



ORGANIC CONDUCTORS

FUNDAMENTALS AND APPLICATIONS

**EDITED BY
JEAN-PIERRE FARGES**

ORGANIC CONDUCTORS

FUNDAMENTALS AND APPLICATIONS

EDITED BY

JEAN-PIERRE FARGES

*Université de Nice – Sophia Antipolis
Nice, France*

Marcel Dekker, Inc.

New York • Basel • Hong Kong

Library of Congress Cataloging-in-Publication Data

Organic conductors : fundamentals and applications / edited by Jean-Pierre Farges.

p. cm. — (Applied physics; 4)

Includes bibliographical references and index.

ISBN 0-8247-9216-5 (alk. paper)

1. Organic semiconductors. 2. Organic superconductors. 3. Organic conductors. I. Farges, Jean-Pierre. II. Series: Applied physics (Marcel Dekker, Inc.) ; 4.

QC611.8.07069 1994

620.1'1797—dc20

94-16958

CIP

The publisher offers discounts on this book when ordered in bulk quantities. For more information, write to Special Sales/Professional Marketing at the address below.

This book is printed on acid-free paper.

Copyright © 1994 by Marcel Dekker, Inc. All Rights Reserved.

Neither this book nor any part may be reproduced or transmitted in any form or by any means, electronic or mechanical, including photocopying, microfilming, and recording, or by any information storage and retrieval system, without permission in writing from the publisher.

Marcel Dekker, Inc.

270 Madison Avenue, New York, New York, 10016

Current printing (last digit):

10 9 8 7 6 5 4 3 2 1

PRINTED IN THE UNITED STATES OF AMERICA

Series Introduction

The Applied Physics series represents a commitment by Marcel Dekker, Inc., to develop a book series that provides up-to-date information in the new and exciting areas of physics emanating from the explosion of discoveries in new materials and new processing techniques. The advances in amorphous materials, layered copper oxide high-temperature superconductors, organic and inorganic cage structures, organic conductors, and a host of new thin-film deposition and nanofabrication processes have led to a host of new applications. It is the intent of the series editor to invite experts in the most important of these areas to assemble book-length manuscripts describing the latest developments. Many volumes will take the form of comprehensive multiauthored compendia that are linked logically by judicious choice of subject matter and editing.

The Applied Physics series is designed to bring the nonspecialist scientist/engineer to the forefront of each area. Researchers wishing to enter a particular area will find these volumes of significant benefit as a detailed introduction to the field. The books in the series are also expected to provide important summaries and to serve as reference guides to the experts in each field.

The scope of the series is broad. We will encourage volumes relating to new or improved sensors, memories, processing units, displays, energy conversion, storage and delivery, and to semiconducting and superconducting devices generating technologies in areas ranging from communications and computers to medical physics.

We sincerely hope that through this series we can help today's discoveries rapidly become tomorrow's technology.

Allen M. Hermann

This Page Intentionally Left Blank

Foreword

This book brings together a crew of acknowledged experts dealing with the main topics within the wide area of charge-transport effects in organic materials. For many years this subject has been essentially of academic relevance only. A brief spell of industrial interest in the early 1960s, as exemplified by the Chicago Inter-Industry Conference on Organic Semiconductors in 1961, evaporated rather quickly because of unrealistically high expectations and an unrealistically short time scale. At that time, neither a firm theoretical framework nor a body of reasonably extensive, reproducible, and meaningful experimental data was in existence.

Today, the position, as evident from the material presented in this book, is vastly improved. In addition, several phenomena not even suspected, say, 30 years ago, such as organic semimetals, organic superconductors, and virtually loss-free surface charge transfer, are all discussed in the present volume. Even now, though, theory lags behind experiment; thus organic and high-temperature superconductivity are good examples of Gauss's dictum, "I have had my results for a long time but I do not yet know how to arrive at them" (quoted in A. Arber, *The Mind and the Eye*, 1954, p. 471).

Many of the experimental advances are due to sophisticated methodology, some of it having come into use only during the last few decades. It is good to see several chapters devoted to such matters, which so often

are treated merely peripherally. Still—“Absolutum Obsoletus” (St. Thomas Aquinas, ca. A.D. 1350): “If it works, it’s obsolete.”

Considerations of charge transport are becoming increasingly relevant to an astonishingly wide area of applied as well as pure science. As a topic, organic conductivity transcends conventional boundaries between physics, chemistry, biology, and engineering. Like all interdisciplinary subjects that refuse to be compartmentalized, its study requires intimate cooperation among practitioners of several branches of science. It is the merit of this book that it not only provides a broad overview of this rapidly developing field but also presents each special, separate topic as a contribution from well-known researchers active in that area, each of whom has made significant advances in the topic under review.

Fundamental as well as applied aspects are well and thoughtfully covered, and I am sure that this cooperative effort will become, and remain, a standard reference for years to come.

*Felix Gutmann
Macquarie University
Sydney, Australia*

Preface

No one could introduce this new book better than my old friend Professor Felix Gutmann, of Sydney, Australia. For more than twenty years, we have been together often: in Nice, in Sydney, in Munich, and in Los Angeles. Felix Gutmann is co-author, with Lawrence Lyons of Brisbane, Australia, of a most remarkable volume, *Organic Semiconductors*, published in 1967 by John Wiley & Sons, Inc., New York. This monumental book has received considerable support in the scientific community, and I have seen this book in many solid-state physics and chemistry laboratories and in libraries throughout the world. I hope that the present volume will enjoy the same level of success.

Organic compounds have long been considered the most natural representatives of the insulating state. This point of view started to change significantly about thirty years ago, after the synthesis in 1960 of a beautiful new organic molecule: tetracyanoquinodimethane (TCNQ). This molecule displayed unique chemical and physical properties and gave rise, progressively, to a very rich class of higher and higher conducting crystalline materials. One can state roughly that the 1960s saw the development of organic semiconductors, the 1970s the development of organic metals, and the 1980s the development of organic superconductors. In the meantime, organic molecules more efficient than the basic TCNQ have been discovered. These closely related materials, all with unusual electrical properties, are termed simply *organic conductors*.

The aim of the present book is to offer a comprehensive, up-to-date survey of the numerous facets of the subject. As it falls in the Applied Physics series, the book focuses especially on basic chemical and physical concepts. We have, as much as possible, stressed clarity over completeness, even avoiding some obscuring aspects that, although important, might be too specialized and discourage the reader. In that case, of course, the references help the reader who needs more detailed information to find it easily. On the other hand, all the experimental aspects, original techniques, and specific methods of synthesis, measurement, control, and analysis have been developed thoroughly.

Conducting organic compounds and polymers form, like recent high- T_c superconducting oxides, a promising new generation of functional materials for future technology. Various applications, including thin-film applications, are currently under active development in many research laboratories. Recent advances in novel molecular-scale engineering are widely reviewed throughout the present volume. They include switching and memory systems, Schottky and electroluminescent diodes, field-effect transistors, photovoltaic devices and solar cells, xerography, rechargeable batteries, nonlinear optical devices, thermistors and negative-resistance devices, conducting composites, ferromagnets, and others.

Each chapter is written by a recognized expert or experts, and the chapters are classified to form a coherent whole. Although sometimes unavoidable, the overlap of material between chapters has been minimized. In fact, the authors have supplied a high level of logical continuity between chapters.

The book is intended primarily for researchers, engineers, and managers, and also for teachers, students, and other people who may have only little or no experience in the field, but a broad scientific background, who need to acquire a rapid general knowledge of the subject. Scientists already engaged in the field should find much of interest in the book, by utilizing it somewhat like a handbook for study of or reference to particular aspects, whether or not related to either theory or experiment. In addition, readers may take advantage of a rich compilation of practical information and detailed references covering the entire field of organic conductors.

I wish to thank most warmly the many contributors to this book for their collaboration and the publisher for their confidence in proposing this work and for continuous encouragement.

Jean-Pierre Farges

Contents

Series Introduction *iii*

Foreword Felix Gutmann *v*

Preface *vii*

Contributors *xi*

1. Organic Conductors: An Overview 1
 William A. Little
2. Basic Physical Concepts of Organic Conductors 25
 Laurent G. Caron
3. Molecular Design of Organic Conductors 75
 Vladimir Khodorkovsky and James Y. Becker
4. Chemical Synthesis and Crystal Growth Techniques 115
 Lawrence K. Montgomery
5. Organic Conductors: The Crystallographic Approach 147
 Alain Filhol
6. Optical Properties 229
 Andrzej Graja

7. Magnetic, ESR, and NMR Properties 269
Luís Alcácer
8. Organic Semiconductors 311
André Brau and Jean-Pierre Farges
9. Organic Metals 359
J. R. Cooper and B. Korin-Hamzić
10. Organic Superconductors: From (TMTSF)₂PF₆ to Fullerenes 405
Denis Jérôme
11. Introduction to Conjugated and Conducting Polymers 495
Michel Schott and Maxime Nechtschein
12. Undoped (Semiconducting) Conjugated Polymers 539
Michel Schott
13. Doped Conjugated Polymers: Conducting Polymers 647
Maxime Nechtschein
14. Related Topics I: Charge-Transfer Complexes in Biological Systems 691
Vivian C. Flores, Hendrik Keyzer, Cissy Varkey-Johnson, and Karen Leslie Young
15. Related Topics II: Thallium-Based High- T_c Superconducting Oxides 735
M. Paranthaman and Allen M. Hermann
16. Applications of Organic Conductors: Molecular Electronics 759
Mutsuyoshi Matsumoto, Hiroaki Tachibana, and Takayoshi Nakamura
17. Organic Photoconductors and Photovoltaics 791
Piergiulio Di Marco and Gabriele Giro
- Index* 825

Contributors

Luís Alcácer Department of Chemistry, Instituto Superior Técnico, Lisbon, Portugal

James Y. Becker Department of Chemistry, Ben-Gurion University of the Negev, Beer-Sheva, Israel

André Brau Laboratoire de Physique de la Matière Condensée, Université de Nice–Sophia Antipolis, Nice, France

Laurent G. Caron Centre de Recherche en Physique du Solide, Université de Sherbrooke, Sherbrooke, Québec, Canada

J. R. Cooper* Interdisciplinary Research Centre in Superconductivity, University of Cambridge, Cambridge, England

Piergiulio Di Marco Istituto di Fotochimica e Radiazioni d'Alta Energia del CNR, Bologna, Italy

Jean-Pierre Farges Laboratoire de Physique de la Matière Condensée, Université de Nice–Sophia Antipolis, Nice, France

*On leave of absence from the Institute of Physics of the University, Zagreb, Croatia

Alain Filhol Division Science/Calcul Scientifique, Institut Laue Langevin, Grenoble, France

Vivian C. Flores Department of Chemistry and Biochemistry, California State University, Los Angeles, Los Angeles, California

Gabriele Giro Istituto di Fotochimica e Radiazioni d'Alta Energia del CNR, Bologna, Italy

Andrzej Graja Institute of Molecular Physics, Polish Academy of Sciences, Poznań, Poland

Allen M. Hermann Department of Physics, University of Colorado at Boulder, Boulder, Colorado

Denis Jérôme Laboratoire de Physique des Solides, Université Paris–Sud, Orsay, France

Hendrik Keyzer Department of Chemistry and Biochemistry, California State University, Los Angeles, Los Angeles, California

Vladimir Khodorkovsky Department of Chemistry, Ben-Gurion University of the Negev, Beer-Sheva, Israel

B. Korin-Hamzić Institute of Physics of the University, Zagreb, Croatia

William A. Little Department of Physics, Stanford University, Stanford, California

Mutsuyoshi Matsumoto Department of Molecular Engineering, National Institute of Materials and Chemical Research, Tsukuba, Ibaraki, Japan

Lawrence K. Montgomery Department of Chemistry, Indiana University, Bloomington, Indiana

Takayoshi Nakamura Department of Molecular Engineering, National Institute of Materials and Chemical Research, Tsukuba, Ibaraki, Japan

Maxime Nechtschein Département de Recherche Fundamentale sur la Matière Condensée, Centre d'Etudes Nucléaires de Grenoble, Grenoble, France

M. Paranthaman Chemical and Analytical Sciences Division, Oak Ridge National Laboratory, Oak Ridge, Tennessee

Michel Schott Groupe de Physique des Solides, Université Paris VII (Denis Diderot), Paris, France

Hiroaki Tachibana Department of Molecular Engineering, National Institute of Materials and Chemical Research, Tsukuba, Ibaraki, Japan

Cissy Varkey-Johnson Department of Chemistry and Biochemistry, California State University, Los Angeles, Los Angeles, California

Karen Leslie Young Department of Chemistry and Biochemistry, California State University, Los Angeles, Los Angeles, California

This Page Intentionally Left Blank

1

Organic Conductors: An Overview

William A. Little

Stanford University, Stanford, California

I. INTRODUCTION

The study of organic conductors has become a major part of modern condensed-matter physics and in many institutes it now involves collaborative, multidisciplinary research in chemical synthesis, polymer preparation, materials science, physics, and applied physics. In distinguishing this field from that of conventional conductors, it is appropriate to ask what it is about the organic state that is different from that of the inorganic, and what it is that one can learn from the study of these materials that one has not, or cannot, learn from the study of conventional metals. To answer these questions we need to define what we mean by *organic*. Organic compounds are traditionally considered to be those containing the element carbon, often in association with nitrogen, oxygen, and hydrogen. Originally, *organic* referred to compounds derived solely from plants and animals, but with the growth of synthetic organic chemistry a vast number of new compounds now are synthesized in the laboratory that have never been associated with living organisms. The vast majority of organic conductors fall in this category. However, many of the features that make the organic conductors especially interesting and different from those of the inorganic conductors lie in the unique chemistry of carbon that give such organic compounds the rich variety of properties and structures used by

living organisms. An enormous amount has been learned from the study of such natural products, and these serve as an inspiration to many and examples, par excellence, of the range of compounds that can be made that are based on a carbon skeleton.

It is the 4 valence of carbon that allows it to bond with so many other elements and to form structures of great complexity—large conjugated structures as in the polyacetylenes; the flexible polymeric chains of nylon and rubber; rigid molecular skeletal structures of the steroids; and huge, complex, but precisely defined structures of tens of thousands of atoms, as in enzymes and other biologically active compounds. In addition, the relatively large molecular substituents of which these larger structures are built and the presence in them of elements other than carbon (heteroatoms) give different molecular substituents different electron affinities and different ionizing potentials, thus readily permitting the transfer of charge from one to another and the ability of the *molecules* to mimic the behavior of many different types of *atoms*. This is one reason why organic conductors can offer a richer palette of properties than can the simple metals and why so much more can be learned from them. It is this rich range of structural and electronic properties, all of which, in principle, can be controlled by the synthetic chemist, that has attracted the interest of chemist and physicist alike, and that promises to yield ever more interesting materials in the future.

Hideo Akamatu [1], one of the pioneers of organic semiconductors, put the argument in a concise and instructive form. He made the point that “organic” as applied to “conductive” compounds means more than that the compounds are based simply on carbon. It also means that the molecules of such compounds can be organized into a unified, *organic* whole, similar to what occurs in living systems, where the tertiary structures of the compounds play so large a role in controlling their overall physical and chemical behavior. This is even more to the point in the case of organic superconductors than with organic semiconductors, because the transport behavior of superconductors is not a local property but depends in a critical manner on the properties of the atomic or molecular substituents over a rather large extended region.

In this chapter we give a broad overview of the field of organic conductors, discussing in a general way the key issues that distinguish these from the more conventional conductive compounds. In later chapters, each topic is treated in greater detail by experts in these areas. Our effort will be to paint a broader picture and to attempt to show how the study of these systems fits with the rest of condensed-matter physics.

II. EARLY HISTORY

Most organic solids at room temperature are insulators, but what must have intrigued some early chemists was the fact that a few such compounds have a metal-like appearance, a “metallic luster,” a “glistening silvery sheen,” or “coppery luster,” to quote some early descriptions of such complex, organic compounds. This gave a hint that such materials or derivatives of them might exhibit true metallic behavior. So began the study of what has become the field of organic conductors. One should be aware, however, that such appearances can be quite misleading and may say little about the conductive properties of the materials. Moreover, the term *metallic* used to describe the appearance of some of these materials can mean different things to different people. Chemists and physicist often disagree. We begin by describing some of the early history of the study of such materials.

A. Metallic Ions

The similarity between the chemistry of substituted ammonium ions and that of the alkali metals was noted early in the century. McCoy and Moore [2] in 1911, and Kraus [3] a little later, studied a number of amalgams of such organic moieties and discussed their physical properties: crystallinity, metallic luster, and possible electrical conductivity, without making any systematic measurements of these properties. Reading these early papers makes one realize the range of meanings of the term *metallic state* and what it conveys to persons of different disciplines—from chemical behavior similar to that of the elemental metals, to mechanical properties, to optical properties, to what we are focusing on here, the electrical properties. This early work did recognize the important fact that molecular groups, or clusters of atoms, could behave both chemically and physically like a different class of “atoms” with new and different properties from those of their constituents, the ammonium group being a prime example. This work on the substitute ammonium ions inspired later work and can be linked directly to present-day studies in this field.

B. Organic Semiconductors

Interest in organic semiconductors was stimulated by a suggestion in 1941 by Szent-Györgi [4], and stressed again in a paper [5] in 1946, that some processes in biological systems might be accounted for by the transfer of π -electrons over large distances along molecular stepping stones. In 1948, Eley [6] found that the conductivity of a number of organic compounds varied exponentially with the reciprocal of the absolute temperature. Shortly

after this, in 1950, Akamatu and Inokuchi [7] in Japan studied the conductivity of polycrystal samples of violanthrone and pyranthrone, which are large polycyclic fused-ring systems with a quinoid structures. They, too, found an activated conductivity that followed the same temperature dependence as that of inorganic semiconductors, $\sigma = \sigma_0 \exp(-\Delta/2kT)$, suggesting that these were intrinsic semiconductors with a semiconductor gap Δ between a valence and a conduction band. The magnitude of this gap was found to be between 0.75 and 1 eV, but the resistivity at room temperature was high, being greater than $10^9 \Omega\text{-cm}$ for this class of compounds.

A much more conductive compound was discovered a few years later by Akamatu et al. [8]. This was a perylene–bromine complex that was found to have a conductivity on the order of $1 (\Omega\text{-cm})^{-1}$, which is comparable to that of some of the doped inorganic semiconductors. This is one example from a large class of compounds that have since been prepared in which an organic moiety is complexed to a halogen or, as we will see from later work, another more complicated multiatom anion. These were among the first of the highly conductive organics to be studied. At much the same time that this work was done, it also became known that in the condensed aromatic hydrocarbons such as anthracene and naphthalene, excitons (bound particle–hole pairs) could move over considerable distances in crystalline samples, and this suggested a high mobility for the charge carriers in the upper bands. Then, in the early 1960s, enhanced conductivity was discovered in polymers doped with iodine [9]. The field of organic semiconductors blossomed during this period with the publication of a number of books and review articles [10–12].

The enhanced conductivity of the perylene–bromine complex results from a transfer of charge from one molecular substituent to another, with the formation of a donor–acceptor complex. The resultant particle and hole are then only weakly bound to one another, so that in many cases the two can be separated thermally, creating a thermally activated conductivity with a relatively small gap. Studies of these and of poorly conducting inorganic compounds began to reveal the importance of this binding energy in determining the overall electrical behavior of the compound. As we describe shortly, and as is described in greater detail elsewhere in this volume, there are many factors that determine the strength of this binding. Most of these are not discussed in undergraduate texts dealing with condensed matter and are touched upon only lightly in introductory graduate texts. Conductivity of metals is usually discussed from a band picture alone, which is that of electrons moving in the periodic field of the ions, disregarding the finer details of the electron–electron correlations. The band picture is, of course, an important and essential ingredient to the understanding of the metallic state, but what is seldom discussed in detail and

which needs to be appreciated in the study of the organics are the factors that make the band theory applicable. A useful and brief introduction to this can be found in Ashcroft and Mermin's book, *Solid State Physics* [13].

The reason these factors are so much more important in the organics than in the conventional metals is that most of the organic conductors consist of molecular moities bound to one another by van der Waals forces or, in the charge-transfer compounds, by a weak contribution from the Coulomb field. These weak or broadly acting forces lead to a small overlap of the atomic orbitals of neighboring molecular substituents, whereas in conventional metals the overlap is usually large, and strong covalent binding occurs between adjacent atoms. The weak overlap means that the time for a charge to transfer from one molecule to another is comparatively long, and consequently, the kinetic energy for such motion is small compared to the Coulomb repulsion between the charges. As a result, an electron does not respond just to the field determined by the average distribution of the other electrons but rather, to that given by their instantaneous configuration. The other electrons simply cannot respond fast enough to redistribute themselves to give a field based upon an average distribution. Although this description is a simplified classical one, it is the essence of the physics of the Hubbard model [14], which provides a description of the effects of correlations. These correlations are essential to an understanding of the conductivity of the organics.

C. Organic Metals

A major breakthrough in the field of organic conductors came with the discovery of salts of the radical anion formed by the addition of an electron to tetracyanoquinodimethane (TCNQ) by Kepler et al. [15] in 1960. The quinolinium–[TCNQ·]–[TCNQ]⁰ salt had an activation energy for conduction of less than 0.01 eV, and a room temperature conductivity of 100 (Ω-cm)^{−1} along the direction of highest conductivity in the crystal. The electrons appeared to form a conventional degenerate system with a temperature-independent paramagnetism similar to that of conventional metals. In the following years a large class of these materials were prepared and studied [16]. Although none of these remained metallic down to liquid nitrogen temperatures, near room temperature some single-crystal specimens appeared to have an immeasurably small activation energy and thus to be true metals. This opened up a vast area of study and salts based on these materials, and related analogs became the most active area of research in conductive organics.

A second breakthrough followed with the synthesis of tetrathiofulvalene (TTF) by Wudl and co-workers [17] in 1970 and the discovery by Coleman et al. [18] in 1973 of *metallic* conductivity in TTF–TCNQ down to about

59 K, where the conductivity reached a maximum $\approx 8000 (\Omega\text{-cm})^{-1}$ but below which it fell rapidly to a small value. Excellent discussions of this area of study can be found in a number of conference proceedings [19,20]. Other donors and other acceptors were synthesized during the 1970s and their complexes prepared and studied. This set the stage for the discovery in the early 1980s, of the first organic superconductors.

D. Organic Superconductors

Some of the factors that are now recognized as important to an understanding of the conductivity and superconductivity of the organics can be found in two papers by Ogg [21,22] published in 1946, well before most others had given the subject any serious consideration. Ogg studied the conductivity of solutions of alkali metals in liquid ammonia. He suggested that the solvated electron from the metal would be self-trapped in a cavity created in the solvent medium due to the large dielectric constant of the ammonia, which would thus provide a stabilizing polarization energy. This, he argued, could lead to pairs of electrons becoming bound in a singlet state in such cavities, and that these would undergo Bose–Einstein condensation at temperatures as high as 180 to 190 K, yielding superconductivity at these temperatures. It is worthy of note that these papers predated by 10 years Cooper’s paper [23], in which he showed that the Fermi sea was unstable to the formation of such pairs if the electron–electron interaction was attractive. These “Cooper pairs” became central to the successful Bardeen–Cooper–Schrieffer (BCS) theory of superconductivity [24]. It is now generally believed that the experimental work upon which Ogg based this theoretical model was flawed, and the superconducting-like behavior claimed by Ogg for the solutions has not been reproduced; nevertheless, the papers constitute a remarkable contribution, ahead of their time. He estimated the magnitude of the polarization energy and stressed its role in stabilizing the structure. He noted the fact that Bose–Einstein condensation of pairs of electrons would lead to superconductivity, and that superconductivity might not be confined to the conventional metals.

To thoughtful persons both in and out of the biological sciences, the existence and evolution of living organisms and their development have posed and continue to pose enormously challenging intellectual problems. Fritz London, who had contributed much to the phenomenological theory of superfluidity and superconductivity, was also fascinated by these problems. From his earlier work on superfluid helium and superconductivity he knew of the unifying effect that the existence of a Bose–Einstein condensate had upon a superfluid system. Today we would describe this as the effect on the system of the existence of an order parameter—in par-

ticular, one with off-diagonal long-range order. It appears that he felt that something analogous to this might also exist in living organisms. In the introduction to his book *Superfluids* [25] published in 1950, there is a brief statement in which London suggests that application of the concept of superfluidlike states to macromolecules might explain the ability of large molecules to act as single units, a theme similar to that voiced by Szent-Györgi a few years earlier. He did not expand on this suggestion or clarify what he meant by it in later publications.

In the early 1960s I, too, became interested in some of the problems of biology and was struck by the fact that a certain type of DNA was biologically active only if it existed in the form of a closed ring. Struck by the similarity between this and the ability of a closed superconducting ring to maintain a persistent current, and knowing of London's remarks, I asked if a molecule with the general structure of DNA, consisting of a sugar-phosphate helical backbone with a regular array of bases bonded to it, might be able to exist in a superconducting state. The microscopic BCS theory was now well established and it became an interesting exercise to see whether it could be applied to this problem. The system was modeled by the now-well-known postulated structure of a polyene "spine" with attached polarizable side-chain molecules [26,27]. Using the simplest formalism of the BCS model, I found that an attractive interaction between the electrons in the spine could be obtained through the virtual electronic polarization of the side chains. Surprisingly, the calculated transition temperature, T_c , came out to be well above room temperature. I soon recognized the formal reason for this, which was that the high transition temperature resulted from replacement of the phonon frequency ω by a much higher electronic excitation energy of the electrons in the side chains in the BCS expression for the transition temperature:

$$kT_c = 1.13 \hbar\omega \exp\left[\frac{-1}{N(0)V}\right] \quad (1)$$

This showed for the first time that superconductivity at relatively *high temperatures* might be possible if a system could be devised in which the electronic states of the system played the role that the phonon states normally play in providing an attractive interaction between electrons in the conduction band. It suggested that superconductivity might occur in a suitably synthesized *organic* system. It suggested that superconductivity could occur in a *polymeric* system and raised the question whether a phase transition from the normal to a quantum phase could occur in *one dimension*, knowing full well that phase transitions between classical phases (e.g., liquid-gas or ferromagnetic transition of the Ising lattice were forbidden under these circumstances.

Although the concept of organic semiconductors and organic superconductors was originally inspired by phenomena in biology, we believe today that that is as far as it goes. Charge transfer in biological molecules such as cytochrome c_3 may well occur [28] by processes similar to those of conventional semiconductors, but there are no biological molecules or macromolecules known where superconductivity could be expected to exist at any temperature, nor in the light of our present understanding does it seem likely that such conditions could prevail in such structures. Furthermore, while the ideas of the possible role of long-range order in a biological system were appealing, the same ends appear to be met by all the wondrous workings of molecular biology. The value of the suggestion of the possibility of synthesizing an organic superconductor lay not in this area, but rather, in stimulating both theoretical and experimental work on systems of limited dimensionality, which prior to this had never been considered or discussed; in considering an alternative mechanism of superconductivity; and in stimulating interest in the synthesis of organic conductors and the search for organic superconductors. The suggestions raised many questions relating to the basic assumptions of the metallic state and the existence of superconductivity in systems of limited dimensionality. A detailed discussion of these problems and the prospects of attaining high-temperature superconductivity in these systems can be found in a review article by Gutfreund and Little [29] published in 1979.

From today's perspective, there are perhaps three major milestones in the search for superconductivity in the organics and the search for high-temperature superconductivity based on these ideas that are worthy of special comment. The first was the discovery of superconductivity in the polymer $(\text{SN})_x$ by Greene et al. [30] in our laboratory in 1975. This was a remarkable discovery even though the superconductivity occurred only at temperatures well below 1 K. The compound $(\text{SN})_x$ is not an organic, of course, as it has no carbon in it; nor is the superconductivity believed to be of a nonphonon variety; and the band structure is not even truly one-dimensional. Nevertheless, the occurrence of superconductivity in such a polymer provided a tremendous boost to the field and provided positive proof that superconductivity could occur in systems of limited dimensionality.

Shortly after this polyacetylene [31] doped with iodine was found to exhibit an enormously enhanced conductivity, reaching a value of $30 (\Omega\text{-cm})^{-1}$ for the composition $(\text{CHI}_{0.22})_x$, and although this was not found to superconduct at any temperature, its study introduced a number of new insights [32] into the conduction process, including the existence of solitons, topological defects, and the separation of charge and spin degrees of freedom. Many of these have since reappeared in models of the superconduc-

tivity of the recently discovered high-transition-temperature superconducting cuprates.

The second milestone was the discovery of the first organic superconductor, $(\text{TMTSF})_2\text{PF}_6$, by Jerome et al. [33] in 1980 with a transition temperature of 0.9 K at a pressure of 12 kbar. This opened the door to the discovery of other charge-transfer superconductors that were found to superconduct at ambient pressure and with higher transition temperatures. Today more than 30 such superconductors have been synthesized and characterized, and the highest transition temperature among this class is now in excess of 12 K.

The third was the more recent discovery of superconductivity in the salts of the fullerenes, C_{60} , with transition temperatures [34,35] ranging from 18 K for K_3C_{60} to 45 K for $\text{Rb}_x\text{Tl}_y\text{C}_{60}$. Were it not for the fact that high-temperature superconductivity had been discovered in the cuprates [36] in 1986, the discovery of superconductivity in the fullerides at these temperatures undoubtedly would have set off a frenzy of activity among workers in condensed matter similar to that which occurred after the discovery of the cuprates.

Of course, the discovery of the cuprates also has had a significant impact on work in the organics, with the realization, first, that high-temperature superconductivity was indeed possible, and second, that in the search for better superconductors, the previous narrow, limited focus on alloys of the conventional metals to the exclusion of all other classes of materials had been misdirected and had, indeed, missed the boat. A broader, less parochial view has now emerged among workers in the field who have interests in exploring the organics, organometallics, oxides, and other more exotic materials. This is a healthy, promising development that can be expected to lead to the discovery of new and interesting materials, some of which may well be novel superconductors and some, perhaps, which may have still higher transition temperatures.

III. KEY ISSUES

Future developments in this field will surely be dominated by issues relating to the limited dimensionality of the compounds so often found in the organics. As alluded to earlier, such concepts as limited dimensionality and quasi-one-dimensionality were not part of the everyday vocabulary of condensed-matter physics, nor were they part of the world of superconductivity until work focused on problems of organic superconductors. It was this that brought these concepts to the fore, notably through work in the late 1960s of Ferrell [37], Rice [38], and Hohenberg [39] on fluctuations and the innovative microscopic treatment of competition between super-

conductivity and other instabilities by Bychkov et al. [40]. The importance of taking into account effects of limited dimensionality was brought into clear perspective by the controversy following the announcement of the discovery of a huge conductivity anomaly in the TTF–TCNQ salt by Heeger et al. [41] in 1973 and in subsequent studies of $(\text{SN})_x$ and $(\text{CH})_x$. Since then the role of limited dimensionality has become inextricably entwined in the fabric of the field.

There are many problems in mathematical physics that can be formulated in one spatial dimension rather than in three, and much can be learned from these models. Such treatments are considered to be truly one-dimensional. However, the sense in which the terms, *limited dimensionality* and *quasi-one-dimensional* are used in regard to the organics differs somewhat from this. The difference has now become part and parcel of their meaning in this context, but one should be aware that it was not always so. The different sense in which it is being used today should be recognized. For example, in the treatment of the behavior of linear chain compounds one can idealize the structure as a chain of atoms linked to one another and isolated from the rest of the universe by vacuum. In a sense this is a one-dimensional problem even though the individual atoms and the bonds between the atoms are all treated in three dimensions and the Coulomb field is treated in its real-world, three-dimensional form. Furthermore, because the angle between the incoming and outgoing bonds is usually not 180° , the chain is not even linear. Nevertheless, we consider this a quasi-one-dimensional problem. It is clearly not one-dimensional at the atomic level, but it differs from the actual three-dimensional problem by the neglect of interactions between adjacent chains, and it is this neglect that makes the problem “quasi”-one-dimensional. These subtle differences in terminology between the strictly one-dimensional models and these models have caused confusion between the more mathematical theorists and experimental chemists and physicists. It is as well to be sensitive to these differences in perspective in reading the literature, particularly the early literature on theoretical models.

Systems that are quasi-one-dimensional thus are those in which the interactions within the chain are considered to be much stronger than those between adjacent chains, and quasi-two-dimensional systems are similarly considered to be those in which interactions between atoms within a plane or layer are much larger than those between layers. The approximations, and the sense of the terms used, can be complicated further by taking into account in one case and not in another the Coulomb field that couples together adjacent chains or planes, which is long ranged, but neglecting the tunneling of particles from one to the other because this depends on the overlap of atomic wavefunctions, which is short ranged.

Systems that are of limited dimensionality in the sense just defined are found to be more sensitive to certain instabilities than are systems with comparable coupling in all three dimensions. The presence of these instabilities profoundly affects the physical and thermodynamic properties of these systems. Moreover, they are temperature dependent, and their latent presence at temperatures above those at which the systems become unstable also have an effect on the system's physical properties.

IV. INSTABILITIES

A. Peierls Instability

It has long been believed that metallic conduction cannot occur in a one-dimensional system. This is based on what is now considered a classic instability of such a system, the Peierls instability. Peierls [42] considered a linear chain of atoms regularly spaced in one dimension and the energy levels of electrons moving in the periodic field of the atoms. He showed that if each alternate atom was moved slightly closer to one of its neighbors, all in the same direction, this distorted chain would have a reduced translational symmetry and the additional periodicity would introduce a new gap in the density of states at a point in k space corresponding to this periodicity. States near the gap with momenta less than this would be depressed in energy, and those with greater momenta would be raised in energy. If the band were only partially filled with electrons, so that the states with momenta less than this were all occupied and those with momenta greater unoccupied, the distorted structure would have a lower total electronic energy than the undistorted structure. The system thus would have the tendency to dimerize and a gap would appear at the Fermi energy, and thus the system would become an insulator.

For this distortion to occur, the reduction in energy of the electrons in the distorted lattice must be greater than the energy increase of the system from the elastic energy involving the structural bonds between the atoms of the chain. Further analysis shows that the electronic energy contains a term essentially linear in the displacement coordinates, whereas the elastic energy is quadratic, so the linear term wins at a small enough displacement. However, this may not be true at higher temperatures because electrons can be excited across the gap to states that are raised in energy by the effects of the distortion. It then becomes energetically less advantageous to support this distortion and the displacement decreases, reducing the gap and making it easier for other electrons to be excited across the gap, depressing the gap still more. Eventually, the distortion is driven to zero

and above a certain temperature the Peierls distortion does not occur and the system reverts to the metallic state.

As one approaches the Peierls temperature from above, the restoring force for a distortion which has the symmetry that would create a gap at the Fermi surface gets smaller and smaller, until at the Peierls temperature it goes to zero and the lattice distorts spontaneously to the new structure. Thus phonons with the symmetry of this distortion become soft as one approaches this temperature and the amplitude of thermal excitation of the mode grows enormous. These effects show up in x-ray studies of such compounds and allow the identification of the instability.

The analogous lattice instabilities can occur in two and three dimensions, too, but the effects are more accentuated in one. In two dimensions it occurs when the Fermi surface approaches the shape of a square cylinder, leading to a “nested Fermi surface.” In three dimensions, it results in a distortion that lowers the symmetry of the lattice and in which the Fermi surface, treated in a first approximation as a sphere, is found just to touch the Brillouin zone boundary of the distorted structure. Because the states just adjacent to a zone boundary on the low-energy side are depressed in energy, the occupied levels that lie within the Brillouin zone of this distorted structure are lowered in energy relative to those of the undistorted structure. As a result the distorted structure is stabilized in energy over a range of alloy compositions for which the number of electrons/atom lie close to that which gives a Fermi surface touching the zone boundary. This relationship between composition and structure of metallic alloys is known as one of the Hume–Rothery rules [43,44].

Peierls was careful to point out that his conclusion was not complete because it assumed the validity of the adiabatic approximation. This approximation cannot be strictly valid in the case of a metal because of the close spacing of energy levels, and thus the motion of the nuclei must be taken into account in a more rigorous treatment of the problem. Peierls result is based on a simple one-electron treatment of the problem in which electron–electron interactions are neglected. Such electron–electron interactions mix states above and below the gap in a manner somewhat analogous to that of raising the temperature and so also affect the tendency to distort. Consequently, a more sophisticated analysis is needed before one can draw any definite conclusions on the stability of a particular system against the Peierls distortion.

In a system that has undergone a Peierls distortion, the partially dimerized lattice of atoms will have a different density of electrons in the region between the close partners than between more distant neighbors. As a result, an additional modulation will occur in the density of the electrons of the distorted chain compared to that of the undistorted chain.

One can describe this as the presence of a charge-density wave in the electronic system. In this case the charge-density wave follows from displacement of the atoms. One can ask the question whether in a rigid lattice the electron system itself can distort spontaneously to lower its symmetry, producing an effect that would then attempt to force the nuclei to follow suit. The driving force in this case would not be the movement of the atoms as in the Peierls instability but rather the inherent instability of the electron system itself. The answer to this question is “yes.” The study of these types of instabilities and associated instabilities in the spin system of the electrons has become an important part of the physics of limited dimensionality.

B. Electronic Instabilities

The origin of the energy gap in long conjugated molecules has long been of interest to theoretical chemists. Early work [45] attributed this to the Peierls instability but it later was realized that correlations in the electron gas itself could give rise to a similar instability along the lines mentioned above. In an important paper in 1960 Overhauser [46] showed the existence of low-energy solutions to the electron gas problem within the Hartree–Fock approximation that had a lower symmetry than that of the original Hamiltonian. These were spin waves, which are now believed to account for the antiferromagnetism of the metal, chromium. Cizek and Paldus [47] in 1967 showed similarly that the symmetric Hartree–Fock state could be unstable to the formation of a charge-density wave, resulting in an alternation of bond order in a polyene. The instabilities that lead to these two types of states are known as triplet and singlet instabilities, respectively. The resultant states now go under the names *spin-density wave* (SDW) and *charge-density wave* (CDW) *states*. Their occurrence has been found to be much more common among the organics and inorganic layered structures than in the more conventional metals, due to the restricted dimensionality of these more unusual systems. The strength of the interactions, their energy dependence, the presence of interchain coupling, and many other factors determine the relative strength of the driving forces leading to these different instabilities. Competition among the different instabilities is common, and often a delicate balance between two or more phases can exist which is sensitive to small changes in the compounds.

C. Metal–Insulator Transition

An essential feature of a metal is that a current induced in it by an applied voltage should be proportional to the voltage, *however small that voltage might be*; in other words, it should obey Ohm’s law at *all* voltages. This imposes an demanding criterion on the properties of a conductor in order

for it to be a true metal. For example, in the charge-transfer salts, where an electron is transferred from a donor molecule to an acceptor, and these two molecules are surrounded by similar molecules, the electron and the hole are still bound to each other. Their mutual potential will be given by the usual expression for the potential in vacuum modified by a dielectric constant ϵ of the medium resulting from the polarization of the molecules in the neighborhood. Clearly, this dielectric constant will not be strictly isotropic or position independent but will contain local corrections to accommodate the details of the local environment. However, all of these factors can be taken into account in ϵ . The general form of the potential will be

$$V(\mathbf{r}) = -\frac{e^2}{4\pi\epsilon\mathbf{r}} \quad (2)$$

Given reasonable conditions on the form of ϵ , one finds that in three dimensions this always leads to the existence of bound states between the electron and the hole. As a result, the application of a weak field cannot break these two apart and the only means for conductivity is by thermal dissociation of the pair, resulting in thermally activated semiconductive behavior, not metallic conductivity.

Mott [48] has given a model that explains in a simple manner how true metallic conductivity can occur. He considered one electron in a metal surrounded by a large number of other electrons. The Coulomb field keeps these electrons away from one another so that in the immediate vicinity of each, the electron density will be reduced. Within this region of reduced electronic density the background charge of the positive ions will remain, so the net charge within this region will be the sum of the two. The resultant effective electron–electron potential from the sum of the actual field and that of the background positive charge brought into play by the locally depressed electron density is then in the simplest model, one of a screened [13, pp. 340–342], or Yukawa, form:

$$V(\mathbf{r}) = -\frac{e^2}{4\pi\epsilon\mathbf{r}} \exp(-\kappa r) \quad (3)$$

Now, depending on the density of carriers present, which determines the screening factor κ in the exponential, one may or may not have bound states upon solving the Schrödinger equation for the particle–hole system. If the density is high enough, the screening will be strong and no bound states will occur. The particle and hole will then be free to move independently of one another, and true metallic conductivity will result.

This argument explains the behavior of two classes of phenomena. If a system has too low a density of carriers, it cannot exhibit metallic con-

ductivity. A sharp transition to a highly conducting state can be expected, though, if the number of free carriers is increased. This increase can occur either through doping or through thermal excitation of the carriers. This then leads to a transition from a nearly insulating to a metallic state known as a Mott, or metal-to-insulator, transition.

In systems of limited dimensionality, screening is more inhibited than in isotropic three-dimensional systems because the charge carriers are confined to move along a stack of molecules or along the polymer direction for quasi-one-dimensional systems, or in a plane for the quasi-two-dimensional systems. The simple isotropic model of Mott then needs to be generalized to accommodate the resultant change of screening. This screening is inevitably less than for a comparable three-dimensional system, and thus metallic conductivity is more difficult to obtain in systems of limited-dimensionality.

Much thought has gone into the problem of designing organic metals taking into account many chemical and physical considerations. Among the physical factors that have been considered are the tendency toward dimerization or the Peierls instability, the tendency toward a charge-density or spin-density wave instability, means for inhibiting these instabilities, the role of disorder, and the role of doping. Among the chemical considerations are the design and synthesis of novel donors and acceptors, minimization of inherent disorder, polarizability of the anions and cations, planarity of the structures, and many more. Excellent reviews by Cowan [49], Bloch [50], Miller [51], and others cited by these authors can be found in the literature.

Thus far we have confined ourselves to considering essentially perfect crystals. This is not what one finds in the real world. Real materials have various degrees of disorder, contain impurities, dislocations, grain boundaries, and may not be in true thermodynamic equilibrium. It is essential, therefore, to take into account the role of disorder, impurities, nonstoichiometry, and other factors that cause such real materials to deviate from that of the unattainable, theoretically ideal, compounds. Once again one finds that the limited dimensionality of most organic materials make them more susceptible to the effects of such disorder, resulting in a tendency for the carriers to be localized and for the conductivity to be dominated by variable range hopping between the localized states.

D. Effects of Disorder

As can be expected on simple physical grounds, impurities and disorder play an accentuated role in systems of reduced dimensionality upon the conductivity of the system. The effect is most dramatic in one dimension,

as shown by Mott and Twose [52]. These authors showed that for a strictly one-dimensional system with an arbitrarily weak random potential, all the eigenstates are localized and conduction is possible only by thermally activated hopping. The effect can be demonstrated by application of the transfer matrix method [53] to an evaluation of the amplitudes of the wavefunctions as one steps along the chain.

It was generally believed that this proof of localization was rigorous. But in a beautiful piece of work, Phillips [54] has found a counterexample, at least in a practical sense. He has shown that for a polymer chain containing dimers inserted at random in a chain of other monomers, a group of states can exist that are not localized. The reason for this is that for the range of energies where localization does not occur, the matrix representing the dimer can be shown to approximate closely the unit matrix. Thus the random insertion of a unit matrix in the chain leaves the states unchanged and the dimers become effectively transparent. What is important is that this condition is satisfied over a sufficiently large range of energies for the effect to have a physically significant impact on the conductivity of the system. In a sense this is a pathological case, though, and more often the effects of disorder are damaging to the conduction processes. However, this is not always the case, as we explain below.

Disorder can in some cases help a system to remain conductive. As an example, disorder in a linear chain partially frustrates the tendency of the chain to undergo a Peierls distortion by destroying the translational symmetry. This depresses the Peierls temperature. Such an effect was expected theoretically and has been shown experimentally, for example, by Pouget et al. [55], with orientationally disordered NMP–TCNQ and other salts [56]. Impurities affect other types of ordered states, too, including the spin-density wave state and superconductivity. A detailed treatment of the effect of both magnetic and nonmagnetic impurities on all the different types of instabilities has been given for one-dimensional metals [57], including the effect these have on the superconducting phases.

E. Effects of Pressure

Just as impurities can play a part in suppressing the Peierls or other instabilities, so, too, can pressure. The importance of this was recognized by Jérôme and Weger [58] early in the 1970s and a program was initiated at that time for the systemic study of the effects of pressure on the organics. This led ultimately to the discovery of the first organic superconductor [33] in 1980. It was the extra degree of freedom contributed by the application of pressure that revealed the existence of superconductivity in $(\text{TMTSF})_2\text{PF}_6$ which would have been missed had the study been restricted to ambient

pressure. In this case the applied pressure suppressed the metal-to-insulator transition temperature to a value below that of the transition to the superconducting state.

Since that time, the combination of pressure and the application of high magnetic fields have been used extensively in the study of the organics. This has revealed a bewildering array of new phases, in particular, a number of field-induced spin-density wave phases (FI-SDW) [59] in $(\text{TMTSF})_2\text{PF}_6$ and related salts. Great progress has been made in the use of such techniques. Measurements of magnetoresistance and of the Shubnikov–de Haas effect on well-formed single crystals have given detailed information of the Fermi surface of many salts, and theoretical models [60–62] have provided a good explanation of the complex phenomena brought to light. A comprehensive treatment of these subjects can be found in Ishiguro and Yamaji's book [60] on organic superconductors.

V. SIMILARITIES OF ORGANIC AND OXIDE SUPERCONDUCTORS

A number of similarities [63] have been noted between properties of the organic superconductors such as $(\text{BEDT-TTF})_2\text{X}$, also known as $(\text{ET})_2\text{X}$, one of the “ET” salts, and those of the recently discovered cuprates, such as $\text{YBa}_2\text{Cu}_3\text{O}_7$. Both have strong interactions in a plane with weak interactions out of the plane, giving a two-dimensional Fermi surface in both cases. The organics have portions of their Fermi surface that nest, and it appears now that this is also typical of the cuprates [64]. Both systems have a low density of carriers, with the result that screening is reduced, and therefore the electron–electron interactions are stronger than in an ordinary metal and electron–electron correlations are important in both cases.

In the cuprates the superconducting state lies close to an antiferromagnetic state, and it is believed by some that the antiferromagnetism plays a role in the superconducting phase of the cuprates. In the $(\text{TMTSF})_2\text{X}$ compounds the spin-density wave state lies close to the superconducting state. Thus both appear to have some incipient tendencies toward a magnetic state while in the superconducting state. In both systems it is believed the superconducting gap is anisotropic and the coherence length small compared to that of conventional elemental superconductors. Fluctuations are important in the cuprates because of the short coherence length and to a lesser extent in the organics.

What is notably different between the cuprates and the organics is their ease of synthesis. While the cuprate superconductors can, and have been made by relatively inexperienced workers, including high school students, the synthesis of most of the organics requires talented and experienced

chemists. This difference is partly the reason the study of the high-temperature cuprates developed at such remarkable speed, whereas progress in the organics has been relatively slow. The typical multistep synthesis of each of the key donors, acceptors, and monomers needed for the preparation of even the simpler organic conductors is time consuming and to be successful requires long-term funding, a dedicated team, and access to a wide range of modern instrumentation.

VI. FUTURE PROSPECTS

Before attempting to assess what the future holds for the field of organic conductors it is as well to look back first to review briefly what the subject has contributed to date. It has clearly stimulated an enormous amount of work on many subjects bearing on the physics of the solid state [60], including problems pertaining to the stability of matter, the nature of instabilities in molecular and polymer systems, incipient instabilities, and the role of fluctuations; the development of x-ray and neutron scattering as tools for the study of structures, soft modes, and modulated lattices [65]; the nature of the metallic state, localization, mechanisms of conductivity, and of superconductivity; solitons; and topological defects. Impressive advances have been made in the chemistry and materials science of molecular systems [66], particularly in the design and synthesis of new donors and acceptors [49,50,67], in preparatory techniques [68] for growing of organic crystals of semiconductor-like perfection [61], electrocrystallization [69], and rapid structural determinations; and the exquisite techniques of solid-state synthesis of polymer single crystals [70]. The chemistry and physics of these areas has gone far beyond what we dreamed of 30 years ago.

In addition to these advances in the core areas of the disciplines of physics, chemistry, and materials science, we have seen a change in the sociology of the participants working in this field. Interdisciplinary groups have been formed in Europe, Japan, the United States, and internationally, incorporating in each a wide range of disciplines where active participation of individuals occurs across traditional disciplinary boundaries. Today there are many experimental chemists with an understanding of second quantization and the intricacies of many-body physics; physicists with a working knowledge of the chemistry of TCNQ and TTF and preparatory techniques of polymer science; and chemists and materials scientists sensitive to the exacting demands of quality crystal growth, four-probe resistance measurements, cryogenics, and high-pressure experimentation. This cross-fertilization can be expected to have a stimulating effect well beyond the field of organic conductors in many other areas of science.

In looking to the future, probably the one factor that will have the greatest impact on the long-term importance of the field will be the synthesis and, of course, characterization of new materials. The important advances of the past decade have resulted from following the path of least resistance, progressing step by step from compounds whose properties were relatively well understood to new compounds by making relatively minor modifications to the old. Ultimately, new ground will have to be broken. At a recent conference a number of interesting and novel new approaches were suggested by a blue ribbon panel of experts [71]. Clearly, there is no shortage of ideas and opportunities, but to explore even one new area takes a significant commitment in time and resources. Because of the large number of combinations of possible donors, acceptors, monomers, and polymers it is not even possible in a short time to determine whether a new entry is a winner or a loser. Extensive work is needed to find the right crystal environment or a compatible class of partners in the case of donor–acceptor synthesis. These considerations are among the barriers to entry into the field.

It seems likely that the most dramatic advances that will be made will come through advances in other areas of chemistry being assimilated into the field. A limiting factor in the present design of organic conductors is the lack of control over the crystal structure of the end product. On the other hand, much progress has been made in recent years in the area of molecular engineering [72] and what has been called “supramolecular chemistry” by Jean-Marie Lehn [73,74], wherein consideration is given to the synthesis of supramolecular entities. This is in the spirit of Akamatu’s remarks on the nature of the organic state alluded to earlier, where the object is to prepare or organize in the crystal a functioning entity. Some work along these lines has already been done, notably that of Wegner and co-workers [70] on the solid-state polymerization of diaminodiacetylenes; the structural modification of crystals by incorporation in them of solvent molecules by Kuroda [75], the work of Whangbo and co-workers, and others on the role of donor–donor and donor–anion interactions in the ET salts [66, pp. 270–283]; and indeed, many years ago [76] the concept was suggested of building a “macrometal” using instead of atoms, tightly bound metal clusters or molecular entities. The possibility now exists for doing this or using the functionalized fullerenes to construct the scaffolding and large-scale architectural entities for such supramolecules. It is this design and control of the molecular architecture over distances on the order of 10 to 100 nm that is important for conduction processes for good conductors and superconductors. This is precisely the distance range where one is dealing with the organization of assemblies of molecules rather than simply with the synthesis of individual molecules and where the special considerations of supramolecular chemistry come into play.

Factors that matter in the design of assemblies of molecules are the packing forces, determined by the shape of the molecules defined by the repulsive part of the van der Waals interaction, multipolar forces from electrostatic interactions of charges on the molecules, hydrogen bonding where applicable, and the attractive contribution of the van der Waals force. Many of these and the role they play in determining crystal structures are described in Kitaigorodskii's classic work [77], *Molecular Crystals and Molecules* published in 1973. The concept of "crystal engineering" dates back to about the same era with the pioneering work of Gerhardt Schmidt [78] and his group at the Weizmann Institute, beginning with their elegant contribution on the topochemical synthesis of photodimerizable olefins. The detailed structural work of a huge number of organic compounds [79], the steering effect of dichloro-substituted aromatic molecules in crystal structures recognized by Schmidt and Green [80], and the role of hydrogen bonding [81] are among the many contributions of this group. Desiraju's recent book [72], *Crystal Engineering: The Design of Organic Solids*, is a gold mine of information on this field. It will be an essential aid to those working in conductive organics in the 1990s, putting in one place, as it does, the work of all the major contributors and providing an expert's guidance to the key issues.

In the more distant future one may well ask whether we will ultimately see the biosynthesis of conductive or other magnetic or novel organic compounds. The question was asked many years ago by a student of mine, Norman Kagan [82], who proposed an artificial, Darwinian environment for the selective breeding of microorganisms exhibiting high electrical conductivity or large diamagnetism in a proposed search for an ambient-temperature organic superconductor. This was before the discovery of DNA cloning and the biotechnology revolution. Although we have no reason today to believe that such organic superconductors exist in living organisms, the ideas he espoused may yet prove to be a feasible approach to the synthesis of important, new materials if done with the use of powerful modern techniques of gene manipulation. This would then complete the circle, taking one from the inspiration gained from observation of the incredibly rich spectrum of biomolecules in nature and the remarkably precise synthetic processes in which they participate, to the actual synthesis of human-made or human-designed compounds by biological means.

ACKNOWLEDGMENT

We gratefully acknowledge financial support for this work from the U.S. Department of Energy (grant DEFG03-86ER45245).

REFERENCES

1. H. Akamatu, in *Energy and Charge Transfer in Organic Semiconductors* (K. Masuda and M. Silver, eds.), Plenum Press, New York, 1973, pp. 3–4.
2. H. N. McCoy and W. C. Moore, *J. Am. Chem. Soc.* 33:273 (1911).
3. H. J. Kraus, *J. Am. Chem. Soc.* 34:1732 (1913).
4. A. Szent-Györgi, *Science* 93:609 (1941).
5. A. Szent-Györgi, *Nature* 157:875 (1946).
6. D. D. Eley, *Nature* 162:819 (1948).
7. H. Akamatu and H. Inokutchi, *J. Chem. Phys.* 18:810 (1950).
8. H. Akamatu, H. Inokutchi, and Y. Matsunaga, *Nature* 173:168 (1954).
9. A. H. Hermann and A. Rembaum, *J. Polym. Sci. C*, 107 (1967).
10. Y. Okamoto and W. Brenner, *Organic Semiconductors*, Reinhold, New York, 1964.
11. F. Gutmann and L. E. Lyons, *Organic Semiconductors*, Wiley, New York, 1967.
12. A. Rembaum and R. F. Landel, eds., *Electrical Properties of Polymers*, *J. Polym. Sci. C*, 17 (1967).
13. N. W. Ashcroft and N. D. Mermin, *Solid State Physics*, Holt, Rinehart, and Winston, New York, 1976, p. 186, 685–687.
14. J. Hubbard, *Proc. Roy. Soc.* A276:238 (1963); A277:237 (1964); A281:401 (1964).
15. R. G. Kepler, P. E. Bierstedt, and R. E. Merrifield, *Phys. Rev. Lett.* 5:503 (1960).
16. W. J. Siemons, P. E. Bierstedt, and R. G. Kepler, *J. Chem. Phys.* 39:3523 (1963).
17. F. G. Wudl, G. M. Smith, and E. J. Hufnagle, *Chem. Commun.*, 1453 (1970).
18. L. B. Coleman, M. J. Cohen, D. J. Sandman, F. G. Yamagishi, A. F. Garito, and A. J. Heeger, *Solid State Commun.* 12:1125 (1973).
19. J. S. Miller and A. J. Epstein, eds., *Synthesis and Properties of Low Dimensional Materials*, *Ann. N.Y. Acad. Sci.* 313 (1978).
20. A. J. Epstein and E. M. Conwell, eds., *Proc. International Conference on Low-Dimensional Conductors*, Colorado, *Mol. Cryst. Liq. Cryst.* 82 (1982).
21. R. A. Ogg, *Phys. Rev.* 69:243 (1946).
22. R. A. Ogg, *Phys. Rev.* 69:668 (1946).
23. L. N. Cooper, *Phys. Rev.* 104:1189 (1956).
24. J. Bardeen, L. N. Cooper, and J. R. Schrieffer, *Phys. Rev.* 108:1175 (1957).
25. F. London, *Superfluids*, Vol. 1, Wiley, New York, 1950.
26. W. A. Little, *Phys. Rev.* 134:A1416 (1964).
27. W. A. Little, *Sci. Am.* 212:21 (1965).
28. Y. Nakahara, K. Kimura, and H. Inokuchi, *Chem. Phys. Lett.* 47:251 (1977).
29. H. Gutfreund and W. A. Little, in *Highly Conducting One-Dimensional Solids* (J. T. Devreese, R. P. Evrard, and V. E. van Doren, eds.), Plenum Press, New York, 1979, p 305.
30. R. L. Greene, G. B. Street, and L. J. Suter, *Phys. Rev. Lett.* 34:577 (1975).

31. C. K. Chiang, Y. W. Park, A. J. Heeger, H. Shirakawa, E. J. Louis, and A. G. MacDiarmid, *Phys. Rev. Lett.* **39**:1098 (1977).
32. W. P. Su, J. R. Schrieffer, and A. J. Heeger, *Phys. Rev. Lett.* **42**:1698 (1979); *Phys. Rev. B* **22**:2099 (1980).
33. D. Jerome, A. Mazaud, M. Ribault, and K. Bechgaard, *J. Phys. Lett.* **41**:L-95 (1980).
34. A. F. Hebard, M. J. Rosseinsky, R. C. Haddon, D. W. Murphy, S. H. Glarum, T. T. Palstra, A. P. Ramirez, and A. R. Kortan, *Nature* **350**:600 (1991).
35. Z. Iqbal, R. H. Baughman, B. L. Ramakrishna, S. Khare, N. S. Murthy, H. J. Bornemann, and D. E. Morris, *Science* **254**:826 (1991).
36. J. G. Bednorz and K. A. Müller, *Z. Phys. B* **64**:189 (1986).
37. R. A. Ferrell, *Phys. Rev. Lett.* **13**:330 (1964).
38. T. M. Rice, *Phys. Rev.* **140**:1889 (1965).
39. P. C. Hohenberg, *Phys. Rev.* **158**:383 (1967).
40. Y. A. Bychkov, L. P. Gorkov, and I. E. Dzyaloshinskii, *Sov. Phys. JETP* **23**:489 (1966).
41. L. B. Coleman, M. J. Cohen, D. J. Sandman, F. G. Yamagishi, A. F. Garito, and A. J. Heeger, *Solid State Commun.* **12**:1125 (1973).
42. R. E. Peierls, *Quantum Theory of Solids*, Oxford University Press, Oxford, 1955.
43. W. Hume-Rothery, *The Metallic State*, Oxford University Press, Oxford, 1931.
44. N. F. Mott and H. Jones, *The Theory and Properties of Metals and Alloys*, Oxford University Press, Oxford, 1936.
45. H. C. Longuet-Higgins and L. Salem, *Proc. Roy. Soc. A* **251**:172 (1959).
46. A. W. Overhauser, *Phys. Rev. Lett.* **4**:462 (1960).
47. J. Cizek and J. Paldus, *J. Chem. Phys.* **47**:3976 (1967).
48. N. F. Mott, *Phil. Mag.* **6**:287 (1961).
49. D. Cowan, P. Shu, C. Hu, W. Krug, T. Carruthers, T. Poehler, and A. Bloch, in *Chemistry and Physics of One-Dimensional Metals* (H. Keller, ed.), NATO Advanced Study Institute Series B: Physics 25, Plenum Press, New York, 1977, pp. 25–45.
50. A. N. Bloch, T. F. Carruthers, T. O. Poehler, and D. O. Cowan, in *Chemistry and Physics of One-Dimensional Metals* (H. Keller, ed.), NATO Advanced Study Institute Series B: Physics 25, Plenum Press, New York, 1977, pp. 47–85.
51. J. S. Miller, *Ann. N.Y. Acad. Sci.* **313**:25–60 (1978).
52. N. F. Mott and W. D. Twose, *Adv. Phys.* **10**:107 (1961).
53. E. Merzbacher, *Quantum Mechanics*, Wiley, New York, 1961, pp. 78–111.
54. D. H. Dunlap, H.-L. Wu, and P. Phillips, *Phys. Rev. Lett.* **65**:88 (1990); P. Phillips and H.-L. Wu, *Science* **252**:1805 (1991).
55. J. P. Pouget, S. Megtert, R. Comés, and A. J. Epstein, *Phys. Rev. B* **21**:486 (1980).
56. J. P. Pouget, in *Semiconductors and Semimetals*, Vol. 27 (E. Conwell, ed.), Academic Press, New York, 1988, pp. 87–214.

57. H. Gutfreund and W. A. Little, *Felix Bloch and Twentieth Century Physics*, Rice University Studies 66, Rice University, Houston, 1980, pp. 1–18.
58. D. Jérôme and M. Weger, in *Chemistry and Physics of One-Dimensional Metals* (H. Keller, ed.), NATO Advanced Study Institute Series B: Physics 25, Plenum Press, New York, 1977, pp. 341–367.
59. J. F. Kwak, J. E. Shirber, R. L. Greene, and E. M. Engler, *Phys. Rev. Lett.* 46:1296 (1981).
60. T. Ishiguro and K. Yamaji, *Organic Superconductors*, Springer-Verlag, Berlin, 1990.
61. M. Tokumoto, A. G. Swanson, J. S. Brooks, C. C. Agosta, S. T. Hannahs, N. Kinoshita, H. Anzai, M. Tamura, H. Tajima, H. Kuroda, and J. R. Anderson, in *Organic Superconductivity* (V. Z. Kresin and W. A. Little, eds.), Plenum Press, New York, 1990, pp. 167–190.
62. L. P. Gorkov and A. G. Lebed, *J. Phys. Lett.* 45:403 (1984).
63. R. L. Greene, in *Organic superconductivity* (V. Z. Kresin and W. A. Little, eds.), Plenum Press, New York, 1990, pp. 7–13; see also Y. J. Uemura, L. P. Le, G. M. Luke, B. J. Sternlieb, J. H. Brewer, T. M. Riseman, G. Saito, and H. Yamochi, in the same book, pp. 23–29.
64. C. G. Olsen, R. Liu, A.-B. Yang, D. W. Lynch, A. J. Arko, and R. S. List, *Science* 245:731 (1989).
65. R. Comés, in *Chemistry and Physics of One-Dimensional Metals* (H. Keller, ed.), NATO Advanced Study Institute Series B: Physics 25, Plenum Press, New York, 1977, pp. 315–339.
66. J. M. Williams, J. R. Ferraro, R. J. Thorn, K. D. Carlson, U. Geiser, H. H. Wang, A. M. Kini, and M.-H. Whangbo, *Organic Superconductors (Including Fullerenes)*, Prentice Hall, Englewood Cliffs, N.J., 1992.
67. F. Wudl, in *Chemistry and Physics of One-Dimensional Metals* (H. Keller, ed.), NATO Advanced Study Institute Series B: Physics 25, Plenum Press, New York, 1977, pp. 233–256.
68. J. R. Andersen, E. M. Engler, and K. Bechgaard, in *Synthesis and Properties of Low Dimensional Materials* (J. S. Miller and A. J. Epstein, eds.), *Ann. N.Y. Acad. Sci.* 313:293 (1978).
69. K. Bechgaard, K. Carneiro, R. B. Rasmussen, M. Olsen, G. Rindorf, C. S. Jacobsen, H. J. Pedersen, and J. C. Scott, *J. Am. Chem. Soc.* 103:2440 (1981).
70. G. Wegner, in *Chemistry and Physics of One-Dimensional Metals* (H. Keller, ed.), NATO Advanced Study Institute Series B: Physics 25, Plenum Press, New York, 1977, pp. 297–314.
71. D. Cowan, R. Elsenbaumer, F. Wudl, J. Collman, G. Saito, and P. Erk, in *Organic Superconductivity* (V. Z. Kresin and W. A. Little, eds.), Plenum Press, New York, 1990, pp. 295–316.
72. G. R. Desiraju, *Crystal Engineering: The Design of Organic Solids*, Elsevier, Amsterdam, 1989.
73. J.-M. Lehn, *Pure Appl. Chem.* 50:871 (1978).
74. J.-M. Lehn, *Science* 260:1762 (1993).

75. H. Kuroda, in *Energy and Charge Transfer in Organic Semiconductors* (K. Masuda and M. Silver, eds.), Plenum Press, New York, 1973, pp. 177–182.
76. W. A. Little, *J. Less-Common Met.* 62, 361 (1978).
77. A. I. Kitaigorodskii, *Molecular Crystals and Molecules*, Academic Press, New York, 1973.
78. G. M. J. Schmidt, *Pure Appl. Chem.* 27:647 (1971).
79. F. H. Herbstein, *Perspect. Struct. Chem.* 4:166 (1971).
80. B. S. Green and G. M. J. Schmidt, *Israel Chem. Soc. Annu. Meet. Abstr.* 190 (1971); see also A. Elgavi, B. S. Green, and G. M. J. Schmidt, *J. Am. Chem. Soc.* 95:2058 (1973).
81. L. Leiserowitz and G. M. J. Schmidt, *J. Chem. Soc. A*, 2372 (1969).
82. N. E. Kagan, in *Proc. International Conference of Organic Superconductors* (W. A. Little, ed.), *J. Polym. Sci. C* 29:191 (1970).

2

Basic Physical Concepts of Organic Conductors

Laurent G. Caron

Université de Sherbrooke, Sherbrooke, Québec, Canada

I. INTRODUCTION

As discussed in Chapter 1, organic conductors, because of their intrinsic lower dimensionality, can show very diversified thermodynamic behavior [1]. This proved very early to be an unexpected challenge to theorists and experimentalists. New phenomena were explored; new theoretical tools and new experimental techniques had to be developed. It is the purpose of this chapter to present an overview of the phenomena and the tools that have occupied the theorists in the 20 years of existence of the field covered by this book.

The approach I have chosen for this chapter is more pedagogical than historical. I do not cover all topics: a selection had to be made. Critical phenomena are not discussed, for instance. Neither do I pretend to do a thorough literature survey; I will rely on past review articles and books whenever advantageous. My apologies to the many authors of excellent articles I will not directly quote. I will try to present the physics behind the phenomena and the theoretical approaches.

I have subdivided this chapter in five parts. In the next section the particularities of low-dimensional physics are introduced. I then present the basic ingredients of organic conductors in the form of one- and two-body interactions, which are the input to the various models of interest, and discuss the origin of the strong anisotropy in the electronic properties.

The following section treats the one-dimensional aspects and focuses on the importance of fluctuations. Section V treats the two-dimensional regime, and the one after, the three-dimensional situation and the mechanisms of phase transitions.

II. LOW-DIMENSIONAL PHYSICS

What is so special about low-dimensional solids? The key element here is the Mermin–Wagner theorem [2]. It states [3] that systems with short-range forces that are at finite temperature cannot undergo any phase transition to a state that breaks (1) a discrete symmetry in one dimension ($d = 1$) or (2) a continuous symmetry in one or two dimensions ($d = 2$). Why is this so?

Let us start with the discrete symmetry. Inversion symmetry is an example. Any state that breaks this symmetry can be characterized by a scalar order parameter $\psi(x)$ ($n = 1$ component) which measures the local average of the observable associated with the broken symmetry [4]. This can be the average spin component in the z direction in the Ising ferromagnet or the amplitude of the local bond-length distortion due to π bonding in polyacetylene. At low temperatures the putative long-range-ordered (LRO) state is degenerate with $\psi = \pm|\psi_0|$. The elementary excitations are kinks (the solitons to be discussed later), well localized in space and with energy of the order of the interaction energy, with the sign of the order parameter changing from one side to the other. The LRO can be studied by the correlation function $\lim_{x \rightarrow \infty} \langle \psi(x)\psi(0) \rangle$, the thermodynamic average measuring the coherence of the order parameter over large distances. This correlation function would give $|\psi_0|^2$ in the LRO state. In the presence of kinks, $\psi(x)\psi(0) = (-1)^{N_k}|\psi_0|^2$, where N_k is the number of kinks in the interval $[0, x]$. It is thus quite obvious that the thermal fluctuations in N_k , a large value in the thermodynamic limit, will wipe out the correlation function and any pretense to LRO. Entropy arguments also lead to conclude the instability of LRO to kink formation [4,5]. Things are quite different for $d > 1$. Kink production is prohibitive because of the high energy involved, proportional to the length L of the system. The excitations have finite perimeter and form domains. The correlation at large distance can thus survive to a fair amount of excitations as long as most of these do not enclose the points $(0, \mathbf{r})$.

As far as the continuous symmetry breaking is concerned, the Goldstone theorem states [4] that this will generate hydrodynamic modes, that is, gapless excitations. The order parameter is multicomponent ($n > 1$): a vector $\boldsymbol{\psi}$ for magnetism breaking the rotational symmetry, a complex variable $\psi = |\psi|e^{i\theta}$ for charge-density waves and for superconductivity which

break translational or gauge symmetry, respectively. It costs no energy to rotate the direction of ψ or to translate the complex order parameter along the “direction” of the broken translational symmetry (change the phase). It is these gapless excitations that destroy LRO for $d \leq 2$. Let me illustrate this with a complex order parameter. In a presumed ordered state, the amplitude of ψ is homogeneous but the phase can vary in space $\psi(\mathbf{r}) = |\psi|e^{i\theta(\mathbf{r})}$. In the phenomenology of the Landau–Ginzburg theory discussed in Section IV.C.1, the gapless thermal excitations can be treated classically [6] and have an energy proportional to $\int d^d x |\Delta\psi|^2 = |\psi|^2 \int d^d x |\Delta\theta|^2$. Fourier transforming $\theta(\mathbf{r}) = \int d^d k e^{i\mathbf{k}\cdot\mathbf{r}} \theta_{\mathbf{k}}$, one immediately sees that the energy of an excitation of wave vector \mathbf{k} is proportional to $k^2 |\theta_{\mathbf{k}}|^2$. Boltzmann averaging on such a mode, one gets $\langle |\theta_{\mathbf{k}}|^2 \rangle \propto T k^{-2}$. It follows that the contribution of the long-wavelength hydrodynamic modes to the fluctuations in the phase coherence is $\lim_{x \rightarrow \infty} \langle (\theta(x) - \theta(0))^2 \rangle \propto \int d^d k \langle |\theta_{\mathbf{k}}|^2 \rangle \sin^2(k_x x/2) \propto T \int d^d k k^{-2} \sin^2(k_x x/2)$. This last integral is singular for $d \leq 2$ and $T \neq 0$, implying lack of phase correlation and thus a total instability of the ordered state to the phase fluctuations.

The impact of this is tremendous. No long-range order (LRO) can exist at finite temperature in one dimension: no crystals, no magnets, no superconductors. Only special transitions are possible in two dimensions. The Ising model ($n = 1$ component) is an example [7]. The Kosterlitz–Thouless transition [8], *without LRO*, is another case for $d = 2$ and $n = 2$, discussed in Section V.C. The thermal fluctuations are very destructive in lower dimensions. Quantum fluctuations (i.e., those associated with the dynamics of a system) also tend to suppress LRO and can sometimes destroy it even at 0 K when the Mermin–Wagner theorem does not apply. Such is the case of the quantum spin- $\frac{1}{2}$ antiferromagnetic models [9] in one dimension.

We will see that it is the interactions between chains or sheets that is responsible for finite temperature transitions. That is the reason for labeling systems of chains or sheet as quasi-one- or two-dimensional. They exhibit one- or two-dimensional behavior until there occurs a crossover to higher dimensionality. Obviously, crystals do exist and as such must be three-dimensional. Binding forces are intrinsically three-dimensional. Let us then take for granted the existence of the crystalline backbone of organic conductors and concentrate on the electronic properties which are of interest to conduction. It is the strong anisotropy in these which is responsible for the stamp of quasi-one- or quasi-two-dimensional solids.

III. INTERACTIONS IN ORGANIC CONDUCTORS

The nature of the fundamental interactions is common to all types of low-dimensional solids. They differ mostly because of the constraints imposed

by the molecular arrangements. I shall thus review the basic interactions and then specialize them to the specific categories of organic conductors.

The conduction band(s) of organic conductors (but not of the superconducting oxides) are constructed from π -molecular orbitals. The electrons in a π orbital can tunnel (hop) from one orbital to a nearest neighbor with a strength t . π Orbitals are directional and, as a result, the hopping integral is highly anisotropic, being maximal when the orbitals make good contact. The tight-binding single-electron Hamiltonian is given by $\mathcal{H}_e = - \sum_{i \neq j, s} t_{ij} c_{js}^+ c_{is}$, where c_{is} annihilates an electron of spin s on molecule i and t_{ij} is the hopping matrix element between molecules i and j . The resulting energy band has the generic form

$$\varepsilon(\mathbf{k}) = -2t_a \cos k_a a - 2t_b \cos k_b b - 2t_c \cos k_c c$$

where t_a , t_b , and t_c are the hopping amplitudes between nearest-neighbor molecules along the three lattice directions and so chosen that the t values are ordered with decreasing magnitude. Shapes of the Fermi surface are illustrated in Fig. 1.

The Coulomb interaction between electrons is often taken to be limited to the intramolecular part, $\mathcal{H}_{e-e} = U \sum_i n_{i\uparrow} n_{i\downarrow}$, and one gets the famous

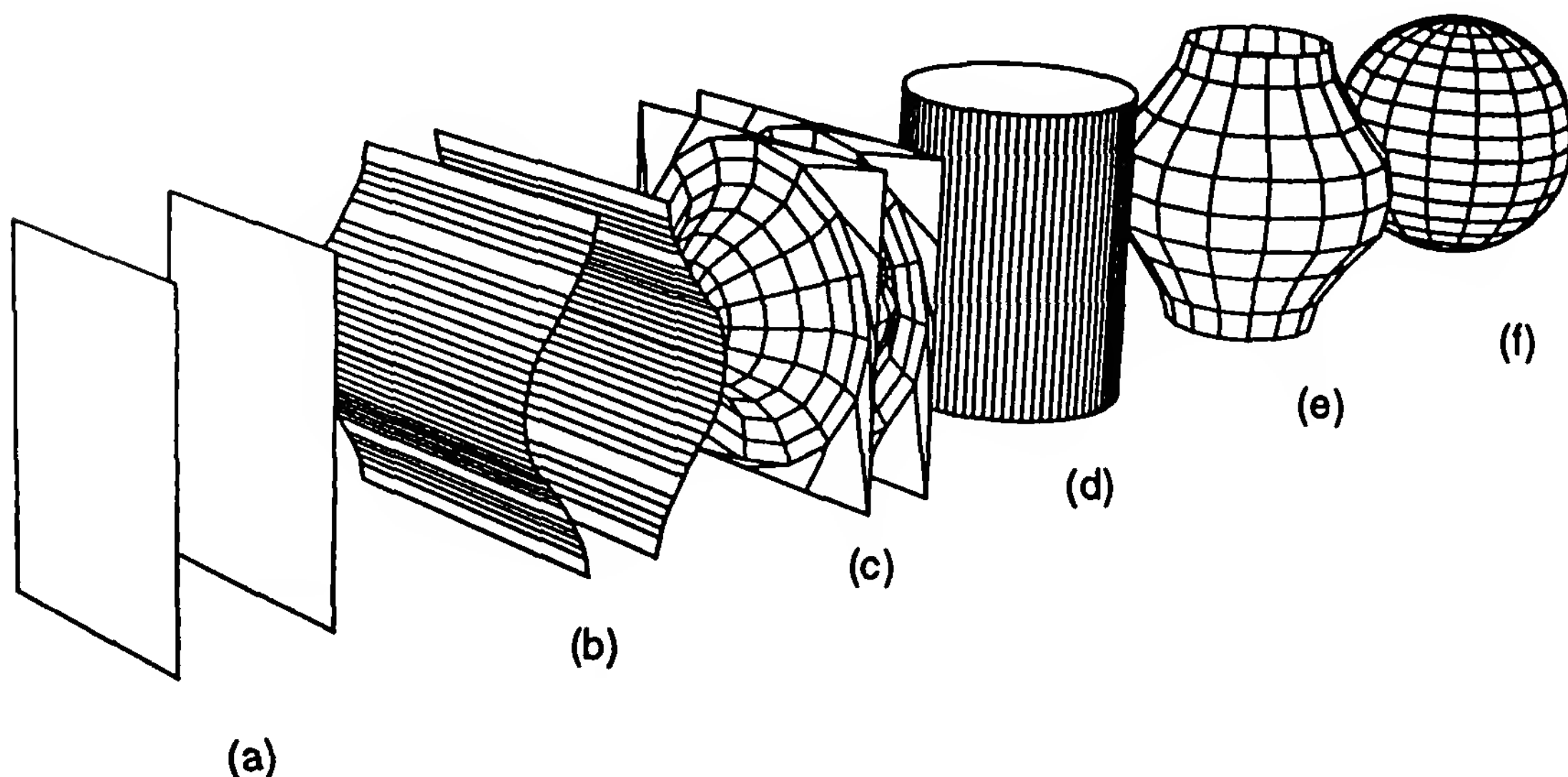


Figure 1 Effect of dimensionality on the shape of the Fermi surface. The surfaces shown are for (a) $t_b, t_c = 0$ (one-dimensional), (b) $t_b \ll t_a, t_c = 0$ (quasi-one-dimensional), (c) transverse isotropic quasi-one-dimensional, (d) isotropic two-dimensional, (e) $t_c \ll t_a, t_b$ (quasi-two-dimensional), and (f) isotropic three-dimensional. (Courtesy of J. Lefebvre.)

Hubbard Hamiltonian [10],

$$\mathcal{H}_H = - \sum_{i \neq js} t_{ij} c_{js}^+ c_{is} + U \sum_i n_{i\uparrow} n_{i\downarrow} \quad (1)$$

Here $n_{is} = c_{is}^+ c_{is}$ is the occupation operator for electrons of spin s at molecule i . The extensions to near neighbors or to further neighbors yield the extended Hubbard or the Pariser–Parr–Pople [11] Hamiltonians, respectively:

$$\mathcal{H}_{PPP} = - \sum_{i \neq js} t_{ij} c_{js}^+ c_{is} + U \sum_i n_{i\uparrow} n_{i\downarrow} + \frac{1}{2} \sum_{i \neq j} V_{ij} n_i n_j$$

This simple modeling accounts fairly well for the short-range part of the Coulomb interaction. The long-range part is presumed to play a less important role near the Fermi surface, due to screening.

The electron–phonon interaction can take on two different forms, depending on the type of phonons involved. The interaction with optical phonons is intramolecular and of the form $\mathcal{H}_{e-o} = \lambda \sum_i q_i n_i$, where λ is the coupling strength and q_i is the phonon normal coordinate at molecule i . The interaction with acoustical phonons is through the hopping integrals, which are modulated by intermolecular motion. The hopping between two molecules at the crystal positions \mathbf{R}_i and \mathbf{R}_j is $t_{ij} = t + (\nabla_{ij} t_{ij}) \cdot (\mathbf{u}_j - \mathbf{u}_i) + \dots$, so

$$\mathcal{H}_{e-a} = - \sum_{i \neq js} (\nabla_{ij} t_{ij}) \cdot (\mathbf{u}_j - \mathbf{u}_i) c_{js}^+ c_{is}$$

where \mathbf{u}_i is the displacement of molecule i from the equilibrium position.

A. Quasi-One-Dimensional Conductors

1. Charge-Transfer Salts

The charge-transfer salts are constructed with either (1) two species of relatively flat molecules with π orbitals perpendicular to the planes, or (2) one molecular species with a counterion. Soos [12] had early on catalogued the different types of arrangements in π -molecular complexes. Conductors and semiconductors show a segregated stack structure like $A^+ A^+ A^+ A^+ \oplus B^- B^- B^- B^-$, where A and/or B are flat molecules piling up in chains with good π -orbital contact, while in case (2) the counterions distribute themselves between the molecular chains. The Coulomb interaction between the ionic species determines the basic crystalline structure, that is, composition of the high-temperature unit cell. The charge transfer need not be integer as for TTF–TCNQ [13]. The necessary condition for con-

duction along the chains is that the charge transfer leave the π orbitals partially occupied.

Although there can be a modulation of the hopping strength t_a along the chain due to the counterion potential, in A_2B compounds for instance, the physics of quasi-one-dimensional conductors is contained in the standard uniform-hopping model. One has $t_a \gg t_b \gg t_c$, which explains the large anisotropy in the electronic properties. The Fermi surface is open with two slightly warped sheets at $k_a \approx \pm |k_F|$, as shown in Fig. 1b. Theorists often linearize the intrastack component around the Fermi level to get $\varepsilon(\mathbf{k}) = \varepsilon_{\parallel}(k_a) + \varepsilon_{\perp}(\mathbf{k}_{\perp})$, where

$$\varepsilon_{\parallel}(\mathbf{k}) = v_F \hbar (|k_a| - k_F) \quad (2a)$$

$$\varepsilon_{\perp}(\mathbf{k}_{\perp}) = -2t_b \cos k_b b - 2t'_b \cos 2k_b b - 2t_c \cos k_c c \quad (2b)$$

$v_F = (2t_a a \sin k_F a)/\hbar$ the Fermi velocity, k_F the Fermi momentum, and $t'_b \sim t_b^2/t_a$ compensates for the lost dispersion in the chain direction.

An alternative approach to the Coulomb repulsion is that of “g-ology” [14–18]. On the premise that the interesting physics occurs in an energy shell on the order of the thermal energy around each sheet of the Fermi surface, the interaction is divided into wave-number independent g_i and V_i interactions acting within these shells. Here $g_i(V_i)$ are the intrachain (interchain) backward ($i = 1$), forward ($i = 2, 4$), and umklapp ($i = 3$) processes shown in Fig. 2. At $T = 0$, the umklapp processes are present only when the number of carriers (electrons or holes) per the unit cell is one. They can be felt close to half-filling at finite temperature. The correspondence between the g-ology model and the extended Hubbard models for a one-dimensional half-filled band is discussed in Ref. 16: $g_1, g_3 \leftrightarrow U - 2V$, $g_2, g_4 \leftrightarrow U + 2V$. As discussed in Barisic [19], the long-range part of the Coulomb interaction can naturally be included in the intrachain forward scattering. The g-ology Hamiltonian in the one-dimensional situation is

$$\mathcal{H}_g = \sum_{k\sigma} \varepsilon_{\parallel}(k) (a_{ks}^{\dagger} a_{ks} + b_{ks}^{\dagger} b_{ks}) + H_{e-e} \quad (3a)$$

$$\begin{aligned} \mathcal{H}_{e-e} = & \frac{g_1}{L} \sum_{kk'q,ss'} b_{k+qs}^{\dagger} a_{k'-qs'}^{\dagger} b_{k's'} a_{ks} + \frac{g_2}{L} \sum_{kk'q,ss'} a_{k+qs}^{\dagger} b_{k'-qs'}^{\dagger} b_{k's'} a_{ks} \\ & + \frac{g_3}{2L} \sum_{kk'q,ss'} (b_{k+qs}^{\dagger} b_{k'-qs'}^{\dagger} a_{k's'} a_{ks} + \text{h.c.}) \\ & + \frac{g_4}{2L} \sum_{kk'q,ss'} (a_{k+qs}^{\dagger} a_{k'-qs'}^{\dagger} a_{k's'} a_{ks} + b_{k+qs}^{\dagger} b_{k'-qs'}^{\dagger} b_{k's'} b_{ks}) \end{aligned} \quad (3b)$$

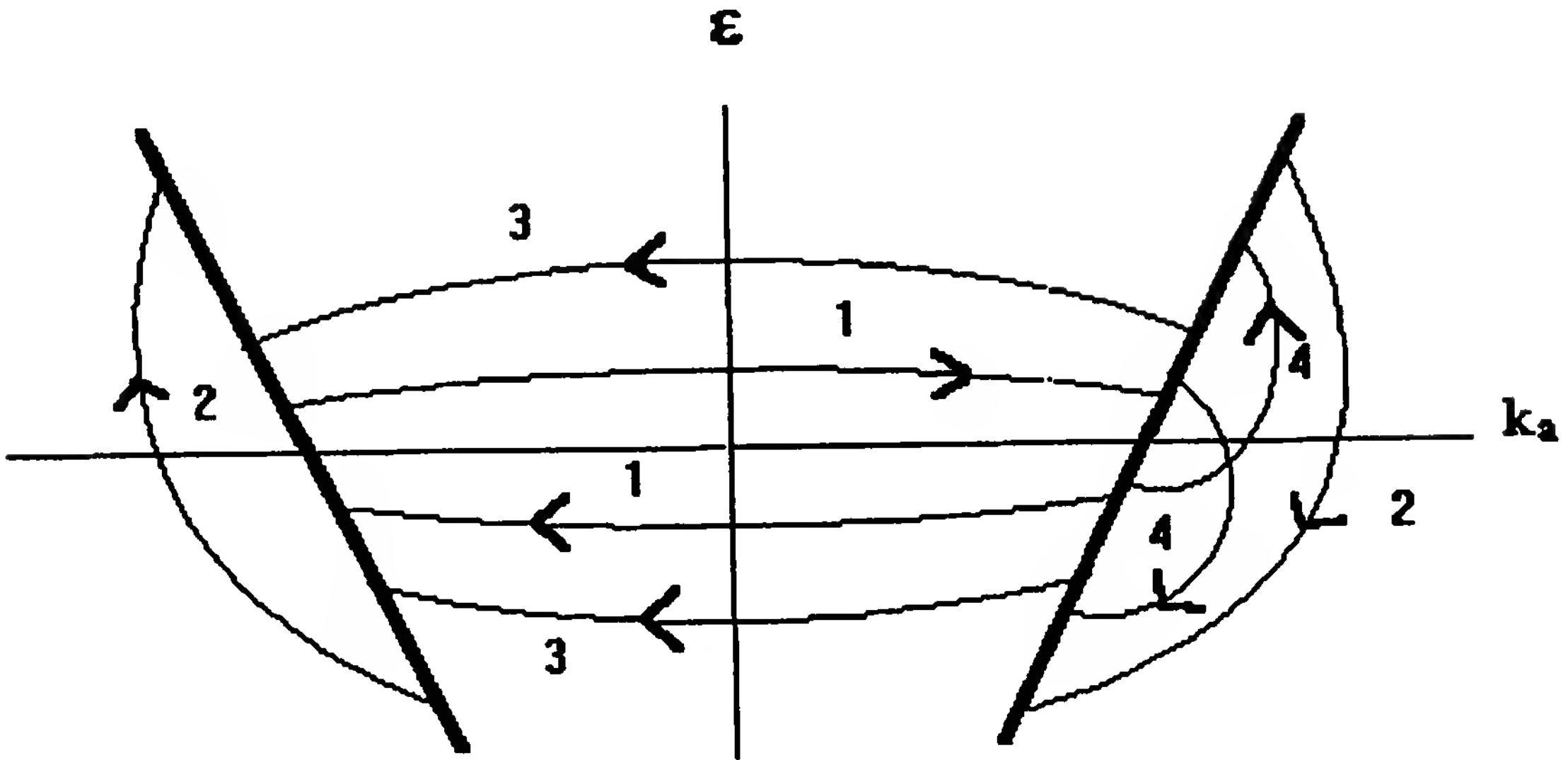


Figure 2 Various scattering processes in one-dimensional conductors. The linearized electronic energy spectrum is shown around the Fermi surface ($k = \pm k_F$). The processes are depicted by trajectories showing the transfer of electrons in momentum space. i refers to backward ($i = 1$), forward ($i = 2, 4$), and umklapp ($i = 3$) processes.

where a_{ks} (b_{ks}) annihilates a carrier (electron or hole) of spin s with $k > 0$ ($k < 0$) and L is the length of the chain.

The interaction with optical phonons is at the core of the molecular crystal (MC) Hamiltonian [20]. In one dimension this becomes

$$\mathcal{H}_{\text{MC}} = - \sum_{is} t(c_{i+1s}^+ c_{is} + \text{h.s.}) + \lambda \sum_i q_i n_i + \sum_i \left[\frac{p_i^2}{2M} + \frac{1}{2} \kappa q_i^2 \right] \quad (4)$$

In the one-dimensional limit, the coupling to acoustic phonons is at the heart of the Su–Schrieffer–Heeger (SSH) Hamiltonian [21]:

$$\begin{aligned} \mathcal{H}_{\text{SSH}} = & - \sum_{is} [t - \lambda(u_{i+1a} - u_{ia})](c_{i+1s}^+ c_{is} + \text{h.c.}) \\ & + \sum_i \left[\frac{p_i^2}{2M} + \frac{1}{2} \kappa (u_{i+1} - u_i)^2 \right] \end{aligned} \quad (5)$$

One should realize that the anisotropy of the electronic properties (in the t 's) imparts a similar anisotropy to the electron–acoustic–phonon interaction. Details and refinements of these concepts can be found in Ref. 22.

2. Polymers

Conjugated polymers differ mostly through the bonding, which is covalent. The chains are A – A – A like with a sigma bond between the basic

units A and an “itinerant” π bond for every two units (half-filled band). The interchain coupling is very weak and the polymers are thus the most one-dimensional of all organic conductors. The interactions are otherwise similar to those in Section III.A.1. Details and refinements of the concepts for polymers can be found in Ref. 23.

B. Quasi-Two-Dimensional Conductors

1. Charge-Transfer Solids

These are the members of the ET (BEDT-based organic solids) family. The structure can be chainlike, as in α -, β -, or θ -(ET)₂X, with strong interchain coupling along **b**, resulting in sheets with $t_a \approx t_b$ and a slightly open or most often closed quasi-two-dimensional Fermi surface (Fig. 1d and e). The chainlike structure can even disappear, as in κ -(ET)₂X, in favor of a more complex two-dimensional mesh of molecules. It should be mentioned that the single-electron energies have a form more complicated than the generic one proposed at the beginning of this section. Details and refinements of the concepts for ET salts can be found in Refs. 22 and 24.

2. Oxide Superconductors

Although not strictly speaking organic conductors, the high-temperature superconductors (HTSs) have often shared the podium with the organics, as is the case with this book. The band structure is complicated by degeneracies [25]. The two-band modeling of Emery [26] was an attempt at dealing with this degeneracy and describing the holes on the oxygens and the magnetic moments on the copper sites. It turns out, however, that the tight-binding single-band description seems to possess the essential ingredients for an understanding of the physics behind the HTSs. The two models I discuss briefly in this chapter are akin to those used in the organics. These are the Hubbard model [Eq. (1)] and the t - J model,

$$\mathcal{H}_{t-J} = -t \sum_{\langle ij \rangle_s} (d_{js}^+ d_{is} + \text{h.c.}) + J \sum_{\langle ij \rangle} \mathbf{S}_j \cdot \mathbf{S}_i \quad (6)$$

where $d_{is} = c_{is}(1 - n_{i-s})$ and $\langle ij \rangle$ refers to nearest-neighbor pairs. The latter contains the physics of the former for large U , in which situation $J \sim t^2/U$ is an antiferromagnetic coupling between otherwise “itinerant” electrons that must avoid one another. See Ref. 27 for a demonstration.

3. The Fullerenes

The fullerenes are new and special organic superconductors [28]. The fundamental units are the spherical C₆₀ molecules. These can be thought of as spherically folded two-dimensional sheets of carbons with real periodic boundary conditions. The foregoing considerations of low-dimensional sol-

ids can thus be ascribed to the intramolecular part of these solids. Carrier transport is three-dimensional, however.

4. Microtubes

Perhaps the recently studied graphitic microtubes [29] with their cylindrically folded two-dimensional carbon sheets will, like the fullerenes, mix quasi-two- and three-dimensional properties.

IV. PHYSICS IN ONE DIMENSION

We will proceed here with the usual convention that $\hbar, k_B = 1$.

A. Free Carriers

The physics of free carriers is dominated by the Fermi surface. Looking at the linearized spectrum of Fig. 2, one realizes that electron–hole or electron–electron excitations involving quasiparticles (electrons or holes) on each side of the Fermi surface are gapless. This greatly influences the response functions to external fields. Let an external field $F_\alpha(q)$ couple to the operator $O_\alpha(q)$, where

$$\begin{aligned} O_{\text{CDW}}(q) &= \sum_{ks} b_{ks}^+ a_{k+qs} & O_{\text{SDW}}(q) &= \sum_{kss'} b_{ks'}^+ \boldsymbol{\sigma}_{s's} a_{k+qs} \\ O_{\text{SS}}(q) &= \sum_{ks} s b_{ks} a_{-k+q-s} & O_{\text{TS}}(q) &= \sum_{kss'} s b_{ks'} \boldsymbol{\sigma}_{s's} a_{-k+q-s} \end{aligned} \quad (7)$$

and $\boldsymbol{\sigma}_{ss'}$ are the Pauli matrices. These are the charge-density wave (CDW), the spin-density wave (SDW), the singlet superconductivity (SS), and the triplet superconductivity (TS) observables relevant to organic conductors. The corresponding frequency- and momentum-dependent response functions are defined to be (of opposite sign to usual convention)

$$\chi_\alpha(q, \omega_m) = \int_0^\beta d\tau e^{-i\omega_m\tau} \langle O_\alpha(q, \tau) O_\alpha^+(q, 0) \rangle \quad (8)$$

where τ is the usual imaginary time of statistical physics, $\omega_m = 2\pi Tm$ is a Matsubara frequency, and $\beta = 1/k_B T$. In one dimension the free-electron susceptibilities are all logarithmic, behaving like

$$\chi_{\text{CDW,SDW}}^\circ(2k_F + q, \omega_m) \quad \chi_{\text{SS,TS}}^\circ(q, \omega_m) \approx \frac{\ell}{\pi v_F} \quad (9a)$$

$$\ell = \ln[\zeta] \quad \zeta^2 = \frac{E_0^2}{(\pi T)^2 + (v_F q)^2 + (\omega_m)^2} \quad (9b)$$

where E_0 is of the order of the Fermi energy. This contrasts with the three-dimensional behavior when only the particle–particle response functions

(SS, TS) are logarithmic, due to time-inversion symmetry. In one dimension, the particle–hole susceptibilities (CDW, SDW) are also logarithmic, due to the property of nesting of the Fermi surface: The left sheet of Fig. 1a superimposes on the right sheet in a translation by $2k_F$. The static, uniform magnetic susceptibility is the usual Pauli one measuring the density of states at the Fermi level:

$$\chi_{\text{SDW}}^0(0, 0) = N(E_F) = \frac{2}{\pi v_F} \quad (9c)$$

B. Electron–Electron Interaction

1. The Hubbard Model

Let us now try to understand the effect of the Coulomb interaction in one dimension. The Hubbard Hamiltonian [Eq. (1)] provides the simplest model for this. There is an exact solution for the ground state and the excitations when $U > 0$ [30], obtained by the Bethe ansatz. The physics has recently been reviewed by Schulz [31]. The collective excitations are of two types. At arbitrary filling, there are “ $4k_F$ ” singlet excitations which are gapless at wave number $k = 0$ and $4k_F$ (a wavelength equal to the average distance between electrons). These are charge excitations whose velocity u_ρ is given by the slope of the excitation spectrum at $k = 0$. At half filling (one electron per site), the $4k_F$ and $k = 0$ excitations are coupled by a reciprocal lattice vector for $U \neq 0$ (umklapp processes) and a gap opens in the charge excitations, yielding $u_\rho = 0$. This gap for small U is given [30] by

$$\Delta \sim 8\pi^{-1} \sqrt{UE_0} \exp\left(-\frac{\pi v_F}{U}\right) \quad (10)$$

and is of order U when large. There are also degenerate “ $2k_F$ ” singlet and triplet excitations which are gapless at $k = 0$, $2k_F$, and $4k_F$ and whose velocity at $k = 0$ is u_σ . This degeneracy implies the existence of two noninteracting spin- $\frac{1}{2}$ objects called spinons. This picture is confirmed by calculating the energy needed to add (or remove) an electron (the quasiparticle energy). The total energy of the added particle is just the sum of the charge and spinon components. The charge and spin degrees of freedom do not interact. This is a central feature of electron behavior in one dimension. This spin and charge separation had been seen early on in the large U limit since the system was shown to behave as a decoupled set of spinless fermions (the carriers) and localized magnetically coupled spins [32]. We can see this in the case of a half-filled band by following the arguments of Schulz. There is strong short-range antiferromagnetic order [33] with the typical configuration $\uparrow \downarrow \uparrow \downarrow \uparrow \downarrow \uparrow \downarrow \uparrow \downarrow$. Introducing a hole leads to $\uparrow \downarrow \uparrow \downarrow \uparrow 0 \uparrow \downarrow \uparrow \downarrow$. If the hole moves, this changes to

$\uparrow \downarrow 0 \uparrow \downarrow \uparrow \uparrow \downarrow \uparrow \downarrow$, whereas spin flips lead to $\uparrow \downarrow 0 \uparrow \downarrow \uparrow \downarrow \uparrow \uparrow \downarrow$. The original configuration has evolved into a configuration with a hole surrounded by antiferromagnetically aligned spins (charge, no net spin) and an independent spin misalignment (no charge, excess spin $\frac{1}{2}$), which are the holons and spinons postulated in the context of the HTS [34]. The static magnetic susceptibility is $\chi_{\text{SDW}}(0, 0) = N(E_F)(v_F/u_\sigma)$. The spinon velocity being smaller than the Fermi velocity, the Coulomb repulsion thus increases the magnetic susceptibility.

For $U < 0$, the analysis of Emery [16] captures the essence. The attractive interaction favors singlet pairing and the system develops superconducting fluctuations. The charge- or pair-density fluctuations are gapless in the absence of umklapp processes. The spin excitations develop a gap of order U since singlet pairs need to be broken to create spin excitations.

2. Bosonization

The model Hamiltonian [Eq. (3)] defined on a continuum has some exact solutions [35]. These have culminated in what is now known as the bosonization technique, in which the interacting fermion fields can be expressed in terms of boson field operators. This method is reviewed in Refs. 15, 16, and 31.

For a repulsive interaction, one obtains two decoupled free boson field equations and thus recovers the separation of charge and spin central to the Hubbard Hamiltonian. The ground state is shown to be a Luttinger liquid. The electron occupation is no longer discontinuous at the Fermi level. It is continuous albeit with a singularity of the form $(n_{k\sigma} - \frac{1}{2}) \propto -\text{sign}(k - k_F)|k - k_F|^\alpha$. The density of states vanishes at the Fermi level. This power law singularity is characteristic of one-dimensional correlations and also appears in the various response functions [Eq. (8)]. $\chi_{\text{CDW,SDW}}(2k_F + q, \omega)$, $\chi_{\text{SS,TS}}(q, \omega)$ are found to have the following power laws:

$$\chi_\alpha \sim (\zeta)^{\gamma_\alpha} |\ln(\zeta)|^{\beta_\alpha} \quad (11)$$

where ζ is as in Eq. (9b). Here $(\gamma, \beta) = (1 - K_\rho, -\frac{3}{2})$ for CDW, $(1 - K_\rho, \frac{1}{2})$ for SDW, $(1 - 1/K_\rho, -\frac{3}{2})$ for SS, and $(1 - 1/K_\rho, \frac{1}{2})$ for TS. K_ρ is a single parameter associated with the charge excitations. The one associated with the spin excitations, K_σ , is not relevant to these low-temperature exponents. They are given in bosonization by [15–17]

$$K_\rho \approx \left[\frac{1 + \tilde{g}_4 - (\tilde{g}_2 - \tilde{g}_1/2)}{1 + \tilde{g}_4 + (\tilde{g}_2 - \tilde{g}_1/2)} \right]^{1/2} \quad K_\sigma \approx \left[\frac{1 - \tilde{g}_4 + \tilde{g}_1/2}{1 - \tilde{g}_4 - \tilde{g}_1/2} \right]^{1/2} \quad (12)$$

where $\tilde{g}_i = g_i/\pi v_F$. SS and TS response functions are large if $K_\rho > 1$, CDW and SDW otherwise. It should also come as no surprise, because of the gapless charge excitations in the Hubbard model at $k = 4k_F$, that the

charge response function also develops a power law dependence at $4k_F$: $\chi_{\text{CDW}}(4k_F + q, \omega) \sim (\zeta)^{2-4K_\rho}$. This would become singular if \tilde{g}_2 were large enough and might explain the $4k_F$ fluctuations seen in x-ray measurements seen in a number of compounds [13, 36]. The behavior of K_ρ for the repulsive Hubbard Hamiltonian is nontrivial especially close to half-filling (it quickly goes to the value $\frac{1}{2}$) but one always has $\frac{1}{2} < K_\rho < 1$ [31]. The $4k_F$ charge response is thus not singular for the Hubbard Hamiltonian.

In the presence of umklapp processes, the charge bosons are no longer free. They are bound by a cosine potential energy term of amplitude $|g_3|/2\pi$, so the charge excitations have a gap of this magnitude which can be felt at low temperatures. Under those circumstances, only the SDW susceptibility remains singular with $\gamma_{\text{SDW}} = 1$ (see, however, the refinement when umklapp are present in Section IV.B.3.d).

For attractive interactions (actually, for negative g_1) a similar cosine term appears in the spin equation. The spins develop a gap of order $|g_1|/2\pi$. The CDW and SS susceptibilities keep their power law behavior with

$$\gamma_{\text{CDW}} = 2 - K_\rho \quad \gamma_{\text{SS}} = 2 - \frac{1}{K_\rho} \quad (13)$$

3. Renormalization

(a) Method

There are also renormalization group (RG) treatments of the Coulomb interactions. Although less precise quantitatively, they have proven to be very useful qualitatively. The basic ideas of renormalization can be found in Refs. 4 and 37. The underlying principle is that of self-similarity. Although the value of the parameters composing the Hamiltonian is arbitrary, this Hamiltonian is presumed to retain its form at different length (energy) scales. The parameters should tend asymptotically to their fixed-point value as the lengths (energies) tend to infinity (zero). In this way, one can presumably describe systems close to phase transitions when the correlation length becomes infinite (or in one dimension when the temperature goes to zero). One tries to find a recursion relation for the (smooth) variation in the value of the parameters and of all functions of interest as the scales change. This can be done in momentum or coordinate (see Refs. 4 and 37) space.

In momentum space, one uses the logarithmic behavior characteristic of the free-electron gas response (in Section IV.A) to add the contributions at various energy (or momentum) scales. One does this using perturbation theory at the higher energies. It is, as such, a weak-coupling theory, whose range of validity is restricted to small values of $\tilde{g}_\alpha = g_\alpha/\pi v_F$. Multiplicative

renormalization [15] laid the ground rules in this respect. Working with the g-ology Hamiltonian, it construed recursion relations at a given external frequency by varying the natural high energy or momentum cutoff. This cutoff was scaled to small values and the flow behavior of the various parameters of the model was deduced. I will not describe this method since its results are contained in a more general approach developed by Bourbonnais [18].

This method is more in the traditional philosophy of the Kadanoff–Wilson [38] procedure. The guiding hypothesis is that the short-length (high-energy) behavior is not singular. The former can thus be integrated out, leaving a renormalized Hamiltonian acting on the lower-energy degrees of freedom that are left. This Hamiltonian can then be rescaled back to its original scale, if one wishes, to bring out fully the self-similarity of the procedure and to assess the relevance of the various parameters. One starts from the linearized single-electron band of Fig. 3 (although this is not essential in the Bourbonnais formalism). A high-energy cutoff E_0 is introduced to regularize the procedure (restore the bandwidth and remove singularities in momentum integrations). It is of the order of the Fermi energy. At each step of the RG, the degrees of freedom (k values) in the shells of width $dE_0/2 = E_0 dl/2$ (i.e., those contributing to the *quantum*

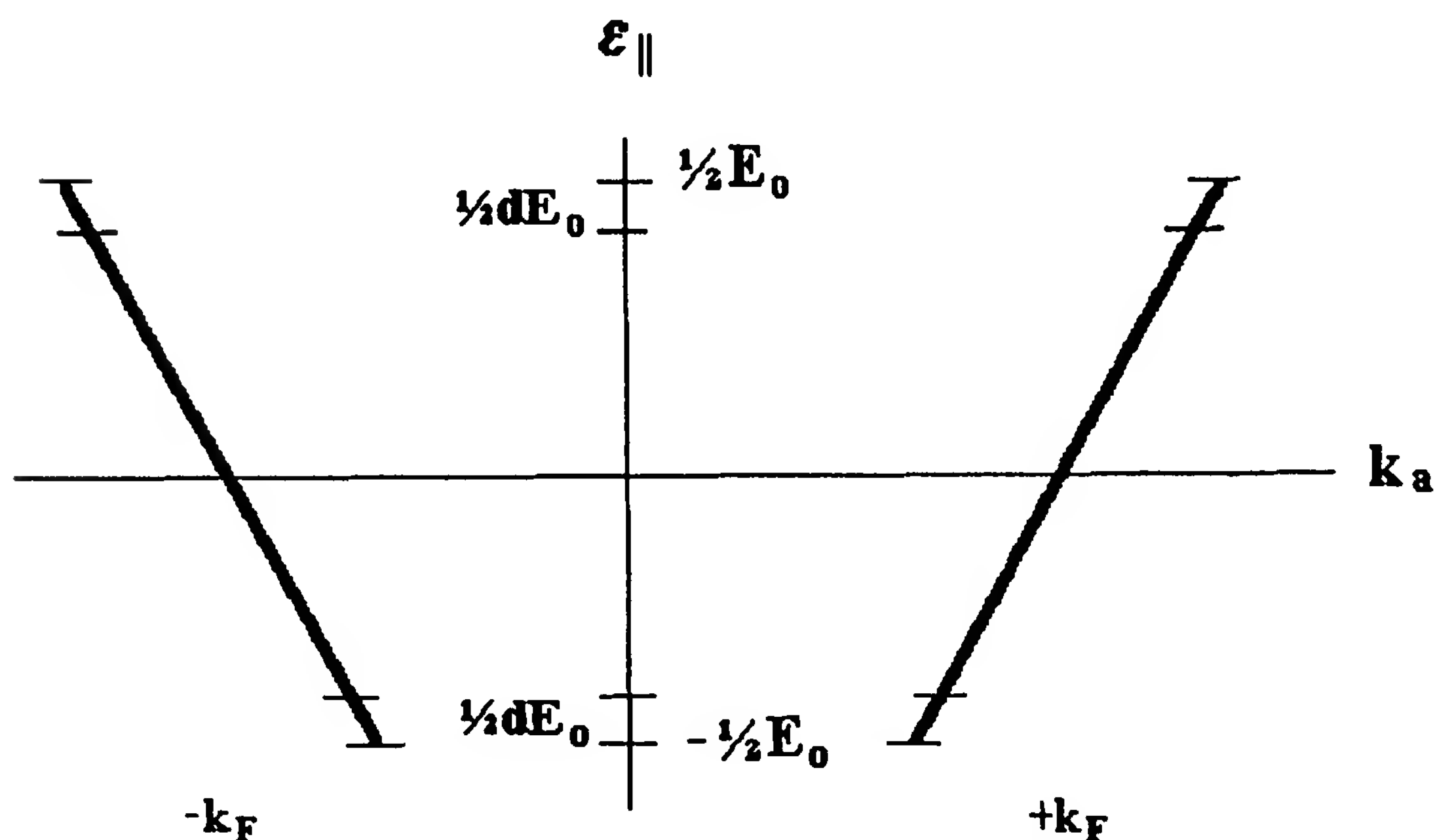


Figure 3 Linearized electronic energy spectrum around the Fermi surface ($k = \pm k_F$). The degrees of freedom in the energy shells of width $dE_0/2$ at the extrema of the spectrum are integrated over in each step of the renormalization group.

fluctuations) are integrated on. Let me illustrate this. Although formulated using Grassmann variables in Ref. 18, the partition function of statistical physics can be thought of as $Z = \text{Tr}_< \text{Tr}_\eta e^{-\beta(H_{0<} + H_{0\eta} + H'_< + H'_{<\eta} + H'_\eta)}$, where the index $<$ refers to those degrees of freedom that are left and η to those in the shells, and H_0 and H' correspond to the free particle and interaction terms, respectively. Loosely speaking, integration over η can be performed using the cumulant expansion

$$Z = Z_{0\eta} \text{Tr}_< \exp \left[-\beta(H_{0<} + H'_<) + \sum_n \frac{C_{n<}}{n} \right]$$

where

$$C_{n<} = (-1)^n T_\tau \int_0^\beta d\tau_1 \cdots d\tau_n \langle (H'_{<\eta}(\tau_1) + H'_\eta(\tau_1)) \cdots (H'_{<\eta}(\tau_n) + H'_\eta(\tau_n)) \rangle_{0\eta,c}$$

is the n th cumulant. This is only approximately correct since one has to neglect any nonlocality in time for the degrees of freedom that are left in $C_{n<}$. Here $\langle \cdots \rangle_{0\eta,c} \propto dE_0$ is the connected part of the thermodynamic average over the shells using the unperturbed $H_{0\eta}$ and $Z_{0\eta} = \text{Tr}_\eta e^{-\beta H_{0\eta}}$. The cumulant expansion is perturbative and thus so is the RG. Under the scaling, one has $E_0 \rightarrow E_0(1 - dl)$. dl is thus the generator of the RG. As the energy scales down, the quantum coherence length (the length over which the quantum fluctuations have been integrated on) scales up: $\xi \rightarrow \xi(1 + dl)$. As a result, $H'_< \rightarrow H'_< - \beta^{-1} \sum_n C_{n<}/n$. The cumulants $C_n \propto dl$ are dimensionless. This proportionality to $dl = -d \ln(E_0)$ gives the RG its characteristic logarithmic structure. The nature of the cumulants is such that they breed single-particle, two-particle, and multiparticle (>2) terms. The single-particle term leads to self-energy corrections, whereas the two-particle term generates corrections to the coupling g_i . The multiparticle terms are irrelevant in the sense that they do not grow in the scaling process. So are nonlocal, in space and *time*, changes in the interactions or the nonlinear corrections to the electronic spectrum.

The following RG structure is obtained. The single-particle Green function, whose poles give the quasiparticle energies and whose residues measure the effective weight of the quasiparticles, transforms as $G(k, \omega_n)_{E_0(l+dl)} = z^{-1}(dl) G(k, \omega_n)_{E_0(l)}$. Note that the free-electron Green function is $G^0(k, \omega_n) = [i\omega_n - \varepsilon_{\parallel}(k)]^{-1}$. The interactions transform as $g_i(l + dl) = z_i(dl) z^{-2}(dl) g_i(l)$. Now what about the response functions. These can be probed by adding the contributions $O_\alpha(q, \omega_n) F_\alpha(q, \omega_n)$ to the Hamiltonian, where the O_α are as in Eq. (7). This field is shown to evolve as $F_\alpha(l + dl) = z_\alpha(dl) F_\alpha(l)$. The $q = 2k_F$ CDW and SDW, and

the $q = 0$ SS and TS susceptibilities are given by

$$\chi_\alpha(l) = \int_0^l \Gamma_\alpha^2(l') \left[\frac{d}{d\ell} \chi_\alpha^0(\ell) \right]_{\ell=l'} dl' \quad (14)$$

In this formula, both vertices of the elementary response [see Eq. (9a)] at every energy scale (in the shell η) are dressed by the vertex correction $\Gamma_\alpha(l) = F_\alpha(l)/F_\alpha(0)$. It is the form of $z(dl)$, $z_i(dl)$, and $z_\alpha(dl)$ which determines the evolution of the parameters.

But when does the scaling process stop? It must stop when (1) the quantum coherence length $\xi = \xi_0 e^l$, where $\xi_0 \approx v_F/E_0$, becomes equal to the thermal coherence length $\xi_{th} = v_F/\pi T$, at which point the thermal fluctuations take over, (2) $E_0(l) = E_0 e^{-l}$ becomes equal to the energy $v_F q$ of the quasiparticles involved in the q dependent response functions [the q of Eq. (9a)] or (3) equal to the external Matsubara frequency ω_m . At that point, one replaces l with ℓ of Eq. (9b).

(b) Renormalization Equations

In second-order renormalization, that is, including second-order corrections in g_i for the z 's, one has

$$\frac{d}{dl} \ln z^{-1}(l) = -\frac{1}{2} \Phi(\tilde{g}_1, \tilde{g}_2, \tilde{g}_3) \quad (15)$$

$$\begin{aligned} \frac{d\tilde{g}_1}{dl} &= -\tilde{g}_1^2 - \frac{1}{2}\tilde{g}_1^3 & \frac{d}{dl}(2\tilde{g}_2 - \tilde{g}_1) &= \tilde{g}_3^2 \left(1 - \frac{2\tilde{g}_2 - \tilde{g}_1}{2} \right) \\ \frac{d\tilde{g}_3}{dl} &= \tilde{g}_3(2\tilde{g}_2 - \tilde{g}_1) \left(1 - \frac{2\tilde{g}_2 - \tilde{g}_1}{4} \right) - \frac{\tilde{g}_3^3}{4} \end{aligned} \quad (16)$$

$$\Phi(\tilde{g}_1, \tilde{g}_2, \tilde{g}_3) = \frac{1}{2} \left(\tilde{g}_1(l)^2 - \tilde{g}_1(l)\tilde{g}_2(l) + \tilde{g}_2(l)^2 + \frac{\tilde{g}_3(l)^2}{2} \right) \quad (17)$$

These equations result from the intimate mixing of electron–electron and electron–hole channels (the Parquet summation). This is of crucial importance in one dimension. The t -matrix or random-phase approximations are incapable of doing this and are fundamentally wrong in one dimension. Notice also that g_4 is absent because it does not alone contribute any logarithmic term. It leads only to charge and spin velocity corrections. It is normally neglected in the RG treatments (see Refs. 15 and 39 for a discussion of this). It will only be taken into account for the uniform susceptibility in part d.

As pointed out by Kimura [40], *when umklapp processes are relevant*, the system can differentiate between site (on the molecules) and bond (in

the intermolecular regions) combinations

$$O_\alpha^M(q) = \frac{O_\alpha(q) + MO_\alpha(-q)}{1 + |M|} \quad (18)$$

for CDW and SDW, where $M = +1$ refers to the site and $M = -1$ to the bond responses. Such combinations are irrelevant for SS and TS, and the value $M = 0$ can be used. The RG equations for the external-field vertices are

$$\frac{d}{dl} \ln(\Gamma_\alpha^M) = \frac{1}{2} \tilde{g}_\alpha^M(l) - \frac{1}{2} \Phi(\tilde{g}_1, \tilde{g}_2, \tilde{g}_3) \quad (19)$$

where

$$\begin{aligned} \tilde{g}_{\text{CDW}}^M &= \tilde{g}_2 - M\tilde{g}_3 - 2\tilde{g}_1 & \tilde{g}_{\text{SDW}}^M &= \tilde{g}_2 + M\tilde{g}_3 \\ \tilde{g}_{\text{SS}} &= -\tilde{g}_1 - \tilde{g}_2 & \tilde{g}_{\text{TS}} &= \tilde{g}_1 - \tilde{g}_2 \end{aligned} \quad (20)$$

(c) Behavior Without Umklapp

Let me first describe the situation without umklapp ($g_3 = 0$). For positive \tilde{g}_1 , the fixed points are at $\tilde{g}_1^* = 0$ and $\tilde{g}_2^* = \tilde{g}_2 - \tilde{g}_1/2$. For negative \tilde{g}_1 , the g 's scale to the strong-coupling values $\tilde{g}_1^* = -2$, $\tilde{g}_2^* = \tilde{g}_2 - \tilde{g}_1/2 - 1$. This can be understood in the following way. g_1 is known from bosonization to be associated with the spin excitations. If g_1 is positive, the electrons will make use of the Pauli principle to avoid one another efficiently. Parallel-spin (triplet) correlations will be favored on which g_1 has no effect. For $g_1 < 0$, the opposite situation prevails. The electrons want to take advantage of the interaction and will thus prefer singlet correlations in which there is nothing to prevent an intimate contact. A gap opens up in the spin excitations.

The single-particle properties are controlled by

$$z^{-1}(\ell) = D(\ell)\zeta^{-\theta} \quad D(\ell) = \exp\left[-\frac{3}{16} \int_0^\ell \tilde{g}_1^2(l) dl\right] \quad \theta = \frac{(2\tilde{g}_2 - \tilde{g}_1)^2}{16} \quad (21)$$

This shows that the weight of the quasiparticles shrinks to zero in a power law fashion, as $\ell, \zeta \rightarrow \infty$, again confirming the results of bosonization. The reason for this is that more and more of the electrons are engulfed into collective quantum fluctuations as the RG proceeds, leaving little time for independent-particle behavior.

One finds that $\chi_\alpha^M \sim (\zeta)^{\gamma_\alpha^M}$. The susceptibility power law exponents close to the fixed point are $\gamma_\alpha^{M*} = \tilde{g}_\alpha^{M*} - \Phi(\tilde{g}_1^*, \tilde{g}_2^*)$. The logarithmic part of

(11) can be obtained by looking at the effect of deviations from scaling [18] that are specific to the particular trajectories to the fixed points. One word of caution is in order: The results of bosonization should be used whenever $\tilde{g}_i(l) < -1$ (for $T < T_\sigma$) since the RG is perturbative and cannot be used quantitatively in the strong-coupling regime.

The general picture emerging from the RG and bosonization at this point for the dominant singular behavior of the response functions is shown in the standard phase diagram of Fig. 4. Depending on the initial value of the g_i couplings, the interacting electron gas in one dimension will develop *quantum fluctuations* favoring one type of response function or another. This diagram is easy to understand. For $\tilde{g}_1 > 0$, we have seen that the electrons prefer triplet pairing over the singlet type. For negative \tilde{g}_1 , singlet pairs form, thus favoring SS or the correlation of pairs into a CDW. $2g_2 - g_1$, the combination associated with the charge excitations [Eq. (12)], will favor the Cooper pairing for negative, attractive values.

(d) *Behavior with Umklapp*

The solutions of Eq. (16) for which the umklapp is relevant (i.e., \tilde{g}_3 flows to strong-coupling values) are for $2\tilde{g}_2 - \tilde{g}_1 > -|\tilde{g}_3|$. A Hubbard gap forms for repulsive charge-excitation interactions. At temperatures below $T_p \sim E_0 \exp(-1/\tilde{g}_3)$ [see Eq. (10)], when the gap in the charge excitations is felt, the perturbative RG results have to be discarded in favor of more exact ones. The calculations of Voit [41] show that the susceptibility power

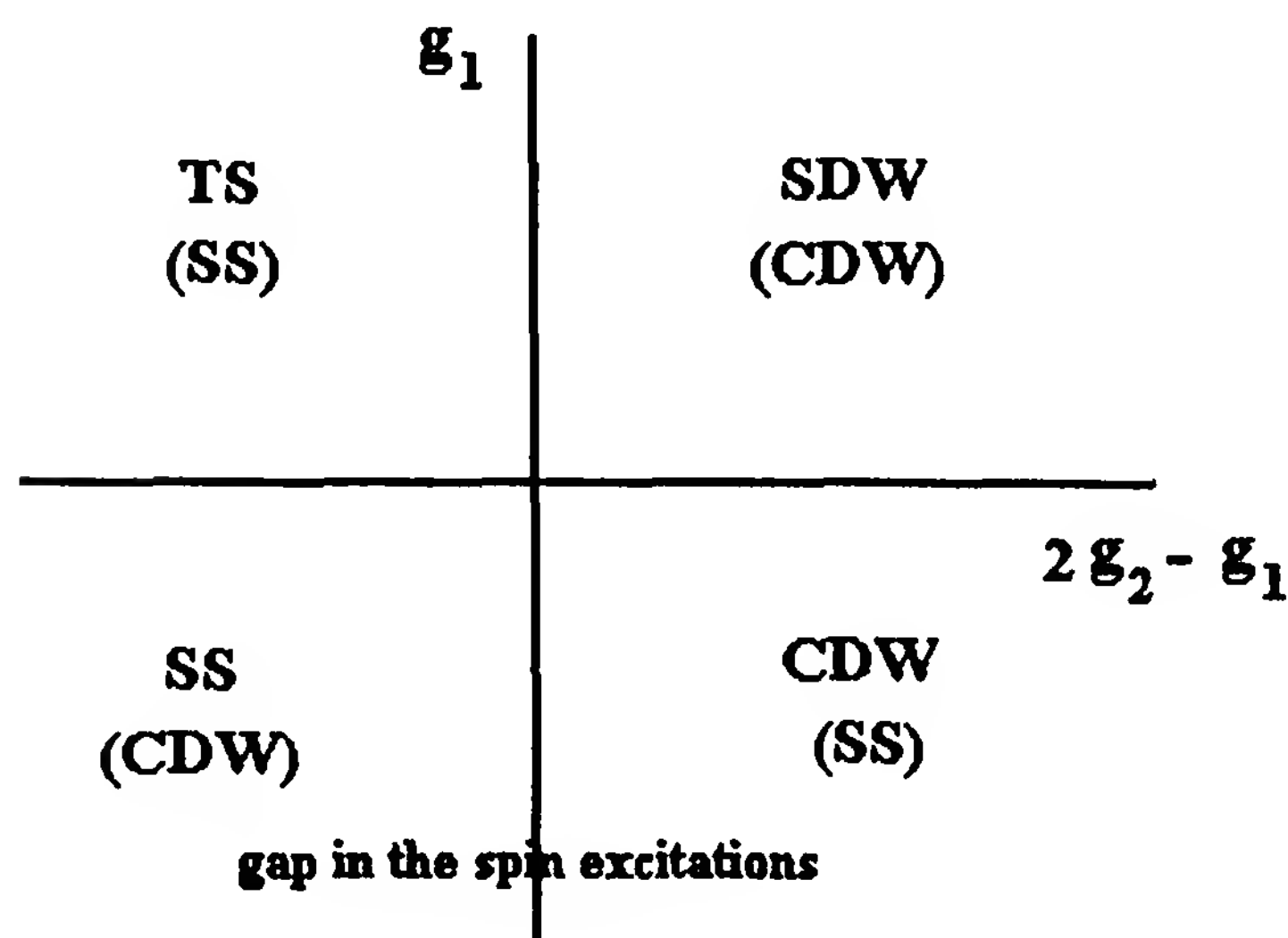


Figure 4 Phase diagram of the interacting electron gas showing the competing response functions with positive power law exponent in the absence of umklapp processes. Those in parentheses have a smaller prefactor.

law exponents of the Hubbard model are

$$\gamma_{\text{SDW}}^{*+1} = \gamma_{\text{CDW}}^{*-1} = 1 \quad (22)$$

whereas all other response functions are nonsingular. The dichotomy between bond and site responses is important to the conducting polymers. It should be noticed that the charge-density operator is proportional to $O_{\text{CDW}}^{+1}(q)$. Consequently, only the site CDW feels the Hubbard gap and not the bond-ordering wave (bond CDW or BOW).

Otherwise, the umklapp interaction flows to zero and the fixed points \tilde{g}_1^* , \tilde{g}_2^* are as before. One also has $z^{-1}(\ell) \sim \zeta^{-\theta^*}$, where $\theta^* = \Phi(\tilde{g}_1^*, \tilde{g}_2^*, \tilde{g}_3^*)/4$, that is, $\theta^* = \frac{3}{4}$ in both the repulsive and attractive sectors. This again confirms the existence of the Luttinger liquid ground state. Figure 5 shows how the phase diagram of Fig. 4 is modified in the presence of umklapp.

(e) *Static Uniform Magnetic Susceptibility*

Let me finally look at the uniform magnetic susceptibility $\chi_{\text{SDW}}(0, 0)$. This susceptibility is affected only indirectly by renormalization. Moreover, it is quite sensitive to g_4 through its noncritical effect on the velocity of the spin excitations (see Section IV.B.1). It is found to be approximately given

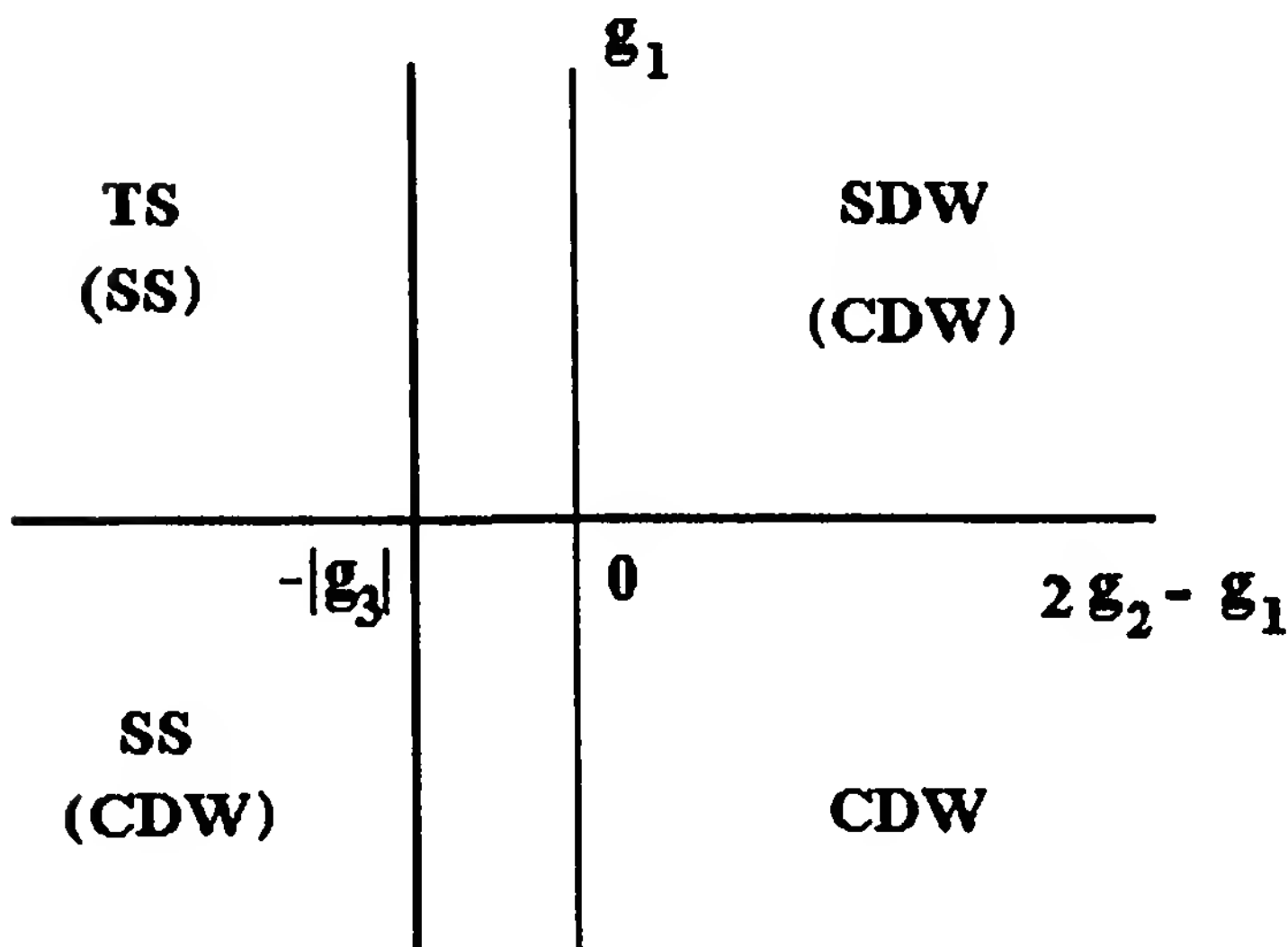


Figure 5 Phase diagram of the interacting electron gas showing the competing response functions with positive power law exponent in the presence of umklapp processes. Those in parentheses have a smaller prefactor. There is a gap in the charge excitations to the right of the $-|g_3|$ line and one in the spin excitations for negative g_1 .

by [39]

$$\chi_{\text{SDW}}(0, 0) = \frac{N(E_F^*)}{1 - g_1(\ell)/2\pi v_F^*} \quad v_F^* = v_F \left(1 - \frac{g_4}{2\pi v_F} \right) \quad (23)$$

although nonlogarithmic corrections are required at finite temperatures and large interactions [42]. The susceptibility is seen to be enhanced by repulsive interactions, a trait readily observed in random-phase-approximation (RPA) or mean-field estimations. This has the well-known Stoner enhanced form $\chi \sim N(E_F)/(1 - \tilde{U})$. But Eq. (23) says more. This enhancement is modulated in one dimension, due to the variation of g_1 with temperature. This is an observed feature in the charge-transfer salts [39].

4. t - J Model

It is proper to say a few words about the one-dimensional t - J model (6) at this point. Its ground-state phase diagram is by now fairly well understood [43,44]. As mentioned previously, the $J/t < 1$ region has the signature of the Hubbard model at large U . For larger J/t , a limit in which the parental ties to the Hubbard model are severed, things are different. First, K_p can be larger than 1, indicating a dominance of superconducting fluctuations (diverging susceptibility exponent). There is, moreover, a phase separation for J/t approximately larger than 3 into a segment of spins (site occupancy of 1) and a vacuum.

C. Electron–Phonon Interaction

The Hamiltonians of relevance here are the molecular crystal [Eq. (4)] and the SSH Hamiltonians [Eq. (5)]. The electron–phonon interactions have the following forms [45]:

$$H_v = N^{-1/2} \sum_{q,k,s} g_v(k, q) \varphi(q) c_{k+qs}^+ c_{ks} \quad (24)$$

where $v = \text{MC, SSH}$, c_{ks} is the Fourier transform of c_{is} , $\varphi(q) = b_q + b_{-q}^+$, b_q is the usual phonon annihilation operator, $\omega_0(\omega_q)$ is the optical (acoustical) phonon frequency, and

$$g_{\text{MC}}(k, q) = \frac{\lambda}{(2M\omega_0)^{1/2}}$$

$$g_{\text{SSH}}(k, q) = \frac{i4\lambda \sin(qa/2) \cos(ka + qa/2)}{(2M\omega_q)^{1/2}} \quad (25)$$

Note that this equation implies that the phonons of the SSH (MC) model couple to the combination O_{CDW}^{-1} (O_{CDW}^{+1}), that is, to the BOW (site CDW) response function.

1. Phonon Softening

The phonon propagator has a definition akin to Eq. (8):

$$\begin{aligned} D(q, \omega_m) &= - \int_0^\beta e^{-i\omega_m \tau} \langle \varphi^+(q, \tau) \varphi(q, 0) \rangle \\ &= \frac{-2\omega_q}{\omega_m^2 + \omega_q^2} \end{aligned} \quad (26)$$

It is obviously ideally suited to measuring the effect of the electron quantum fluctuations on the phonon frequency. What one immediately learns from Eq. (26) is that the propagator is quasistatic; that is, the $\omega_m = 0$ component dominates for $T > \omega_q/2\pi$. This comes from the definition of the Matsubara frequencies for bosons [under Eq. (8)]. As far as the electrons are concerned, the atoms move very slowly (the adiabatic limit). If $2g_2 - g_1 > -|g_3|$ (see Fig. 5), the electrons are able to screen the slow lattice motion and thus soften the interactions. We are obviously interested in the $2k_F$ phonons, which will be screened most effectively by the dominant $2k_F$ charge response of the one-dimensional electron gas.

(a) Incommensurate Systems

Let me first illustrate the approach with incommensurate systems, that is, those for which the band filling n_f (the average number of electrons of a given spin in the conduction band per unit cell) is an irrational number. There are no electronic umklapp processes.

The standard RPA “bubble” diagram summation prevails for static processes. The result is

$$D(q, 0) = D^\circ(q, 0)[1 + g_{1\text{ph}}\chi_{\text{CDW}}(\ell)]^{-1} \quad (27)$$

where $g_{1\text{ph}} = |g_v(-k_F, 2k_F)|^2 D^\circ(2k_F, 0) < 0$ is an effective electronic backward scattering term and D° is the undressed (bare) phonon propagator. As $g_{1\text{ph}}$ is negative, a growing χ_{CDW} will result in a softening of the $2k_F$ phonon frequency $\omega_q(\ell)/\omega_q = D^\circ/D(\ell) < 1$. We know that χ_{CDW} increases at least logarithmically with ℓ for free electrons and in a power law fashion for an interacting electron gas. When the denominator of Eq. (27) becomes equal to zero, at $T = T_P^\circ$ or $\chi_{\text{CDW}}(\ell_P^\circ) = -g_{1\text{ph}}^{-1}$, the RPA structure has already become unreliable. This is interpreted as signaling the presence of the Peierls or periodic lattice distortion (PLD) instability in the phonons at $2k_F$, a CDW for the MC model and a BOW for the SSH model. This is commonly seen in various organic conductors [36]. A mean-field treatment, although inappropriate in one dimension, can be found in Ref. 46. T_P° is the mean-field Peierls transition temperature. It is given by $T_P^\circ \sim \pi^{-1}E_0(|\tilde{g}_{1\text{ph}}|)^{1/\gamma_{\text{CDW}}}$ for a strongly correlated system and by $T_P^\circ \sim \pi^{-1}E_0 \exp(-1/|\tilde{g}_{1\text{ph}}|)$, the well-known BCS expression, without correla-

tions. The electrons are affected similarly. Indeed, the electrons feel the quasistatic lattice fluctuations that couple the electronic states at $\pm k_F$. As a result, a pseudogap (fluctuating) of amplitude $2\Delta_{\text{PLD}} \approx \pi T_P^\circ$ wants to open at $\pm k_F$.

The RPA can be improved on by the Landau–Ginzburg (LG) formalism [47] appropriate in a quasistatic regime. One introduces a complex order parameter $\psi(x)$ (dimensions of energy) associated with $\Delta_{\text{PLD}}(x)$, which can also be related to the amplitude of the lattice distortion [Eqs. (4 and 5)] $u_i, q_i \propto e^{i2k_F x_i} \psi(x_i) + e^{-i2k_F x_i} \psi^*(x_i)$. It is complex because the phase of the CDW or BOW at $+2k_F$ is independent of the one at $-2k_F$. The partition function is expressed as a functional integral weighing all fluctuations in the order parameter $Z = \int \mathcal{D}\psi e^{-\beta F\{\psi\}}$, where the free-energy functional is

$$F\{\psi\} = \int_0^L dx \left[a|\psi(x)|^2 + b|\psi(x)|^4 + c \left| \frac{d\psi(x)}{dx} \right|^2 \right] \quad (28)$$

Here $a = a'(t - 1)$, $t = T/T_P^\circ$, and a', b, c are either phenomenological parameters or else they can be calculated from mean-field calculations [48] or better yet, by using the Hubbard–Stratonovich transformation to convert the partition function into a functional integral [39]. In the latter case, one obtains around $t = 1$ the values

$$a \approx (g_{1\text{ph}})^{-1} [1 + g_{1\text{ph}} \chi_{\text{CDW}}(\ell)]$$

$$a' \approx T_P^\circ \left[\frac{\partial \chi_{\text{CDW}}(\ell)}{\partial T} \right]_{T=T_P^\circ}$$

$$c \approx \left[\frac{\partial \chi_{\text{CDW}}(\ell)}{\partial q^2} \right]_{T=T_P^\circ, q=0}$$

$$b \approx \frac{7\Gamma_{\text{CDW}}^4(\ell_P^\circ)}{16\pi^3 v_F (T_P^\circ)^2}$$

The parameter c measures the rigidity of the system to spatial variations in the order parameter and is intimately linked to the excitation spectrum. Equation (28) can be solved by the transfer matrix method. It maps the problem into that of a quantum particle of mass $m^* = 2c/T^2$ moving in a two-dimensional potential well $a|\psi|^2 + b|\psi|^4$. The axial symmetry implies that $\langle \psi \rangle = 0$, that is, no LRO, as expected from the Mermin–Wagner theorem. For temperatures less than T_P° , one has $a < 0$ and the well develops a minimum at $|\psi|^2 = |a|/2b$. At low temperatures, the effective particle gets confined to the well and $\langle |\psi|^2 \rangle = a'/2b \sim (\pi T_P^\circ / \Gamma_{\text{CDW}})^2$. The amplitude of the order parameter is rather well defined at low temperatures. It can undergo only high-energy oscillations, the amplitudons. Things are different for the phase, however. It is related to the azimuthal position

of the effective particle in the well. The latter can move freely at the bottom of the well, due to the axial symmetry. The phase is not fixed. This corresponds to the Frölich mode of an incommensurate system whereby the PLD can freely slide (the Goldstone mode) and give rise to a collective contribution to the electrical conductivity [49]. It is also related to the phasons of Rice [50]. The order parameter correlation function is given by $\langle \psi^*(x)\psi(0) \rangle \approx |\langle 0|\psi|1 \rangle|^2 e^{-|x|/\xi(T)}$, where $|0\rangle$ ($|1\rangle$) refers to the ground (first excited) state of the effective particle and

$$\xi(T) = \frac{T}{\varepsilon_1 - \varepsilon_0} \approx \frac{2a'c}{bT}$$

is the thermal correlation distance. It is finite because of the thermal-phase fluctuations. Notice the exponential behavior of the correlation function, a signature of thermal fluctuations. The static response function for the order parameter is

$$\chi_{\text{PLD}}(2k_F + q) \approx \frac{2\xi(T)\langle |\psi|^2 \rangle}{T(1 + q^2\xi(T)^2)} \quad (29)$$

As already mentioned, the LG theory is valid inasmuch as the quasistatic picture prevails [i.e., the cutoff energy $E_0(\ell) \approx \pi T$ is larger than ω_q]. On the one hand, if it should happen that $\pi T_P^\circ > \omega_q$, the fluctuations and the pseudogap will both develop for $T \approx T_P^\circ$, while the renormalization procedure is still active. This will, in turn, quickly wipe out the density of states around the Fermi level and freeze out any further contribution of the electrons to the various response functions. This puts an end to the RG process and consecrates the low-temperature static (classical) nature of the system. There is a quantum-classical crossover. This occurs in TTF-TCNQ, for which the fluctuating PLD is seen at temperatures larger than the phonon energy [13]. On the other hand, if $\pi T_P^\circ < \omega_q$, the PLD instability is quenched by the quantum fluctuations before they have a chance to develop. The RG parameter space is enlarged following the crossover to a nonretarded (nonadiabatic) regime at $E_0(\ell) \approx \omega_q$. This is obviously most likely to occur for the MC model. In this new quantum regime, the dynamics of the phonons is no longer negligible compared to the electron energies that are left. There are new effective electronic interactions $g_i \rightarrow g_i + g_{\text{iph}}(\ell_{\omega_q})$ in action. Here

$$\tilde{g}_{1\text{ph}}(\ell) = \tilde{g}_{1\text{ph}}\Gamma_{\text{CDW}}^2(\ell)[1 + \tilde{g}_{1\text{ph}}\chi_{\text{CDW}}(\ell)]^{-1}$$

while $\tilde{g}_{2\text{ph}}$ is not affected by the PLD [39,45]. The phase diagram of Fig. 4 points to the leading fluctuations at lower temperatures.

(b) *Weakly Commensurate Systems*

If $n_f = p/r$ is a fraction other than $\frac{1}{2}$, the system is said to be weakly commensurate. There now appears in the LG free-energy functional a weak commensurability term [51] of the form $\frac{1}{2}d\{[\psi(x)]^r + [\psi^*(x)]^r\} = d|\psi(x)|^r \cos r\theta$, coming from an r -vertex bubble in which $r2k_F$ is equal to a reciprocal lattice wave number ($2\pi p/a$). Here $d \sim B\Gamma_{\text{CDW}}(\pi v_F)^{-1}(E_0)^{-r+2}$, where

$$B = \prod_{m=1}^{r-1} [|g_v(-k_F + m2k_F, 2k_F)|^2 D^\circ(2k_F, 0)/g_{1\text{ph}}]$$

accounts for the fact that $(r - 1)$ phonon-mediated electron interactions in the r -vertex bubble are off the energy shell (off the Fermi surface). The transfer-matrix solution now involves an effective particle in the potential $a|\psi|^2 + b|\psi|^4 + d|\psi(x)|^r \cos r\theta$. This is quite a change from the incommensurate situation for the phase part of the distortion. It now sees a periodic potential and bands form. The energy-level spacing $(\varepsilon_1 - \varepsilon_0)$ thus decreases and $\xi(T)$ increases. Commensurability has a stabilizing effect on the phase fluctuations. At low enough temperatures, the bandwidth will become small as the effective particle gets contained within the well minima in which it undergoes harmonic motion. But it can also tunnel through the potential barrier separating two minima. Assuming a barrier height of $V_B \approx d|\psi(x)|^r$, a width π/r , and an azimuthal mass $m_\theta^* = m^*\langle|\psi|^2\rangle$, the tunneling probability per unit time is

$$S \approx \exp\left(-\frac{\pi}{r} \sqrt{\frac{m_\theta^* B \Gamma_{\text{CDW}} \langle|\psi|^r\rangle}{2\pi v_F E_0^{r-2}}}\right) \\ \approx \exp\left[-\frac{AB^{1/2}}{r(\Gamma_{\text{CDW}})^{1/2}} \frac{\pi T_P^\circ}{T} \left(\frac{\pi T_P^\circ}{\Gamma_{\text{CDW}} E_0}\right)^{r/2-1}\right],$$

where A is a constant of order 1. S is a measure of the bandwidth. Consequently, $(\varepsilon_1 - \varepsilon_0)$ gets multiplied by S while the correlation length $\xi(T)$ gets increased by the factor S^{-1} . It thus acquires an exponential dependence on the temperature, as does the susceptibility χ_{PLD} . The commensurability acts as a weak pinning potential, which quickly becomes irrelevant as r increases, the more so the larger the Coulomb enhancement of the vertex (Γ_{CDW}).

The phasons of the incommensurate situation now have a gap. They have become the finite-energy harmonic-phase oscillations in one of the r “pinning” minima. They will couple to external electric fields and can explain why the intramolecular symmetric phonons can show up in optical reflectivity measurements as in TEA-TCNQ₂ [52]. The tunneling at low temperature is the manifestation of solitonic excitations [53]. The solitons

here are phase discommensurations or misadaptations. The system would like to be phase-ordered (in one of the minima of the well), but the thermal fluctuations can produce a local excitation separating two ordered regions with different phases (the tunneling). From the form of S , one deduces that the solitons have an energy

$$E_S = A \frac{\pi T_P^\circ}{r(\Gamma_{\text{CDW}})^{1/2}} \left(\frac{\pi T_P^\circ}{\Gamma_{\text{CDW}} E_0} \right)^{r/2-1}$$

This is in general agreement with Refs. 54 and 55 when $\Gamma_{\text{CDW}} = 1$, although, as realized in Ref. 55, the situation when r is a multiple of 4 is special in the SSH case since $B = 0$, due to the disappearance of one of the $g_\nu(-k_F + m2k_F, 2k_F)$. For instance, when $r = 4$ and $\Gamma_{\text{CDW}} = 1$ they found that $E_S \sim \pi T_P^\circ (\pi T_P^\circ / E_0)^2$. Following the arguments of Ref. 56, one deduces that a soliton has a width

$$w = \frac{E_S}{V_B} = \frac{A \pi (\Gamma_{\text{CDW}})^{1/2}}{r B^{1/2}} \left(\frac{\Gamma_{\text{CDW}} E_0}{\pi T_P^\circ} \right)^{r/2-1} \xi_{\text{th}}^P$$

where ξ_{th}^P is the thermal coherence length at T_P° . We can thus foresee a soliton energy smaller by $\pi T_P^\circ / \Gamma_{\text{CDW}} E_0$ and a width correspondingly larger for the case $r = 4$. The soliton wavefunction is $\delta\theta = (\pi/r) \tanh[(x - x_0)/w]$. It is a kink soliton corresponding to a phase shift of $2\pi/r$ from one side to the other. It has a fundamental fractional charge of $\pm e/r$ and may carry spin [57]. The case $p = 2, r = 3$ can be used to illustrate this. Suppose that we have a charge transfer of two electrons for three molecules from cations. The idealized trimerized ground state would show alternating sequences of two electrons in the bonding orbital of each trimer: $\cdots \bullet-\bullet-\bullet \quad \bullet-\bullet-\bullet \cdots$. One of the three possible tightly confined soliton would look like $\cdots \bullet-\bullet-\bullet \quad \bullet \quad \bullet-\bullet-\bullet \cdots$. The “isolated” molecule can have an electron or not and sits in an ionic environment with charge $+2e/3$ per molecule. This soliton thus has effective charge $-e/3$ with spin $\frac{1}{2}$ or $+2e/3$ and no spin.

It might happen that there are umklapp processes present because of the presence of a weak lattice modulation at $4k_F$ which results in the presence of a small gap Δ_D at $k = \pm 2k_F$ but none at $\pm k_F$. This is the case for TEA-TCNQ₂ [52] or in the TMTTF₂X and TMTSF₂X families [36,58], for instance, in which $r = 4$. There then appear weak umklapp terms $g_3 \approx g_1(\Delta_D/E_0)$ [59] and $g_{3\text{ph}} \approx \pm g_{1\text{ph}}(\Delta_D/E_0)$. The plus sign (negative sign) is for the MC (SSH) model [39]. The preceding theory must be modified to account for these. $g_{1\text{ph}}$ is replaced with $g_{\text{ph}} = g_{1\text{ph}} + M g_{3\text{ph}}$, where $M = 1$ for site and $M = -1$ for bond PLD. $\chi_{\text{CDW}}(\ell)$ and $\Gamma_{\text{CDW}}(\ell)$ are replaced with $\chi_{\text{CDW}}^M(\ell)$ and $\Gamma_{\text{CDW}}^M(\ell)$. Since a negative g_{ph} is required for any insta-

bility, it is apparent that the BOW (site CDW) instability is favored if g_3 is positive (negative), as in the SSH (MC) model, and if the temperature is low enough for the umklapp to be relevant (see Ref. 59). There also appears an additional umklapp term in the free-energy functional because of this coming from a three-vertex bubble: $(\Gamma_{\text{CDW}})^2(\pi v_F)^{-1}|\psi(x)|^2(\Delta_D/E_0)\cos 2\theta$. The solitonic structure is thus profoundly modified by this term, which dominates over the commensurability one. The solitons have

$$E_s = A \frac{\pi T_P^\circ}{2} \left(\frac{\Delta_D}{E_0} \right)^{1/2} \quad w = \frac{A\pi}{2} \left(\frac{E_0}{\Delta_D} \right)^{1/2} \xi_{\text{th}}^P$$

They are quite a bit narrower and have a larger energy.

If the system is nearly commensurate, discommensurations will naturally form and separate ordered commensurate phases. These discommensurations have a gapless excitation spectrum [60]. This subject has been reviewed in Ref. 61.

(c) *Half-Filled Band*

The case of a half-filled band, with strong commensurability, is quite similar to the weakly commensurate situation with umklapp. It just requires a slight adaptation. The main difference is that the order parameter is real since there is no difference between the distortion at $+2k_F = 2\pi/a$ or the one at $-2k_F$. Again the BOW instability is favored in the SSH model. One should again be reminded that the BOW carry no net charge. This corresponds to the situation in the conducting polymers [23]. The effective particle of the LG theory now sits in a one-dimensional potential $a\psi^2 + b\psi^4$. At low temperature, the only excitations are the high-energy amplitudons (no more phasons) and tunneling from one well minimum to the next. The amplitude solitons are otherwise quantitatively similar to the phase solitons with umklapp in Section IV.B.3.d if one puts $\Delta_D = E_0$. They correspond to a change of sign of the order parameter from one side to the other, $\text{sign}(\psi) = \pm \tanh[(x - x_0)/w]$, and are labeled soliton or antisoliton depending on the sign change. Discommensurations (soliton lattice) are also possible and are believed to occur at intermediate doping in the polymers. This is discussed fully in Refs. 57 and 62.

It is an interesting exercise to examine the BOW and its excitations in the tightly bound situation used to illustrate the third-filled band solitons in the preceding section. The dimerization is shown in Fig. 6a, along with the bonding and antibonding dimer-orbital energies. One of the two possible amplitude solitons is shown in Fig. 6b. There is a trimer at the soliton location with its three molecular orbitals shown. There is an insertion of one level at midgap, the nonbonding orbital. It is made up of one-half of an antibonding orbital (conduction band) state and one-half of a bonding

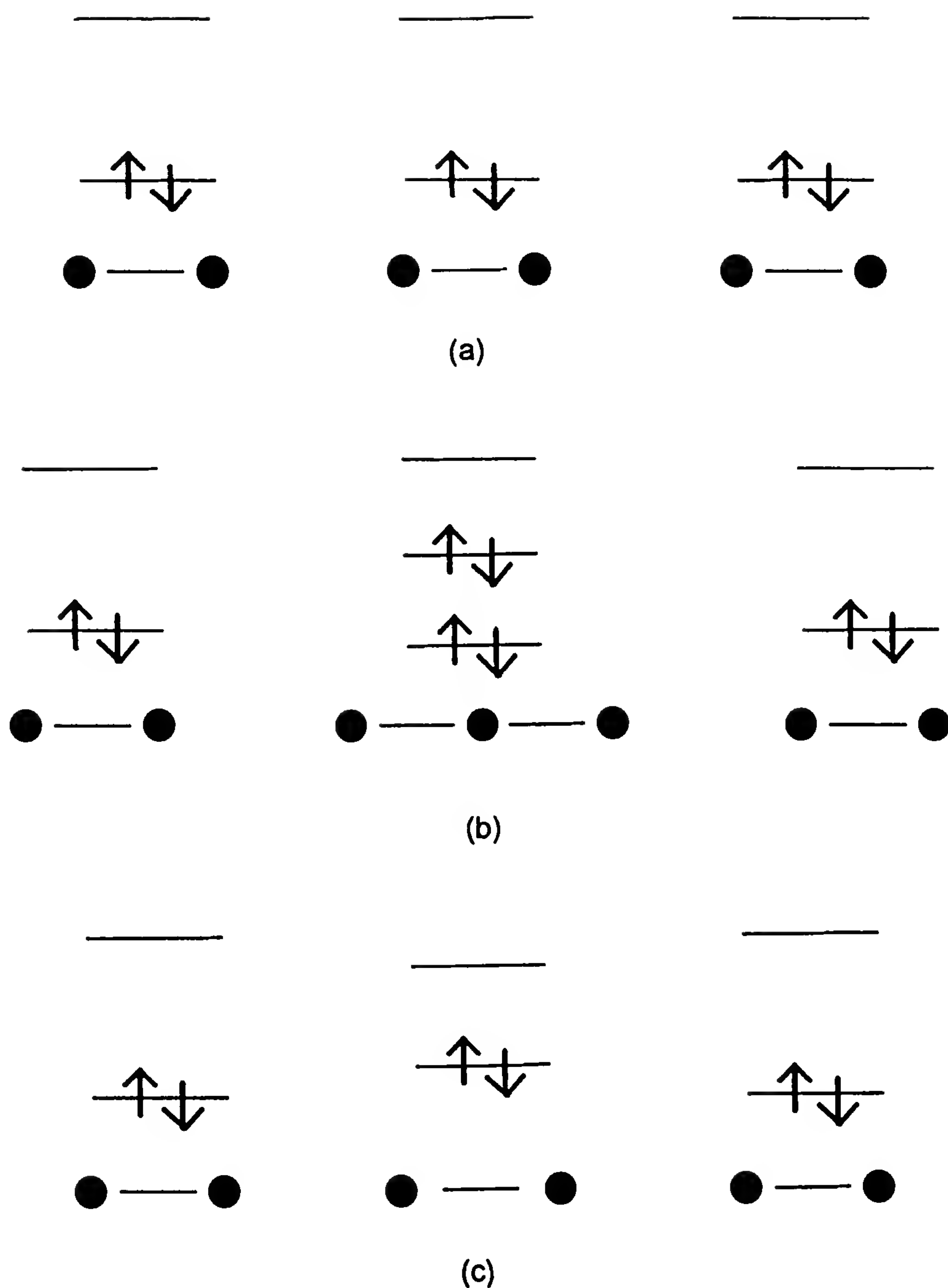
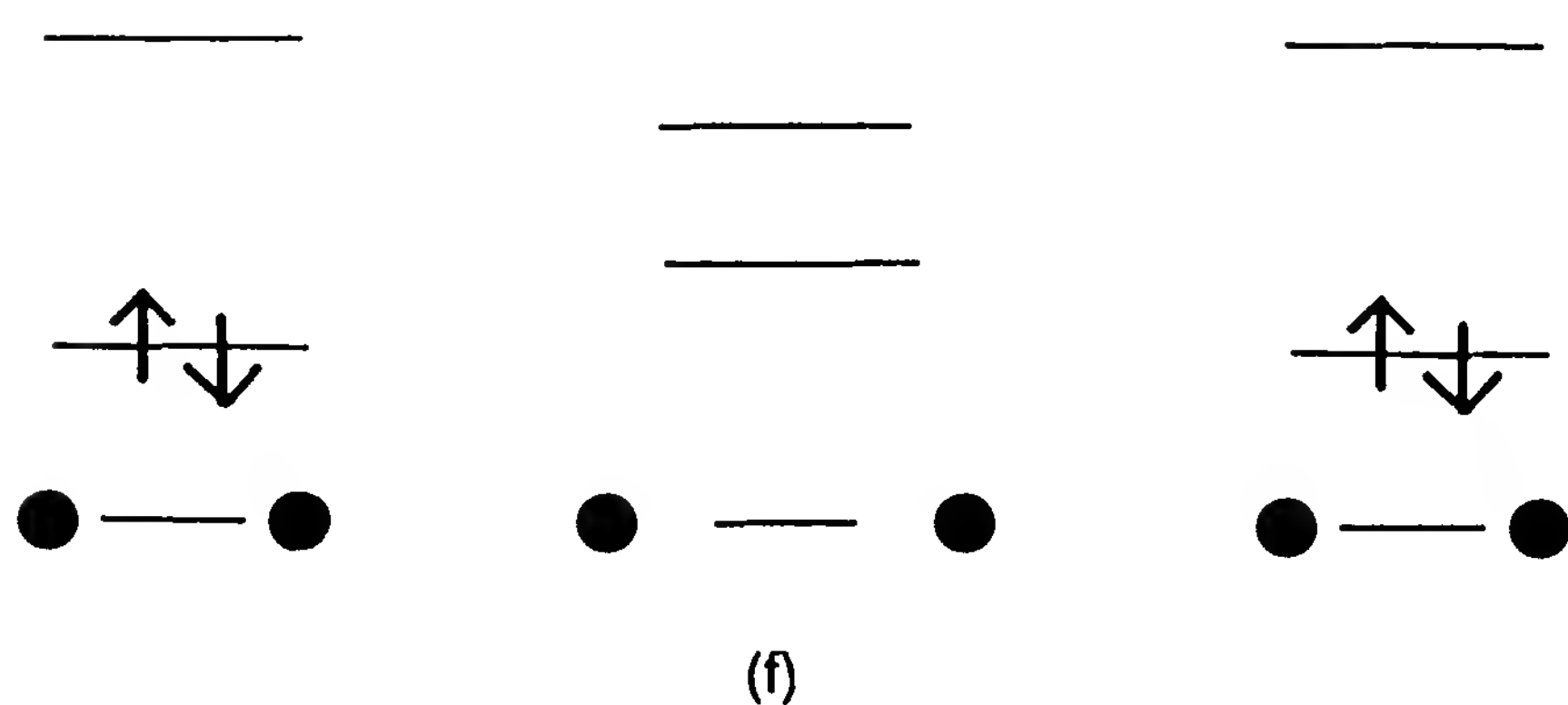
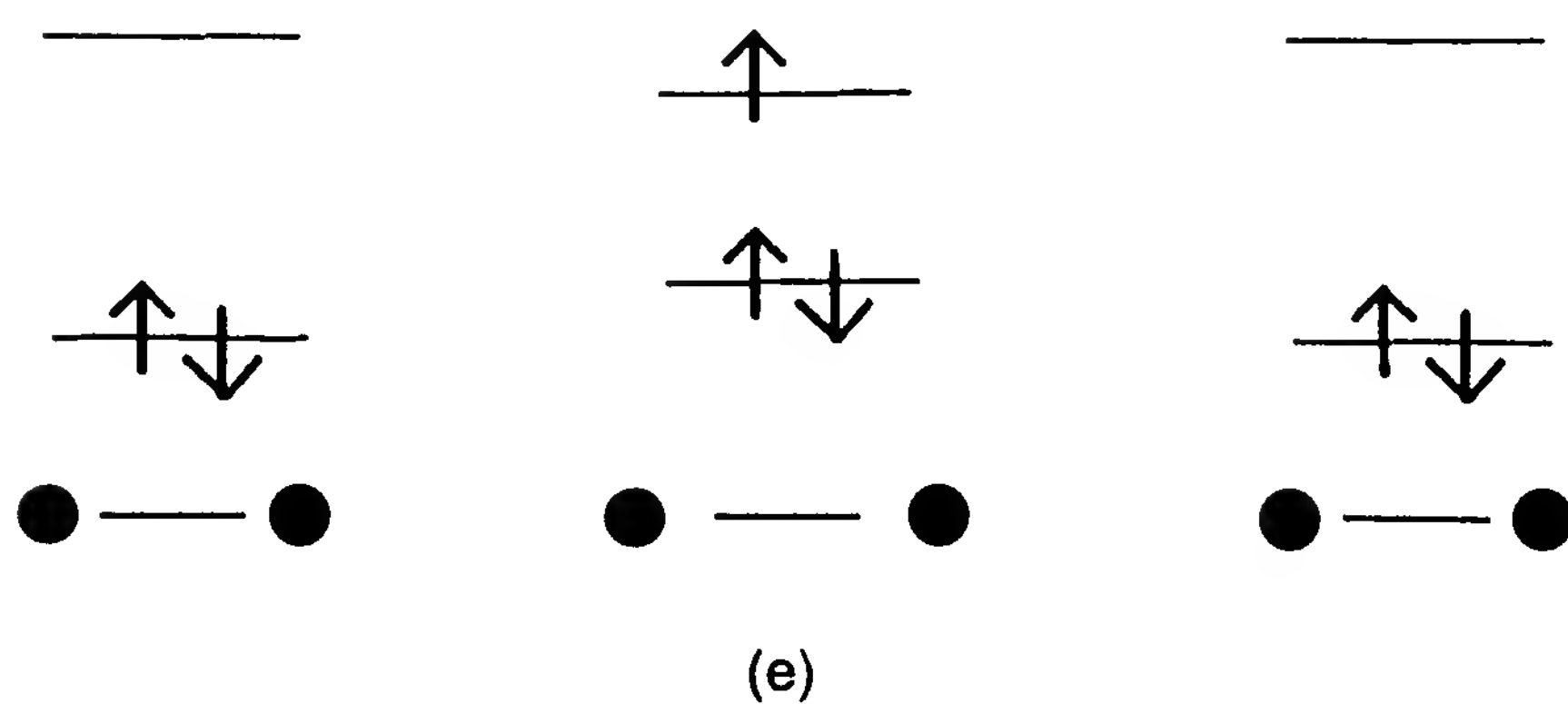
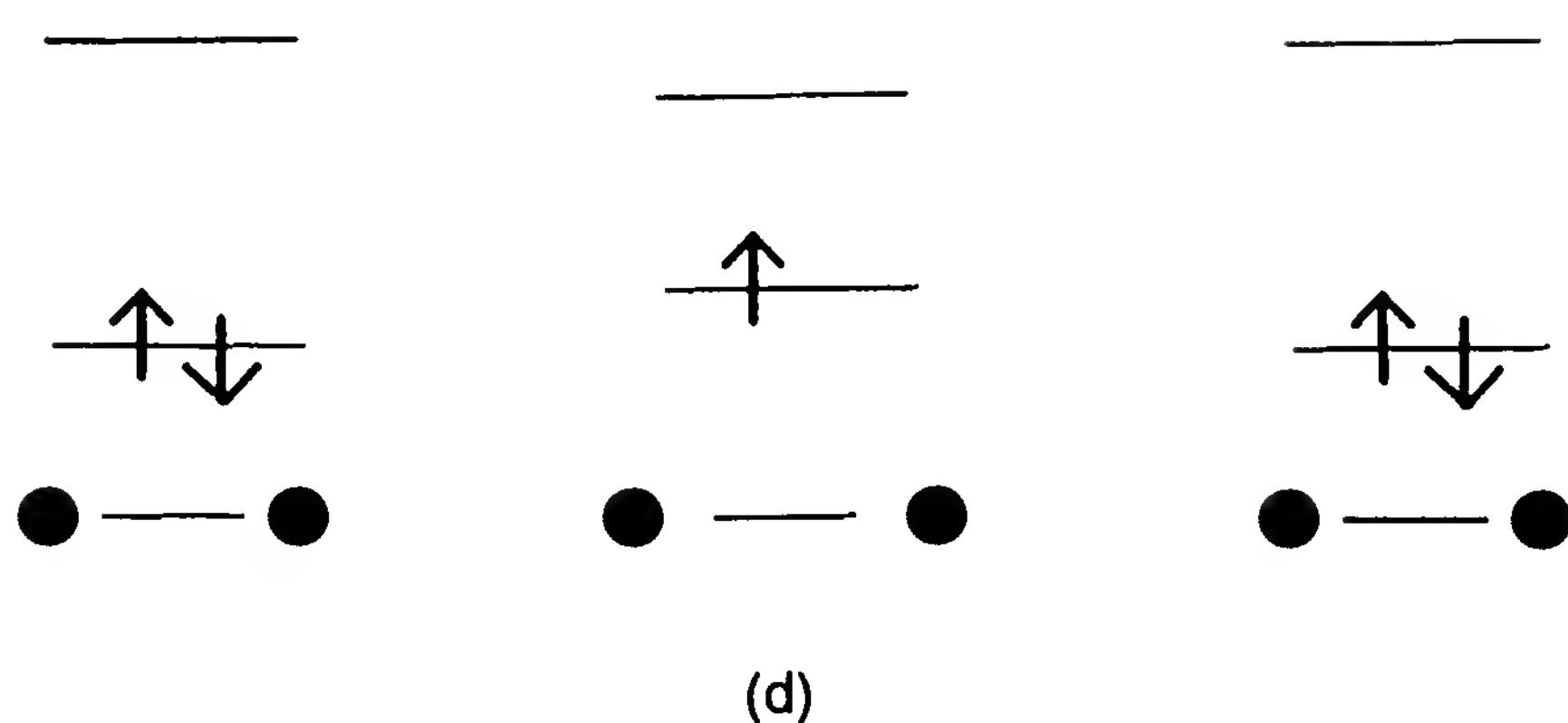


Figure 6 Segments of dimerized linear chains showing the spatial molecular arrangements of the dimers with their bond (lower part), and the molecular orbital energy level positioning with the electron distribution (upper part). The electrons and their spin are shown as upward or downward pointing arrows. They show (a) a perfectly dimerized chain, (b) a negatively charged soliton, (c) a local stretching fluctuation (unstable) of a dimer and its gap, (d) a positively charged polaron, (e) a negatively charged polaron, (f) a doubly charged positive bi-polaron, (g) a doubly negatively charged bi-polaron, and (h) a neutral bi-polaron.



orbital (valence band) state. This is the soliton level. The soliton shown is the one with charge $-e$. It has no spin. The sibling neutral soliton is the one with one of the electrons in the nonbonding orbital missing. It has spin $\frac{1}{2}$. If one tries to remove a second electron in the midgap state, the structure becomes unstable against the formation of a neutral soliton and a positively charged polaron. Polarons and bi-polarons are excitations shown in Fig.

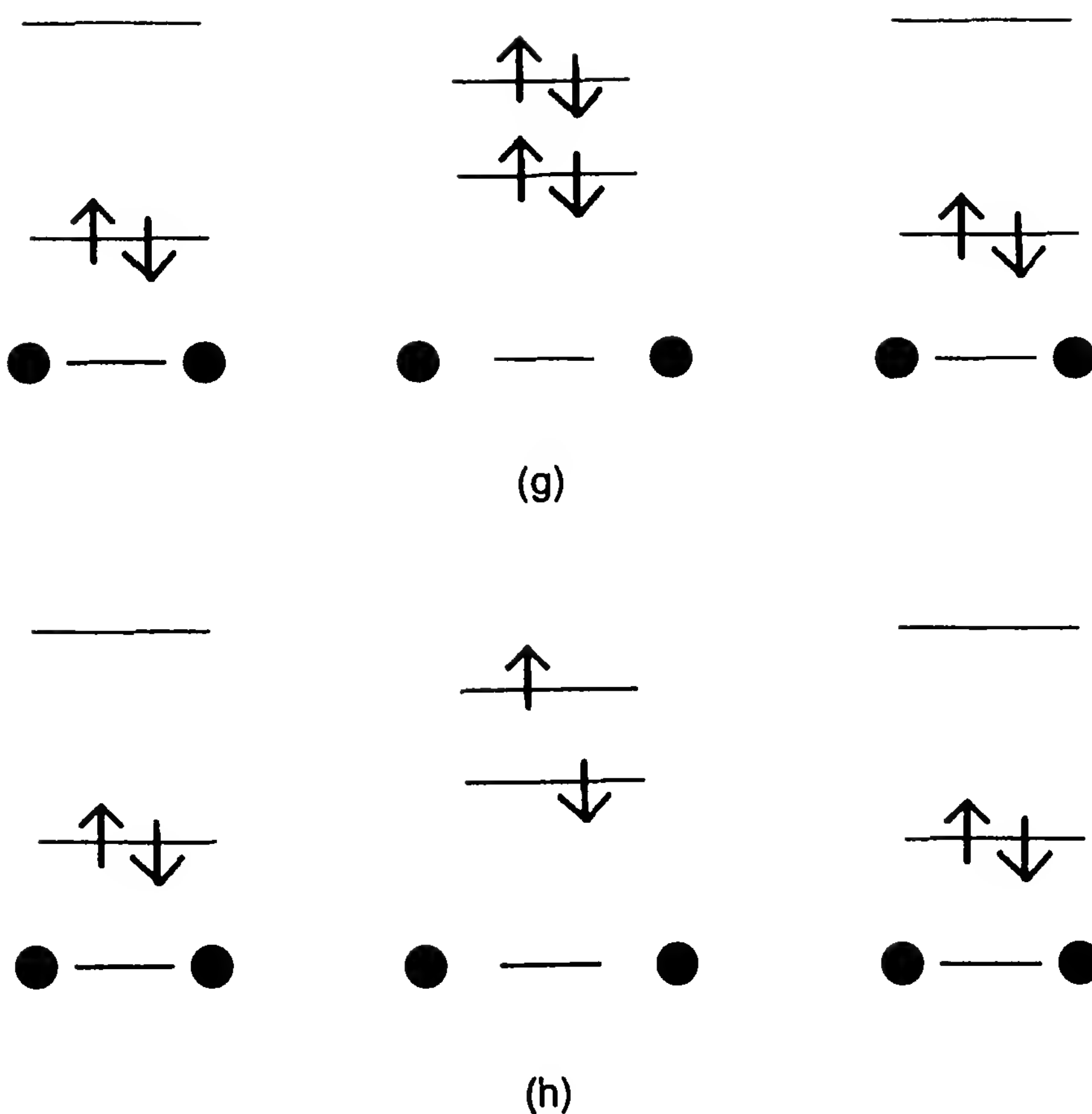


Figure 6 Continued

6d to h. They are formed in a local gap modulation. Such a modulation without electron rearrangement is shown in Fig. 6c. One dimer has stretched and the gap (bonding–antibonding energy difference) has decreased, introducing two states in the gap (one from each orbital or band). As is, this modulation is unstable since there is nothing to hold back the stretched bond. The stretching can be stabilized by weakening the bonding in this dimer. This can be done in a number of ways. One electron can be removed from the bonding orbital (Fig. 6d) or one added to the antibonding one (Fig. 6e). These are the $+e$ and $-e$ charged, spin- $\frac{1}{2}$ polarons, respectively. Starting from the configuration of Fig. 6c, the two electrons in the bonding orbital can be removed (Fig. 6f), two more can be added to the antibonding orbital (Fig. 6g), or one can be removed from the bonding orbital and put in the antibonding one (Fig. 6h). These are the $+2e$, $-2e$, and neutral bipolarons, respectively.

2. Superconducting Fluctuations

The only window for superconducting fluctuations in the repulsive sector (Section IV.C.1.a) is below the nonadiabatic crossover $\pi T_P^\circ < \omega_q$ under the conditions of small Coulomb interactions and sizable (negative) \bar{g}_{2ph}

and $\bar{g}_{1\text{ph}}(\ell_{\omega_q})$. The condition is most likely for the MC model. This is the approach in Ref. 22 to a conventional phonon-mediated binding mechanism for Cooper pairs.

A less constraining situation in which the superconducting fluctuations can prosper is the attractive sector $2g_2 - g_1 < -|g_3|$ (Fig. 5). The relevant combination for the Cooper channels is $g_{\alpha\text{ph}} = \pm g_{1\text{ph}} - g_{2\text{ph}}$, the minus (plus) sign describing the SS (TS) situations (20). LG theory is not possible. Superconducting quantum fluctuations ($g_\alpha + g_{\alpha\text{ph}} > 0$) are more likely for SS than for TS, remembering that the bare phonon interactions are negative. The instability is easier to sustain in the MC model than in the SSH model, which has a small $\bar{g}_{2\text{ph}}$ value. Umklapp and commensurability have no effect on superconducting fluctuations in this sector.

D. Effect of Disorder

One-dimensional conductors are very sensitive to localization [63]. The reason is that the electrons cannot possibly avoid defects or impurities in one dimension and that the backscattering part easily leads to localized states (coherent backscattering between two defects) at low enough temperature. The effect of this is seen in resistivity and magnetic measurements [64]. The analysis of Giamarchi and Schulz [65] for disorder and nonmagnetic impurities is quite revealing. They have looked at the effect of forward and backward defect scattering using a RG approach and bosonization.

1. Forward Scattering

The effect of forward scattering is quite simple. There is no effect on conductivity or on the TS and SS response functions. Forward scattering does not break the single-particle coherence or the $q = 0$ pair coherence because of the fundamental time-reversal symmetry in the model used, which leads to a persistent degeneracy of the paired particles. But it is not so for the $2k_F$ CDW and SDW particle-hole pairs. The lifetime broadening is felt by these pairs. Their RG growth process is halted by it roughly when $E_0(\ell) \approx \tau^{-1}$, where τ is the scattering lifetime. Their response functions are no longer divergent.

2. Backward Scattering

The effect of backward defect scattering is more subtle. There are coupled flow equations for τ^{-1} , g_1 , and K_ρ [see Eq. (12) for its definition]. The main effect of the disorder is to generate an effective electron backward scattering proportional to τ^{-1} that subtracts to g_1 and accordingly acts to decrease K_ρ . There are three possible sets of fixed points.

(a) Delocalization

The fixed points are $(\tau^*)^{-1}$, $g_1^* = 0$. There is a line of fixed points for K_ρ . This situation requires that $K_\rho^* > 2$, that is, $2\bar{g}_2 - \bar{g}_1 < -(1 + \bar{g}_4)/3$, and

g_1 be reasonably large and positive. The disorder is irrelevant and the regular power law exponents for the response functions are recovered. Thus the superconducting fluctuations are not affected.

(b) Strongly Attractive Sector

The fixed points are $(\tau^*)^{-1} = 0$ and $g_1^* \rightarrow -\infty$. This situation requires that $K_\rho^* > 3$ and g_1 be small or negative. The disorder is irrelevant and the normal results for the attractive sector prevail. There is a gap in the spin excitations. Only the SS fluctuations can diverge with $\gamma_{SS} = 2 - (K_\rho^*)^{-1}$. The CDW response is nondivergent for such a large K_ρ .

(c) Localization

This is the region where one is more likely to find the organic conductors. The fixed point is $(\tau^*)^{-1} \rightarrow \infty$ and g_1^* is smaller than the bare value (a line of fixed points). The system crosses over to the strong-coupling regime, in which localization sets in. If $g_1^* < 0$, the spin excitations have a gap and the system will have evolved into one of randomly localized singlet pairs. The localization length is estimated to be $L_{\text{loc}} \propto (E_0/\tau^{-1})^{1/(3-K_\rho)}$, so the localization temperature is given approximately by $\xi_0 \approx L_{\text{loc}}$, that is, $\pi T_{\text{loc}} \sim E_0(\tau^{-1}/E_0)^{1/(3-K_\rho)}$. The static uniform magnetic susceptibility is zero. The resistivity is predicted, from the RG equations, to increase sharply below T_{loc} . But if $g_1^* > 0$, the system develops into a spin-glass-like state. The localization length is now estimated to be $L_{\text{loc}} \propto (E_0/\tau^{-1})^{1/(2-K_\rho)}$, so the localization temperature is approximately $\pi T_{\text{loc}} \sim E_0(\tau^{-1}/E_0)^{1/(2-K_\rho)}$. The resistivity similarly increases below T_{loc} . The susceptibility is typical of the random antiferromagnet [66,67] and has a characteristic power law dependence on temperature $\chi_{\text{SDW}}(0, 0) \propto T^{-(1-2c)}$. These properties have been seen in some compounds [64]. In the localized regime, the various response functions will have frozen to their value at the crossover $\chi_\alpha \approx \chi_\alpha(\ell_{\text{loc}})$.

3. Umklapp

Giamarchi and Schulz [65] have not considered the situation with umklapp. The recent work of Sandvik [68] on the repulsive Hubbard Hamiltonian is instructive, however. Monte Carlo simulations of off-diagonal (bond or hopping) disorder for the half-filled band show that K_ρ , which is zero for the BOW response function in the absence of disorder [Eqs. (11) and (22)], gradually increases with disorder and seems to want to approach 1 for large disorder. What may be happening is that just as the disorder subtracts a term proportional to an upward scaling τ^{-1} off of g_1 , so may g_3 be reduced and have a fixed-point value gradually going to zero by increasing amounts of disorder. Perhaps, too, the effect of site disorder will prove to reduce the effect of umklapp. This is the view of Firsov et al. [17] who argue that

the gap in the charge excitations caused by umklapp will gradually decrease and go to zero beyond a critical defect density. It is otherwise expected that the qualitative effect of disorder described above would apply in the presence of umklapp.

4. Magnetic Impurities

Magnetic impurities affect all response functions [17]. The spin conserving (Ising) part suppresses the power law growth of the triplet SDW and TS susceptibilities, while the spin-flipping part does similar damage to the singlet CDW and SS responses. Any gap in the spin excitations for $\tilde{g}_1^* < 0$ may also disappear beyond a critical impurity concentration. This is in addition to the normal nonmagnetic defect contribution described above. Magnetic impurities thus always lead to localization.

5. Effect on PLD

It is quite obvious from the above that disorder of any kind will reduce the CDW or BOW responses and the PLD fluctuations. Consequently, T_P^0 will decrease and will eventually disappear for large enough disorder [69]. Defects will also pin the Frolich mode and produce phase and amplitude modulations in the order parameter. Impurities may ionize (dopants) and produce charged solitons and discommensurations [70]. The commensurability pinning will decrease, affecting the soliton energy and width, as does the umklapp pinning.

V. PHYSICS IN TWO DIMENSIONS

A. Quasi-One-Dimensional Solids

1. Dimensionality Crossover

Rigorous one-dimensionality is of course a myth in organic conductors. The Coulomb interaction is inherently long range. There is also an unavoidable finite overlap and thus hopping between chains. These lead to two- and three-dimensional couplings and to dimensionality crossovers.

(a) *Single-Particle Crossover*

As seen in Section III, interchain single-particle tunneling leads to a warping of the Fermi surface. As long as the thermal coherence time $\xi_{\text{th}}/v_F = 1/(\pi T)$ is longer than the tunneling time $1/t_b$, the interchain motion will be diffusive. This is shown in Fig. 7a. The system remains one-dimensional but with perturbative effects of hopping. I illustrate the consequence of this incoherent motion in the following section. This effective one-dimensionality also means that the hopping is part of the parameter space that is modified

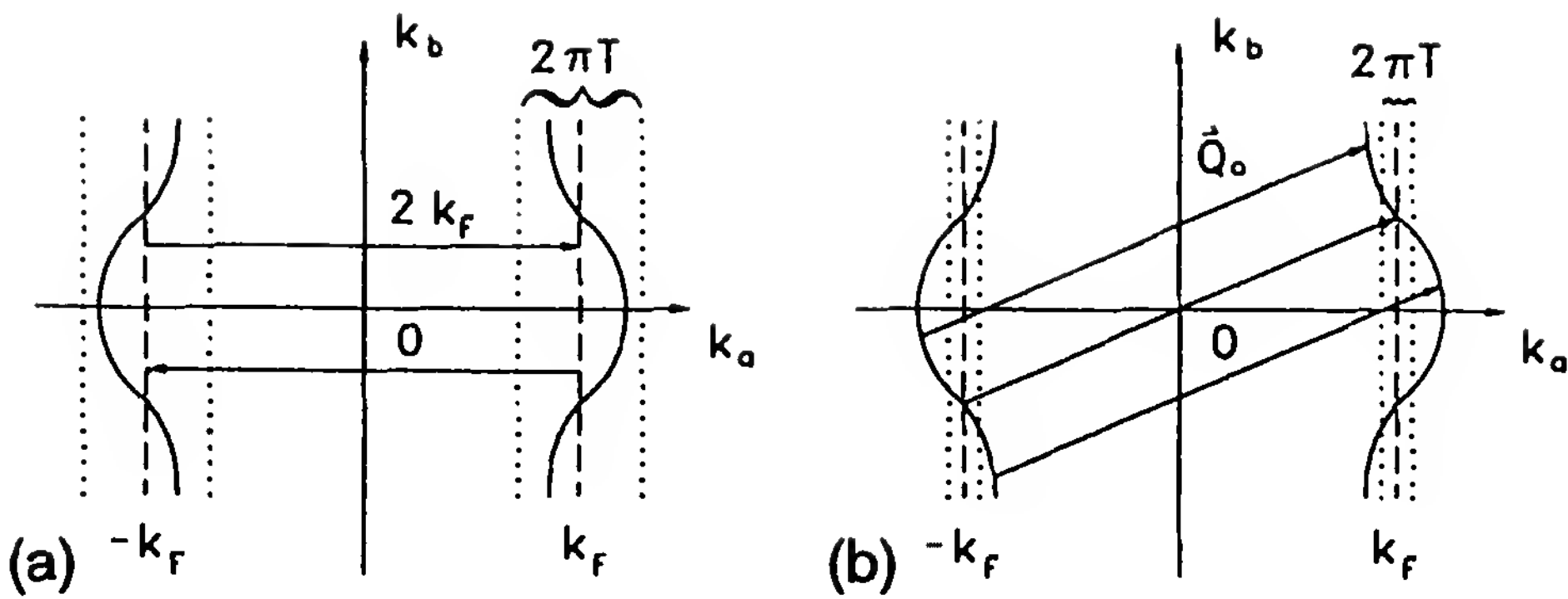


Figure 7 Nesting of the Fermi surface of quasi-one-dimensional conductors. At high temperature (a), the thermal fluctuations hide the warping of the surface and the conductor has a one-dimensional nesting vector $\mathbf{Q}_0 = 2k_F \hat{a}$. At low temperature (b), the warping is felt and there is coherent interchain tunneling with $\mathbf{Q}_0 \approx 2k_F \hat{a} + (\pi/b)\hat{b}$.

by the renormalization procedure. It is in fact reduced to

$$t_b(\ell) = z^{-1}(\ell)t_b \quad (30)$$

In short, all electrons are dressed by the intrachain fluctuations and can only hop to another chain by carrying this fluctuation cloud along with them. This becomes harder and harder the more correlated the electrons are. Because of this, the dimensionality crossover is pushed back because the effective tunneling time $1/t_b(\ell)$ is increased. It will occur at the temperature

$$T_x^1 = \frac{t_b(\ell_x^1)}{\pi} \sim t_b \left(\frac{t_b}{E_0} \right)^{\theta/(1-\theta)} \quad (31)$$

where θ was defined in Eq. (21). It is thus possible, if θ is large enough, that the crossover be pushed to vanishingly small temperatures. This has not been observed in organic conductors, however. For temperatures below T_x^1 , the transverse electron motion is coherent and the conductor becomes two-dimensional; that is, the full Fermi surface becomes relevant.

(b) Two-Particle Crossover

When the transverse hopping is diffusive, the effect of t_b can only be felt through virtual (perturbative) processes that are faster than the quantum coherence time $1/E_0(\ell)$ and in which energy conservation is not required (uncertainty principle). These processes involve pairs of correlated particles in all channels. For instance, a correlated electron-hole pair on one chain can be broken temporarily, one particle hopping to a nearest-neighbor chain (a virtual process) followed a bit later by the other particle, there

reforming the pair. The probability that this process can occur within the quantum coherence time is [71] $P_p P_h P_h P_p$, where $P_p \sim g_\alpha^M(\ell)/\pi v_F$ is the probability that the particles are paired (beginning and end) and $P_h \sim t_b(\ell)/E_0(\ell)$ is the probability that each of the particles can hop within the quantum coherence time. The generator for these pair-tunneling terms is $f_\alpha^M = 2\pi v_F S_\alpha (\tilde{g}_\alpha^M(\ell) t_b(\ell)/E_0(\ell))^2$ [18,39], where $S_{SS,TS} = -1$, $S_{CDW,SDW} = 1$. In short, the RG generates new terms in the Hamiltonian. This is a well-known aspect of RG in the context of real-space renormalization of block spins [4,37]. It is this distinctive capability of the Bourbonnais RG that makes it more attractive than previous formulations for applications to organic conductors.

These interchain terms have a form $V_\alpha^M(Q, \ell) O_\alpha^{M*}(Q) O_\alpha^M(Q)$ [18,39] [see Eqs. (7) and (18)]. All are affected by the RG:

$$\begin{aligned} \frac{d\tilde{V}_\alpha^M(Q, \ell)}{d\ell} &= f_\alpha^M \cos Q_b b \\ &+ 2\tilde{V}_\alpha^M \frac{d\ln(\Gamma_\alpha^M)}{d\ell} - \frac{1}{2} (\tilde{V}_\alpha^M)^2 \end{aligned} \quad (32)$$

where the second and third terms on the right-hand side are the vertex and RPA contributions, respectively. The boundary condition is that $\tilde{V}_\alpha^M(Q, \ell_0)$ be set equal to the bare interchain interaction (Coulomb plus phonon-mediated) $\tilde{G}_\alpha^M(Q, \ell_0) \cos Q_b b$, where $\ell_0 = 0$ in most instances (the bare values at the start of the RG) or $\ell_0 = \ell_{\omega_q}$ in the special case of an unquenched electron–phonon system (see the end of Section IV.C.1.a). The RG equation has a RPA-like pole structure and thus \tilde{V}_α^M would be expected to become singular at some critical $T_{c,\alpha}^{o,M}$. The perturbative analysis above will, however, become unreliable when $|\tilde{V}_\alpha^M| \sim 1$, that is, in the strong-coupling regime for interchain interactions. This defines a two-particle dimensionality crossover $\ell_x^2 = T_x^2$ beyond which the solid is two-dimensional. The expression for this crossover is rather complicated [18]. Note also that the RG procedure will be halted by any CDW or BOW pseudogap developing at T_P^o (see Section IV.C.1).

(c) Classical Crossover

In the situation where a PLD distortion has succeeded in quenching all quantum effects ($T < T_P^o$), any further evolution is controlled by the classical thermal fluctuations. Within the RPA, one has, from Dieterich [47] [see Eq. (29)],

$$\chi_{\text{PLD}}(Q, T) \approx \frac{\chi_{\text{PLD}}(Q_a, T)}{1 + V_{\text{CDW}}^M(Q, T_P^o) \chi_{\text{PLD}}(Q_a, T) / \langle |\psi|^2 \rangle} \quad (33)$$

The dominant part is at $Q_a = 2k_F$ and $Q_b = \pi/b$, where $V_{\text{CDW}}^M(Q, T_P^\circ)$ has its most negative value because of the $\cos Q_b b$ dependence of these interactions. Expanding around $Q_b = \pi/b$, this can be rewritten as

$$\chi_{\text{PLD}}(Q_0 + q_b \hat{b}, T) \approx \frac{\chi_{\text{PLD}}(Q_{0a}, T)}{1 - V_\perp \xi(T) + (V_\perp \xi(T) b^2/2) q_b^2} \quad (33')$$

where $Q_0 = 2k_F \hat{a} + (\pi/b) \hat{b}$ and $V_\perp = 2|V_{\text{CDW}}^M(Q_0, T_P^\circ)|/T$. This defines a transverse correlation length

$$\xi_\perp = b \left[\frac{V_\perp \xi(T)}{2(1 - V_\perp \xi(T))} \right]^{1/2} \quad (34)$$

The crossover occurs when $\xi_\perp = b$. At lower temperatures, the system is two-dimensional with strong correlations between PLD on different chains.

2. Two-Dimensional Regime

At the crossover, a new problem emerges with a new cutoff $E_0(\ell_x^i)$, new interactions $g_\alpha^M(\ell_x^i)$ and $V_\alpha^M(\ell_x^i)$, and new “bare” susceptibilities $\chi_\alpha^M(\ell_x^i)$. The problem is then of characterizing the evolution in temperature of the system below the crossover temperature.

(a) Nesting

When the conductor is at $T < T_x^1$, any further evolution of the solid will be dominated by the two-dimensional Fermi surface, in which the phenomenon of nesting is all important. Figure 7b illustrates this peculiar property of the Fermi surface, where part of the Fermi surface, say at $k < 0$, can superimpose on the other part when translated by wave vector Q_0 . The response functions at this wave vector is dominant. In two dimensions, the mixing between electron–electron and electron–hole channels (see Section IV.B.3.b) does not occur. The RPA structure emerges. At $Q = Q_0$, one has, putting $W_\alpha^M = \tilde{V}_\alpha^M - \tilde{g}_\alpha^M$,

$$W_\alpha^M(Q_0, \ell) = \frac{W_\alpha^M(Q_0, \ell_x^1)}{1 + \frac{1}{2} N_\alpha \tilde{W}_\alpha^M(Q_0, \ell_x^1)(\ell - \ell_x^1)} \quad (35)$$

the boundary conditions being that all model parameters at the crossover ℓ_x^1 be those obtained from the one-dimensional regime. Here N_α is the nesting fraction important to the CDW and SDW channels (SS and TS are unaffected by nesting because of time-reversal symmetry). It is given roughly by the fraction of the Fermi surface for which $|\epsilon(\mathbf{k}_F) - \epsilon(-\mathbf{k}_F + Q_0)| < \pi T$. The susceptibilities are in turn given by the nontrivial expressions with

vertex corrections

$$\chi_{\alpha}^M(Q_0, \ell) = \chi_{\alpha}^M(2k_F, \ell_x^1) + (\pi v_F)^{-1} N_{\alpha} (\Gamma_{\alpha}^M(\ell_x^1))^2 \ln \frac{T_x^1}{T} \times \left[1 + \frac{1}{2} N_{\alpha} \tilde{W}_{\alpha}^M(Q_0, \ell_x^1) \ln \frac{T_x^1}{T} \right]^{-1} \quad (36)$$

The RPA structure can be recognized in the denominator. It is built on the logarithmic bare response of the two-dimensional Fermi surface. The dominant singularity is singled out by the most negative of the $\tilde{W}_{\alpha}^M(Q_0, \ell_x^1)$. This signals the occurrence of an instability at the mean-field temperature $T_{c,\alpha}^{o,M} \approx T_x^1 \exp(-2/N_{\alpha} \tilde{W}_{\alpha})$ (BCS-like equation).

(b) Correlation Regime

Should the solid undergo a two-particle or a classical crossover before the single-particle one, nesting at Q_0 is not relevant. Below the two-particle crossover, the RPA pole defines the attractive fixed point. Equation (32) can be simplified to the bare essential elements

$$\frac{d\tilde{V}_{\alpha}^M(Q, \ell)}{d\ell} = \tilde{V}_{\alpha}^M \gamma_{\alpha}'^M - \frac{1}{2} (\tilde{V}_{\alpha}^M)^2 \quad (32')$$

where $\gamma_{\alpha}'^M$ are strong-coupling exponents similar to Eqs. (13) and (22) [18]. The susceptibility is also RPA-like,

$$\chi_{\alpha}^M(Q_0, \ell) \approx \chi_{\alpha}^M(2k_F, \ell_x^2) + (\pi v_F)^{-1} \left(\frac{T_x^2}{T} \right)^{\gamma_{\alpha}'^M} \times \left[1 + \frac{1}{2} \tilde{V}_{\alpha}^M(Q_0, \ell_x^2) \left(\frac{T_x^2}{T} \right)^{\gamma_{\alpha}'^M} \right]^{-1} \quad (37)$$

Again, as with any RPA approach, this predicts an instability in the channel with the most negative $V_{\alpha}^M(Q_0, \ell_x^2)$. In the case of the classical crossover, the RPA susceptibility is still given by Eq. (33) and corresponds to an “isotropic” interacting systems.

B. Closed Fermi Surface

Whenever $t_a \approx t_b$ the Fermi surfaces will be closed. This is the case with most of the ET salts and the high-temperature superconductors. These solids are intrinsically quasi-two-dimensional. The RG does not apply since there is no one-dimensional regime. Nesting is relevant to only few ET, a

recent example of this being (BEDT-TTF)₂TlHg(SCN)₄ (see Section VI.E). But it is germane to the HTS. Those compounds without nesting will have uneventful CDW and SDW response functions and a Stoner enhanced Pauli susceptibility. The RPA SS and TS susceptibilities resemble Eq. (36):

$$\chi_{\alpha}(0) = \frac{1}{2} N(E_F) \ln \frac{\omega_{\text{ph}}}{T} \times \left[1 + \frac{1}{2} N(E_F) W_{\alpha}(0) \ln \frac{\omega_{\text{ph}}}{T} \right]^{-1} \quad (36')$$

where $W_{\alpha} < 0$ is the effective (RPA screened) two-dimensional Cooper attractive interaction and ω_{ph} is the crossover at which the phonons are no longer retarded. Let us examine two popular models for two-dimensional physical systems.

1. Hubbard Model

The two-dimensional Hubbard model (1) has been studied extensively. Nesting is excellent in the half-filled band defined by $|k_a|a + |k_b|b = \pi$ and deteriorates gradually as the occupancy moves away from this value. As a consequence [see Eqs. (35) and (36)] the CDW and SDW responses will decrease away from $n = 1$. There is also a van Hove singularity in the noninteracting electronic density of states at midband. Note that the inclusion of second-neighbor hopping modifies this considerably.

The attractive Hubbard model is fairly well understood [72]. At half-filling, the ground state exhibits both long-range CDW and SS pairing. Away from half-filling, the CDW is subdued due to imperfect nesting and the system undergoes a Kosterlitz–Thouless transition into a SS state with power law correlations [73] and a gap in the density of states.

The physics of the repulsive model is a bit more uncertain. At half-filling there is definitely SDW LRO in the ground state. Away from half-filling, there is no LRO. Otherwise, things are uncertain. Quantum Monte Carlo simulations [72,74] are inconclusive and indicate that any enhancement would be short distance. This is borne out in Ref. 75. There are signs, however, coming from other approaches [76–79], indicating that *d*-wave pairing might be privileged. A simple view of *d*-wave pairing involves two electrons on nearest-neighbor sites in a spin-singlet configuration. The attractive pairing mechanism here would be through SDW fluctuations. In two dimensions the pairing operator combinations for

superconductivity, akin to Eq. (7), are

$$\Delta_{\beta} = \sum_{\mathbf{k}} A_{\beta}(\mathbf{k}) c_{\mathbf{k}\uparrow} c_{-\mathbf{k}\downarrow} \quad (38)$$

$$A_s(\mathbf{k}) = \cos k_a a + \cos k_b b$$

$$A_p(\mathbf{k}) = \sin k_a a \text{ or } \sin k_b b$$

$$A_{d_{xy}}(\mathbf{k}) = \sin k_a a \sin k_b b$$

$$A_{d_{x^2-y^2}}(\mathbf{k}) = \cos k_a a - \cos k_b b$$

Note that *p*-wave pairing is triplet. Giamarchi and Lhuillier [77] claim that between zero and a critical doping ($\delta = 1 - n \sim 0.2$), SDW and potentially *d*-wave SS coexist. This SS persists until $\delta \sim 0.3$, after which the system would be paramagnetic. It is most likely that the pairing is *d*_{*x*²-*y*²}-like since it is strongest near the [100] parts of the Brillouin zone, thus calling on those regions of the Fermi surface that are at the source of the van Hove singularities (large density of states). It should be noted that the *s*-wave combination in Eq. (38) is not favored on the Fermi surface near half-filling. All other symmetries have zeros on the Fermi surface.

2. *t*-*J* Model

Knowledge about the *t*-*J* model is about at the same level of uncertainty as for the Hubbard model [43]. There is a small Nagaoka ferromagnetic region for $\delta < 0.3$ and $J/t < 0.1$. There is also probably a phase separation, for $J/t > 1$ to 3, depending on band filling, as for the one-dimensional model (Section IV.B.4). The system has antiferromagnetic LRO for $n = 1$. The evidence [79,81] indicates that away from half-filling, this order is only short-range and eventually disappears at $\delta = 0.04$ in favor of *d*-wave pairing (perhaps of resonating-valence-bond, i.e., RVB, type [82]), which in turn would disappear in favor of a Fermi liquid at $\delta = 0.4$ [80]. There is evidence for *s*-wave or perhaps a more exotic hybridized *s*-*d*-wave pairing at the larger values of δ .

C. Transitions in Two Dimensions

As mentioned in Section II, LRO in two dimensions can exist only for a real order parameter, that is, for CDW in a half-filled band. This would be the case for BOW in the polymers or the Peierls state, which would be stabilized by transverse hopping or interchain coupling. This is also the case of the CDW state of the $n = 1$ two-dimensional Hubbard model. All other types of instabilities, such as those treated in the RPA previously in Section V, require three-dimensional coupling to stabilize any LRO.

There is, however, another type of transition possible in two dimensions, a transition between states without LRO. This is the Kosterlitz–Thouless transition [8] mentioned in Sections II and V.B.1. It is relevant to superconductivity, commensurate–incommensurate transitions [61], planar magnetism, the electron gas system, and to many other systems in two dimensions. It involves vortices (thus the requirement of a two-component order parameter) characterized by a winding number $q = (1/2\pi) \oint d\mathbf{r} \cdot \nabla\theta$, in which θ is the phase of the order parameter (see also Ref. 4), the amplitude being fixed. These free vortices have an energy [see Eq. (28)] given by

$$E_V = \frac{J}{2} \int d^2r |\nabla\theta|^2 \approx \pi J q^2 \ln \frac{L}{a} \quad (39)$$

where J is a measure of the microscopic interaction energy scale and L is the length of the system. The logarithmic dependence is typical of vortices. One can estimate the entropy of a free vortex to be $S \approx \ln[(L/a)^2]$, since there are $(L/a)^2$ different nonoverlapping possible positions for it. Vortices will exist in great numbers (a free-vortex gas phase) when their creation energy E_V is overcome by the gain in entropy S . This occurs for $q = 1$ at temperatures above $T_K = E_V/S \approx \pi J/2$, the Kosterlitz–Thouless transition temperature. Below this temperature, vortices will bind in opposite-winding-number pairs with algebraically decaying pair correlations (quasi-LRO). This fluid is permeated with the LRO-destroying phase fluctuations of Section II.

VI. PHYSICS IN THREE DIMENSIONS

We have just seen that some form of three-dimensional coupling is necessary to stabilize most types of LRO. The two-dimensional/three-dimensional crossover will occur very close to the two-dimensional RPA “transition temperatures.” Simply put, the three-dimensional susceptibilities $\chi_\alpha^{3D}(\mathbf{q})$ are related to the two-dimensional ones $\chi_\alpha^{2D}(Q, \ell)$ of Section IV through intersheet interactions $X_\alpha(q_c)$ in an RPA fashion:

$$\chi_\alpha^{3D}(\mathbf{q}) \approx \frac{\chi_\alpha^{2D}(Q, \ell)}{1 + \frac{1}{2} X_\alpha(q_c) \chi_\alpha^{2D}(Q, \ell)} \quad (40)$$

A divergence in (40) identifies a mean-field transition temperature to a state with LRO. Below the transition temperature, there will be an order parameter describing this LRO in which all chains are synchronized. If it is incommensurate, it will be able to slide (the Frölich mode). Close to the transition temperature, there is a critical region in which fluctuations will play an important role [4,5,37]. The RG is a key ingredient in the

study of critical phenomena and critical exponents. Nuclear magnetic resonance (NMR) has proven to be an excellent probe in the quasi-one-dimensional conductors [83]. Various types of transitions are observed in organic conductors.

A. Anion Ordering

In the $(\text{TMTTF})_2\text{X}$ and $(\text{TMTSF})_2\text{X}$ salts with noncentrosymmetric anions X, there can occur an orientation ordering transition [22,36]. This transition originates from the interchain interactions and results in a superlattice structure. This is often coupled to the $2k_F$ CDW response function of the conducting chains and results in the opening of a gap at the Fermi level. There then occurs a metal–semiconductor transition. In the particular case of the very interesting superconductor $(\text{TMTSF})_2\text{ClO}_4$, the anion ordering does not open a gap at the Fermi level but modulates the crystal potential in the b transverse direction. This actually splits the conduction band in two and opens a gap at $k_b = \pi/2b$ [84]. As a result, nesting is destroyed. This has profound consequences for superconductivity.

B. Spin-Peierls Transition

Highly correlated quasi-one-dimensional conductors that have repulsive interactions and electronic umklapp processes will develop a “Hubbard” gap in the charge excitations at $T_\rho \approx E_0 \sqrt{\bar{g}_3} e^{-1/\bar{g}_3}$ [Eq. (10)] provided that this occurs before a one-dimensional/two-dimensional crossover. There is a resistivity minimum at this temperature. This is observed in $(\text{TMTTF})_2\text{X}$, where $\text{X} = \text{Br}, \text{PF}_6$, or in $(\text{TMTSF})_2\text{PF}_6$ (see references in Ref. 39). The umklapp is caused by a slight dimerization [36,58,59] (see Section IV.C.1.b) involving the $4k_F$ response function (see Section IV.B.2). The dimerization gap is observed to decrease under pressure, and thus so do \bar{g}_3 and T_ρ [1,39]. At lower temperatures, the BOW and site-SDW response functions have a power law exponent of 1 [see Eq. (22)]. The RG-generated interchain interactions get frozen to their values at T_ρ . There is then a competition between a phonon instability of the type described in Section IV.C.1 caused by the electron–phonon interaction and a SDW instability. Depending on the relative importance of phonon and interchain interactions, one of these will be favored. This is the BOW in the more correlated systems such as $(\text{TMTTF})_2\text{PF}_6$ [1,39], since the larger T_ρ is, the smaller the RG-generated magnetic interchain coupling $\propto (t_b/T_\rho)^2$ is and the larger $T_P^\rho \propto |\bar{g}_{1\text{ph}}|T_\rho$ is. At T_x^2 , the system becomes two-dimensional and will undergo a transition to a spin-Peierls state at lower temperature due to the RG-generated BOW interchain interaction V_{CDW}^{-1} . The static uniform magnetic susceptibility vanishes exponentially in this state made of local spin-singlet pairs. The

magnetic excitations are to triplet states. This transition is called spin-Peierls because it is magnetically driven in view of the gap of the charge excitations. A traditional view of the spin-Peierls transition can be found in Ref. 85.

C. Antiferromagnetism

There are two mechanisms for antiferromagnetism (AFM). The first one is interchain driven. This was explained in Section VI.B. (TMTTF)₂Br and (TMDTDSF)₂PF₆ are examples [1,39]. T_x^2 is often preceded by a minimum in the resistivity at T_p and is controlled by the SDW interchain interaction V_{SDW}^{+1} generated by the RG above T_p . At lower temperatures the system is two-dimensional and quickly becomes three-dimensional and undergoes a transition to the AFM state at the temperature $T_{c,\text{SDW}}^{\circ,+1} \propto (t_b/T_p)^2$. Under pressure, t_b increases, as does $T_{c,\text{SDW}}^{\circ,+1}$ [1,39].

The alternative mechanism is nesting. If the one-dimensional/two-dimensional crossover is determined by the transverse hopping and occurs before a gap in the charge excitations can develop, the SDW response function will be privileged for repulsive interactions. This is the case in quenched (TMTSF)₂ClO₄ (no anion ordering) and in (TMTSF)₂PF₆ under pressure [1,39]. The effect of external pressure is interesting. It increases t_b and T_x^1 but decreases the repulsive forces. But this is occurring at temperatures at which deviations from nesting caused by $t'_b \propto t_b^2$ [see Eq. (2b) for the definition of t'_b] can be felt. The larger t'_b is, the smaller the nesting factor N_{SDW} . There is also a readjustment of Q_0 to a new value Q'_0 [22]. The overall effect is to lower $T_{c,\text{SDW}}^{\circ} \propto T_x^1 e^{-2[N_{\text{SDW}} W_{\text{SDW}}(Q'_0, \ell_x^1)]^{-1}}$ dramatically [Eq. (36)]. As a matter of fact, the AFM transition temperature is quickly destroyed by this deviation [22] in favor of other incipient instabilities. The nesting mechanism is also at the heart of AFM in the two-dimensional Hubbard and t - J models as well as in the high-temperature superconductors. It should be pointed out that the transverse ordering wave vector is the same for both mechanisms in quasi-one-dimensional solids [86]. The SDW can also be set in motion by electric fields [22,87,88].

D. Field-Induced SDW Transitions

The effect of a magnetic field H on nesting in quasi-one-dimensional solids is quite spectacular. For materials such as (TMTSF)₂X, where X = ClO₄ [89] or PF₆ [90], which are in a low-temperature metallic regime, a sufficiently strong magnetic field (~ 5 T) in the c direction will induce a sequence of transitions to insulating phases [1,22] with a Hall voltage that is reminiscent of the quantum Hall effect. As the field increases, the transverse magnetic length $2\pi/\kappa$, where $\kappa = ebH$, decreases and the electrons get more and more confined to their chains. Transverse single-particle coher-

ence starts to be affected when the magnetic energy $\omega_M = ebHv_F$ becomes larger than the thermal energy. At yet higher fields, the deviation from nesting caused by t'_b (see Section VI.C) slowly gets washed away when $\omega_M > t'_b$. The system then can sustain SDW sub phases with a nesting wave vector Q'_0 that depends sensitively on the field strength. This wave vector corresponds to the most negative $N_\alpha \tilde{W}_\alpha^M(Q'_0, \ell_x^1)$ of Eq. (35). Nesting models [91] have shown how Q'_0 can vary with field and temperature. $Q'_0 = Q_{0a} + n\kappa$ jumps discontinuously from one value of n to the next smaller value until it gets to $n = 0$ around $H = 8$ T in $(\text{TMTSF})_2\text{ClO}_4$. At a higher field yet, around 27 T, there is a reentrance to a paramagnetic phase. This reentrance may be due to a two-dimensional/one-dimensional crossover when $\omega_M = T_x^1$, the system becoming fully quantum and deprived of LRO at higher fields. There are, however, other explanations. There is the g-ology model of Yakovenko [92] and the anion-superlattice-potential model of Ref. 84. These models profess a new assignment of the subphases.

E. Peierls Transition

The Peierls transition is the first to have been observed in organic conductors, that is, for TTF–TCNQ [13]. This transition requires nesting and a sufficiently important electron–phonon interaction to overwhelm the competing SDW instability should the Coulomb interaction be important. It will occur when $V_\perp \xi(T) = 1$ [Eq. (33)] at a temperature slightly less than T_P° [46,47]. It is observed in a great number of salts [24]. Curiously, the soliton does not play an important role in the behavior of the commensurate charge-transfer quasi-one-dimensional Peierls semiconductors. Perhaps this is because their width in third-filled-band compounds $w \approx (\Gamma_{\text{CDW}} E_0 / \pi T_P^\circ)^{1/2} \xi_{\text{th}}^P$ can be as large as 100 to 1000 lattice distances, and also be large in one-quarter-filled bands with a dimerization gap $w = (E_0 / \Delta_D)^{1/2} \xi_{\text{th}}^P$ or yet larger $w \approx (\Gamma_{\text{CDW}} E_0 / \pi T_P^\circ)^2 \xi_{\text{th}}^P$ without umklapp. These widths are much longer than the coherence length in most experimental situations and the solitons cannot form. This is in contrast with a width of only a few unit cells in the polymers. The Frölich mode can be seen in incommensurate systems. If there is pinning, this mode will oscillate in the pinning potential and can be depinned by a strong enough electric field.

The Peierls transition knows no boundary and can be observed in all types of organic conductors, even the ET salts, which are presumably more isotropic. $(\text{BEDT-TTF})_2\text{TiHg}(\text{SCN})_4$, an example mentioned in Section V.B, is believed to go through a Peierls transition caused by nesting in an open part of the Fermi surface (another part being closed) [93].

The situation in the polymers as been described in Section IV.C.1. There is a rich excitation spectrum: solitons, polarons, and bi-polarons. The effect of three-dimensional coupling would be to confine soliton–antisoliton pairs

along the chain direction but perhaps also allow them to hop between chains [23,57,62].

F. Superconductivity

1. Quasi-One-Dimensional Conductors

A mean-field treatment gives the following gap equation [71] for *singlet* superconductivity:

$$\Delta(\mathbf{k}_\perp) = \frac{1}{2} \sum_{\mathbf{k}'} \Delta(\mathbf{k}'_\perp) \left[g_{ss} - V_{ss}(0) - \frac{1}{2} V_{CDW}(\mathbf{k}'_\perp + \mathbf{k}_\perp) + \frac{3}{2} V_{SDW}(\mathbf{k}'_\perp + \mathbf{k}_\perp) \right] \frac{\tanh[\varepsilon(\mathbf{k}')/2T]}{\varepsilon(\mathbf{k}')} \quad (41)$$

The origin of superconductivity in the quasi-one-dimensional solids is still a matter of debate, however. The correlation school believes that the proximity of the superconducting phase to the AFM phase [1,39,94] indicates that there are important repulsive Coulomb interactions at play. These would favor a SDW-mediated pairing mechanism, the attractive part coming from V_{SDW} . This leads to a gap varying as $\cos k_\perp b$. The electrons in the Cooper pairs would thus be on different chains and the superconductivity would be “*d*-wave.” The evidence for strong correlations also comes from NMR relaxation rate measurements both above the transition temperature [39,83], a clear deviation from the Korringa law is seen, and below [95] in the form of a power law decrease that best fits *d*-wave pairing. Note that superconductivity and SDW share different parts of the Fermi surface in this model.

The phonon school believes that the pairing is of electron–phonon origin [22]. As discussed in Section IV.C.2, this is possible if the Coulomb interactions are weak and if there is important coupling to optical phonons such that there emerges a net positive renormalized electron–electron coupling $g_{ss} \approx -g_{1ph} - g_{2ph}$ at low temperature. Since nesting is known to be weakened (Section VI.C) in the superconducting state, this prevents any Peierls instability from benefiting from the attractive phonon-mediated coupling. Conventional superconductivity could then occur, stabilized by interchain pair tunneling $V_{ss}(0) < 0$ (see Section V.A.1.b) and even with some *d*-wave modulation coming from V_{SDW} [see Eq. (41)]. This superconductivity would be very sensitive to impurities, even the nonmagnetic ones (see Section IV.D).

2. ET Conductors

Conductors with closed Fermi surfaces clearly belong to the phonon-pairing category. A mean-field treatment of the gap yields the equation

$$\Delta(\mathbf{k}) = \frac{1}{2} \sum_{\mathbf{k}'} \Delta(\mathbf{k}') \left[-W_{ss}(0) - X_{ss}(0) - \frac{1}{2} X_{CDW}(k'_c + k_c) + \frac{3}{2} X_{SDW}(k'_c + k_c) \right] \frac{\tanh[\epsilon(\mathbf{k}')/2T]}{\epsilon(\mathbf{k}')} \quad (42)$$

where W [see Eq. (35)] is the net in-plane Cooper pairing and the X [see Eq. (40)] are the intersheet couplings. Superconductivity is generally believed to be s -wave, although recent penetration depth measurements by muon spin resonance and microwave [96] indicate that there might be zeros of the gap on the Fermi surface. So nonconventional superconductivity is not excluded from Eq. (42). The gap could easily be modulated by X_{CDW} or even go to zero in the c direction because of its $\cos k_c c$ dependence.

3. High-Temperature Superconductors

There seems to be a growing consensus that the superconductivity is d -wave [97], more specifically, $d_{x^2-y^2}$ type. Recent microwave measurements [98] would indicate that the penetration depth is linear in temperature, a sign that the gap has zeros. As pointed out in Ref. 99, this does not exclude s -wave pairing since harmonics of the basic combinations [Eq. (38)] can also lead to zeros of the gap on the Fermi surface. It is interesting to note that d -wave pairing is quite in line with the extrapolations of the two-dimensional Hubbard and t - J models (Section V.B) and the observed competition with AFM. This would point to a spin-exchange mechanism. The parallel with the quasi-one-dimensional superconductors is striking.

4. Fullerenes

The pairing mechanism is assuredly intramolecular. The large “bucky balls” should be quite polarizable, sufficiently so for this to lead to an attraction. Again there are two schools of thought. This attraction can be caused by phonons or correlations. This has been reviewed in Ref. 28. The large fullerene molecules have a great number of low-energy vibrational modes which could provide the attractive force for superconductivity, in a fashion similar to the discussion in Section IV.C. The two-dimensional correlation models discussed in Section V.B are also relevant to the fullerene molecule (Section III.B.3). They point to the perhaps dominant intramolecular d -type singlet pairing, which would be the attractive mechanism for this otherwise three-dimensional superconductivity. The recent discovery of ferromagnetism in one fullerene [100], a dopant-sensitive prediction of the correlation model [101], confirms the importance of correlations. Indeed,

p -wave pairing is germane to two-dimensional correlation models [Eq. (38)]. This can provide the essential triplet-type intramolecular interactions that can lead to ferromagnetism. The recent NMR results of Ref. 102 on K_3C_{60} confirm the importance of both correlations and electron/high-frequency-phonon contributions.

G. Ferromagnetism

Ferromagnetism is observed in a number of organic solids. This has been reviewed recently [100]. The generic mechanism for this is, as in the fullerenes, of intramolecular origin and has not been covered by any of the preceding dimensionality-based arguments. It can occur with degenerate or nearly degenerate molecular orbitals in which a molecular Hund rule might apply: parallel spin alignment for two electrons on the same molecule but in different orbitals in order to benefit from exchange and minimize the Coulomb interaction. There are other possibilities involving three electrons on the same molecule. These are known as the McConnell model and their variants.

VII. CONCLUDING REMARKS

There is a fair amount of unity, as seen in Section VI, in the mechanisms of phase transitions of the organic conductors and the oxide superconductors. Correlations, be they inter- or intramolecular, play an important role. Quantum and thermal fluctuations are important in the quasi-one-dimensional solids and, to a lesser extent, in the quasi-two-dimensional conductors. There is a striking richness of phases and unusual phenomena in the organic conductors. These are explored in the following chapters of this book.

ACKNOWLEDGMENTS

I wish to thank the following people for useful discussions: C. Bourbonnais, K. Maki, A. Sandvik, D. J. Scalapino, A.-M. S. Tremblay. I have also benefited from financial support from the Natural Sciences and Engineering Research Council of Canada and the "Fonds pour la formation de chercheurs et d'aide à la recherche" of the Québec government.

REFERENCES

1. D. Jérôme, in *Earlier and Recent Aspects of Superconductivity* (J. G. Bednorz and K. A. Müller, eds.), Springer-Verlag, New York, 1990, p. 113.
2. N. D. Mermin and H. Wagner, *Phys. Rev. Lett.* **17**:1133 (1966).

3. G. Parisi, *Statistical Field Theory*, Addison-Wesley, Reading, Mass., 1988, p. 188.
4. N. Goldenfeld, *Lectures on Phase Transitions and the Renormalization Group*, Addison-Wesley, Reading, Mass., 1992.
5. H. E. Stanley, *Introduction to Phase Transitions and Critical Phenomena*, Oxford University Press, Oxford 1971.
6. J. A. Hertz, Phys. Rev. B 14:1165 (1976).
7. L. Onsager, Phys. Rev. 65:117 (1944). Many textbooks on statistical physics discuss the two-dimensional Ising model.
8. J. M. Kosterlitz and D. J. Thouless, J. Phys. C Solid State Phys. 5:L124 (1972); 6:1181 (1973); Prog. Low Temp. Phys. VIIB:373 (1978).
9. E. Fradkin, *Field Theories of Condensed Matter Systems*, Addison-Wesley, Reading, Mass., 1991.
10. J. Hubbard, Proc. R. Soc. London A 276:238 (1963).
11. R. Pariser and R. G. Parr, J. Chem. Phys. 21:767 (1953); J. A. Pople, Trans. Faraday Soc. 42:1375 (1953).
12. Z. Soos, Annu. Rev. Phys. Chem. 25:121 (1974); Z. Soos and D. J. Klein, in *Molecular Interactions* (R. Foster, ed.), Academic Press, New York, 1974, pp. 1–109.
13. R. Comès and G. Shirane, in *Highly Conducting One-Dimensional Solids* (J. T. Devreese, R. P. Evrard, and V. E. van Doren, eds.), Plenum Press, New York, 1979, p. 17.
14. Y. Bychkov, L. P. Gor'kov, and I. E. Dzyaloshinskii, Sov. Phys. JETP 23:489 (1966).
15. J. Solyom, Adv. Phys. 28:201 (1979).
16. V. J. Emery, in *Highly Conducting One-Dimensional Solids* (J. T. Devreese, R. P. Evrard, and V. E. van Doren, eds.), Plenum Press, New York, 1979, p. 247.
17. Yu. A. Firsov, V. N. Prigodin, and Chr. Seidel, Phys. Rep. 126:245 (1985).
18. C. Bourbonnais and L. G. Caron, Int. J. Mod. Phys. B 5:1033 (1991); also in *The Hubbard Model: Recent Results* (M. Rasetti, ed.), World Scientific, River Edge, N.J., 1991, p. 169.
19. S. Barisic, J. Phys. 44:119 (1983); also in *Low-Dimensional Conductors and Superconductors* (D. Jérôme and L. G. Caron, eds.), Plenum Press, New York, 1987, Vol. 155, p. 395.
20. T. Holstein, Ann. Phys. (N.Y.) 8:325 (1959); D. J. Scalapino and R. L. Sugar, Phys. Rev. B 24:4295 (1981).
21. S. Barisic, J. Labbé, and J. Friedel, Phys. Rev. Lett. 25:919 (1970); W. P. Su, J. R. Schrieffer, and A. J. Heeger, Phys. Rev. B 22:2099 (1980).
22. T. Ishiguro and K. Yamaji, *Organic Superconductors*, Springer-Verlag, New York, 1990.
23. D. Baeriswyl, D. K. Campbell, and S. Mazumdar, in *Conjugated Conducting Polymers* (H. Kiess, ed.), Springer-Verlag, New York, 1992.
24. J. R. Ferraro and J. M. Williams, *Introduction to Synthetic Electrical Conductors*, Academic Press, New York, 1987; J. M. Williams, J. R. Ferraro,

- R. J. Thorn, K. D. Carlson, U. Geiser, H. H. Wang, A. M. Kini, and M.-H. Whangbo, *Organic Superconductors (Including Fullerenes): Synthesis, Structure, Properties, and Theory*, Prentice Hall, Englewood Cliffs, N.J., 1992.
25. W. E. Pickett, *Rev. Mod. Phys.* **61**:433 (1989).
 26. V. J. Emery, *Phys. Rev. Lett.* **58**:2794 (1987).
 27. A. P. Balachandran, E. Ercolessi, G. Morandi, and A. M. Srivastava, *Hubbard Model and Anyon Superconductivity*, World Scientific, River Edge, N.J., 1990.
 28. A. F. Hebard, *Phys. Today* **45**(11):26 (1992).
 29. N. Hamada, S. Sawada, and A. Oshiyama, *Phys. Rev. Lett.* **68**:1579 (1992).
 30. E. H. Lieb and F. Y. Wu, *Phys. Rev. Lett.* **20**:1445 (1968); A. A. Ovchinnikov, *Sov. Phys. JETP* **30**:1160 (1970); C. Coll, *Phys. Rev. B* **9**:2150 (1974).
 31. H. Schulz, *Interacting Fermions in One Dimension: From Weak to Strong Correlation*, preprint; *Int. J. Mod. Phys. B* **5**:57 (1990); *Phys. Rev. Lett.* **64**:2831 (1990).
 32. G. Beni, T. Holstein, and P. Pincus, *Phys. Rev. B* **8**:312 (1973); see more recently H. Shiba and M. Ogata, *Int. J. Mod. Phys. B* **5**:31 (1990).
 33. D. Baeriswyl and W. von der Linden, *Int. J. Mod. Phys. B* **5**:999 (1991); also in *The Hubbard Model: Recent Results* (M. Rasetti, ed.), World Scientific, River Edge, N.J., 1991, p. 135.
 34. S. Kivelson, D. Rokhsar, and J. Sethna, *Phys. Rev. B* **35**:8865 (1987); Z. Zou and P. W. Anderson, *Phys. Rev. B* **37**:627 (1988).
 35. S. Tomonaga, *Prog. Theoret. Phys.* **5**:349 (1950); J. M. Luttinger, *J. Math. Phys.* **4**:1154 (1963); D. C. Mattis and E. H. Lieb, *J. Math. Phys.* **6**:304 (1965); A. Luther and I. Peschel, *Phys. Rev. B* **9**:2911 (1974); A. Luther and V. J. Emery, *Phys. Rev. Lett.* **33**:589 (1974).
 36. J. P. Pouget, in *Low-Dimensional Conductors and Superconductors* (D. Jérôme and L. G. Caron, eds.), Plenum Press, New York, 1987, Vol. 155, p. 17.
 37. S. K. Ma, *Modern Theory of Critical Phenomena*, W. A. Benjamin, Menlo Park, Calif., 1976.
 38. L. P. Kadanoff, W. Götze, D. Hamblen, R. Hecht, E. A. S. Lewis, D. Aspnes, and J. Kane, *Rev. Mod. Phys.* **39**:395 (1967); K. G. Wilson and R. Kogut, *Phys. Rep.* **12**:75 (1974); K. G. Wilson, *Rev. Mod. Phys.* **47**:773 (1975).
 39. C. Bourbonnais, in Proc. "Les Houches," Ecole d'été de physique théorique, *Highly Correlated Fermion Systems and High- T_c Superconductors*, July 1991 (B. Doucot and R. Rammal, eds.), Elsevier, New York, 1993.
 40. M. Kimura, *Prog. Theor. Phys.* **53**:955 (1975).
 41. J. Voit, *Phys. Rev. B* **45**:4027 (1992).
 42. H. Nelisse, Simulations Monte-Carlo et groupe de renormalisation pour le gaz d'électrons unidimensionnel, M.Sc. thesis no. III-743, Université de Sherbrooke, Nov. 1991.

43. M. Luchini, M. Ogata, W. Putikka, and T. M. Rice, *Physica C* 185–189:141 (1991).
44. M. Ogata, M. U. Luchini, S. Sorella, and F. F. Assaad, *Phys. Rev. Lett.* 66:2388 (1991).
45. L. G. Caron and C. Bourbonnais, *Phys. Rev. B* 29:4230 (1984).
46. G. A. Toombs, *Phys. Rep.* 40:181 (1978).
47. D. J. Scalapino, M. Sears, and R. A. Ferrell, *Phys. Rev. B* 6:3409 (1972); W. Dieterich, *Adv. Phys.* 25:615 (1976).
48. P. A. Lee, T. M. Rice, and P. W. Anderson, *Phys. Rev. Lett.* 31:462 (1973).
49. H. Frölich, *Proc. Roy. Soc. London A* 223:296 (1954); M. J. Rice, S. Strässler, and W. R. Schneider, in *One-Dimensional Cooperative Phenomena* (H. J. Keller, ed.), Plenum Press, New York, 1975, p. 215; D. Jérôme and H. J. Schulz, in *Extended Linear Chain Compounds* (J. S. Miller, ed.), Plenum Press, New York, 1982, Vol. 2, p. 159.
50. M. J. Rice, *Phys. Rev. Lett.* 37:36 (1976); M. J. Rice, L. Pietronero, and P. Brüesch, *Solid State Commun.* 21:757 (1977).
51. W. L. McMillan, *Phys. Rev. B* 12:1187 (1975).
52. J.-P. Farges, in *The Physics and Chemistry of Low Dimensional Solids* (L. Alccacer, ed.), D. Reidel, Amsterdam, 1980, p. 223.
53. A. R. Bishop and T. Schneider, eds. *Solitons and Condensed Matter Physics*, Springer-Verlag, New York, 1978.
54. W. L. McMillan, *Phys. Rev. B* 14:1496 (1976).
55. B. Horovitz and J. A. Krumhansl, *Phys. Rev. B* 29:2109 (1984).
56. M. J. Rice, *Phys. Lett.* 71A:152 (1979).
57. Yu, Lu, *Solitons and Polarons in Conducting Polymers*, World Scientific, River Edge, N.J., 1988.
58. V. J. Emery, R. Bruisma, and S. Barisic, *Phys. Rev. Lett.* 48:1039 (1982).
59. S. Barisic and S. Brazovskii, in *Recent Developments in Condensed Matter Physics* (J. T. Devreese, ed.), Plenum Press, New York, 1981, Vol. 1, p. 327.
60. W. L. McMillan, *Phys. Rev. B* 16:4655 (1977).
61. P. Bak, *Rep. Prog. Phys.* 45:587 (1982).
62. A. J. Heeger, S. Kivelson, J. R. Schrieffer, and W.-P. Su, *Rev. Mod. Phys.* 60:781 (1988).
63. A. A. Abrikosov and J. A. Ryzhkin, *Adv. Phys.* 27:147 (1978).
64. L. Zuppiroli, in *Low-Dimensional Conductors and Superconductors* (D. Jérôme and L. G. Caron, eds.), Plenum Press, New York, 1987, Vol. 155, p. 307.
65. T. Giamarchi and H. J. Schulz, *Phys. Rev. B* 37:325 (1988).
66. G. Theodorou, *Phys. Rev. B* 16:2264 (1977); G. Theodorou and M. H. Cohen, *Phys. Rev. B* 16:4104 (1977).
67. G. Theodorou and M. H. Cohen, *Phys. Rev. B* 16:3955 (1977).
68. A. Sandvik, D. Scalapino, and P. Henelius, *Bull. Am. Phys. Soc.* 38:583 (1993), and recent unpublished results.
69. B.-C. Xu and S. E. Trullinger, *Phys. Rev. Lett.* 57:3113 (1986).

70. W. Rehwald and H. G. Kiess, in *Conjugated Conducting Polymers* (H. Kiess, ed.), Springer-Verlag, New York, 1992, p. 135; H. G. Kiess and G. Harbeke, in the same book, p. 175.
71. C. Bourbonnais and L. G. Caron, *Europhys. Lett.* 5:209 (1988).
72. D. J. Scalapino, *Physica C* 185–189:104 (1991).
73. A. Moreo, D. J. Scalapino, and S. R. White, *Phys. Rev. B* 45:7544 (1992).
74. A. Moreo, *Phys. Rev. B* 9:5059 (1992).
75. T. Koma and H. Tasaki, *Phys. Rev. Lett.* 68:3248 (1992).
76. N. E. Bickers, D. J. Scalapino, and S. R. White, *Phys. Rev. Lett.* 62:961 (1989).
77. T. Giamarchi and C. Lhuillier, *Phys. Rev. B* 43:12943 (1991).
78. A. V. Chubukov and J. P. Lu, *Phys. Rev. B* 46:11163 (1992).
79. E. Dagotto, J. Riera, and A. P. Young, *Phys. Rev. B* 42:2347 (1990).
80. T. K. Lee and S. Feng, *Phys. Rev. B* 38:11809 (1988); G. J. Chen, R. Joynt, F. C. Zhang, and C. Gros, *Phys. Rev. B* 42:2662 (1990).
81. E. Dagotto, A. Moreo, F. Ortolani, D. Poilblanc, and J. Riera, *Phys. Rev. B* 45:10741 (1992); E. Dagotto and R. Riera, *Phys. Rev. B* 46:12084 (1992).
82. Interesting historical work on the RVB can be obtained in J. Woods Halley, ed., *Theories of High Temperature Superconductivity*, Addison-Wesley, Reading, Mass., 1988; Zi-Zhao Gan and Zhao-Bin Su, eds., *Two-Dimensional Strongly Correlated Electronic Systems*, Gordon and Breach, New York, 1988.
83. C. Bourbonnais, *J. Phys. I* 3:143 (1993); P. Wzietek, F. Creuzet, C. Bourbonnais, D. Jérôme, K. Bechgaard, and P. Batail, *J. Phys. I* 3:171 (1993).
84. T. Osada, S. Kagoshima, and N. Miura, *Phys. Rev. Lett.* 69:1117 (1992).
85. J. W. Bray, L. V. Interrante, I. S. Jacobs, and J. C. Bonner, in *Extended Linear Chain Compounds* (J. S. Miller, ed.), Plenum Press, New York, 1983, Vol. 3, p. 353.
86. L. G. Caron and B. Bourbonnais, *J. Phys. (Colloque)* 8:1419 (1988).
87. S. Tomic, J. R. Cooper, and K. Bechgaard, *Phys. Rev. Lett.* 62:462 (1989).
88. W. Kang, S. Tomic, J. R. Cooper, and D. Jérôme, *Phys. Rev. B* 41:4862 (1990).
89. R. V. Chamberlin, M. J. Naughton, X. Yan, L. Y. Chiang, S.-Y. Hsu, and P. M. Chaikin, *Phys. Rev. Lett.* 60:1189 (1988).
90. J. F. Kwak, J. E. Schirber, P. M. Chaikin, J. M. Williams, H.-H. Wang, and L. Y. Chiang, *Phys. Rev. Lett.* 56:972 (1986).
91. K. Maki, *Phys. Rev. B* 33:4826 (1986); A. Virosztek, L. Chen, and K. Maki, *Phys. Rev. B* 34:3371 (1986); L. Chen and K. Maki, *Phys. Rev. B* 35:8462 (1987); D. Poilblanc, M. Héritier, G. Montambaux, and P. Lederer, *J. Phys. C* 19:L321 (1986); G. Montambaux, *J. Phys. C* 20:L327 (1987); G. Montambaux and D. Poilblanc, *Phys. Rev. B* 37:1913 (1988).
92. V. M. Yakovenko, *Europhys. Lett.* 3:1041 (1987).
93. M. V. Kartsovnik, A. E. Kovalev, and N. D. Kushch, *J. Phys. I* 3:1187 (1993).
94. V. J. Emery, *Synth. Met.* 13:21 (1986).

95. M. Takigawa, H. Yasuoka, and G. Saito, *J. Phys. Soc. Jpn.* 56:873 (1987); Y. Hasegawa and H. Fukuyama, *J. Phys. Soc. Jpn.* 56:877.
96. L. P. Le, G. M. Luke, B. J. Sternlieb, W. D. Wu, Y. J. Uemura, J. H. Brewer, T. M. Riseman, C. E. Stronach, G. Saito, H. Yamochi, H. H. Wang, A. M. Kini, K. D. Carlson, and J. M. Williams, *Phys. Rev. Lett.* 68:1923 (1992); D. Achkir, M. Poirier, C. Bourbonnais, G. Quirion, C. Lenoir, P. Batail, and D. Jérôme, *Phys. Rev. B* 47:11595 (1993).
97. B. Goss Levi, *Phys. Today*, 46(5):17 (1993).
98. W. N. Hardy, D. A. Bonn, D. C. Morgan, R. Liang, and K. Zhang, *Phys. Rev. Lett.* (to be published); these measurements have been confirmed by M. Poirier et al. (to be published).
99. L. Chen and A.-M. S. Tremblay, *Proc. Santa Fe Conference on Spectroscopies in Novel Superconductors*, Santa Fe, N.Mex., Mar. 17–19, 1993.
100. F. Wudl and J. D. Thompson, *J. Phys. Chem. Solids* 53:1449 (1992).
101. S. Chakravarty, M. P. Gelfand, and S. Kivelson, *Science* 254:970 (1991).
102. G. Quirion, C. Bourbonnais, E. Barthel, P. Auban, D. Jérôme, J. M. Lambert, A. Zahab, P. Bernier, C. Fabre, and A. Rassat, *Europhys. Lett.* 21:233 (1993).

This Page Intentionally Left Blank

3

Molecular Design of Organic Conductors

Vladimir Khodorkovsky and James Y. Becker

Ben-Gurion University of the Negev, Beer-Sheva, Israel

I. INTRODUCTION

The content of this chapter is confined exclusively to *molecular* organic conductors. From a chemist's point of view, one of the most important questions to be raised is whether it is possible to *design* organic conducting materials. Although a vast amount of data in the field of organic metals has accumulated over the past 20 years, there are still too many unknowns to permit the a priori prediction with any degree of assurance whether a newly designed material will actually exhibit metallic, semiconducting, or insulating properties. However, attempts to design organic metals according to general guidelines have been made, and some indeed have led to enhanced electrical conductivity. Even before the discovery of the first organic metal [1,2], Little [3] suggested to design high-temperature superconductors. The necessary requirements to obtain organic metals have been reviewed and discussed in detail by Garito and Heeger [4], and later revised by others (e.g., Refs. 5 to 11). Most criteria for the suitability of organic derivatives as components for organic metals have been formulated for the case of charge-transfer donor–acceptor complexes. However, in general, the most significant results have been obtained for mixed-valence cation-radical salts. Some requirements, which were initially thought to be of fundamental importance, later appeared not to be so crucial (e.g., planarity in the neutral and ionic states). Thus bis(ethylenedithio)tetrathiafulvalene (BEDT-TTF), which is

a parent donor for a series of superconducting cation-radical salts, is not planar in its neutral solid state [12]. Another example is the former requirement of a high symmetry of both donor and acceptor molecules, which was found to be unimportant in several organic metals and even in a superconductor based on unsymmetrical donor molecules (for a recent review, see, e.g., Ref. 13). Moreover, the number of common features of known organic conductors decreased significantly with the discovery of high-temperature superconductors based on fullerenes (see, e.g., Ref. 14). Our follow up discussion will be limited to molecular donors and acceptors, leaving the important class of conducting polymers, discussed in Chapters 11 to 13.

The generally accepted set of necessary conditions (Refs. 4 to 11) for electrical conductivity in organic compounds can be divided into two groups:

1. Requirements for electronic structure of organic metal components
2. Requirements for molecular and crystal structure in the solid state

The basic and absolute requirement in the first group is the presence of unpaired electrons in the donor and/or acceptor molecules. The most important feature in the second set of criteria is the formation of uniform spacing between donor or acceptor component molecules to permit intermolecular delocalization of charge, forming a single metallic band or overlap between partially filled and partially empty bands.

The electronic structure of donor and acceptor components is more or less predictable and the general relationship between, for example, structure and donor (acceptor) strength or structure and stability of ion radicals, is quite familiar to organic chemists. The design of new "electronic structures" is not only quite possible but represents the main trend of current research activities in the field. On the other hand, only preliminary steps have been made toward predicting and designing of crystal structure [15–17].

The formation of an organic conductor from a donor, acceptor, or mixed donor–acceptor molecules is depicted schematically in Figs. 1 and 2. Ion-radical species, formed by oxidation of a donor, reduction of an acceptor, or electron transfer from a donor to an acceptor, might undergo further transformations, such as dimerization, fragmentation, and reactions with solvent, moisture, or oxygen from air. In the case of stable ion radicals, further donor–acceptor interactions between a donor and its cation radical, acceptor and its anion radical, or between a donor and acceptor, usually lead to the desired ion-radical (IR) salts or charge-transfer (CT) complexes. If the spacing between components in such IR or CT salts is uniform and stacking in CT salts is segregated, and the degree of CT in donor–acceptor complex is partial, electrical conductivity can be achieved.

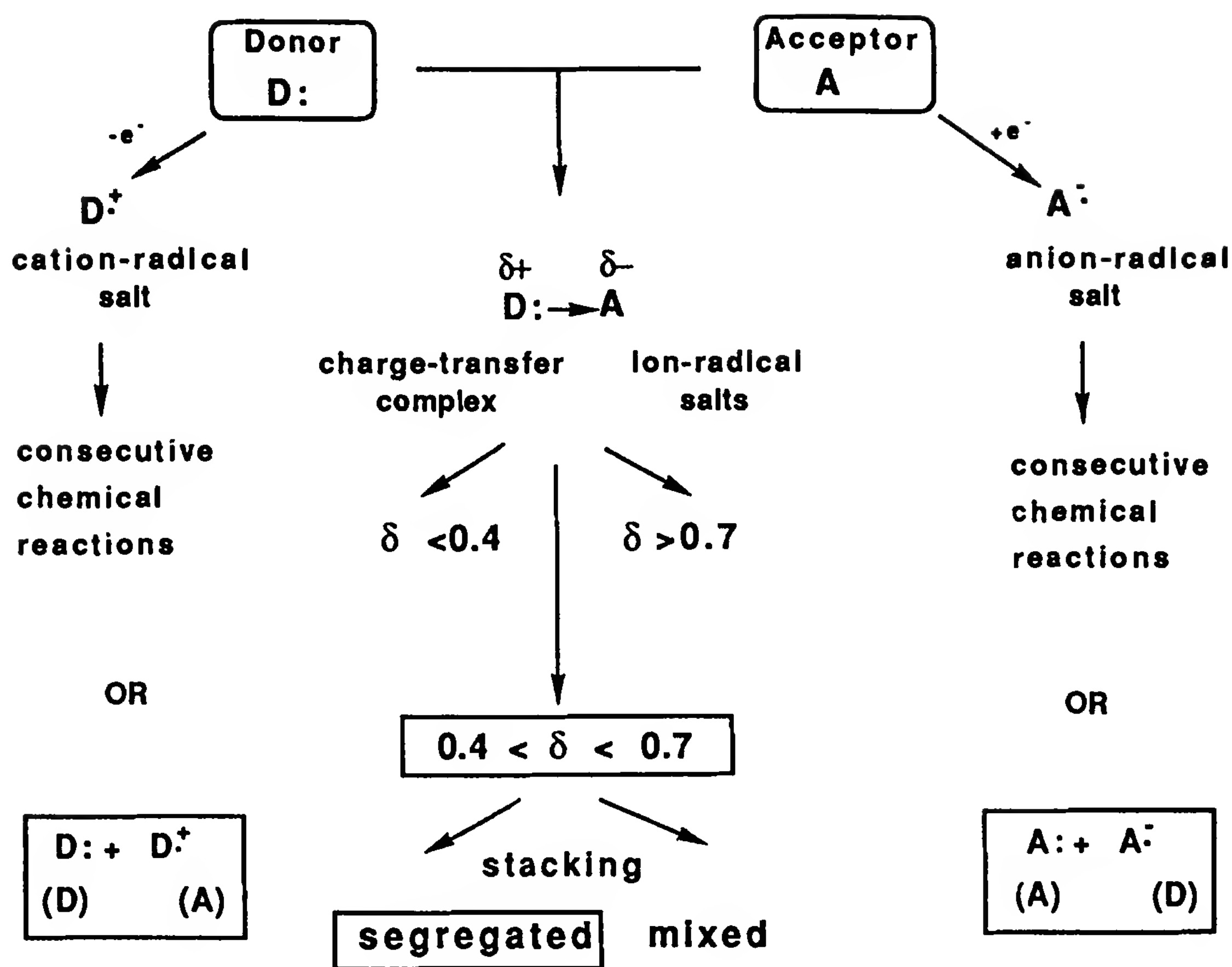


Figure 1 Schematic representation of the formation of IR salts and CT complexes.

As one can see from Figs. 1 and 2, the stability of ion-radical species is one of the most crucial requirements for the formation of conducting salts. Therefore, neutral donors and acceptors, as well as ion radicals, should not oxidize or reduce water, or react with oxygen. On the other hand, components of conducting materials should be chemically inactive, namely weak electrophiles or nucleophiles. Ion radicals must also exhibit sufficient degree of spin delocalization and be thermodynamically stable, to avoid, for example, dimerization or disproportionation. A sufficiently large energy gap should prevent the disproportionation of ion radicals into neutral and dicationic species. These requirements are presented schematically in Fig. 3.

The aim of this chapter is to provide the reader with some general information about organic donors and acceptors, quantitative measure of their strength, and their suitability as components for organic conductors. Outlines of important requirements (e.g., structural, redox potentials, degree of charge transfer, stacking modes, etc.), which are necessary conditions for obtaining organic conductors, are discussed.

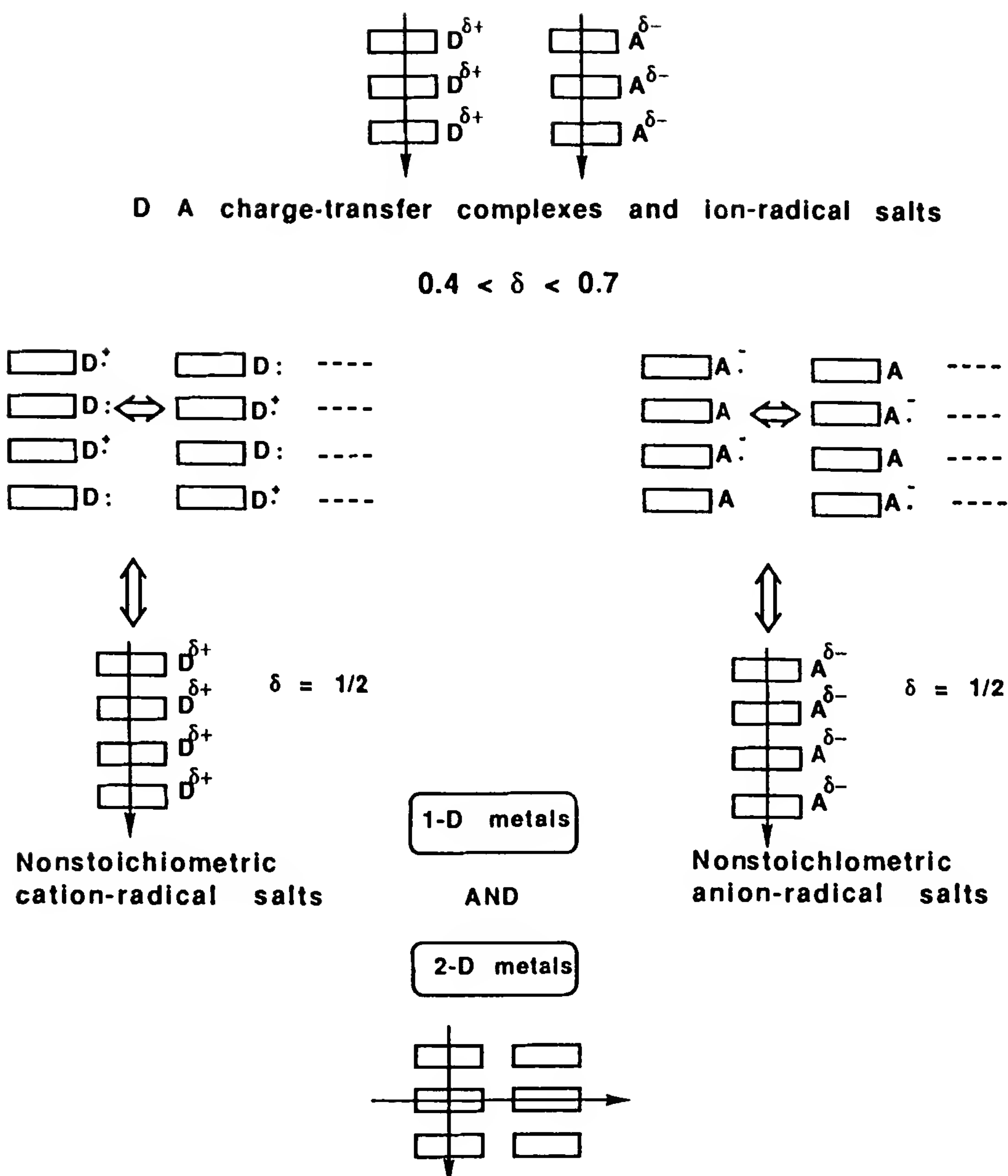


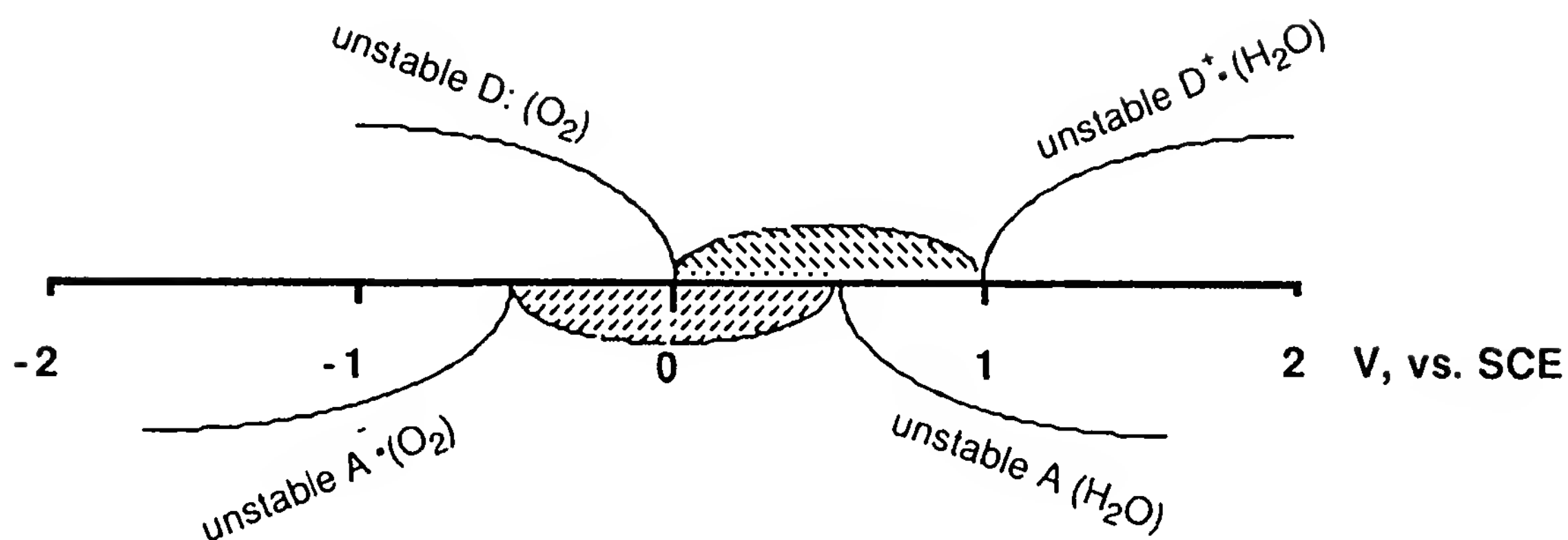
Figure 2 Schematic representation of the formation of one- and two-dimensional conductors.

Furthermore, attempts are made to furnish answers that are addressed to the following issues:

1. How can we chemically tune the strength of donors and acceptors, and stabilize their corresponding ion radicals?
2. Can we forecast the solid-state structure of CT complexes that result from combination of chosen donors and acceptors?
3. Can chemists design organic conductors?

1. Kinetic

A) Redox properties

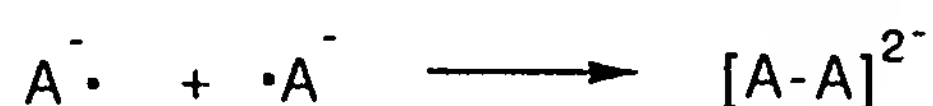
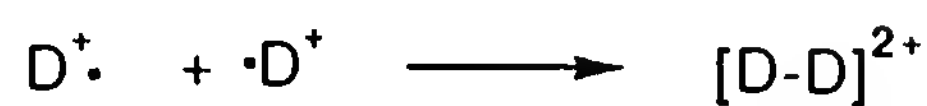


B) Charge and spin delocalization to minimize (1) and (2)

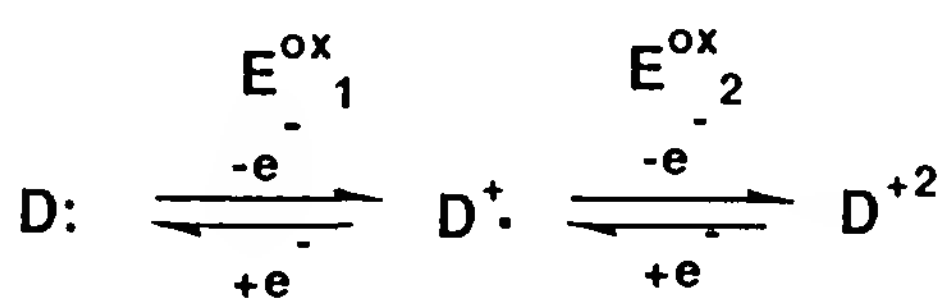
(1)

 $D^{\cdot+}$ - electrophile properties $A^{\cdot-}$ - nucleophile properties

(2)

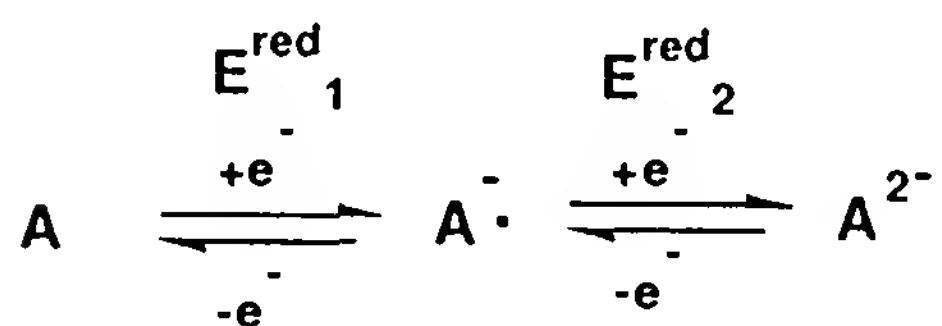


2. Thermodynamic

Two-stage reversible REDOX systems

$$\Delta E = E_{ox}^2 - E_{ox}^1$$

$$\lg K = \frac{\Delta E}{0.059}$$



K - ion-radical stability constant

Figure 3 Stability requirements for components of organic metals.

II. DONOR AND ACCEPTOR COMPONENTS OF MOLECULAR ORGANIC CONDUCTORS: ELECTRONIC ASPECTS

A. Electron Donor Ability

1. Ionization Potentials of Donor Molecules

Previously we have indicated that the most important characteristics of donor and acceptor molecules which lead to the formation of conducting organic compounds are both the energy required for the conversion of a closed-shell donor or acceptor to the corresponding cation or anion radical, and the stability of the products of such a process. Both theoretical (quantum-chemical calculations) and experimental approaches are suitable for the purpose of studying and predicting these properties. Although simple computation methods can provide valuable information about donor-acceptor ability and stability of open-shell state of unknown derivatives, no systematic studies have been carried out. The most important experimental approaches to this issue utilize gas-phase ionization potentials (IPs) for donor molecules, electron affinity (EA) determination for acceptor molecules, and measurement of redox potentials in solutions for both donor and acceptor molecules (usually by cyclic voltammetry, which also provides information about thermodynamic and kinetic stability of ion radicals formed). Although several quantitative correlations between IP values (determined by means of ultraviolet photoelectron spectroscopy) and electrochemical oxidation potentials (e.g., Refs. 18 and 19) are available, one should bear in mind that there is not much physical meaning in such comparisons, because an IP is a vertical ionization process and the oxidation potential is an adiabatic measure, which also includes the energies of substrate-solvent and substrate-electrode interactions. However, because an IP is a vertical ionization process, it is an excellent tool for evaluating new strong electron donors, as long as a comparison is made for *different* classes of organic compounds. The EA determination is not as straightforward, and therefore the available EA data for organic acceptors are rather limited (for a more detailed discussion, see Ref. 20). To obtain valuable quantitative information about donor and acceptor strength *within* a definite class of compounds, electrochemical redox potentials could be utilized for this purpose, since the energies of interactions with solvent and electrode could be considered to be constant at first approximation.

The IP values of neutral electron donor molecules used as components for organic metals are within the limits of $6.3 < \text{IP} < 6.9$ eV. These low IP values are exhibited by several classes of organic compounds. Thus IP values of arenes decrease rapidly in a series of linearly annelated polyacenes (Table 1). Tetracene (**4**) and especially pentacene (**5**) and rubrene (**6**) can

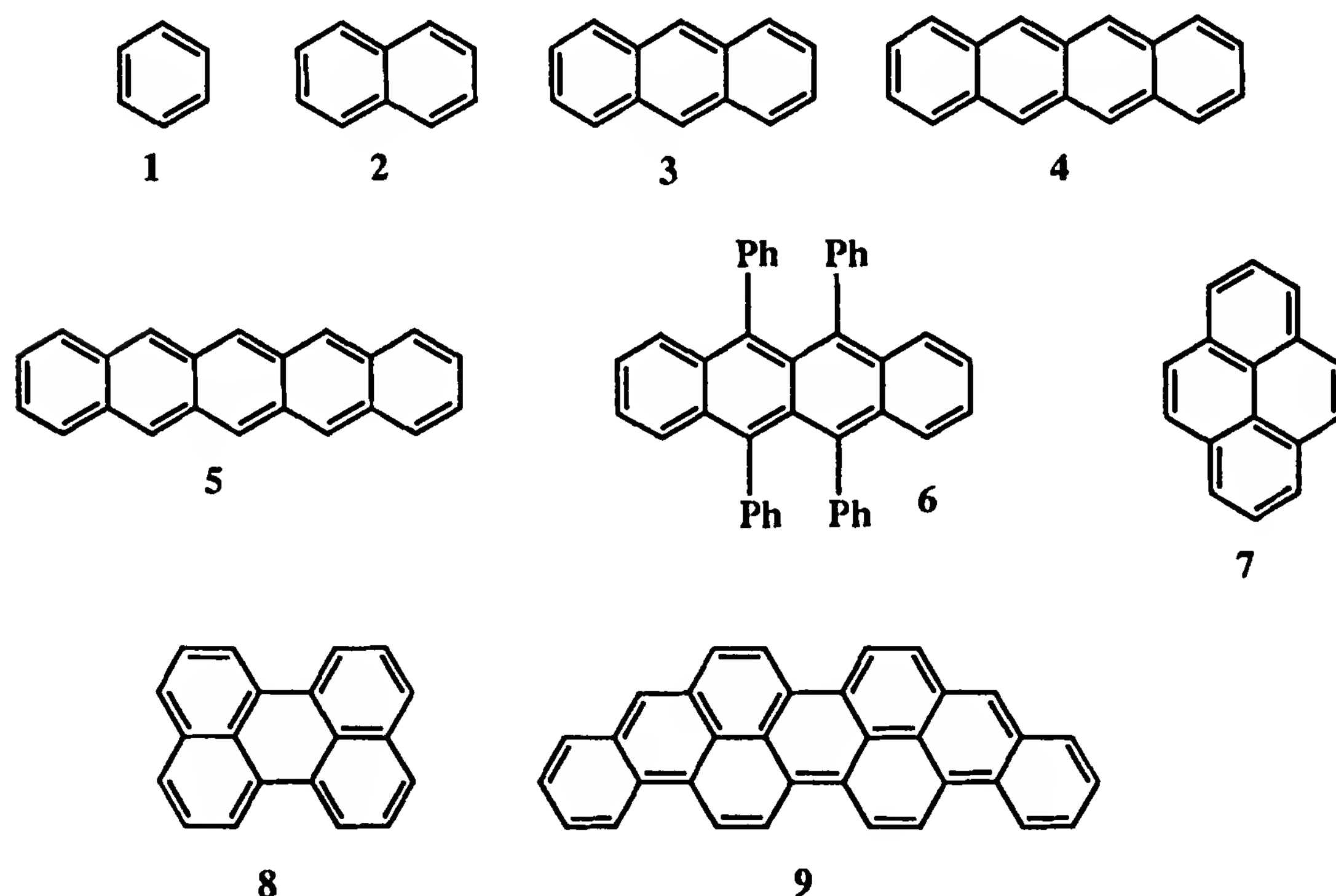
Table 1 Ionization Potentials of Arenes

Compound	IP	Compound	IP
1	9.24	7	7.41
2	8.15	8	7.00
3	7.40	9	6.50
4	7.01	10	6.85 ^a
5	6.64	11	6.65 ^a
6	6.44		

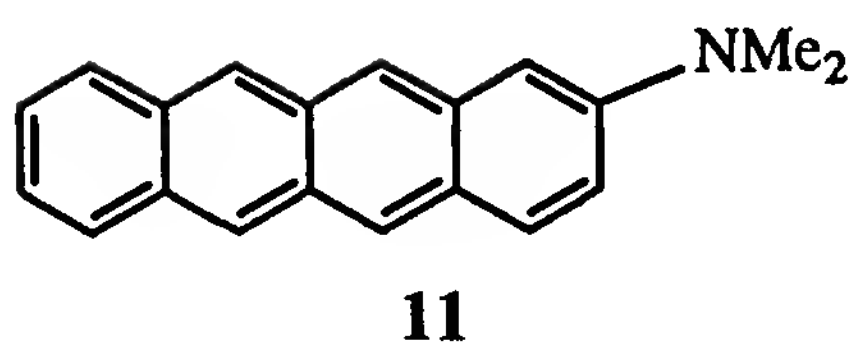
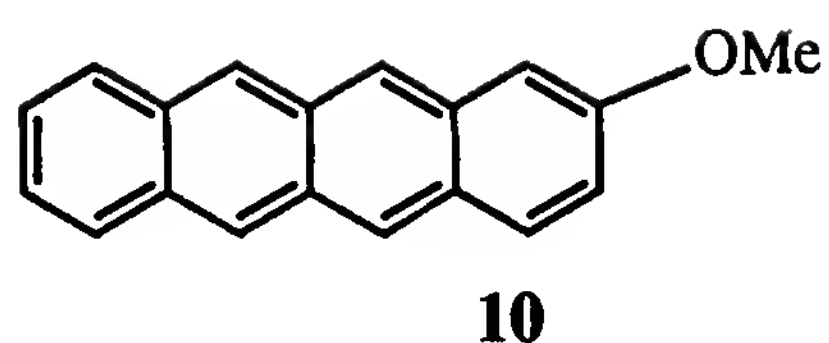
^aFrom Ref. 24.

Source: Ref. 22.

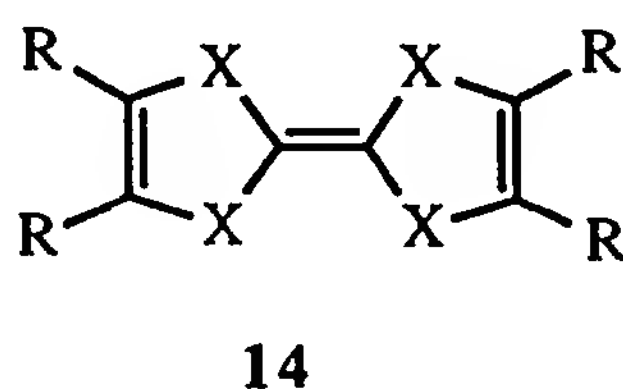
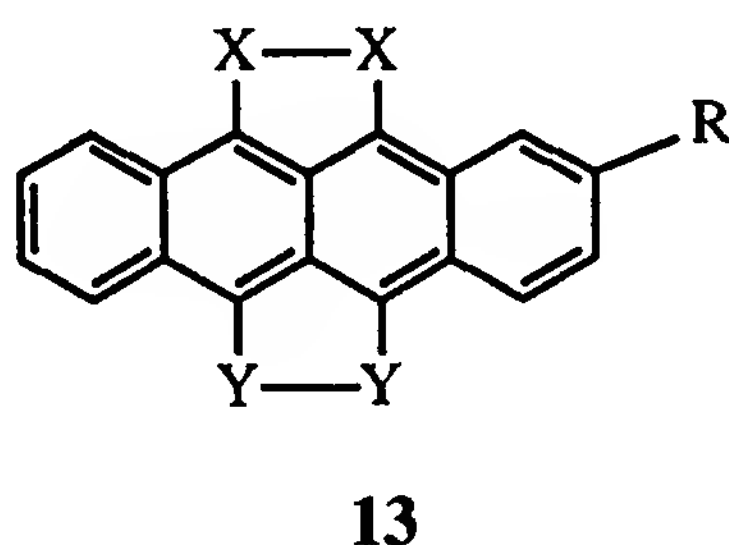
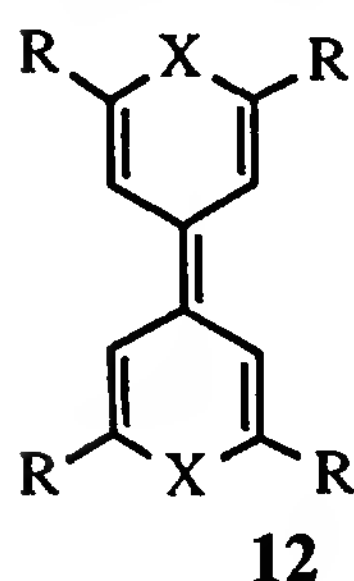
readily be oxidized in solutions, but their cation radicals are unstable and their solubility drops drastically upon increasing annelation. Pericondensed arenes are poorer donors, but their cation radicals are more stable. Thus nonstoichiometric salts of perylene (**8**) do afford conducting crystals [21].



The introduction of alkyl, alkoxy, alkylthio, and especially dialkylamino groups to an arene molecule results in substantial decrease of their IP values. Thus the IPs of methoxy (**10**) and dimethylamino (**11**) tetracenes fit within the IP range of interest, although to the best of our knowledge, they have never been used as donor components for organic metals.



Heterocycles such as furane, thiophene, and pyrrole have rather moderate donor ability. However, substituting them with appropriate electron-donating substituents might decrease their IP values and make them suitable components for organic metals. Pyranylidenes and their chalcogena analogs (**12**) have very low IP values (6.3 eV for R = Ph, X = S) and have been utilized for the preparation of conducting materials [23].



To date, it has been shown that multisulfur heterocycles and their seleno and telluro analogs are most promising candidates as components for organic metals. The introduction of chalcogen atoms in organic unsaturated derivatives decreases its IP and stabilizes the corresponding cation radicals, as well as enhances intermolecular interactions in the solid state. Tetrachalcogenoarenes (**13**) and tetrachalcogenafulvalenes (**14**) are the most widely investigated derivatives of this type (Table 2).

2. Electrochemical Oxidation Potentials of Donor Molecules

An extensive body of information on oxidation potentials of organic compounds, usually determined by cyclic voltammetry, is available. In fact, almost every newly synthesized organic electron donor is characterized by its electrochemical properties. The differences in the energy of solvation for different classes of donors make the comparison of their electron-donor ability on the basis of these measurements not very straightforward. However, within the same structural class of compounds these differences may often be neglected. The majority of electron donors that are used as components for organic metals exhibits two-stage one-electron reversible behavior. The kinetic stability (e.g., toward water and other nucleophiles in solution) of cation radicals and dications formed after one- and two-electron oxidation can easily be appreciated by measurement of the relative heights of the oxidation and the corresponding reduction current amplitudes and by the anodic and cathodic peak potentials separation for each species. The thermodynamic stability of a cation radical (i.e., its tendency to dis-

Table 2 Ionization Potentials of Tetrachalcogenotetracenes and Tetrachalcogenafulvalenes

Compound	IP	Refs.	Compound	IP	Refs.
13 R = H, X = Y = S	6.2	24	14 R = H, X = S	6.92	25, 26
13 R = <i>t</i> -Bu, X = Y = S	6.2	24	14 R = H, X = S	6.83	27
			14 R = H, X = S	6.70	28
13 R = MeO, X = Y = S	6.1	24	14 R = Me, X = S	6.38	25
13 R = H, X = S, Y = Se	6.2	24	14 R = MeS, X = S	6.63	29
13 R = H, X = Y = Se	6.25	24	14 R + R = (CH) ₄ , X = S	6.41	29
13 R = H, X = Se, Y = Te	6.15	24	14 R = H, X = Se	6.90	30
13 R = H, X = Y = Te	5.9–6.0	24	14 R = Me, X = Se	6.58	30

proportionate to a neutral donor and the corresponding dication species) could be evaluated from the difference between the first and second oxidation potentials, $\Delta E = E_2 - E_1$. This difference is linked to the cation-radical stability constant by the expression $\log K = \Delta E/0.059$ V and was widely used by Huenig and co-workers [31], for instance, for the evaluation of “semiquinone” stability constants.

The comparison between redox properties data taken from different literature sources is also somewhat complicated because of the use of different experimental conditions: solvent, working electrode, reference electrode, sweep rate, electrolyte, and so on. On the other hand, it is quite helpful that most of the authors cite their data with respect to a reference compound under the same experimental conditions (usually compared to unsubstituted TTF or TCNQ). Cyclic voltammetry data for TTF, under various experimental conditions, are given in Table 3. The particular influence of solvent on TTF oxidation potentials was discussed in Ref. 28.

Cyclic voltammograms of unsubstituted arenes usually exhibit irreversible oxidation waves. Often, the introduction of heteroatoms enhances both donor ability and stability (due to better charge delocalization) of the corresponding cation radicals. The electrochemical behavior of amino-substituted derivatives **15** [41], **16** [42], and **17** [43] can serve as representative examples. Thus compound **15** oxidizes extremely easily at a potential as low as -0.2 V (two-electron process), whereas compound **16** oxidizes at higher potentials, but in two one-electron steps: $E^1 = 0.29$ V,

Table 3 Electrochemical Redox Potentials of TTF Under Different Experimental Conditions

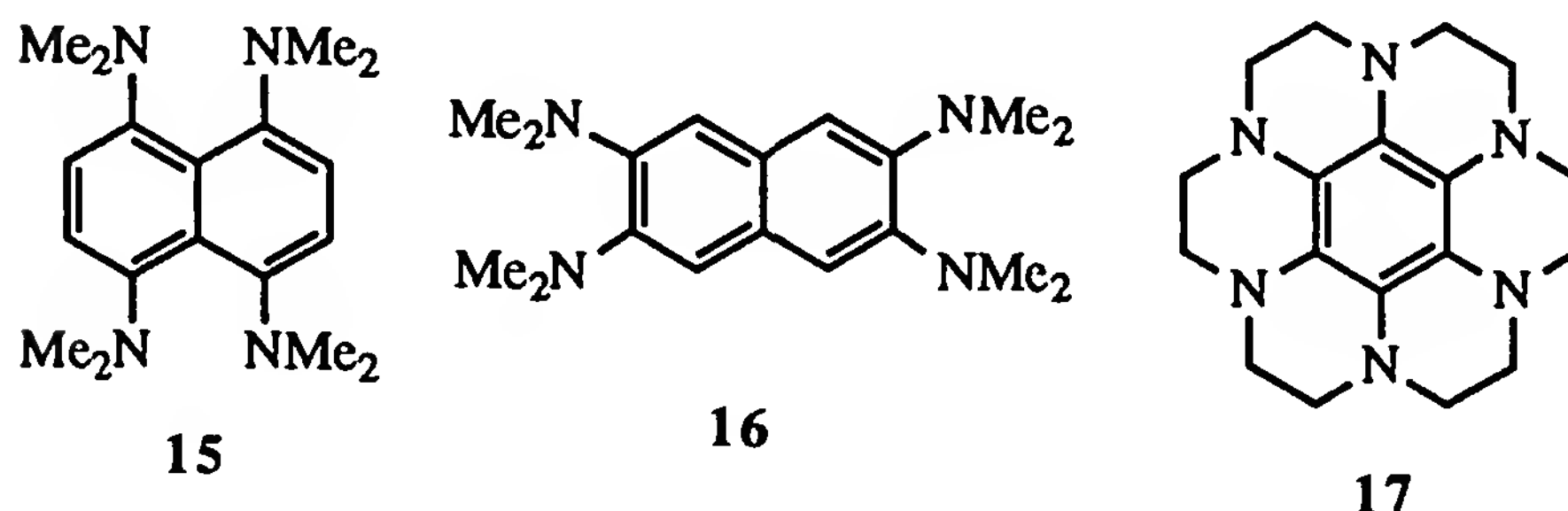
E^1 (V)	E^2 (V)	$\log K$	Working electrode	Reference electrode	Solvent	Electrolyte ^a	Ref.
0.35 ^b	0.71	6.10	GC ^c	SCE	MeCN	TBAP	32
0.33	0.70	6.27	Pt	SCE	MeCN	TEAP	33
0.47	0.81	5.75	Pt	SCE	CH ₂ Cl ₂	TBAF	34
0.34	0.78	7.46	Pt	Ag/AgCl	CH ₂ Cl ₂	TEAHF	35
0.46 ^b	0.87	6.95	Pt	SCE	PhCN	TBAP	36
0.40	0.82	7.12	Pt	SCE	CH ₂ Cl ₂	TBAHF	37
0.30	0.56	4.41	Pt	SCE	DMF	TBAHF	38
0.34	0.71	6.27	Pt	Ag/AgCl	CH ₂ Cl ₂	TBAHF	39
0.45 ^b	0.71	4.41	GC ^c	SCE	DMF	TBAP	40

^aTEAP, Et₄NClO₄; TBAP, *n*-Bu₄NClO₄; TBAF, *n*-Bu₄NBF₄; TEAHF, Et₄NPF₆; TBAHF, *n*-Bu₄NPF₆.

^bPeak potential.

^cGlassy carbon.

$E^2 = 0.37$ V (data for **15** and **16** in MeCN, recalculated for Ag/AgCl). Hexaazaoctadecahydrocoronene **17**, one of the strongest known donors, exhibits four reversible one-electron redox couples at -0.44 , 0.06 , 0.52 , 0.92 V (versus SCE, in MeCN) [43].



Other examples of heteroatom-substituted arenes are tetrathionaphthalene (TTN) and the previously mentioned tetrachalcogenotetracenes (**13**). The former exhibits two one-electron oxidation waves and its cation radical is relatively stable [44]. The latter, with the exception of tetrathiotetracene, undergo one two-electron oxidation step. Oxidation potentials for these derivatives, together with two other examples of tetraselena analogs of perylene, are collated in Table 4.

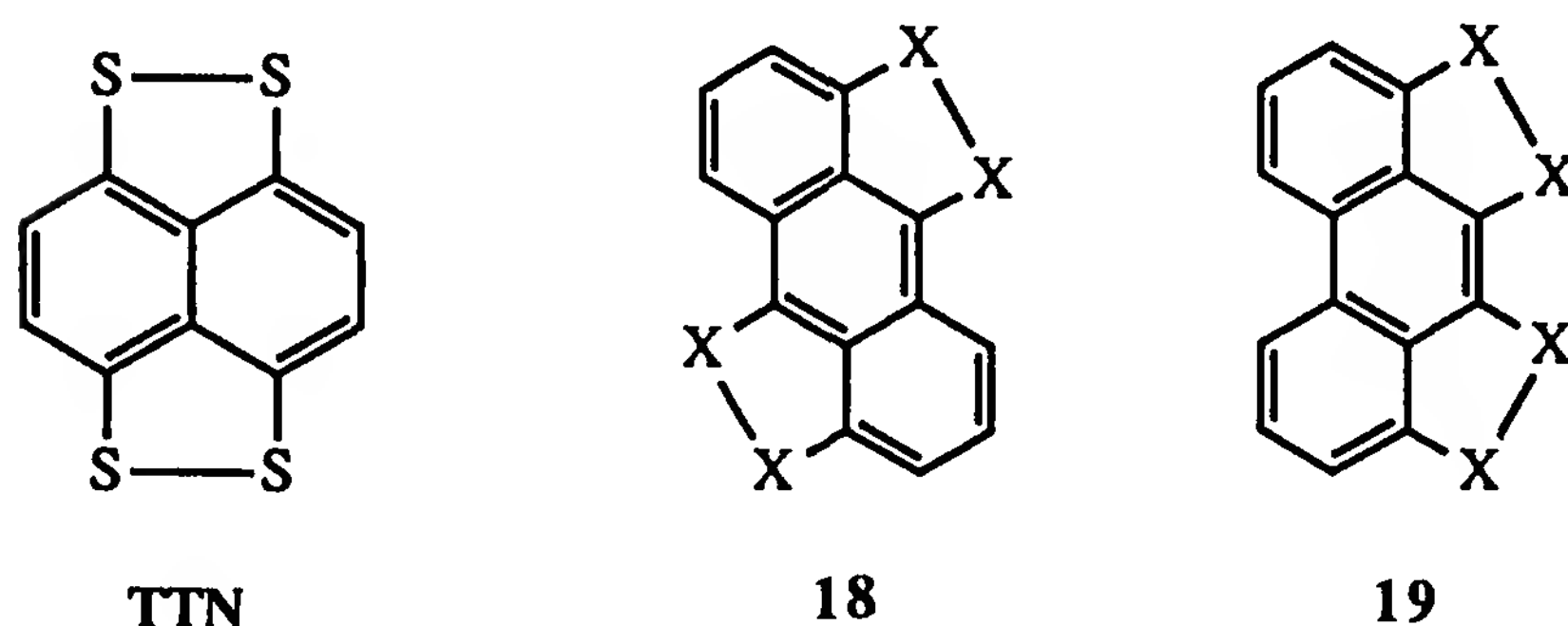


Table 4 Electrochemical Redox Potentials of Tetrachalcogenotetracenes **13** (R = H) and Tetraselenaperylenes **18** and **19**

Compound	E^1 (V)	E^2 (V)	$\log K$	Reference electrode	Ref.
13 X = Y = S	0.12	0.49	6.27	SCE	45
13 X = Y = Se ^a	0.32	—	—	Ag/AgCl	46
13 X = Y = Te	0.22	—	—	Ag/AgCl	46
18	0.47	0.78	5.25	Ag/AgCl	47
19	0.64	1.02	6.44	Ag/AgCl	48

^a E^1 value of TTF under these conditions: 0.37 V.

Undoubtedly, the most important class of organic electron donors is presented by electron-rich tetrasubstituted ethylenes, which exhibit a full range of redox properties: from irreversible oxidation at positive potentials greater than 1 V to reversible oxidation at potentials close to -1 V (see Table 5). For instance, whereas an ethylene diphenyldithio-substituted derivative, exemplified by 1,1'-bi(3,3-diphenyl-1,3-dihydrobenzo[*c*]thiophen-2-ilydene) **20** and TTF analog **21**, in which one sulfur atom is substituted by a carbonyl group, undergo irreversible oxidations, the tetraaza analog of TTF, **26**, oxidizes reversibly to a more stable form (**26a**). Other TTF derivatives present an intermediate case, as illustrated in Table 5.

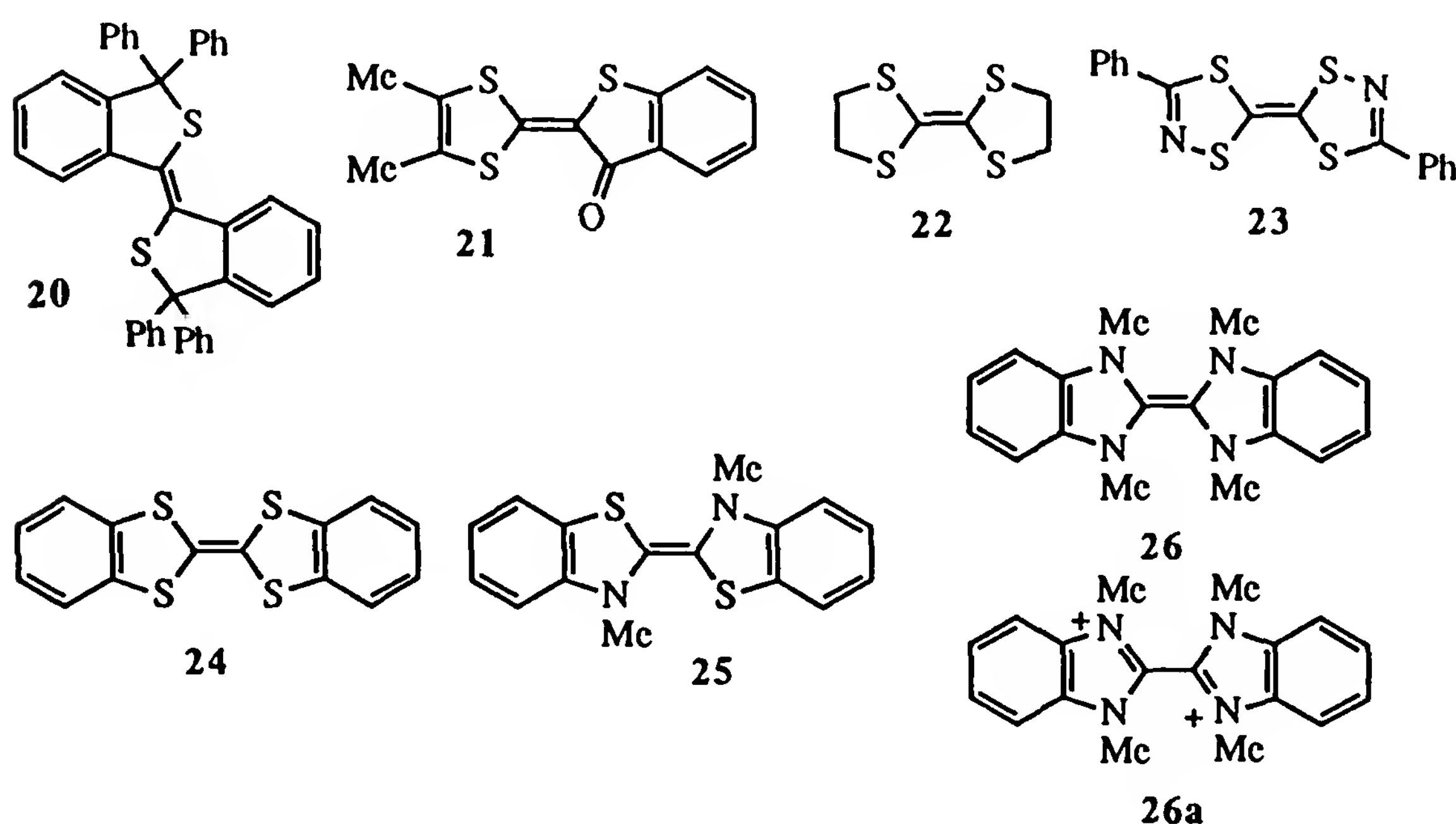


Table 5 Electrochemical Redox Potentials of Electron-Rich Tetrasubstituted Ethylenes^a

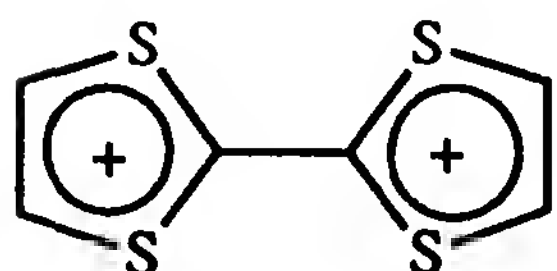
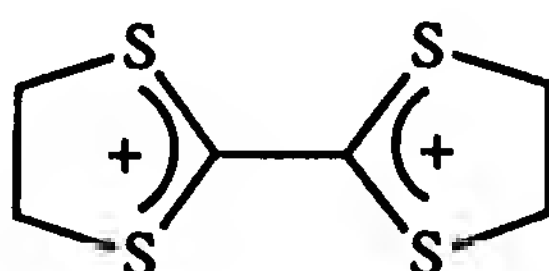
Compound	E^1 (V)	E^2 (V)	$\log K$	Reference electrode	Ref.
20	1.35 ^{b,c}	—	—	Ag/AgCl	49
21	1.18 ^b	—	—	Ag/AgCl	50
22	0.74 ^b	1.19	7.63	SCE	32
23	0.65	0.98	5.59	SCE	51
24	0.67	1.02	5.93	Ag/AgCl	52
TTF	0.35	0.71	6.10	SCE	32
25	-0.02	-0.17	2.54	SCE	52
26	-0.81	—	—	SCE	52

^aIn CH₃CN.

^bPeak potentials.

^cIn PhCN.

The delocalization of positive charges in the dication of TTF (see below, TTF^{2+}) is extended to two outer double bonds, and therefore the intramolecular coulombic repulsion is smaller than in the dication of tetrahydro-TTF (22^{2+}). As a result, a higher value of $\log K$ for **22** has been observed, and although the first oxidation of **22** takes place at a higher potential, its cation radical is thermodynamically more stable than that of TTF.

**TTF** $^{2+}$ **22** $^{2+}$

The insertion of an additional double bond between the two 1,3-dithiole moieties in TTF molecule leads to a diminished coulombic repulsion and to a less stable cation radical. This trend is observed in cases of the vinylog of TTF, **27**, vinylog of BEDT-TTF, **28**, and other TTF vinylogs listed in Table 6. It is noteworthy that further accumulation of double bonds (compounds **31** to **34**) leads to the coalescence of the two one-electron oxidation waves into one two-electron wave.

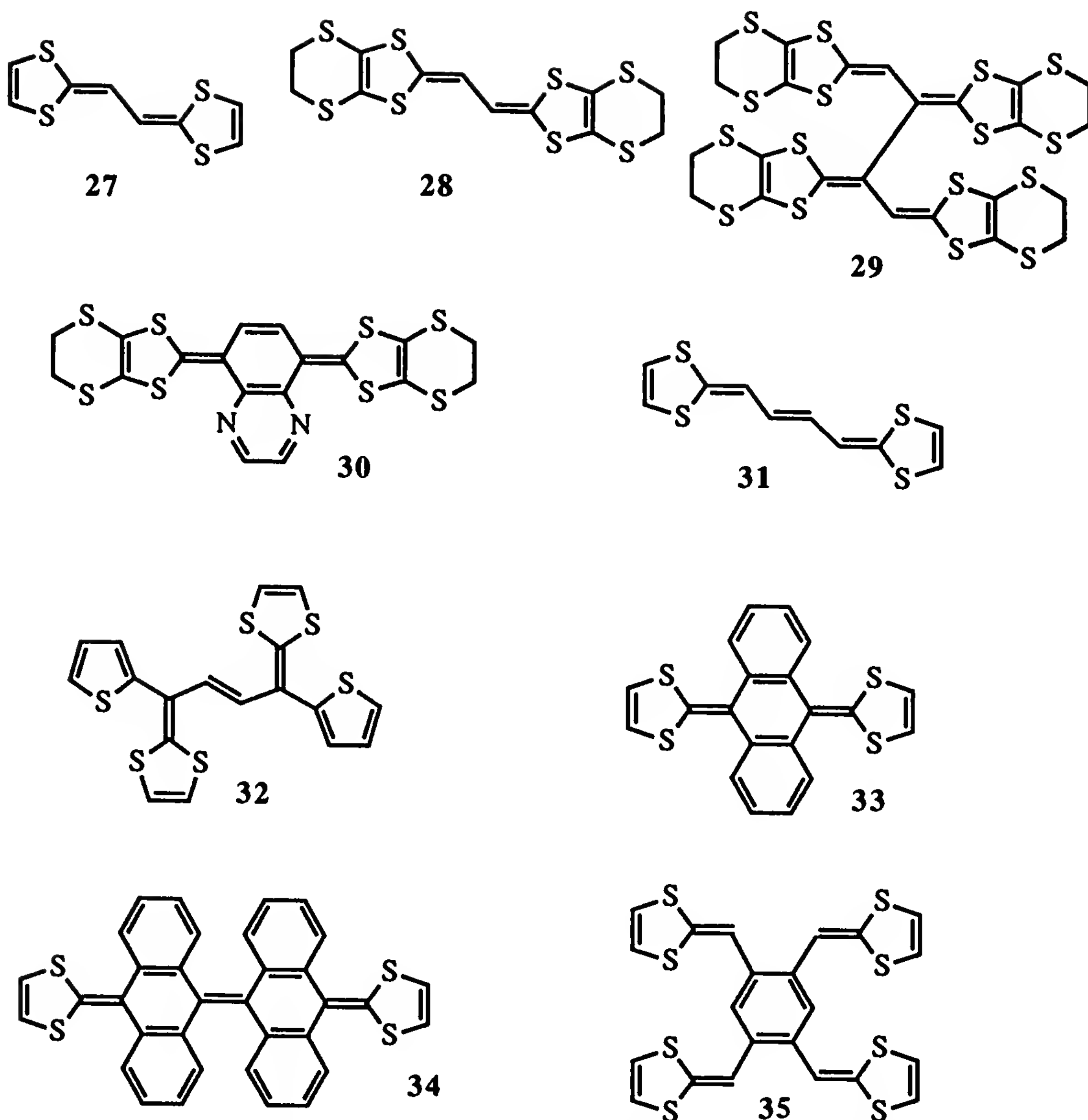
Table 6 Electrochemical Redox Potentials of TTF Vinylogs

Compound	E^1	E^2	$\log K$	Reference electrode	Ref.
27	0.20	0.36	2.71	Ag/AgCl	53
28	0.36	0.59	3.90	SCE	54
	0.45	0.66	3.56	Ag/AgCl	55
	0.48	0.71	3.90	Ag/AgCl	56
29^a	0.227	0.393	2.81	Ag/AgCl	57
30	0.33	0.49	2.71	SCE	58
31	0.22	—	—	Ag/AgCl	59
32	0.02	—	—	Ag/Ag +	60
33	0.40	—	—	Ag/AgCl	61
34	0.48	—	—	Ag/AgCl	61
35	0.46 ^b	—	—	SCE	62
	0.57 ^c	0.72	2.54	SCE	62

^a $E^3 = 0.807$, $\log K_2 = 7.02$.

^bIn DMF.

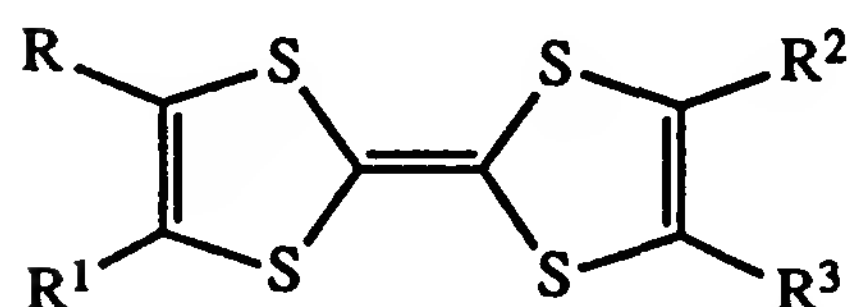
^cIn trichloroethane.



The oxidation potentials of TTF derivatives can be varied in a controlled way over a wide range by the introduction of appropriate substituents. The influence of substituents on oxidation potentials values of TTF has been discussed in many articles. For instance, the oxidation potentials of about 40 different substituted TTF derivatives have been measured under the same conditions [32]. In general, all substituents, with the exception of alkyl groups, increase oxidation potentials and the mesomeric effect of substituents have been shown to have an insignificant influence on the donor ability of TTF, in contrast to the trends observed for aromatic and heteroaromatic series. Some representative examples of oxidation potentials for substituted TTF derivatives are collected in Table 7. In the case of aryl-substituted TTFs, a usual $E_{\text{ox}}-\sigma_p^+$ correlation has been reported [63].

Table 7 Electrochemical Oxidation Peak Potentials of TTF Derivatives **36** (in MeCN versus SCE)

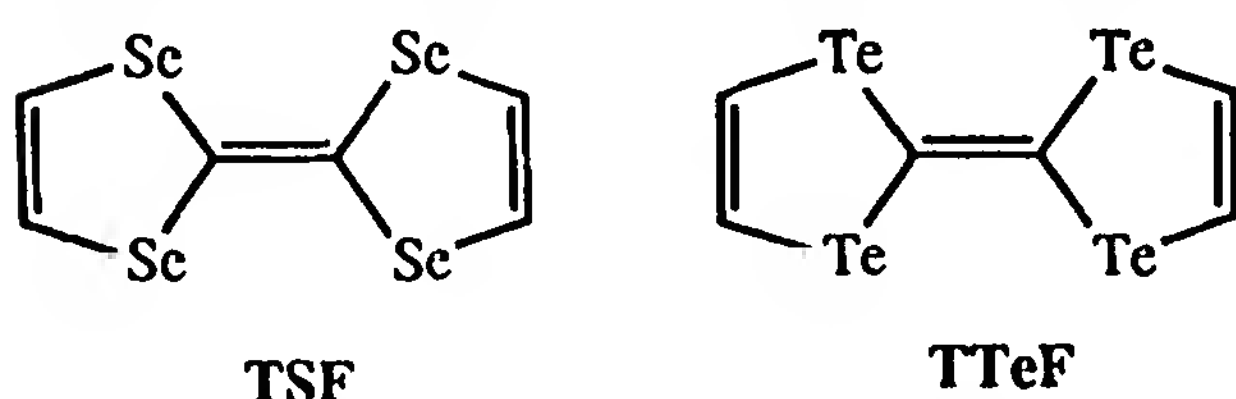
R	R ¹	R ²	R ³	E _p ¹	E _p ²	log K	Ref.
H	H	H	H	0.35	0.71	6.10	32
Me	Me	H	H	0.28	0.67	6.61	32
Me	Me	Me	Me	0.29	0.65	6.10	32
Ph	H	Ph	H	0.43	0.78	5.93	32
Ph	Ph	Ph	Ph	0.45	0.77	5.42	32
BuOOC	H	H	H	0.51	0.86	5.93	32
BuOOC	H	BuOOC	H	0.65	0.98	5.59	32
BuOOC	EtOOC	BuOOC	H	0.76	1.14	6.44	32
MeOOC	MeOOC	MeOOC	MeOOC	0.83	1.10	4.58	32
MeS	H	H	H	0.33	0.69	6.10	^a
MeS	MeS	H	H	0.42	0.73	5.25	^a
MeS	H	MeS	H	0.47	0.77	5.08	^a
MeS	MeS	MeS	H	0.50	0.76	4.41	^a
MeS	MeS	MeS	MeS	0.53	0.77	4.07	^a
MeSe	H	MeSe	H	0.46	0.77	5.25	^a
MeSe	MeSe	MeSe	H	0.48	0.78	5.08	^a
MeSe	MeSe	MeSe	MeSe	0.49	0.77	4.75	^a
Cl	Cl	Cl	Cl	1.05 ^b	1.38	5.59	^a
Br	Br	Br	Br	0.96 ^b	1.30	5.76	^a
I	H	H	H	0.45	0.83	6.44	^a
I	H	I	H	0.58	0.96	6.44	32
—CH=CH—CH=CH—		—CH=CH—CH=CH—		0.62	0.93	5.25	32
—SCH ₂ CH ₂ S—		—SCH ₂ CH ₂ S—		0.56	0.80	4.07	32
—SCH ₂ CH ₂ CH ₂ S—		—SCH ₂ CH ₂ CH ₂ S—		0.54	0.81	4.58	32
—S(CH ₂) ₄ S—		—S(CH ₂) ₄ S—		0.67	1.01	5.76	32
—SCH=CHS—		—SCH=CHS—		0.70	0.94	4.39	32

^aFrom unpublished results of V. Y. Khodorkovsky and J. Y. Becker.^bSimilar oxidation potentials for tetrachloro- and tetrabromo-TTF in CH₂Cl₂ have been reported, with irreversible E² in this solvent [64].**36**

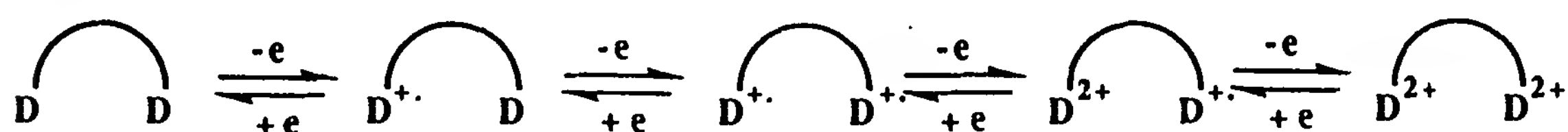
Interestingly, the introduction of methylthio groups leads to an increase in oxidation potentials and a decrease in log *K*. The substituents attached to the outer sulfur atoms also affect both oxidation potentials and the

stability of the corresponding cation radical, as demonstrated by the last four entries in Table 7.

An interesting trend in the variation of donor ability of these compounds can be observed upon replacing the sulfur atoms in TTF molecule by heavier selenium or tellurium atoms. Whereas the replacement of sulfur by selenium gives rise to an increase in the oxidation potentials, tetratellurafulvalene (TTeF) oxidizes more easily than the tetraselenium analog (TSF). The value of $\log K$ increases in the series $\text{TTeF} < \text{TSF} < \text{TTF}$, indicating that there is an increase in intramolecular coulombic repulsion (Table 8).



A series of derivatives involving several TTF units in a molecule has been designed and synthesized recently [32,65–75]. In the case where two equally substituted TTF moieties are linked together by a linking group, the molecules could exhibit a variety of cyclic voltammetry patterns, from two two-electron to four one-electron oxidation waves, depending on the degree of intramolecular interaction between the two TTF moieties. When the two donor (D) moieties can interact (through-conjugation or through-space), the coulombic repulsion between positively charged species leads to a separation between the oxidation potentials of the neutral molecule, its mono cation radical, dication radical, cation radical dication, and dication, as shown below for the case of through-space interaction:



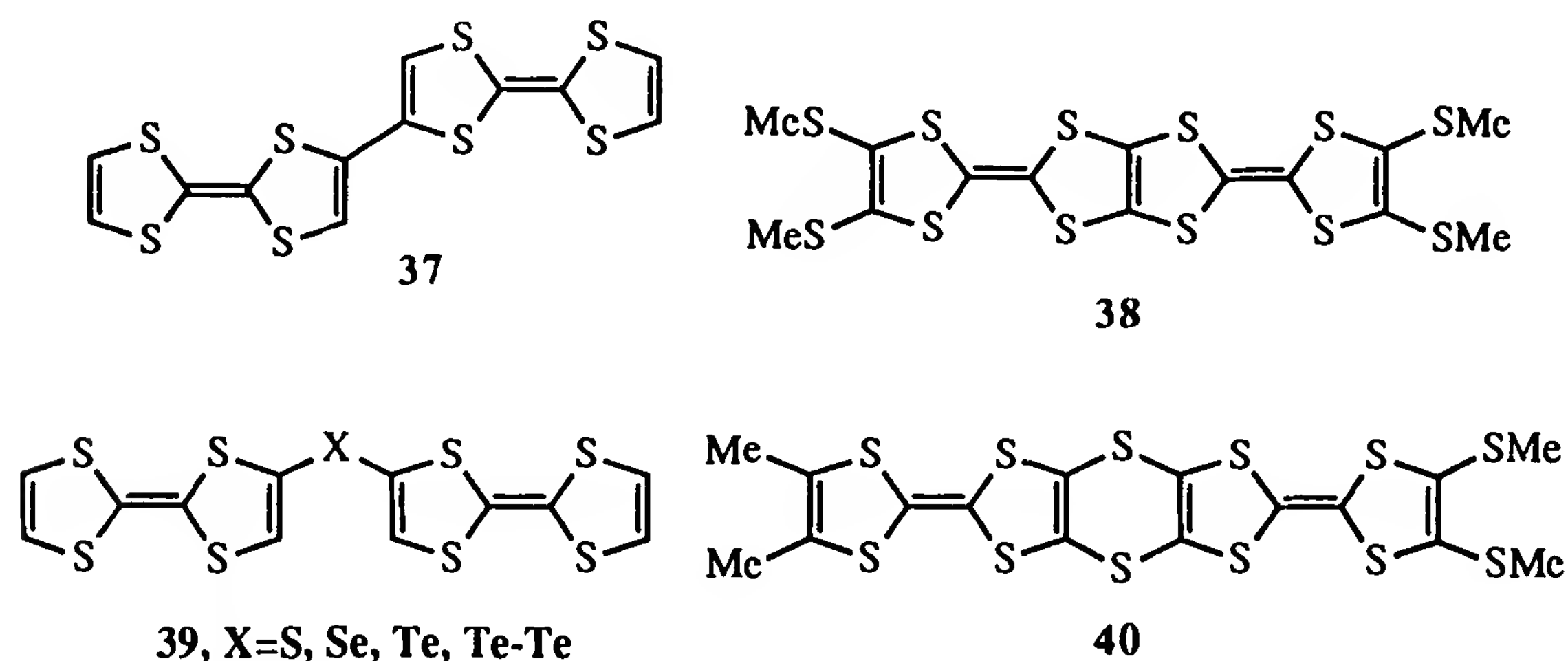
As a result, up to four redox waves can be observed by cyclic voltammetry. The separation is proportional to the degree of interaction, and if the interaction is small, some waves can overlap and therefore decrease the number of oxidation waves observed. For instance, three reversible oxidation waves have been observed for 2,2'-bis(tetrathiafulvalenyl) (37) [32]

Table 8 Redox Potentials of TTF, TSF, and TTeF (in CH_2Cl_2 versus SCE)

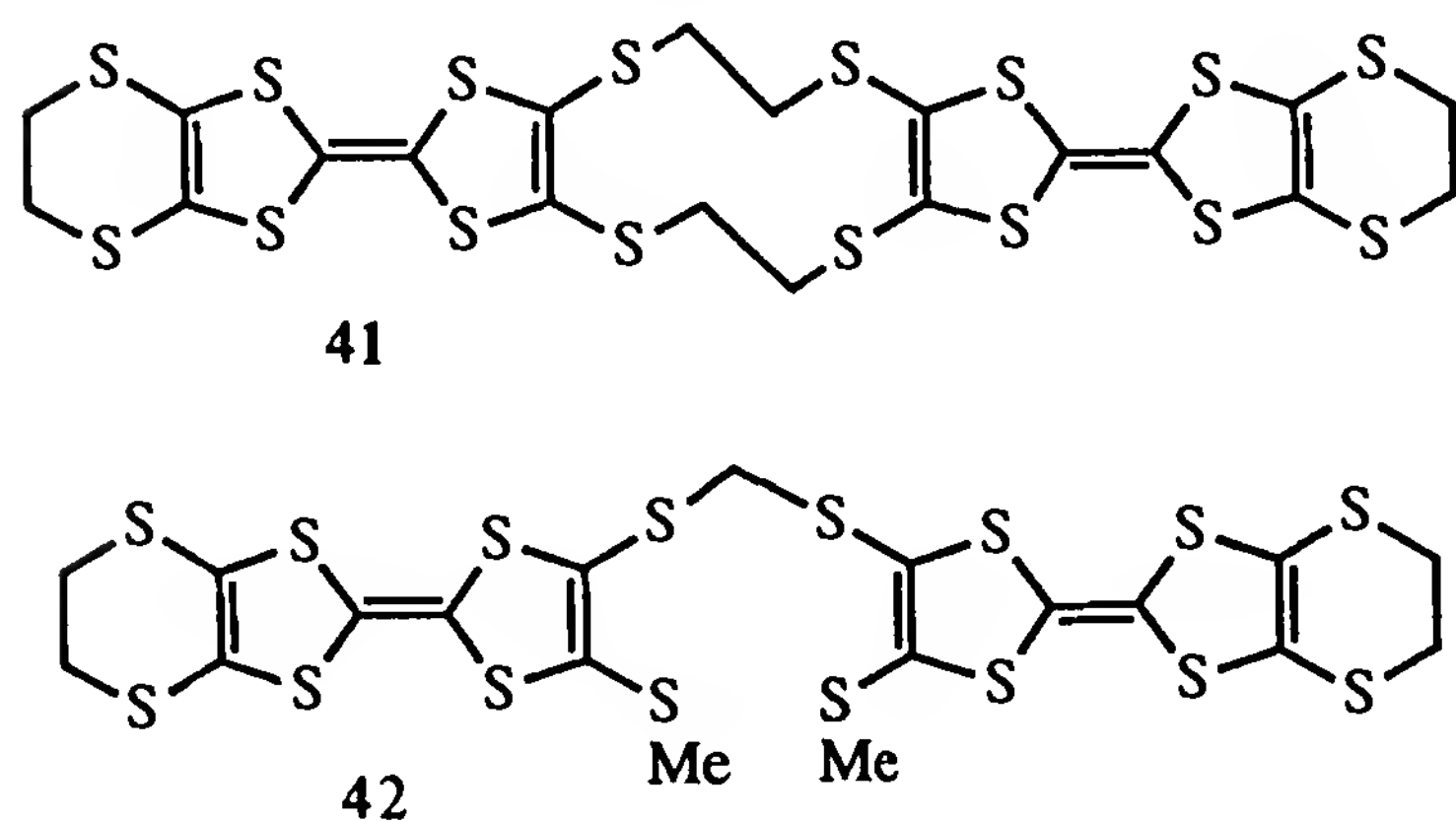
Compound	E^1	E^2	$\log K$
TTF	0.47	0.81	5.76
TSF	0.62	0.90	4.75
TTeF	0.59	0.84	4.24

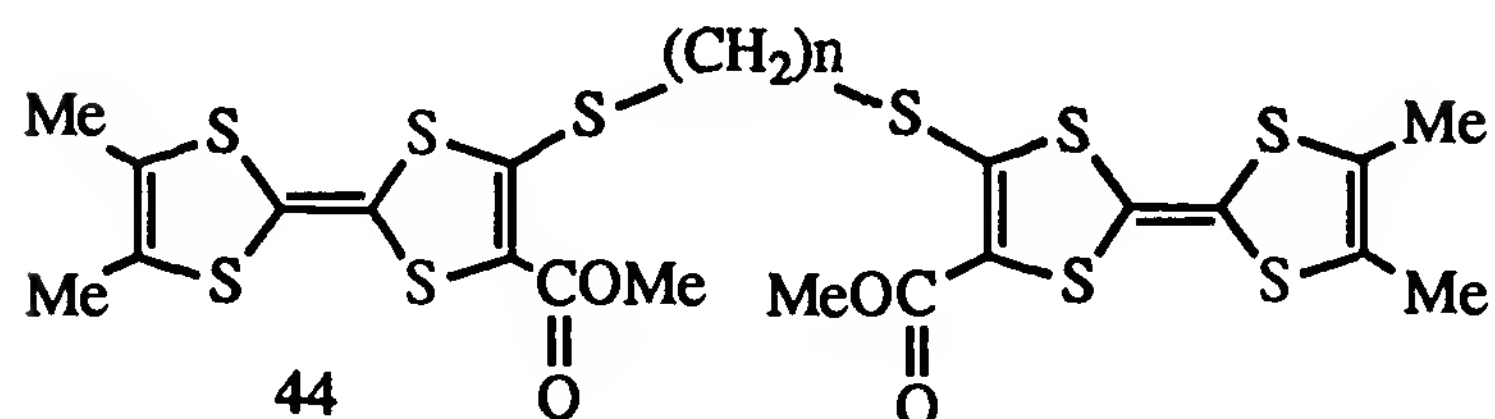
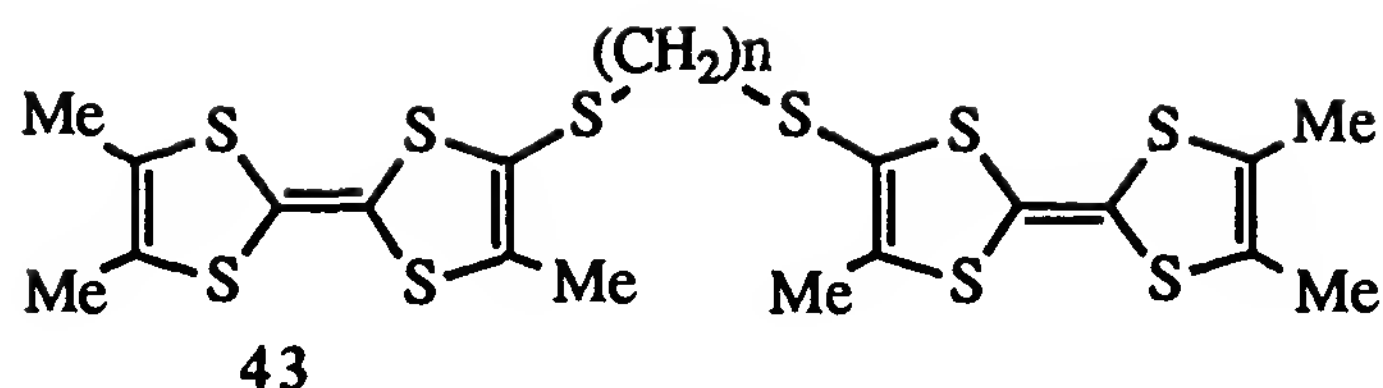
Source: Ref. 34.

and its methylthio derivative [65] and four waves for the fused analog **38** [66]. Derivatives of type **39** exhibit three oxidation waves, of which the third is irreversible. The crystal structures of **39** ($X = S$ [67] and Te [68]) reveal that both TTF moieties, in each structure, are almost orthogonal and the third oxidation wave in **39** ($X = Te$) was ascribed to the oxidation of the Te atom. The possibility of through-space interaction was considered in the cases of $X = S$ and Se . The redox properties of **39** ($X = Te-Te$) [69] are unknown because of limited solubility of this derivative. Three reversible redox waves have been detected for the condensed 1,4-dithiino derivative **40** [70]. A different behavior was observed for tri(tetrathiafulvalenyl) phosphine $(TTF)_3P$, which shows only two reversible three-electron redox waves, corresponding to the formation of three cation radicals and three dications [38].



Derivatives involving two TTF units connected by a saturated spacer exhibit interesting features as well. Thus the BEDT-TTF analog **41**, which contains two TTF moieties [71] shows only two oxidation waves at similar potentials to that of BEDT-TTF. Three redox waves have been detected for compounds **42** [72], **43** [73] ($n = 1, 2$) and **44** [74] ($n = 3$), whereas they collapse into two waves for a longer chain ($n > 2$ for **43**, $n > 3$ for **44**). Three reversible oxidation waves have been observed for a cyclophane derivative containing two TTF units [75]. Some representative data are collected in Table 9.





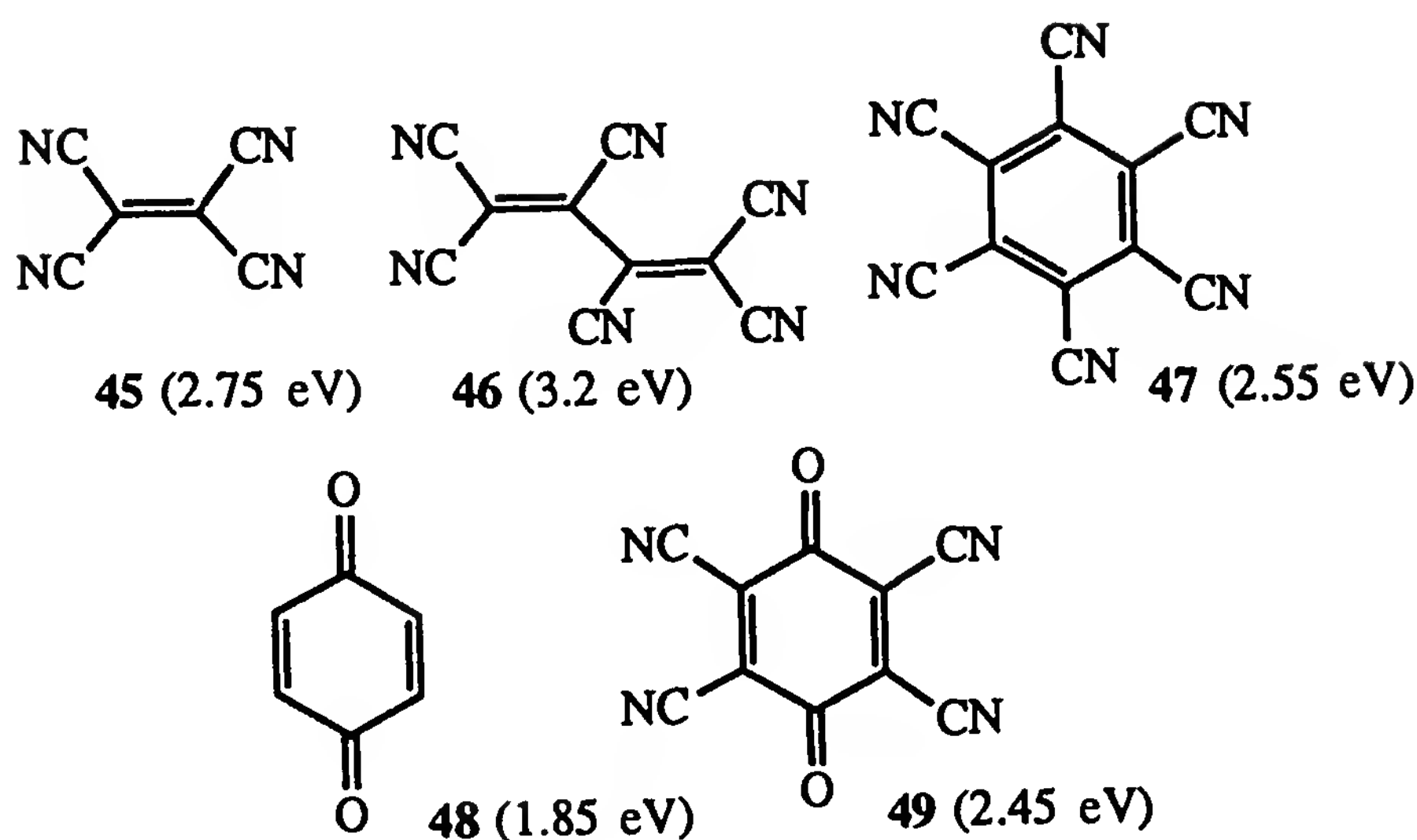
B. Electron Acceptor Ability

1. Electron Affinity of Electron Acceptors

The determination of electron affinity (EA) of neutral acceptors is not so straightforward as the determination of the ionization potential of neutral donors. Although several methods of EA determination have been employed (for a discussion, see, e.g., Ref. 20), the vast majority of data accumulated to date have been obtained by indirect methods, which do not provide absolute EA values. On the other hand, if one considers only relative EA values, satisfactory correlation between EA values obtained in the gas phase and EA values obtained indirectly, in solutions (e.g., by polarographic methods, charge-transfer complexes method), is observed. EAs for some organic neutral electron acceptors are presented below (compounds 45-49).

Table 9 Electrochemical Redox Potentials for Derivatives Containing Two TTF Moieties

Compound	E^1	E^2	E^3	E^4	$\log K_1$	$\log K_2$	Reference electrode
37	0.36	0.74	0.90	—	6.44	2.71	SCE
38	0.53	0.72	0.99	1.11	3.22	4.58	SCE
39, X = S	0.49	0.61	0.86	—	2.03	—	Ag/AgCl
39, X = Te	0.31	0.65	0.8	—	5.76	—	Ag/AgCl
40	0.51	0.68	0.94	—	2.88	4.41	Ag/AgCl
43, $n = 1$	0.22	0.36	0.80	—	2.37	7.46	SCE
43, $n = 2$	0.23	0.36	0.74	—	2.20	6.44	SCE
43, $n = 3$	0.28	0.75	—	—	7.97	—	SCE



2. Electrochemical Reduction Potentials

Electrochemical reduction potentials of neutral organic acceptor molecules vary in a wide range, from about -0.6 V for weak acceptors such as naphthoquinone, to $+0.9$ V for tetracyano-*p*-benzoquinone, which is the strongest π -acceptor known to date. The choice of strong electron acceptors as components for organic metals is not as large as that for electron donors. In fact, the great majority of conducting charge-transfer complexes known contain a *p*-benzoquinone derivative as the acceptor component, usually tetracyano-*p*-quinodimethane (TCNQ) or dicyanoimino-*p*-quinodimethane (DCNQI) derivatives. Their first reduction potentials ($+0.1$ to $+0.2$ V versus SCE) do correspond well to the oxidation potentials of common electron donors ($+0.35$ to $+0.6$ V versus SCE). In comparison, acceptors such as tetracyanoethylene (TCNE, **45**), chloranil (**50**), and dichlorodicyano-*p*-benzoquinone (DDQ), are too strong to lead to partial degree of charge transfer, whereas quinones like *p*- and *o*-benzoquinone or their fused analogs are too weak (their anion radicals are rather strong nucleophiles) for this purpose. Reduction potentials for selected organic acceptors are gathered in Table 10. The difference between first and second reduction potentials (ΔE) is also informative: TCNE, chloranil, and DDQ give extremely stable anion radicals but never gave conducting materials even in combination with weaker donors.

An extensive review of the redox properties of several substituted *p*-ben-

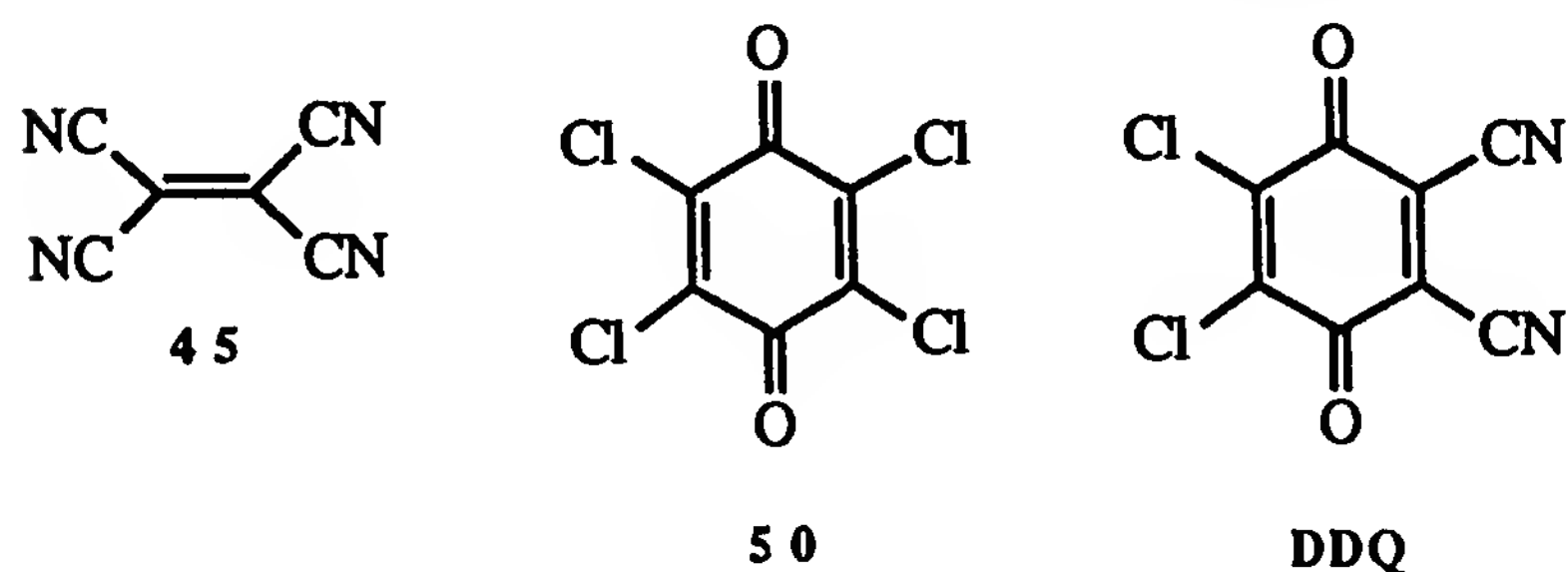
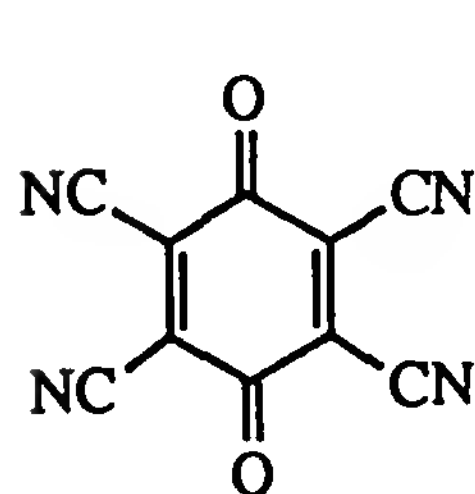
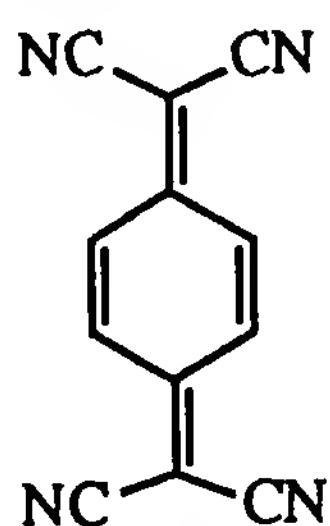
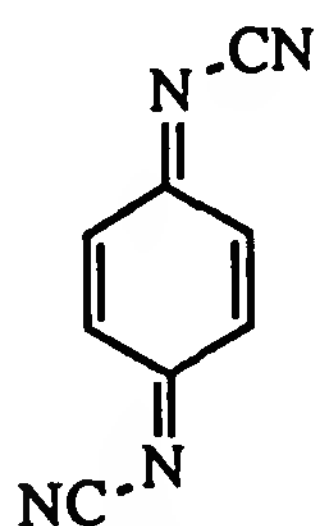


Table 10 Electrochemical Redox Potentials of Some Common Organic π -Electron Acceptors^a

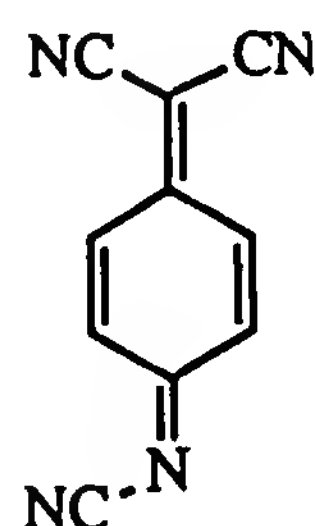
Compound	E^1	E^2	log K	Refs.
45	0.15	−0.57	12.20	76
50	0.05	−0.79	14.24	77
DDQ	0.59	−0.25	14.24	77
49	0.90	0.09	16.78	77
TCNQ	0.17	−0.37	9.15	77 ^b
DCNQI	0.17	−0.34	8.64	^b
51^c	0.16	−0.42	9.83	78

^aIn MeCN versus SCE.^bV. Y. Khodorkovsky and J. Y. Becker, unpublished results.^cIn CH₂Cl₂ versus Ag/AgCl.**49**

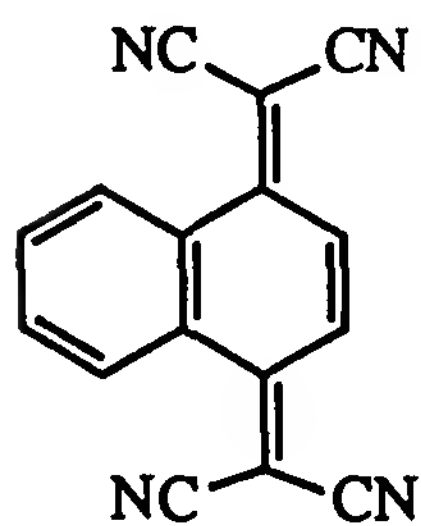
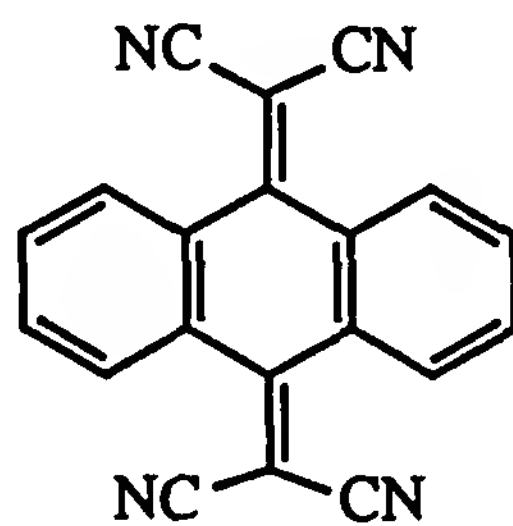
TCNQ

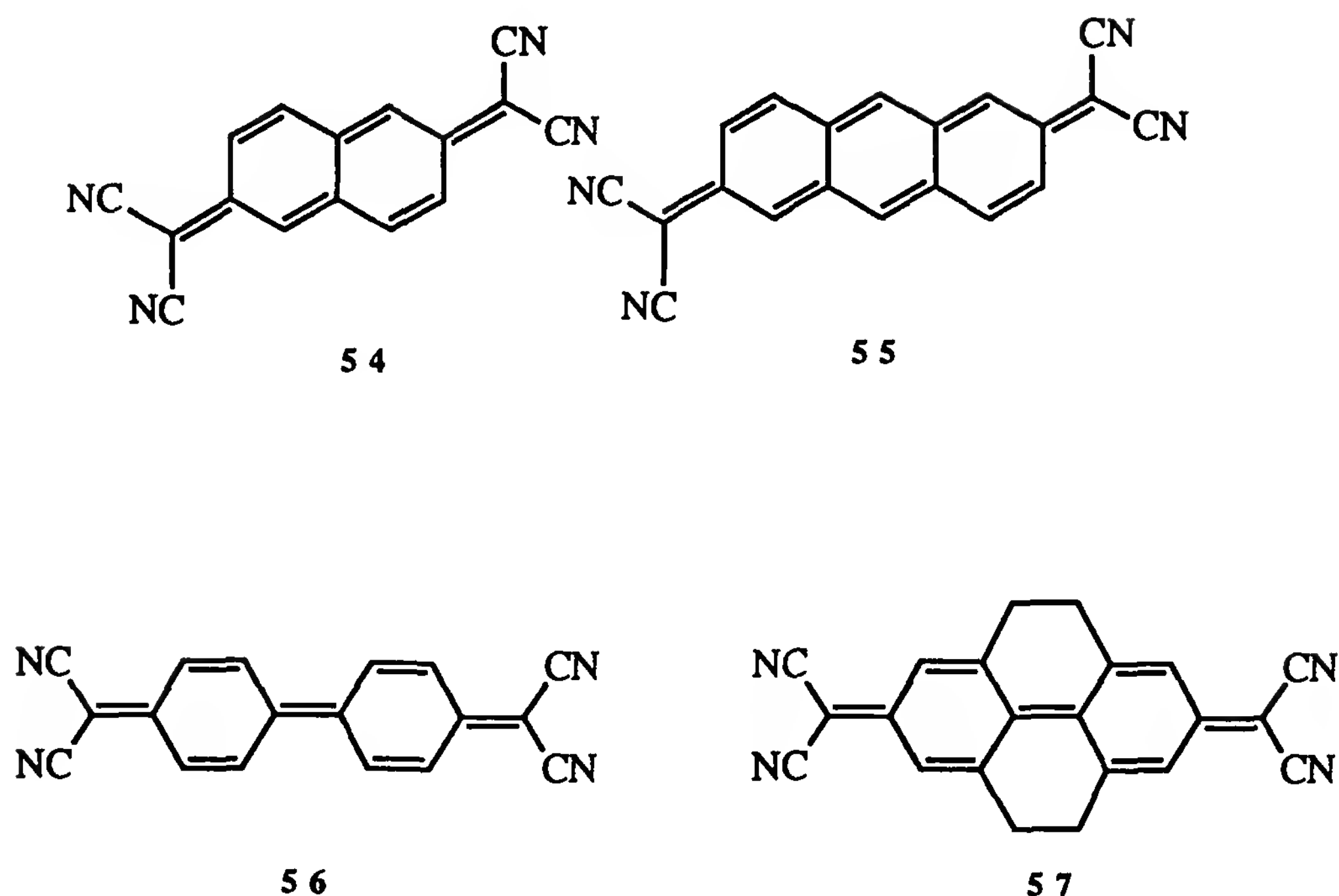


DCNQI

**51**

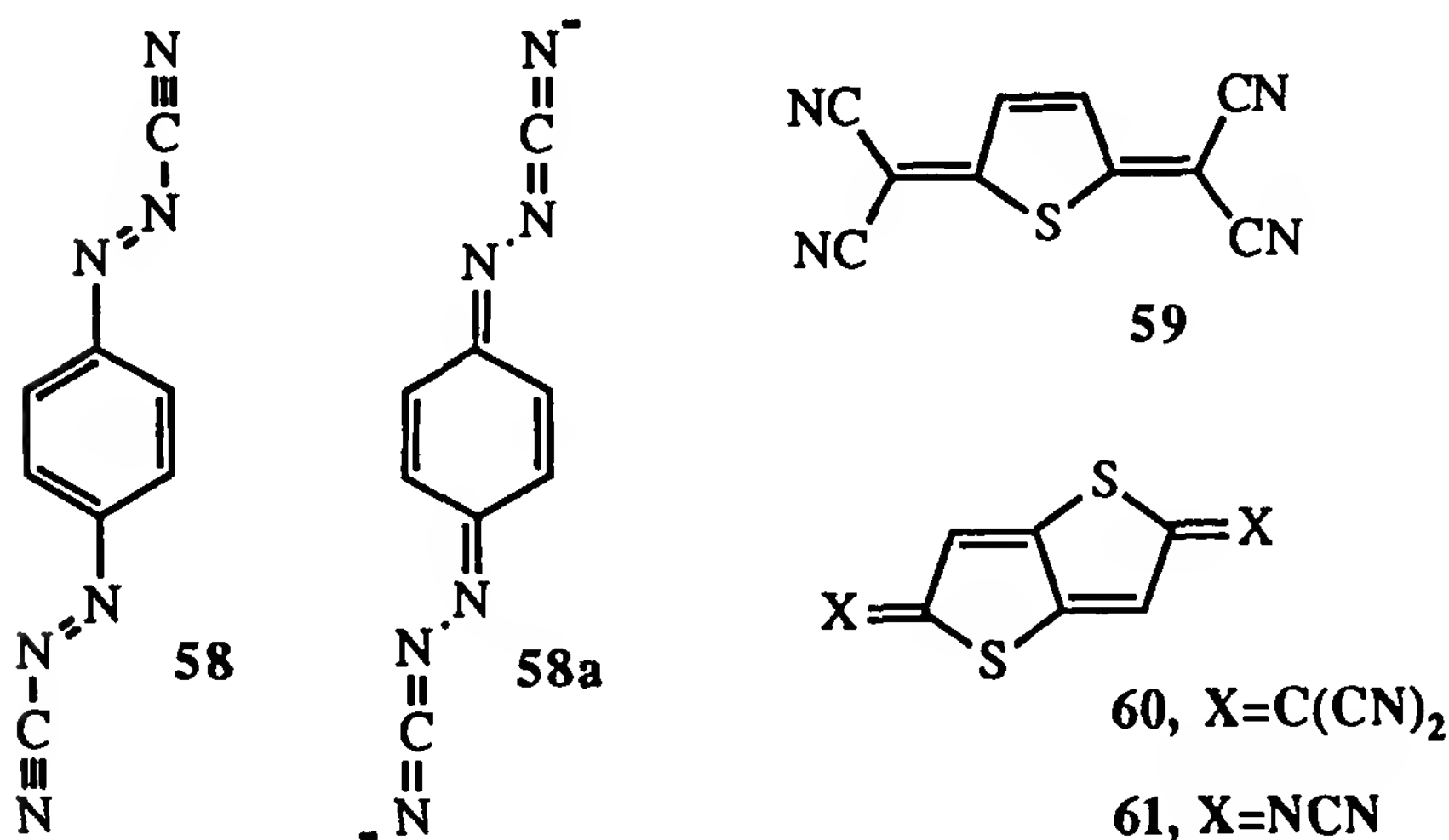
zoquinones and the corresponding TCNQ and DCNQI derivatives is presented in Ref. 79. It is noteworthy that upon increasing steric hindrance in the series TCNQ–benzo-TCNQ (**52**) and dibenzo-TCNQ (**53**), a drastic decrease in acceptor ability occurs. For instance, the first reduction potentials of 2,6-naphthoquinone (**54**) and 2,6-anthraquinone (**55**) derivatives are essentially similar to that of TCNQ because of the absence of steric hindrance [80]. The difference between the second and first reduction potentials decrease for TCNQ > **54** > **55**, due to a decrease in coulombic repulsion. Fused DCNQI derivatives are stronger acceptors than the corresponding TCNQ derivatives, because the steric hindrance is smaller in the former ones [81]. Tetracyano-diphenodiquinodimethane (**56**) and tetracyanotetrahydropyrenoquinodime-

**52****53**



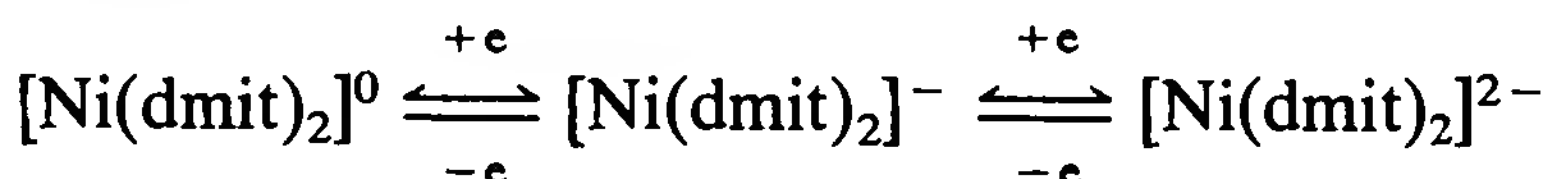
thane (57) are other examples of strong quinoid acceptors, with first reduction potentials similar to that of TCNQ [82].

Most organic acceptors employed in the preparation of organic conducting materials belong to a class of polycyano compounds. The reasons are quite obvious if one takes into consideration the unique properties of the cyano group, which is one of the strongest acceptor substituents known, and also the smallest to cause minimal steric strain. Among other polycyano derivatives to be mentioned are 1,4-phenyl-bis(diazocyanide) **58** [83], which its reduced form corresponds to a quinoid structure **58a**, and thieno derivatives **59** [84,85], **60**, and **61** [86], with acceptor properties similar to those of TCNQ.

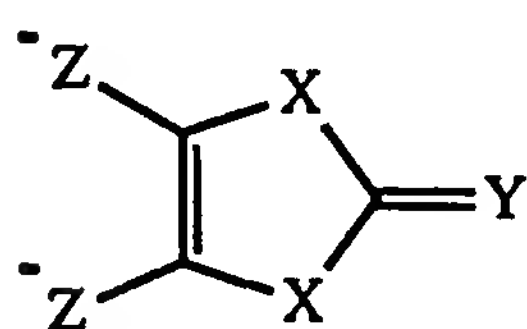


Another very important group of organic acceptors employed as components for organic metals during the last decade is presented by dithiolene metal complexes [e.g., 1,3-dithiole-2-thione-4,5-dithiolate (dmit) ligand and

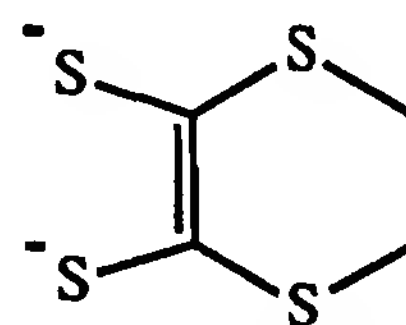
its structural analogs]. DMIT metal complexes are the only known acceptors to date (except for C_{60}), which give rise to superconducting materials [87] and could undergo two-stage one-electron redox conversions according to the equation



Metal complexes of other isologous 1,3-dichalcogene-2-chalcogenone-4,5-dichalcogenolates of general formula **62** have also been described (e.g., Ref. 88). The redox potentials in this series, for example, Ni complexes, vary in the narrow range of -0.175 V for “dmit” to -0.108 V for “dsis” (in DMF, versus SCE).

**62**

X = Y = Z = S, dmit
 X = Z = S; Y = Se, dmise
 X = Y = S; Z = Se, dsit
 X = S; Y = Z = Se, dsise
 X = Y = Z = Se, dsis

dddt **63**

A close structural relationship with TTF derivatives, especially BEDT-TTF, is exhibited by “dddt” metal complexes [dddt = 5,6-dihydro-1,4-dithiin-2,3-dithiolate (**63**)]. The most interesting feature of this dithiolene ligand is the ability of its metal complexes to form not only anionic salts like dmit, but also cationic salts like TTF derivatives [89], to afford non-stoichiometric IR salts of type $[M(dddt)_2]_m X_n$. Thus the cyclic voltammogram of $[Bu_4N][Ni(dddt)_2]$, after its initial oxidation, exhibits the reduction of neutral $[Ni(ddt)_2]^0$ to anion $[Ni(ddt)_2]^-$ at 0 V, and its further reduction to the dianion $[Ni(dddt)_2]^{2-}$, as well as the oxidation of $[Ni(dddt)_2]^0$ to the cation $[Ni(dddt)_2]^+$ at 0.8 V (MeCN versus Ag/Ag/Cl). The feasible synthesis of conducting donor–acceptor complexes involving dddt metal derivatives as donors and dmit metal derivatives as acceptors has also been demonstrated [90].

C. Degree of Charge Transfer in Ion-Radical Salts and CT Complexes

The vast majority of strong donors and acceptors employed in the synthesis of conducting organic materials are reversible two-step redox systems. This reversible behavior ensures electron transfer from a donor to an acceptor molecule without decomposition of the charged intermediates formed. Another important conclusion is that for CT systems, the degree of charge transfer from a donor to an acceptor determines most of the electronic characteristics (and sometimes also the crystal structure [91]) of such sys-

tems. It is evident that there is no sharp boundary between charge-transfer complexes (which are characterized by neutral ground state and ionic excited state) and ion-radical salts (ionic ground state and neutral excited state).

The results from research on donor–acceptor systems accumulated to date show that the existence of partial charge transfer is a prerequisite for conducting CT complexes and ion-radical salts. In general, weak π – π complexes with a degree of charge transfer less than 0.4 exhibit semiconducting and photo-semiconducting properties. Ion-radical salts with a degree of charge transfer more than 0.7 are usually insulators. The degree of charge transfer can be determined experimentally by several methods, such as dipole moment measurements, nuclear quadrupole resonance, x-ray electronic spectroscopy, IR spectroscopy, and so on. Such relevant data and methodology have been reviewed and discussed in the literature (e.g., Ref. 92). The charge-transfer complex of TTF with tetracyanoquinodimethane (TCNQ) was historically the first organic metal-like conductor obtained [1,2] and the degree of charge transfer in this complex was found to be 0.59 [93]. Selected examples of the degree of charge transfer in tetrathiafulvalene (TTF) complexes with different acceptors are listed in Table 11.

The degree of charge transfer in the solid state depends on the ionization potential (IP) of the donor, the electron affinity (EA) of the acceptor, and Madelung energy. In solutions, the analog of the Madelung energy is presented by the difference in solvation energies of ion radicals and the parent neutral molecules. Both theoretical and experimental investigations demonstrated that the dependence of the degree of charge transfer δ with the difference $IP - EA$ is not linear. The transition from weak complexes with $\delta < 0.4$ to strong complexes with $\delta > 0.7$ proceeds sharply within the limits $3.5 < IP - EA < 4.1$ eV. Essentially the same dependence was

Table 11 Degree of Charge Transfer (δ) Between TTF and Different Acceptors^a

Acceptor (selected examples)	δ
Chloranyl	0.27
3,3,5,5-Tetrabromo- <i>p</i> -diphenoquinone	0.36
TCNQ	0.59
3,3,5,5-Tetrachloro- <i>p</i> -diphenoquinone	0.81
Tetrafluoro-TCNQ	1

^aFrom Ref. 92, determined by x-ray electronic spectroscopy.

observed when electrochemical redox potentials of donors and acceptors were used as a measure of donor–acceptor ability, within the limits [92] $-0.25 \text{ V} < E_{\text{ox}} - E_{\text{red}} < 0.34 \text{ V}$.

The formation of nonstoichiometric cation-radical and anion-radical salts can be treated in an analogous manner to the formation of CT complexes. For instance, chemical or electrochemical oxidation of some of the donor molecules in solution leads to the formation of some oxidized molecules, namely cation radicals, which are actually strong acceptors. The latter could easily interact with neutral donor molecules to produce partially positively charged stacks in which the charges are compensated by the counter anions. Such interactions in cation-radical or anion-radical salts could afford nonstoichiometric salts with a formal partial degree of charge transfer, which is determined by the ratio $m:n$ in D_mX_n , where X is a counteranion. Representative examples are listed in Table 12.

III. DONOR AND ACCEPTOR COMPONENTS OF MOLECULAR ORGANIC CONDUCTORS: STRUCTURAL ASPECTS

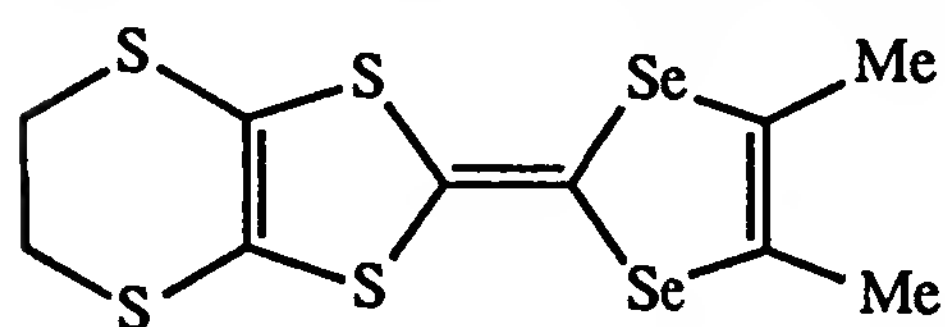
Initial studies on the first example of an “organic metal,” TTF–TCNQ, and other conducting one-dimensional CT complexes have shown an important structural feature: the presence of strong intrastack delocalization of charge and weak interstack interactions between segregated stacks of donor and acceptor molecules. Their tendency to undergo metal–insulator transition was observed and ascribed to a Peierls distortion, characteristic for one-dimensional systems. Further studies on the highly conducting complex of tetramethyl-TSF and 2,5-dimethyl-TCNQ under pressure [98] led to the conclusion that its properties are mostly determined by spatial arrangement of the donor component within the crystal, in particular the tetramethyl-TSF stacking. Therefore, succeeding endeavors focused to a large extent on this particular donor, which successfully led (in 1980) to

Table 12 Formal Degree of Charge Transfer in TTF Cation-Radical Salts

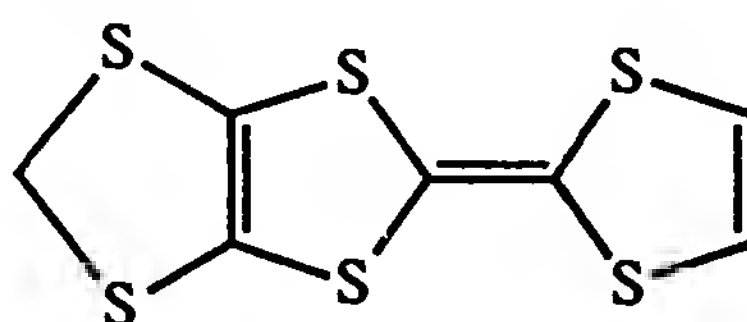
Compound	Formal δ	Conductivity (S/cm) (ambient pressure)	Ref.
(TTF)Cl ₂	2	Insulator	94
(TTF)Cl	1	Insulator	94
(TTF)Cl _{0.68}	0.68	100–500	94
(TTF)(NO ₃) _{0.55}	0.55	1200	95
(TMTSF) ₂ ClO ₄	0.5	Superconductor at 1.3 K	96
κ -(BEDT-TTF) ₂ Cu(SCN) ₂	0.5	Superconductor at 10.4 K	97

the discovery of the first organic superconductors, involving the salts $(\text{TMTSF})_2\text{PF}_6$ (under hydrostatic pressure) [99] and $(\text{TMTSF})_2\text{ClO}_4$ (under ambient pressure [96]. The most important structural feature of these superconductors, as deduced from their x-ray structure, is the presence of two- and even three-dimensional inter- and intrastack network of $\text{Se} \cdots \text{Se}$ interactions.

The second family of superconducting materials is based on cation-radical salts of another donor, bis(ethylenedithio)-TTF (abbreviated BEDT-TTF or ET), which exhibit two-dimensional network mostly due to interstack $\text{S} \cdots \text{S}$ interactions [100]. Another important feature of BEDT-TTF salts is their tendency to give polymorphs. For instance, $(\text{BEDT-TTF})_2\text{I}_3$ salt affords four polymorphs (α , β , θ , and κ phases), of which only the first undergoes metal-insulator transition, while the others are superconductors at ambient pressure (see Chapter 10 of this book). It is quite surprising that of all numerous BEDT-TTF structural analogs synthesized to date, only two salts of *unsymmetrical* derivatives, DMET [101] and MDT-TTF [102], led to superconductors.



DMET

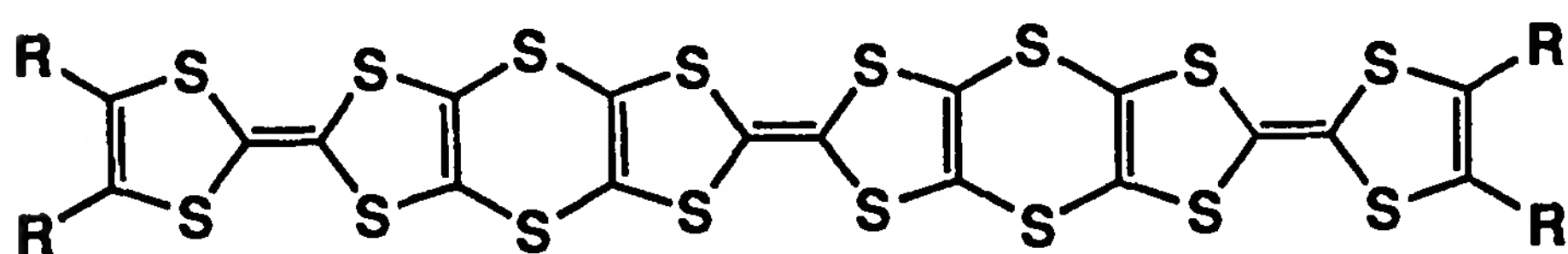


MDT-TTF

The third family of superconductors is based on “dmit” nickelate complex ion as the acceptor, which gives a CT complex with TTF [103], or anion-radical superconducting salt with tetramethylammonium cation [104].

The results above illustrate that high conductivity and superconductivity could be observed in various kinds of IR salts and CT complexes involving very different components. However, they do not provide us with sufficient data to postulate guidelines for designing new conducting systems. The crystallographic approach is discussed in detail in Chapter 5, so here we mention only some general trends, related to the effect of introduction of specific substituents into the TTF moiety on the stacking modes. The main goal during the search for new TTF derivatives was to obtain new substances, possessing not only the desired electron-donating ability, but also strong intermolecular interactions. The latter property, which should permit delocalization of an unpaired electron along the uniform stack, is achievable (e.g., by increasing the number of relatively voluminous heteroatoms). Indeed, the addition of four sulfur atoms to the TTF skeleton, to form BEDT-TTF, has led to a family of superconductive salts. The striking observation that the nature and size of donor or acceptor have no substantial effect on the intermolecular distance within a stack (3.2 to 3.5

Å) leads to the notion of improving intermolecular interactions within a given stack by increasing the volume of heteroatoms. The enhanced intermolecular interactions were indeed observed by substitution of sulfur with selenium. Whereas various organic salts of tetramethyltetrathiafulvalene never exhibited superconductivity, those of tetramethyltetraselenatetrathiafulvalene, known as Bechgaard salts, were the first organic superconductors to be discovered [99]. The next reasonable step was to synthesize a seleno analog of BEDT-TTF, but this compound appeared to possess very limited solubility, even to the extent that its oxidation potential could be determined [105]. In general, the solubility problem implies severe limitations in choosing proper components for organic metals. Thus derivatives involving three TTF structural units **64** cannot be dissolved even in boiling nitrobenzene [106]. Another restriction stems from synthetic difficulties; for instance, only a very small number of tetratellurafulvalenes are known to date: TTeF [34], dibenzo [107], hexamethylene [108], β,β' -dimethylhexamethylene [109], and thienocondensed [110] derivatives. So far, attempts to synthesize tetramethyl-TTeF have been unsuccessful.



64 (R = H, Me)

Another important way to increase the intermolecular interactions is the use of the effect of a “molecular fastener” [111]. This effect has been observed in tetrakis(alkylthio)tetrathiafulvalenes (alkyl is longer than C₈), for which a relatively high conductivity was observed even in neutral donors [111]. This phenomenon was explained by the enhancement of intermolecular interaction induced by van der Waals interactions of the alkyl side chains. Interestingly, a high intrinsic conductivity has been observed also for tetrakis(methyltelluro)tetrathiafulvalene, for which tellurium atoms were claimed to play the role of “molecular fasteners” [112].

Although there exist many other correlations of the type “structure conductivity,” discussed in other chapters of this book (see also Refs. 4 to 11), none of them can be used for real design of a crystal lattice. We limit ourselves to a consideration of the possibility to construct molecules with a “built-in” tendency to give a crystal lattice required for a high metallic conductivity.

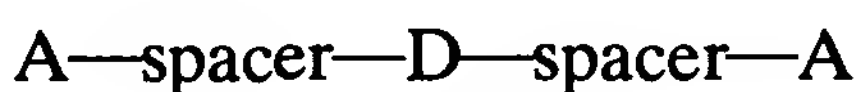
A. Strategic Design of Molecular Organic Conductors

As stated above, in donor–acceptor complexes, which are comprised of individual donor (D) and acceptor (A) molecules, the factors that influence

the formation of a desired crystal structure are essentially at random and are not readily susceptible to chemical control. The randomization can be reduced significantly by considering molecules of types **65** and **66**, in which the D and A are *chemically bonded* to one another by nonconjugated spacers (hydrocarbon chain or heteroatoms) [114].



65



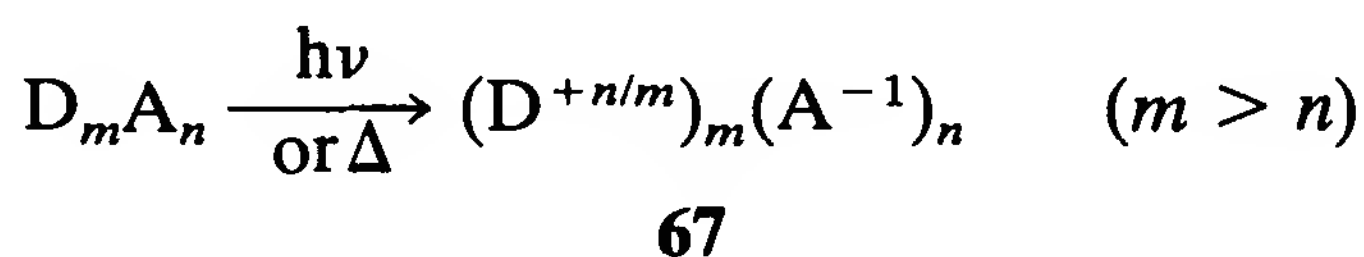
66

These types of molecules belong to a general class of materials that can be represented by the formula $\text{D}_m\text{—A}_n$ and in which the D and A moieties are included in the same molecule with a predetermined stoichiometric ratio $[m:n]$. Prototype molecules of this type will fulfill the following conditions:

1. The stoichiometric ratio is predetermined and can be modified chemically.

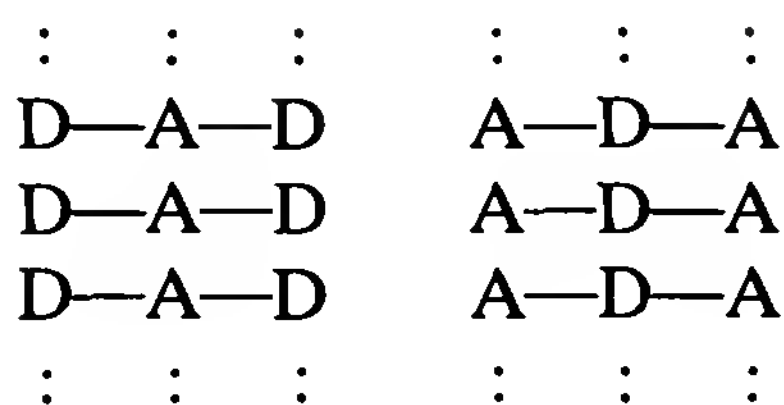
2. The ionization potential of D and the electron affinity of A may be modified by altering the mode of chemical substitution. In this manner it is possible to create molecules in which D and A are in the neutral ground state or in the charged state (as a result of the transfer of an electron from D to A). In principle, the former will behave like photoconductors or semiconductors, while the latter will behave like metallic conductors or superconductors, depending on the factors enumerated below.

3. For a fixed stoichiometry between A and D, the maximum degree of charge transfer (δ) is also determined. For instance, for **65** we would obtain a value of $\delta_{\text{Dmax}} = 0.5$ while $\delta_{\text{Amax}} = -1$, and exactly the opposite will hold for **66**. In general, for molecules of the motif $\text{D}_m\text{—A}_n$, the values of δ will be $+n/m$ and -1 , respectively (for $m > n$). When D is a very good donor and A is an excellent acceptor, these values will determine the maximum degree of charge transfer in the ground state. When the donor and acceptor abilities of D and A are not high, it is possible to obtain the desired degree of charge transfer via photo or thermal excitation, as shown in **67**.



4. The symmetrization of the two ends of the molecule *increases the chances* for packing in segregated stacks [115]. The ideal packing is rep-

resented in a schematical way, although other possibilities cannot be ruled out.



It is important to point out here that in principle, by utilizing the armory of synthetic tools available to the organic chemist, it is relatively easy to modify the symmetric architecture of the D's or A's in **65** or **66** in a way that will increase the likelihood for aggregation in segregated stacks. Possible asymmetric modifications of this type of molecules are represented schematically by **68** and **69**.

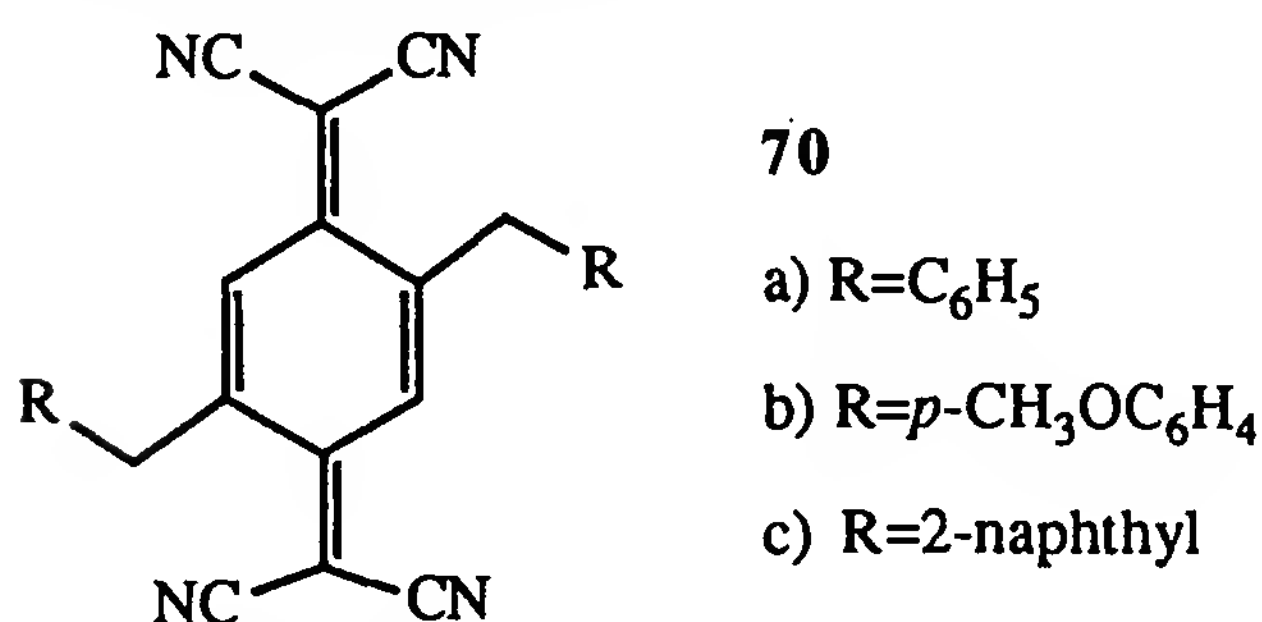


5. By chemically linking A and D moieties in the same molecule one could, in principle, obtain arrays containing three segregated stacks of moieties. This type of structure has not been found in any of the crystalline donor-acceptor complexes. The existence of direct interactions between stacks of D moieties and A moieties in the same material tends to increase electronic stabilization in the same way that mixed stacks are stabilized [11]. This type of electronic stabilization will *increase* the possibility of obtaining the desired structural isomer with segregated stacks. The degree of interaction between D and A can be tuned by chemical and geometrical modification of the molecule. One of the possibilities is to change the number of CH₂ groups, or introduce heteroatoms as spacers.

6. The barrier to electron hopping along the columns of molecules may be reduced by introducing heavy atoms into the donor moieties in **65**, **66**, **68**, and **69**. This type of substitution will lead at least to two important effects: first and foremost there will be an increase in the overlap between the molecules along the stack due to the large size of the atomic orbitals of the heavier atoms. A secondary effect is the lowering of the reorganization energy in the process $\text{D}^0 \rightarrow \text{D}^+$ due to concentration of the frontier orbital (HOMO) of the donor on the heavy atom [11]. As a result, the nonbonding character of this orbital increases and the reorganization energy concomitantly decreases. Despite the combination of these two effects, it is possible to reduce the reorganization energy of a molecule to zero [113].

1. Prototype Molecules

A prototype molecule for D₂A motif is presented by dibenzyl TCNQ (**70a**) [114]. Although the phenyl group is a very weak donating group, the crystal structure exhibits a unique space architecture. Most of the known weak charge-transfer complexes give mixed stacking. Figure 4 shows that for dibenzyl TCNQ there is a tendency of the molecules to form infinite segregated stacks of TCNQ moieties along the *c* crystallographic axis. It seems that the factor which prohibits the formation of desired stacking is the tendency of the plane of the donor moieties to be nearly perpendicular to the TCNQ plane, apparently due to both steric factors and free rotation of the phenyl groups.



Interestingly, the other derivatives containing stronger *p*-anisyl and 2-naphthyl donor substituents (**70b** and **c**) are isostructural with the structure of **70a** (see Table 13), and all of them crystallize in the same manner [115]. Recently, it was found that 2,5-[Ph(CH₂)₃]₂ TCNQ is also isostructural to **70** [116].

The degree of charge transfer (D → A) of the members of this family was determined according to the methods of Kistenmacher et al. [117] and Chappell et al. [118] and was found to be similar (about 0.2) for all of them. This degree of charge transfer is low and is characteristic for donor–acceptor complexes with a neutral electronic ground state. The donors in **70** are not strong ones, and hence the transfer of an electron from D to A does not take place to a very large extent, so that the ground state of the resulting molecular crystal remains uncharged.

It is noteworthy that the color of compounds **70a** to **c**, which is yellow for all of them in solution, changes from transparent orange for the weakest donor (Ar = C₆H₅) to violet-black for the better donors (e.g., Ar = C₆H₄OCH₃) in the solid state. This solid-state phenomenon shows that there is indeed an influence of the substituents on the donor entities, which changes the energy gap ΔE between the neutral ground state and the excited ionic state in subtle ways.

Diquinone isomeric derivatives **71a** and **71b** can serve as examples of the A—D—A motif [119]. Interestingly, although both derivatives contain weak donors and weak acceptors moieties, they do give segregated stack-

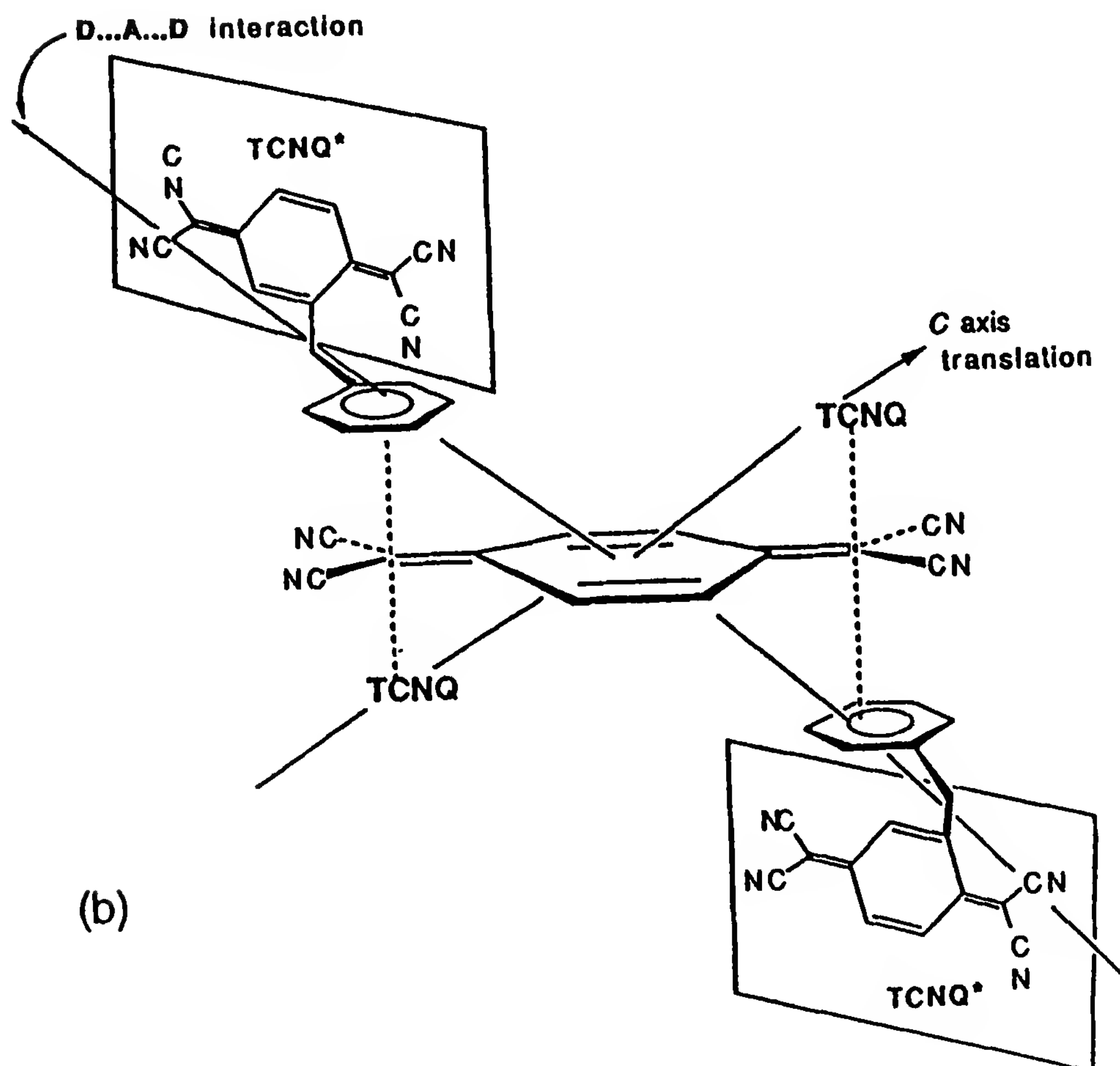
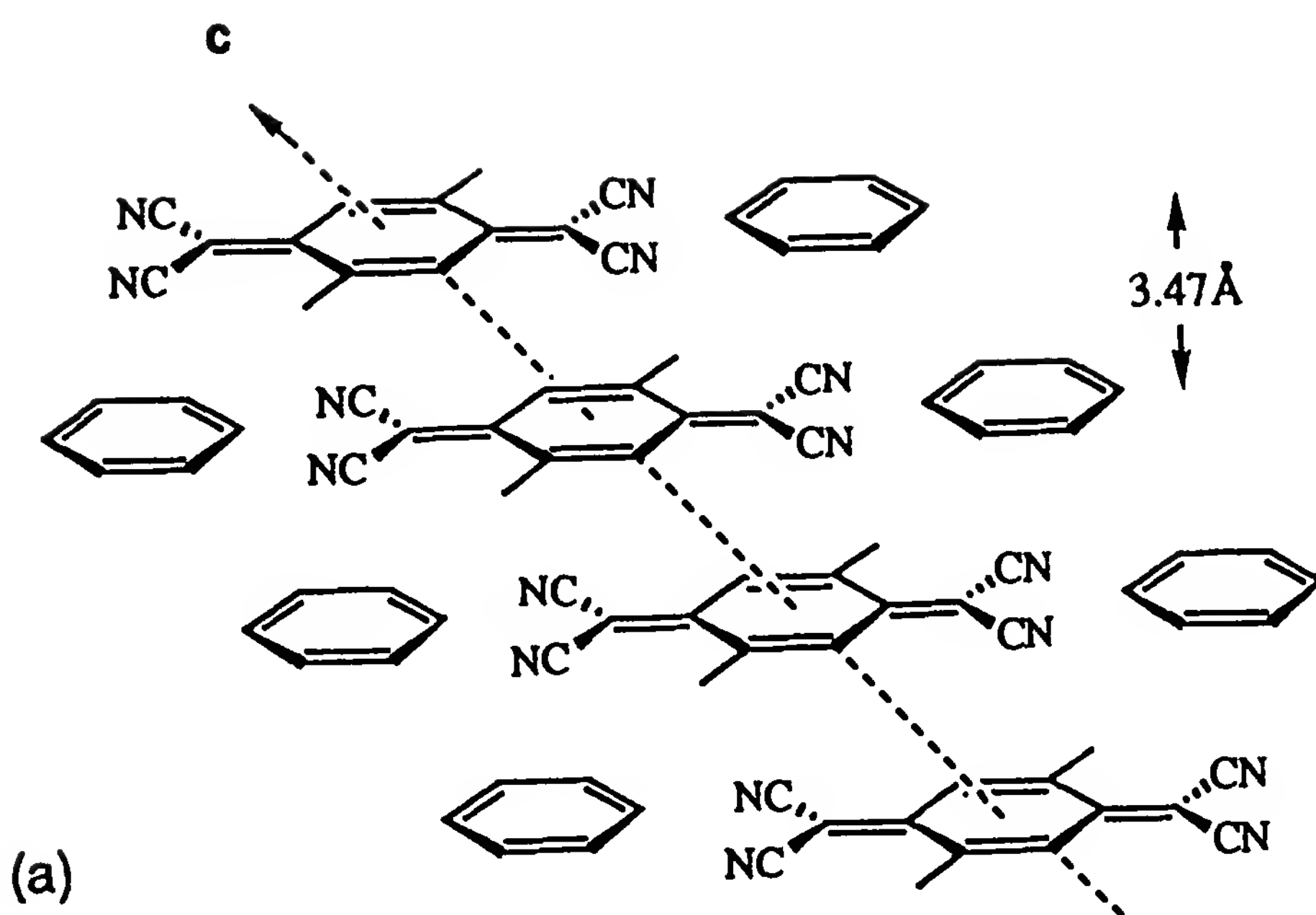


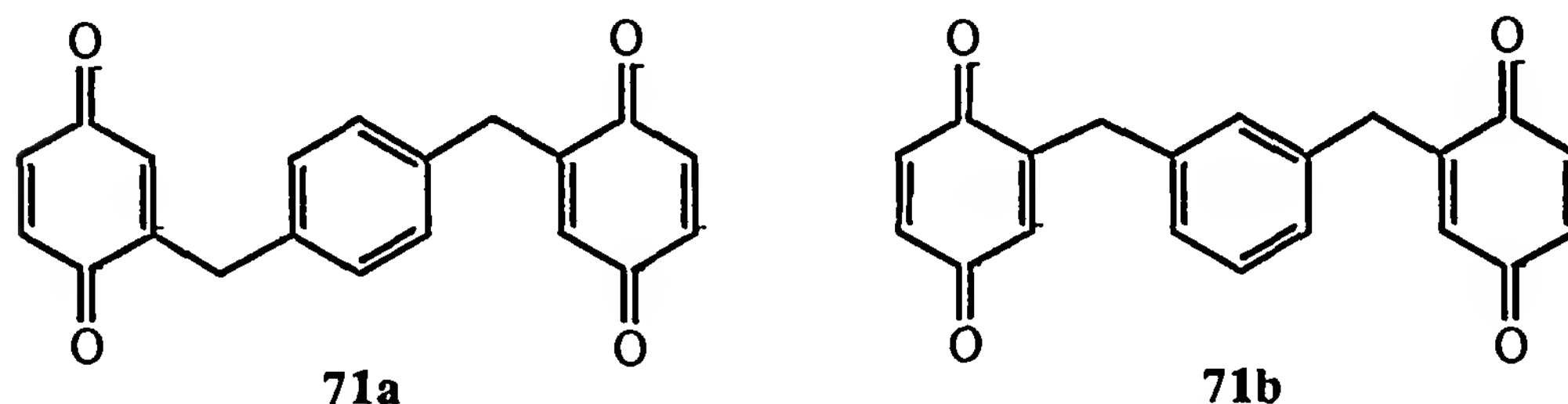
Figure 4 D...A...D solid state interactions in **70**.

Table 13 Crystallographic Constants for the Isostructural Compounds **70**^a

	Compound		
	70a	70b	70c
a (Å)	13.999 (6)	16.87 (6)	16.98 (3)
b	10.760 (2)	10.235 (6)	11.62 (2)
c	6.970 (3)	7.172 (4)	7.11 (1)
β (°)	102.51 (3)	107.80 (4)	115.3 (1)

^aAll three materials crystallize in the space group $P2_1/a$, $z = 2$; I, D = C₆H₅; II, D = *p*-C₆H₄OCH₃; III, D = 2-naphthyl.

ing. Diquinone **71a** shows an almost ideal one-dimensional array of quinone and phenyl moieties (Fig. 5), but even more surprising, by small geometrical changes, its isomer **71b** affords two-dimensional stacking, which is the most prominent feature of its crystal packing (Fig. 6).



Derivatives **70a** to **c** are not conducting, probably due to the low degree of charge transfer (the alkali and copper salts of **70c** are semiconductors, and **70c** itself is a photoconductor [119]. Nevertheless, the internal structure D—A—D or A—D—A can provide a driving force for the development of segregated stacks. However, to obtain the desired stacking arrangement, in which both the donor and acceptor moieties in the molecule are overlapping with their neighbors, in a face-to-face manner, a greater degree of planarity (in which the free rotation of individual molecular units is restricted) is required.

2. Recent Advances

The existence of a tendency to crystallize in segregated stacks discussed above has been confirmed by later investigations, for instance, in a series of compounds **72** to **74**, in which the spacers are sulfur atoms. No segregated structure was found in the crystals of derivative **72a**. However, the desired packing can be induced by some definite modifications, such as by geometrical changes as in 2,6-isomer (**72b**) [120], by increasing the donor ability in **73**, or by increasing the acceptor ability in **74**. In all these compounds,

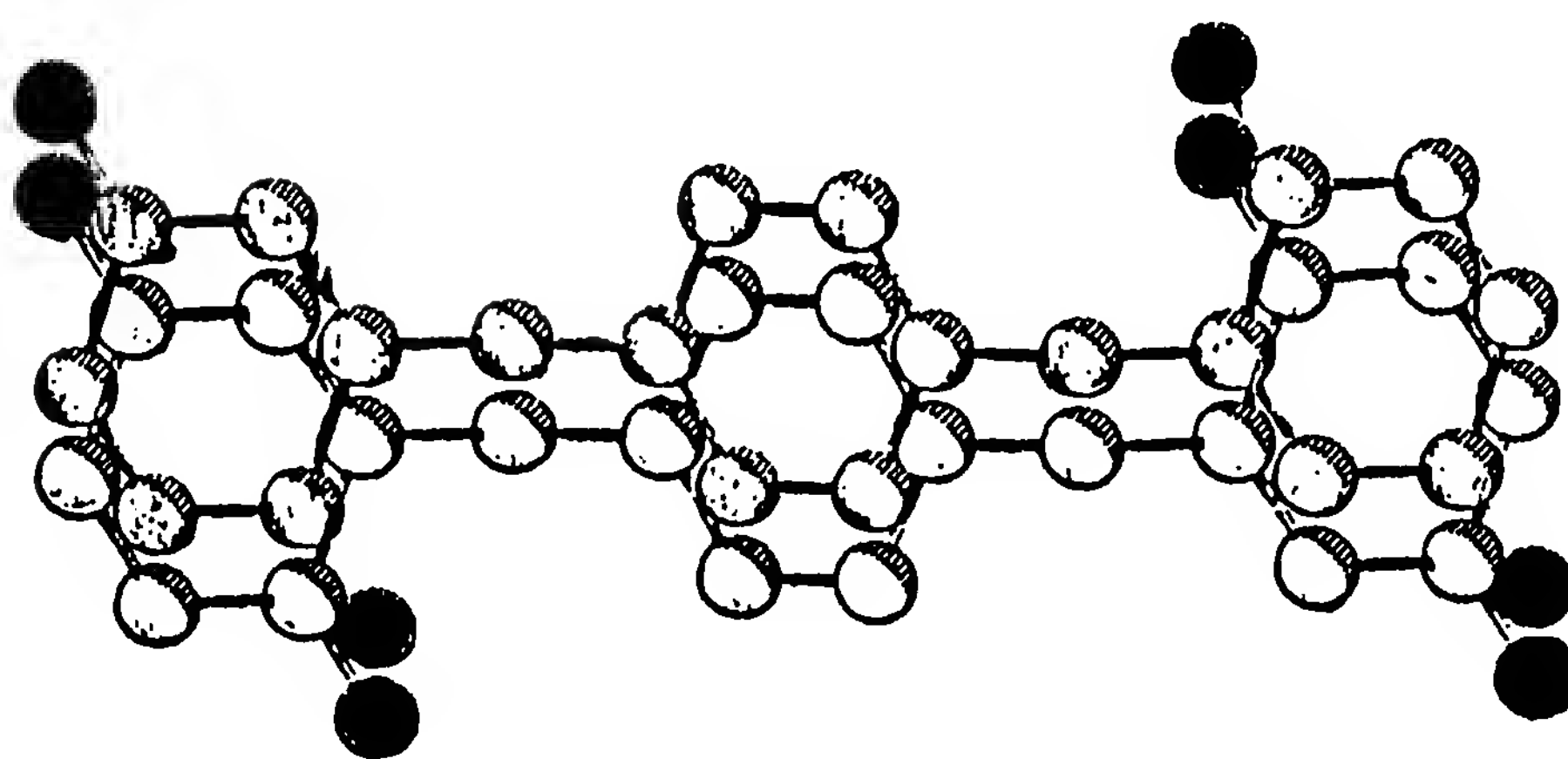
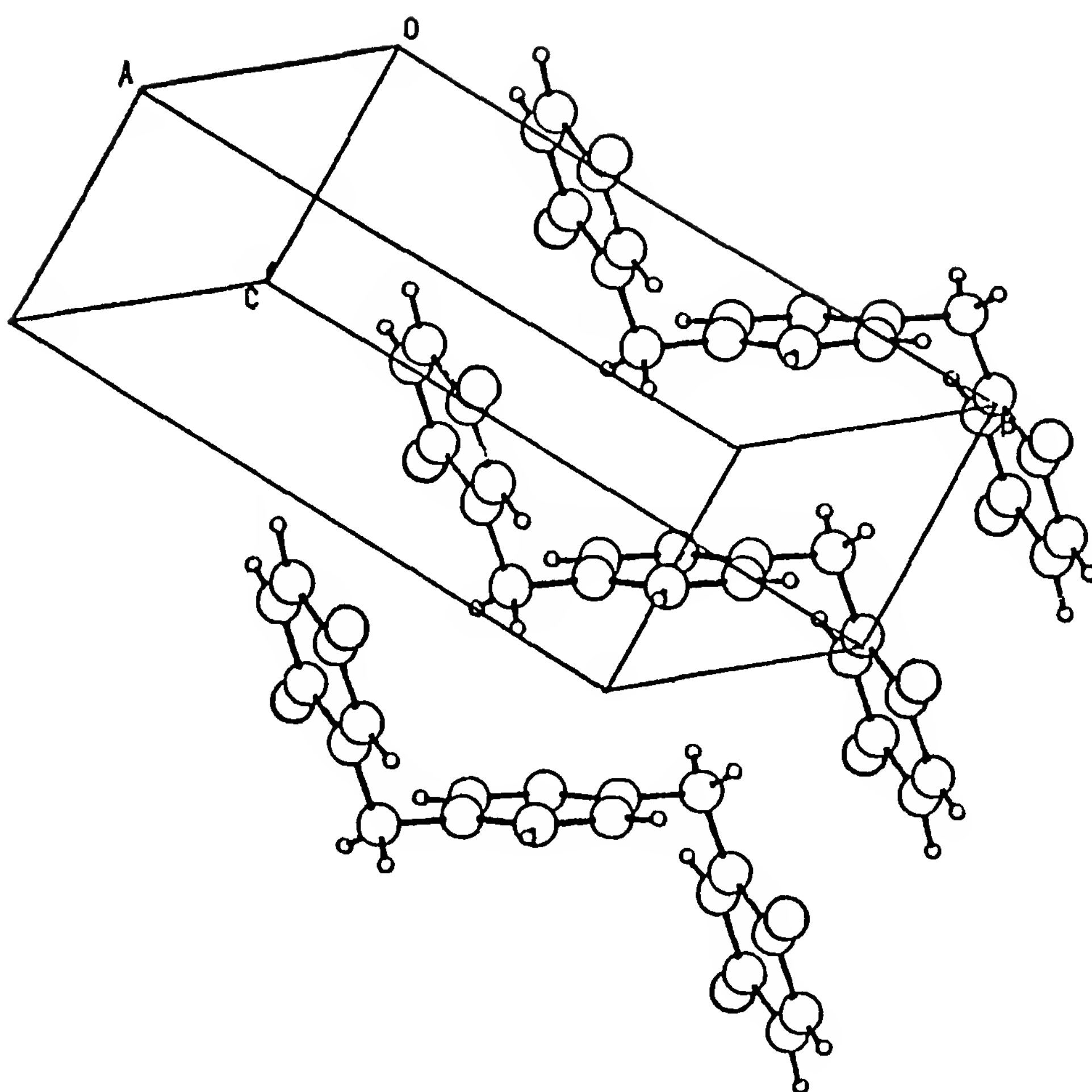


Figure 5 Packing of 71a showing the mutual overlap of both donor and acceptor. Oxygen atoms on the quinone moieties are darkened.

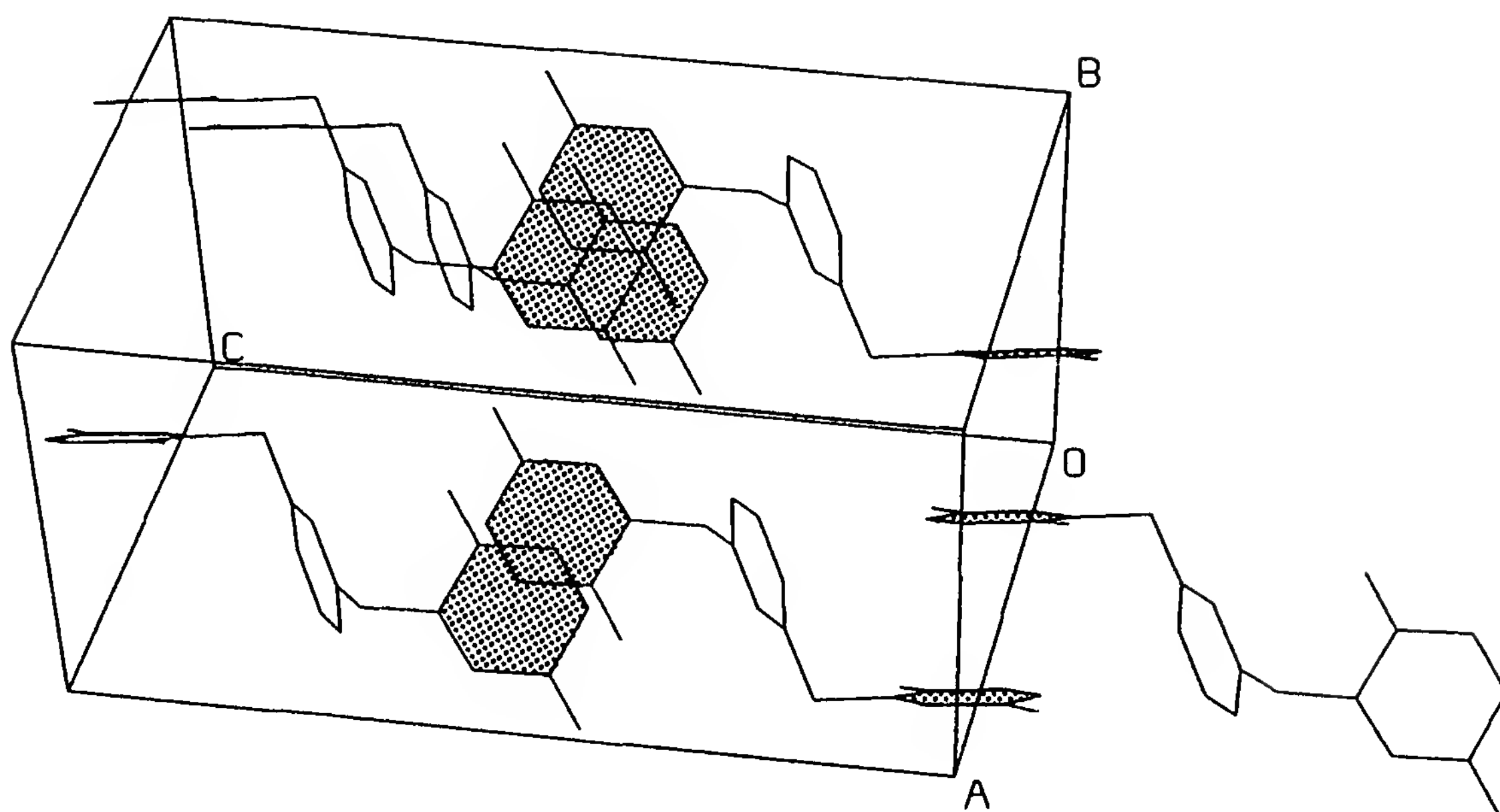
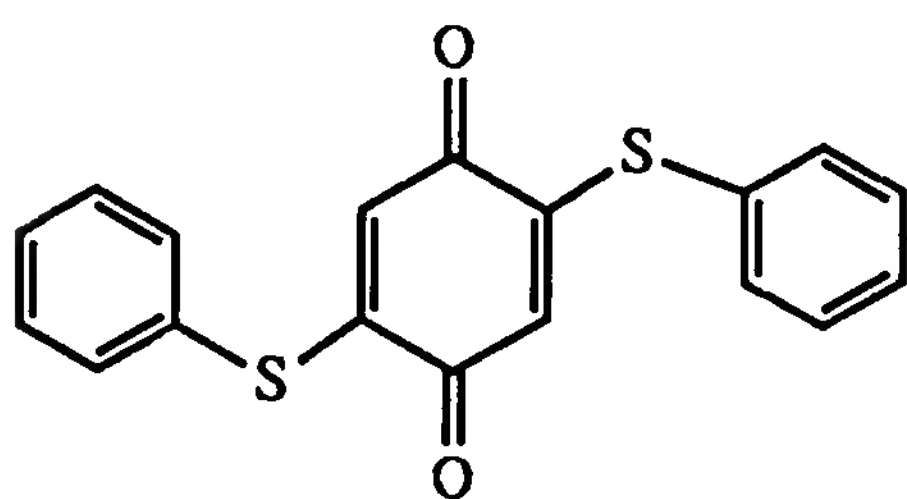
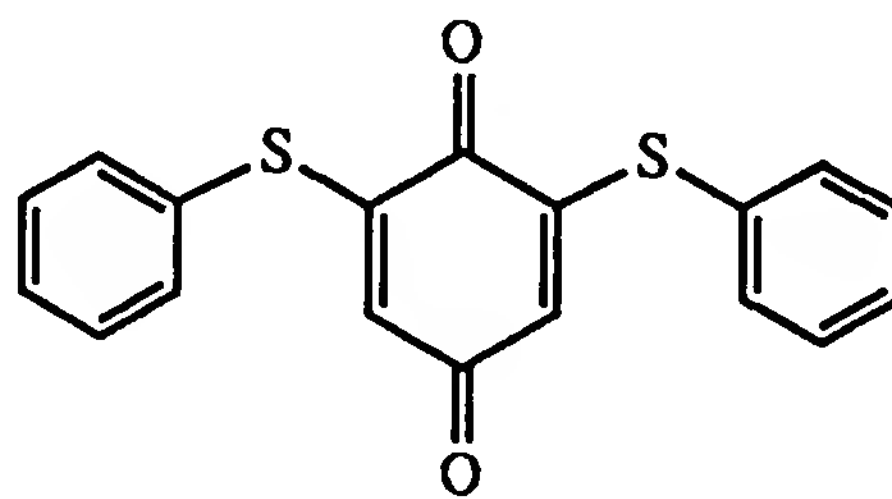


Figure 6 Packing diagram of **71b**, showing the two-dimensional overlap of acceptors (shaded rings).

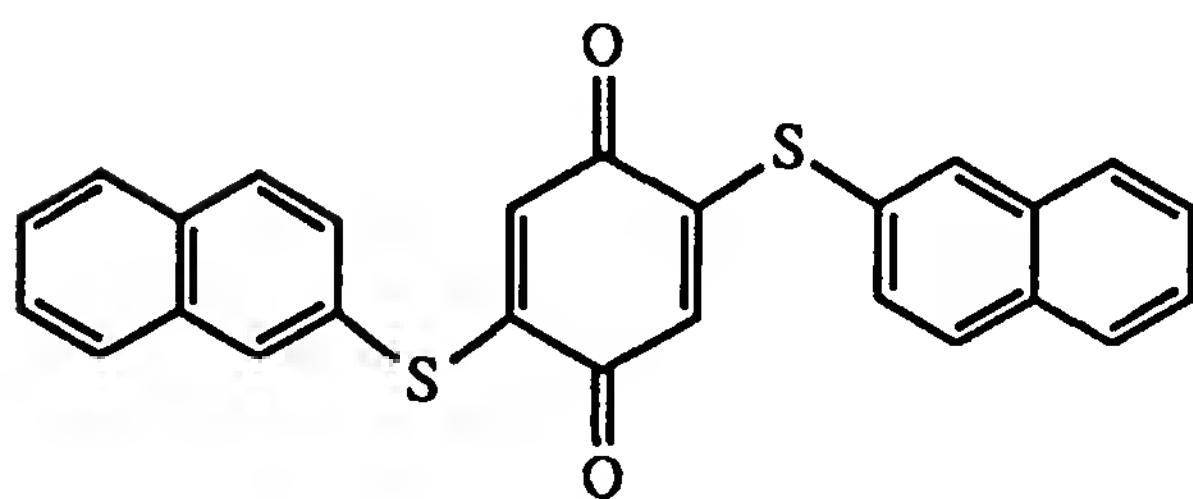
a segregated packing characteristic of conducting materials has been achieved [121]. New A—D—A systems based on TTF derivatives have been synthesized [122]. One of them, 2,6-(ArCH₂S)₂TTF exhibits stacking of both donor and acceptor moieties.



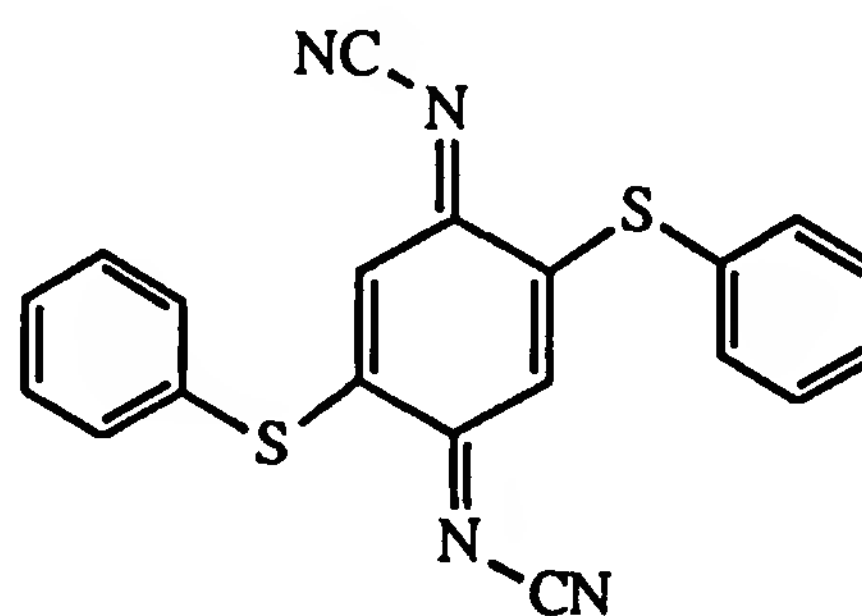
72a



72b

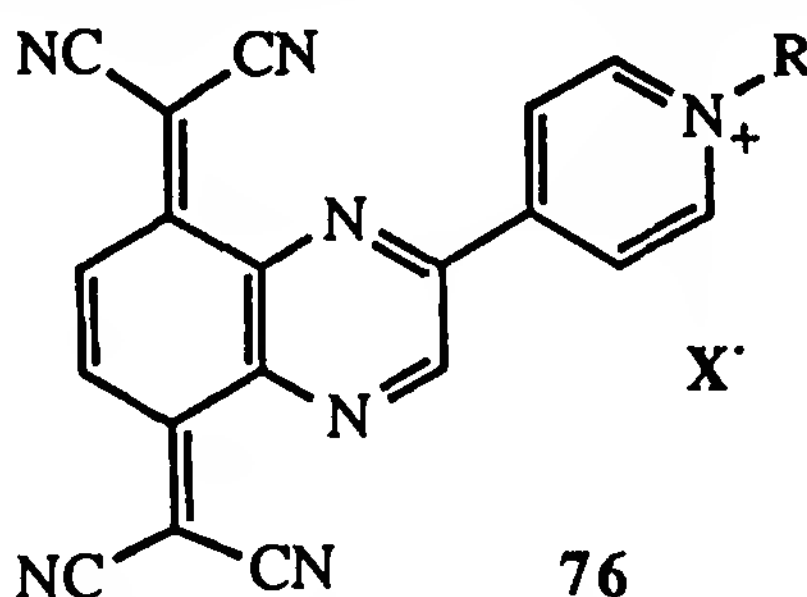
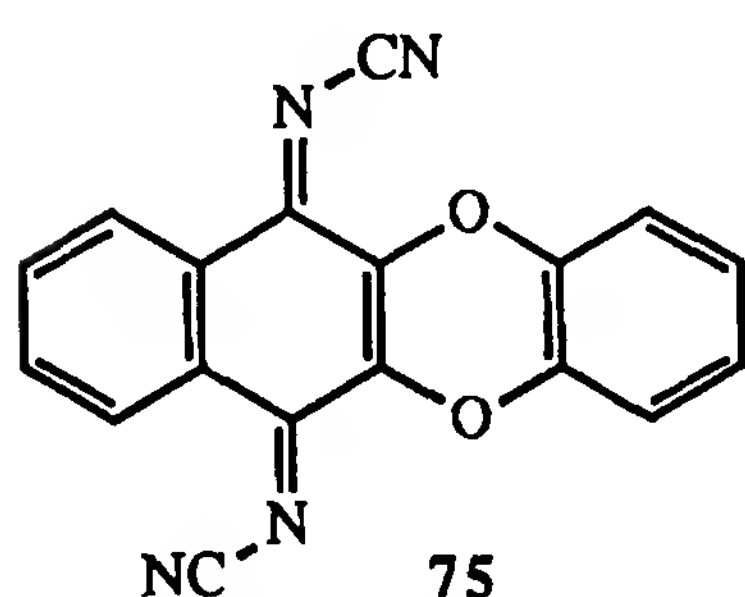


73



74

As mentioned earlier, the tendency of the plane of the donor moieties to be nearly perpendicular to the TCNQ plane prohibits formation of the desired stacking mode. A series of naphtho-1,4-dioxin derivatives (**75**) has been synthesized to obtain more planar molecules of this type (benzene ring as a donor) [123]. These compounds appeared to be strong acceptors and give rise to conducting salts (e.g., Cu derivatives) (J. Y. Becker, M. Hanack, J. Bernstein, and L. Kaufman-Orenstein, unpublished results).



TCNQ derivatives containing *N*-alkylpyridinium substituents **76** formally belong to A—A compounds, and upon their reduction they afford neutral radicals with the properties of single-component organic conductors [124]. Derivatives consisting of two donor moieties (D—D) or two acceptor (A—A) moieties connected by a nonconjugating linking bridge could also be considered as D—A type, because after one-electron oxidation or reduction they might become D—D⁺, or A—A[−], respectively. The electrochemical behavior of this kind of derivative was discussed earlier, and we would like to mention here that available crystallographic data for **39** (X = S, Te, Te—Te), for example, exhibit essentially the same trend in packing: stacks along the *c* crystallographic axis. Both **39** (X = Te) and **39** (X = Te—Te) afford highly conducting complexes with TCNQ [125]. Interestingly, the donor di(tetrathiafulvalenyl) ditelluride **39** (X = Te—Te) has an intrinsic conductivity and is actually a semiconductor [69,126].

IV. ORGANIC CONDUCTORS AND SUPRAMOLECULAR CHEMISTRY: CONCLUDING REMARKS

Achievements in the field of organic conductors and superconductors have promoted the development of the field of molecular electronics as well. The latter is a nascent field of research, suggesting the use of organic molecules with the tunability of their electronic structure, instead of conventional inorganic microelectronics. It has been suggested that molecular electronic devices could utilize a variety of optoelectronic and conductivity phenomena of organic substances at the nanometer level. Whereas the conductivity and superconductivity of organic metals is a result of bulk electrical behavior of lower-dimensional systems, molecular electronics deals

with optical and charge-transfer properties of a single molecule, which is a part of a molecular assembly (Langmuir–Blodgett film, chemically modified electrode, etc. [127]). This field of research is discussed in detail in Chapter 16. The design of most molecular electronic devices has been based on the incorporation of molecular “building blocks” with well-characterized chemical or physical properties into a single molecular unit. Molecular electronics is thus closely related to the concept of supramolecular chemistry. According to the latter, supermolecules are constructed from special molecular subunits, in the same manner that molecules are “constructed” from atoms. In addition, further investigations on monomolecular films will provide a deeper insight on the behavior of donor–acceptor systems. This will offer a genuine possibility for “constructing” complicated systems such as crystal lattice, hopefully followed by design of high-temperature molecular organic superconductors.

ACKNOWLEDGMENT

The authors thank Joel Bernstein for fruitful discussions and for his valuable suggestions and comments.

REFERENCES

1. J. Ferraris, D. O. Cowan, V. V. Walatka, and J. H. Perlstein, *J. Am. Chem. Soc.* **95**:948 (1973).
2. L. B. Coleman, M. J. Cohen, D. J. Sandman, F. G. Yamagishi, A. F. Garito, and A. J. Heeger, *Solid State Commun.* **12**:1125 (1973).
3. W. A. Little, *Phys. Rev. A* **134**:1416 (1964).
4. A. F. Garito and A. Heeger, *Acc. Chem. Res.* **7**:232 (1974).
5. J. H. Perlstein, *Angew. Chem. Int. Ed. Engl.* **16**:519 (1977).
6. J. M. Williams, J. R. Ferraro, R. J. Thorn, et al., *Organic Superconductors*, Prentice Hall, Englewood Cliffs, New Jersey, 1992.
7. G. Saito and J. P. Ferraris, *Bull. Chem. Soc. Jpn.* **53**:2141 (1980).
8. M. L. Khidekel and E. I. Zhilyaeva, *Synth. Met.* **4**:1 (1981).
9. R. N. Lyubovskaya, *Russ. Chem. Rev.* **52**:736 (1983).
10. F. Wudl, *Acc. Chem. Res.* **17**:227 (1984).
11. S. S. Shaik, *J. Am. Chem. Soc.* **104**:5328 (1982).
12. H. Kobayashi, A. Kobayashi, Y. Sasaki, G. Saito, and H. Inokuchi, *Bull. Chem. Soc. Jpn.* **59**:301 (1986).
13. M. R. Bryce, *Chem. Soc. Rev.* **20**:355 (1991).
14. *Acc. Chem. Res.* **25**(3) (1992).
15. A. Gavezzotti, *J. Am. Chem. Soc.* **113**:4622 (1991).
16. H. R. Karfunkel and R. J. Gdanitz, *J. Comput. Chem.* **13**:1171 (1992).
17. J. R. Holden, Z. Du, and H. L. Ammon, *J. Comput. Chem.* **14**:422 (1993).
18. V. D. Parker, *J. Am. Chem. Soc.* **96**:4646 (1974).

19. L. L. Miller, G. D. Nordblom, and E. A. Mayeda, *J. Org. Chem.* 37:916 (1972).
20. V. Kampar and O. Neilands, *Russ. Chem. Rev.* 46:503 (1977).
21. C. Kroenke, V. Enkelmann, and G. Wegner, *Angew. Chem. Int. Ed. Engl.* 19:912 (1980).
22. N. Sato, K. Seki, and H. Inokuchi, *J. Chem. Soc. Faraday Trans. II* 77:1621 (1981).
23. D. J. Sandman, A. J. Epstein, T. J. Holmes, J.-S. Lee, and D. D. Titus, *J. Chem. Soc. Perkins Trans. II*, 1578 (1980).
24. O. Neilands, K. Balodis, J. Kacens, J. Kreicberga, R. Medne, L. Paulins, G. Pukitis, V. Khodorkovsky, and A. Edzina, *Izv. Akad. Nauk Latv. SSR Ser. Khim.* 64 (1986); *C.A.* 106:11470.
25. N. Sato and H. Inokuchi, *Chem. Phys.* 60:327 (1981).
26. A. Berlinsky, J. F. Carolan, and L. Weiler, *Can. J. Chem.* 52:3373 (1974).
27. R. Gleiter, E. Schmidt, D. O. Cowan, and J. P. Ferraris, *J. Electron Spectrosc. Relat. Phenom.* 2:207 (1973).
28. D. L. Lichtenberger, R. L. Johnston, K. Hinkelmann, T. Suzuki, and F. Wudl, *J. Am. Chem. Soc.* 112:3302 (1990).
29. N. Sato, G. Saito, and H. Inokuchi, *Chem. Phys.* 76:79 (1983).
30. A. Schweig, N. Thon, and E. M. Engler, *J. Electron. Spectrosc.* 12:335 (1977).
31. S. Huenig and H. Berneth, *Adv. Org. Chem.* 92:1 (1980).
32. V. Khodorkovsky, A. Edzina, and O. Neilands, *J. Mol. Electron.* 5:33 (1989).
33. E. M. Engler, F. B. Kaufman, D. C. Green, C. E. Klots, and R. N. Compton, *J. Am. Chem. Soc.* 97:2921 (1975).
34. R. D. McCullough, G. B. Kok, K. A. Lerstrup, and D. O. Cowan, *J. Am. Chem. Soc.* 109:4115 (1987).
35. A. J. Moore, M. R. Bryce, D. A. Ando, and M. B. Hursthouse, *J. Chem. Soc. Chem. Commun.*, 320 (1991).
36. Y. Yamashita, S. Tanaka, K. Imaeda, H. Inokuchi, and M. Sano, *J. Chem. Soc. Chem. Commun.*, 1132 (1991).
37. J. M. Fabre, J. Garin, and S. Uriel, *Tetrahedron Lett.*, 32:6407 (1991).
38. M. Fourmigue and P. Batail, *J. Chem. Soc. Chem. Commun.*, 1370 (1991).
39. M. R. Bryce, G. J. Marshallsay, and A. J. Moore, *J. Org. Chem.* 57:4859 (1992).
40. V. Khodorkovsky, J. Y. Becker, and J. Bernstein, *Synthesis*, 1071 (1992).
41. T. Barth, C. Krieger, F. A. Neugebauer, and H. A. Staab, *Angew. Chem. Int. Ed. Engl.* 30:1028 (1991).
42. K. Elbl-Weiser, C. Krieger, and H. A. Staab, *Angew. Chem. Int. Ed. Engl.* 29:211 (1990).
43. J. S. Miller, D. A. Dixon, J. C. Calabrese, C. Vasquez, P. J. Krusic, M. D. Ward, E. Wasserman, and R. L. Harlow, *J. Am. Chem. Soc.* 112:318 (1990).
44. F. Wudl, D. E. Scafer, and B. Miller, *J. Am. Chem. Soc.* 98:252 (1976).
45. R. C. Wheland and J. L. Gilson, *J. Am. Chem. Soc.* 98:3916 (1976).

46. D. J. Sandman, J. C. Stark, and B. M. Foxman, *Organometallics* 1:739 (1982).
47. H. Endres, H. J. Keller, J. Queckborner, J. Veigel, and D. Schweitzer, *Mol. Cryst. Liq. Cryst.* 86:111 (1982).
48. K. Takimiya, A. Ohnishi, Y. Aso, T. Otsubo, and F. Ogura, *J. Chem. Soc. Chem. Commun.*, 278 (1992).
49. V. Y. Khodorkovsky and D. A. Oparin, *Zh. Org. Khim. (USSR)* 25:1343 (1989); *C.A.* 112:76839.
50. V. Y. Khodorkovsky, A. S. Edzina, Y. Y. Kacens, and O. Y. Neilands, *Izv. Akad. Nauk Latv. SSR Ser. Khim.*, 365 (1987); *C.A.* 108:112285.
51. S.-L. Chu, K.-F. Wai, T.-F. Lai, and M. P. Sammes, *Tetrahedron Lett.* 34:847 (1993).
52. S. Huenig, H. Schlaf, G. Kiesslich, and D. Scheutzow, *Tetrahedron Lett.* 27:2271 (1969).
53. Z. Yoshida, T. Kawase, H. Awaji, I. Sugimoto, and S. Yoneda, *Tetrahedron Lett.* 24:3469 (1983).
54. V. Y. Khodorkovsky, L. N. Vesselova, and O. Y. Neilands, *Khim. Geterotsikl. Soed.*, 130 (1990); *C.A.* 113:22868.
55. T. K. Hansen, M. V. Lakshmikantham, M. P. Cava, R. M. Metzger, and J. Becher, *J. Org. Chem.* 56:2720 (1991).
56. A. J. Moore, M. R. Bryce, D. J. Ando, and M. B. Hursthouse, *J. Chem. Soc. Chem. Commun.*, 320 (1991).
57. M. A. Coffin, M. R. Bryce, A. S. Batsanov, and J. A. K. Howard, *J. Chem. Soc. Chem. Commun.*, 552 (1993).
58. Y. Yamashita, S. Tanaka, K. Imaeda, H. Inokuchi, and M. Sano, *J. Chem. Soc. Chem. Commun.*, 1132 (1991).
59. Z. Yoshida, T. Kawase, H. Awaji, and S. Yoneda, *Tetrahedron Lett.* 24:3473 (1983).
60. A. Ohto, T. Kobayashi, and H. Kato, *J. Chem. Soc. Chem. Commun.*, 431 (1993).
61. A. J. Moore and M. R. Bryce, *J. Chem. Soc. Perkin Trans. I*, 157 (1991).
62. M. Salle, A. Belyasmine, A. Gorgues, M. Jubault, and N. Soyer, *Tetrahedron Lett.* 32:2897 (1991).
63. G. Schukat and E. Fanghaenel, *J. Prakt. Chem.* 327:767 (1985).
64. M. Jorgensen and K. Bechgaard, *Synthesis*, 208 (1989).
65. H. Tatemitsu, E. Nishikawa, Y. Sakata, and S. Misumi, *Synth. Met.* 19:565 (1987).
66. Y. Misaki, H. Nishikawa, K. Kawakami, S. Koyanagi, T. Yamabe, and M. Shiro, *Chem. Lett.*, 2321 (1992).
67. M. Bryce, G. Cooke, A. S. Dhindsa, D. J. Ando, and M. Hursthouse, *Tetrahedron Lett.* 33:1783 (1992).
68. J. Y. Becker, J. Bernstein, S. Bittner, J. A. R. P. Sarma, and L. Shahal, *Tetrahedron Lett.* 29:6177 (1988).
69. J. Y. Becker, J. Bernstein, M. Dayan, and L. Shahal, *J. Chem. Soc. Chem. Commun.*, 1048 (1992).

70. V. Khodorkovsky, E. Aqad, J. Y., Becker, and J. Bernstein, submitted for publication.
71. T. Tacikawa, A. Izuoka, R. Kumai, T. Sugawara, and Y. Sugawara, *Solid State Commun.* 82:19 (1992).
72. A. Izuoka, R. Kumai, and T. Sugawara, *Chem. Lett.*, 285 (1992).
73. M. Jorgensen, K. A. Lerstrup, and K. Bechgaard, *J. Org. Chem.* 56:5684 (1991).
74. I. Sudmale, G. V. Tormos, V. Y. Khodorkovsky, A. S. Edzina, O. Neilands, and M. P. Cava, *J. Org. Chem.* 58:1355 (1993).
75. M. Adam, V. Enkelmann, H.-J. Raeder, J. Roehrich, and K. Muellen, *Angew. Chem. Int. Ed. Engl.* 31:309 (1992).
76. M. D. Ward, *Electroanal. Chem.* 16:182 (1989).
77. C. Vazquez, J. C. Calabrese, D. A. Dixon, and J. S. Miller, *J. Org. Chem.* 58:65 (1993).
78. M. R. Bryce, S. R. Davies, A. M. Grainger, J. Hellberg, M. B. Hursthouse, M. Mazid, R. Bachmann, and F. Gerson, *J. Org. Chem.* 57:1690 (1992).
79. A. Aumuller and S. Huenig, *Liebigs Ann. Chem.*, 165 (1986).
80. T. Yanagimoto, K. Takimiya, T. Otsubo, and F. Ogura, *J. Chem. Soc. Chem. Commun.*, 519 (1993).
81. N. Martin, J. A. Navarro, C. Seoane, A. Albert, F. H. Canob, J. Y. Becker, V. Khodorkovsky, and E. Harlev, *J. Org. Chem.* 57:5726 (1992).
82. E. Aharon-Shalom, J. Y. Becker, and I. Agranat, *Nouv. J. Chim.* 3:643 (1979).
83. H. Almen, T. Bauer, S. Huenig, V. Kupcik, U. Langohr, T. Metzenthin, K. Meyer, H. Rieder, J. Ulrich von Schuetz, E. Tillmanns, and H. C. Wolf, *Angew. Chem.* 103:608 (1991).
84. S. Gronowitz and B. Uppstroem, *Acta Chem. Scand. B* 28:981 (1974).
85. M. L. Kaplan, R. C. Haddon, F. B. Bramwell, F. Wudl, J. H. Marshall, D. O. Cowan, and S. Gronowitz, *J. Phys. Chem.* 84:427 (1980).
86. E. Guenther and S. Huenig, *Chem. Ber.* 125:1235 (1992).
87. P. Cassoux, L. Valade, H. Kobayashi, A. Kobayashi, R. A. Clark, and A. E. Underhill, *Coord. Chem. Rev.* 110:115 (1991).
88. R.-M. Olk, B. Olk, J. Rohloff, J. Reinhold, J. Sieler, K. Truebenbach, R. Kirmse, and E. Hoyer, *Z. Anorg. Allg. Chem.* 609:103 (1992).
89. E. B. Yagubsky, A. I. Kotov, E. E. Laukhina, A. A. Ignatiev, L. I. Buravov, A. G. Khomenko, V. E. Shklover, S. S. Nagapetyan, and Yu. T. Struchkov, *Synth. Met.* 42:2515 (1991).
90. C. Faulmann, A. Errami, J.-P. Legros, P. Cassoux, E. B. Yagubski, and A. I. Kotov, *Synth. Met.* 55-57:2057 (1993).
91. I. B. Torrance, *Molecular Metals Proc., NATO Conf., New York-London*, p. 7 (1979).
92. V. Kampar and O. Neilands, *Russ. Chem. Rev.* 55:334 (1986).
93. J. S. Chappell, A. N. Bloch, W. A. Bryden, M. Maxfield, T. O. Poehler, and D. O. Cowan, *J. Am. Chem. Soc.* 103:2442 (1981).

94. B. A. Scott, S. J. LaPlaca, J. B. Torrance, B. D. Silverman, and B. Welber, *J. Am. Chem. Soc.* **99**:6631 (1977).
95. P. Kathirgamanathan, M. A. Mazid, and D. R. Rosseinsky, *J. Chem. Soc. Perkin Trans. II*, 592 (1982).
96. K. Bechgaard, K. Carneiro, M. Olsen, F. B. Rasmussen, and C. S. Jacobsen, *Phys. Rev. Lett.* **46**:852 (1981).
97. H. Urayama, H. Yamochi, G. Saito, K. Nozawa, T. Sugano, M. Kinoshita, S. Sato, K. Oshima, A. Kawamoto, and J. Tanaka, *Chem. Lett.* **55** (1988).
98. C. S. Jacobsen, K. Mortensen, J. R. Andersen, and K. Bechgaard, *Phys. Rev. B Cond. Matter* **18**:905 (1978).
99. D. Jerome, A. Mazaud, M. Ribault, and K. Bechgaard, *J. Phys. Lett.* **41**:L195 (1980).
100. J. M. Williams, M. A. Beno, H. H. Wang, P. C. W. Leung, T. J. Emge, U. Geiser, and K. D. Carlson, *Acc. Chem. Res.* **18**:261 (1985).
101. K. Kikuchi, K. Murata, Y. Honda, T. Namiki, K. Saito, T. Ishigura, K. Kobayashi, and I. Ikemoto, *J. Phys. Soc. Jpn.* **55**:3435 (1987).
102. G. C. Papavassiliou, G. A. Mousdis, J. S. Zambounis, A. Terzis, A. Hountas, B. Hilti, C. W. Mayer, and J. Pfeiffer, *Synth. Met. B* **27**:379 (1988).
103. L. Brossard, M. Ribault, L. Valade, and P. Cassoux, *Physica B* **143**:378 (1986).
104. A. Kobayashi, H. Kim, Y. Sasaki, H. Kobayashi, S. Moriyama, Y. Nishio, K. Kajita, and W. Sasaki, *Chem. Lett.*, 1819 (1987).
105. V. Y. Lee, E. M. Engler, R. R. Schumaker, and S. S. P. Parkin, *J. Chem. Soc. Chem. Commun.*, 235 (1983).
106. V. Khodorkovsky, J. Y. Becker, and J. Bernstein, *Synth. Met.* **55–57**:1919 (1993).
107. K. A. Lerstrup, D. Talham, A. Bloch, T. O. Poeler, and D. O. Cowan, *J. Chem. Soc. Chem. Commun.*, 336 (1982).
108. F. Wudl and E. Aharon-Shalom, *J. Am. Chem. Soc.* **104**:1154 (1982).
109. A. R. Bailey, R. D. McCullough, M. D. Mays, D. O. Cowan, and K. A. Lerstrup, *Synth. Met.* **27**:B425 (1988).
110. K. A. Lerstrup and D. O. Cowan, *J. Phys. Colloq.*, **44**(C3):1247 (1983).
111. H. Inokuchi, G. Saito, P. Wu, K. Seki, T. B. Tang, T. Mori, K. Imaeda, T. Enoki, Y. Higuchi, K. Inaka, and N. Yasupka, *Chem. Lett.*, 1263 (1986).
112. H. Inokuchi, K. Imaeda, T. Enoki, T. Mori, Y. Maruyama, G. Saito, N. Okada, H. Yamochi, K. Seki, Y. Higuchi, and N. Yasuoka, *Nature* **329**:39 (1987).
113. S. S. Shaik and M.-H. Whangbo, *Inorg. Chem.* **25**:1201 (1986).
114. J. Y. Becker, J. Bernstein, S. Bittner, N. Levi, and S. S. Shaik, *J. Am. Chem. Soc.* **105**:4468 (1983); Idem and N. Zer-Zion, *J. Org. Chem.*, **53**:1689 (1988).
115. J. Y. Becker, J. Bernstein, S. Bittner, J. A. R. P. Sarma, and S. S. Shaik, *Chem. Mater.* **1**:412 (1989); Idem, *Synth. Met.* **27**:B197 (1988).
116. N. Martin and C. Seoane, VII Centennial Universidad Compludense de Madrid Meeting, Madrid, Spain, January 17–19 (1994).

117. T. J. Kistenmacher, T. J. Emge, A. N. Bloch, and D. O. Cowan, *Acta Cryst. B* 38:1193 (1982); K. Bechgaard, T. J. Kistenmacher, A. N. Block, and D. O. Cowan, *Acta Cryst. B* 33:417 (1977).
118. J. S. Chappell, A. N. Bloch, W. A. Bryden, M. Maxfield, T. O. Poehler, and D. O. Cowan, *J. Am. Chem. Soc.* 103:2442 (1981).
119. J. Y. Becker, J. Bernstein, S. Bittner, Y. Giron, E. Harlev, L. Kaufman-Orenstein, D. Peleg, L. Shahal, and S. S. Shaik, *Synth. Met.* 41–42:2523 (1991); J. Y. Becker, J. Bernstein, S. Bittner, and S. S. Shaik, *Pure & Appl. Chem.*, 62:467 (1990).
120. J. Y. Becker, J. Bernstein, S. Bittner, E. Harlev, J. A. R. P. Sarma, and S. S. Shaik, *New J. Chem.* 12:875 (1988).
121. E. Harlev, Ph.D. thesis, Ben-Gurion University of the Negev, Beer-Sheva, Israel, 1991.
122. M. P. Le Pailard, A. Robert, C. Garrigou-Lagrange, et al., *Synth. Met.*, 58:223 (1993).
123. T. Czekansky, M. Hanack, J. Bernstein, J. Y. Becker, S. Bittner, L. Kaufman-Orenstein, and D. Peleg, *J. Org. Chem.* 56:1569 (1991).
124. Y. Tsubata, T. Suzuki, T. Miyashi, and Y. Yamashita, *J. Org. Chem.* 57:6749 (1992).
125. J. Y. Becker, J. Bernstein, M. Dayan, A. Ellern, and L. Shahal, submitted for publication.
126. J. D. Martin, E. Canadel, J. Y. Becker, and J. Bernstein, *Chem. Mater.*, 5:1199 (1993).
127. D. Seebach, *Angew. Chem. Int. Ed. Engl.* 29:1367 (1990).

4

Chemical Synthesis and Crystal Growth Techniques

Lawrence K. Montgomery

Indiana University, Bloomington, Indiana

I. INTRODUCTION

The study of organic conductors begins with synthesis. Before the structure, physical properties, and detailed physics of a conductor can be examined, it must be prepared. Synthesis, in consort with theory and existing knowledge concerning organic conductors, also plays a key role in designing new conducting systems. Organic and organometallic chemistry have produced a bountiful and varied supply of compounds that can serve as building blocks for new conductors; chemical synthesis furnishes the methodology for uniting these building blocks to form new conducting and superconducting systems.

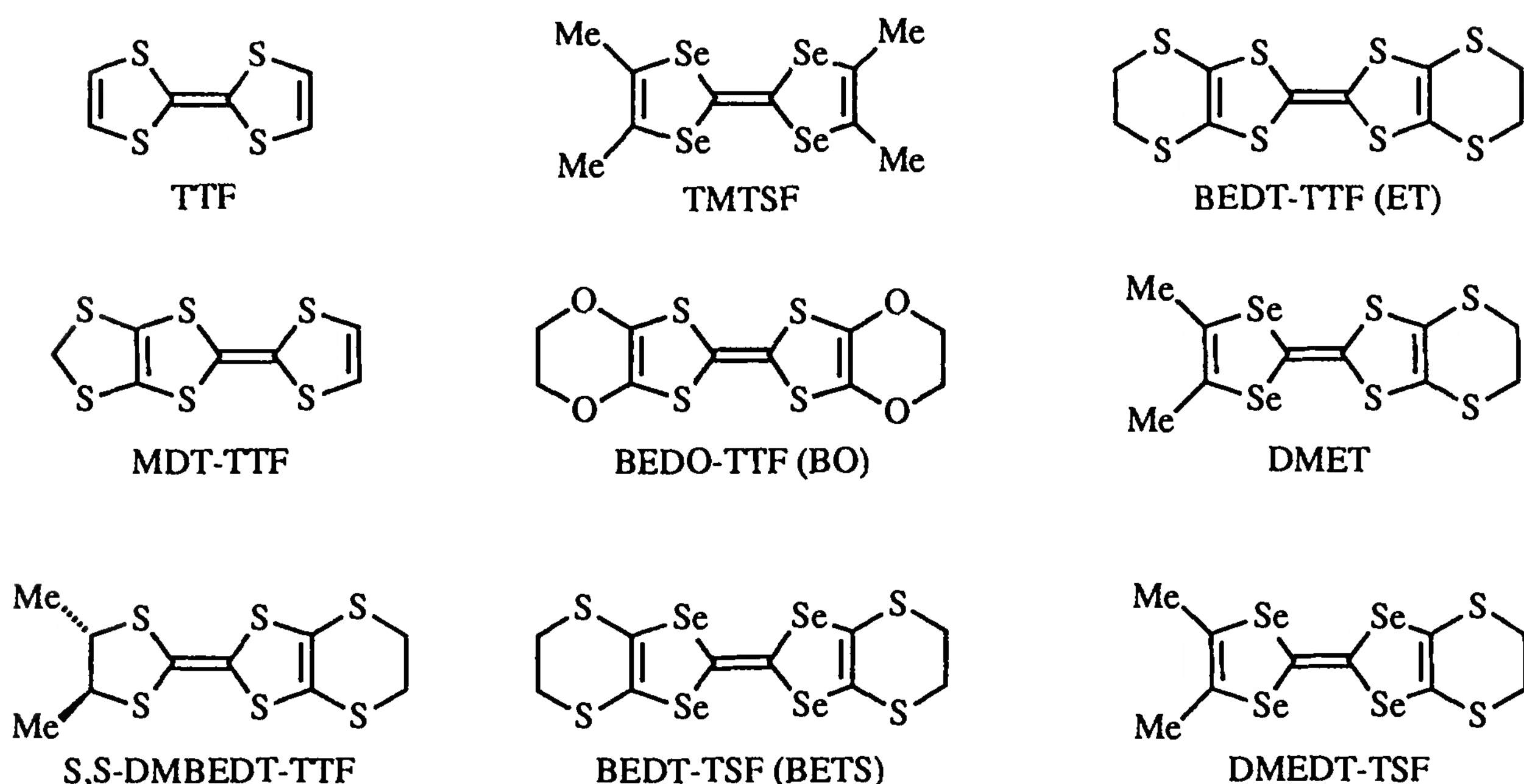
Organic conductors are so numerous that it is impossible to provide adequate coverage of their syntheses in a single chapter. Even if general compound classes are considered, the task is still overwhelming. In the discussion that follows, the selection of subject matter and emphasis undoubtedly reflect the tastes and interests of the author; it is, however, intended to give an overview of the more important conducting systems. The content is obviously biased toward organic superconductors. This seems appropriate, since superconductivity is one of the areas of organic conductor research that has received the most attention. A very important topic that is not covered is organic conducting polymers; their preparation is considered in Chapters 11 through 13.

Although the depth of coverage of the individual subjects in this chapter varies somewhat, in no instance is the treatment considered comprehensive. Numerous references are supplied that contain more detailed information. Also, there are a number of fine review articles on organic conductor synthesis that complement and supplement the present chapter [1–8].

Organic molecular solids with high conductivities are invariably radical-cation or radical-anion salts. Consequently, organic conductors are usually prepared by adding (reduction) or removing (oxidation) electrons from closed-shell molecules. Figure 1 shows several electron-donor molecules that furnish important radical-cation conductors. In Fig. 2 acceptors are shown that afford radical-anion conductors, including Buckminsterfullerene (C_{60}), whose alkali metal salts possess the highest superconducting transition temperatures (T_c) to date for organic materials [e.g., K_3C_{60} ($T_c = 19$ K), Rb_3C_{60} ($T_c = 29$ K), and Cs_2RbC_{60} ($T_c = 33$ K)] [9].

It is convenient to divide the synthesis of organic molecular conductors into two basic processes: (1) the synthesis of donor and acceptor molecules, and (2) the oxidation and reduction of the donors and acceptors to radical cations and radical anions. The chapter is organized along these lines. Donor and acceptor synthesis is discussed first, followed by a brief coverage of the formation and growth of radical cation- and radical anion-based crystals.

Several independent methods of synthesis are discussed for selected donors, acceptors, and compound classes. For someone unfamiliar with chemical synthesis, it might seem curious that more than one synthetic



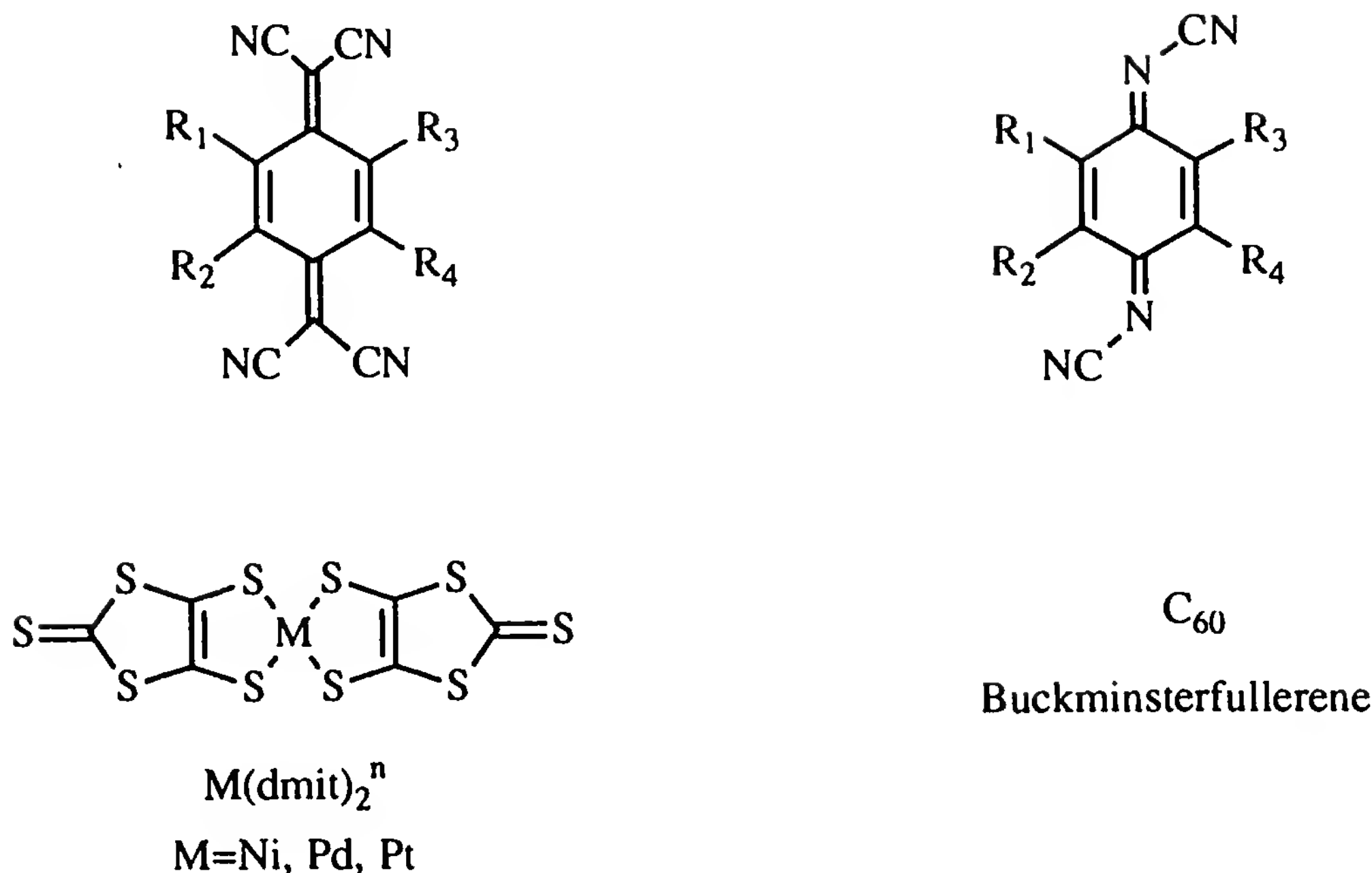
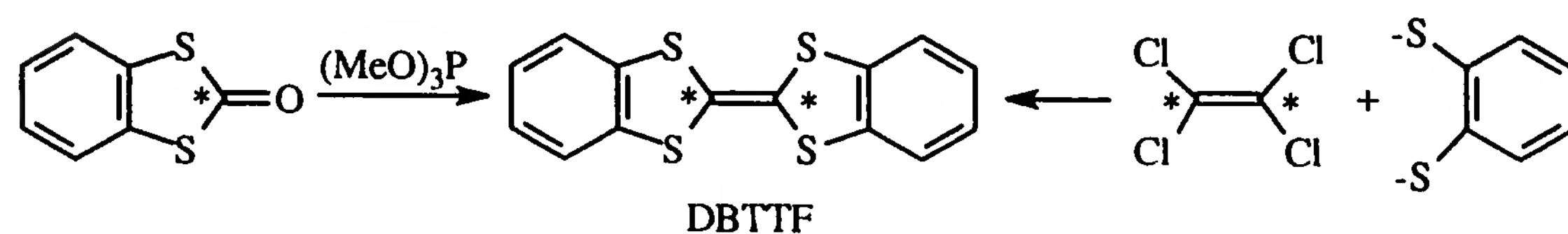


Figure 2 Important organic and organometallic acceptors.

method is worthy of discussion when one “good” procedure has already been described. The circumstances surrounding a synthesis frequently dictate what constitutes a “good” synthetic pathway. If one is interested in making a *known conducting material* for the purpose of carrying out a new type of experiment, the synthetic route of choice is probably the one that is the easiest, quickest, and least expensive.

On the other hand, if a *new potential donor or acceptor* is being prepared, the most expeditious route may be unacceptable for a variety of reasons. Frequently, substituent groups or other molecular constituents are incompatible with the chemical reaction conditions of a required synthetic step. This can rule out one or more possible synthetic approaches.

The synthesis of isotopically substituted molecules imposes even greater restrictions on syntheses. For example, consider the synthesis of dibenzotetrathiafulvalene (DBTTF), where the two central carbons are to be labeled with ^{13}C (*). Two possible routes are shown in Scheme 1. In ad-



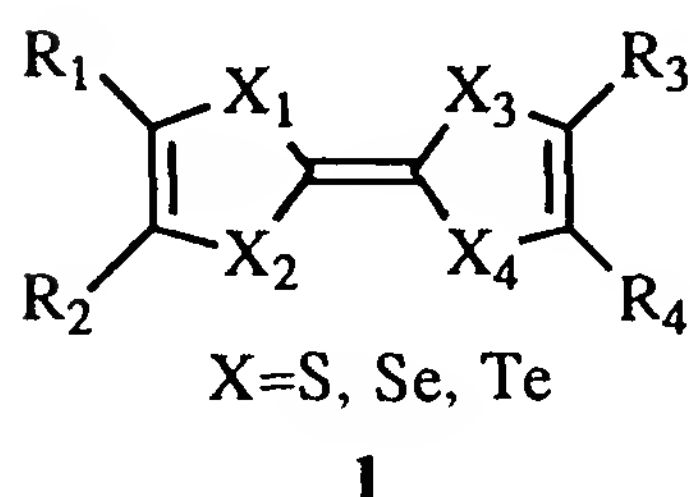
Scheme 1 Synthesis of $^{13}C(*)$ -labeled dibenzotetrathiafulvalene.

dition to the usual synthetic considerations such as ease of execution and yield, the availability and cost of the labeled precursors must be considered. Accordingly, the chemist's repertoire of synthetic alternatives must be extensive.

II. SYNTHESIS OF ORGANIC CONDUCTOR PRECURSORS

A. Electron Donors

No class of donor molecules has played a more important role in organic conductor research than the tetrachalcogenafulvalenes (**1**). In fact, all known



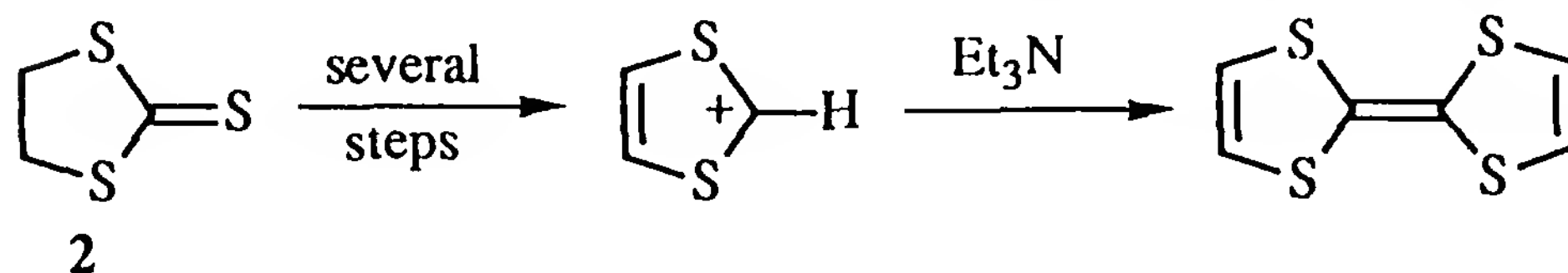
organic radical-cation superconductors are derived from tetrachalcogenafulvalenes [10]. Syntheses of the four parent tetrachalcogenafulvalenes, ($R_{1-4} = H$), tetrathiafulvalene (TTF), tetraselenafulvalene (TSF), and tetratellurafulvalene (TTeF) are discussed briefly, although TTF and TSF are commercially available. A host of substituted tetrachalcogenafulvalenes have been prepared [e.g., $R = \text{alkyl}, (CH_2)_n, \text{aryl}, \text{halogen}, OR, SiR_3, SR, S(CH_2)_nS, Se(CH_2)_2Se, CH_2OH, CHO, CO_2R, CONR_2, CN, CF_3, \text{benzo}, \text{and ethe no}$]. Although it is not feasible to discuss all such systems, general methods will be considered that offer routes to many of the known tetrachalcogenafulvalene derivatives.

1. Tetrathiafulvalene and Its Symmetrical Derivatives

(a) Deprotonation of 1,3-Dithiolium Salts

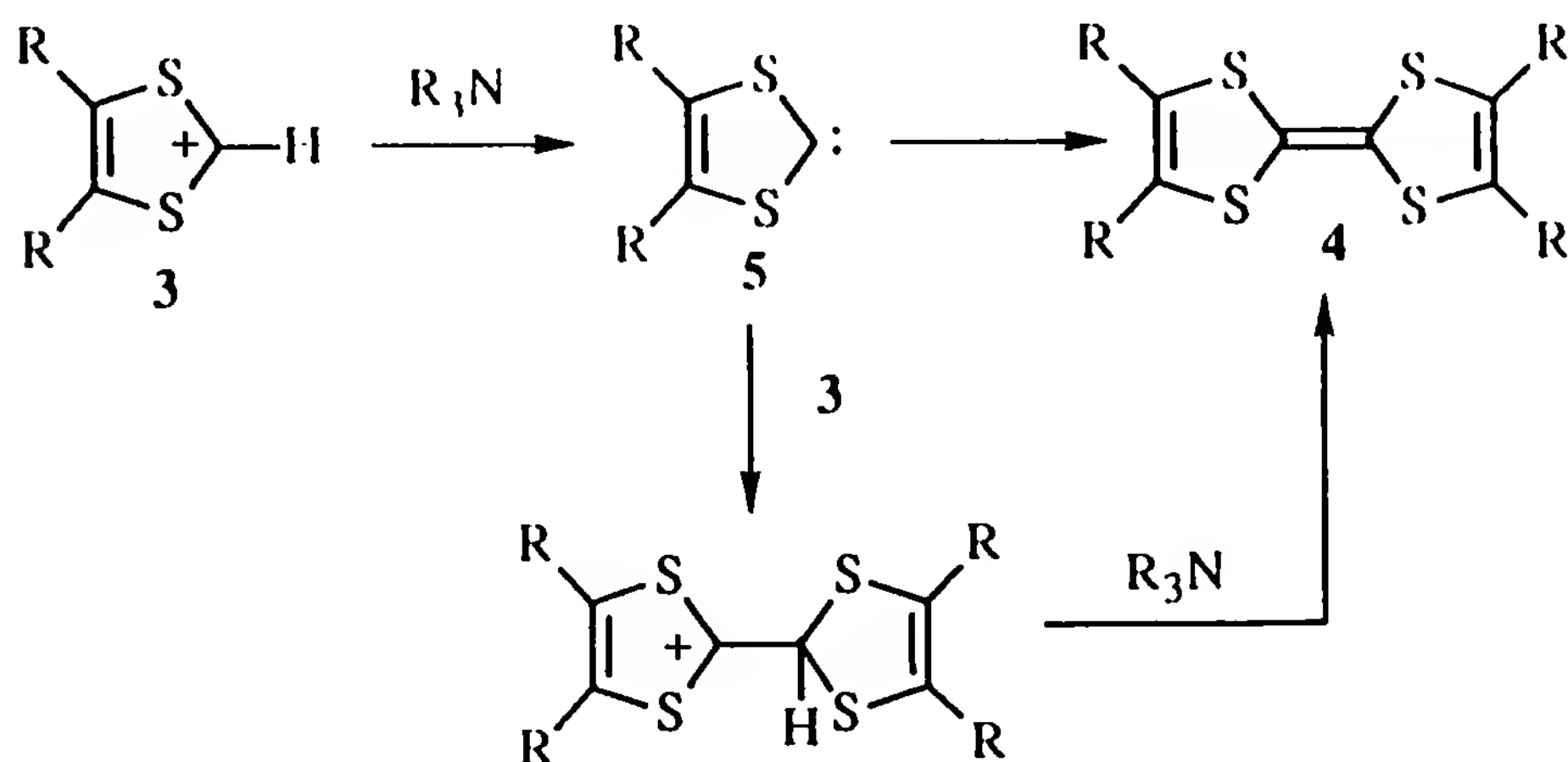
TTF was independently synthesized by three different groups about 1970 [11–18]. Many alternative pathways to TTF and its derivatives are now available.

In 1974 a multistep synthesis of TTF was published that starts from a readily available starting material, ethylene trithiocarbonate (**2**), and af-



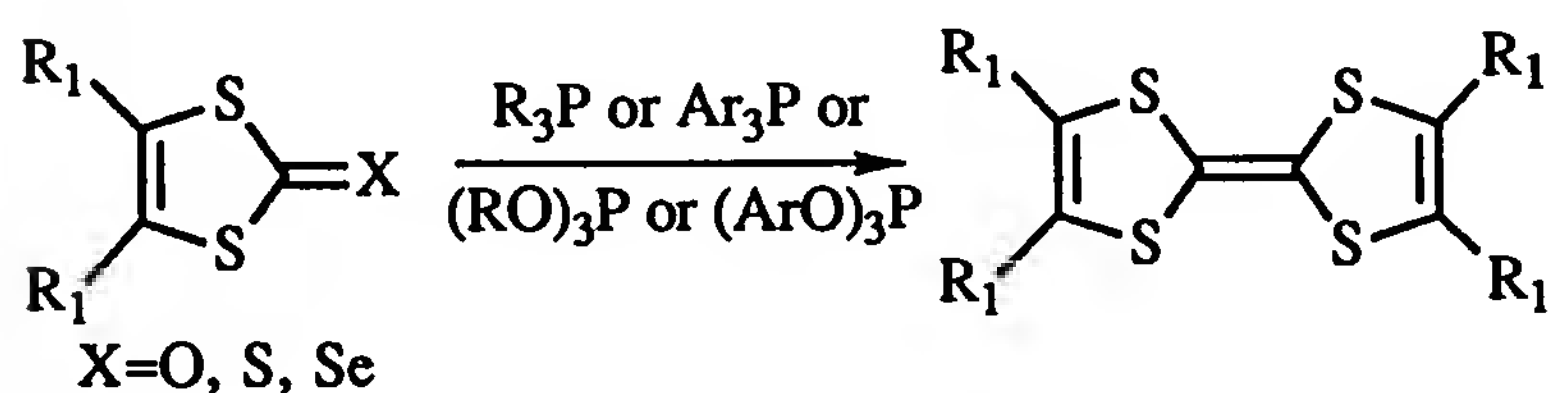
fords TTF in good overall yield [19]. In general, the deprotonation of 1,3-dithiolium salts (**3**) with tertiary amines provides an efficient route to sym-

metrically substituted tetrathiafulvalenes (**4**) [11,13,14,18]. The coupling reactions are believed to take place by way of short-lived carbene intermediates (**5**), either by direct carbene dimerization to **4** or reaction with a second cation followed by proton removal. The method works well with electron-releasing substituents that stabilize 1,3-dithiolium cations but not with electron-withdrawing substituents [1,5]. 1,3-Dithiolium cations can be prepared by a number of methods [5].

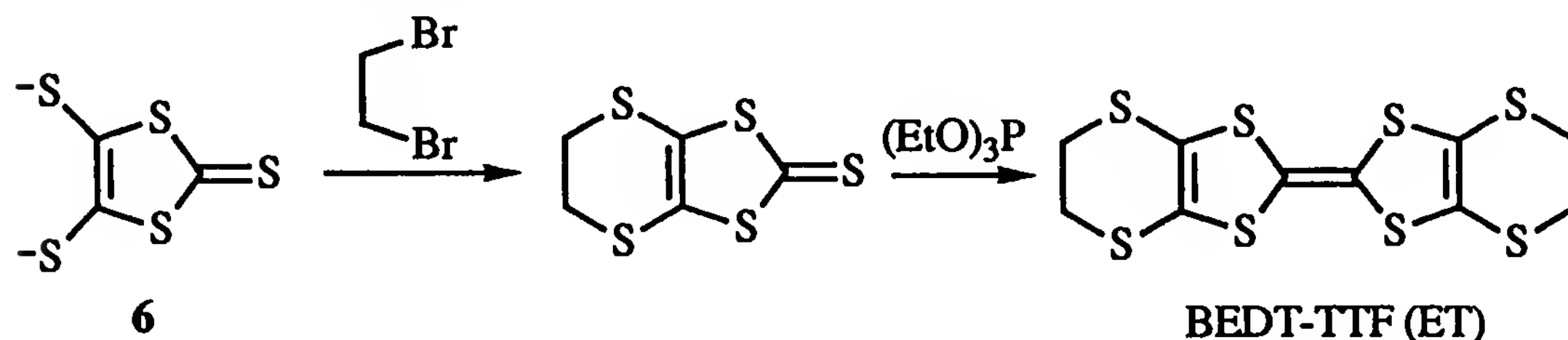


(b) Trivalent Phosphorus Coupling Routes

Probably the most general method for preparing tetrathiafulvalenes involves the coupling of 1,3-dithiole-2-chalcogenones utilizing phosphines or phosphites [1–8]. A number of factors (R_1 substituents, nature of X, solvent, temperature, and the trivalent phosphorus reagent) are important in determining the optimum yield [1–8]. In contrast with the 1,3-dithiolium salt coupling route, good yields are obtained with electron-withdrawing substituents [8].



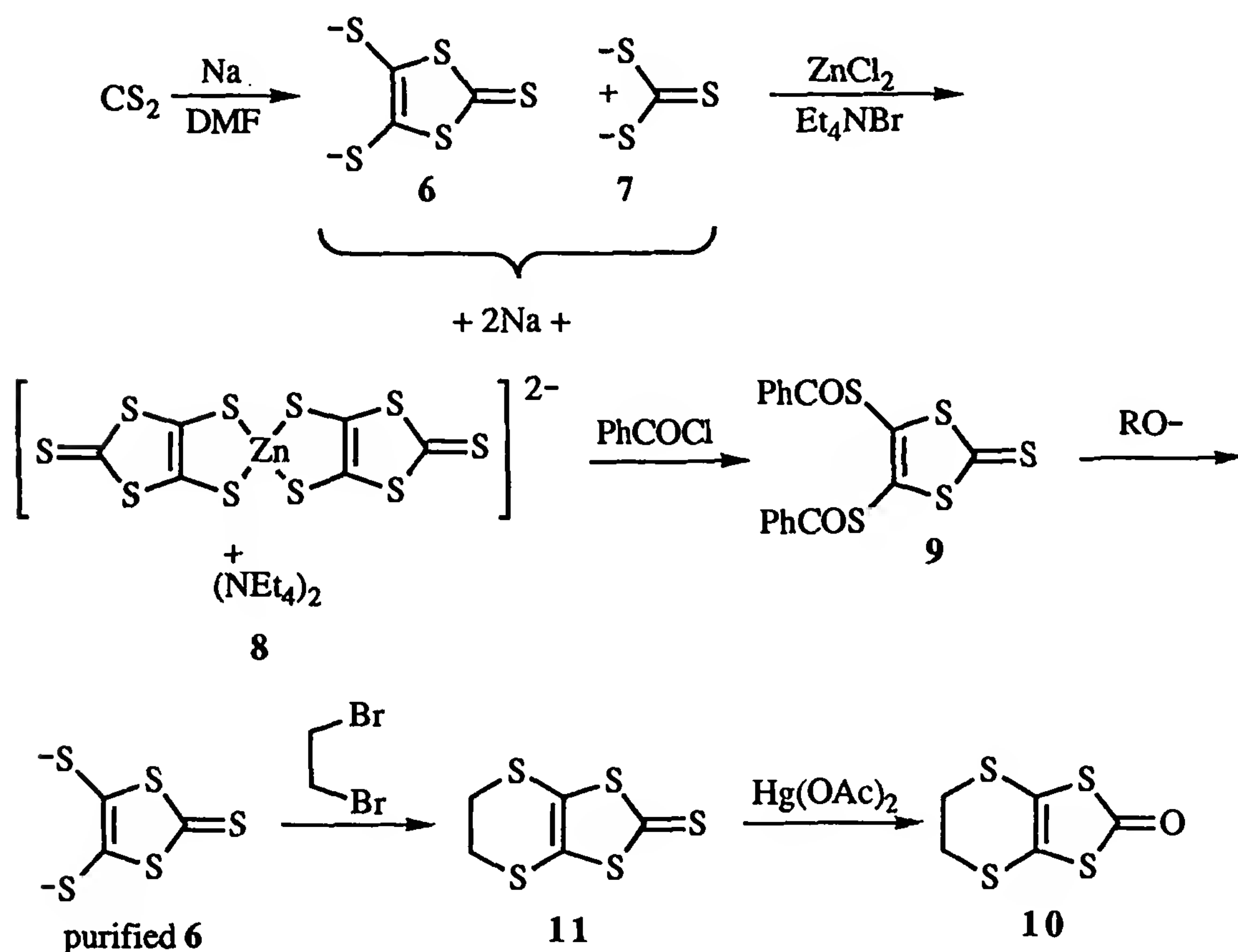
Bis(ethylenedithio)tetrathiafulvalene (BEDT-TTF or ET) was first synthesized in 1978, starting from dithiolate salt (**6**) [20]. The 1,3-dithiole-2-



thione-4,5-dithiolate anion (**6**) is obtained by the chemical [Na or K in dimethylformamide (DMF)] [21] or electrochemical (acetonitrile) [22] re-

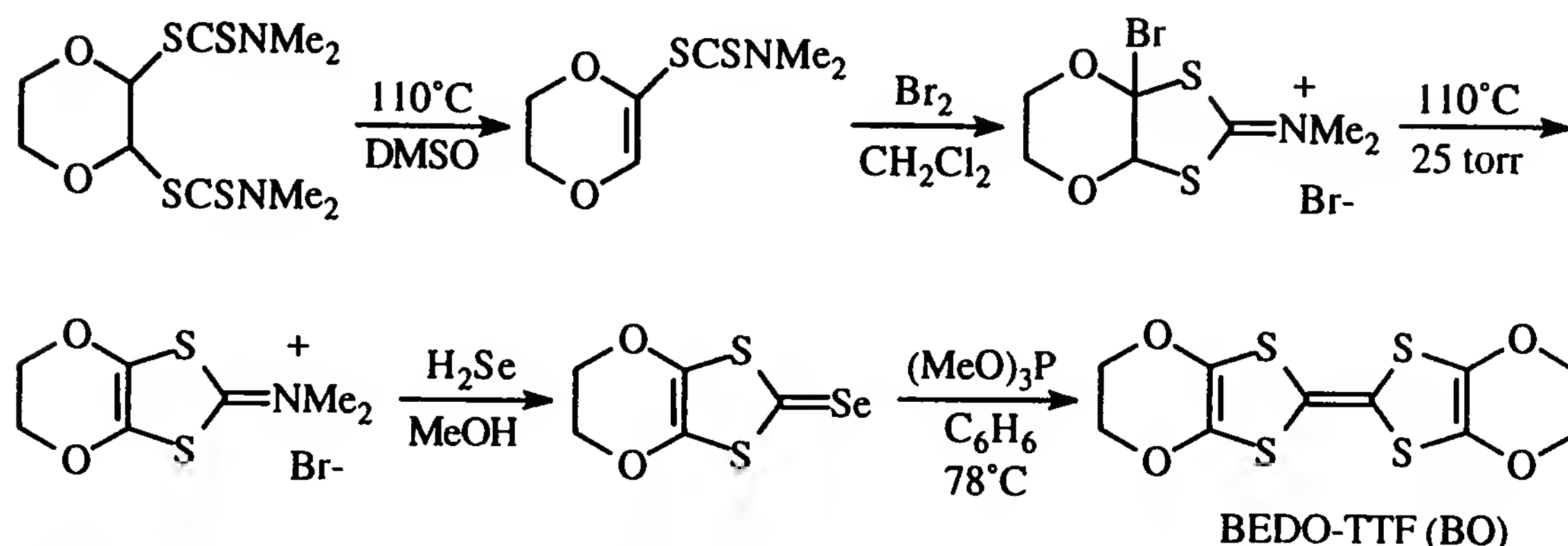
duction of carbon disulfide. Since the trithiocarbonate anion (**7**) is also produced, various procedures have been developed for purifying and storing the dithiolate anion (Scheme 2). Treatment of the reduction products with zinc chloride and tetraethylammonium bromide produces an insoluble tetraethylammonium zincate salt (**8**) that can be isolated and converted to a stable dibenzoate (**9**) [23]. Alkoxide regenerates the dithiolate anion when required in purified form. If desired, 1,3-dithiole-2-thiones can be converted to 1,3-dithiole-2-ones with mercuric acetate [24] to take advantage of the generally improved coupling yields with the 2-ones [8]. One of the most straightforward routes to BEDT-TTF, however, is to conduct the sodium reduction of carbon disulfide in DMF, rigorously remove the DMF, dissolve the reaction products in methanol, and alkylate the dithiolate anion in methanol with ethylene dibromide. The sequence takes place in a single reaction vessel and does not require the isolation of the dithiolate anion (**6**). 1,3-Dithiole [4,5-*b*][1,4]dithiin-2-thione (**11**) is obtained in 52% yield and can be converted to BEDT-TTF in one more step with neat, freshly distilled triethyl phosphite [25].

The synthesis of bis(ethylenedioxy)tetrathiafulvalene (BEDO-TTF or BO) represented a formidable synthetic challenge; its preparation was



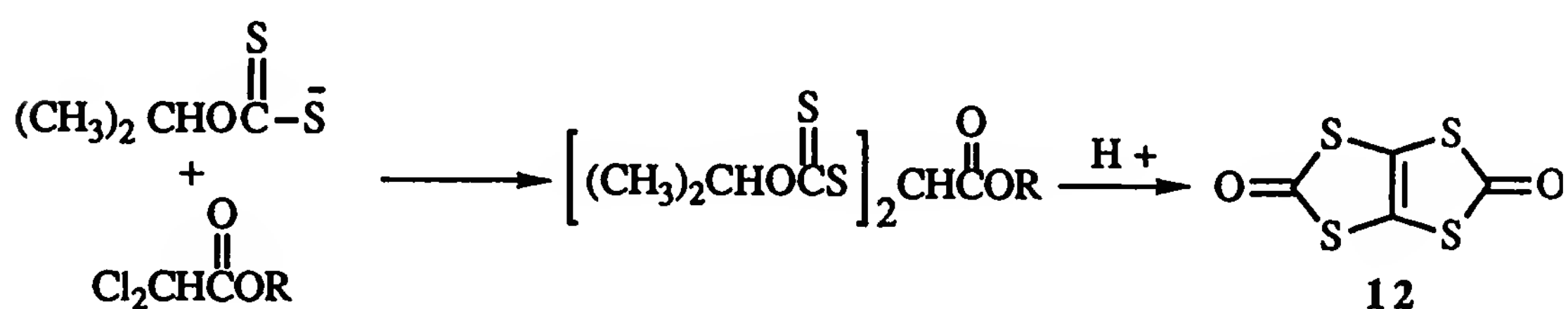
Scheme 2 Purification and handling of dithiolate anion **6**.

reported by Wudl in 1989 [26]. The final step involves a trimethyl phosphite-promoted coupling reaction (Scheme 3).

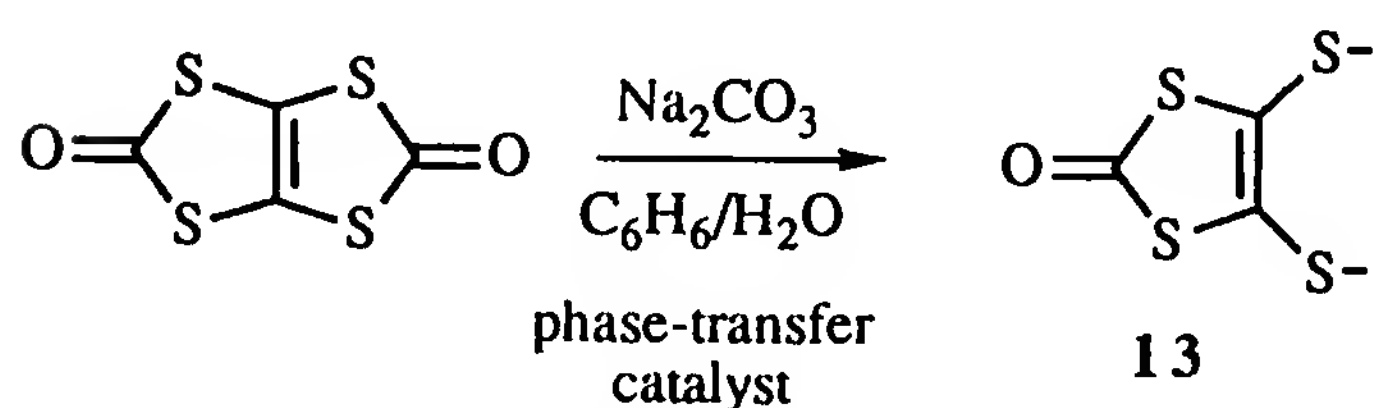


Scheme 3 Synthesis of BEDO-TTF.

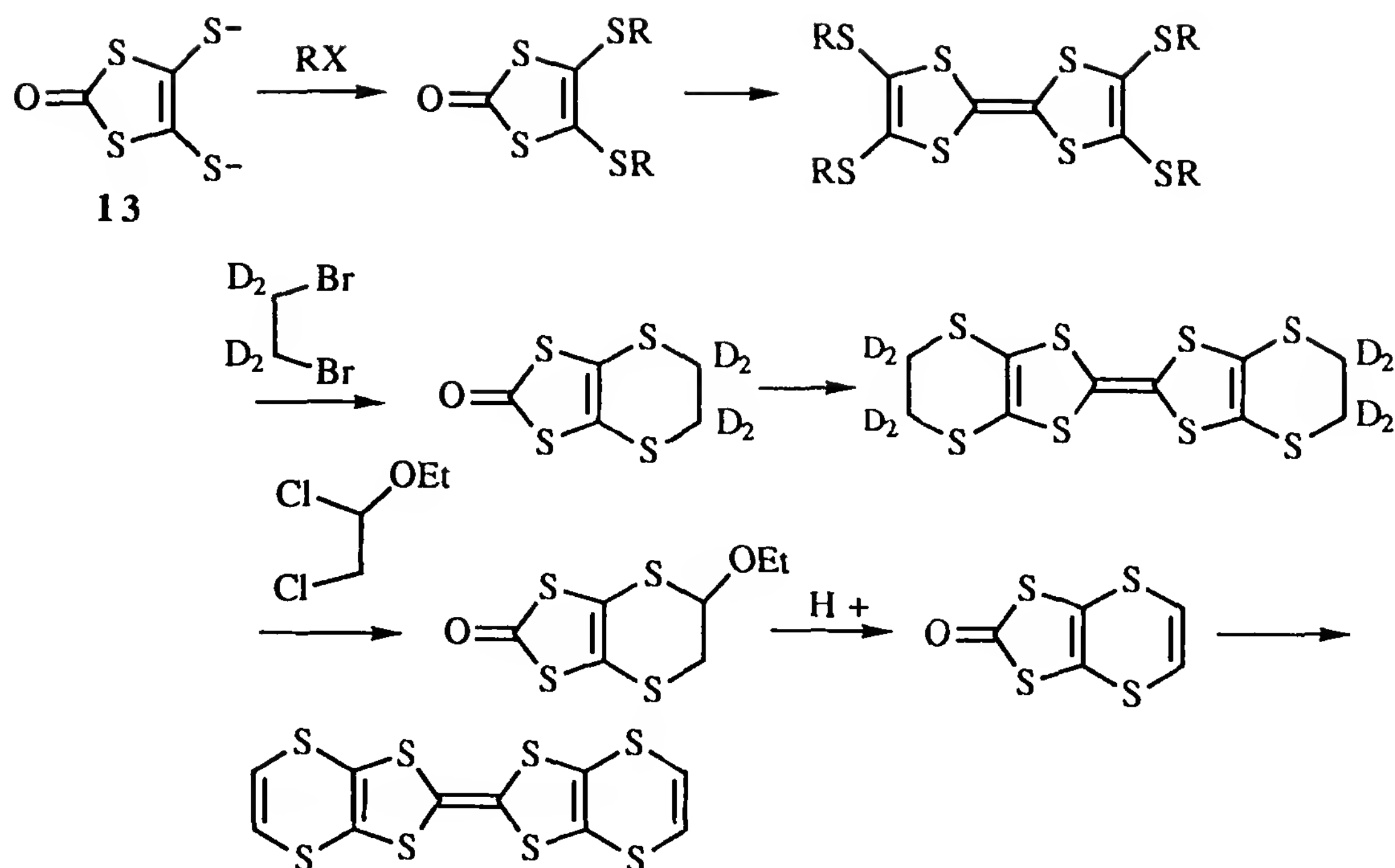
Thiapendione (**12**) also serves as a convenient starting material for the preparation of symmetrically substituted tetrathiofulvalenes [6]. It is formed by refluxing α,α -dichloroacetate esters with potassium *O*-isopropyl dithiocarbonate, followed by an acid-catalyzed cyclization [27]. One carbonyl group of thiapendione can be selectively cleaved in benzene–water in the



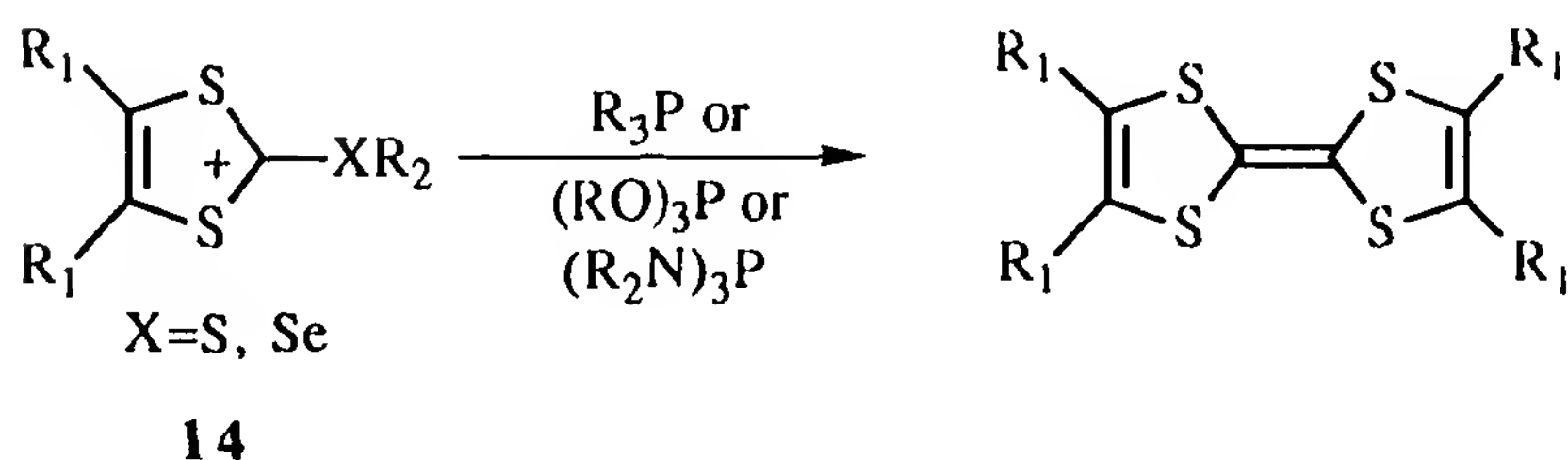
presence of a phase-transfer catalyst [28] to form the 1,3-dithiole-2-one-4,5-thiolate dianion (**13**), a versatile synthetic intermediate (Scheme 4). The thiapendione route to BEDT-TTF is one of the best for large-scale preparations [29].



Phosphines, phosphites, and phosphoramides also promote the coupling of 2-thio- and 2-seleno-substituted 1,3-dithiolium salts (**14**) [30].

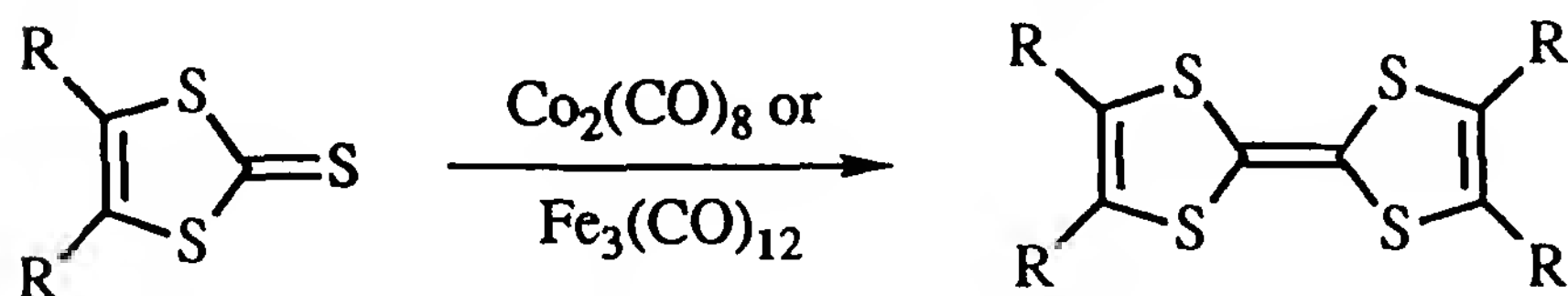


Scheme 4 Conversion of dithiolate anion **13** to several donor molecules.



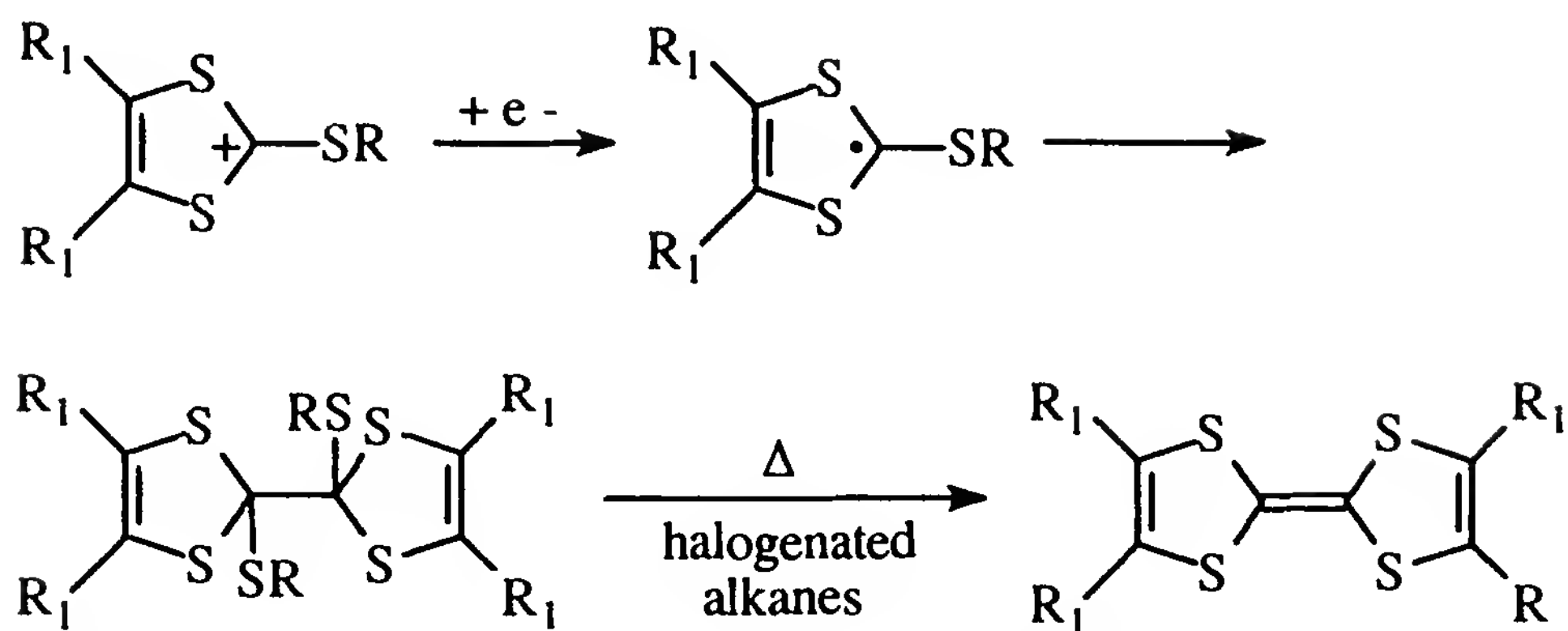
(c) *Transition Metal–Promoted Coupling*

1,3-Dithiole-2-thiones combine under the influence of dicobalt octacarbonyl [31–33] or triiron dodecacarbonyl [34,35] in aromatic hydrocarbons. Poor to good yields are obtained for a broad spectrum of substituents.

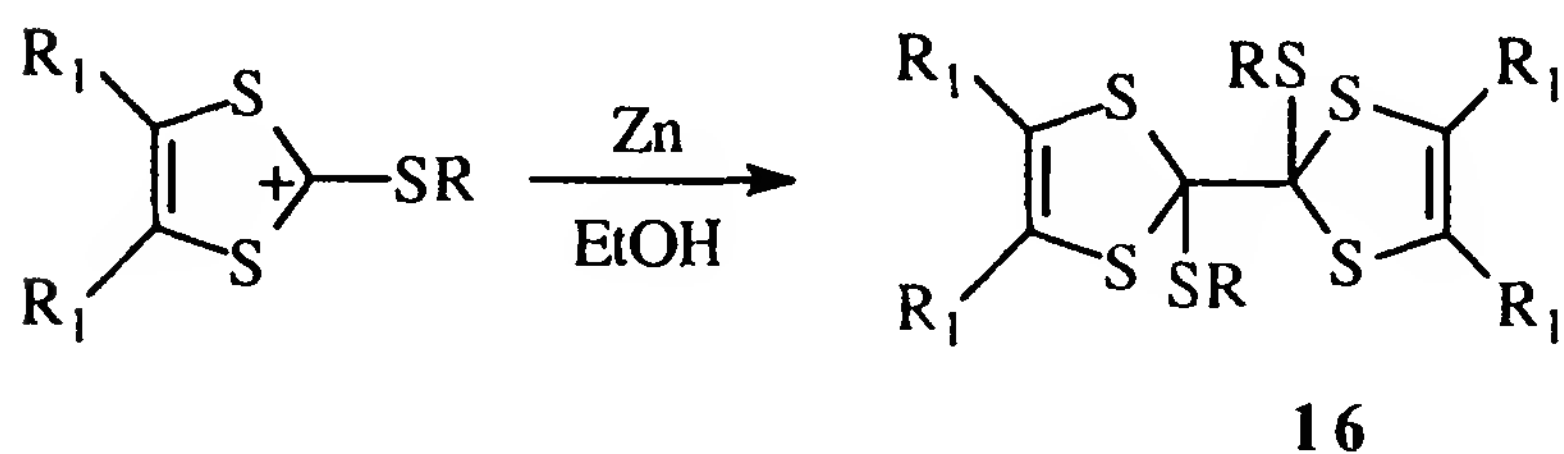


(d) *Reduction of 2-Alkylthio-1,3-Dithiolium Salts*

2-Alkylthio-1,3-dithiolium salts are reduced electrochemically in acetonitrile [36] (Scheme 5). The reductions proceed through radical intermediates (**15**), giving dimeric hexathioorthoxalates (**16**). The dimers can be converted to tetrathiafulvalenes by heating in carbontetrachloride, 1,1,2-trichloroethane (TCE), or 1,2-dichloroethane [36,37]. The reductive dimerization to hexathioorthoxalates can also be affected chemically [38].

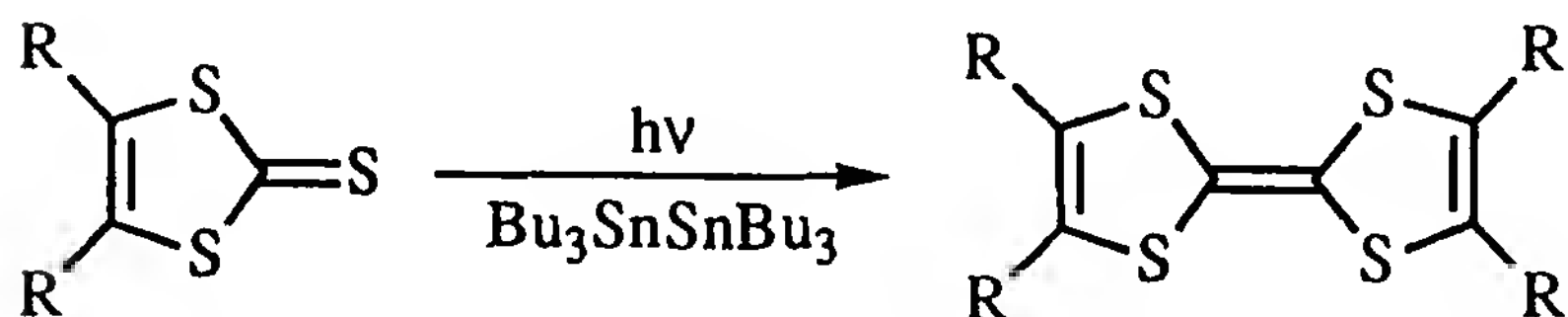


Scheme 5 Electrochemical reduction of 2-alkylthio-1,3-dithiolium salts.



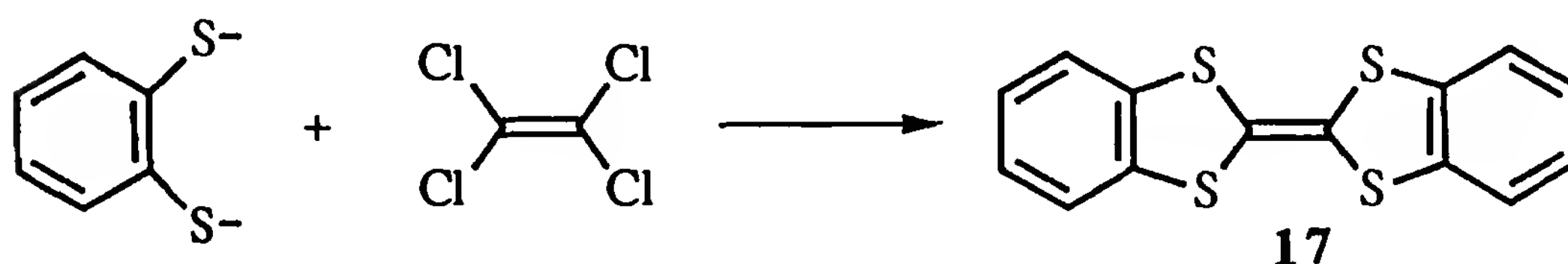
(e) *Photochemical Coupling*

1,3-Dithiole-2-thiones provide tetrathiafulvalenes upon irradiation in the presence of hexabutylditin [39,40]. Satisfactory yields are obtained for both electron-releasing and electron-withdrawing substituents.



(f) *Reaction of Tetrahaloethylenes with 1,2-Dithiolates*

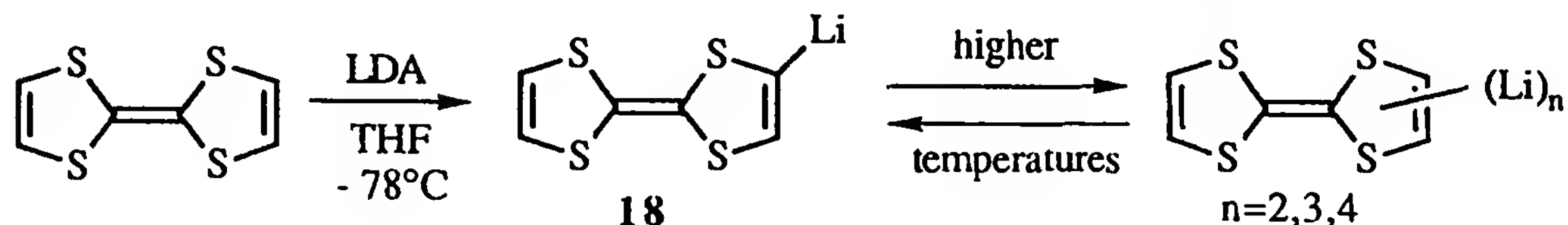
1,2-Dithiolate anions react with tetrahaloethylenes to furnish substituted tetrathiofulvalenes. This method has proven particularly useful in preparing dibenzotetrathiafulvalene (**17**) and its derivatives [41–43].



(g) *Lithiation of TTF*

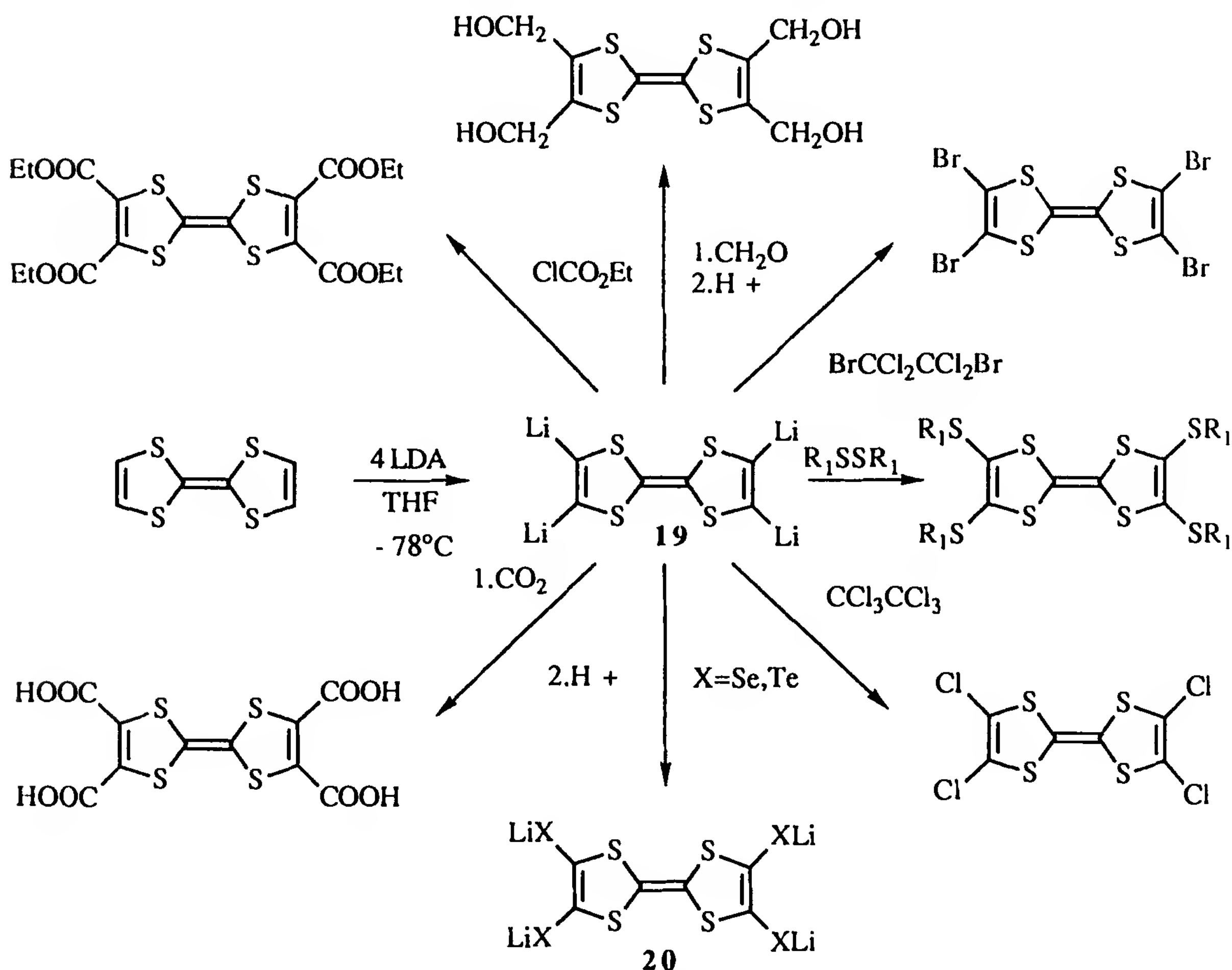
TTF is metallated [44–46] by either butyllithium or lithium diisopropylamide (LDA) in THF or ether at -78°C , producing monolithiotetrathioful-

valene (**18**). If the temperature is raised, lithium-equilibration reactions take place giving a mixture of mono-, di-, tri- and tetralithiated TTFs.



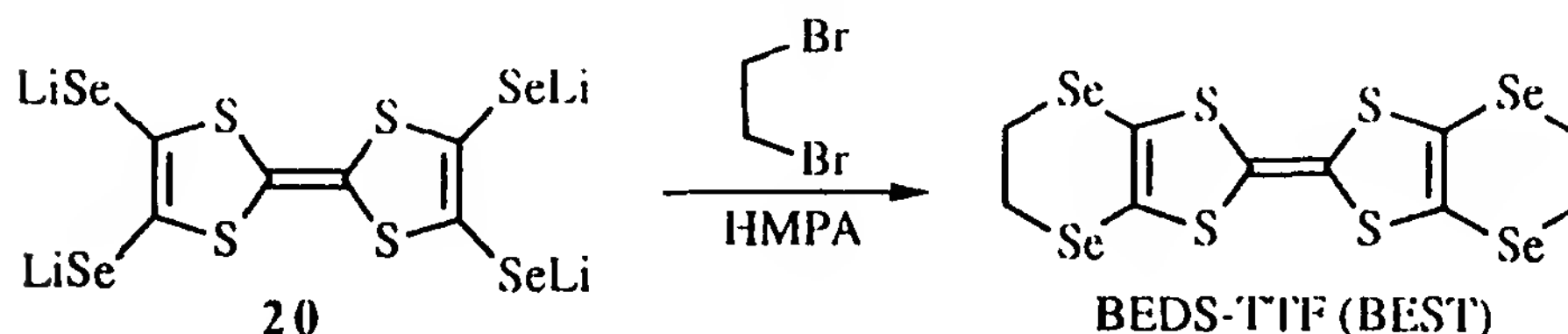
Many monosubstituted tetrathiafulvalenes have been made from monolithiotetrathiafulvalene [46,47]. By and large, these compounds are of little value in the search for new and improved organic conductors and superconductors; they are of considerable interest in other areas, such as the construction of Langmuir–Blodgett films.

If four molar equivalents of LDA are used in the metallation [48], all four protons of TTF can be replaced (**19**). Numerous products can be prepared from this intermediate [48–52] (Scheme 6). This is the preferred route for preparing tetrahalotetrathiafulvalenes; pathways involving electrophilic aromatic substitution are not practical in general. Chalcogen insertion (Se, Te) offers a good pathway to mixed chalcogen donors. For



Scheme 6 Some reactions of tetralithiotetrathiafulvalene **19**.

example, bis(ethylenediseleno)tetrathiafulvalene (BEDS-TTF, BEST) can be obtained in excellent yield by the alkylation of **20** in hexamethylphosphorus triamide (HMPA) [53].

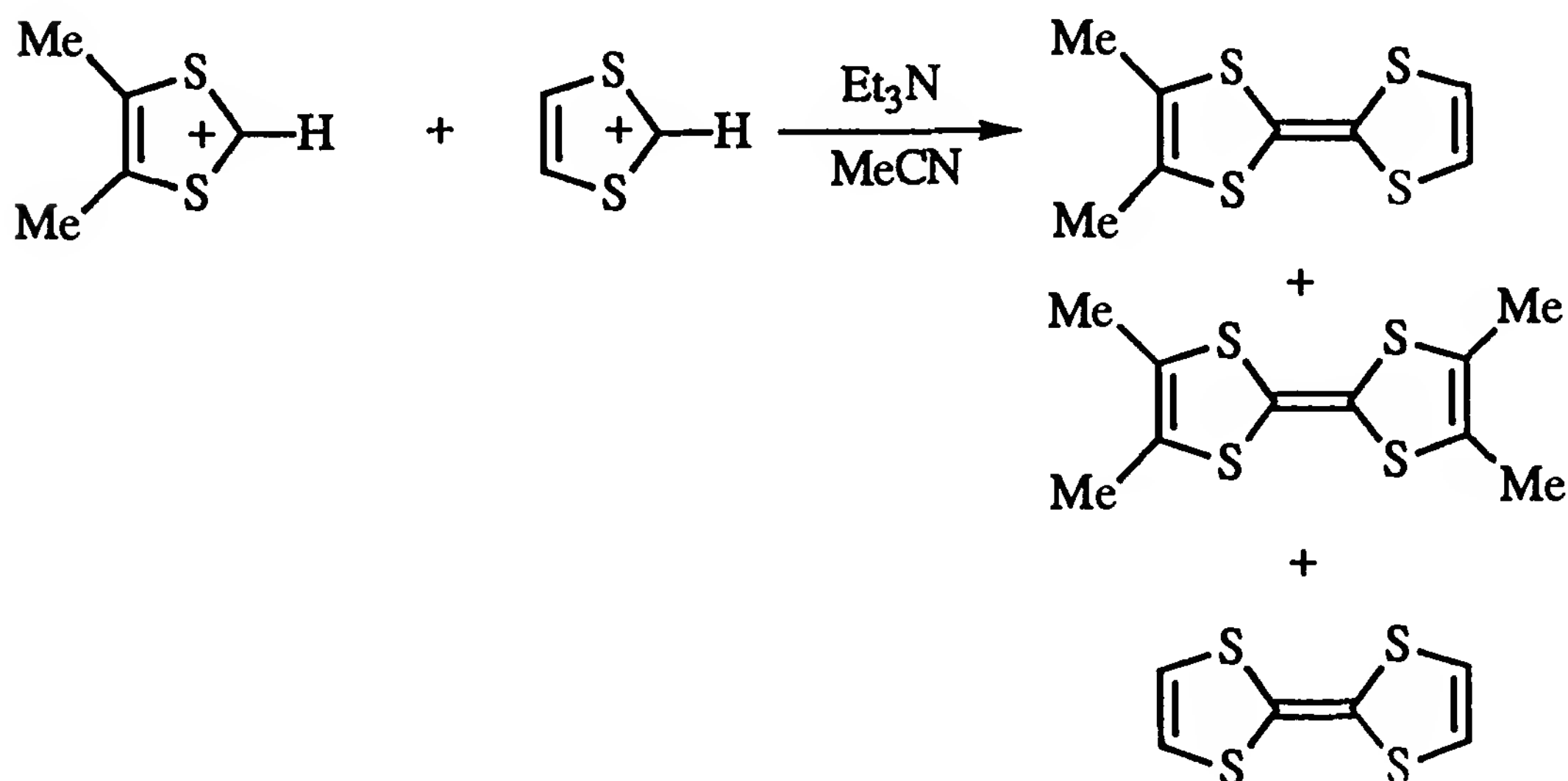


(h) Miscellaneous Methods

More limited routes to symmetrical tetrathiafulvalenes are available and can be of value in particular circumstances. Discussions of alternative pathways are available in the review articles cited previously [1–8].

2. Unsymmetrically Substituted Derivatives of TTF

The majority of synthetic approaches to TTF derivatives that have been discussed to this point involve the coupling of two like halves to form a symmetrical molecule. Several of the important donor molecules shown in Fig. 1 have unsymmetrical substitution patterns [methylenedithiotetrathiafulvalene (MDT-TTF), S,S-dimethyl-bis(ethylenedithio)tetrathiafulvalene (S,S-DMBEDT-TTF) and dimethyl(ethylenedithio)tetraselenafulvalene (DMEDT-TSF)] or different chalcogens in the two tetrachalcogenafulvalene rings [dimethyl(ethylenedithio)diselenadithiafulvalene (DMET)]. One obvious approach to the synthesis of donors of this type is to couple two different donor halves employing the methodologies outlined above. This has, in fact, been done in a number of cases [e.g., Refs. 54 to 57]. The union of two dissimilar 1,3-dithiolium cations is shown in (Scheme 7) [56].



Scheme 7 Coupling of two different 1,3-dithiolium salts.

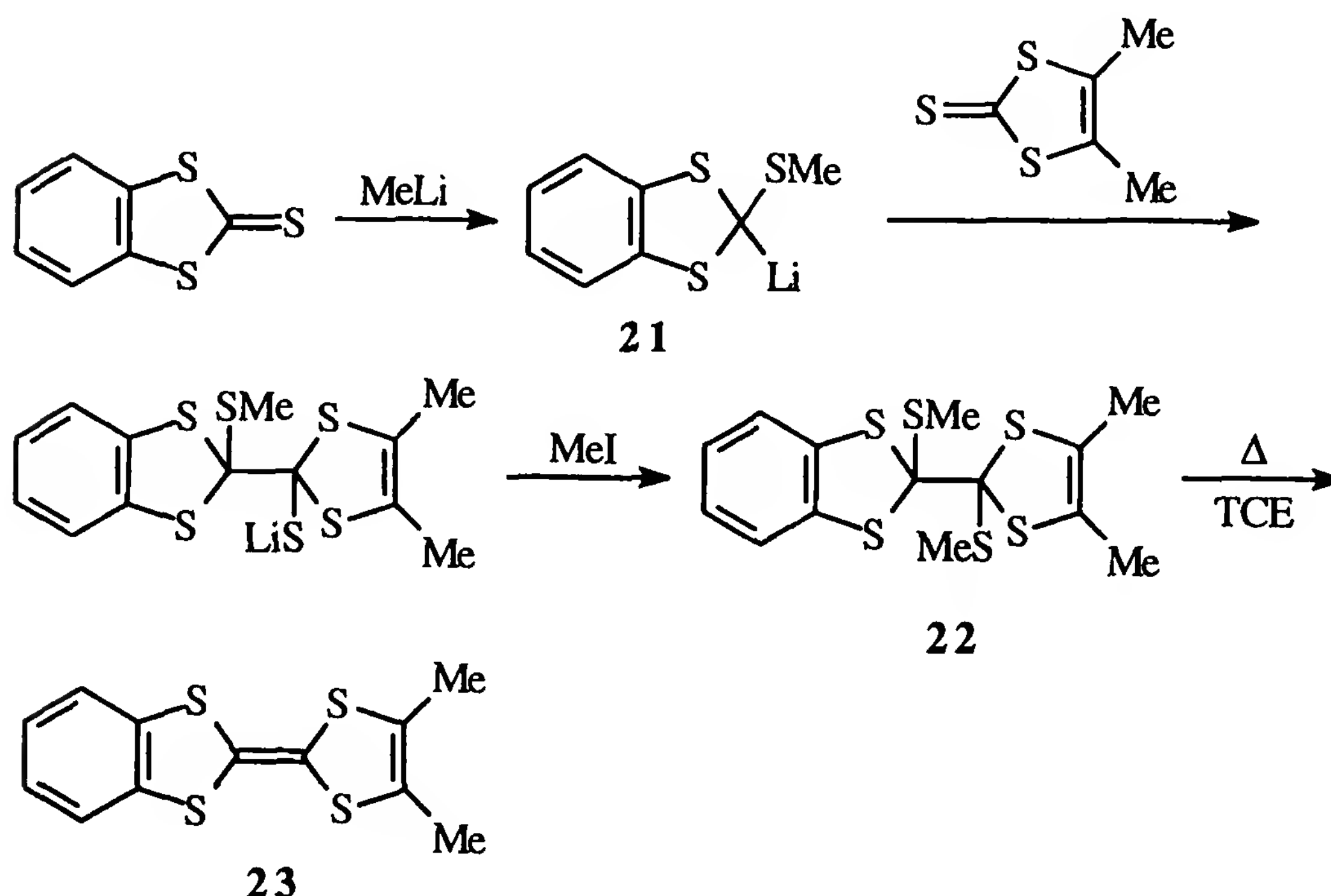
There are two serious drawbacks to such an approach. First, the theoretical yield of the desired cross-coupling product is reduced by the production of three different TTF derivatives. In the case of statistical coupling, the maximum yield of unsymmetrical donor is only 50%. The second problem is that the desired product must be separated from two very similar compounds. This is usually a difficult task. Because of these limitations, more efficient routes to unsymmetrical donors have been developed.

(a) *Hexathioorthoxalate Pathway*

Unsymmetrical hexathioorthoxalates are obtained in good yields (60 to 90%) by coupling two different 1,3-dithiole-2-thiones in the following manner [59]: Methyl lithium is added to the first 1,3-dithiole-2-thione; S-alkylation occurs to form **21**. A second 1,3-dithiole is reacted with the adduct (**21**), and the resulting product is alkylated with methyl iodide. The hexathioorthoxalate obtained in this way (**22**) can be converted to a tetrathiafulvalene as outlined above [36,37] (75 to 95%). The overall sequence is shown for the preparation of benzodimethyltetrathiafulvalene (**23**) in Scheme 8.

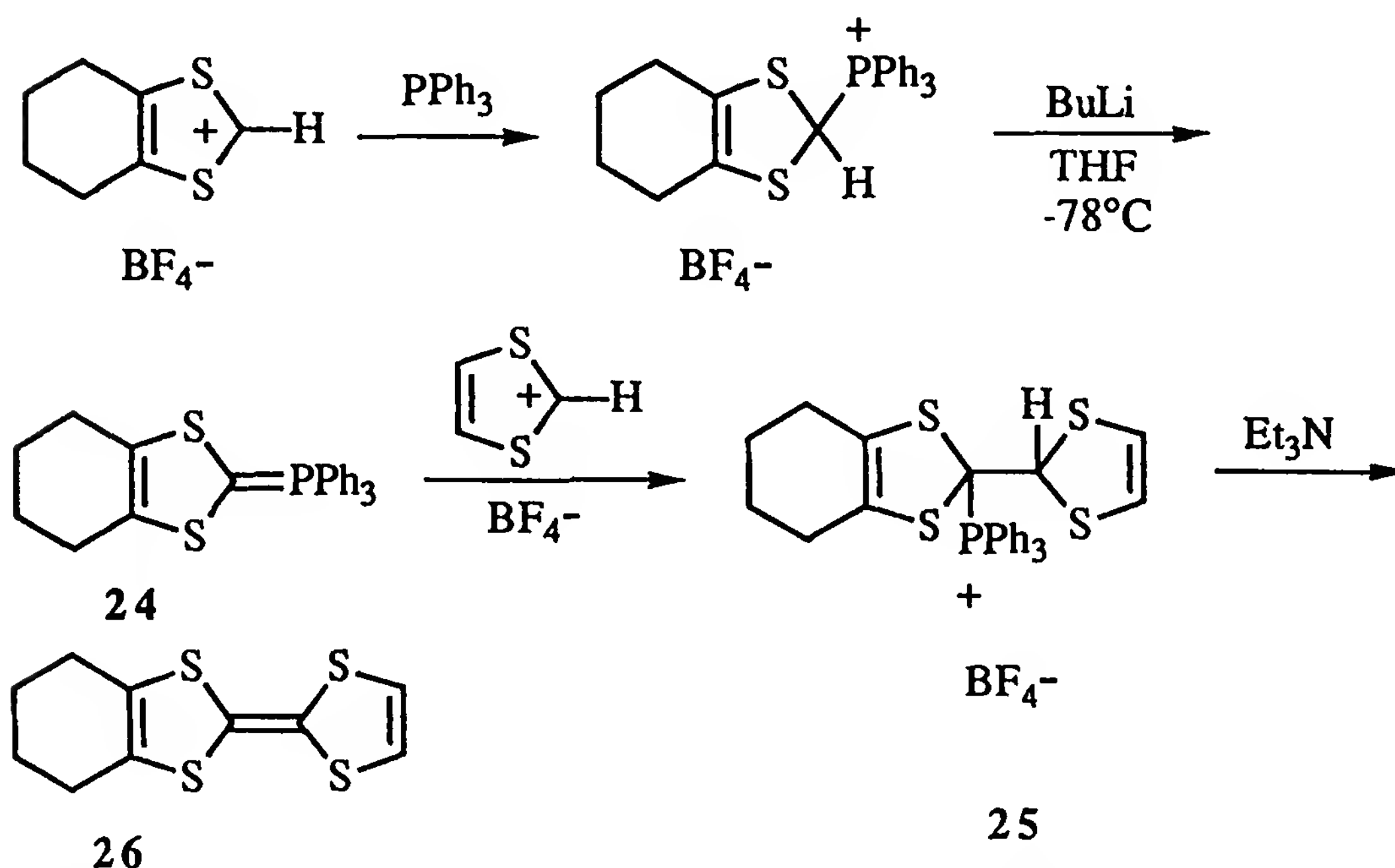
(b) *Coupling of 1,3-Dithiole-2-Phosphoranes with 1,3-Dithiolium Salts*

In 1978, Cava published a general procedure for the preparation of unsymmetrical TTF derivatives based on a phosphorane (**24**) -1,3-dithiolium



Scheme 8 Synthesis of benzodimethyltetrathiafulvalene *via* the hexathioorthoxalate pathway.

salt coupling reaction [59] (Scheme 9). Treatment of the resulting adduct (**25**) with base leads to an unsymmetrical TTF derivative [60,61]. The complete sequence is illustrated in Scheme 9 for the preparation of tetramethylenetetrafulvalene (**25**, 41% yield).



Scheme 9 The phosphorane-1,3-dithiolium salt coupling procedure.

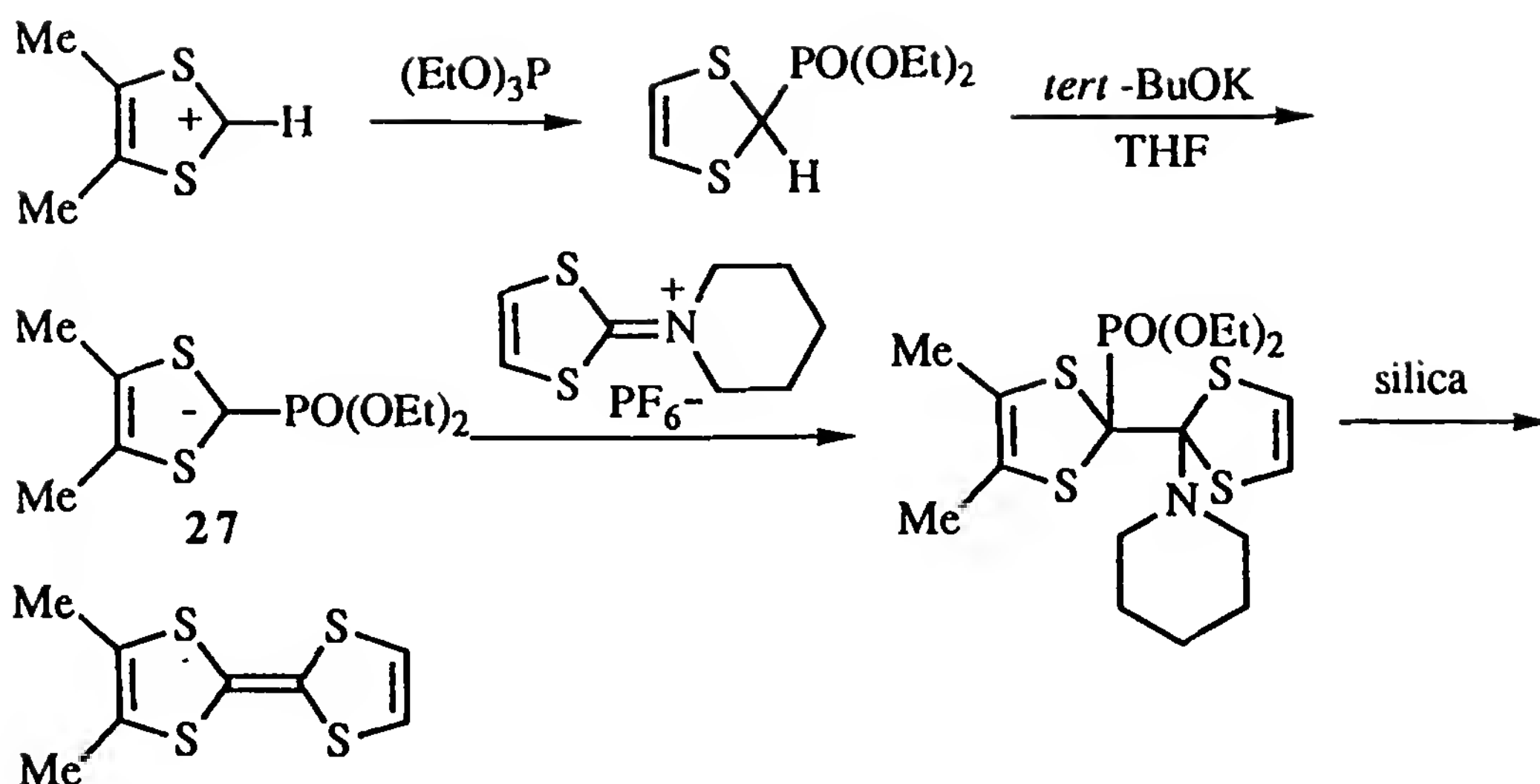
(c) *Coupling of 1,3-Dithiole-2-Phosphonates with 1,3-Dithiole-2-Iminium Salts*

In the reaction outlined in Section II.A.2.b, the desired cross-coupled product is sometimes contaminated with small amounts of symmetrical TTFs. The contaminants are believed [61] to arise because of the instability of the phosphonium salt intermediate (**25**). Lerstrup has reported an improved synthesis utilizing phosphonate reagents (**27**) that presumably circumvents this problem [62]. Dimethyltetrafulvalene can be synthesized in good yield with no contaminating TTF by products following the sequence in Scheme 10.

3. Tetraselenafulvalene and Its Derivatives

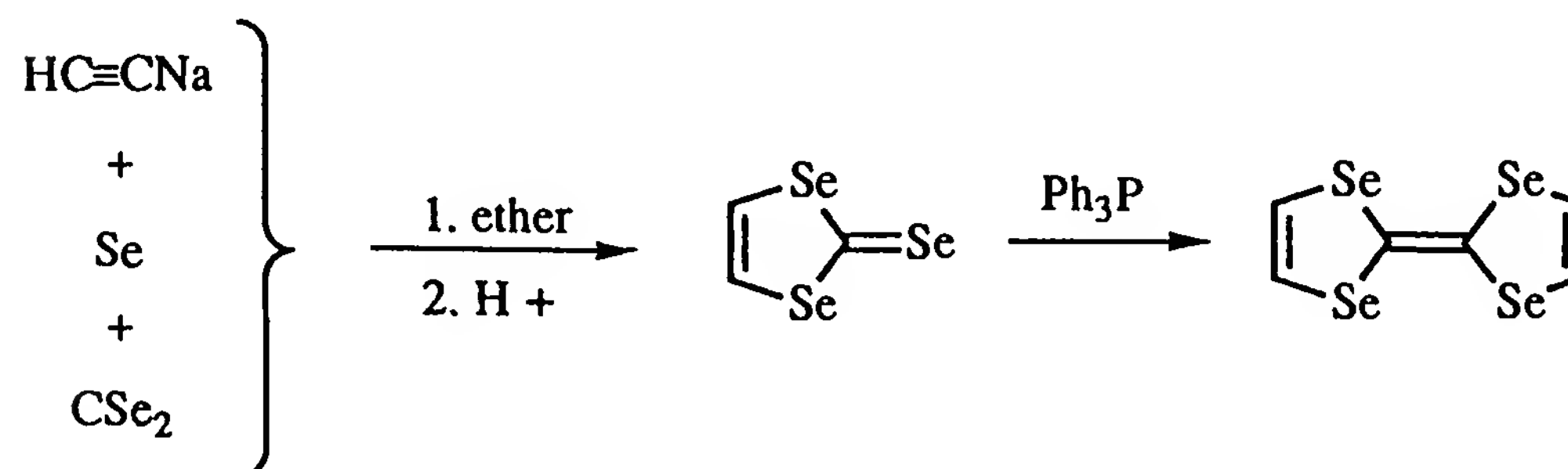
(a) *Tetraselenafulvalene (TSF)*

Engler and Patel published the first synthesis of TSF in 1974 [63]. 1,3-Diselenole-2-selenone was obtained from sodium acetylide, selenium, and



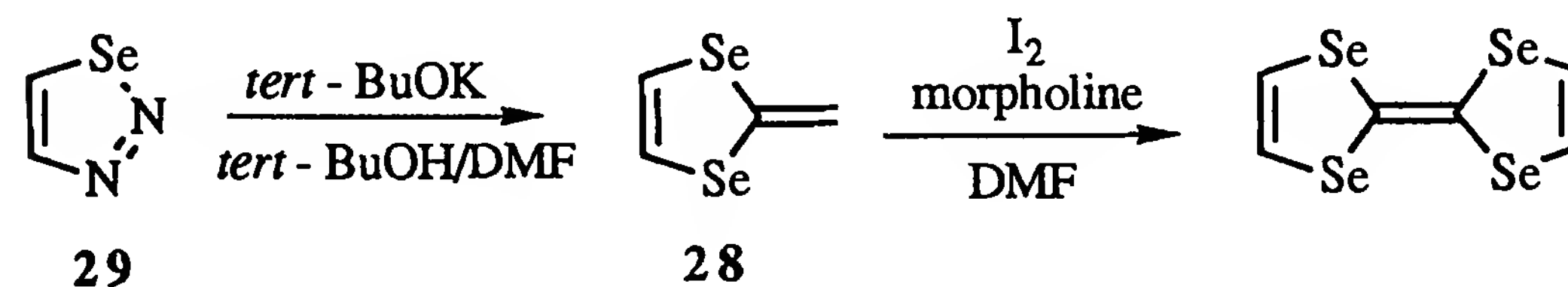
Scheme 10 The phosphonate-iminium salt route to dimethyltetrathiafulvalene.

carbon diselenide in low yield (15 to 25%). Coupling of the selenone with triphenylphosphine afforded TSF in 70 to 80% yield. Because of problems



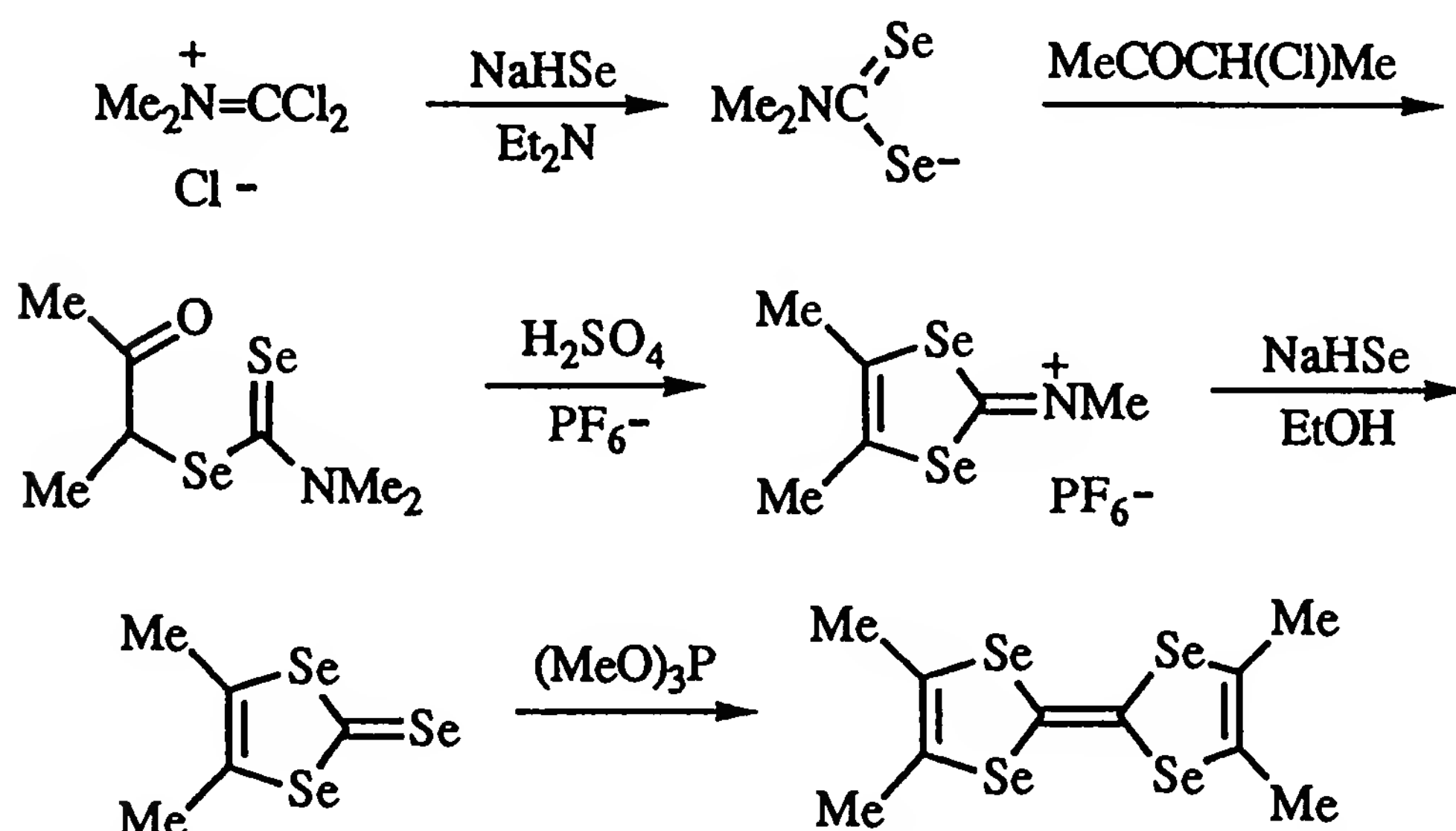
associated with the elemental selenium and carbon diselenide employed, this procedure has been one of the most verbally maligned [4,6–8] in the history of organic synthesis (highly toxic, very expensive, malodorous, extremely fetid, and ill-ventable). Fortunately, improved syntheses of TSF followed.

The most convenient route to TSF was reported by Cava in 1987 [64]. The procedure utilizes a novel iodine-promoted coupling of 2-methylene-1,3-diselenole (**28**). The starting 1,2,3-selenadiazole (**29**) is easily obtained from the oxidation of the semicarbazone of acetaldehyde with selenium dioxide.



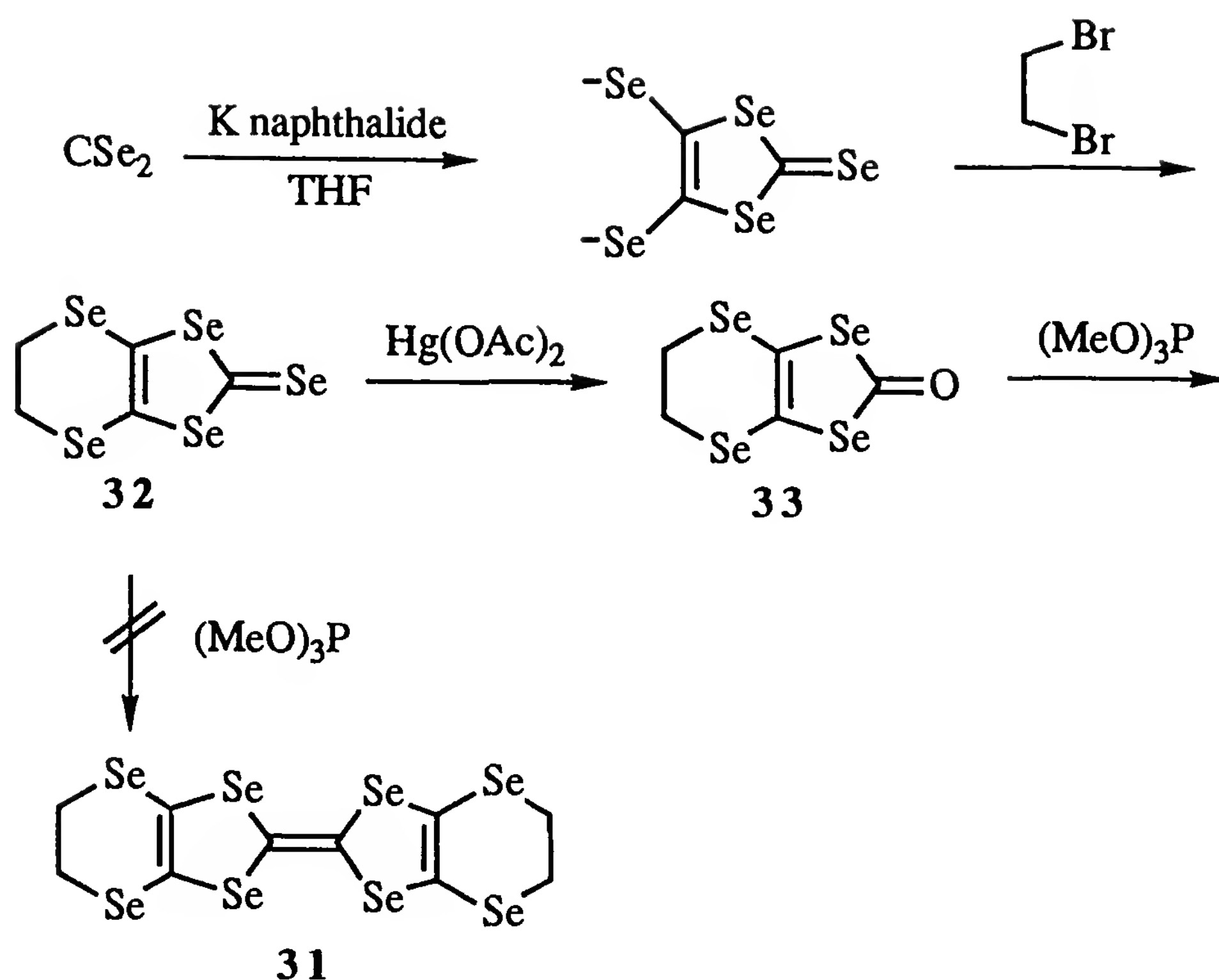
(b) *Substituted Tetraselenafulvalenes*

Tetramethyltetraselenafulvalene (TMTSF) has yielded numerous conducting salts with rich and varied physics, including six superconductors [10]. TMTSF was prepared originally by the phosphine-promoted coupling of a selenone precursor [65]. As in the case in the first TSF synthesis, carbon diselenide was utilized in the formation of the selenone intermediate. More recently, NaHSe has been used as the selenium source [66] (Scheme 11) (30). TMTSF is commercially available.

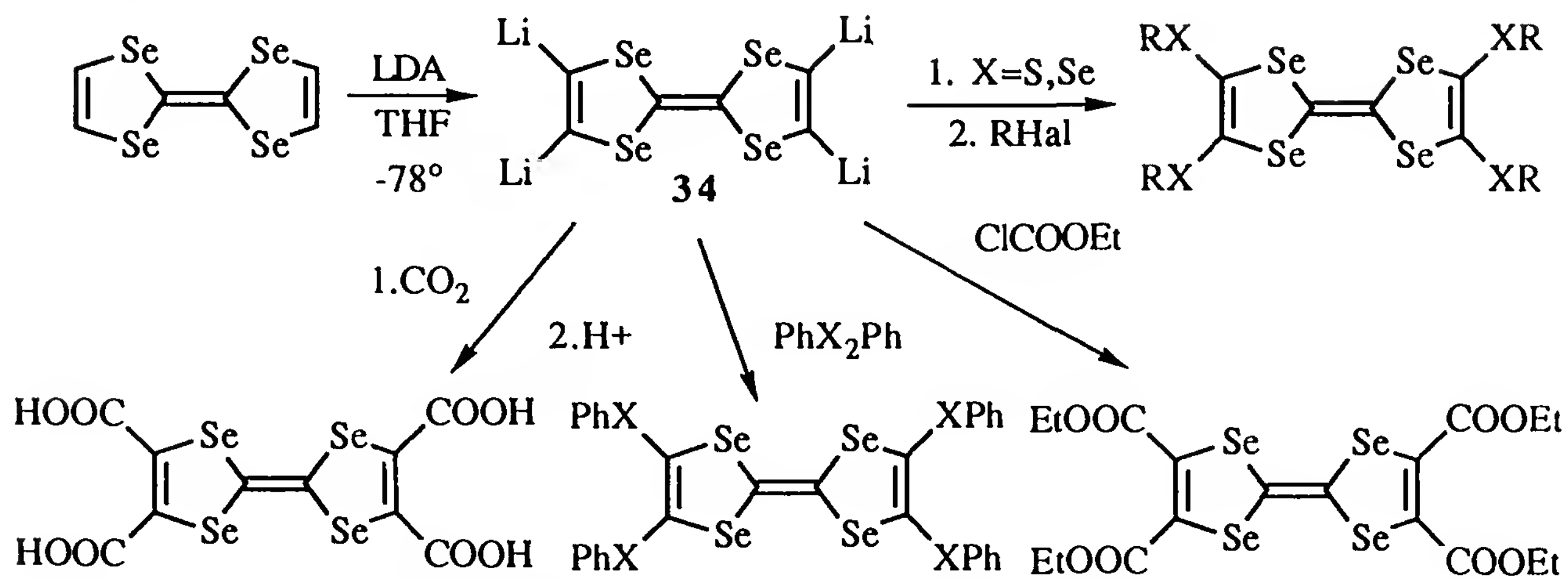


Scheme 11 Synthesis of TMTSF.

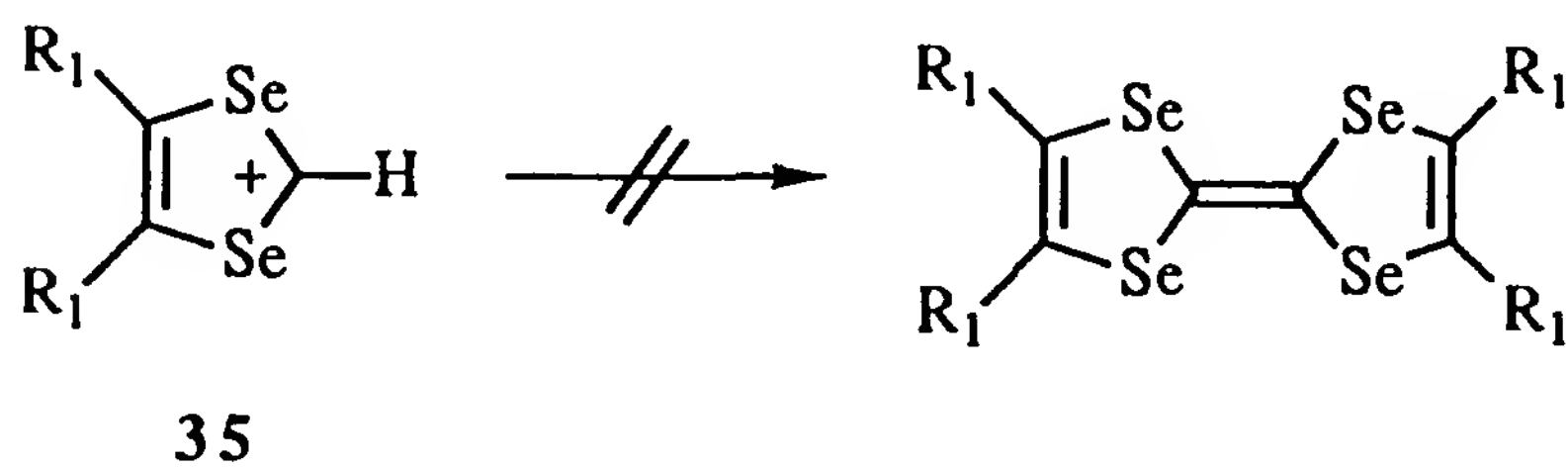
An assortment of other selenium-containing donors have been made. In preparing selenium compounds there are many parallels with the TTF chemistry that was outlined above, as well as some important differences. The octaselenium analog of BEDT-TTF, bis(ethylenediseleno)tetraselenafulvalene (BEDS-TSF) (31), can be synthesized from carbon diselenide (Scheme 12) [67]. In contrast to the usual situation [8], the selenone intermediate (32) does not undergo facile coupling to BEDS-TSF but must be converted to the oxo derivative (33). BEDS-TSF has not received much attention as a synthetic metal component because of its extremely limited solubility in organic solvents. TSF can be tetralithiated with LDA but not butyllithium, which leads to ring-opened products [68,69]. The tetralithio product (34) can be utilized in a number of useful ways (Scheme 13). One significant difference between the methodology for preparing TTF and TSF derivatives is that 1,3-diselenolium cations (35) do not afford coupled products with amines [70].



Scheme 12 Synthesis of BEDS-TSF.

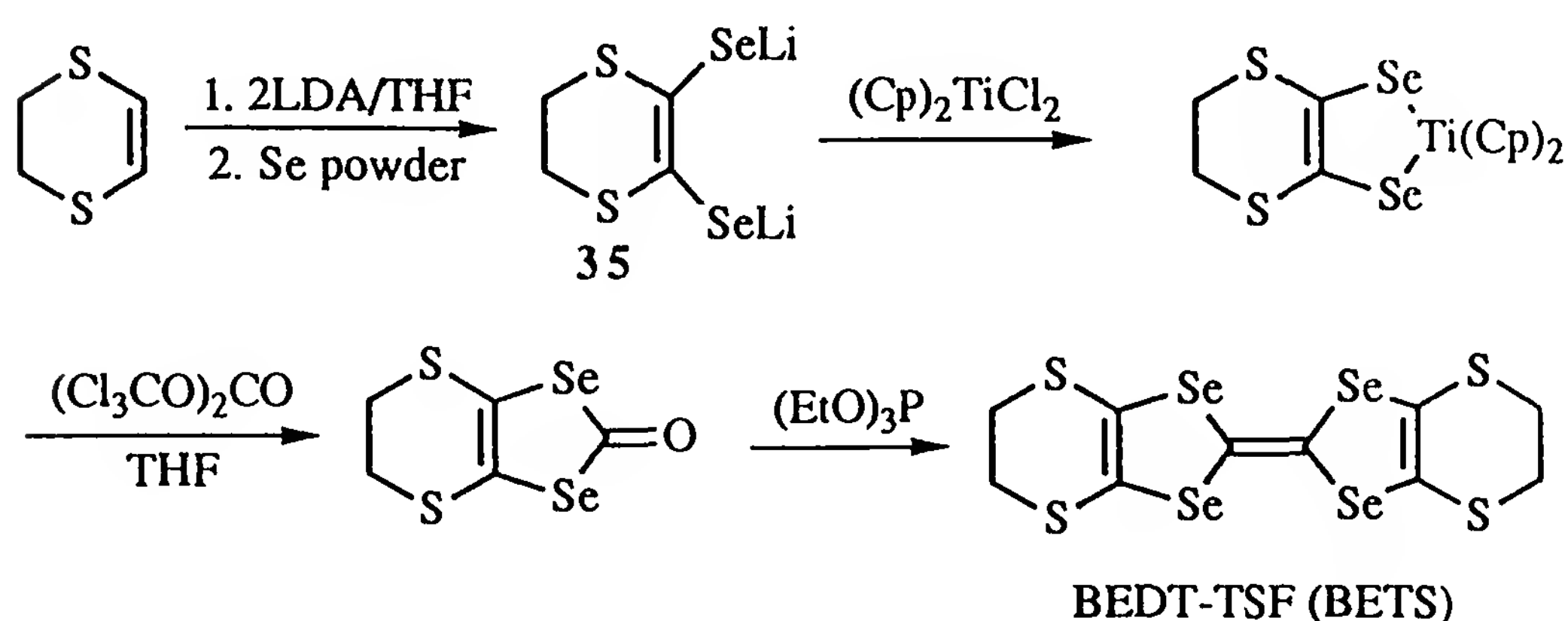


Scheme 13 Some useful reactions of tetralithiotetraselenafulvalene.



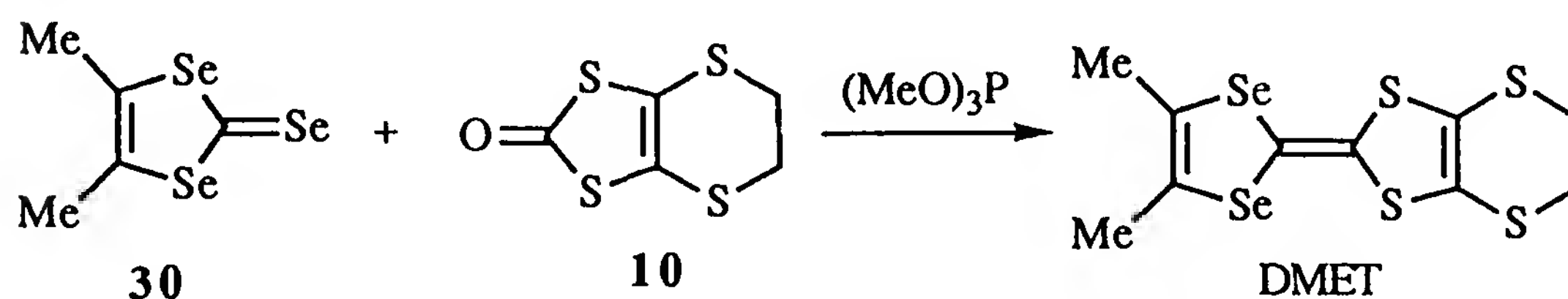
4. Mixed Sulfur–Selenium Donors

The synthesis of the mixed sulfur–selenium donor BEDS-TTF (BEST) via the tetralithiation of TTF was mentioned above [53]. Bis(ethylenedithio) tetraselenafulvalene (BEDT-TSF, BETS) is obtained in good yield following the sequence outlined in Scheme 14. The synthesis makes use of a titanium–cyclopentadiene complex to stabilize a problematic, unstable synthetic intermediate (**35**) [7].



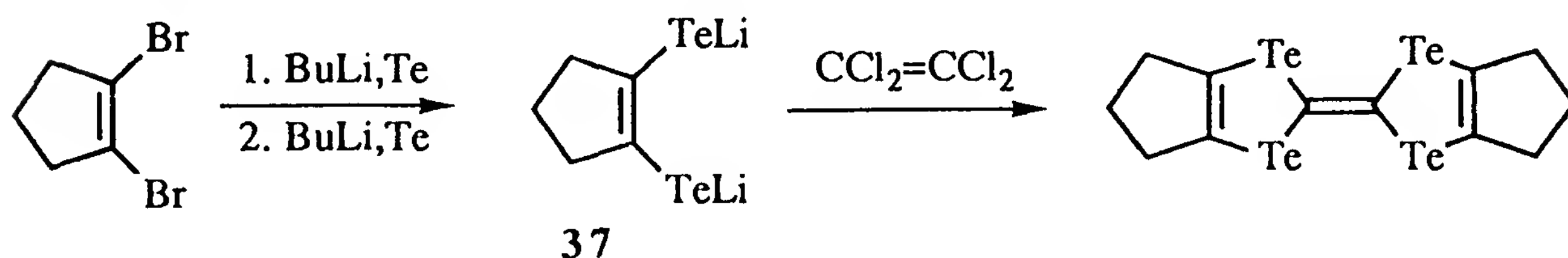
Scheme 14 Synthesis of BETS.

The unsymmetrical, mixed donor DMET has produced a number of superconducting salts [10]. DMET can be prepared in acceptable yield by way of a mixed coupling reaction [72]. Preparation of **30** and **10** has been discussed previously.

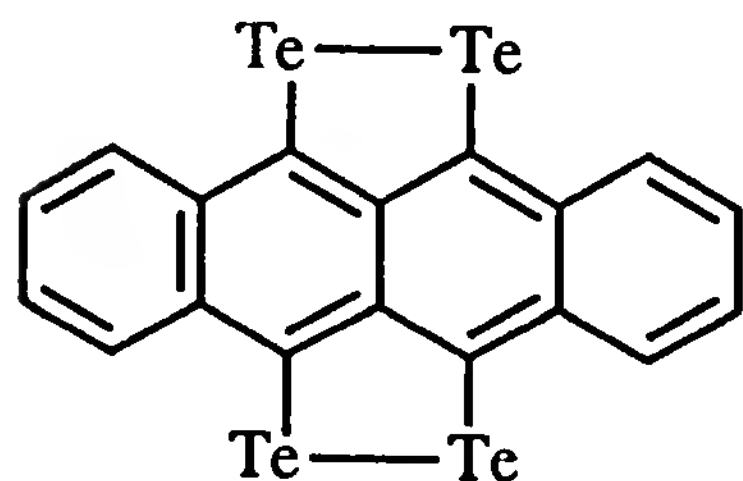
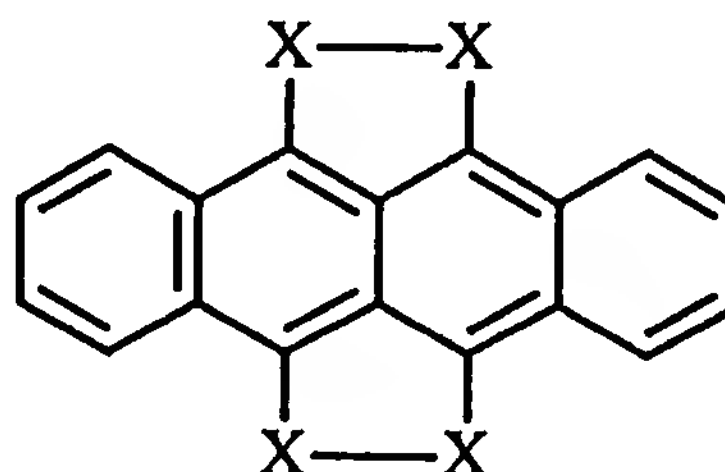


5. Tetratellurafulvalene and Its Derivatives

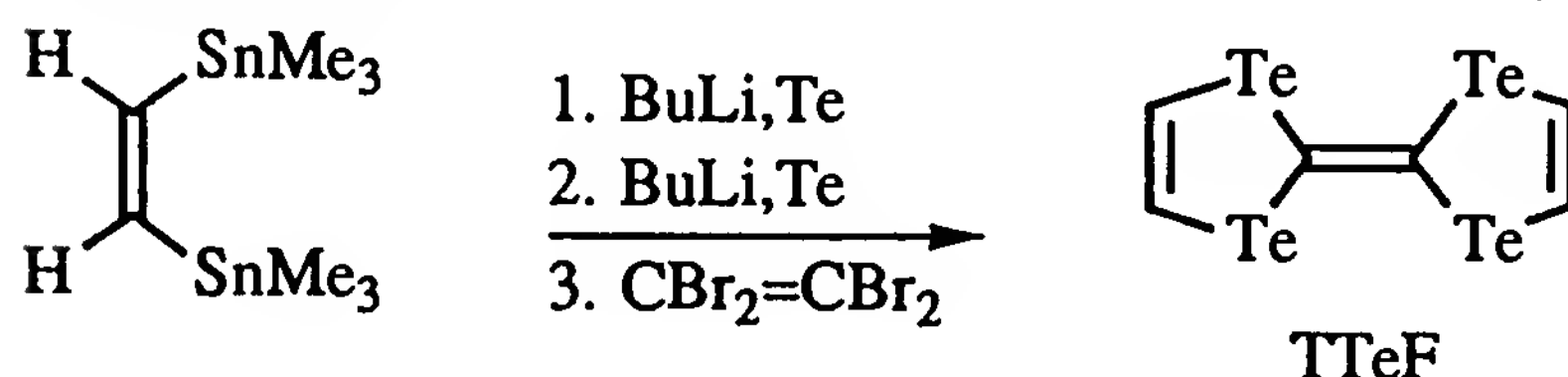
Relatively few tetratellurafulvalenes have been prepared. The first substituted tetratellurafulvalenes were reported by Cowan and Wudl and shared a common synthetic approach, ditellurolate (**37**) displacements on tetrachloroethylene [73–76].



Tetratelluratetracene (**38**) was also reported about the same time [77]. Tetrathiatetracene (**39**) [78], tetraselenatetracene (**40**) [79], and other tetra-chalcogenapolyacenes are also known [4,8].

**38**X=S, Se (**39,40**)

Cowan published the first synthesis of tetratellurafulvalene (TTeF) in 1987, utilizing a multistep, one-flask approach [80,81]. Improvement of

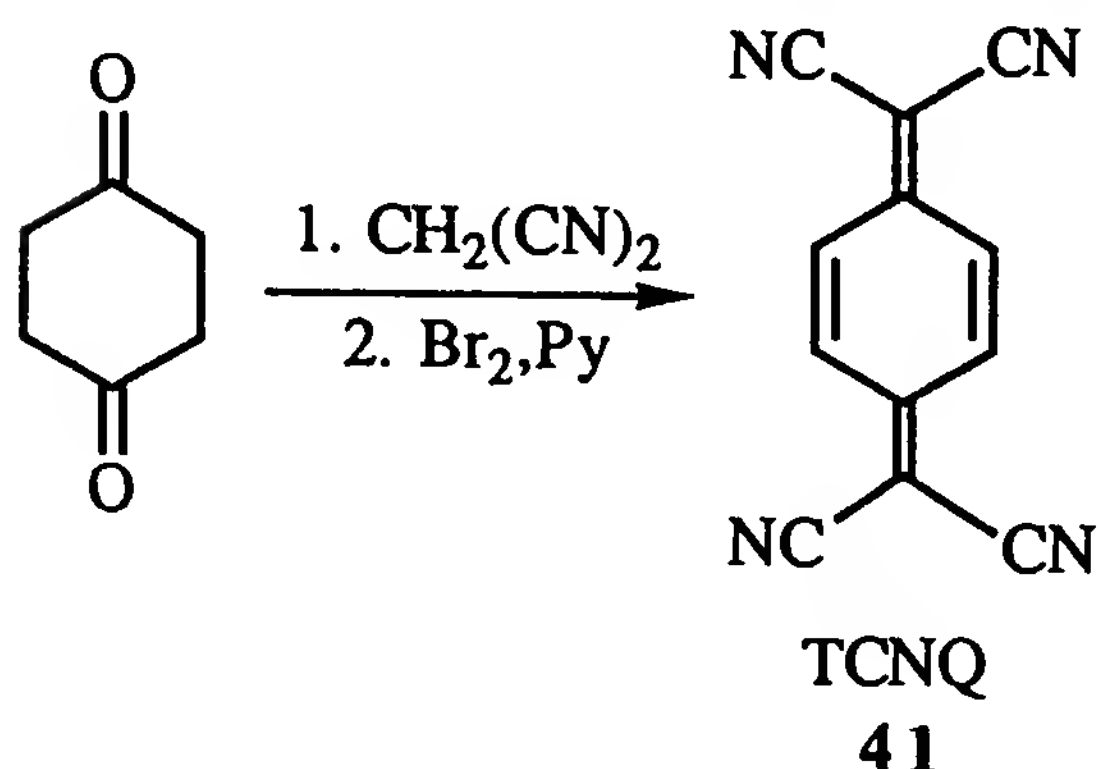


this difficult synthesis and its modification for use in the preparation of TTeF derivatives continues in the Cowan group.

B. Electron Acceptors

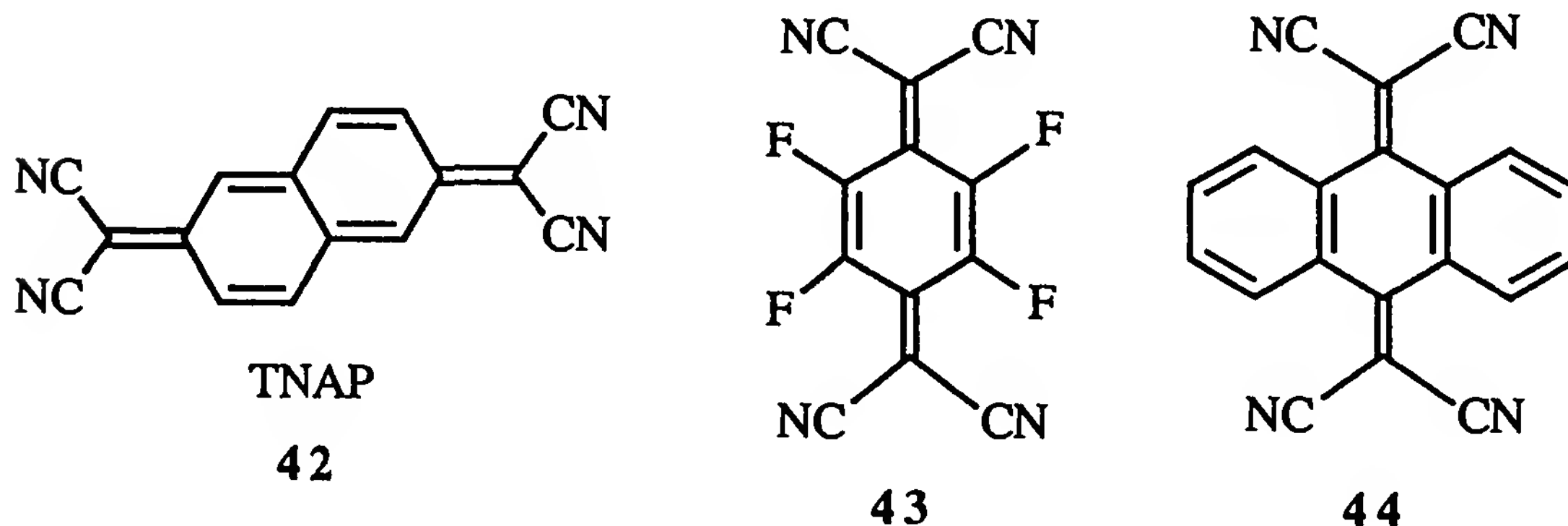
1. Salts Derived from 7,7,8,8-Tetracyano-*p*-quinodimethane (TCNQ, **41**)

Although the 1960s and 1970s were the most active decades of TCNQ research [82], there is still considerable interest in the magnetic and electrical properties of TCNQ salts. TCNQ was synthesized in 1962 as shown below [83]. Research in conductive organic solids developed rapidly with



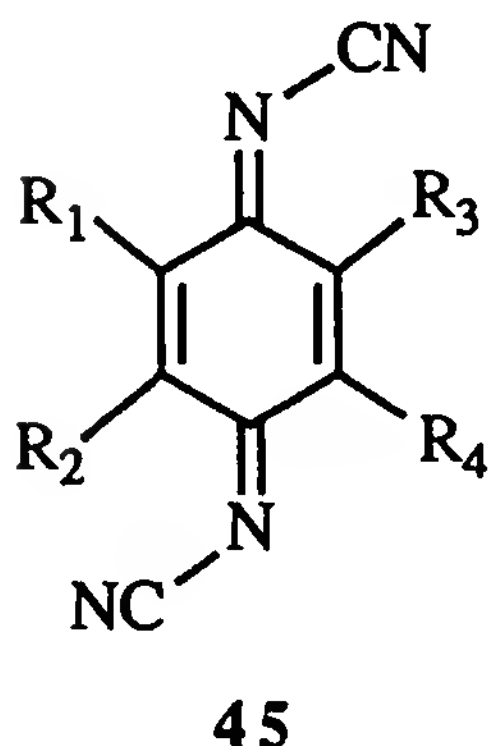
the report that many TCNQ salts possessed low resistivities [84]. The observation of metallic conductivity in TTF-TCNQ ushered in the area of

organic metals [85,86]. TCNQ, several of its derivatives, and related polycyano compounds are commercially available [e.g., 11,11,12,12-tetracyanonaphtho-2,6-quinodimethane (TNAP, **42**) and tetrafluorotetracyanoquinodimethane, **43**]. Tetrasubstituted tetracyanoquinodimethanes with large substituents are nonplanar (e.g., **44**) [87].

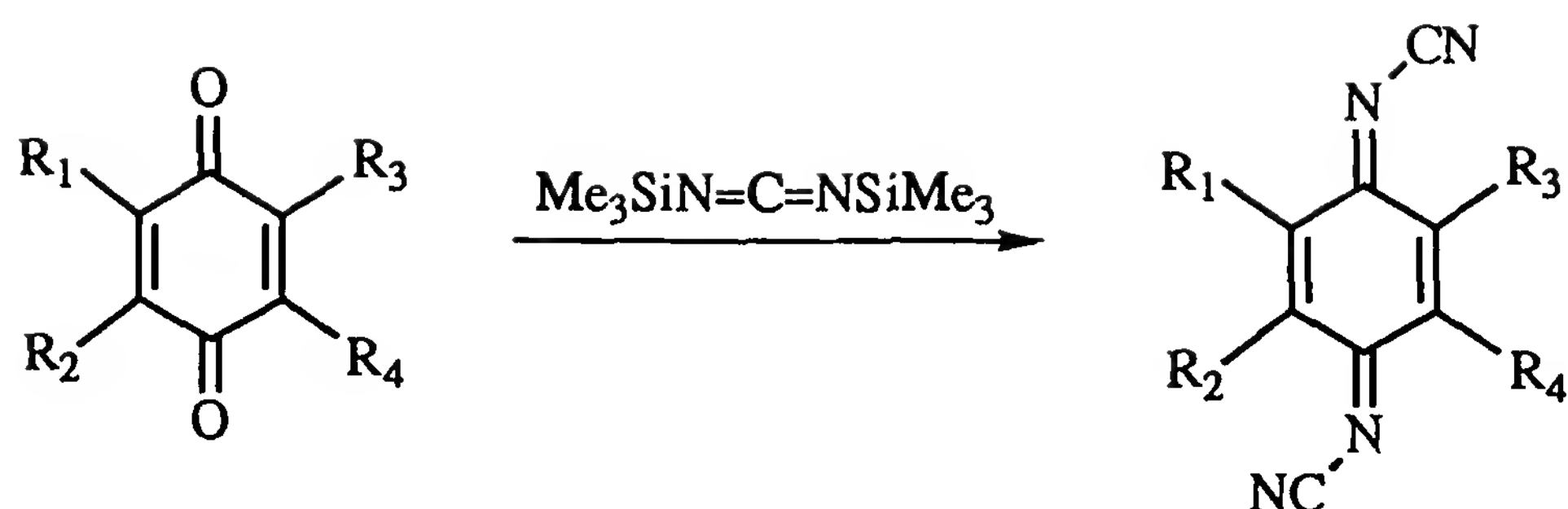


2. *N,N'*-Dicyanoquinonediimine (DCNQI) Acceptors

The chemistry and physics DCNQI acceptors (**45**) were pioneered by Hünig. DCNQI salts represent an extremely interesting class of molecular con-

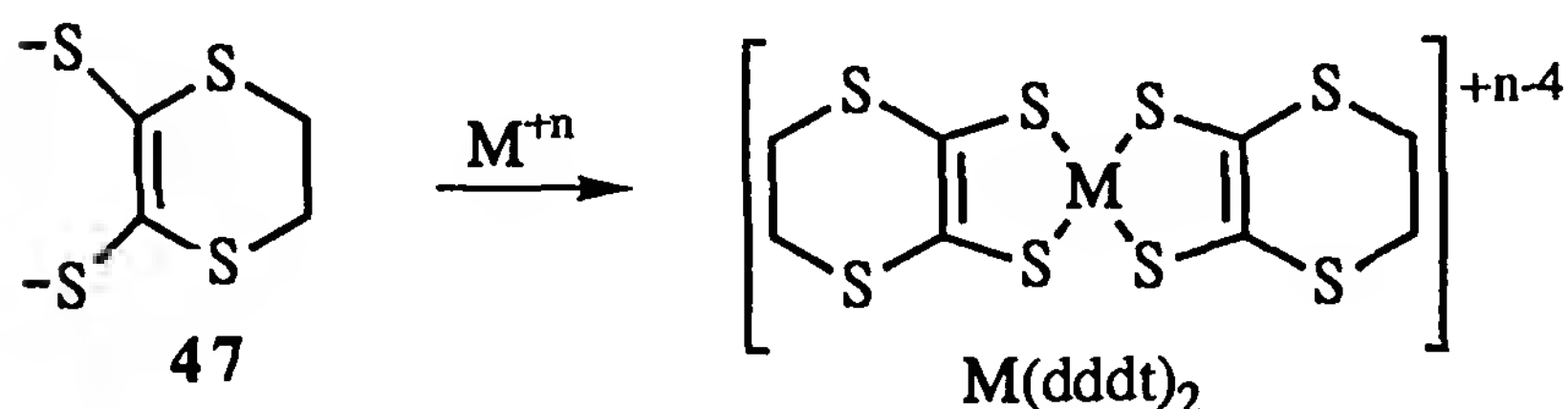
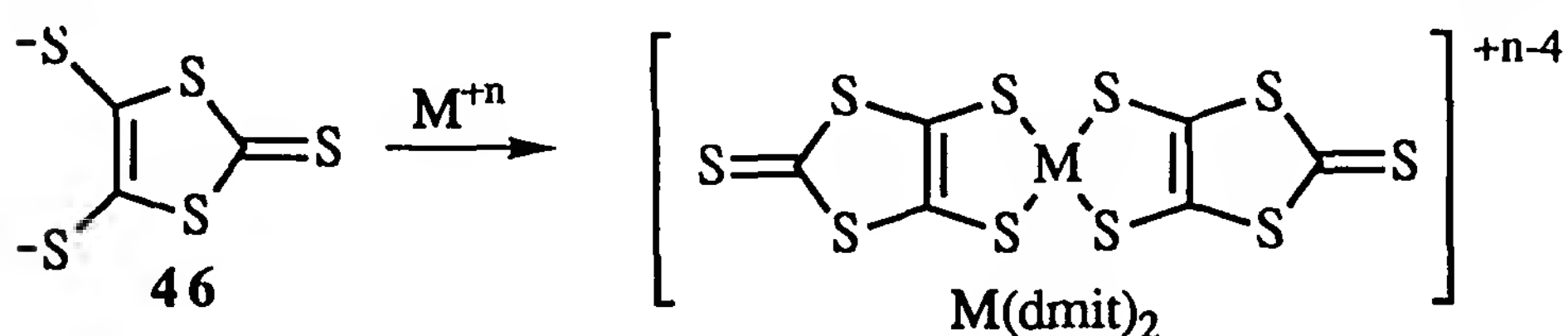


ductors because of their unusually high electrical conductivities [88]. Hünig and his co-workers have synthesized numerous mixed valence salts possessing the general formula $M(R_1R_2R_3R_4 \text{ DCNQI})_2$, where $M = \text{Cu, Ag, Tl, Li, Na, K, and Rb}$, and R_1, R_2, R_3 , and R_4 represent various substituents [88]. The cyanoimine groups on the DCNQI acceptors are smaller than the $=C(CN)_2$ units on TCNQ, permitting up to four substituents to be attached to the DCNQI nucleus without forcing the system out of planarity [87]. The copper salt of 2,5-dimethyl DCNQI [$\text{Cu}(2,5\text{-DMDCNQI})_2$] has a room-temperature conductivity of $\sigma = 10^3 \text{ S/cm}$. This value steadily increases to $\sigma = 5 \times 10^5 \text{ S/cm}$ at 3.5 K [89]. Although DCNQI has produced some of the best organic metals to the present, none of its salts exhibit superconductivity. DCNQI derivatives can be synthesized in a straightforward manner from substituted 1,4-benzoquinones [90].



3. Bis-Dithiolene-Transition Metal Conductors

4,5-Dimercapto-1,3-dithiole-2-thione (dmit, **46**) and 4,5-dihydro-1,4-dithiin-2,3-dithiolate (dddt, **47**) ligands can be reacted with transition metal ions to give $\text{M}(\text{dmit})_2$ and $\text{M}(\text{dddt})_2$ complexes ($\text{M} = \text{Pt}, \text{Pd}, \text{Ni}, \text{and Au}$) [91]. The $\text{M}(\text{dmit})_2$ and $\text{M}(\text{dddt})_2$ anions, like BEDT-TTF, have numerous peripheral sulfur atoms and are planar. Additionally, they have variable redox potentials that can be adjusted through the metal that is selected.



In combination with tetraalkylammonium salts and TTF^+ , $\text{M}(\text{dmit})_2$ and $\text{M}(\text{dddt})_2$ form conducting salts with various stoichiometries. Several dmit salts are superconducting under pressure (T_c values ~ 1.5 to 5.0 K at 7 to 22 kbar) [10].

4. Buckminsterfullerene (C_{60})

The synthesis of C_{60} in macroscopic quantities by Krätschmer and Huffman in 1990 [92] produced a flurry of research activity that is rarely seen in chemistry and physics. Studies were initiated in a multitude of areas. Certainly, the most significant as far as this chapter is concerned was the discovery of superconductivity in K_3C_{60} ($T_c = 18$ K) [93] and other alkali metal fullerenes [9].

In the Krätschmer and Huffman procedure, C_{60} is produced by the resistive heating of graphite at high temperatures in an inert atmosphere [92]. If the soot that is obtained is extracted with toluene, a mixture of compounds is obtained that consists of C_{60} , C_{70} , and smaller amounts of higher

C_n materials [94]. Good procedures have been developed for isolating the C_{60} , the simplest being continuous extraction of the C_n mixture with hexane [95]. Special reactors have been designed for the laboratory preparation of C_{60} -rich soot [e.g., Refs. 92 and 96]. A number of companies now market soot and pure C_{60} , however, and the prices are quite reasonable.

III. SYNTHESIS OF CONDUCTING SALTS AND CRYSTAL GROWTH

Organic conductor precursors are generally closed-shell and neutral. The redox reactions that produce conducting salts can be performed by (1) mixing oxidants and reductants directly (chemical redox methods) or (2) by carrying out the oxidations and reductions electrochemically (electrocrystallization).

A. Chemical Redox Methods

1. General Considerations

Detailed studies of organic conductors demand high-quality crystals. Crystallization and recrystallization, if carefully controlled, are purifying processes [97,98]. Even so, it is prudent to exercise considerable care in performing any crystal growth procedure. The purity of the starting materials is obviously important, although there has been debate over how meticulous one should be in purifying conducting solid precursors [99]. Solvents should be purified according to standard procedures immediately prior to use. Although it is not always necessary, it is common to conduct crystal growth in an inert atmosphere (dry, oxygen-free nitrogen or argon) and in the absence of light. Vibrations enhance the rate of crystal growth and should be minimized. Some authors have worried about ferromagnetic contaminants being leached from glass equipment and have coated the glass with Teflon [100].

2. Combined Synthesis and Crystal Growth

(a) *Solution Reaction Procedures*

The simplest method of forming charge-transfer salts consists of mixing a donor and an acceptor in a hot solvent and letting the system cool slowly [100–102]. Chemical reaction takes place, and crystallization follows.

A slightly more complicated variation on this method utilizes an H-shaped glass reaction vessel [100,103,104]. The donor is placed in the bottom of one of the vertical compartments and the acceptor in the other. Solvent is added. The donor and acceptor slowly diffuse together, react, and form crystalline product. The success of the method relies on the fact

that all of the processes take place in a slow, controlled manner. A simple modification consists of separating the two halves of the cell with a fitted glass disk (medium, fine, or ultrafine) to slow diffusion.

Alternatively, a linear three-compartment apparatus can be constructed where the three compartments are separated by two fitted disks. The donor and the acceptor are placed in the outer two compartments, and diffusion occurs into the center cell where reaction and crystallization takes place. TTF–TCNQ crystals grow well in this type of apparatus (acetonitrile, 30°C) [103,104].

(b) Vapor-Phase Diffusion

Conducting solids can be grown by diffusion of one or more of the reacting components through the vapor phase [100,105,106]. A classic example is the reaction between iodine vapor and BEDT-TTF. A complex mixture of redox products is obtained [107–110]. Superconducting films of alkali metal C_{60} compounds (M_3C_{60}) were first prepared at AT&T Bell Laboratories employing the vapor diffusion method [111]. The high-vacuum glass apparatus that was employed for the initial experiments is shown in Fig. 3. C_{60} films were deposited on a square glass substrate that had four evaporated silver pads for conductivity measurements. An alkali metal was placed in the bottom of the apparatus in a dry box and the system evacuated to about 10^{-5} torr. The initial conductivity of the C_{60} film was $<10^{-5}$ S/cm. The bottom of the tube was placed in a heating bath to promote diffusion of the alkali metal. As diffusion and reaction with the C_{60} took place, the conductivity increased, reached a maximum, and then decreased. The maximum varied with each metal ($M = \text{Li, Na, K, Rb, and Cs}$). In the case of potassium, the maximum conductivity occurred at 500 S cm^{-1} . Subsequent experiments showed that a stoichiometric compound, K_3C_{60} , was formed at the point of maximum conductivity, and it was superconducting ($T_c \sim 18 \text{ K}$) [112]. A more sophisticated, high-vacuum apparatus was employed in subsequent experiments because of the extreme air sensitivity of the alkali metal– C_{60} films [9]. Other routes now exist for the synthesis of the superconducting C_{60} salts. K_3C_{60} can be prepared simply by mixing potassium metal and C_{60} in toluene [113,114].

A clever improvement on the original vapor-phase method was reported by Zetl and co-workers [115], who treated sizable single crystals of C_{60} with potassium vapor to form K_3C_{60} . Superconducting resistive transitions were obtained with the doped crystals that were sharper ($<200 \text{ mK}$) and higher ($T_c = 19.8 \text{ K}$) than the original K_3C_{60} films. The doped crystals have been referred to as “single crystals,” although single-crystal diffraction data supporting this assumption have not been provided.

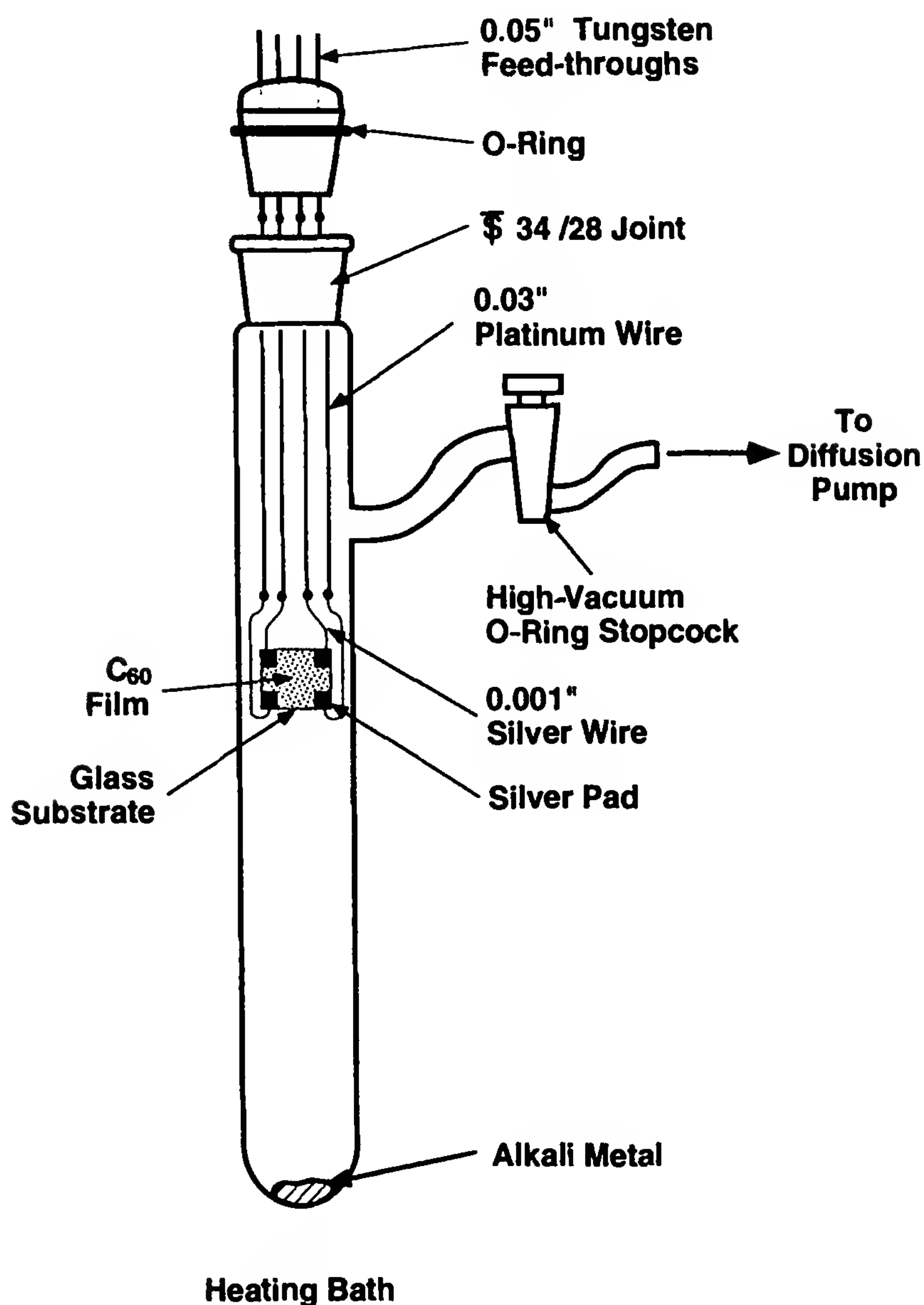


Figure 3 Apparatus for the vapor-phase doping of C_{60} films. (From Ref. 111.)

(c) *Growth from a Viscous Medium*

This is essentially a modification of the solution diffusion technique. Diffusion is slowed by conducting the reaction of the donor and the acceptor in an organic solvent that contains a polymer to increase the viscosity of the solution [100,116].

3. Recrystallization of Preformed Conducting Salts

Conducting solids can be synthesized, isolated, and recrystallized like any other solid. The quality of crystals obtained in this fashion is usually not as high as that of crystals prepared by the methods outlined above. The

procedures in Section II.A.2 probably form crystals at slower rates. The recrystallization techniques that are employed are fairly standard: slow cooling, evaporation, and two-solvent precipitation [100]. In the last method, the conducting solid is dissolved in a solvent and placed in a closed system that contains a second solvent in which the solid is less soluble. Over a period of time, the second solvent diffuses into the container containing the conducting solid and induces a slow precipitation of the solid. Under favorable circumstances good crystals are formed.

B. Electrocrystallization

The electrocrystallization technique has provided the most general method for the synthesis of high-quality organic molecular conductors and has given rise to the majority of organic superconductors. In an electrocrystallization experiment, a donor or an acceptor is oxidized or reduced electrochemically to form radical cations or radical anions. Crystal formation takes place at the working electrode when the radical cations/anions combine with suitable counterions that are furnished by the supporting electrolyte.

Several different types of electrochemical cells have been proposed to carry out electrocrystallization. One of the most popular designs is shown in Fig. 4. The basic component is an H-shaped glass cell that has an ultrafine fritted glass disk separating the two halves of the cell. Although larger cells can be used, one that holds about 15 mL of solution is convenient for most studies. Electrodes are connected to the H cell by way of standard taper joints. The electrode assemblies have inlet tubes for providing an inert atmosphere (dry nitrogen or argon). Platinum (0.5 to 2 mm in diameter by ~ 30 mm) is commonly employed as an electrode material. Other inert metals appear to work as well [29]. The use of Nafion polymer films [118] and graphite electrodes [29,119] have been explored briefly. The α and β forms of (BEDT-TTF)₂I₃ can be grown selectively on graphite electrodes, depending on how the electrodes are treated prior to electrocrystallization [119]. After each experiment the H-cell should be washed briefly in aqua regia, rinsed with distilled water and methanol, and stored in a drying oven. Prolonged contact of the cell with aqua regia causes deterioration of the fritted disk. Other experimental setups for electrocrystallization include a commercial voltammetric cell [120] and a concentric tube system [121].

All of the general precautions that hold for chemical crystal growth methods (Section III.A.1) must be observed in electrocrystallization experiments also (purity of starting materials and solvent; light- and vibration-free environment). If a radical-cation salt is to be prepared, 5 mL of donor solution (1 to 5 mM) is placed in the half-cell that contains the anode.

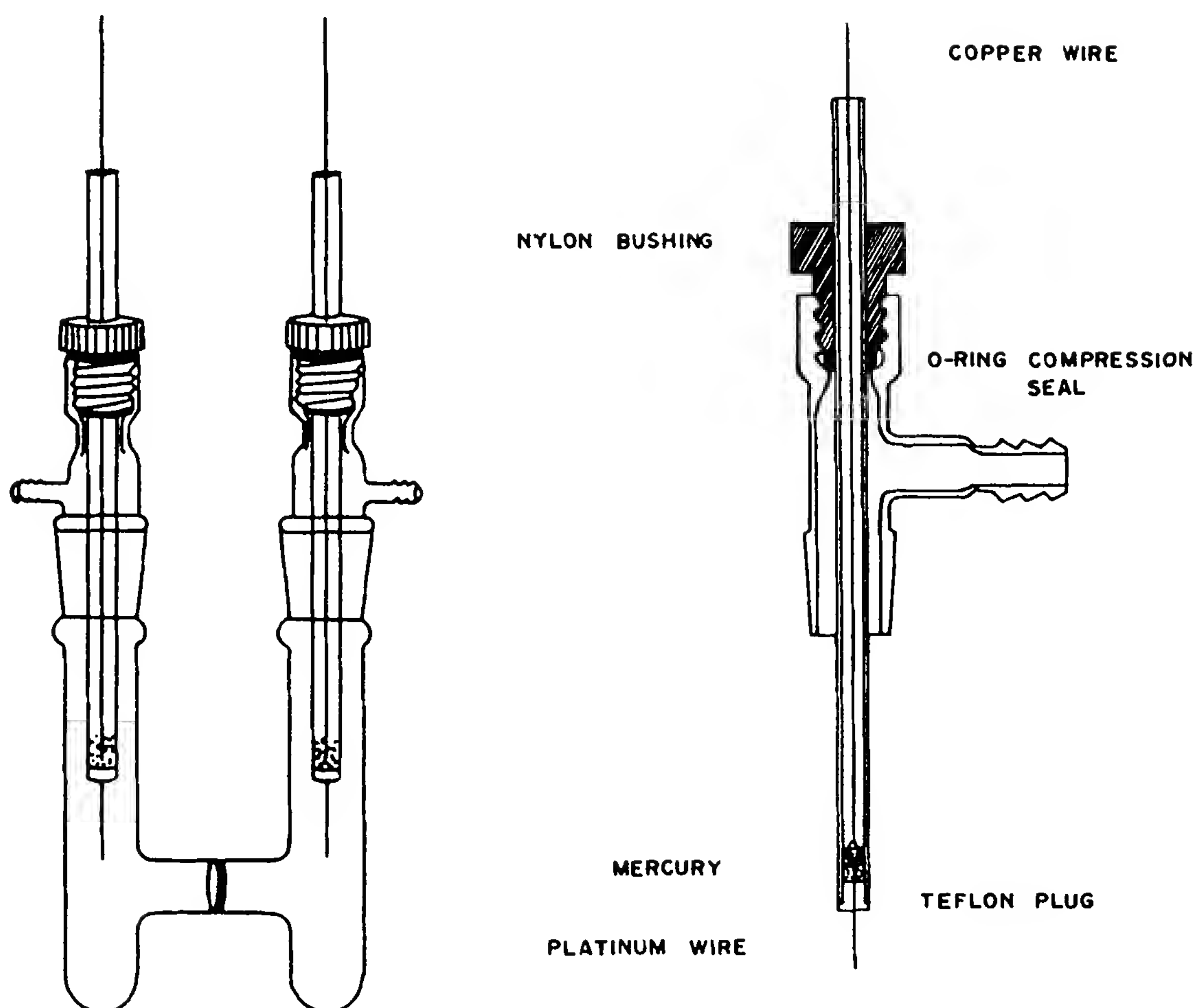


Figure 4 Electrocrystallization cell and electrode insert. (From Ref. 117.)

Because typical donors possess fairly high molecular weights, the choice of solvents is somewhat limited. Hydrocarbon solvents do not give good crystals [121]. Most donors are very sparingly soluble in the best non-aqueous electrochemical solvents. Moreover, the conducting salts produced on electrocrystallization are highly soluble in polar nonhydroxylic solvents. Accordingly, moderately polar organic solvents are generally employed [tetrahydrofuran (THF), TCE, methylene chloride, chlorobenzene, benzonitrile]. Next, 10 mL of a supporting electrolyte solution (tetraalkylammonium or tetraphenylphosphonium salt) is divided between the two chambers so as to make the total solution volumes equal. The electrolyte facilitates electrical conduction and supplies the organic conductor counter ion. The electrolyte concentration is maintained at 5 to 10 times the donor concentration, depending on its solubility and availability. In general, the higher the concentration, the better. The ability to vary the nature of counter ion is one of a number of strengths of the electrocrystallization method. Over 150 BEDT-TTF salts have been prepared by electrocryst-

tallization. Such versatility is rarely encountered in a synthetic method. The synthesis of supporting electrolytes has been summarized [6].

Preparation of the electrodes prior to electrocrystallization is crucial. A reliable method has been described [122]. The electrodes are immersed in 1 M H₂SO₄ solution. The working electrode is connected to the negative pole of a 3-V battery; the remaining electrode is attached to the positive pole. Electrolysis ensues and is continued for 4 min. The polarity is reversed for 4 min, then returned to the original configuration for 8 min. The electrodes are washed in water, absolute methanol, and dried with a heat gun.

Electrocrystallization can be conducted under conditions of constant current or constant voltage. The former is more common. In a constant-current experiment, the initial current density should be low and increased as required. For BEDT-TTF salts, a starting current density of about 0.1 $\mu\text{A}/\text{cm}^2$ is reasonable. Optimum current densities are usually in the range 0.1 to 0.5 $\mu\text{A}/\text{cm}^2$. For TMTSF the current densities must be somewhat larger (0.8 to 2.0 $\mu\text{A}/\text{cm}^2$). The influence of the current density (voltage) on the size, quality, phases, and stoichiometry of the crystals that are obtained has been discussed [8,121,123,124]. Early in the electrocrystallization experiment the voltage varies erratically (constant-current mode). After a period of several hours, it stabilizes. The crystals are harvested (few days to several weeks) when the voltage starts to increase or decrease sharply from the constant state or significant color change takes place. Unfortunately, there have been few systematic studies of the details of crystal growth by electrocrystallization. This situation appears to be changing, however [123,125–129].

REFERENCES

1. M. Narita and C. U. Pittman, Jr., *Synthesis*, 489 (1976).
2. M. R. Bryce, *Aldrichim Acta* 18:73 (1985).
3. A. Krief, *Tetrahedron* 42:1209 (1986).
4. D. Cowan and A. Kini, in *The Chemistry of Organic Selenium and Tellurium Compounds*, Vol. 2 (S. Patai, ed.), Wiley, Chichester, West Sussex, England, 1987, p. 463.
5. G. Schukat, A. M. Richter, and E. Fanghänel, *Sulfur Rep.* 7:155 (1987).
6. J. M. Williams, H. H. Wang, T. J. Emge, U. Geiser, M. A. Beno, P. C. W. Leung, K. D. Carlson, R. J. Thorn, A. J. Schultz, and M.-H. Whangbo, *Prog. Inorg. Chem.* 35:51 (1987).
7. M. R. Bryce, *Chem. Soc. Rev.* 20:355 (1991).
8. J. M. Williams, J. R. Ferraro, R. J. Thorn, K. D. Carlson, U. Geiser, H. H. Wang, A. M. Kini, and M.-H. Whangbo, *Organic Superconductors (Including Fullerenes)*, Prentice Hall, Englewood Cliffs, N.J., 1992, Chapter 2.

9. R. C. Haddon, *Acc. Chem. Res.* 25:127 (1992).
10. Reference 8, Chapter 1.
11. G. Kiesslich, Dissertation, Universität Würzburg, 1968.
12. D. L. Coffen and P. E. Garrett, *Tetrahedron Lett.*, 2043 (1969).
13. F. Wudl, G. M. Smith, and E. J. Hufnagel, *J. Chem. Soc. Chem. Commun.*, 1453 (1970).
14. D. L. Coffen, J. Q. Chambers, D. R. Williams, P. E. Garrett, and N. D. Canfield, *J. Am. Chem. Soc.* 93:2258 (1971).
15. W. F. Cooper, N. C. Kenny, J. W. Edmonds, A. Nagel, F. Wudl, and P. Coppens, *J. Chem. Soc. Chem. Commun.*, 889 (1971).
16. R. Zahradník, P. Cársky, S. Hünig, G. Kiesslich, and D. Scheutzow, *Int. J. Sulfur Chem. C* 6:109 (1971).
17. F. Wudl, D. Wobschall, and E. J. Hufnagel, *J. Am. Chem. Soc.* 94:671 (1972).
18. S. Hünig, G. Kiesslich, H. Quast, and D. Scheutzov, *Liebigs Ann. Chem.*, 310 (1973).
19. L. R. Melby, H. D. Hartzler, and W. A. Sheppard, *J. Org. Chem.* 39:2456 (1974).
20. M. Mizuno, A. F. Garito, and M. P. Cava, *J. Chem. Soc. Chem. Commun.*, 18 (1978).
21. K. Hartke, T. Kissel, J. Quante, and R. Matusch, *Chem. Ber.* 113:1898 (1980).
22. S. Wawzonek and S. M. Heilmann, *J. Org. Chem.* 39:511 (1974).
23. G. Steimecke, H. Sieler, R. Kirmse, and E. Hoyer, *Phosphorus Sulfur* 7:49 (1979).
24. H. Poleschner, W. John, G. Kempe, E. Hoyer, and E. Fanghänel, *Z. Chem.* 18:345 (1978).
25. P. E. Reed, J. M. Braam, L. M. Sowa, R. A. Barkau, G. S. Blackman, D. D. Cox, G. A. Ball, H. H. Wang, and J. M. Williams, *Inorg. Synth.* 26:386 (1980).
26. T. Suzuki, H. Yamochi, G. Srdanov, K. Hinkelmann, and F. Wudl, *J. Am. Chem. Soc.* 111:3108 (1989).
27. R. R. Schumaker and E. M. Engler, *J. Am. Chem. Soc.* 99:5521 (1977).
28. R. R. Schumaker, V. Y. Lee, and E. M. Engler, *J. Org. Chem.* 49:564 (1984).
29. E. M. Engler, V. Y. Lee, R. R. Schumaker, S. S. P. Parkin, R. L. Greene, and J. C. Scott, *Mol. Cryst. Liq. Cryst.* 107:19 (1984).
30. E. Fanghänel, A. M. Richter, and G. Schukat, *J. Prakt. Chem.* 326:479 (1984).
31. J. Le Costumer and Y. Mollier, *J. Chem. Soc. Chem. Commun.*, 38 (1980).
32. M. Sallé, A. Gorgues, J.-M. Fabre, K. Bechgaard, M. Jubault, and F. Texier, *J. Chem. Soc. Chem. Commun.*, 1520 (1989).
33. A. Gorgues, P. Batail, and A. Le Coq, *J. Chem. Soc. Chem. Commun.*, 405 (1983).

34. M. G. Miles, J. S. Wager, J. D. Wilson, and A. R. Seidle, *J. Org. Chem.* **40**:2577 (1975).
35. H. Alper and H.-N. Paik, *J. Chem. Soc. Chem. Commun.* **42**:3522 (1977).
36. P. R. Moses and J. Q. Chambers, *J. Am. Chem. Soc.* **96**:945 (1974).
37. A. M. Kini, S. F. Tytko, J. E. Hunt, and J. M. Williams, *Tetrahedron Lett.* **28**:4153 (1987).
38. E. Fanghänel, L. van Hinh, and G. Schukat, *Z. Chem.* **16**:317 (1976).
39. Y. Ueno, A. Nakayama, and M. Okawara, *J. Am. Chem. Soc.* **98**:7440 (1976).
40. W. Chen, M. P. Cava, M. A. Takassi, and R. M. Metzger, *J. Am. Chem. Soc.* **110**:7903 (1988).
41. W. R. H. Hurtley and S. Smiles, *J. Chem. Soc.*, 2263 (1926).
42. G. S. Bajwa, K. D. Berlin, and H. A. Pohl, *J. Org. Chem.* **41**:145 (1976).
43. M. Mizuno and M. P. Cava, *J. Org. Chem.* **43**:416 (1978).
44. D. C. Green, *J. Chem. Soc. Chem. Commun.*, 161 (1977).
45. D. C. Green and R. W. Allen, *J. Chem. Soc. Chem. Commun.*, 832 (1978).
46. D. C. Green, *J. Org. Chem.* **44**:1476 (1979).
47. A. S. Dhindsa, M. R. Bryce, J. P. Lloyd, and M. C. Petty, *Synth. Met.* **27**:B563 (1988).
48. E. Aharon-Shalom, J. Y. Becker, J. Bernstein, S. Bittner, and S. Shaik, *Tetrahedron Lett.*, 2783 (1985).
49. N. Okada, H. Yamochi, F. Shinozaki, K. Oshima, and G. Saito, *Chem. Lett.*, 1861 (1986).
50. S.-Y. Hsu and L. Y. Chiang, *J. Org. Chem.* **52**:3444 (1987).
51. V. Y. Lee, *Synth. Met.* **20**:161 (1987).
52. H. Yamochi, N. Iwasawa, H. Urayama, and G. Saito, *Chem. Lett.*, 2265 (1987).
53. A. M. Kini, B. D. Gates, M. A. Beno, and J. M. Williams, *J. Chem. Soc. Chem. Commun.*, 169 (1989).
54. J. M. Fabre, L. Giral, E. Dupart, C. Coulon, J. P. Manceau, and P. Delhaes, *J. Chem. Soc. Chem. Commun.*, 1477 (1983).
55. J. M. Fabre, E. Torreilles, J. P. Gilbert, M. Chanaa, and L. Giral, *Tetrahedron Lett.*, 4033 (1977).
56. J. M. Fabre, L. Giral, E. Dupart, C. Coulon, and P. Delhaes, *J. Chem. Soc. Chem. Commun.*, 426 (1983).
57. J. P. Morand, L. Brzezinski, and C. Manigand, *J. Chem. Soc. Chem. Commun.*, 1050 (1986).
58. C. A. Brown, R. D. Miller, C. M. Lindsay, and K. Smith, *Tetrahedron Lett.*, 991 (1984).
59. N. C. Gonnella and M. P. Cava, *J. Org. Chem.* **43**:369 (1978).
60. H. Tatemitsu, E. Nishikawa, Y. Sakata, and S. Misumi, *J. Chem. Soc. Chem. Commun.*, 106 (1985).
61. L. Giral, J. M. Fabre, and A. Gouasmia, *Tetrahedron Lett.*, 4315 (1986).
62. K. Lerstrup, I. Johannsen, and M. Jørgensen, *Synth. Met.* **27**:B9 (1988).
63. E. M. Engler and V. V. Patel, *J. Am. Chem. Soc.* **96**:7376 (1974).

64. Y. A. Jackson, C. L. White, M. V. Lakshmikantham, and M. P. Cava, *Tetrahedron Lett.*, 5635 (1987).
65. K. Bechgaard, D. O. Cowan, and A. N. Bloch, *J. Chem. Soc. Chem. Commun.*, 937 (1974).
66. A. Moradpour, V. Peyrussan, I. Johansen, and K. Bechgaard, *J. Org. Chem.* 48:388 (1983).
67. V. Y. Lee, E. M. Engler, R. R. Schumaker, and S. S. P. Parkin, *J. Chem. Soc. Chem. Commun.*, 235 (1983).
68. N. Iwasaka, G. Saito, K. Imaeda, T. Mori, and H. Inokuchi, *Chem. Lett.*, 2399 (1987).
69. S. Rajeswari, Y. A. Jackson, and M. P. Cava, *J. Chem. Soc. Chem. Commun.*, 1089 (1988).
70. E. M. Engler and V. V. Patel, *Tetrahedron Lett.*, 1259 (1975).
71. R. Kato, H. Kobayashi, and A. Kobayashi, *Synth. Met.* 42:2093 (1991).
72. K. Kikuchi, T. Namiki, I. Ikemoto, and K. Kobayashi, *J. Chem. Soc. Chem. Commun.*, 1472 (1986).
73. F. Wudl and E. Aharon-Shalom, *J. Am. Chem. Soc.* 104:1154 (1982).
74. K. Lerstrup, D. Talham, A. N. Bloch, T. O. Poehler, and D. O. Cowan, *J. Chem. Soc. Chem. Commun.*, 336 (1982).
75. K. A. Lerstrup and D. O. Cowan, *J. Phys.* 44:C3-1247 (1983).
76. K. Lerstrup, D. O. Cowan, and T. J. Kistenmacher, *J. Am. Chem. Soc.* 106:8303 (1984).
77. D. J. Sandman, J. C. Stark, and B. M. Foxman, *Organometallics* 1:739 (1982).
78. C. Marschalk and C. Stumm, *Bull. Chem. Soc. France*, 418 (1948).
79. K. A. Balodis, A. D. Livdane, R. S. Medne, and O. Y. Neiland, *Z. Org. Chem. (Russ.)* 15:391 (1979).
80. R. D. McCullough, G. B. Kok, K. A. Lerstrup, and D. O. Cowan, *J. Am. Chem. Soc.* 109:4115 (1987).
81. R. D. McCullough, M. D. Mays, A. B. Bailey, and D. O. Cowan, *Synth. Met.* 27:B487 (1988).
82. J. R. Ferraro and J. M. Williams, *Introduction to Synthetic Electrical Conductors*, Academic Press, Orlando, Fla., 1987, Chapter 2.
83. D. S. Acker and W. R. Hertler, *J. Am. Chem. Soc.* 84:3370 (1962).
84. L. R. Melby, R. J. Harder, W. R. Hertler, W. Mahler, R. E. Benson, and W. E. Mochel, *J. Am. Chem. Soc.* 84:3374 (1962).
85. J. Ferraris, D. O. Cowan, V. Walatka, Jr., and J. H. Perlstein, *J. Am. Chem. Soc.* 95:948 (1973).
86. L. B. Coleman, M. J. Cohen, D. J. Sandman, F. G. Yamagishi, A. F. Garrito, and A. J. Heeger, *Solid State Commun.* 12:1125 (1973).
87. U. Schubert, S. Hünig, and A. Aumüller, *Liebigs Ann. Chem.*, 1216 (1985).
88. S. Hünig and P. Erk, *Adv. Mater* 3:225 (1991).
89. A. Aumüller, P. Erk, G. Klebe, S. Hünig, J. V. von Schütz, and H.-P. Werner, *Angew. Chem. Int. Ed. Engl.* 25:740 (1986).
90. A. Aumüller and S. Hünig, *Angew. Chem. Int. Ed. Engl.* 23:447 (1984).

91. Reference 6, pp. 191–202.
92. W. Krätschmer, L. D. Lamb, K. Fostiropoulos, and D. R. Huffman, *Nature* 347:354 (1990).
93. A. F. Hebard, M. J. Rosseinsky, R. C. Haddon, D. W. Murphy, S. H. Glarum, T. T. M. Palstra, A. P. Ramirez, and A. R. Kortan, *Nature* 350:600 (1991).
94. F. Diederich and R. L. Whetten, *Acc. Chem. Res.* 25:119 (1992).
95. K. C. Khemani, M. Prato, and F. Wudl, *J. Org. Chem.* 57:3254 (1992), and pertinent references cited therein.
96. A. S. Koch, K. C. Khemani, and F. Wudl, *J. Org. Chem.* 56:4543 (1991), and pertinent references cited therein.
97. H. E. Buckley, *Crystal Growth*, Chapman & Hall, London, 1951.
98. P. Hartman, *Crystal Growth*, North-Holland, Amsterdam, 1973.
99. J. R. Andersen, E. M. Engler, and K. Bechgaard, in *Synthesis and Properties of Low-Dimensional Materials* (J. S. Miller and A. J. Epstein, eds.), *Ann. N.Y. Acad. Sci.* 313:293 (1978).
100. J. C. Scott, D. F. Garito, and A. J. Heeger, *Phys. Rev. B* 10:3131 (1974).
101. Y. Tomkiewicz, R. A. Craven, T. D. Schultz, E. M. Engler, and A. R. Taranko, *Phys. Rev. B* 15:1011 (1977).
102. E. M. Engler, R. A. Craven, Y. Tomkiewicz, B. A. Scott, K. Bechgaard, and J. R. Andersen, *J. Chem. Soc. Chem. Commun.* 337 (1976).
103. M. L. Kaplan, *J. Cryst. Growth* 33:161 (1976).
104. J. Anzai, *J. Cryst. Growth* 33:185 (1976).
105. T. J. Kistenmacher, T. E. Phillips, J. P. Ferraris, D. O. Cowan, A. N. Bloch, and T. O. Poehler, *Acta Cryst. B* 32:539 (1976).
106. E. Ehrenfreund, S. K. Khanna, A. F. Garito, and A. J. Heeger, *Solid State Commun.* 22:139 (1977).
107. R. P. Shibaeva, V. F. Kaminskii, and É. B. Yagubskii, *Mol. Cryst. Liq. Cryst.* 119:361 (1985).
108. R. P. Shibaeva, R. M. Lobkovskaya, É. B. Yagubskii, and E. E. Kostyuchenko, *Kristallografiya* 31:455 (1986); *Sov. Phys. Crystallogr.* 31:267 (1986).
109. M. A. Beno, U. Geiser, K. L. Kostka, H. H. Wang, K. S. Webb, M. A. Firestone, K. D. Carlson, L. Nuñez, J. M. Williams, and M.-H. Whangbo, *Inorg. Chem.* 26:1912 (1987).
110. R. P. Shibaeva, R. M. Lobkovskaya, É. B. Yagubskii, and E. E. Kostyuchenko, *Kristallografiya* 31:1110 (1986); *Sov. Phys. Crystallogr.* 31:657 (1986).
111. R. C. Haddon, A. F. Hebard, M. J. Rosseinsky, D. W. Murphy, S. J. Duclos, K. B. Lyons, B. Miller, J. M. Rosamilia, R. M. Fleming, A. R. Kortan, S. H. Glarum, A. V. Makhija, A. J. Muller, R. H. Eick, S. M. Zahurak, R. Tycko, G. Dabbagh, and F. A. Thiel, *Nature* 350:320 (1991).
112. A. F. Hebard, M. J. Rosseinsky, R. C. Haddon, D. W. Murphy, S. H. Glarum, T. T. M. Palstra, A. P. Ramirez, and A. R. Kortan, *Nature* 350:600 (1991).

113. H. H. Wang, A. M. Kini, B. M. Savall, K. D. Carlson, J. M. Williams, K. R. Lykke, P. Wurz, D. H. Parker, M. J. Pellin, D. M. Gruen, U. Welp, W.-K. Kwok, S. Fleshler, and G. W. Crabtree, *Inorg. Chem.* **30**:2838 (1991).
114. H. H. Wang, A. M. Kini, B. M. Savall, K. D. Carlson, J. M. Williams, M. W. Lathrop, K. R. Lykke, D. H. Parker, P. Wurz, M. J. Pellin, D. M. Gruen, U. Welp, W.-K. Kwok, S. Fleshler, and G. W. Crabtree, *Inorg. Chem.* **30**:2962 (1991).
115. X.-D. Xiang, J. G. Hou, G. Brinceño, W. A. Vareka, R. Mostovoy, A. Zettl, V. H. Crespi, and M. L. Cohen, *Science* **256**:1190 (1992).
116. C. Berg, K. Bechgaard, J. R. Andersen, and C. S. Jacobsen, *Tetrahedron Lett.*, 1719 (1976).
117. M. M. Lee, J. P. Stokes, F. M. Wiygul, T. J. Kistenmacher, D. O. Cowan, T. O. Poehler, A. N. Bloch, W. W. Fuller, and D. U. Gubser, *Mol. Cryst. Liq. Cryst.* **79**:145 (1982).
118. T. P. Henning, H. S. White, and A. J. Bard, *J. Am. Chem. Soc.* **104**:5862 (1982), and previous papers in series.
119. H. H. Wang, L. K. Montgomery, C. A. Husting, B. A. Vogt, J. M. Williams, S. M. Budz, M. J. Lowry, K. D. Carlson, W.-K. Kwok, and V. Mikheyev, *Chem. Mater.* **1**:484 (1989).
120. E. M. Engler, R. Greene, P. Halen, Y. Tomkiewicz, K. Mortensen, and J. Berendzen, *Mol. Cryst. Liq. Cryst.* **79**:15 (1982).
121. H. Anzai, M. Tokumoto, and G. Saito, *Mol. Cryst. Liq. Cryst.* **125**:385 (1985).
122. T. J. Emge, H. H. Wang, M. A. Beno, J. M. Williams, M.-H. Whangbo, and M. Evain, *J. Am. Chem. Soc.* **108**:8215 (1986).
123. M. D. Ward, *J. Electroanal. Chem.* **273**:79 (1989).
124. S. Sakura, H. Imai, H. Anzai, and T. Moriya, *Bull. Chem. Soc. Jpn.* **61**:3181 (1988).
125. M. D. Ward, in *Electroanalytical Chemistry*, Vol. 16 (A. J. Bard, ed.), Marcel Dekker, New York, 1989, p. 181.
126. S. L. Li, H. S. White, and M. D. Ward, *J. Phys. Chem.* **96**:9014 (1992).
127. S. L. Li, H. S. White, and M. D. Ward, *Chem. Mater.* **4**:1082 (1992).
128. C. Faulmann, P. Cassoux, E. B. Yagubskii, and L. V. Vetoshkina, *New J. Chem.* **17**:385 (1993).
129. J.-B. Tommassino, B. Pomarede, D. Medus, D. de Montauzon, and P. Cassoux, *Mol. Cryst. Liq. Cryst.* **237**:445 (1993).

This Page Intentionally Left Blank

5

Organic Conductors: The Crystallographic Approach

Alain Filhol

Institut Laue Langevin, Grenoble, France

I. WHY USE CRYSTALLOGRAPHY?

Structural crystallographic techniques are essential in the study of organic conductors. Indeed, confronted with materials exhibiting a new type of behavior, one of the first questions is, or should be: What is the molecular structure? In other words, in the case of organic conductors, a good knowledge of the medium in which the carriers move and interact is essential to an understanding of their electrical properties, especially because of their low dimensionality and of a crystal packing that is far more intricate than that of inorganic conductors and superconductors. Thus crystallography provides some essential basic data at the atomic level, necessary to interpret the results of physical measurements and to build theories of transport properties.

Of course, the first task of crystallographers was the determination of the room-temperature crystal structure of new compounds for the design of better conductors. The earliest explanations of the gross features of electrical conductivity were based mostly on these room-temperature structural data. Very soon after, crystallographers had to deal with the problem of low temperature and high pressure because organic conductors exhibit electronic behavior under constraints that cannot be fully explained without the knowledge of the corresponding lattice changes or distortions. A new aspect of the problem is thus the detection of all kinds of phase transitions,

lattice distortions, and pretransitional fluctuations, some of which are distinctive to the materials of interest here. This has been done by means of distinctive techniques. The interpretation of results of the latter have reached a high level of sophistication to get as much information as possible on the foregoing lattice modifications, because several years passed before full structure determination could be performed at very low temperature, at high pressure, and on weakly distorted lattices.

Neither the relation between transport properties and structures of different compounds nor the relation between temperature and pressure dependence and structure change of a given material are obvious. In the latter case temperature and/or pressure modifies the sample structure either smoothly (no phase transition) or more abruptly (phase transition), but both changes are of importance to explain physical properties. Since organic conductors are built from complicated organic molecules with many internal degrees of freedom, their behavior is not easy to model. Structures were first discussed mainly on the basis of a few characteristic intra- and intermolecular distances, but the approach is now more global and tries to account for the competing bonding and antibonding character of molecular interactions. We can summarize the crystallographic problem as follows:

1. *Phase transitions.* Low-dimensional conductors undergo several types of specific structural phase transitions, such as the Peierls distortion (electron–phonon coupling), the spin-Peierls distortion (spin–phonon coupling), anion-ordering transitions, and so on. These first have to be detected and then measured and understood. However, the foregoing distortions may be very small and difficult to observe, and up to now, only a few lattice distortions have been fully measured and described.

2. *No phase transition.* Typically, thermal expansion and compressibility of organic conductors are large and anisotropic. Even in the absence of a phase transition, they are responsible for many changes (intra- and interstack distances; molecular overlap changes; molecular reorientation, bending, twisting, etc.) intermixed in an unpredictable manner. The observed behavior of the material is the result of the sum of small changes in atom-to-atom distances which modify the transfer integrals. Thus crystallography may provide sets of accurate atom coordinates necessary for, for example, the computation of the shape of the Fermi surface or may even try to give a direct observation of the shape of the electron cloud and thus of the interactions within the material.

II. WHICH KIND OF CRYSTALLOGRAPHY?

The crystallographic study of organic conductors has involved a number of techniques. Three main types of radiation—x-rays, neutrons, elec-

trons—have been largely used together with different kinds of sample environments: low temperature, high pressure, magnetic field. A few powder diffraction studies have been performed (thermal expansion, compressibility) with limited success because the large cell dimensions and low symmetry give very dense diffraction patterns. Thus most crystallographic work was performed on single-crystal samples.

The crystallography of organic low-dimensional conductors is, in many ways, similar to that of other organic materials, but nevertheless has some specific aspects:

1. *Molecular packing.* The “low dimensionality” of organic conductors is associated with a specific stacking of large flat molecules. Understanding their electronic properties through the crystal packing is not trivial. The description of the latter (molecular overlap and interchain coupling) was first made in terms of simple distances and angles. Subsequent attempts have been made to estimate, more or less accurately, transfer integrals, and ultimately, the latter together with Fermi surfaces have been computed from the structural data. The quantum approach leads to results that sometimes contradict the geometrical approach. For example, “good” stacking (geometrically speaking) may correspond to small axial transfer integrals and strong transverse ones.

2. *Commensurability.* Incommensurate lattice distortions and commensurate–incommensurate phase transitions are often observed in these materials. The incommensurability comes either from an incommensurate Fermi wave vector ($2k_F$, $4k_F$ scattering in charge-transfer salts) or from the counterion stacks (e.g., triiodide-containing materials).

3. *Disorder.* This is important since electronic properties of organic conductors are very sensitive to disorder (e.g., it may prevent a long-range coherence of charge density waves or strongly influence the superconductivity transition). *Intrinsic* disorder is often present (compositional; positional either static or dynamic). It is responsible for diffuse layers and order–disorder phase transitions, for example, and has been responsible for reporting of some “mean” (or even inaccurate) structure determinations. *Extrinsic* disorder (irradiation effect) can also make some crystallographic studies difficult.

4. *Atomic and molecular displacement under constraint.* Thermal expansion and compressibility are large and anisotropic. Sometimes structural data have been extrapolated from the room temperature (RT) down to low temperature (LT) simply by considering changes in lattice dimensions. This has led to disappointing results since, even in the absence of a phase transition, molecular shapes and orientations may change substantially. Similarly, if we find an isostatic pressure at room temperature whose effect is equivalent to a given temperature decrease at ambient pressure for, say, the chain contraction, the equivalence will not usually match for, say, the

transverse transfer integrals. This is one of the justifications for full structural studies under constraints.

5. *Structural transitions.* Very low-temperature and/or high-pressure crystallographic studies of organic materials were very rare until they became really necessary for the study of organic conductors. Indeed, quasi-one-dimensional conductors exhibit a set of original lattice distortions driven or influenced by the instability of the low-dimensional electron gas. An impressive amount of crystallographic work has been devoted to a study of the corresponding lattice fluctuations and distortions, mainly by means of diffuse scattering techniques but also by means of the structure determination of the distorted phase. Organic conductors with a higher dimensionality generally undergo more classical structural transitions.

III. STRUCTURAL CRYSTALLOGRAPHY

Determining the structure of a crystalline material remains an important step toward an understanding of that material's properties. Indeed, the crystal structure provides the nature, the position, the population factor, and the thermal motion parameters of each atom in the asymmetric unit of the lattice cell. Thus, instead of giving a direct atomic-scale “view” of the material, crystallography gives an accurate N -parameter “model” structure which can be used for quantitative comparisons or theoretical calculations (see Section VIII). Nowadays, some microscopy techniques do reach atomic resolution, but this is either on materials other than low-dimensional conductors or to a much lower resolution than crystallography allows (see Section XII.D). We cannot give a course on crystallography here, but we can recall some basic ideas before discussing the various techniques and their specific applications to the study of low-dimensional conductors.

A. Fundamentals

In the following we give only the main lines of the structure determination process, without trying to be complete, and assume that the reader is familiar with basic crystallography. More details can be found in a number of monographs, but, among others, the paper of Hirshfeld [1] is a good primer.

In a typical structure determination experiment, a sample—powder or single crystal—is placed in a radiation beam—usually x-rays or neutrons—the wavelength of which is in the order of the interatomic distances to be observed in the sample. The incident beam is diffracted by the sample if the Bragg law is satisfied:

$$n\lambda = 2d_{hkl} \sin \theta_{hkl}$$

where λ is the wavelength, n the harmonic order, d_{hkl} the distance between the crystal lattice planes hkl , and $2\theta_{hkl}$ the corresponding diffraction angle (Bragg angle). n is usually incorporated in the indices hkl as a multiplying factor. Each lattice plane family hkl has a different structure factor F_{hkl} (i.e., a different diffraction power), which is given by the expression

$$F_{\mathbf{H}} = \sum_{j=1,m} f_j \exp[2\pi i(\mathbf{H} \cdot \mathbf{r}_j)] \exp\left(-B_j \sin^2 \frac{\theta}{\lambda^2}\right) \quad (1)$$

where $\mathbf{H} = h\mathbf{a}^* + k\mathbf{b}^* + l\mathbf{c}^*$ is a reciprocal-lattice vector denoting a Bragg reflection; $\mathbf{r}_j = x_j\mathbf{a} + y_j\mathbf{b} + z_j\mathbf{c}$ is a direct-lattice vector denoting the position of the j th atom in the cell; B_j is the atomic temperature factor (Debye–Waller factor); f_j is the atomic scattering factor (x-rays) or the elastic scattering length (neutrons); the sum is over the m atoms in the unit cell. Therefore, each atom in the unit cell (and hence in the crystal) contributes to the intensity of each reflection. X-rays are scattered by the electron cloud of the atoms while neutrons interact with the atom nucleus,* and this makes x-rays and neutron crystallography complementary techniques. Indeed, x-ray scattering factors vary roughly like the atomic number (the number of electrons), while neutron scattering lengths vary erratically from one element to another and from one isotope to another.

The structure factors are related to the density of scatterers in the unit cell through the Fourier transform:

$$\rho(\mathbf{r}) = \frac{1}{V} \sum_{\mathbf{H}} F_{\mathbf{H}} \exp[-2\pi i(\mathbf{H} \cdot \mathbf{r})] \quad (2)$$

where V is the crystal volume and ρ is the electron density (x-rays) or the nuclear density (neutrons) at point \mathbf{r} in the cell. In practice, obtaining ρ from Eq. (2) is not trivial. Equation (1) can be rewritten $F_{\mathbf{H}} = A_{\mathbf{H}} + iB_{\mathbf{H}}$, and the measured intensities $I_{\mathbf{H}}$, once corrected for several factors (e.g., absorption, extinction, etc.) provide only the amplitude $(A_{\mathbf{H}}^2 + B_{\mathbf{H}}^2)^{1/2}$ of the structure factors $F_{\mathbf{H}}$. The phase is lost and thus, roughly speaking, the art of determining a structure is to derive or estimate “correctly” the phase by any appropriate method.

In the formulation above, each atom of a structure model has typically nine parameters (three coordinates, one to six thermal motion parameters, plus optionally one population factor) which must be refined by means of a minimization technique since the measured intensities are affected by errors. A rule of thumb is that 5 to 10 structure factors must be observed per parameter to be refined. As we shall see in Section VI.C, this ratio

*Neutrons are also scattered by unpaired electrons.

cannot easily be satisfied for weakly modulated structures since the reflections carrying the information on modulation may be extremely weak. In the following we do not discuss either how accurate intensities can be measured and corrected (see, e.g., Ref. 2) or how the structure is practically determined (see, e.g., Refs. 3 and 4) but simply explain how structural crystallography has been applied to the specific domain of low-dimensional conductors. Indeed, these materials have offered crystallographers a wide range of nonstandard and, sometimes, difficult problems to solve.

Several kinds of radiation sources are available which can be used in several ways and with several measurement strategies to collect sets of diffracted intensities $I_{\mathbf{H}}$. The number of possible combinations is thus large, but as we shall see, only a small number of these are presently of practical interest for the study of organic conductors, even if some are clearly promising for the near future.

The types of radiations that are used in structural crystallography are mainly x-rays, neutrons, and electrons. The use of electrons is still difficult for structure determination but can be a useful tool for the detection of structural transitions (see Section X). White or monochromatic x-ray beams can conveniently be obtained from sealed tubes, rotating anode generators, or synchrotron sources [5], with relative flux magnitudes on the order of 1, 10, >100 , respectively.* The first two x-ray sources are continuous and are generally designed to produce almost monochromatic beams, while synchrotron radiation is pulsed and “white.” Neutron sources are comparatively much weaker and are either continuous (nuclear reactor) or pulsed (spallation source [6]).

Bragg intensities can be collected either from a powder sample or from a single crystal. High-resolution powder diffraction nowadays produces rich diffraction patterns, with very narrow lines, from which structures can be determined [7,8] and then refined by mean of the Rietveld method [9,10]. This method clearly has many advantages, such as experimental simplicity, samples generally easier to obtain in the form of a powder than in the form of a single crystal, and insensitivity to crystal twinning. However, the drawbacks for the materials of interest here are as follows. The unit cell must be relatively small—the present upper limit with neutrons is about 1500 \AA^3 . While the situation may change in the future, the study of struc-

*According to Coppens et al. [12], intensities of the monochromatic beam at the sample table as high as $6 \times 10^{11} \text{ photons mm}^{-2} \text{ s}^{-1}$ can be obtained with the best synchrotron sources, while the flux achieved with sealed tubes is approximately $10^9 \text{ photons mm}^{-2} \text{ s}^{-1}$. Furthermore, the increase in brilliance is of 6 to 10 orders of magnitude as compared to sealed tubes. A few months ago the European Synchrotron Radiation Facility (ESRF) at Grenoble became operational and now offers fluxes several orders of magnitude larger than those ever obtained.

tures of organic conductors has been performed exclusively by single-crystal diffraction, which remains the most accurate method to date.

Single-crystal crystallographic studies are classically performed in *angle-dispersive* mode, that is, that a fixed monochromatic radiation is used while the Bragg angle θ is varied. However other approaches are possible. For example, since synchrotron sources now produce strong white beams, *energy-dispersive* diffraction or *Laue techniques* can be used. In the *energy-dispersive* method the detector is set at a fixed scattering angle while an energy (wavelength) scan is performed. This fixed diffraction geometry is well suited to the geometrical restrictions of sample environment devices, but the resolution is intrinsically low and the counting statistics are poor when samples are small [11]. In the Laue geometry all wavelengths—within a certain range—from a white beam are allowed to diffract at the same times. Advances are being made in this direction mainly in the field of protein crystallography [12]. Similarly with neutrons, the time-of-flight technique used with pulsed sources now makes possible the structure study of molecular crystals [13]. Unfortunately, white beam crystallography is more complicated because of the considerable burden of λ -dependent corrections and associated uncertainties (absorption, extinction, harmonics, detector response, etc.) and full crystal structures obtained by this method so far are few.

Finally, concerning low-dimensional organic conductors, almost all crystallographic studies have been performed with the conventional angle-dispersive method (i.e., with single-crystal monochromatic-beam diffraction techniques). Again, this may change in the future since considerable efforts are invested in the development of new techniques for the best use of synchrotron and pulsed neutron sources. Although we have considerably narrowed the field of interest above, there are still many instrument setups and measuring techniques. For the organic conductors, photographic detection has been used only marginally for crystal structural studies but widely used for transition, disorder, and lattice modulation studies* (see Section VI). Thus, in the following, we will be interested primarily in automated diffractometers with quantum detectors and using x-rays from conventional generators or installed at synchrotron or neutron sources. More specifically, we will pay attention to the use of sample environment devices on these instrument, since one of the interesting aspects of the structural crystallography of organic conductors is that it has been per-

*There is a tendency nowadays to use quantum position-sensitive detectors instead of photographic film or movable single detectors. This is especially true for x-rays following the introduction of the so-called “image plate” detectors [14]. The latter have the advantage of high sensitivity and of a linear response over a large dynamic range with a good resolution.

formed down to very low temperatures and to high pressures (see Section IV.C).

B. Instrument Geometries

Let us recall some characteristics of the primary instrument geometries (e.g., Ref. 15) for single-crystal diffractometers designed for use in the angle-dispersive mode (Fig. 1), since this will be useful for the discussion on low-temperature and high-pressure equipment. The data to be recorded are integrated intensities of a series of hkl reflections by rotating each reflection through its reflection condition.

1. *Four-circle with Euler geometry.* The sample is placed at the center of a Eulerian cradle and the detector rotates in the equatorial plane. Data can be recorded from full spheres in the reciprocal lattice except if blind regions are introduced on the Euler angles (ω , χ , ϕ) by, for example, the sample environment assembly.
2. *Four-circle with κ -geometry.* It is similar to the previous one, but the three orienting rotations are no longer orthogonal.
3. *Three-circle with normal-beam geometry* (also called "lifting counter technique"). This is the simplest one since the sample only rotates around a vertical axis. The detector arm rotates around the same axis and can also be lifted out of the equatorial plane.

For a long time, normal-beam geometry was not in favor with crystallographers because, as compared to the two others, the measurable part of the reciprocal space is smaller. However, this drawback is serious only

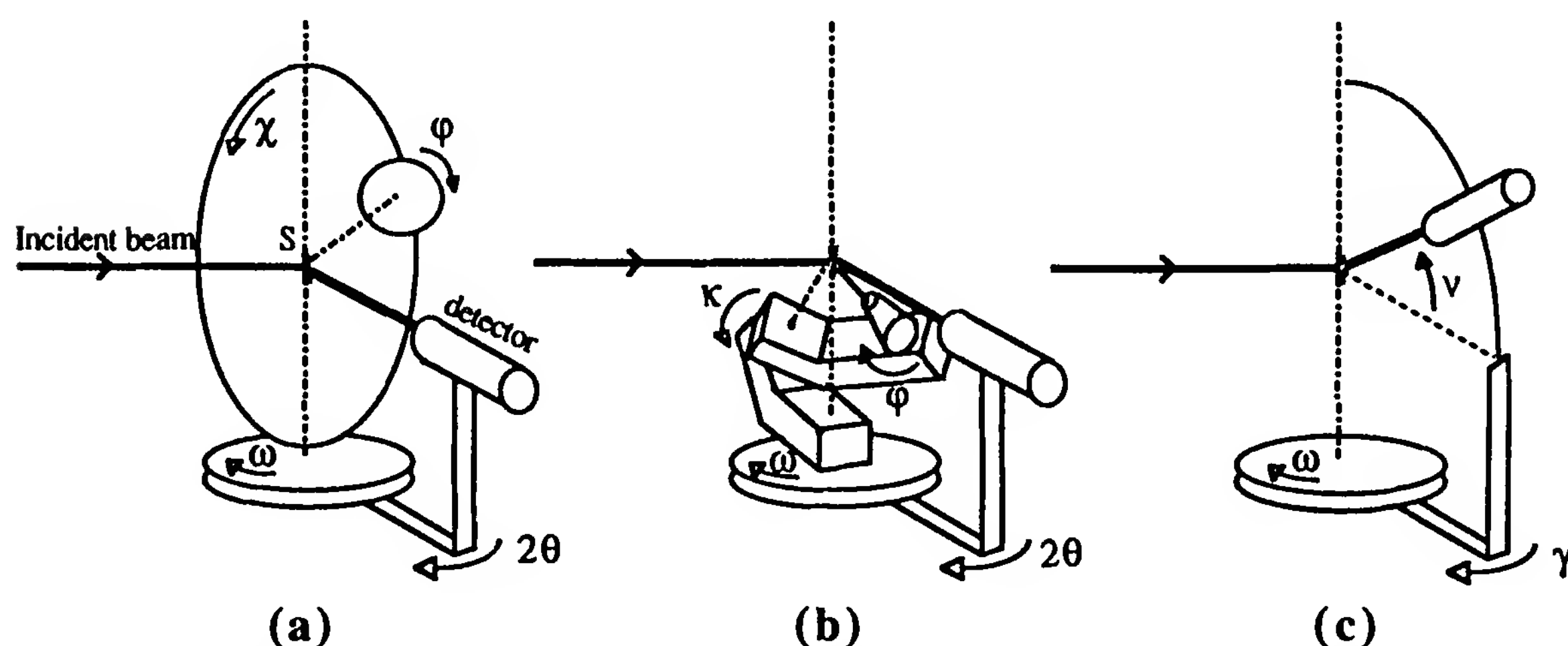


Figure 1 Schematic representation of the three main geometries of automated x-ray or neutron single-crystal diffractometers: (a) four-circle geometry; (b) κ -geometry; (c) normal-beam geometry. S is the sample position.

when high accuracy is crucial (e.g., electron density studies) and is often made up for by the fact that it is a geometry well suited to the use of complicated sample environment devices. Indeed, regular quality data collections are generally limited to $\sin(\theta_{\max})/\lambda \sim 0.6 \text{ \AA}^{-1}$ since diffraction intensity vanishes for large Bragg angles θ , due to both the effect of the Debye–Waller factor and, for x-rays, to the decrease of atomic scattering factors. Thus the reciprocal volume (V_{4C}) in which a four-circle diffractometer will collect data is the resolution sphere with radius $2 \sin(\theta_{\max})/\lambda$. A normal-beam diffractometer can access reflections within a torus with zero internal radius and external radius $2/\lambda$, but the true measurement volume (V_{NB}) is the intersection of the torus and of the resolution sphere (V_{4C}) as given by the formula

$$V_{NB} = \frac{2\pi}{\lambda^3} \left[2\theta_{\max} - \frac{1}{2} \sin(4\theta_{\max}) \right]$$

An extra blind region may exist since the detector must not be lifted too high, due to a worsening of the instrument resolution. In practice, fewer than 10% of measurable reflections are lost under normal measuring conditions. For example, with radiation MoK_α and $\sin(\theta_{\max})/\lambda \sim 0.6 \text{ \AA}^{-1}$, the percentage of normal-beam blind regions is only about 6% for the intrinsic one $(V_{4C} - V_{NB})/V_{4C}$ and less than about 10% with the usual limits on the detector lift angle.

IV. STRUCTURAL STUDIES

There is no space here for a discussion of the various kinds of crystal packing exhibited by low-dimensional organic conductors, since this has already been discussed in this book (e.g., in Chapter 8 for semiconductors, in Chapter 9 for metals, and in Chapter 10 for superconductors). Instead, we present some specific aspects in the measuring and the interpretation of the structures of organic conductors, and we will take most of the examples from the following five typical materials:

1. $\text{TEA}(\text{TCNQ})_2$ [triethylammonium-di(7,7,8,8-tetracyano-*p*-quinodimethane)], a one-dimensional semiconductor
2. TMA.TCNQ.I [trimethylammonium-(7,7,8,8-tetracyano-*p*-quinodimethane) iodine], a ternary salt that behaves as a “bad” one-dimensional metal
3. TTF.TCNQ [tetrathiafulvalene-7,7,8,8-tetracyano-*p*-quinodimethane], the first true one-dimensional synthetic metal
4. $(\text{TMTSF})_2\text{ClO}_4$ [TMTSF is tetramethyltetraselenafulvalene], an ambient-pressure one-dimensional superconductor of the Bechgaard salt family

5. β -(BEDT-TTF)₂I₃ [where BEDT-TTF (or ET) is bis-(ethylene-dithio)tetrathiafulvalene], an ambient-pressure two-dimensional superconductor

The selection above is somewhat arbitrary but has been directed by the availability of large numbers of crystallographic studies for each of these compounds. These are representative of many low-dimensional organic conductors; however, this must not hide the fact that the stacking of flat molecules is not an inevitable requirement for the design of molecular metals [16]. For example, in θ -(BEDT-TTF)₂I₃, the BEDT-TTF moieties form a two-dimensional sulfur network through short S...S contacts between molecules, the planes of which make a dihedral angle of about 80°. In κ -(BEDT-TTF)₂I₃ the metal sheets are made of paired molecules, and adjacent pairs are almost perpendicular to each other (87°). Organic conductors of this kind are relatively recent but are clearly a new important step in the design of better organic metals and superconductors. However, they are absent from our selection because, so far, they do not exhibit original structural behaviors that we can discuss here. On the contrary, materials with a quasi-one-dimensional crystal packing have been studied for several decades and, due to this specific molecular arrangement, exhibit an exceptionally wide range of interesting crystallographic features.

A. Selected Characteristic Structures

We briefly describe here the main features of the crystal packing and of the phase transitions of the five materials listed earlier.

1. TEA(TCNQ)₂ is one of the very first organic compounds in which a noticeable and highly anisotropic electrical conductivity has been observed [17,18]. This ion-radical salt with stoichiometry 1:2 is a quasi-one-dimensional semiconductor which, despite modest performances ($\sigma_{\parallel 300\text{K}}$ a few $\text{S} \cdot \text{cm}^{-1}$; $\sigma_{\parallel}/\sigma_{\perp} \sim 100$) as compared to those of the best organic conductors available nowadays, was one of the materials most studied in the early days of organic conductor investigations. The unit cell is triclinic $P\bar{1}$ with $Z = 2$ and the asymmetric unit contains two independent TCNQ moieties (TCNQ_A and TCNQ_B) and one TEA site [19–21] (Fig. 2). The crystal packing is characterized by the existence of independent linear chains of nearly planar TCNQ ions stacked face to face. The stacking sequence is ABBA, leading to three different interplanar distances and two overlapping modes (tetrads) in the conducting chain. The TEA cations are arranged in the space between the columns. Low-temperature studies showed that the cation site is disordered, with two nonequivalent TEA

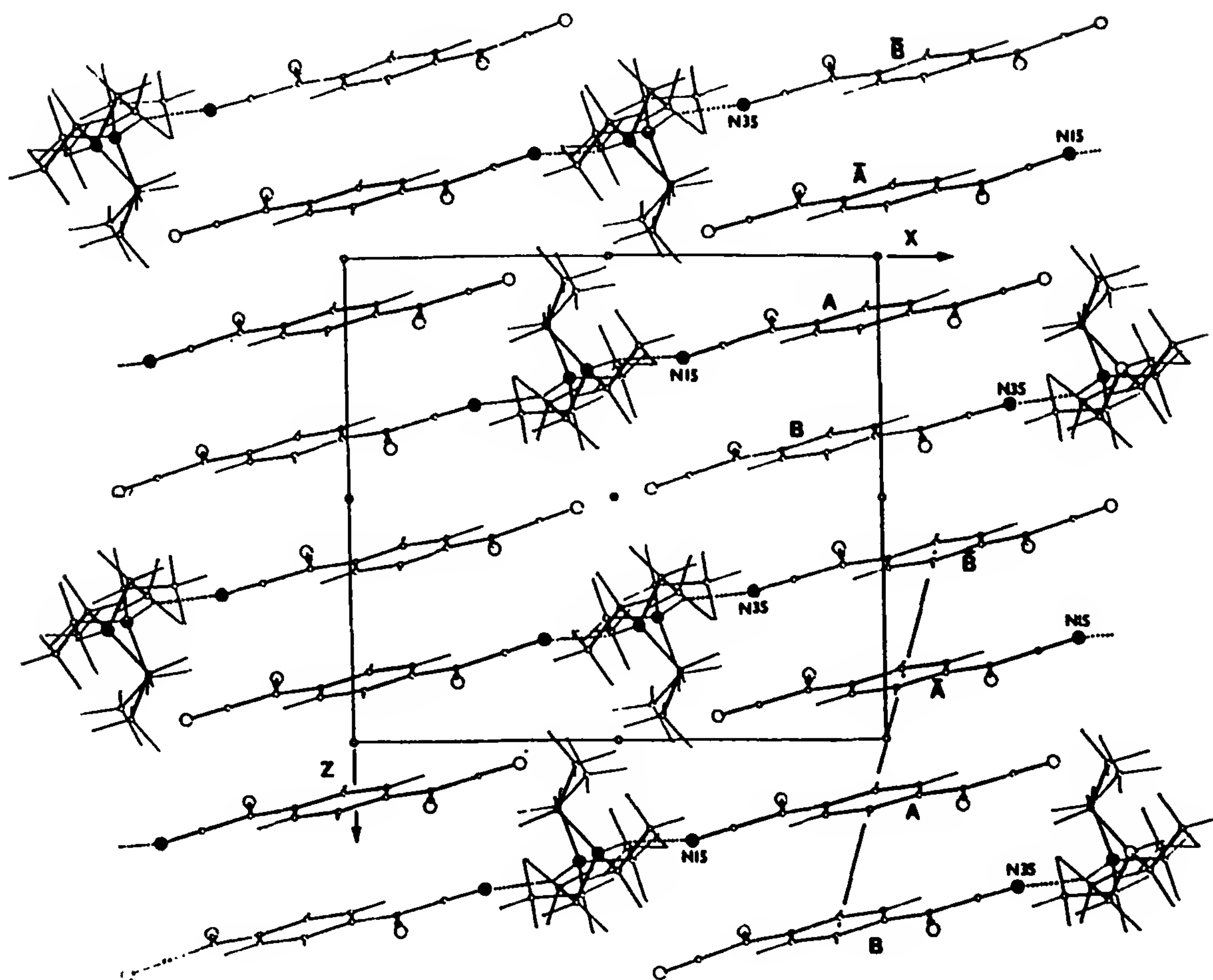


Figure 2 Structure of $\text{TEA}(\text{TCNQ})_2$ at 40 K. Projection along axis b onto the (ac) plane. On the right-side stack the two independent TCNQ moieties are labeled A and B. Each cation site contains two half-filled positions, TEA' and TEA'' , displayed superimposed. (From Ref. 22.)

moieties (TEA' and TEA'') randomly distributed along the cation stacks [22,23].

2. $\text{TMA}^+\text{TCNQ}^{(2/3)-}(\text{I}_3^-)_{1/3}$ is the first ternary organic conductor ever synthesized. Depending on the batches, samples are either semiconductors with $\sigma_{\parallel 300\text{K}} \sim 20$ to $40 \text{ S} \cdot \text{cm}^{-1}$ [24,25] or weakly metallic above 240 K with an anisotropy $\sigma_{\parallel}/\sigma_{\perp} \sim 400$ [26]. The organic lattice (A) is monoclinic with space group C2/m . The TCNQ moieties are located on crystallographic mirror planes and form regular zigzag stacks along the b axis with intrastack distance $b/2$. The TMA moieties are also situated on the crystallographic mirrors and exchange a $\text{N}-\text{H} \cdots \text{N}$ interaction with adjacent TCNQ molecules [24,27] (Fig. 3). In some samples, the lattice (B) of I_3^- columns is disordered and responsible for diffuse layers at $\frac{2}{3}b^*$; the study of ordered

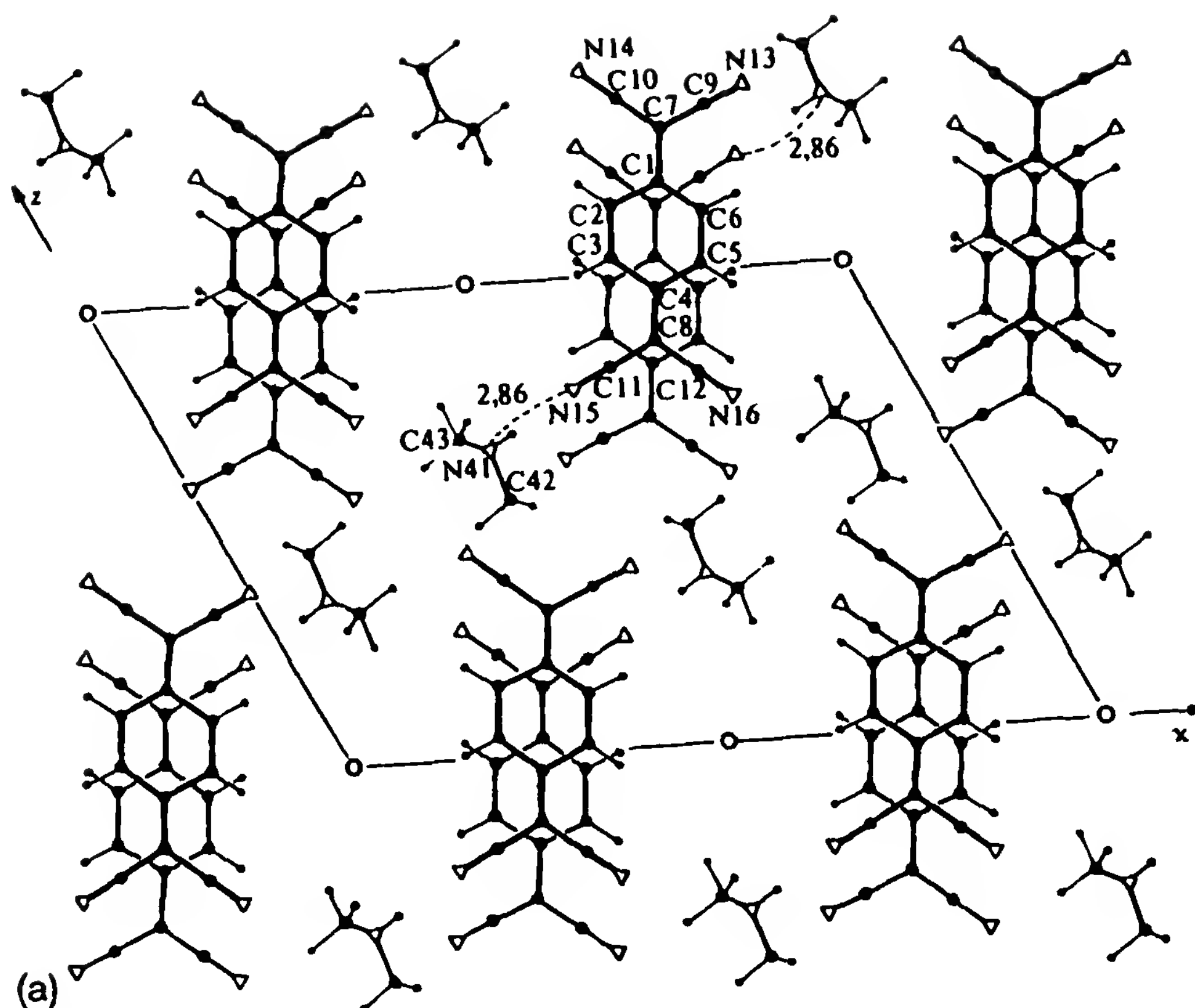
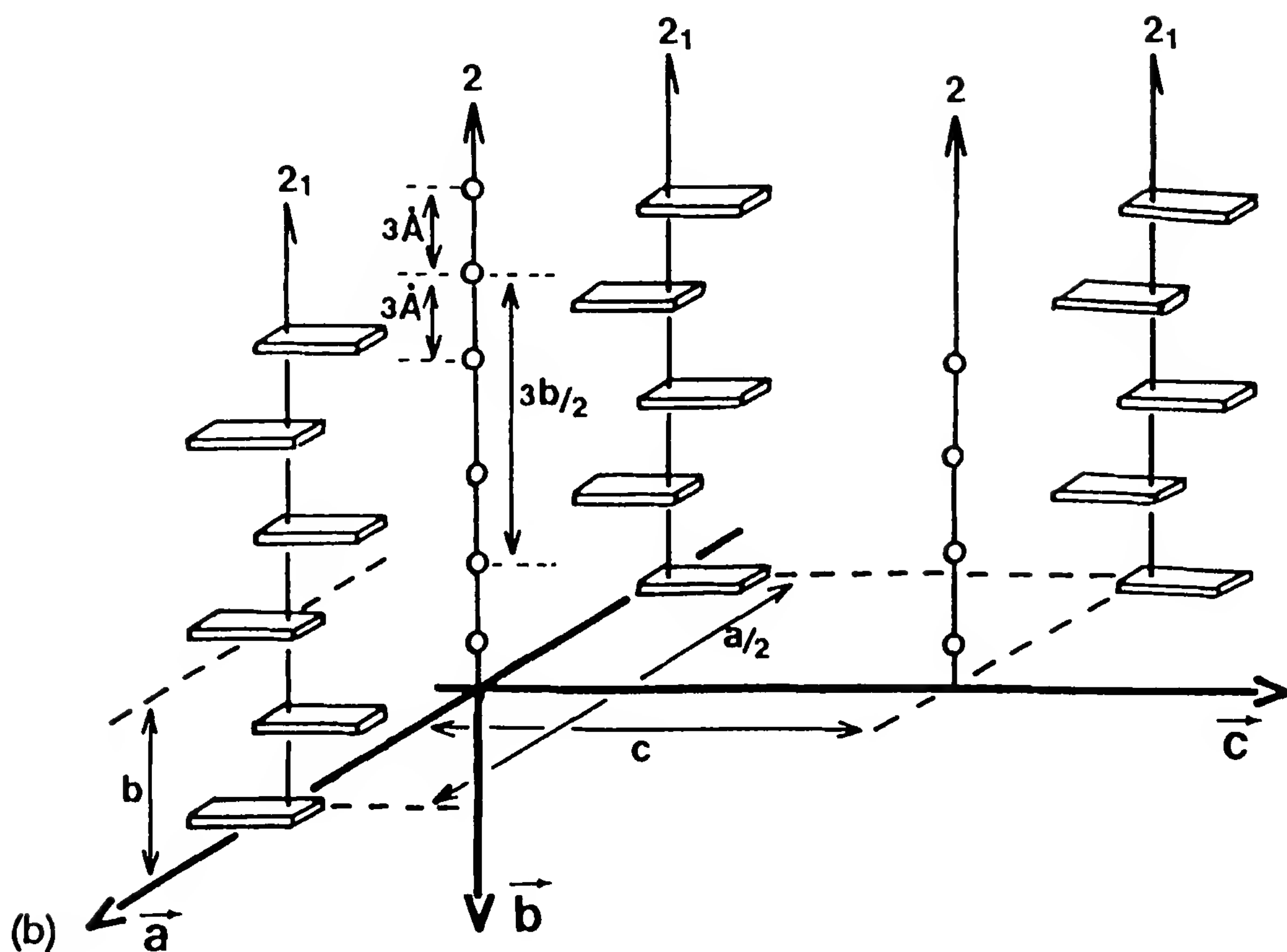


Figure 3 (a) Structure of TMA.TCNQ.I in the monoclinic $C2/m$ symmetry as described in Refs. 24 and 27; (b) how iodine columns and zigzag TCNQ stacks are arranged in the crystal.

samples showed that lattice (B) is triclinic and incommensurate with (A) [28]. Thus the room-temperature crystal packing is made of segregated columns of cations and anions but with two interpenetrating lattices with nonparallel axes. Structural studies have been performed as a function of temperature [27,29] with the following salient results. At 150 K the compound undergoes a “generalized Peierls transition,” with wave vector $(0a^*, \frac{1}{3}b^*, 0c^*)$, which only distorts the organic chains [30]. At 95 K a twinning of the sublattice (A) occurs and the satellite wave vector starts to change to reach the “lock-in” value $(\frac{1}{6}a^*, \frac{1}{3}b^*, 0c^*)$ at 65 K; this last transition is thus of the incommensurate–commensurate type [30,31].

3. TTF-TCNQ is the first true organic metal ever prepared [32] ($\sigma_{\parallel 300K} \sim 300$ to $500 \text{ S} \cdot \text{cm}^{-1}$; $\sigma_{\parallel 54K} \leq 10^4 \text{ S} \cdot \text{cm}^{-1}$) [33]. This charge-transfer salt is well known for its quasi-one-dimensional electronic-transport properties and its sequence of Peierls ($T_c = 54 \text{ K}$) and collective phase transitions at low temperature. Its physical properties have thus been the subject of detailed studies as a function of various physical conditions (for



a review, see, e.g., Ref. 34). The room-temperature crystal packing is characterized by a monoclinic unit cell ($P2_1/c$, $Z = 2$) and the segregated regular stacking of flat molecules along the b axis (Fig. 4). The molecular planes are tipped with respect to the column axis so that TTF and TCNQ stacks can have the same repeat distance, while their respective intermolecular distances are different [35–37]. The partial charge transfer between donor and acceptor chains and the extensive π overlap between adjacent molecules in both types of columns is responsible for a high degree of *intrachain* electronic delocalization and thus for a very anisotropic electrical conductivity. The electronic gas exhibits a strong one-dimensional character since *interchain* coupling, via short transverse $S \cdots N$ contacts, is relatively weak. The structure of TTF-TCNQ has also been determined at 100 K [38]; 60, 53, 45 K [39]; 13 K [40]; or at room temperature under 0.46 GPa [36].

4. $(TMTSF)_2ClO_4$ is a member of the family of compounds known as the “Bechgaard salts” [41] with formula $(TMTSF)_2X$, with X a small anion (e.g., PF_6 , ClO_4 , AsF_6 , etc.). Bechgaard salts have given several of the very first organic superconductors but with critical temperatures of only 1

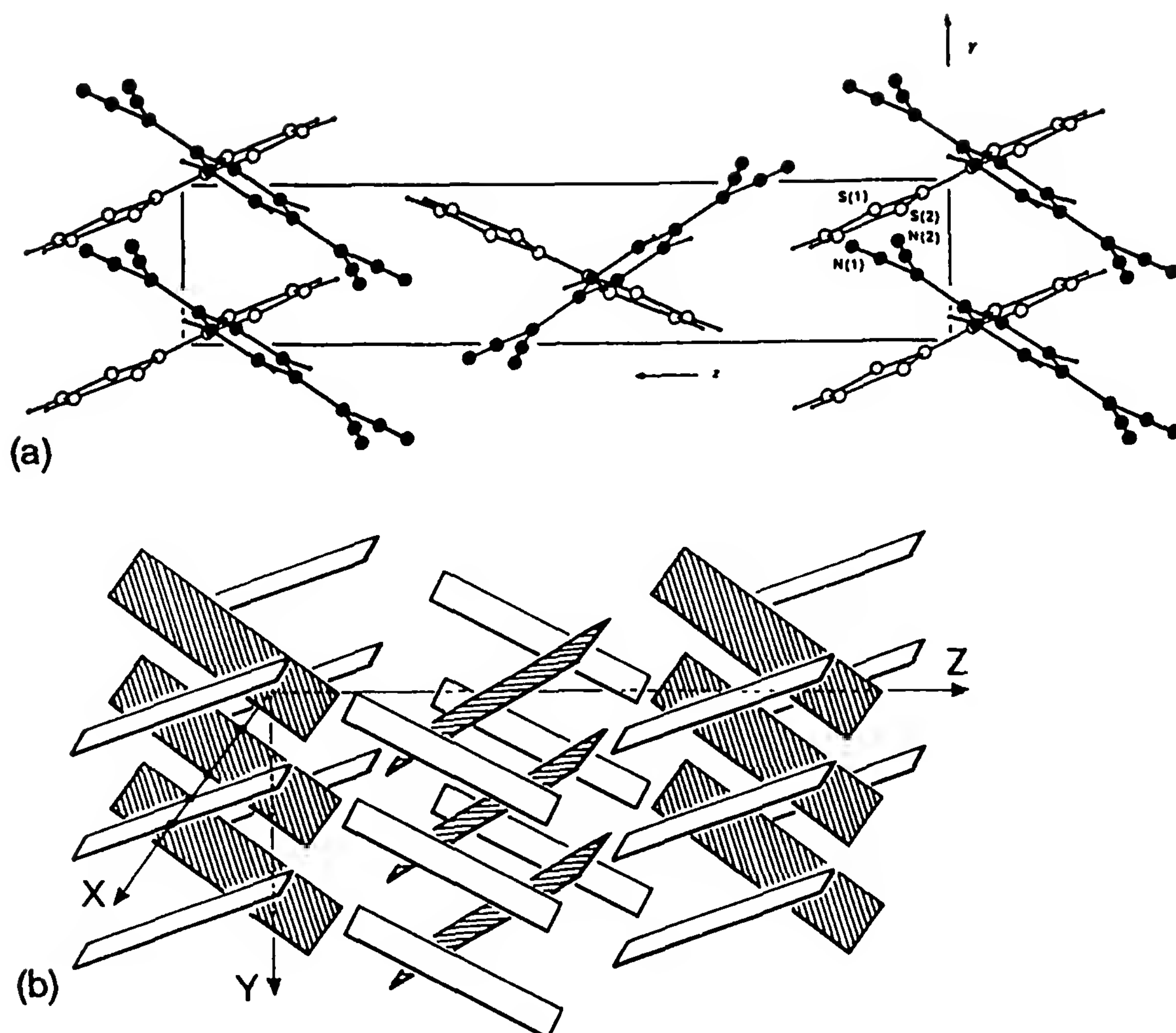


Figure 4 Room-temperature crystal packing of TTF-TCNQ. (a) View normal to the (ac) plane. (From Ref. 35.) (b) Schematic representation of the structure (shaded rectangles: TCNQ; white rectangles: TTF). The molecular planes are tilted about the a axis; there are two identical molecules with opposite tilts for one repeat unit along c , and TCNQ and TTF stacks alternate in the a direction.

to 2 K. For example, $(\text{TMTSF})_2\text{PF}_6$ is superconductor under a pressure of about 1 GPa [42], while $(\text{TMTSF})_2\text{ClO}_4$ is a superconductor at room pressure [43]. Bechgaard salts are isostructural [41,44,45] and their room-temperature crystal packing (Fig. 5) can be described as follows. The unit cell is triclinic $P\bar{1}$ and the crystal is formed of TMTSF molecules stacked along the a axis. The anions are located at inversion centers of the lattice, in the spaces between the methyl groups of adjacent organic chains in the $[011]$ direction. The organic moieties are nearly planar and almost perpendicular to the chain axis. Two adjacent TMTSFs in a chain are associated by an inversion center, and thus organic moieties are all parallel.

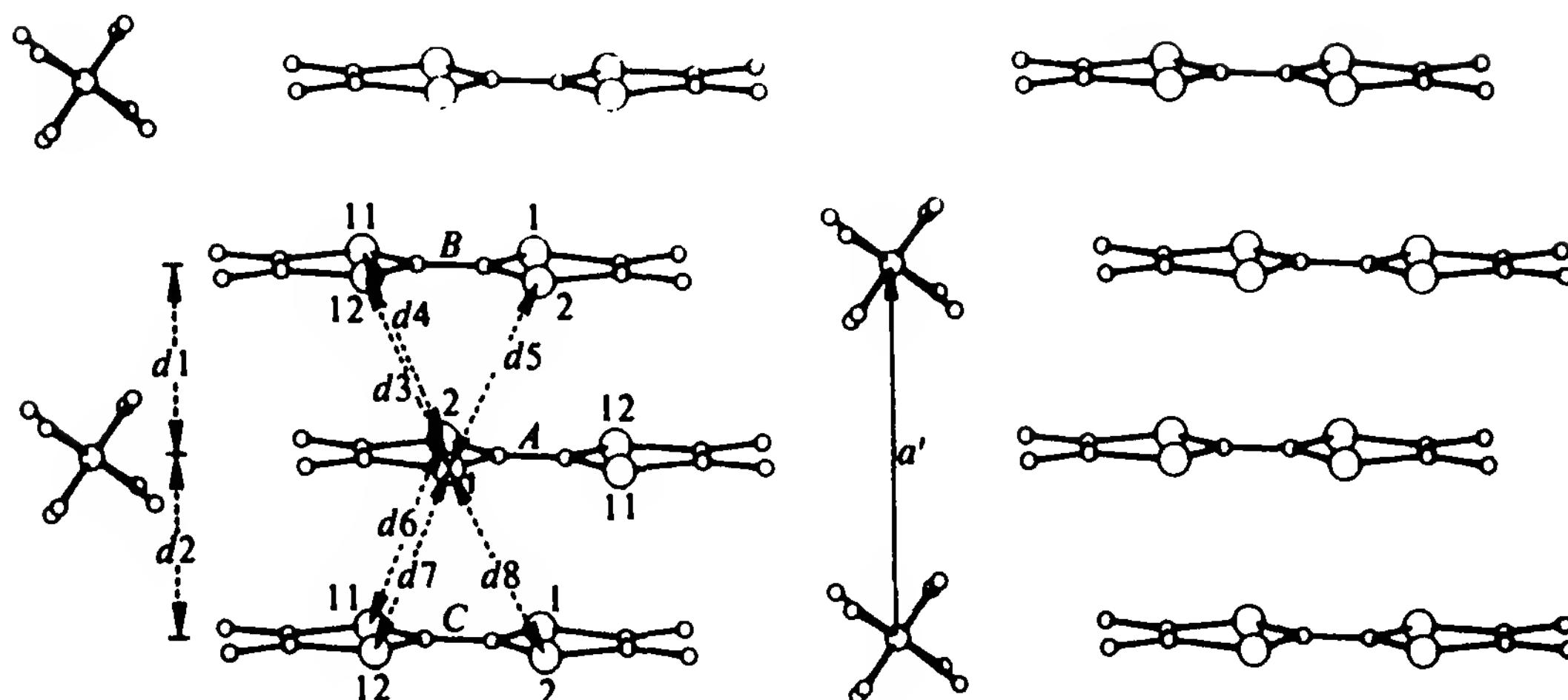


Figure 5 Crystal packing of the Bechgaard salt $(\text{TMTSF})_2\text{ClO}_4$. The independent intermolecular spacings within a TMTSF stack are labeled $d1$ and $d2$. The dashed lines show the short $\text{Se}\cdots\text{Se}$ distances. (From Ref. 45.)

The organic chains are almost regular (weakly dimerized), with two independent intrachain distances and with zigzag stacking. Since short $\text{Se}\cdots\text{Se}$ interchain distances exist between organic stacks, the electronic properties have some two-dimensional character and the crystal packing is often described in terms of (**a**,**b**) conducting organic sheets separated by insulating sheets of anions. In these $(\text{TMTSF})_2\text{X}$ salts, centrosymmetric anions (e.g., PF_6 , AsF_6) have a definite orientation, while noncentrosymmetric ones (e.g., ClO_4 , ReO_4) exhibit a disorder between (at least) two orientations related by inversion symmetry. In all salts, when X is noncentrosymmetric, anions order at low temperature, and a structural order–disorder transition is observed. (For a review, see, e.g., Ref. 46.) Various types of ordering can occur depending on the anion (symmetry, size, etc.) to which different reduced wave vectors of the superstructure reflections correspond [47].

5. $\beta\text{-(BEDT-TTF)}_2\text{I}_3$ is part of the $(\text{BEDT-TTF})_2\text{X}$ family of compounds (X is a small inorganic anion), which is known to provide a wide variety of polymorphic structures labeled β , θ , κ , and so on, in the literature (for a review, see, e.g., Ref. 48) and has given many superconductors with a critical temperature as high as $T_c \sim 12.8$ K for $\kappa\text{-(BEDT-TTF)}_2\text{Cu}[\text{N}(\text{CN})_2]\text{Cl}$ [49]. In this chapter, examples are mainly from $\beta\text{-(BEDT-TTF)}_2\text{I}_3$, the first ambient temperature sulfur-based organic superconductor. The latter has critical temperature $T_c = 1.4$ K (β_L state) [50–52] but a high- T_c state (β_H or β^* state), with $T_c = 7.4$ K, can be obtained under a moderate pressure [53–55] and can be preserved with $T_c = 8.1$ K if depressurization is performed below 125 K [56,57]. The crystal packing is characterized by a triclinic unit cell $\text{P}\bar{1}$ in which the nearly

planar BEDT-TTF molecules form chains in the $\mathbf{a} + \mathbf{b}$ direction. These chains are packed side by side, thus forming two-dimensional “corrugated sheets” parallel to the (a,b) plane (Fig. 6). Along c the organic sheets alternate with the triiodide anion planes [51,58–61]. In the β_L form, the terminal ethylene groups of the BEDT-TTF moieties, which are in close contact with the I_3^- ions, are disordered with two nonequivalent orientations labeled A and B in the literature. Only the B orientation exists in the β_H phase [62,63]. The electron gas in $\beta\text{-(BEDT-TTF)}_2\text{I}_3$ is clearly two dimensional, due to a network of $\text{S}\cdots\text{S}$ interactions in the crystal. Upon cooling, no metal–insulator transition is observed, but the compound undergoes a structural transition at about 175 to 200 K with satellites at $\pm \mathbf{q} = 0.075(3)\mathbf{a}^* + 0.275(5)\mathbf{b}^* + 0.205(5)\mathbf{c}^*$ [64–67]. This incommensurate modulation of the lattice exists only for the β_L form and does not significantly change the electrical behavior of the material.

B. Room-Temperature Approach

As a guide for new synthesis, hundreds of x-ray structures of organic conductors have been determined throughout the world. Indeed, in the early days of the study of quasi-one-dimensional conductors, almost every new freshly synthesized compound, whatever its conductivity, was a candidate for a structure determination. However, there is not much to say on the determination of room-temperature (RT) structure of organic conductors since this is classical crystallography only. The interpretation of the results is, by some aspects, more interesting since it became progressively more and more sophisticated.

For example, let us consider the TCNQ-based salts of the 1980s, which exhibited a wide range of crystal packing and of RT conductivities (from insulator to good one-dimensional semiconductors). Their room-temperature structures showed the specific stacking of large flat molecules which favors the one-dimensional overlap of π orbitals. As illustrated by the review of André et al. [68], attempts were soon made to explain the longitudinal conductivities of the various salts by means of a comparison of the regularity of TCNQ stacks (intrastack distances), of the overlap of adjacent molecules within chains, of the shortest intermolecular distances, and so on. But this is again standard crystallography.

More specific to low-dimensional organic conductors is the approach of Chasseau [69]. The conductivity was assumed to be directly related to the efficiency of the molecular overlap between adjacent moieties within TCNQ stacks. This overlap efficiency was quantized on the basis of the total intersection volume between van der Waals spheres attached to each atom. This method, although very approximate, gave good results for ammonium

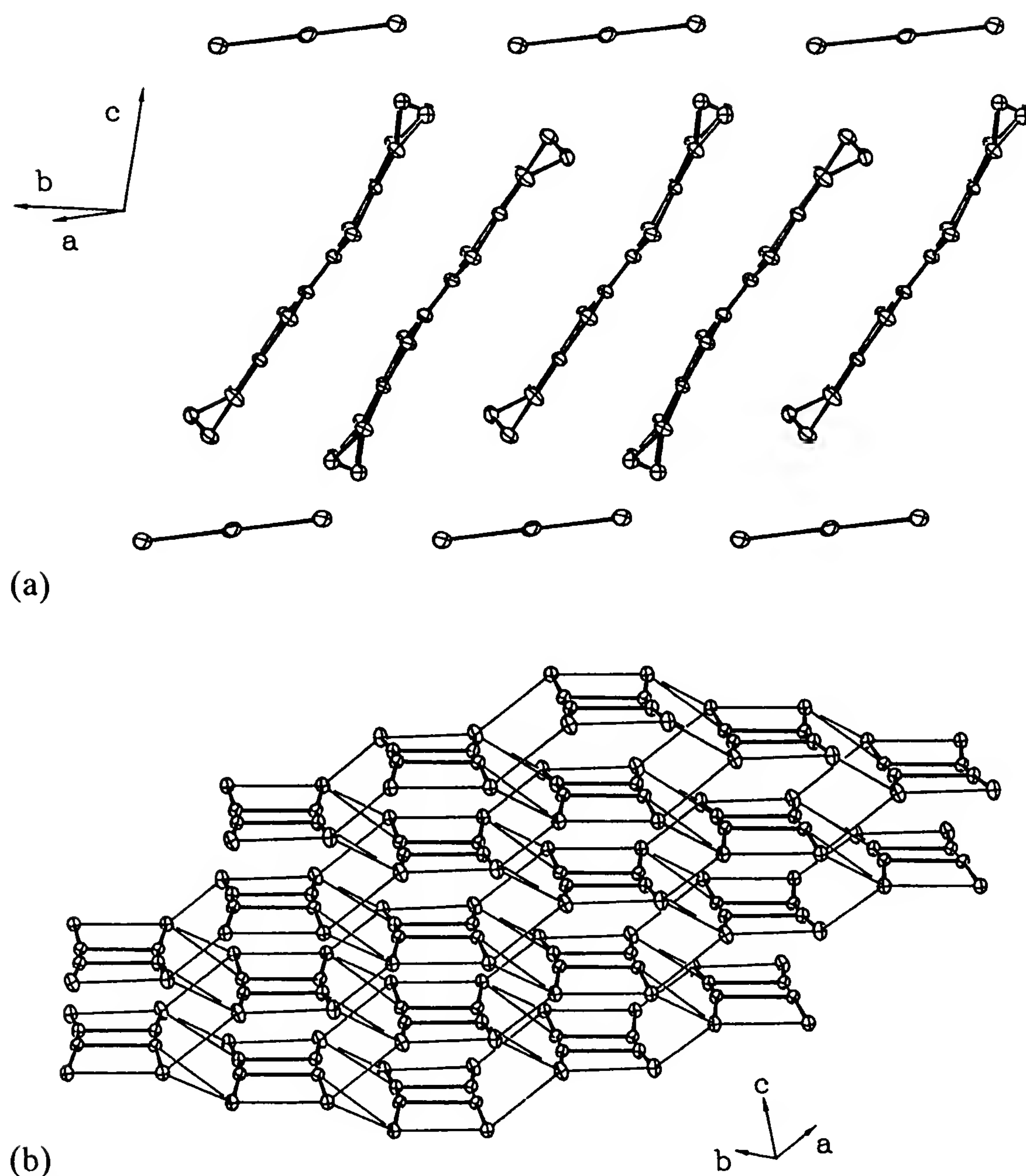


Figure 6 Room-temperature crystal packing of β -(BEDT-TTF) $_2$ I $_3$: (a) loose intrastack packing of BEDT-TTF molecules ($d_{s-s} > 3.60$ Å) and I_3^- anions; (b) "corrugated sheet network" of short ($d_{s-s} < 3.60$ Å) interstack S—S interactions. Only S atoms of the BEDT-TTF molecules are given. (From Ref. 64.)

TCNQ salts; however, this was only a substitute for a more quantitative approach through the calculation of transfer integrals (see Section VII) or for the direct observation of the charge density between molecules (see Section XI). However, in series of isostructural materials such as the Bechgaard salts, it is clearly possible to estimate intra- and interstack interactions

qualitatively, through a few geometrical parameters (distances and angles) accounting for the shape and orientation of orbitals [70,71]. This will be more uncertain in the case of BEDT-TTF-based materials, which exhibit a wide range of different crystal packing.

Among other original interpretations of room-temperature structural results, we may quote here the work of Flandrois and Chasseau [72], who have evaluated the amount of charge transfer in TCNQ-based salts by means of the study of combinations of intramolecular bond lengths (see Section VII.C).

C. Low-Temperature and High-Pressure Approach

The room-temperature approach rapidly reached its limits since a simple examination of the room-temperature structure cannot explain the low-temperature (LT) or high-pressure (HP) electronic behavior of organic conductors. Indeed, very different temperature and pressure dependences of transport properties are observed, leading to various kinds of transitions and ground states.

In earlier theoretical approaches of the temperature and pressure transport properties, structural changes were accounted for by simple changes in the stacking and interchain distances, the latter being deduced from the room structure through the variation in the lattice constants. This was a rigid-molecule approach of the crystal packing evolution. Unfortunately, organic crystals are highly deformable and the corresponding structural changes are complicated. Even in the rigid-body approximation above, the intra- and interchain distance changes are always accompanied by a more or less pronounced molecular rotation which modifies the overlap of orbitals. Ultimately, since transport properties may depend on extremely small relative atomic displacements which cannot be intuited, an effort has been made toward the computing of transfer integrals and of Fermi surfaces, from low-temperature and high-pressure structural data. Such studies have also been performed as a function of temperature and/or pressure (see Section VIII).

To emphasize the importance of structural studies at LT or HP, let us take the example of TTF-TCNQ. This prototype charge density wave (CDW) system undergoes at ambient pressure a succession of three structural and electronic phase transitions, from a high-temperature metallic phase down to a low-temperature insulator phase. There has been a considerable debate about the mechanism of these transitions, and many distortional modes have been proposed to account for the physical properties of this material (e.g., rigid molecule displacement as translations [73,74] or librations [75,76] or even internal deformations of the molecules [77,78]. Indeed, an experi-

mental confirmation was missing, and this point is discussed in more detail in Section VI.C.

Low-temperature and high-pressure structural studies started slowly because, in the 1970s there were few appropriate sample environment setups. However, since organic conductors exhibit a set of interesting lattice changes correlated with their exceptional electronic properties, it is not by chance that most of the first very low-temperature and/or high-pressure x-ray and neutron structure determinations of molecular structures were performed on organic conductors. The role of neutron diffraction is important here since sample environment devices are easier to design when the radiation is able to pass through thick metallic walls. However, neutron experiments were often hindered by the lack of large enough single crystals (see Section XII.A). Nowadays x-ray LT and HP setups have made great progress and can often compete with neutron setups. In the following we discuss the evolution of sample environment techniques and their use in the study of organic conductors.

D. Low-Temperature and High-Pressure Techniques

The number of low-temperature, high-pressure (LT + HP) structure determinations of organic conductors is not yet very large, but a number of other crystallographic studies under constraint have also been reported. To limit the field of the discussion below, we consider only the case of techniques allowing for the measurement of full crystal structures, since collecting a three-dimensional diffraction data set is more demanding than simple observation of a few main or satellite reflections.

1. Low-Temperature Techniques

Single-crystal x-ray or neutron diffractometers equipped with a low-temperature device were sparse in the 1970s. At present, several tens exist in the world, but very few are capable of handling temperatures below 10 K. As stated in Section III, until now crystal structure studies have been performed only by means of the angle-dispersive method. We discuss below the three main kinds of cryostats that can be used on the instrument geometries described in Section III.B. More details can be found, for example, in Ref. 79, which compares LT setups suitable for accurate electron density map studies.

1. *Gas-stream cryostats.* These were the first kind of setup available. Their advantage is that they are cheap and that no shields or windows are required (no absorption, no parasitic scattering). The device is fixed while the crystal rotates in the cold gas stream. With nitrogen the limit temperature is about 100 K; helium is rarely used since it cannot be recuperated easily in such an arrangement. The reliability is not particularly good. Icing

of the sample often occurs even with the best assemblies and the temperature of the sample can be misjudged by more than 10°.

2. *Gas-flow cryostats*. The sample is mounted on a cooling block through which the coolant (usually helium) passes. The cold parts are enclosed in vacuum by shrouds generally made of beryllium (x-rays) or of aluminum (neutrons). The inner wall is kept in contact with the cooling block, in which a sensor is embedded. This ensures that at thermal equilibrium, the crystal temperature is known with high precision. Here, to orient the sample in the beam, either the entire assembly is moved or the cryogenic reservoir is kept fixed while only the sample chamber is moved. In the latter case rotating seals and/or some kind of articulated or flexible cryogen transfer line must be used, and this is the critical part of most designs. Argoud and Muller [80] have recently reported a very sophisticated fixed flow cryostat with no rotating seals and 5-K capability. The crystal is mounted on a small, delicate, gimbaled holder coupled magnetically to diffractometer axes.

3. *Cryocoolers*. These are closed-cycle cryogenic refrigeration systems employing helium gas as a working medium. The system consists of a compressor module with electrical controls, flexible interconnecting gas lines, and an expander module in which the refrigeration is produced by means of adiabatic expansion of the helium. Single-stage units are relatively small and capable of a minimum temperature of 45 K, double-stage units are larger and capable of 10 K, while bulky, heavy, and expensive three-stage units can reach 3.6 K. The sample is mounted at the end of the last-stage heat station and insulated from the room temperature by several shrouds. Cryocoolers are reliable and less expensive than flow cryostats since they consume no cryogen.

In the following we discuss which kind of cryostat can be used for each instrument geometry, and their advantages and drawbacks.

1. *Normal-beam geometry*. Since the sample rotates only around the vertical axis, it is very easy to attach a two- or three-stage cryorefrigerator, a standard reservoir-type liquid helium cryostat, or even a compact dilution cryostat, to the ω cradle of the instrument. This is the simplest assembly, which also offers the lowest temperatures and, as we shall see later, is also most appropriate for LT + HP studies. Three-circle diffractometers are relatively common in neutron laboratories but a few x-ray diffractometers have also been built (R. Moret, unpublished, 1993; J. Gaultier, unpublished, 1993) and used for measurements on organic conductors.

2. *Kappa geometry*. Kappa geometry was thought initially to be very convenient for low-temperature studies because the sample can be freely accessed from the top of the instrument without reducing the measurable part of reciprocal space. This was true for gas-stream devices, which are

fixed and independent of the diffractometer, but turned out to be a serious drawback when a device must be attached to the instrument. Indeed, this is mainly because the κ arm of commercial diffractometers is mechanically weaker than the annular cradle of four-circle diffractometers.* The helium flow cryostat of Albertson et al. [81] also had this kind of problem; however the device of Argoud and Muller [80] does not because it applies almost no extra stress to the diffractometer axes.

3. *Four-circle geometry.* Since the crystal rotates around three orthogonal axes, this instrument geometry may seem inappropriate to measurements at very low temperatures. In fact, several good mechanical solutions have been found. Here the main constraints come from the absence of a nodal plane (or axis) for the multiaxial sample rotations, from space limitations due to the internal diameter of the χ cradle, from the mechanical strength of the χ cradle, which must hold the cryostat without deformation,[†] and from the power of motors, which must be able to rotate heavy parts and to drag more or less flexible links.

If we exclude marginal designs, such as the use of an unusually large Eulerian cradle able to internally hold a two-stage cryocooler (T. F. Koetzle and J. L. Henriques, unpublished, 1976) or the use of a very small full-circle Eulerian cradle mounted completely inside the sample room of a helium cryostat [82], the LT device must fit a commercial Eulerian cradle. At present, χ shafts with inner diameters in the range 250 to 400 mm in diameter are common; the plane of the χ circle may either contain the axis of the ϕ circle or be offset.

With a normal χ shaft (no offset) the cryostat must fit within the inner part of the cradle. Coppens et al. [83] used a small helium flow cryostat mounted within a Eulerian cradle for a 40-K x-ray study of TTF-TCNQ [39]. Samson et al. [84] used an intricate design in which the sample rotates relative to the cold station of a cryocooler but is thermally coupled to it through a flexible high-purity copper cable. The minimum temperature is then only 18 K, but this made possible, for example, the 19-K study of $\text{TTT}_2\text{I}_{3+\delta}$ [85] (TTT is tetrathiotetracene). To reach temperatures down to 3 K, Zeyen et al. [86] have built a helium flow cryostat with spherical geometry and full 360° freedom of motion for all three Euler angles. This result was obtained due to a clever helium siphon with two rotating Johnston joints. The helium consumption is reasonable owing to a special low-loss transfer line with magnetically suspended helium ducts. This assembly

*A kappa diffractometer with a strong κ arm is presently being built at the European Synchrotron Radiation Facility (ESRF) at Grenoble.

[†]Annular cradles are sensitive to stress. They may buckle or become oval with, as a consequence, an increase in the radius of the confusion sphere of the rotation axes.

(Fig. 7) was operated routinely for many years on the neutron diffractometer D10 at the Institut Laue Langevin and was used for studies on, for example, Bechgaard salts at temperatures close to the superconducting transition [87,88]. Since 1990, 1.6 K can be reached routinely with an improved design and a dilution cryostat has been tested successfully in the laboratory which fits the Eulerian cradle and is capable of 70 mK (C. M. E. Zeyen and S. Pujol, private communication, 1993). The helium flow cryostat of Argoud and Muller [80] is also well adapted to four-circle geometry and can be installed even on a small Eulerian cradle.

However, at present the most popular design is certainly the mounting of a two-stage cryocooler on a Eulerian cradle with an offset χ circle. The cryorefrigerator may be either fixed to the offset χ circle through a ball bearing and coupled to the ϕ shaft as proposed by Filhol et al. [89] or may be held and driven directly by the ϕ shaft itself as proposed by Henriksen et al. [79,90] (Fig. 8). Those devices are easy to operate since they have no rotating seal. Cryocooler-based setups have been installed successfully on both neutron and x-ray diffractometers and have been used often for low-temperature studies on organic conductors down to 10 K.

Most cryostats and instruments initially designed for neutrons or x-rays have been adapted successfully to the other radiation. There is not much difference between the two kinds of instruments since x-ray diffractometers now often use the same large and strong Eulerian cradles as those developed for neutrons. In both cases the absorption by windows is not large ($<5\%$); aluminum shrouds can be manufactured in the form of spheres (constant absorption), and beryllium shrouds are generally in the form of cups (angle-dependent absorption). Recently, other materials, such as thin carbon foils [91], have been used as shrouds in the x-ray case. Synchrotron radiation must be considered separately due to its high intensity, low divergency, and wavelength tunability. This is clearly beneficial for data accuracy but also affects the design of sample environment units since it makes possible the use of shorter wavelengths which are more penetrating. As a conclusion of the present section, we can say that structural studies down to 1.6 K are now routine.

2. High-Pressure Techniques

Some sophisticated cells now make possible diffraction experiments at pressures higher than 400 GPa, thus approaching those at the earth's center, but this has a cost in terms of reduced sample size, nonhydrostaticity, and so on [92]. At such high pressures only powder diffraction patterns can be obtained, while the unrestricted three-dimensional collection of single-crystal diffraction data is possible only up to a few gigapascal. Fortunately,

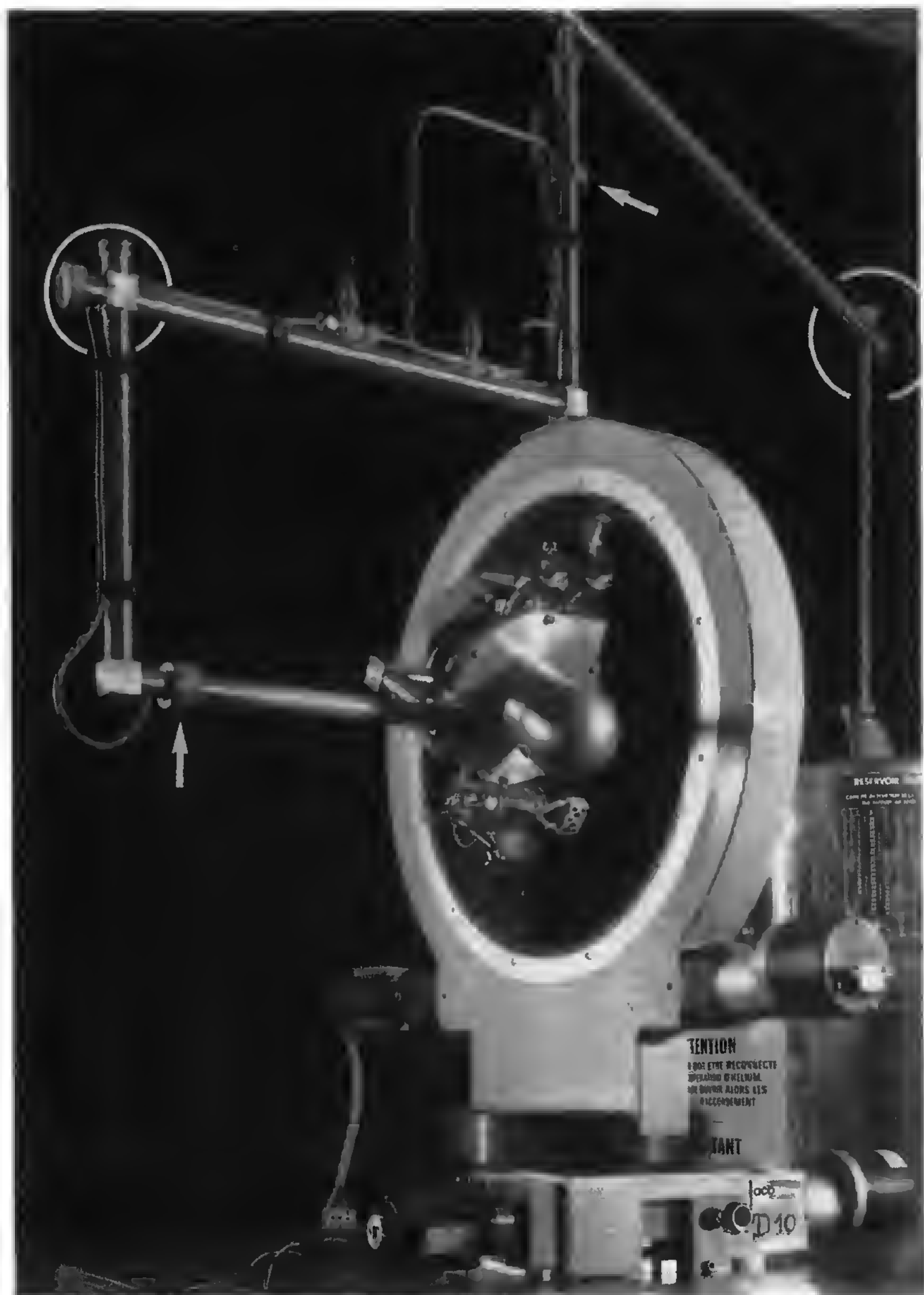


Figure 7 Continuous-gas-flow cryostat of Ref. 86, with its special helium siphon installed on the Eulerian cradle of the neutron diffractometer D10 at the Institut Laue Langevin (Grenoble, France). The arrows indicate the two rotating Johnstons; the circles indicate the corners with magnetic spacers.

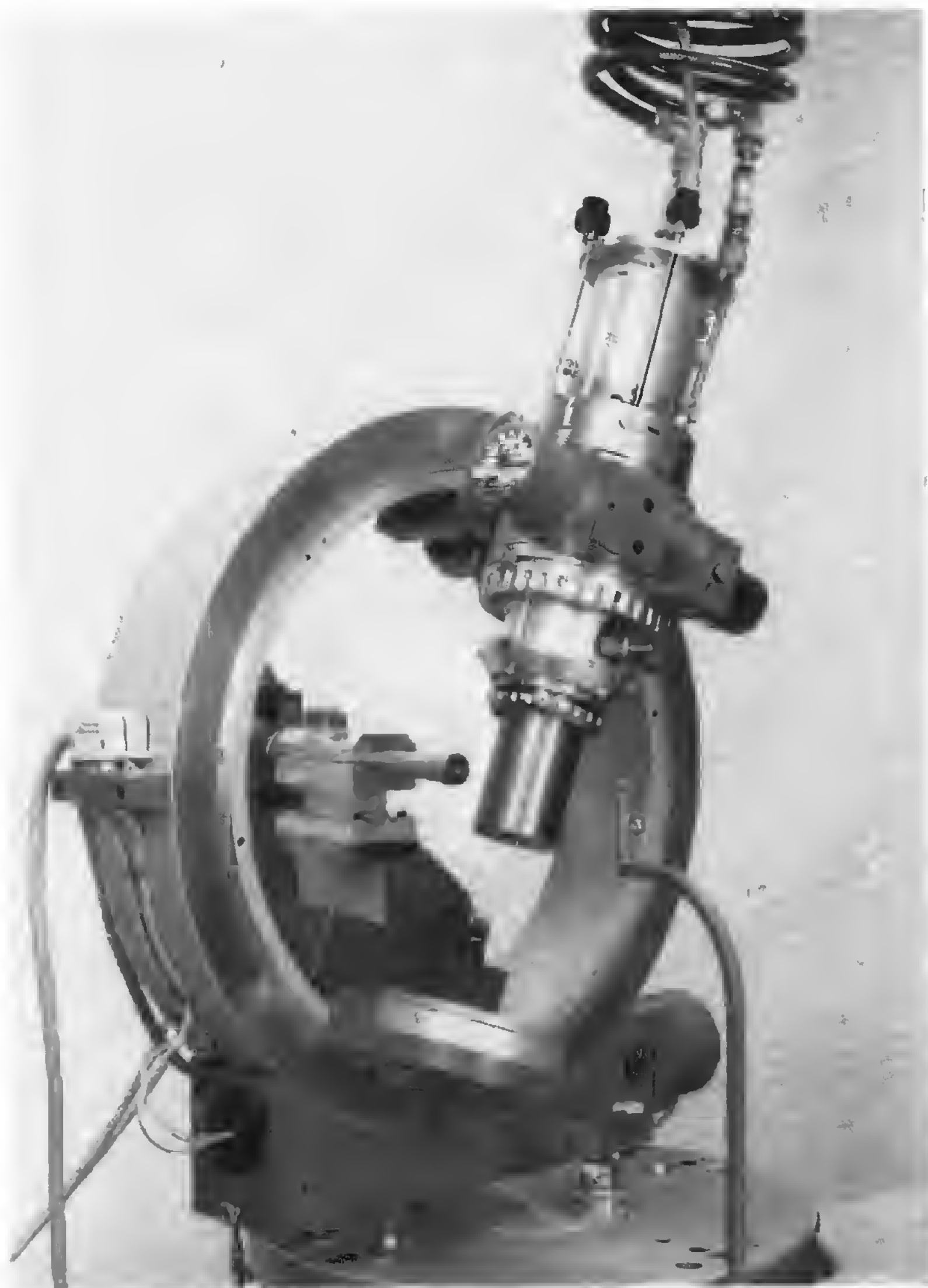


Figure 8 Two-stage Displex CS201 cryocooler mounted on the ϕ -bearing of a Huber 512 four-circle diffractometer. Helium gas lines and electrical connections are supported from the ceiling by a swinging link suspension. (From Ref. 90.)

if extreme pressures are clearly useful, as for the study of the equation of state of geophysically interesting mineral materials, in practice, pressures up to about 2 GPa only can be used for single-crystal structure studies of organic conductors. At higher pressure the Bragg reflections are broadened, which prevents accurate data analysis (J. Gaultier, private communication, 1993; and Ref. 93).

What are the specific characteristics of the high-pressure structure studies of organic conductors? Compared to simple minerals, the pressure range is lower, but molecular materials are more sensitive to nonhydrostatic stress, diffract an order of magnitude less, the cell dimensions are larger, and thus more reflections must be collected. In practice, three types of pressure vessels are often used in the diffraction experiments.

(a) *Gas-Pressurized Cells*

The sample is placed in a thick-walled container continuously pressurized with a gas [94]. The pressure is isotropic and may be varied without any mounting/dismounting by adjusting the gas pressure. In case of pressure cell failure, the stored energy in the gas is very high; the cell may explode and must thus be surrounded by a thick safety shield. Since many materials are transparent to neutrons, gas-pressurized cells were first designed for use in neutron-scattering experiments. For example, the neutron structure of TTF-TCNQ at 4.6×10^2 MPa was measured by Filhol et al. [36] using a pressure vessel made of high-strength Al alloy (AZ8GU) with inside and outside diameter of 10 and 30 mm, respectively, at the sample position. The cell, surrounded by an Al-alloy shield with outside diameter of 60 mm and pressurized with helium gas, was mounted on the ϕ -table of the Eulerian cradle of a neutron diffractometer (Fig. 9). The entire assembly introduced no extra angular blind spots, but the 40 mm of Al alloys in the beam were responsible for 35% absorption at 1.269 Å and introduced some powder lines in the background.

(b) *Clamp Pressure Cells*

The sample is mounted in a small cylinder containing a fluid, and the cylinder is, in turn, mounted in a piston cylinder cell. Load is applied to the piston until the desired pressure is reached inside the cell. The piston is then clamped with a locking nut. The advantage of the piston cylinder device is that it may break but not explode since a liquid does not expand dramatically. The drawback is that changing the pressure requires dismounting the cell to load it again. Steel or copper–beryllium clamps can be used for neutron structure studies since they allow almost three-dimensional studies. Clamps capable of higher pressures are made with an alumina

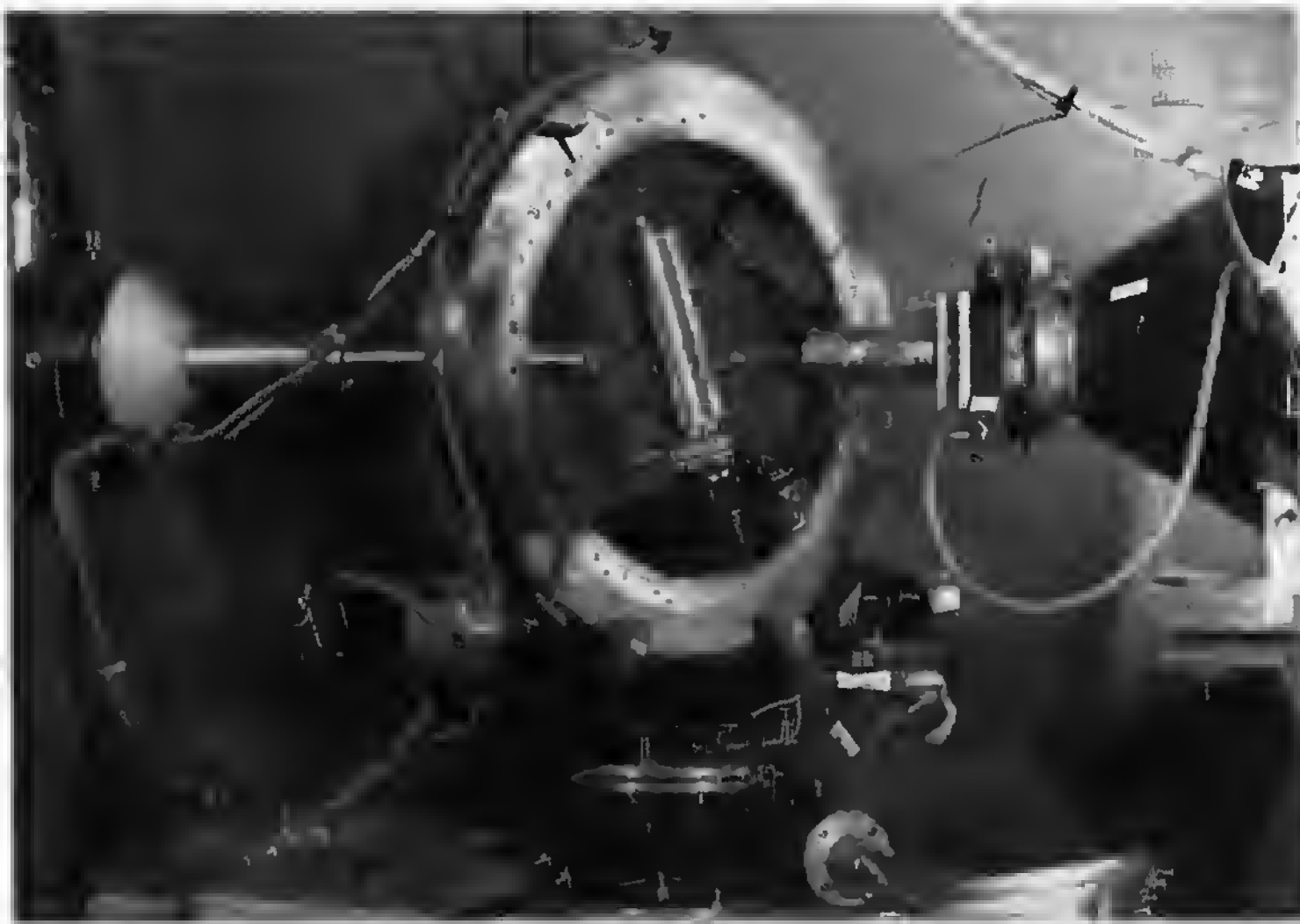


Figure 9 Helium-pressurized cell mounted on the neutron four-circle diffractometer D8 of the Institut Laue Langevin. (From Ref. 36.)

cylinder which must be supported with reinforcing steel rings [95]. In this case data can be collected in the equatorial plane only.

(c) Gasketed Anvil Cells

The sample is placed in the hole of a gasket pressed by two anvils made of a hard material, generally diamond for the x-ray case. The pressure-transmitting medium is a liquid that fills up the sample space. When applying load on the anvils, the gasket deforms, the sample volume decreases, and the pressure in the fluid increases. Diamond anvil cells are very compact, but the available sample space is also very small (generally, a fraction of a cubic millimeter). The latter is limited by the availability of gemstones of good quality with required dimension and by the price, which goes up as the seventh power of their dimension. Efforts are currently being made to design anvil cells offering a larger sample space. For example, neutron experiments require sample sizes of several cubic millimeters.

Generally, the x-ray diffraction measurements are made with the incident and diffracted beam passing through the diamond anvils (Fig. 10a) and thus the absorption is typically 25% for MoK_α radiation. The Bragg angle θ is limited to about 45° and thus either a short wavelength is used or the angle-dispersive mode is preferred, especially in the case of the

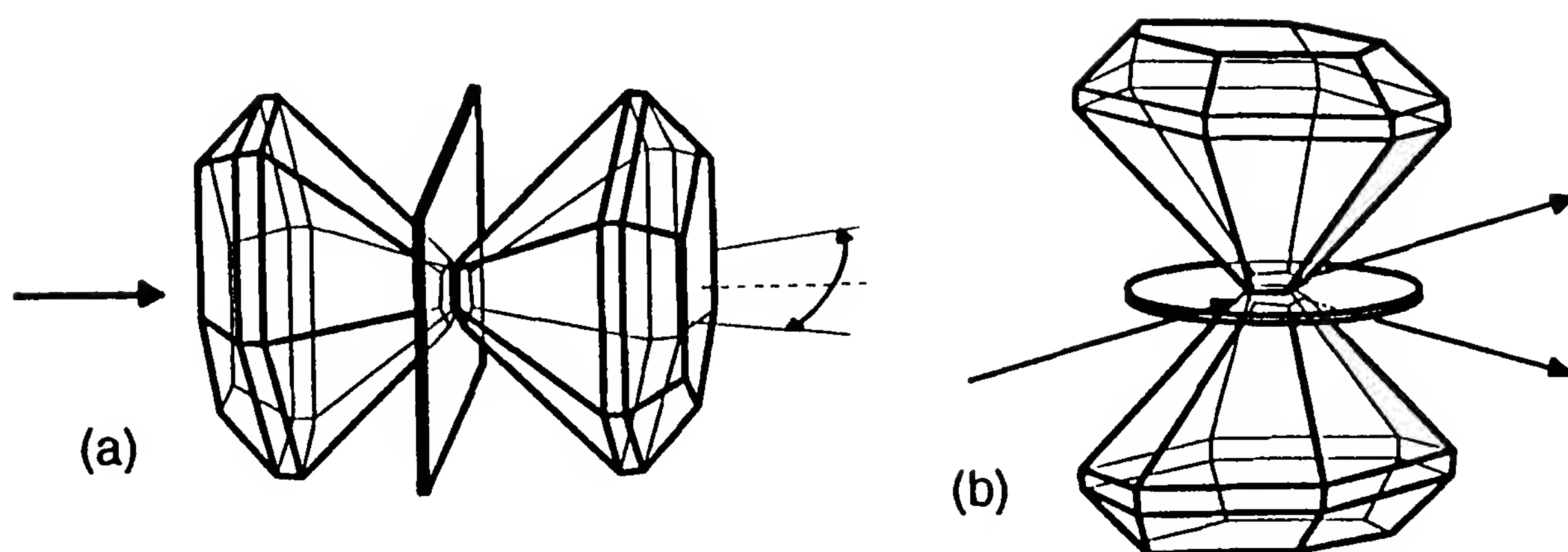


Figure 10 Diffraction geometry with diamond anvils; (a) Merrill-Bassett-like geometry; (b) Bridgman-like geometry but with both transparent anvils and gasket. (From Ref. 96.)

synchrotron radiation. However, if we consider the specific case of organic conductors, the geometry above is probably not the most appropriate.

With molecular crystals the diffraction lines are weaker than with mineral materials, and perhaps with the exception of the strong synchrotron sources, the counting statistics are not good enough (absorption, small sample size). However, Ahsbahr [96] designed an opposed anvil cell, with a beryllium gasket transparent to x-rays, so that the beam passes through the gasket instead of the anvils (Fig. 10b). When mounted on a four-circle diffractometer, all reflections up to $2\theta \sim 90^\circ$ can be measured in the usual bisecting angle setting. In fact, here the limitation on θ is a function of the setting angle χ and disappears when χ is less than 30° . When the beam is orthogonal to the anvil axis ($\chi = 0^\circ$), it passes through the transparent gasket only; when the cell is inclined, the beam also crosses the thinner end of the anvils (i.e., a small quantity only of the anvil material), and thus the absorption is always much smaller (5 to 8% with $\text{CuK}\alpha$) than in the previous design. On a normal-beam diffractometer, almost no extra blind spots are introduced [93]. For x-rays, beryllium-gasketed diamond anvils allow for a maximum pressure of about 3.5 GPa; a description of the instrument setup and measurement technique can be found in Refs. 71, 93, and 97 (Fig. 11). For neutrons, sapphire or sintered tungsten carbide anvils and titanium–zirconium gaskets allow for maximum pressure of 2 GPa, but the probe volume can be made much larger (e.g., 2 mm diameter \times 2 mm height) [98].

X-ray diamond anvil cells made feasible the challenge of measuring full high-pressure structures of, for example, some Bechgaard salts (Refs. 70

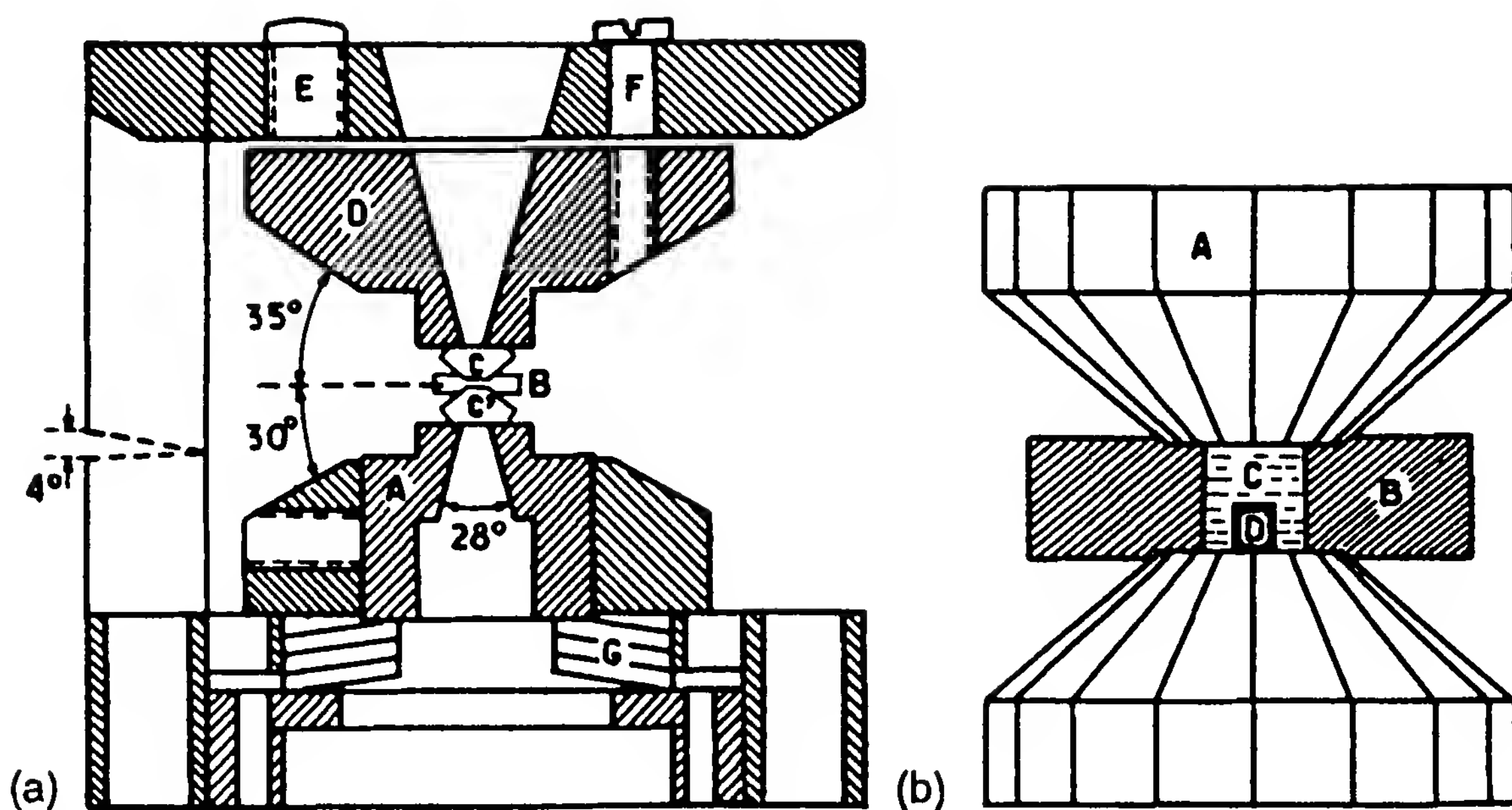


Figure 11 Schematic view of a beryllium-gasketed diamond anvil cell. (a) The entire assembly. A, Movable diamond seat; B, beryllium gasket; C, diamond anvils; D, adjustable diamond seat; E, adjusting screws; F, locking screws; H, buffer springs. (b) Magnified view of the sample setting. A, diamond anvil; B, beryllium gasket; C, liquid; D, sample. (From Refs. 71 and 93.)

and 99) and some BEDT-TTF salts [63]^{*} [93,100][†] [97] [101].[‡] While typical sample dimensions were about 0.001 mm³, more than one order of magnitude less than for usual x-ray samples, high-quality structures have been obtained even with a standard x-ray tube [93]. Of course, the use of a rotating anode is nevertheless advisable.

3. High Pressure at Low Temperature

For structure studies under high pressure at low temperature (HP + LT) the pressure cell must fit in a cryostat and the pressure transmitting medium must not freeze or, if it does, must not produce a large uniaxial additional component. Several combinations of devices described in Sections IV.D.1 and IV.D.2 are possible. While four-circle diffractometers have been often used for room-temperature and LT structural studies of organic conductors,

^{*}The measurements were performed on a four-circle diffractometer, but no detail is given on the diamond anvil cell geometry.

[†]Some measurements were performed on an equi-inclination automated diffractometer, others on a normal-beam diffractometer.

[‡]A Merrill-Bassett diamond anvil cell was used. To get a large enough data set, the data collection was performed from two platelike crystals with the large flat face indexed as (101) and (010), respectively.

almost all HP + LT studies have been performed on normal-beam diffractometers. Let us indicate here some typical instrument setups.

(a) Helium-Pressurized Cells

Schultz et al. [57] used a helium cell mounted on a cryocooler to study the ordering in the high- T_c phase of β_H -(BEDT-TTF) $_2$ I $_3$ with the help of a time-of-flight single-crystal diffractometer at the Argonne Intense Pulsed Neutron Source (IPNS). Then the full structure of β_H -(BEDT-TTF) $_2$ I $_3$ at 4.5 K and 0.15 GPa was measured by Schultz et al. [62] by means of a helium cell placed in a top-loading helium reservoir cryostat installed on the neutron normal-beam diffractometer D15 at the Institut Laue Langevin (ILL). It is worth noting here the advantage of helium as a pressure-transmitting medium; even when it freezes the pressure remains almost hydrostatic since the solid is isotropic and very soft.

(b) Clamps

In HP + LT experiments, the pressure-transmitting medium must be chosen carefully (usually, a fluorocarbon or alcohol) and precautions taken. For example, the pressure must be applied first since the sample generally breaks when pressure solidifies the liquid, while freezing does not destroy the crystal. Also, the change in pressure on cooling, due to a differential thermal expansion between the cell components and the sample must be taken into account. As an example, let us quote the determination of the structure of (TMTSF) $_2$ PF $_6$ at 1.7 K and 0.7 GPa by Gallois et al. [102]. The diffraction data were recorded at the ILL on the neutron diffractometer D15 equipped with a top-loading liquid-helium cryostat; the sample was mounted in a maraging steel (Marval 18) clamp with Fluorinert* FC 75 as the pressure-transmitting medium since it crystallizes at much higher pressures (Fig. 12).

(c) Diamond Anvil Cells

A diffraction geometry with the beam penetrating the anvils has been used for phase-transition studies. For example, Nogami et al. [103] measured some satellites of β -(BEDT-TTF) $_2$ I $_3$ to establish its T,P phase diagram. They used a three-axis x-ray diffractometer, a gas-flow cryostat, and a specifically designed diamond anvil cell with a large volume of sample space (0.8 mm diameter \times 0.3 mm height). Similarly, Moret et al. [104] used a normal-beam x-ray diffractometer with a Merrill–Bassett cell mounted on a cryocooler to study the anion-ordering phase diagram of (TMTSF) $_2$ ReO $_4$. No HP + LT structure measurements performed with a gasketed anvil cell have been reported so far, although such devices seem fairly well suited to that task.

*A trademark of 3M Company.



Figure 12 Clamp made of maragin steel with Fluorinert FC 75 as pressure-transmitting medium. Inside diameter 6 mm, height 10 mm, wall thickness 25 mm, absorption $\sim 50\%$ for a neutron wavelength of 1.175 Å. (From Ref. 102.)

V. THERMAL EXPANSION AND COMPRESSIBILITY

As discussed in Section I, thermal expansion and compressibility must be taken into account in the discussion of the T and P effect on the electronic properties of organic conductors. These quantities can be obtained by several methods, but in practice, mainly single-crystal diffraction, and marginally, powder diffraction, have been used on these materials. For example, Debray et al. [105] measured the compressibility of TTF-TCNQ up to 2 GPa with the help of neutron powder diffraction; however, their results were not in good agreement with subsequent single-crystal measurements [36]. Nowadays, high-resolution neutron diffractometers equipped with poly- or multidetectors and with computer-controlled environment setups make possible quick and automated recording of powder diffraction patterns while the constraint (temperature or pressure) is applied progressively. Then results are displayed in the form of three-dimensional plots of the diffracted intensity versus Bragg angle and constraint, making even small changes in the lattice dimensions or symmetry easily observable. This is, in some aspects, a modern version of the Guinier–Lenne camera but with the advantages of computer control* and of computer data processing.

Usually, low-temperature or high-pressure single-crystal or powder diffraction experiments provide a set of cell parameters as a function of T or

*See, for example, the discussion of “time-resolved crystallography” by Pannetier [106].

P. The latter have to be interpreted in terms of thermal expansion and compressibility, respectively. Both quantities are described by a second-rank deformation tensor U which can be directly computed from the six sets of parameters versus constraint [37,107]:

$$U_{ii} = a_i da_i$$

$$U_{ij} = \frac{1}{2} [(a_i da_j + a_j da_i) \cos \xi_k - a_i a_j d\xi_k \sin \xi_k] \quad \text{if } i \neq j$$

where a_i are the three cell dimensions and ξ_k the three cell angles.

It must be emphasized here that due to the low symmetry of crystals of organic conductors (often triclinic or monoclinic), the directions of the principal axes may take any direction that satisfies Neumann's principle (see, e.g., Ref. 108). Indeed, principal directions and values of the deformation tensor are the relevant parameters to be compared to the structure since they indicate the directions of the highest and weakest deformations in the material. In the vicinity of a phase transition, the orientation of principal axes is fixed either by the strongest intermolecular interactions (axis of weakest deformation) or by the largest deformation (e.g., molecular ordering). Thus, looking at their orientation may help to understand transition driving forces. For example, the conductivity of TEA(TCNQ)₂ exhibits an anomaly at about 200 to 220 K [18,109], but no evidence of structural transition has been found. However, changes in the orientation of principal thermal expansion axes at that temperature suggest that something occurs in the direction of the N—H · · · N interaction between anion and cation [23] (Fig. 13). Indeed, Travers [110] concluded, from nuclear magnetic resonance (NMR) studies, that TEA cations are dynamically disordered above 270 K but their motion progressively freezes down to 200 K. Grassi et al. [111] confirmed that an energy path exists which allows for a room-temperature dynamical disorder of such a large molecule in the crystal packing of TEA(TCNQ)₂.

The remarks above can be extended to alloying between similar organic conductors since the compositional deformation of the cell can also be described by a second-rank tensor [107]. For example, computation of the compositional tensor of the alloy (TMTTF)₂(SbF₆)_{1-x}(AsF₆)_x (TMTTF is tetramethyltetrathiofulvalene) has been reported by El Amrani [112].

VI. PHASE TRANSITIONS, LATTICE FLUCTUATIONS AND DISTORTIONS, AND INCOMMENSURABILITY

For more than 20 years, the study of structural phase transitions has played a key role in the investigation of the physics of the various families of low-dimensional conductors that have been discovered. The reason is that

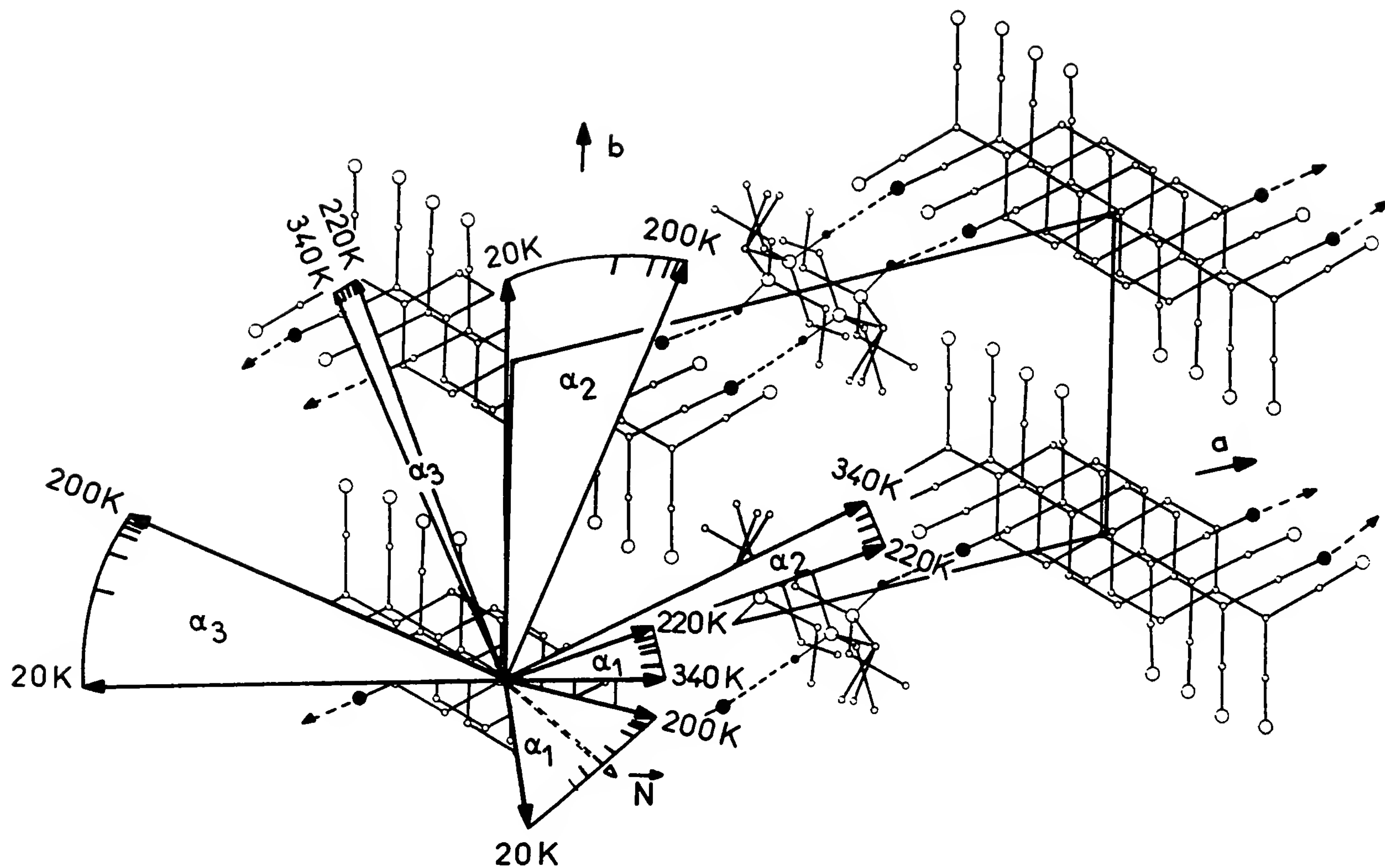


Figure 13 Thermal expansion of TEA(TCNQ)₂. The largest principal expansion α_1 is along the chain axis at any temperature. Above 200 K α_2 and α_3 are roughly parallel and perpendicular to the N—H...N interchain interactions; below 200 K, α_2 and α_3 are directed roughly along the transverse and elongation axes of the average bonded molecular species. (From Ref. 23.)

quasi-one-dimensional materials exhibit low-temperature periodic lattice distortions related to the instability of the one-dimensional electronic gas and driven either by the electron–phonon or spin–phonon interactions (e.g., TTF-TCNQ family) or by the counterion ordering (e.g., Bechgaard salts). Considerable attention has been devoted to these new kinds of behavior, which are now well understood. In BEDT-TTF-based conductors and superconductors the electronic interactions have pronounced two-dimensional character, and thus these materials exhibit a more classical set of structural phase transitions.

It is not the purpose here to develop the theory of structural instabilities of quasi-one-dimensional conductors, which has already been treated extensively in a number of papers (e.g., Refs. 34, 46, and 113 to 116). We simply show how lattice fluctuations, lattice distortions, and phase transitions in organic conductors are detected and studied.

A. Principal Features

Besides their remarkable electronic properties, low-dimensional organic conductors exhibit themselves by their structural phase transitions, which can be classified as follows.

1. *Transitions driven by the electron gas instability* (Peierls or spin-Peierls). These transitions are typical of quasi-one-dimensional conductors and lead to lattice distortions which are generally weak and which may be incommensurate. They are associated with a critical one-dimensional diffuse scattering, which is often observed in an unusually wide temperature range above the critical temperature. Both pretransitional structural fluctuations and lattice distortions have been the subject of a large number of experimental and theoretical studies and are well understood now (see, e.g., Ref. 114). X-ray diffuse scattering is the favored technique for their detection and study (see Section VI.D). Results of the latter technique have often been discussed in great detail; for example, the study of one-dimensional scattering and/or of some satellite reflections may provide a description of the main features of the lattice modulation via a rigid-molecule model [74,117,118]. However, as we shall see in Section VI.C, only a full structure determination of the distorted phase gives an exact description of intra- and intermolecular changes.

2. *Transitions due to the frustration of interchain interactions.* The best example is that of TTF-TCNQ. The Peierls distortion at 54 K is followed by two transitions at 45 K and 38 K which are due to a competition between the modulations on TTF and TCNQ stacks (see, e.g., Ref. 114).

3. *Counterion ordering.* This occurs when insulating ions are dynamically disordered in the high-temperature phase but order at low temper-

ature. The coupling between the counterion sublattice and the conducting stacks introduces an external potential which may induce a $2k_F$ or $4k_F$ charge density wave response of the conducting stacks. However, this generally occurs at a temperature much higher than that at which a true Peierls or spin-Peierls transition would have occurred in the material. A typical case is the well-known anion ordering (AO) transition in the Bechgaard salts. In these materials, which have a one-dimensional stacking type, one-dimensional pretransitional fluctuations are either absent or very weak. In the latter case the weak one-dimensional scattering vanishes near T_{AO} , while a broad three-dimensional diffuse scattering takes place [119], thus indicating that the transition is anion driven rather than electron-phonon driven. For a review, see Ref. 120.

4. *Ordering of conducting stacks or layers.* For example, in β -(BEDT-TTF)₂I₃ a disordered ethylene group may partially or fully order, depending on temperature and pressure conditions (see Section IV.A). Crystallographically speaking, this is a more classical structural phase transition (strong superlattice reflections) but has a specific influence on the electron gas of organic conductors.

5. *“Classical” transitions.* These can be viewed as crystal packing rearrangements with no straightforward connection with the low dimensionality of the electron gas (but which, of course, influence it) or with the one- or two-dimensional character of the molecular stacking in these materials. Superstructure (or satellite) reflections are strong and little sensitive to radiation damage, whereas in the cases discussed above they were often several orders of magnitude weaker than main reflections* and are also much more sensitive to defects (see Section IX.C). For example, a classical transition has been observed by Rahal [93] in α' -(BEDT-TTF)₂Ag(CN)₂ at room temperature and ~ 0.8 GPa, which can be interpreted as follows. At ambient pressure the material has a less compact crystal packing than that of similar BEDT-TTF salts, but at about 0.8 GPa its compressibility is strongly reduced, with one principal compressibility nearly zero. At that pressure the structure reorganizes, thus restoring a significant amount of compressibility capability. At higher pressure, both the magnitude and the anisotropy of the compressibility drops again and then the material starts to lose its crystalline organization. The crystal packing has exhausted its ability to counteract the applied pressure simply by reducing intermolecular distances.

*Of course, this may not be true when the compound contains heavy atoms [e.g., (TMTSF)₂ReO₄ undergoes an AO phase transition leading to relatively strong superlattice reflections]. In fact, Re is a very strong x-ray scatterer compared to other atoms in the material [121,122].

B. Incommensurability

Incommensurate structures have been known for a long time in minerals, whereas TTF-TCNQ is one of the very first organic material in which an incommensurate phase has been observed. There are two main types of incommensurate crystal structures. The first class is that of intergrowth or composite structures, where two (or more) mutually incommensurate substructures coexist, each with a different three-dimensional translational periodicity. As a result, the composite crystal consists of several modulated substructures, which penetrate each other and we cannot say which is the host substructure. The second class is that of a basic triperiodic structure which exhibits a periodic distortion either of the atomic positions (displacive modulation) and/or of the occupation probability of atoms (density modulation). When the distortion is commensurate with the translation period of the underlying lattice, the result is a superstructure; otherwise, it is an incommensurately modulated structure (IMS) that has no three-dimensional lattice periodicity.

Composite structures are characterized by strong main reflections on several three-dimensional reciprocal lattices, part of which is overlapped, but others are incommensurate. This is the case of TMA.TCNQ.I, where the organic and iodine sublattices have nonparallel axes (see Section IV.A). The signature of an IMS in a diffraction pattern is a subset of satellite reflections, generally much weaker than the intense main Bragg reflections corresponding to the basic structure. This is often observed in organic conductors since an incommensurate lattice distortion may occur at low temperature when the Fermi wave vector is incommensurate. A prototype charge density wave system is TTF-TCNQ (see Section VI.C). The structure determination of composite structure has often been performed by separate processing of the data set relative to each sublattice. However, this is only approximate since sublattices are intermodulated and thus, and, as a consequence, even when the structure refinement appears successful, some Debye–Waller factors may have a tendency to diverge. In fact, it has been demonstrated [123–126] that the use of a superspace with dimensionality higher than three makes possible the refinement of composite structures and of IMSs as a whole. Nevertheless, the full structural study of modulated structures is not trivial. For example, in the case of IMSs, satellites reflections may be very weak and thus difficult to observe, the superspace group must be found, and preliminary experiments must permit inference of a model. Photographic methods such as the fixed-crystal fixed-film technique (see Section VI.D) or electron microdiffraction (see Section X) are well adapted to these first steps. Finally, specific structure refinement procedures must be used which account for the appropriate superspace symmetry.

C. Structural Study of Lattice Distortions

Up to now we have seen how lattice distortions are detected and characterized. This does not provide a direct observation of the molecular translations, rotations, and deformations associated with the distortion. However, for a few compounds it has been possible to measure a large enough number of satellite or superstructure reflections so that the distorted structure can be parametrized and refined (rigid-body or full structural study). We consider below four examples, taken from materials selected in Section IV.A, which show that such studies are not easy and that the data collection requires special attention. Indeed, it is generally difficult to measure enough satellite reflections, especially if several kinds of the latter coexist (e.g., $2k_F$ and $4k_F$ satellites, high-order satellites, etc.).

1. $TMA^+TCNQ^{(2/3)-}(I_3^-)_{1/3}$. As explained in Section IV.A, the crystal packing of this ternary salt is made of segregated columns of cations and anions but with two interpenetrating incommensurate lattices: lattice (A) of TMA and TCNQ moieties is monoclinic with space group $C2/m^*$; lattice (B) of I_3^- columns is triclinic [27,28,30]. At 150 K the compound undergoes a “generalized Peierls transition” in which only the organic lattice (A) is distorted. Gallois et al. [31] collected a set of superstructure reflections with wave vector $(0a^*, \frac{1}{3}b^*, 0c^*)$ and performed a rigid-body structure refinement. They concluded that the TCNQ chain distortion corresponds mainly to in-plane translations with helicoidal distribution.

2. *TTF-TCNQ*. X-ray and neutron diffuse scattering studies, combined with magnetic, vibronic absorption, and specific-heat measurements, have established that the synthetic metal TTF-TCNQ undergoes a series of electron-driven collective phase transitions which can be described schematically as follows. First, the TCNQ stacks are distorted[†] by a $2k_F$ Peierls transition at 54 K; second, the TTF stacks also undergo displacement at 49 K; and finally, a locking of the distortion wave vector occurs at 38 K. Thus, below 38 K, the waves on the TCNQ and TTF stacks are assumed to coexist and interfere. (For a detailed discussion, see Refs. 114 and 115.) Furthermore, diffuse scattering measurements showed that the $2k_F$ scattering is mainly transverse to the molecular stacks but with a longitudinal component below 54 K, while the $4k_F$ one is purely longitudinal [74,118]. However, this does not establish the exact nature of the distortion itself.

*The monoclinic symmetry is an average since the A lattice is in fact twinned (see Section IV.A).

[†]This is, of course, a simplified picture since the donor and acceptor stacks are not completely decoupled and a finite charge density wave amplitude on one type of stack induces a small distortion on the other type of stack.

Since satellite intensities are only about 10^{-4} times that of the main reflections, Coppens et al. [127] used high-intensity synchrotron radiation to collect a set of 137 unique $2k_F$ satellite intensities at 15 K. Rigid-body molecular displacements were assumed and the five-dimensional superspace group $P_m^{P2_1/c}$ was selected (i.e., the incommensurate modulated crystal is described in a five-dimensional space in which the two additional dimensions act on the phase of the modulation wave). The final refinement (24 independent parameters) showed that the main displacement is a translation of the TTF molecules, polarized along the axis of the molecule and with amplitude 0.0191(8) Å. Thus the $2k_F$ charge density wave in the low-temperature phase has a significantly larger amplitude on the TTF chains with both transverse and longitudinal components, the main feature being a relative slip of the TTF molecules.

An improved description of the distortion at 15 K has been given by Bouveret and Megtert [40] from a bigger experimental data set. The intensities of 621 satellites were collected on a three-circle x-ray diffractometer equipped with a rotating anode and a cryocooler. The refinement was performed using the same superspace group as above but with a semirigid molecular displacement model (60 independent parameters) instead of the rigid-body model. This showed that the TTF molecule rigidity is preserved in the locking phase, the dominant displacement being a sliding in the molecular plane in the longest axis direction. By contrast, the TCNQ molecules undergo a large out-of-plane intramolecular distortion resembling that observed in TEA(TCNQ)₂ [23], that is, mainly a displacement of the quinoid ring perpendicular to the mean molecular plane (Fig. 14).

Both structural studies confirm the charge density polarizations observed by other methods but allow a much better understanding of the distortion. However, it must be stressed that despite the huge efforts devoted to this work, data sets are still too limited to allow for an unconstrained refinement and only the first-order satellites have been measured. “ $4k_F$ ” satellites are about one order of magnitude weaker than “ $2k_F$ ” ones.

3. *(TMTSF)₂ClO₄*. The lattice distortion in this room-pressure superconductor is a cell doubling ($a \times 2b \times c$) due to an anion-ordering (AO) structural transition at $T_{AO} \sim 24$ K (see Section IV.A). The structural study of the ordered phase was performed first from x-ray data only [128] and then from joint neutron and x-ray data sets [129]. Neutron intensities of main reflections were measured at 7 K [130], and x-ray intensities of superstructure reflections were measured at 11 K [129]. Gallois et al. [129] then performed a rigid-body refinement from the joint x-ray/neutron data set. They observed that the distorted ClO_4^- tetrahedrons exhibit two orientations which alternate along cell axis *b* and are related through inversion

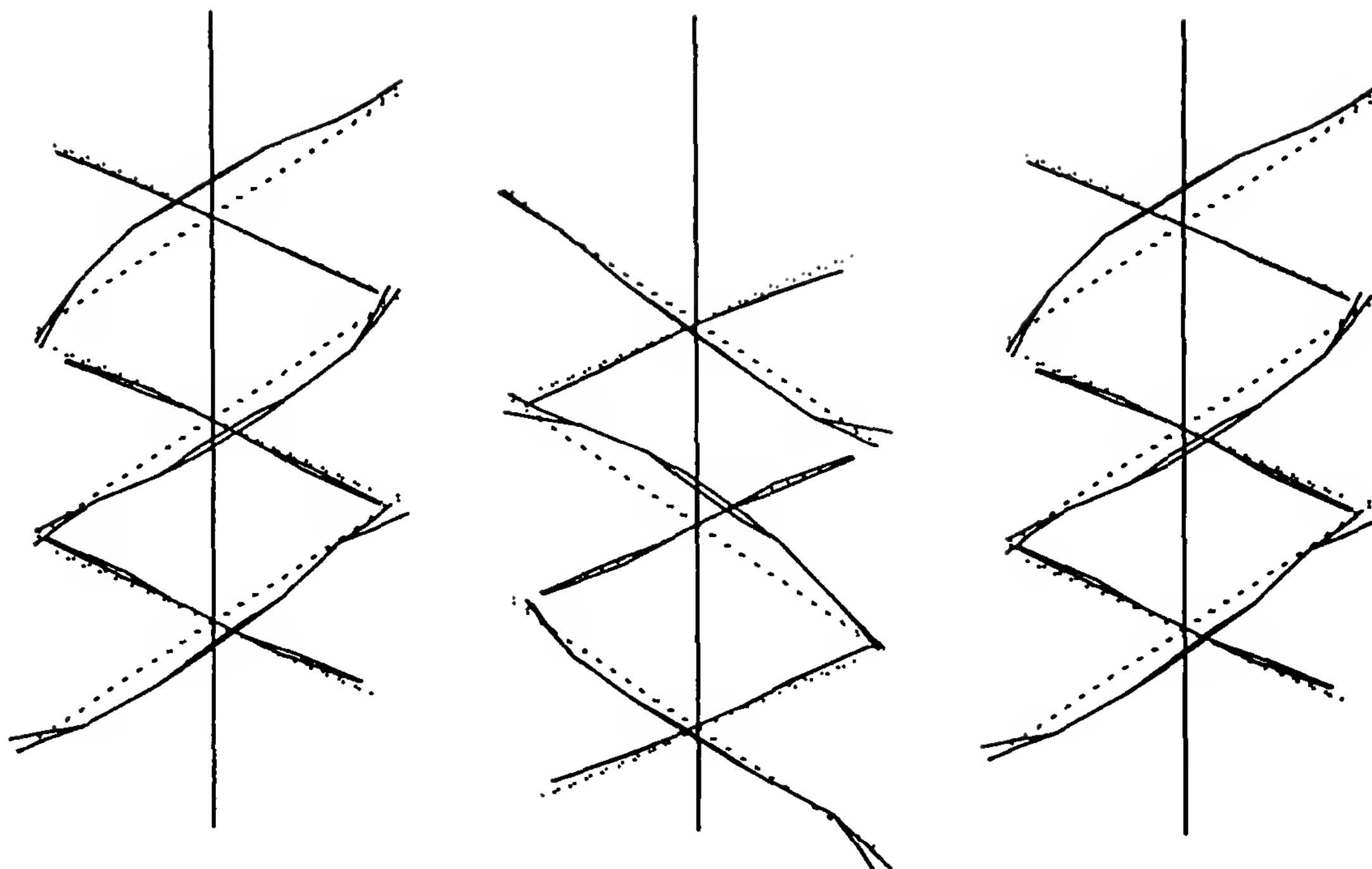


Figure 14 Representation of the chain distortion in TTF-TCNQ. Projection along the a axis of the TTF sheet lying at $x = 0$ and the TCNQ sheet lying at $x = a/2$. Continuous line, real position in the modulated structure; dashed line, mean position in the average structure. (From Ref. 40.)

centers. The organic lattice is found to be only weakly distorted and dimerized. This confirmed that the size of the ClO_4^- anion is too small to induce structural changes leading to an insulating ground state at the anion-ordering temperature T_{AO} . A similar study has been performed by Rindorf et al. [122] on $(\text{TMTSF})_2\text{ReO}_4$ and Emge et al. [131] on $(\text{TMTSF})_2\text{BF}_4$. For a detailed discussion on AO transitions in $(\text{TMTSF})_2\text{X}$ and $(\text{TMTTF})_2\text{X}$ salts, see, for example, Ref. 113.

4. $\beta\text{-(BEDT-TTF)}_2\text{I}_3$. This compound provides another interesting example of a lattice distortion study but this time, on a two-dimensional organic conductor. Upon cooling, the β_{L} phase of the compound (see Section IV.A) undergoes a structural phase transition at $T_c \sim 175$ to 200 K leading to an incommensurate modulation of the lattice [57,64] which does not exist in the case of the β_{H} phase (Fig. 15). The lattice modulation of the β_{L} phase at 120 K has been analyzed by Leung et al. [65] in terms of rigid-body sinusoidal displacement waves of the I_3^- ions and of the BEDT-TTF molecules with respective amplitudes $U_{\text{I}_3} = 0.27 \text{ \AA}$ and $U_{\text{BEDT-TTF}} = 0.11 \text{ \AA}$. Ravy et al. [67] discussed a number of additional structural features of the transition. They used a normal-beam lifting-detector x-ray diffractometer equipped with a closed-cycle helium cryocooler and ob-

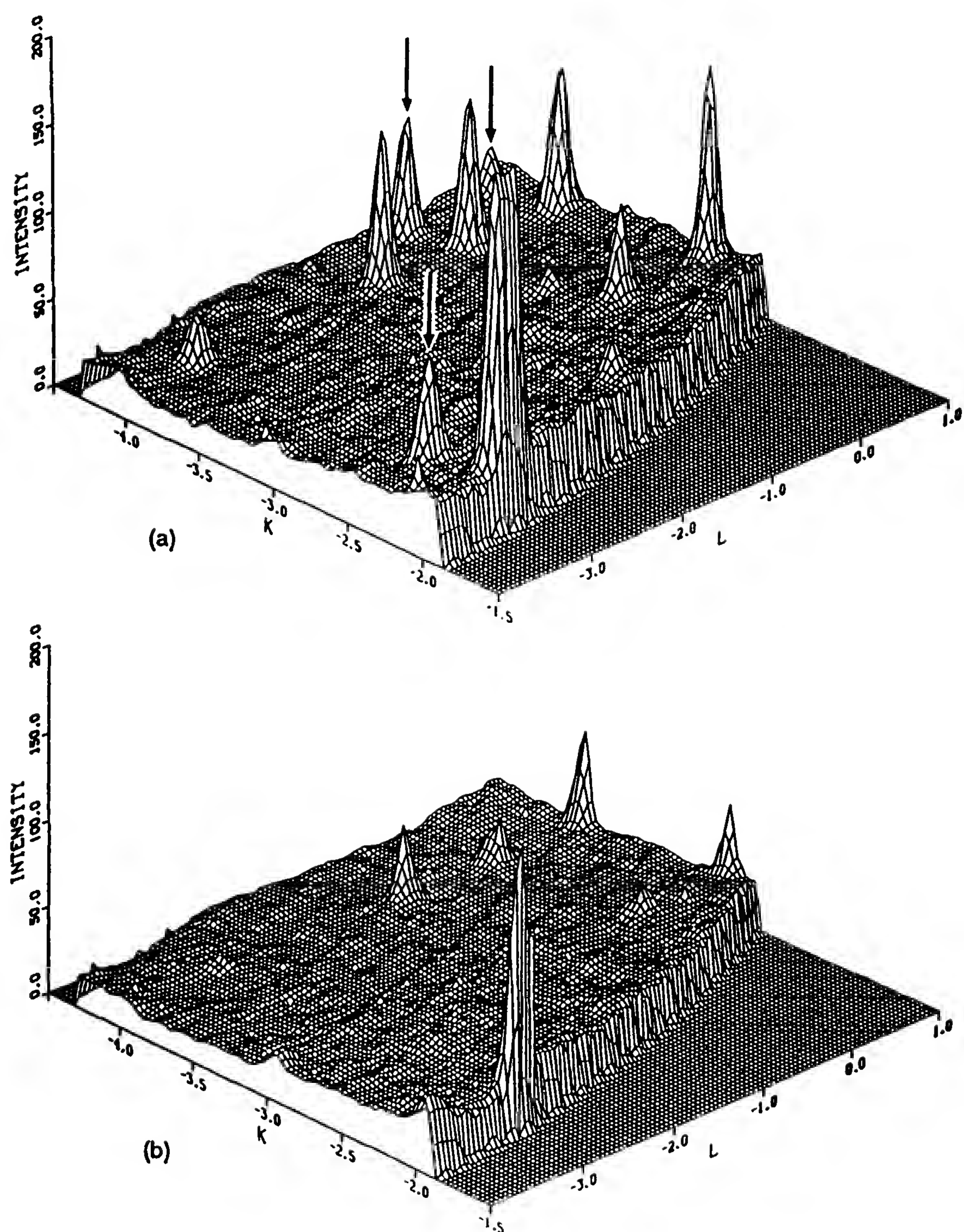


Figure 15 Neutron time-of-flight study of β -(BEDT-TTF) $_2$ I $_3$ performed at the IPNS pulsed source (Argonne). (a) Neutron diffraction intensity distribution in the $h = 4.92$ reciprocal lattice plane at 20 K and ambient pressure. Satellite peaks are observed (arrows); (b) the same reciprocal plane after applying a pressure of 0.14 GPa, warming to room temperature, and cooling back down to 20 K. (From Ref. 64.)

served pretransitional fluctuations in the form of slightly anisotropic and broad diffuse spots centered at the position of first-order satellite reflections [i.e., at $(hkl) \pm \mathbf{q}_c$ with $\mathbf{q}_c = 0.075 \pm 0.003\mathbf{a}^* + 0.275 \pm 0.005\mathbf{b}^* + 0.205 \pm 0.005\mathbf{c}^*$]. The corresponding spatial correlation length is anisotropic $\xi_{c^*}:\xi_{a^*}:\xi_{b^*} = 6:3:2$ and is large in a direction orthogonal to the BEDT-TTF sheets, where the electron gas has a two-dimensional character. It is thus concluded that the transition is not driven by the electron gas but rather by the $\text{CH}_2\cdots\text{I}$ coupling along \mathbf{c}^* between BEDT-TTF molecules and I_3^- anions. Below T_c , sharp and strong first-order satellites ($\frac{1}{10}$ of the intensity of main reflections) are observed as well as higher-order satellites at $Q_n = Q_0 + n\mathbf{q}_c$ with $n = \pm 1, \pm 2, \pm 3, 4, 5$. The relative intensities of the latter indicate that the modulation is not strictly sinusoidal. Among many other interesting results of Ravy et al. is their analysis of the modulation. The wave vector is triply incommensurate and the period in the \mathbf{q}_c direction corresponds approximately to six molecules. However, within experimental error, the wave vector is almost commensurate with $\mathbf{q}_c = \frac{1}{14}(\mathbf{a}^* + 4\mathbf{b}^* + 3\mathbf{c}^*)$, but Ravy et al. postulated that a lock-in effect due to the weak potential of commensurability will be effective only at low temperature.

What is apparent from the examples above is that, in most cases, the key problem is the measuring of a large enough number of weak (or even very weak) satellites or superstructure reflections. A limited data set forces the use of rigid-body refinements and may lead to inaccurate results. However, we may expect that new, very high flux synchrotron sources may help to solve this problem in the near future.

D. Diffuse Scattering

The x-ray monochromatic Laue technique or fixed-crystal fixed-film technique was pioneered by the Laboratoire de Physiques des Solides at Orsay (France). The instrument, as described in Ref. 132, consists of a low-temperature photographic camera with the film in the form of a cylinder normal to the beam axis. The crystal is mounted at the cold end of a cryocooler ($T_{\min} = 10$ K), closed by a shroud filled with helium gas to ensure good thermal exchange (Fig. 16). The shroud has Mylar windows on both the incident and diffracted beam sides. The vacuum shield has a Mylar window on the incident beam side and on the diffracted beam side a beryllium window (0.4 mm thick) against which the photographic film is simply pressed. A doubly curved graphite monochromator provides an incident beam with a large divergence, and thus the flux received by the sample is much larger than for normal photographic cameras. Finally, the radiation used is CuK_α since the sample diffracting power is larger at longer

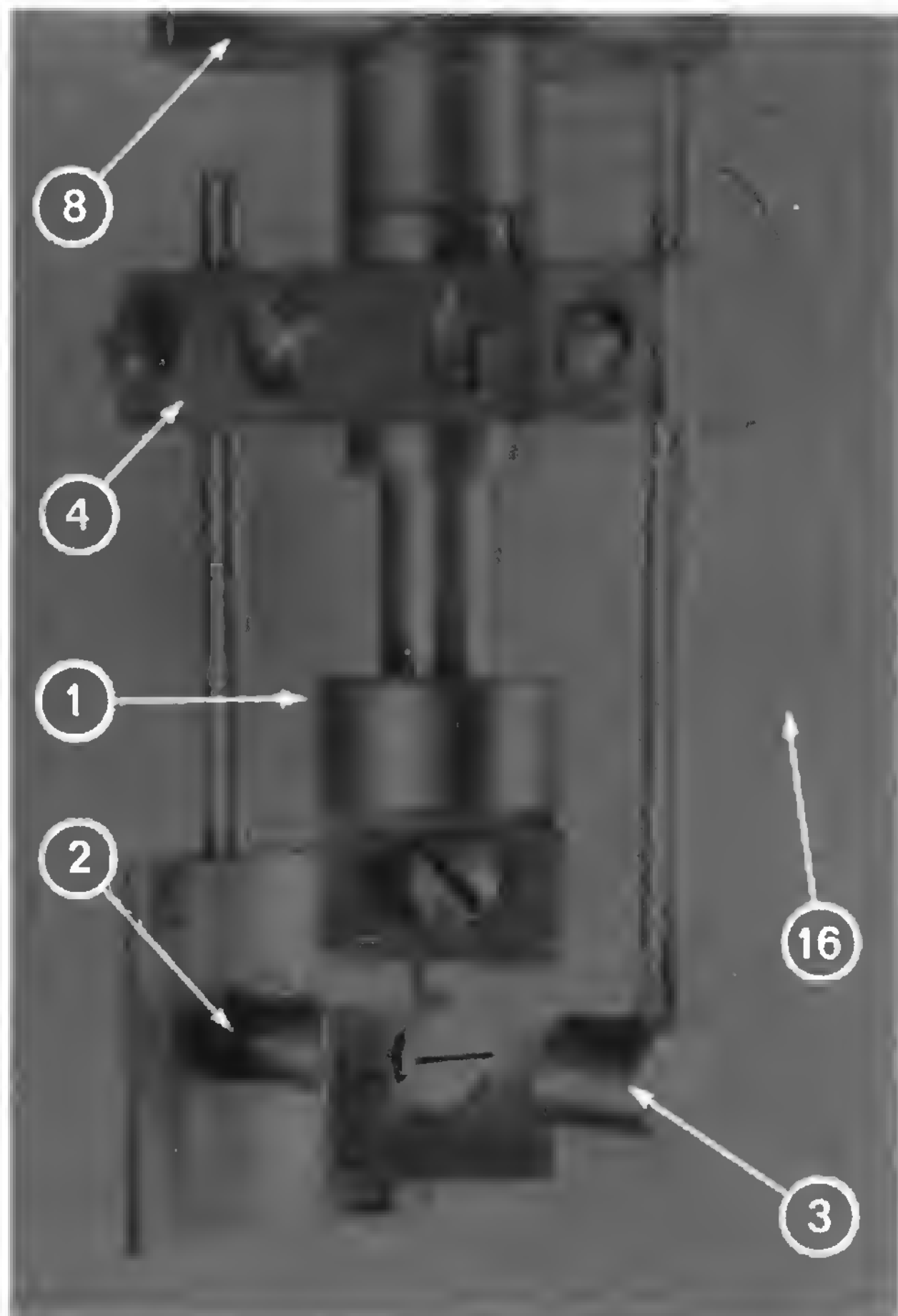


Figure 16 Sample holder assembly of a "monochromatic Laue" camera. 1, Brass sample holder; 2, collimator; 3, beam stop; 4, orienting arm; 8, part attached to the cold tip of the cryocooler and holding the cold shroud; 16, thermocouple. (From Ref. 132.)

wavelengths. In other words, beam intensity is favored to the detriment of resolution, while absorption and scattering by walls and air are kept to a minimum.

The diffraction observed comes from the intersection volume of the sample reciprocal space and the Ewald sphere thickened by the beam divergency.

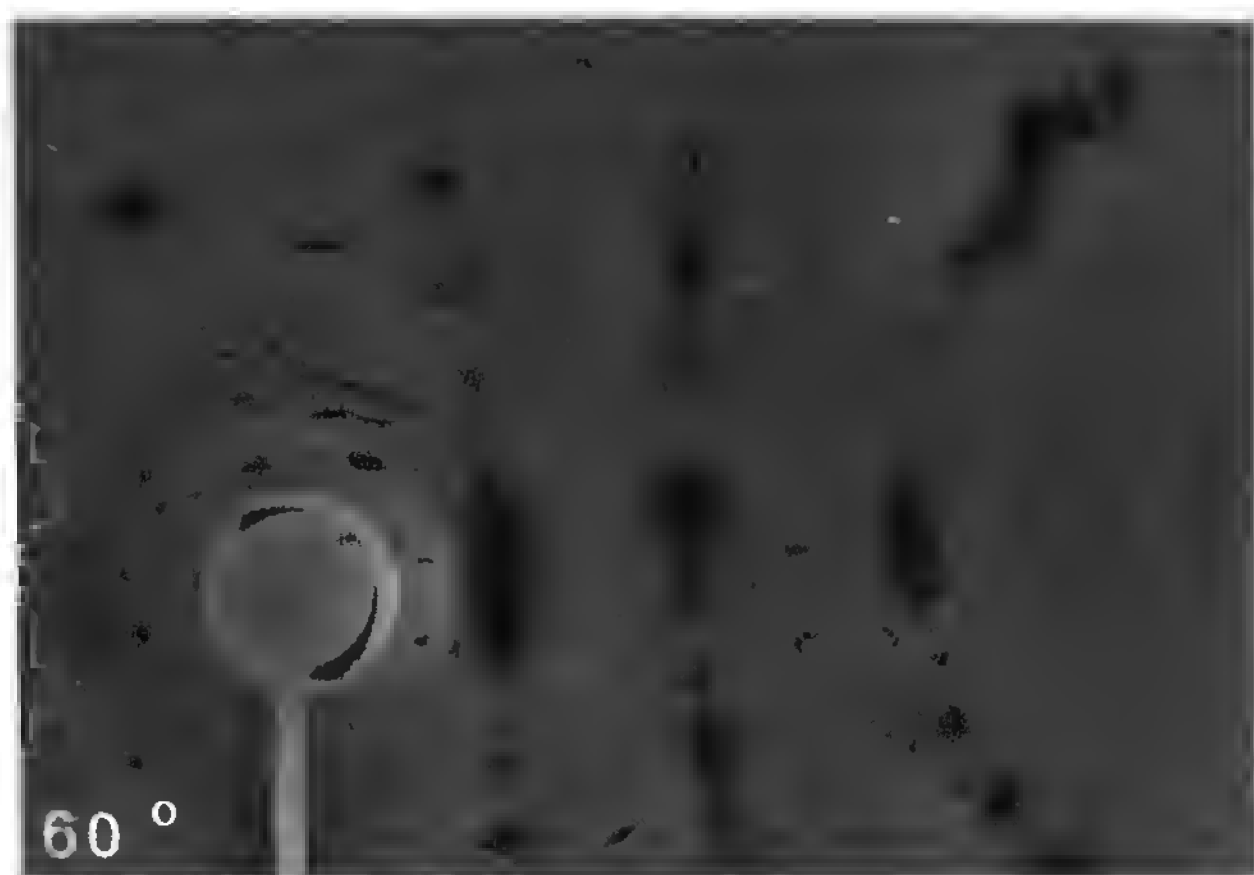
Since crystal and film are fixed, only a small part of reciprocal space can be observed at a time, but a reciprocal point of the diffracting volume scatters during the whole exposure time. By contrast, scanning techniques such as Weissenberg or precession cameras see a larger part of reciprocal space, but each reciprocal point stays only a short time on the Ewald sphere.

The diffracting volume generally contains a few main Bragg peaks, which give very large saturated spots covering part of the pattern but may also exhibit additional scattering due to disorder or to phonons of exceptionally low frequency. To illustrate the use of this technique in the case of quasi-one-dimensional conductors, we consider a material exhibiting $2k_F$ and/or $4k_F$ pretransitional fluctuations. Due to their one-dimensional nature, the fluctuations are responsible for a set of diffuse reciprocal planes normal to the conducting chain axis. The scattering coming from the intersection of the diffuse planes and the Ewald sphere produces a set of continuous or interrupted diffuse lines (Fig. 17). At lower temperature, if a Peierls or spin-Peierls transition occurs, the weak diffuse precursor lines condense into weak satellite reflections.

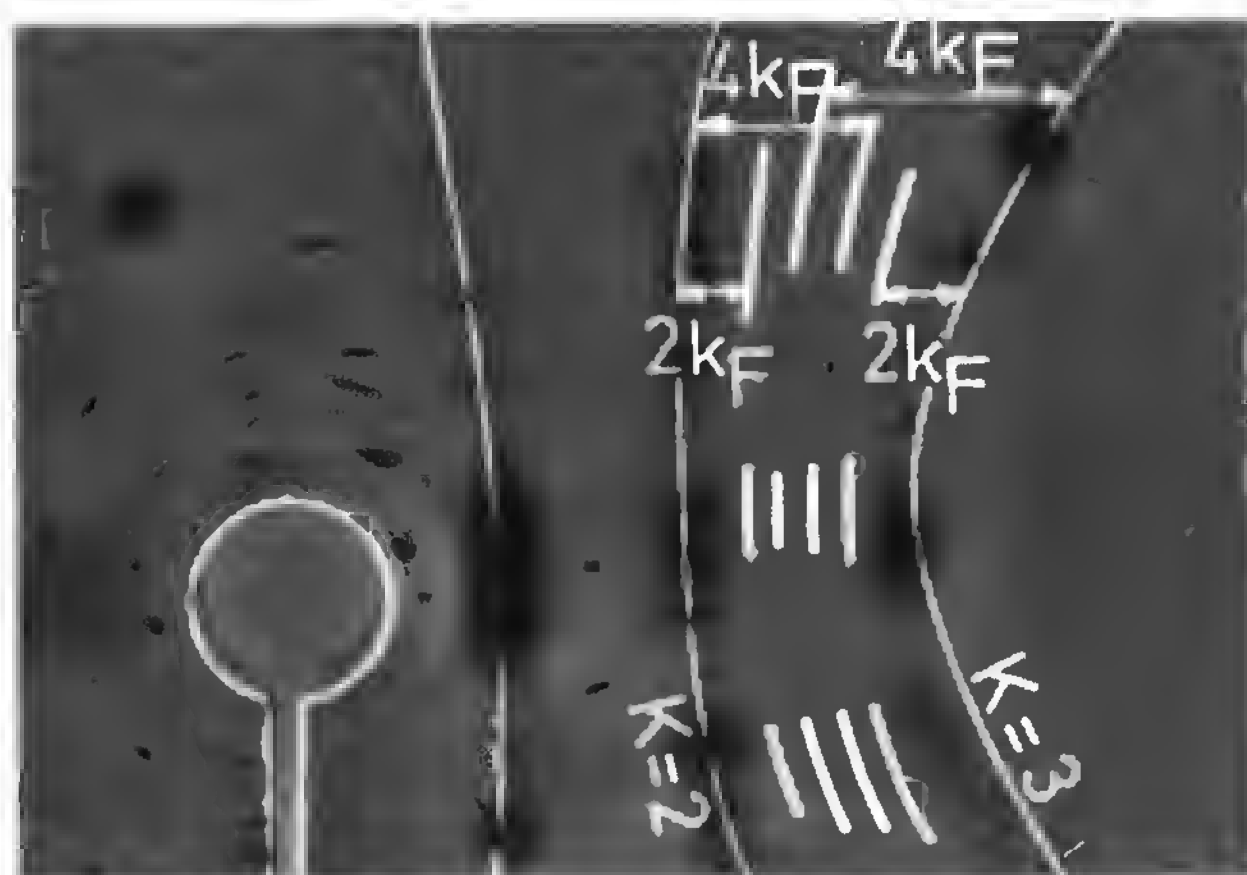
One of the great advantages of the fixed-film fixed-crystal technique is that even with a conventional x-ray tube, it makes possible the observation of extremely weak diffuse lines or satellites. It is thus an outstanding tool for the study of low-dimensional conductors, but some experience is required to read the patterns. To improve the accuracy of the measurements (e.g., extraction of accurate wave vector coordinates) a microdensitometer reading is often necessary (see, e.g., Ref. 119). Film results can also be used as a starting point for counter measurements (see, e.g., Ref. 74).

A better compromise of intensity versus resolution can be obtained on synchrotron radiation sources since the beam flux is several orders of magnitude higher than with conventional sources, even for very small divergences. This is illustrated in Fig. 18, where satellites very close to a Bragg peak can easily be observed. However, the drawback is that the very small beam divergence leads to a very small diffracting reciprocal space volume thus making some observations more difficult.

Because x-ray and neutron atomic scattering factors are very different, neutron diffuse scattering could be a very useful complementary tool to the x-ray technique for the study of lattice distortions. Unfortunately, even the best neutron sources are relatively weak, less effort has been made to design a high-performance instrument, and low-dimensional organic conductors are rarely available in the form of large enough single crystals (see Section XII.A). Nonetheless, some fixed-film fixed-crystal patterns have been recorded on the neutron Weissenberg camera D12 at the ILL. Superstructure reflections were observed at low temperature in TMA.TCNQ.I [135] and $\text{TTT}_2\text{I}_{3+\delta}$ [136], but the satellite reflections in TTF-TCNQ below



(a)



(b)

Figure 17 Diffuse x-ray pattern of TTF-TCNQ at 60 K. (a) Pattern showing the $2k_F$ and $4k_F$ one-dimensional precursors at $0.294b^*$ and $0.59b^*$ from the layer of Bragg reflections. They appear as interrupted diffuse lines due to the structure factor of scattering molecules. (b) Schematic representation of the diffuse lines. (From Ref. 133.)

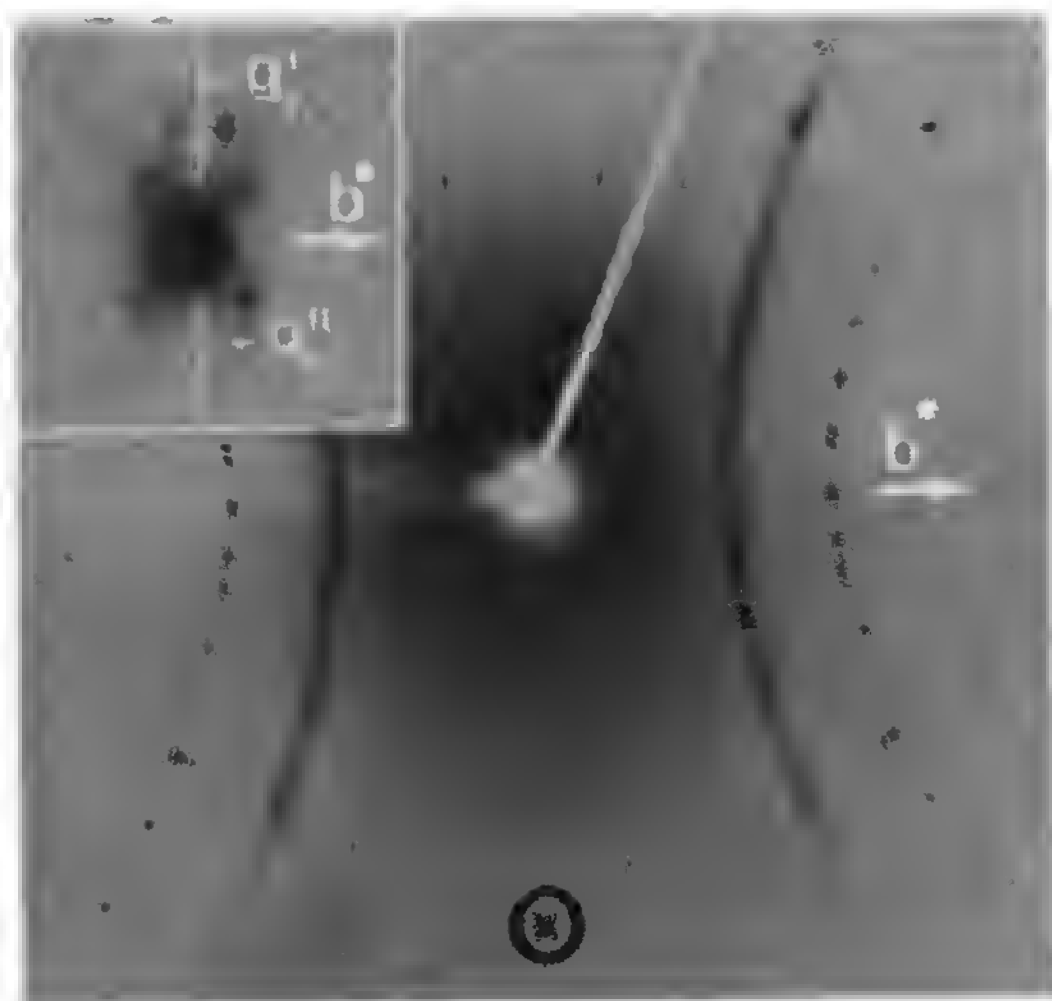


Figure 18 Synchrotron fixed-film fixed-crystal pattern obtained at LURE (France) on $\text{TTT}_2\text{I}_{3+\delta}$ at 120 K. The sample has its b^* axis horizontal. The diffuse lines are due to a one-dimensional disorder of the I_3 columns. Top left corner: a magnified detail of a main Bragg reflection surrounded by two families of satellites. The latter are attributed to the existence of two families of iodine chains. (From Ref. 134.)

the Peierls distortion could not be detected (J. P. Pouget and A. Filhol, unpublished). In another study, these satellites were observed successfully with neutrons but with the help of very large TTF-TCNQ samples mounted on triple-axis spectrometers [137].

VII. CHARGE TRANSFER AND CHARGE DISTRIBUTION

The physical properties of low-dimensional organic conductors depend greatly on the amount of charge transferred, ρ , between the constituent donor (D) and acceptor (A) molecules:



and/or on the charge distribution within a conducting column. However, each family of materials behaves differently. In charge-transfer complexes, both segregated D and A stacks conduct. In these salts, the charge transfer is incomplete and, generally, ρ cannot be guessed from the stoichiometry. In radical-ion salts (RISs), typically one stack conducts, the other is made of totally ionized counterions, and thus ρ is fixed by the stoichiometry. For

example, in many TCNQ salts the cation gives one electron to the TCNQ stack and thus $\rho = 1e^-$ for a 1:1 stoichiometry and $\rho = \frac{1}{2}e^-$ for a 1:2 stoichiometry (see Chapter 8 of this volume). In the latter case, if the two TCNQs are independent, the effective charge distribution over those moieties cannot be predicted.* In $(\text{TMTSF})_2\text{X}$ or $(\text{TMTTF})_2\text{X}$ salts, the inorganic anion X is singly charged, and owing to the 1:2 stoichiometry, $\rho = \frac{1}{2}$ hole per donor molecule. Since there is only one independent organic moiety in the unit cell, each TMTSF receives the same charge, but this may change at low temperature if the material undergoes a phase transition leading to a superstructure. In $(\text{BEDT-TTF})_2\text{X}$ or $(\text{BEDT-TTF})_n\text{X}$ materials there are generally several independent organic ions and a charge localization may exist.

However, for RIS the hypothesis of some participation of the counterions in the conductivity and superconductivity has sometimes been raised [138–141]. This would imply a back transfer of the charges and thus observed values of ρ slightly different from the formal ones. This phenomenon has not been confirmed so far, perhaps because measurements of ρ are not accurate enough.

The study of the T and/or P dependence of charge transfer or charge localization in organic conductors is very useful since their transport properties are directly influenced by these quantities. Except when fixed by stoichiometry or lattice symmetry, charge transfer and/or charge localization are the result of a delicate balance between the various contributions to the cohesion energy, which, of course, is modified by external constraints. Thus we show below how crystallographic results can be used for such studies, although another approach is possible through band structures computed from structural data (see Section VIII).

A detailed discussion of charge transfer in quasi-one-dimensional organic conductors can be found in Refs. 114 and 142. According to the classification of Ref. 114, three methods can be used to evaluate the charge transfer:

1. *Calculations.* In theory, ρ can be obtained by minimizing the part of the cohesive energy that depends on it. In practice, for large structures, the various contributions cannot be calculated with enough accuracy to give reliable results, and thus such a calculation is far beyond what is presently feasible.

*Of course, more complicated situations may exist, such as $n:m$ stoichiometries or ternary salts. See, for example, Graja [142] for a classification of molecular conductors on the basis of conductivity, crystal packing, and charge transfer. See also Pouget [114] for a discussion of charge transfer and instabilities in a number of materials.

2. *Direct methods.* The charge per molecule is measured either directly (e.g., very accurate structural determination, x-ray photoelectron spectroscopy) or through the relative change of an intramolecular parameter sensitive to the charge (e.g., intramolecular bond length, intramolecular vibration frequency). The accuracy is relatively poor ($\geq 10\%$).
3. *Structural methods.* ρ is obtained, with an accuracy of a few percent, through measurement of the critical wave vector of the structural instability accompanying the $2k_F$ or $4k_F$ instability of the one-dimensional electron gas.

In the following sections we consider crystallographic techniques only.

A. X-Ray or Neutron Diffuse Scattering

In quasi-one-dimensional conductors, the one-dimensional electron gas instability is responsible for the formation of a charge density wave (CDW) with wave vector $2k_F$ and/or $4k_F$ via electron-phonon coupling. Thus the measurement, in reciprocal wave vector units, of the corresponding $4k_F$ and $2k_F$ scattering wave vectors gives the value and twice the value of the charge transfer ρ , respectively (e.g., see Ref. 114).

In practice there are three main difficulties in the use of this technique. The $2k_F$ and $4k_F$ scattering is not observed in all materials or at all temperatures. Fortunately, pretransitional effects (one-dimensional fluctuations) are often observed in a wide temperature range above T_c [114]. Second, the corresponding scattering is often very weak and requires special measurement techniques. For example, in the case of TTF-TCNQ, the intensity of $2k_F$ satellites is 10^{-4} that of main reflections and the one-dimensional scattering at 60 K is a further 10^{-2} to 10^{-3} weaker [133]. Third, to get ρ , one must decide whether the observed instability occurs at the $2k_F$ or at the $4k_F$ electronic wave vector.

The difficulty in assigning the observed scattering to a $2k_F$ or $4k_F$ instability is illustrated by the case of NMP-TCNQ (NMP is *N*-methylphenazinium), which is discussed in detail by Pouget [114]. First, Pouget et al. [143] showed that the room temperature x-ray diffuse scattering at reduced wave vectors $\pm 0.094na^*$ (n integers in the range 0 to 5) is not critical and cannot be attributed to $2k_F$ or $4k_F$ scattering. Then, real quasi-one-dimensional critical scattering was observed at wave vectors $q_1 = \frac{1}{8}a^*$ and $q_2 = \frac{1}{3}a^*$, but due to their special values, q_1 and q_2 could neither be ascribed directly to $2k_F$ and $4k_F$ instabilities nor attributed to a given stack. As a consequence it was not possible to decide whether the charge transfer was $\frac{2}{3}$ or $\frac{1}{3}$. Finally, the ambiguity was removed by means of the study of the alloy $\text{NMP}_x\text{Phen}_{1-x}\text{TCNQ}$, where non-totally symmetric NMP molecules are substituted by neutral phenazine (Phen). Without going into detail, let us simply

note here that the disorder introduced by a small amount of phenazine molecules only suppresses the q_1 scattering, and as a consequence, q_1 was attributed to the NMP stacks, and the correct value of charge transfer is thus $\rho = \frac{2}{3}e^-$.

Several methods can be used to detect and measure the lattice instabilities and distortions. The most popular one is certainly the x-ray fixed-film fixed-crystal technique described in Section VI.D, which was first applied to an organic metal by Denoyer et al. [144]. However x-ray counter measurements, using photographic results as a starting point, generally provide more quantitative results. Electron microdiffraction is probably sensitive enough, but its use is difficult with organic conductors (see Section X). Neutron diffractometers provided excellent results, especially when a complicated sample environment is necessary. For example, Megtert et al. [145] established the T,P phase diagram of TTF-TCNQ with the help of the high neutron flux available at the ILL, the high signal to noise ratio of a triple-axis spectrometer, and large deuterated samples. They observed a rapid increase in ρ with pressure toward a locking value of $\frac{2}{3}e^-$ at 1.45 GPa (Fig. 19). This was the first direct evidence of commensurability effects on the Fermi wave vector of one-dimensional conductors. However, the behavior of the conductivity [146] suggests that the locking exists only in the pressure range 1.4 to 1.8 GPa and that ρ again increases at higher pressures.

B. Numerical Integration of X-Ray Diffraction Amplitudes

It was shown long ago that accurate electron density maps can be obtained from three-dimensional x-ray diffraction data (see Section XI). Furthermore, Coppens [147], one of the pioneers in the technique, demonstrated that a direct estimate of the amount of charge transferred can be obtained by means of a numerical charge integration in the volume occupied by each molecule in the asymmetric unit. The method, applied to TTF-TCNQ at 100 K, provided one of the very first reliable estimates of the charge on TTF and TCNQ ions [i.e., 0.48 and 0.60 (± 0.15) electrons, respectively]. However, it cannot be of routine use since highly accurate data sets are mandatory.

Coppens [147] analyzed the difficulties of the numerical integration method as follows. In the centrosymmetric case, the total electron population P is given by

$$P = \int \sum \frac{F_{\text{obs}}}{k} \cos 2\pi \mathbf{H} \cdot \mathbf{r} \, d\tau + \int F_{000} \, d\tau$$

where the integrals are over the molecular volume, k is the scale factor defined by $F_{\text{obs}} = kF_{\text{calc}}$, and F and H are the structure factor and reciprocal-

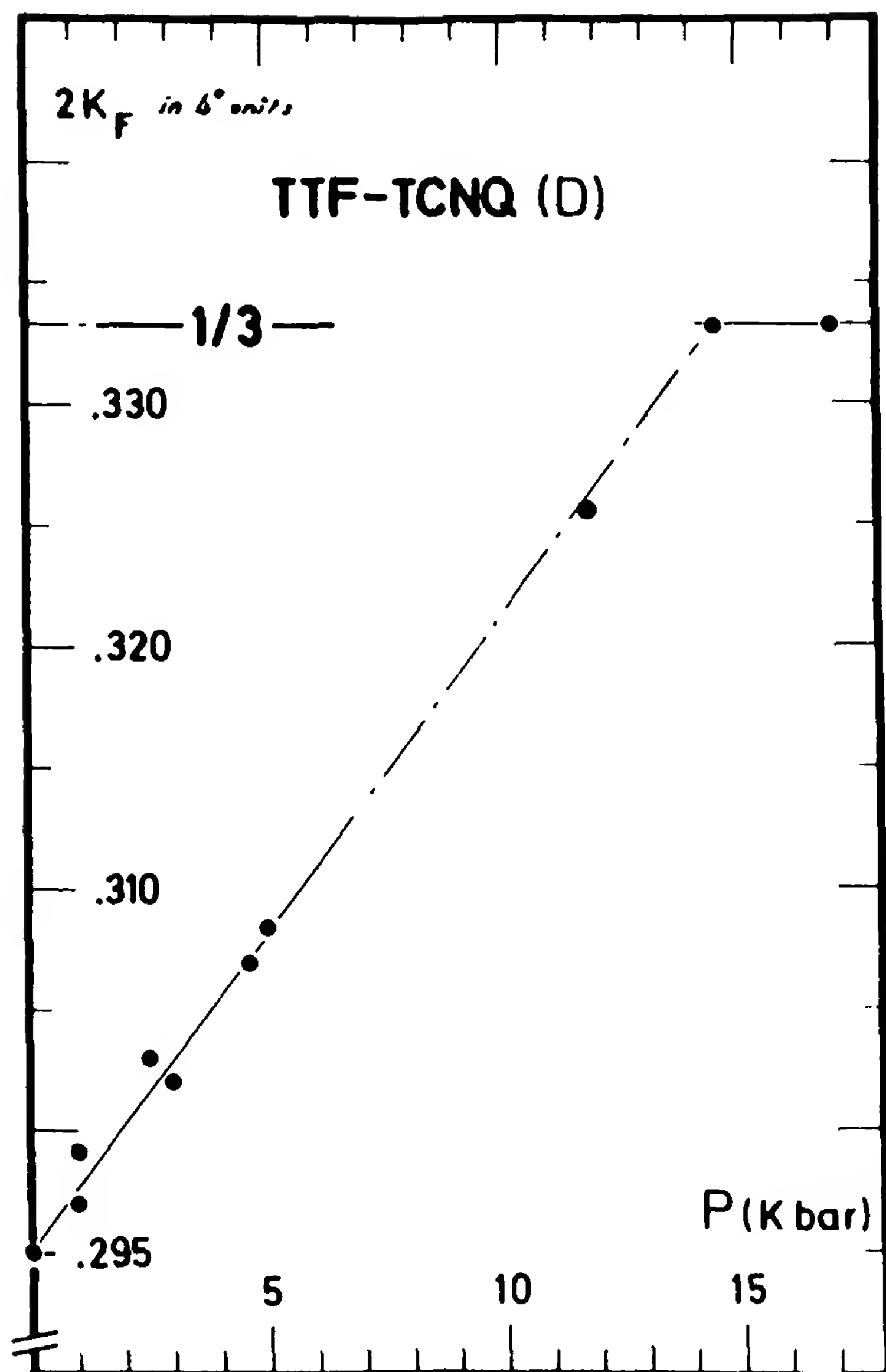


Figure 19 Pressure dependence of the $2k_F$ wave vector in TTF-TCNQ. $2k_F$ locks at the value $\frac{1}{3}b^*$ at 1.45 GPa, corresponding to the modulation period $3b$ and to a charge transfer of $\frac{1}{3}$ electron. (From Ref. 145.)

lattice vector, respectively. This tells us that the mean value of the computed charge transfer will be sensitive to the estimated value of the scale factor k , a quantity that is not obtained easily with very good accuracy. Also, the space must be subdivided among the molecules, and thus Coppens used a method based on the ratio of the van der Waals radii of contacting atoms. He observed that integrated charges are not very dependent on the boundary location, which is indeed consistent with the fact that the regions between the molecules contain little density. Finally, the measured in-

tensities from which the F_{obs} are derived must be very accurate and carefully corrected for absorption and extinction, since this acts directly on error bars on the electron density. Integration of a fitted multipolar model could also be used and should be less prone to errors in F_{obs} . Measurements and analysis techniques have developed quite a bit since 1975 [148], but these structures are still considered to be difficult for such work.

C. Bond Lengths

Generally speaking, molecular bond length and angles are expected to be slightly modified by a gain or loss of charge. In organic conductors the change is small but perceptible, especially on intramolecular bond lengths. To analyze this, Flandrois and Chasseau [72] collected all x-ray structural data available in 1977 on TCNQ-based materials. First, they observed that the C=C bond labeled c (Fig. 20) exhibits the largest change (1.373 Å in the neutral TCNQ⁰; 1.420 Å in the anion TCNQ⁻), thus indicating a modification in the quinoid character of the TCNQ. Second, they found an almost linear relationship between the difference in bond lengths (b–c) and (c–d) and the ionicity of a given TCNQ molecule. This resulted in a very simple, easy-to-use method which provides good estimates of the degree of charge transfer and of the charge distribution in TCNQ-based organic conductors. However, it must be kept in mind that the results of this “bond length method” are very sensitive to the accuracy of structure determinations.

To illustrate the latter statement, let us consider the case of TEA(TCNQ)₂, in which two independent cations TCNQ_A and TCNQ_B share one unpaired electron. The stacking in a conducting column is formally tetramerized

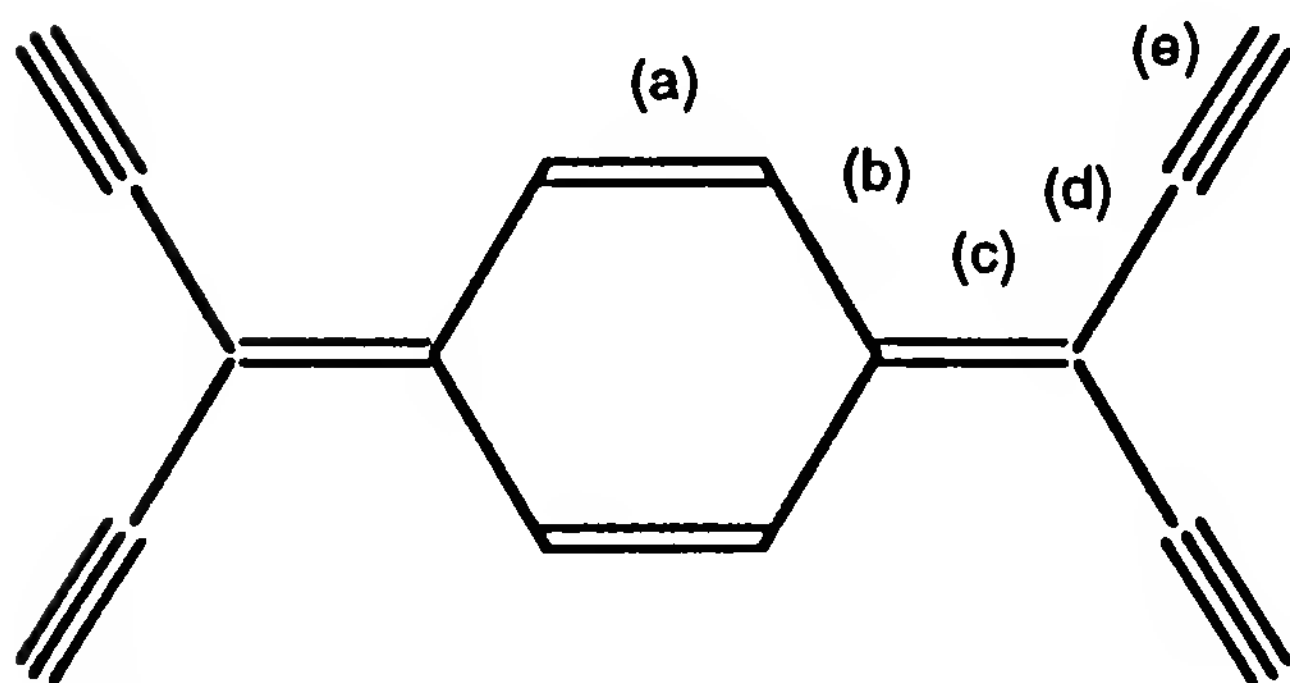


Figure 20 TCNQ molecule.

but dimers A–B exhibit the shortest interplanar spacing and the best molecular overlap. From the structural data of Ref. 19, Flandrois and Chasseau found a strong charge localization of 0.84 e and 0.30 e, respectively, the largest charge being on TCNQ_A, which forms a N—H · · · N bond with the cation. This result was in good agreement with observations on other TCNQ salts but in disagreement with spectroscopic results [149], for which the charge should be equidistributed. Subsequently, Filhol et al. [22,23] demonstrated that the TEA cation is disordered over two nonequivalent sites and that both TCNQ_A and TCNQ_B are involved in a N—H · · · N bond. Finally, accounting for the disorder in the refinement of the room-temperature structure led to a nearly symmetrical charge distribution of 0.54(6) e on TCNQ_A and 0.46(4) e on TCNQ_B.

The bond length method of Flandrois and Chasseau can be used to study the variation of charge transfer or charge distribution with temperature or pressure. Indeed, while intermolecular distances exhibit large changes with T and P , intramolecular ones are much more insensitive; furthermore, since only length differences are used, this guarantees that the method is valid at least in the usual T and P range. To emphasize this point, we now consider the temperature dependence of the charge distribution in TEA(TCNQ)₂. Using the values obtained by Filhol and Thomas [23] for five temperatures between 345 and 110 K, Farges [109] showed that the charge distribution in that compound follows the simple law $q_A = (\frac{1}{2} + T_0/T)$ e and $q_B = (\frac{1}{2} - T_0/T)$ e with $T_0 = 24$ K and exhibits the remarkable limit $q_A = q_B = e/2$ if $T \rightarrow \infty$. From these findings, several unexplained aspects of the electrical properties of that material could be clarified—in particular, the sign anomaly of the thermopower.

We should note here that the bond length versus charge-transfer relationship in TCNQ molecules has been established by Flandrois and Chasseau [72] from x-ray data and is thus valid for x-ray data only. In fact, x-rays and neutrons provide atom positions which generally do not coincide. The former radiation measures the charge centroid location, while the latter measures the nuclear position. As a consequence, a different parametrization must be used for neutron data [36].

A similar approach can be tried on other molecules. For example, Kobayashi et al. [150] and Fettouhi [151] have tabulated some intramolecular distances in BEDT-TTF molecules as a function of the charge transfer. However, the use of combinations of intramolecular bond lengths lead to results less sensitive to experimental errors (D. Chasseau, private communication, 1993).

VIII. BAND STRUCTURE AND FERMI SURFACE

The electronic properties of organic conductors are discussed by physicists in terms of band structure and Fermi surface. The shape of the band structure is defined by the dispersion energy and characterizes the electronic properties of the material (semiconductor, semimetals, metals, etc.); the Fermi surface is the limit between empty and occupied electronic states, and its shape (open, closed, nested, etc.) characterizes the dimensionality of the electron gas. From band dispersion and filling one can easily deduce whether the studied material is a metal, a semiconductor, or an insulator (occurrence of a gap at the Fermi energy). The intra- and interchain bandwidths can be estimated, for example, from normal-incidence polarized reflectance, and the densities of state at the Fermi level can be used in the modeling of physical observations. The Fermi surface topology is of importance to predict or explain the existence of instabilities of the electronic gas (nesting vector concept; see Chapter 2 of this book). Fermi surfaces calculated from structural data can be compared to those observed by means of the Shubnikov–de Hass method in the case of two- or three-dimensional metals [152].

The calculations may be done either at the *ab initio* or semiempirical level. In the case of organic conductors the large number of atoms per unit cell precludes the use of *ab initio* methods. In fact, calculations at the latter level have been done once by Kasowki and Whangbo [153] for β -(BEDT-TTF)₂I₃ and showed a close agreement between the *ab initio* band structures and those calculated using the extended Hückel (EH) approach (semiempirical). Therefore, in practice, the latter approach is the one used to calculate the band structures of organic conductors [61,154–158]. Moreover, the different calculations have shown that the energy dispersion and Fermi surfaces may be described correctly from the transfer integrals calculated by the EH method. These transfer integrals characterize the electronic coupling between interacting molecules.

Evaluation of the electronic coupling between interacting molecules has been somewhat controversial in the past since structural data were interpreted in terms of simple atom–atom distances (van der Waals contacts) or geometrical molecular overlap, disregarding the bonding and antibonding character of interactions. In fact, a quantitative characterization of the electronic coupling requires computation of the transfer integrals from the atomic positions provided by a structural study. For example, Grant [154,155] has studied the (TMTSF)₂X salts using the room-temperature structure data. However, one of the most interesting aspects of these materials is that their low-temperature ground state (nonmagnetic insulating, antiferromagnetic, or superconducting) is pressure sensitive. Thus Grant used

mainly room-temperature structural data but with modified cell dimensions to account for compressibility. On the other hand, Ducasse et al. [156,157] used true LT and HP structural data sets and showed that nonexact atomic positions substantially modify the results. In particular, Grant's data implied that the nesting vector should be commensurate with the lattice, whereas the LT and HP results have shown that this vector might be incommensurate. This has been confirmed by NMR experiments [159,160], and there is good agreement between the anisotropy of the calculated transfer integrals and the conductivity anisotropy observed.

Another demonstration of the validity of these calculations is provided by BEDT-TTF-based salts. The calculated Fermi surface of these materials exhibit closed orbits characteristic of two-dimensional electronic interactions and this has been confirmed experimentally. For example, in the case of $(\text{BEDT-TTF})_2\text{I}_3$, the calculated surface of these orbits (Fig. 21) [61] agrees well with the one measured by magnetic experiments [161]. However, the overall good agreement between calculation and experiment must not hide the fact that some qualitative discrepancies may arise in some cases. For example, $(\text{TMTTF})_2\text{X}$ salts exhibit a resistivity minimum at a temperature at which no structural transition has yet been observed. The resistivity minimum is not explained by the one-electron band structure, and to account for this progressive electron localization, it is necessary to include in the calculations the effect of the electronic correlations [162]. Another difficulty has been met in the case of the semiconducting materials $\alpha'-(\text{BEDT-TTF})_2\text{X}$, for which the calculated band structure exhibits the characteristic features of a metal [93,97,100] and it is not yet understood

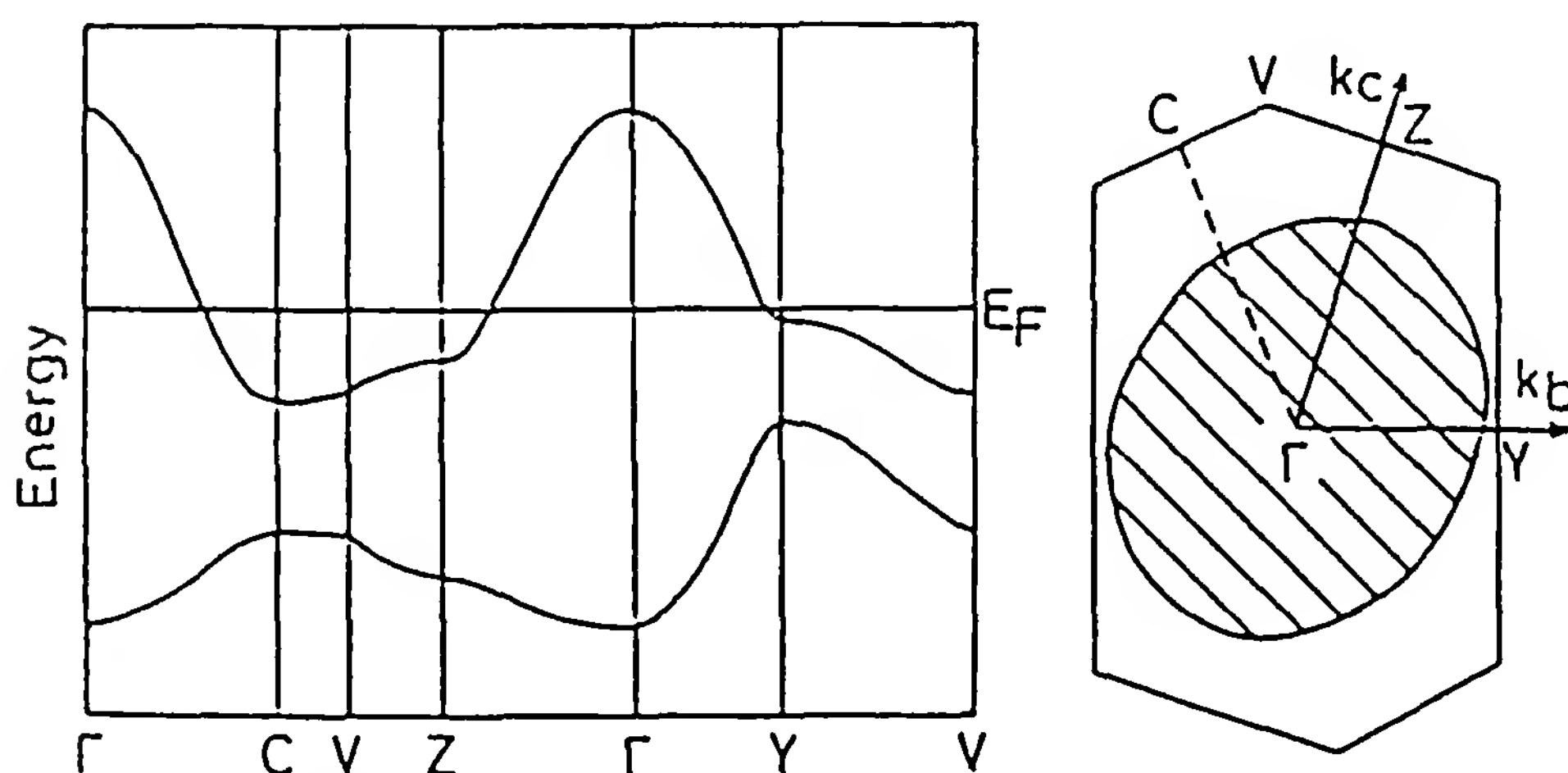


Figure 21 Energy band structure and the Fermi surface of $\beta-(\text{BEDT-TTF})_2\text{I}_3$. Energy in arbitrary units. The shaded region indicates the holelike part. (From Ref. 61.)

if this comes from inadequate calculations or from some missing information in the structural data.

IX. LATTICE IMPERFECTIONS

Perfect crystals do not exist in real life and it has long been known that the physical properties of materials may depend at least as much on some deviations from the perfect periodicity as on the structure itself. Indeed, the structure is always averaged over a large number of unit cells and thus does not show atomic scale defects or disorder. Further, while the introduction of a controlled amount of imperfection in samples tells us very much about the physics of the material, on the contrary, uncontrolled sample imperfections may lead to incorrect or inaccurate deductions.

We consider here two types of lattice imperfections, twinning and disorder. They may preexist in crystals of organic conductors or appear during measurements. Their magnitude is either controlled or uncontrolled. Twinning, a result of growth conditions, is generally uncontrolled; however, in a few cases, a controlled amount of stress-induced twinning can be introduced in the sample, thus allowing for the study of its influence on physical properties. Disorder can be either intrinsic (compositional or positional) or extrinsic (irradiation-induced defects) (i.e., introduced during crystal growth or created afterward, respectively). Both may be either controlled (chemical alloying,* sample irradiation for the production of known amounts of defects, etc.) or uncontrolled (chemical impurities, irradiation during a diffraction experiment, etc.). Many papers have been devoted to controlled disorder because they are useful probes for the study of electronic properties in organic conductors (see, e.g., Ref. 166). However, in the following, we are more interested in uncontrolled lattice imperfections for their consequences on crystallographic studies. Clearly, uncontrolled lattice imperfections have something to do with sample quality, which is discussed in Sections XII.A and XII.B.

A. Twinning

Twinning, like disorder, may be responsible for altering physical properties of organic conductors and may also be a serious obstacle to high-quality structure studies. To emphasize the importance of accounting for twinning in crystallographic studies, let us consider the case of the high- T_c super-

*Chemical alloying is simply replacing parts of the molecules by isostructural and isoelectronic parts. For example, alloys such as $(\text{TTF})_{1-x}(\text{TSeF})_x\text{TCNQ}$ [163], $(\text{TMTSF})_{1-x}(\text{TMTTF})_x\text{ClO}_4$ [164], and $(\text{TMTSF})_2(\text{ClO}_4)_{1-x}(\text{ReO}_4)_x$ [165] have been obtained.

conductor YBaCuO, a material in which the oxygen plays an important role. An early single-crystal structure determination [167] led to disordered oxygen sites, while neutron powder diffraction, which is insensitive to twinning, showed ordered oxygen sites [168]. In the following we give a few examples of the influence of twinning on crystallographic results in the case of organic conductors.

The first structure determination of TTF-TCNQ was performed from a twinned sample, and thus with the exception of sulfur atoms, the refinement was limited to isotropic atomic thermal parameters [35]. Although of excellent quality ($R = 0.04$), this structure is not accurate enough to allow for some detailed analysis. For example, the agreement between chemically equivalent intramolecular bond lengths is poor and discrepancies as large as $0.010(3) \text{ \AA}$ have been observed with more recent structural data [37]. The difference is not large and could be thought of as being negligible. This is not the case because some aspects of the structural analysis of organic conductors are sensitive to subtle bond length and angle differences. For example, such an error of 0.01 \AA has notable consequences on the method of Flandrois and Chasseau [72], which estimates the charge transfer in TCNQ-based organic conductors from intramolecular bond lengths in the TCNQ moiety (see Section VII.C).

Many other examples of sample twinning can be found in the literature, from which we have selected the following. The room structure of TMA.TCNQ.I was first described as being monoclinic $C2/m$ with regular stacks of strictly flat TCNQ [27]. Later it was found that the iodine sublattice is triclinic [28], and finally, Gallois et al. [31] demonstrated that the organic lattice (A) and the iodine lattice (B) are both triclinic, twinned, and with nonparallel axes. As a result, TCNQ columns in this material are not regular but instead, weakly dimerized. The analysis of this twinning was not trivial since it is hidden by iodine disorder in some samples, and since at room temperature, lattice points of twin domains A' and A'' are superimposed strictly with $(h, k, l)_{A'}$ equal to $(h + k, \bar{k}, l)_{A''}$. However, the twinning becomes apparent below 95 K since lattice A' and A'' are no longer superimposed, due to a change in cell dimensions. In needle crystals of $(\text{TMTSF})_2\text{ClO}_4$, Ishiguro et al. [169] observed stress-induced reversible kinks and antikinks due to twinning (Fig. 22). In the superconducting materials $\beta\text{-(BEDT-TTF)}_2\text{X}$ (where $\text{X} = \text{I}_3, \text{IBr}_2$, and AuI_2), twinning can be induced by plastic deformation of the crystal with, as a consequence, T_c values increased by up to 30% [170]. In $\theta\text{-(BEDT-TTF)}_2\text{I}_3$ the orthorhombic structure reported by Kobayashi et al. [171] is an average one since a more detailed analysis of the iodine sublattice [16] has indicated that samples are twinned, each domain being monoclinic with space group

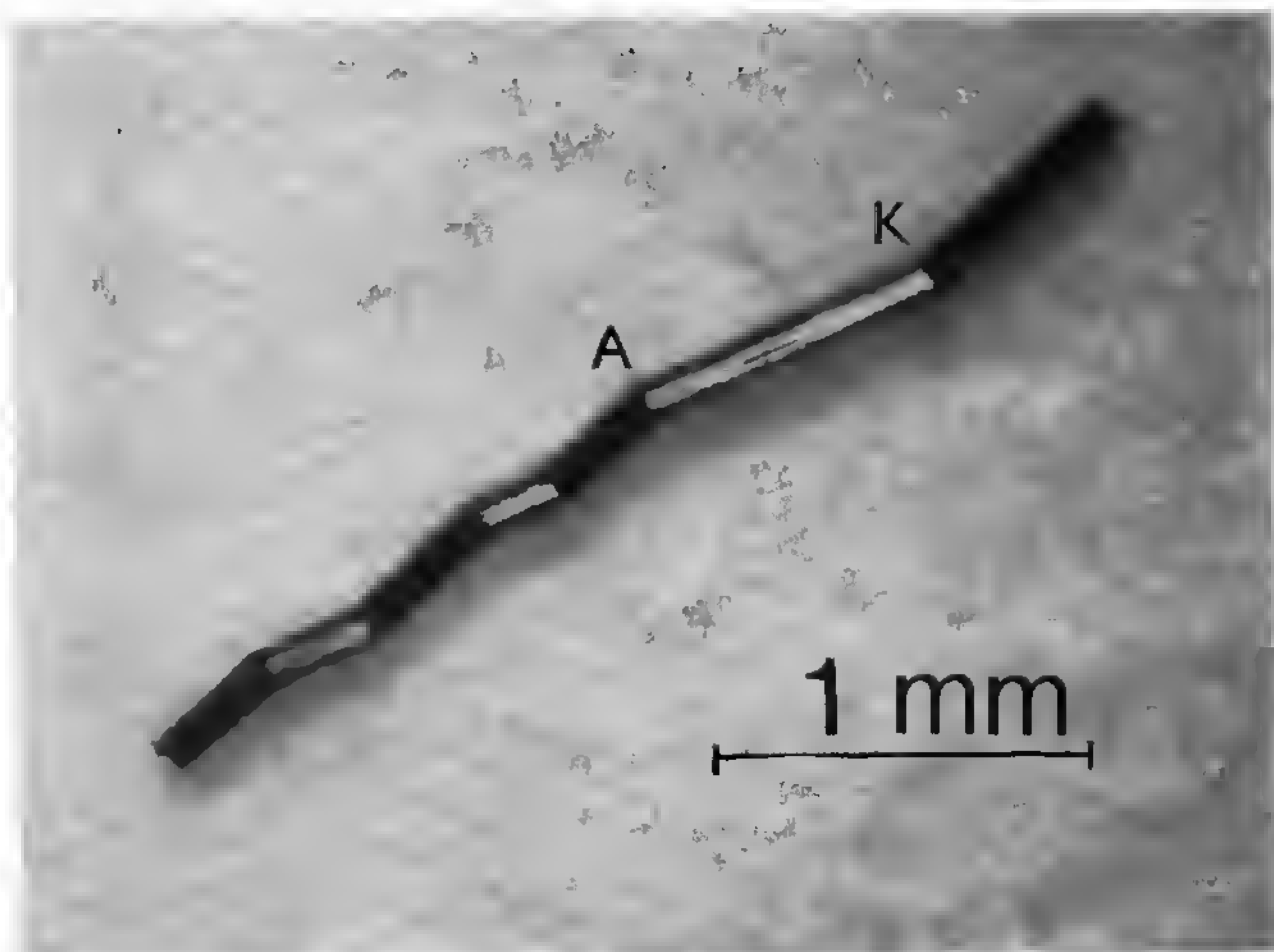


Figure 22 If a needle crystal of $(\text{TMTSF})_2\text{ClO}_4$ is pressed with a force perpendicular to the needle axis, kink (K) and antikink (A) pairs are formed. The kinks can be annihilated, reproduced, and moved back and forth along the needle axis by applied stress. The reproducibility and mobility of the kinks indicate that the samples are of high crystallinity (few dislocations or defects). (From Ref. 169.)

$P2_1/c$. The absence of a superconductivity transition in some samples of the latter material is attributed to twinning. Twinning in $\kappa\text{-(BEDT-TTF)}_2(\text{Cu})\text{NCS})_2$ is described by Watanabe et al. [172].

From the examples above of TMA.TCNQ.I and $\beta\text{-(BEDT-TTF)}_2\text{I}_3$ and others in the literature, it can be seen that the structure study of iodine-containing organic conductors needs special attention. Before starting an x-ray or a neutron diffraction study it is good practice to check that the sample is twin-free. This can be conveniently performed with photographic x-ray cameras and especially with the Laue technique (white beam diffraction). This is easy with small samples, while crystals larger than the beam cross section must be checked point by point. Neutron beams are generally much larger than x-ray beams, and thus a neutron Laue camera would be the most appropriate tool. Indeed, Schultz et al. [173] have reported the use of a time-of-flight neutron diffractometer to obtain Laue patterns quickly from a series of large crystals of $\kappa\text{-(BEDT-TTF)}_2\text{Cu}(\text{NCS})_2$. Marmeggi [174] has designed a neutron Laue camera for sample testing and superstructure and lattice modulation studies [175].

B. Intrinsic Disorder

We discuss here the influence of uncontrolled compositional or positional disorder on the crystallography of organic conductors. To some extent, structure studies are fairly insensitive to isotropic disorder because they are the result of an average over a large number of unit cells. But, for example, discrepancies in the cell dimensions for samples from different batches of the same material can be, at least partially, attributed to chemical impurities and/or other lattice defects. The specific molecular packing of organic conductors favors one-dimensional disorder, which can easily be observed in the form of diffuse reciprocal planes, this being especially true with x-rays and iodine-containing organic conductors, since iodine atoms are strong scatterers.

1. Compositional Disorder

Uncontrolled compositional disorder comes either from chemical impurities (e.g., oxidation of the bath during crystal growth, partial degradation of one of the reactants during the synthesis, etc.) or from fluctuations in reactant proportions (nonuniform stoichiometry). As stated above, disorder may not affect the accuracy of structure studies; however, some synthesis or crystal growth process may occasionally lead to unusually large amounts of chemical impurities, which can both modify the physical properties of the material significantly and/or lead to specific diffraction features.

Consider, for example, the case of the quasi-one-dimensional organic metal $\text{TTT}_2\text{I}_{3+\delta}$. This material often exhibits a set of disordered iodine sublattices either commensurate or incommensurate with the main lattice. Lowe-Ma et al. [85] have analyzed the intensity of the corresponding set of diffuse reciprocal layers and postulated that, in their samples, part of the I_3^- ions are substituted by I_2 and I^- moieties. In fact, the intensity of the zero layer is not negligible and no three-dimensional ordering of iodine chains is observed at low temperature. However, $\text{TTT}_2\text{I}_{3+\delta}$ crystals are often characterized by a varying amount of positional disorder [136] of iodine columns rather than by a chemical disorder.

2. Positional Disorder

One-dimensional positional disorder is often observed in low-dimensional organic conductors and especially in the case of iodine-containing materials because I_3^- columns may exhibit random longitudinal relative shifts. Such a disorder in TMA.TCNQ.I and some of its consequences have been discussed in Sections IV.A and VI.C. In the latter material the period of the one-dimensional scattering is commensurate with the host lattice, but commensurate and incommensurate diffuse reciprocal layers can also be observed simultaneously in, for example, $\text{TTT}_2\text{I}_{3+\delta}$ [176]. The structure re-

finement is then hampered by the disordered iodine atoms, and their Debye–Waller parameters often diverge. A discussion of this effect can be found in Refs. 177 and 178. If no ordered samples can be prepared, refining parameters of a simple disorder model [27,136,176] will help, at least, in understanding the perturbing effects of the disorder on the physical properties of the material.

In quasi-one-dimensional conductors the positional disorder may affect both conducting and insulating stacks and may affect ions as a whole (e.g., inversion movement) or only a given part of each ion (e.g., disorder of an ethylene group). Furthermore, a noncentrosymmetric molecules may exhibit a stacking disorder of the possible orientations. For example, in NMP-TCNQ the NMP molecules have a disordered ethylene group [179], while in $\text{Qn}(\text{TCNQ})_2$ [Qn is quinoleinium] the cations are disordered over two equiprobable orientations related by an inversion center [180]. When the disorder is dynamic at room temperature, it freezes at low temperature with or without ordering of the ions, and this may substantially influence the electronic properties of the material. For example, in $\text{TEA}(\text{TCNQ})_2$ the large TEA cation undergoes a thermally activated inversion movement at room temperature, which freezes at 200 to 220 K with, as a consequence, a non-symmetry-breaking $2k_F$ distortion of the TCNQ stacks [22,23,109]. In $(\text{TMTSF})_2\text{ClO}_4$ the anions order at 24 K and a superstructure ($0a^*$, $\frac{1}{2}b^*$, $0c^*$) is observed [181]. Because ClO_4 anions are small and weakly linked to the TMTSF stacks, negligible distortion is induced in the latter [128,129], whereas, for example, in $(\text{TMTSF})_2\text{ReO}_4$ the ReO_4 anions being in strong contact with the organic stacks, the ordering ($T_{AO} \sim 180$ K) leads to an antiferromagnetic ground state [45,182].

Similarly, in the BEDT-TTF series, which exhibits two-dimensional packing, partial disorder of the organic molecule is often observed. For example, in $(\text{BEDT-TTF})_2\text{I}_3$ one of the ethylene groups, which strongly interacts with the triiodide anions, is disordered at room temperature but orders [62,63] under given T and P conditions to lead to a high- T_c superconducting ground state (see Section IV.A).

The examples above demonstrate that when observed in an organic conductor, positional disorder must be analyzed in detail. Several approaches are possible depending on the kind of disorder; for example, it may be through the interpretation of the diffuse scattering due to the disorder [183] or by means of an improved structural analysis. The effect of positional disorder on structural determinations is that, especially at room temperature, disordered atoms generally exhibit unusually large and anisotropic atomic thermal parameters. The corresponding atomic positions are thus averaged over the partially populated sites between which the atoms move. Decreasing the temperature considerably helps resolving

a positional disorder because the atomic temperature factors are smaller and peaks on the Fourier maps are sharper. For example, in the case of $\text{TEA}(\text{TCNQ})_2$, the intricate disorder of the TEA moiety was resolved at 40 K, a task that was facilitated by the use of neutrons because all atoms in the compounds have positive scattering lengths except for hydrogen atoms, which have negative ones [22]. If the material undergoes an order–disorder phase transition, the measuring of superstructure reflections makes possible the determination of the structure of the ordered phase (see Section VI).

C. Extrinsic Disorder

As stated above, extrinsic disorder, produced by introducing known amounts of defects by irradiation, is a tool often used in the study of organic conductors [166], but we are interested here in its “dark side,” that is, the limitations it may introduce in some crystallographic measurements. Generally speaking, when an organic crystal is irradiated with an ionizing radiation* [ultraviolet (UV), x-rays, γ -rays, electrons], the incoming photons interact with the material in a manner that depends largely on their energy. If the latter is high enough (UV) molecules are activated and/or chemical bonds are broken into ions. Activated molecules and ions react in situ and strongly damage the lattice structure. Low-dimensional organic conductors are not excluded from this general behavior but also exhibit some specific aspects since irradiation can also suppress a superconducting transition, smear fluctuations, pin charge density waves, localize electrons, and stabilize the metallic state [166].

The Peierls and spin-Peierls transitions are extremely sensitive to defects. Indeed, because the coherence between charge density waves or spin-density waves is due to interchain coupling, the defects destroy the coherence and thus avoid wave ordering below the critical temperature. Zuppiroli et al. [184,185] using γ -rays, first demonstrated that in TTF-TCNQ, a concentration of 10^{-3} of radiation-induced defects suppresses the Peierls transition. Superconductivity is also very sensitive to defects. For example, in $(\text{TMTSF})_2\text{ClO}_4$ it is suppressed by the introduction of $\geq 5\%$ ReO_4 anions in ClO_4 chains [165], by 0.5% TMTTF molecules in the organic chain [186,187], or by only 0.01% irradiation-induced defects per mole [188]. Even the anion ordering at 24 K in $(\text{TMTSF})_2\text{ClO}_4$ [128] is sensitive to irradiation; the transition temperature is lowered and the intensity of superstructure reflections is reduced. On the other hand, a

*In the case of neutrons (nonionizing radiation) the main effect is atom recoil if the energy momentum of the neutron is large enough. In diffraction studies being performed with thermal neutrons, very few defects are produced compared to ionizing radiations.

defect concentration of several percent is necessary to suppress the first-order structural phase transition at 315.7 K of MTPP(TCNQ)₂ (MTPP is methyltriphenylphosphonium) [189].

As discussed in Section X, irradiation effects are the main enemy in the case of electron microdiffraction. Granier et al. [31,190] found that not only does the irradiation rapidly destroy the sample, but long before, satellite reflections vanish (Fig. 23). In fact, the coherence between charge density waves is much more sensitive than the material itself.

At least in normal experimental conditions,* x-ray irradiation has less dramatic effects than electrons. Indeed, the main reflections are little affected during regular data collection; however, the situation might be different when the quantity measured is the intensity of a set of satellites or superstructure reflections. In the latter case the intensity decay is visible and data must be carefully corrected. For example, Bouveret and Megtert [40] report that in TTF-TCNQ the intensity of three reference satellites exhibits about a 0.5% decrease per irradiation hour during structural measurements performed using a rotation anode (12-kW Rigaku 200, Copper anode) (Fig. 24). For the ordered phase of (TMTSF)₂ClO₄, Moret et al. [128] observed a 50% intensity decrease of superstructure reflections after only 16 h of irradiation (1.5-kW x-ray tube, CuK_α radiation).

Another example of the perturbing effect of irradiation on diffraction experiments is described by Pouget et al. [119]. The study of the structural fluctuations of the (TMTTF)₂X spin-Peierls order was precluded by the sensitivity of this ground state to x-ray irradiation.

X. ELECTRON MICRODIFFRACTION

Transmission electron microscopes produce greatly magnified images, but it is less well known that they may also give the diffraction pattern from the very small part of the sample that is being observed (typically, a few hundred square angstroms). The latter technique, called *electron microdiffraction*, is able to observe the local structure of the sample while x-ray or neutron scattering provides precise information on the average structure of a much larger volume of the material. Electron microscopy is thus of interest for the study of domains, of twins, or of very small regions localized either on or between defects of the crystal. Furthermore, the short wave-

*X-ray tube or rotating anode. A synchrotron radiation source being more intense, the irradiation effect might be expected to be larger. However, in practice this may not be true, since the beam divergency and the $\Delta\lambda/\lambda$ ratio are much smaller, the signal/noise ratio is much better, and thus shorter wavelength and shorter measuring times can be used.

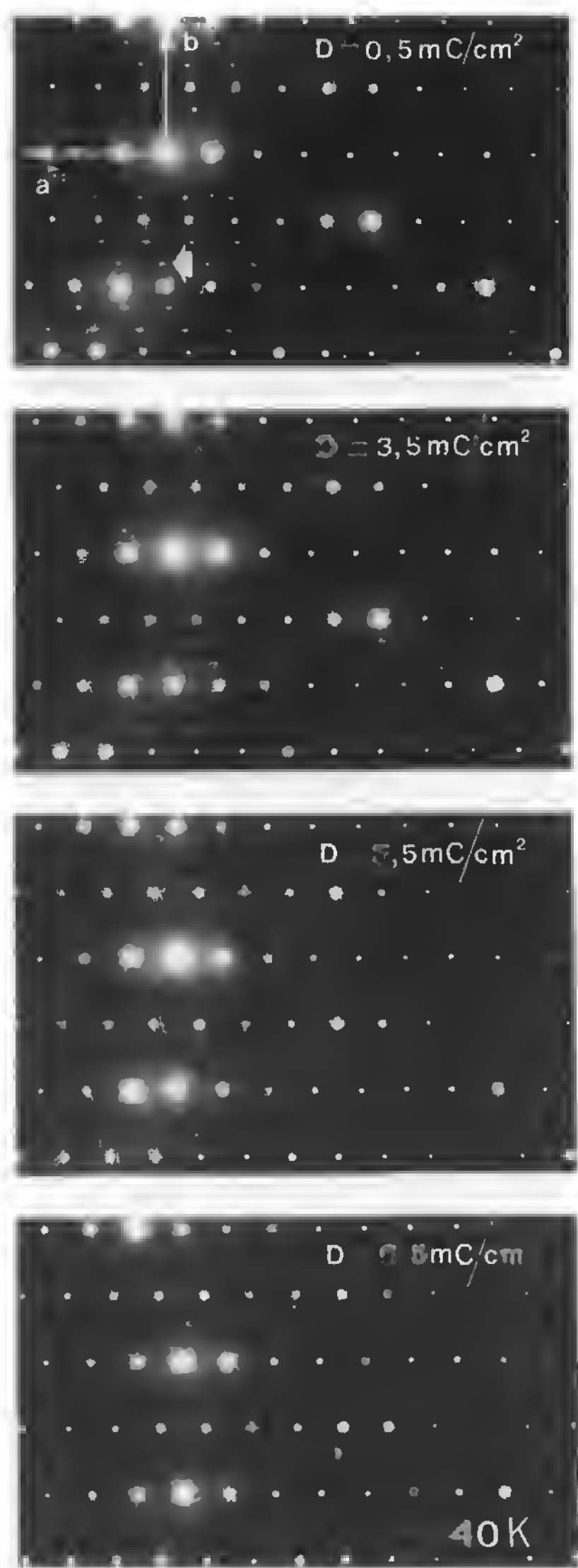


Figure 23 Electron microdiffraction study of TMA.TCNQ.I. Changes in superstructure reflections at about 40 K as a function of the irradiation dose. (From Ref. 190.)

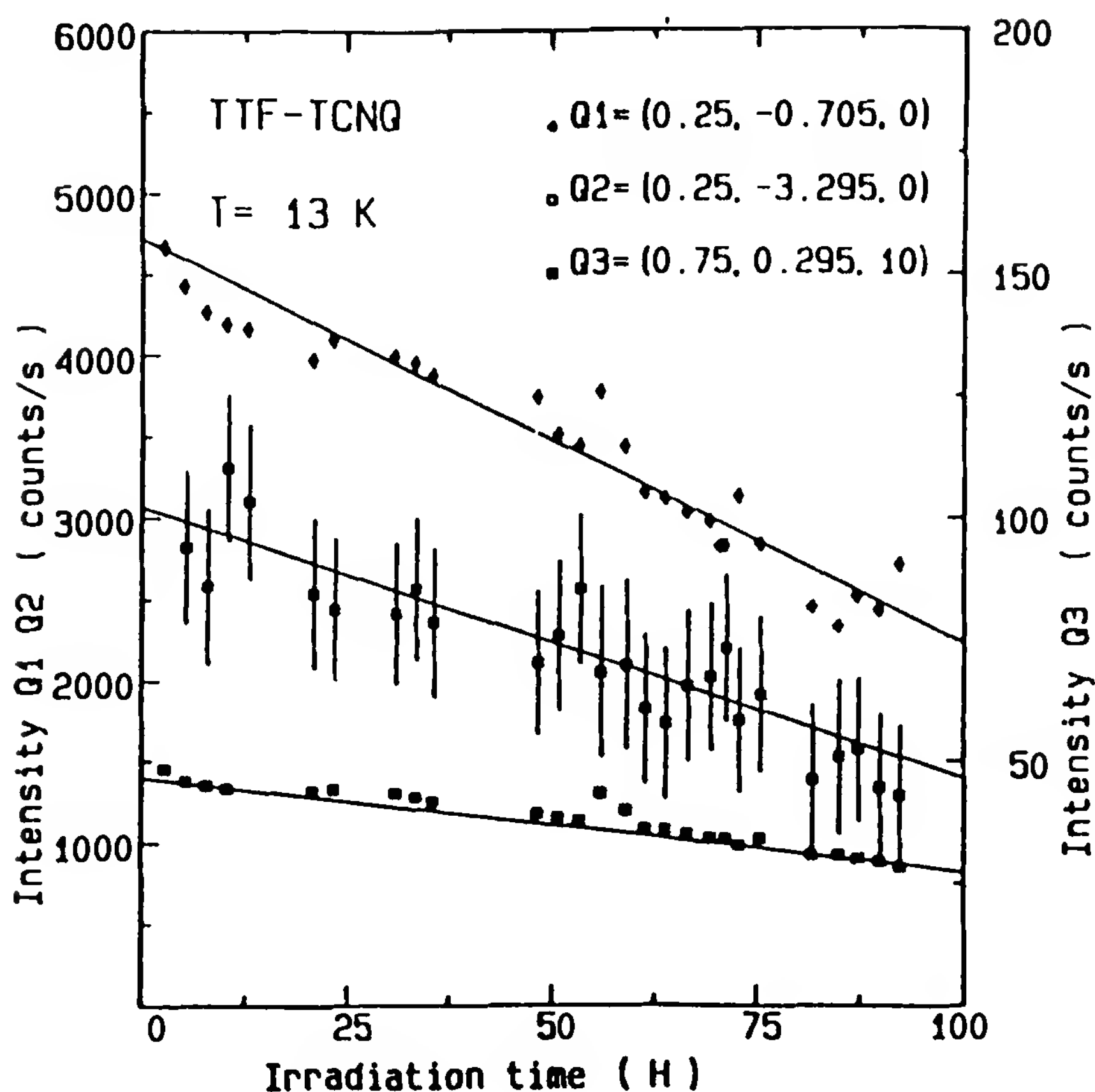


Figure 24 Integrated intensity behavior of three satellite reflections versus exposure time in TTF-TCNQ at 13 K. With a rotating copper anode generator (12-kW Rigaku 200) an $\sim 0.5\%$ intensity decrease per irradiation hour is observed. (From Ref. 40.)

length of the electrons* makes it possible to observe a large area of reciprocal space.

However, although electron microdiffraction is often used in the study of inorganic materials (e.g., one-dimensional conductors such as NbSe_3 or TeS_3), this is not the case with organic compounds. Most of the latter are so sensitive to electron irradiation that the crystal lattice is rapidly destroyed and the diffraction pattern vanishes. This sensitivity is due first to the inelastic scattering of some of the incoming electrons with an energy transfer to electrons and molecules of the sample (excitations ranging from plasmons to deep energy levels of heavy atoms). Then, excited or ionized atoms and molecules react chemically and release the energy received. With low-dimensional organic conductors, an extra difficulty arises from

* $\lambda_e = 0.0054 \text{ \AA}$, with an accelerating voltage of 2000 kV.

the fact that the coherence between charge density waves is destroyed long before the material itself (see Section IX.C).

Despite all these difficulties, at least one electron microdiffraction study of a low-dimensional organic conductor has been carried out successfully [31,190]. This is indeed the first use of electrons to observe structural modifications in an organic compound, the ternary salt $\text{TMA}^+(\text{TCNQ})^{(2/3)-}(\text{I}_3^-)_{1/3}$. TMA.TCNQ.I crystals are destroyed in only 2 or 3 s in an electron beam of the usual intensity ($6.25 \times 10^{17} \text{ e}^-/\text{cm}^2$ per second; $0.1 \text{ A}/\text{cm}^2$) and thus the irradiation damage had to be minimized to reach long enough exposure times.* This was achieved by the use of low temperatures and of high accelerating voltages (up to 2000 kV). The former reduces the chemical reactions resulting from irradiation† (e.g., the sample lifetime is multiplied by 2.5 if temperature is decreased from 80 K to 40 K). The higher voltage allows for the use of a much lower electron beam intensity; the lifetime is increased by 1.5 going from 1000 to 2000 kV. In addition, some extra experimental tricks made it possible to improve the heat transfer between the sample and its holder.

The goal of the electron microdiffraction study of TMA.TCNQ.I [31,190] was an understanding of the lattice distortions associated with two successive phase transitions. The first one ($T_{\text{MI}} \sim 150 \text{ K}$) is a metal–insulator transition with a generalized Peierls-like lattice distortion [30] followed by a structural transition at 90 K. However, the structure of TMA.TCNQ.I is complicated (see Section IV.A) and exhibits two triclinic twinned sublattices with nonparallel axes that evolve differently as a function of temperature. Electron microdiffraction gave beautiful diffraction patterns which exemplified and clarified x-rays and neutron results (Fig. 25). Only electrons made it possible to obtain diffraction patterns from a single crystal domain. It helped the understanding of the sample twinning and also gave the most convincing observations of some additional low-intensity satellites and of the continuous increase, from 0 to a locking value, of one of the components of the distortion wave vector in the temperature range 95 to 65 K.

This demonstrates that electron microdiffraction may compete with other diffraction techniques but is not easy to use. Nowadays synchrotron radiation is probably more convenient, in most cases, for the observation of very weak sublattice reflections even from small crystallites however not as small as with electron microdiffraction.

*Exposure times up to 30 s with high-speed film plates were necessary to observe very weak superlattice reflections.

†However, some organic compounds are more sensitive to electron irradiation at low temperature than at room temperature.

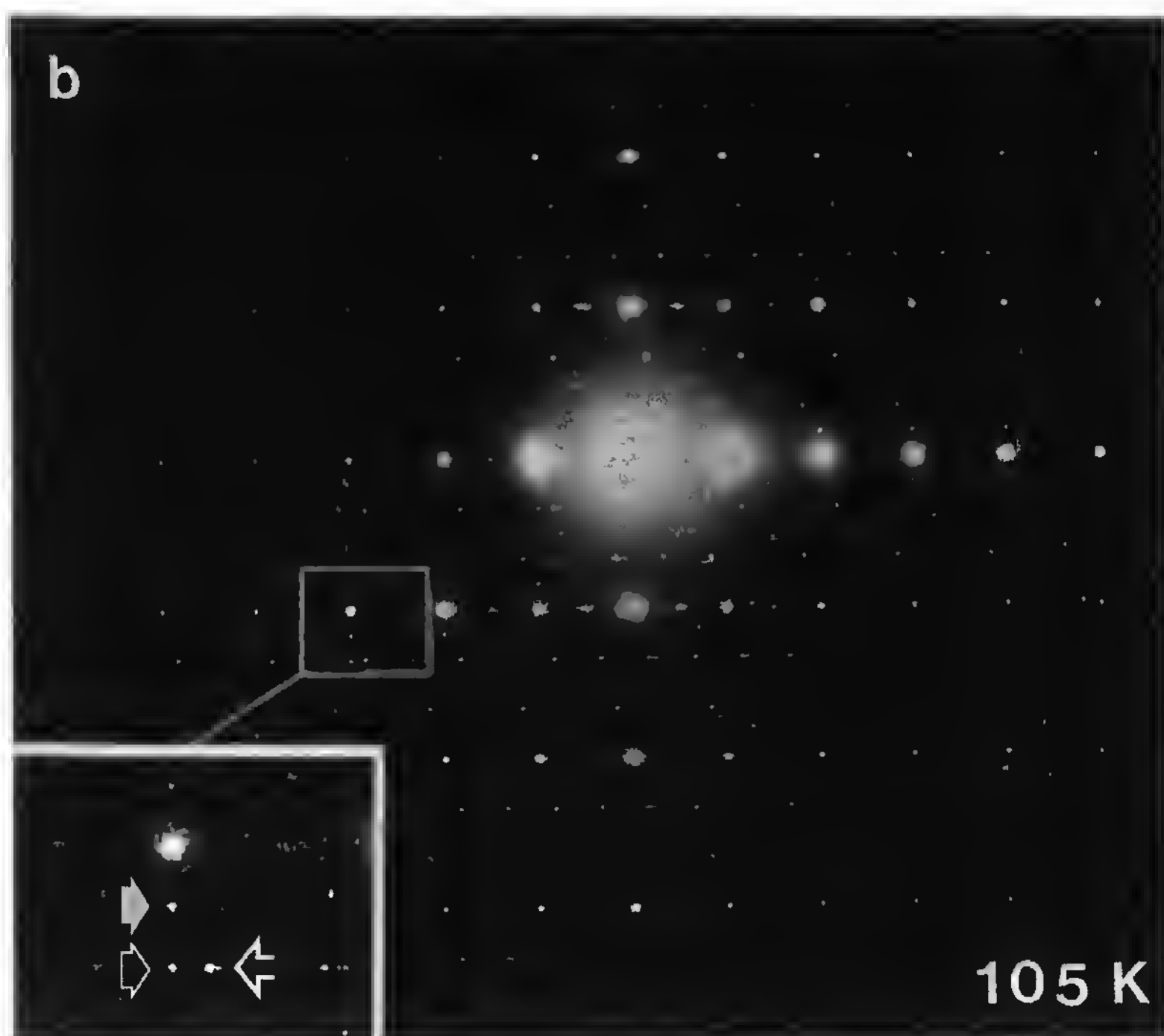


Figure 25 Electron microdiffraction diagram of plane $\{[40\bar{1}].b^*\}$ of TMA.TCNQ.I taken at 2000 kV and $T \sim 105$ K. The satellites (solid arrows) are visible at $\pm \frac{1}{3}b^*$ and are accompanied by a second series of reflections at $\pm \frac{2}{3}b^*$ (fine hollow arrows) with the same component in the direction $[40\bar{1}]$. (From Ref. 31.)

XI. ELECTRON DENSITY MAPS

The low dimensionality of organic conductors is due to a specific molecular packing which allows for the strong overlapping of some orbitals, leading to a long-range delocalization of the electrons. We have already seen that structural results (bond lengths and angles) have been discussed more or less successfully in terms of longitudinal and transverse transfer integrals. But this is only a substitute for the lack of a direct and precise observation of the electron cloud distribution within the crystal lattice. Thus the question is: Can we have a direct measure of the charge transfer, of the electron cloud distortion due to the overlap of bonding and antibonding orbitals? As we shall see below, the answer from crystallographers is “yes,” but the proposed methods have rarely been used on organic conductors.

Let us recall here that the core electrons have an almost isotropic distribution around the atom, while the orbitals of peripheral electrons (valence electrons) are often very anisotropic due to bonding effects. X-rays are scattered by electrons, while neutrons are scattered by the nuclei of atoms. Therefore, two methods can be used. The so-called *X-N method* combines neutron and x-ray data measured at the same temperature. Neutron data provide nuclear mean positions and thermal parameters unbiased by the effects of the nonsphericity of the atomic electron density due to chemical bonding. The contribution of the core electron (spherical-atom model) is then subtracted from the total electron distribution provided by x-ray data. The remainder, the *deformation density map*, shows the distortions of the peripheral electron cloud. The *X-X' method* relies on specific processing of x-ray data. The core density contributes mainly to large diffraction angles, whereas peripheral electrons diffract primarily at low angles. Thus the data set is split into two parts at $\sin(\theta)/\lambda \sim 0.6 \text{ \AA}^{-1}$. The refinement of the high-angle part, using a spherical-atom model, provides the positional and displacement parameters of the core electrons. The distribution of peripheral electrons is thus obtained from the low-angle data set processed with the atomic parameters provided by the high-angle data set. For a review of the X-N and X-X' methods, see, for example, references [1,12,191,192].

Both methods are successful only when highly accurate data can be obtained. The second method also implies that data can be collected up to large $\sin(\theta)/\lambda$ values (typically up to 1.2 \AA^{-1}) despite the decrease in diffraction intensity due to the Debye–Waller factor and to the falloff in the atomic scattering factor. As far as we know, only two examples of electron density studies performed on organic conductors can be found in the literature.

As discussed in Section VII.B, Coppens et al. [147], pioneers in the X-N and X-X' methods, obtained a direct estimate of the charge transfer in TTF-TCNQ from the electron density deduced from accurate x-ray data. Electron density maps from $(\text{TMTSF})_2\text{AsF}_6$ have been published by Wudl et al. [193]. The density in the TMTSF plane (Fig. 26) is higher for the C2–C3 and C1–C6 double bond and lower for the C7–C8 double bond. The near absence of in-plane selenium lone-pair density suggests that these atoms may be sp^3 hybridized. “Slices” in other directions show the intermolecular electron density in the form of an alternating pattern between TMTSF molecular centers. Wudl et al. note that this is a “microscopic view of electron density distribution along a one-dimensional conduction band.” Even more striking is the fact that they observed electron density only along the longest Se–Se interstack distance (Se2–Se4', 4.151 \AA), whereas no electron density is observed in the shortest selenium atom contact (Se2–Se2, 3.905 \AA). This is indeed the direct observation of what

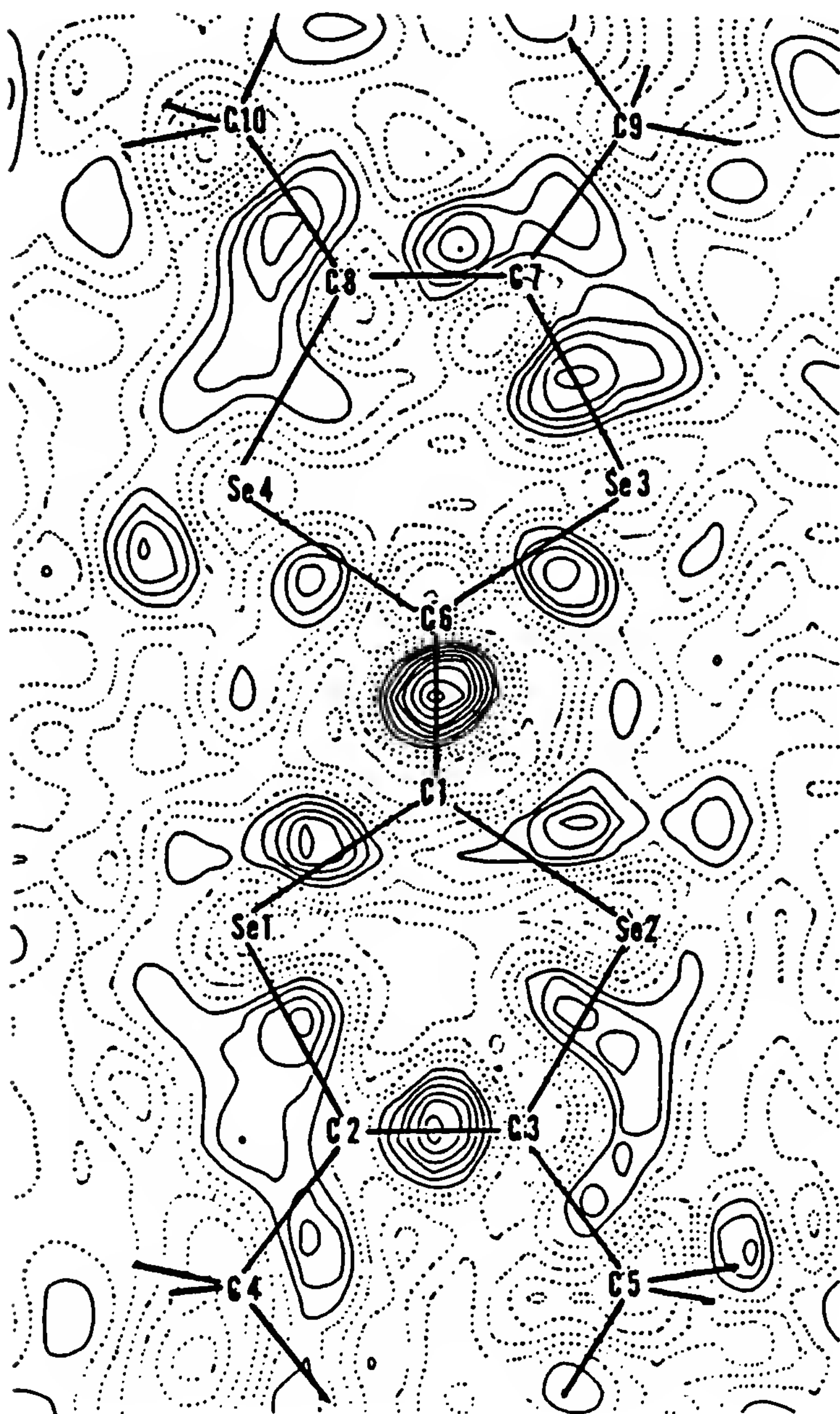


Figure 26 Electron densities in the plane of a TMTSF molecule of $(\text{TMTSF})_2\text{AsF}_6$. Contours are $0.05 \text{ e}/\text{\AA}^3$ per line starting at $0.05 \text{ e}/\text{\AA}^3$; negative contours are shown by dashed lines. (From Ref. 193.)

Grant [154] demonstrated independently by means of transfer integral computations. In other words, this again emphasizes that one must be careful in discussing the properties of organic conductors on the basis of inter- and intrastack distances, since the bonding and antibonding character of the interactions cannot be neglected.

In view of the results above we may ask: Why are there so few electron density studies of organic conductors? Clearly, even if the required ex-

perimental conditions and accuracy are well known nowadays and can be met in many laboratories, getting good electron density maps is still difficult. Furthermore, Wudl et al. [193] noted that they could not find good enough crystals of TCNQ-based metals, and thus some effort has also to be made to obtain a sample with the desired quality. However, Coppens [12] claimed that synchrotron sources, which now produce fluxes more than 100 times higher than sealed tubes and which also have a much higher brilliance, will soon make highly accurate measurements much easier, even from smaller samples.

XII. OTHER TECHNIQUES

The foregoing sections have been devoted primarily to structural crystallography and phase-transition studies; hereafter we discuss briefly the use of other crystallographic techniques in the study of low-dimensional organic conductors. Our goal is not an exhaustive review but simply to give some leads toward a different approach to these materials. For example, since crystallography is the science of crystals, two of the sections below are on sample size and quality.

A. Crystal Growth and Sample Size

In Chapter 4 in this book organic conductor synthesis and crystal growth techniques are discussed; here we put the emphasis on sample size and quality as regards crystallographic techniques. As a matter of fact, some compounds are synthesized in the form of a more or less crystalline powder (spontaneous seeding), while others are obtained directly in the form of relatively small needle-shaped or thin plate single crystals (e.g., electrochemical synthesis). Larger crystals are generally difficult to obtain whether through recrystallization of the powder or by means of improved electrochemical synthesis. Thus physicists usually say that a crystal is “large” if it is substantially larger than regular ones, whatever its actual size, which can be very small indeed.

For a long time, sample size has limited the use of some investigation techniques. For example, polarized neutron studies failed in part for sample-size problems (see Section XII.C). Similarly, to perform neutron inelastic scattering experiments on TTF-TCNQ, Shirane et al. [73] had to use an assembly of 17 aligned crystals to reach a total volume of about 0.015 cm^3 . Of course, there is a gradual improvement in both measurement techniques and crystal growth, but almost every time a new type of material is found, problems recur. In this section we first recall the needs of the main crys-

tallographic techniques and then mention some of the largest sample sizes obtained.

In the case of structural studies with x-rays, sample size is rarely a serious problem since single crystals as small as about 0.001 mm^3 (sealed x-ray tube) or 10^{-9} mm^3 (synchrotron radiation) will do. In the case of x-ray diffuse scattering measurements with the assembly described in Section VI.D, the crystal must be 2 mm long at least but can be relatively thin. With neutrons, however, sample size is more critical. Indeed, for structure measurements, 0.1 mm^3 is a minimum, with the highest neutron fluxes available nowadays, and more usual sizes are in the range of several cubic millimeters to several tens of cubic millimeters. For polarized neutrons or inelastic scattering studies, much larger samples are necessary.

The growth of large single crystals of organic conductors is generally not easy, and despite the efforts expended in many laboratories to produce large samples, the results are modest compared to those in inorganic chemistry. First, the effort has been put mostly into the growth of the conductors easiest to crystallize, even if their transport is of less interest. Then special attention has been devoted to the most interesting synthetic metals or superconductors. To fix one's ideas, let us recall here some of the best results.

The largest crystals of low-dimensional organic conductors ever obtained are probably those grown by Almeida et al. [194,195] for inelastic neutron experiments. They improved the growth method first used by Dupuis [196] (i.e., controlled cooling of acetonitrile solution) and reached sizes up to $30 \times 10 \times 3$, $18 \times 13 \times 11$ and $15 \times 15 \times 8 \text{ mm}^3$ for organic semiconductors $\text{TEA}(\text{TCNQ})_2$, $\text{MNEB}(\text{TCNQ})_2$, and $\text{MTPP}(\text{TCNQ})_2$, respectively (here MNEB is *N*-ethylbenzimidazolium and MTPP is methyltriphenylphosphonium). A special effort has been devoted by several laboratories to TTF-TCNQ, the first organic one-dimensional metal. For example, Joansen et al. [197] planned to grow crystals in space; unfortunately, the experiment was canceled due to scheduling problems in the U.S. space program. The largest sample size obtained so far is probably about 20 mm^3 , but the mosaic was not good and composite crystals have been used to substitute for large single crystals [73]. Crystals of Bechgaard salts (black needles) with dimensions up to $10 \times 0.5 \times 0.5 \text{ mm}^3$ can be routinely obtained [198] and narrow dimensions of at least $1 \text{ mm} \times 1 \text{ mm}$ have been reached (L. K. Montgomery, private communication). However, one should note that, even for crystallographic studies for which large sample sizes were essential, $(\text{TMTSF})_2\text{ClO}_4$ or $(\text{TMTSF})_2\text{PF}_6$ crystals with volumes of 0.3 to 0.85 mm^3 only have been used. For $\beta\text{-(BEDT-TTF)}_2\text{I}_3$, Schultz et al. used [57] single crystals of about 1 mm^3 in a neutron diffraction experiment.

B. Topography and Sample Quality

Several of the interesting physical properties of organic conductors (especially transport properties) are expected to be sensitive to crystal defects. It is thus surprising that little has been done up to now to assess crystal quality. For example, a technique that may be used is x-ray transmission topography, a powerful method to obtain information about the internal perfection of not too small crystals, since it provides direct observation of defects.

The first use of topography on organic conductors was on TTF-TCNQ samples [199], which were found to exhibit a very large mosaic spread. Almeida et al. [195,200] performed a more detailed study of several compounds [TEA(TCNQ)₂, MTPP(TCNQ)₂, MNEB(TCNQ)₂] to improve the growth of very large crystals from controlled cooling of acetonitrile solutions. For example, crystals of TEA(TCNQ)₂ obtained by spontaneous nucleation and fast cooling ($\sim -4^\circ\text{C}/\text{day}$) exhibit a good external appearance but contain solvent inclusions surrounded by severe long-range strain fields, indicating a poor crystal quality. Slower cooling ($-0.6^\circ\text{C}/\text{day}$) leads to better quality, but microchannels and screw dislocations are still numerous. Larger crystals were grown from seeds, and a lot of effort was necessary to avoid or drastically reduce the number of inclusions, dislocations, and growth bands resulting from varying impurity concentration (Fig. 27). One important conclusion of the studies described above is that if large crystals of organic conductors often exhibit perfect mirrorlike faces, this is not a guarantee of internal perfection.

C. Polarized Neutron Diffraction

The spin of the neutron interacts with the spins in the sample, and this is responsible for a magnetic contribution to the structure factors of Bragg peaks, the sign of which changes on reversal of the neutron spin direction:

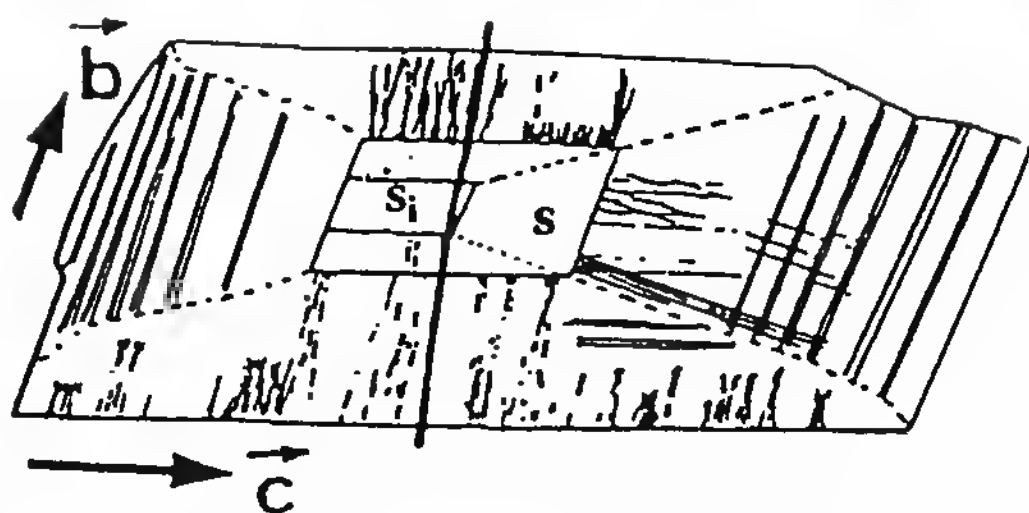
$$F^2 = (F_{\text{nuclear}} \pm F_{\text{magnetic}})^2$$

Polarized neutron diffraction makes it possible to measure magnetic structure factors and thus to obtain the distribution of unpaired spins in magnetic materials (see, e.g., Ref. 201). Let us discuss here the use of this technique for the study of low-dimensional organic conductors.

Since organic conductors are paramagnetic, a first approach is to place the sample in a strong magnetic field to orient all the spins and then to measure the flipping ratios $R = I^+/I^-$ for a number of Bragg peaks. From the latter the spin-density map is then reconstructed and shows the spin localization in the structure. The difficulty with organic conductors is that the magnetic susceptibility is small ($\chi_p < 20 \times 10^{-4}$ emu cgs/mol). An



(a)



(b)

Figure 27 X-ray topograph (Lang's technique) of a crystal of $\text{TEA}(\text{TCNQ})_2$ grown from thin stationary seed by fast cooling ($4^\circ\text{C}/\text{day}$): (a) topography image; (b) interpretation: *s* is the seed, *s_i* is an internal seed; *x*, inclusions; *-*, dislocations; *=*, growth bands; *---*, growth section boundary; *—*, suspending fiber. The crystal size is $12 \times 5 \times 0.3 \text{ mm}^3$. (From Ref. 200.)

attempt was made by A. Filhol and J. Schweizer (unpublished, 1985) to measure the spin-density map in $\text{TEA}(\text{TCNQ})_2$. The compound being a radical-ion salt, the charge transfer is total, but if the mean charge on each TCNQ is $\frac{1}{2}$, Farges [109] showed that the charge distribution on the two TCNQ molecules is not equal and changes with temperature. The magnetism of the compound mainly follows a singlet-triplet law [202,203] and the susceptibility is maximum at room temperature. Thus an attempt to observe the spin localization on TCNQ moieties could be performed only at room temperature. A test experiment was done on the polarized neutron diffractometer D3 at the ILL with a field of 4.6 T. The sample was a 190-mm^3 single crystal of partially deuterated $\text{TEA}(\text{TCNQ})_2$ ($\chi_{p(300\text{K})} \sim 7 \times 10^{-4} \text{ emu cgs/mol}$). Three strong Bragg peaks were measured with counting times of 18 h and a weak magnetic signal [$R = 1.00066(14)$] was observed for the $3\bar{1}1$ reflection. The main experiment on samples of about 1 cm^3

could not be carried out because of the overdemand for the instrument. This is unfortunate because up to now, the spin distribution in these organic conductors is known only by theoretical calculations and from EPR spectroscopy [204], and results are not in good agreement.

The approach of Aeppli et al. [205] is different since they tried to measure the magnetic contribution to the superlattice intensity in the spin-Peierls ground state of $\text{MEM}(\text{TCNQ})_2$ (MEM is *N*-methyl-*N*-ethylmorpholinium) by means of a polarization analysis technique. The goal of the experiment was to demonstrate that, as predicted, there is no ordered magnetic moment in the spin-Peierls ground state. The experiment was performed at the Brookhaven High-Flux Beam Reactor on a deuterated single crystal ($5 \times 3 \times 0.5 \text{ mm}^3$) mounted on a two-axis diffractometer. They worked at 6 K, that is, below the spin-Peierls phase transition ($T_{\text{SP}} = 17.4 \text{ K}$) of $\text{MEM}(\text{TCNQ})_2$. The conclusion was that the ordered moment is zero within an experimental uncertainty of roughly one-third of a Bohr magneton and that a 30-fold improvement in sample size and polarized neutron efficiency is needed to make the spin fluctuations driving the spin-Peierls transition observable.

In both cases, sample size was found to be a crucial parameter. As we have seen in Section XII.A, growing very large crystals of organic conductors is not easy. To make the experiment feasible one can think of a bunch of carefully aligned smaller crystals and/or take advantage of improvements in polarized neutron techniques since the 1980s.

D. Scanning Tunneling Microscopy and Atomic Force Microscopy

A few physical methods are capable of viewing the crystal structure with atomic resolution. Diffraction (mainly x-rays and neutron diffraction), the most popular method, provides accurate time-averaged structural data. High-resolution transmission electron microscopy is able to “see” atoms in crystals, but organic compounds are rarely able to survive the intense electron irradiation. Scanning tunneling microscopy (STM), scanning tunneling spectroscopy (STS) [206,207], and atomic force microscopy (AFM) [208] have emerged as powerful tools for the real-time observation of surfaces with atomic resolution. In the three methods, the sample surface is scanned with a microtip that approaches it very closely (down to a few angstrom for the STM) or that contacts it (AFM). STM measures the change in the tunneling current between the surface and the tip, thus giving a topography of the surface (i.e., the distribution of orbitals pointing out from the surface). STS observes the distribution of surface electrons on a given energy level. AFM works in the constant-force mode, and the tip is moved vertically by the repulsion due to surface atoms. For STM and STS

the material should be a conductor or a semiconductor, while AFM can be performed on insulating materials. The sample may be in vacuum, in the air, or even in a liquid.

Several organic conductors have been studied by these methods, and we mention here some works relative to compounds discussed in Section IV.A [i.e., TTF-TCNQ [209], (TMTSF)₂PF₆, (TMTSF)₂ClO₄ [210], and several BEDT-TTF salts (e.g., Refs. 211 and 212)]. However, the resolution is not as good as in the case of metals or inorganic low-dimensional conductors. The images are more difficult to interpret and individual atoms are visible only in special cases. Nevertheless, even with molecular resolution only, the STM images are very interesting and show several features that can be compared with what is already known on the bulk crystal structure.

The simplest observations show steps on the crystal surface with one or more molecular heights. Furthermore, flat crystal faces exhibit sets of bright and less-bright protrusions which can be attributed to anions, cations, or part of them. Indeed, Magonov et al. [211] postulate that "the STM image [of TTF-TCNQ] could not be explained well by the geometric atomic arrangement. The evident electronic effects observed in this case correlate better with molecular orbital calculations than with the effective charge distribution." However, it is sometimes possible to decide if the crystal ends with an anion or a cation layer [213]. When the sample orientation is favorable, the image exhibits corrugations that correspond to chains of molecules. For example, Pan et al. [209] observed from TTF-TCNQ samples double rows attributed to CN radicals in the TCNQ molecules and single rows attributed to the π -bond electron cloud of the TTF molecules (Fig. 28). At temperatures below 80 K they also observed strong corrugations (Fig. 29), with an average period $2a$ consistent with the a component of the commensurate $2k_F$ CDW ($0.5a^*$, $0.29b^*$, $0c^*$) measured with x-rays [214].

Because orbitals pointing out of the surface are not bonded, to minimize its energy the surface may adopt an atom distribution which differs from that of the bulk structure. The surface is said to be "reconstructed." For example, the various phases with different T_c values of β -(BEDT-TTF)₂I₃ are due to the instability of its anion layers [64]; according to STM, there are many vacancies of BEDT-TTF molecules and the surface is reconstructed [212]. In a number of other organic conductors, the surface structure is in good agreement with the crystallographic data for the bulk material.

XIII. CONCLUSIONS

In the 1970s the structural crystallography of molecular compounds was essentially confined to room-temperature structure determinations. The



Figure 28 Room-temperature STM image of a (001) face of a TTF-TCNQ crystal. The image is 18 Å wide. The white lines are the unit cell in the (a,b) plane. The one-dimensional conduction band is formed by the wave functions of p electrons on TTF and TCNQ molecules. It is suggested that the double-row features (small arrows) can be identified as the CN radicals at the extremes of the TCNQ molecules, and the row between (bigger arrow) as the π -bond electron clouds of the TTF molecules. (From Ref. 209.)

main motivation of such work was, for example, drug design, in which physicists had little interest. The discovery of quasi-one-dimensional electrical conductivity in TCNQ-based salts [215,216], Little's proposal that superconductivity may exist in organic materials (Ref. 217 and Chapter 1 in this book), and the successive discovery of synthetic metals and superconductors all contributed strongly to push this discipline toward new fields of interest. Physicists discovered that molecular materials may exhibit a number of interesting properties, such as displacive or incommensurate phase transitions and, more specific to organic conductors, novel phonon-electron coupling, a variety of ground states, and so on. Thus it is not surprising if most of the first structure studies of molecular compounds at very low temperature and/or high pressure have been performed on low-dimensional organic conductors and superconductors. Similarly, the original set of lattice fluctuations and distortions that can be observed in quasi-one-dimensional materials with relatively simple diffuse scattering experiments has opened a rich field of investigation and led to extremely sophisticated interpretations. We have thus shown here how crystallographic

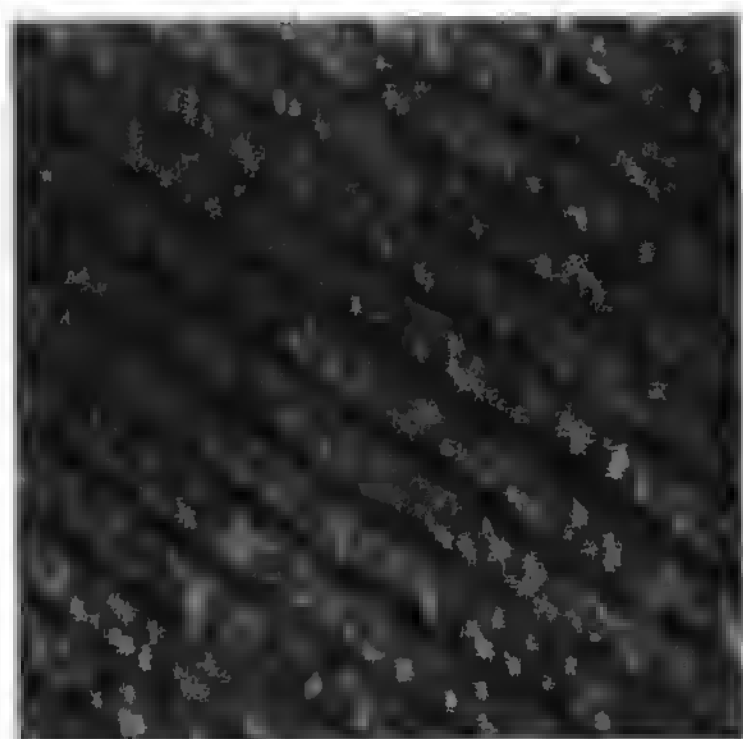


Figure 29 STM image (120 Å wide) of a TTF-TCNQ crystal at temperatures below 80 K. A one-dimensional superlattice commensurate with the underlying lattice, but with double the period, starts to appear. It is attributed by Pan et al. [209] to the commensurate $2k_F$ CDW ($0.5a^*$, $0.29b^*$, $0c^*$) observed by x-ray diffraction study at 50 K [214]. However, the modulation in the b direction was never observed. (From Ref. 209.)

techniques have evolved and how they have, in many aspects, contributed to the present understanding of the physics of organic conductors.

ACKNOWLEDGMENTS

The author would like to thank to D. Chasseau, J. Gaultier, D. Gray, M. S. Lehmann, and S. A. Mason for checking the typescript. He is also very indebted to J. P. Aimé, J. Laugier, G. McIntyre, J. P. Pouget, and C. Vettier for their help on specific sections and for fruitful discussions. Special thanks are due to L. Ducasse for its contribution to Section VIII.

REFERENCES

1. L. Hirshfeld, in *Accurate Molecular Structures: Their Determination and Importance*, (A. Domenicano and I. Hargittai, eds.), International Union of Crystallography, Oxford University Press, Oxford, 1992.
2. J. Baruchel, J. L. Hodeau, M. S. Lehmann, J. R. Regnard, and C. Schlenker, eds., *Neutron and Synchrotron Radiation for Condensed Matter Studies*, Vol. I, Les Editions de Physique and Springer-Verlag, Berlin, 1993.
3. G. H. Stout and L. H. Jensen, *X-ray Structure Determination: A Practical Guide*, Macmillan, New York, 1968.
4. J. D. Dunitz, *X-ray Analysis and the Structure of Organic Molecules*, Cornell University Press, Ithaca, N.Y., 1979.

5. J. D. Jackson, *Classical Electrodynamics*, Wiley, New York, 1962, Chap. 14.
6. *Advanced Neutron Sources 1988: Proceedings of the 10th Meeting of the International Collaboration on Advanced Neutron Sources (ICANS X)*, Los Alamos, N. Mex., Oct. 3–7, 1988, (D. K. Hyer, ed.), Institute of Physics Conference Series No. 97, Institute of Physics, Bristol, 1988.
7. L. B. McCusker, *Proceedings of the International Conference: Accuracy in Powder Diffraction II*, Gaithersburg, Md., May 26–29, 1992, NIST Special Publication 846, pp. 75–79.
8. J. M. Newsam, M. W. Deem, and C. M. Freeman, *Proceedings of the International Conference: Accuracy in Powder Diffraction II*, Gaithersburg, Md., May 26–29, 1992, NIST Special Publication 846, pp. 80–91.
9. H. M. Rietveld, *J. Appl. Cryst.* 2:65 (1969).
10. D. L. Bish and J. E. Post, eds., *Modern Powder Diffraction*, Reviews in Mineralogy, Vol. 20, Mineralogical Society of America, Washington, D.C., 1989.
11. D. Häusermann, *High Pressure Res.* 8:647 (1992).
12. P. Coppens, D. Cox, E. Vlieg, and I. K. Robinson, *Synchrotron Radiation Crystallography*, Academic Press, London, 1992.
13. A. J. Schultz, K. Srinivasan, R. G. Teller, J. M. Williams, and C. M. Lukehart, *J. Am. Chem. Soc.* 106:99 (1984), and references therein.
14. Y. Amemiya, T. Matsushita, A. Nakagawa, Y. Satow, J. Miyahara, and J.-I. Chikawa, *Nucl. Instr. Methods Phys. Res. A* 266:645 (1988).
15. A. J. C. Wilson, ed., *International Tables for Crystallography*, Vol. C, Kluwer, Norwell, Mass., 1992.
16. H. Kobayashi, R. Kato, A. Kobayashi, S. Moriyama, Y. Nishio, K. Kajita, and W. Sasaki, *Synth. Metals* 27:A283 (1988).
17. R. G. Kepler, P. E. Bierstedt, and R. E. Merrifield, *Phys. Rev. Lett.* 5:503 (1960).
18. J. P. Farges, in *Physics and Chemistry of Low-Dimensional Solids*, NATO ASI C 56 (L. Alcácer, ed.), D. Reidel, Dordrecht, The Netherlands, 1980, p. 223.
19. H. Kobayashi, Y. Ohashi, F. Marumo, and Y. Saito, *Acta Cryst. B* 26:459 (1970).
20. J. Jaud, D. Chasseau, J. Gaultier, and C. Hauw, *C.R. Acad. Sci. Sér. C* 278:769 (1974).
21. J. A. Potworowski, Ph.D. thesis, Univ. Toronto, Canada, 1974.
22. A. Filhol, C. M. E. Zeyen, P. Chenavas, J. Gaultier, and P. Delhaes, *Acta Cryst. B* 36:2719 (1980).
23. A. Filhol and M. Thomas, *Acta Cryst. B* 40:44 (1984).
24. A. Cougrand, S. Flandrois, P. Delhaes, P. Dupuis, D. Chasseau, J. Gaultier, and J. L. Miane, *Mol. Cryst. Liq. Cryst.* 32:165 (1976).
25. P. Delhaes, A. Cougrand, S. Flandrois, D. Chasseau, J. Gaultier, C. Hauw, and P. Dupuis, *Lect. Notes Phys.* 65:494 (1977).

26. A. Abokowitz, A. J. Epstein, C. H. Griffiths, J. S. Miller, and M. L. Slade, *J. Am. Chem. Soc.* **99**:5304 (1977).
27. A. Filhol, M. Rovira, C. Hauw, J. Gaultier, D. Chasseau, and P. Dupuis, *Acta Cryst. B* **35**:1652 (1979).
28. P. Coppens, P. Leung, K. E. Murphy, P. R. V. Tilborg, A. J. Epstein, and J. S. Miller, *Mol. Cryst. Liq. Cryst.* **61**:1 (1980).
29. A. Filhol and J. Gaultier, *Acta Cryst. B* **36**:592 (1980).
30. B. Gallois, J. Gaultier, J. P. Pouget, C. Coulon, and A. Filhol, *J. Phys.* **44**:C3-1307 (1983).
31. B. Gallois, J. Gaultier, T. Granier, R. Ayroles, and A. Filhol, *Acta Cryst. B* **41**:56 (1985).
32. J. Ferraris, D. O. Cowan, V. Walatka, Jr., and J. H. Perlstein, *J. Am. Chem. Soc.* **95**:948 (1973).
33. J. P. Ferraris and T. F. Finnegan, *Solid State Commun.* **18**:1169 (1976).
34. D. Jérôme and H. J. Schultz, *Adv. Phys.* **31**:299 (1982).
35. T. J. Kistenmacher, T. E. Phillips, and D. O. Cowan, *Acta Cryst. B* **30**:763 (1974).
36. A. Filhol, G. Bravic, J. Gaultier, D. Chasseau, and C. Vettier, *Acta Cryst. B* **37**:1225 (1981).
37. A. Filhol, Thesis 835, Univ. Bordeaux I, France, 1985.
38. R. H. Blessing and P. Coppens, *Solid State Commun.* **28**:215 (1974).
39. A. Schultz, G. D. Stucky, R. H. Blessing, and P. Coppens, *J. Am. Chem. Soc.* **98**:3194 (1976).
40. Y. Bouveret and S. Megtert, *J. Phys. (France)* **50**:1649 (1989).
41. K. Bechgaard, C. S. Jacobsen, K. Mortensen, H. J. Pedersen, and N. Thorup, *Solid State Commun.* **33**:1119 (1980).
42. D. Jérôme, A. Mazaud, M. Ribaud, and K. Bechgaard, *J. Phys. Lett.* **41**:L95 (1980).
43. K. Bechgaard, K. Carneiro, M. Olsen, and F. B. Rasmussen, *Phys. Rev. Lett.* **46**:852 (1981).
44. N. Thorup, G. Rindorf, H. Soling, and K. Bechgaard, *Acta Cryst. B* **37**:1236 (1981).
45. G. Rindorf, H. Soling, and N. Thorup, *Acta Cryst. B* **38**:2805 (1982).
46. R. Moret and J. P. Pouget, in *Crystal Chemistry and Properties of Materials with Quasi-One-Dimensional Structures* (J. Rouxel, ed.), D. Reidel, Dordrecht, The Netherlands, 1986, pp. 87–143.
47. R. Moret, J. P. Pouget, R. Comès, and K. Bechgaard, *J. Phys.* **44**:C3-957 (1983).
48. J. M. Williams, J. R. Ferraro, R. J. Thorn, K. D. Carlson, U. Geiser, H. H. Wang, A. M. Kini, and M.-H. Whangbo, *Organic Superconductors (Including Fullerenes): Synthesis, Structure, Properties and Theory*, Prentice Hall, Englewood Cliffs, N.J., 1992.
49. J. M. Williams, A. M. Kini, H. H. Wang, K. D. Carlson, U. Geiser, L. K. Montgomery, G. J. Pyrka, D. M. Watkins, J. M. Kommers, S. J. Boryschuk,

- A. V. Strieby Crouch, W. K. Kwok, J. E. Schirber, D. L. Overmyer, D. Jung, and M.-H. Whangbo, *Inorg. Chem.* 29:3272 (1990).
50. É. B. Yagubskii, I. F. Shchegolev, V. N. Laukhin, P. A. Kononovich, M. V. Kartsovnik, A. V. Zvarykina, and L. I. Buravov, *Pis'ma Zh. Eksp. Teor. Fiz.* 39:12 (1984) [*JETP Lett.* 39:12 (1984)].
 51. J. M. Williams, T. J. Emge, H. H. Wang, M. A. Beno, P. T. Copps, L. N. Hall, K. D. Carlson, and G. W. Crabtree, *Inorg. Chem.* 23:2558 (1984).
 52. H. Schwenk, C. P. Heidmann, F. Gross, E. Hess, K. Andres, D. Schweitzer, and H. J. Keller, *Phys. Rev. B* 31:3138 (1985).
 53. V. N. Laukhin, E. É. Kostyuchenko, Y. V. Sushko, I. F. Shchegolev, and É. B. Yagubskii, *Pis'ma Z. Eksp. Teor. Fiz.* 41:68 (1985) [*JETP Lett.* 41:81 (1985)].
 54. K. Murata, M. Tokumoto, H. Anzai, H. Bando, G. Saito, K. Kajimura, and T. Ishiguro, *J. Phys. Soc. Jpn.* 54:1236 (1985).
 55. H. Veith, C.-P. Heidmann, F. Gross, A. Lerf, K. Andres, and D. Schweitzer, *Solid State Commun.* 56:1015 (1985).
 56. F. Creuzet, G. Creuzet, D. Jérôme, D. Schweitzer, and H. J. Keller, *J. Phys. Lett.* 46:L1079 (1985).
 57. A. J. Schultz, M. A. Beno, H. H. Wang, and J. M. Williams, *Phys. Rev. B* 33:7823 (1986).
 58. V. F. Kaminskii, T. G. Prokhorova, R. P. Shibaeva, and É. B. Yagubskii, *Pis'ma Zh. Eksp. Teor. Fiz.* 39:15 (1984) [*JETP Lett.* 39:17 (1984)].
 59. R. P. Shibaeva, V. F. Kaminskii, and V. K. Bel'skii, *Kristallografiya* 29:1089 (1984) [*Sov. Phys. Crystallog.* 29:638 (1984)].
 60. R. P. Shibaeva, V. F. Kaminskii, and É. B. Yagubskii, *Mol. Cryst. Liq. Cryst.* 119:361 (1984).
 61. T. Mori, A. Kobayashi, Y. Sasaki, H. Kobayashi, G. Saito, and H. Inokuchi, *Chem. Lett.* 6:957 (1984).
 62. A. J. Schultz, H. H. Wang, J. M. Williams, and A. Filhol, *J. Am. Chem. Soc.* 108:7853 (1986); *Physica B* 143:354 (1986).
 63. V. N. Molchanov, A. P. Shibaeva, V. N. Kachinshii, E. B. Yagubskii, V. N. Simonov, and B. K. Vainshtein, *Dokl. Akad. Nauk SSSR* 286:637 (1986) [*Sov. Phys. Dokl.* 31:6 (1986)].
 64. T. J. Emge, P. C. W. Leung, M. A. Beno, A. J. Schultz, H. H. Wang, L. M. Sowa, and J. M. Williams, *Phys. Rev. B* 30:6780 (1984).
 65. P. C. W. Leung, T. J. Emge, M. A. Beno, H. H. Wang, J. M. Williams, V. Petricek, and P. Coppens, *J. Am. Chem. Soc.* 106:7644 (1984); *J. Am. Chem. Soc.* 107:6184 (1985).
 66. Y. Nogami, S. Kagoshima, T. Sugano, and G. Saito, *Synth. Met.* 16:367 (1986).
 67. S. Ravy, J. P. Pouget, R. Moret, and C. Lenoir, *Phys. Rev. B* 37:5113 (1988).
 68. J. J. André, A. Bieber, and F. Gautier, *Ann. Phys.* 1:145 (1976).
 69. D. Chasseau, Thesis 632, Univ. Bordeaux I, France, 1979.

70. B. Gallois, J. Gaultier, C. Hauw, T. Lamcharfi, and A. Filhol, *Acta Cryst. B* 42:564 (1986).
71. T. Lamcharfi, Thesis 28, Univ. Bordeaux I, France, 1986.
72. S. Flandrois and D. Chasseau, *Acta Cryst. B* 33:2744 (1977).
73. G. Shirane, S. M. Shapiro, R. Comès, A. F. Garito, and A. J. Heeger, *Phys. Rev. B* 14:2325 (1976).
74. S. K. Khanna, J. P. Pouget, R. Comès, A. F. Garito, and A. J. Heeger, *Phys. Rev. B* 16:1468 (1977).
75. M. Weger and J. Friedel, *J. Phys.* 38:241 (1977).
76. H. Morawitz, *Phys. Rev. Lett.* 34:1096 (1975).
77. H. Gutfreund, B. Horowitz, and M. Weger, *J. Phys. C* 7:383 (1974).
78. M. J. Rice, C. B. Duke, and N. O. Lipari, *Solid State Commun.* 17:1089 (1975).
79. F. K. Larsen, in *The Application of Charge Density Research to Chemistry and Drug Design*, (G. A. Jeffrey and J. F. Piniella, eds.), Plenum Press, New York, 1991, pp. 187–208.
80. R. Argoud and J. Muller, *J. Appl. Cryst.* 22:584 (1989).
81. J. Albertson, Å. Oskarsson, and K. Ståhl, *J. Appl. Cryst.* 12:537 (1979).
82. F. Elf, G. Will, J. Chatzipetros, and B. Dujka, *Rev. Phys. Appl.* 19:793 (1984).
83. P. Coppens, F. K. Ross, R. H. Blessing, W. F. Cooper, F. K. Larsen, J. G. Leipoldt, B. Rees, and R. Leonard, *J. Appl. Cryst.* 7:315 (1974).
84. S. Samson, E. Goldish, and C. J. Dick, *J. Appl. Cryst.* 13:425 (1980).
85. C. Lowe-Ma, R. Williams, and S. Samson, *J. Chem. Phys.* 74:1966 (1981).
86. C. M. E. Zeyen, R. Chagnon, F. Disdier, and H. Morin, *Rev. Phys. Appl.* 19:789 (1984).
87. B. Gallois, J. Gaultier, C. Hauw, T. Lamcharfi, and A. Filhol, *J. Phys.* 44:C3-1071 (1983).
88. B. Gallois, D. Chasseau, J. Gaultier, C. Hauw, and A. Filhol, *Acta Cryst. B* 42:564 (1986).
89. A. Filhol, J. M. Reynal, J. M. Savariault, P. Simms, and M. Thomas, *J. Appl. Cryst.* 13:343 (1980).
90. K. Henriksen, F. K. Larsen, and S. E. Rasmussen, *J. Appl. Cryst.* 19:390 (1986).
91. D. D. Coppens, P. Coppens, R. Li, and P. Lee, *J. Appl. Cryst.* 26:226 (1993).
92. R. J. Nelmes and D. Häusermann, *Proceedings of the IUCr Workshop on Synchrotron Radiation Instrumentation for High Pressure Crystallography*, High Pressure Res. 8 (1992).
93. M. Rahal, Thesis 906, Univ. Bordeaux I, France, 1993. J. Gaultier and M. Rahal, to be published.
94. C. Vettier, in *Neutron Scattering: 1981* (J. Fabert, ed.), AIP Conf. Proc. 89:121 (1982).
95. D. B. McWhan, *Rev. Phys. Appl.* 19:715 (1984).
96. H. Ahsbahs, *Rev. Sci. Instrum.* 55:99 (1984).

97. D. Chasseau, J. Gaultier, G. Bravic, L. Ducasse, M. Kurmoo, and P. Day, *Proc. R. Soc. London* 442:207 (1993).
98. H. Ahsbahr, *Rev. Phys. Appl.* 19:819 (1984).
99. B. Gallois, J. Gaultier, C. Hauw, D. Chasseau, A. Meresse, and A. Filhol, *Mol. Cryst. Liq. Cryst.* 119:225 (1985).
100. D. Chasseau, J. Gaultier, M. Rahal, L. Ducasse, M. Kurmoo, and P. Day, *Synth. Metals* 41–43:2039 (1991).
101. A. J. Schultz, U. Geiser, H. H. Wang, J. M. Williams, L. W. Finger, and R. M. Hazen, *Physica C* 208:277 (1993).
102. B. Gallois, J. Gaultier, F. Bechtel, A. Filhol, and C. Vettier, *Mol. Cryst. Liq. Cryst.* 148:279 (1987).
103. Y. Nogami, S. Kagoshima, H. Anzai, M. Tokumoto, N. Môri, N. Kinoshita, and G. Saito, *J. Phys. Soc. Jpn.* 59:259 (1990).
104. R. Moret, S. Ravy, J. P. Pouget, R. Comès, and K. Bechgaard, *Phys. Rev. B* 57:1915 (1986).
105. D. Debray, R. Millet, D. Jérôme, S. Barisic, L. Giral, and J. M. Fabre, *Phys. Rev. Lett.* 38:715 (1977).
106. J. Pannetier, in *Neutron and Synchrotron Radiation for Condensed Matter Studies*, Vol. 1 (J. Baruchel, J. L. Hodeau, M. S. Lehmann, J. R. Regnard, and C. Schlenker, eds.), Les Editions de Physique and Springer-Verlag, Berlin, 1993.
107. N. B. Chanh, J. Clastre, J. Gaultier, Y. Haget, A. Meresse, J. Lajzerowicz, A. Filhol, and M. Thomas, *J. Appl. Cryst.* 21:10 (1988).
108. J. F. Nye, *Physical Properties of Crystals*, Clarendon Press, Oxford, 1957.
109. J. P. Farges, *J. Phys.* 46:465 (1985); 46:1249 (1985).
110. J. P. Travers, F. Devreux, and M. Nechtschein, *J. Phys.* 44:C3-1295 (1983).
111. H. Grassi and H. Broch, *Theochem* 60:371 (1989).
112. B. El Amrani, Thesis 29, Univ. Bordeaux I, France, 1986.
113. J. P. Pouget, in *Low Dimensional Conductors and Superconductors*, NATO ASI B 155 (D. Jérôme and L. C. Caron, eds.), Plenum Press, New York, 1987, pp. 17–45.
114. J. P. Pouget, in *Highly Conducting Quasi-One-Dimensional Organic Crystal Semiconductors and Semimetals*, Vol. 27 (E. M. Conwell, ed.), Pergamon Press, New York, 1988, p. 87.
115. J. P. Pouget and R. Comès, in *Charge Density Waves in Solids* (L. P. Gor'kov and G. Grüner, eds.), Elsevier, Amsterdam, 1989, pp. 85–136.
116. J. P. Pouget, S. Ravy, and B. Hennion, *Phase Transitions* 30:5 (1991).
117. K. Yamaji, S. Megtert, and R. Comès, *J. Phys.* 42:1327 (1981).
118. S. Kagoshima, T. Ishiguro, and H. Anzai, *J. Phys. Soc. Jpn.* 41:2061 (1976).
119. J. P. Pouget, R. Moret, R. Comès, K. Bechgaard, J. M. Fabre, and L. Giral, *Mol. Cryst. Liq. Cryst.* 79:129 (1982).
120. J. P. Pouget, in *Organic and Inorganic Low-Dimensional Materials*, NATO ASI B 168 (P. Delhaes and M. Drillon, eds.), Plenum Press, New York, 1987.

121. R. Moret, J. P. Pouget, R. Comès, and K. Bechgaard, *Phys. Rev. Lett.* **49**:1008 (1982).
122. G. Rindorf, H. Soling, and N. Thorup, *Acta Cryst. C* **40**:1137 (1984).
123. P. M. De Wolff, *Acta Cryst. A* **30**:777 (1974).
124. A. Janner and T. Janssen, *Phys. Rev. B* **15**:643 (1977).
125. P. M. De Wolff, T. Janssen, and A. Janner, *Acta Cryst. A* **37**:625 (1981).
126. A. Yamamoto, *Acta Cryst. A* **48**:476 (1992).
127. P. Coppens, V. Petricek, D. Levendis, F. K. Larsen, A. Paturle, G. Yan, and A. D. Legrand, *Phys. Rev. Lett.* **59**:1695 (1987).
128. R. Moret, J. P. Pouget, R. Comès, and K. Bechgaard, *J. Phys.* **46**:1521 (1985).
129. B. Gallois, A. Méresse, J. Gaultier, and R. Moret, *Mol. Cryst. Liq. Cryst.* **131**:147 (1985).
130. B. Gallois, D. Chasseau, J. Gaultier, C. Hauw, A. Filhol, and K. Bechgaard, *J. Phys. Colloq.* **44**:1071 (1983).
131. T. J. Emge, J. M. Williams, P. C. W. Leung, A. J. Schultz, M. A. Beno, and H. H. Wang, *Mol. Cryst. Liq. Cryst.* **119**:237 (1985).
132. S. Megtert, Thesis, Univ. Paris–Sud, Orsay, France, 1978.
133. J. P. Pouget, S. K. Khanna, F. Denoyer, R. Comès, A. F. Garito, and A. J. Heeger, *Phys. Rev. Lett.* **37**:437 (1976).
134. S. Megtert, J. P. Pouget, R. Comès, and R. Fourme, *Lect. Notes Phys.* **96**:196 (1979).
135. A. Filhol, B. Gallois, J. Laugier, P. Dupuis, and C. Coulon, *Mol. Cryst. Liq. Cryst.* **84**:17 (1982).
136. A. Filhol, J. Gaultier, C. Hauw, B. Hilti, and C. W. Mayer, *Acta Cryst. B* **38**:2577 (1982).
137. S. Megtert, R. Comès, C. Vettier, R. Pynn, and A. F. Garito, *Mol. Cryst. Liq. Cryst.* **85**:159 (1982).
138. T. Doi, K. Oshima, H. Maeda, H. Yamazaki, H. Maruyama, H. Kimura, M. Fujita, H. Mori, S. Tanaka, H. Yamochi, and G. Saito, *Physica C* **185–189**:2671 (1991).
139. J. Williams, A. J. Schultz, U. Geiser, K. D. Carlson, A. M. Kini, H. H. Wang, W.-K. Kwok, M.-H. Whangbo, and J. E. Schirber, *Science* **252**:1501 (1991).
140. P. Delhaès, J. Ameill, L. Ducasse, B. Hilti, C. W. Mayer, and J. Zambounis, *Physica B* **182**:99 (1992).
141. K. Oshima, T. Doi, Y. Tokuoka, H. Yamazaki, K. Kato, Y. Maruyama, H. Mori, and S. Tanaka, *Synth. Metals* **55–57**:2339 (1993).
142. A. Graja, *Low-Dimensional Organic Conductors*, World Scientific, Singapore, 1992.
143. J. P. Pouget, S. M. Shapiro, G. Shirane, A. F. Garito, and A. J. Heeger, *Phys. Rev. B* **19**:1792 (1979).
144. F. Denoyer, R. Comès, A. F. Garito, and A. J. Heeger, *Phys. Rev. Lett.* **35**:445 (1975).

145. S. Megtert, R. Comès, C. Vettier, R. Pynn, and A. F. Garito, *Solid State Commun.* 31:977 (1979); 37:875 (1981); *Mol. Cryst. Liq. Cryst.* 85:159 (1982).
146. A. Andrieux, H. J. Schulz, D. Jérôme, and K. Bechgaard, *Phys. Rev. Lett.* 43:227 (1979); *J. Phys. Lett.* 40:L385 (1979).
147. P. Coppens, *Phys. Rev. Lett.* 35:98 (1975).
148. P. Coppens, *J. Phys. Chem.* 93:7979 (1989).
149. J. S. Chappell, A. N. Bloch, W. A. Bryden, M. Maxfield, T. O. Poehler, and D. O. Cowan, *Am. Chem. Soc.* 103:2442 (1981).
150. H. Kobayashi, R. Kato, T. Mori, A. Kobayashi, Y. Sasaki, G. Saito, T. Enoki, and H. Inokuchi, *Mol. Cryst. Liq. Cryst.* 107:33 (1984).
151. M. Fettouhi, Thesis 977, Univ. Rennes I, France, 1993.
152. E. Canadell and M.-H. Whangbo, *Chem. Rev.* 91:965 (1991).
153. R. V. Kasowski and M.-H. Whangbo, *Inorg. Chem.* 29:360 (1990).
154. P. M. Grant, *Phys. Rev. B* 26:6888 (1982).
155. P. M. Grant, *J. Phys.* 44(C3):847 (1983).
156. L. Ducasse, M. Abderraba, and B. Gallois, *J. Phys. C* 18:L947 (1985).
157. L. Ducasse, M. Abderraba, J. Hoarau, M. Pesquer, B. Gallois, and J. Gaultier, *J. Phys. C* 18:3805 (1986).
158. D. Jung, M. Evain, J. J. Novoa, M.-H. Whangbo, M. A. Beno, A. M. Kini, A. J. Schultz, J. M. Williams, and P. J. Nigrey, *Inorg. Chem.* 28:4516 (1989).
159. A. Kobayashi, R. Kato, H. Kobayashi, Y. Nishio, K. Kajita, and W. Sasaki, *Chem. Lett.*, 789 (1986).
160. J. M. Delrieu, M. Roger, Z. Toffano, A. Moradpour, and K. Bechgaard, *J. Phys.* 47:839 (1986).
161. N. Toyota, T. Sasaki, K. Murata, Y. Honda, M. Tokumoto, H. Bando, N. Kinochita, H. Anzai, T. Ishiguro, and Y. Muto, *J. Phys. Soc. Jpn.* 57:2616 (1988).
162. A. Fritsh and L. Ducasee, *J. Phys. I* 1:855 (1991).
163. T. D. Schultz and R. A. Craven, in *Highly Conducting One-Dimensional Solids* (J. T. Devereese, R. P. Evrard and V. E. van Doren, eds.), Plenum Press, New York, 1979.
164. C. Coulon, *J. Phys. Coll.* 44:C3-885 (1983).
165. S. Tomic, D. Jérôme, D. Mailly, M. Ribault, and K. Bechgaard, *J. Phys. Colloq.* 44:C3-1075 (1983).
166. L. Zuppiroli, in *Low-Dimensional Conductors and Superconductors*, NATO ASI B 135 (D. Jérôme and L. G. Caron, eds.), Plenum Press, New York, 1987.
167. T. Siegrist, S. Sunshine, D. W. Murphy, R. J. Cava, and S. M. Zahurak, *Phys. Rev. B* 13:7137 (1987).
168. J. J. Capponi, C. Chaillout, A. W. Hewat, P. Lejay, M. Marezio, N. Nguyen, B. Raveau, J. L. Soubeyroux, J. L. Tholence, and R. Tournier, *Europhys. Lett.* 3:1301 (1987).
169. T. Ishiguro, T. Ukachi, M. Tokumoto, K. Murata, K. Kajimura, H. Anzai, K. Kato, and G. Saito, *J. Phys.* 44:C3-1063 (1983).

170. A. V. Zvarykina, M. V. Kartsovnik, V. N. Laukhin, E. É. Laukhina, R. B. Lyubovskii, S. I. Pesotskii, R. P. Shibaeva, and I. F. Shchagolev, *Zh. Eksp. Teor. Fiz.* 94:277 (1988) [*Sov. Phys. JETP* 67:1891 (1988)].
171. H. Kobayashi, R. Kato, A. Kobayashi, Y. Nishio, K. Kajita, and W. Sasaki, *Chem. Lett.*, 2017 (1986).
172. Y. Watanabe, T. Sasaki, H. Sato, and N. Toyota, *J. Phys. Soc. Jpn.* 60:927 (1991).
173. A. J. Schultz, M. A. Beno, U. Geiser, H. H. Wang, A. M. Kini, J. M. Williams, and M.-H. Whangbo, *J. Solid State Chem.* 94:352 (1991).
174. J. C. Marmeggi, in *Position-Sensitive Detection of Thermal Neutrons*, (P. Convert and J. B. Forsyth, eds.), Academic Press, New York, 1983, pp. 391–399.
175. J. C. Marmeggi, J. Laugier, and A. Filhol, *La Revue de Métallurgie-CIT/ Science et Génie des Matériaux*, Sept 1993, p. 1182.
176. H. R. Luss and D. L. Smith, *Acta Cryst. B* 33:1744 (1977).
177. H. R. Luss and D. L. Smith, *Acta Cryst. B* 36:1580 (1980).
178. P. A. Albouy, J. P. Pouget, and H. Strzelecka, *Phys. Rev. B* 35:173 (1987).
179. H. Kobayashi, *Bull. Chem. Soc. Jpn.* 48:1373 (1975).
180. H. Kobayashi, F. Marumo, and Y. Saito, *Acta Cryst. B* 27:373 (1971).
181. J. P. Pouget, G. Shirane, K. Bechgaard, and J. M. Fabre, *Phys. Rev. B* 27:5203 (1983).
182. C. S. Jacobsen, H. J. Pedersen, K. Mortensen, G. Rindorf, N. Thorup, J. B. Torrance, and K. Bechgaard, *J. Phys. C* 15:2651 (1982).
183. Q. Liu, S. Ravy, J. P. Pouget, I. Johannsen, and K. Bechgaard, *J. Phys. I France* 3:803 (1993).
184. L. Zuppiroli and S. Bouffard, *J. Phys.* 41:291 (1980).
185. L. Zuppiroli, H. Mutka, and S. Bouffard, Boulder Conference, Saclay, France, Sept. 9, 1980.
186. C. Coulon, P. Delhaes, J. Amiell, J. P. Manceau, J. M. Fabre, and L. Giral, *J. Phys.* 43:1721 (1982).
187. J. P. Pouget, R. Moret, R. Comès, G. Shirane, K. Bechgaard, and J. M. Fabre, *J. Phys. Colloq.* 44:C3-969 (1983).
188. R. L. Greene, P. Haen, S. Z. Huang, E. M. Engler, M. Y. Choi, and P. M. Chaikin, *Mol. Cryst. Liq. Cryst.* 79:183 (1982).
189. G. Sekretarczyk and A. Graja, *Synth. Metals* 35:53 (1990).
190. T. Granier and R. Ayroles, *J. Phys. Colloq.* 44:C3-1301 (1983).
191. J. M. Troup, M. W. Extine, and R. F. Ziolo, in *Proceedings of the American Chemical Society Symposium on Electron Distribution and the Chemical Bond* (M. B. Hall and P. Coppens, eds.), Plenum Press, New York, 1982, p. 285.
192. H. Fuess, in *The Application of Charge Density Research to Chemistry and Drug Design*, NATO ASI B 250 (G. A. Jeffrey and J. F. Piniella, eds.), Plenum Press, New York, 1991.
193. F. Wudl, D. Nalewájek, J. M. Troup, and M. W. Extine, *Science* 222:415 (1983).
194. M. Almeida and L. Alcácer, *J. Cryst. Growth* 62:183 (1983).

195. M. Almeida, L. Alcácer, and A. Lindegaard-Andersen, *J. Cryst. Growth* 72:567 (1985).
196. P. Dupuis and J. Néel, *C. R. Acad. Sci. (Paris) C* 265:1297 (1967).
197. J. Joansen, L. Groth-Andersen, and K. F. Nielsen, *J. Cryst. Growth* 51:627 (1981).
198. J. R. Ferraro and J. M. Williams, *Introduction to Synthetic Electrical Conductors*, Academic Press, New York, 1987, p. 26.
199. J. D. Begg, R. S. Narang, K. J. Roberts, and J. N. Sherwood, *J. Cryst. Growth* 49:735 (1980).
200. A. Lindegaard-Andersen, M. Almeida, L. Alcácer, and K. Mortensen, *J. Phys. Colloq.* 44:C3-1325 (1983).
201. P. J. Brown, *Sci. Prog. Oxford* 73:213 (1989).
202. S. Flandrois, J. Amiell, F. Carmona, and P. Delhaes, *Mol. Cryst. Liq. Cryst.* 32:255 (1976).
203. S. Oostra, Thesis, Rijksuniversiteit Groningen, The Netherlands, 1985, pp. 56–60.
204. S. Flandrois and J. Boissonade, *Chem. Phys. Lett.* 58:596 (1978).
205. G. Aepli, J. L. de Boer, J. P. Pouget, and G. Shirane, *Phys. Rev. B* 29:5165 (1984).
206. G. Binning, H. Rohrer, Ch. Gerber, and E. Weibel, *Appl. Phys. Lett.* 40:178 (1982); *Phys. Rev. Lett.* 49:57 (1982).
207. P. K. Hansma and J. Tersoff, *J. Appl. Phys.* 61:R1 (1987).
208. G. Binning, C. F. Quate, and Ch. Gerber, *Phys. Rev. Lett.* 56:930 (1986).
209. S. Pan, A. L. de Lozanne, and R. Fainchtein, *J. Vac. Sci. Technol. B* 9:1017 (1991).
210. R. Fainchtein and J. C. Murphy, *J. Vac. Sci. Technol. B* 9:1013 (1991).
211. S. N. Magonov, G. Bar, E. Keller, E. B. Yagubskii, and H.-J. Cantov, *Synth. Metals* 40:247 (1991).
212. M. Yoshimura, H. Shigekawa, H. Yamochi, G. Saito, Y. Saito, and A. Kawazu, *Phys. Rev. B* 44:1970 (1991).
213. R. Fainchtein, S. T. d'Arcangelis, S. S. Yang, and D. O. Cowan, *Science* 256:1012 (1992).
214. S. K. Khanna, J. P. Pouget, R. Comès, A. F. Garito, and A. J. Heeger, *Phys. Rev. B* 19:1792 (1979).
215. L. R. Melby, R. J. Harder, W. R. Hertler, W. Mahler, R. E. Benson, and W. E. Mochel, *J. Am. Chem. Soc.* 84:3374 (1962).
216. D. S. Acker and D. C. Blomstrom, U.S. Patent 3,162,641 (1964).
217. W. A. Little, *Phys. Rev. A* 134:1416 (1964).

6

Optical Properties

Andrzej Graja

Polish Academy of Sciences, Poznań, Poland

I. INTRODUCTION

Optical—in particular spectral—studies play an important role in the investigation of electronically low-dimensional organic conductors. The materials are characterized by highly anisotropic optical properties, with one crystal direction often displaying metal-like behavior, while others appear to be lower conducting. Previous reviews of optical properties of these materials have been elaborated by numerous authors (e.g., Refs. 1 to 10). It was shown that optical studies provide information on a number of fundamental interactions and basic properties of organic conductors.

Within a variety of measurements, optical reflectivity investigation of indicatrix and the study of spectra in a wide frequency range help to clarify, for example, the interaction of electronic and vibrational transitions, the role of electron–electron and electron–phonon couplings, intermolecular interactions, and so on. The orientation of the polarizability tensor related to the molecule axes (i.e., to the crystal structure) is investigated by measuring the orientation and dispersion of the indicatrix. On the other hand, electronic spectroscopy can be naturally considered as a useful technique for determining the electronic structure of organic conductors. The interest in the vibrational spectroscopy (e.g., infrared, Raman) is justified by the fact that the interaction between electrons and intramolecular vibrations plays an important role in determining the physical properties of low-

dimensional molecular conductors, both molecular complexes and ion-radical salts.

The properties of low-dimensional organic conductors are determined by different interactions and instabilities (see, e.g., Chapter 2). It is commonly assumed that it can be treated as in ordinary metals with a frozen long-range interaction part, while the short-range part gives rise to quasiparticles with screened interactions. Thus the proper model Hamiltonian is of the extended Hubbard type [11].

The optical properties of organic conductors may be described by the simplest model, which assumes noninteracting electrons (one-electron model). In this approximation the infrared (IR) properties may be derived in the self-consistent field approximation. Assuming a frequency-independent relaxation rate, γ , and a background dielectric constant arising from virtual high-frequency transitions, ϵ_0 , the result takes the Drude form [12]:

$$\epsilon^*(\omega) = \epsilon_0 - \frac{\omega_p^2}{\omega^2 + i\omega\gamma} \quad (1)$$

where ω_p is the plasma frequency. Expression (1) is frequently used to describe the low-frequency optical properties of organic metal-like conductors and to estimate some of its electron parameters.

In organic conductors the electron-phonon couplings play a fundamental role. In general, the interaction of the electrons with intramolecular vibrations can be written in the form given by Rice [13]:

$$H = H_e + H_v + \sum_{i,\alpha} g_\alpha n_i Q_{\alpha i} \quad (2)$$

The first two terms describe, respectively, the radical electrons and the molecular vibrations in the absence of vibronic coupling. Linear electron-molecular vibration (e-mv) coupling is described explicitly by the third term in Eq. (2). The set of G constants $\{g_\alpha\}$ denotes linear monomer π -electron-molecular vibration coupling constants. In the following sections, the indicatrix measurements, electronic and molecular spectroscopies, and other techniques are analyzed as methods of characterizing the organic conductors.

II. REMARKS ON BASIC OPTICAL PROPERTIES OF LOW-DIMENSIONAL ORGANIC SOLIDS

A. Complex Dielectric Function

There are many ways to determine the optical constants of bulk or thin-film solids. However, only some of them are useful for organic conductors.

Usually, the absorption coefficient of the conducting crystals is so high that producing a crystal sufficiently thin and suitable for absorption measurements presents a great difficulty. If this is so, the bulk optical constants of a solid may be computed from the normal-incidence reflectivity of that material over an extended range of frequencies, followed by a Kramers–Kronig analysis of the measurements [12,14]. In this method the real, n , and imaginary, k , parts of the complex index of refraction

$$n^* = n - ik \quad (3)$$

are related to the measured reflectivity by

$$n = \frac{1 - r^2}{1 - 2|r| \cos \theta + r^2} \quad (4)$$

$$k = \frac{2|r| \sin \theta}{1 - 2|r| \cos \theta + r^2} \quad (5)$$

where r and θ are defined in terms of the measured reflectivity R by the equation

$$r = \sqrt{R} e^{i\theta} \quad (6)$$

Application of the Kramers–Kronig procedure then allows us to express the phase shift, θ , in terms of R [14]:

$$\theta(\omega') = \frac{1}{\pi} \int_{-\infty}^{+\infty} \frac{\ln[R(\omega)]^{1/2}}{\omega - \omega'} d\omega \quad (7)$$

In practice, this integral is performed on a digital computer using a measured spectrum of R versus ω , the frequency of electromagnetic radiation. The index of refraction of anisotropic solids is described by a biaxial indicatrix. In triclinic crystals the indicatrix is a triaxial ellipsoid formed by three principal axes of the length $2n_\alpha$, $2n_\beta$, and $2n_\gamma$ which lie along the X , Y , and Z optical directions, respectively. n_α , n_β , and n_γ are the three principal indices of refraction ($n_\alpha < n_\beta < n_\gamma$). For absorbing crystals the indicatrix is complex [15].

The response of a pure, homogeneous medium to the applied fields may be characterized quite generally by a complex frequency-dependent dielectric function $\epsilon(\omega)$, which can be written in terms of its real and imaginary parts as

$$\epsilon(\omega) = \epsilon'(\omega) + i\epsilon''(\omega) \quad (8)$$

The relationship between the optical parameters (n , k) and the dielectric parameters (ϵ' , ϵ'') is given by

$$\epsilon'(\omega) = n(\omega)^2 - k(\omega)^2 \quad (9)$$

and

$$\epsilon''(\omega) = 2n(\omega)k(\omega) \quad (10)$$

In the case of conducting materials the frequency-dependent conductivity, $\sigma(\omega)$, is often used. The $\sigma(\omega)$ is defined by the equation

$$\sigma(\omega) = \epsilon''(\omega)\epsilon_0\omega = 2n(\omega)k(\omega)\epsilon_0\omega \quad (11)$$

where ϵ_0 is the vacuum permittivity. The dielectric functions $\epsilon'(\omega)$ and $\epsilon''(\omega)$ have a simpler mathematical form than the optical parameters $n(\omega)$ and $k(\omega)$. Classical dispersion theory provides a simple approximation for physical understanding of dielectric and optical parameters. When the medium is highly anisotropic, as are the organic conductors, $\epsilon(\omega)$ and $\sigma(\omega)$ become tensor quantities. In general, the principal directions of the tensors may vary in space with frequency.

B. Electron–Molecular Vibration Couplings

This type of interaction determines above all the optical properties of low-dimensional organic conductors in the middle infrared region. It leads to activation of modes that are normally nonactive in the IR. For the tetracyano-*p*-quinodimethane (TCNQ), tetrathiafulvalene (TTF), and other symmetrical molecules, π molecular orbital occupied by the radical electron are nondegenerate, so linear e-mv coupling is possible only for the totally symmetric (a_g) modes. For example, TCNQ molecule has 54 normal modes, among which only 10 are the a_g modes. They cover a range of frequencies from about 130 cm^{-1} to about 3050 cm^{-1} [16], while TTF molecules has seven totally symmetric modes of the range $250 \text{ cm}^{-1} < \omega_\alpha < 3100 \text{ cm}^{-1}$ [17].

The absorption IR spectra of the organic conductors, of both ion-radical salts and charge-transfer (CT) complexes, created by a given electron acceptor with various donors, share plenty of characteristic features. In addition to rather narrow and weak bands characteristic of the donor D and acceptor A molecules, a few novel absorption bands appear. They are polarized in the plane perpendicular to that of D and A molecules, broad and very intensive. The presence of such unusually polarized bands can be accounted for by the activation of totally symmetric donor or acceptor vibrations resulting from e-mv coupling. Typical polarized reflection spectra of the triethylammonium (TEA) (TCNQ)₂ salt for three light polarizations [18] are shown in Fig. 1. It is fascinating that the reflectivity for

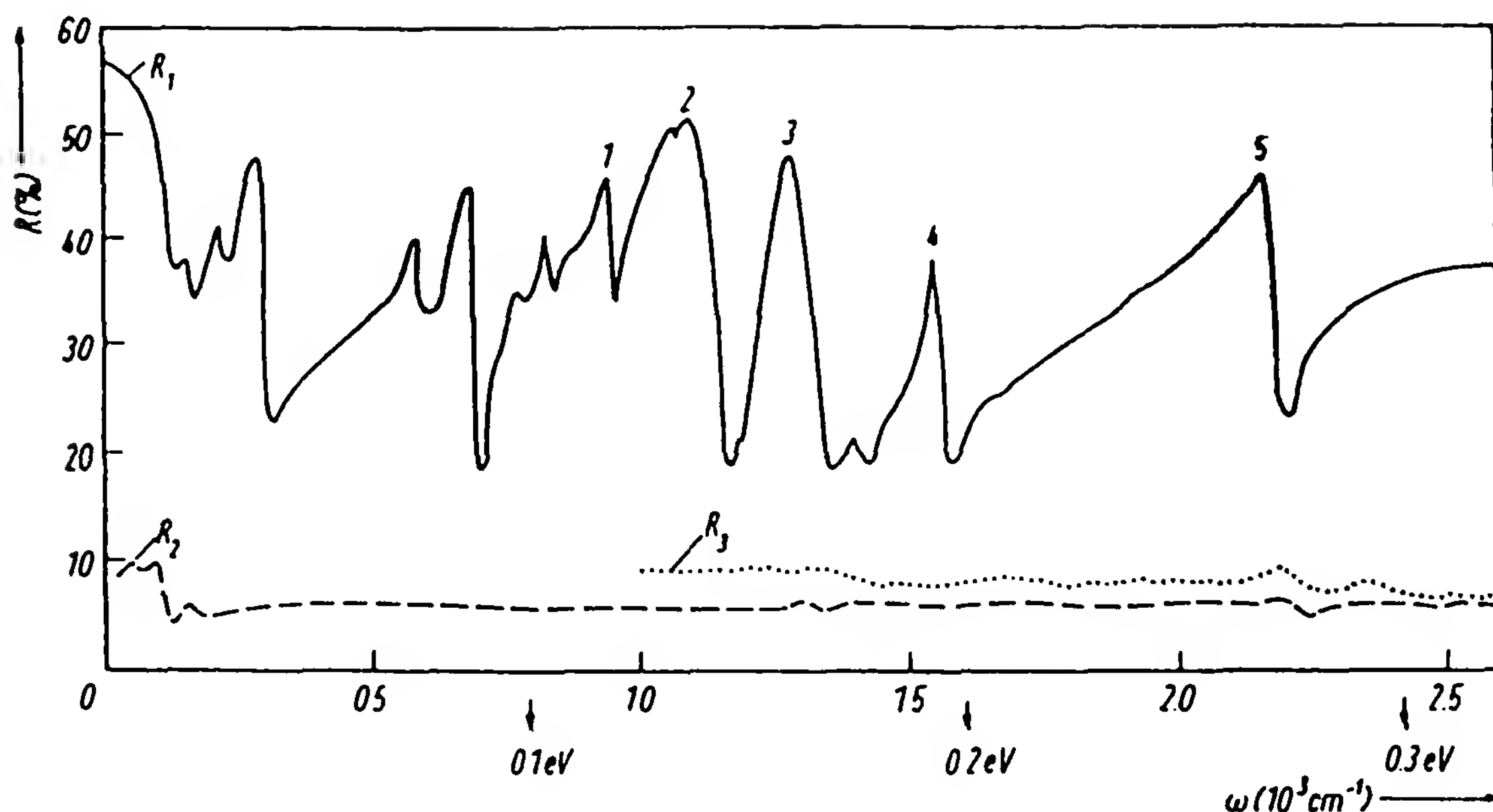


Figure 1 Polarized near-normal-incidence reflection spectra of TEA(TCNQ)₂ at room temperature in the far-infrared and infrared region. The spectra show the details for three light polarizations: 1, parallel to the TCNQ chains; 2 and 3, perpendicular to the chains (2 being within and 3 perpendicular to the alternating layers of TCNQ and TEA molecules). (From Ref. 18.)

the electric vector polarization parallel to stacks (nearly perpendicular to the acceptor plane) reflects intramolecular vibrations in the plane of the molecules.

A more precise interpretation of the electron–phonon coupling mechanism has been offered by Rice and his co-workers [19,20]. Let us consider a linear chain composed of organic molecules whose semiconducting properties are due to Peierls distortion. The ground state of this system is determined by a set of charge density waves (CDWs), each bound to an oscillation system of ion radicals coupled with electrons. Small-amplitude oscillations in the phase of the component CDWs about their stationary equilibrium values involve bodily displacement of the condensed radical electron charge along the chain axis and lead to abnormal optical activity. In the microscope theory [19] they are described by a phase phonon propagator $D_\phi(\omega)$, which depends on the details of the CDW ground state and, in particular, on the magnitude of the e-mv coupling constants. The complex conductivity, $\sigma(\omega)$, may be expressed in terms of $D_\phi(\omega)$, as a function of e-mv coupling constants.

In the majority of low-dimensional organic conductors the molecules are arranged to form linear clusters of two, three, or four molecules. A somewhat different mechanism is responsible for the e-mv couplings in

these systems. Their optical properties may be described as a simple superposition of the optical responses from isolated n -mers ($n = 2, 3, 4, \dots$) [9,20]. Such optical response is related to localized electronic CT excitations coupled to the intramolecular vibrational modes.

In organic conductors composed of isolated dimers, the synchronization of a_g vibrations in both moieties of the dimer may result in their symmetrical or antisymmetrical vibrations. It is just the antisymmetrical type of vibrations that is capable of coupling to electron oscillations. As a consequence of this interaction, an abnormal optical absorption of the system can be observed. It is polarized in the direction of the dimer's axis and characterized by a frequency close to that of symmetrically vibrating molecules forming a dimer.

Despite some model differences, dielectric susceptibility can be expressed by the same equation [7]:

$$\epsilon(\omega) = \epsilon_\infty \left\{ 1 + \omega_p^2 \left[\chi_{el}(\omega) - \frac{(\lambda/\omega_0^2)f^2(\omega)}{D_0^{-1}(\omega) + b + \lambda cf(\omega)} \right] \right\} \tag{12}$$

valid for both phase phonon and dimer models. $\chi_{el}(\omega)$ determines the electronic part of $\epsilon(\omega)$, while the second part of the expression in square brackets determines the electron-phonon share. However, the form of values is different for the two models:

Phase phonon model	Dimer model
$\chi_{el} = \frac{f(\omega) - f(0)}{\omega^2}$	$\chi_{el} = \frac{f(\omega)}{\omega_0^2}$
$f(\omega) = \frac{\pi i + \ln[(1 - s)/(1 + s)]}{2s(\omega/\omega_0)^2}$	$f(\omega) = \frac{\omega_0^2}{\omega_0^2 - \omega^2 - i\omega\Gamma}$
$s = \left[1 - \left(\frac{\omega_0}{\omega} \right)^2 \right]^{1/2}$	
$\hbar\omega_0 = 2\Delta =$ energy gap in the electron spectrum	$\hbar\omega_0 =$ CT energy in the dimer $\Gamma =$ electron damping
$f(\omega) \rightarrow f(\omega + i\Gamma)$ $b = 1 - V/\Delta$, where $2V =$ energy gap in the absence of e-mv couplings	$b = 0$

$$c = \left(\frac{\omega}{\omega_0} \right)^2 \quad c = 1$$

$$\lambda_\alpha = \frac{g_\alpha^2}{\hbar\omega_\alpha} N(0); \quad \omega_\alpha = \omega_\alpha(2k_F) \quad \lambda_\alpha = \frac{g_\alpha^2}{\hbar\omega_\alpha} \frac{\epsilon_\infty\omega_p^2}{\omega_0^2\pi N_d e^2 a^2}$$

$N(0)$ = density of electron states

N_d = density of dimers

ω_p = plasma frequency

ω_p = CT band frequency

Trimerized organic conductors are of special interest, because two electrons per three sites constitute the simplest situation, where both electronic transitions resulting in single- and double-site occupation take place [21]. As one considers larger n -mers, two complications arise. First, the number of equations that should be solved sharply increases. The second complication is the increase in the number of n -meric normal modes, which are coupled to an external electromagnetic field. Recently, Yartsev et al. [22] have proposed using the linear response theory for several variables to describe the optical properties of trimers with arbitrary equilibrium charge density distribution. This approach can be extended to any cluster—the size is limited only by computer facilities.

Different approaches have also been proposed. For instance, Painelli et al. [23] have expressed the frequency-dependent conductivity of dimerized and trimerized organic conductors on the base of vibronic adiabatic Mulliken theory. They have shown that the calculated spectrum is virtually identical to the one obtained from linear response theory.

An analysis of the IR reflection spectra of organic conductors with activated a_g modes makes it possible to determine, among others, the values of e-mv coupling constants, which are instrumental in estimating the electric conductivity of the system or calculating the temperature of a potential metal–superconductor transition.

III. EXPERIMENTAL TECHNIQUES

The orientation of the polarizability tensor related to the planar molecule axes (i.e., to the crystal structure) is investigated by measuring the orientation and dispersion of the indicatrix. Usually, the principal axes of polarizability coincide with the directions of the three principal axes of the indicatrix: X , Y , and Z . Perpendicular to each of the two circular sections of radius n_β is an optic axis. The maximum absorption is always parallel to one of the three optical directions.

Investigations of the interference figures may be performed with a polarizing microscope equipped with a four-axis universal stage. Normally, for polarizing microscope measurements, transparent crystal thin sections

about 10 to 50 μm thick are needed. In the case of the organic conductors the required thickness is only about 1 μm , due to the optical absorption. In some cases the transparency and quality are so good that observation of interference figures by conoscopic illumination is possible. A specially equipped microscope works in the visible (VIS) and near infrared (NIR). Thus measurements of the dispersion of indicatrix and birefringence can be performed in the range 400 to 2000 nm. An additional photometer makes it possible to measure absorption in the principal directions.

The light absorption of an anisotropic crystal depends on the direction of the propagated light with regard to the crystal axes. Further, it depends on the plane of polarization of the radiation. The radiation is absorbed only if the phonon energy coincides with a vibrational energy spacing, and there is a component of the electric field of the radiation parallel to the transition moment associated with the vibration. When the light is propagated inside a crystal, the absorption is determined by the component ϵ'' [Eq. (10)] of the complex dielectric function. Investigation of light transmission (or absorption) in anisotropic crystals requires measuring it along different symmetry axes using polarized light.

For organic conductors it is usually impossible to obtain sample sections thin enough to determine the absorption coefficients of the strongest absorption bands. In this case reflection spectra can be recorded at near-normal incidence using polarized radiation. Microspecular reflection inserts or special microscopes are necessary for obtaining reflection spectra of small single-crystal organic conductors. Provided that the spectral range of observations is wide enough, the dielectric parameters $\epsilon'(\omega)$ and $\epsilon''(\omega)$ and optical parameters $n(\omega)$ and $k(\omega)$ can be calculated using Kramers–Kronig analysis.

If quality or size of the single crystals is not sufficient for reflectance measurement, the IR spectra of powdered solids may be measured in mulls, containing liquid mulling agent (e.g., Nujol or Fluorolube). However, the alkali halide pellet method is a very useful technique involving a solid dispersing medium. This requires a mixture of the sample with an alkali halide (usually KBr) to be finely ground and pressed into the form of a pellet for measurement. The main disadvantage of this method is averaging of the spectrum, which slurs the spectral anisotropy.

Raman light scattering, submitted to different selection rules, is complementary to infrared spectroscopy. Raman spectroscopy not only gives additional information on vibrational properties of organic conductors, but makes it possible to determine a polarizability tensor as a function of frequency. Resonant Raman scattering is of special importance for studying highly conducting conjugated polymers.

IV. EXPERIMENTAL STUDIES OF PHENOMENA AND PROPERTIES OF ORGANIC CONDUCTORS

A. Polarizability and Absorption Tensors

The indicatrix orientation, birefringence, optic axes angle, absorption tensor, and so on, can be measured in small crystals of organic conductors in the near infrared and the visible spectral range by polarizing microscope techniques adopted by Helberg [24–29]. Indicatrix measurements in the NIR and VIS of some TCNQ salts [24,25] show that the orientation of the polarizability tensor is governed by the orientation of the planar TCNQ molecules of the stack in the entire frequency range. In methyltriphenylarsonium (MTPA) (TCNQ)₂, for example, the optical directions coincide with the directions of the TCNQ molecule axes in the crystal: the *X* axis parallels the normal of the TCNQ molecule plane; *Y*, the transverse axis; and *Z*, the longitudinal axis. The axial angle $2V_Z$ (related to bisectrix *Z*) changes drastically from the visible range ($<90^\circ$) to the infrared range ($>90^\circ$) at about 10^4 cm^{-1} . That means that the shape of the indicatrix changes from “rodlike” parallel *Z* to “platelike” normal *X*. Maximum absorption was found parallel to *Z* in the visible and parallel to *X* in the IR [24,25].

The indicatrix orientation in TTF-TCNQ is also directed by the orientation of the stack molecules. It seems that in the case of intramolecular excitation the optic sign of the low-dimensional crystal is positive, and the absorption is greatest for light electrical vector vibrating parallel to the long axes of the molecules. In the case of intermolecular excitation the optic sign is negative, and the absorption is greatest for vibrations perpendicular to the planes of the molecules, not parallel to the stack [24].

Recently, Helberg et al. [26] have studied polarizabilities of the intermolecular contacts in bis(ethylenedithiolo)tetrathiafulvalene (BEDT-TTF) and bis(ethylenedioxy)tetrathiafulvalene (BEDO-TTF) molecular crystals by polarizing microscope techniques. The principal refractive indices and the corresponding optical axes have been calculated by tensorial addition of the bond polarizabilities of all bonds in the molecules. Comparison of calculated and measured values of the relative polarizabilities showed that the polarizabilities of the molecules only cannot yield the measured indicatrix and axes angle. Thus polarizabilities with other orientations must be involved. From the crystal structure of the molecular crystals it is known that 10 and four different contacts exist between the molecules of BEDT-TTF and BEDO-TTF, respectively, with contact distances lower than van der Waals distances. Assigning of polarizabilities of these contacts can explain the measured behavior.

The indicatrix orientation, the birefringence, and the transmission spectra were measured in small crystals of organic conductors, α -(BEDT-TTF) $_2$ I $_3$ and α -(BEDT-TTF) $_3$ (NO $_3$) $_2$, in the near-infrared and the visible spectral range [27,28]. It was shown that at high energies (≥ 2 eV) in the visible, the orientation of the polarizability tensor is governed by the orientation of the stack-forming molecules due to the intramolecular excitations. In the near-infrared region the intermolecular excitations become dominant. In both materials the principal axes of the absorption tensor coincide with the principal axes of the indicatrix.

A direct comparison of the structural properties of different phases in the same crystal sample, studied by means of polarizing microscope techniques and microspectroscopy, gives very interesting information. It is known that the tempering of α -(BEDT-TTF) $_2$ I $_3$ crystals above 70°C for several days leads to a transformation into the superconducting α_r phase [30]. The properties of the α_r phase and the high T_c phase of β -(BEDT-TTF) $_2$ I $_3$ crystals are found to be similar; this gives reason to suppose that the tempering of the α phase leads to some kind of β phase. But the indicatrix orientation indicates rather a new phase than the β phase [29].

Stereographic projections related to the plane (001) of α -(BEDT-TTF) $_2$ I $_3$ and α_r phase (Fig. 2a) and β -(BEDT-TTF) $_2$ I $_3$ (Fig. 2b) are shown. The indicatrix orientation of the α phase is governed by the direction L of the longitudinal axes of BEDT-TTF molecules and by the stack direction.

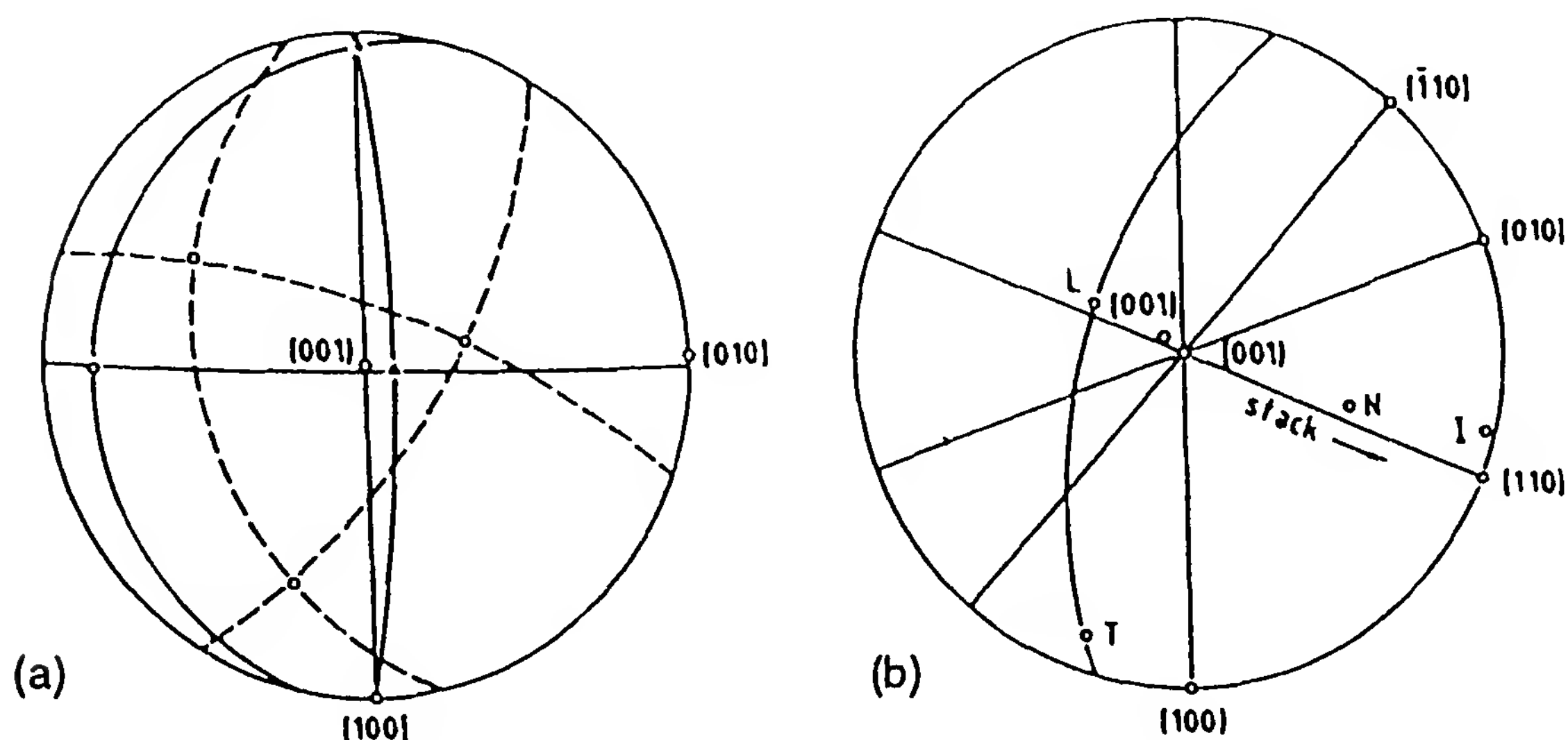


Figure 2 Stereographic projection: (a) related to the plane (001) of α -(BEDT-TTF) $_2$ I $_3$; measured indicatrix orientation in the α -phase (solid line) and in the α_r -phase (dashed line); principal axes X (\circ), Y ($+$), and Z (Δ) are marked; (b) related to the plane (001) of β -(BEDT-TTF) $_2$ I $_3$; L , longitudinal; T , transversal, and N , normal molecule axes; I , iodine molecule axis. (From Ref. 29.)

Assuming that the α_r phase is a kind of β phase, the indicatrix orientation should be compared to the structure of β -(BEDT-TTF)₂I₃ (Fig. 2). However, analysis of the stereographic projections shows that a transformation of α phase into this transformed β phase requires large movements of molecules. In a first step the BEDT-TTF molecules of the α phase should be rotated around the L axis by 78°, 42°, or 30°, respectively, and then all L axes should be further inclined by 15°. On the other hand, the transformation from the α phase into the α_r phase needs a rotation by only 34°, 3°, or 16° around L , and then the same inclination by 15°. This led to the assumption that the α_r -(BEDT-TTF)₂I₃ is a newer phase than the β -(BEDT-TTF)₂I₃ [29].

B. Charge Transfer

The charge-transfer electronic transition of a typical electron donor–acceptor complex has the character $DA \rightarrow D^+A^-$ and is associated with a strong, broad, visible, or NIR absorption band. Investigations of the electronic spectra of TCNQ salts indicated that their spectra are very similar to each other. The following four strong absorption bands are usually observed: 2 to $4 \times 10^3 \text{ cm}^{-1}$, 7 to $11 \times 10^3 \text{ cm}^{-1}$, 16 to $18 \times 10^3 \text{ cm}^{-1}$, and 27 to $30 \times 10^3 \text{ cm}^{-1}$ (Fig. 3). The electronic transitions fall into two classes: those at high energies generally result from excitations of single TCNQ molecules and are called localized excitations: LE_1 , LE_2 , and so on. The lower-energy bands, polarized in the stacking direction, are due to interactions among the molecules and are called charge-transfer bands: CT_1 , CT_2 , and so on. The former is usually attributed to the charge-transfer transition of the type $A^-A^- \rightarrow A^0A^{2-}$, the latter to the transition $A^-A^0 \rightarrow A^0A^-$. The frequencies and oscillator strengths of these CT bands are related to the electronic structure of the compound [31,32]. Exact interpretation of these bands is more complicated and requires attention to the special properties of the solid as well as the main interactions that determine its optical properties. In an extreme case Hubbard [11] and Kamaràs et al. [33] attempted to interpret the absorption spectra of TCNQ complex salts as the superposition of the spectra of $TCNQ^0$, $TCNQ^-$, and $(TCNQ)_2^{2-}$.

Optical studies of TCNQ salts have been reported by numerous authors (see, e.g., Refs. 2, 6, 8, 10, 18, and 31 to 33). Typical and very informative are the reflectance study of K-TCNQ by Tanner et al. [34] for $\vec{E} \parallel \vec{a}$ and for $\vec{E} \parallel \vec{b}$, \vec{c} , shown in Fig. 4. The near-infrared dispersion is strongly polarized in the direction of the stacking axis, while the visible one is polarized in the direction of the long axis of the TCNQ molecule, so that

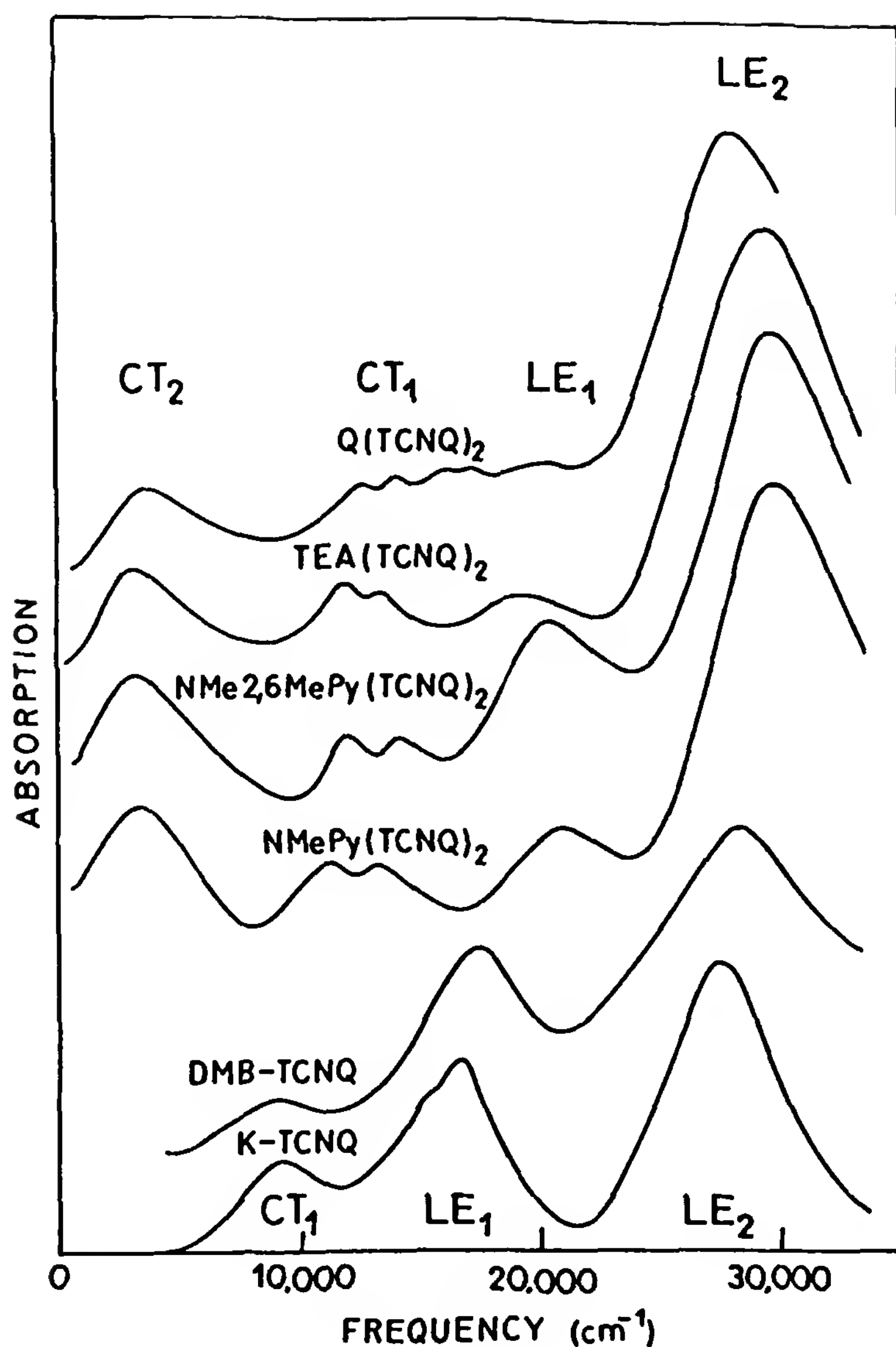


Figure 3 Powder absorption spectra measured on KBr pellets and normalized per mole TCNQ for some typical TCNQ salts.

the former is attributed to the CT and the latter to the intramolecular excitation. The data indicate structure associated with molecular stretching and bending modes at low frequencies, and a broad “metallic reflection” peak from direct electronic transitions at higher frequencies.

There are a number of examples of monovalence salts, the spectra of which are very closely related to that of the solution dimer: for example, K-TCNQ, tetramethyl-*p*-phenylenediamine (TMPD)-ClO₄, K-chloranil, and cation-radical salts of TTF. The powder absorption spectrum for TTF-Cl is shown by the dashed line in Fig. 5, where it is compared with the spectrum of the solution (TTF⁺)₂ dimer [35]. Analyzing the reflectivity spectrum for light polarized parallel and perpendicular to the *c* axis, one

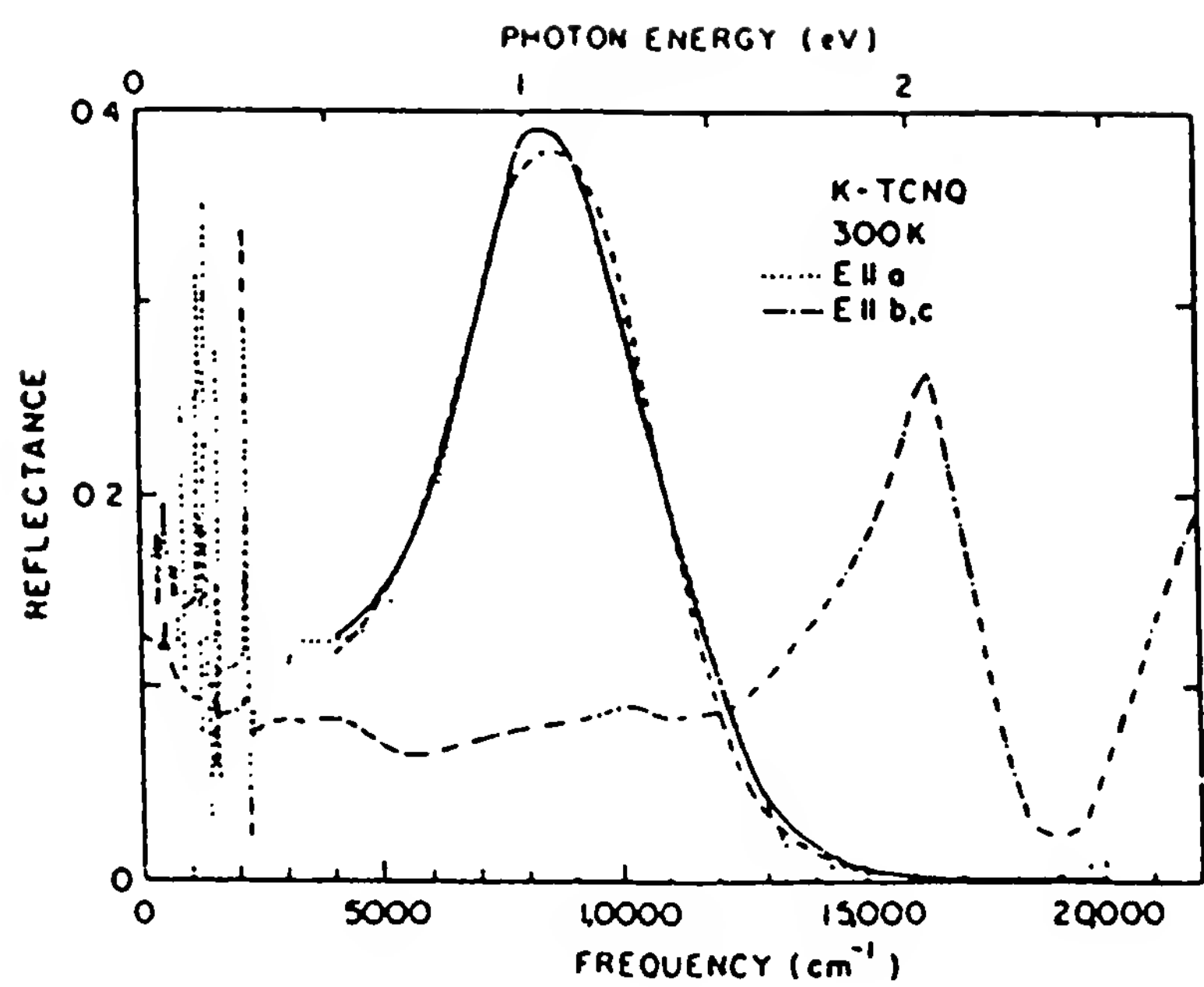


Figure 4 Reflectance of K-TCNQ single crystal, for two polarizations. The dashed line is a fit of the reflectance for the electric field parallel to the chain axis by a single Lorentzian oscillator; the solid line is a fit to the two-oscillator model. (From Ref. 34.)

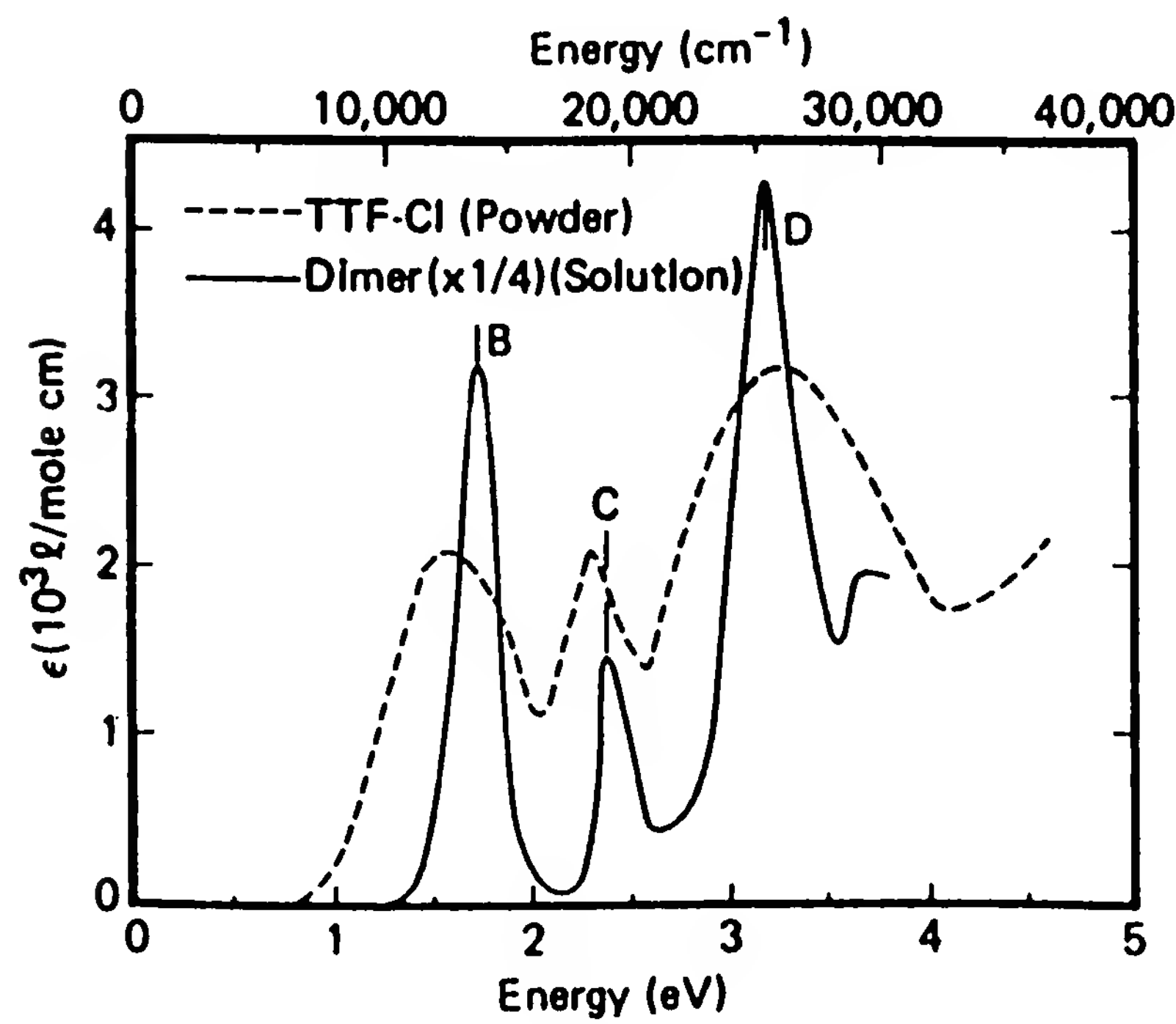


Figure 5 Powder absorption spectrum of TTF-Cl compared with that of the (TTF⁺)₂ dimer in solution. (From Ref. 35.)

can confirm identification of the absorption peaks: peak C is an intramolecular excitation (polarized primarily perpendicular to the *c* axis), while peak B is a CT band (polarized primarily along the *c* axis). The spectrum of a mixed-valence stack of TTF molecules consists of four distinct absorption peaks about 5000, 14,000, 19,000, and 25,000 cm^{-1} . The two low-energy peaks are CT bands, polarized along the stack.

Similar examinations of the CT spectra for bis(propylenedithio)-tetrathiafulvalene (BPDT-TTF) salts [36], BEDT-TTF salts [37], and bis-tetramethylenetetraselenafulvalene-(4,5-dimercapto-1,3-dithiole-2-thione)nickel [OMTSF-Ni(DMIT)₂] salt [38] have been performed. The latter salts are examples of organic conductors that are almost isotropic in two dimensions. Thus only weak polarization dependence is found in the entire frequency range. The analysis of the spectra within a simple DA-charge oscillator model, which takes into account the coupling to intramolecular vibrational modes, demonstrates how IR and optical measurements can provide estimates for a number of physical parameters for low-dimensional organic conductors.

Although the localization and shape of the CT bands depend on a degree of charge transfer from the electron donor-to-acceptor molecule, this spectral region is not suitable for evaluation of the amount of transferred electrons in organic conductors. Raman scattering and vibrational spectra are more useful for this purpose.

Infrared absorption spectroscopy was used by Farges et al. [39,40] as a tool to investigate the degree of CT and charge distribution in a collection of TCNQ sites. They showed that a particular vibrational mode of the TCNQ molecule, namely, an out-of-plane CH bending, b_{3u} mode could be of special interest. A dramatic modification of the relative intensities of the bands associated with a vibrational out-of-plane *u* mode of the TCNQ⁰ molecule and TCNQ⁻ radical for TEA(TCNQ)₂ salt is shown in Fig. 6. These modifications can be attributed to a reduction of the charge delocalization in the salt. The three peaks at 825, 838, and 863 cm^{-1} may then serve as sensitive indicators of the amount of transferred electrons in the solid. This method was applied to a quantitative analysis of charge distribution in some TCNQ compounds and mixtures of various solid-state products [39].

Recently, the method of Brau and Farges [40] was adopted [41,42] for temperature investigation of charge localization effects in TCNQ salts with various cations. Temperature dependences of the amounts of TCNQ⁰, TCNQ^{-δ}, and TCNQ⁻ were determined from the relative integral intensities of the respective bands for three organometallic TCNQ salts with ferrocene stacks. It was shown that the amount of TCNQ⁻ decreases with increasing temperature; at low temperatures the salts are characterized by

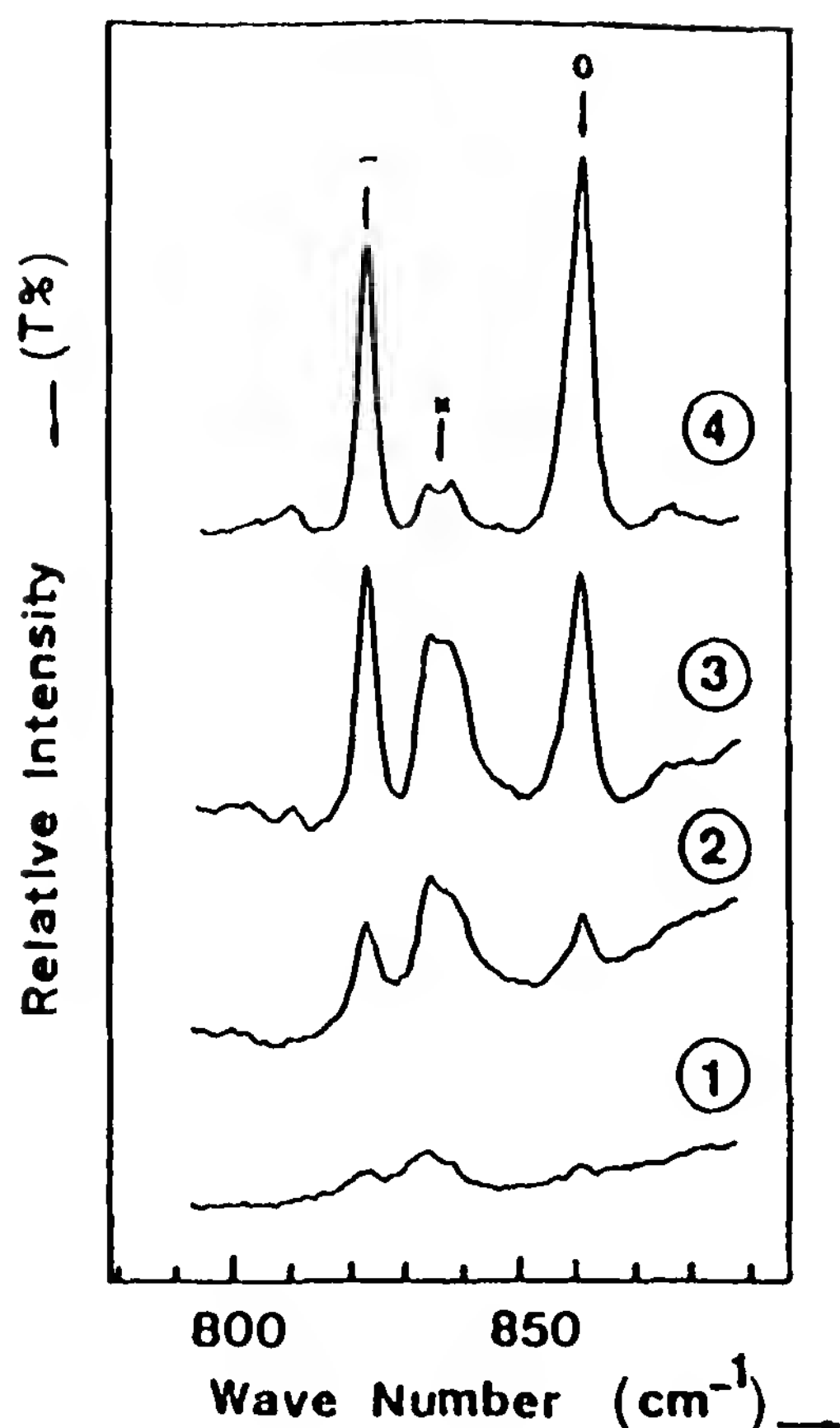


Figure 6 Powder IR absorption spectra of $\text{TEA}(\text{TCNQ})_2$ in a KBr pellet. Several steps (spectra 2, 3, and 4) of the relative evolution of a vibrational out-of-plane u mode of TCNQ resulting from an extensive recrushing of KBr pellet. Comparison is made with the spectrum of the initial pellet (spectrum 1). (From Ref. 39.)

a nonregular charge distribution along the chains, the electrons becoming partially localized.

The foregoing remarks show that optical properties of organic conductors, in particular their UV-VIS, Raman, and IR spectra, can be used to estimate a number of physical parameters; and among other things, the formal charge of the molecules or ions; their evolution versus temperature, CT reactions, and so on, can be studied as well. Besides, examination of the IR spectra of low-dimensional organic conductors permits one to draw some conclusions about the stoichiometry and electronic properties of the salt.

C. Plasma Reflectance

High electrical conductivity of organic conductors manifests itself in the IR spectra as anisotropic metal-like reflectivity associated with intermolecular charge transfer. Although an electron gas giving the plasma edge

does not occur in organic metals, a quasifree transport of electrons along the one-dimensional axis produces metallic properties at NIR frequencies.

Measurements of the polarized reflectance in the NIR have frequently been used to obtain estimates for the transfer integrals. The method consists in fitting a reflectance model based on the Drude expression [Eq. (1)] to the experimental data. The Drude expression should be considered as a tool in estimating the plasmon frequency, Ω_p ; the background dielectric constants, ϵ_0 ; plasma frequency, ω_p ; and so on. The validity of the Drude analysis is limited to the conducting organic materials, with the electrical conductivity not less than a few $\text{S} \cdot \text{cm}^{-1}$.

Some applications of the method will be shown for the ternary salt trimethylammonium (TMA)–TCNQ-I. Tanner et al. [43] have obtained a best fit with a Drude–Lorentz dielectric function with $\omega_p = 5290 \text{ cm}^{-1}$, $\gamma = 2560 \text{ cm}^{-1}$, $\epsilon_c = 2.65$, $\omega_L = 4960 \text{ cm}^{-1}$, and $\Gamma = 4480 \text{ cm}^{-1}$, where ω_L is the frequency and Γ is the relaxation rate of the second oscillator. The average value of the frequency-dependent conductivity below 200 cm^{-1} should be $19 \pm 1 \text{ S} \cdot \text{cm}^{-1}$. The energy gap of 0.10 to 0.14 eV, the effective quantity of electrons participating in the electric transport $N_{\text{eff}} = 0.67$ per molecule, and the effective mass of the carriers $m^* = 5.2 m$ were found from the plasma frequency.

Organic metals such as TTF-TCNQ consist of segregated stacks of donor and acceptor molecules. IR study has shown that there is an energy gap 0.14 eV above which the single-particle conductivity is Drude-like, with $\omega_p = 9600 \text{ cm}^{-1}$, $\Omega_p = 500 \text{ cm}^{-1}$, effective mass $M^* = 300m^*$, where the band mass is $m^* = 3m_c$, and $\tau_c^{-1} = 0.5 \text{ cm}^{-1}$ [44]. Polarized IR reflectance measurements have also been made at temperatures between 25 and 300 K by Tanner et al. [45]. The temperature change of the reflectance at higher frequencies consists of a sharpening of the plasma edge and an increase in the reflectance with decreasing temperature. The conductivity at 60 K has a strong maximum at the lowest frequencies. At 25 K a strong peak appears at 40 cm^{-1} , attributed to the CDW pinned by the three-dimensional ordering that occurs in TTF-TCNQ at 38 K. IR measurements support a CDW mechanism for the high dc conductivity of TTF-TCNQ, and provide estimates for the 60-K lifetime and the low-temperature pinning frequency of the CDW.

The Drude parameters for typical one-dimensional organic conductors are $6400 \text{ cm}^{-1} < \omega_p < 8000 \text{ cm}^{-1}$, $2 < \epsilon_0 < 3$, charge carriers density $-(1 \div 3) \times 10^{21} \text{ cm}^{-3}$, $0.8e < m^* < 2e$, $0.1 \text{ eV} < t < 0.3 \text{ eV}$.

There are two groups of organic conductors which, contrary to one-dimensional TCNQ salts, show considerable interchain coupling. They are both of single-stack type, with donor molecules of tetramethyltetrafulvalene (TMTTF) or tetramethyltetraselenafulvalene (TMTSF) and BEDT-

TTF type. The optical anisotropy of such two-dimensional conductors and their electron parameters may also be deduced from reflectance studies. As an example, from the $(\text{TMTSF})_2\text{X}$ family we present the polarized reflectance of $(\text{TMTSF})_2\text{PF}_6$ at three temperatures (Fig. 7). It is evident that optical anisotropy decreases at low temperature, and a reasonably well-defined plasma edge appears in the b' direction at 25 K. The transverse reflectance edge appears at the frequency about 10 times lower than that of the stacking axis edge ($t_{b'}$ = 22 meV, about 10 times smaller than t_a) [46]. Drude parameters for typical $(\text{TMTSF})_2\text{X}$ salt are $\epsilon_0 = 3.5$, $1500 \text{ cm}^{-1} < \omega_p < 2000 \text{ cm}^{-1}$, $250 \text{ cm}^{-1} < \gamma < 500 \text{ cm}^{-1}$, and $t_b = 0.02 \text{ eV}$.

The BEDT-TTF trihalides and the related salts attract much attention because of a relatively high superconducting transition temperature. Figure 8 shows the polarized reflectance of α - and β -(BEDT-TTF) $_2\text{I}_3$ crystals for two light polarizations. For both phases the electronic reflection bands with a Drude-like edge are observed in two perpendicular polarizations [47]. Drude parameters and transfer integrals of typical (BEDT-TTF) $_2\text{X}$ salts are $5000 \text{ cm}^{-1} < \omega_p < 9600 \text{ cm}^{-1}$, $500 \text{ cm}^{-1} < \gamma < 2000 \text{ cm}^{-1}$, and $0.08 \text{ eV} < t < 0.20 \text{ eV}$. Near isotropy of the optical properties of typical BEDT-TTF salts is confirmed by electrical transport studies. Rather small values of t are consistent with relatively low room-temperature conductivity.

The analysis of reflectance data in the plasma region yields reliable estimates for transfer integrals, electrical conductivity, carrier concentration, effective mass, collision time, bandwidth, and Fermi vector of the crystals. However, it is necessary to notice that some deviations from the Drude rule were observed in the spectra of highly conducting materials below the plasma edge. Formally, it can be described by coupling of two electron oscillators (Drude–Lorentz model). The physical reasons for the appearance of the conductivity maximum in the region 1000 to 3000 cm^{-1} may be various: for example, a gap in the electron energy spectrum, conduction electron correlations, electron–electron interactions in the site, e-mv couplings, and so on.

D. Electron–Phonon Interactions

Several methods, perturbative and nonperturbative, have been proposed to account for the introduction of $H_{e\text{-ph}}$ in the adiabatic solution of $H_e + H_v$ [Eq. (2)]. The interesting physics of e-mv coupling is associated with the linear term, which is able to mix ground and excited states, giving rise to peculiar vibronic phenomena in the IR spectra.

Kaplunov et al. [48] and particularly Brau et al. [18] have observed for the first time and explained a remarkable series of strong IR absorption bands polarized in the chain direction in the quasi one-dimensional organic

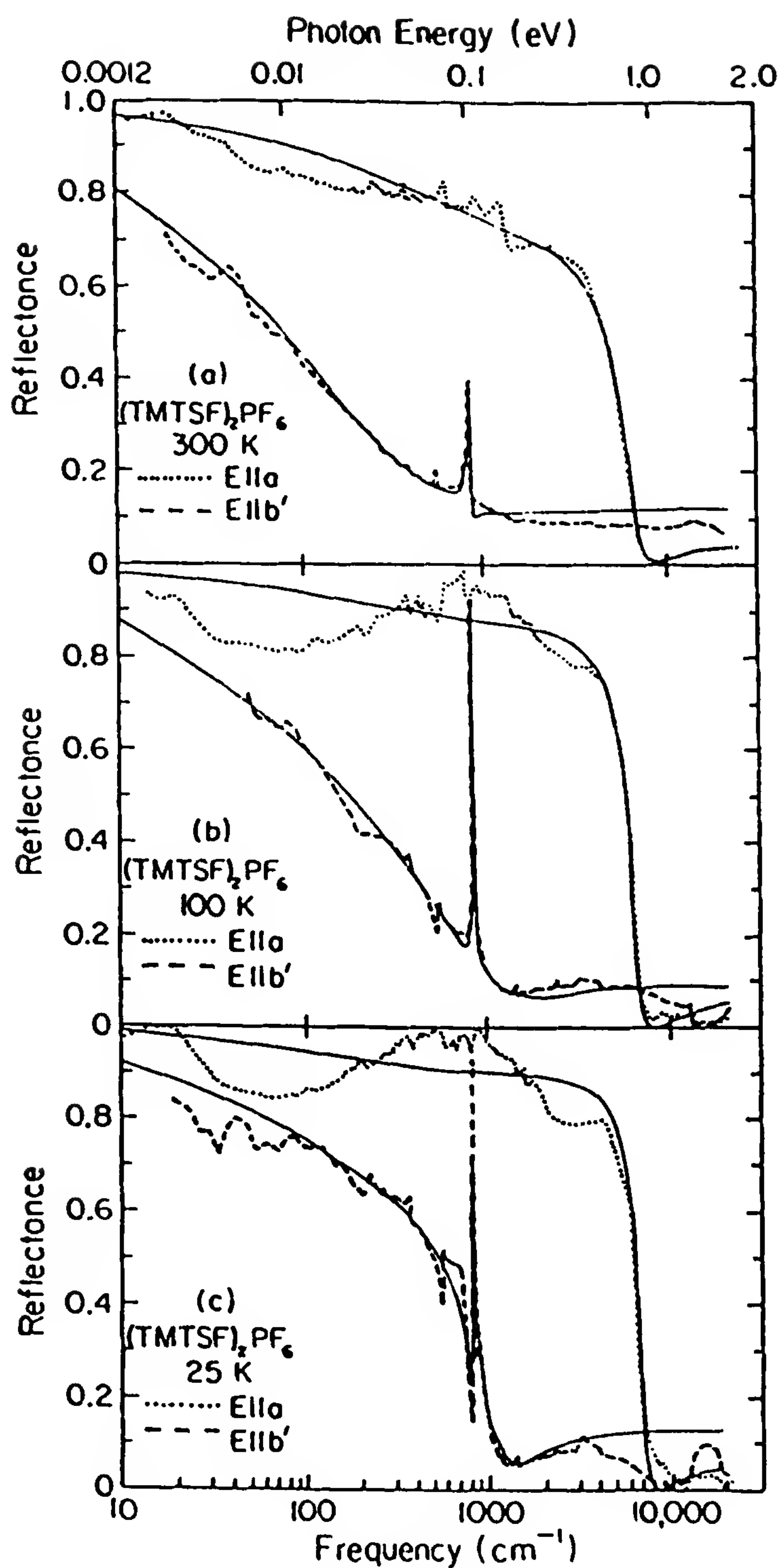


Figure 7 Polarized reflectance of $(\text{TMTSF})_2\text{PF}_6$ at 300, 100, and 25 K. The solid lines are Drude fits. (From Ref. 46.)

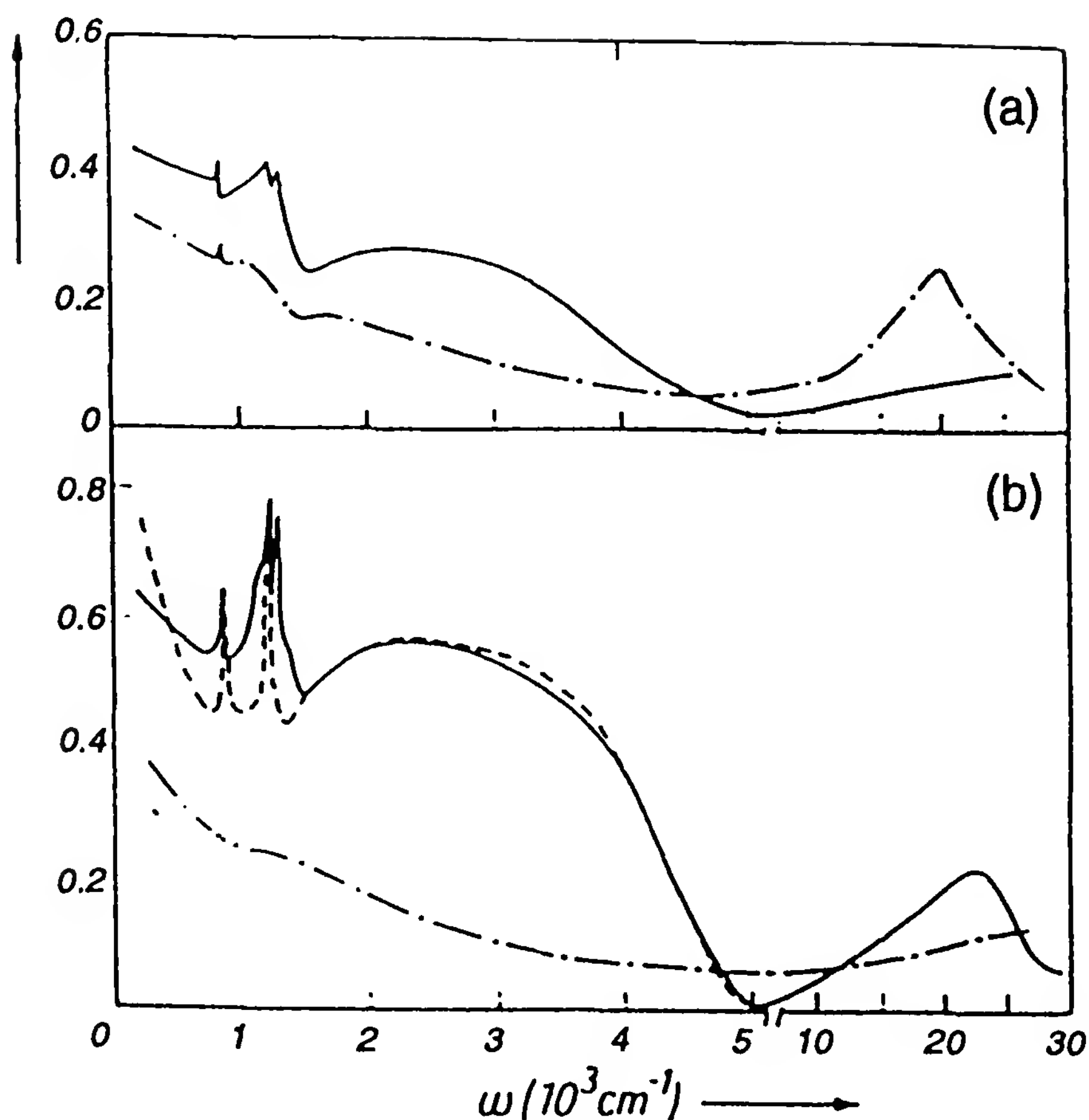


Figure 8 Polarized reflectance of $(\text{BEDT-TTF})_2\text{I}_3$ single crystals: (a) α -phase: —, $E \perp b$; -·-·-, $E \parallel b$; (b) β -phase: —, $E \parallel d$; -·-·-, $E \perp d$; ----, calculated. (From Ref. 48.)

semiconductor $\text{TEA}(\text{TCNQ})_2$ (Fig. 1). Its origin has been explained as a result of interaction of conduction electrons with intramolecular TCNQ vibrations. Despite some simplifications, a model of phase phonons describes fairly well the observed vibrational excitations in the salt. The values of 10 a_g intramolecular e-mv coupling constants, g_α , deduced from a fit of the equation found by Rice et al. [49] to the experimental data of Brau et al. [18] are in agreement with the theoretical values of the e-mv coupling constants obtained by Lipari et al. [50]. The sum of the dimensionless e-mv coupling constants, λ_α is $\lambda_{\text{intra}} = 0.51$. Addition of the assumed intermolecular coupling $\lambda_{\text{inter}} = 0.1$ to λ_{intra} gives a total coupling parameter $\lambda = 0.61$, which yields $V/\Delta = 0.13$, where 2Δ denotes the energy gap of the stabilized semiconducting state and $2V$ the energy gap in the hypothetical absence of e-mv coupling. The smallness of V/Δ indicates that the semiconducting state in $\text{TEA}(\text{TCNQ})_2$ arises predominantly from periodic intramolecular distortion [49].

Different theoretical models have been adopted to interpret the spectra of TEA(TCNQ)₂ salt. More exact description requires regard to the tetramerization or dimerization of the chains in TEA(TCNQ)₂. Thus the interpretation of TEA(TCNQ)₂ spectra should be made in terms of the theory of e-mv coupling in tetramers with two radical electrons [51] or the dimer CT oscillation mechanism [13,20,52]. The application of the latter mechanism to the TEA(TCNQ)₂ salt is shown in Fig. 9.

A very good model system for studying the spectral properties of isolated TCNQ dimers with one radical electron is tetraethylammonium (TeEA) (TCNQ)₂ salt [54,55]. The IR reflectivity was studied from various well-developed crystal faces. The fit of a dimer model with inequivalent molecules to the experimental data is shown in Fig. 10. The optimum values for the electronic mode parameters are $\omega_{CT} = 3222 \text{ cm}^{-1}$, $\gamma_e = 2216 \text{ cm}^{-1}$, $|t| = 1864 \text{ cm}^{-1}$, and $\Delta = 938 \text{ cm}^{-1}$ [55].

The dimer models were also used or proposed to interpretation of the reflectivity spectra of K-TCNQ [34], methylethylmorpholinium (MEM) (TCNQ)₂ [52], decamethylferrocenium (DMeFc)-TCNQ [56], *N*-methyl-

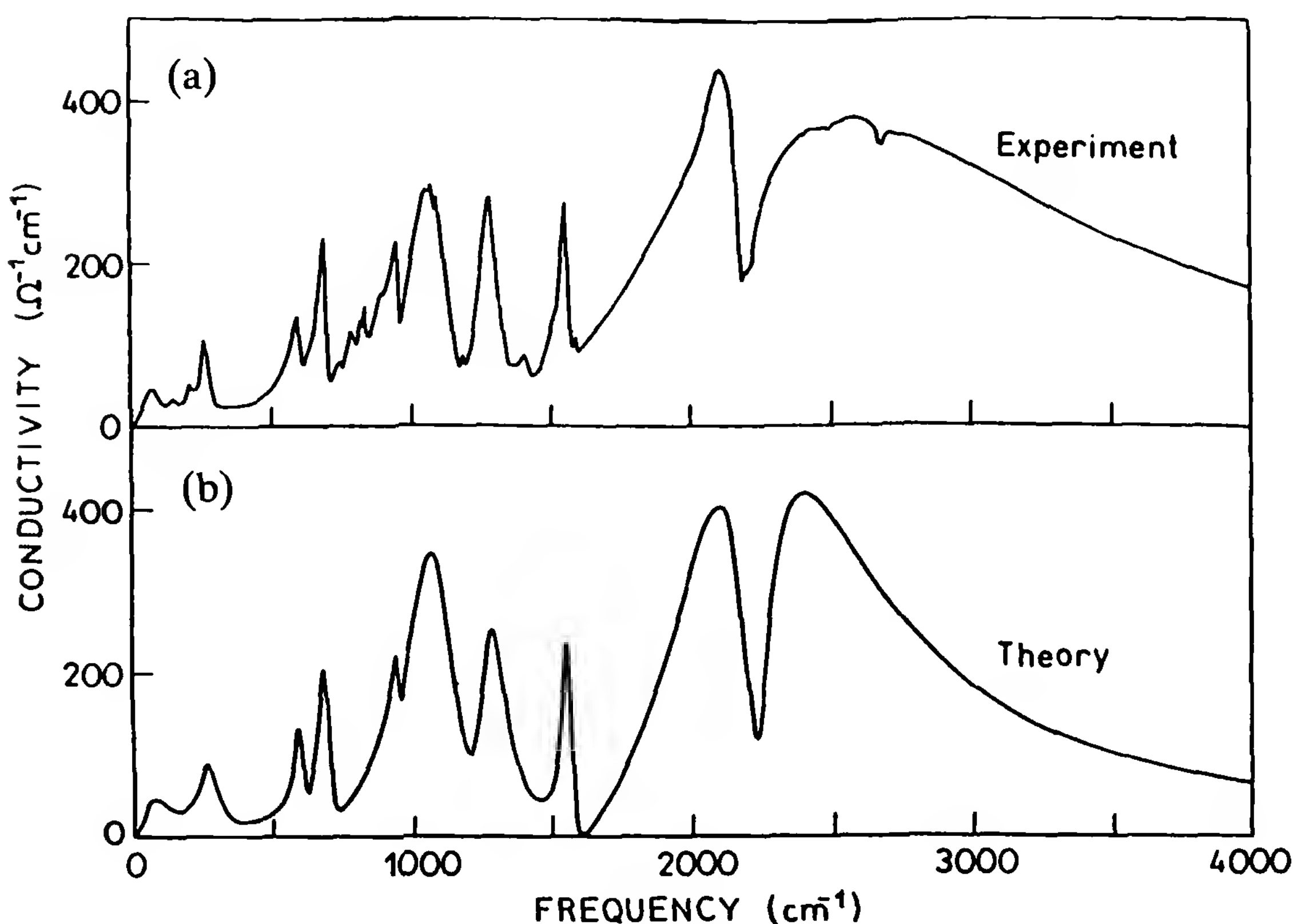


Figure 9 Real part of the frequency-dependent conductivity of TEA(TCNQ)₂ as deduced by dispersion analysis of the measured reflectivity at 300 K (a) and calculated theoretically according to the dimer model (b). (From Ref. 53.)

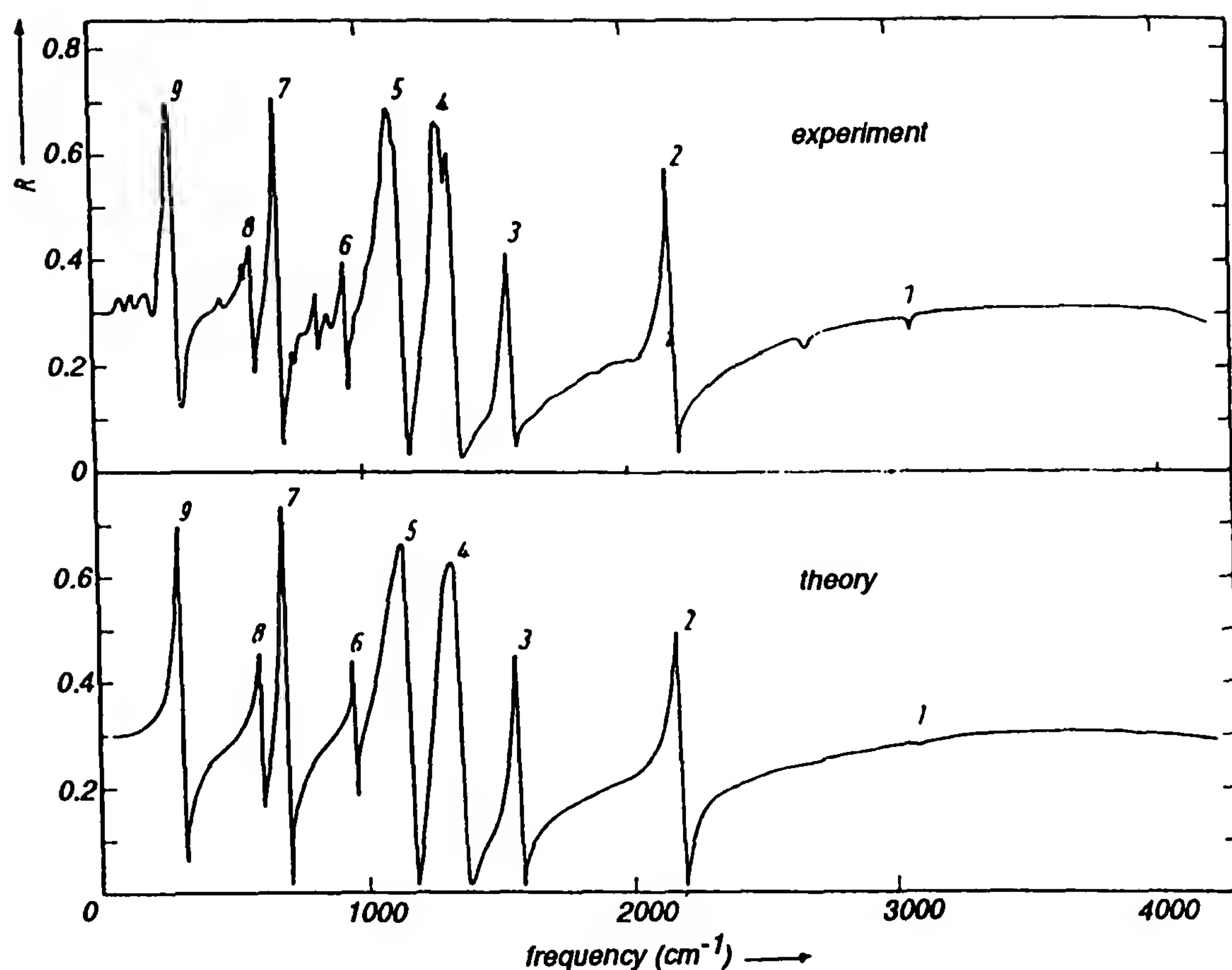


Figure 10 Measured and calculated reflectance of face $g(100)$ for $\text{TeEA}(\text{TCNQ})_2$. (From Ref. 55.)

2,6-dimethylpyridinium (NMe-2,6-MePy) $(\text{TCNQ})_2$ [57], methyl-*N*-ethylbenzimidazolium (MNEB) $(\text{TCNQ})_2$ [58], dimethyldibenzophosphonium (DMDBP) $(\text{TCNQ})_2$ [59], and *N*-dimethylthiomorpholinium (DMTM) $(\text{TCNQ})_2$ [60]. On the basis of polarized reflectance measurements and a theoretical analysis, two basic conclusions have been arrived at: (1) each unpaired electron is localized on a dimeric TCNQ unit, and (2) two-site molecular orbital involves molecular distortion, which is driven by a steric site inequivalence of the individual TCNQ monomers.

The IR conductivity spectra of $(\text{TMTSF})_2\text{X}$ and $(\text{TMTTF})_2\text{X}$ compounds consist of a broad electronic band with superimposed vibrational fine structure. The spectra can be taken as evidence of considerable electronic coupling to some vibrational modes of TMTTF or TMTSF molecules, in particular to the methyl group modes. The model based on isolated dimers describes the experimental results quite well. Jacobsen et al. [61] have fitted the dimer model to the reflectance of some salts of this family. The chain-axis reflectance of $(\text{TMTTF})_2\text{PF}_6$ at $T = 300\text{ K}$, measured and cal-

culated by fitting the dimer model to the data is shown in Fig. 11. The e-mv coupling constants for TMTSF and TMTTF appear to be qualitatively similar to those of TTF. A new feature is the presence of considerable coupling to modes involving methyl groups, suggesting that a sizable charge density is located near these groups.

Recently, Graja et al. [62] have focused on a giant analog of TTF, in which the dihydro-TTF core is bearing two conjugated, 1,4-dithiafulven-6-yl side arms (DDTF-DHTTF). It was shown that Yartsev and Jacobsen's idea [63] of treating the donor molecules as an aggregate of two parts

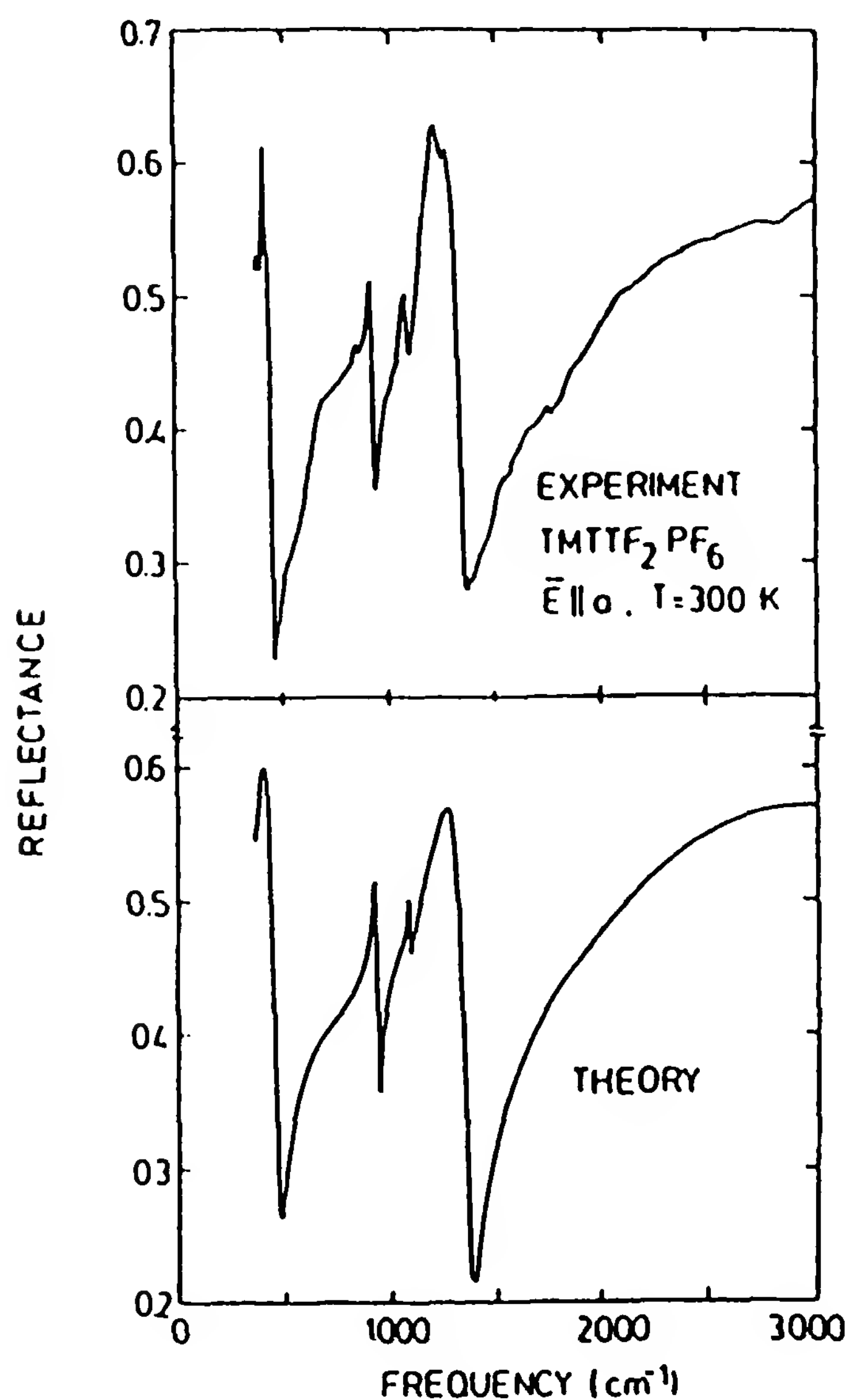


Figure 11 Chain-axis reflectance of $(\text{TMTTF})_2\text{PF}_6$ as measured and as calculated by fitting the dimer model to the data. (From Ref. 61.)

excited by the intramolecular charge transfer is an acceptable first approximation of the e-mv coupling in the giant π donors. The e-mv coupling constants estimated for the DDTF-DHTTF molecule nicely compare with those determined for the parent TTF molecule. The IR spectral study of (DDTF-DHTTF)ClO₄ has shown that the e-mv coupling can be established despite the absence of totally symmetric a_g modes of the donor or acceptor molecule (due to its low symmetry). The temperature dependence of the band intensities (Fig. 12) showed that some bands at 83 K are stronger than at room temperature by 10 to 20%. Some bands increase 2.6 to 3.0 times, whereas the intensities of the others increase about 1.6 times when going from room to low temperatures. It suggests that the two last-mentioned

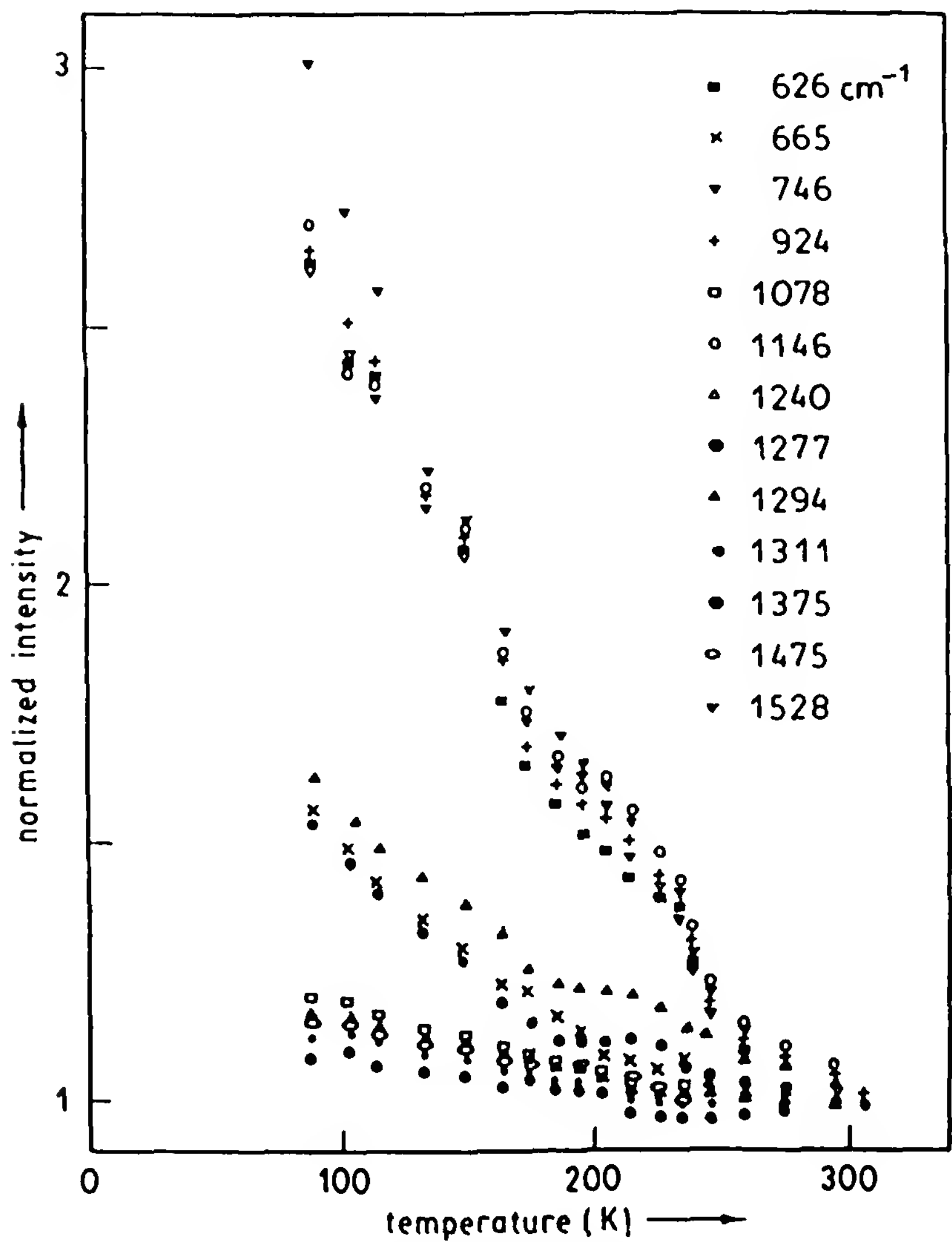


Figure 12 Normalized to room-temperature intensities of selected absorption bands of the (DDTF-DHTTF)ClO₄ salt. (From Ref. 62.)

groups of absorption bands should be attributed to the vibronic bands, which are due to a coupling of intramolecular vibrations of different symmetries with charge-transfer electronic excitations.

The spectral properties of the TCNQ salts where the TCNQ molecules are present as quasi-isolated trimers are of special interest. The mode corresponding to the charge transfer between noncentric molecules was shown to be responsible for the indirect IR activity [21]. The interpretation of the absorption and reflection spectra of the Cs, (TCNQ), has been suggested by various authors using the Yartsev model [21,64] or a phenomenological model of interacting oscillators [65,66]. Recently, the spectrum of this salt has been reinterpreted by Painelli et al. [23] in terms of a model for trimerized compounds based on vibronic adiabatic Mulliken theory. The model takes into consideration the coupling of the TCNQ a_g modes with both the intra- and intertrimer charge-transfer transitions. The agreement between the theoretical and experimental spectra for Cs, (TCNQ)₃ [23], using the parameters of g_α , demonstrates that these values can be transferred from one TCNQ compound to another.

Recently, the trimer theory has been used for the interpretation of the optical properties of the S-methylthiouronium salt [(MT)₂(TCNQ)₃ · 2H₂O] [67,68]. The dominant feature of the polarized reflection spectrum of (MT)₂(TCNQ)₃ · 2H₂O (Fig. 13) is a broad intensive band of electronic reflection, with a sharp edge and low minimum at the frequency $\omega = 9090 \text{ cm}^{-1}$. The intensive structure observed in the middle IR range (lines 1 to 8) is attributed to the e-mv coupling. Lines 2 and 4 have a fine structure which could be understood if one takes into account the equilibrium charge density shift $\rho'_B = 0.25e$ and $\beta''_B = 0.15e$ in the two halves of TCNQ (€3).

The fine structure related to the inequivalence of TCNQ molecules within the tetramer is seen in the reflectivity spectra of, for example, TEA(TCNQ) at low-temperature phase and methyltriphenylphosphonium (MTPP) (TCNQ), [69], as shown in Fig. 14. The presence of a specific fine structure of a_g bands in the IR spectra of tetramerized TCNQ salts is an interesting feature of these materials. One usually observes doublets formed by a wide (bandwidth up to 100 cm^{-1}), relatively strong component of lower frequency and a narrow (bandwidth between 10 and 20 cm^{-1}), relatively weak component of higher frequency. The narrow components exhibit stronger temperature dependence, and in some salts with higher conductivity are not observed at room temperature. Świetlik et al. [70] have noticed that narrow components of activated a_g bands have the same frequency as the bands in dimerized simple TCNQ salts, and consequently, they have suggested the existence of long-living pairs of neighboring TCNQ⁻

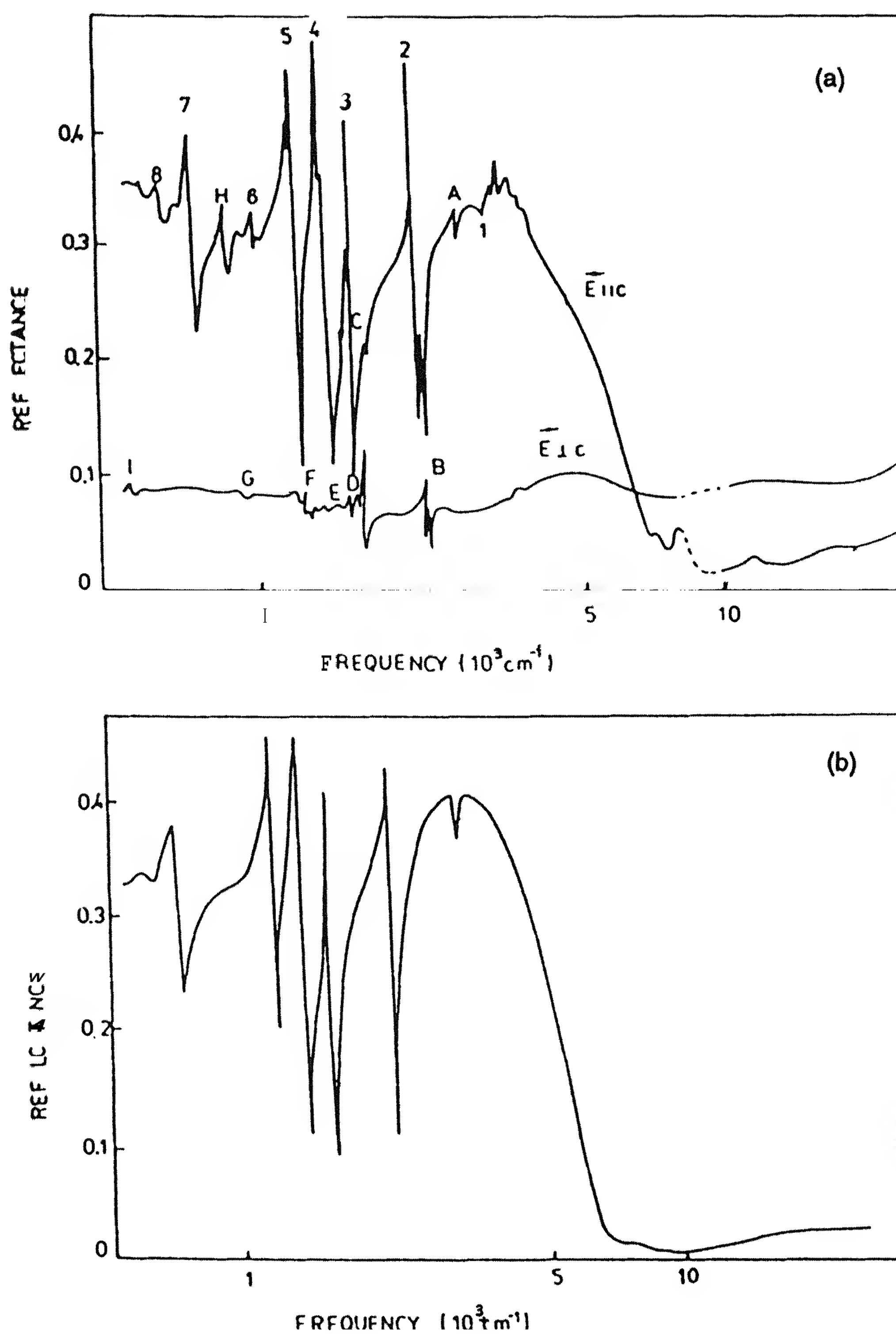


Figure 13 Polarized reflectance of $(MT)_2(TCNQ)_3 \cdot 2H_2O$ for two polarizations (a) and calculated spectrum for $\vec{E} \parallel \vec{c}$ (b). (From Ref. 67.)

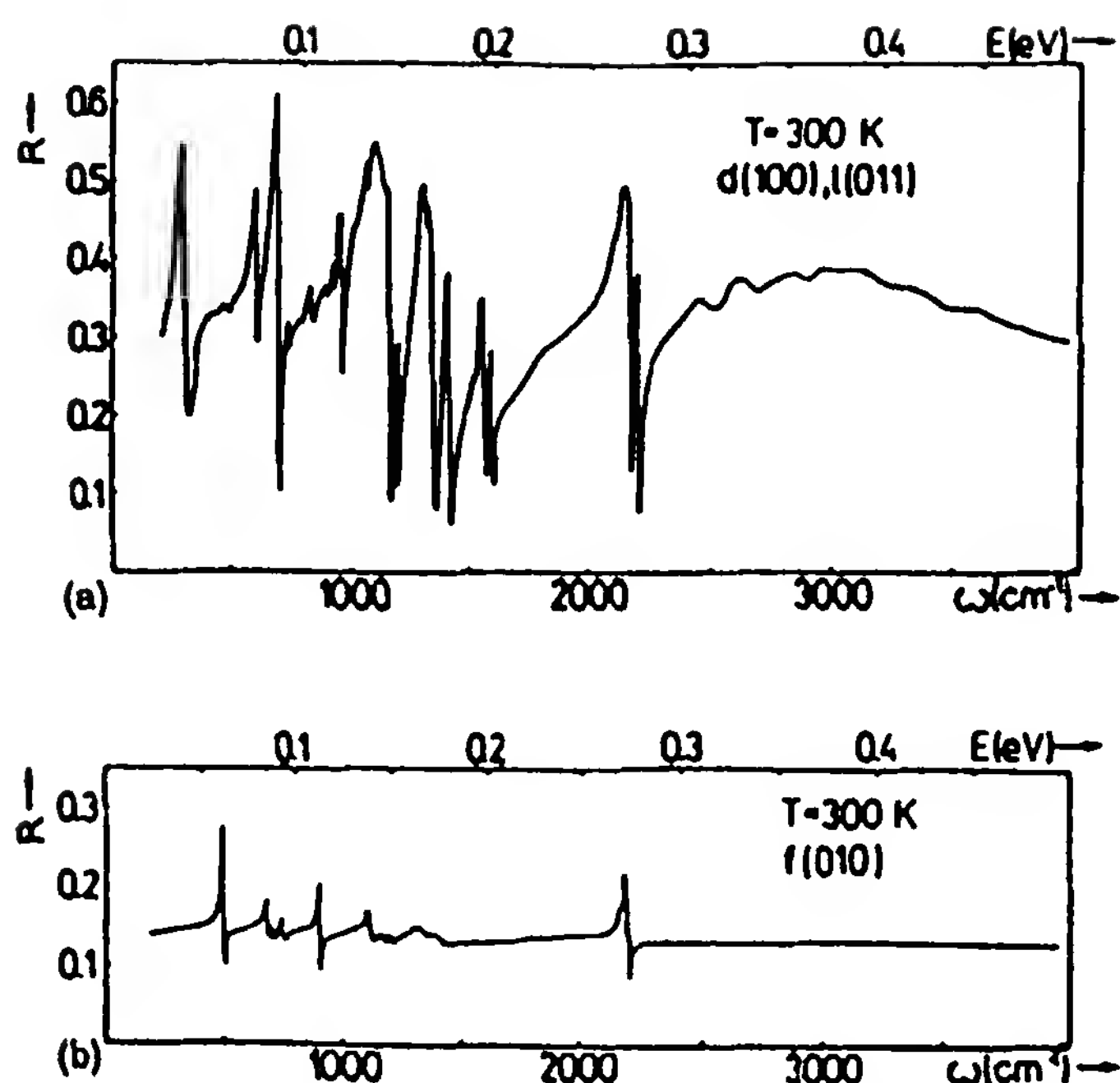


Figure 14 Polarized reflectance of MTPP(TCNQ)₂ for different crystal faces. The electric vector is parallel to the TCNQ stacks direction in the case of faces *d*(100) and *l*(011) (a) and is parallel to the TCNQ long axis for *f*(010) (b). (From Ref. 69.)

ions, attributing the narrow bands to e-mv coupling phenomena in (TCNQ)₂²⁻ dimers. In this approach the fine structure is expected to appear even in the case of uniform charge distribution. Another explanation has been given by Yartsev and Rice [71], who have attributed the phenomenon of *a_g* bands splitting to a nonuniform charge distribution.

The e-mv coupling constants g_α characterize the molecule while the dimensionless e-mv coupling constants λ_α describe all molecular stacks. This is why the g_α values determined for various ion-radical salts of the same donor (or acceptor) molecule are close to one another. Thus the average values of g_α can be calculated and compared with g_α values calculated using a quantum chemistry method [50]. Mean values of g_α for about 20 TCNQ salts are collected in Table 1. From these data one can evaluate the energy of polaron formation:

$$E_p = \sum_{\alpha} \frac{g_{\alpha}^2}{\hbar\omega_{\alpha}} \quad (13)$$

For TCNQ, $E_p \approx 0.1$ eV and is comparable with transfer integral value $t = 0.1 \div 0.3$ eV. This means that the electrons can be localized in the TCNQ salts.

Table 1 Electron–Molecular Vibration Coupling Constants for TCNQ Salts

a_g mode	ω_α (cm^{-1})	g_α (meV)	
		Averaged	Calculated [50]
1	3048	4	3.8
2	2229	47	52.4
3	1602	59	131.0
4	1454	53	48.6
5	1207	37	28.4
6	948	17	29.4
7	711	20	32.6
8	602	9	2.2
9	334	24	24.0
10	144	13	9.7

The e-mv couplings play an important role in superconductivity in organic materials, which contributes to static dielectric susceptibility. It is necessary to notice that not only totally symmetric modes couple with the electrons: some out-of-plane molecular modes and intermolecular modes can also couple with the electron excitations.

The role of e-mv coupling in organic conductors is quite peculiar. In fact, although the strength of the single e-mv couplings does not appear to be very great, the high number of e-mv coupled modes makes the collective contribution important in modulating the on-site energies.

E. Instabilities

The authors of other chapters in this book are occupied in more detail with different low-dimensional instabilities. Just as an example, we mention here the effect of instability on the IR spectra.

Optical study indicates that at low temperatures the low-energy electronic properties of some organic metal-like conductors (e.g., TTF-TCNQ) are dominated by charge density wave (CDW) effects. Frequency-dependent conductivity of TTF-TCNQ, obtained from the IR reflectance, at 25 K displays a double-peak structure with a low-frequency band near 35 cm^{-1} and a very intense band near 300 cm^{-1} [45]. The intense band may be ascribed to single-particle transitions across the gap in a $2k_F$ (Peierls) semi-conducting state, while the 35-cm^{-1} band is assigned to the Fröhlich (i.e., CDW) pinned mode. Low-temperature results based on the bolometric technique [72,73] (Fig. 15) confirm the IR reflectance data. Such a con-

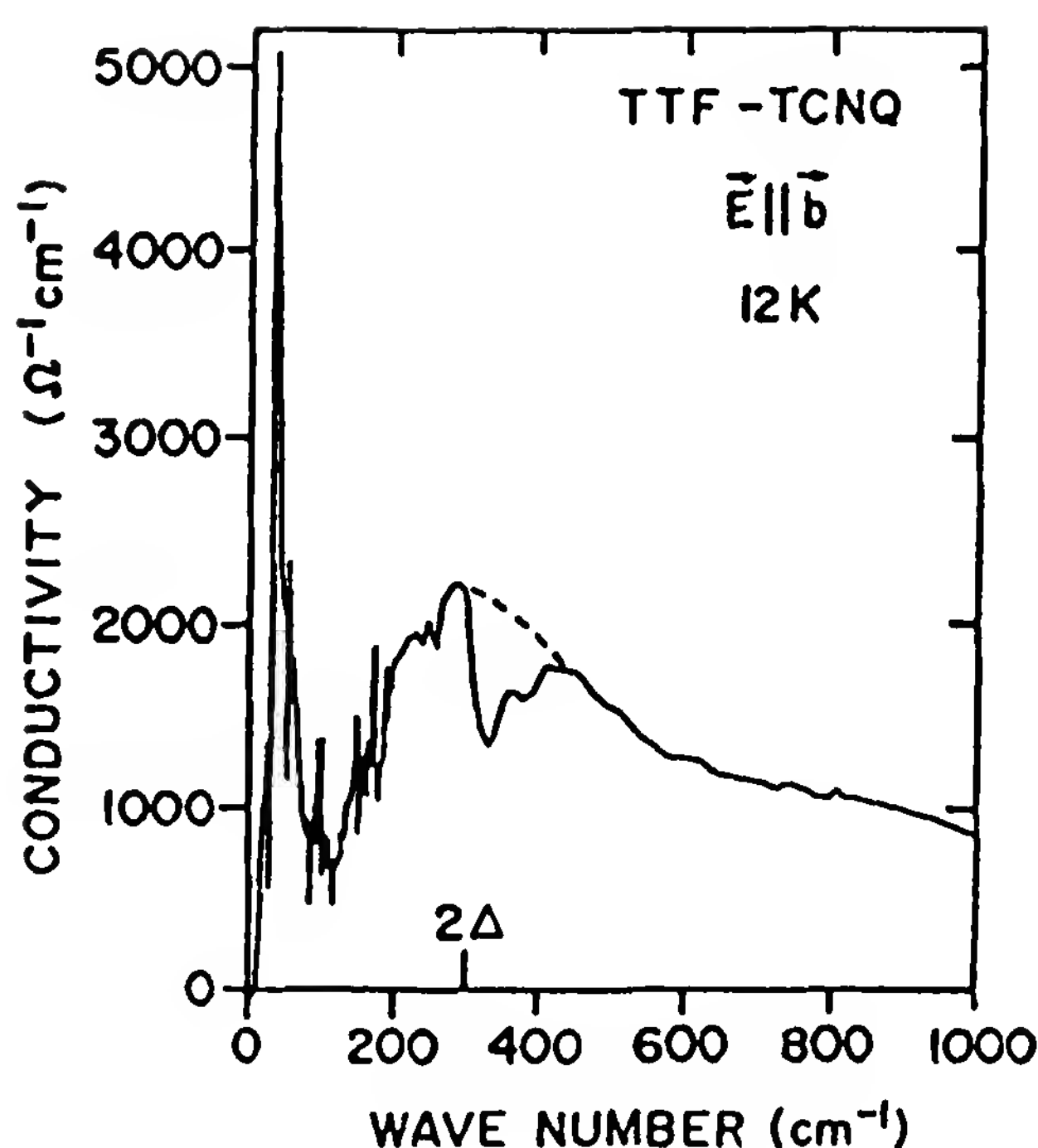


Figure 15 Frequency-dependent conductivity of TTF-TCNQ at 12 K. The dashed line is the expected $\sigma(\omega)$ in the absence of the strong antiresonance at 330 cm^{-1} due to the TCNQ internal mode ν_9 (a_g). (From Ref. 73.)

ductivity spectrum has been predicted theoretically by Lee et al. [74] for a one-dimensional system with an incommensurate CDW. The single-particle response is an inverse-square-root singularity with the peak near the energy gap, and the pinned CDW is optically active in the gap. The 60 K data show a broadening of the 300-cm^{-1} structure, and apparently the oscillator strength of the 35-cm^{-1} band has moved to zero frequency. This is consistent with a depinning of the CDWs at the phase transition.

The $4k_F$ instability gives rise to the only detectable superstructure at 300 K. The IR properties of the $4k_F$ CDW consist of a maximum in $\sigma(\omega)$, corresponding to a pseudogap, plus a number of sharper features near the a_g vibrational modes. It was shown [75] that the T dependence of the vibrational modes of TCNQ follows that of the $2k_F$ scattering. Thus the $4k_F$ instability must take place on the TTF stacks. This conclusion agrees with other studies of TTF-TCNQ salt.

F. Raman Scattering

Raman spectroscopy is used widely to study the vibrational and structural properties of single crystals and conducting polymers. Since this spectral method is a convenient, nondestructive tool, it is not surprising that it has

been used widely to characterize organic conducting materials. There already exists considerable literature on the Raman scattering in conducting ion-radical salts and complexes of TCNQ, TTF, TMTSF, TMTTF, BEDT-TTF, and so on.

One of the motivations of the Raman study is the need to complement the findings on the IR activation of the symmetric modes of acceptors or donors in organic conductors. For instance, Bandrauk et al. [76] have found that the intensities of the Raman spectra of organic semiconductor K-TCNQ correlate fairly well with the dimerization phase transitions proposed for the salt. They have suggested that librations are important in describing the physical properties of the systems.

Raman spectroscopy is a useful tool in the study of optically induced or electric field-induced transformation of some TCNQ salts (e.g., Cu TCNQ, Ag TCNQ) from a high-impedance to a low-impedance state [77]. On the other hand, Raman spectroscopy is considered to be a good technique to estimate the degree of charge transfer, owing to the linear dependence of TCNQ frequency on the formal charge [78,79]. Raman spectroscopy has been used not only to study properties of TCNQ salts but also to investigate various phenomena in organic CT complexes.

There already exists considerable literature on the optical properties of the salts and complexes of TMTTF and TMTSF molecules, either neutral or fully ionized [80,81]. BEDT-TTF is the second organic donor, which forms ambient pressure superconductors. The Raman scattering method is widely used to study the BEDT-TTF-based organic superconductors [82–85]; (BEDT-TTF)₂I₃ family is of special interest. The resonance Raman spectra of I₃[−] anions in the organic superconductor α - and β _H-(BEDT-TTF)₂I₃ were studied and compared with the nonsuperconducting phases of (BEDT-TTF)₂I₃ by Świetlik et al. [83]. For example, an interesting splitting of the band of about 120 cm^{−1} into two or three lines was observed at low temperature. The splitting is related to the commensurate superstructure developed below 125 K, contrary to the α phase, where the observed structure is related to a crystal-field effect. It was also shown that electronic excitation of the β -phase crystals by laser light can induce a structural transformation. The structural change was related to a transformation from the commensurate superstructure with a superconducting transition temperature $T_c = 1.3$ K into a more ordered and symmetric structure which becomes superconducting at $T_c = 8.1$ K.

Light scattering is a useful tool for investigating a superconducting gap in the electronic energy spectrum because it is based on electron–phonon interaction and therefore is able to sensitively probe both phonon and electronic states. This idea and experimental studies have recently been developed for (BEDT-TTF)₂I₃ family superconductors [85,86]. The van-

ishing of phonon bands, accompanied by a decrease of the electronic background, was observed below T_c .

Optical properties of organic conductors also reflect the appearance of the energy gap, 2Δ , in the electronic energy spectrum of low-dimensional solids. The approximate value for the total gap from the a_g -mode line shapes can be estimated by comparing the IR spectra of the organic conductor, measured for the frequencies above and below the energy gap; sharp absorption bands are produced at the frequencies $\omega < 2\Delta$, whereas for $\omega > 2\Delta$ sharp indentations occur [87,88].

Raman spectroscopy is also widely used to study the physical properties of polymers. Considerable interest and some controversies have arisen on the doping mechanisms responsible for high conductivity of doped polyacetylene, $(\text{CH})_x$. Undoped $(\text{CH})_x$ is a semiconductor with a gap of 1.4 eV; the gap is maintained upon doping, so that the new IR modes are within the gap. This behavior was recognized as evidence of the soliton configuration in $(\text{CH})_x$. Horowitz [89] showed that this behavior is a general consequence of the translational degree of freedom of additional charge, independent of its configuration. He explained all the phonon anomalies occurring in $(\text{CH})_x$ and $(\text{CD})_x$ in terms of the amplitude modes of the Peierls gap and the IR active vibrations induced by the added charge. It is impressive that the resonant Raman vibrations and the IR-active modes induced by doping or photogeneration are all described by the same form of dressed phonon propagator, $D_0(\omega)$.

The optical properties of conducting polymers are important to the development of an understanding of the basic electronic structure of the material. These and other problems were described in various books and review papers [90–93]. Raman spectroscopy is also an ideal tool for predicting many important electronic properties of molecular materials, organic conductors, and superconductors as well as for understanding their different physical properties, since it is a nondestructive tool, which can be used in situ and with spatial resolution as good as 1 μm .

G. Temperature Dependence and Phase Transitions

The temperature dependences of optical properties of organic conductors beyond the phase-transition region have not been investigated sufficiently so far. The quantitative temperature studies of the e-mv coupling are very difficult and possible only for some selected low-dimensional salts. It was shown [94,95] that an analysis of T dependence of the IR spectra of the salts composed of isolated dimers $(\text{TCNQ})_2^{2-}$ makes it possible to pinpoint the main mechanisms responsible for thermal evolution of the IR spectra and changes in the absorption coefficients. Among other things it was

shown that the activated a_g modes exhibit stronger temperature dependence than that of other bands. Nevertheless, the T dependence of other bands can also give interesting information.

Optical properties of organic conductors are strictly related to interactions between electrons and intramolecular vibrations. Therefore, the electron and IR spectra are sensitive to changes in charge distribution induced by temperature, structural disorder, or phase transition. Let us consider some examples of phase transitions studied by spectral methods. Among a number of organic CT compounds, the family of segregated-stack compounds of the radical anion TCNQ^- has been subject for considerable investigations [60,96,100]. For example, the ion-radical salt $\text{MEM}(\text{TCNQ})_2$ undergoes first-order structural phase transitions, at temperatures $T_{\text{EP}} = 335$ K and $T_{\text{SP}} = 19$ K. The former is an electronic Peierls phase transition, whereas the latter is a spin-Peierls transition; both transitions are accompanied by rearrangements in the stacks. These rearrangements are observed by IR spectral methods. The reflectivity spectra of $\text{MEM}(\text{TCNQ})_2$ single crystals for $T < T_{\text{EP}}$ (Fig. 16) are similar to the spectra of semiconducting TCNQ salts, and the spectra for $T > T_{\text{EP}}$ are similar to other TCNQ salts which exhibit metallic properties. During thermal cycling a thermal hysteresis extended on 3° was observed [97]. Recently, a soft-mode phonon associated with the spin-Peierls transition has been found below the T_{SP} in $\text{MEM}(\text{TCNQ})_2$ by far-IR spectroscopy [99]. From the residual profiles below T_{SP} shown in Fig. 17, one can see that as temperature is increased from 4 K to 17 K, the frequency of the lowest phonon decreases and its line width is broadened; the lowest phonon is a softened vibration associated with the spin-Peierls transition.

Among the many intriguing features of the physical behavior of TTF-TCNQ is the sequence of successive phase transitions at 54, 49, and 38 K.

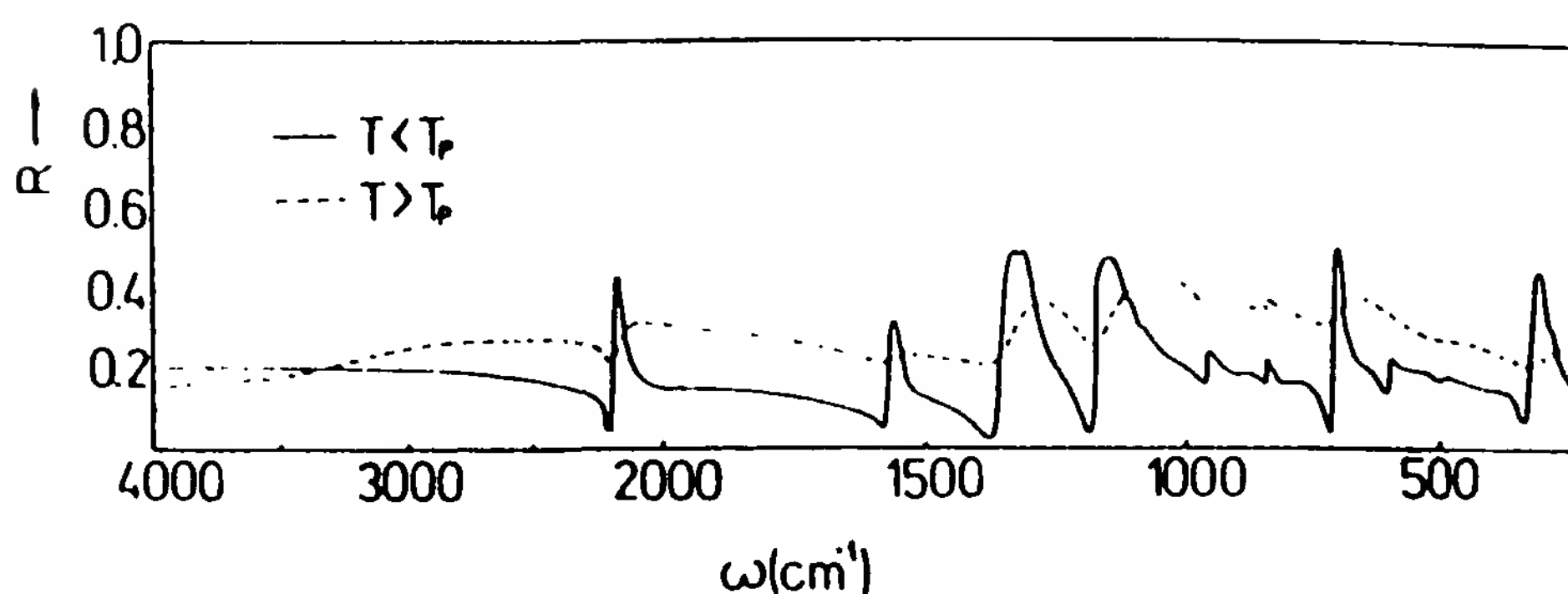


Figure 16 IR reflectivity of the low-temperature (solid line) and high-temperature (dashed line) phases of $\text{MEM}(\text{TCNQ})_2$ single crystals. (From Ref. 97.)

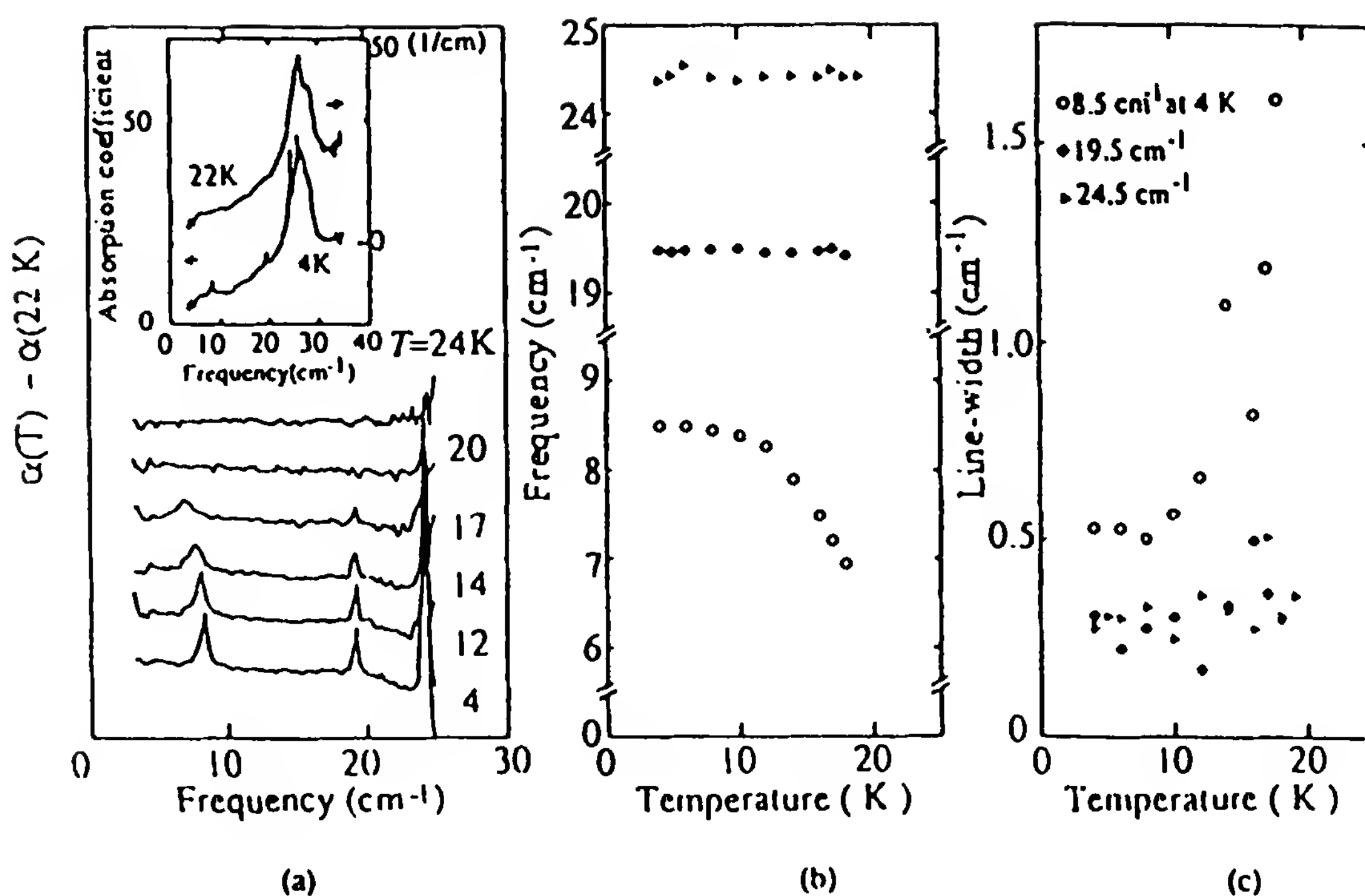


Figure 17 Absorption spectra of $\text{MEM}(\text{TCNQ})_2$ at a temperature T minus that at 22 K. Absorption spectra at 4 and 22 K are shown in the inset in (a). Frequency of absorption lines (b) and the line width (c) as a function of temperature. (From Ref. 99.)

The origin of these transformations is very difficult to investigate. Yet it appears that the optical study should be very helpful for this purpose. An analysis of T dependence of the phase phonon absorptions at 317 and 253 cm^{-1} show that the 54 K metal–insulator transition is driven by the Peierls distortion on the TCNQ sublattice, whereas the distortion on the TTF chains increases markedly around 49-K phase transition [100]. It is a typical example of a close relationship between the optical properties of organic conductors and a molecular mechanism of the phenomena that occur in the material.

Recently, the spectral study of $\text{DMTM}(\text{TCNQ})_2$ phase transition was performed [60]. The salt is a quarter-filled organic semiconductor containing segregated chains of TCNQ dimers and DMTM counterions. This material undergoes an “inverted Peierls transition,” which has tentatively been explained in terms of a crystal-field distortion. It was shown that the experimental values of unperturbed phonon frequencies and e-mv coupling constants are nearly independent of temperature. The dimer model fails to reproduce the phonon intensities and line shapes and underestimates the coupling constants, whereas the CDW model produces better results

in both cases. The electronic parameters, most notably the transfer integral, show an unusual T dependence and may have important implications on charge transport in the TCNQ stacking direction. The spectral data do not support the idea that the unusual properties of DMTM(TCNQ)₂ are caused by low-energy interchain charge transfer [60].

IR study of TMTTF with nonsymmetrical anions (ClO_4^- , NO_3^- , SCN^- , and SeCN^-) versus temperature was performed by Garrigou-Lagrange et al. [101]. At low temperature the authors observed an increase in both intensity and frequency of the a_g $\nu(\text{C}=\text{C})$ mode. It was shown that these changes are due to an order–disorder transition of the noncentrosymmetric counterion, which can induce a tetramerization of the organic stacks. We close this section by emphasizing that in some cases vibrational spectroscopy yields structural information that is not easy to obtain by means of other methods.

H. Structural Disorder

Irradiation of the crystal by electrons or neutrons is the simplest way of introducing the defects by controlled means. Optical properties of organic conductors are sensitive to changes in the electron distribution induced by irradiation defects (i.e., their spectra are sensitive to the localization of the carriers, due to random potentials in the environment of the defects). The electronic absorption spectra give information on the density of charge carriers and their localizations as well as on the electronic energy levels.

Neutron [102] and electron [70,103] irradiated TCNQ salts were investigated by IR spectroscopy. The spectra of irradiated samples gradually become weaker when the dose is increased: the broad lines change shape and decrease in intensity; some even vanish (Fig. 18). It was shown [103] that the vibrational features connected with the totally symmetric modes of the TCNQ are particularly sensitive to structural disorder. In some cases, for example, in MTPP(TCNQ)₂ irradiated by electrons, the disappearance of distinct doublets of activated a_g modes was noticed. Different mechanisms of the excitation of both the narrow and wide components explain their different dose and temperature dependences [70]. The changes of band intensity in the UV-VIS region imitate the electrical conductivity as a function of dose.

It has been shown that electron irradiation of the semiconducting TCNQ salts leads to extensive spectral changes. Some of these changes were described and explained, but many still remain unexplained. Almost untouched is the subject of spectral studies of irradiated organic metal-like materials. One must emphasize that although the optical investigations of disordered organic conductors are focused on the molecular approach, the

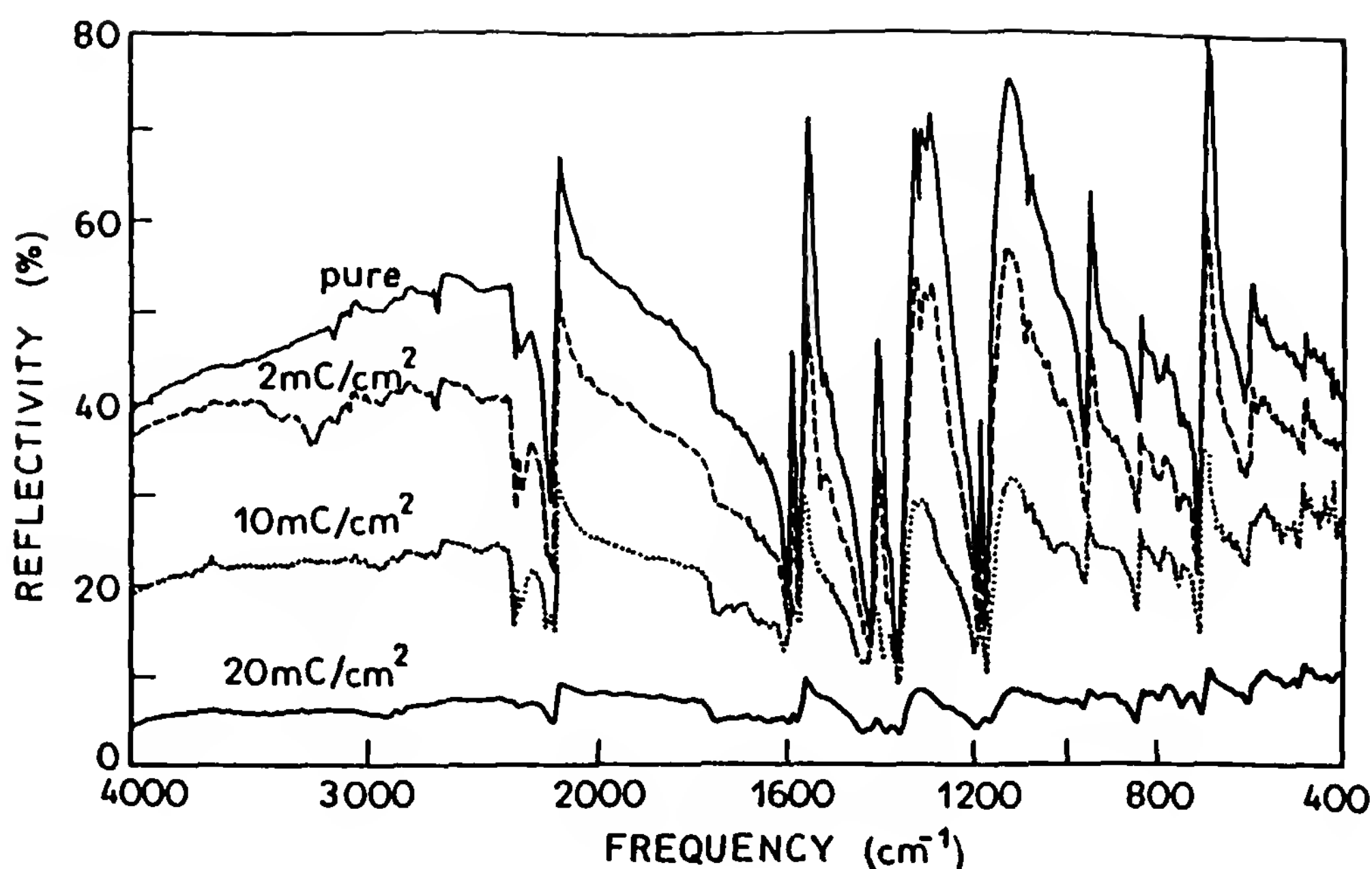


Figure 18 Dose dependence of the TEA(TCNQ)₂ reflectance at 80 K with light polarized along the maximum reflectance direction. (From Ref. 53.)

conclusions drawn from this study are useful for understanding various physical properties of nominally pure and disordered crystals.

V. CONCLUDING REMARKS

In this chapter we have summarized the principal optical properties of characteristic organic semiconductors, metal-like conductors, molecular superconductors, and polymers (on a limited scale). The optical properties of these molecular materials are crucial to the development of understanding of basic electronic interactions and structures of the organic conductors. The basic information comes from the studies in the wide spectral region, from far infrared to vacuum ultraviolet. Other phenomena of fundamental importance described in this paper are various interactions and couplings in molecular conductors, which determine their physical properties and their usefulness to applications. Optical investigations of the organic conductors can provide specific information about localization of the charges on a one-dimensional chain, electron–electron and electron–phonon interactions, vibronic activations of the modes, distortions of the one-dimensional chains, nature of the phase transitions, and changes of the properties of the organic solids under extreme conditions. Very important issues have motivated a number of studies of the spectra in the far-IR region. These

included the measurements of the gaps induced by the formation of spin density waves or by the onset of superconductivity at low temperature.

On the other hand, there are a number of open questions, some of which have been touched on briefly in the chapter. A principal goal of the field of conducting polymers is to achieve an understanding of the relationship between the chemical structure of the monomer units and electronic properties of the resulting conjugated polymer. In situ spectral technique has made it possible to determine the nature of the charge-storage states and to monitor the kinetics of the CT reaction. Such investigations have played an important role in clarifying the chemistry and physics of conducting polymers.

The general trend in the study of organic conductors is to modify, through an imposed molecular organization, the bulk properties of these materials on a mesoscopic or even microscopic scale. The optical studies of such materials (e.g., Langmuir–Blodgett films) are in the process. Finally, it was shown that the optical study of various organic conducting materials permits us to solve many specific problems.

REFERENCES

1. R. Bozio and C. Pecile, in *The Physics and Chemistry of Low-Dimensional Solids* (L. Alcácer, ed.), D. Reidel, Dordrecht, The Netherlands, 1980.
2. D. B. Tanner, in *Extended Linear Chain Compounds*, Vol. 2 (J. S. Miller, ed.), Plenum Press, New York, 1982.
3. C. S. Jacobsen, in *Sixteen Research Reports by the Niels Bohr Fellows of the Royal Danish Academy of Sciences and Letters*, Matematisk-fysiske Meddelelser 41, Copenhagen, 1985.
4. C. S. Jacobsen, *J. Phys. C Solid State Phys.* 19:5643 (1986).
5. C. S. Jacobsen, in *Low Dimensional Conductors and Superconductors*, NATO ASI Series (D. Jérôme and L. G. Caron, eds.), Plenum Press, New York, 1987.
6. A. Graja, *Les interaction électron–électron et électron–phonon dans les systèmes unidimensionnels des sels de TCNQ; nature et conséquences spectrales*, Les Editions Science de Pologne, Varsovie-Poznań, 1985.
7. M. G. Kaplunov and Y. G. Borod'ko, *Khim. Fiz.* 6:1529 (1987).
8. R. Bozio, in *Molecular Electronics* (M. Borisov, ed.), World Scientific, Singapore, 1987.
9. V. M. Yartsev and R. Świetlik, *Rev. Solid State Sci.* 4:69 (1990).
10. A. Graja, in *Molecular Electronics and Molecular Electronic Devices* (K. Sienicki, ed.), CRC Press, Boca Raton, Fla. (in press).
11. J. Hubbard, *Phys. Rev. B* 17:494 (1978).
12. M. Born and E. Wolf, *Principles of Optics*, Pergamon Press, New York, 1959.
13. M. J. Rice, *Solid State Commun.* 31:93 (1979).

14. R. G. J. Miller and B. C. Stace, eds., *Laboratory Methods in Infrared Spectroscopy*, Heyden, New York, 1972.
15. G. N. Ramachandran and S. Ramaseshan, in *Handbook of Physics*, Vol. XXV/1 (S. Flügge, ed.), Springer-Verlag, New York, 1961, p. 1.
16. A. Girlando and C. Pecile, *Spectrochim. Acta A* 29:1859 (1973).
17. R. Bozio, A. Girlando, and C. Pecile, *Chem. Phys. Lett.* 52:503 (1977).
18. A. Brau, P. Brüesch, J. P. Farges, W. Hinz, and D. Kuse, *Phys. Status Solidi (b)* 62:615 (1974).
19. M. J. Rice, *Phys. Rev. Lett.* 37:36 (1976).
20. M. J. Rice, N. O. Lipari, and S. Strässler, *Phys. Rev. Lett.* 39:1359 (1977).
21. V. M. Yartsev, *Phys. Status Solidi (b)* 112:279 (1982).
22. V. M. Yartsev and A. V. Filimoshkina, *Mater. Sci.* 17:93 (1991).
23. A. Painelli, A. Girlando, and C. Pecile, *Mol. Cryst. Liq. Cryst.* 134:1 (1986).
24. H. W. Helberg, *Phys. Status Solidi (a)* 33:453 (1976).
25. H. W. Helberg, *Mol. Cryst. Liq. Cryst.* 85:91 (1982).
26. H. W. Helberg and H.-Chr. Lenz, *Synth. Metals* 55–57:2431 (1993).
27. H. W. Helberg, *Physica* 143B:488 (1986).
28. H. W. Helberg, *Ber. Bunsenges. Phys. Chem.* 91:899 (1987).
29. H. W. Helberg, D. Schweitzer, and H. J. Keller, *Synth. Metals* 27:A347 (1988).
30. G. O. Baram, L. I. Buravov, L. S. Degtyarev, M. E. Kozlov, V. N. Laukhin, E. E. Laukhina, V. G. Onishchenko, K. I. Pokhodnya, M. K. Sheinkman, R. P. Shibaeva, and E. B. Yagubskii, *Pis'ma Zh. Eksp. Teor. Fiz.* 44:293 (1986).
31. J. B. Torrance, B. A. Scott, and F. B. Kaufman, *Solid State Commun.* 17:1369 (1975).
32. A. Graja, *Low-Dimensional Organic Conductors*, World Scientific, Singapore, 1992.
33. K. Kamaràs, G. Grüner, and G. A. Sawatzky, *Solid State Commun.* 27:1171 (1978).
34. D. B. Tanner, C. S. Jacobsen, A. A. Bright, and A. J. Heeger, *Phys. Rev. B* 16:3283 (1977).
35. J. B. Torrance, B. A. Scott, B. Welber, F. B. Kaufman, and P. E. Seiden, *Phys. Rev. B* 19:730 (1979).
36. K. Yakushi, H. Tajima, T. Ida, M. Tamura, H. Itayashi, H. Kuroda, A. Kobayashi, H. Kobayashi, and R. Kato, *Synth. Metals* 24:301 (1988).
37. H. Tajima, K. Yakushi, H. Kuroda, G. Saito, and H. Inokuchi, *Solid State Commun.* 49:769 (1984).
38. C. S. Jacobsen, V. M. Yartsev, D. B. Tanner, and K. Bechgaard, *Synth. Metals* 55–57:1925 (1993).
39. J. P. Farges, A. Brau, and P. Dupuis, *Solid State Commun.* 54:531 (1985).
40. A. Brau, J. P. Farges, and E. H. Ghezzal, *Solid State Ionics* 44:331 (1991).
41. M. Pawlak and A. Graja, *Synth. Metals* 24:145 (1988).
42. W. Pukacki, M. Pawlak, A. Graja, M. Lequan, and R. M. Lequan, *Inorg. Chem.* 26:1328 (1987).

43. D. B. Tanner, J. E. Deis, A. J. Epstein, and J. S. Miller, *Solid State Commun.* 31:671 (1979).
44. D. B. Tanner, C. S. Jacobsen, A. F. Garito, and A. J. Heeger, *Phys. Rev.* 13:3381 (1976).
45. D. B. Tanner and C. S. Jacobsen, *Mol. Cryst. Liq. Cryst.* 85:137 (1982).
46. C. S. Jacobsen, D. B. Tanner, and K. Bechgaard, *Phys. Rev. Lett.* 46:1142 (1981).
47. M. G. Kaplunov, E. B. Yagubskii, L. P. Rosenberg, and Yu. G. Borodko, *Phys. Status Solidi (a)* 89:509 (1985).
48. M. G. Kaplunov, T. P. Panova, and Yu. G. Borodko, *Phys. Status Solidi (a)* 13:K67 (1972).
49. M. J. Rice, L. Pietronero, and P. Brüesch, *Solid State Commun.* 21:757 (1977).
50. N. O. Lipari, C. B. Duke, R. Bozio, A. Girlando, C. Pecile, and A. Padva, *Chem. Phys. Lett.* 44:236 (1976).
51. V. M. Yartsev, *Phys. Status Solidi (b)* 126:501 (1984).
52. M. J. Rice, V. M. Yartsev, and C. S. Jacobsen, *Phys. Rev.* 21:3437 (1980).
53. I. Olejniczak and A. Graja, *Acta Phys. Polonica* 83:517 (1993).
54. R. Świetlik, A. Graja, and E. Sopa, *J. Mol. Struct.* 115:165 (1984).
55. V. Železný, J. Petzelt, and R. Świetlik, *Phys. Status Solidi (b)* 140:595 (1987).
56. D. B. Tanner, J. S. Miller, M. J. Rice, and J. J. Ritsko, *Phys. Rev.* 21:5835 (1980).
57. A. Szyszkowski, *Phys. Status Solidi (b)* 91:K95 (1979).
58. E. F. Steigmeier, H. Anderset, D. Baeriswyl, and M. Almeida, *Mol. Cryst. Liq. Cryst.* 120:163 (1987).
59. G. J. Ashwell, D. W. Allen, A. Graja, and R. Świetlik, *J. Chem. Soc. Faraday Trans. II* 82:83 (1986).
60. J. L. Musfeldt, C. C. Homes, M. Almeida, and D. B. Tanner, *Phys. Rev. B* 46:8777 (1992).
61. C. S. Jacobsen, D. B. Tanner, and K. Bechgaard, *Phys. Rev. B* 28:7019 (1983).
62. A. Graja, V. M. Yartsev, C. Garrigou-Lagrange, M. Sallé, and A. Gorgues, *Phys. Status Solidi (b)* 174:119 (1992).
63. V. M. Yartsev and C. S. Jacobsen, *Phys. Status Solidi (b)* 145:K149 (1988).
64. K. D. Cummings, D. B. Tanner, and J. S. Miller, *Phys. Rev. B* 24:4142 (1981).
65. M. V. Belousov, A. M. Vainrub, R. M. Vlasova, and V. N. Semkin, *Fiz. Tverd. Tela* 20:107 (1978).
66. A. Graja, A. Szyszkowski, J. Petzelt, N. Ryšavá, and K. Král, *Acta Phys. Polon. A* 61:123 (1982).
67. V. N. Semkin, S. Y. Prieв, R. M. Vlasova, V. M. Yartsev, G. G. Abashev, and V. S. Russkikh, *Mater. Sci.* 14(4):71 (1988).
68. V. N. Semkin, R. M. Vlasova, N. F. Kartenko, S. Y. Prieв, O. A. Usov, V. M. Yartsev, L. S. Agroskin, K. V. Petrov, G. G. Abashev, and V. S. Russkikh, *Fiz. Tverd. Tela* 31:89 (1989).

69. R. Świetlik and A. Graja, *J. Phys.* 44:617 (1983).
70. R. Świetlik, A. Graja, and K. I. Pokhodnya, *Synth. Metals* 35:17 (1990).
71. V. M. Yartsev and M. J. Rice, *Phys. Status Solidi (b)* 100:K97 (1980).
72. J. E. Eldridge and F. E. Bates, *Phys. Rev. B* 28:6972 (1983).
73. J. E. Eldridge, *Phys. Rev. B* 31:5465 (1985).
74. P. A. Lee, T. M. Rice, and P. W. Anderson, *Solid State Commun.* 14:703 (1974).
75. D. B. Tanner, K. D. Cummings, and C. S. Jacobsen, *Phys. Rev. Lett.* 47:597 (1981).
76. A. D. Bandrauk, K. D. Troung, and S. Jandl, *Can. J. Chem.* 60:1881 (1982).
77. E. I. Kamitsos and W. M. Risen, Jr., *Solid State Commun.* 45:165 (1983).
78. H. Kuzmany and M. Elbert, *Solid State Commun.* 35:597 (1980).
79. S. Matsuzaki, R. Kuwata, and K. Toyoda, *Solid State Commun.* 33:403 (1980).
80. M. Krauzman, H. Poulet, and R. M. Pick, *Phys. Rev. B* 33:99 (1986).
81. S. Matsuzaki, Z. S. Li, M. Sano, G. Saito, and M. Soma, *Synth. Metals* 38:269 (1990).
82. S. Sugai and G. Saito, *Solid State Commun.* 58:759 (1986).
83. R. Świetlik, D. Schweitzer, and H. J. Keller, *Phys. Rev. B* 36:6881 (1987).
84. R. Świetlik, H. Grimm, D. Schweitzer, and H. J. Keller, *Z. Naturforsch.*, 42a:603 (1987).
85. A. Graja, K. I. Pokhodnia, M. Weger, and D. Schweitzer, *Synth. Metals* 55–57:2477 (1993).
86. K. I. Pokhodnia, A. Graja, M. Weger, and D. Schweitzer, *Z. Phys. Condensed Matter* 90:127 (1993).
87. R. P. McCall, I. Hamberg, D. B. Tanner, J. S. Miller, and A. J. Epstein, *Phys. Rev. B* 39:7760 (1989).
88. A. M. Vainrub, G. S. Zavt, and A. Graja, *Phys. Status Solidi (b)* 155:147 (1989).
89. B. Horowitz, *Synth. Metals* 9:215 (1984).
90. J. C. W. Chien, *Polyacetylene: Chemistry, Physics and Materials Science*, Academic Press, Orlando, Fla., 1984.
91. T. A. Skotheim, ed., *Handbook of Conducting Polymers*, Marcel Dekker, New York, 1986.
92. A. O. Patil, A. J. Heeger, and F. Wudl, *Chem. Rev.* 88:183 (1988).
93. J. Kürti and H. Kuzmany, *Phys. Rev. B* 44:597 (1991).
94. A. Graja, R. Świetlik, G. Sekretarczyk, and K. Král, *Acta Phys. Polon. A* 59:77 (1981).
95. A. Graja, P. V. Huong, and J.-C. Cornut, *Solid State Commun.* 39:929 (1981).
96. H. Okamoto, Y. Tokura, and T. Koda, *Phys. Rev. B* 36:3558 (1987).
97. R. Świetlik and A. Graja, *J. Phys. Colloq.* 44:C3-1457 (1990).
98. Y. Tanaka and K. Nagasaka, *Solid State Commun.* 73:735 (1990).
99. Y. Tanaka, N. Satoh, and K. Nagasaka, *Synth. Metals* 41–43:2503 (1991).
100. R. Bozio and C. Pecile, *Solid State Commun.* 37:193 (1981).

101. C. Garrigou-Lagrange, A. Graja, C. Coulon, and P. Delhaès, *J. Phys. C Solid State Phys.* *17*:5437 (1984).
102. K. Kamarás, K. Holczer, and J. Jánossy, *Phys. Status Solidi (b)* *102*:467 (1980).
103. A. Graja and R. Świetlik, *J. Phys.* *46*:1417 (1985).

This Page Intentionally Left Blank

7

Magnetic, ESR, and NMR Properties

Luís Alcácer

Instituto Superior Técnico, Lisbon, Portugal

I. INTRODUCTION

This chapter serves as an overview of the magnetic, electron spin resonance (ESR), and nuclear magnetic resonance (NMR) properties of organic conductors. Instead of trying to be exhaustive, we focus on general aspects and discuss typical examples. Besides conductivity and optical reflectance, the spin susceptibility and ESR properties usually provide a very good characterization of the electronic properties of organic conductors: namely, bandwidths, role of electron–electron interactions, and nature of the ground state. On the other hand, a very direct proof of the one-dimensional character of the electronic motion is given by the NMR properties.

Organic conductors are quasi-one-dimensional solids with relatively narrow bandwidths. The conventional band theory has some limitations due to the importance of electron–electron and electron–phonon interactions. The difficulties are aggravated by the great sensitivity to disorder, defects, and impurities usually present in these materials. The variety of transport processes makes rationalization very difficult. Since the magnetic, ESR, and NMR properties are related to the electronic properties, we could start by phenomenologically distinguishing [1] between materials with a metallic regime above a metal–insulator transition, at a characteristic temperature, $T_{\text{M-I}}$, or a superconducting transition at T_c ; materials with a broad maximum in the conductivity at a characteristic temperature, T_ρ ; and materials

with temperature-activated conductivity. We deal mainly with materials with a high-temperature metallic regime above a metal–insulator transition, since superconductors are treated elsewhere and other types of organic conductors are much diversified and less well characterized.

In the metallic regime the properties can usually be interpreted within the one-dimensional model. The low-temperature behavior is determined by the shape of the Fermi surface. If it is open as in the case of the TMTTF and TMTSF salts, the description of the properties is based on the physics of one-dimensional systems. This does not mean that the dynamics of the electrons is one-dimensional. The coupling between chains has an important role, allowing transitions at $T > 0$, derived from one-dimensional instabilities.

We start with a review on the basic theory and experiments followed by an analysis of typical experimental data. Considerable attention will then be devoted to the emerging field of molecular ferromagnets and to applications.

II. BASIC THEORY AND EXPERIMENTS

A. Introduction

Under this heading we review the basic concepts, in general, first (see, e.g., Ref. 2), and then in the context of quasi-one-dimensional organic conductors. Several previous good and profound reviews have appeared in the literature. Among them, we particularly recommend those by Scott [3] and Jérôme and Schulz [4].

B. Magnetic Susceptibility

The application of a magnetic field, \mathbf{H} , to a material induces a magnetization, \mathbf{M} , defined as the magnetic moment per unit volume. The magnetic susceptibility is

$$\chi = \frac{\mathbf{M}}{\mathbf{H}} \approx \frac{\mu_0 \mathbf{M}}{\mathbf{B}} \quad (1)$$

since $\mathbf{B} \approx \mu_0 \mathbf{H}$ where μ_0 is the vacuum permeability. The susceptibility defined in this way is adimensional. It is, however, frequent to use the molar susceptibility, $\chi_M = \chi M/\rho$, where M is the molecular weight and ρ is the specific mass. χ_M is expressed in $\text{m}^3 \text{mol}^{-1}$ in the SI system and in $\text{cm}^3 \text{mol}^{-1}$ in the emu system. Since most results in the literature are in emu/mol, we use these units from here on.

The total magnetic susceptibility of a solid is, in general, the sum of various terms: namely, the diamagnetic susceptibility, χ_D (negative and

small), due to induced currents which tend to screen the applied field; the spin susceptibility, χ_S (positive), due to the unpaired spins; the Van Vleck susceptibility, χ_{VV} , which is due to band mixing, is zero in one-dimensional band structures, and has been neglected in organic metals; and the Landau diamagnetic susceptibility, χ_L , due to effects of the Landau orbits.

Static magnetic susceptibility is usually one of the first experiments to be performed in a new organic conductor. It can immediately provide information on its magnetic nature. Important information can also be extracted from the susceptibility on the nature of phase transitions which are common in quasi-one-dimensional organic conductors.

Several techniques are used to measure the magnetic susceptibility: namely, the Faraday balance, which is the most precise and easy to use over a large temperature range; the SQUID, magnetometer particularly good for very small samples; and other less precise methods. In all these methods one measures the total susceptibility $\chi_T = \chi_D + \chi_S + \chi_{VV} + \chi_L$. χ_D can be calculated from the Pascal constants, and in the context of organic conductors, the important temperature-dependent term is χ_S , the other terms being negligible, with a few exceptions.

C. Spin Susceptibility

The spin susceptibility of the conduction electrons in conventional metals, and within the free-electron Fermi gas model, is temperature independent and is called the Pauli susceptibility. It arises from the fact that in the presence of an applied field, the density of states will split into two components, one with the spins parallel to the field and the other antiparallel. The energies of the electrons with magnetic moment parallel to the field ($E \downarrow = -\mu_B B$, μ_B being the Bohr magneton) will be lower than those with magnetic moment antiparallel ($E \uparrow = +\mu_B B$). Since the Fermi energy in thermal equilibrium will be the same for both spin states and since usually $\mu_B B \ll E_F$, the excess moments parallel to the field will be $\Delta n = \frac{1}{2} D(E_F) 2\mu_B B$, and the corresponding magnetization $M = \Delta n \mu_B = \mu_B^2 D(E_F) B$, where $D(E_F)$ is the density of states at the Fermi level. Taking $B \approx \mu_o H$ we can compute the Pauli susceptibility:

$$\chi_S = \mu_B^2 D(E_F) \quad (2)$$

If the electrons of a lattice ion or molecule contributing to the magnetic moment are sufficiently tightly bound for the ions or molecules to be taken as isolated, but on the other hand, that the nearest neighbors are close enough for a significant exchange interaction to arise, we need to consider a different approach, which is as follows.

The spin contribution to the magnetic susceptibility comes from the exchange term of the Coulomb interaction. If we take into account the exchange interaction in the Hartree–Fock approximation, the ground state of an electron gas is the *ferromagnetic* state, in which all spins are parallel.

The exchange Hamiltonian can be written in the Heisenberg form:

$$\mathbf{H}^{\text{exchange}} = - \sum_{ij}' J_{ij} \mathbf{S}_i \cdot \mathbf{S}_j \quad (3)$$

in which \mathbf{S}_i and \mathbf{S}_j are the spin operators, J_{ij} is the exchange integral, and the sum is over all pairs of spins ($i \neq j$). A detailed study of the Heisenberg model leads to collective excitations or spin waves, which have dispersion relations similar to those of phonons.

In a lattice with a basis, each molecule or ion of the primitive cell can have a different spin or a different orientation. This leads to the necessity of considering sublattices. For two sublattices with opposite spins of different moduli, the total spin is the difference between spins. This is a *ferrimagnet*. If two sublattices have opposite spins of the same moduli, the resulting spin is zero and we have an *antiferromagnet*.

To understand the behavior above the Curie temperature, we will use the *molecular field approximation*. In the presence of an applied external field \mathbf{B} , we have to add the term due to the N spins interacting with the field,

$$H = - \sum_{ij}' J_{ij} \mathbf{S}_i \cdot \mathbf{S}_j - g\mu_B \mathbf{B} \cdot \sum_{i=1}^N \mathbf{S}_i \quad (4)$$

where g is the Landé factor ($g = 2.0023$ for the free electron).

This Hamiltonian cannot be solved exactly because the first term is nonlinear. We can, however, use the molecular field approximation, which consists of taking the mean value $\langle \mathbf{S}_j \rangle$ over the j spins:

$$H = - \sum_{i=1}^N \left(g\mu_B \mathbf{B} + \sum_{j=1(\neq i)}^N J_{ij} \langle \mathbf{S}_j \rangle \right) \cdot \mathbf{S}_i \quad (5)$$

Besides the external field, \mathbf{B} , a *mean internal field*, \mathbf{B}_M , is introduced. This is called the Weiss field:

$$\mathbf{B}_M = \frac{1}{g\mu_B} \sum_{j=1(\neq i)}^N J_{ij} \langle \mathbf{S}_j \rangle \quad (6)$$

Since the magnetic moment is $\mu = g\mu_B \langle \mathbf{S}_j \rangle$, we can write the magnetization:

$$\mathbf{M} = N\mu = g\mu_B \langle \mathbf{S}_j \rangle N \quad (7)$$

and the internal field $\mathbf{B}_M = \lambda \mathbf{M}$ with $\lambda = \nu J / g^2 \mu_B^2 N$, ν being the number of nearest neighbors and J the exchange integral.

For the case where $k_B T \gg g \mu_B B$, the Boltzmann distribution leads to a magnetization and the corresponding susceptibility, in thermal equilibrium:

$$\chi_s = \frac{N \mu^2}{3 k_B T} \quad (8)$$

or, since $\mu^2 = g^2 \mu_B^2 \langle S^2 \rangle$, and $\langle S^2 \rangle = S(S + 1)$:

$$\chi_s = \frac{N g^2 \mu_B^2 S(S + 1)}{3 k_B T} = \frac{C}{T} \quad (9)$$

which is the well-known Curie law. It implies that for the case where spin interactions are negligible, the spin susceptibility is proportional to the inverse temperature.

If there is an orbital angular momentum, L , besides the spin, S , we should use the total moment $J = L + S$, and we would get a Landé factor:

$$g = 1 + \frac{J(J + 1) + S(S + 1) - L(L + 1)}{2J(J + 1)} \quad (10)$$

The effective magnetic moment, μ_{eff} , is of the form

$$\mu_{\text{eff}} = g \sqrt{J(J + 1)} \mu_B \quad (11)$$

When the ferromagnetic interactions are nonnegligible but small, the spin susceptibility takes the form

$$\begin{aligned} \mathbf{M} &= \frac{C}{T} (\mathbf{B} + \lambda \mathbf{M}) \quad \text{or} \quad \mathbf{M} \\ &= \frac{C}{T - C\lambda} \mathbf{B} \quad \text{or still} \quad \mathbf{M} = \frac{C}{T - T_c} \mathbf{B} \end{aligned} \quad (12)$$

implying that above T_c (Curie temperature) the susceptibility increases with $(T - T_c)^{-1}$. In general, we can write

$$\chi = \frac{C}{T - \Theta} \quad (13)$$

which is the Curie–Weiss law. Θ is positive if the interactions are *ferromagnetic* and it is negative if they are *antiferromagnetic*. Usually, Θ is used when the interactions are antiferromagnetic and T_c when they are ferromagnetic.

This model only considers the interaction between spins in the nearest neighbors. Long-range interactions can also occur, through the paramagnetic ions, which can transmit the interaction. It is the case of MnO, for example, in which, each d electron interacts with one of the two p electrons of the oxygen lone pair. This leads to effective interaction between the d electrons of the Mn atoms, giving rise to *superexchange*.

There are also cases in which the unpaired localized electrons of the lattice interact with the conduction electrons. The information of the spin state of a given ion is transmitted to another one, via the conduction electrons. Since the Pauli exclusion principle cannot be violated, the spins, feeling the interaction, will comply. This is called the *Ruderman–Kittel interaction*.

D. Spin Susceptibility in One-Dimensional Systems

Most organic conductors behave as quasi-one-dimensional systems, at least at high temperatures. It is generally accepted that due to the narrow bandwidths, the strongest interactions are the electron–electron Coulomb interaction, U for two electrons on the same site, and V for electrons in nearest-neighbor sites, in agreement with the extended Hubbard Hamiltonian, which is usually taken as a good approximation.

Most organic conductors have segregated stacks, one of which is conducting, the other being formed by diamagnetic counterions. In the metallic regime, above the usual metal–insulator transition at a characteristic temperature, T_{M-I} , or the superconducting transition at T_c , the susceptibility should, in principle, be Pauli type [Eq. (2)] with $D(E_F)$ calculated within the tight-binding approximation (Hubbard model):

$$D(E_F) = \left(2\pi t \sin \frac{\pi\rho}{2} \right)^{-1} \quad (14)$$

where $t \equiv t_{||}$ is the intrachain transfer integral and ρ is the amount of charge transfer.

We will consider two limiting cases:

1. In the weak-coupling limit ($t \gg U, V$), the effect of electron–electron interactions measured in terms of an effective, U_{eff} , lead to a Stoner-type enhancement factor, which can slightly reduce the deviation from the expected Pauli susceptibility [5]:

$$\chi_s(T) = \frac{\chi_s^0}{1 - U_{\text{eff}}D(E_F)} = \chi_s^0(1 - \alpha)^{-1} \quad (15)$$

where χ_s^0 is the Pauli susceptibility given by Eq. (2). U_{eff} is the effective Coulomb repulsion from the bare Hubbard U . It depends on U and V . In

the case of full charge transfer ($\rho = 1$), $U_{\text{eff}} = U - V^2$. In the Hartree–Fock approximation χ_S is given by the same expression [6], but $U_{\text{eff}} \approx U$. As we shall see, for the quasi-one-dimensional systems, χ_S does not exactly follow this behavior, and in most cases it is still a matter of controversy.

2. In the limit of strong coupling (for $U, V \gg t$) the electron–electron interactions lead to localization. The concept of Fermi surface loses its significance and the spin and charge degrees of freedom are uncoupled. For a description of the spin degrees of freedom the simplest approach consists in taking the molecular limit, $t = 0$. In this case the Hubbard one-dimensional Hamiltonian is equivalent to the isotropic Heisenberg Hamiltonian [7]:

$$\mathbf{H}^{\text{exchange}} = J_{\text{eff}} \sum_i \mathbf{S}_i \cdot \mathbf{S}_{i+1} \quad (16)$$

with an effective exchange coupling constant, $J_{\text{eff}} \approx t^2/U$.

Bonner and Fisher [8] computed χ_S for a Heisenberg infinite linear chain of $S = \frac{1}{2}$ spins. They obtained a maximum value for χ_S such that

$$\frac{\chi^{\text{max}}}{Ng^2\mu_B^2/J_{\text{eff}}} \approx 0.07346 \quad (17)$$

at a temperature $T_{\text{max}} \approx 1.282J_{\text{eff}}/k_B$. For temperatures $T > T_{\text{max}}$ the Curie–Weiss law is followed with $\theta = J_{\text{eff}}$. According to the Bonner and Fisher approximation,

$$\chi(T = 0) = \frac{g^2\mu_B^2\rho}{2\pi^2J_{\text{eff}}} \approx 0.7\chi_{\text{max}} \quad (18)$$

where ρ is the degree of charge transfer and ρ and J_{eff} are the only parameters. Also,

$$J_{\text{eff}} = \frac{2t^2}{U} \rho \left(1 - \frac{\sin 2\pi\rho}{2\pi\rho} \right) \quad (19)$$

3. In a more general case of a nonregular chain, for which the nearest-neighbor exchange coupling constant changes along the chain, supposed nonregular, the Hamiltonian can be written as:

$$H = -2J \sum_i [\mathbf{S}_{i-1} \cdot \mathbf{S}_i + \alpha \mathbf{S}_i \cdot \mathbf{S}_{i+1}] \quad (20)$$

where $\alpha = 1$ for a regular chain. When $\alpha < 1$, the Heisenberg chain is alternate and the exchange coupling constant between the closest neighbors is $2J$. The exchange coupling constant between the farthest near neighbors (on the other side) is $2\alpha J$.

The computed values for a linear alternate Heisenberg chain of $S = \frac{1}{2}$

spins show a broad maximum [9] for all values of α . It is also shown (for $\alpha < 1$) that the susceptibility decreases exponentially as the temperature goes to zero. Only in the case of the Bonner–Fisher uniform chain ($\alpha = 1$) does the susceptibility tend to a finite value when the temperature goes to zero, in agreement with Eq. (18).

When $\alpha = 0$ (isolated dimmers), the situation is described by [10]

$$\chi = \frac{2Ng^2\mu_B^2}{k_B T} \frac{1}{3 + \exp(-2J/k_B T)} \quad (21)$$

E. Electron Spin Resonance

1. ESR Parameters

The interaction of the electronic spins with an applied magnetic field, H , splits the spin energy levels and the transitions between those levels can be observed. For the particular case of $S = \frac{1}{2}$, the splitting between the two $m_s = \pm \frac{1}{2}$ spin levels gives

$$\Delta E = g\mu_B H \quad (22)$$

Transitions can be induced by applying an oscillating magnetic field perpendicular to the static field, and the resonance condition is

$$h\nu = g\mu_B H \quad (23)$$

The application of the oscillating field satisfying the resonance condition deviates the system from equilibrium and induces transitions between the two states. On the other hand, the relaxation processes lead the system to equilibrium, in agreement with the Bloch equations (for a static field perpendicular to z):

$$\begin{aligned} \frac{dM_x}{dt} &= (\mathbf{M} \times \mathbf{M})_x - \frac{M_x}{T_{2e}} \\ \frac{dM_y}{dt} &= (\mathbf{M} \times \mathbf{M})_y - \frac{M_y}{T_{2e}} \\ \frac{dM_z}{dt} &= (\mathbf{M} \times \mathbf{M})_z - \frac{M_0 - M_z}{T_{1e}} \end{aligned} \quad (24)$$

where T_{1e} is the spin-lattice relaxation time and T_{2e} is the spin-spin or transverse relaxation time.

The ESR technique is very useful in the characterization of organic conductors. Three parameters can be studied: (1) the intensity of the ESR absorption, (2) the g tensor, and (3) the linewidth.

2. Intensity of the ESR Absorption

The Kramers–Kronig relation gives the spin susceptibility as the integrated intensity of the ESR absorption [11]:

$$\chi_s = \frac{2}{\pi H_0} \int_0^\infty \chi''(H) dH \quad (25)$$

$\chi''(H)$ is the imaginary part of the susceptibility, $\text{Im}(\chi_s)$ and is proportional to the microwave absorption. H_0 is the resonance field. The spin susceptibility alone can best be measured by comparing the integrated intensity of the ESR line with a standard sample of known spin susceptibility.

3. The g Tensor

The g tensor [Eq. (10)] depends on the paramagnetic species present, since it essentially depends on the spin environment. In many cases it is possible to obtain structural information, as well as information on spin–spin interactions, through analysis of the g value and anisotropy as a function of temperature.

In compounds where both the donor and the acceptor molecules (or ions) are paramagnetic, two situations may arise: (1) if the interchain interactions are negligible, the ESR spectrum is the superposition of the ESR spectra of each individual species; or (2) if they are weak but there is significant fast spin exchange between the two spin systems, a single spectrum is observed with a g value that is averaged by the contributions to the spin susceptibilities of each chain [12]:

$$g = \frac{g_A \chi_s^A + g_D \chi_s^D}{\chi_s^A + \chi_s^D} \quad (26)$$

In this expression, the subscripts and superscripts A and D refer to the acceptor and donor stacks, respectively.

4. Linewidth

The linewidth (peak to peak), ΔH_{pp} , depends on the relaxation times T_{1e} and T_{2e} . If the line is Lorentzian, the following expression is valid:

$$\Delta H_{pp} = \hbar(g\mu_B T_{2e})^{-1} \quad (27)$$

where T_{2e} is the transverse relaxation time. The spin-lattice relaxation time, T_{1e} , occurs primarily due to interchain scattering events.

In isotropic three-dimensional conventional metals $T_{2e} \approx T_{1e}$ and the linewidth has a temperature dependence which is similar to that of the resistivity [13]. The dominant process leading to the spin-lattice relaxation rate, $1/T_{1e}$, comes from the modulation of spin-orbit interactions by phonons. Elliot [14] has shown that in this case, the ESR linewidth, ΔH_{pp} , is

related to the g shift, Δg , relative to the free electron:

$$\Delta H_{\text{pp}} = \frac{1}{T_{1e}} \approx \frac{(\Delta g)^2}{\tau} \quad (28)$$

However, this relation is not valid for organic conductors.

In one-dimensional organic metals, T_{1e} , which is due to spin-phonon scattering, is the dominant term [15]. The diversity of this parameter among the variety of organic conductors has posed difficulties to the formulation of a consistent theory, but despite the limitations, the study of this parameter has been of great value. The remarkably narrow lines of most one-dimensional conductors have been attributed to a considerable weakening of the efficiency of the spin-orbit-induced relaxation in one-dimensional conductors, due to (1) strong mismatch between the energy of a phonon and the excitation energy of an electron-hole pair, implying that scattering events involving $\Delta q \approx 0$ (forward) is inefficient for the spin reversal; (2) the $\Delta q = 2k_F$ contribution is also inefficient since the spin-orbit operator has no matrix elements between Kramers conjugate states such as $|+k_F, \uparrow\rangle$ and $|-k_F, \downarrow\rangle$. This also implies that the Elliot relation does not hold for one-dimensional conductors. Spin-reversal mechanisms are weakened by dimensional effects. However, the interchain integral, t_\perp , admixes some three-dimensionally to the originally flat Fermi surface specified through the ratio between the intrachain and the interchain scattering times, $\tau_\parallel/\tau_\perp$. Weger et al. [16] suggested taking the deviation from the one-dimensional behavior into account in the spin relaxation mechanism and proposed an expression that relates the linewidth to interchain coupling:

$$\Delta H_{\text{pp}} \sim \frac{(\Delta g)^2}{\tau_\parallel} \frac{\tau_\parallel}{t_\perp} = (\Delta g)^2 t_\perp^{-1} \quad (29)$$

5. Antiferromagnetic Resonance

Antiferromagnetic resonance (AFMR) is a very sensitive technique to probe long-range magnetic order and can be performed in organic conductors if no Se atoms are present [17,18]. The AFMR theory [18,19] is a generalization of ESR when long-range magnetic order is present. The frequencies of the collective excitations of the spins that experience both the external field and internal fields (exchange and anisotropy) depend strongly on the orientation and magnitude of the external field. Figure 1 presents the dependence of the resonance frequencies, for $T = 0$, when the field is applied along the *easy direction* (along which the anisotropy energy is minimum). The relevant parameters are $r = 1 - \chi_\parallel/\chi_\perp$ ($r = 1$ for $T = 0$) and the zero-field resonance frequencies related to the magnetic energies $\hbar\Omega_- = (\mu/\mu_B)\sqrt{2JW_{\text{ei}}}$ and $\hbar\Omega_+ = (\mu/\mu_B)\sqrt{2JW_{\text{en}}}$, where μ is the local

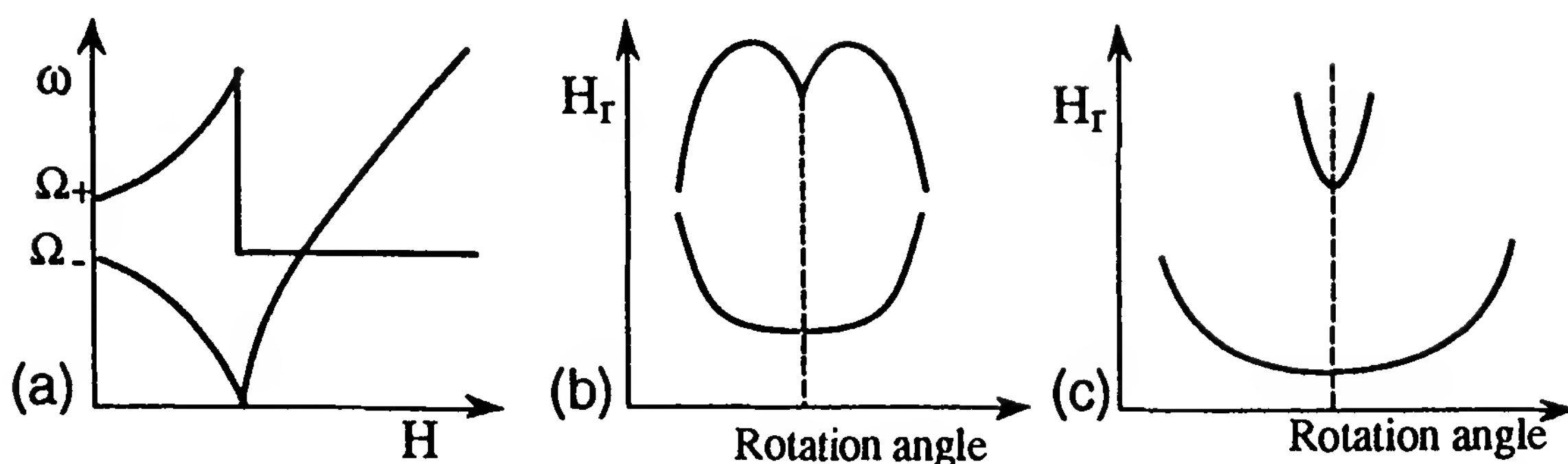


Figure 1 (a) Frequency versus field when H is applied along the easy axis. (b) Rotation patterns in the easy-intermediate plane. (c) Rotation patterns in the easy-hard plane. (From Ref. 18.)

magnetic moment, μ_B the Bohr magneton, J the exchange energy, and W_{ei} and W_{en} the difference of anisotropy energies between the easy and intermediate, and between the easy and hard directions, respectively. In a conventional spectrometer the field can be scanned to find the resonances (for a fixed frequency). When the single-crystal sample is rotated around a given axis, rotation patterns such as those shown in the figure can give the resonance fields as a function of the rotation angle. From the fitting to experimental data the characteristics of the anisotropy and the position of the magnetic axis can be obtained.

F. Nuclear Magnetic Resonance

NMR has proved to be one of the most valuable techniques to obtain information on electron distribution and dynamics [3], as well as on dimensionality and on the role of electron-electron interactions, in organic conductors. Since they contain atoms such as C, H, N, S, and Se, having isotopes with nuclear spin, they have nuclear magnetic moments of the form

$$\mu_n = \gamma_n \hbar \mathbf{I} \quad (30)$$

where \mathbf{I} is the nuclear spin and γ_n is the nuclear gyromagnetic ratio.

To decide which nuclear spins are responsible for observed effects, it is sometimes useful to perform experiments on samples selectively isotopically enriched. The interaction of the nuclear momenta with an applied magnetic field splits the nuclear spin energy levels, and the transitions between those levels can be observed and studied. For the particular case of $I = \frac{1}{2}$, as in proton NMR, the splitting between the two $m_I = \pm \frac{1}{2}$ nuclear

spin levels is

$$\hbar\omega_n = \gamma_n\hbar H \quad (31)$$

ω_n being the nuclear Larmor frequency. At thermodynamic equilibrium there is a small difference in the population of the two sublevels and consequent magnetization, M_0 .

NMR is a very powerful technique either to measure the chemical and Knight shifts or to measure relaxation times due to many phenomena, including, for example, rotations of methyl or other groups in the materials. The recent high-resolution NMR techniques have also already been applied to the study of organic conductors [20]. However, the NMR experimental parameters that have been most studied and which are of great value to an understanding of many aspects of the quasi-one-dimensional organic conductors are the Knight shift, K , and the spin-lattice relaxation rate, T_1^{-1} , which result from the hyperfine interaction, $a\mathbf{S}\cdot\mathbf{I}$, between the nuclear spins and the electron spins. This hyperfine interaction has two main components: the *contact interaction* and the *dipolar interaction*.

The *scalar contact interaction* between one nucleus, n , of spin \mathbf{I} , and electrons i , of spin \mathbf{S}_i is given by the Hamiltonian:

$$H_c = \frac{8\pi}{3} \hbar\gamma_n g\mu_B \sum_i \left[I_z S_{iz} + \frac{1}{2} (I_+ S_{i-} + I_- S_{i+}) \right] \delta(r) \quad (32)$$

where $g\mu_B$ is the electron magnetic moment, $\hbar\gamma_n$ the nuclear moment, and $\delta(r)$ the Dirac δ function for $r = r_e - r_n$.

In an applied magnetic field the electrons gain a magnetic polarization, leading to an effective additional field at the nucleus such that the applied field for resonance, H_0 , is shifted to lower fields than in diamagnetic materials, by the amount

$$K = \frac{\Delta H}{H_0} = \frac{8\pi}{3} \langle |u_k(0)|^2 \rangle_{E_F} \chi_S \quad (33)$$

where $\langle |u_k(0)|^2 \rangle_{E_F}$ is determined by averaging the wavefunctions, $u_k(0)$, over the Fermi surface, and χ_S is the static spin susceptibility.

The spin-lattice relaxation time is found by several techniques, which consist basically of applying an oscillating field, H_1 , perpendicular to the static field H_0 with a duration shorter than T_1 , to obtain a maximum signal amplitude. The measurement is made by preparing the system in a state $M_x = M_y = 0$, $M_z \neq M_0$ at a time $t = 0$ and measuring the decay to the equilibrium state M_0 . According to the Bloch equations the transverse magnetization stays zero and M_z decays exponentially as $M_z(t) = M_0(1 - e^{-t/T_1})$.

The spin-lattice relaxation rate, T_1^{-1} , is due to modulation of the hyperfine interaction by the electronic spin motion of the conduction electrons and therefore probes the electron dynamics. The $(I_+S_{i-} + I_-S_{i+})$ term in H_c induces transitions of the nucleus, giving the *Korringa relation* [21] for a noninteracting electron gas:

$$T_1^{-1} = \frac{4\pi k_B}{\hbar} \left(\frac{\hbar \gamma_n}{g\mu_B} \right)^2 a^2 \chi_S^2 T \quad (34)$$

where a is the hyperfine field in gauss. For conventional metals, with a temperature-independent Pauli susceptibility, this implies that

$$T_1^{-1} \propto T \quad (35)$$

For interacting electrons, χ_S is enhanced, as discussed above, and also K and T_1^{-1} . It has been shown [22] that T_1^{-1} changes proportionally to

$$\eta(\alpha) = \left\{ \frac{(1 - \alpha)^2}{[1 - \alpha F(x)]^2} \right\}_F$$

where α is given by Eq. (15), $F(x = q/2k_F)$ is the Lindhard function and the average is taken over the Fermi surface. The Korringa relation should then be modified to give

$$T_1^{-1} = \frac{4\pi k_B}{\hbar} \left(\frac{\hbar \gamma_n}{g\mu_B} \right)^2 a^2 \chi_S^2 T \eta(\alpha) \quad (36)$$

In organic metals, the nature of the molecular π orbitals that form the conduction bands leads to a *dipolar* hyperfine interaction that may be nonnegligible when compared with the contact contribution discussed above [23]. The various terms in the dipolar interaction modify K and T_1^{-1} in different ways. The dipolar component [3] can be written as a sum of terms, some of which produce anisotropic Knight shifts (or line broadening in powder samples) and contribute to the spin-lattice relaxation rate.

Another complication arises from the shape of the quasi-one-dimensional Fermi surface, which is typical of most organic conductors. This fact implies that important spin density fluctuations (scattering) can occur with wavevectors $q \approx 0$ (forward scattering) and $q = 2k_F$ (backward scattering).

In addition to the *intrachain* contact, $T_{1c\parallel}^{-1}$, and dipolar, $T_{1d\parallel}^{-1}$, terms both for $q \approx 0$ and $q = 2k_F$, considered so far, we should include the *contact* and *dipolar interchain* terms $T_{1c\perp}^{-1}$ and $T_{1d\perp}^{-1}$, especially in the case of two chain compounds. We should then write the spin-lattice relaxation rate as a sum of all these terms [24]:

$$T_1^{-1} = T_{1c\parallel}^{-1} + T_{1d\parallel}^{-1} + T_{1c\perp}^{-1} + T_{1d\perp}^{-1} + \text{other terms} \quad (37)$$

In this work we will be specially concerned with intra- and interchain contact and dipolar interactions and will ignore the above-mentioned “other terms,” despite the fact that they may be relevant in particular cases. We should also make clear that the NMR technique gives the total spin-lattice relaxation rate over all q vectors. Therefore, it will be necessary to make a thorough analysis of the data to extract the relevant components. On the other hand, a complete theory of the spin-lattice relaxation rate in organic conductors is still lacking. In our description we try to point out some of the main features, the temperature and field dependence.

The intrachain contact term, $T_{1c\parallel}^{-1}$, is usually the most important and is related to the one-dimensional regime (i.e., conduction along a stack). The electrons traveling along the chain experience two kinds of scattering, $q \approx 0$ and $q = 2k_F$.

The $q \approx 0$ term, of long wavelength, is responsible for spin diffusion along the chain and is of the form

$$T_{1c\parallel}^{-1}|_{q \approx 0} \sim a^2 \chi_S(T) T (D \omega_e)^{-1/2} \quad (38)$$

where $\chi_S(T)$ is the spin susceptibility (of the chain), D the diffusion constant of the spin excitations, and ω_e the electronic Larmor frequency. This term is field dependent through the relation

$$\frac{d(T_1^{-1}T)}{dH_0^{-1/2}} \propto \frac{\chi_S(T)}{\sqrt{D}} \quad (39)$$

For $U \gg 4t_{\parallel}$ in the Hubbard model, the diffusion constant becomes $D = 2.3J_{\text{eff}}/\hbar$.

The $q = 2k_F$ term is nondiffusive and is given by

$$T_{1c\parallel}^{-1}|_{q=2k_F} \sim a^2 \chi_S^2(T) T \quad (40)$$

similar to the Korringa law, but it may be enhanced by the factor $\eta(\alpha)$, which may even be a function of temperature. The short-wavelength spin excitations ($q = 2k_F$) would give rise to a coherent propagation of the spin excitations and to a field-independent spin-lattice relaxation rate.

The intrachain dipolar term, $T_{1d\parallel}^{-1}$, which in most cases is assumed to contribute $\approx 20\%$ to the total spin-lattice relaxation rate, has two components as well. $T_{1d\parallel}^{-1}|_{q \approx 0}$ has an expression similar to (38) but with ω_n instead of ω_e . It is also diffusive in nature and it will enhance T_1^{-1} with respect to the Korringa law since χ_S is enhanced. $T_{1d\parallel}^{-1}|_{q=2k_F}$ is nondiffusive and field independent. Since the time scale is ω_n^{-1} , this contribution is usually saturated for the fields commonly used, and it is normally ignored.

The interchain contact term, $T_{1c\perp}^{-1}$, can be observed at small enough fields (small ω_e) for which the corresponding intrachain component is saturated. It results from the small probability that the electron may spend

some time in the side chain, and it is therefore important for measuring the escape time, τ_{\perp} . The $q \approx 0$ term is given by

$$T_{1c\perp}^{-1} \propto T\chi_S(T) \sqrt{\frac{\tau_{\perp}}{D}} g(\omega_e) \quad (41)$$

with

$$g(\omega_e) = \sqrt{\frac{1 + \sqrt{1 + \omega_e^2 \tau_{\perp}^2}}{2(1 + \omega_e^2 \tau_{\perp}^2)}} \quad (42)$$

The $q = 2k_F$ contribution is usually assumed to be negligible since the hopping rate $1/\tau_{\perp}$ is much smaller than the Fermi energy.

The measurement of $T_{1c\perp}^{-1}$ is important to probe the three-dimensional regime at low fields and to compute τ_{\perp} . In fact, according to the field dependence of $g(\omega_e)$ there exists a crossover value of the field (given through ω_e) at $\omega_e \tau_{\perp} \approx 1$ between the high-field one-dimensional regime, for which expression (39), applies (i.e., $T_1^{-1} \propto H_0^{-1/2}$) and a low-field three-dimensional regime that is field independent.

The interchain dipolar term may be particularly important in the case of two magnetic chain compounds. The $q \approx 0$ term is diffusive,

$$T_{1d\perp}^{-1}|_{q=0} \propto T\chi_S(T)(D\omega_N)^{-1/2} \quad (43)$$

and is typically due to weakly interacting spins from the two chains. The $2k_F$ term is

$$T_{1d\perp}^{-1}|_{q=2k_F} \propto T\chi_S(T) \quad (44)$$

III. INSTABILITIES AND PHASE TRANSITIONS

There are four different potential instabilities in quasi-one-dimensional conductors at low temperature: the charge density wave, spin density wave, spin-Peierls transition, and superconducting transitions: ST (superconductivity triplet) and SS (superconductivity singlet). Since superconductivity is treated in another chapter, we ignore it in this contribution.

A. Charge Density Wave and the Peierls Transition

Peierls pointed out in 1955 that a one-dimensional metallic chain is not stable at $T = 0$ K, against a periodic lattice distortion of wave vector $2k_F$, as the result of electron-phonon coupling, opening a gap 2Δ at the Fermi level. From this fact a collective electronic state results called a charge density wave (CDW). In the limit where U , the intrasite Coulomb repulsion, is infinite, since a given k state cannot be occupied by more than one

electron, the conduction band will be filled from $-2k_F$ up to $+2k_F$ (if we still define k_F for noninteracting electrons). Similarly to the $2k_F$ Peierls instability, the system is also unstable at $T = 0$ K against a periodic lattice distortion which now occurs at the wave vector $4k_F$. In a half-filled band, the big U limit leads to a Mott–Hubbard insulator.

In real systems we have intermediate situations, depending on the value of U . The one-dimensional system will present CDW instabilities at the $2k_F$ and/or the $4k_F$ wave vector. The interchain interactions lead to Peierls metal–insulator transitions at $T > 0$.

In the case of the $2k_F$ Peierls transition, both charge and spin degrees of freedom are frozen and the ground state of a $2k_F$ CDW is nonmagnetic. In this case the spin susceptibility is expected, in first approximation, to decay exponentially to zero when $T \rightarrow 0$ K, with an activation energy which is similar to that of the conductivity. In a $4k_F$ CDW transition the spin degrees of freedom are not directly affected, since there is only loss of the charge degrees of freedom. The signature of a Peierls transition are the one-dimensional precursor effects, which can be observed by x-ray diffuse scattering, above the metal–insulator transition temperature.

B. Spin Density Wave

The spin density wave (SDW) is a $2k_F$ instability due to spin-spin interactions and the ground state has no lattice distortion. χ_S is typical of an antiferromagnetic ground state and therefore anisotropic below the transition temperature, T_c . Antiferromagnetic resonance (AFMR) may be a good technique to characterize this transition. A particular characteristic is that the T_1^{-1} NMR relaxation rate diverges at T_c .

C. Spin-Peierls Transition

The spin-Peierls $2k_F$ instability usually occurs when U is big and is originated by spin-phonon interactions. As in the CDW case, in real systems, the interchain Coulomb interactions couple the SDW and may lead to phase transitions at $T > 0$.

In solids with strong localization of the charge carriers, there are no charge degrees of freedom, but there will be spin degrees of freedom. In this class we should include systems that underwent a metal–insulator transition for a $4k_F$ CDW state. The ground states of these systems are usually $2k_F$ spin density wave or spin-Peierls states.

D. Summary of the One-Dimensional Instabilities

In Table 1 we summarize the typical behavior of one-dimensional instabilities in organic conductors.

Table 1 Typical Behavior of One-Dimensional Instabilities in Organic Conductors

	Peierls (CDW)	SDW	Spin-Peierls (S-P)
Wave vector	$2k_F$	$2k_F$	$2k_F$
Lattice distortion	Yes	No	Yes
Interaction	Electron–phonon	Spin–spin	Spin–phonon
Ground state	Nonmagnetic	Antiferromagnetic	Nonmagnetic
Susceptibility	$T > T_P$: Pauli (enh.) $T < T_P$: activated	$T > T_c$: Pauli (enh.) or Bonner–Fisher $T < T_c$: anisotropic ($\chi > 0$)	$T > T_{SP}$: Pauli (enh.) or Bonner–Fisher $T < T_{SP}$: activated
ESR	$\Delta H_{pp(max)}$ at T_P	ESR disappears at T_c , ΔH_{pp} diverges at T_c	Similar to Peierls
T_1^{-1} (NMR)	$T > T_P$: \approx Korringa, $T < T_P$: activated	Diverges at T_c	Similar to Peierls
Examples (discussed below)	TTF-TCNQ (Per) ₂ [M(mnt) ₂], M = Cu, Co	(TMTSF) ₂ PF ₆	(BCPTTF) ₂ PF ₆ (BCPTTF) ₂ AsF ₆ MEM-TCNQ

Note: The $4k_F$ CDW (big U) is a Mott–Hubbard insulator in a half-filled band with magnetic disorder but no anomaly in χ_s and leads to a SDW or S-P ground state. There are competitions between these instabilities. In the metallic regime, if there are both charge and spin degrees of freedom, the $2k_F$ CDW competes with SDW, $4k_F$ CDW, SI, ST. The SDW and S-P compete between themselves. If there are only spin degrees of freedom, the SDW will compete with S-P. In the Peierls and spin-Peierls transitions the electrons become paired in a singlet state. The hyperfine interaction is annihilated, and a strong deviation from the Korringa-type law is shown through the fall of T_1^{-1} at the transition temperature.

IV. ANALYSIS OF EXPERIMENTAL DATA

A. Introduction

We will now analyze relevant experimental data, without being exhaustive, but trying to give typical examples that have been well characterized. We focus on a particular family of organic conductors, which has been one of our main concerns and exhibits a variety of magnetic phenomena that we believe to be unique.

B. Spin Susceptibility

None of the approaches described above is completely realistic for quasi-one-dimensional organic conductors since there is always some Coulomb repulsion between them, which does not fall in any of the limits considered above. The U and V terms are essentially molecular, and usually $U > V > 0$, with $U > 1$ eV, which is on the order of magnitude of the bandwidth,

$4t$ [25]. The bandwidth of one-dimensional molecular conductors [26] is typically on the order of 0.2 to 1 eV, although it can be larger, as in the case of (fluoranthene)₂(PF₆), for which $W \approx 2$ eV while U is on the order of 1 to 2 eV and $V \leq U/2$. Therefore, most one-dimensional molecular conductors appear to be in a situation that is closer to the strong-coupling limit ($U, V \gg t$). Despite the limitations of the above-mentioned models (strong coupling and weak coupling), the susceptibility has been analyzed satisfactorily within one or the other of these approximations. However, such models can only be used within restricted temperature limits and the agreement with experiment is only qualitative or semiquantitative.

In the metallic regime, the susceptibility has usually been analyzed within the limit of weak correlations [Eq. (15)] (Pauli enhanced).

However, the applicability of this approximation poses some problems since, in many cases, $U \geq 4t$. Another problem in most of these materials is the temperature dependence of the susceptibility, which deviates considerably from the Pauli temperature-independent paramagnetism. In general, the susceptibility decreases with temperature (on the order of 20% between 300 and 200 K).

Many explanations have been given to account for the departures from the expected enhanced-Pauli χ_S in the metallic regime [3]. First, we have to consider if the compound that we are studying has one or two magnetic stacks. If it has two, we should try to separate the contributions from each one. This has been done successfully in a number of cases. The decomposition can be done through the g factor or through the Knight shift. Second, if a chain is metallic, the susceptibility should, in principle, be Pauli-like. If there are localized spins, the behavior should be of Bonner–Fisher type.

Deviations to the Pauli-like susceptibility have been attributed to several effects:

1. In the one-dimensional fluctuation regime, above the Peierls transition, the $D(E_F)$ will be depressed. χ_S should be proportional to the inverse coherence length, and therefore linear in T . Although there is no good agreement with this model, it is believed that the Peierls pseudogap should be considered as a contributing factor.
2. The thermal expansion coefficient is large in organic conductors compared to conventional metals. Since the overlap integrals depend on lattice parameters, considerable increase in the bandwidth is expected upon cooling, affecting χ_S .
3. If Coulomb interactions are important, χ_S will deviate toward Bonner–Fisher behavior due to exchange interactions.

4. Gutfreund et al. [27] have proposed that strong electron–phonon interactions lead to an enhanced density of states, increasing χ_S .

Below the phase-transition temperatures, the behavior of the susceptibility is as summarized in Table 1 and as discussed further below. In Fig. 2 the magnetic susceptibility with the diamagnetic component χ_D extracted is presented for three typical organic metals.

TTF-TCNQ is a two-conducting (both magnetic) chain compound. In Fig. 2 the total susceptibility is shown. Decomposition into the two components required a study of the g factor weighted by the susceptibilities of the two chains [28] or NMR experiments on isotopically enriched molecules [29].

At 300 K the total susceptibility is reminiscent of the Bonner–Fisher type. The model fits for $J_{\text{eff}} = 1.3t^2/U = 200$ K (for $\rho = 0.59$) (i.e., $U/4t_{\parallel} \approx 2$ if $4t_{\parallel} = 0.4$ eV) [30]. A similar value of $U/4t$ was obtained within the strong correlations limit [31]. NMR data [6] indicate that $U/4t \approx 0.8$ to 1, which is confirmed by the susceptibility at $T \approx 100$ K. The Peierls transitions (which can be globally seen in Fig. 2) show that electron–phonon interactions are important.

(TMTSF)₂PF₆ shows a typical SDW transition as a knee in the susceptibility (powder sample). As expected for a SDW, χ_S does not go to zero as $T \rightarrow 0$. HMTSF-TCNQ is a special case. χ_{Pauli} was calculated from NMR

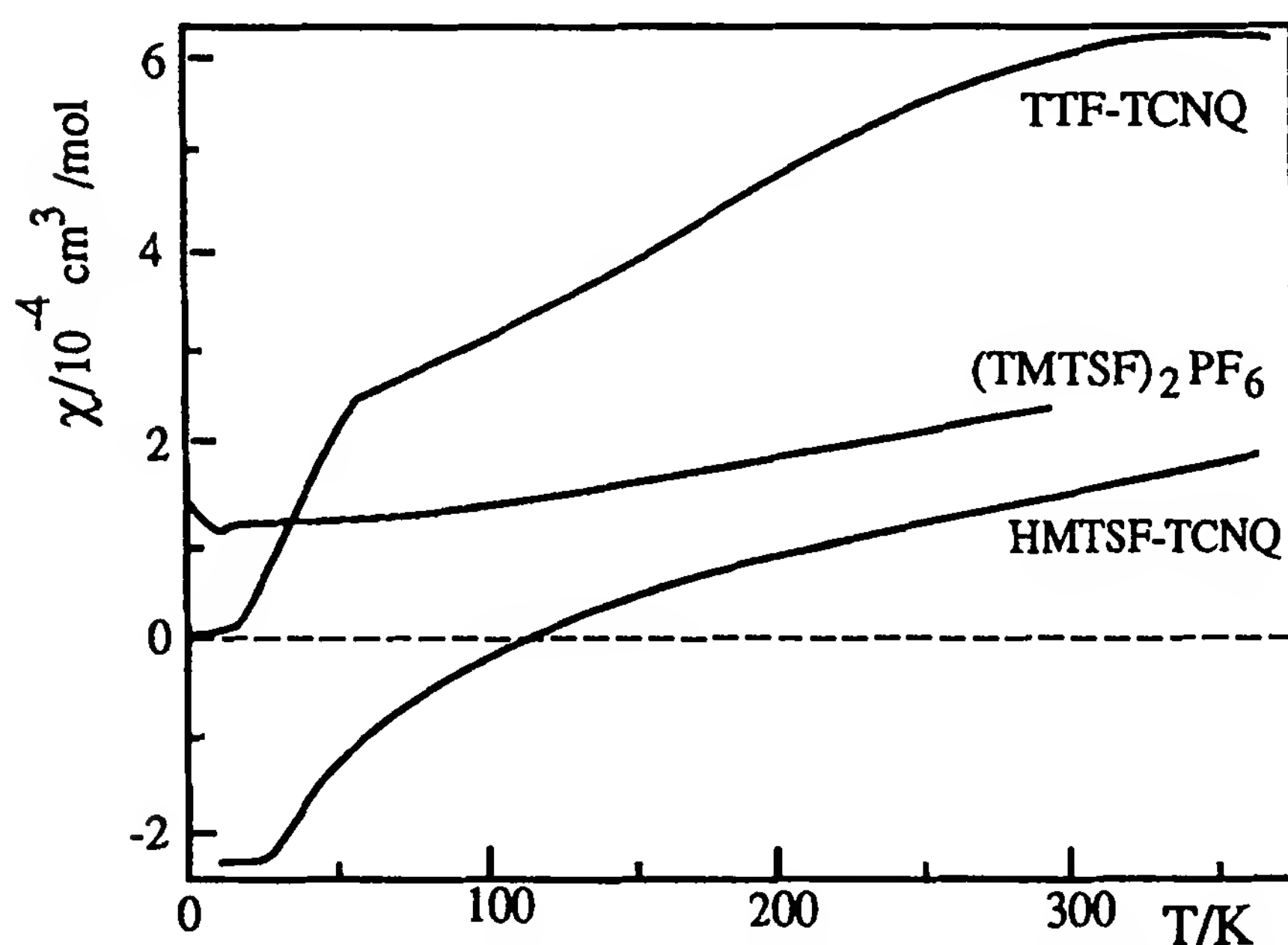


Figure 2 Temperature dependence of the susceptibility (χ_D extracted) for the organic metals TTF-TCNQ, (TMTSF)₂PF₆ (powder), and HMTSF-TCNQ. (From Ref. 3.)

data and the negative susceptibility below 100 K is attributed to a Landau–Peierls diamagnetism. This temperature is taken as a crossover temperature, T_x , where the dimensionality goes from one to two or three dimensions, due to strong interchain coupling. At 24 K there is a transition (Peierls ordering) suggested by x-ray diffuse scattering results. However, despite much study, the behavior of the susceptibility of this material is not yet clear.

The Landau term referred to above depends on the cyclotron effective mass m^* and is given by $\chi_L = -\frac{1}{3}\chi_{\text{Pauli}}(m/m^*)$. It is usually ignored, in quasi-one-dimensional systems, where the interchain motion is accomplished by hopping. In materials that exhibit progressive localization, the susceptibility has been interpreted both within the weak and strong limits. Materials with strong localization of the charge carriers have been analyzed in the limit of strong correlations. Both linear regular and alternate Heisenberg chain models have been used. For example, in the case of the (TMTTF)₂X series, where the susceptibility is similar to that of the analog TMTSF family (within a factor of 2, higher for the first series), the susceptibility has been analyzed within the weak correlation limit, and a value of $\chi/\chi_0 \approx 4$ was obtained [32], which according to Eq. (15) gives $U/4t \approx 2.5$. However, it should be noted that the value of $U/4t$ for the TMTSF series is ≤ 1 [33,34]. The behavior of other materials of this class, such as (NMP)(TCNQ) and Qn(TCNQ)₂, was interpreted within the limit of strong correlations [31] with $U/4t \approx 2$.

Some materials are very sensitive to disorder [3]. In general, the low-temperature susceptibility follows $\chi \propto T^{-\alpha}$ ($\alpha \approx 0.6$ to 0.9). (NMP)(TCNQ) and Qn(TCNQ)₂ are examples of this effect, the disorder being intrinsic, attributed to the asymmetry of the cation. (HMTSF)(TNAP) has a similar behavior at low temperature, the disorder being attributed to the TNAP molecule. In (TTT)₂I_{3+ δ} the disorder results from nonstoichiometry. Similar effects have been obtained when disorder is induced by irradiation [35]. It should be noted that the behavior of the susceptibility due to disorder is distinct from that of paramagnetic impurities. The susceptibility is usually smaller for selenium compounds. HMTSF-TCNQ suggests practically no enhancement due to correlations.

C. ESR

ESR has been used extensively in the study of one-dimensional conductors [36], which usually exhibit narrow ESR signals often at room temperature. The temperature dependence of the linewidth is very diversified and there is no unified theory to explain it. The narrowness of the ESR lines in organic conductors is attributed to low dimensionality, which reduces the

spin-orbit coupling. In fact, in a strictly one-dimensional conductor, the only diffusion process possible is the one with a change in wave vector $\Delta q \approx 0$. In this case, the phonon energies are much different from the energies which are necessary to create or annihilate electron–hole pairs, making the $\Delta q \approx 0$ diffusion probability very small.

The linewidth, ΔH_{pp} , should follow the temperature dependence of the resistivity, and therefore decrease at low T in the metallic regime. For TTF-TCNQ, ΔH_{pp} increases by factor of 3 between 300 and 60 K, but TTF-TCNQ is a special case since there are two chains each with paramagnetic species. ΔH_{pp} and t_1^{-1} derived from NMR in TTF-TCNQ behave similarly in the conducting region. The drop in ΔH_{pp} observed in the Peierls state ($T < 54$ K) is due to the vanishing of the density of states, $D(E_F)$, which is required for electron scattering.

HMTSF-TCNQ, which is believed to have strong coupling between chains, does not show ESR signal at room temperature [37]. The linewidth is presumably on the order of 4000 Oe. On the contrary, TMTSF-DMTCNQ, a Se compound with a narrow line (≈ 70 Oe at 300 K), has been taken as evidence of weak interchain coupling [38].

The ESR properties of single-chain or pseudo-single-chain compounds, such as the $(\text{TMTSF})_2\text{X}$ and $\text{Qn}(\text{TCNQ})_2$, are still a matter of challenge. In particular, in $(\text{TMTSF})_2\text{PF}_6$ and related compounds [39], ΔH_{pp} decreases steadily toward low temperature, while the transversal conductivity, σ_\perp , increases significantly [40]. It has been suggested that the spin relaxation of these compounds may be influenced by the development of the superconducting one-dimensional divergence at low temperature [4].

In nonsuperconducting single-chain compounds, such as $\text{Qn}(\text{TCNQ})_2$, the strong one-dimensionality could also favor the establishment of a one-dimensional pseudogap (Peierls like) at high temperature with a consequent reduction of the density of states. Antiferromagnetic resonance (AFMR) experiments have been reported for several organic conductors [18] [e.g., $(\text{BEDT-TTF})_2\text{ICl}_2$] which present an antiferromagnetic ground state below 20 K well as the AuCl_2 analog.

D. NMR

NMR relaxation experiments have been performed in many organic conductors and have usually been interpreted according to the mechanisms described above. Expression (39), for example, has been used for TTF-TCNQ(D_4). T_1^{-1} in $(\text{TMTTF})_2\text{PF}_6$ [41] and $\text{TTF}[\text{Ni}(\text{dmit})_2]_2$ [42] behave as one-dimensional conductors with deviations to Korringa law (Korringa law: $T_1^{-1} \propto T$).

E. Effects of the One-Dimensional Instabilities on the Magnetic Properties

The typical effects of the one-dimensional instabilities and transitions on the magnetic, ESR, and NMR properties have been summarized in Table 1. Before globally analyzing the experimental data of a particular family of organic conductors in Section IV.F we will refer to a recent reexamination of the spin-Peierls transition reported by Pouget et al. [43]. The spin-Peierls transition is driven by one-dimensional antiferromagnetic fluctuations which couple to the lattice through spin-phonon interactions and is very similar to the Peierls transition in the localized spins limit. The authors conclude that there are two types of spin-Peierls transitions. In systems such as MEM-(TCNQ)₂, the spin-Peierls transition is unusual—there is evidence of tridimensional critical effects that do not affect the Bonner–Fisher behavior of the susceptibility. On the other hand, the spin-Peierls transitions observed in (BCPTTF)₂PF₆ and (BCPTTF)₂AsF₆ (Fig. 3) are more typical of a one-dimensional spin-Peierls instability—the susceptibility follows the Bonner–Fisher law below 300 K, and one-dimensional antiferromagnetic correlations appear at $T \approx J$. At T_F , one-dimensional structural fluctuations begin to be observed by x-ray scattering, and due to spin–phonon coupling, a local spin pairing deviates the susceptibility from the Bonner–Fisher law. The one-dimensional structural fluctuations become progressively three-dimensional, and lattice doubling takes place below T_{SP} when the susceptibility drops.

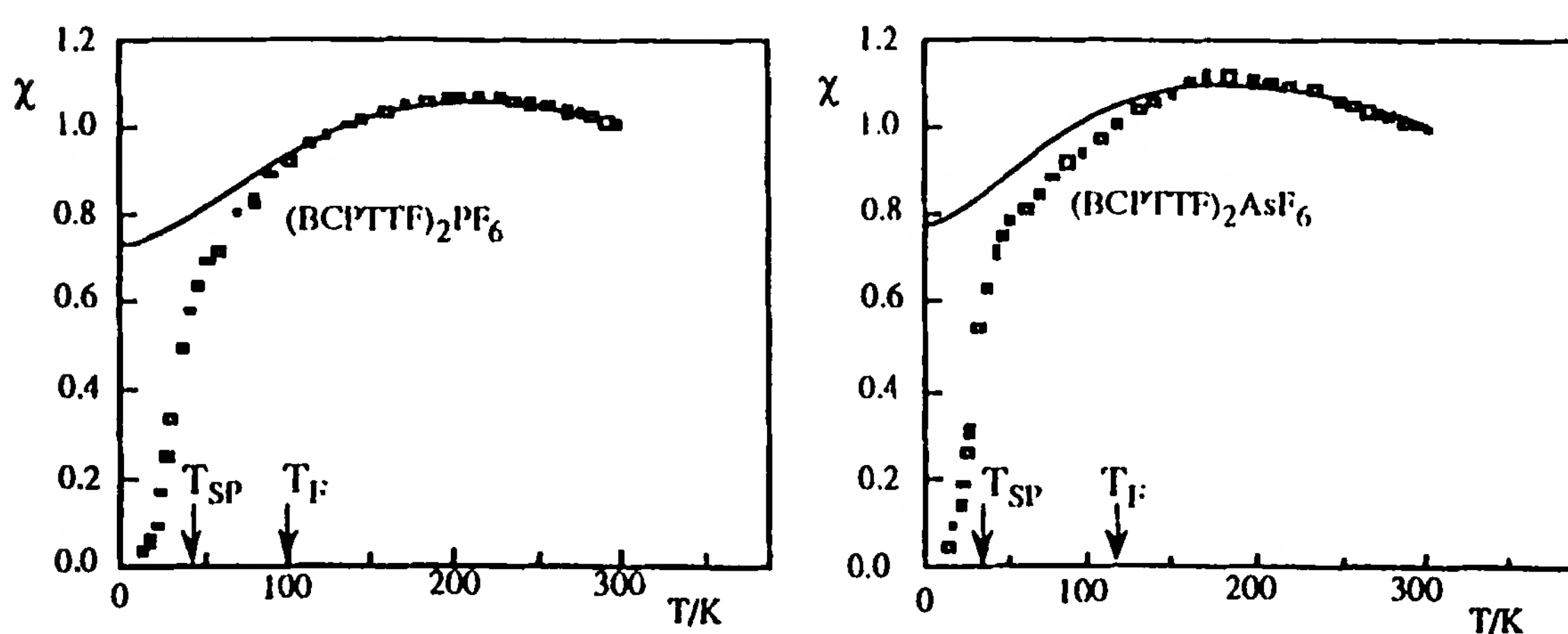


Figure 3 Temperature dependence of the susceptibility, measured by the ESR intensity, of (BCPTTF)₂PF₆ and (BCPTTF)₂AsF₆, normalized at room temperature. The solid lines are fittings to a Bonner–Fisher law. (From Ref. 43.)

F. The Unique (Perylene)₂ [M(mnt)₂] Family

This particular family of organic conductors provides the unique feature of combining a conducting chain (the perylene stack) with a magnetic or nonmagnetic chain, depending on the metal, M, of the bismaleonitriledithiolate chain, [M(mnt)₂], where "mnt" is an abbreviation for maleonitriledithiolate, a common name for the ligand *cis*-(2,3-dimercapto-2-butenedinitrile). Some of these compounds appear in two different crystal structures. The α phases are metallic at room temperature and exhibit metal–insulator transitions at low temperatures which are different for each compound. The β phases are semiconductors with a superlattice modulation along the chain direction, without long-range order in the plane perpendicular to the chain axis.

In Fig. 4 we show the molecular structures of [M(mnt)₂] and perylene and the general scheme of the crystal structure of the α phases. The conduction band of the perylene system is a three-quarter-filled band, whereas the dithiolate chains are either Mott–Hubbard insulators or closed shell. The members of this series cover a number of the situations described above.

To better illustrate and understand the variety of magnetic properties presented by this family of organic conductors, we select the most typical

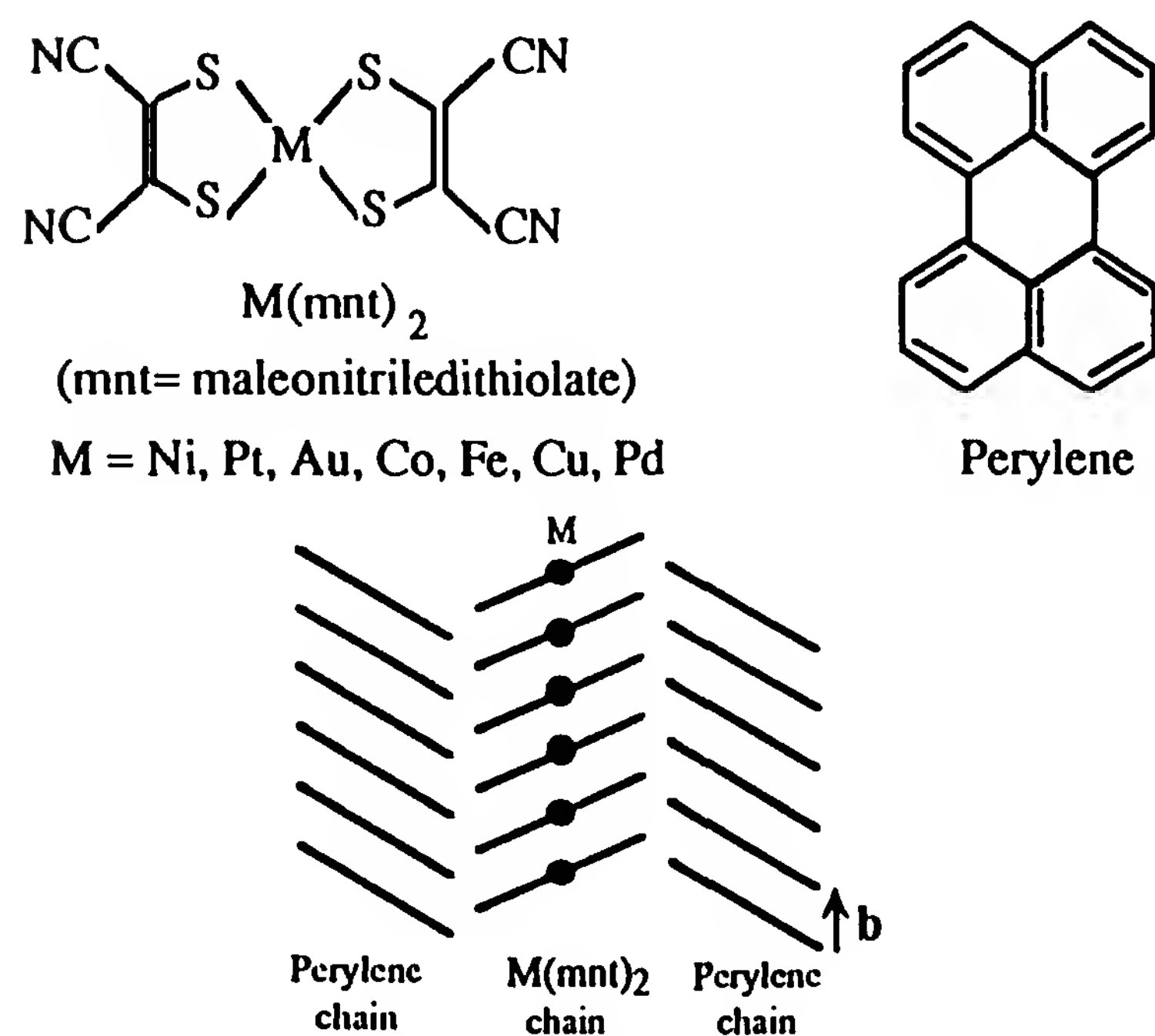


Figure 4 Molecular structures and the general scheme of the crystal structures of (Per)₂[M(mnt)₂] compounds.

compounds of the isostructural α phases and in Table 2 will first review the structural instabilities, since they affect the magnetic properties.

The table indicates the spin of the dithiolate anions specified by the metal atom, M, the temperature of the metal–insulator transition, T_{M-I} , the observed structural instability signatures, and types of transitions occurring at T_{M-I} . It should be noted that due to the crystal structure and band filling (three-quarters) of the conducting perylene chain as well as the insulating character (Mott–Hubbard insulator or closed shell) of the dithiolate chains, the structural instabilities occurring at $b^*/4$ (tetramerization in the perylene chain) correspond to a wave vector $2k_F^P$, the superscript P indicating that it corresponds to the perylene chain. Similarly, the structural instabilities at $b^*/2$ (dimerization in the dithiolate chain) correspond to a wave vector $4k_F^D \equiv 2k_F^D$, the D superscript indicating that it is associated with the dithiolate chain.

Table 2 Structural Instabilities in α -Per₂[M(mnt)]₂; M = Co, Ni, Cu, Pd, Pt, Au

Co(3d ⁶) (<i>S</i> = 0) <i>Structural instabilities:</i> 2 <i>k</i> _F ^P CDW <i>Transitions:</i> Peierls on Per chain	<i>T</i> _{M-I} = 73 K	Ni(3d ⁷) (<i>S</i> = ½) <i>Structural instabilities:</i> 2 <i>k</i> _F ^P CDW 2 <i>k</i> _F ^D “Spin-Peierls” <i>Transitions:</i> Peierls on Per chain “Spin-Peierls” on dithiolate chain	<i>T</i> _{M-I} = 25 K
Cu(3d ⁸) (<i>S</i> = 0) <i>Structural instabilities:</i> 2 <i>k</i> _F ^P CDW <i>Transitions:</i> Peierls on Per chain	<i>T</i> _{M-I} = 32 K	Pd(4d ⁷) (<i>S</i> = ½) <i>Structural instabilities:</i> 2 <i>k</i> _F ^D “Spin-Peierls” <i>Transitions:</i> Peierls on Per chain “Spin-Peierls” on dithiolate chain	<i>T</i> _{M-I} = 28 K
Au(5d ⁸) (<i>S</i> = 0) <i>Structural instabilities:</i> <i>Transitions:</i> Peierls on Per chain	<i>T</i> _{M-I} = 12 K	Pt(5d ⁷) (<i>S</i> = ½) <i>Structural instabilities:</i> 2 <i>k</i> _F ^D “Spin-Peierls” <i>Transitions:</i> Peierls on Per chain? “Spin-Peierls” on dithiolate chain?	<i>T</i> _{M-I} = 8 K

Note: In the “spin-Peierls” transitions on the Ni, Pt, the driving forces seem to be electron–phonon interactions and not spin–phonon, since the field dependence of the transition temperatures are of Peierls type and not spin-Peierls.

1. $M = \text{Co, Au, Cu}$

In the α compounds with $M = \text{Co, Au, Cu}$ [44], the bismaleonitriledithiolate chains are nonmagnetic and the susceptibilities are Pauli-like with enhancement [expression (15)] above the Peierls transitions, occurring at T_{M-I} . Figure 5 shows the temperature dependence of the susceptibility for these compounds. It should be mentioned that the Co analog has a higher susceptibility at high temperatures since the bandwidth is $W = 0.5$ eV, and therefore smaller than the bandwidths of the Au and Cu compounds, which are $W = 0.6$ eV.

Below T_{M-I} , the susceptibility decreases exponentially. As discussed above, this behavior is typical of Peierls transitions. The single ESR lines, which are due to the perylene radical ions, are narrow ($\Delta H_{pp} \approx 0.3$ G for $M = \text{Cu}$) and their intensities follow the spin susceptibility, including the activation energies below T_{M-I} . For $M = \text{Cu}$ and Au, ΔH_{pp} exhibits a maximum near T_{M-I} which is typical of the Peierls transition.

The temperature dependence of the NMR relaxation rate T_1^{-1} for the Au compound (Fig. 9) exhibits a typical behavior of one-dimensional conductors with deviations to the Korringa law ($T_1^{-1} \propto T$) shown by the upward curvature at high temperatures similarly to $(\text{TMTTF})_2\text{PF}_6$ [41] and $\text{TTF}[\text{Ni}(\text{dmit})_2]$ [42]. Since there are no localized spins on the dithiolate chain, the relaxation comes from the hyperfine contact and dipolar interactions, $T_{1c\parallel}^{-1} + T_{1d\parallel}^{-1}$, produced by the spins of the itinerant electrons along the perylene stacks. The enhancement of the relaxation is, however, less important than that shown by the Bechgaard salts [45].

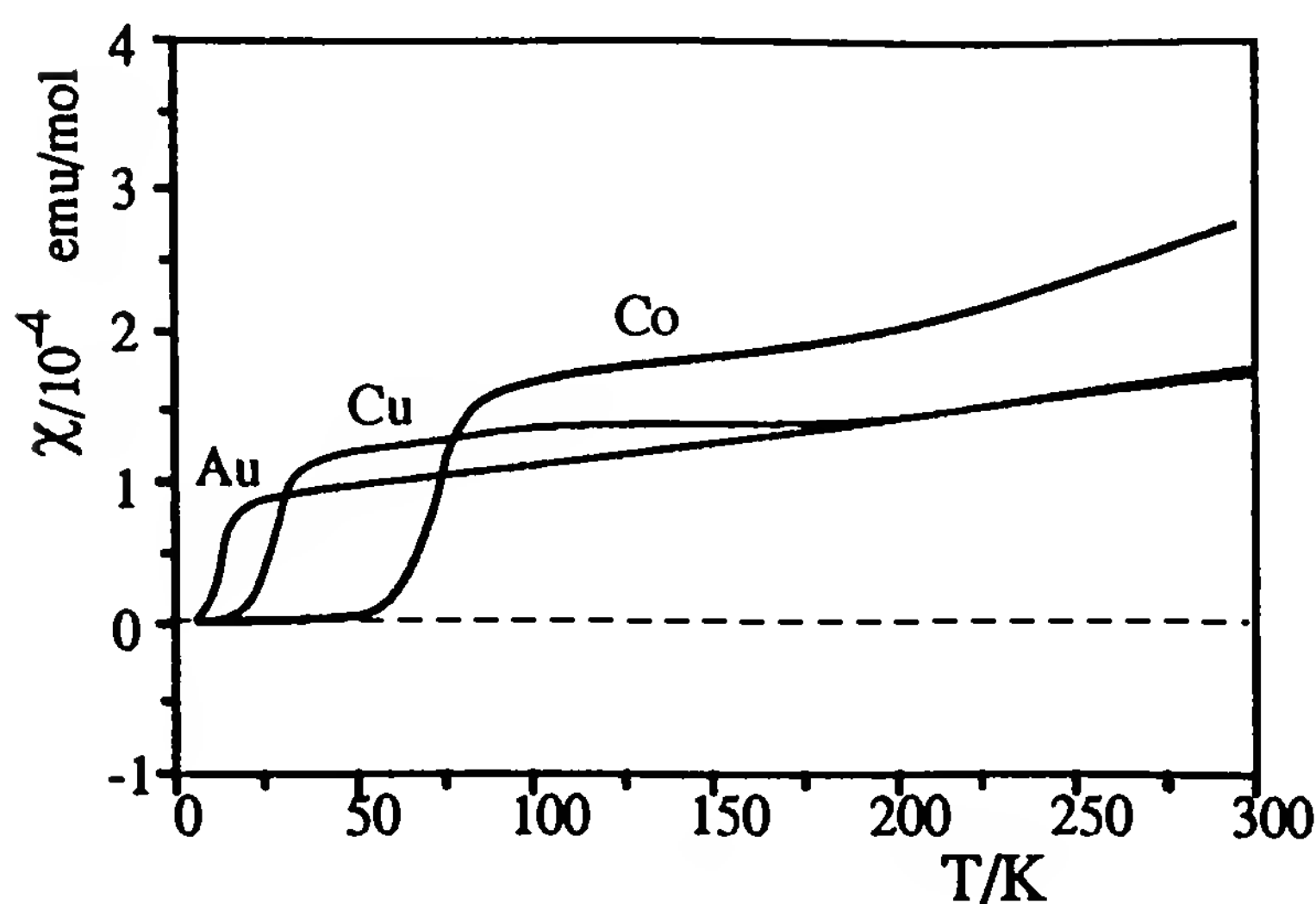


Figure 5 Temperature dependence of the spin susceptibility of $\alpha\text{-Per}_2[\text{M}(\text{mnt})]_2$; $M = \text{Co, Cu, Au}$. (Courtesy of V. Gama, INETI, Sacavem, Portugal.)

2. $M = \text{Ni, Pd, Pt}$

In the $M = \text{Ni, Pd, and Pt}$ compounds, the dithiolate chains have localized spins ($S = \frac{1}{2}$) that interact with the itinerant electrons of the perylene chains in some cases, and at high temperature through a fast spin exchange interaction (Fig. 6). In the high-temperature region, the fast spin exchange interactions between the two spin systems give a single ESR spectrum with a g value that is averaged by the contributions to the spin susceptibilities of each species [Eq. (16)] [46]:

$$g = \frac{g_{\text{Per}}\chi_S^{\text{Per}} + g_{\text{mnt}}\chi_S^{\text{mnt}}}{\chi_S^{\text{Per}} + \chi_S^{\text{mnt}}} \quad (45)$$

The total susceptibility is given by

$$\chi_S(T) = \chi_S^{\text{Per}}(T) + \chi_S^{\text{mnt}}(T) \quad (46)$$

In this expression, Per and mnt refer to perylene and dithiolate, respectively.

For the Pd compound [46], since g_{Pd} is rhombic whereas g_{Per} is isotropic, a rhombic g tensor is the result. The principal values of the averaged tensor are $\bar{g}_i = g_{\text{Per}} + x(g_i - g_{\text{Per}})$, where x is the fraction of interacting Pd spins in the sample and $i = 1, 2, 3$ refer to the principal values of isolated $[\text{Pd}(\text{mnt})_2]^-$ species. The combined analysis of the ESR powder spectra (with each of the three g_i values) and the static susceptibility made possible the separation of the contributions to χ_{Per} and χ_{Pd} (Fig. 7). Since all these compounds are isostructural, the spin susceptibility χ_{Per} was considered to be the same.

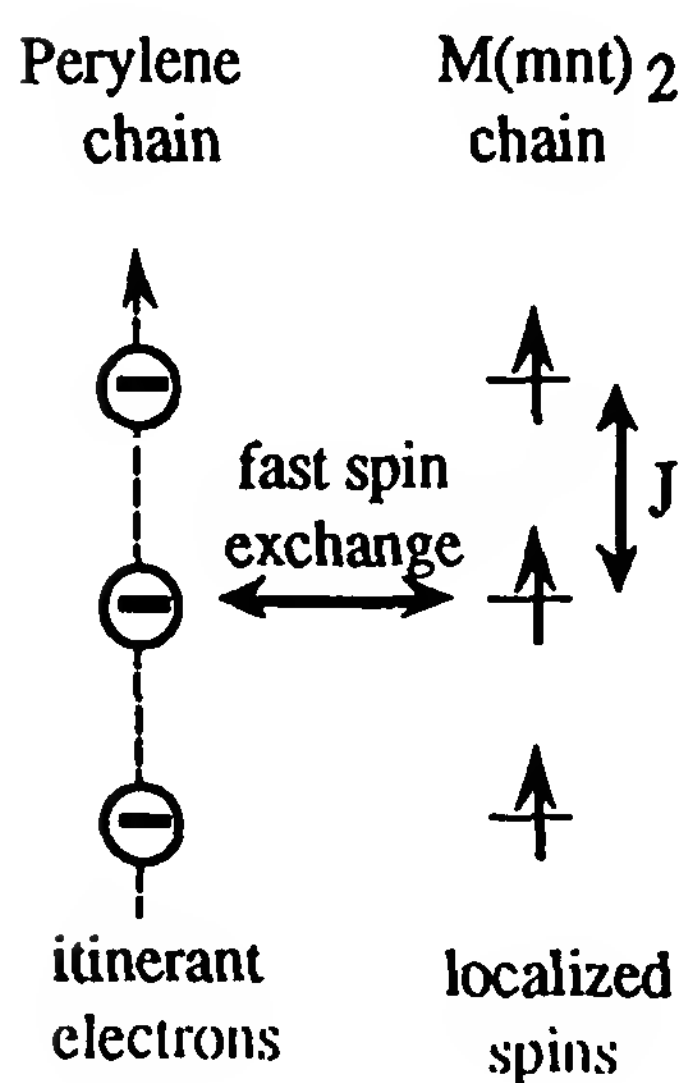


Figure 6 Schematic representation of the interactions exhibited by the $\alpha\text{-Per}_2[\text{M}(\text{mnt})_2]$ compounds.

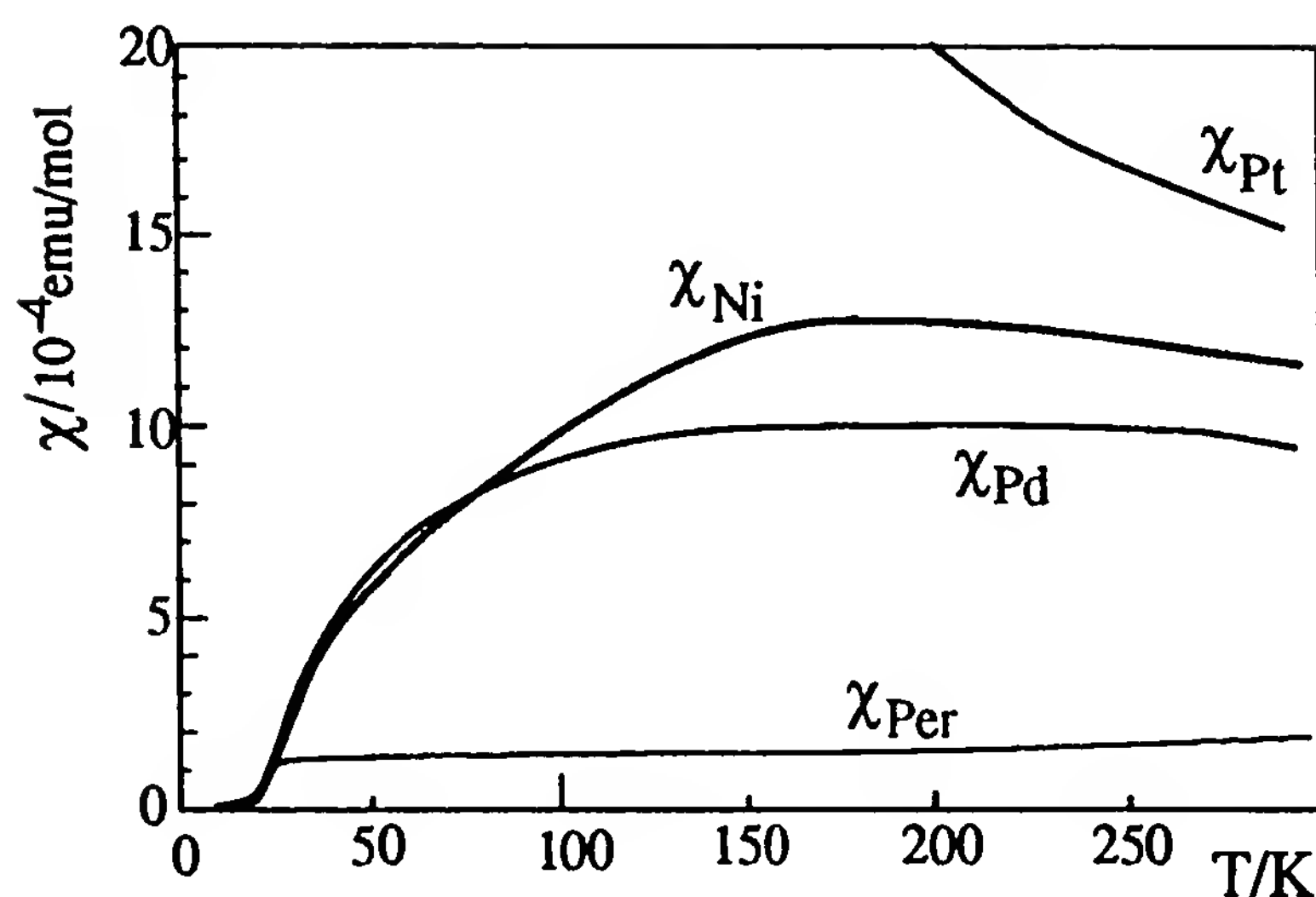


Figure 7 Temperature dependence of the spin susceptibility of $\alpha\text{-Per}_2[\text{M}(\text{mnt})_2]$; $\text{M} = \text{Ni}, \text{Pt}, \text{Pd}$. (Courtesy of V. Gama, INETI, Sacavem, Portugal.)

The contribution to the susceptibility due to the perylene chain is enhanced Pauli-like, similar to the Au, Cu, and Co analogs, while the dithiolate chain contribution $\chi_{\text{Pd}} \equiv \chi_{\text{S}}^{\text{mnt}}(T)$ is of Bonner–Fisher type. The magnitude of the antiferromagnetic intrachain interactions can be estimated from the Θ value of Curie–Weiss law, which can be adjusted at high temperature [expression (13)] and its value is on the order of $\Theta \approx -210$ K.

From a fitting to the Bonner–Fisher law, a value for $|J_{\text{eff}}/k_{\text{B}}|$ can be estimated to be on the order of ≈ 130 K, constant from 300 to 100 K, with enhancement below this temperature. It is interesting to notice that this temperature (100 K) corresponds to the appearance of the $2k_{\text{F}}^{\text{D}}$ diffuse lines. The behavior of the susceptibility below 100 K could be attributed to pretransitional spin-Peierls fluctuations, with a depression on the $\chi_{\text{S}}^{\text{mnt}}(T)$ as observed in $(\text{BCPTTF})_2\text{AsF}_6$ (Fig. 3).

The Ni analog has a very similar behavior. For a powder sample, there is only one ESR line above ≈ 160 K, with a room temperature linewidth on the order of 300 G. The magnitude of the antiferromagnetic intrachain interactions can be estimated to be $\Theta \approx -56$ K and the magnitude of the interchain interactions could also be estimated for $T > 180$ K as

$$\frac{J_{\text{P-Ni}}}{k_{\text{B}}} \gg \frac{\mu_{\text{B}} H_0 (g_{\text{Ni}} - g_{\text{P}})}{k_{\text{B}}} \approx 0.015 \text{ K}$$

which is big compared with the difference between the resonant frequencies of both spin systems [47].

A second ESR line appears below 160 K, gradually approaching g_{Per} , indicating that the interchain spin-coupling constant decreases with temperature. The $\chi_{\text{Ni}} \equiv \chi_{\text{S}}^{\text{mnt}}(T)$ contribution (Fig. 7) has a χ_{max} value at ≈ 190 K, but it does not fit a Bonner–Fisher model unless we consider a temperature-dependent J_{eff} , which is linear in the range 70 to 300 K, increasing as T goes down. Below 100 K the enhancement becomes more pronounced, this being attributed to the above-mentioned pretransitional spin-Peierls fluctuations, with a depression on the $\chi_{\text{S}}^{\text{mnt}}(T)$. The structural instabilities from Table 2 and the behavior of the magnetic susceptibility suggest that for both the Pd and Ni compounds there is a Peierls transition in the perylene chain simultaneous with a spin-Peierls transition in the Ni(mnt) chain.

In the Pt compound [24] we can also separate the total spin susceptibility into two components: the enhanced Pauli type $\chi_{\text{S}}^{\text{Per}}(T)$ and the $\chi_{\text{Pt}} \equiv \chi_{\text{S}}^{\text{mnt}}(T)$ (Fig. 8). However, for the χ_{Pt} , the antiferromagnetic intrachain interaction is negligible and therefore the spin susceptibility at high temperatures is much higher than in the Ni and Pd analogs, as shown in Fig. 7. As in the Pd compound, but more clearly, we can distinguish three temperature ranges with different regimes. Above ≈ 25 K, there is interchain spin exchange, denoted by the ESR spectra, which exhibits a single line with temperature-dependent g . Well above this temperature range, χ_{Pt} is not of Bonner–Fisher type since there is no evidence of spin dynamics, but Curie–Weiss type, $\chi_{\text{Pt}} = ng^2\mu_{\text{B}}/4k_{\text{B}}(T + \Theta)$, with $\Theta \approx 20$ K, which essentially coincides with the maximum in χ_{Pt} . This maximum in χ_{Pt} corresponds to the onset of spin-Peierls instabilities and depression of χ_{Pt} as well as the onset of $2k_{\text{F}}^{\text{D}}$ diffuse lines observed in diffuse x-ray experiments. We denominate this temperature as T_{SP}^0 . Below T_{SP}^0 , χ_{Pt} is activated, taking

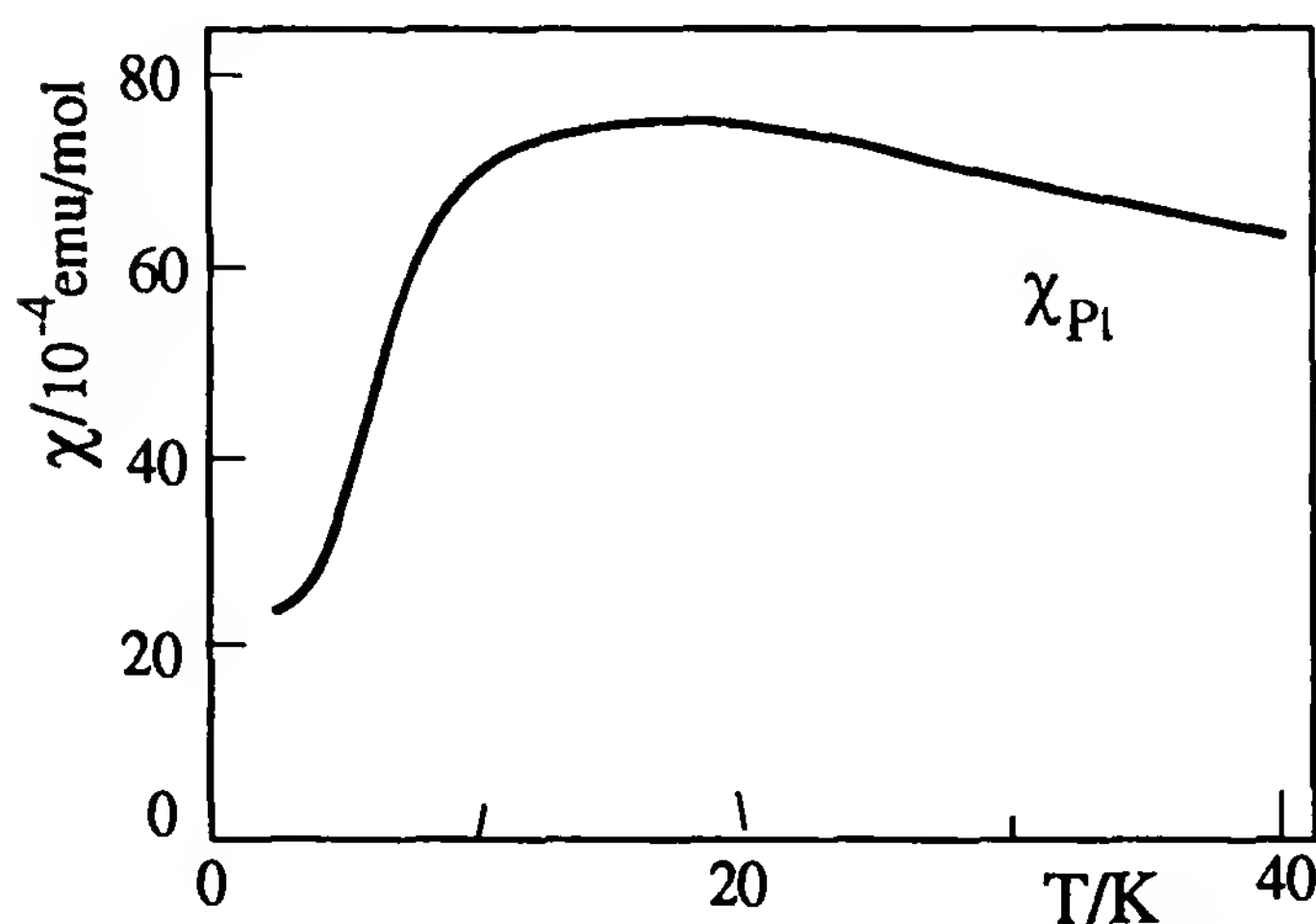


Figure 8 Temperature dependence of the $\chi_{\text{S}}^{\text{mnt}}(T)$ component of $\alpha\text{-Per}_2[\text{Pt}(\text{mnt})_2]$ for $T < 40$ K. (From Ref. 24.)

a singlet–doublet form, attributed to the spin-Peierls pseudogap. At $T = 7$ K the metal–insulator transition occurs, the ESR line disappears, and new signals appear which are attributed to the uncoupled perylene and $[\text{Pt}(\text{mnt})_2]^-$ species.

In Fig. 9, T_1^{-1} is represented as a function of temperature for the Au and Pt compounds. As mentioned above, the Au T_1^{-1} value is reminiscent of one-dimensional conductors with deviations of the Korringa law. In the Pt compound T_1^{-1} is temperature independent above ≈ 30 K, this behavior being attributed to localized spins. Below 30 K there are deviations of the Curie–Weiss law that affect T_1^{-1} . It is interesting to note that $T_1^{-1} \propto T\chi_s(T)$ over the entire temperature range. From the other properties of this compound the main contribution to T_1^{-1} is considered to be the $T_{1d\perp}^{-1}$ term since the contact $T_{1c\perp}^{-1}$ term should be negligible.

V. MOLECULAR FERROMAGNETS

A. Introduction

Extensive literature has been devoted to magnetic molecular materials [48], and we will review the subject only briefly. As we have seen, a ferromagnet has a magnetization of the type $\mathbf{M} = [C/(T - T_c)]\mathbf{B}$, where $T_c = C\lambda$ is the Curie temperature below which there is magnetic order. In principle, in a small enough volume, we should have, below T_c , all moments aligned and a saturation magnetization, M_s . In real materials, the magnetization is not homogeneous but distributed in ferromagnetic domains, with dif-

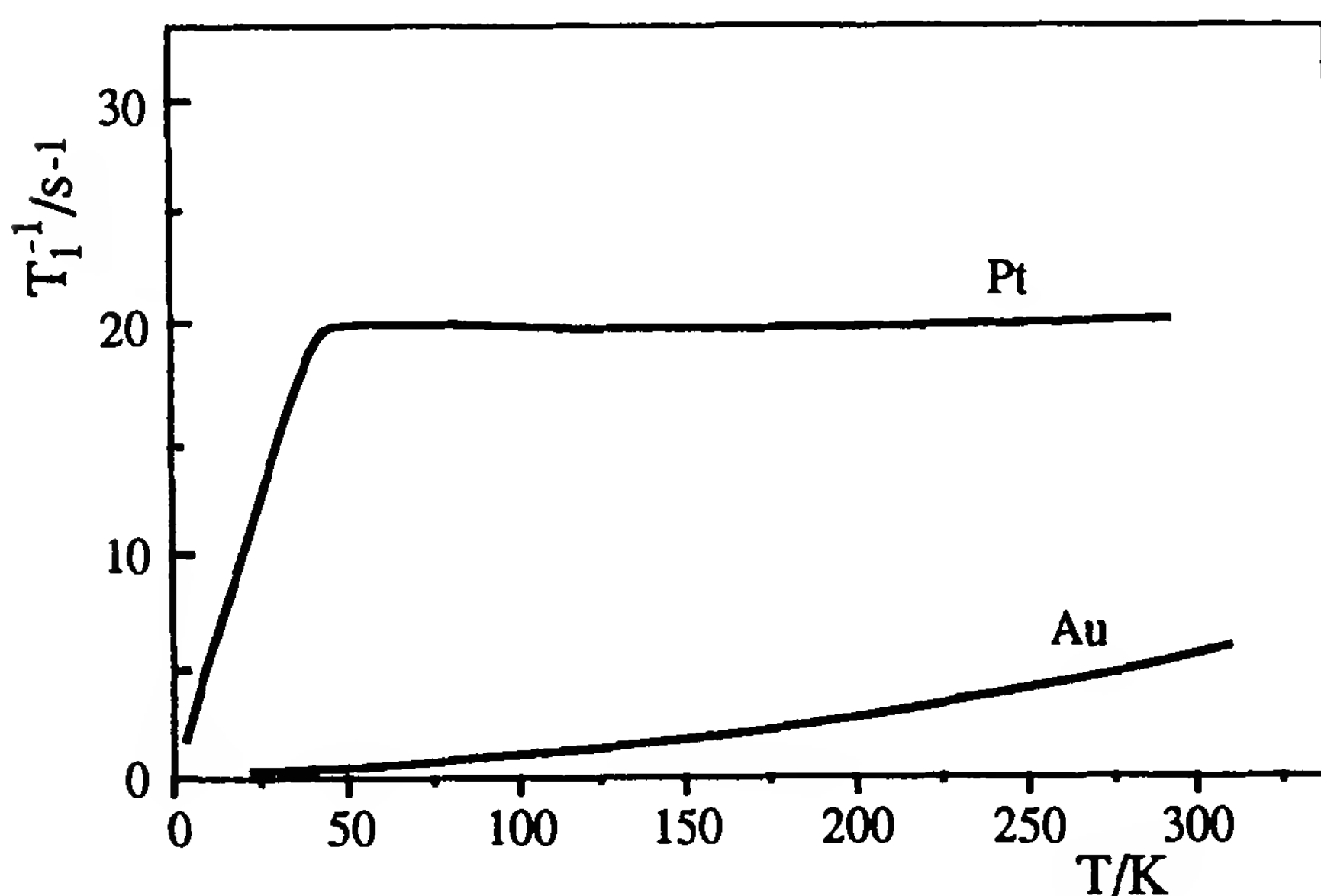


Figure 9 NMR relaxation T_1^{-1} for $\alpha\text{-Per}_2[\text{Pt}(\text{mnt})_2]$ and $\alpha\text{-Per}_2[\text{Au}(\text{mnt})_2]$. (From Ref. 24.)

ferent orientations. When the material is submitted to an intense external field, the magnetic moments will align. The material is characterized by the magnetization curves $M(H)$, which, in general, exhibit hysteresis. A *soft* material responds rapidly to the field, and a *hard* material retains the magnetization when the field is removed.

A great challenge in the field of molecular materials is the design of molecular ferromagnets, especially after the discovery of the organic superconductors. Some of the main objectives are (1) to obtain magnetic order at high enough temperatures; (2) to obtain stable systems, with well-defined hysteresis, remnant magnetization, and high coercive fields; and (3) to obtain transparent films that will keep the ferromagnetic properties below T_c .

Molecular materials present some specific peculiarities: namely, the fact that the magnetic moment is delocalized within the molecule, since half-filled orbitals are, in general, of molecular type. Some typical examples of molecular magnets include:

1. Charge-transfer complexes with alternate chains of the type D^+A^- , in which both species, D^+ (the donor) and A^- (the acceptor), have one unpaired electron (i.e., a local spin of $\frac{1}{2}$). An example is $\text{Fe}(\text{Me}_5\text{Cp})_2(\text{TCNE})$ [49], in which Me_5Cp = pentamethylcyclopentadienyl and TCNE = tetracyanoethylene. This compound exhibits ferromagnetic order below $T_c = 4.8$ K. Recently, a polymeric magnet was reported [50] to have been prepared from $\text{V}(\text{C}_6\text{H}_6)_2$ and TCNE with $T_c > 350$ K.
2. Compounds based on Mn(II) and Ni chains.
3. Bimetallic polymers based on Mn(II)–Cu(II), with bisbidentated ligands.

The basic idea is to make sure that the neighbor magnetic moments become parallel, without compensation. Several approaches have been pursued to achieve that condition. One approach consists in using molecules with a large number of magnetic centers, and consequently, high spin values and large magnetic moments. This can be achieved by placing the neighboring spins in orthogonal magnetic orbitals. Another type of molecular ferromagnets is based on organometallic derivatives in which ferromagnetic coupling is stabilized by configuration interaction.

A number of design strategies to obtain molecular magnets have been proposed [51]. The general idea is to assemble molecules with one or more magnetic centers in such a way that the interactions between the local spins lead to a nonzero spin, always taking advantage of intra- and intermolecular

interactions. In most cases, the onset of a spontaneous magnetization results from a three-dimensional transition.

We now summarize some of the most relevant design strategies.

1. Orthogonality of Magnetic Orbitals [52]

Magnetic orbitals have been defined as orbitals with unpaired electrons. If we consider the interaction between a pair of doublets with unpaired spins, the singlet–triplet energy gap is $\Delta E \approx 4tS + 2J$, where t is the transfer integral, S the overlap integral, and J the two-electron exchange integral. If $S = 0$ (orthogonal orbitals), the ground state is ferromagnetic. If $4tS < 0$, then $\Delta E < 0$ and we obtain an antiferromagnet. Therefore, the way to obtain a ferromagnet with a triplet GS is to minimize the overlap integral, S . This approach has been rather successful. This is O. Kahn's strategy and seeks strict orthogonality of magnetic orbitals: high spin multiplicity in the ground state in order to impose parallel alignment of a $S = \frac{5}{2}$ species (e.g., Mn^{2+} , Fe^{3+}) through antiferromagnetic coupling with a $S = \frac{1}{2}$ species (e.g., Cu^{2+}) leading to a one-dimensional $\text{Mn}^{2+}\text{Cu}^{2+}$ system.

2. McConnell Mechanisms

The McConnell mechanisms [53,54] are based on spin polarization due to the interaction between a positive spin density of a unit and a negative spin density of an adjacent unit, this leading to ferromagnetic intermolecular interactions. In fact, the interaction between the ground state and a high-spin charge-transfer excited state seems to be very efficient for getting intermolecular ferromagnetic interactions. Examples of materials for which this mechanism has been proposed include $[\text{FeCp}_2^*][\text{TCNE}]$ and $\text{Mn}(\text{Cp}_2^*)(\text{TCNQ})$.

3. Weak Ferromagnetism

This strategy is based on the arrangement of antiferromagnetic units to take advantage of the ferromagnetic nearest-neighbor interactions, which result in net ferromagnetic coupling.

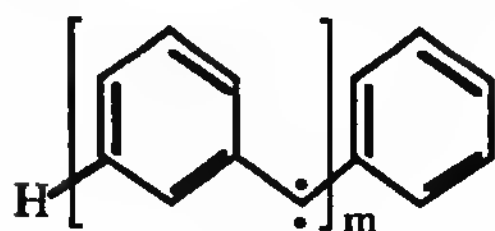
4. Ferrimagnetic Approach

This strategy consists in building ferrimagnetic chains and assemble them in a ferromagnetic arrangement, taking advantage of interchain interactions.

5. Topological Degeneracy

In the approach of high-spin molecules, tetra and penta(*m*-phenylenecarbenes) (I) are reported [55] to have the highest spin multiplicities for purely

organic molecules with ground states $S = 2$ and $S = \frac{5}{2}$, respectively. This



I ($m=4$; 5)

is a potential approach to obtaining ferromagnetic polymers. A still higher-spin ($S = 5$) polycarbene has been reported [56].

B. Some Examples

To better illustrate the general properties of these materials, we will mention the main characteristics of just a few of the best known.

1. $\{\text{Cr}[(\text{ox})\text{Ni}(\text{Me}_6\text{-[14]ane-N}_4)]_3\}(\text{ClO}_4)_3$

An example of the success of orthogonality of magnetic orbitals is given by the organometallic complex [57] $\{\text{Cr}[(\text{ox})\text{Ni}(\text{Me}_6\text{-[14]ane-N}_4)]_3\}(\text{ClO}_4)_3$, which is represented schematically in Fig. 10. In this material, both Cr(III), with three unpaired electrons in t_{2g} orbitals, and Ni(II), with two unpaired electrons in e_g orbitals, have octahedral symmetry. In the C_{2v} symmetry of each Cr–Ni bridging, the t_{2g} and e_g orbitals are quasiorthogonal. The local spins are expected to be parallel with a $S = \frac{9}{2}$ ground state. The

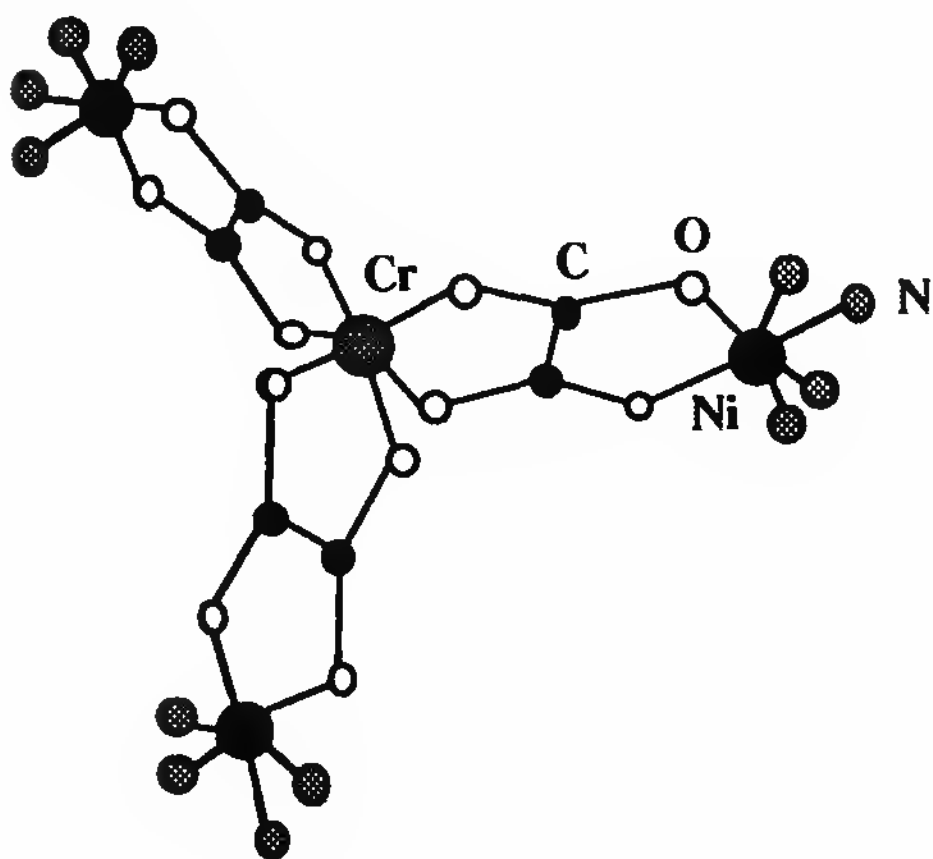


Figure 10 Molecular structure of $\{\text{Cr}[(\text{ox})\text{Ni}(\text{Me}_6\text{-[14]ane-N}_4)]_3\}(\text{ClO}_4)_3$.

temperature dependence of the magnetic susceptibility confirms this prediction reaching a plateau below 6 K. The exchange integral is estimated as -5.3 cm^{-1} .

Another example [58] is given by $\text{NBu}_4[\text{CuCr}(\text{ox})_3]$, which has a ferromagnetic transition at $T_c = 7 \text{ K}$ and exhibits remnant magnetization and a hysteresis loop below T_c .

2. $[\text{Fe}(\text{C}_5\text{Me}_5)_2]^+ \cdot [\text{TCNE}]^-$

The magnetic susceptibility of this material (Fig. 11) follows the Curie-Weiss law [Eq. (13)] at high temperatures ($T > 60 \text{ K}$), exhibiting ferromagnetic interactions, with $\Theta \approx 30 \text{ K}$ and with $\mu_{\text{eff}} = 3.1\mu_B$ at room temperature. An estimation of the exchange integrals give $J = 27 \text{ K}$, $J_{\perp} = 0.35 \text{ K}$, and $J_{\parallel}/J_{\perp} = 77$. For $T > 16 \text{ K}$ it follows the one-dimensional Heisenberg model for $S = \frac{1}{2}$. Below that temperature the susceptibility diverges as $(T - T_c)^{-\gamma}$ with a critical exponent that is typical of a three-dimensional character. The Curie temperature is $T_c = 4.8 \text{ K}$, and below approximately that temperature, spontaneous magnetization remains at $H = 0$ with a three-dimensional ferromagnetic ground state. The saturation magnetization at 4.2 K is $M_s = 1.1 \times 10^4 \text{ emu} \cdot \text{G/mol}$. The hysteresis [60], shown in Fig. 12, indicates a coercive field of $H_c \approx 1000 \text{ G}$ at $T = 2 \text{ K}$.

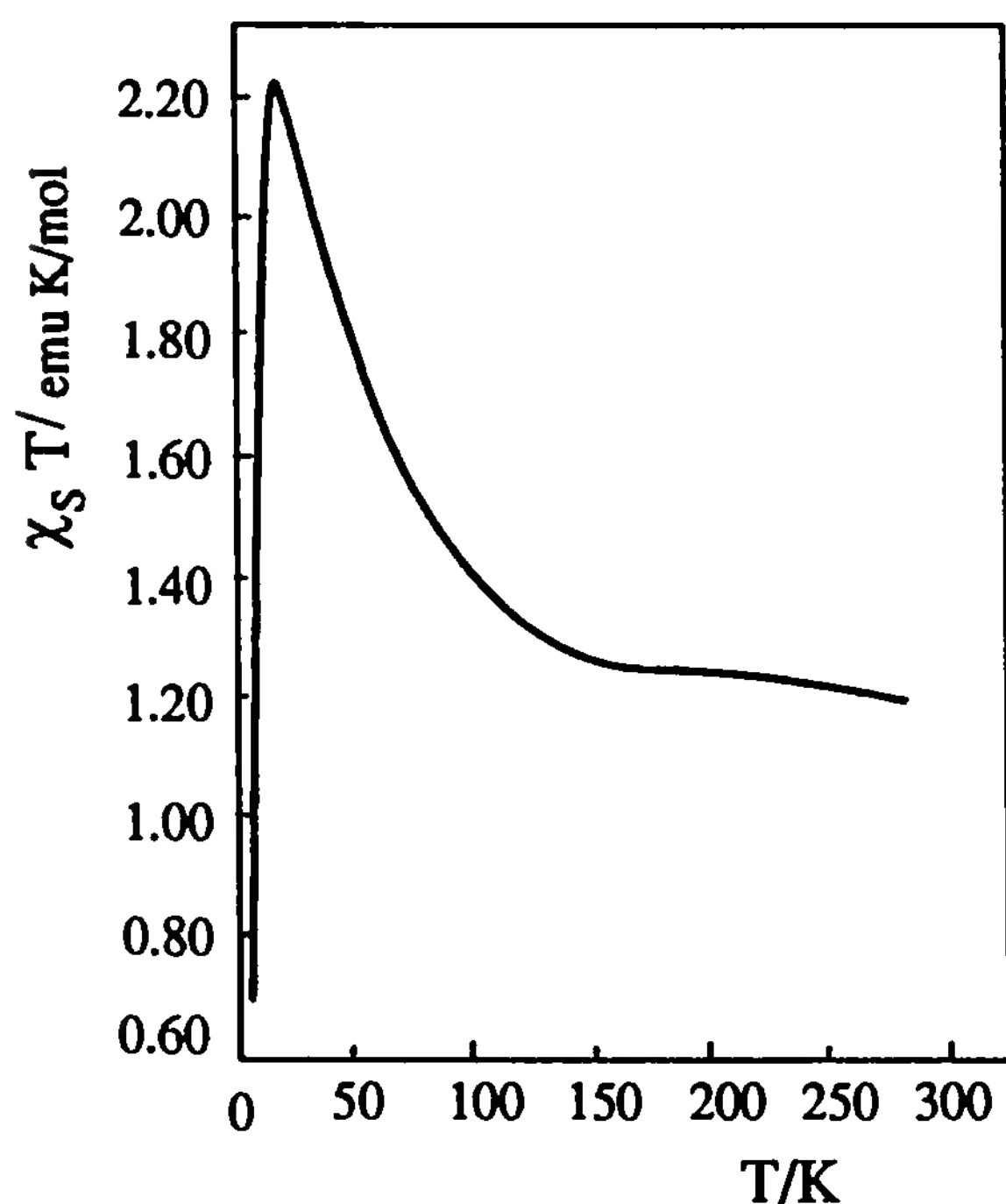


Figure 11 Product of the susceptibility and temperature as a function of temperature for $[\text{Fe}(\text{C}_5\text{Me}_5)_2]^+ \cdot [\text{TCNE}]^-$ (Reprinted with permission from Ref. 59. Copyright 1987 American Chemical Society.)

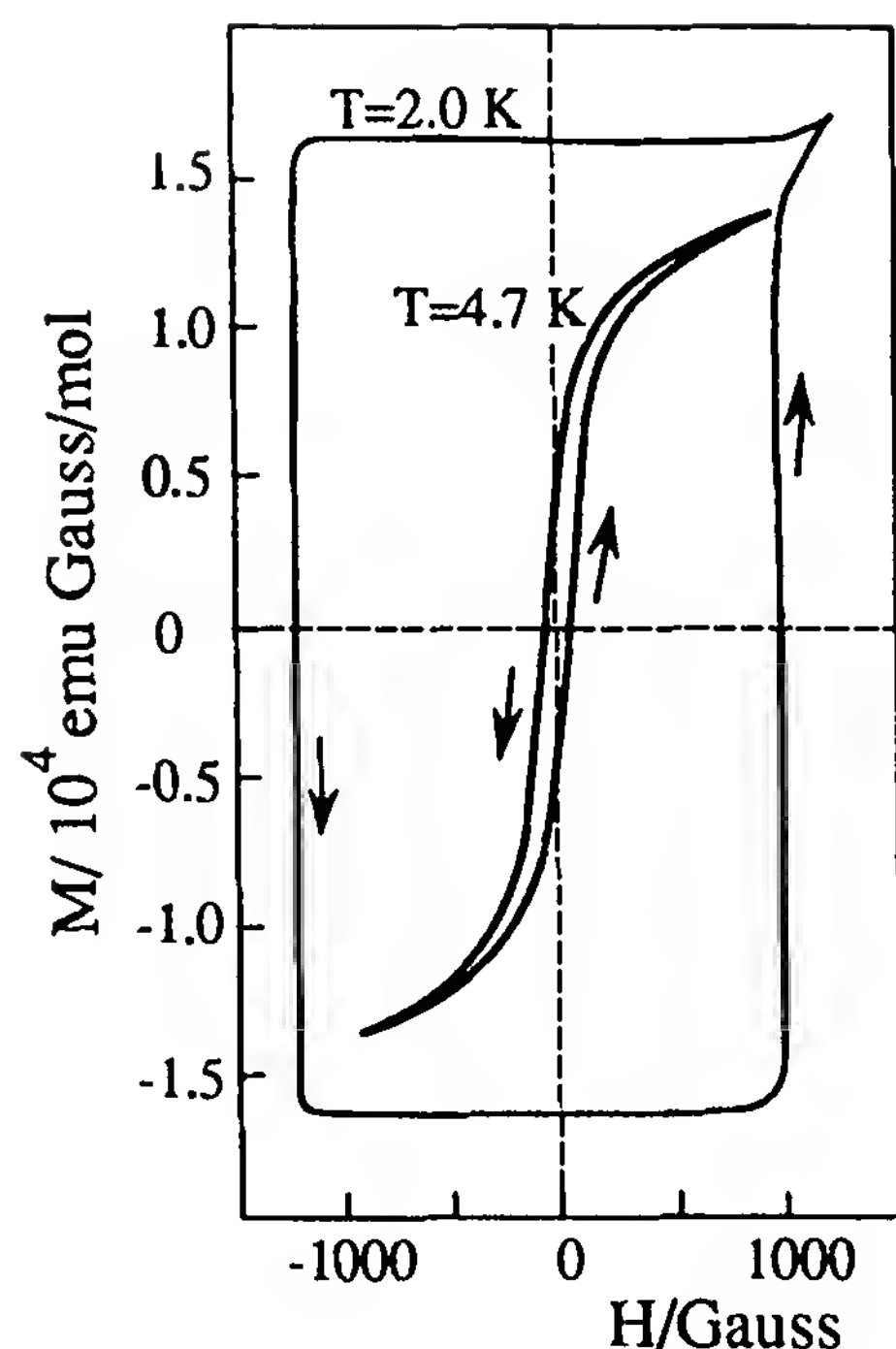


Figure 12 Magnetization M versus applied magnetic field at $T = 4.7$ K and $T = 2$ K. (From Ref. 60.)

The magnetic behavior of this material is explained within the model of mixing excited states with the ground state for stabilizing the ferromagnetic coupling and lead to three-dimensional (bulk) ferromagnetism.

3. $V(\text{TCNE})_x \cdot y$ (Solvent) [61]

An important achievement concerning the challenge of obtaining high Curie temperatures was reported for the compound $V[\text{TCNE}]_x \cdot y\text{CH}_2\text{Cl}_2$ [62]. This is the first room-temperature molecular magnet reported so far. T_c is estimated to be ≈ 400 K, and the coercive field is $H_c = 60$ G. This material has a considerable conductivity, $\sigma_{\text{RT}} \approx 10^{-3} \text{ S} \cdot \text{cm}^{-1}$. Figure 13 shows the hysteresis curve at room temperature.

A similar compound with CH_3CN as solvent—namely, $V[\text{TCNE}]_x \cdot y(\text{CH}_3\text{CN})$ [63] where $x \approx 1.5$, $y \approx 2$ —exhibits random magnetic anisotropy and has a Curie temperature, $T_c = 138$ K. In this material V^{II} has three electrons in $3d$ orbitals ($S = \frac{3}{2}$), and TCNE^- has one electron in a p_z orbital ($S = \frac{1}{2}$). Zhou et al. [63] used the random magnetic anisotropy concepts previously applied to f and d electrons to account for the magnetic phenomena in a molecular magnet for which a substantial fraction of the spin is supplied by p electrons and for which the spinless solvent has a key role in determining the magnetic properties.

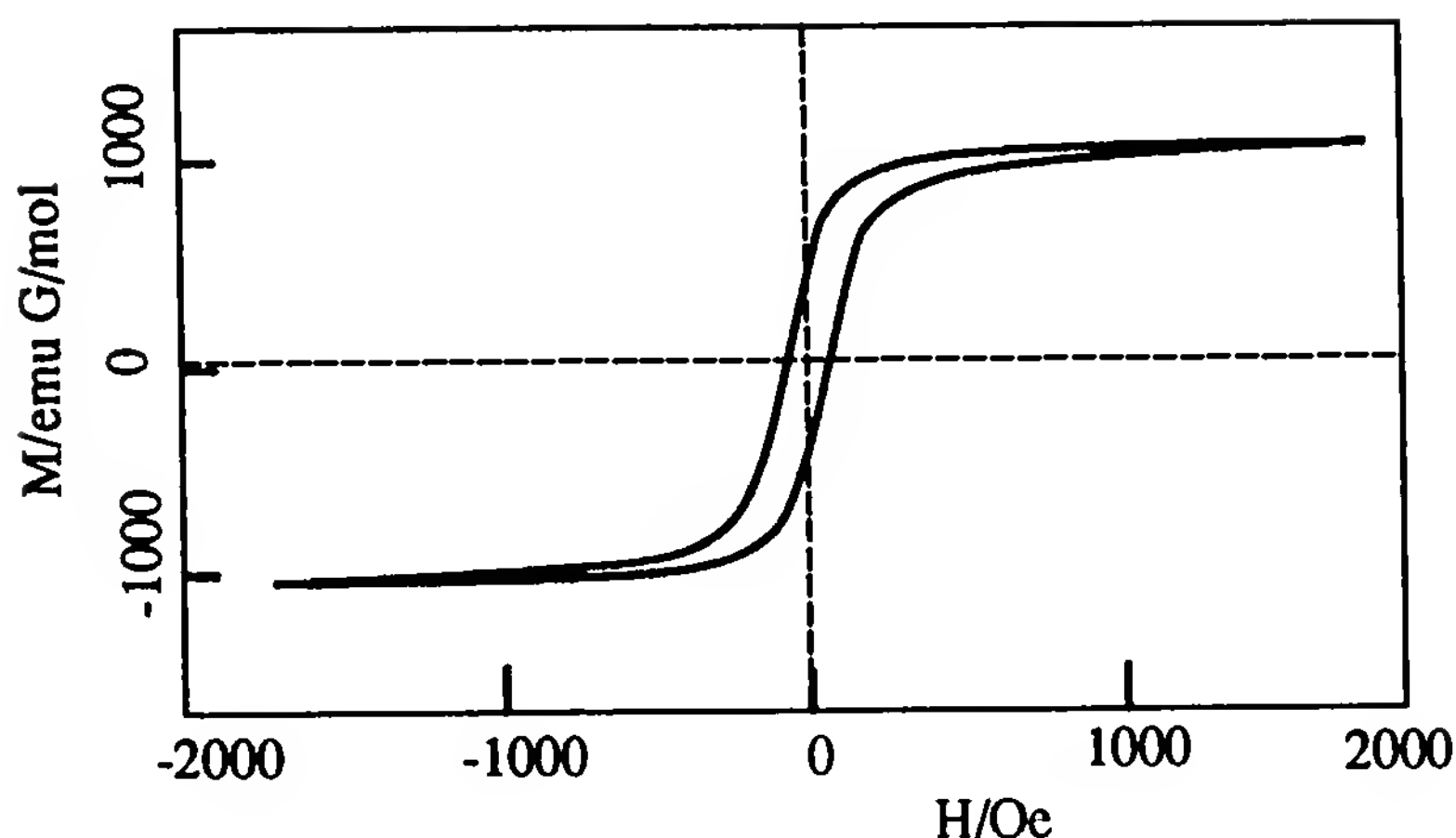


Figure 13 Hysteresis, $M(H)$, of $V(TCNE)_x \cdot y(CH_2Cl_2)$ at room temperature. (Adapted from Ref. 62. Copyright 1991 by the AAAS.)

This material is also conducting, with $\sigma_{RT} \approx 10^{-5} \text{ S}\cdot\text{cm}^{-1}$, and the microwave dielectric constant yields a localization length of $a \approx 5 \text{ \AA}$, comparable to that of the $TCNE^-$ group. The observed strongly temperature-dependent alternating-current (ac) conductivity has been attributed to short-range ferrimagnetic correlations and has been explained within a Mott-type three-dimensional variable range hopping model: $\log(T^{1/2}) \propto T^{-1/4}$. An extensive review on this type of materials has been presented [64].

VI. APPLICATIONS

A. Introduction

The main objective of studying the magnetic, ESR, and NMR properties of organic conductors is to complement information in order to understand the general features of these materials. However, a few spin-off applications have emerged and the very recent field of molecular magnets will certainly lead to important technological applications.

B. Applications of Materials with Narrow ESR Linewidths

Materials with very narrow ESR lines ($\Delta H_{pp} < 20 \text{ mG}$) can be used as small-volume and low-power magnetic sensors of great sensitivity. Such devices would have applications as submarine mine detectors, local terrestrial magnetic field detectors [65,66], and for the identification of objects with an added suitable paramagnetic substance [67].

To give an order of magnitude: A 4-mg sample with a volume of $\approx 3 \text{ mm}^3$, of a material with a 13-mG ESR linewidth, would have a signal-to-

noise ratio on the order of 100 in a field of 8 G. This means that the precision of the field measurement is on order of 0.13 mG. A field of 80 G could be measured with the same precision with a 0.04-mg sample or a field of 0.8 G with 400 mg of material [66].

Several solid materials satisfying the linewidth requirement are known [68]:

1. The graphite bisulfate [69], a graphite insertion compound of formula $C^{m+}(\text{HSO}_4^- \cdot 2\text{H}_2\text{SO}_4)_m$ (m = oxidation state) with $\Delta H_{\text{pp}} = 45$ mG for $m = 0.02$.
2. Radical ion salts of phtalocyanines.
3. Lithium-doped polyacetylene. This material would be practical, but the linewidth is of order $\Delta H_{\text{pp}} \approx 90$ mG, which is larger than most requirements.
4. Radical cation salts of polyaromatic hydrocarbons [70].

The radical cation salts of polyaromatic hydrocarbons (fluoranthene, pyrene, perylene) have particular advantages (i.e., narrower lines) and can easily be improved by chemical modification. In Table 3 we list a few of these materials. Note that the linewidth of the common ESR standard, DPPH (diphenylpicrylhydrazil), is ≈ 1500 mG. The narrow ESR line is due to delocalized conduction electrons on the aromatic chains since the spin-spin interactions are relatively small. The narrowness of the ESR lines in organic conductors is attributed to the low dimensionality of these materials, reducing the spin-orbit coupling. In fact, in a strictly one-dimensional conductor, the only diffusion processes possible are, as we have seen above, those with a change in wave vector, $\Delta q \approx 0$ or $\Delta q = 2k_F$. In the first case, the typical phonon energies, $q\nu_s$, are very different from the energy $q\nu_F$, which is necessary to create or annihilate an electron-hole pair, making the $\Delta q \approx 0$ diffusion probability very small. On the other hand, $\Delta q = 2k_F$ is not diffusive. Therefore, in a strictly one-dimensional

Table 3 Organic Conductors with Particularly Narrow ESR Signals

Material	Linewidth (mG)	Ref.
(Perylene) ₂ (PF ₆)· $\frac{2}{3}$ THF	26	71
(Perylene) ₂ (AsF ₆)· $\frac{2}{3}$ THF	34	71
(Perylene) ₂ (AsF ₆) _{0.45} (PF ₆) _{0.55} · $\frac{2}{3}$ THF	17	71
Lithium phtalocyanine	15	72
(Fluoranthene) ₂ (PF ₆)	15	71
(Naphthalene) ₂ (PF ₆)	2.5	71

system, if the dominating process is the spin-orbit interaction, the linewidth should indeed be very small.

A particular promising application was patented by Jérôme et al. [67]. It claims a method of authenticating an object by electron paramagnetic resonance, and a portable apparatus for implementing the method, as well as an object usable with the method. The invention provides a special portable and small ESR spectrometer using a transient detection method or more particularly a “fast adiabatic pass” method. The apparatus works at microwave frequencies, $\nu < 1$ GHz and uses a magnetic field, H_0 , ranging from 50 to 370 G. A particular substance proposed is tetrahydro1,2,7,8-dicyclopentaperylene, and only a few tens of milligrams are needed.

The proposed applications include the identification of banknote paper, security paper, bank cards, art objects, or even bar codes. The marks can be invisible or hidden. Related patents are mentioned to describe the state of the art, one of which also uses radical-ion organic conductors [73].

C. Potential Applications of Molecular Magnets

Molecular magnets with high Curie temperatures ($T_c > 125$ K) would certainly have important real applications [74] as bulk magnets, in magnetic and magnetooptic storage and recording, magnetic imaging, and so on. As in all emerging research areas, new phenomena may expand to unforeseen applications. One of the greatest challenges is to obtain soluble materials, particularly polymers, allowing easy processibility. Preliminary results suggest this to be possible.

The present market for inorganic magnetic materials has annual sales larger than that of semiconductors. Present magnetic tapes and disks are made such that the magnetic moments are parallel to the plane of the film or disk. Increased data density requires larger demagnetization fields, and therefore materials with larger coercive fields are required. However, increased data density apparently is not needed for the time being, since present technology on inorganic materials largely exceeds the requirements of present and predictable future technologies for magnetic storage. Magnetic storing devices are soon expected to become small components and not peripherals.

Optical disks with high data density will be an increased data storage technology. However, magnetooptic effects remain to be studied in molecular materials. An ultrahigh-density optical storage device with a data density of 10^{18} bits/cm³ based on two-dimensional addressing of 1- μ m³ bits with light could be envisioned. This might be achievable with molecular magnets.

Since in contrast to inorganic-based magnets, most molecular magnets are insulating, this could lead to different applications, such as photomagnetic switches and polarized light manipulation in integrated optical devices. New phenomena may emerge and hence nonpredictable applications. Potential areas of interest may be colloidal dispersions and magnetic inks, Langmuir–Blodgett films, magnetostrictive sensors, magnetic bubbles, and soft magnetic materials with low coercive fields for ac motors, generators, and transformers (especially in micromechanics). Biocompatibility may be important for medical applications such as magnetic imaging and transducers for medical implants. Some of the anticipated properties of molecular/polymeric magnets are:

Chemical stability with time and temperature

Insulation

Low density

Low magnetic anisotropy

Transparency

Optical changes

Low elastic moduli

Moldulate/tuning of properties via chemistry

Solubility and processibility

Large polarizability of constituent molecules

Low environmental contamination

Potential biocompatibility

Photomagnetic effects

ACKNOWLEDGMENTS

We particularly thank Dr. D. Jérôme, Dr. J. P. Pouget, and Professor A. Epstein for sending us relevant new information, as well as R. T. Henriques and V. P. Gama for providing data and help during the preparation of this contribution.

REFERENCES

1. A. J. Epstein, E. M. Conwell, and J. S. Miller, *Ann. N.Y. Acad. Sci.* **313**:183 (1978).
2. O. Madelung, *Introduction to Solid-State Theory*, Springer-Verlag, New York, 2nd printing 1981, p. 155.
3. J. C. Scott, in *Semiconductors and Semimetals*, Vol. 27, *Highly Conducting Quasi-One-Dimensional Crystalline Materials* (E. Conwell, ed.), Academic Press, New York, 1988, p. 385.
4. D. Jérôme and H. J. Shultz, *Adv. Phys.* **31**:299 (1982).

5. S. Mazundar and S. N. Dixit, Phys. Rev. B 34:3683 (1986).
6. T. Takahashi, D. Jérôme, F. Masin, J. M. Fabre, and L. Giral, J. Phys. C 17:3777 (1984).
7. D. J. Klein and W. A. Seitz, Phys. Rev. B 10:3217 (1974).
8. J. C. Bonner and M. E. Fisher, Phys. Rev. A 135:640 (1964).
9. J. C. Bonner, H. W. J. Blöte, J. W. Bray, and I. S. Jacobs, J. Appl. Phys. 50:1810 (1979).
10. B. Bleaney and K. D. Bowers, Proc. R. Soc. A 214:451 (1952).
11. C. P. Slichter, *Principles of Magnetic Resonance*, Springer-Verlag, Berlin, 1978.
12. L. Alcácer, Ph.D. thesis, University of California, 1970; L. Alcácer and A. H. Maki, J. Phys. Chem. 80:1912 (1976); Y. Tomkiewicz, A. R. Taranko, and J. B. Torrance, Phys. Rev. Lett. 36:751 (1976).
13. R. J. Elliot, Phys. Rev. 96:280 (1954).
14. R. J. Elliot, Phys. Rev. 96:266 (1954).
15. Y. Yafet, in *Solid State Physics*, Vol. 14 (F. Seitz and D. Turnbull, eds.), Academic Press, New York, 1963, p. 109.
16. S. Shitzkovsky, M. Weger, and H. Gutfreund, J. Phys. Paris 39:711 (1987).
17. C. Coulon, R. Laversanne, and J. Amiell, Proceedings of the Yamada Conference XV, Lake Kawaguchi, Japan, 1986.
18. C. Coulon and R. Laversanne, in *Low-Dimensional Conductors and Superconductors*, NATO-ASI Series B, Physics, Vol. 155 (D. Jérôme and L. G. Caron, eds.), Plenum Press, New York, 1987, p. 135.
19. T. Nagamiya, Adv. Phys. 4:1 (1954).
20. F. Rachdi, T. Nunes, M. Ribet, P. Bernier, M. Helmle, M. Mehring, and M. Almeida, Phys. Rev. B 45(14):8134 (1992).
21. A. Abragam, *The Principles of Nuclear Magnetism*, Clarendon Press, Oxford, 1961.
22. T. Moriya, J. Phys. Soc. Jpn. 18:516 (1963).
23. F. Devreux, C. Jeandey, M. Nechtschein, J. M. Fabre, and L. Giral, J. Phys. Paris 40:671 (1979).
24. C. Bourbonnais, R. T. Henriques, P. Wzietek, D. Köngeter, J. Voiron, and D. Jérôme, Phys. Rev. B 44:641 (1991).
25. P. Delhaès, in *Lower-Dimensional Systems and Molecular Electronics*, NATO ASI Series B, Vol. 248 (R. M. Metzger, P. Day, and G. C. Papavassiliou, eds.), Plenum Press, New York, 1990, p. 43.
26. J. B. Torrance, in *Low-Dimensional Conductors and Superconductors*, NATO ASI Series B, Vol. 155 (D. Jérôme and L. G. Caron, eds.), Plenum Press, New York, 1987, p. 113.
27. H. Gutfreund, M. Kaveh, and M. Weger, in *Quasi-One-Dimensional Conductors I*, Lecture Notes in Physics, Vol. 95 (S. Barišić, A. Bjelis, J. R. Cooper, and B. Leontic, eds.), Springer-Verlag, Berlin, 1979, p. 105.
28. Y. Tomkiewicz, A. R. Taranko, and J. B. Torrance, Phys. Rev. Lett. 36:751 (1976).

29. E. F. Rybaczewski, L. S. Smith, A. F. Garito, A. J. Heeger, and B. G. Silbernagel, *Phys. Rev. B* **14**:2746 (1976).
30. J. B. Torrance, in *Chemistry and Physics of One-Dimensional Metals* (H. J. Keller, ed.), Plenum Press, New York, 1977, p. 137.
31. J. B. Torrance, *Ann. N.Y. Acad. Sci.* **313**:210 (1978).
32. C. Coulon, *Organic and Inorganic Low-Dimensional Crystalline Materials*, NATO ASI Series B, Vol. 168 (P. Delhaès and M. Drillon, eds.), Plenum Press, New York, 1987, p. 201.
33. T. Takahashi, *Prog. Theor. Phys.* **40**:348 (1970).
34. J. Tanaka and C. Tanaka, *J. Phys. Colloq.* **44**:C3-997 (1983).
35. B. Korin-Hamzic, M. Miljak, and J. R. Cooper, *Mol. Cryst. Liq. Cryst.* **85**:177 (1982).
36. Y. Tomkiewicz, in *Physics and Chemistry of Low-Dimensional Solids* (L. Alcácer, ed.), D. Reidel, Dordrecht, The Netherlands, p. 187.
37. D. Jérôme and M. Weger, in *Chemistry and Physics of One-Dimensional Metals* (H. J. Keller, ed.), Plenum Press, New York, 1977, p. 341.
38. Y. Tomkiewicz, J. R. Andersen, and A. R. Taranko, *Phys. Rev. B* **17**:1579 (1978).
39. H. J. Pedersen, J. C. Scott, and K. Bechgaard, *Solid State Commun.* **35**:207 (1980).
40. C. S. Jacobsen, K. Mortensen, M. Weger, and K. Bechgaard, *Solid State Commun.* **38**:423 (1981).
41. F. Creuzet, C. Bourbonnais, L. G. Caron, D. Jérôme, and K. Bechgaard, *Synth. Metals* **19**:289 (1987).
42. C. Bourbonnais, P. Wzietek, D. Jérôme, F. Creuzet, L. Valade, and P. Cassoux, *Europhys. Lett.* **6**:177 (1988).
43. Q. Liu, S. Ravy, J. P. Pouget, C. Coulon, and C. Bourbonnais, *Synth. Metals* **55–57**:1840 (1993); and references therein.
44. R. T. Henriques, V. Gama, G. Bonfait, I. C. Santos, M. J. Matos, M. Almeida, and M. T. Duarte, *Synth. Metals* **55–57**:1846 (1993).
45. M. Miljak and J. R. Cooper, *Mol. Cryst. Liq. Cryst.* **119**:141 (1985).
46. L. Alcácer and A. H. Maki, *J. Phys. Chem.* **80**:1912 (1976).
47. M. Y. Ogawa, B. M. Hoffman, S. Lee, M. Youdkowsky, and W. P. Halperin, *Phys. Rev. Lett.* **57**:1177 (1986).
48. D. Gatteschi, O. Kahn, J. S. Miller, and F. Palacio, eds., *Magnetic Molecular Materials*, NATO ASI Series, Vol. 198, Kluwer, Norwell, Mass., 1991.
49. J. S. Miller, J. C. Calabrese, H. Rommelmann, S. R. Chittipeddi, J. H. Zhang, W. M. Reiff, and A. J. Epstein, *J. Am. Chem. Soc.* **109**:777 (1987).
50. J. S. Miller and A. Epstein, *International Conference on Science and Technology of Synthetic Metals*, Göteborg, Sweden, Aug. 1992, Abstracts, p. 37.
51. O. Kahn, D. N. Hendrickson, H. Iwamura, and J. Veciana, in *Magnetic Molecular Materials*, NATO ASI Series E, Vol. 198 (D. Gatteschi, O. Kahn, J. S. Miller, and F. Palacio, eds.), Kluwer, Norwell, Mass., 1991, p. 385.
52. O. Kahn, *Struct. Bond.* **68**:89 (1987).
53. H. M. McConnell, *J. Chem. Phys.* **39**:1910 (1963).

54. H. M. McConnell, *Proc. R.A. Welch Found. Chem. Res.* 11:144 (1967).
55. K. Itoh, in *Magnetic Molecular Materials*, NATO ASI Series E, Vol. 198 (D. Gatteschi, O. Kahn, J. S. Miller, and F. Palacio, eds.), Kluwer, Norwell, Mass., 1991, p. 67.
56. I. Fujita, Y. Teki, T. Takui, T. Kinoshita, F. Miko, Y. Sawaki, H. Iwamura, A. Izuoka, and T. Sugawara, *J. Am. Chem. Soc.* 112:4047 (1990).
57. Y. Pei, Y. Journaux, and O. Kahn, *Inorg. Chem.* 28:100 (1989).
58. Z. J. Zhong, N. Matsumoto, H. Okawa, and S. Kida, *Chem. Lett.*, 87 (1990).
59. J. S. Miller, J. C. Calabrese, H. Rommelmann, S. R. Chittipeddi, J. H. Zhang, W. M. Reiff, and A. J. Epstein, *J. Am. Chem. Soc.* 109:777 (1987).
60. A. J. Epstein, S. Chittipeddi, A. Chakraborty, and J. S. Miller, *J. Appl. Phys.* 63(8):2953 (1988).
61. Du et al., *Proceedings of the Conference on Magnetism and Magnetic Materials*, Houston, Dec. 1992; *J Appl. Phys.* (in press).
62. J. M. Manriquez, G. T. Yee, R. S. McLean, A. J. Epstein, and J. S. Miller, *Science* 252:1415 (1991).
63. P. Zhou, B. G. Morin, J. S. Miller, and A. J. Epstein, *Phys. Rev. B Rapid Commun.* (to appear July 1993).
64. A. J. Epstein and J. S. Miller, *Molecular/Polymeric Magnets: Proceedings of the 6th International Conference on Electrical and Related Properties of Organic Solids*, Capri, Italy, May 1992 (J. Kalinowski, ed.); *Mol. Cryst. Liq. Cryst.* (in press).
65. P. Michel, A. Moradpour, and P. Penven, Patent application Thomson-CSF 88 01682 (1988).
66. P. Penven, D. Jérôme, P. Michel, and A. Moradpour, Patent application Thomson-CSF 88 07214 (1988).
67. D. Jérôme, J. Josas, G. Tevanian, H. Roses, P. Batail, and M. Fourmigué, U.S. Patent 5,149,946 (Sept. 22, 1992).
68. P. Michel, Ph.D. thesis, University of Paris–Sud, Centre d’Orsay, 1989.
69. G. R. Henning, B. Smaller, and Y. L. Yasatis, *Phys. Rev.* 95:1088 (1954).
70. W. Stöcklein, B. Bail, M. Schwoerer, D. Singel, and J. Schmidt, *Organic Molecular Aggregates*, Springer-Verlag, New York, 1983, p. 228.
71. P. Penven, Ph.D. thesis, Univ. Paris–Sud, 1989.
72. H. Sugimoto, T. Higashi, and M. Mori, *J. Chem. Soc. Chem. Commun.* 622 (1983); P. Turek, J. J. André, A. Giraudeau, and J. Simon, *Chem. Phys. Lett.* 134(5):471 (1987); H. Sugimoto, M. Mori, M. Masuda, and T. Taga, *J. Chem. Soc. Chem. Commun.* 962 (1986).
73. Patent DK-A-147 737.
74. C. P. Landee, D. Melville, and J. S. Miller, in *Magnetic Molecular Materials*, NATO ASI Series E, Vol. 198 (D. Gatteschi, O. Kahn, J. S. Miller, and F. Palacio, eds.), Kluwer, Norwell, Mass., 1991, p. 395.

This Page Intentionally Left Blank

8

Organic Semiconductors

André Brau and Jean-Pierre Farges

Université de Nice–Sophia Antipolis, Nice, France

I. BRIEF CLASSIFICATION OF ORGANIC CONDUCTORS

A. Introduction

The field of charge-transfer organic conductors has been the object of rapidly growing research activity for more than 30 years (for an early review, see, e.g., Ref. 1, and for more recent reviews, Refs. 2 and 3). It represents the most successful result of close and harmonious collaboration between chemists, crystallographers, and physicists during this time. This field takes advantage of the extreme versatility of modern organic chemistry, which makes it possible to construct, practically at will, an almost unlimited number of new conducting materials. This class of materials as a whole exhibits nonconventional physical properties, which include a great wealth of phase transitions. Thus they present considerable interest not only for pure fundamental research, but also for a lot of potential applications.

The challenge in this field has been to use the power of such molecular engineering to synthesize ever more and more conducting organic systems. This has led to what are currently called *organic metals* and *organic superconductors* in solid-state physics. The advancement in this field is still very fast, and the most significant results have been reported during the last 5 years (see, e.g., the proceedings of ICSM'88 [4], ICSM'90 [5] and

ICSM'92 [6], and also of ICCOSS IX [7], ICCOSS X [8], and ICCOSS XI [9]. One of the actual efforts of workers in this field is, of course, to stabilize the organic superconducting state at still higher and higher temperatures, in keen competition with workers engaged in the field of high- T_c superconducting oxides.

Finally, the field of organic conductors has interesting implications in biological and pharmacological sciences, providing useful concepts and models to any problem concerned with electrochemistry and charge-transfer complex formation [10,11] (see also Chapter 14).

B. Basic Properties

Charge-transfer organic conductors are molecular solids which are characterized, first, by remarkably high electrical conductivity. This gives clear evidence of the existence in these solids of conduction electrons which are significantly delocalized through the crystal lattice even if the electron mobilities are in general much smaller than in the more conventional inorganic conductors. In addition, a specific feature of the electronic system is its low dimensionality, which is due to the particular chainlike molecular architecture of organic conductors. The electronic system has in general either a quasi-one- or a quasi-two-dimensional character, and as a result, the electrical properties of the materials exhibit high anisotropy.

Knowledge of the true dimensionality of the electronic system in such solids is an important prerequisite to an understanding of their electrical properties, which is, however, not always evident. In the actual case of heavily doped conducting polymers, for instance, the dimensionality of the electronic system is still a question of debate, despite obvious chainlike structure, and most recent work is devoted to this important question [12].

The one-electron band structure of organic conductors is typical of molecular solids with a narrow bandwidth. In particular, the bandwidth W is significantly smaller than the on-site Coulomb repulsion U , in general (see also Chapter 2), so that the electrical properties of these conductors are strongly influenced by electron–electron interactions.

Another particular aspect of organic conductors is the extreme multiplicity of intra- and intermolecular vibrational modes to which the conduction electrons may couple. Then electron–phonon interactions are also of critical importance in the materials under the simple effect of such multiplicity. The electrical resistivity ρ is found to cover an extraordinary wide range of values, from exactly zero in superconductors below T_c , to more than $10^{10} \Omega \cdot \text{cm}$ in the most perfect insulators.

The diversity of phase transitions in this class of materials is worthy of mention. These transitions may result from either electronic or purely

structural instabilities, and they may be induced by either temperature or pressure variations. They have already been introduced, from a formal point of view, in Chapter 2, and they are discussed at length, in the case of specific materials, in the present and subsequent chapters.

On the basis of the electrical properties, it is advisable to divide these transitions into three general classes and to consider these classes in the following order: semiconductor-to-semiconductor transitions in the present chapter, and metal-to-semiconductor and metal-to-superconductor transitions in Chapters 9 and 10. The case of polymers is treated separately in Chapters 11, 12, and 13.

II. DEFINITION OF THE NONMETALLIC STATE

A. Existence of an Energy Gap

The nonmetallic state is a direct consequence of the existence of an energy gap E_G at the Fermi level in the electronic excitation spectrum [2,13]. Roughly speaking, in a simple metal, the resistivity ρ increases almost linearly with temperature T . In a nonmetal it is the conductivity σ ($= 1/\rho$) that usually increases with T , according to an activation law of the form $\sigma = \sigma_0 \exp(-\Delta/T)$. Note that in this expression the activation energy Δ is measured in units of kelvin. In a one-electron band description, the energy gap, which is $E_G = 2\Delta$, represents the energy required to create a *pair* of carriers, that is, to promote one electron to the conduction band and, simultaneously, to leave one hole in the valence band [13]. This gap may have a pure structural origin. It may also result from an electronic Peierls distortion, or from electron–electron interactions, as in a Mott–Hubbard localization, or, at least in part, from electron–ion interactions [2,14].

By definition, the electrical conductivity σ due to a concentration n of carriers, all with the (mean) mobility μ , is given by: $\sigma = n|e|\mu$, e being the electronic charge, and in a simple semiconductor, it is in fact the activation of n ($= n_{\text{electrons}} = n_{\text{holes}}$) that produces the activation of σ ($= \sigma_{\text{electrons}} + \sigma_{\text{holes}}$) [13].

The distinction between semiconductors and insulators is only a question of *orders* of magnitude. On the basis of both the energy gap E_G and the electrical conductivity σ , the insulating state will be defined rather arbitrarily in the present chapter by $E_G > 0.5$ to 1 eV and $\sigma < 10^{-3}$ to 10^{-4} S/cm (or $\Omega^{-1} \text{ cm}^{-1}$) at room temperature. The distinction between metals and nonmetals is apparently clear: There is *no* energy gap in the electronic energy spectrum of metals. However, we shall see below that the use of such a criterion is not always simple in practice.

B. Semiconductor-to-Semiconductor Transition

Let us consider, as a first case, a simple semiconductor with a T -dependent energy gap $2\Delta(T)$ but a T -independent mobility $\mu = \mu_0$. Then

$$\sigma(T) = n(T)|e|\mu_0 = \sigma_0 \exp\left[-\frac{\Delta(T)}{T}\right]$$

with $\sigma_0 = \text{constant} = n_0|e|\mu_0$. A plot of the experimental σ data in the appropriate form $\ln\sigma = f(T^{-1})$ then has in general a negative T -dependent slope: $-s(T)$, s being measured here, like Δ , in units of kelvin. One gets in this way the simple differential equation

$$s(T) = \Delta(T) - T\frac{d\Delta}{dT} \quad \text{or} \quad \frac{ds}{dT} = -T\frac{d^2\Delta}{dT^2}$$

by which it is possible to deduce the unknown gap function $2\Delta(T)$ from the experimental slope function $s(T)$ [15]. In particular, for any T range over which Δ is constant, s is also constant and equal to Δ .

Let us assume further that the material undergoes a simple semiconductor-to-semiconductor transition from a state with $\Delta = \text{constant} = \Delta_0$ for $T < T_1$ to a state with $\Delta = \text{constant} = \Delta_\infty < \Delta_0$ for $T > T_2$, and that Δ decreases continuously between T_1 and T_2 from its low- T to high- T values, as shown in Fig. 1. In such a case it is conventional to define the transition temperature T_0 at the inflection point of $\Delta(T)$. Obviously, $T_1 < T_0 < T_2$.

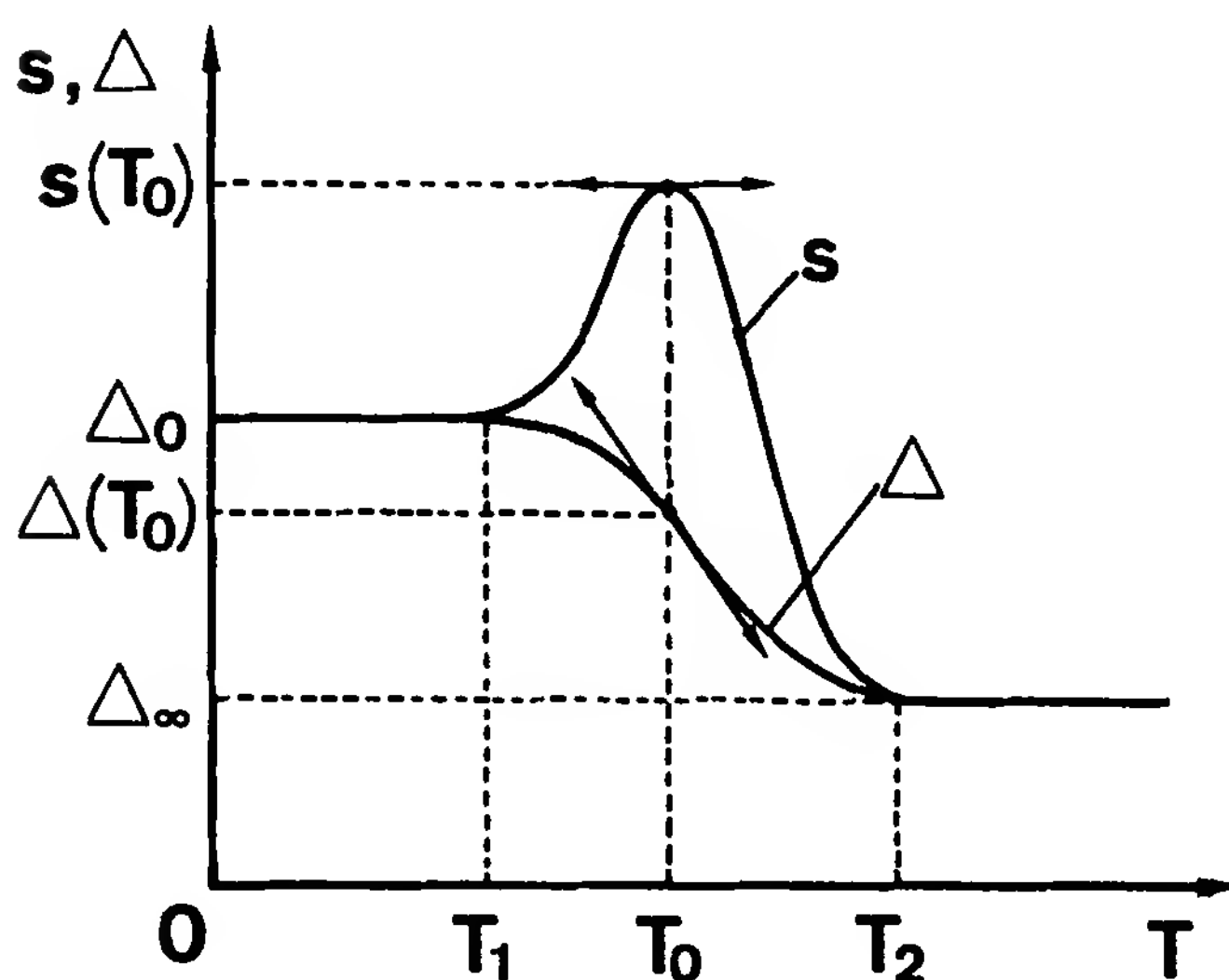


Figure 1 Comparison of the T dependences of the slope function, s , and of the half-gap function, Δ , in the case of a simple semiconductor-to-semiconductor transition (see the text).

It is instructive to compare the T -dependences of s and Δ in this elementary case. The s function is represented schematically together with the Δ function in Fig. 1. One has simply, for $T < T_1$, $s = \Delta = \Delta_0$, and for $T > T_2$, $s = \Delta = \Delta_\infty$. At $T = T_0$, $[d^2\Delta/dT^2] = 0$, $[ds/dT] = 0$, and then s is maximum at the transition [15]. In consequence, when a material presents a well-defined semiconducting state with a constant energy gap 2Δ at low temperature, any subsequent increase in the slope function s upon heating is in fact the indication of a decrease in this gap. These opposite behaviors of s and Δ have sometimes been the source of misleading interpretations in the past.

It is a useful way, in practice, to look for phase transitions in organic conductors by means of the electrical conductivity data. Thus when a “peak” is detected at some temperature in the derivative of the slope function $s(T)$, it is a reasonable indication of the existence of a transition at this temperature. The width of this peak in temperature is also an indication of the width of the transition.

C. Metal-Like Semiconductor

In this second example, we consider a semiconducting material with a T -independent energy gap $2\Delta_0$ but a T -dependent mobility $\mu(T)$. This interesting case has been discussed thoroughly by Epstein et al. [16]. If a standard power law of the form $T^{-\alpha}$, is assumed for $\mu(T)$, in addition to the normal activation law $\exp(-\Delta_0/T)$ for $n(T)$, the resulting conductivity

$$\sigma(T) = n(T)|e|\mu(T)$$

presents in consequence a maximum at a temperature T_m given by $T_m = \Delta_0/\alpha$.

For low enough values of Δ_0 and/or high enough values of α , T_m may well be below room temperature, so that the T -dependence of σ may resemble in this case that of a semiconductor below T_m and that of a metal above T_m (Fig. 2) [16].

Of course, real systems may have a more complex behavior than that shown by the ideal models discussed here and in Section II.B. Some specific applications of these models are considered in Section III.B.1.

III. MATERIALS WITH SEMICONDUCTING BEHAVIOR AT ROOM TEMPERATURE

A. Two Specific Examples: MEM(TCNQ)₂ and TEA(TCNQ)₂

1. General Aspects

The two materials MEM(TCNQ)₂ and TEA(TCNQ)₂ (MEM⁺ = *N*-methyl-*N*-ethylmorpholinium, TEA⁺ = triethylammonium) are among the best

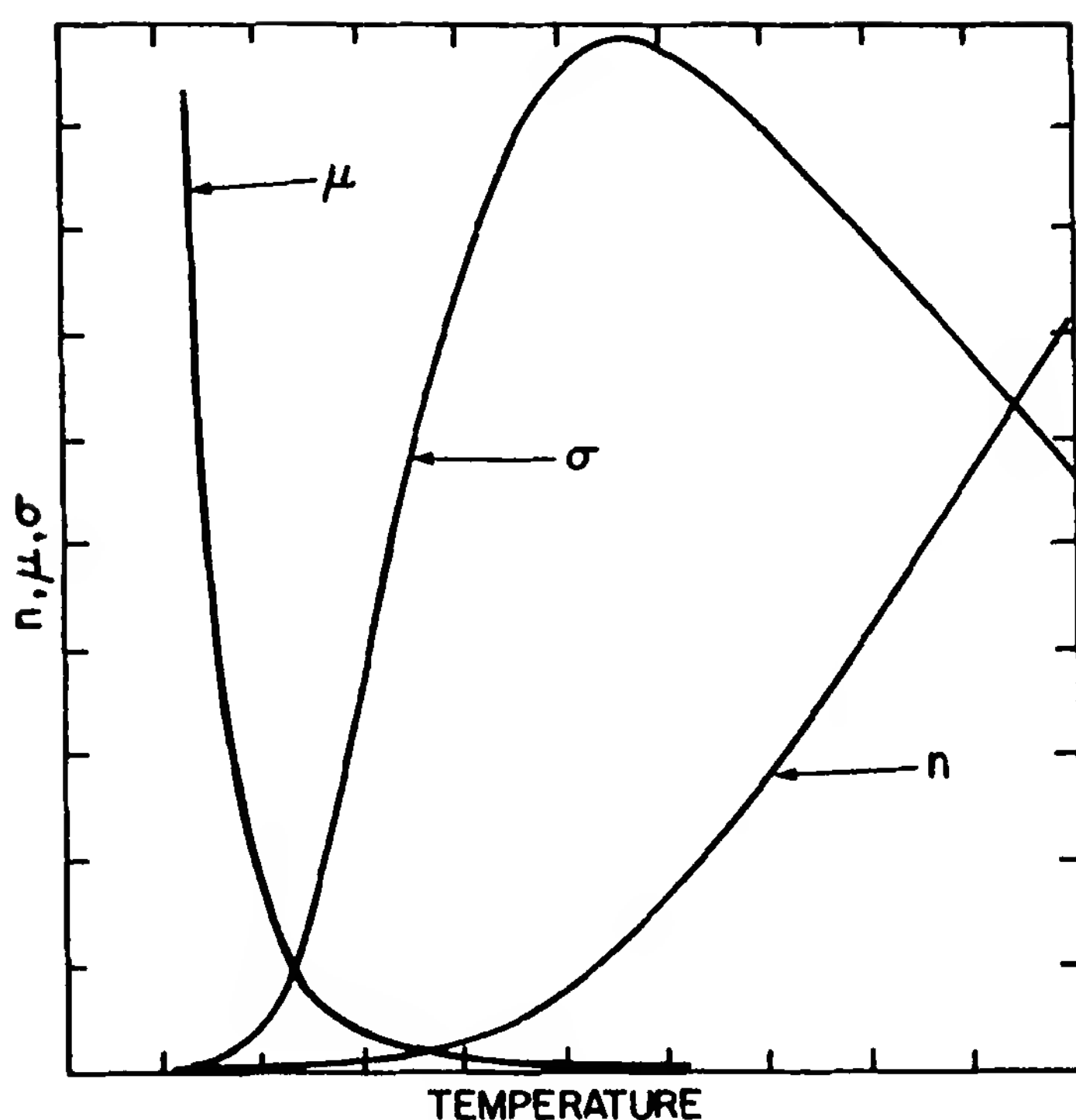
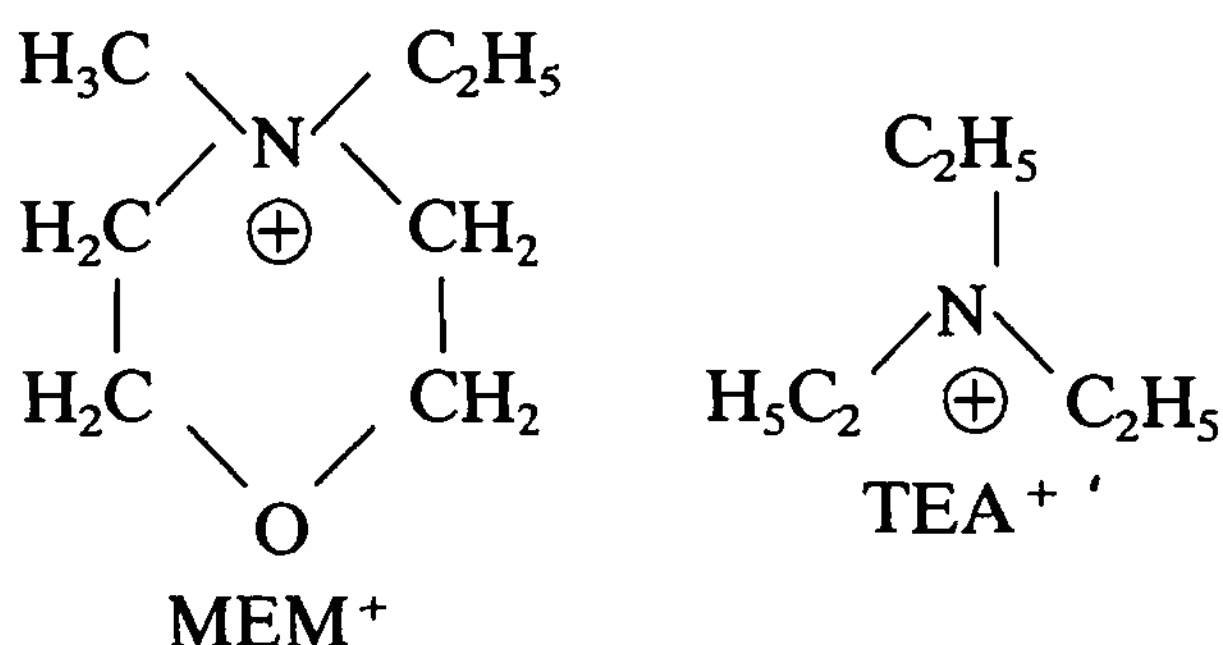


Figure 2 Schematic temperature dependence of charge-carrier concentration: $n \propto e^{-\Delta 0/T}$, mobility $\mu \propto T^{-\alpha}$, and conductivity $\sigma = n|e|\mu$. (After Ref. 16.)

representatives of the wide class of quasi-one-dimensional organic semiconductors, as they have been investigated quite extensively. They present strong analogies, but also strong differences, in their crystal structures as well as in their physical properties. For a comparative description of these two materials, the reader is referred to several review papers devoted to the two materials (see, e.g., Refs. 17 to 20). Here we present only the most recent results and current views of the two materials.



MEM(TCNQ)₂ and TEA(TCNQ)₂ are two 1:2 TCNQ salts, with one MEM or TEA donor molecule per two TCNQ acceptor molecules, in which there is a complete charge transfer from the donor as indicated by the formulas MEM⁺(TCNQ)₂⁻ and TEA⁺(TCNQ)₂⁻. In consequence, the mean

charge ρ per TCNQ molecule is formally one-half of the electronic charge e , or $\rho = \frac{1}{2}$, in units of e , in both of them.

One may recall here that a general criterion for having an organic salt with appreciable semiconducting or metallic electrical conductivity is that $\rho < 1$. However, when $\rho = 1$, as in 1:1 TCNQ salts (i.e., one donor molecule per acceptor molecule) with *complete* charge transfer, the insulating state always prevails [2,3] (see also Section IV).

Crystallographic data [21–23] indicate that for TEA(TCNQ)₂, there are two molecular formulas per unit cell, or $Z = 2$. In the crystal structure, segregated parallel TCNQ chains are built up from identical A–B dimer units according to the tetramerized sequence



The space group is $P\bar{1}$ and two adjacent dimers are related through an inversion center (Fig. 3).

Adjacent monomers A and B are crystallographically inequivalent along the zigzag-like chains, and this is made clear in the figure by considering only their nearest neighbors, although the cations TEA⁺ contribute most significantly to the nonequivalence. There are in general two different interdimer distances, $d(\text{A-A})$ and $d(\text{B-B})$, as well as two different geometrical overlaps. At any temperature, the intradimer distance, $d(\text{A-B})$,

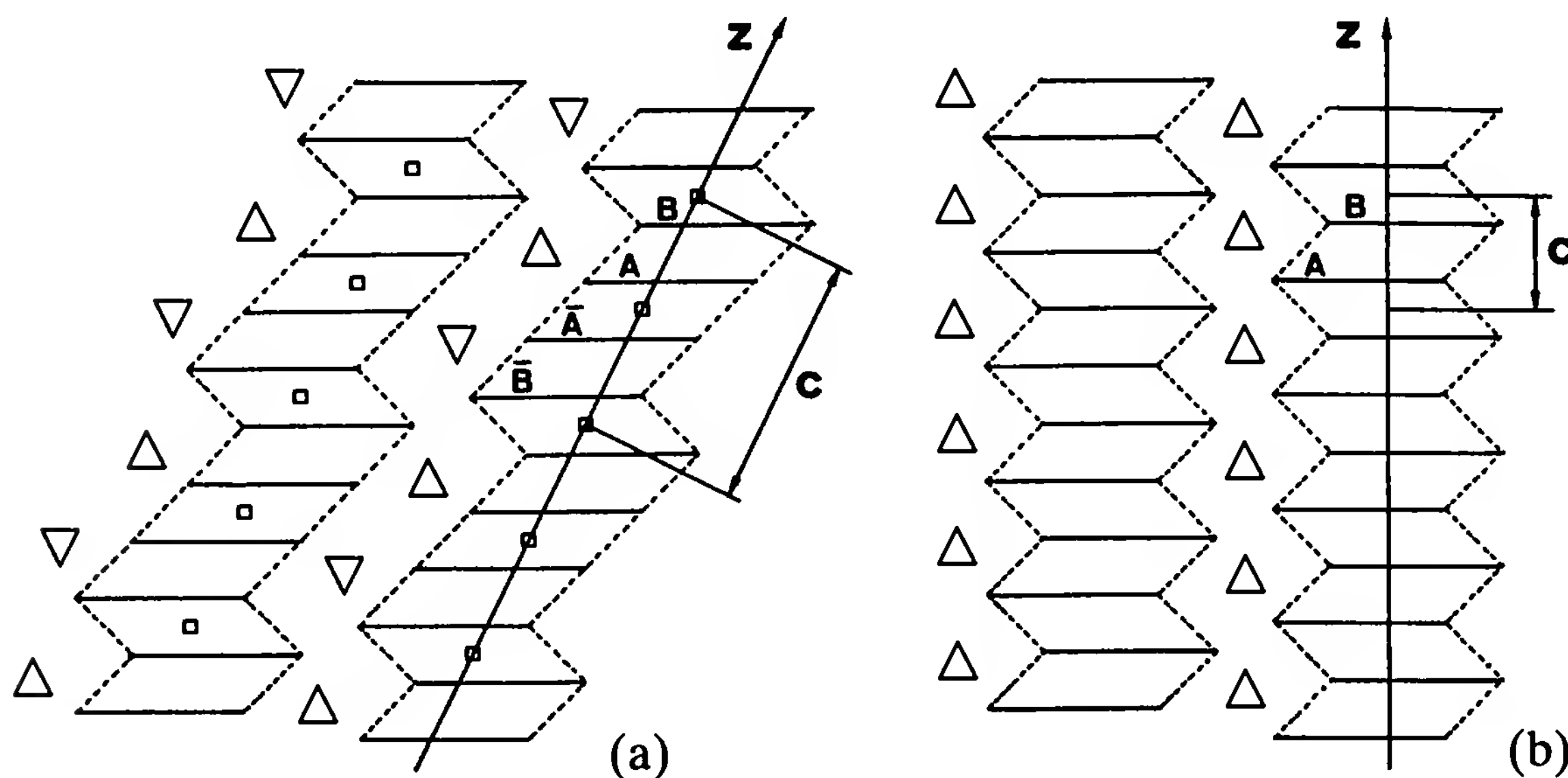


Figure 3 Schematic molecular arrangements in the crystal structures of (a) TEA(TCNQ)₂ (after Ref. 22) and (b) MEM(TCNQ)₂ (after Ref. 24). —, TCNQ monomer; Δ , asymmetric cation; \square , inversion center. Note the lateral shifts of TCNQ monomers that occur in the chains with successive signs: $- + + + - + + + -$ in TEA(TCNQ)₂, and $- + - + - + - + -$ in MEM(TCNQ)₂.

is the shortest one in the sequence and also the intradimer geometrical overlap is optimal.

For $\text{MEM}(\text{TCNQ})_2$ [24,25], there is only one molecular formula per unit cell, or $Z = 1$. In consequence, the segregated TCNQ chains in this salt are built up from identical A–B dimers according to the simple dimerized sequence



The space group is P1 and two adjacent monomers (A,B) are inequivalent in the sequence (Fig. 3). This nonequivalence is the consequence of an asymmetric neighboring cation arrangement.

Then, each TCNQ chain can be viewed as a sequence of *parallel* (A–B A–B) dimers in the case of $\text{MEM}(\text{TCNQ})_2$, and a sequence of *anti-parallel* (A–B B–A) dimers in the case of $\text{TEA}(\text{TCNQ})_2$. This means in particular that according to crystal symmetry, dimerization is intrinsically present in the first salt, and tetramerization is intrinsically present in the second, irrespective of temperature.

More precisely, a tetramerized chain in $\text{TEA}(\text{TCNQ})_2$ may be regarded as resulting from a dimerized one in which one dimer in two is shifted by a length Δ' parallel to the chain axis z and by a length δ' perpendicular to z (Fig. 4) [15,22]. The length Δ' is then found to follow nicely the thermal expansion of the chain, which is the indication of a constant longitudinal distortion. On the contrary, the length δ' , which is a measure of the transverse chain distortion, is found to increase significantly as T decreases (see Section III.A.2) [15].

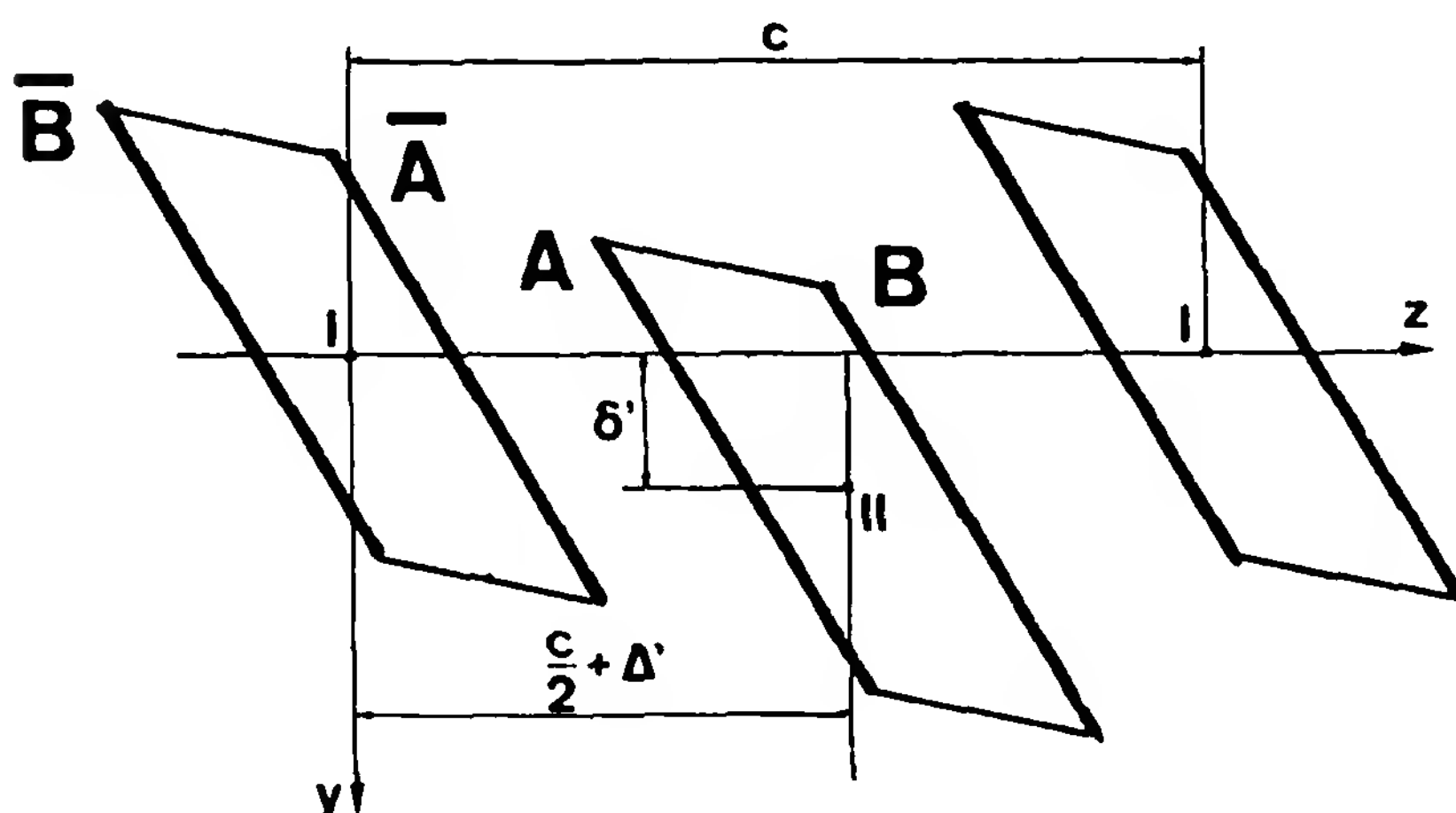


Figure 4 Formation of a tetramerized chain: definition of the two distortion parameters $\Delta' \parallel z$ and $\delta' \perp z$, z being the chain axis, for a simple dimerized chain: $\Delta' = \delta' = 0$ (see also Fig. 3). (After Ref. 15.)

The electrical properties of TCNQ salts are clearly related to the excess electrons provided to the TCNQ chains by the cations. It is a general property of these salts that the intrachain coupling between TCNQ molecules is relatively strong, owing to a quite favorable plane-to-plane close stacking of the molecules, so as to make the electronic system significantly delocalized in the chain direction, at least as far as $\rho < 1$. The electrical properties then reflect the ability of the electrons to move in the easiest direction of the chains, z , as well as in transverse directions, and they exhibit in general a high degree of anisotropy.

Within a one-electron description (i.e., $U = 0$, U being the on-site Coulomb repulsion [2,3], regular conducting TCNQ chains with $\rho = \frac{1}{2}$ electron per molecular site correspond to quarter-filled electronic bands. Consequently, the Fermi wave "vector" is in this case $k_F = \pi/4d$, d being the spacing parameter between adjacent sites, and the chains are metallic. This is the case, for instance, for MEM(TCNQ)₂ and TEA(TCNQ)₂. Note that in these two salts the cations MEM⁺ and TEA⁺ are diamagnetic and do not participate in electrical conduction.

When electron–phonon interactions are taken into account, the regular conducting chains are found to be unstable; they undergo a low-temperature phase transition which results in both a modulation of the chains and the opening of an energy gap at the Fermi level. This is the so-called Peierls transition, at $T = T_P$, a second-order symmetry-breaking transition that is characteristic of the quasi-one-dimensional conductors [2,3].

It may be recalled here that the Peierls transition is basically a one-dimensional effect coming from the divergent response in one dimension of the electron system at $2k_F$. However, because of the fluctuations, any transition is possible only at 0 K in one dimension and not at the temperature T_{MF} predicted by mean-field theory. It is then an effect of the (small) interchain coupling to restore a transition temperature lower than T_{MF} but finite. When the interchain coupling becomes too large (under high pressure, for instance) the one-dimensional character is lost and the Peierls transition is suppressed [2,3].

When electron–electron interactions are subsequently introduced (i.e., $U \neq 0$), $2k_F$ as well as $4k_F$ modulations are in fact found to occur in the two limits $U/t \ll 1$ and $U/t \gg 1$, respectively, t being the transfer integral in the chains [2], with corresponding periods:

$$\lambda(q) = \frac{2\pi}{q} \rightarrow \lambda(2k_F) = \frac{2\pi}{2k_F} = 4d \quad \lambda(4k_F) = \frac{2\pi}{4k_F} = 2d$$

Thus a $2k_F$ modulation results into a tetramerization of the conducting chains, whereas a $4k_F$ modulation results into a dimerization. These dis-

tinctive features are shown schematically in Fig. 5 for the two cases of interest: $\rho = \frac{1}{2}$ and $\rho = 1$.

All the foregoing aspects are also well developed in Chapter 2.

2. Tetramerization and Electronic Gap in TEA(TCNQ)₂

From a very detailed x-ray study at 110, 173, 234, 295, and 345 K [22] as well as from a neutron study at 40 K [21], the chain structure in TEA(TCNQ)₂ has been shown to evolve continuously from weak tetramerization at high temperature to strong tetramerization at low temperature, through a rather wide transition centered at about 210 K. This transition, which occurs with no symmetry breaking, may be considered as a reminiscent second-order $2k_F$ transition. There is also an underlying chain dimerization that is kept *unchanged* during the temperature variation [15].

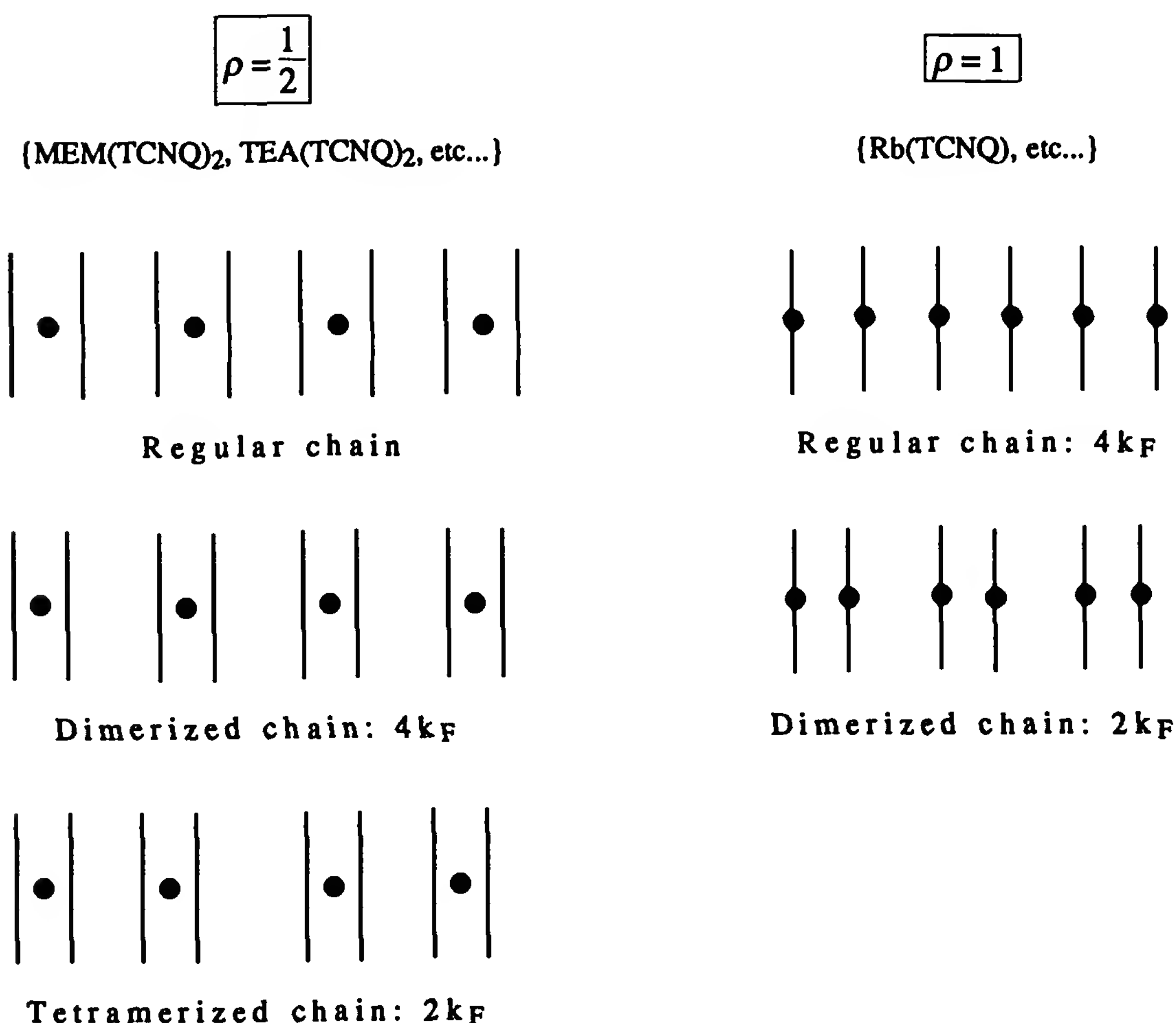


Figure 5 Schematic representation of $2k_F$ and $4k_F$ distortions in a regular conducting chain for the two commensurate cases: $\rho = \frac{1}{2}$ and $\rho = 1$.

Some structural parameters are more sensitive than others to this transition. A good example is presented in Fig. 6. Instead of the cell parameter a defined by Filhol et al. [21,22], it is equivalent to choose the new parameter a' defined from parameters a and b , as shown in the figure inset. It seems that a' is an even better choice, as one obtains $a' < a$ for any T . The T dependence of a (as well as that of the other cell parameters: b , c , α , β , γ) has been investigated carefully by Filhol and Thomas [22] and Filhol and Grassi (unpublished results). There is a clear anomaly in the behavior of $a(T)$ at 210 K, but the derivative da/dT always remains positive [22]. The corresponding behavior for $a'(T)$, as it is deduced from the data of Filhol et al., is shown in Fig. 6. One sees that the derivative da'/dT now has opposite signs above and below 210 K, being positive above and neg-

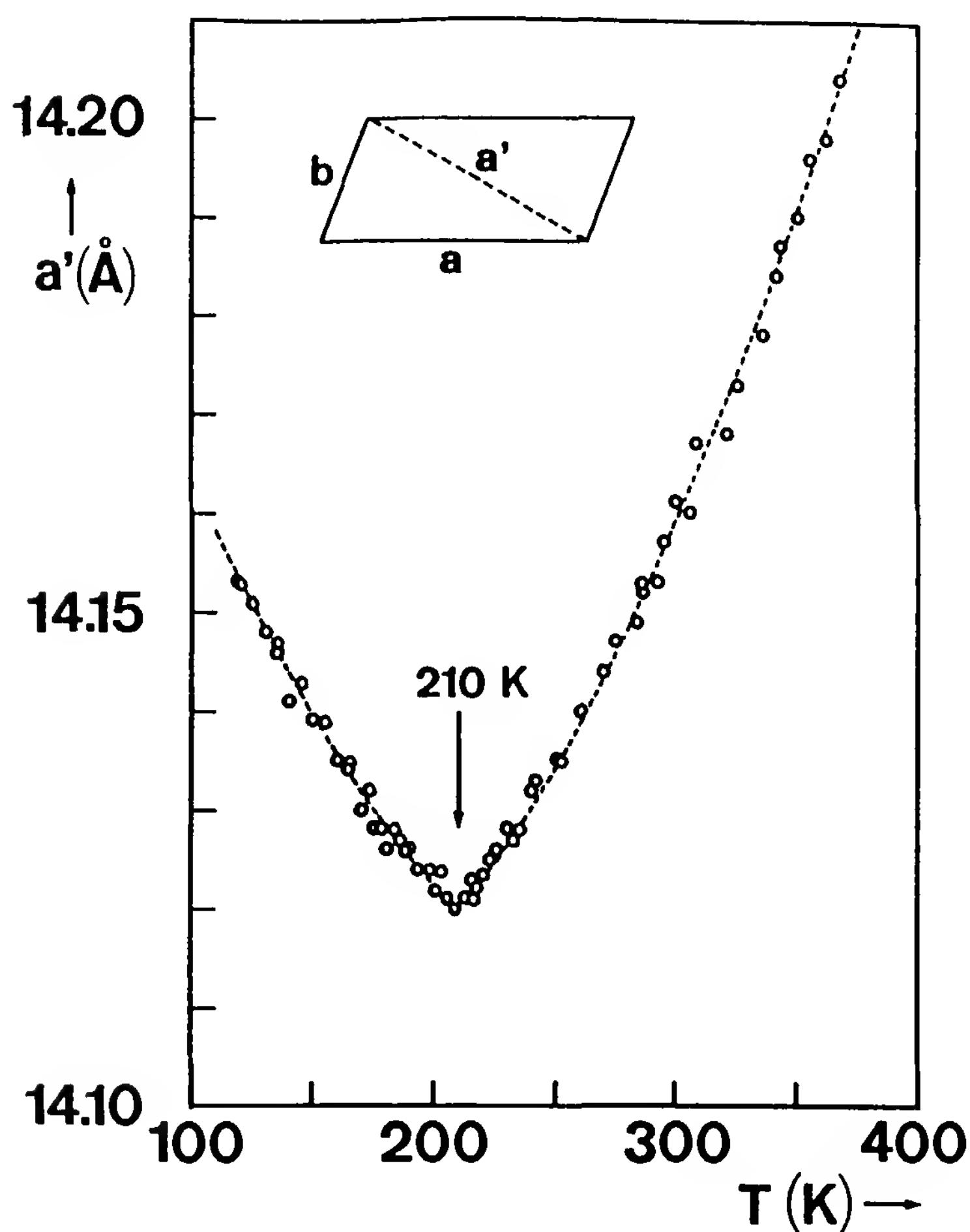


Figure 6 Temperature dependence of the (new) cell parameter a' defined in the text for TEA(TCNQ)₂. (These data are recalculated from those of Ref. 22 and the unpublished results of A. Filhol and H. Grassi.) Inset: Geometrical relation between a' and the cell parameters a and b chosen in Ref. 22.

ative below, which makes the effect of the transition at 210 K much more evident on $a'(T)$ than on $a(T)$.

On a purely structural basis, this view is also well supported by the existence of a short direct link between TCNQ molecules in the a' rather than in the a direction (see Fig. 7) [23].

The chain-axis electrical conductivity $\sigma_{\parallel}(T)$ of $\text{TEA}(\text{TCNQ})_2$ exhibits a continuous semiconducting-like behavior up to the highest temperature investigated (350 K). The energy gap $E_G = 2\Delta$, however, is not constant and varies markedly with T . Discontinuities of various heights have also been reported for $\sigma_{\parallel}(T)$, in the vicinity of 210 K, but not at well-defined temperatures, only on cooling and only for fine crystalline needles, not for larger crystals [26]. Although σ_{\parallel} may jump in this way by two orders of magnitude, the initial room-temperature value is recovered accurately on completion of the thermal cycles.

The T dependence of the half-gap Δ is found to be very well correlated with the T dependence of the structural tetramerization parameter δ' , whose definition, given in Ref. 15, has been recalled in Fig. 4. The functions $\Delta(T)$, normalized to its 0 K value, and $\delta'(T)$ are shown in Fig. 8, curve a, and Fig. 9, respectively. $\Delta(T)$ has been deduced [15,27] from the slope $-s(T)$ of a plot: $\ln \sigma_{\parallel} = f(T^{-1})$, as indicated in Section II.B, and $\delta'(T)$ from a subsequent detailed analysis [15] of the crystallographic data of Filhol and Thomas [22]. The two functions decrease as T increases, their variations being maximum at $T_0 \cong 210$ K [15,28]. Curve b, the characteristic

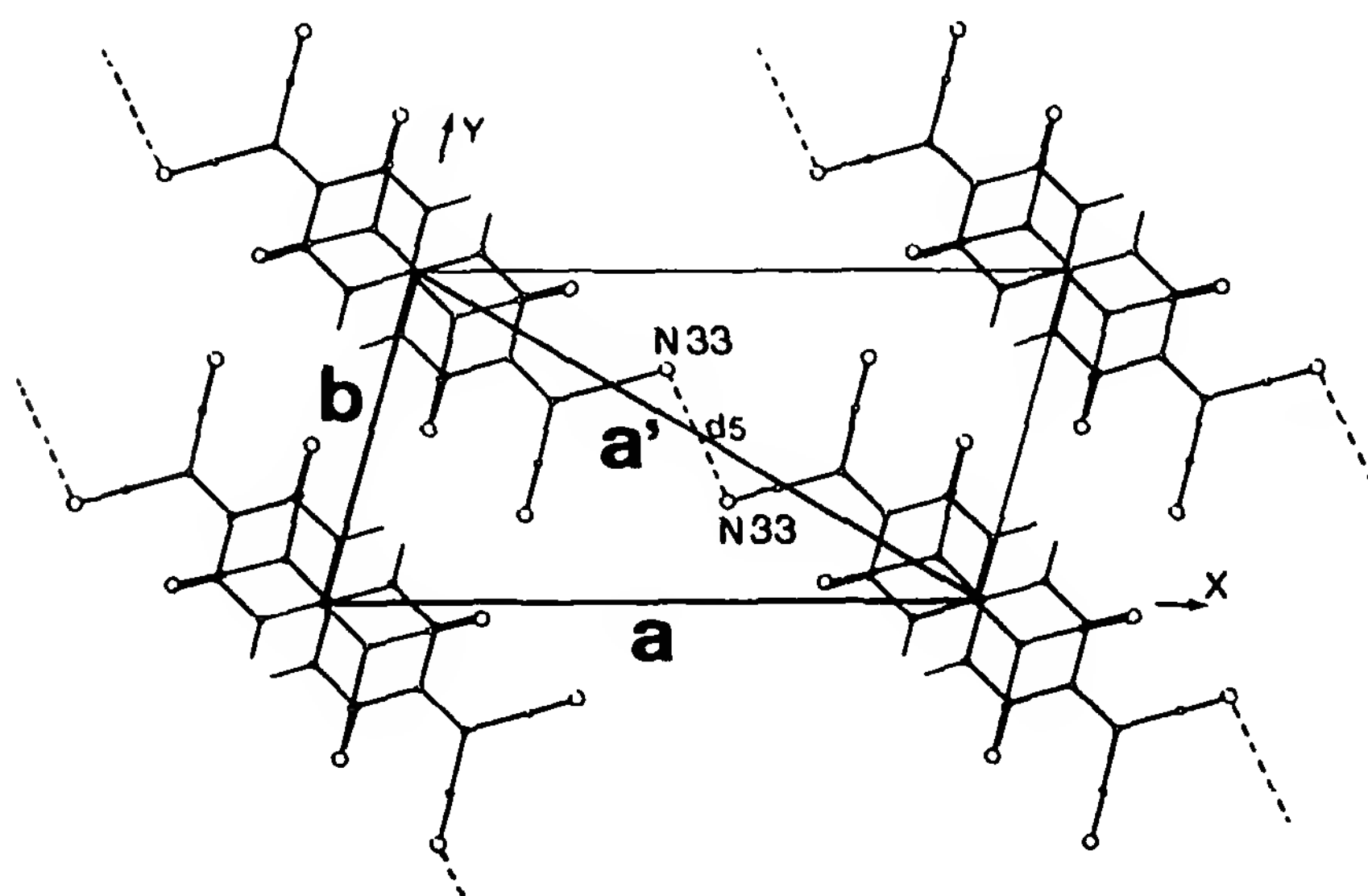


Figure 7 Existence of short links between adjacent TCNQ molecules in the a' rather than in the a direction (see also Fig. 6). Short links which also exist between adjacent molecules in the b direction are not shown in this figure. (From Ref. 23.)

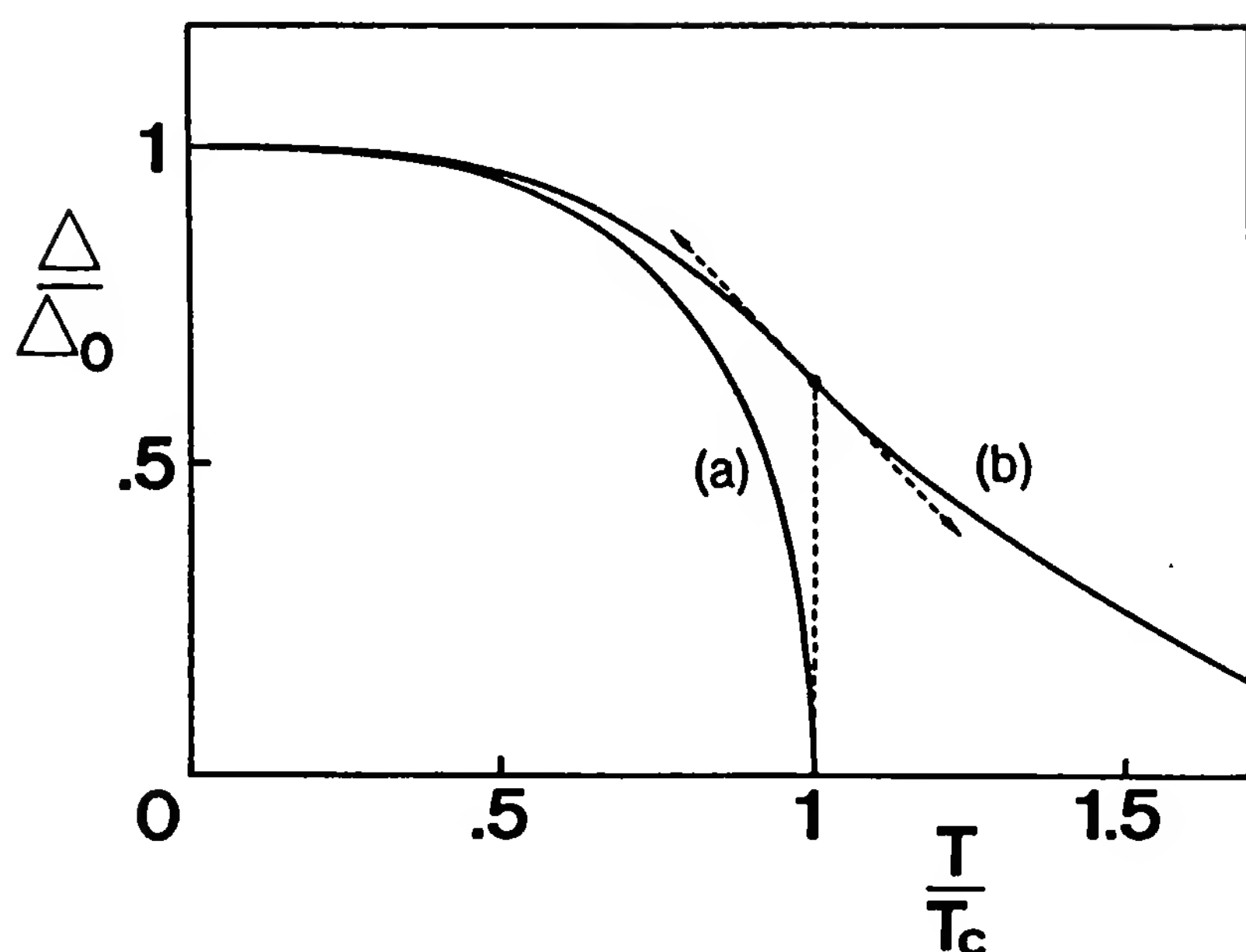


Figure 8 Temperature dependence of (a) BCS-like Peierls gap Δ_p [29] and (b) integrated half-gap Δ of TEA(TCNQ)₂ [15]. The gaps are normalized to their 0 K values and the temperatures to $T_c = 210$ K.

T dependence of the BCS-like Peierls half-gap function when the Peierls temperature is $T_c = T_0 = 210$ K is reproduced for comparison in Fig. 8 (see, e.g., Ref. 29).

Numerical values for the electrical energy gap of TEA(TCNQ)₂ are at 300 K, $2\Delta = 905$ K (78 meV); at 210 K, $2\Delta = 1926$ K (166 meV); and below 60 K, $2\Delta = 2\Delta_0 = 3020$ K (260 meV) [15,27].

The electrical conductivity of TEA(TCNQ)₂ is fairly large: $\sigma_{\parallel} = 7$ S/cm at 300 K. It has a quite pronounced one-dimensional character, as proved by anisotropic ratios $\sigma_{\parallel}/\sigma_{\perp}$ as large as 164 and 2800 obtained for two orthogonal transverse directions at 300 K [20,27].

The considerable electrical anisotropy of this salt is made still more evident on the room-temperature polarized infrared reflection spectra [30] (see also Chapter 6 and Fig. 1 of this chapter). In addition, these reflection spectra give a remarkably clear information on the existence of strong coupling between the quasi-one-dimensional electronic system and the symmetric a_g vibrational modes of the TCNQ molecules. More precisely, under the effect of this coupling, these particular modes, which are normally Raman active but infrared nonactive, acquire an anomalous intense infrared activity together with an anomalous polarization [20,30,31].

An independent information on the nature of the gap in TEA(TCNQ)₂ has been obtained by means of Raman spectroscopy analysis, which supports a description in terms of $2k_F$ Peierls distortion [32]. It was considered

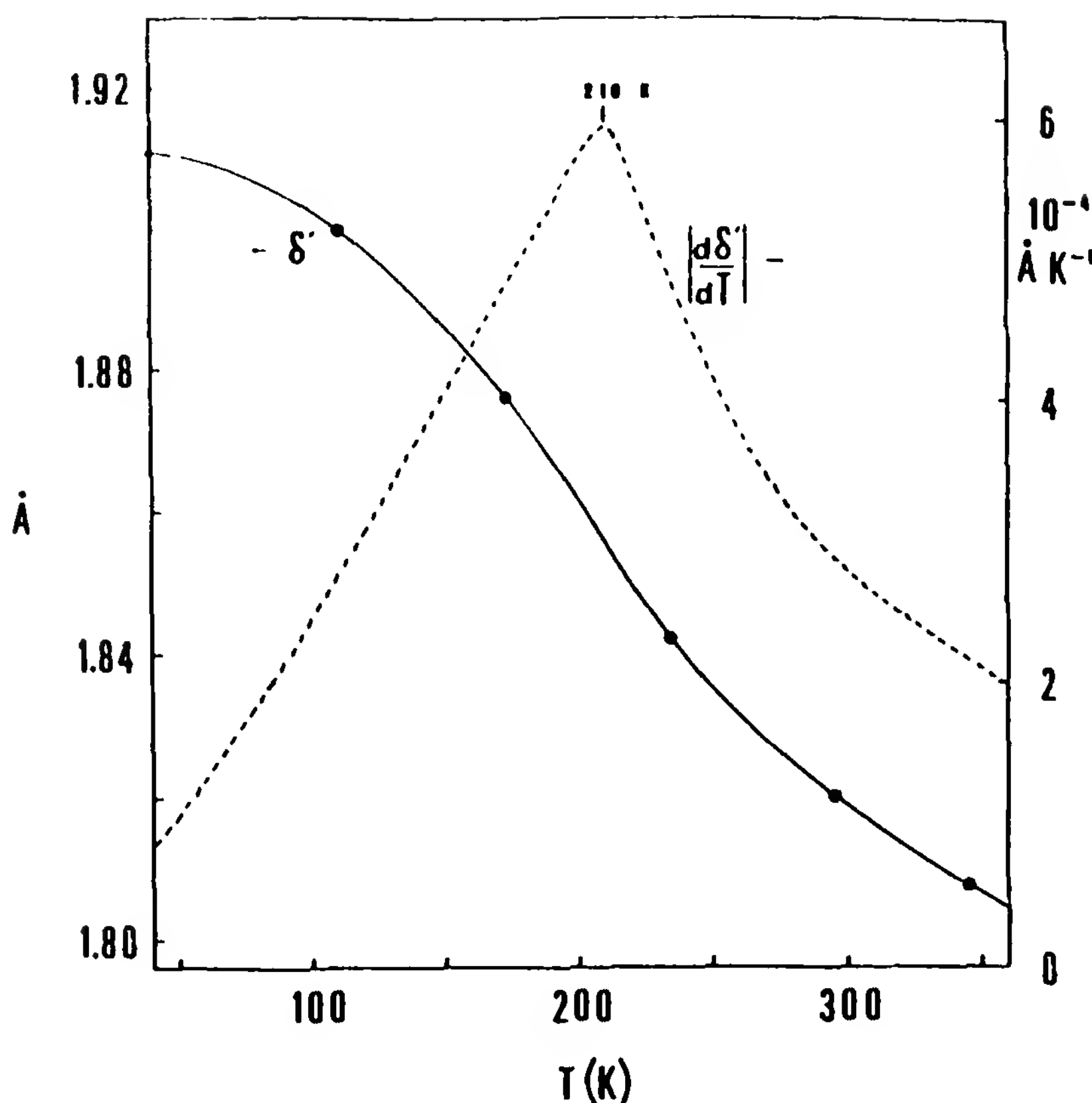


Figure 9 Temperature dependence of the transverse tetramerization parameter δ' defined in Fig. 4 (solid line) and of the corresponding derivative $|d\delta'/dT|$ (dashed line) [15]. Dots represent the values of δ' calculated from the experimental data of Ref. 22.

that the coupling constants of low-frequency vibrational Raman lines should reflect in this case the T dependence of the Peierls gap, and five Raman lines in the spectrum of $\text{TEA}(\text{TCNQ})_2$ have then been investigated between 4 and 300 K and their coupling constants calculated. The results are reported on a normalized scale, as a function of T , in Fig. 10 [32]. The overall T dependence of the half-gap function obtained in this way is very similar to that obtained by means of the electrical conductivity data and shown in Fig. 8. Such agreement then supports the assumption that the carrier mobility in the material is only weakly T -dependent.

An evaluation of the gap value at 300 K was also deduced from the optical data in Ref. 32 on the assumption that the peaks in the infrared conductivity $\sigma(\omega)$ [30] were rather resonances below, roughly, 1000 cm^{-1} but antiresonances above. This is then indicative of an energy gap: $E_G = 2\Delta \approx 1000 \text{ cm}^{-1}$ at 300 K, or $2\Delta \approx 120 \text{ meV}$, a crude value that is not

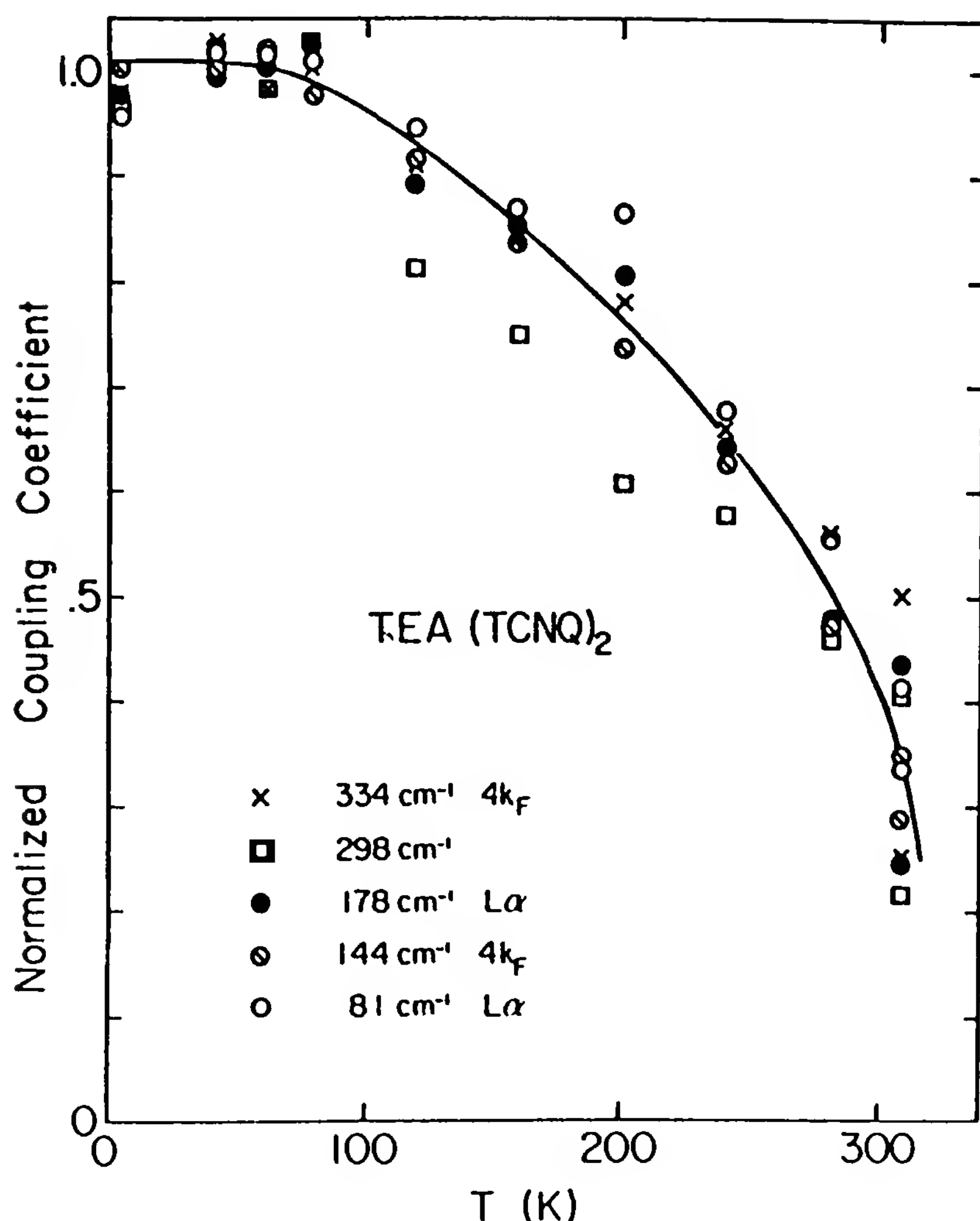


Figure 10 Normalized coupling coefficients for the different low-frequency Raman modes versus temperature. The “universal curve” given approximately by the full line represents a measure of the order parameter of the Peierls transition. (After Ref. 32.)

very far from that of 78 meV deduced above from the electrical conductivity data.

The phonon spectrum of protonated and of deuterated TEA(TCNQ)₂ has been measured by Carneiro et al. [33] and by Pedersen et al. [34,35], respectively. A 2k_F-like anomaly seems to be observed in both cases, together with a zone-boundary gap, at 80 K, although the anomaly seems to be weaker for the deuterated compound [35].

The simple classical theory of a tetramerized chain with four different force constants was found to be unable to describe this phonon spectrum, however [36]. This is an indication that the conduction electrons could be involved in formation of the chain distortion.

On the assumption that the electron correlations are relatively weak in the material, the model of Schulz [37], which takes into account the interaction between the conduction electrons and one acoustic phonon branch, has then been used to calculate the longitudinal phonon spectrum. In the model, two new optical modes are coming up at $2k_F$, corresponding to excitations in the phase and in the amplitude of the distortion. However, the agreement was still very poor in this case, the renormalization of the phase mode being considerably larger in the model than experimentally observed [34].

It is clear from infrared and Raman measurements [20,31,33] (see also above) that the interaction between the electrons and the symmetric vibrational modes of TCNQ is in fact so efficient that a significant part of the electronic gap is actually attributable to static molecular distortions [31]. The most important consequence is that the lattice is then less distorted than one would expect from the magnitude of the electronic gap. When such molecular distortions are correctly included in the model, as an external potential of period $2k_F$, a reasonably good agreement is then obtained with the experimental data for both protonated and deuterated TEA(TCNQ)₂ [35,36].

3. Estimation of Site Charge Distribution in TEA(TCNQ)₂

The distribution of the electrical charge on the sites of the conducting chains is an information of importance to understand the electrical properties of the material. The values of the fractional electronic charges q_A and q_B ($= 1 - q_A$) on the two nonequivalent TCNQ monomers, A and B (see Fig. 3) of the conducting TCNQ chains of TEA(TCNQ)₂, are also given by Filhol and Thomas in their paper [22]. These values are estimated at 110, 173, 234, 295, and 345 K, from the internal bond lengths of the two independent monomers A and B, separately, according to a method suggested by Flandrois and Chasseau [38] (see also Chapter 5). The following averages over the considered temperatures are thereby obtained: $\overline{q_A} = 0.60e$ and $\overline{q_B} = 0.40e$, which clearly show a significant difference [22].

In addition, a closer inspection of all the reported individual values reveals that despite their inherent limited accuracy, they in fact do not vary in some erratic manner from one temperature to the other [39]. On the contrary, they are found to vary with an unexpected regularity and according to a very simple law. This fact should not be entirely fortuitous. The experimental law to which they obey is $q_A = (\frac{1}{2} + T'/T)e$ and $q_B = (\frac{1}{2} - T'/T)e$, with $T' = 24$ K. Although the physical meaning of T' is still not entirely clear, this law also gives the remarkable limit $q_A = q_B = \frac{1}{2}e = \rho e$ when $T \rightarrow \infty$, which is worth of mention [39].

4. Magnetic Properties of TEA(TCNQ)₂

The magnetic susceptibility $\chi(T)$ of TEA(TCNQ)₂ has been the object of several experimental studies in the past. This property has been “revisited” in great detail by Oostra in his Ph.D. thesis, which provides the most recent and accurate set of data on this salt [40]. In view of the tetradic chain structure of TEA(TCNQ)₂, an alternating antiferromagnetic chain of localized $\frac{1}{2}$ spins seems to be a reasonable model to account for the magnetic properties of this salt. In this case, if the spin alternation is strong enough (i.e., if the intratetrad exchange energy J_1 is much larger than the intertetrad exchange energy J_2), a standard singlet–triplet law with a single energy J_1 (or $J_2 = 0$) can be used to fit the data. The singlet–triplet model has a nonmagnetic ground state with all the $\frac{1}{2}$ spins coupled into $S = 0$ pairs.

Oostra showed that such a fit is not good unless J_1 is allowed to change significantly with T . The relative variation of J_1 which is obtained from such a fit has in fact opposite signs above and below 200 K. This variation is about $-1.2 \times 10^{-3} \text{ K}^{-1}$ on cooling from 300 K to 210 K, and then about $+0.4 \times 10^{-3} \text{ K}^{-1}$ on cooling from 190 to 110 K. J_1 attains a maximum at about 200 K with a value of $J_1 = 230 \text{ K}$. At 290 K, one also has $J_1 = 208 \text{ K}$ and $\chi = 0.72 \times 10^{-3} \text{ emu/mol}$ [40].

After Oostra, the condition $J_1 \gg J_2$ may not be fulfilled in the case of TEA(TCNQ)₂; however, the most likely explanation for the reported behavior of $\chi(T)$ is that the cation disorder plays an important role. Oostra observed, in fact, that a noticeable excess magnetic susceptibility could be produced below 210 K, on rapid cooling (see Fig. 11) and he attributed this excess to an effect of the TEA cations, which did not have the time to order completely in the crystal [40].

5. Electrical and Magnetic Properties of MEM(TCNQ)₂

Contrary to TEA(TCNQ)₂, the chain structure in MEM(TCNQ)₂ [24,25] is found to go discontinuously from a very weak dimerization above 335 K to a strong dimerization below 335 K. This is a first-order transition which is reminiscent here of a $4k_F$ transition, although there is still no symmetry breaking [28]. An additional tetramerization also starts to develop continuously below 19 K. This last transition, which now involves symmetry breaking, can be identified with a true second-order $2k_F$ transition [17,18,28] (see Section 7).

In the intermediate phase, $19 \text{ K} < T < 335 \text{ K}$, MEM(TCNQ)₂ is a very poor semiconductor, with a chain axis electrical conductivity σ_{\parallel} of $\cong 10^{-3} \text{ S/cm}$ and with anisotropic ratios $\sigma_{\parallel}/\sigma_{\perp}$ in two transverse directions of $\cong 5$ and $\cong 40$, at room temperature [17,18,41] (see Fig. 12). As in TEA(TCNQ)₂, E_G is also somewhat T -dependent, with $E_G = 0.62 \text{ eV}$ for $316 \text{ K} < T <$

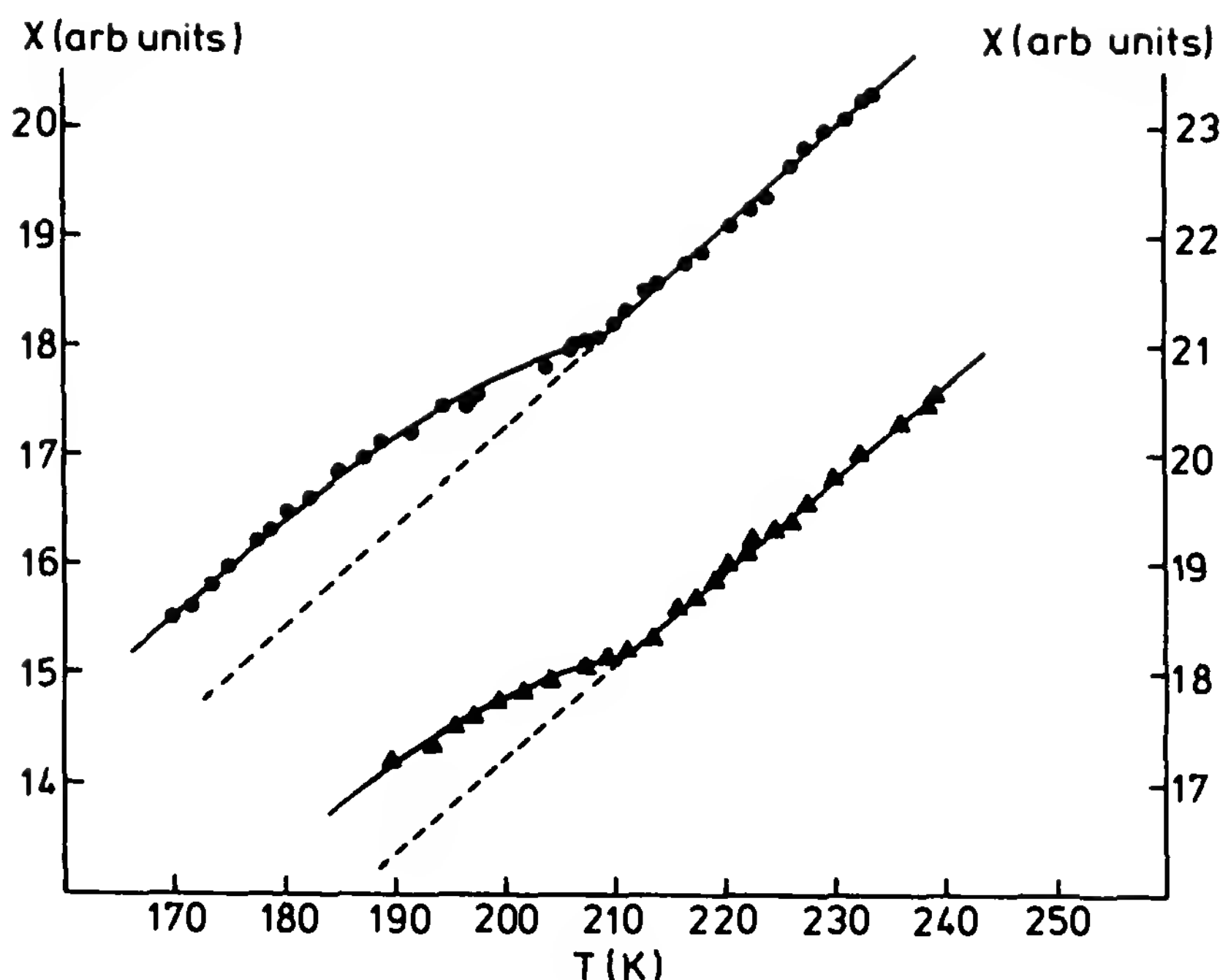


Figure 11 Magnetic susceptibility of TEA(TCNQ)₂ after rapid cooling. The result of two different measurements is shown. The dashed line is the result obtained with slow cooling. (After Ref. 40.)

335 K and $E_G = 0.64$ eV for $T < 250$ K [41]. The magnetic susceptibility $\chi(T)$ fits quite accurately here the standard Bonner–Fisher law for a regular one-dimensional Heisenberg antiferromagnet, with an exchange energy $J = 53$ K. This is a nonconducting Mott–Hubbard-like state, in which the electrons are strongly localized, one on every dimer, which results from strong electron correlations (i.e., $U/t \gg 1$) (see below) [17]. Note that for a salt with a mean charge $pe = \frac{1}{2}e$ per TCNQ site, as in MEM(TCNQ)₂ or in TEA(TCNQ)₂, the metallic behavior is not suppressed by chain dimerization in a one-electron description (the conduction band being only half filled).

The fact that J is T -independent in the case of MEM(TCNQ)₂ is very surprising. After Oostra [40], this is a purely accidental feature which may be associated with the relative constancy of the transfer integrals in this case. On heating, σ_{\parallel} in MEM(TCNQ)₂ increases discontinuously at 335 K by about three orders of magnitude, with a hysteretic effect characteristic of a first-order transition [17–19], whereas χ decreases by only about 7%. In the new phase, above 335 K, σ is almost T independent: $\sigma_{\parallel} \cong 20$ S/cm and $E_G \cong 0$ [41]. χ as a Curie–Weiss-like temperature dependence: $\chi = 1/(T + \Theta)$, with $\Theta = 70$ K. MEM(TCNQ)₂ then resembles a highly cor-

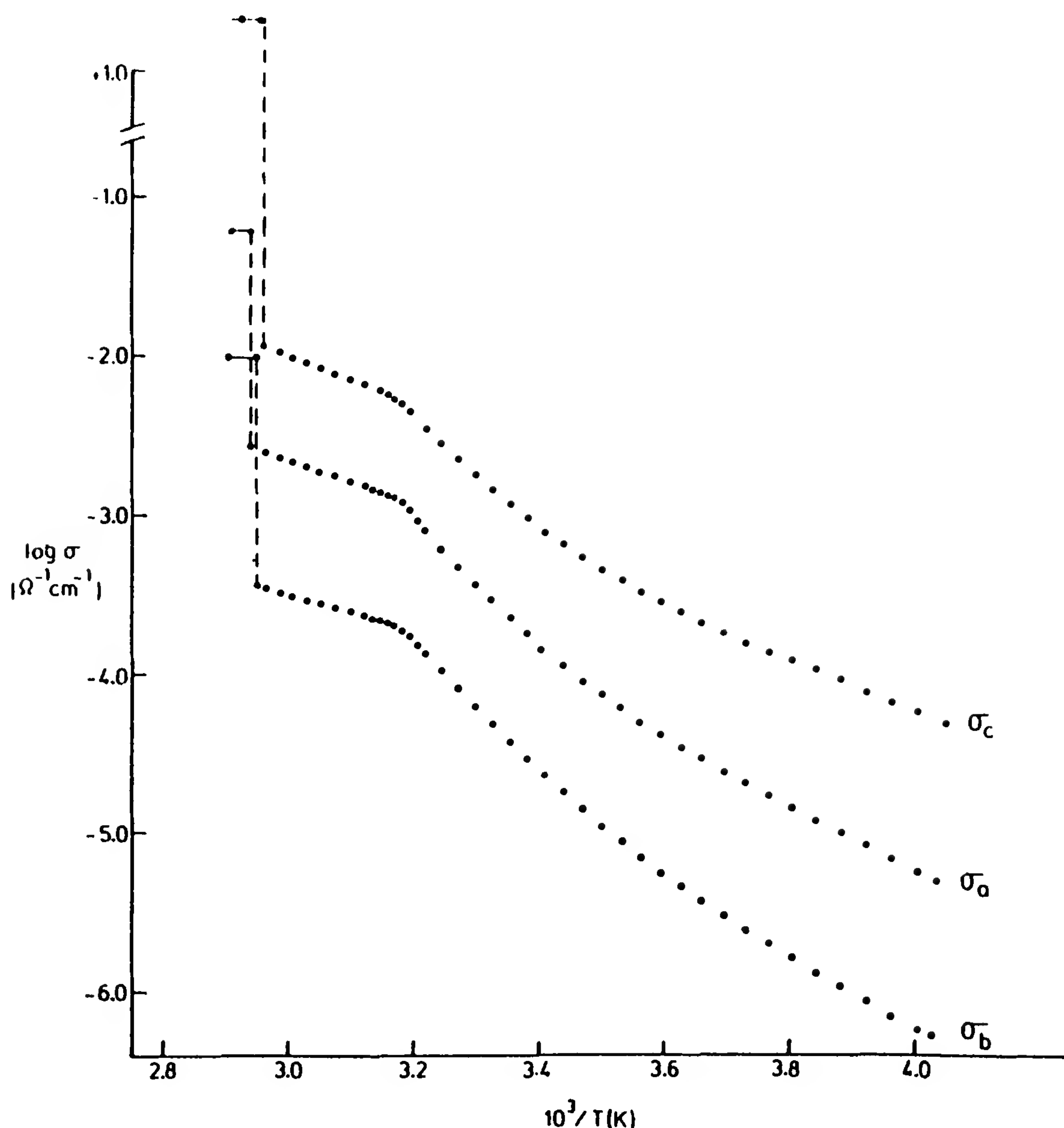


Figure 12 Temperature dependence, above 250 K, of the electrical conductivity of MEM(TCNQ)₂ crystals. Axis *c* is the chain axis and axes *a* and *b* are almost orthogonal to *c*. (After Ref. 41.)

related metal (with $U \gg t$) [17,18]. At last, below the low-temperature transition at 19 K, MEM(TCNQ)₂ becomes a nonmagnetic insulator [17].

6. Correlation Effects in MEM(TCNQ)₂ and TEA(TCNQ)₂

This important aspect has been reviewed in a thorough way by Pedersen et al. [36], in particular for the special case of the two salts under concern here. The experimental magnetic susceptibility has a maximum value of

about 21×10^{-4} emu/mol, at 66 K, in MEM(TCNQ)₂, and of about 7×10^{-4} emu/mol, at 300 K, in TEA(TCNQ)₂ [17,18,40]. In any case, this is much larger than the Pauli value, evaluated to only about 8×10^{-5} emu/mol [36].

Such enhancements of χ are most commonly attributed to strong electronic correlations [2,3]. This conclusion is furthermore well supported by the following two facts. The typical high-temperature limit of $\cong -60 \mu\text{V/K}$ for the chain-axis thermopower S_{\parallel} , found in both salts [41,42] and in many others, is just the theoretical limit $S = -(k/|e|) \ln 2 = -59.8 \mu\text{V/K}$ predicted for strongly correlated systems [43], k being the Boltzmann constant and e the electronic charge. Also, a general trend of the organic semiconductors is that the activation energy of the magnetic susceptibility is different from and significantly lower than the activation energy of the electrical conduction [44,45]. For uncorrelated systems, the two activation energies are simply the same [36].

In MEM(TCNQ)₂, in which $\rho = \frac{1}{2}$, the two well-defined structural phase transitions at 335 and 19 K just coincide with $2k_F$ and $4k_F$ distortions, respectively. It seems, then, a reasonable approach to consider that such transitions result from Peierls instabilities in a one-dimensional electronic system characterized by strong enough electron–electron correlations. In such an approach, the first, at 335 K, is identifiable with an electronic-Peierls transition, and the second, at 19 K, with a spin-Peierls transition. In this process, an electrical gap is formed, below 335 K, with corresponding loss of electronic degrees of freedom, and a new magnetic gap is formed, below 19 K, with corresponding loss of spin degrees of freedom. Actually, these two transitions do not occur at 0 K as in a strictly one-dimensional system but at a finite temperature due to the small three-dimensional interchain coupling [2,3].

The fact that there is apparently only one, $2k_F$, transition in TEA(TCNQ)₂ but two, $2k_F$ and $4k_F$, transitions in MEM(TCNQ)₂ has been considered as an indication that Coulomb repulsions, although significant in both salts, are relatively weaker in the first [36]. This trend is also supported by the fact that the exchange energy $J \approx t^2/U$ [3] is about four times smaller in MEM(TCNQ)₂ ($J = 53$ K) than in TEA(TCNQ)₂ ($J_1 = 230$ K at $T = 200$ K), whereas the (effective) transfer integral t is expected to be about the same (see the discussion above) [36].

After Pedersen and Carneiro, it is mostly the magnitude of the nearest-neighbor Coulomb repulsion energy, V , which is responsible for the difference between TEA(TCNQ)₂ and MEM(TCNQ)₂. The magnitude of V is determined largely by the shape and polarizability of the cations, and the cation TEA⁺ is believed to screen more efficiently than the cation MEM⁺, the intermolecular Coulomb repulsion represented by V [36].

However, it will be seen below that the transitions observed in both $\text{MEM}(\text{TCNQ})_2$ and $\text{TEA}(\text{TCNQ})_2$, although bearing some strong characteristics of Peierls transitions, also present several additional features clearly attributable to *sterical* effects, which make them somewhat more complicated in nature.

Finally, it may be remarked that the two salts $\text{MEM}(\text{TCNQ})_2$ and $\text{TEA}(\text{TCNQ})_2$ bear several points of resemblance in their physical properties with the most interesting salts of the $(\text{TMTTF})_2\text{X}$ series (TMTTF = tetramethyltetrathiafulvalene) [14]. They are all organic conductors with a quasi-one-dimensional character, with $\rho = \frac{1}{2}$ (or $\frac{3}{2}$), and with a dominant electron–electron interaction. They exhibit comparable modest values of the electrical conductivity at high temperature, which indicate that the electrons are not very delocalized in the materials, and in all of them an underlying $4k_F$ dimerization is also present, due to the cations. These common features, which are thought to be at the origin of sizable Umklapp scattering effects in the salts of the $(\text{TMTTF})_2$ series [14], could also be able to produce the same kinds of effects in $\text{MEM}(\text{TCNQ})_2$ and $\text{TEA}(\text{TCNQ})_2$ (see also Chapter 2).

7. Spin-Peierls Transition in $\text{MEM}(\text{TCNQ})_2$ and Related Compounds

The spin-Peierls transition is a genuine structural phase transition which occurs at a temperature $T = T_{\text{sp}}$ in a regular antiferromagnetic chain of localized electrons. The transition results from a $2k_F$ instability existing in the chain under the effect of the spin–phonon coupling. In such a transition, inherent in the one-dimensional character of the electronic spin system, a magnetic gap is produced together with a chain distortion, the magnetic energy gained in the formation of the gap being larger than the elastic energy lost in the formation of the distortion. The net effect of the distortion is in fact to couple the $s = \frac{1}{2}$ electronic spins of the chain into nonmagnetic $S = 0$ pairs [3].

Practical realizations of regular antiferromagnetic chains are provided either by regular chains of monomers, with one electron per monomer or $\rho = 1$, or by regular chain of dimers, with one electron (one hole) per dimer or $\rho = \frac{1}{2}(\frac{3}{2})$. Then the $2k_F$ distortion results in a dimerization of the molecular chains in the first case, and in a tetramerization, or, more correctly, a dimerization of dimers [19] in the second case (see also Fig. 5).

In any case the spin-Peierls transition is driven by one-dimensional pretransitional structural fluctuations [46]. Such fluctuations start to develop at some temperature T_F above T_{sp} . The effect of these critical fluctuations is to induce a *local* pairing of the spins which leads to an observable deviation of the magnetic susceptibility χ below T_F from the general Bon-

ner–Fisher law. These fluctuations first are of a one-dimensional nature at T_F and become progressively three-dimensional, on cooling from T_F to T_{SP} . Below T_{SP} , a long-range order is finally achieved: there is a lattice doubling and the magnetic susceptibility then falls sharply to zero.

The spin-Peierls transition has been the object of several recent papers. Examples of the first case, with $\rho = 1$, are provided by the insulating alkali metal simple salts [47] (see below), and examples of the second case, with $\rho = \frac{1}{2}$ or $\frac{3}{2}$, are given by the salt MEM(TCNQ)₂ [17–19,46], by the salts of the (TMTTF)₂X series [46,48], or by the salts of the (BCPTTF)₂X series (BCPTTF = benzocyclopentyltetrathiafulvalene) [46,49].

The characteristic behavior described above is particularly well observed with the salts of the last series. For instance, for the representative salt: (BCPTTF)₂PF₆ [46], pretransitional structural fluctuations are found by x-rays to exist on cooling from $T_F \cong 100$ K to $T_{SP} \cong 37$ K, these fluctuations being almost one-dimensional between 100 and 50 K. The magnetic susceptibility of this salt with “regular” behavior fits well the Bonner–Fisher law at high T , with $J = 165$ K, and it starts to deviate appreciably from this law below 100 K, that is, well above T_{SP} .

However, in the case of MEM(TCNQ)₂, which is considered as one of the most representative spin-Peierls materials, with $T_{SP} = 19$ K, the results are quite at variance with the normal behavior described above [46]. For this material, critical fluctuations are also observed correctly, by x-rays, below $T_F \cong 40$ K, but they are only of a three-dimensional nature. Moreover, these fluctuations do not produce any detectable effect below T_F on the Bonner–Fisher dependence of the magnetic susceptibility. Consequently, this law is perfectly followed, with $J = 53$ K, down to 19 K [17,18,46]. Some earlier comments on this point have also been given by Schulz [50].

8. Role of Cations

There is considerable experimental evidence that the physical properties of the organic conducting salts are influenced significantly by the associated counterion subsystems. The specific effects of the counterions, MEM⁺ and TEA⁺, are considered in more detail below.

In ideally one-dimensional systems, only intrachain electron–phonon and spin–phonon couplings are, within mean-field approximation, at the origin of electronic-Peierls and/or spin-Peierls transitions, respectively. In real systems, such as the TCNQ salts under concern here, it is clear, however, that one should take properly into account the coupling of the electrons to external potentials also and, in the first case, to the periodic electrostatic cation potential.

The effects of an external periodic potential V_Q with $Q = 2k_F$ on an electronic-Peierls transition at $T = T_P$ have been investigated in detail by Hansen and Carneiro [51] within a mean-field theory. They have found in this case that the Peierls transition is somewhat smeared out around T_P , but not depressed. The modified gap $2\Delta(T)$ is larger than the original Peierls gap $2\Delta_P(T)$ below T_P and it does not vanish above T_P . Thus only a change in the slope of $\Delta(T)$ at T_P recalls in this case the underlying transition [28,51]. If V_Q is small enough [$V_Q < 0.1\Delta_P(0)$], then $\Delta(T)$ varies dramatically around T_P with $|d\Delta/dT| \approx \text{maximum}$, at T_P . One also gets in this case the two limits

$$\Delta(0) = \Delta_P(0) \exp\left[\frac{V_Q}{\lambda\Delta_P(0)}\right] \quad \text{and} \quad \Delta(\infty) = V_Q$$

λ being a dimensionless electron–phonon coupling constant [51].

It is useful to recall here the example of Fig. 8, which reports, for the special case of TEA(TCNQ)₂, both the experimental gap $2\Delta(T) = E_G(T)$ (curve a) and the BCS-like Peierls gap $2\Delta_P(T)$ (curve b), on normalized scales. In this figure the temperature $T_0 = 210$ K at which $|d\Delta/dT|$ is maximum has been identified simply with T_P , as in the small V_Q limit.

It is established from the work of Ref. 51 that any external periodic potential V_Q breaks the symmetry even above T_P , and that, consequently, there is no longer a real phase transition. However, in most compounds of interest the external potential has both periodic and random components, and this would require in fact a more complex analysis (see also below).

It is important to remark here that the periodicity of the cation sublattice in the chain direction z just coincides with $2k_F$ periodicity in the case of TEA(TCNQ)₂, and with $4k_F$ periodicity in the case of MEM(TCNQ)₂. This fact would suffice by itself to account, in terms of electron–cation interaction and commensurability effect, for the intrinsic chain tetramerization of TEA(TCNQ)₂ and for the intrinsic chain dimerization of MEM(TCNQ)₂, in particular for the residual dimerization still above 335 K. However, the cation subsystem certainly has a more direct, steric influence than through only the electron–ion interaction discussed above on the overall structural properties of the organic salts.

A detailed study between 80 and 300 K of the temperature dependence of the polarized reflection spectra of TEA(TCNQ)₂ single crystals has been performed quite recently by Olejniczak and Graja [52]. The observed thermal evolution of the spectra is consistent with a wide semiconductor-to-semiconductor transition centered at about 220 K. The transition is

manifested optically by distinct changes in those bands which are assigned to the TEA⁺ cation vibrations, and this is a proof that the transition occurs mainly in the cation sublattice.

In real three-dimensional materials, it is clear that the various molecular constituents are all of importance in determining the equilibrium crystal structures. They obey complex steric rules according to which a structural close packing can be optimized at every temperature. All these constituents should then be taken into account correctly in the description of structural phase transitions. In the case of TCNQ salts, this means that the entire molecular system formed by the conducting TCNQ chains plus the cations has in fact to be considered.

In particular, the rather strong rearrangements observed in the cation sublattices could play a major steric role in the structural transformations of the materials. Also, they could eventually render the electronic systems still more unstable and thus force the electronic transitions to take place at temperatures somewhat higher than their “natural” ones.

9. Static Disorder and Thermal Motion of Cations

Significant modifications of the thermal motion of cations, corresponding to the loss of degrees of freedom on cooling, are observed in both MEM(TCNQ)₂ and TEA(TCNQ)₂, near 335 K and 210 K, respectively. Such cation rearrangements appear better as the cause rather than as the consequence of the correlative $2k_F$ and $4k_F$ electronic transitions. In effect, structural changes are so important that they can hardly be attributed to instabilities of the electronic subsystems.

In both salts, cations are found, from x-ray studies, to be disordered between *two* preferential orientations. In MEM(TCNQ)₂, the occupancies, x and $1 - x$, of these two orientations are found to be T dependent. Below 113 K, $x = 1$, and from 113 to 243 K, x varies from 1 to 0.5 [24,25]. In TEA(TCNQ)₂, the two occupancies are almost identical: $x \cong 1 - x \cong 0.5$ [22]. This twofold disorder is definitely static at low temperature. However, due to thermal factors, it becomes more and more difficult to resolve the two orientations at high temperature and also to conclude whether the disorder is static or dynamic in nature [22,24].

An appropriate analysis of the dynamics of the orientational disorder of the cations can be performed by means of proton NMR second-moment studies [53–55]. Such studies have established in the case of TEA(TCNQ)₂ that the cation disorder is dynamic above 270 K while it is static below 205 K, with some transitional regime in between [53,54]. The wide transition of TEA(TCNQ)₂ at about 210 K may then be considered to be a continuous structural transition from a state of dynamic disorder at high T to a state

of static disorder at low T , or, eventually, to an ordered state, as in the case of an order–disorder transition.

In effect, a hypothetical superstructure of TEA cations at low temperature, implying long-range ordering, has not been ruled out [22,23]. Diffuse scattering experiments could help clarify this point (in fact, at least two families of diffuse sheets, parallel to c^* and parallel to a^* , and with a modulated intensity, have been observed but never explained) [23].

Let us finally also mention here the results of proton nuclear relaxation time T_1 measurements on TEA(TCNQ)₂ [53,54]. From the frequency dependence of T_1 , it is deduced that the spin motion is a nearly one-dimensional diffusion. Moreover, the temperature dependence of the on-chain spin diffusion rate shows a quite remarkable feature: while it is thermally activated below 220 K, it suddenly becomes temperature independent above 220 K.

To summarize, the considerable amount of experimental data now available on the salt TEA(TCNQ)₂, concerning both its structural and electrical properties [20,22,36], provides a rather clear indication that this organic semiconductor is in fact approaching a metallic behavior at high temperature, like MEM(TCNQ)₂, but in a continuous way. This is certainly due in part to the increasingly fast thermal motion of cations at high temperature, which produces on the cation potential an averaging effect somewhat assimilable to a new form of order [54]. One may also remark that the measured room-temperature chain-axis electrical conductivity of 7 S/cm in TEA(TCNQ)₂ is unusually high for a semiconducting salt [27].

Proton NMR second moment has also been studied in MEM(TCNQ)₂ [54,55]. A large decrease in the second moment M_2 is observed in the range 280 to 320 K, which is associated with increasing disorder of the MEM cations. This disorder is apparently of a dynamic type and consists of flipping over of the cations between the two preferred positions at an increasing rate. The first-order phase transition at 335 K is accompanied by a drop in the NMR second moment, indicating that a *new* motion sets in, probably a rotation of the MEM ions as a whole about the N–O axis. The entropy change due to these extra rotational degrees of freedom plus that due to the electronic degrees of freedom is found to be in reasonable agreement with specific heat data. The stabilization of the metallic state in MEM(TCNQ)₂ at high T is probably associated, at least in part, with the new thermal motion of the MEM ions.

A still more singular case than MEM(TCNQ)₂ is provided by DMTM(TCNQ)₂, a salt of the same family (DMTM = dimethylthimorpholinium) [19,40]. This salt is also found to undergo a first-order phase transition, at $T_c = 272$ K; but below T_c , the electrical conductivity increases

discontinuously by a factor of about 500, as in a semiconductor-to-metal transition (i.e., in a reversed Peierls transition), whereas the magnetic susceptibility drops by only about 15%. This behavior is then the opposite of that observed for $\text{MEM}(\text{TCNQ})_2$, described above. Very recently, ^1H and ^{13}C NMR measurements have been performed on this material. The results indicate that it is a mode of motion of $\text{DMTM}(\text{TCNQ})_2$ which is frozen out at the transition at 272 K, thereby reducing the crystal symmetry and introducing the observed changes in the electrical conductivity and magnetic susceptibility [56].

B. Selected New Materials

1. $\text{Qn}(\text{TCNQ})_2$, $(\text{DMDCNQI})_2\text{Ag}$, and $(\text{TMTTF})_2\text{PF}_6$

The metal-like semiconductor model of Epstein et al. (see Section II.C) has been found to fit rather nicely the electrical conductivity data $\alpha(T)$ of the quinolinium salt $\text{Qn}(\text{TCNQ})_2$, for instance [16]. In this case, the experimental values of the fitting parameters were $\Delta_0 = 600$ K, $\alpha = 2.7$, and $T_m = \Delta_0/\alpha = 240$ K.

From more recent optical data it is proved that $\text{Qn}(\text{TCNQ})_2$ is a semiconductor up to 300 K, with an energy gap due mainly to a Peierls distortion on the conducting TCNQ chains [57]. However, this gap $E_G = 2\Delta$ is not constant, as is simply assumed in the model of Epstein et al. In fact, Δ appears to decrease significantly from $\cong 1200$ K at $T = 0$ K to $\cong 300$ K at $T = 300$ K, somewhat like in the salt $\text{TEA}(\text{TCNQ})_2$ (see above). This requires a modified approach in which the existence of a conductivity maximum σ_m still implies a T -dependent mobility μ but not so steep as would require a constant gap.

A weak $2k_F$ diffuse x-ray scattering [58], seen only at low temperature, confirms that $\rho = \frac{1}{2}$ in this salt and indicates that the Fermi wave vector is rather well defined despite structural cation disorder. A stronger $4k_F$ scattering [58] observed from 25 K to 300 K is an indication of large Coulomb effects in this salt, with $U \gg t$, in agreement with other known magnetic and thermopower data [57,58].

We may incidentally remark that the same kinds of arguments could also be reasonably invoked for the electrical properties of some materials of more recent concern. For instance, a resistivity minimum that is not related to a phase transition is observed at T_p in $(\text{DMDCNQI})_2\text{Ag}$ (DMDCNQI = dimethylcicyanoquinonediimine) [59] as in $(\text{TMTTF})_2\text{PF}_6$ [60]. This minimum is attributed to the opening of a gap in the electronic spectrum of the materials below T_p , under the effect of Umklapp scattering, with a corresponding Mott–Hubbard localisation [14]. It is, however, also

observed that the thermopower approaches semiconducting behavior *even* for $T > T_p$ when the resistivity has a metal-like behavior [60]. Moreover, recent detailed analysis of the optical data of Bechgaard salts, $(\text{TMTSF})_2\text{X}$, and sulfur analogs, $(\text{TMTTF})_2\text{X}$, gives evidence for large on-site Coulomb correlations, or $U \gg t$, in the materials, and for the existence of semiconducting gaps even at room temperature [61]. Apparently, all these features might also be rather well reconciled, as in the case of $\text{Qn}(\text{TCNQ})_2$, by utilizing a slightly modified version of the model of Epstein et al. However, different views concerning the electronic properties of $\text{Qn}(\text{TCNQ})_2$ which emphasize the role of disorder and utilize for this salt the original concept of granularity have been developed by Zuppiroli [62].

2. $(\text{BCPTTF})_2\text{X}$ Series

The magnetic properties of these salts have been discussed above in relation with the spin-Peierls transition of $\text{MEM}(\text{TCNQ})_2$ (see Section III.A.7). BCPTTF is an unsymmetrical substituted TTF molecule. Room-temperature electrical conductivities for the salts $\text{X} = \text{PF}_6$ and $\text{X} = \text{AsF}_6$, are 10 and 4 S/cm, respectively. These two salts have a semiconducting behavior up to 300 K with a low-temperature activation energy $\cong 1000$ K in both cases. There is a probable resistivity minimum at T_p above 300 K. The behavior of these salts resembles that of the salts of the $(\text{TMTTF})_2\text{X}$ series (low-temperature activation energy $\cong 600$ K, $T_p \cong 220$ to 250 K, for $\text{X} = \text{PF}_6$ and $\text{X} = \text{AsF}_6$), but apparently with a larger charge localization [49].

3. $\text{NPrQn}(\text{TCNQ})_2$

This salt (NPrQn , *N*-propylquinolinium) consists of tetramerized TCNQ chains. It undergoes a phase transition at 220 K which is considered to be a second-order metal-to-semiconductor transition. Optical reflectivity measurements on crystals, with the light polarized in the chain direction, indicate that the charge distribution on the TCNQ sites in the tetrads is less uniform at 100 K than at 300 K. This is as in $\text{TEA}(\text{TCNQ})_2$ (see Section III.A.3). However, estimation of this charge distribution from the bond lengths at 300 K [38] gives ambiguous results for this material [63].

4. $\text{MDT}(\text{TCNQ})_2$

In this salt ($\text{MDT} = 1\text{-methyl-1,4-dithianium}$), there is a brick wall stacking arrangement of TCNQ dimers. It is a quasi-one-dimensional semiconductor up to 300 K with an energy gap $E_G \cong 0.22$ eV. The magnetic susceptibility follows quite well a Bonner–Fisher law with $J = 76$ K. At room temperature: $\chi = 9.5 \times 10^{-4}$ emu/mol and there is a maximum $\chi_M = 14.5 \times 10^{-4}$ emu/mol at $T_M = 100$ K. There is also a probable spin-Peierls transition at 5.5 K [64].

5. α' -(BEDT-TTF)₂X Series

The salts of this series [BEDT-TTF = bis(ethylenedithiolo)tetrathiafulvalene], with X = AuBr₂, CuCl₂, or Ag(CN)₂, are all semiconductors with narrow bandwidths and strong Coulomb repulsions. For this series the magnetic susceptibility has room-temperature values of $\cong 8$ to 9×10^{-4} emu/mol, and maximum values of $\cong 16$ to 18×10^{-4} emu/mol, at $T_M \cong 60$ to 70 K. However, it does not fit well a Bonner–Fisher law in any case. A spin-Peierls transition is found to occur, at 7 K, for the Ag(CN)₂ salt only [65].

6. (BEDT-TTF)₂GaCl₄

The structure of this salt consists of stacks of twisted dimers. It is a semiconductor with an energy gap $E_G \cong 0.42$ eV. At room temperature the electrical conductivity is $\sigma_{\parallel} \cong 0.1$ S/cm and the magnetic susceptibility is: $\chi = 8 \times 10^{-4}$ emu/mol. As in the preceding α' -(BEDT-TTF)₂X series, the magnetic susceptibility does not fit well a Bonner–Fisher law [66].

IV. MATERIALS WITH INSULATING BEHAVIOR AT ROOM TEMPERATURE

A. Introduction

As mentioned at the beginning of Section III, the conducting properties of organic charge-transfer materials are critically dependent on (1) their stoichiometry (i.e., the number of donor to acceptor molecules), and (2) the degree of charge transfer ρ per acceptor molecule. In particular, as a result of inherently strong Coulomb repulsions, all 1:1 TCNQ salts with complete ionization, or $\rho = 1$, are insulators [45].

Let us illustrate this point by considering, for instance, the two representative charge-transfer compounds TTF-TCNQ and RbTCNQ formed between donors TTF and Rb, respectively, and the acceptor TCNQ. The crystal structures of the two compounds consist of segregated molecular chains of donor and acceptor moieties, and these chains are regular at high temperature [2,67]. These two compounds exhibit extraordinarily different electrical properties. TTF-TCNQ is typically an organic metal, with an electrical conductivity increasing from $\cong 500$ S/cm at 300 K up to $\cong 10^4$ S/cm at 60 K [2], whereas RbTCNQ is only an insulator with an electrical conductivity lower than 10^{-5} S/cm already at room temperature [68]. The reason is actually because charge transfer is complete in RbTCNQ, or $\rho = 1$, whereas it is incomplete in TTF-TCNQ: $\rho < 1$ [45]. In this sense, RbTCNQ is a charge-transfer salt, but not TTF-TCNQ.

Let us recall here that in a one-electron description ($U \ll t$), RbTCNQ and TTF-TCNQ should be metals, as the conduction band is not filled in

both cases (it is half-filled and less than half-filled, respectively). However, due to the narrowness of the electron bands in these organic solids, Coulomb correlations have in fact a dominant effect ($U \gg t$), so that two electrons can hardly be on the same site at the same time. In consequence, electron motion not requiring double-site occupancies is possible in a chain only when $\rho < 1$. However, when $\rho = 1$, Coulomb repulsions cause the electrons to be localized, one on each site, as in a Mott–Hubbard insulator [2,45]. In summary: a regular chain of acceptor molecules is a metal when $\rho < 1$ and it is an insulator when $\rho = 1$.

In TTF-TCNQ, both segregated TCNQ and TTF chains actually contribute to the electrical conduction, with mean charges per acceptor and donor molecules which have just opposite values: $\rho_D = -\rho_A$ [2]. In RbTCNQ, the cation Rb^+ is diamagnetic and does not participate in the conduction.

Both compounds are also unstable and undergo a structural distortion at low temperature with a marked change in their electrical properties. It is properly an electronic-Peierls transition, at 53 K, in the case of TTF TCNQ [2], and a spin-Peierls transition, at 381 K, in the case of RbTCNQ [67,69] (see the next section).

B. Specific Examples: Alkali Metals–TCNQ Salts

It has long been known that alkali metals Na, K, Rb, and Cs form with the acceptor TCNQ 1:1 segregated charge-transfer salts, with complete ionization: $\rho = 1$. They have regular chains at high temperature but are insulators due to Coulomb repulsions as discussed in the preceding section. They are then primarily one-dimensional magnetic materials whose properties have been studied extensively in the past [69].

At some critical temperature, a structural distortion to dimerized chains occurs together with the opening of a gap in the magnetic excitations. Such a distortion is attributable to a $2k_F$ spin-Peierls transition, just as in $\text{MEM}(\text{TCNQ})_2$ (cf. Section III.A.7). A $2k_F$ transition results into chain tetramerization for $\rho = \frac{1}{2}$ and into chain dimerization for $\rho = 1$, as also shown in Fig. 5. For instance, the spin-Peierls transition takes place at $T_{\text{SP}} = 395$ K in KTCNQ and at $T_{\text{SP}} = 381$ K in RbTCNQ [67] (a second form, called RbTCNQ II, also exists for the Rb salt [69], but it is not considered here). By analogy with the case of polymers, the dimerized phase at low temperature is also called a bond-ordered-wave (BOW) phase [47].

A very interesting feature, which appeared fully only recently, however, is that when in the dimerized state, these salts exhibit a significant nonlinear conductivity and a related (differential) negative resistance at high electric fields [47]. Nonlinear current density electric field J - E characteristics of RbTCNQ single crystals are shown for several temperatures (below T_{SP})

in Fig. 13 [47]. An instability from low- to high-conductivity states is observed to occur at some electric field threshold E_{th} which depends on temperature, and the dashed lines in Fig. 13 then correspond to rather discontinuous jumps of the current density.

Such an effect is not due to a trivial Joule heating of the samples. From a detailed experimental study based mainly on electrical [68], optical [70], and x-ray [71] measurements, this effect has been attributed to the motion of charged soliton-like defects existing in the TCNQ chains. A soliton in a dimerized chain is expected to have the following general form [47]:



It may be either a charged $+$ or $-$ soliton, if $*$ = 0 or $-$, or a spin soliton, if $*$ = $-$. A charged soliton is thus a charge plus a local lattice distortion.

After the authors of Ref. 47, the motion of charged solitons in dimerized chains requires a relatively low excitation energy, and it could take place according to the following scenario. At low electric field, this motion is hindered by the three-dimensional interactions between molecular chains. The current is then due to a few defects more or less free from these interactions. As the field is increased, more and more charged solitons are driven to motion and by a cooperative effect of these mobile solitons, a critical field E_{th} is finally attained at which value the three-dimensional order is lost. The solitons are then able to move in one chain almost independent of the others, and this new degree of freedom is believed to

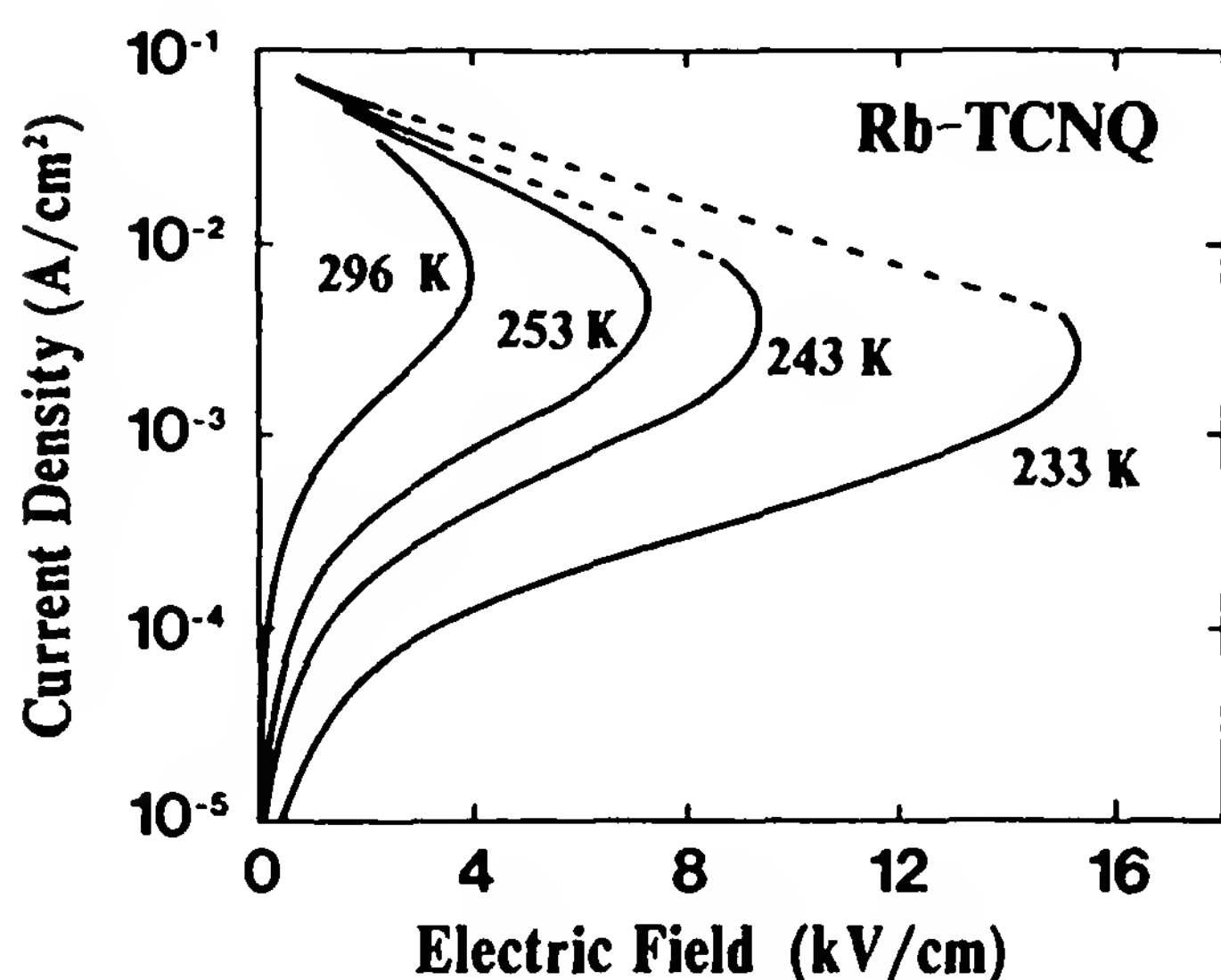


Figure 13 J - E characteristics for a RbTCNQ crystal at various temperatures. (After Ref. 47.)

be at the origin of the negative-resistance regime ($dJ/dE < 0$) shown above E_{th} in Fig. 13.

V. NEUTRAL-TO-IONIC TRANSITION

Most organic charge-transfer complexes are composed of mixed chains in which donor, D, and acceptor, A, molecules stack alternatively. By definition, for a 1:1 charge-transfer salt, $\rho = 1$, whereas for a 1:1 charge-transfer complex $\rho < 1$ [44]. In consequence, unlike the large family of segregated chain materials discussed up to now, the mixed chain materials are always poor conductors with a ground state largely influenced by the degree of charge transfer ρ from D to A.

The materials may be in a quasi-ionic phase when $1 > \rho > 0.5$, or in a quasi-neutral phase when $0.5 > \rho > 0$. In the simplest theoretical approach, the value of ρ depends on only three parameters: I_D , the ionization potential of D; A_A , the electron affinity of A; and M , the electrostatic Madelung energy of the crystal lattice. A fully ionic lattice ($\rho = 1$) is then realized when $I_D - A_A > M$, and a fully neutral lattice ($\rho = 0$) when $I_D - A_A < M$. This result is, however, greatly obscured by the neglect of transfer integral t and of other relevant parameters [44].

Interestingly, several of these materials are rather close to the neutral–ionic boundary and they can be driven from the (quasi) ionic to the (quasi) neutral phases, in reversible phase transitions, by means of temperature or/and pressure variations. Such variations are thought to act primarily on the Madelung energy parameter [72,73]. The first observation of such neutral-to-ionic transition in any kind of materials was curiously in the form of a distinct color change of the samples when pressure was applied above a certain threshold [72].

A significant amount of work has been devoted to mixed-chain complexes during the last 10 years, mostly by the Japanese school [74–79]. The central material for such studies has been TTF-*p*-chloranil [72,73]. At room temperature and ambient pressure, this material is quasi-neutral with $\rho = 0.3$, with an electrical conductivity $\sigma \cong 10^{-6}$ S/cm and with an energy gap $2\Delta \cong 0.2$ eV [79]. At ambient pressure, the degree of charge transfer changes from $\rho = 0.3$ above $T_c = 81$ K to $\rho = 0.7$ below T_c [79]. This neutral-to-ionic transition is not first order and not simple, and it appears to involve an intermediate region of width $\cong 30$ K below T_c in which both the neutral and ionic phases coexist [73]. At room temperature, the neutral-to-ionic transition is also observed to take place at a pressure of 11 kbar. A detailed phase diagram of the material (ρ, T, P), which includes the degree of charge transfer ρ , as estimated from infrared spectroscopy, is presented in Fig. 14 [75].

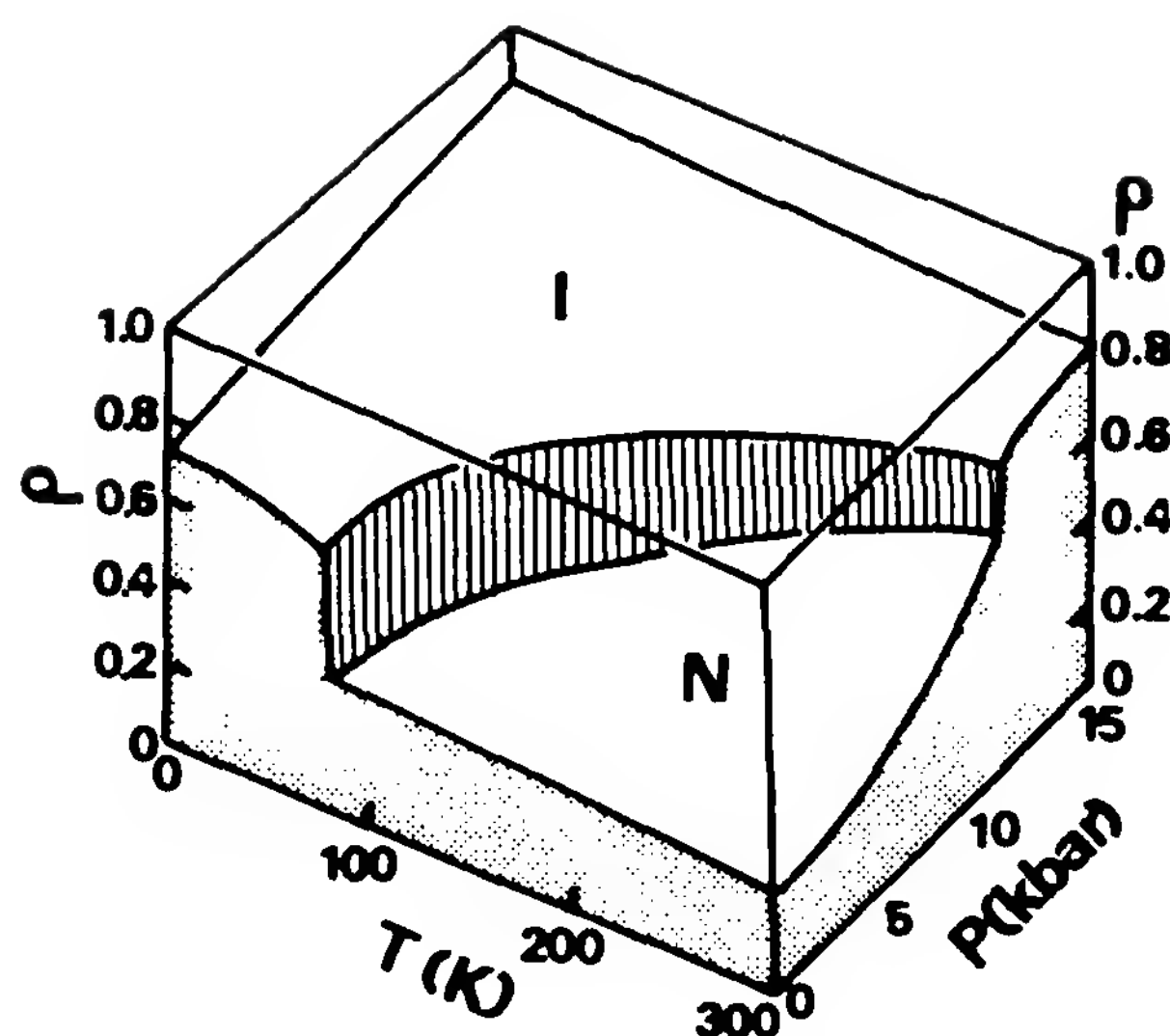


Figure 14 Degree of charge transfer ρ in TTF-chloranil as a function of temperature and pressure. (After Ref. 75.)

Mixed-chain charge-transfer complexes are characterized by a regular chain structure when in the quasi-neutral phase at high temperature. Often, but not always, the chains undergo dimerization in the low-temperature quasi-ionic phase, at T_c or below, as a possible consequence of one-dimensional spin-Peierls-like transition [74,76].

A negative-resistance effect very similar to those discussed above for 1:1 segregated-chain TCNQ salts is also present in various mixed-chain complexes. A stable and reproducible negative-resistance effect has been observed in the J - E characteristics of a selection of nine complexes, in either quasi-neutral or quasi-ionic phases but all thought to be near the neutral-ionic boundary [77]. This clearly establishes that such an effect is a rather general property. Moreover, from a comparative study on various materials it was also shown that the negative-resistance effect was a characteristic of chain dimerization, the nonlinearity being significantly less pronounced in the case of regular chain structures, either neutral or ionic [78]. A discussion of the microscopic origin of the nonlinear effect in both regular and dimerized structures is also given in Ref. 78. The much stronger effect present in the dimerized state is attributed to the motion of charged soliton-like defects, just as in the 1:1 alkali simple salts [78,47] (see above).

All the results above lead consistently to the conclusion that the negative-resistance effect is a common property of mixed-chain 1:1 charge-transfer complexes and segregated-chain 1:1 charge-transfer salts, the only requirement being the dimerization of the molecular chains in both cases [47].

A (somewhat reduced) neutral-to-ionic first-order-like transition has been reported for another material: TMB-TCNQ (TMB = 3,3',5,5'-tetramethylbenzidine) [79]. At room temperature: $\rho \cong 0.6$, $\sigma \cong 10^{-4}$ S/cm, and $2\Delta \cong 0.2$ eV. At ambient pressure, the transition is at $T_c = 205$ K and in this case ρ goes only from $\cong 0.6$ to $\cong 0.7$. At ambient temperature, the transition occurs at a pressure of 4.3 kbar. In contrast to the case of TTF-*p*-chloranil, the high-temperature phase is not really a neutral phase ($\rho = 0.6$) and the low-temperature phase is found to consist of both ionic and neutral molecules. Lattice dimerization also occurs in this compound below 205 K [79].

VI. POTENTIAL APPLICATIONS OF ORGANIC SEMICONDUCTORS

A. Negative-Resistance Devices

In a number of cases it has been demonstrated that the negative-resistance effect in the J - E characteristics of both 1:1 mixed-chain complexes or 1:1 segregated-chain salts could be utilized to obtain switching effects with large hysteresis [47,76–78]. Such an effect can be produced in a simple electrical circuit consisting of a single-crystal sample of (nonlinear) resistance R in series with a dc voltage V_0 and an appropriate load resistor R_L . The switching effect is observable when the sample is cooled well below the temperature at which lattice dimerization occurs. The temperature T of the sample is lower and the switching effect is larger. More precisely, as V_0 is increased at fixed T , the current I is switched to a high-conductivity or on-state at some threshold voltage V_{th} . Then as V_0 is decreased, I is switched back to the initial low-conductivity or off-state, at some other threshold voltage V'_{th} lower than V_{th} . The current $I = V_0/(R + R_L)$ is determined by the choice of R_L , which must be such that $R \ll R_L$ in the on-state, and $R \gg R_L$ in the off-state [76]. The switching effect is quite reproducible. For instance, more than 10^6 switching cycles could be repeated with a 100-Hz ac voltage [77]. As discussed above, the negative resistance and related switching effects are attributed to a current-induced breakdown of the dimerized state.

Let us mention the case of tetrakis(methyltelluro)TTF [76]. This material is (already) in the quasi-ionic phase at 300 K and it undergoes dimerization below 240 K. Some measured values of the threshold field E_{th} above which jumps of current density occur are $\cong 300$ V/cm at 200 K, $\cong 600$ V/cm at 180 K, and $\cong 1100$ V/cm at 160 K. Crystals have typical dimensions of $0.8 \times 0.8 \times 0.2$ mm³. This material was also chosen to build a prototype bistable device which utilized the switching effect [76].

A crystal sample kept at 155 K was in series with a load resistor and a constant-voltage V_0 such that $V'_{th} < V_0 < V_{th}$. Then a sequence of positive and negative pulse voltages of absolute height V_p such that $V_p > V_{th} - V_0$ and $V_p > V_0 - V'_{th}$ was superposed to V_0 . This made the device to switch on and off repeatedly from high- to low-resistance states, as shown in Fig. 15 [76]. More than 10^3 switching cycles could thus be repeated. The switching speed depends on the values of T , R_L , and V_0 , and the response time to a step voltage is on the order of 10 to 100 ms, in contrast with the very fast switching times of less than 10 ns found on thin CuTCNQ films [76,80] (see also Chapter 16).

Let us mention a somewhat different form of differential negative-resistance regime reported in the case of thin-film polymer electronic devices [81]. This negative regime is limited in the $I = f(V)$ characteristics by turning points given by $dI/dV = 0$ rather than by $dV/dI = 0$ as in the preceding case, and in this case it involves a different mechanism, based on quantum tunneling.

B. Thermistor Effect

The thermistor effect provides an indirect way to realize nonlinear current-voltage characteristics and (differential) negative resistances in conventional semiconducting samples which takes advantage here of sample self-

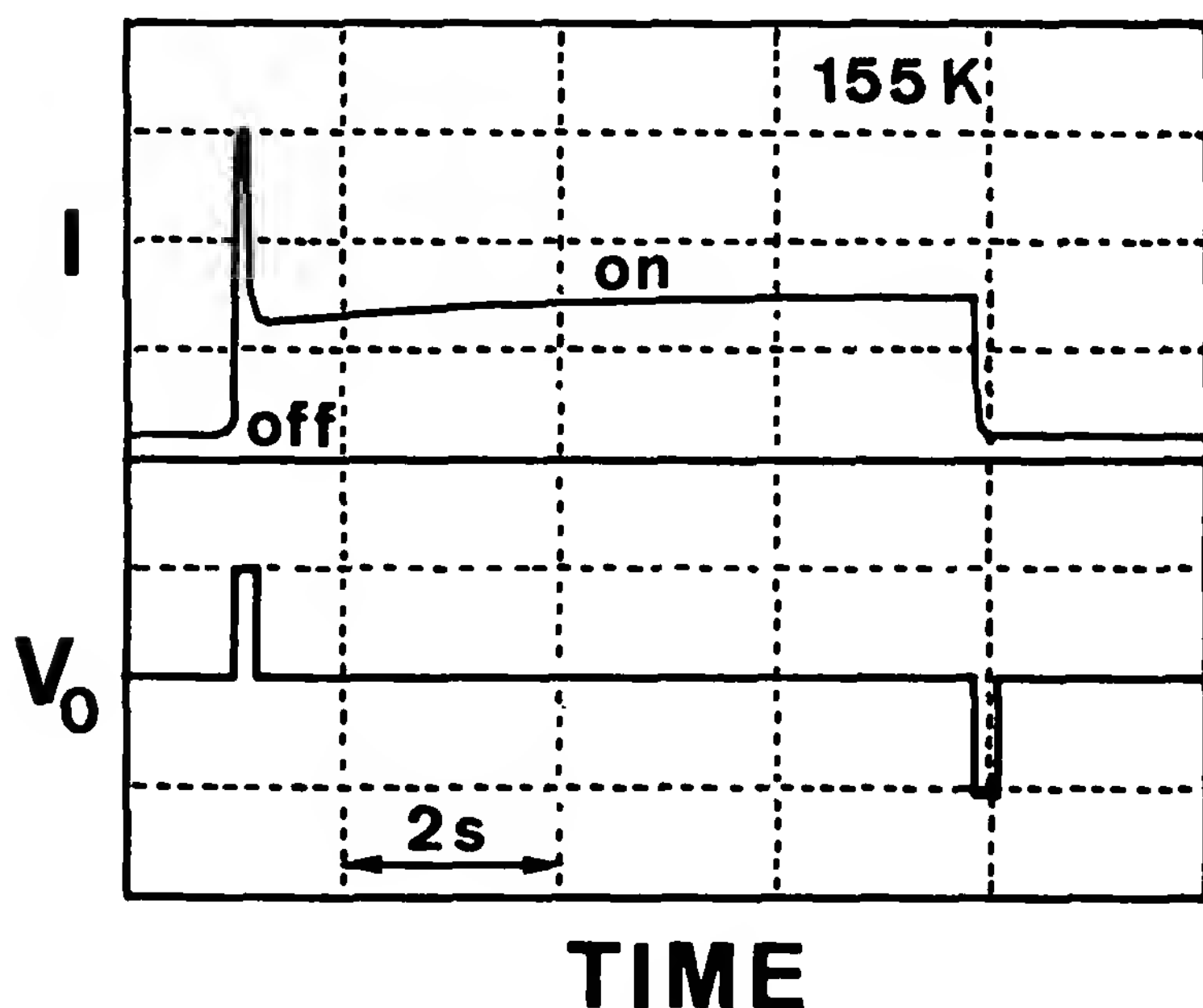


Figure 15 Time-dependent characteristics of a bistable device utilizing a crystal of the organic mixed-chain charge-transfer complex: tetrakis(methyltelluro)TTF cooled at 155 K. (From Ref. 76.)

heating by the Joule effect [82]. Let us consider a sample of an ideal semiconducting material whose electrical resistance R depends on the absolute temperature T according to a simple activation law of the form

$$R(T) = R_{\infty} \exp\left(\frac{\Delta}{kT}\right)$$

In this expression, Δ , the activation energy (half the semiconducting energy gap E_G of the material), and R_{∞} , the preexponential factor, are assumed to be independent of T (R_{∞} is the lower limit of R when $T \rightarrow \infty$); k is the Boltzmann constant.

The thermistor effect consists of the occurrence of strong nonlinearities in the current–voltage characteristics $I = f(V)$ of the semiconducting sample, which in this case are a direct consequence of sample self-heating by the Joule effect. As a result, the equilibrium temperature T of the sample in the thermistor regime is higher than the ambient temperature T_0 . In fact, the sample temperature T is an increasing function, and the sample resistance $R = V/I$, a decreasing function, of the electrical current I across the sample, and T and R also depend on the thermal coupling of the sample with the external medium. Conversely, $T \rightarrow T_0$ and $R \rightarrow R(T_0) = R_0$ when $I \rightarrow 0$.

Let us assume that when at temperature T , the thermal losses in the sample are simply proportional to the difference $T - T_0$. This linear approximation is reasonable provided that $T - T_0 \ll T$. Under a given current I , the equilibrium condition is then

$$RI^2 = H(T - T_0)$$

H being a constant loss factor that is determined in part by sample geometry.

Let us now define for convenience the two dimensionless parameters

$$x = \frac{R_0}{R} \quad \text{and} \quad c = \frac{\Delta}{kT_0}$$

as well as the new loss factor, with dimension of an electrical current:

$$J = \sqrt{\frac{HT_0}{R_0}}$$

From the first assumption, x is defined within the range

$$e^c \geq x \geq 1$$

and for a sample with given values of T_0 , R_0 , E , and H , we can, from the foregoing assumptions, express current I , voltage V , and temperature T ,

as a function of x , as [82]

$$I(x) = J \sqrt{\frac{x \ln x}{c - \ln x}} \quad V(x) = RI = \frac{R_0 I}{x} \quad T(x) = \frac{T_0}{1 - \ln x/c}$$

These expressions give, in particular, for the current–voltage characteristics $I = f(V)$ of the sample in the thermistor regime the following two limits:

$$(1) \quad V \rightarrow 0 \text{ (or } T \rightarrow T_0): I \rightarrow \frac{V}{R_0}$$

$$(2) \quad V \rightarrow \infty \text{ (or } T \rightarrow \infty): I \rightarrow \frac{V}{R_0} e^c$$

The current-to-voltage derivative dI/dV is also

$$\frac{dI}{dV} = \frac{dI/dx}{dV/dx} = \frac{x}{R_0} \frac{1 + (1 - \ln x/c) \ln x}{1 - (1 - \ln x/c) \ln x}$$

Divergent values of this derivative occur for particular values of x which are the roots of the equation

$$1 - \left(1 - \frac{\ln x}{c}\right) \ln x = 0$$

These roots, x_I and x_{II} , are given by

$$\ln x = \frac{c}{2} \left(1 \pm \sqrt{1 - \frac{4}{c}}\right)$$

The condition for having a pseudo-negative-resistance regime, $dI/dV < 0$, is clearly that for the existence of turning points in the $I = f(V)$ characteristics (i.e., for having *two* roots). This condition is

$$c > 4 \quad \text{or} \quad \Delta > 4kT_0$$

For instance, with $T_0 = 300$ K, we obtain in this way $\Delta > 0.1$ eV.

Figure 16 provides three illustrative examples of theoretical current–voltage characteristics, in a reduced form: $\log(I/J) = f(\log(V/R_0 J))$, which are obtained respectively for the values $c = 2$ (no root), $c = 4$ (one root), and $c = 8$ (two roots).

In the particular representation of Fig. 16, isothermal curves $T = \text{constant}$ are simply given by parallel straight lines with slope -1 . This results from the following equivalent log-log expression of the current–voltage

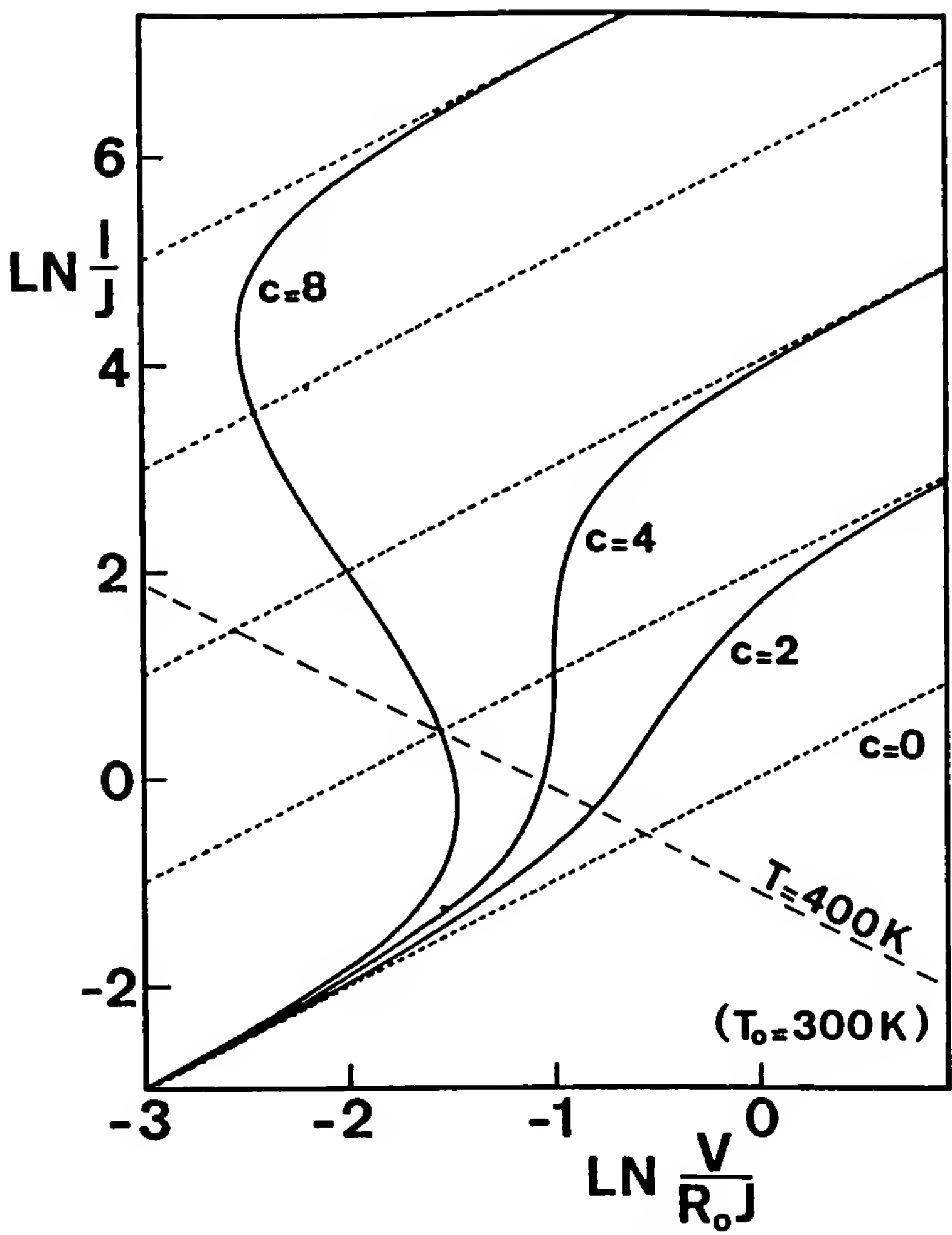


Figure 16 Theoretical I – V characteristics for an ideal thermistor in the reduced form $\ln(I/J) = f[\ln(V/R_0J)]$ for several values of the parameter c defined in the text. J is a thermal loss factor and R_0 the resistance of the thermistor in the limit $I \rightarrow 0$. In this particular representation, each characteristic $c = x$ has two parallel asymptotes with slope $+1$ (dotted lines), distant by x along the ordinate axis, and an inversion center at middistance from the asymptotes. Also, isotherms $T = \text{constant}$ are represented by parallel straight lines with slope -1 (dashed line) [82].

characteristics:

$$\log \frac{I}{J} = \log \left(\frac{T}{T_0} - 1 \right) - \log \frac{V}{R_0J}$$

In practice, it is usual to characterize a thermistor element by its temperature coefficient β , which is defined by

$$\beta = \frac{1}{R} \frac{dR}{dT}$$

This coefficient is then negative for a semiconductor ($dR/dT < 0$) and positive for a metal ($dR/dT > 0$). Within the approximations above it is also given by

$$\beta = -\frac{\Delta}{kT^2}$$

For instance, for a semiconductor with a gap $E_G = 2\Delta = 0.4$ eV, then $c = \Delta/kT_0 = 8$ (cf. Fig. 16), and $\beta = -\Delta/kT_0^2 \cong -0.03$ K⁻¹ at 300 K.

An illustrative example of a thermistor effect in an organic crystal, the segregated charge-transfer salt $\text{Cs}_2(\text{TCNQ})_3$, is reproduced in Fig. 17. In this case the gap is high: $2\Delta = 0.69$ eV, and the pseudo-negative-resistance regime is well established. One also gets $c = 13.3$ and $\beta = 0.044$ K⁻¹ [83,84].

Another example of $I = f(V)$ thermistor characteristic is presented in Fig. 18 together with what is believed to be the best fit with the foregoing theory. The organic sample here is a compacted powder of the segregated salt $\text{TEA}(\text{TCNQ})_2$ [82] (already discussed in Section III.A). Both the semiconducting gap 2Δ and loss factor J can be deduced from the fit. One gets in this way $2\Delta = 0.11$ eV, a value close to the single-crystal value at 300 K: $2\Delta = 0.08$ eV (cf. Section III.A.2) and which nearly gives $c = 2$ and $\beta = -0.007$ K⁻¹. In this case, as discussed above and shown in Fig. 16, a pseudo-negative-resistance regime ($dI/dV < 0$) cannot be attained, the value of c being too small.

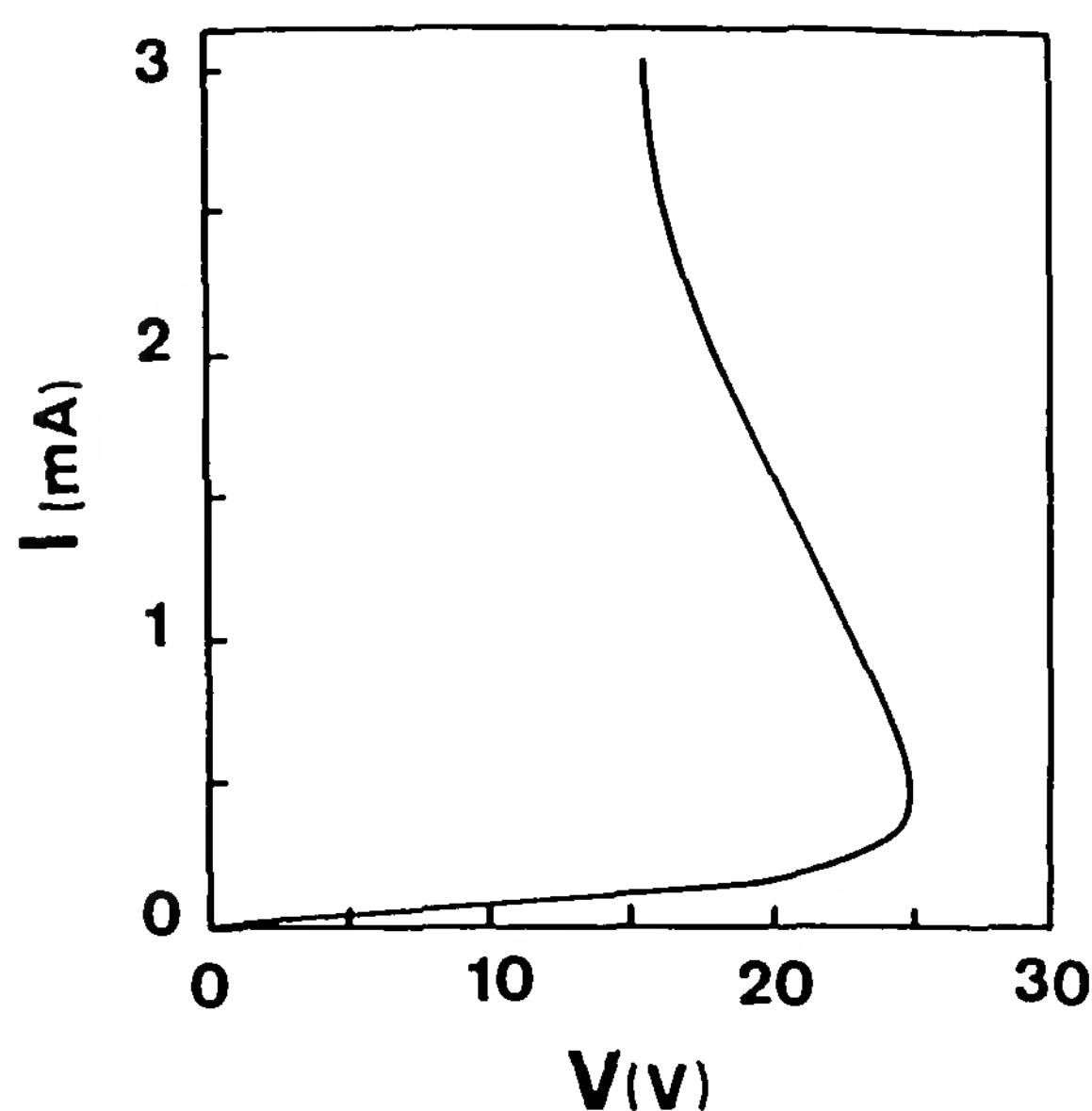


Figure 17 I - V characteristic of a sample of the 2:3 organic segregated-chain charge-transfer salt $\text{Cs}_2(\text{TCNQ})_3$ utilized as a thermistor. (From Refs. 83 and 84.)

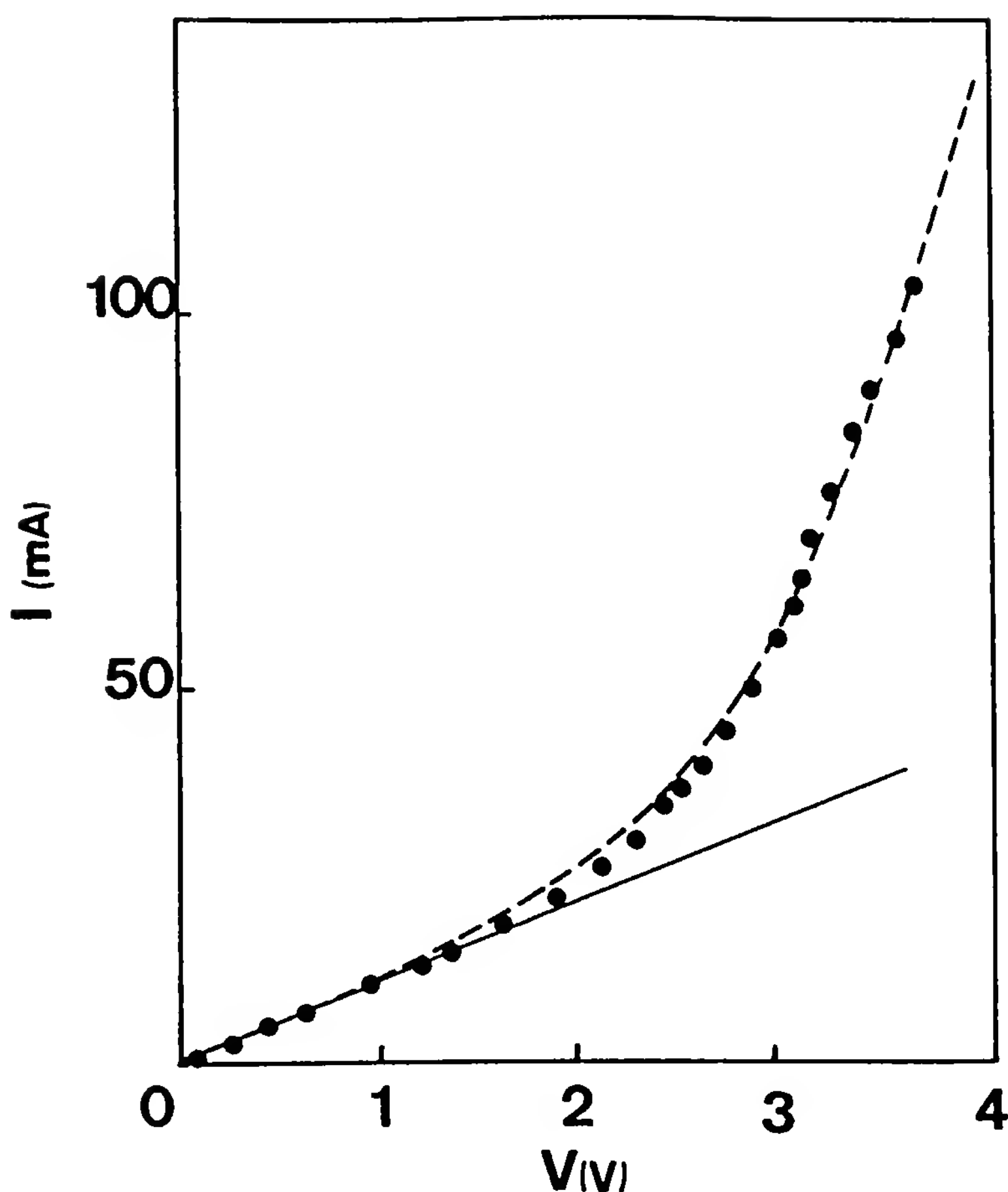


Figure 18 Experimental nonlinear I - V data for a sample of the 1:2 organic segregated-chain charge-transfer salt: TEA(TCNQ)₂ [82] (dots) and best fit with the theory given in the text [dashed line ($R_0 = 92 \, \Omega$, $2\Delta = 0.11 \, \text{eV}$, $J = 73 \, \text{mA}$)]. The solid line shows Ohm's law in the limit $I \rightarrow 0$.

C. Conducting Composites Formed by Direct Charge-Transfer Reaction Between Two Solid Components

It has been demonstrated that significant charge-transfer reactions between two organic components could be achieved directly in the solid state, without any solvent, simply by grinding the crystalline compounds thoroughly together at room temperature [85–87]. Such an effect is observable with a great variety of organic solids, being a function of the relative donor versus acceptor character of the two moieties.

The most remarkable property, worthy of mention here, is that an enormous gain of conductivity is realized in such mixtures in comparison with the insulating character of the two individual components. This implies a significant charge mobility in addition to the strong charge-transfer ef-

iciency. However, until now, no x-ray data are available to ascertain the mechanisms of these reactions.

One of the best examples is given by the solid-state reaction between donor TTF and acceptor TCNQ [86,87]. The same reaction, in solution, produces the well-known complex TTF-TCNQ, which is an organic metal [2] (see also Section IV.A). The powdered TTF/TCNQ mixture is at first highly colored in orange and yellow, and it turns rapidly dark on grinding. It also gains an intense infrared activity, intense ESR signal, and high electrical conductivity after compaction under moderate pressure (2.4 kbar) chosen for use in all the experiments. The electrical properties of such composites depend on four main parameters: temperature T , pressure P , molar fraction of donor x , and grinding time t . At given T and P , a conductivity maximum σ_M is obtained, for each value of x , after a time t_M . This value of t_M is significantly dependent on x [87].

The observed T dependence of σ_M is that of a semiconductor for any x . The measured values of σ_M and of the corresponding activation energy $\Delta = E_a$ at 300 K are reported in function x in Fig. 19 [87]. For equimolar mixtures, $x = 0.5$, the conductivity σ_M goes through a rather sharp maximum as high as 8 S/cm. For $x = 0.03$, the value of σ_M is still fairly high: $\cong 10^{-2}$ S/cm, whereas for pure TCNQ ($x = 0$) it approaches 10^{-9} S/cm (being less than 10^{-10} S/cm for the purest samples [88]).

The thermopower S at 300 K is also shown for comparison in function of x in Fig. 20 [87]. This dependence of S is surprisingly simple: S is negative

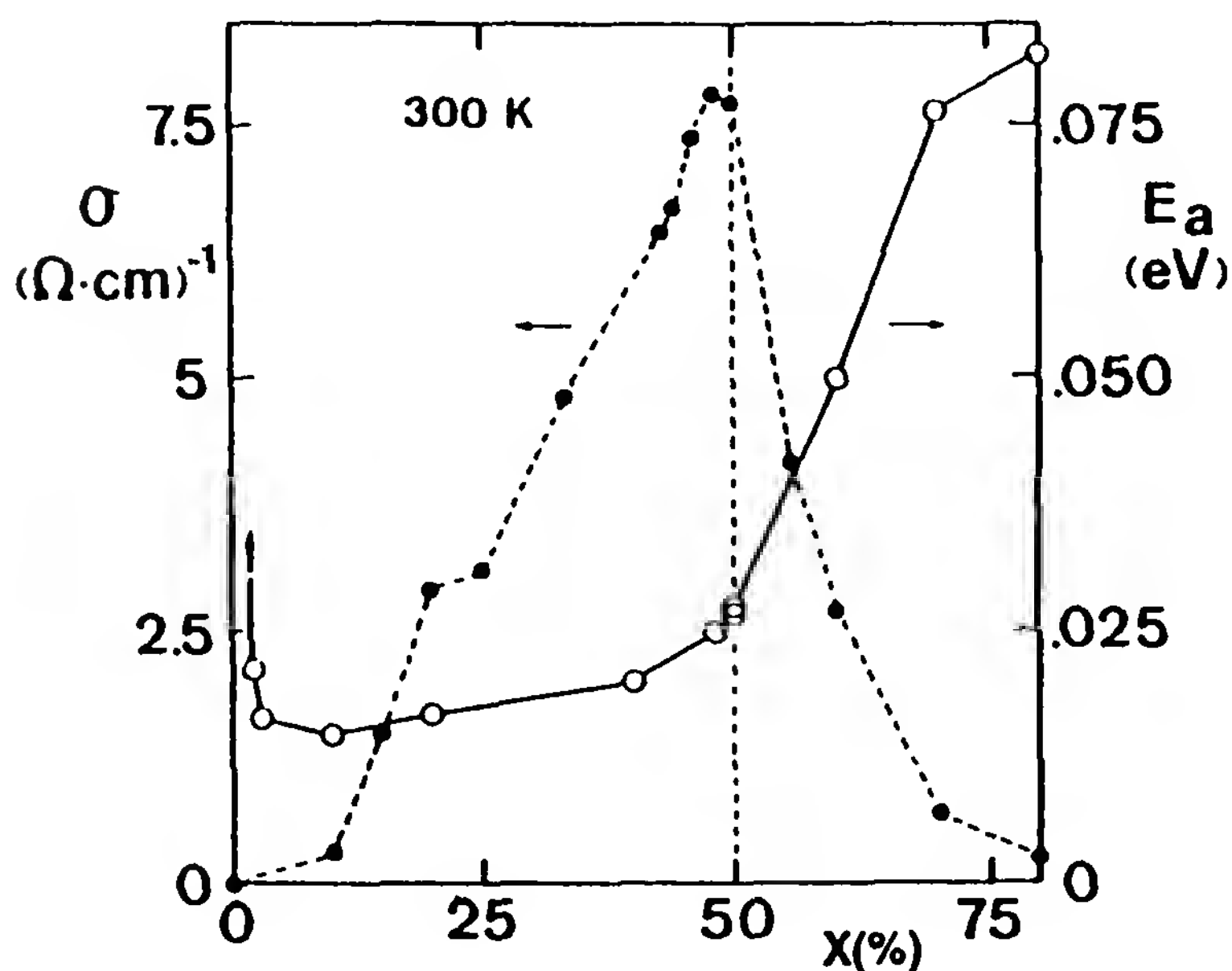


Figure 19 Dependence of electrical conductivity σ_M and activation energy E_a of TTF/TCNQ composites on molar fraction x of donor TTF. (From Ref. 87.)

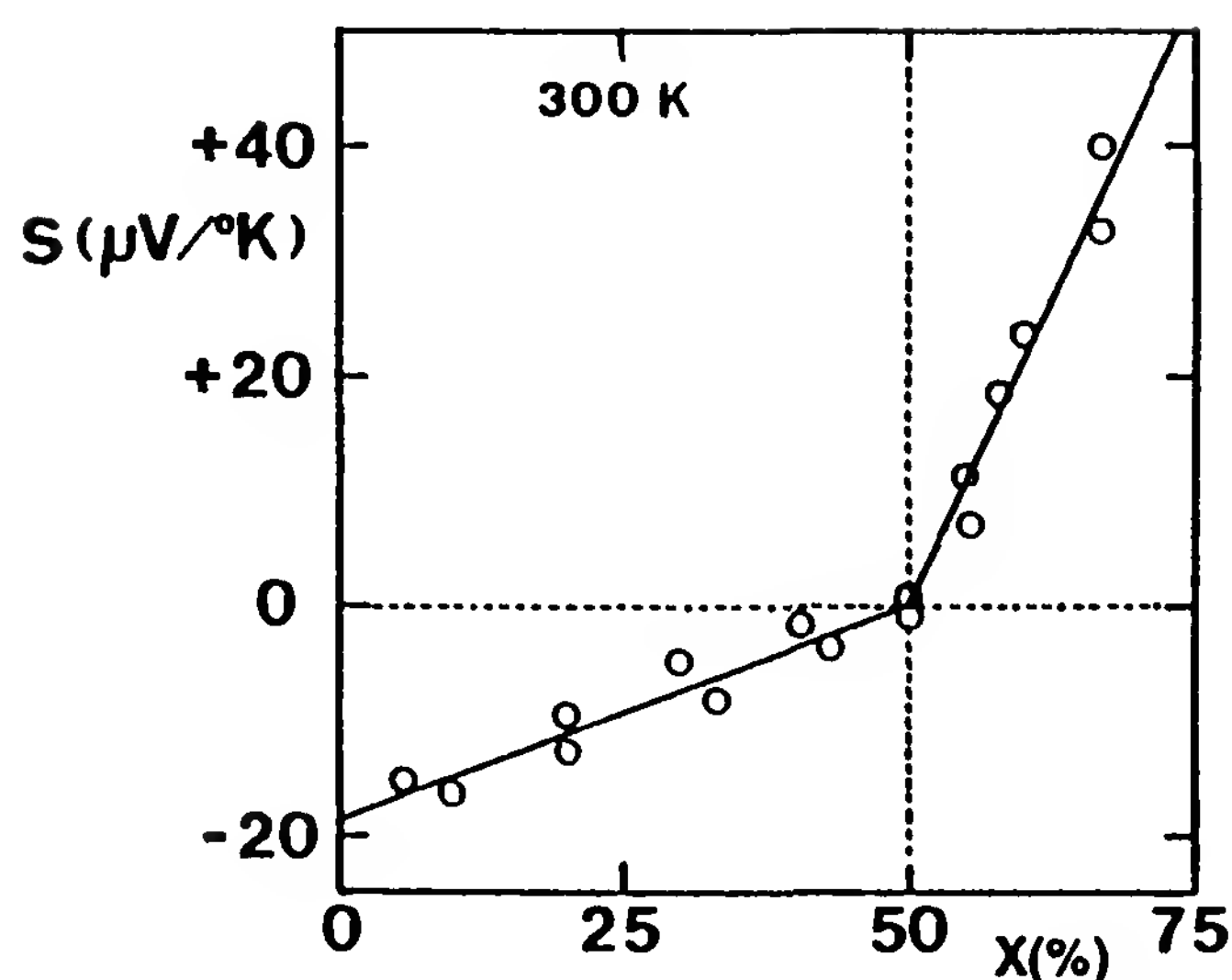


Figure 20 Dependence of thermopower S of TTF/TCNQ composites on molar fraction x of donor. (From Ref. 87.)

when acceptor TCNQ is in excess, it is positive when donor TTF is in excess, and it is then just zero for the equimolar mixture.

The particular behavior of both σ_M and E_a , at low values of the donor concentration x , are shown in detail, on a logarithmic scale, in Fig. 21 [86]. These behaviors are typical of a percolation threshold, with, however, a remarkably low critical x value of less than 0.03.

To summarize, this method offers an interesting new possibility of producing quite simply, from two initially insulating components, a great variety of conducting composites with widely adjustable electrical properties. The only thing one has, in fact, to do is to grind the two solid components together.

D. Ionizing Radiation Dosimetry

Irradiation techniques are more and more widely utilized for industrial applications: for instance, for food preservation, medical sterilization, and polymer processing. Such techniques require specific rules of control by means of accurate dosimetry [89]. In this context, new promising dosimeters based on resistance measurements of organic conducting crystals have been reviewed by Zuppiroli et al. [89]. The crystals utilized as dosimeters are either small needles ($0.01 \times 0.01 \times 3 \text{ mm}^3$) or larger plates ($0.1 \times 0.5 \times 3 \text{ mm}^3$), and their electrical resistances ($\approx 1 \text{ k}\Omega$ in the first case, $\approx 1 \Omega$ in the second) increase exponentially with the adsorbed radiation dose, up to quite high doses.

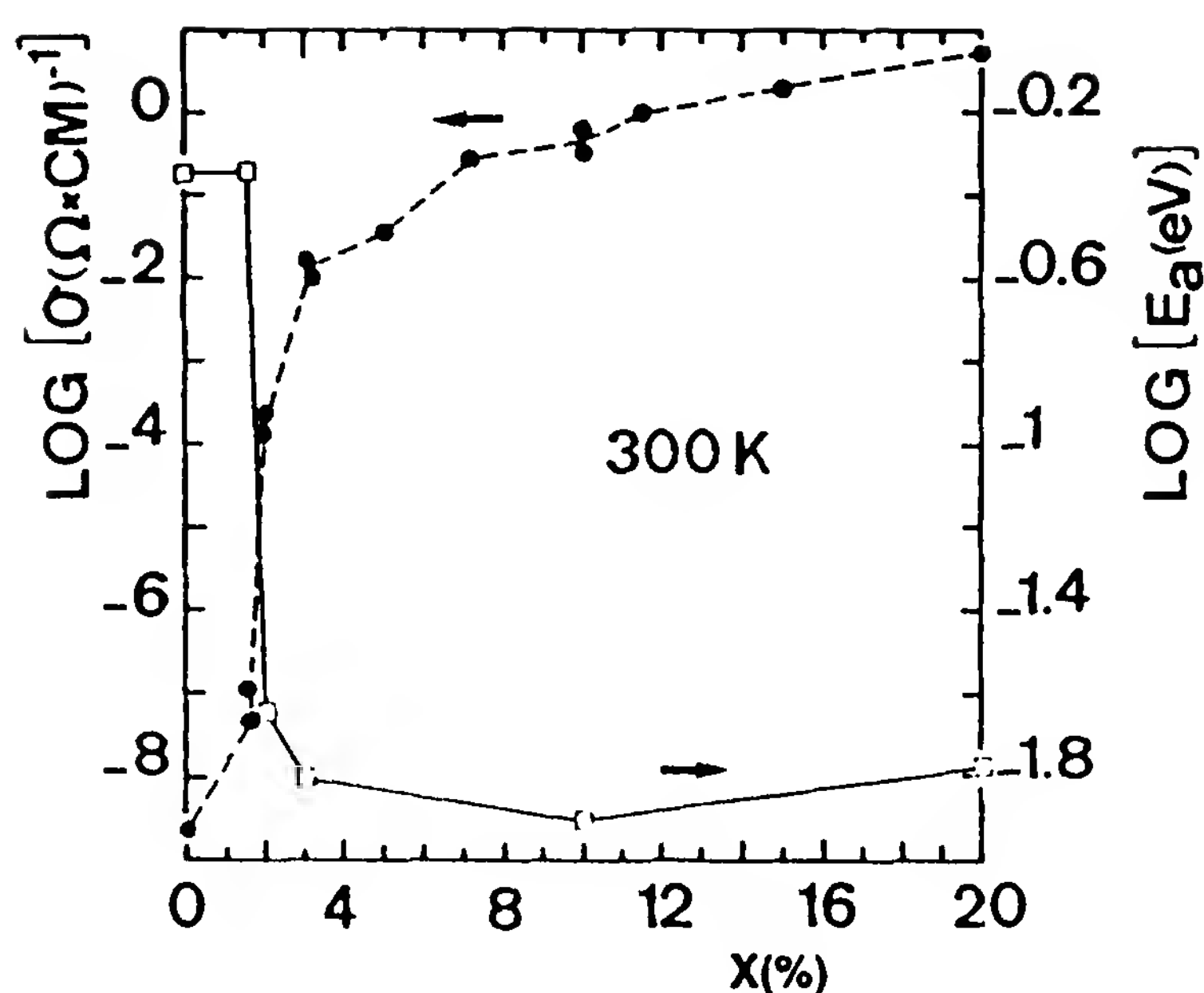


Figure 21 Dependence of σ_M and of E_a at low x values (TTF/TCNQ composites). Note the logarithmic scales. (From Ref. 86.)

The following organic materials have been investigated for dosimetric applications by Zuppiroli et al. over a wide range of adsorbed doses, from 0.01 to 50 MGy (1 Gy = 1 Grey = 1 J/kg): the metals TTT_2I_3 , TTF-TCNQ, TMTSF-DMTCNQ, and $(\text{TMTSF})_2\text{ClO}_4$ and the semiconductors $\text{Qn}(\text{TCNQ})_2$ and $\text{TEA}(\text{TCNQ})_2$ (TTT = tetrathiotetracene, TMTSF = tetramethyltetraselenofulvalene, DMTCNQ = dimethyl-TCNQ).

A particularity of some of these materials, such as $\text{Qn}(\text{TCNQ})_2$ and $\text{TEA}(\text{TCNQ})_2$, is that they contain only elements H, C, or N, not heavy atoms. In consequence, their mass energy-absorption coefficients at low photon energies are about the same as those of various substances of special dosimetric interest, such as water, biological tissues, or polymers.

In the review by Zuppiroli et al. it is concluded that one promising candidate for high absorbed dose measurements, from 0.01 up to 50 MGy, is the organic conductor (TMTSF)DMTCNQ. The measurements are particularly stable and reproducible with this material, whatever the incident particles are, photons or electrons (see Fig. 22). When a material with a mass absorption coefficient close to the value for water is required, the organic semiconductor $\text{TEA}(\text{TCNQ})_2$ is also a good candidate, and it is even more sensitive at low doses. Conducting polymers are also quite sensitive to irradiations; however, it appears that they are generally less stable and more sensitive to water and oxygen than to organic crystals.

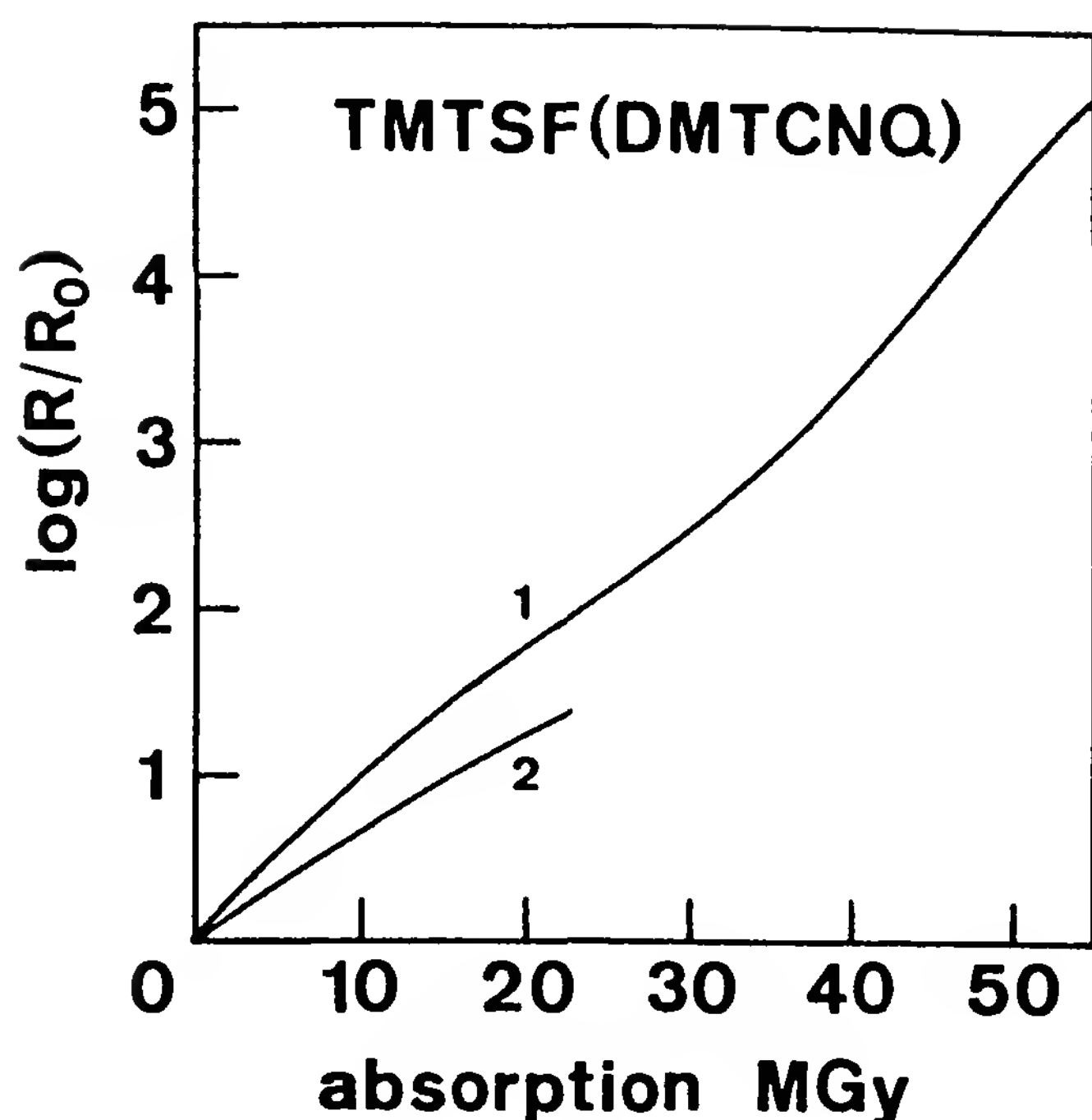


Figure 22 Logarithm of the normalized resistance $\log(R/R_0)$ versus the absorbed ionizing dose for samples of the organic charge-transfer salt TMTSF-DMTCNQ: 1, electron irradiations; 2, x-ray irradiations. (Adapted from Ref. 89.)

REFERENCES

1. F. Gutman and L. E. Lyons, *Organic Semiconductors*, Wiley, New York, 1967.
2. D. Jérôme and H. J. Schulz, *Adv. Phys.* 31:299 (1982).
3. D. Jérôme and L. G. Caron, eds., *Low-Dimensional Conductors and Semiconductors*, NATO ASI Series, Vol. 155, Plenum Press, New York, 1987.
4. *Proceedings of the International Conference on Science and Technology of Synthetic Metals (ICSM'88)*, Santa Fe, N.Mex., June 26–July 2, 1988; *Synth. Metals* 27 (1988), 28–29 (1989).
5. *Proceedings of the International Conference on Science and Technology of Synthetic Metals (ICSM'90)*, Tübingen, Germany, Sept. 2–7, 1990; *Synth. Metals* 41–43 (1991).
6. *Proceedings of the International Conference on Science and Technology of Synthetic Metals (ICSM'92)*, Göteborg, Sweden, Aug. 12–18, 1992; *Synth. Metals* (in press, 1993).
7. *Proceedings of the 9th International Conference on the Chemistry of the Organic Solid State (ICCOSS IX)*, Como, Italy, July 2–7, 1989; *Mol. Cryst. Liq. Cryst.* 186 (1990).
8. *Proceedings of the 10th International Conference on the Chemistry of the Organic Solid State (ICCOSS X)*, Vancouver, British Columbia, Canada, July 7–12, 1991; *Mol. Cryst. Liq. Cryst.* 211 (1992).

9. *Proceedings of the 11th International Conference on the Chemistry of the Organic Solid State (ICCOSS XI)*, Jerusalem, Israel, July 5–9, 1993; Mol. Cryst. Liq. Cryst. (to be published).
10. J.-P. Farges and F. Gutmann, in *Modern Aspects of Electrochemistry*, Vol. 12 (J. O'M. Bockriss and B. E. Conway, eds.), Plenum Press, New York, 1977, pp. 267–314.
11. F. Gutmann and J.-P. Farges, in *Modern Aspects of Electrochemistry*, Vol. 13 (B. E. Conway and J. O'M. Bockriss, eds.), Plenum Press, New York, 1979, pp. 361–421.
12. Z. H. Wang, E. M. Scherr, A. G. MacDiarmid, and A. J. Epstein, Phys. Rev. B 45:4190 (1992).
13. C. Kittel, *Introduction to Solid State Physics*, 4th ed., Wiley, New York, 1971.
14. C. Bourbonnais, in Ref. 3, pp. 155–183.
15. J.-P. Farges, J. Phys. 46:465 (1985).
16. A. J. Epstein, E. M. Conwell, and J. S. Miller, Ann. N.Y. Acad. Sci. 313:183 (1978).
17. G. A. Sawatzky, S. Huizinga, and J. Kommandeur, in *Quasi One-Dimensional Conductors II: Proceedings of the International Conference*, Dubrovnik, Yugoslavia, Sept. 1978 (S. Barišić, A. Bjelis, J. R. Cooper, and B. Leontic, eds.), Springer-Verlag, Berlin, Lecture Notes in Physics, Vol. 96, 1979, pp. 34–44; S. Huizinga, J. Kommandeur, G. A. Sawatzky, K. Kopinga, and W. J. M. De Monde, Ibid., pp. 45–49.
18. S. Huizinga, Thesis, Groningen, The Netherlands, 1980.
19. J. Kommandeur, in Ref. 3, pp. 87–94.
20. J.-P. Farges, in *Physics and Chemistry of Low-Dimensional Solids: Proceedings of the NATO-ASI Conference*, Tomar, Portugal, Aug. 26–Sept. 7, 1979 (L. Alcácer, ed.), D. Reidel, Dordrecht, The Netherlands, 1980, pp. 223–232.
21. A. Filhol, C. M. E. Zeyen, P. Chenavas, J. Gaultier, and P. Delhaes, Acta Cryst. B 36:2719 (1980).
22. A. Filhol and M. Thomas, Acta Cryst. B 40:44 (1984).
23. A. Filhol, Thesis, Bordeaux, France, 1985.
24. A. Bosh and B. v. Bodegom, Acta Cryst. B 33:3013 (1977).
25. B. v. Bodegom, Thesis, Groningen, The Netherlands, 1979.
26. H. Grassi, A. Brau, and J.-P. Farges, Phys. Status Solidi (a) 55:K179 (1979).
27. A. Brau and J.-P. Farges, Phys. Status Solidi (b) 61:257 (1974).
28. J. P. Pouget, in Ref. 3, pp. 17–45.
29. A. A. Abrikosov, *Fundamentals of the Theory of Metals*, North-Holland, Amsterdam, 1988, p. 348.
30. A. Brau, P. Bruesch, J.-P. Farges, W. Hinz, and D. Kuse, Phys. Status Solidi (b) 62:615 (1974).
31. M. J. Rice, L. Pietronero, and P. Buesch, Solid State Commun. 21:757 (1977).
32. E. F. Steigmeier, H. Auderset, D. Baeriswyl, M. Almeida, and K. Carneiro, J. Phys. C3, 44:1445 (1983).

33. K. Carneiro, M. Almeida, and L. Alcácer, *Solid State Commun.* **44**:959 (1982).
34. J. S. Pedersen, K. Carneiro, L. K. Hansen, and M. Almeida, *Synth. Metals* **19**:433 (1987).
35. J. S. Pedersen, K. Carneiro, and M. Almeida, *J. Phys. C Solid State Phys.* **20**:1781 (1987).
36. J. S. Pedersen and K. Carneiro, *Rep. Prog. Phys.* **50**:995 (1987).
37. H. J. Schulz, *Phys. Rev. B* **18**:5756 (1987).
38. S. Flandrois and D. Chasseau, *Acta Cryst. B* **33**:2744 (1977).
39. J.-P. Farges, *J. Phys.* **46**:1249 (1985).
40. S. Oostra, Thesis, Groningen, The Netherlands, 1985.
41. M. Almeida, L. Alcácer, and S. Oostra, *Phys. rev. B* **30**:2839 (1984).
42. J.-P. Farges and A. Brau, *Phys. Status Solidi (b)* **64**:269 (1974).
43. P. M. Chaikin, in *Thermoelectricity in Metallic Conductors: Proceedings of the First International Conference on Thermoelectric Properties of Metallic Conductors*, Michigan State University, Aug. 10–12, 1977 (F. J. Blatt and P. A. Schroeder, eds.), Plenum Press, New York, 1978, pp. 359–375.
44. Z. G. Soos and D. J. Klein, in *Treatise on Solid State Chemistry*, Vol. 3, *Crystalline and Noncrystalline Solids* (N. B. Hannay, ed.), Plenum Press, New York, 1976, pp. 679–767.
45. J. B. Torrance, in Ref. 3, pp. 113–133.
46. Q. Liu, S. Ravy, J. P. Pouget, C. Coulon, and C. Bourbonnais, in Ref. 6 (in press).
47. N. Watanabe, Y. Isawa, and T. Koda, *Phys. Rev. B* **44**:11111 (1991).
48. L. G. Caron, F. Creuzet, P. Butaud, C. Bourbonnais, D. Jérôme, and K. Bechgaard, in Ref. 4, pp. B123–B128.
49. L. Ducasse, C. Coulon, D. Chasseau, R. Yagbasan, J. M. Fabre, and A. K. Gouasmia, in Ref. 4, pp. B543–B548.
50. H. J. Schulz, in Ref. 3, pp. 95–112.
51. L. K. Hansen and K. Carneiro, *Solid State Commun.* **49**:531 (1984).
52. I. Olejniczak and A. Graja, preprint, 1993.
53. J. P. Travers, F. Devreux, and M. Nechtschein, *J. Phys. C3* **44**:1295 (1983).
54. J. P. Travers, Thesis, Grenoble, France, 1986.
55. S. Oostra, B. v. Bodegom, S. Huizinga, G. A. Sawatzky, G. Grüner, and J. P. Travers, *Phys. Rev. B* **24**:5004 (1981).
56. G. Zimmer, A. C. Kolbert, F. Rachdi, P. Bernier, M. Almeida, and M. Mehring, in Ref. 6 (in press).
57. E. M. Conwell and I. A. Howard, *Phys. Rev. B* **31**:7835 (1985).
58. J. P. Pouget, *Chem. Scr.* **17**:85 (1981).
59. R. T. Henriques, S. Tomic, W. Kang, D. Jérôme, F. Brisset, P. Batail, P. Erk, S. Hünig, and J. U. von Schütz, in Ref. 4, pp. B333–B338.
60. K. Mortensen, E. M. Conwell, and J. M. Fabre, *Phys. Rev. B* **28**:5856 (1983).
61. R. Bozio, D. Pedron, M. Meneghetti, and C. Pecile, in Ref. 5, pp. 1653–1656.
62. L. Zuppiroli, in Ref. 3, pp. 307–333.

63. K. Kamaras, C. S. Jacobsen, V. Zelezny, J. L. Musfeldt, and D. B. Tanner, in Ref. 5, pp. 1839–1842.
64. S. D. Obertelli, R. H. Friend, A. J. Moore, M. R. Bryce, and P. Bates, in Ref. 4, pp. B327–B332.
65. S. D. Obertelli, R. H. Friend, D. R. Talham, M. Kurmoo, and P. Day, in Ref. 4, pp. A375–A380.
66. M. Kurmoo, M. Allan, R. H. Friend, D. Chasseau, G. Bravic, and P. Day, in Ref. 5, pp. 2127–2130.
67. H. Endres, in *Extended Linear Chain Compounds*, Vol. 3 (J. S. Miller, ed.), Plenum Press, New York, 1983, pp. 263– .
68. N. Sakai, I. Shirotani, and S. Minomura, Bull. Chem. Soc. Jpn. 45:3321 (1972).
69. J. Kommandeur, in *Physics and Chemistry of Low-Dimensional Solids: Proceedings of the NATO-ASI Conference*, Tomar, Portugal, Aug. 26–Sept. 7, 1979 (L. Alcácer, ed.), D. Reidel, Dordrecht, The Netherlands, 1980, pp. 197–212.
70. H. Okamoto, Y. Tokura, and T. Koda, Phys. Rev. B 36:3858 (1987).
71. H. Terauchi, Phys. Rev. B 17:2446 (1978).
72. J. B. Torrance, J. E. Vazquez, J. J. Mayerle, and V. Y. Lee, Phys. Rev. Lett. 46:253 (1981).
73. J. B. Torrance, A. Girlando, J. J. Mayerle, J. I. Crowley, V. Y. Lee, P. Batail, and S. J. la Placa, Phys. Rev. Lett. 47:1747 (1981).
74. H. Okamoto, Y. Tokura, T. Koda, and G. Saito, Synth. Metals 19:527 (1987).
75. H. Okamoto, T. Komatsu, Y. Isawa, T. Koda, Y. Tokura, S. Koshihara, T. Mitani, and G. Saito, in Ref. 4, pp. B189–B196.
76. Y. Iwasa, T. Koda, Y. Tokura, S. Koshihara, N. Iwasawa, and G. Saito, Appl. Phys. Lett. 55:2111 (1989).
77. Y. Iwasa, T. Koda, S. Koshihara, Y. Tokura, N. Iwasawa, and G. Saito, Phys. Rev. B 39:10441 (1989).
78. Y. Iwasa, N. Watanabe, T. Koda, S. Koshihara, Y. Tokura, N. Iwasawa, and G. Saito, in Ref. 5, pp. 1675–1678.
79. Y. Iwasa, I. Soga, T. Koda, Y. Tokura, and G. Saito, in Ref. 5, pp. 1827–1830.
80. R. S. Potember, T. O. Poehler, and R. C. Benson, Appl. Phys. Lett. 41:548 (1982).
81. P. H. E. Meijer and A. van Roggen, J. Mol. Electron. 4:119 (1988).
82. J.-P. Farges, A. Brau, and E. Ghezzal (to be published).
83. S. Kosimi, K. S. Karimov, and B. P. Bepalov, in *Elektronika Organicheskikh Materialov* (Electronics of Organic Materials) (A. A. Ovchinnikov, ed.), Nauka, Moscow, 1985 (in Russian).
84. A. Graja, *Low-Dimensional Organic Conductors*, World Scientific, Singapore, 1992.
85. J.-P. Farges, A. Brau, and P. Dupuis, Solid State Commun. 54:531 (1985).
86. A. Brau, J.-P. Farges, and F. Ali Sahraoui, Synth. Metals 27:B71 (1988).

87. J.-P. Farges, A. Brau, and F. Ali Sahraoui, *Mol. Cryst. Liq. Cryst.* **186**:143 (1990).
88. S. Hiroma, H. Kuroda, and H. Akamatu, *Bull. Chem. Soc. Jpn.* **44**:974 (1971).
89. L. Zuppiroli, S. Bouffard, and J. J. Jacob, *Int. J. Appl. Radiat. Isot.* **36**:843 (1985).

This Page Intentionally Left Blank

9

Organic Metals

J. R. Cooper*

University of Cambridge, Cambridge, England

B. Korin-Hamzić

Institute of Physics of the University, Zagreb, Croatia

I. INTRODUCTION

This chapter is devoted to some of the basic physical properties of those organic metals that are formed from large planar molecules such as the TTF (tetrathiafulvalene) molecule and its derivatives. Many hundreds of such organic conductors have been synthesized since the early 1970s when transport and structural studies of single crystals of TTF-TCNQ (tetrathiafulvalenetetracyanoquinodimethane) first caught the imagination of organic chemists, crystallographers, and solid-state physicists.

Several excellent review articles have been written on this subject. Early work, mostly on compounds containing the TCNQ acceptor molecule, is summarized in the article by Schegolev [1]. Ten years later a comprehensive review of the current experimental and theoretical situation was given by Jérôme and Schulz [2], and since then the field has continued to develop rapidly. Much attention has been paid to layer compounds of the BEDT-TTF [bis(ethylenedithio)tetrathiafulvalene or ET] family, some of which have superconducting transition temperatures as high as 13 K, and whose properties are reviewed by Bulaevskii [3]. Organic superconductors are reviewed in detail by Ishiguro and Yamaji [4], while several articles give short overviews of the subject [5–7].

In preparing this chapter we have focused mainly on fairly straightforward electronic properties such as electrical resistivity, resistivity aniso-

*On leave of absence from the Institute of Physics of the University, Zagreb, Croatia.

tropy, and magnetoresistance of a few representative organic metals. Even then, because of the existence of the review articles cited above and time limitations, we have decided to deal mainly with our own work or the closely related work of other groups. So at the outset we offer sincere apologies to colleagues and friends in the field who have made important contributions that are not adequately cited here. On the other hand, we have tried to emphasize points that we feel are still not entirely settled and that may perhaps be amenable to further study in the future.

Earlier chapters in this volume have dealt with the molecular properties and crystal structures of organic metals. The large planar molecules under consideration here are usually stacked face to face in chains; sometimes the molecular planes are perpendicular to the stacking axis, as in the case of the Bechgaard salts, or they may be tilted by as much as 30° , as in TTF-TCNQ. Because the overlap of the partially occupied π orbitals is much better along the stacking axis, their electronic band structures are often quasi-one-dimensional.

II. HISTORY OF ORGANIC CONDUCTORS

A. Early Conductors

Most of the early organic conductors were based on the TCNQ acceptor molecule [1]. Many of these are radical-ion salts having nonuniform stacks composed of dimers, trimers, or tetramers and are thus semiconductors at room temperature (see, e.g., Ref. 8 or Chapter 8 in this volume). From the crystal structures and molecular arrangements [8], it is clear that for the vast majority of these salts, this nonuniformity is driven by Coulomb attraction between the positive donor ions and the π -electron density on the TCNQ molecules, which is larger in the regions where they are more closely spaced. A few materials with uniform stacks were known before 1972, such as $\text{Qn}(\text{TCNQ})_2$ and $\text{TTF Br}_{0.7}$, and these were the best organic conductors known until the discovery of TTF-TCNQ, but their conductivity was limited by intrinsic disorder.

B. Compounds with Uniform Chains

Compounds synthesized in the past two decades, which have uniform stacks with no intrinsic disorder and which make the best organic conductors, can be roughly classified as follows:

1. Two chain compounds, such as TTF-TCNQ and its derivatives, where both donor (TTF) stacks and acceptor (TCNQ) stacks give comparable contributions to the electrical conductivity. Although these compounds

exhibit a rich variety of interesting physical phenomena, especially in their structural properties, which are now quite well understood (see, e.g., the reviews by Pouget [9] and by Barišić and Bjeliš [10]), it is often more difficult to separate out the contributions of the two types of chain to their transport properties.

2. Some compounds, such as $(\text{TSeT})_2\text{Cl}$, have only one type of conducting molecule but still have two (or more) types of chain because there are two (or more) inequivalent molecules per unit cell.
3. Single-chain compounds such as the Bechgaard salts $(\text{TMTSF})_2\text{X}$, where the chains are (nearly) uniform and all chains are equivalent.
4. Two-dimensional compounds such as the ET salts. Here there is often significant dimerization along the chains, but metallic behavior is maintained by strong interchain interactions (e.g., sulfur–sulfur interactions) in one perpendicular direction, giving rise to two-dimensional conducting sheets.

III. ANISOTROPIC COMPOUNDS

A. Physical Characteristics

1. Conductivity and Its Anisotropy

The crystal symmetry of most organic metals is low, often only monoclinic, and the principal axes of the conductivity tensor (σ) are not precisely defined. However, in practice the conductivity along the chain direction (σ_h) is particularly high, usually 300 to $2500 (\Omega \cdot \text{cm})^{-1}$ at room temperature, while that in one direction perpendicular to the chains (σ_l) is very low [2]. Therefore, these two directions must be very close to the principal axes of σ . The third perpendicular direction has intermediate conductivity (σ_i). So in the situation, where $\sigma_h \gg \sigma_i \gg \sigma_l$, which is quite common, the principal axes of the conductivity and resistivity (ρ) tensors are known reasonably well. When measuring these quantities on a single crystal, care must be taken either to ensure that the current distribution is uniform, or alternatively, special methods such as those of Montgomery [11] or van der Pauw [12] must be used. Some insight into these problems can be obtained by consideration of the equivalent isotropic sample [11,13].

Figure 1 shows the overall T dependence of the resistivity in the highly conducting chain direction ($\rho_h = 1/\sigma_h$) on a log-log scale for some representative organic metals [14–20]. The points of interest are firstly that $\rho_h(T)$ falls approximately as T^2 in all cases except for $(\text{TSeT})_2\text{Cl}$, where the dependence is close to T^1 . Second, the β -(BEDT-TTF) $_2\text{I}_3$ compound, like others of its family [3], has a particularly large room-temperature resistivity.

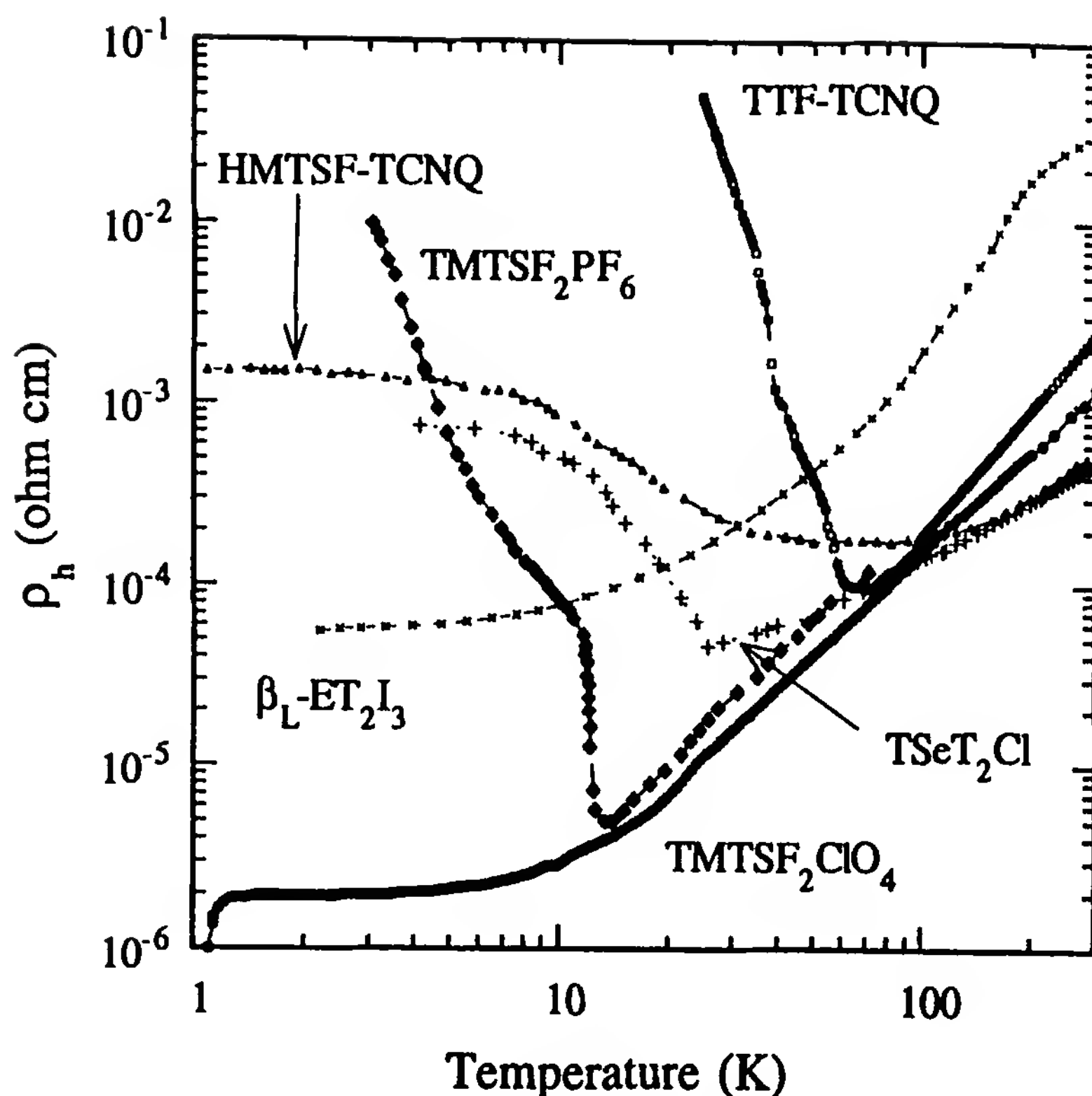


Figure 1 Log-log plots of longitudinal resistivity ρ_h versus temperature T for representative organic conductors: TTF-TCNQ (from Ref. 14), HMTSF-TCNQ (from Ref. 15), $(\text{TMTSF})_2\text{PF}_6$ (from Refs. 17 and 19), $\text{TMTSF}_2\text{ClO}_4$ (from Ref. 16), $(\text{TSeT})_2\text{Cl}$ (from Ref. 18), and $\beta_{\text{L}}\text{-ET}_2\text{I}_3$ (from Ref. 20).

The resistivity in the weakly conducting direction (ρ_l) has been investigated to a much lesser extent. Some representative $\log \rho_l$ versus $\log T$ plots are given in Fig. 2 [21–26] (also, unpublished results of L. Forró, B. Korin-Hamzić, and B. Hilti) and show that there is a wider variation in the room-temperature values of ρ_l than in ρ_h . The large differences between ρ_l of the $\text{X} = \text{ClO}_4$ and $\text{X} = \text{PF}_6$ Bechgaard salts may be relevant for understanding the competition between superconductivity and antiferromagnetism; however, as shown in Table 1, there are also substantial differences in ρ_l . The principal resistivities of various compounds and their T dependences [14–27] (also, unpublished results of L. Forró, B. Korin-Hamzić, and B. Hilti) are summarized in Table 1. It is clear from the table that $\beta\text{-(BEDT-TTF)}_2\text{I}_3$ (and other ET salts [3]) can be regarded as two-dimensional, while TTF-TCNQ is definitely one-dimensional. The Bechgaard salts are one-dimensional but occasionally can be regarded as two-dimensional materials with substantial remanent anisotropy in the conducting planes. $(\text{TSeT})_2\text{Cl}$ is the closest of all these materials to being

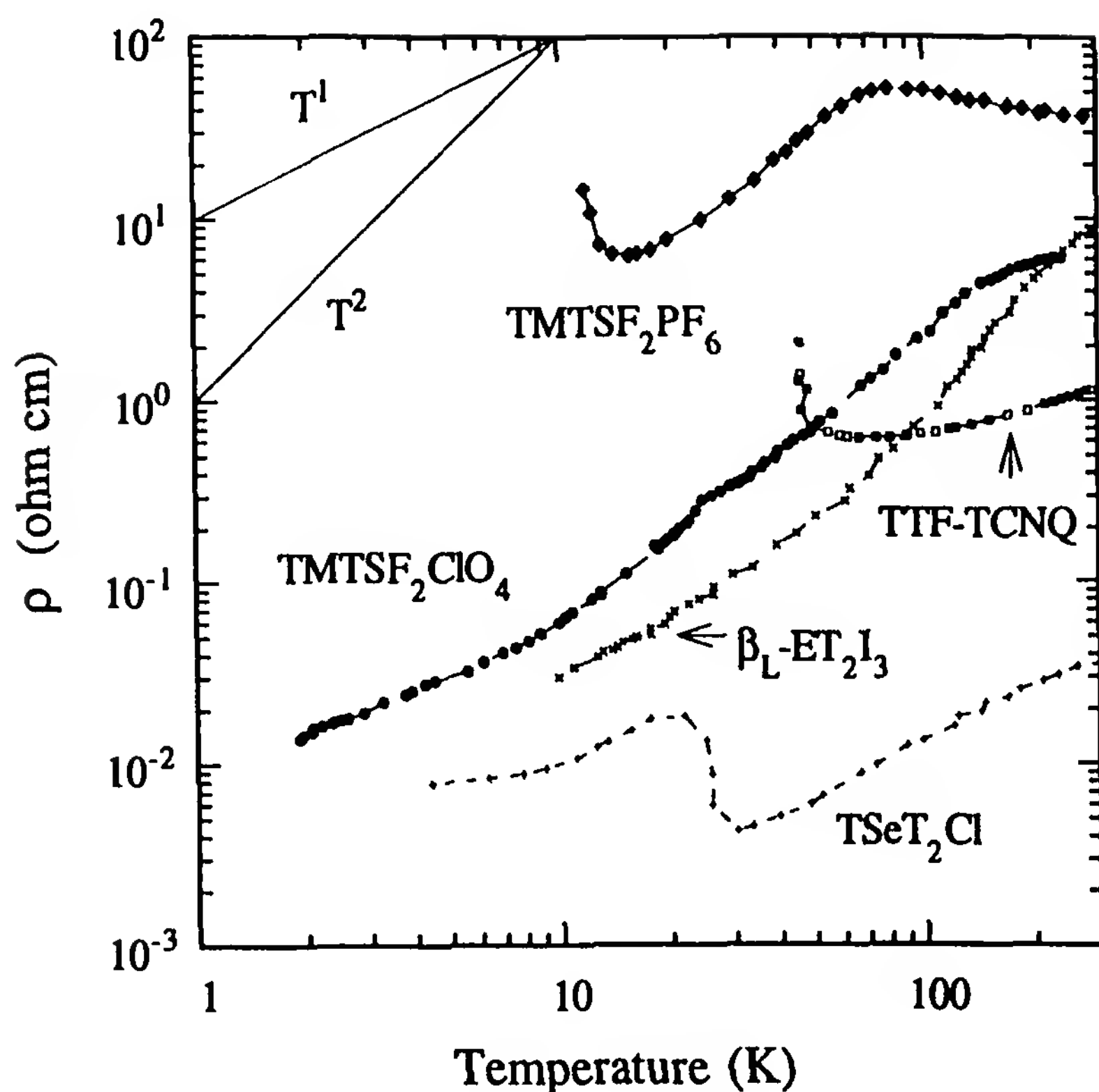


Figure 2 Log-log plots of transverse resistivity ρ_t (in the low-conductivity direction) versus temperature T for representative organic conductors: TTF-TCNQ (from Ref. 21), TMTSF₂PF₆ (from Ref. 23), TMTSF₂ClO₄ (from Ref. 22), TSeT₂Cl (from unpublished results of L. Forró, B. Korin-Hamzić, and B. Hilti), and β_L -ET₂I₃ (from Ref. 26).

three-dimensional, in that it has a relatively large and isotropic transverse conductivity, although there is still substantial anisotropy, $\sigma_h/\sigma_i = \sigma_h/\sigma_t \approx 30$.

The anisotropy in conductivity is temperature dependent; it is quite common for the intermediate resistivity ρ_i to obey a T^1 law ($\rho_i \approx \rho_0 + \alpha T$, where ρ_0 can be considered to be a residual resistivity), and since ρ_h often varies as T^2 , the anisotropy ρ_i/ρ_h increases as T is lowered. Surprisingly, ρ_t often shows a T^2 dependence and ρ_t/ρ_h varies less as the temperature is lowered.

2. Phase Transitions

Figure 1 also illustrates the fact that many of these anisotropic compounds undergo metal–semiconductor transitions below about 50 K [2]. For TTF-TCNQ, which was investigated intensively in the 1970s, diffuse x-ray scattering studies first showed conclusively that this was a Peierls transition [28]. There are, in fact, three phase transitions, at 53, 48, and 38 K.

Table 1 Representative Behavior of Electrical Conductivity of Some Organic Metals at Ambient Pressure

Compound	$\sigma_h(300)$ ($\Omega\cdot\text{cm}$) ⁻¹	T dep.	Range (K)	$\sigma_i(300)$ ($\Omega\cdot\text{cm}$) ⁻¹	T dep.	Range (K)	$\sigma_r(300)$ ($\Omega\cdot\text{cm}$) ⁻¹	T dep.	Range (K)	Refs.
TTF-TCNQ	400	$T^{-2.3}$	70–300	4–6	T^{-1}	80–300	0.5–1	T^{-1}	200–300	21
HMTSF-TCNQ	1800	?	—	60	—	—	4	—	—	27,128
(TMTSF) ₂ PF ₆	800	T^{-2}	30–300	3	T^{-1}	30–300	0.03	T^{-2}	20–70	23,24
(TMTSF) ₂ ClO ₄	800	T^{-2}	10–300	20	—	—	0.17	T^{-1}	2–10	16,122
(TSeT) ₂ Cl	2000	T^{-1}	40–200	60	T^{-1}	40–300	60	T^{-2}	10–120	104
β -(BEDT-TTF) ₂ T ₃	20–70	T^{-2}	10–100	12–45	T^{-2}	10–100	0.1	T^{-1}	40–300	18 ^a
								T^{-2}	10–100	3,25,26

^aAlso, unpublished results of L. Forró, B. Korin-Hamzić, and B. Hilti.

However, as discussed extensively in review articles by Pouget [9] and by Barišić and Bjeliš [10], the presence of both $2k_F$ and $4k_F$ anomalies, where k_F is the Fermi wave vector of the quasi-one-dimensional electron gas, the fact that phonon softening at $2k_F$ is relatively small, combined with theoretical considerations, have lead to the present-day viewpoint that electron–electron Coulomb interactions play an important role.

For $(\text{TMTSF})_2\text{PF}_6$ the metal–semiconductor transition is to a spin density wave or itinerant antiferromagnetic ground state. The evidence for this has been reviewed previously (e.g., Ref. 2). A conclusive demonstration was the measurement of magnetic susceptibility for three field directions on a single crystal of $(\text{TMTSF})_2\text{AsF}_6$, which showed the classical behavior for an antiferromagnet, including a spin flop transition [29]. For the almost identical compound, $(\text{TMTSF})_2\text{PF}_6$, x-ray scattering studies do show the presence of weak $2k_F$ lines between 125 and 35 K, but these disappear again at lower temperatures [30], indicating that the ground state is indeed a pure spin-density wave (SDW), not a mixed charge (C)- and spin-density wave state. This is most important when discussing the SDW conduction (Chapter 10).

For HMTSF-TCNQ the conductivity remains relatively high at low T [15], and in early work the application of relatively modest pressures stabilized a metallic state down to millikelvin temperatures [31]. As discussed later, subsequent measurements of the Hall effect showed that only a very small number of carriers were responsible for conduction at low T , even under pressure [32]. Combined with other evidence, such as anomalous diamagnetism [33], this showed that the ground state was semimetallic rather than truly metallic. This was originally ascribed to strong hybridization of the HMTSF and TCNQ bands [33]. However, observation of strong diffuse x-ray scattering lines at $2k_F$ arising from the HMTSF chains [9,34] implies that the electronic states may also be strongly modified by a charge density wave or Peierls distortion that has only short-range order in the transverse directions.

For $(\text{TSeT})_2\text{Cl}$ there is a sharper transition to a semimetallic state below 25 K [18]. The origin of this transition is still unclear, but it can be suppressed by applying pressures greater than 5 kbar [66].

B. Anisotropic Tight-Binding Model

1. Introduction

In the 1970s it was generally thought that transport in extremely anisotropic organic metals could not be understood in terms of the traditional concepts of a Fermi surface (FS) and a relaxation time (τ) that were developed and used successfully for metallic elements and their alloys in the previous two

decades [35]. However, it gradually became clear that in the materials studied, the interchain coupling was sufficiently strong for there to be a “crossover” from one- to two-dimensional and then eventually to three-dimensional behavior as the temperature was lowered. As explained by Emery [36] and in Chapter 2, these crossover temperatures are of order t_i/k_B and t_l/k_B , respectively, where k_B is Boltzmann’s constant and t_i and t_l are the tight-binding transfer integrals for the intermediate- and low-conductivity directions. As a result, characteristic one-dimensional features, such as the power law divergences discussed in Chapters 2 and 10, occur only above certain crossover temperatures, which vary from one compound to another and which can be increased by the application of hydrostatic pressure. It is important to note that even in the low-temperature region; the one- and two-dimensional characteristics are still expected to affect the *magnitudes* of the electron–electron and electron–lattice interactions (S. Barišić, private communication).

Because of this crossover behavior, the concepts of a FS and a relaxation time are still useful at low T . Early experimental evidence for this was that in several cases the effect of a magnetic field on the resistivity could be described by Kohler’s rule (Section VII.B). Furthermore, an anisotropic tight-binding band structure together with a mean field (nesting) theory of itinerant antiferromagnetism turned out to be useful starting points for understanding the field-induced spin density wave (FISDW) transitions in the Bechgaard salts [37]. Therefore, it is now believed that expressions for the conductivity of an anisotropic FS summarized in the following section are of some help in understanding the transport properties of organic metals.

2. Hall Effect and Magnetoresistance in the Relaxation-Time Approximation

For an orthorhombic material a useful approximation to the electron energy bands is given by the simple dispersion law

$$\varepsilon = -2t_h \cos k_x a - 2t_i \cos k_b b - 2t_l \cos k_z c \quad (1)$$

where as elsewhere in this chapter, h , i , and l are the high-, intermediate-, and low-conductivity directions, respectively, and t_h , t_i , and t_l are the corresponding tight-binding transfer integrals, which represent the electronic overlap along a given chain (t_h) and between chains in two perpendicular directions (t_i , t_l). The molecular spacing along the chains is a , and the interchain spacings are b and c .

If $t_h \gg t_i \gg t_l$ and ε is not too small, the FS is open in both transverse directions, as sketched in Fig. 3. The standard expression for the ij th

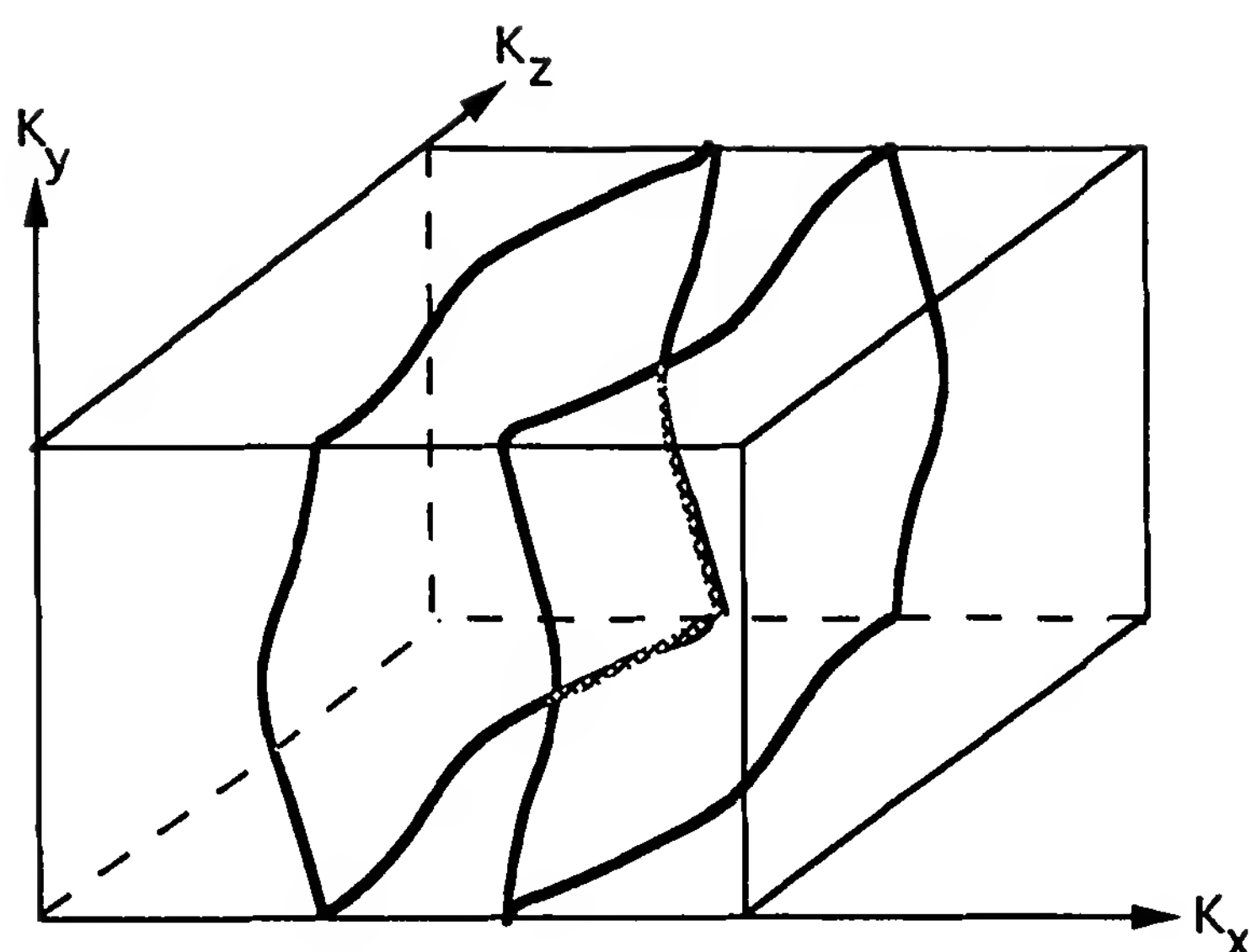


Figure 3 Sketch of open Fermi surface for anisotropic tight-binding model (not to scale).

element of the conductivity tensor is [38]

$$\sigma_{ij} = -\frac{e^2}{4\pi^3} \int \frac{dS}{\hbar|\mathbf{v}|} \int_0^\infty v_i(0)v_j(t)e^{-t/\tau} dt \quad (2)$$

where τ is the relaxation time, $\int dS$ is over the area of the FS, e is the electronic charge, and \hbar is Planck's constant. $v_j(t)$ is obtained from $v_j(\mathbf{k})$ by using the Lorentz force equation to calculate the time dependence of \mathbf{k} :

$$\hbar \frac{d\mathbf{k}}{dt} = -\frac{e}{c'} \mathbf{v} \times \mathbf{H} \quad (3)$$

where c' is the velocity of light. Using Eqs. (1) and (2), the following expressions can be obtained for the zero-field components of σ [13,22]:

$$\sigma_h = \frac{2}{\pi} \frac{e^2}{\hbar} \frac{v_h \tau}{bc} \quad (4)$$

Here v_h is the average Fermi velocity along the chains:

$$v_h = \frac{2t_h}{\hbar} a \sin k_F a = \frac{2t_h}{\hbar} a \sin \frac{\pi\rho}{2} \quad (5)$$

and ρ is the number of carriers per molecule ($\rho = \frac{1}{2}$ for the Bechgaard salts). In this picture the anisotropy is temperature independent and given

by

$$\frac{\sigma_h}{\sigma_i} = 2 \frac{t_h^2}{t_i^2} \frac{a^2}{b^2} \sin^2 \frac{\pi\rho}{2} \quad (6)$$

The corresponding formula for σ_l is obtained by substituting l for i and c for b in Eq. (6). In the low-field limit the Hall coefficient is given by [39]

$$R_H = \frac{1}{nec'} \frac{\pi\rho/2}{\tan(\pi\rho/2)} \quad (7)$$

This formula has been derived using a different method by Maki and Virosztek [40], who give a correction term that depends on the ratio of t_l/t_h , as well as deriving formulas for nonlinear SDW contributions to R_H .

The low-field magnetoresistance is given by

$$\frac{\Delta\rho_h}{\rho_h} = \omega_h^2 \tau^2 \quad (8)$$

when the magnetic field (H) is along l , and there are corresponding formulas for ρ_i and ρ_l . The largest effect occurs when the current is along the low-conductivity axis and the magnetic field along the i axis. In this case

$$\omega_l \tau = \frac{eH}{c' \hbar} c v_h \tau \quad (9)$$

that is, the magnetoresistance can be used to determine the mean free path ($v_h \tau$) along the chains. Since t_h is often known approximately from the measured plasma frequency and band structure calculations, various other parameters (e.g., τ and t_l) can be obtained from the measured values of ρ and $\Delta\rho$ using the equations above. When the current flows along the highly conducting (h) axis and the magnetic field is applied along the l axis, the treatment described above predicts only a very small magnetoresistance, because $\omega_h \approx \omega_l t_i/t_h$. Initially [22], we proposed that the large magnetoresistance actually observed for this geometry might be understandable in terms of the low symmetry and the precise direction of the principal axes of σ . The observed deviations from Kohler's rule were ascribed to magnetic breakdown. As more data have become available, especially for $(\text{TMTSF})_2\text{PF}_6$ under pressure, as discussed in Section VII.B, it is more likely that for the high-conductivity direction, the magnetoresistance is truly anomalous.

C. Calculations of Scattering Rates

Many different scattering mechanisms have been proposed to account for the T dependence of the electrical resistivity of organic metals. Electron-electron scattering was proposed by the experimentalists who made some

of the first resistivity measurements on single crystals of TTF-TCNQ (D. O. Cowan, private communication), and later by others [41] as the experimental situation became clearer, and evidence for approximate T^2 behavior in $\rho(T)$ of several compounds accumulated. Bulaevskii [3] has argued rather persuasively that for the two-dimensional ET salts, electron-electron Umklapp scattering is the dominant process. Very recently [42] it has been shown that the T^2 and T^1 terms often observed in $\rho_i(T)$ and $\rho_l(T)$ of the Bechgaard salts might well be consistent with electron-electron scattering, but calculations of $\rho_h(T)$ have not yet been made.

The most orthodox model involving a quasi-one-dimensional tight-binding band with electron scattering by acoustic phonons and molecular vibrations (one-phonon processes) has been analyzed carefully and in great detail [43,44]. Good agreement with experimental data is claimed by the proponents of this model.

Other more unusual pictures that have been proposed include the libron model [45], where librations (molecular rotations) are responsible for $\rho_h(T)$. It was suggested that the T^2 behavior arose from the dominance of two-libron processes, and that the first-order, single-libron contribution is small by symmetry. The T dependence of the spin susceptibility was discussed within the same framework, in terms of a band-narrowing effect [46]. However, this approach has been criticized [44], and furthermore, no evidence has been found that librations play any role in metal-semiconductor transitions [9].

Friedman [47] suggested that in materials such as TTF-TCNQ, modulation of the polarization energy by lattice vibrations could substantially increase coupling of the conduction electrons to lattice modes. This energy is associated with polarization of one molecule by a conduction electron on a neighboring molecule. It is very dependent on the intermolecular distance a , the coupling constant varies as a^{-10} , and it would be extremely pressure dependent.

J  rome [48] proposed that the T^2 -behavior of $\rho_h(T)$ could be caused by electron-spin fluctuation scattering. This approach can be viewed as an extension of electron-electron scattering to larger effective interaction strengths, which are perhaps caused by the lower dimensionality. The dominant process is scattering of electrons by collective excitations of the electron gas (the spin fluctuations) rather than first-order electron-electron scattering.

A whole class of models involving localization by phonons and static defects has been reviewed by Abrikosov and Ryzkhin [49]. These models also give a T^2 law for $\rho_h(T)$ in the "weak inelasticity" limit when $\omega_D\tau^* \ll 1$, where ω_D is a typical phonon frequency and $1/\tau^*$ is the total electron scattering rate. Roughly speaking, these models reflect the strong tendency

toward localization in low-dimensional systems. If the phonon frequency is low compared with the electron scattering rate, phonons act as static impurity potentials and enhance localization.

Finally, one should not forget the purely one-dimensional models, such as calculation of the conductivity of the one-dimensional interacting electron gas [50]. Such a model also gives a power law for the resistivity. For an attractive long-range electron–electron interaction there is an enhancement of σ_h and a different power law from that expected for (say) phonon scattering. However, it is not clear whether such a model applies to the compounds in Fig. 1, which have different ground states, yet still show similar resistivity behavior.

It is difficult for experimentalists to follow the right path through this veritable forest of interesting theoretical ideas, and the subject is certainly not closed. The results reviewed later in this chapter, particularly Figs. 8 and 9, indicate to us that something unusual is happening at ambient pressure, although the standard electron–phonon picture might well apply to $(\text{TSeT})_2\text{Cl}$ there, and to many of the other compounds at pressures of 30 kbar or more. In view of the fact that $\rho_h(T)$ of the single-chain Bechgaard salts is similar to that of the two-chain compounds (Fig. 1), further work on the effect of alloying on the electronic properties of single-chain compounds could be fruitful. For example, does $\rho_h(T)$ of the Bechgaard salts obey Matthiessen's rule up to room temperature (at ambient pressure and at high pressure) as would be expected in the single-particle band pictures but not for those involving localization? In the past, such studies were hampered by the occurrence of microcracks in these fragile crystals, but this is no longer such a problem because of recent improvements in experimental technique.

IV. MAGNETIC SUSCEPTIBILITY

Several research groups have made measurements of the static magnetic susceptibility of organic metals on a few milligrams of high-purity crystals often using the Faraday method with a sensitive (and delicate) electrobalance (e.g., Ref. 51), or more recently, a commercially available SQUID magnetometer [52]. To obtain the quantity of most interest, the spin susceptibility $\chi_s(T)$, corrections have to be made for the core diamagnetism of the constituent atoms. These corrections can be checked by measuring appropriate insulating compounds such as pure TMTSF or (below 150 K) $(\text{TMTSF})_2\text{ReO}_4$ and nearly always give sensible results. $\chi_s(T)$ has also been measured directly by electron paramagnetic resonance for many of the organic metals containing sulfur. The selenium-based compounds have much broader ESR lines but may become more accessible to this method

in the near future as higher-frequency ESR equipment becomes more widespread.

One characteristic feature of the behavior of $\chi_s(T)$ for organic metals is illustrated in Fig. 4. In contrast to ordinary metals, $\chi_s(T)$ increases quite substantially with temperature from (say) 60 to 300 K. This increase is strongest for the most one-dimensional compound, TTF-TCNQ [53], and becomes progressively weaker for $(\text{TMTSF})_2\text{ClO}_4$ [54], $\beta\text{-(BEDT-TTF)}_2\text{I}_3$ (a genuine two-dimensional compound) [25,26], and the more three-dimensional compound $(\text{TSeT})_2\text{Cl}$ [18] (also, unpublished results of M. Miljak and B. Hilti). For HMTSF-TCNQ [33] such a discussion is complicated by the presence of Landau–Peierls diamagnetism from small pockets of electrons and holes, although estimates of $\chi_s(T)$ have been made by Soda

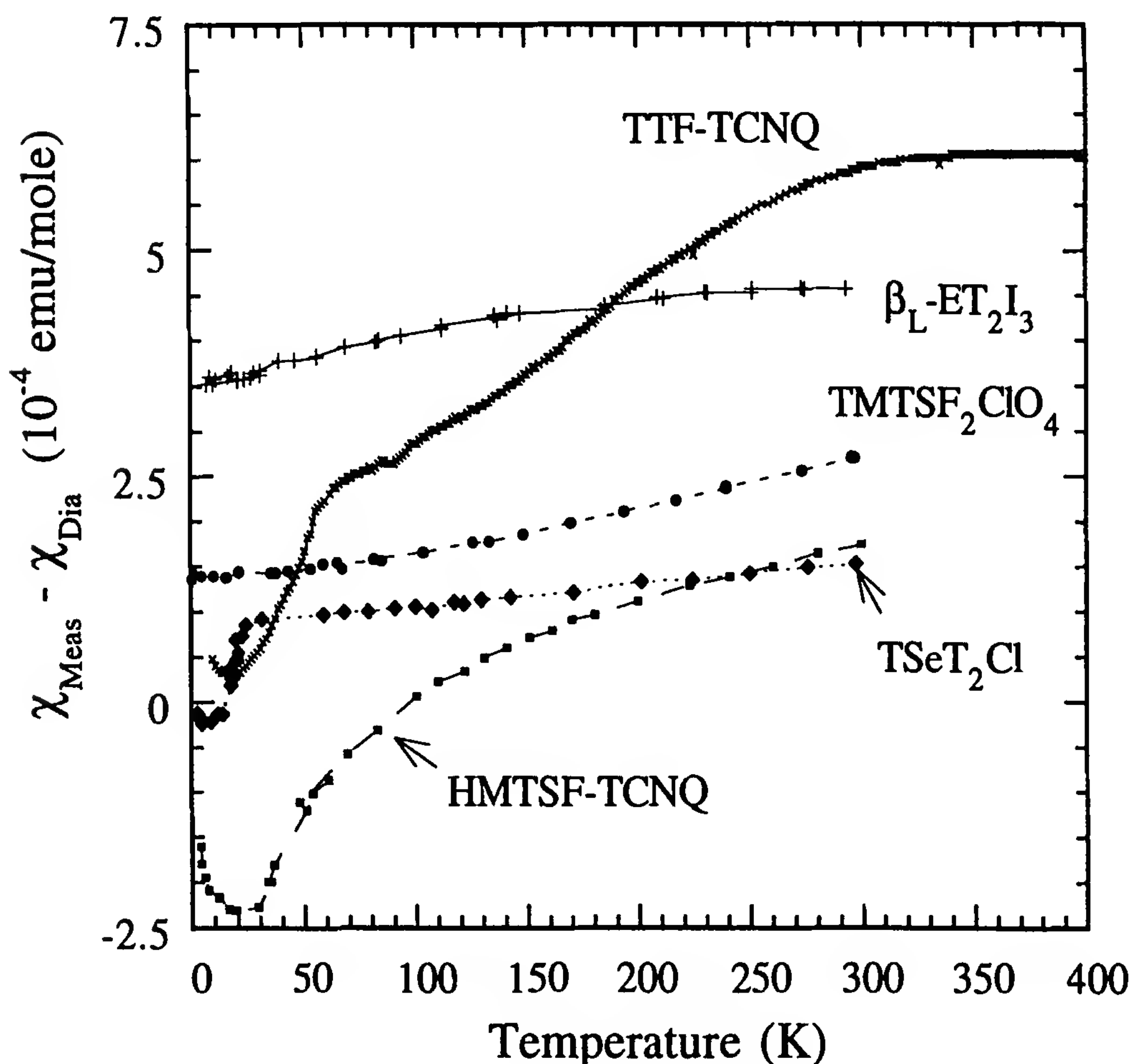


Figure 4 Static susceptibility for randomly oriented crystals, corrected for core diamagnetism: TTF-TCNQ (from Ref. 79), HMTSF-TCNQ (from Ref. 33), $\text{TMTSF}_2\text{ClO}_4$ (from Ref. 57), $(\text{TSeT})_2\text{Cl}$ (from unpublished results of M. Miljak and B. Hilti), and $\beta\text{-ET}_2\text{I}_3$ (from Ref. 26).

et al. [33]. The magnitudes of $\chi_s(300)$ and $\chi_s(60)$ for many organic metals are summarized in Fig. 5, where they are plotted with molecular weight as a parameter. From this figure it can be seen that nearly all the quasi-one-dimensional chain compounds studied show a strong T dependence of χ_s . Also, as emphasized by Delhaes [55], in many cases the enhancement of $\chi_s(60)$ (or the value obtained by extrapolation to $T = 0$) over that expected from a tight-binding band of noninteracting electrons with a typical transfer integral $4t_h = 1$ eV [i.e., $\chi_s = \mu_B^2 n(E_F)$, where in the notation of Section II, $n(E_F) = 1/(\pi abct_h \sin k_F a)$] is not particularly large. The notable exception is $\beta_L - (\text{BEDT-TTF})_2\text{I}_3$ [26] and its high T_c modification [57].

Another interesting point about the results for TTF-TCNQ in Fig. 4 is that there is an increase in slope of $\chi_s(T)$ near 150 K, the temperature below which $2k_F$ diffuse lines first appear in x-ray scattering studies [9]. From the separation of the TTF and TCNQ contributions to $\chi_s(T)$ made

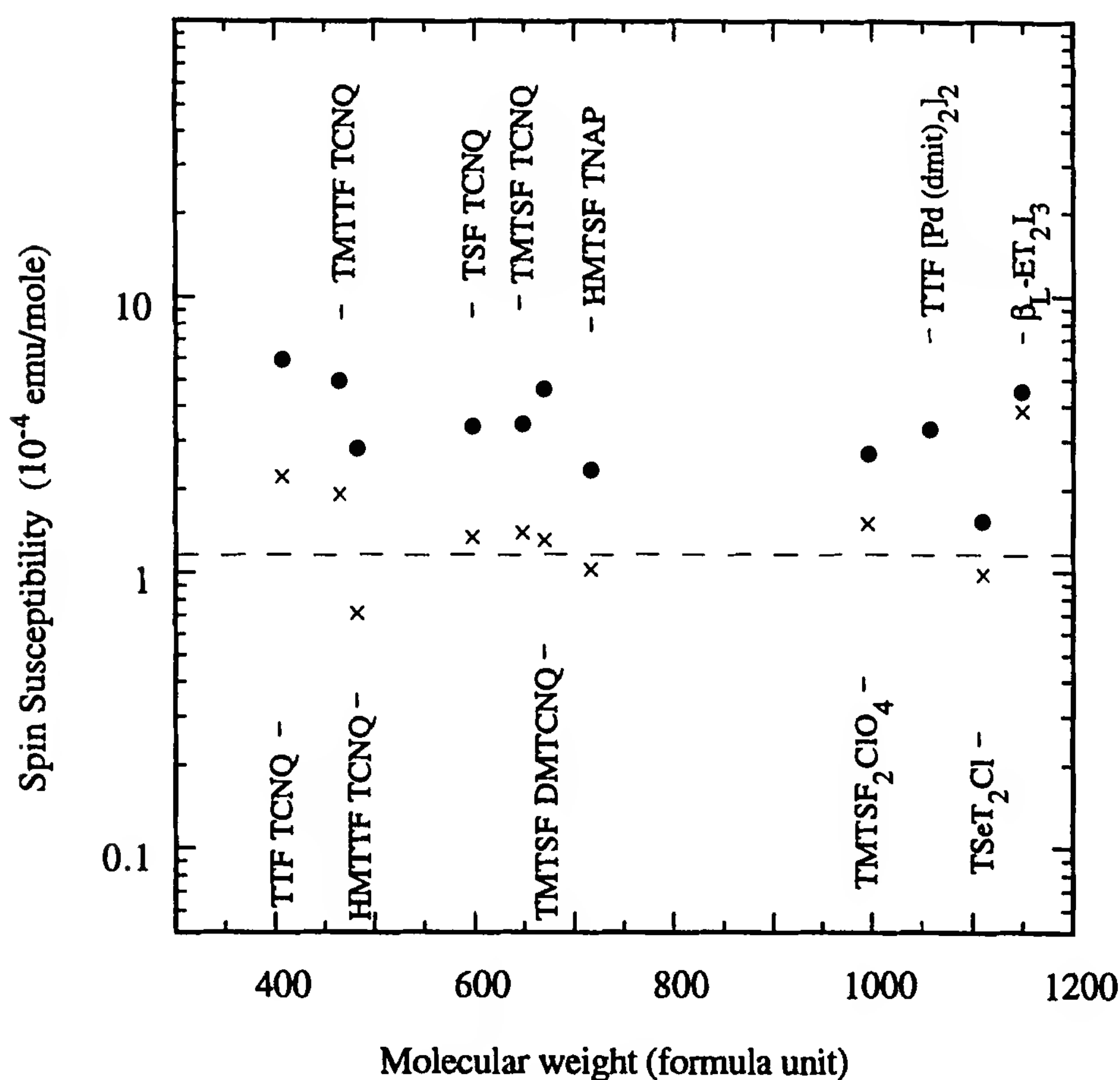


Figure 5 Spin susceptibility of various organic conductors at 300 K (circles) and 60 K (crosses). [Adapted from Ref. 59, with extra data for $(\text{TMTSF})_2\text{ClO}_4$ (from Ref. 54), $\text{TTF}[\text{Pd}(\text{dmit})_2]_2$ (from Ref. 52), $(\text{TSeT})_2\text{Cl}$ (from unpublished results of M. Miljak and B. Hilti), and $\beta_L\text{-ET}_2\text{I}_3$ (from Ref. 26).]

by Tomkiewicz et al. [53] using an ESR g -factor decomposition procedure, it is clear that this anomaly arises from the TTF stacks, as do the $2k_F$ x-ray lines. Namely, χ_s^{TTF} is constant up to 150 K and then increases [53]. At first sight it is strange that there should be an empirical connection between the uniform ($q = 0$) static spin susceptibility and the $q = 2k_F$ response function probed by x-rays. However, examination of available data shows similar effects at appropriate temperatures for most other compounds studied, such as TSeF-TCNQ [9,58], HMTSF-TNAP, HMTTF-TCNQ [9,59], and TMTTF-TCNQ [9,60]. So in this type of organic metal there really does appear to be a connection between the enhancement of χ_s , presumably arising from the electron–electron Coulomb repulsion, and the response of the lattice at $2k_F$.

As shown in Fig. 4, for TTF-TCNQ $\chi_s(T)$ falls to zero as the semiconducting (Peierls) gap opens up below 52 K. However, it can be seen from Fig. 6 that the energy gap determined by plotting $\ln \chi_s$ versus $1/T$ is much less than that obtained by plotting $\ln \sigma$ versus $1/T$ [56]. This feature has been attributed to the effect of electron–electron correlations, which result in magnetic excitations having a lower gap than charge excitations [56]. Although this is clear in the simple case of the strongly localized, dimerized system sketched in Fig. 7, it is not as obvious how it arises in TTF-TCNQ, where the $2k_F$ distortion is small and incommensurate with the lattice. One possibility is that there are spin-wave excitations with lower activation energy than charge excitations, by analogy with the results of Coll [61] for a uniform one-dimensional Hubbard model at arbitrary band fillings. However, certain theoretical treatments [62] in which the low-energy excitations of a Peierls semiconductor are solitons, also give rise to different gaps for charge and spin excitations and should be compared more closely with experimental data. At present it is difficult to rule out more prosaic interpretations, such as those involving a mobility edge, where states in a certain energy range below and above the gap are localized and contribute to χ_s without contributing to σ . We note that there is also evidence [63] for a large difference in magnetic and conductivity gaps in $(\text{BEDT-TTF})_2(\text{ClO}_4)_3$, which also appears to be a Peierls semiconductor, and where the potential complication of two conducting stacks (one possibly giving a gap in χ_s and the other in σ) is absent.

V. PRESSURE EFFECTS

Studies of the effect of hydrostatic pressure on the properties of organic metals have proved to be particularly fruitful. The major success was the discovery of the first organic superconductor, $(\text{TMTSF})_2\text{PF}_6$ in 1980 [64],

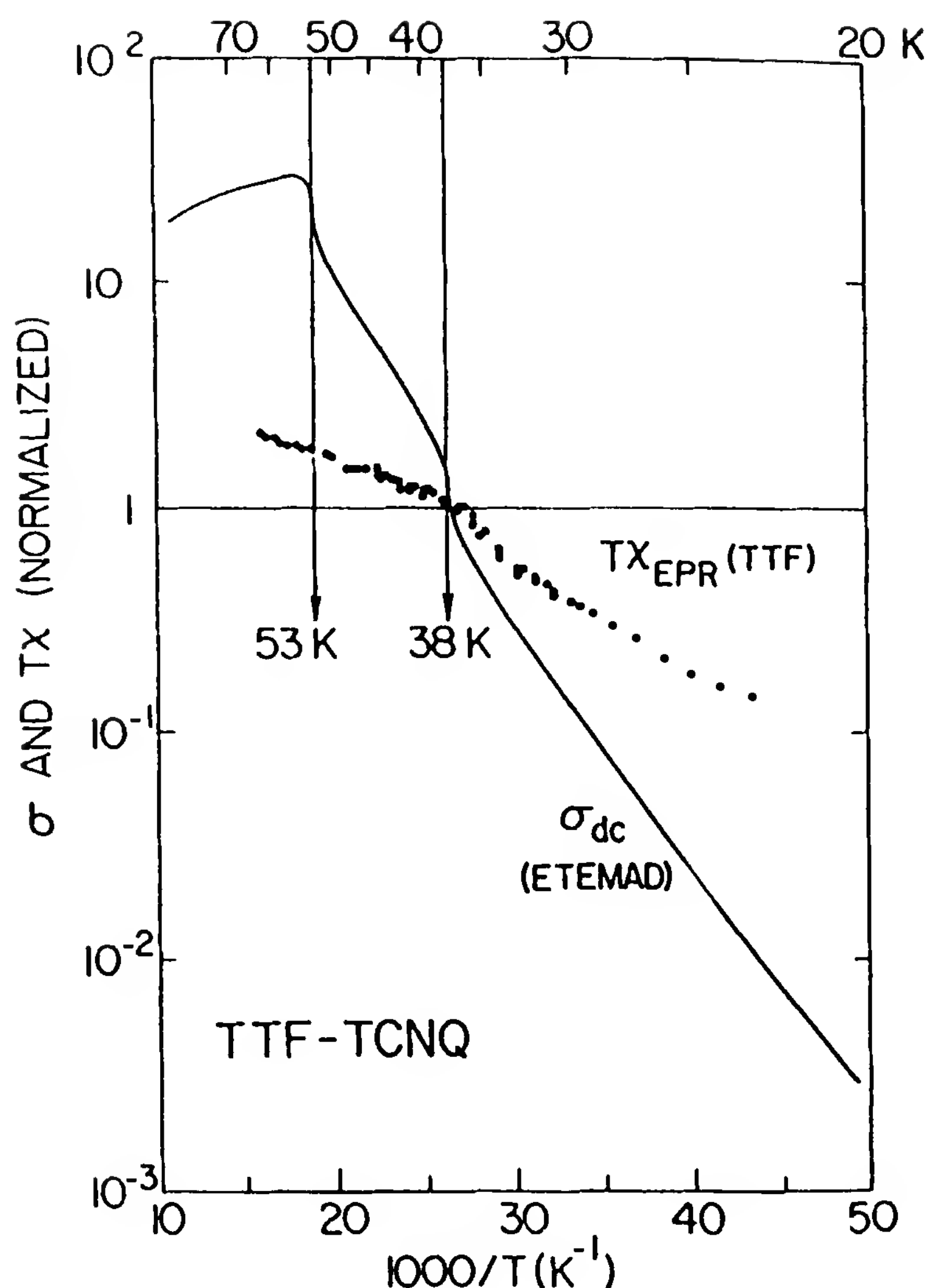


Figure 6 Arrhenius plots of the conductivity of TTF-TCNQ and the spin susceptibility from the TTF chains, showing the different energy gaps for charge and spin excitations. (From Ref. 56.)

but many other interesting areas of research have been opened up by pressure experiments.

A. Conductivity and Its Anisotropy

The effect of pressure on the room-temperature conductivity of several organic metals is summarized in Fig. 8 [65–68] (also, unpublished results of J. R. Cooper, D. Jérôme, and E. M. Engler, 1978). There is a strong initial increase in σ_h of between 20 and 30% per kilobar for the various quasi-one-dimensional compounds. This is a factor of 10 larger than the expected changes in single-particle parameters such as the tight-binding bandwidths. On the other hand, measurements of the plasma frequency (ω_p) under pressure by Welber et al. [69] are in agreement with calculated

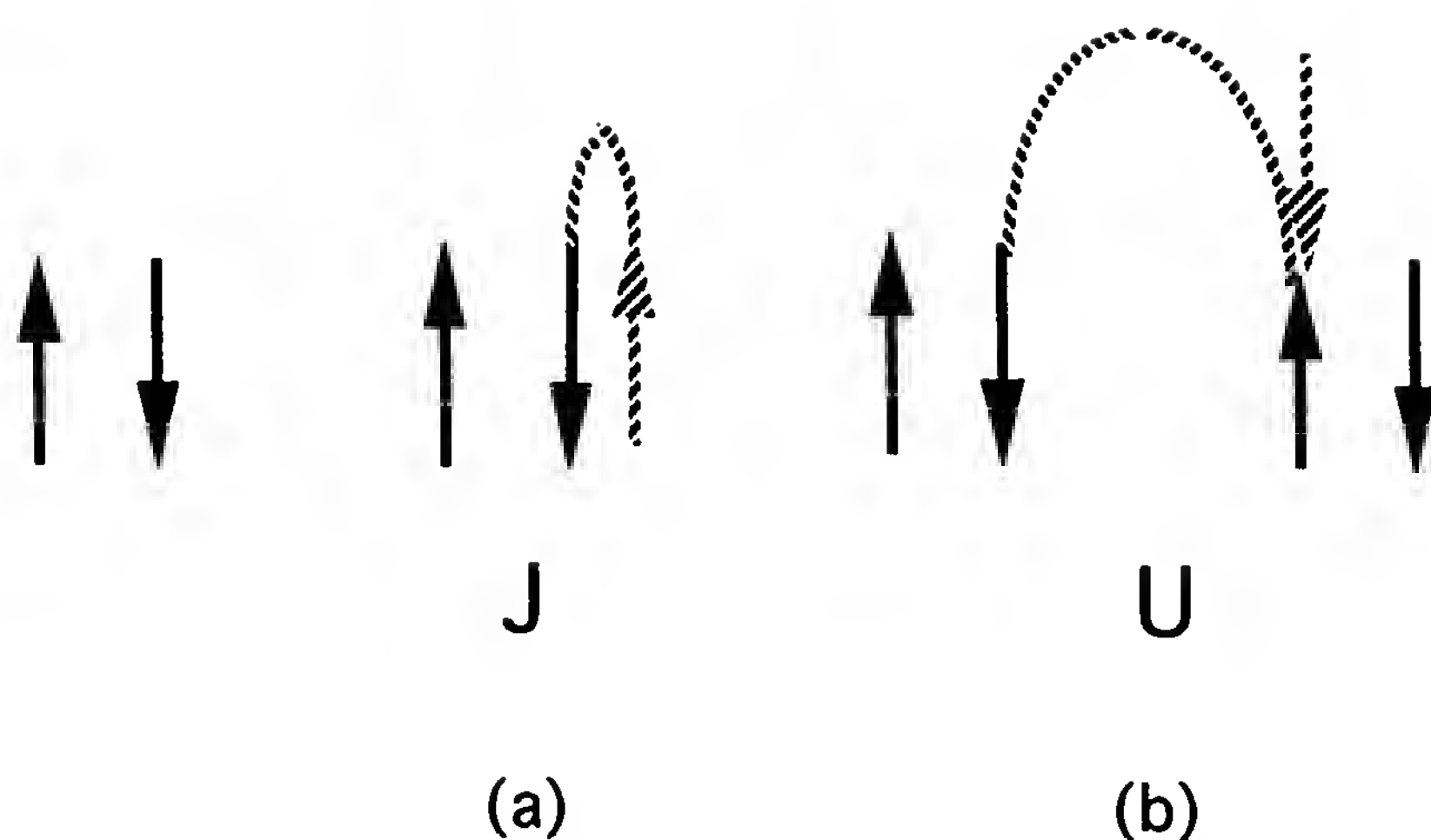


Figure 7 Sketch of the processes responsible for (a) spin or (b) charge excitations in a half-filled Hubbard band.

changes in t_h . For β -(BEDT-TTF) $_2$ I $_3$, which has a particularly large resistivity, $d \ln \sigma_h / dp$ is even larger, in the range 60 to 100% per kilobar [67]. (TSeT) $_2$ Cl is again an exception; the increase in σ_h is only 6% per kilobar [70]. As also shown in Fig. 8, for the other compounds the anomalous increase in σ_h disappears above 20 to 30 kbar, where both σ_h and ω_p change at similar rates. At these high pressures the behavior of $\rho_h(T)$ is essentially linear in T , as shown in Fig. 9 [66,70] (also, unpublished results of J. R. Cooper, D. Jérôme, and E. M. Engler, 1978). Thus the T^2 behavior observed at ambient pressure must be linked in some way with the anomalous pressure dependence, and this is entirely consistent with the result for (TSeT) $_2$ Cl mentioned above ($\rho_h \approx T^1$ and weak pressure dependence at ambient pressure). One possible reason for such a link could be that the pressure dependence arises from a strong dependence of σ_h on the intra-chain molecular spacing (a). In such a case it is more appropriate to consider the behavior of $\rho_h(T)$ at constant a . Using the known thermal expansion [71] and compressibility of TTF-TCNQ [72] and the measured pressure dependence of ρ_h , it was shown that at constant a , $\rho_h(T) \approx T^1$ and not T^2 [65,68]. Despite considerable theoretical work (summarized in Section III.C) there is still no consensus as to the scattering mechanism responsible for the single-particle resistivity $\rho_h(T)$, so on theoretical grounds alone there is no compelling reason to believe that the “constant a ” behavior is necessarily relevant. However, there is some experimental evidence in favor of this viewpoint in that uniaxial strain along the chain direction accounts for about 60% of the observed hydrostatic pressure dependence [73].

For TTF-TCNQ the anomalous pressure derivative $d \ln \sigma_h / d \ln p$ falls approximately linearly with T [68], while for the single-chain Bechgaard salt (TMTSF) $_2$ ClO $_4$ it remains in the range 22 to 25% per kbar between

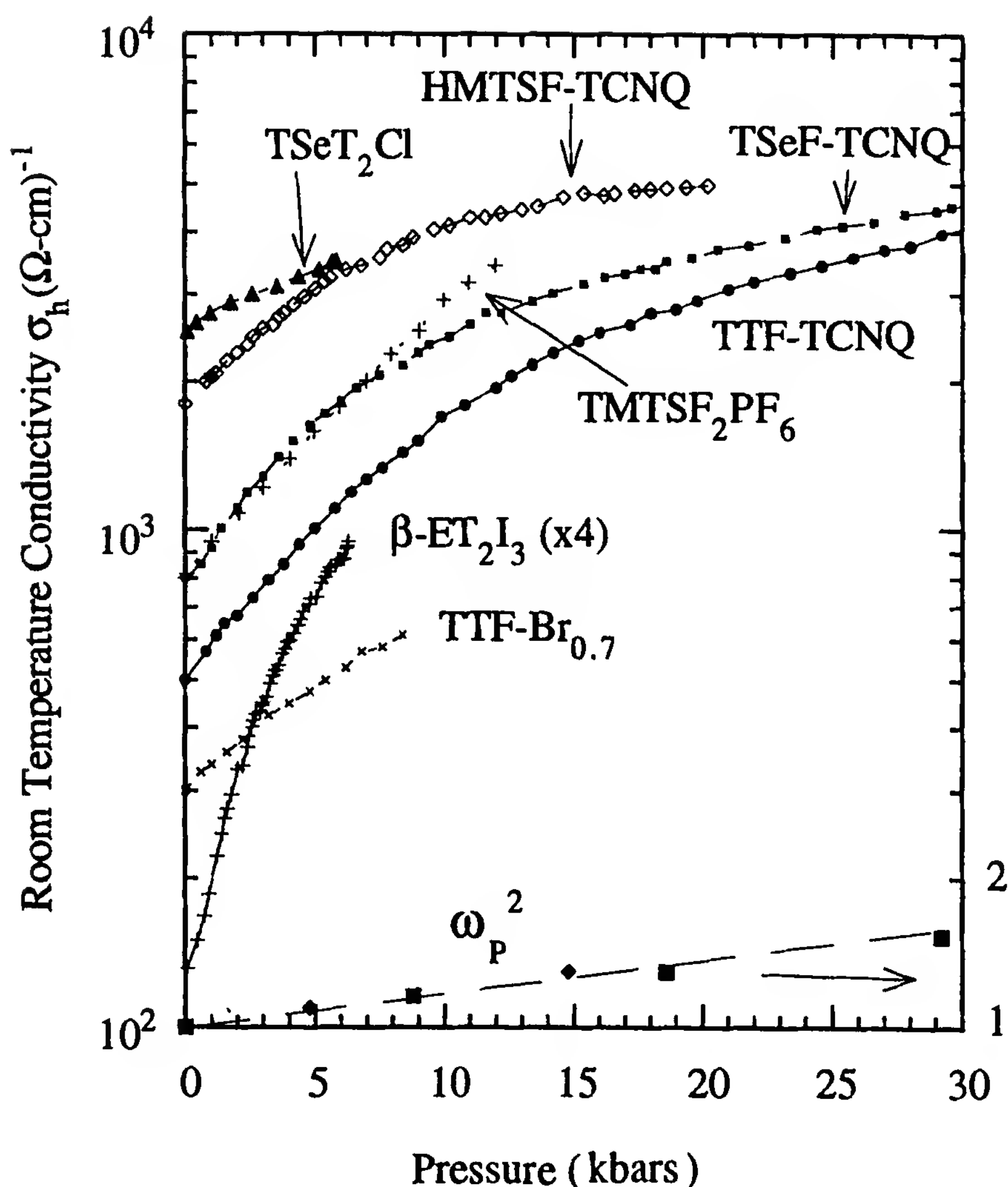


Figure 8 Room-temperature conductivity σ_h of various organic metals versus pressure. [Adapted from Ref. 65, with additional data for $(\text{TSeT})_2\text{Cl}$ (from Ref. 66) and $\beta\text{-ET}_2\text{I}_3$ (from Ref. 67). The relative changes in the square of the plasma frequency for TTF-TCNQ and TSeF-TCNQ are also shown (from Ref. 69).]

32 K and room temperature [74]. Several interpretations of this anomalous pressure dependence have been proposed along with the calculations of the ambient pressure resistivity mentioned previously. The fact that $(\text{TSeT})_2\text{Cl}$ is an exception and the disappearance of the anomalous pressure dependence of σ_h at high pressure seems to indicate that it is a specific property of quasi-one- and quasi-two-dimensional materials.

One of the surprising results of the early pressure studies is shown in Fig. 10 [27]. In the range investigated, both transverse components of the conductivity increased with pressure at the same rate as σ_h . This observation was one of the important factors in the development of Weger's theory of the transverse conductivity of anisotropic metals [75]. In this

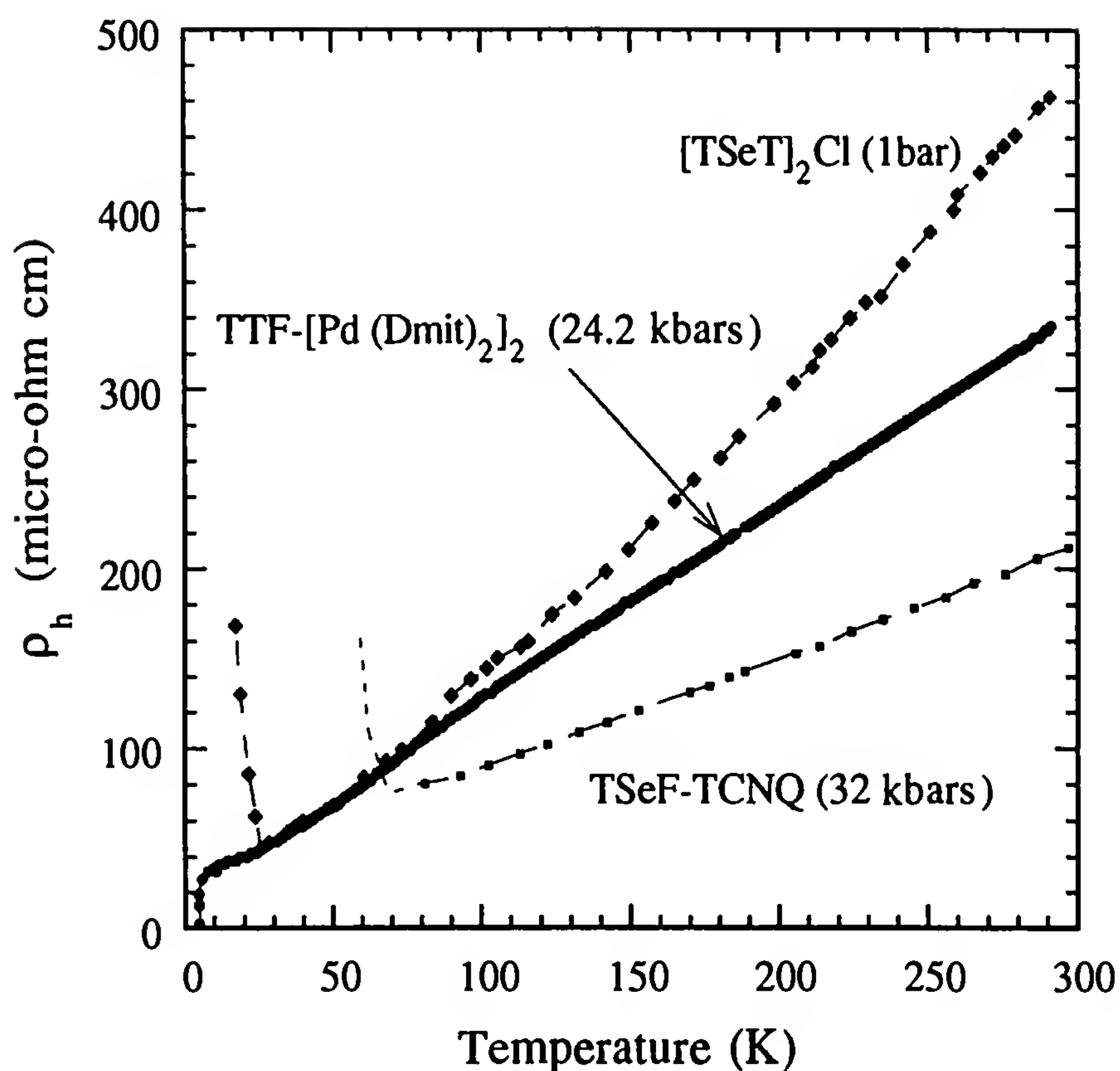


Figure 9 Longitudinal resistivity ρ_h versus temperature for $(\text{TSeT})_2\text{Cl}$ at ambient pressure (from Ref. 18), TTF $[\text{Pd}(\text{dmit})_2]_2$ at 24 kbar (from Ref. 70), and TSeF-TCNQ at 32 kbar (from unpublished results of J. R. Cooper, D. Jérôme, and E. M. Engler, 1978).

theory the interchain hopping rate is related to the on-chain scattering time τ_h , and the latter quantity is responsible for the anomalous pressure dependence of all three components of σ . However, this theory is less successful in accounting for the observed temperature dependence of the anisotropy, which as noted previously (Table 1) is often rather strong. A further puzzle involves the expression derived for the anisotropy within this theory, namely $\sigma_h/\sigma_l = t_h^2 a^2 / t_l^2 c^2$, where t_h and t_l are the overlap integrals and a and c the molecular spacings parallel and perpendicular to the chains. Within a factor of 2, exactly the same expression is given by Bloch–Boltzmann theory in the relaxation-time approximation [Eq. (6), Section III.B.2]. It is conceivable that the latter theory still applies when the inelastic mean free path is much less than c and that it breaks down only when the *elastic* mean free path (L_{el}) is less than c . In support of this speculation and as discussed in Section VII.B.3, we could see no qualitative changes in the magnetoresistance of two Bechgaard salts up to temperatures where the inelastic mean free path perpendicular to the chains became much less than

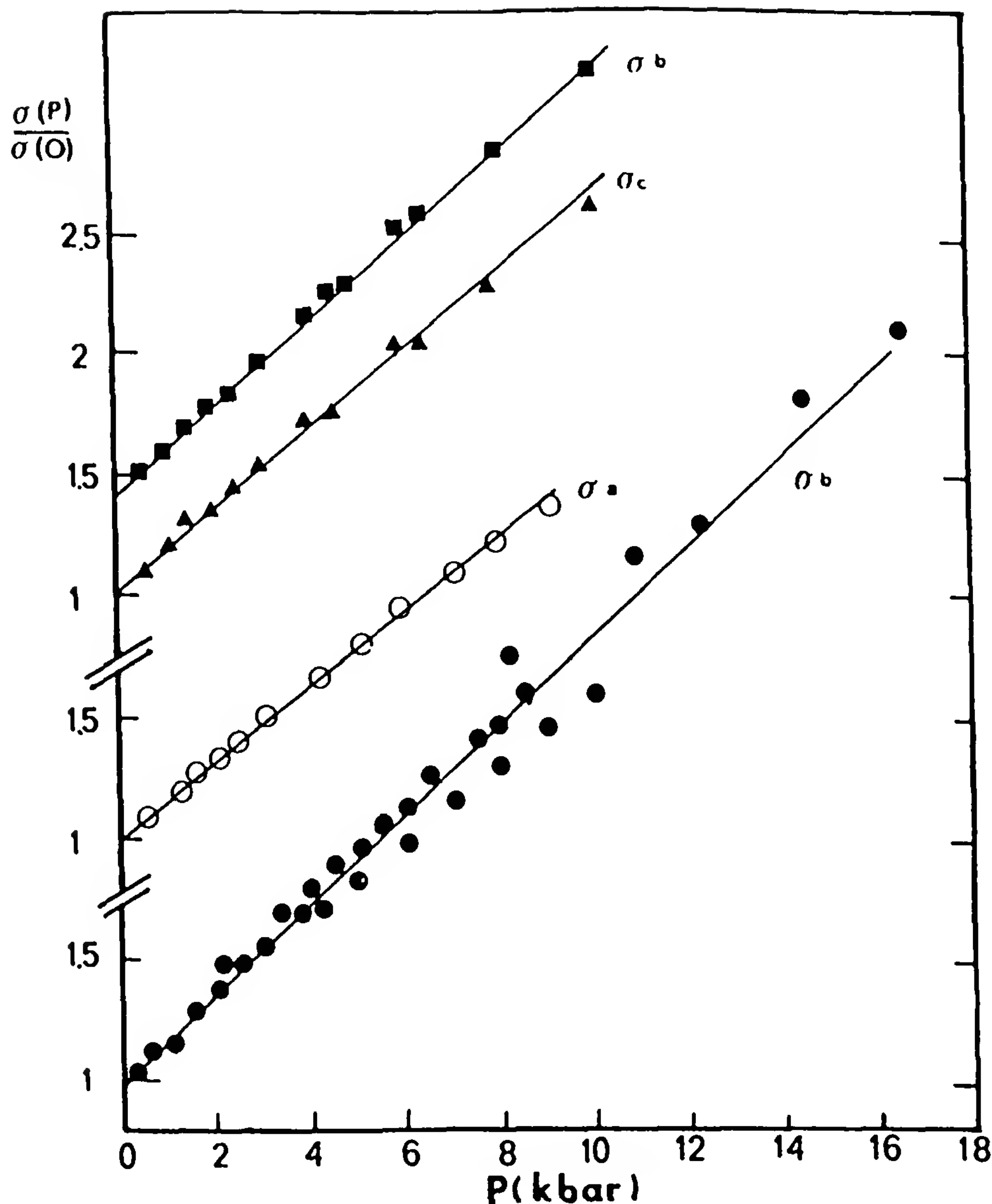


Figure 10 Normalized room-temperature conductivities versus pressure for single crystals of TSeF-TCNQ. At ambient pressure $\sigma_b = 800 \pm 100 (\Omega \cdot \text{cm})^{-1}$, and σ_a and σ_c are $4 \pm 2 (\Omega \cdot \text{cm})^{-1}$. (From Ref. 27.)

c [23]. The implication is that for an anisotropic metal, and provided that inelastic scattering is dominant, the perpendicular conductivity can be arbitrarily small, corresponding to arbitrarily small values of v_l , and yet still be metallic. There is no minimum metallic conductivity for the transverse direction.

Using a scaling theory of localization, adapted for anisotropic materials, Apel and Rice [76] find that the condition $L_{el} \approx c$ does correspond to the Anderson metal-insulator transition of a quasi-one-dimensional system.

But it is not clear how to apply their treatment to the experiments described above where there is significant inelastic scattering.

B. Effect of Pressure on χ_s

Early work on the pressure dependence of the spin susceptibility χ_s focused on ESR measurements under pressure, initially at low frequencies (40 MHz) [60] and later at the normal X-band frequency of 9 GHz [77]. More recently, a series of organic metals was investigated rather thoroughly by Schilling and colleagues using the Faraday technique and a miniature high-purity Cu–Be pressure cell [57,78,79]. The behavior of $-d \ln \chi_s/dp$ ($\equiv \Delta\chi_s$) versus temperature is summarized for three representative compounds in Fig. 11 [79]. The derivative is large for TTF-TCNQ, rising substantially at lower temperatures in contrast to the behavior of $d \ln \sigma_h/dp$. $\Delta\chi_s$ is smaller for $(\text{TMTSF})_2\text{PF}_6$ and the other Bechgaard salts studied, but has similar T dependence to TTF-TCNQ. For β -(BEDT-TTF) $_2\text{I}_3$, $\Delta\chi_s$ is even smaller and shows very little T dependence. We do not believe that any straightforward interpretation of these results has yet been proposed. In general terms they show that for TTF-TCNQ both the $q = 0$ and $q = 2k_F$ responses of the material are highly pressure dependent, whereas for the other two materials the pressure dependence of the $q = 0$ response becomes progressively weaker. In contrast, assuming that σ_h reflects a response at

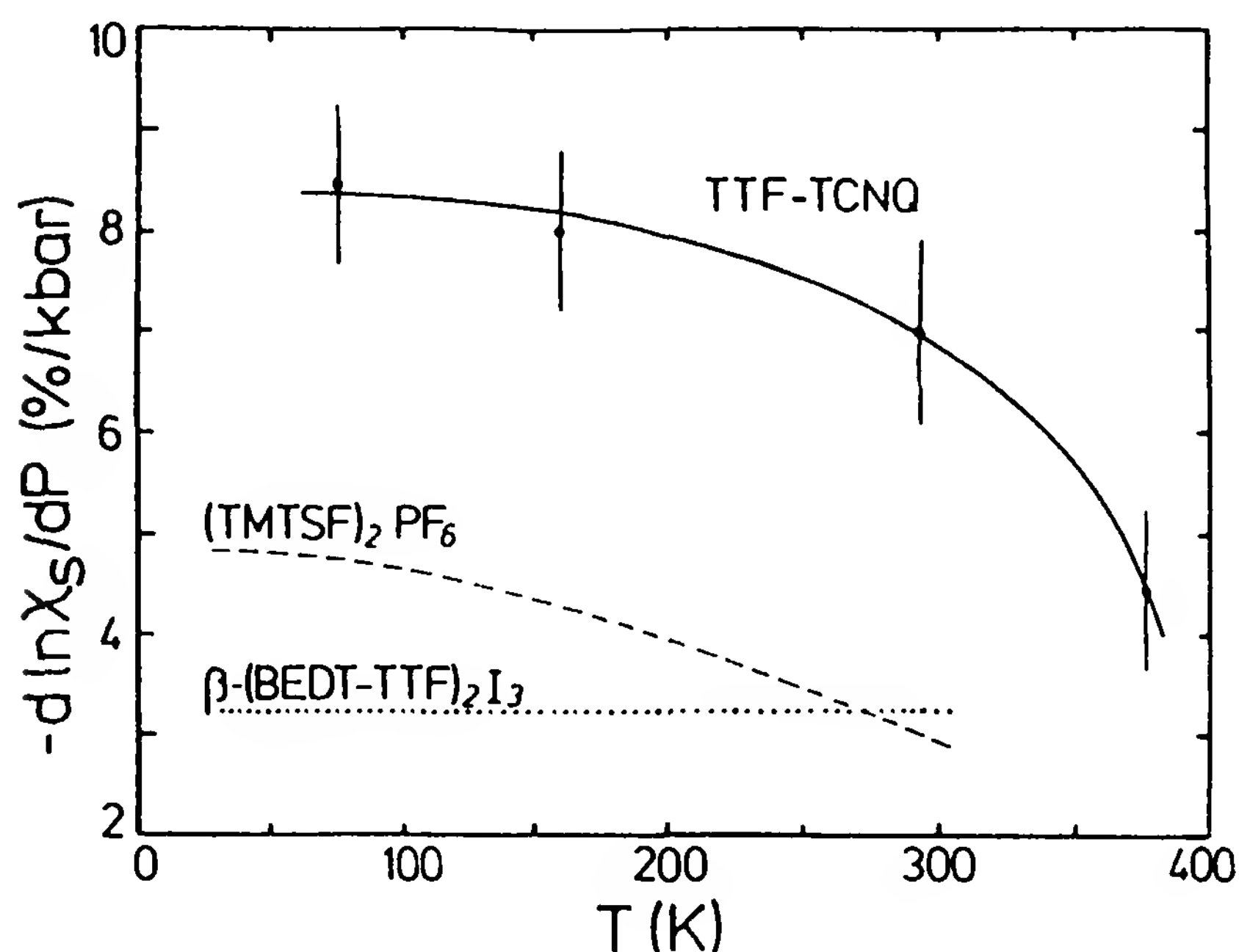


Figure 11 Pressure dependence of the spin susceptibility, $d \ln \chi_s/dp$, versus temperature for three representative organic metals. (From Ref. 79.)

$2k_F$, the latter quantity is strongly pressure dependent for all materials studied (with the usual exception of $(TSeT)_2Cl$ [70]).

The ESR line widths are also [60,77] strongly pressure dependent; for the salts of the TTF-TCNQ family they change at the same rate as σ_h , but for β -(BEDT-TTF) $_2I_3$ the change (10% per kbar) is much less than that in σ_h .

C. Suppression of Instabilities

One of the initial motivations for pressure studies was to suppress the CDW transitions in TTF-TCNQ and its derivatives and thereby stabilize a metallic, and possibly superconducting, state at low temperatures [2]. Experiments on TTF-TCNQ and TSeF-TCNQ [27] showed an increase in the CDW or Peierls transition temperatures (T_p) with pressure, as shown in Fig. 12 [80]. Later work on materials such as HMTTF-TCNQ showed that the transitions could be suppressed by pressure, but a true metallic state was not obtained up to about 30 kbar [81]. Instead, the ground state was very reminiscent of the semimetallic behavior observed for HMTSF-TCNQ, as shown by the resistivity data in Fig. 13. One possible mechanism for the formation of a semimetallic state is that, as proposed by Weger [82], it arises simply from hybridization of donor and acceptor wave functions. However, diffuse x-ray scattering lines [34] and reasonably sharp conductivity anomalies are often observed, so in many cases incommensurate lattice distortions must play a role. In other words, a semimetallic state can also arise when the Q vector of the CDW does not destroy the whole Fermi surface (FS) but leaves small pockets of holes and electrons. Such a situation is particularly likely in two-chain materials, where the direction of Q is determined not just by the FS nesting properties but by the Coulomb interaction between CDWs on the two chains [10].

An important precursor to the Bechgaard salts, TMTSF-DMTCNQ [2], also showed evidence for a low-temperature semimetallic state at pressures below ca. 12 kbar [83], but in view of the similarities with the Bechgaard salts, it is probable that a fully metallic state is formed at higher pressures [2].

D. Commensurability of TTF-TCNQ Under Pressure

The sudden increase in T_p of TTF-TCNQ near 19 kbar and associated hysteresis in the transition [80] lead to the suggestion that in this pressure region (Fig. 12), the charge transfer is $\frac{2}{3}$, and $2k_F$ is commensurate with the crystalline lattice. This was later confirmed directly by neutron scattering on deuterated samples for which it occurred at somewhat lower pressures [84].

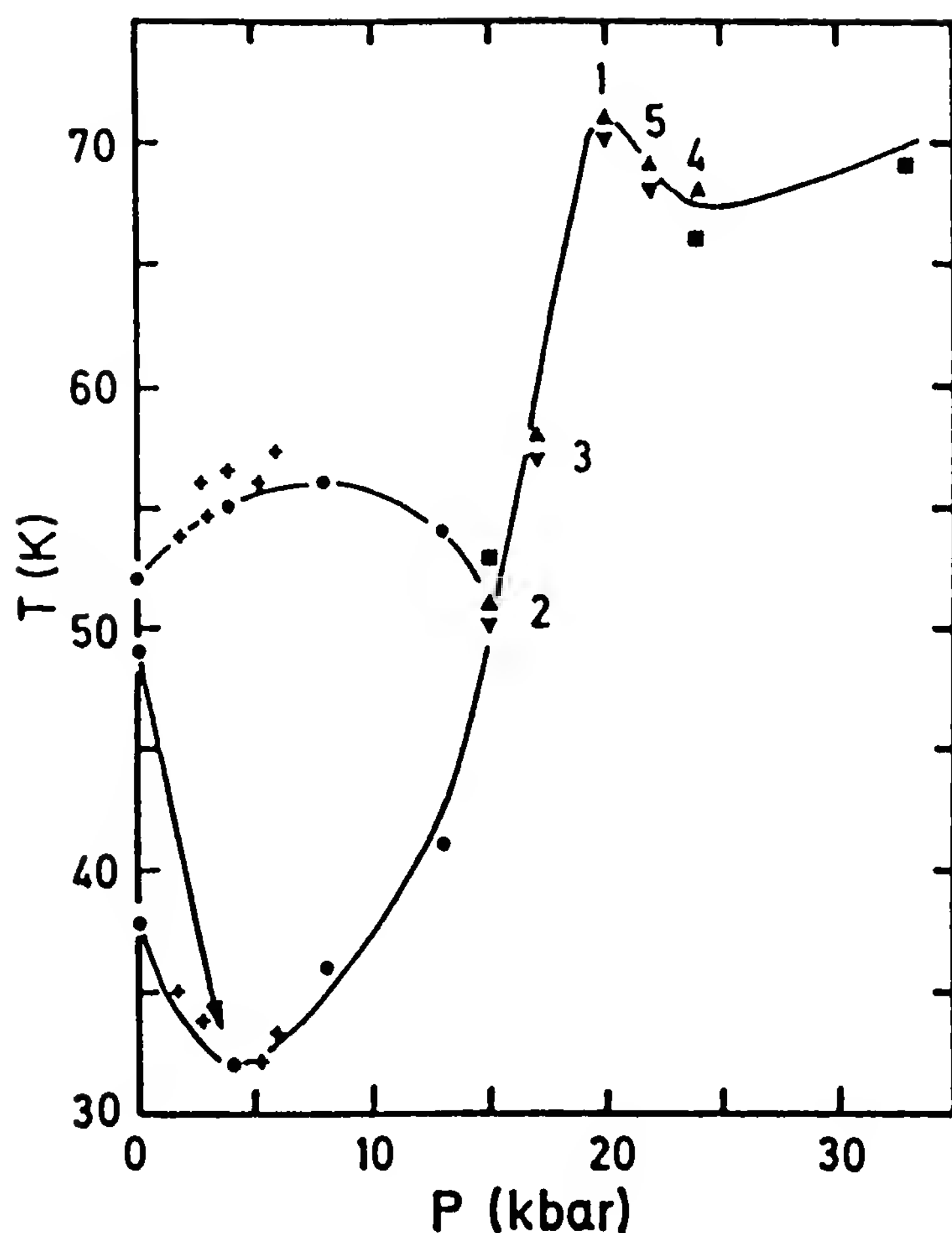


Figure 12 Effect of pressure on the three phase-transition temperatures of TTF-TCNQ. (From Ref. 80.)

Knowledge of the pressure-induced commensurability led to a series of beautiful experiments searching for evidence for a collective electron-phonon or CDW contribution to the *low* field conductivity in TTF-TCNQ *above* T_p . Clear evidence was indeed found for a substantial fall in σ_h between about 150 and 80 K in the narrow commensurability domain, as shown in Fig. 14 [85]. No such dip was found for the transverse conductivity [86], and the dips in σ_h were also shown to be suppressed by only a 2×10^{-3} molecular fraction of irradiation induced defects [87]. All of this leads to a consistent picture in favor of a collective electron-phonon CDW contribution to σ_h above T_p of TTF-TCNQ, as discussed in Ref. 2. However, the extra CDW conductivity is not more than $6000 (\Omega \cdot \text{cm})^{-1}$ at 80 K, that is, about one-half of the ambient pressure conductivity of $(\text{TMTSF})_2\text{PF}_6$ at the same temperature (Fig. 1) and the latter is usually considered to be a single-particle contribution. So until the mechanism

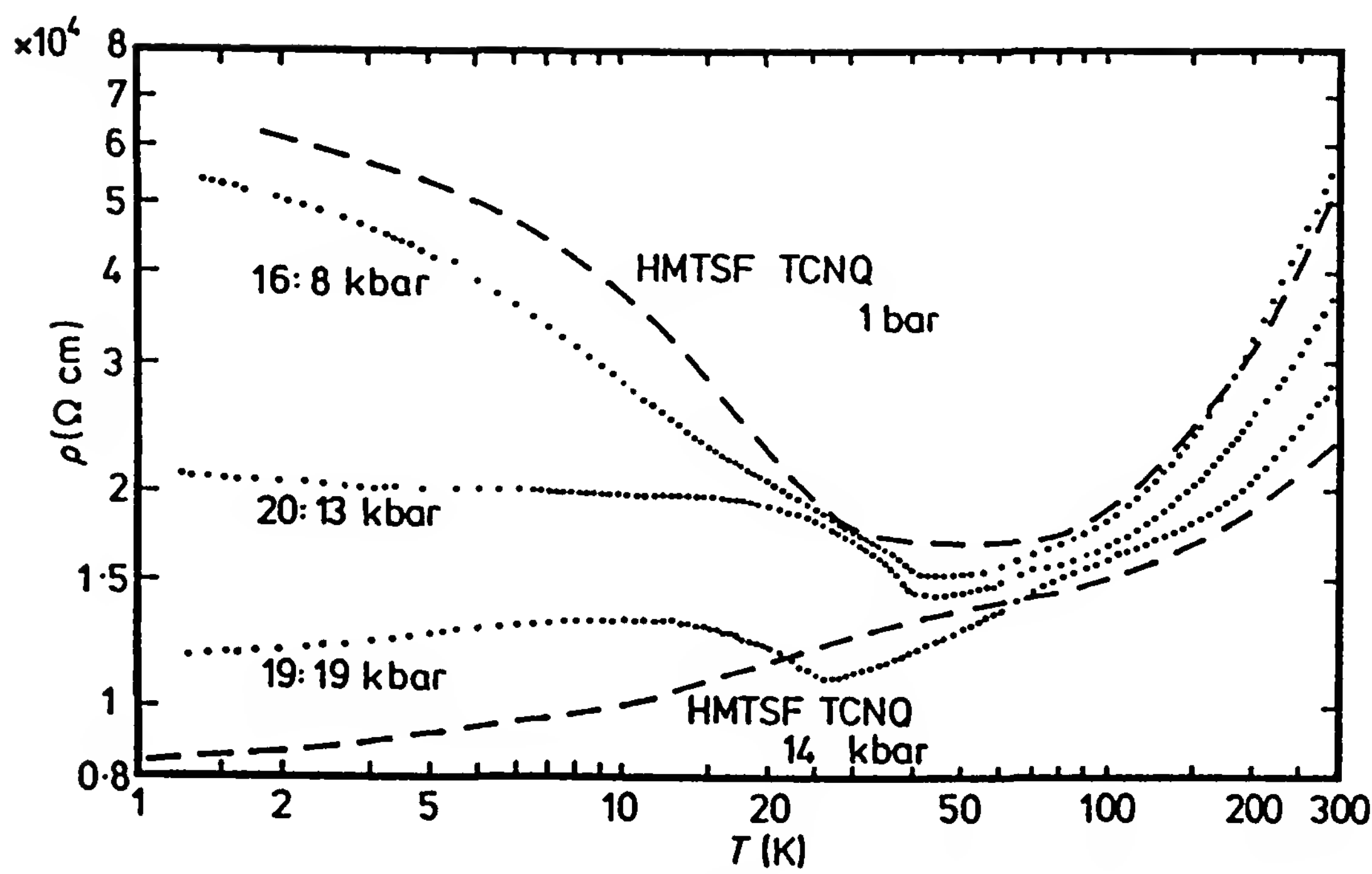


Figure 13 Longitudinal resistivity of HMTTF-TCNQ at various pressures, compared with HMTSF-TCNQ. (From Ref. 81.)

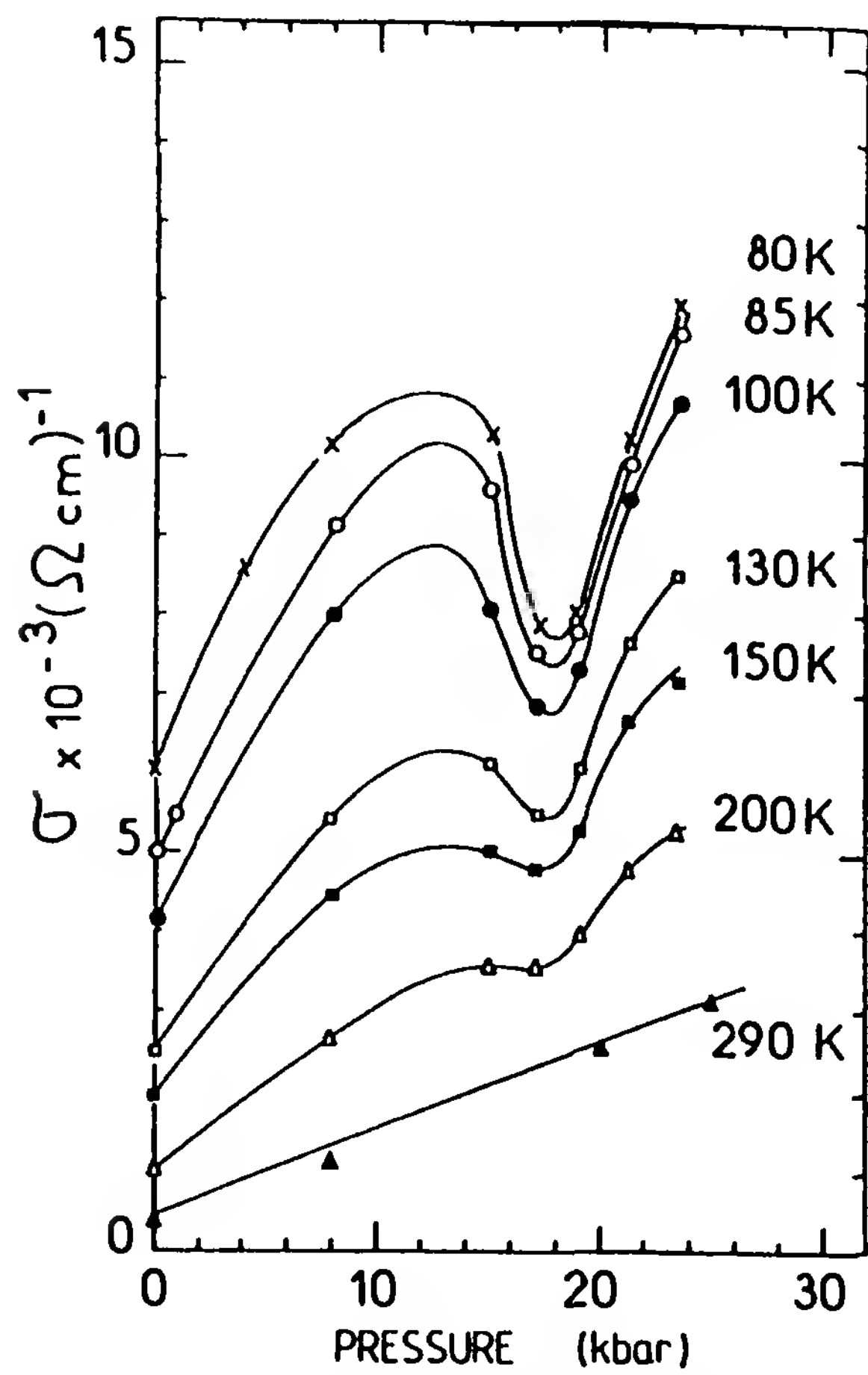


Figure 14 Longitudinal conductivity of a single crystal of TTF-TCNQ versus pressure at various temperatures showing the sharp dip at commensurability. (From Ref. 85.)

limiting the single-particle conductivity in these compounds is definitely identified, one cannot be completely sure that it is not reduced when $2k_F$ becomes commensurate with the lattice.

VI. CDW CONDUCTION

Several experiments show that at atmospheric pressure and between 38 and 53 K, the CDW in TTF-TCNQ is associated predominantly with the TCNQ chain [2,9]. Measurements by Lacoë and colleagues [88] did indeed show evidence for a sliding CDW contribution to the conductivity in this region above a certain threshold field ≈ 0.3 to 3 V/cm. Until then this had only been observed in inorganic CDW systems such as the trichalcogenides [89,90]. This behavior was subsequently followed under pressure. First, as shown in Fig. 15, in the low-pressure region (e.g., at 4 kbar) clearer evidence for CDW conduction was found [91] because the TCNQ CDW is dominant over a wider temperature range. Second, as shown in Fig. 16, there was a very strong increase in the threshold field at commensurability. There was also a sharp fall in the CDW current, indicating that near commensurability, CDW discommensurations may have been responsible for the nonlinear effects rather than uniform translations of the CDW. Further evidence in favor of CDW sliding is given in Fig. 17, where there is a particularly low threshold field that is drastically increased by low concentrations of radiation-induced defects. Below 38 K the threshold field is much larger and less sensitive to defects because of the Coulomb interaction with the CDW on the neighboring TTF chains. These experiments also gave an important impetus to the discovery of analogous effects caused by sliding *spin*-density waves in organic conductors, which are reviewed in Chapter 10.

VII. CHARACTERISTICS OF THE HALL EFFECT AND MAGNETORESISTANCE

A. Hall Effect

The first measurements of the Hall effect for quasi-one-dimensional organic metals were made on single crystals of HMTSF-TCNQ and TTF-TCNQ [32,39], although Hall effect studies of an organic semiconductor TEA(TCNQ)₂ had been made earlier [93]. For TTF-TCNQ the mobility is rather small near room temperature [39], so the signal-to-noise ratio in Hall measurements is usually not very good. To obtain good data it is usually necessary to evaporate gold contact areas on the sides and over the ends of the crystal, as sketched in Fig. 18a. It is often convenient to

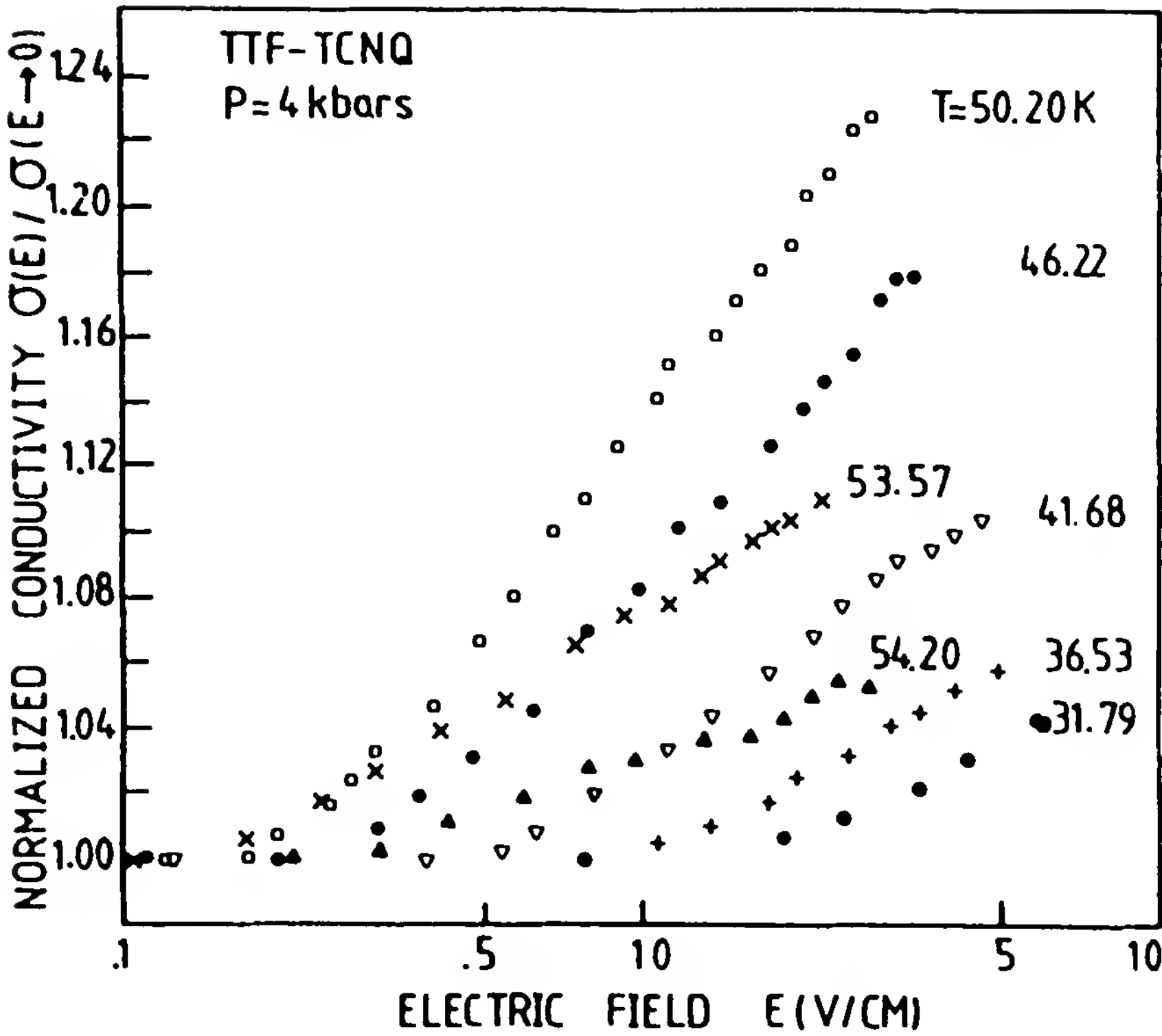


Figure 15 Conductivity of TTF-TCNQ versus electric field showing the onset of CDW conduction. (From Ref. 91.)

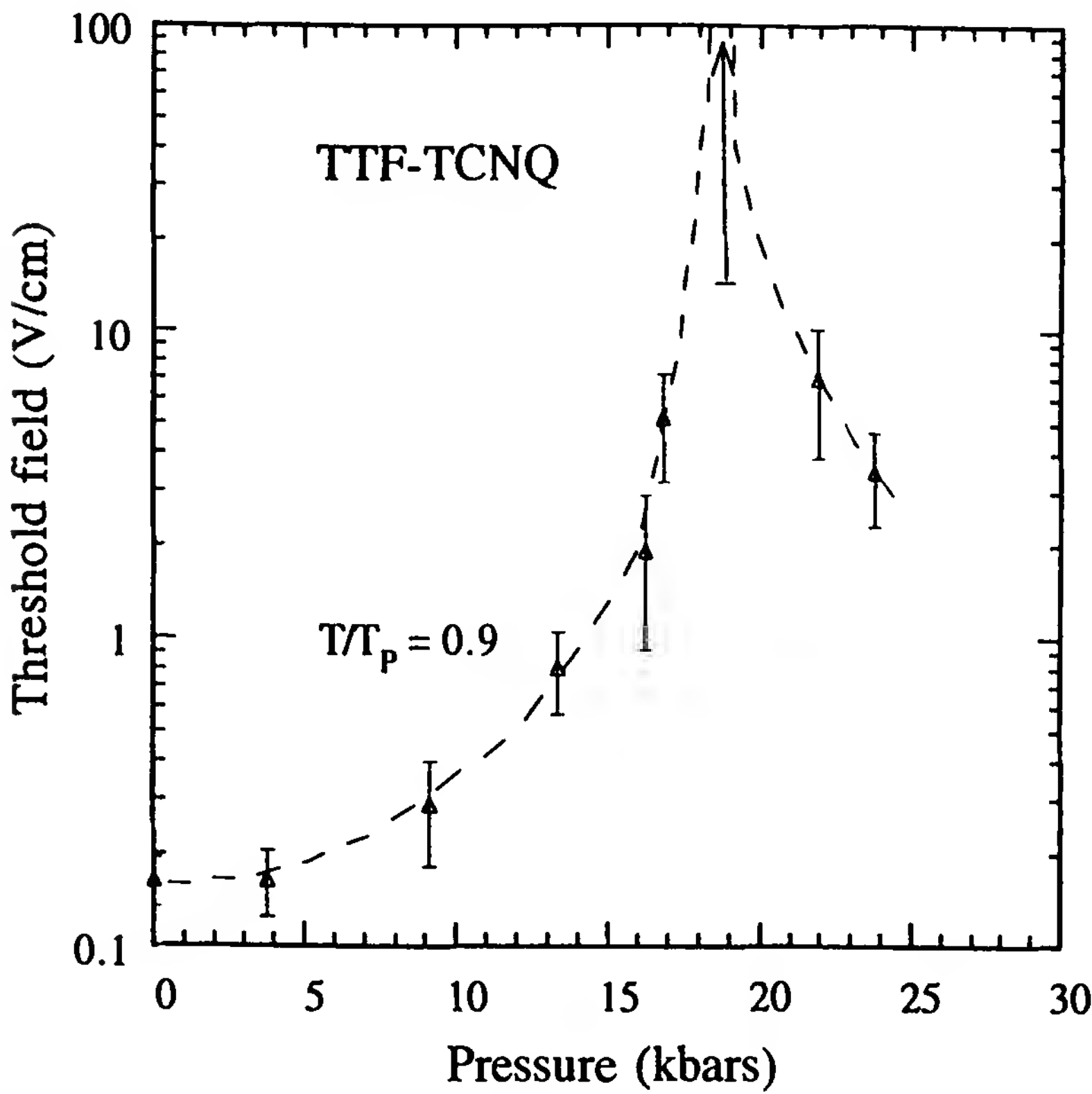


Figure 16 Threshold field for CDW sliding versus applied pressure for TTF-TCNQ, showing a strong increase at commensurability. (Adapted from Ref. 91.)

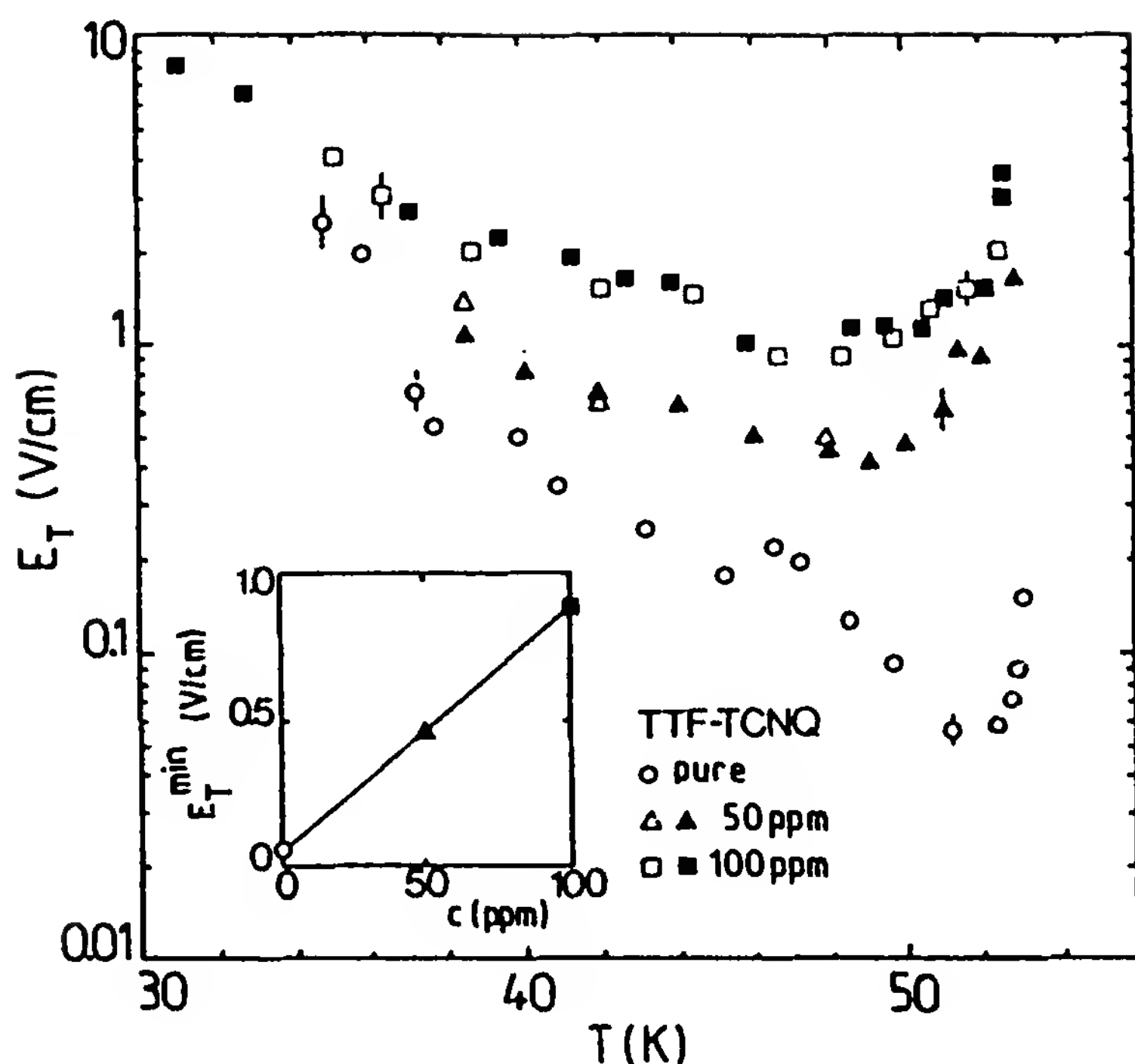


Figure 17 Threshold field versus temperature for TTF-TCNQ at ambient pressure, showing the effect of low defect concentrations. (From Ref. 92.)

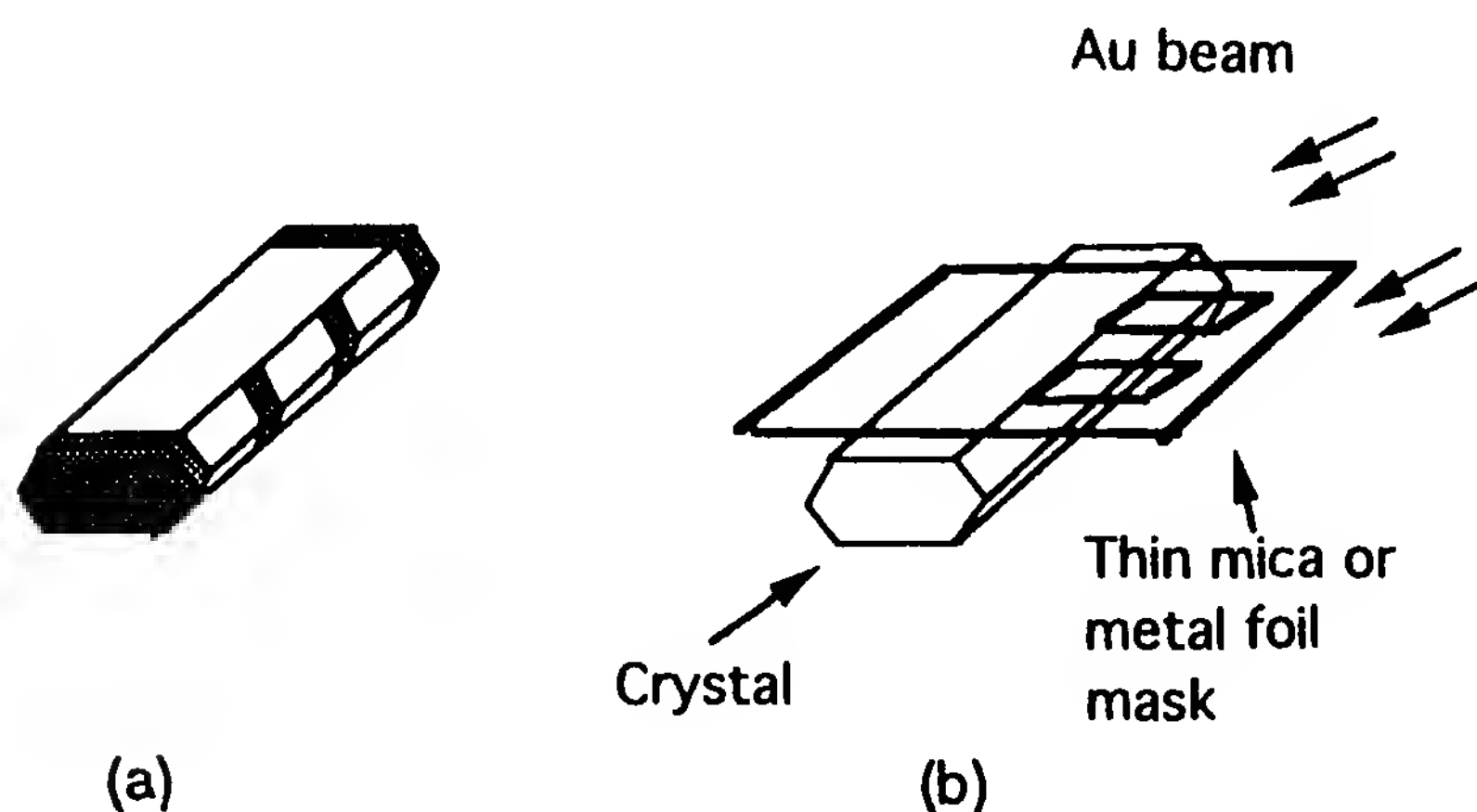


Figure 18 (a) Sketch of evaporated gold contacts for Hall measurements on single crystals of $(\text{TMTSF})_2\text{X}$; (b) masking arrangement used for evaporation of gold.

be able to rotate the sample holder by a suitable angle to prevent any gold from reaching the wider face of the crystal, as sketched in Fig. 18b. Thin (10- or 25- μm -diameter) gold wires are then attached to these gold contact areas using silver paint. The strain-free method introduced by Buravov et al. [94] enables good $\rho_h(T)$ data to be obtained without microcracks, even for the fragile crystals of the Bechgaard salts, but it is less suitable for the

Hall geometry. In the method of Kang [95] (used for much of the later low- T , high-field Hall work summarized in Chapter 10) the gold wires were held firmly against the contact pads by a suitable jig while applying the silver paint, in an attempt to optimize the gold/gold contact and place less reliance on the conductivity of the silver paint.

As far as we know, the Hall constant of the Bechgaard salts has not been measured above liquid helium temperatures. A summary of $R_H(T)$ for other representative compounds is given in Fig. 19. For TTF-TCNQ, R_H is negative in the metallic region, pointing toward the dominance of the TCNQ chains, and somewhat T dependent, especially under pressure where it follows a $1/T$ law [41]. There is a minimum in $|R_H|$ near 150 K where the $2k_F$ lines become visible in x-ray diffuse scattering. The presence of two conducting chains makes any detailed discussion difficult without having access to more data, such as for other field orientations, alloys, and lower temperatures.

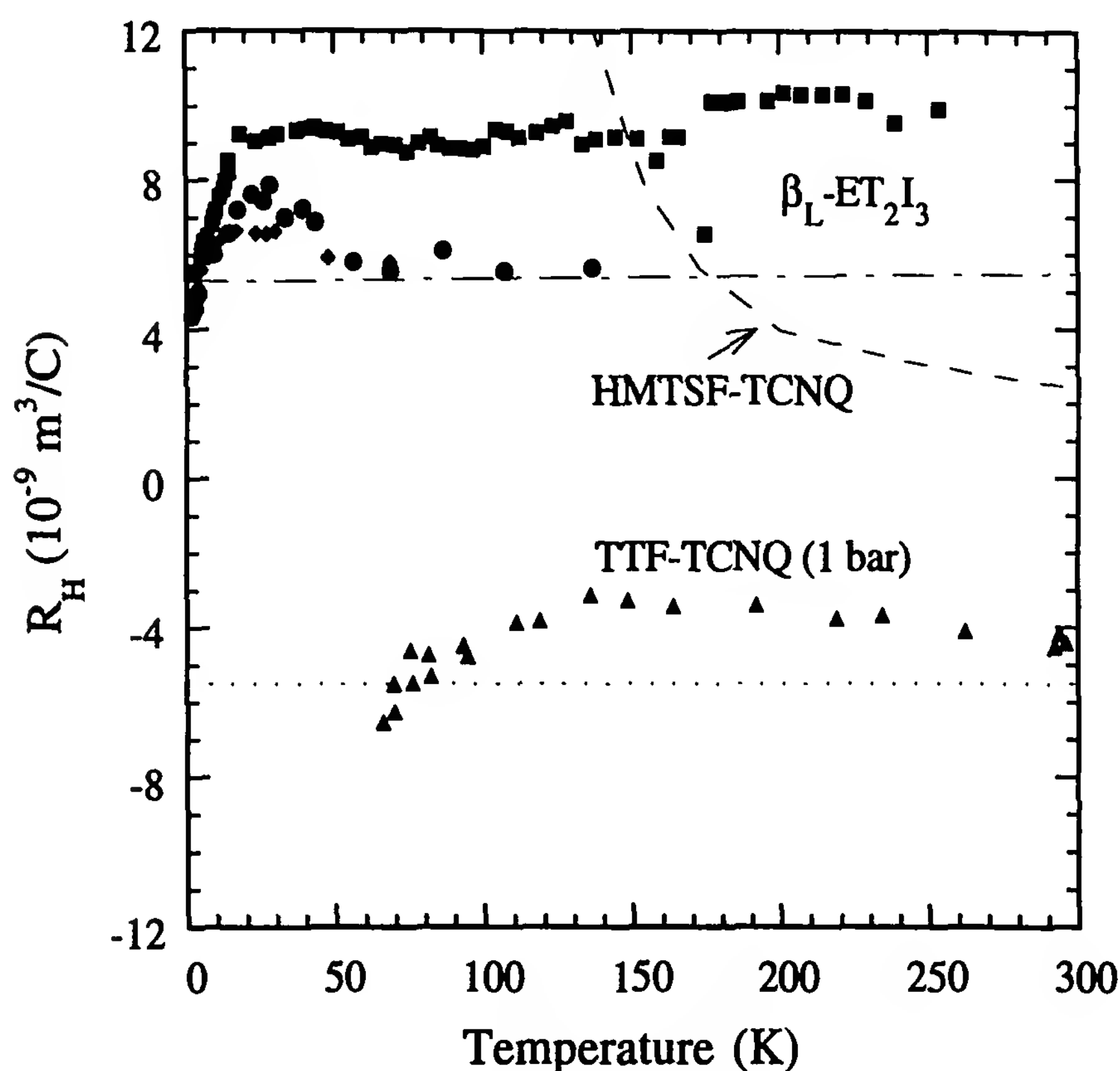


Figure 19 Hall coefficient versus temperature for three organic metals, with current flowing along the highly conducting axis: HMTSF-TCNQ and TTF-TCNQ (from Ref. 39) and β_L -ET₂I₃ [from Refs. 20 (circles and diamonds) and 98 (squares)]. The horizontal dashed line corresponds to a carrier concentration of 0.5 hole per ET molecule, the dotted line to Eq. (7) for the TCNQ chains of TTF-TCNQ.

For HMTSF-TCNQ [32,39], R_H is about the same magnitude down to 200 K, and is positive, pointing toward the dominance of the HMTSF chains, but becomes extremely large and changes sign at lower temperatures. As mentioned before, these data provided the crucial evidence that the conducting state at low temperatures was semimetallic rather than truly metallic. For the Bechgaard salts some measurements have been made in the metallic state at low T as part of the work on the field-induced SDW [96] and quantized Hall effects (Chapter 10). R_H is positive and of the expected magnitude for a quarter-filled quasi-one-dimensional band [Eq. (7), Section III.B.2]; together with specific heat data [97] and the absence of any unusual magnetic anisotropy associated with possible Landau–Peierls diamagnetism [54], this shows conclusively that for the Bechgaard salts there is a true metallic state at low temperatures, which depending on the applied pressure, may become antiferromagnetic or superconducting.

Data for β -(BEDT-TTF) $_2$ I $_3$ [20,98] are also included in Fig. 19. R_H is positive and falls sharply below 20 K. Fortune et al. [99] attribute this fall to the effect of a phase transition at 23 K (possibly a SDW) and suggest that the latter causes a reduction of about 50% in the electronic density of states. This is the reason put forward for the lower superconducting transition temperature ($T_{sc} = 1.5$ K) of the ambient pressure β_L phase compared with the β_H phase, which is stable above 0.5 kbar and has $T_{sc} = 8$ K. However, in contrast to this, Bulaevskii [3] attributed the suppression of T_{sc} to the larger disorder, corresponding to a residual resistivity of about $170 \mu\Omega\cdot\text{cm}$, which is larger than for other (BEDT-TTF) $_2$ X superconductors. So more experiments are needed to verify the above hypothesis. Susceptibility anisotropy measurements may be useful in this respect, because they are more sensitive to the formation of a SDW than the static susceptibility of randomly oriented single crystals (Fig. 4, Section IV).

B. Magnetoresistance

1. Kohler's Rule

In the band picture outlined in Section III.B, the effect of a magnetic field on the electrical resistivity (ρ) is to give an increase ($\Delta\rho \equiv \rho - \rho_0$) that obeys Kohler's rule (KR) [35,100], namely:

$$\frac{\Delta\rho}{\rho_0} = F\left(\frac{H}{\rho_0}\right) \quad (10)$$

and in the low-field limit, $F(H/\rho_0) = \alpha(H/\rho_0)^2$, where α is a constant. KR will not be obeyed if the number of carriers or density of states varies with

temperature, and indeed, for HMTSF-TCNQ there were large deviations from KR [31,32]. Our first measurements of magnetoresistance for the Bechgaard salts [22] were made as part of a study of the effect of magnetic field on the perpendicular (c^*) axis resistivity. The starting idea was that a transverse field would make the electronic states more one-dimensional! Although this did turn out to be the case (see Chapter 10), it is now clear that the novel physics occurs when the magnetic field is applied along the c^* direction and the electronic motion along the other transverse direction (b') is suppressed [101,102]. This is what restores the one-dimensionality and stabilizes spin-density-wave ground states. So, as shown in Fig. 20, when magnetoresistance data for current flow $j \parallel l(c^*)$ and $H \parallel l(b')$ are plotted as $\Delta\rho/\rho_0$ versus H/ρ_0 , KR is obeyed. As explained in various papers [13,22], this and similar data could be analyzed using the formulas in Section III.B.2 to obtain the relaxation time (τ), the mean free path along the chains, and the tight-binding transfer integral in the least conducting direction (t_l or t_c^*). Similar analysis has been made for various other materials [e.g., the β_L and β_H states of $(\text{BEDT-TTF})_2\text{I}_3$] [26,103]. The effects of temperature

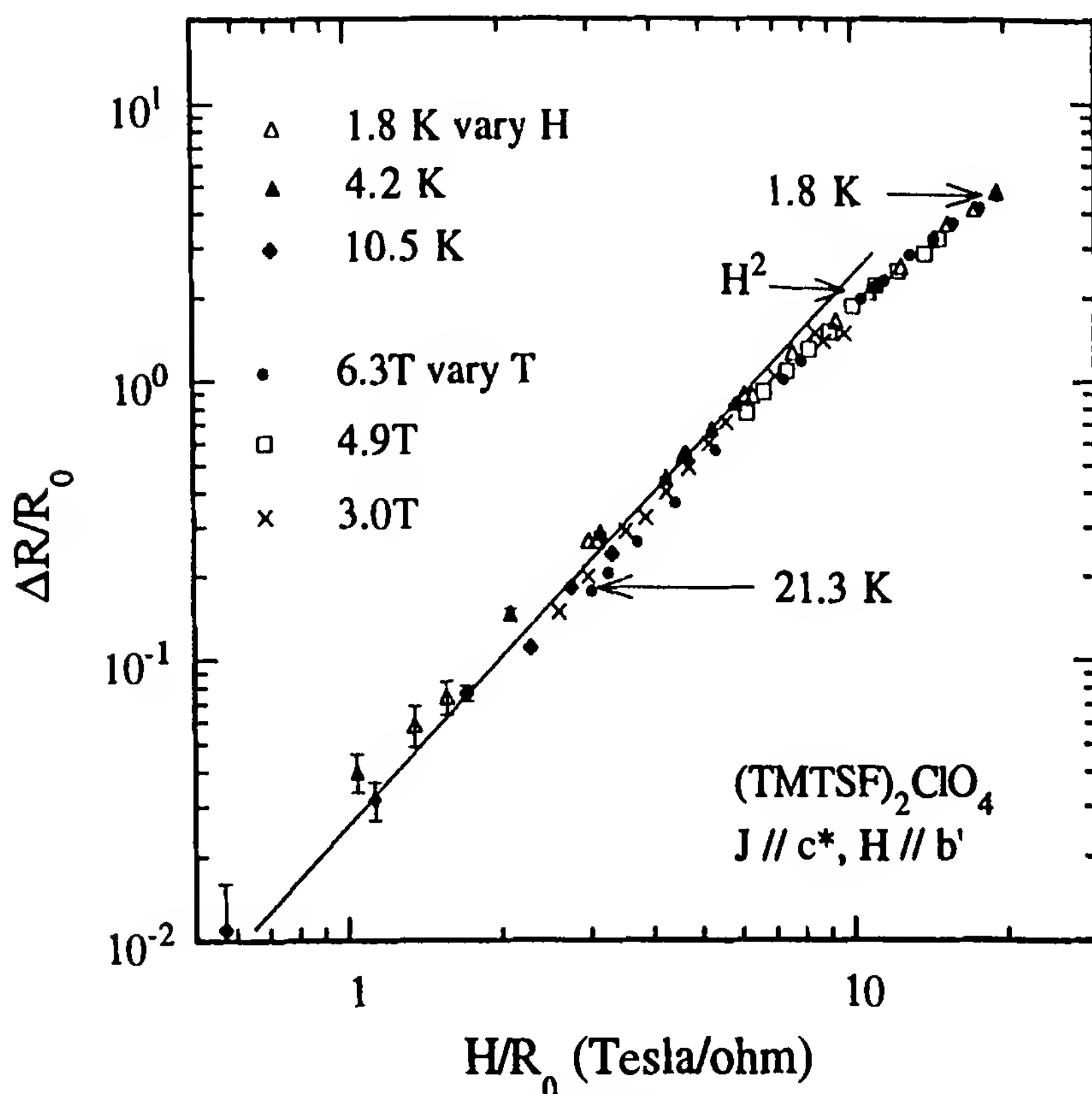


Figure 20 Kohler's plots for the transverse resistivity (ρ_l) of $(\text{TMTSF})_2\text{ClO}_4$ at various temperatures between 1.8 and 21 K and fields of up to 6 T in the intermediate direction. (From Ref. 13.)

[23], alloying, and irradiation-induced defects [104] on ρ_l of the Bechgaard salts have also been studied, and the main results are outlined in Sections VII.B.3 and IX.

2. Anomalous Magnetoresistance for ρ_h

Although the effect of a magnetic field on ρ_l of the Bechgaard salts is well understood, as mentioned in Section II.B.2, there is an anomalously large increase in ρ_h when H is along the low-conductivity direction. The clearest example is in the metallic state of $(\text{TMTSF})_2\text{PF}_6$ under pressure, because for $(\text{TMTSF})_2\text{ClO}_4$ there can be complications associated with anion ordering. An example of the large magnetoresistance (unpublished results of W. Kang, J. R. Cooper, D. Jérôme, and K. Bechgaard) of $(\text{TMTSF})_2\text{PF}_6$ is shown in Fig. 21 and corresponding Kohler's plots in Fig. 22. From the latter it can be seen that KR is partially obeyed because *in fixed fields* there are regions at higher temperatures where $\Delta\rho/\rho_0 \sim \rho_0^{-2}$. One attractive interpretation is that the effect of the field is to increase the one-dimen-

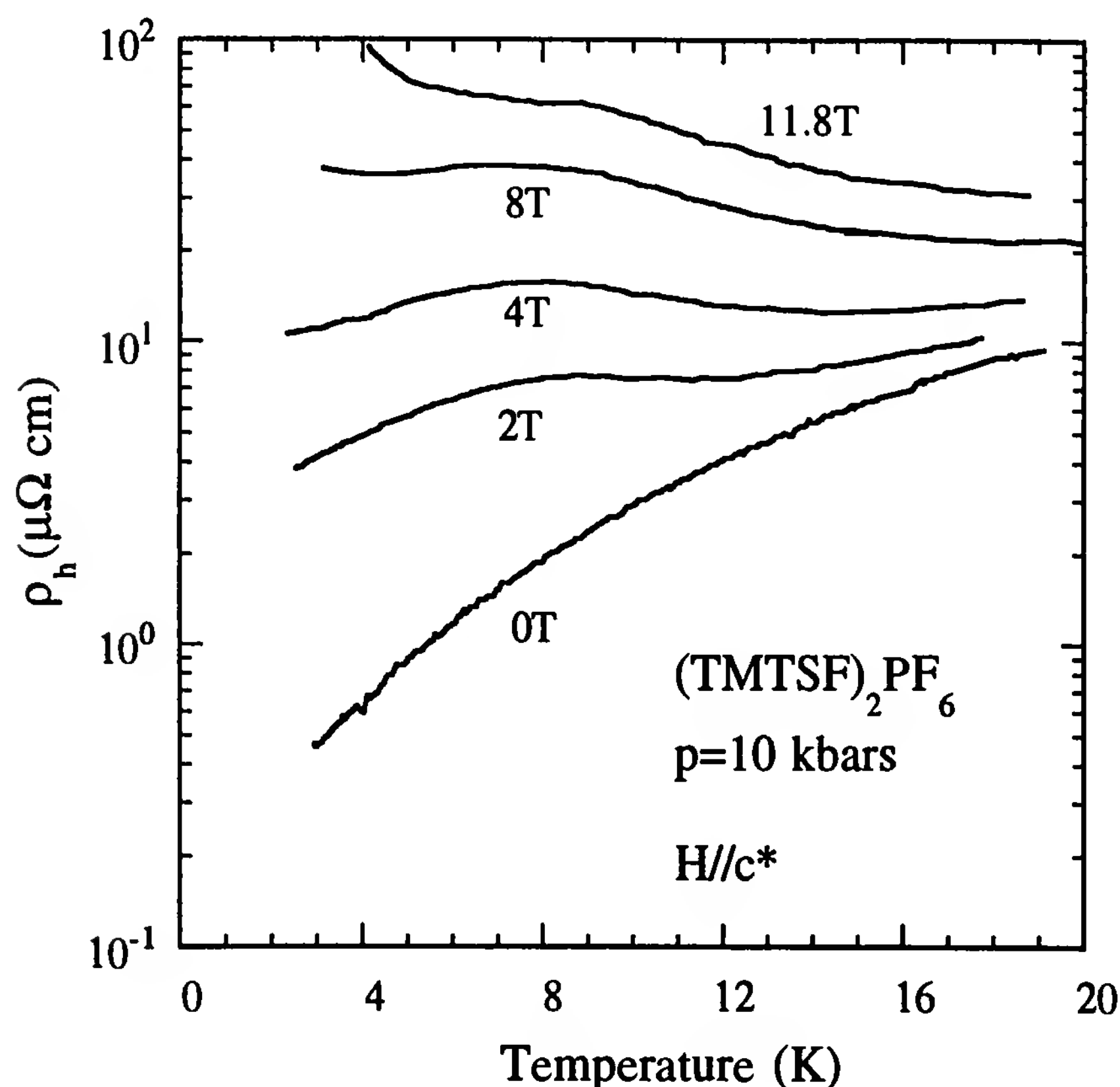


Figure 21 Resistivity of $(\text{TMTSF})_2\text{PF}_6$ for current flow in the high-conductivity direction (*a*) with various magnetic fields applied in the low-conductivity direction (*c**). (From unpublished results of W. Kang, J. R. Cooper, D. Jérôme, and K. Bechgaard.)

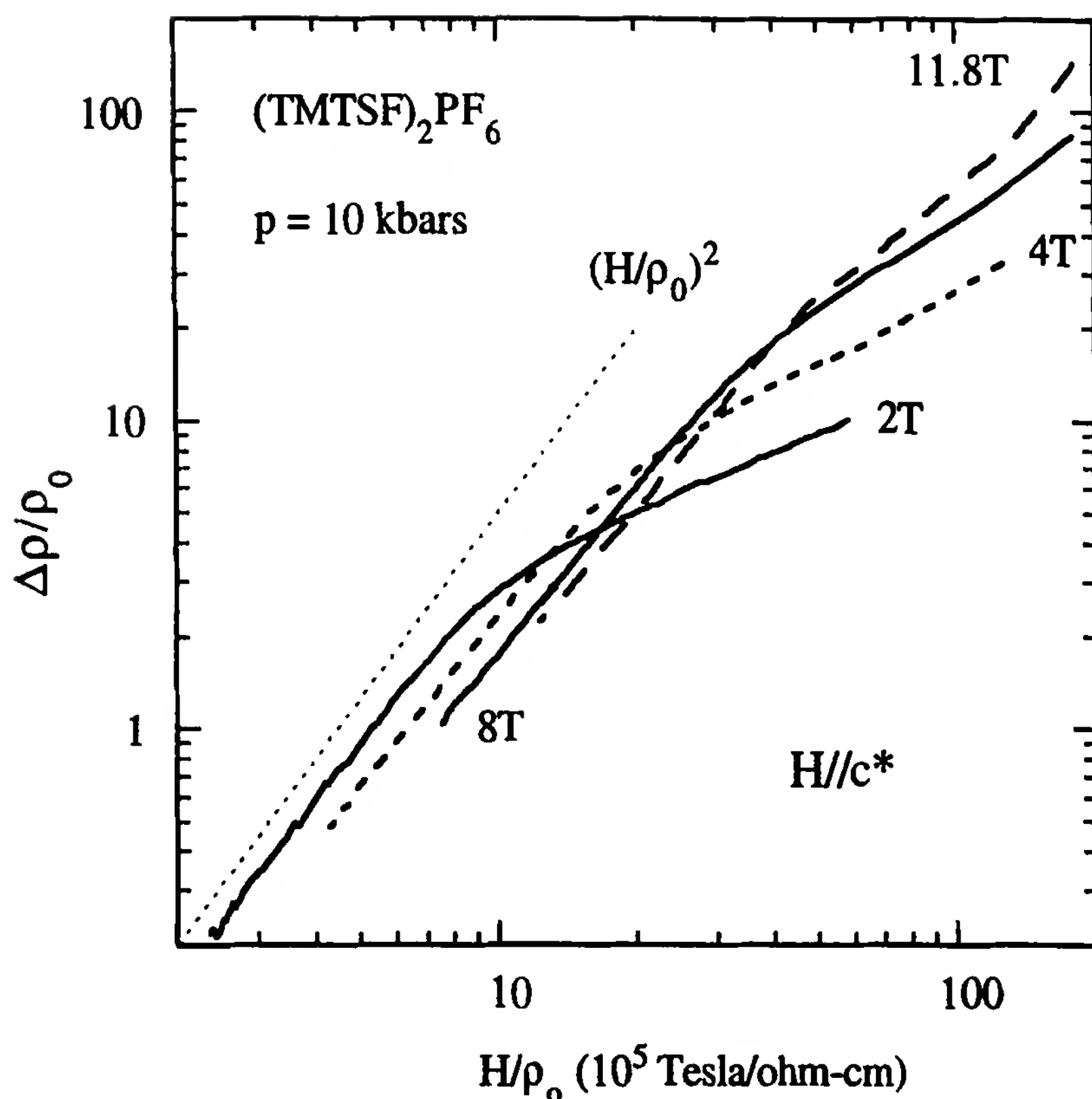


Figure 22 Kohler plots of the data in Fig. 21. In fixed fields and at higher temperatures there is evidence for a $1/\rho_0^2$ behavior. The effect of a field is to extend this $1/\rho_0^2$ behavior down to lower temperatures. $\Delta\rho/\rho_0$ is not proportional to H^2 .

sionality, as in the theory of the field-induced SDW [101,102] and thereby increase the resistivity. Another approach would be to ascribe the large magnetoresistance to the effect of a magnetic field on the selection rules for electron–electron scattering. At the present time this seems to be an interesting, unsolved problem.

3. Magnetoresistance at Higher Temperatures

Given that below 20 K, $\rho_l(H)$ of $(\text{TMTSF})_2\text{ClO}_4$ could be understood in terms of band theory, as summarized in Sections III.B and VII.B.1, it was interesting to extend the measurements up to higher T . Deviations from KR were expected in the diffusive region [80] when the mean free path in the c direction becomes much less than the lattice constant. For organic semiconductors such as naphthalene, this is referred to as the band-hopping transition [105–107]. Deviations from KR were observed for $(\text{TMTSF})_2\text{PF}_6$ above 60 K [23]. However, as shown in Fig. 23, plots of $\sqrt{\Delta\rho/\rho}$ (equivalent to $\omega\tau$ in band theory) versus T were essentially the same for the PF_6 and ClO_4 salts and both followed a $T^{-1.5}$ power law, even though data for the

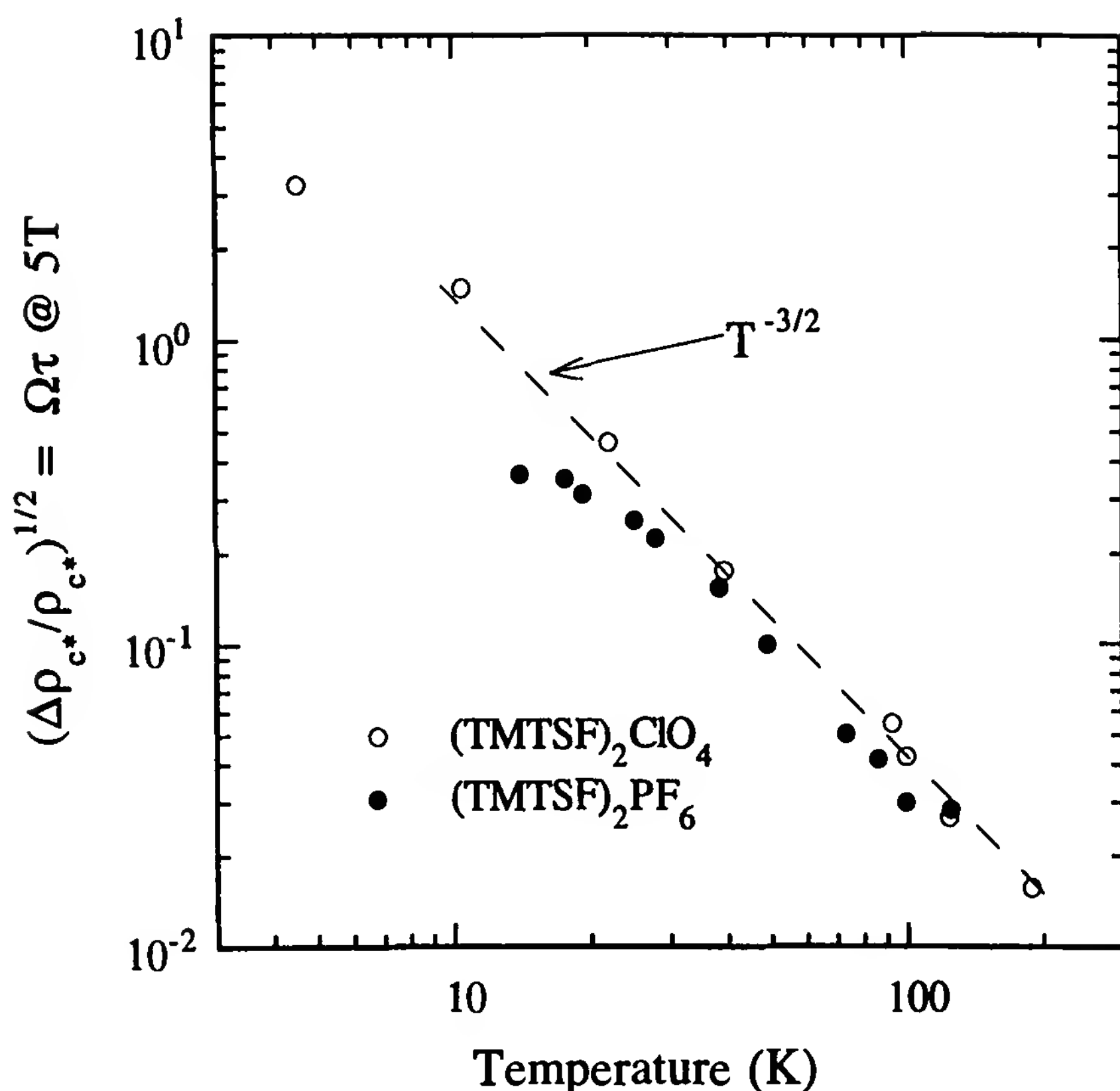


Figure 23 Plots of $\sqrt{\Delta\rho/\rho}$ (i.e., $\omega\tau$) for the high resistivity (l or c^*) direction of $(\text{TMTSF})_2\text{ClO}_4$ and $(\text{TMTSF})_2\text{PF}_6$ in a fixed field of 5.4 T along the i or b' direction.

ClO_4 salt did obey KR approximately. We concluded [23] that there was no qualitative change in magnetoresistance even though the (inelastic) mean free path became as low as 1/250 of a lattice parameter in the c direction. This is the experimental basis for the remarks in Section III about the possible applicability of the Boltzmann formulas even when the inelastic mean free path perpendicular to the chains is very small, and the apparent absence of a minimum metallic conductivity in the transverse directions.

VIII. MOLECULAR VIBRATIONS AND THE ISOTOPE EFFECT IN TTF-TCNQ

Organic semiconductors such as K-TCNQ and $\text{TEA}(\text{TCNQ})_2$ have anomalous infrared (IR) absorption lines at frequencies corresponding to the totally symmetric (a_g) vibration modes of the TCNQ molecule. Normally, these modes would not be IR active, but because they modulate the electron overlap integrals, they induce charge oscillations along the (nonuniform) TCNQ stacks [108]. This is perhaps the clearest experimental evidence for

the importance of electron–molecular vibration (EMV) coupling in organic conductors, and it is possible that molecular modes also play a role in organic superconductivity (Chapter 10). EMV coupling is certainly relevant in the CDW state of TTF-TCNQ, as shown by the IR data [109] reproduced in Fig. 24. The IR absorption by the a_g mode of the TCNQ molecule at 317 cm^{-1} increases in intensity below 65 K with an increased slope at the first transition ($T_1 = 53\text{ K}$). In contrast, the intensity of the 253-cm^{-1} TTF mode only rises below 46 K, and there is an increase in slope at T_3 (38 K). This behavior is consistent with other experiments, including the CDW work summarized in Section VI, which suggest that the upper transition affects only the TCNQ stacks and the lower one mainly the TTF stacks. It also implies that the CDW causes small static distortions of the molecules [109].

Further evidence for the relevance of EMV coupling to the Peierls transition of TTF-TCNQ is given in Fig. 25, which shows how the temperatures T_1 and T_3 of the two phase transitions are affected by various isotopic substitutions of the TTF or TCNQ molecules [110]. The resistive transitions do not all have the same widths ΔT , and as it is known that T_1 and T_3 can be suppressed and broadened by very small defect levels, in the figure T_1 and T_3 are plotted versus ΔT . This enables any shifts caused by defects to be distinguished from true isotope shifts. The observed isotope

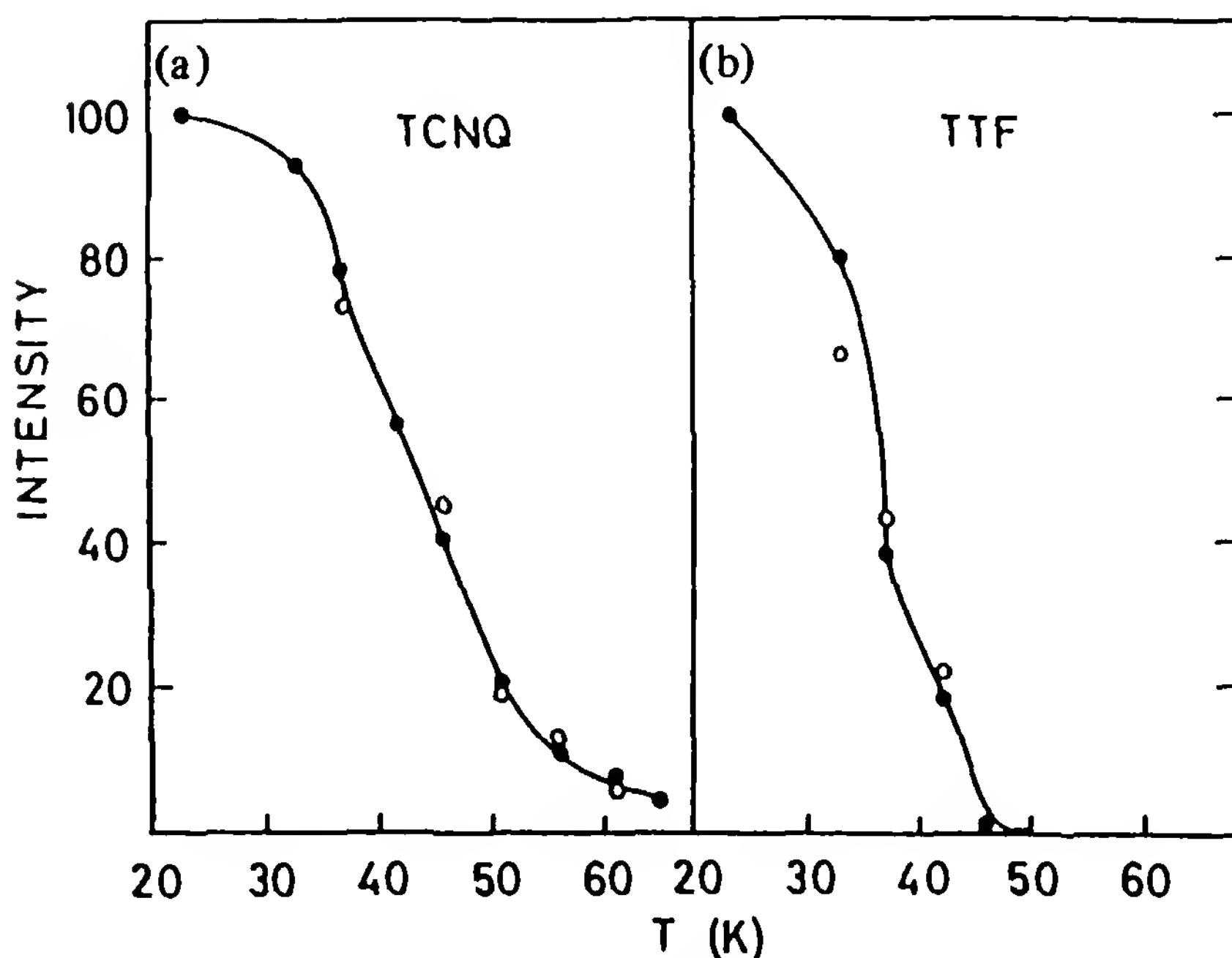


Figure 24 Temperature-dependent infrared absorption intensities of TTF-TCNQ at 317 cm^{-1} (a) and 253 cm^{-1} (b). Solid circles, heating; open circles, cooling. (From Ref. 109.)

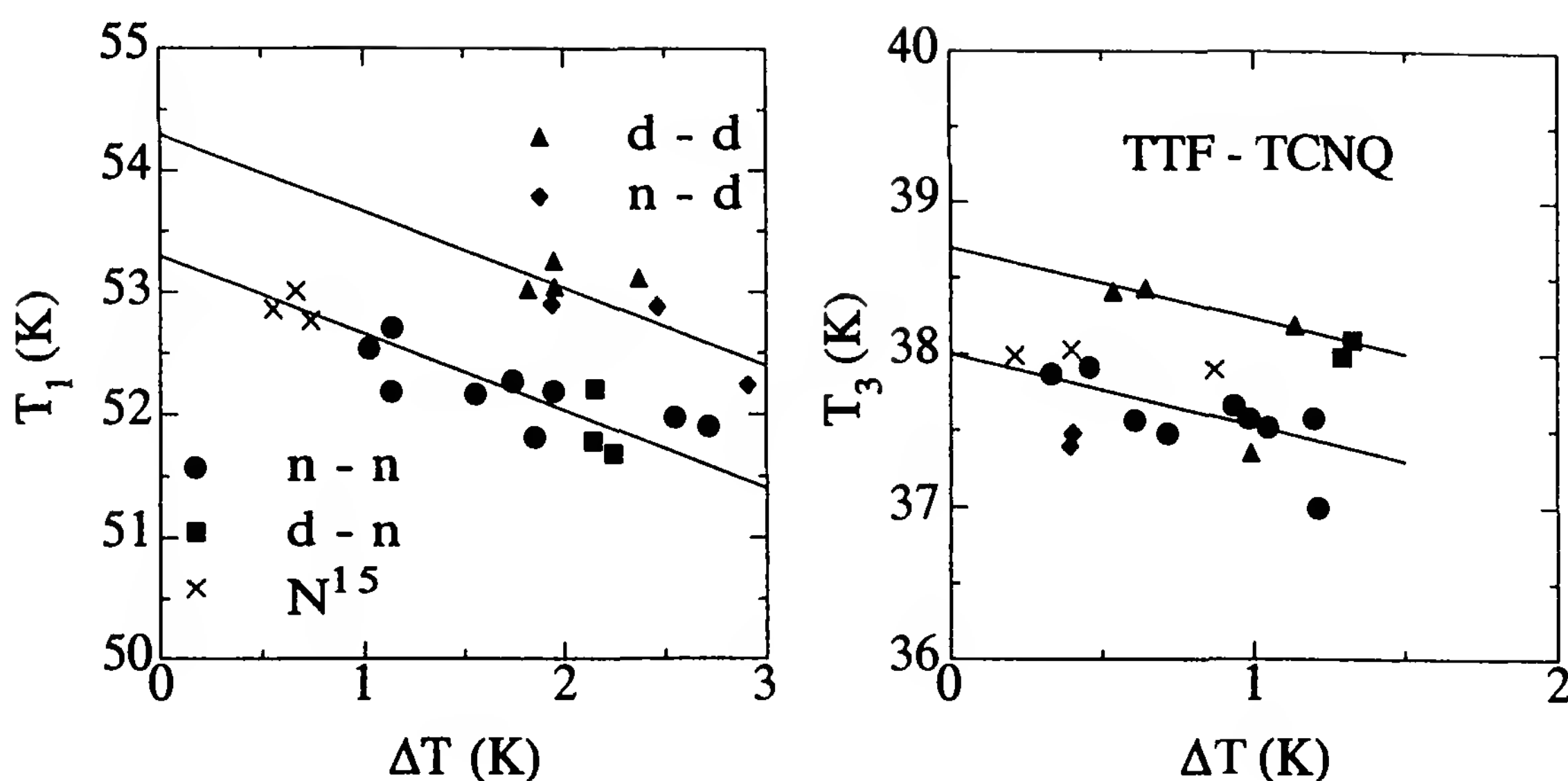


Figure 25 Transition temperatures of single crystals of TTF-TCNQ, with different isotopic substitutions, plotted versus the transition width ΔT (FWHM of the peak in $d\rho_n/dT$). “d-n” indicates fully deuterated TTF molecules and normal TCNQ molecules, and so on. (From Ref. 110.)

shifts are consistent with a theory of Horovitz [111] in which the input parameters are the known EMV coupling constants and the frequency shifts of the a_g modes.

IX. INFLUENCE OF DISORDER

The introduction of controlled amounts of disorder into organic metals has proved to be quite fruitful for understanding the properties of the pristine compounds. Disorder can either be introduced by chemical substitution (alloying) or by irradiation with neutrons or ionizing irradiation such as x-rays, γ -rays, or electrons. These two methods are complementary in that substitution produces a relatively large number of weaker impurity potentials, while irradiation produces completely different chemical species and creates strong perturbing potentials [112], as well as often introducing an unpaired spin [113].

Several solid solutions (alloys) of organic metals have been prepared. Studies of $(TSeF)_x(TTF)_{1-x}TCNQ$ were important at an early stage in unraveling the relative influence of donor and acceptor stacks on the electronic and structural properties of TTF-TCNQ, and are reviewed by Schultz and Craven [114]. Since then there have been interesting results regarding the effect of disorder on the SDW transition in $\{(TMTSF)_x(TMTTF)_{1-x}\}_2PF_6$ [115], on the threshold electric field for SDW sliding in $(TMTSF)_2(AsF_6)_{1-x}(SbF_6)_x$

[116], and on superconductivity in $\{(\text{TMTSF})_x(\text{TMTTF})_{1-x}\}_2\text{ClO}_4$ [117] and $(\text{TMTSF})_2(\text{ClO}_4)_{1-x}(\text{ReO}_4)_x$ [118].

In a classical Boltzmann transport picture, a defect will scatter electrons if its spatial range is less than the electron mean free path, but if it is larger than the mean free path, it will act as a macroscopic region of lower conductivity and electrons will flow around it. The latter type of picture is thought to apply to the organic conductor TMTSF-DMTCNQ, where irradiation-induced defects break up the conducting chains into segments [119] and current flows around the defect perpendicular to the chains (in the i direction). However, the distinction between such a model and those involving localization (with a localization length equal to the segment length) is not clear-cut. Experimentally [119], the chain conductivity is found to obey a law of the form given below, corresponding to the fact that some current flows in the i direction:

$$\rho_h(C, T) = \rho_h(0, T) + C \frac{b}{a} \rho_i(C, T) \quad (11)$$

where C is the molecular fraction of radiation-induced defects, while a and b are the lattice parameters (the transverse hopping length is equal to b). The transverse resistivity ρ_i is found to obey the law [119]

$$\rho_i(C, T) = \rho_i(0, T) \exp\left(\frac{C \Delta\varepsilon}{k_B T}\right) \quad (12)$$

When Eqs. (11) and (12) are fitted to experimental data for TMTSF-DMTCNQ, the parameter $\Delta\varepsilon$ is typically found to be on the order of the bandwidth $4t_h$; that is, $C \Delta\varepsilon$ represents the average energy-level spacing in a metallic strand that is $\approx 1/C$ lattice parameters long. Equations (11) and (12) were found to give a good description of the data even at low values of C (≤ 0.1 mol %). At first sight this implies that in the pure compound, where $\rho_i/\rho_h \approx 100$ and $\rho_t/\rho_h \approx 200$ at room temperature, $\rho_i(0, 300)$ also arises from an inelastic tunneling process despite the fact that it has a metallic temperature dependence. If this were not so, one would expect to see deviations from Eq. (12) at low values of C which were not observed [119]. However, this is not the only possibility. First, all mean free paths are small at 300 K, so there must be an analogous contribution to ρ_i from current flowing around the defects in the lowest-conductivity (l) direction. Second, as discussed below [104], the low- T magnetoresistance for ρ_i of irradiated $\text{TMTSF}_2\text{ClO}_4$ can be understood in terms of a metallic band picture combined with a decrease in the effective value of t_l with C (by about 25% for 0.1 mol % defects). This decrease was ascribed [104] to the defect potentials causing variations ($\approx 4 C t_h$) in the energies of the mo-

lecular orbitals and reducing electron overlap integrals in the transverse direction. Or in other words, irradiation can alter the band parameters, but at low values of C a metallic band picture remains valid. It would not be easy to distinguish this effect from the initial increase with C given by Eq. (12). So although in principle, irradiation experiments can prove whether or not ρ_i or ρ_l of the pristine compound arises from an interchain hopping process, in our opinion this has not yet been done.

Figure 26 shows the effect of x-ray irradiation on the longitudinal resistivity ρ_h [112] of $(\text{TMTSF})_2\text{ClO}_4$ at 4.2 K. Here the two regions hinted at in the preceding paragraph *can* be clearly distinguished, probably because the mean free paths are much longer at low T . From 0 to about 0.2 mol % defects, the resistivity increases linearly with C , as expected for

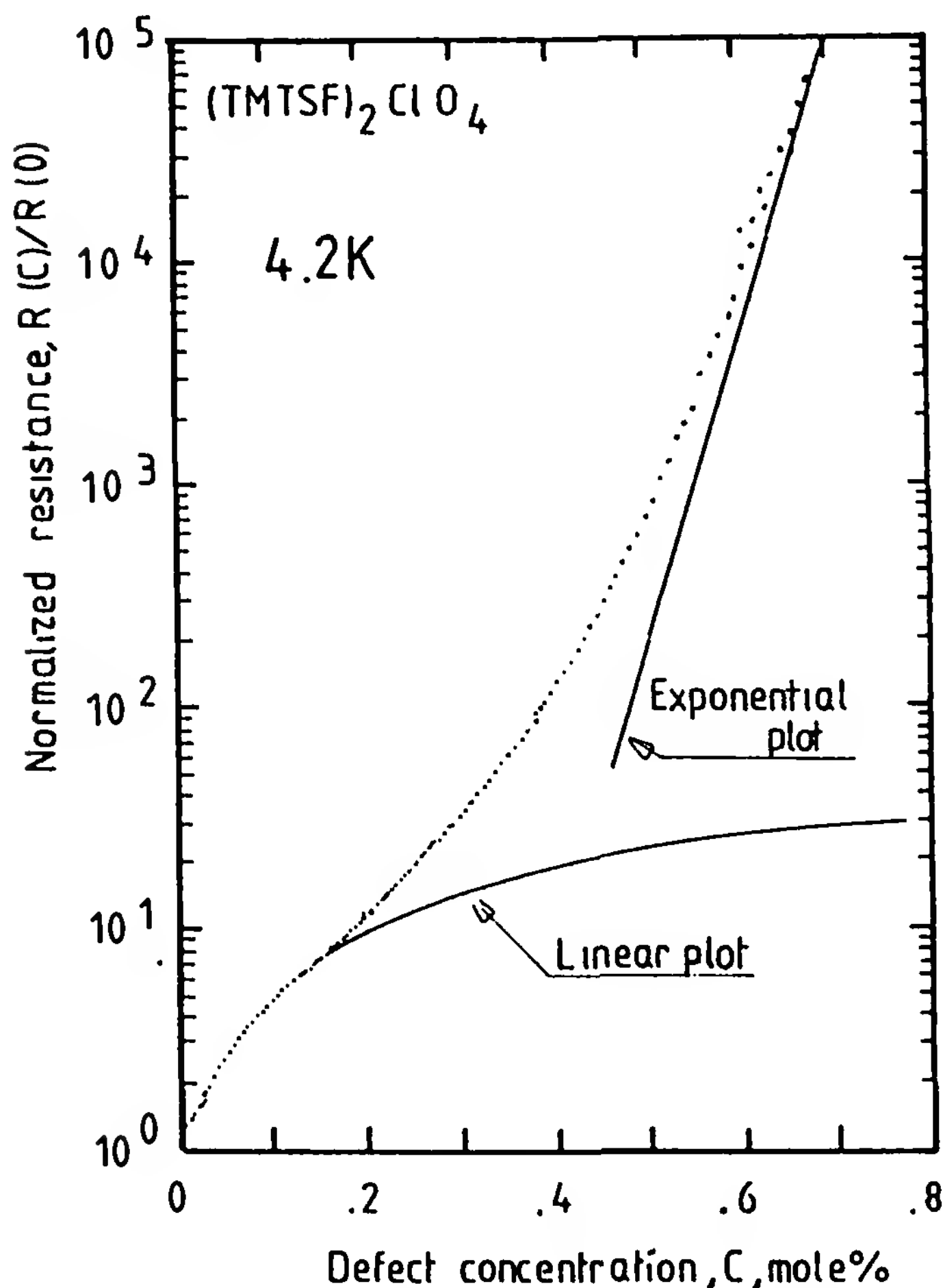


Figure 26 Normalized longitudinal resistivity ρ_h of a single crystal of $(\text{TMTSF})_2\text{ClO}_4$ at 4.2 K versus concentration of irradiation-induced defects (mole %). Initially, linear behavior is observed, corresponding to Matthiessen's rule, followed by an exponential behavior corresponding to Eqs. (11) and (12) (see the text). (From Ref. 112.)

ordinary metallic alloys, where the number of independent scattering centers is proportional to C , before changing over to the faster exponential dependence given by Eq. (12). This plot also shows the high purity of the parent crystal since $\rho_h(0)$ is doubled by the introduction of only 0.02 mol % defects.

An interesting point, which as far as we know is still not understood, is that the superconductivity of $(\text{TMTSF})_2\text{ClO}_4$ is rapidly suppressed both by irradiation-induced defects and by alloying. T_{sc} is reduced by approximately a factor of 10 by 0.01% irradiation-induced defects [112]: substitution of 0.05% TMTSF molecules by TMTTF [117] or 5% of the ClO_4 anions by ReO_4 [118]. It is possible that this happens at approximately the same value of the residual resistivity (i.e., the elastic scattering rate) in all cases, which could point toward the existence of an unconventional superconducting pairing mechanism. [In ordinary superconductors elastic (non-spin-flip) scattering does not suppress T_c because a perturbation that is invariant under time reversal does not cause pair breaking.] However, for the Bechgaard salts there are problems, partly technical (microcracks in the crystals make it difficult to determine the resistivity precisely) and partly caused by the proximity and possible influence of the spin-density-wave instability. [If $(\text{TMTSF})_2\text{ClO}_4$ is cooled rapidly from 40 K to 10 K, the tetrahedral ClO_4 anions remain disordered and a spin-density-wave state is formed below 6 K.] Also, as mentioned below, weak localization effects could play a role in suppressing T_{sc} .

Figure 27 shows the effect of alloying on the transverse resistivity of $(\text{TMTSF})_2(\text{ClO}_4)_{1-x}(\text{ReO}_4)_x$ alloys [104]. The room-temperature resistivity was not altered by alloying, so it can be seen that at low T , Matthiessen's rule is obeyed because the $\rho_l(T)$ curves remain parallel to each other. To a first approximation the ReO_4 ions act as independent scattering centers which do not alter the electronic structure of $(\text{TMTSF})_2\text{ClO}_4$. This was confirmed by a Kohler's rule analysis of the magnetoresistance, which showed that t_l was not altered. In contrast, irradiation-induced defects lead to the reduction in t_l mentioned above and to corresponding deviations from Matthiessen's rule.

Up to now we have discussed two extreme limits, the band picture on the one hand, and strong localization associated with interruptions in the metallic chains on the other. In fact, from work on thin metallic films and metallic glasses it is known that there is an intermediate region, that of weak localization. This occurs when the mean free path for elastic scattering (L_{el}) is only somewhat larger than, or comparable with, that for inelastic processes (L_{in}). In the first approximation there are corrections to the Boltzmann transport formula which depend on the ratio $L_{\text{in}}/L_{\text{el}}$ in different ways for one-, two-, and three-dimensional materials. Weak localization

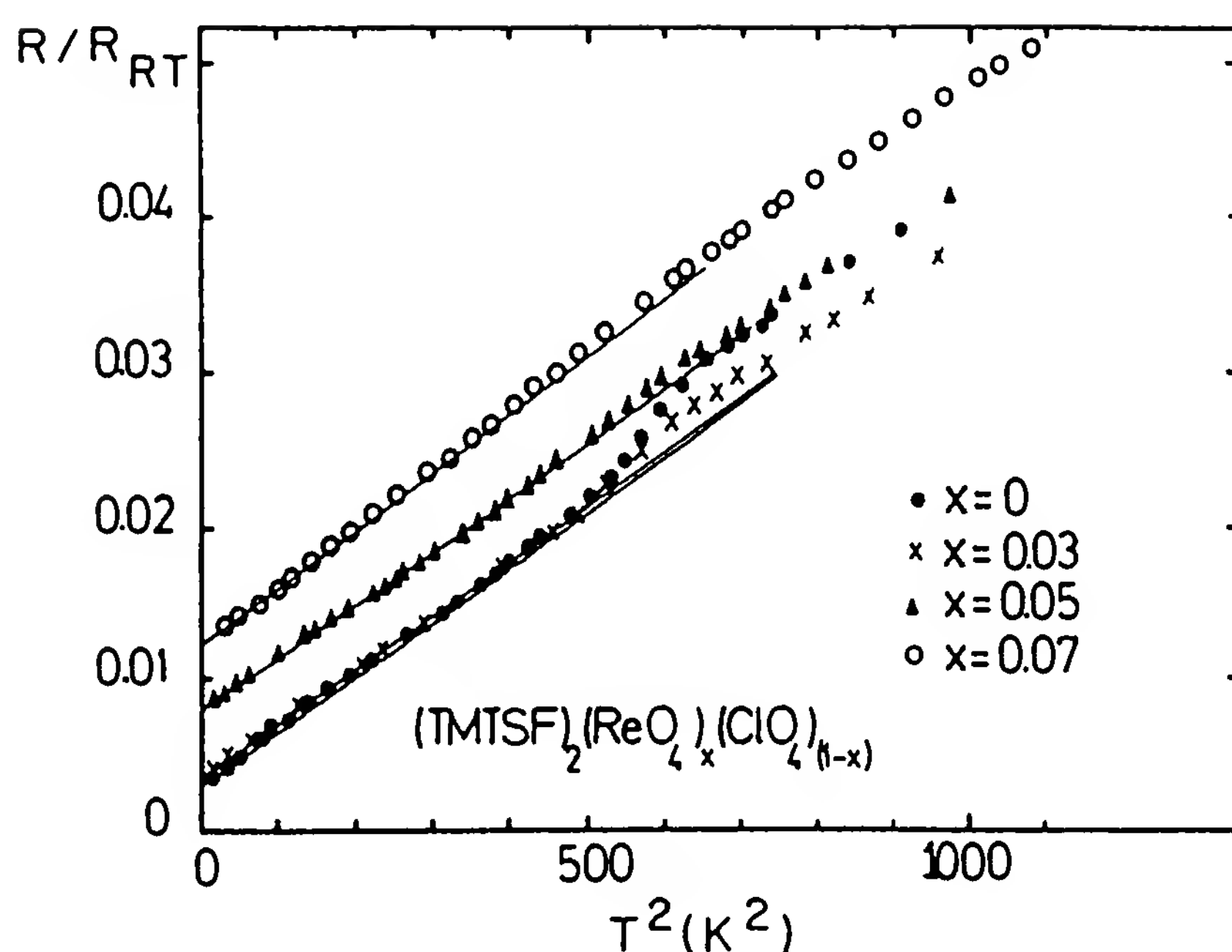


Figure 27 Transverse resistivity ρ_t versus T^2 for $(\text{TMTSF})_2\text{ClO}_4$ doped with small quantities of ReO_4 . There is evidence for a T^2 law and for Matthiessen's rule. The anomaly associated with ordering of the ClO_4 anions at 24 K is also visible. (From Ref. 104.)

effects have been reviewed by Altshuler et al. [120], Bergmann [121], and Lee and Ramakrishnan [122]. One characteristic feature is a negative magnetoresistance which in the simplest case arises because the magnetic field destroys the quantum interference between the scattered electrons and reduces the weak localization effects.

Negative magnetoresistance has been observed [123] in a series of $(\text{DMTTSF})_2\text{X}$ salts, which are isomorphous with the Bechgaard salts and which have very similar electrical properties apart from the occurrence of superconductivity. The magnetoresistance could be understood quite well in terms of weak localization [123], and the latter may also be relevant when discussing the competition between superconductivity and disorder in the Bechgaard salts. There is evidence that disorder suppresses superconductivity in several ET compounds if the in-plane resistivity is greater than $170 \mu\Omega\cdot\text{cm}$ [124]. This corresponds to a resistance of 1100Ω per molecular layer, compared with the value of 8000Ω per (bi)layer found at the separatrix between superconductivity and localization for single crystals of $\text{Bi}_2\text{Ca}_{1-x}\text{Y}_x\text{SrCuO}_8$ [125]. For thin metallic films, where the competition between localization and superconductivity in two dimensions has been studied intensively [126,127], this characteristic resistance is precisely 6450Ω ($h/4e^2$) per square.

ACKNOWLEDGMENTS

We would like to thank many scientists for their interest and cooperation over a long period, especially S. Barišić, K. Bechgaard, A. Bjeliš, L. Forró, G. Grüner, B. Hilti, D. Jérôme, W. Kang, R. C. Lacoe, B. Leontić, M. Miljak, J. P. Pouget, J. S. Schilling, D. Schweitzer, S. Tomić, and M. Weger.

REFERENCES

1. I. F. Schegolev, *Phys. Status Solidi (a)* **12**:9 (1972).
2. D. Jérôme and H. J. Schulz, *Adv. Phys.* **31**:299 (1982).
3. L. N. Bulaevskii, *Adv. Phys.* **37**:443 (1988).
4. T. Ishiguro and K. Yamaji, *Organic Superconductors*, Series in Solid State Sciences, Vol. 88, Springer-Verlag, Berlin, 1990.
5. J. M. Williams, A. J. Schultz, U. Geiser, K. D. Carlson, A. M. Kini, H. H. Wang, W.-K. Kwok, M.-H. Whangbo, and J. E. Schirber, *Science* **252**:1501 (1991).
6. D. Jérôme, *Science* **252**:1509 (1991).
7. I. F. Schegolev, *Europhys. News* **22**:12 (1991).
8. J. J. André, A. Bieber, and F. Gautier, *Ann. Phys.* **1**:145 (1976).
9. J. P. Pouget, in *Highly Conducting Quasi-One-Dimensional Organic Crystals*, Vol. 27 (E. M. Conwell, ed.), Academic Press, New York, 1988, p. 87.
10. S. Barišić and A. Bjeliš, in *Theoretical Aspects of Band Structures and Electronic Properties of Pseudo-One-Dimensional Solids* (H. Kamimura, ed.), D. Reidel, New York, 1985, p. 49.
11. H. C. Montgomery, *J. Appl. Phys.* **42**:2971 (1971); B. F. Logan, S. O. Rice, and R. F. Wick, *J. Appl. Phys.* **42**:2975 (1971).
12. L. J. van der Pauw, *Phillips Res. Rep.* **16**:187 (1961) and **13**:1 (1958).
13. J. R. Cooper, L. Forró, and B. Korin-Hamzić, *Mol. Cryst. Liq. Cryst.* **119**:121 (1985).
14. S. Etemad, *Phys. Rev. B* **13**:2254 (1976).
15. A. N. Bloch, D. O. Cowan, K. Bechgaard, R. E. Pyle, R. H. Banks, and T. O. Poehler, *Phys. Rev. Lett.* **34**:1561 (1975).
16. K. Murata, T. Ukachi, H. Anzai, G. Saito, K. Kajimura, and T. Ishiguro, *J. Phys. Soc. Jpn.* **51**:1817 (1982).
17. K. Bechgaard, C. S. Jacobsen, K. Mortensen, H. J. Pedersen, and N. Thorup, *Solid State Commun.* **23**:1119 (1979).
18. S. P. Zolotukhin, V. F. Kaminskii, A. I. Kotov, R. B. Lyubovskii, M. L. Khidekel', R. P. Shibaeva, I. F. Schegolev, and E. B. Yagubskii, *Pis'ma Z. Eksp. Teor. Fiz.* **25**:480 (1977).
19. S. Tomić, J. R. Cooper, W. Kang, D. Jérôme, and K. Maki, *J. Phys. (Paris)* **1**:1603 (1991).
20. B. Korin-Hamzić, L. Forro, and J. R. Cooper, *Phys. Rev. B* **41**:11646 (1990).

21. M. J. Cohen, L. B. Coleman, A. F. Garito, and A. J. Heeger, *Phys. Rev. B* 10:1298 (1974).
22. L. Forró, K. Biljaković, J. R. Cooper, and K. Bechgaard, *Phys. Rev. B* 29:2839 (1984).
23. J. R. Cooper, L. Forró, B. Korin-Hamzić, K. Bechgaard, and A. Moradpour, *Phys. Rev. B* 33:6810 (1986).
24. C. S. Jacobsen, K. Mortensen, N. Thorup, D. B. Tanner, and K. Bechgaard, *Chem. Scr.* 17:103 (1981).
25. L. I. Buravov, M. V. Karcovnik, P. A. Kononovich, V. N. Laukhin, S. I. Pesockii, and I. F. Schegolev, *Zh. Eksp. Teor. Fiz.* 91:2198 (1986).
26. J. R. Cooper, L. Forró, B. Korin-Hamzić, M. Miljak, and D. Schweitzer, *J. Phys. (Paris)* 50:2741 (1989).
27. J. R. Cooper, D. Jérôme, S. Etemad, and E. M. Engler, *Solid State Commun.* 22:257 (1977).
28. F. Denoyer, R. Comès, A. F. Garito, and A. J. Heeger, *Phys. Rev. Lett.* 35:445 (1975).
29. K. Mortensen, Y. Tomkiewicz, and K. Bechgaard, *Phys. Rev. B* 25:3319 (1982).
30. J. P. Pouget, R. Moret, R. Comès, K. Bechgaard, J. M. Fabre, and J. Giral, *Mol. Cryst. Liq. Cryst.* 79:129 (1982).
31. J. R. Cooper, M. Weger, D. Jérôme, D. Lefur, K. Bechgaard, A. N. Bloch, and D. O. Cowan, *Solid State Commun.* 19:749 (1976).
32. J. R. Cooper, M. Weger, G. Delplanque, D. Jérôme, and K. Bechgaard, *J. Phys. Lett. (France)* 37:L349 (1976).
33. G. Soda, D. Jérôme, M. Weger, K. Bechgaard, and E. Pedersen, *Solid State Commun.* 20:107 (1976).
34. C. Weyl, E. M. Engler, S. Etemad, K. Bechgaard, and G. Jehanno, *Solid State Commun.* 19:925 (1976).
35. A. B. Pippard, *Magnetoresistance in Metals*, Cambridge University Press, Cambridge, 1989.
36. V. J. Emery, *J. Phys. (Paris), Colloq.* 44, C3-977 (1983). For a review see Y. A. Firsov, V. N. Prigodin, and C. Seidel, *Phys. Repts.* 126, 245 (1983).
37. M. Héritier, G. Montambaux, and P. Lederer, *J. Phys. Lett. (Paris)* 45:L943 (1984).
38. R. Kubo and T. Nagamiya, *Solid State Physics*, McGraw-Hill, New York, 1969, Sec. 58.
39. J. R. Cooper, M. Miljak, G. Delplanque, D. Jérôme, M. Weger, J. M. Fabre, and L. Giral, *J. Phys. (Paris)* 38:1097 (1977).
40. K. Maki and A. Virosztek, *Phys. Rev. B* 41:557 (1990).
41. P. E. Seiden and D. Cabib, *Phys. Rev. B* 13:1846 (1976).
42. I. Batistić, B. Korin-Hamzić, and J. R. Cooper, *Phys. Rev. B* 48:16849 (1993).
43. E. M. Conwell, *Phys. Rev. B* 22:1761 (1980).
44. S. van Smaalen, J. Kommandeur, and E. M. Conwell, *Phys. Rev. B* 33:5378 (1986).

45. M. Weger, *Phil. Mag.* 56:889 (1987), and references therein.
46. O. Entin-Wohlman, H. Gutfreund, and M. Weger, *J. Phys. C* 18:L61 (1985).
47. L. Friedman, *Solid State Commun.* 40:41 (1981).
48. D. Jérôme, *J. Phys. Lett. (Paris)* 38:L489 (1977).
49. A. A. Abrikosov and I. A. Ryzkhin, *Adv. Phys.* 27:147 (1978).
50. A. Luther and I. Peschel, *Phys. Rev. Lett.* 18:992 (1974).
51. M. Miljak and J. R. Cooper, *Fizika* 7:49 (1975).
52. L. Brossard, G. Canadell, L. Valade, and P. Cassoux, *Phys. Rev. B* 47:1674 (1993).
53. Y. Tomkiewicz, A. R. Taranko, and J. B. Torrance, *Phys. Rev. Lett.* 36:751 (1986).
54. M. Miljak, J. R. Cooper, and K. Bechgaard, *J. Phys. (Paris) Colloq.* 44:C3-893 (1983).
55. P. Delhaes, in *Physics and Chemistry of One-Dimensional Solids* (L. Alcácer, ed.), D. Reidel, New York, 1980, p. 281.
56. Y. Tomkiewicz, A. R. Taranko, and J. B. Torrance, *Phys. Rev. B* 15:1017 (1977).
57. L. Forró, J. R. Cooper, B. Rothaemel, J. S. Schilling, M. Weger, and K. Bechgaard, *Solid State Commun.* 60:11 (1986).
58. J. C. Scott, S. Etemad, and E. M. Engler, *Phys. Rev. B* 17:2269 (1978).
59. J. R. Cooper, M. Miljak, and B. Korin, *Phys. Scr.* 17:79 (1981).
60. D. Jérôme, G. Soda, J. R. Cooper, J. M. Fabre, and L. Giral, *Solid State Commun.* 22:319 (1977).
61. C. F. Coll, *Phys. Rev. B* 9:2150 (1974).
62. I. A. Krumhansl, B. Horovitz, and A. J. Heeger, *Solid State Commun.* 34:945 (1980).
63. S. S. P. Parkin, M. Miljak, and J. R. Cooper, *Phys. Rev. B* 34:1485 (1986).
64. D. Jérôme, A. Mazaud, M. Ribault, and K. Bechgaard, *J. Phys. Lett. (Paris)* 41:L95 (1980).
65. J. R. Cooper, *Phys. Rev. B* 19:2404 (1979).
66. V. N. Laukhin, A. I. Kotov, M. L. Khidekel', I. F. Schegolev, and E. B. Yagubskii, *Pis'ma Z. Eksp. Teor. Fiz.* 28:284 (1978).
67. K. Murata, M. Tokumoto, H. Anzai, H. Bando, G. Saito, K. Kajimura, and T. Ishiguro, *J. Phys. Soc. Jpn.* 54:2084 (1985).
68. R. H. Friend, M. Miljak, D. Jérôme, D. L. Decker, and D. Debray, *J. Phys. Lett. (Paris)* 39:L134 (1978).
69. B. Welber, P. E. Seiden, and P. M. Grant, *Phys. Rev. B* 18:2962 (1978).
70. L. Brossard, M. Ribault, L. Valade, and P. Cassoux, *J. Phys. (Paris)* 50:1521 (1989).
71. D. A. Schafer, G. A. Thomas, and F. Wudl, *Phys. Rev. B* 12:5532 (1975).
72. D. Debray, R. Millet, D. Jérôme, S. Barišić, L. Giral, and J. M. Fabre, *J. Phys. Lett. (Paris)* 38:L227 (1977).
73. S. Bouffard, A. Bittar, and L. Zuppiroli, in *Quasi One-Dimensional Conductors*, Lecture Notes in Physics, Vol. 95 (S. Barišić et al., eds.), Springer-Verlag, New York, 1979, p. 183.

74. G. Creuzet, J. R. Cooper, F. Creuzet, D. Jérôme, and A. Moradpour, J. Phys. Lett. (Paris) 46:L1133 (1985).
75. G. Soda, D. Jérôme, M. Weger, J. Alizon, J. Gallice, H. Robert, J. M. Fabre, and L. Giral, J. Phys. (Paris) 38:931 (1977).
76. W. Apel and T. M. Rice, J. Phys. C Solid State Phys. 16:L1151 (1983).
77. L. Forró, J. R. Cooper, G. Secretarczyk, M. Krupski, and K. Kamaras, J. Phys. (Paris) 48:413 (1987).
78. B. Rothaemel, L. Forró, J. R. Cooper, J. S. Schilling, M. Weger, P. Mele, H. Bruner, D. Schweitzer, and H. J. Keller, Phys. Rev. B 34:704 (1986).
79. S. Klotz, J. S. Schilling, M. Weger, and K. Bechgaard, Phys. Rev. B 38:5878 (1988).
80. R. H. Friend, M. Miljak, and D. Jérôme, Phys. Rev. Lett. 40:1048 (1978).
81. R. H. Friend, D. Jérôme, J. M. Fabre, L. Giral, and K. Bechgaard, J. Phys. C 11:263 (1978).
82. M. Weger, Solid State Commun. 19:1149 (1976).
83. U. Hardebusch, W. Gerhardt, J. S. Schilling, K. Bechgaard, M. Weger, M. Miljak, and J. R. Cooper, Solid State Commun. 32:1151 (1979).
84. S. Megtert, R. Comès, C. Vettier, R. Pynn, and A. F. Garito, Solid State Commun. 37:875 (1981).
85. A. Andrieux, H. J. Schulz, D. Jérôme, and K. Bechgaard, Phys. Rev. Lett. 43:227 (1979).
86. D. Jérôme and H. J. Schulz, in *Extended Linear Chain Compounds*, Vol. 2 (J. S. Miller, ed.), Plenum Press, New York, 1982, p. 159.
87. S. Bouffard, R. Chipaux, D. Jérôme, and K. Bechgaard, Solid State Commun. 37:405 (1981).
88. R. C. Lacoe, H. J. Schulz, D. Jérôme, K. Bechgaard, and I. Johannsen, Phys. Rev. Lett. 55:2351 (1985).
89. P. Monceau, ed., *Electronic Properties of Inorganic Quasi One-Dimensional Conductors*, D. Reidel, Dordrecht, The Netherlands, 1985.
90. G. Gruner and A. Zettl, Phys. Rep. 119:117 (1985).
91. R. C. Lacoe, J. R. Cooper, D. Jérôme, F. Creuzet, K. Bechgaard, and I. Johannsen, Phys. Rev. Lett. 58:262 (1987) and R. C. Lacoe, J. R. Cooper, D. Jérôme, H. J. Schulz, F. Creuzet, K. Bechgaard, and I. Johannsen, Physica 143B:41–45 (1986).
92. L. Forró, R. C. Lacoe, S. Bouffard, and D. Jérôme, Phys. Rev. B 35:5884 (1987).
93. J. P. Farges, A. Brau, D. Vasilescu, P. Dupuis, and J. Néel, Phys. Status Solidi 37:745 (1970).
94. L. I. Buravov, V. N. Loukhin, and A. G. Khomenko, Zh. Eksp. Teor. Fiz. 88:2185 (1985).
95. W. Kang, Doctoral thesis, Orsay, 1989.
96. M. Ribault, D. Jérôme, J. Tuchlender, C. Weyl, and K. Bechgaard, J. Phys. Lett. (Paris) 43:L147 (1982).
97. F. Pesty, P. Garoche, and K. Bechgaard, Phys. Rev. Lett. 55:2495 (1985).

98. K. Murata, M. Ishibashi, Y. Honda, M. Tokumoto, N. Kinoshita, and H. Anzai, *J. Phys. Soc. Jpn.* 58:3469 (1989).
99. N. A. Fortune, K. Murata, K. Ikeda, and T. Takahashi, *Phys. Rev. Lett.* 68:2933 (1992).
100. J. M. Ziman, *Electrons and Phonons*, Oxford University Press, London, 1960.
101. L. P. Gor'kov and A. G. Lebed, *J. Phys. Lett. (Paris)* 45:L433 (1984).
102. P. M. Chaikin, *Phys. Rev. B* 31:4770 (1985).
103. B. Hamzić, G. Creuzet, and C. Lenoir, *J. Phys. F Metal Phys.* 17:2267 (1987).
104. B. Korin-Hamzić, L. Forró, and J. R. Cooper, *Phys. Rev. B* 38:11177 (1988).
105. L. B. Schein and A. R. McGhie, *Phys. Rev. B* 20:1631 (1979).
106. H. Sumi, *J. Chem. Phys.* 70:3775 (1979).
107. P. Gosar, in *Recent Developments in Condensed Matter Physics* (J. T. Devreese, ed.), Vol. 1, Plenum Press, New York, 1981, p. 593.
108. M. J. Rice, *Phys. Rev. Lett.* 37:36 (1976); and in *Quasi One-Dimensional Conductors* (S. Barišić et al., eds.), *Lecture Notes in Physics*, Vol. 95, Springer-Verlag, New York, 1979, p. 230.
109. R. Bozio and C. Pecile, *Solid State Commun.* 37:193 (1981).
110. J. R. Cooper, J. Lukatela, M. Miljak, J. M. Fabre, L. Giral, and E. Aharon-Shalom, *Solid State Commun.* 25:949 (1978); J. R. Cooper and J. Lukatela, in *Quasi One-Dimensional Conductors*, *Lecture Notes in Physics*, Vol. 95 (S. Barišić et al., eds.), Springer-Verlag, New York, 1979, p. 174.
111. B. Horovitz, *Phys. Rev. B* 16:3943 (1977).
112. L. Zuppiroli, in *Low-Dimensional Conductors and Superconductors*, NATO ASI Series B (D. Jérôme and L. G. Caron, eds.) Plenum Press, New York, 1987, p. 307, and references therein.
113. M. Miljak, B. Korin, J. R. Cooper, K. Holczer, and A. Janossy, *J. Phys. (Paris)* 41:639 (1980).
114. T. D. Schultz and R. A. Craven, in *Highly Conducting One-Dimensional Solids* (J. T. Devreese, R. P. Evrard, and V. E. Van Doren, eds.), Plenum Press, New York, 1979.
115. K. Mortensen and E. M. Engler, *Phys. Rev. B* 29:842 (1984).
116. O. Traetteberg, G. Kriza, C. Lenoir, Y. S. Huang, P. Batail, and D. Jérôme, *Synth. Metals* 56:2785 (1993).
117. S. S. P. Parkin, C. Coulon, D. Jérôme, J. M. Fabre, and L. Giral, *J. Phys. (Paris)* 44:603 (1983).
118. S. Tomić, D. Jérôme, D. Mailly, M. Ribault, and K. Bechgaard, *J. Phys. (Paris) Colloq.* 44:C3-1075 (1983).
119. G. Mihaly, S. Bouffard, L. Zuppiroli, and K. Bechgaard, *J. Phys. (Paris)* 41:1495 (1980).
120. B. L. Altshuler, A. G. Aronov, D. E. Khmel'nitskii, and A. I. Larkin, in *Quantum Theory of Solids* (I. M. Lifshitz, ed.), MIR, Moscow, 1982, Chap. 3.
121. G. Bergmann, *Phys. Rep.* 107:1 (1984).
122. P. A. Lee and T. V. Ramakrishnan, *Rev. Mod. Phys.* 57:287 (1985).

123. J. P. Ulmet, L. Bachere, S. Askenazy, and J. C. Ousset, *Phys. Rev. B* 38:7782 (1988).
124. M. Tokumoto, H. Anzai, K. Murata, K. Kajimura, and T. Ishiguro, *Synth. Metals* 27:A251 (1988).
125. D. Mandrus, L. Forró, C. Kendzoria, and L. Mihaly, *Phys. Rev. B* 44:2418 (1991).
126. Y. Liu, K. A. Mcgreer, B. Nease, D. B. Haviland, G. Martinez, J. W. Halley, and A. M. Goldman, *Phys. Rev. Lett.* 67:2068 (1991).
127. M. Paalanen, A. F. Hebard, and R. R. Ruel, *Phys. Rev. Lett.* 69:1604 (1992).
128. B. Korin, J. R. Cooper, M. Miljak, A. Hamzić, and K. Bechgaard, *Chem. Scr.* 17:45 (1981).

This Page Intentionally Left Blank

Organic Superconductors: From $(\text{TMTSF})_2\text{PF}_6$ to Fullerenes

Denis Jérôme

Université Paris–Sud, Orsay, France

I. INTRODUCTION

Molecular conductors are basically different from the common metallic conductors, in that they are solids made of building blocks (the molecules) presenting their own specific properties: that is, molecular orbitals with their ionization energy or electron affinity, characteristic infrared or Raman active modes, and nuclear magnetic resonance (NMR) chemical shifts of different atomic sites. At variance with conventional molecular crystals made of neutral organic molecules held together by weak van der Waals forces, organic conductors contain molecules with unpaired carriers in π molecular orbitals (open shells) which allow the delocalization over all molecular sites in the crystal via a strong intermolecular π overlap. The open-shell character comes from a partial oxidation (reduction) of donor (acceptor) molecules in the formation of a salt with an inorganic anion (cation). These molecular conductors are therefore different from the extended conjugated polymers or graphite, where the π system of the extended molecules provides the conducting pathway.

The development of molecular conductors (superconductors) has been stimulated to a large extent by the suggestion of Little in 1964 [1] that the arrangement of chain conductors in a polarizable medium could give rise to superconductivity at high temperature. The prerequisite for the formation of a conductor is first, the requirement for having charged molecules

in the solids, and second, to allow these charges to delocalize between molecular entities. Charging the molecules is achieved either by a charge-transfer reaction (see our subsequent discussion of dmit superconductors) or by the formation of an organic salt. For the charges to be delocalized between the molecules, the on-site Coulomb repulsion must not overcome the energy, which is gained by the formation of energy bands in the solid. Thus a condition such as $U \leq 4t_{\parallel}$ should prevail where U and $4t_{\parallel}$ are the on-site repulsion and the bandwidth, respectively, for the molecular crystal to be a metal-like conductor.

In a rough approximation the on-site Coulomb interaction can be estimated from the Coulomb repulsion between two additional electrons located on the same molecule. If it is possible for the two electrons to be far from each other in a large molecule of size 10 to 20 Å, the Coulomb repulsion is on the order of 1 to 5 eV and the dielectric screening by the environment may reduce it by an order of magnitude, making it about 0.3 to 0.5 eV. However, the most stringent criterion is established by the strong tendency toward the formation of insulating phases at low temperature, as they may arise from possibilities of distortions opening energy gaps over the entire Fermi surface in conductors of low dimensionality.

Although the superconducting instability requires three-dimensional long-range order, it is customary to make the difference between the physical properties at low temperature, which are three-dimensional (and possibly very anisotropic) and those at high temperature, where one- or two-dimensional features may prevail [2]. Both the geometry of the building bricks and their packing in a three-dimensional lattice govern the dimensionality of the transport properties of these particular conductors, which ranges from one to three (Fig. 1). The intermolecular overlap between molecular orbitals is optimized by the stacking of the planar molecules on top of each other like pancakes or by the packing of similar molecules in two-dimensional conducting sheets.

As far as one-dimensional conductors are concerned, the planar shape of the molecules is responsible for their particular crystal structure (Fig. 1). All these molecules are modifications of the flat fulvalene skeleton [3]. Noticeable intermolecular overlap is allowed when they form stacks and the conduction band derives from π orbitals directed along the stacks. The overlap of the molecular orbitals is greatest along the stacks of molecules and much weaker between them, making the conductivity greater along the stacking axis than along any other directions. Typical bandwidths in segregated stacks of molecules are in the range 0.4 to 1 eV [4].

The salts of the tetramethylselenafulvalene (TMTSF) molecule [5] are considered as prototype materials for one-dimensional molecular conductors. The overlap between organic stacks along the transverse **b** direction

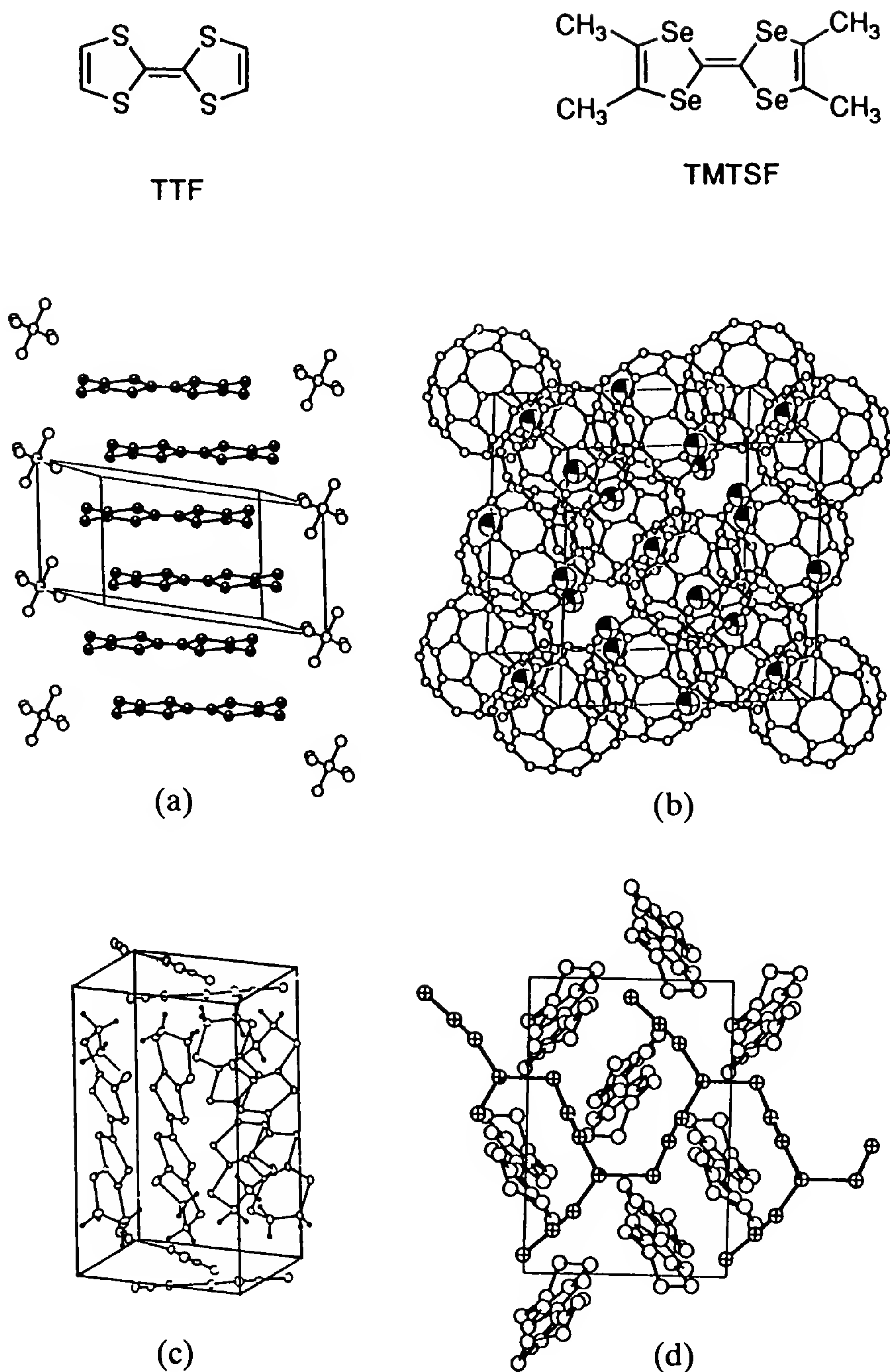


Figure 1 Prototype molecules TTF (tetrathiafulvalene) and TMTSF (tetramethyltetraselenafulvalene) which are used for the elaboration of organic conductors TTF-TCNQ or superconductors $(\text{TMTSF})_2\text{X}$. View of the crystal structure of some molecular superconductors: (a) $(\text{TMTSF})_2\text{PF}_6$; (b) $(\text{alkali})_3 \text{C}_{60}$; (c) $(\text{BEDT-TTF})_2\text{Cu}(\text{SCN})_2$ side view; (d) view along the axis perpendicular to the conducting plane.

amounts to $t_{\perp b} \approx 20$ to 30 meV, which is about one-tenth the value for the intrastack overlap ($t_{\parallel} \approx 200 - 300$ meV), and makes the conduction band about 1 eV wide. The overlap is negligible along the c direction. Such a marked anisotropy causes the Fermi surface to be nearly planar, intersecting the k_{\parallel} axis at wave vectors $\pm k_F$, where the Fermi wave vector for a one-dimensional conductor is related to the density of carriers ρ per unit cell by the relation $2k_F = \rho\pi/a$ [6].

These one-dimensional salts are members of a much broader isostructural family: the $(TM)_2X$ series, which includes salts of selenium containing molecules with a variety of inorganic anions as well as sulfur-containing molecules [7]. The stabilization of superconductivity below a certain critical temperature T_c requires overcoming the strong divergence developing at low temperature in a one-dimensional electron gas toward an insulating behavior, which is discussed later in the chapter [8]. $(TMTSF)_2PF_6$ is actually the compound in which superconductivity has been observed for the first time albeit under a pressure of 9 kbar [9]. However, $(TMTSF)_2ClO_4$ is the only compound pertaining to the one-dimensional family undergoing a transition toward superconductivity at $T_c = 1.2$ K under ambient pressure [10]. These are rather low values for a transition toward superconductivity, but this feature is closely related to the competition between superconductivity and other instabilities arising in one-dimensional conductors, as we shall see below.

In another interesting series of one-dimensional conductors where the cation is an arene such as perylene, the anion is a transition-metal-coordinated complex $[M(mnt)_2]^-$ which provides an additional degree of freedom, depending on whether the metal atom carries a spin $M = Ni, Pd, Pt$, etc. or not for $M = Au$ [11]. Superconductivity has also been found in another series of materials based on transition metal complexes $M(dmit)_2$, where $M = Ni$ or Pd with $T_c = 1.6$ K under 6 kbar [12].

Higher-dimensionality conductors also derive from similar planar molecules, which form dimers with strong overlap between heteroatoms both within each dimer and between neighboring dimers (Fig. 1). This crystal structure gives rise to considerable conductivity within molecular layers and about 10^4 less conduction between the sheets. They are considered as two-dimensional conductors (see Ref. 13 for an overview). Their Fermi surface is tubular with $t_{(a,b)} = 100$ to 150 meV, $t_{\perp c} \approx 0.5$ meV and consequently, T_c rises above 8 K in $(BEDT-TTF)_2I_3$ [14,15] and even up to 10 to 12 K for anions such as $Cu(SCN)_2^-$ [16] and $Cu [N(CN)_2]Cl^-$ [17] or Br^- [18] since superconductivity is no longer competing in these two-dimensional conductors with typical one-dimensional instabilities.

The recent discovery of spherical molecules containing 60 carbon atoms arranged over the surface of a sphere, each atom being linked to three

neighbors forming the C_{60} molecule, has opened the gate to isotropic molecular conductors (the so-called fullerene materials) [19]. Three among the four valence electrons of each carbon atom are engaged in sp^2 bonding with the three neighbors. There remains one electron per carbon atom in a p -state which is delocalized over the entire surface of the sphere in π molecular orbitals. The neutral C_{60} molecule possesses a closed-shell electronic structure giving rise to an insulating molecular solid. However, populating the lowest unoccupied molecular levels (the LUMO) with carriers given by inorganic cations such as alkali or alkaline earth metals gives rise to a partly filled conduction band. This band is half-filled in the prototype material A_3C_{60} ($A_3 = K_3, Rb_3, Cs_2 Rb$, etc.) [20]. The C_{60} spheres are packed in a face-centered-cubic lattice, leaving cavities with octahedral and tetrahedral local symmetry which are all occupied in the A_3C_{60} compound (Fig. 1). Very much like one- or two-dimensional molecular conductors, the conductivity in fullerenes is due to the overlap of π molecular orbitals between near-neighbor molecules, counterions playing essentially no role in the conduction process. The shape of the molecules together with the crystal structure make A_3C_{60} a three-dimensional conductor with a conduction band that is very narrow (≤ 0.5 eV) due to the weakness of intermolecular interactions. However, it is the elaboration of a preparation route based on graphite sublimation and allowing a mass production of C_{60} molecules that boosted the discovery of superconductivity in this new family of molecular conductors [21]. Superconductivity ranges from 19 K in K_3C_{60} [22] up to 28 K in Rb_3C_{60} [23]. The highest T_c value stabilized at the moment for a molecular conductor is 33 K in Cs_2RbC_{60} [24].

II. ONE-DIMENSIONAL ELECTRON GAS

A. Mean-Field Solution of the One-Dimensional Problem

Although a mean-field approximation will not provide the correct answer to the problem of interacting one-dimensional electrons, a brief survey using such an approach is still useful to show that the competition between superconducting and dielectric order is the basic problem of one-dimensional conductors [25a,b].

We are concerned with low-energy processes (near the Fermi energy). Consequently, the only pertinent wave vectors of electron-hole pair excitations will be those close to $q = 0$ and $2k_F$ since the electron-hole pair excitation energy is zero for these vectors in the one-dimensional noninteracting electron gas. The Fourier transform of the Coulomb interaction will contain terms near $q = 0$ and $q = 2k_F$ which are approximated by

various constants g_i in the interaction term of the Hamiltonian (g-ology model) [26] (Fig. 2a).

The one-dimensional Hamiltonian reads.

$$H = H_0 + H_{\text{int}} \quad (1)$$

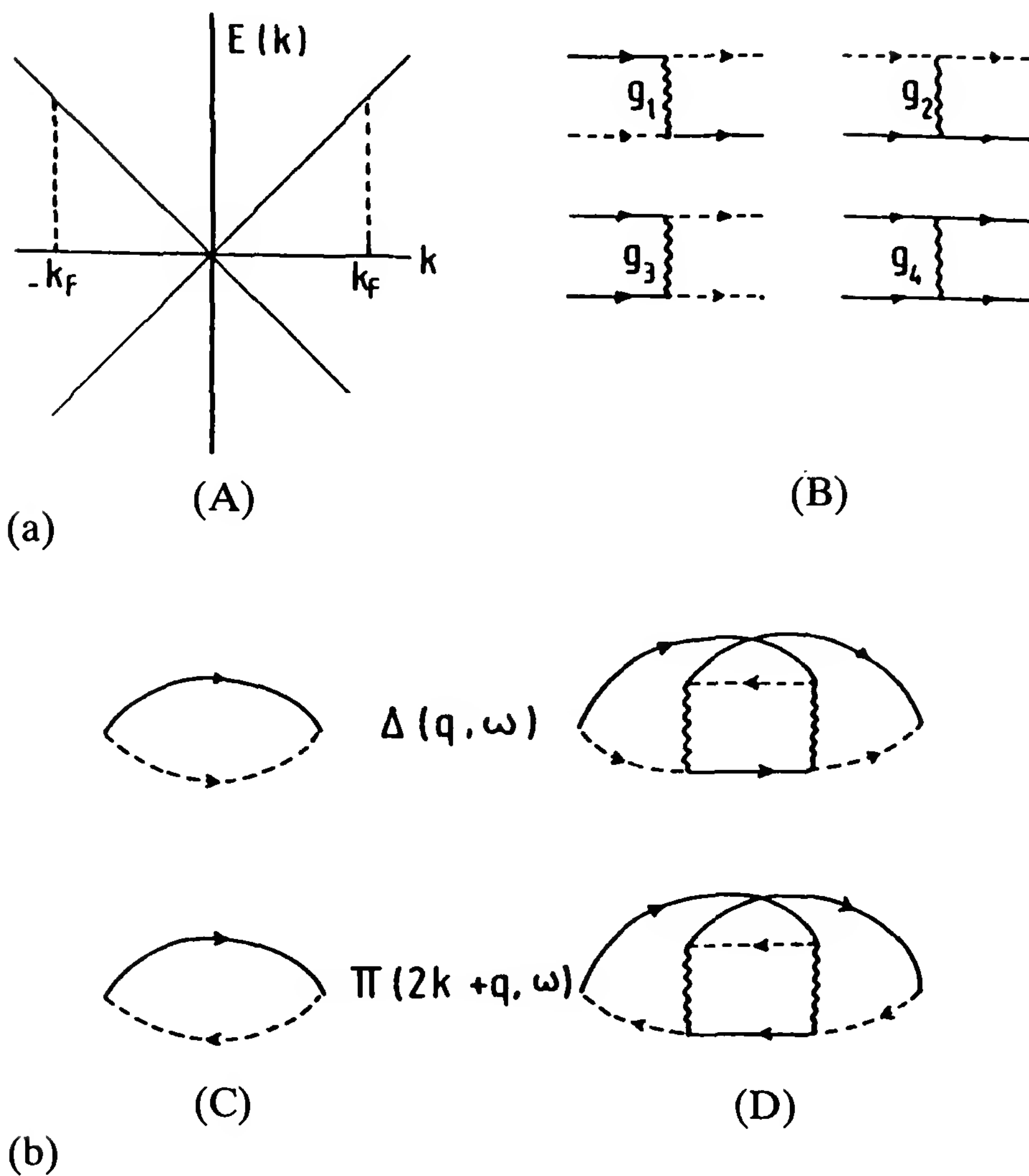


Figure 2 (a) Linearized electron dispersion in the Luttinger approximation (A) and diagrammatic representation of elementary interactions $g_1 \cdots g_4$ (B). Solid and dashed lines represent electrons near k_F and $-k_F$, respectively. The g_3 interaction exists only in case of a half-filled band; (b) Diagrammatic representation of the Cooper pair susceptibility $\Delta(q, \omega)$ and the density wave susceptibility $\Pi(2k_F + q, \omega)$ at lowest order (C) and second order (D) which shows the mixture between Cooper and Peierls channels.

where the noninteracting contribution is linearized in q near the Fermi energy (Luttinger approximation), namely,

$$H_0 = \sum_{k,\sigma} V_F \left[(k - k_F) a_{k,\sigma}^+ a_{k,\sigma} + (-k - k_F) b_{k,\sigma}^+ b_{k,\sigma} \right] \quad (2)$$

and

$$H_{\text{int}} = \sum_{k_1 k_2}^{Q, \sigma \sigma'} g_1 a_{k_1 \sigma}^+ b_{k_2 \sigma'}^+ a_{k_2 + 2k_F + Q, q, \sigma'} b_{k_1 - 2k_F - Q, \sigma} \\ + g_2 a_{k_1 \sigma}^+ b_{k_2 \sigma'}^+ b_{k_2 + Q, \sigma'} a_{k_1 - Q, \sigma} \quad (3)$$

where g_1 and g_2 are the amplitudes of the elementary scattering amplitude [with change of momentum $q = 0$, forward (g_2) and $q = 2k_F$, backward (g_3)].

In addition to the g_1 and g_2 terms in Eq. (3) there are g_3 terms involving the transfer of two particles from one side of the Fermi surface to the other. Since the total momentum transfer is $4k_F$, this process is allowed only if $4k_F$ is a reciprocal lattice vector (Umklapp scattering).

We now define new operators $O_\alpha(q)$, which are the Fourier components of operators characterizing the various ordered states of the interacting one-dimensional gas, namely $\alpha = \text{CDW}$, SDW , or singlet, triplet superconductivity SS and TS, for example:

$$O_{\text{CDW}}(q) = \sum_{k,\sigma} b_{k-q,\sigma}^+ a_{k,\sigma} \quad (4a)$$

$$O_{\text{SDW},i}(q) = \sum_{k,\sigma,\sigma'} b_{k-q,\sigma}^+ \sigma_i^{\sigma\sigma'} a_{k,\sigma'} \quad (4b)$$

where $\sigma_i^{\sigma\sigma'}$ are the elements of the Pauli matrices for $i = x, y, z$.

Using the definitions, Eqs. (4), H_{int} can be rewritten

$$H_{\text{int}} = \sum_q (g_1 - \frac{1}{2}g_2) O_{\text{CDW}}^+(q) O_{\text{CDW}}(q) \\ + g_2 \sum_{q,i} O_{\text{SDW},i}^+(q) O_{\text{SDW},i}(q) \quad (5)$$

One can also rewrite operators such as $O_{\text{CDW}}(q)$ like

$$O_{\text{CDW}}^+(q) O_{\text{CDW}}(q) = (O_{\text{CDW}}^+ \langle O_{\text{CDW}} \rangle + O_{\text{CDW}} \langle O_{\text{CDW}}^+ \rangle) - |\langle O_{\text{CDW}} \rangle|^2 \\ + [O_{\text{CDW}}^+(q) - \langle O_{\text{CDW}}^+(q) \rangle] [O_{\text{CDW}}(q) - \langle O_{\text{CDW}}(q) \rangle] \quad (6)$$

In the mean-field approximation, the possibility for fluctuations of the order parameter is forbidden. Therefore, the last term in Eq. (6) is zero and H_{int} reduces to the mean-field Hamiltonian.

$$\begin{aligned} \bar{H}_{\text{int}} = \sum_k \langle O_{\text{CDW}}(q) \rangle & (a_{k_F+k \uparrow}^+ b_{k_F+k-q \uparrow} + a_{k_F+k \downarrow}^+ b_{k_F+k-q \downarrow}) \\ & + \langle O_{\text{CDW}}^+(q) \rangle (b_{k_F+k-q \uparrow}^+ a_{k_F+k \uparrow} + b_{k_F+k-q \downarrow}^+ a_{k_F+k \downarrow}) \end{aligned} \quad (7)$$

The Hamiltonian (7) can be diagonalized by a Bogoliubov transformation. A gap Δ_{CDW} is opened at the Fermi surface for $q = 2k_F$.

$$\Delta_{\text{CDW}} = 2E_F \exp\left(-\frac{1}{\lambda_{\text{CDW}}}\right) \quad \text{where} \quad \lambda_{\text{CDW}} = -\frac{2g_1 - g_2}{2\pi V_F}$$

The gap Δ_{CDW} is finite if $\Delta_{\text{CDW}} > 0$, which sets the condition,

$$2g_1 - g_2 < 0$$

One could have looked similarly for a finite value of the SDW order parameter which is obtained when the condition $g_2 > 0$ is fulfilled. Consequently, no electron–hole instability exists in the domain of the g_1, g_2 plane limited by

$$g_2 < 0 \quad \text{and} \quad g_1 > \frac{g_2}{2}$$

In addition, the stability of singlet and triplet superconductivity requires $g_1 + g_2 < 0$ and $g_1 - g_2 > 0$, respectively. If all four instabilities are now treated on an equal footing, the diagram leading to the most stable ground state is as given in Fig. 3. Singlet (SS, CDW) and triplet (TS, SDW) phases occur for $g_1 < 0$ and $g_1 > 0$, respectively. Superconducting and density wave orders are separated by the line $g_1 = 2g_2$.

The diagram for the stability of different ground states in quasi-one-dimensional interacting electron gases has had a powerful impact on the development of the field. This was the first suggestion for a common border between electron–electron pairing instability and the spin-modulated ground state. It has also been suggested that superconductivity could be stabilized in one-dimensional conductors by repulsive interactions.

B. Beyond Mean-Field Approximation

However, the mean-field treatment of the one-dimensional system suffers from serious drawbacks. The first and most important of these is the prediction of long-range order at a finite temperature, whereas in a one-dimensional system fluctuations are known to destroy long-range order [25a], as can easily be illustrated by the stability of a ferromagnetic Ising

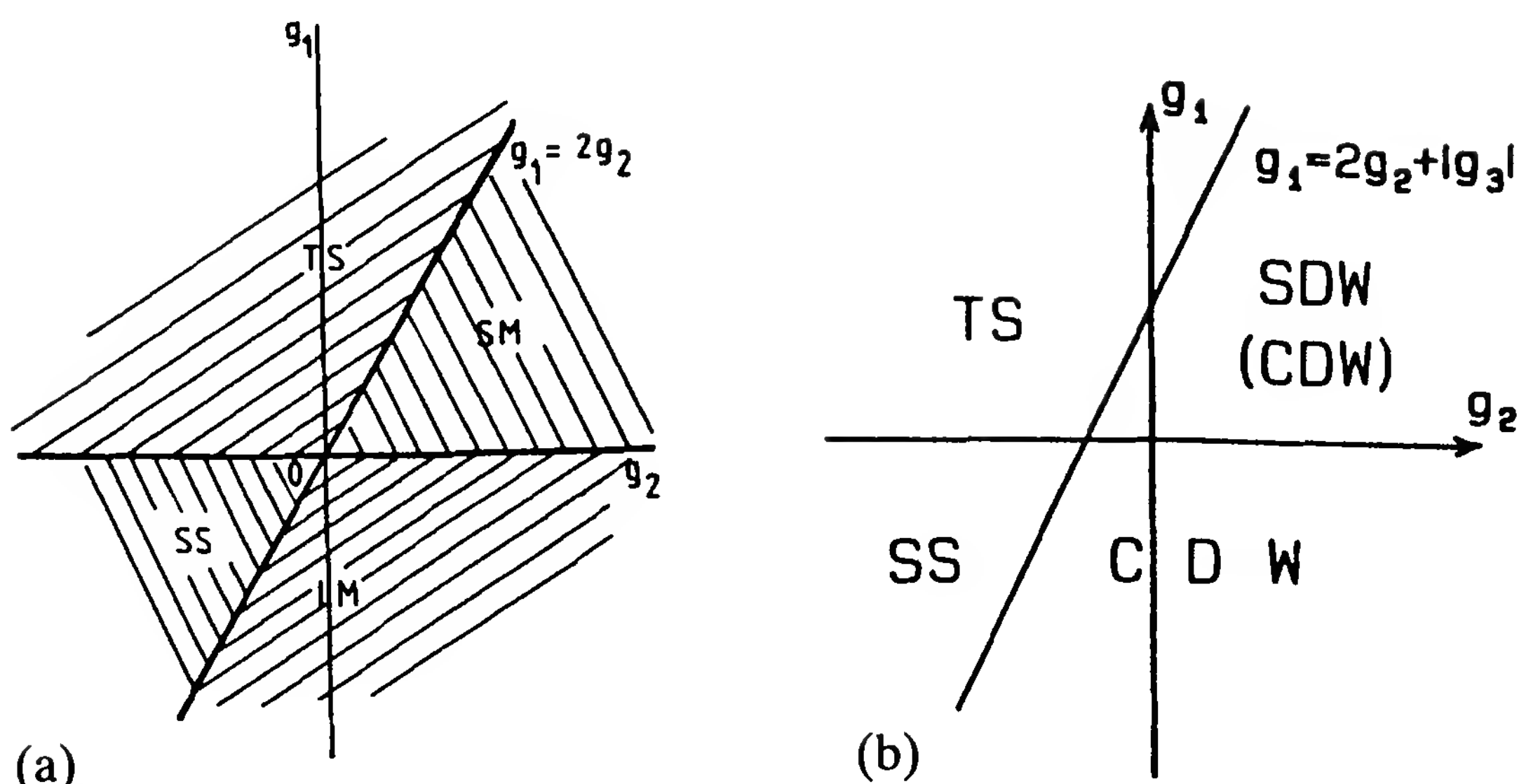


Figure 3 (a) Ground states of the one-dimensional mean-field model. SM, LM, TS, and SS indicate spin modulation, lattice modulation, and triplet and singlet superconductivity, respectively. (b) The most divergent correlations of the one-dimensional Hamiltonian in the presence of Umklapp scattering SDW correlations are more divergent than CDW correlations in the $g_1 > 0$ region.

chain. Starting with a configuration corresponding to ferromagnetic order, the reversal of a spin leads to a change in internal energy J (>0). If a concentration n of such reversed spins exists in the chain, the change of free energy with respect to the ferromagnetic configuration reads [2]

$$\Delta F = nJ + kT[n \log n + (1 - n)\log(1 - n)] \quad (8)$$

Its minimization $\delta \Delta F / \delta n = 0$ when n is small leads to $n = \exp[-(1 + J/kT)]$ or equivalently, to the temperature-dependent correlation length:

$$\frac{\xi(T)}{a} = \exp\left(1 + \frac{J}{kT}\right) \quad (9)$$

$\xi(T)$ reaches infinity only at zero temperature. Thermal fluctuations destroy the onset of long-range order at any finite temperature.

The previous treatment deals with a one-component order parameter (such as for a commensurate Peierls distortion) but does not apply to situations where the order parameter is complex with an amplitude and a phase (superconductivity, incommensurate Peierls, or spin density wave transitions). The latter situation is analogous to classical moments which can rotate freely in an XY plane. The coherence length of the XY model is less strongly divergent at low temperature than for the Ising model,

namely:

$$\frac{\xi(T)}{a} = \frac{J}{kT} \quad (10)$$

The second drawback of the mean-field approximation is neglect of electron–phonon interaction, which should contribute attractively to the g_1 contribution and lead to a lattice modulation (Peierls instability). However, a ground state of such a nature is not stabilized in the TM_2X family. The absence of long-range order is deeply rooted in the one-dimensional problem and arises when the effect of interactions on the different response functions is calculated perturbatively [26].

Response functions $R(\omega)$ for all instabilities contain at all orders in perturbation logarithmic terms, such as $\ln(\omega/E_F)$, which give rise to infrared divergencies. Similar arguments apply to the bare couplings g_1 , which must be replaced by effective couplings (vertex) representing perturbative expansions of the bare coupling. The perturbation expansion reveals a mixture of divergent contributions coming from electron–electron pairs and electron–hole pair divergences. An example of mixture of two types of instabilities in Cooper and Peierls susceptibilities is shown for typical diagrams in Fig. 2b. The mixture of diverging channels is specific to a one-dimensional conductor and is responsible for the absence of long-range order. The one-dimensional problem (i.e., the determination of the temperature dependence of response functions) can be solved using various approximations [26].

In the diagrammatic expansion, the most trivial approximation neglects the mixture of channels. For example, calculating the Cooper pair susceptibility, we neglect contributions coming from density wave fluctuations; this approximation amounts to the mean-field treatment. Some improvements have been provided by the summation of a specific class of diagrams (the parquet diagrams) [25b], which takes into account the channel mixture but still gives rise to long-range order at $T > 0$.

An improved treatment is obtained by renormalization group methods, which lead to the absence of long-range order at any finite temperature [26]. However, interactions now become temperature dependent. A very simple illustration of the one-dimensional behavior is provided by the first-order renormalization calculation of g_1 and g_2 , which become

$$g_1(T) = \frac{g_1}{1 - (g_1/\pi v_F) \ln(T/E_F)} \quad (11a)$$

$$g_2(T) = g_2 - \frac{1}{2}g_1 - g_1(T) \quad (11b)$$

where g_1 and g_2 are the amplitudes taken at high temperature ($T > E_F$).

The response functions $R_i(q, \omega)$ for instabilities i are found to behave like

$$R_i(q, \omega) \approx |\omega^2 - V_F^2 q^2|^{-\alpha_i/2} \quad \text{at } T = 0 \tag{12a}$$

and

$$R_i(0, 0) \approx T^{-\alpha_i} \quad \text{at } \omega = q = 0 \tag{12b}$$

where α_i is an exponent for the divergence of correlations in the channel i (CDW, SDW, TS, SS) which depends on the bare couplings g_1 and g_2 . The diagram for the most diverging fluctuations is analogous to the mean-field diagram in Fig. 3. In the one-dimensional regime, the temperature dependence of response functions are characterized by power law dependences, Eq. (12b).

C. Spin-Charge Separation

Together with the power law dependence and the absence of phase transitions, the separation of the Hamiltonian into spin and charge parts is a peculiar feature of one-dimensional conductors. The concept of spin-charge separation can be visualized very easily with a one-dimensional half-filled band model in the limit of large U preventing double-site occupancy. Strong short-range antiferromagnetic order due to $J \approx t^2/U$ is expected in such a chain.

Removing a carrier at $t = 0$ creates both additional charge and spin locally. After some time the charge will have evolved due to the kinetic term of the Hamiltonian without flipping the spins. Therefore, the original situation of a coupled charge-spin excitation will decay in time into a charge excitation carrying no spin (holon) and at a different place a spin excitation carrying no charge (spinon).

$\uparrow \downarrow \uparrow \downarrow \uparrow \downarrow \uparrow \downarrow \uparrow$	Ground state
$\uparrow \downarrow 0 \downarrow \uparrow \downarrow \uparrow \downarrow \uparrow$	Excited state at $t = 0$
$\uparrow \downarrow \downarrow \uparrow \downarrow \uparrow 0 \downarrow \uparrow$	Excited state at time t
	[spinon ($\downarrow \downarrow$) + holon (0)]

We may also consider a one-dimensional chain of electrons with one electron per site in the large U limit of the Hubbard model ($U > t$). The ground state of the chain is insulating since it costs an energy U to move an electron from one unit cell to its neighbor. The spins adopt an antiferromagnetic configuration which provides the antisymmetrization of the ground-state wavefunction. Double occupancy of \mathbf{k} states in the conduction band is thus forbidden by coulombic repulsions.

If we now consider the band picture, each \mathbf{k} state is doubly occupied when U is negligible. But when U is switched on, one may consider that

double occupancy is forbidden, and therefore for a given concentration of carriers the number of (singly) occupied k states below the Fermi energy should double. These carriers can thus be defined as a noninteracting gas of spinless fermions [27]. The Fermi vector for these new particles becomes $2k_F$ instead of k_F in the initial noninteracting gas. This effect gives rise to the well-known $4k_F$ diffusion in diffuse x-ray scattering [28].

The band splits into a lower singly degenerate Hubbard band and an other singly degenerate Hubbard band at the energy U above the former band. When the site occupancy is $\rho = 1$, the lower Hubbard band is fully occupied and conducting configurations correspond to the excitation of carriers into the upper band at the energy U . The ground state of such a system is thus a Mott–Hubbard insulator.

There exists a major difference between a band insulator and a Mott–Hubbard insulator as far as spin excitations are concerned. Flipping a spin in a band insulator is forbidden by the Pauli principle and requires an excitation of the carrier through the energy gap. Therefore, spin and charge degrees of freedom are coupled. However, flipping a spin in a Mott insulator requires only the exchange energy $J \approx t^2/U$, which is much smaller than the energy U that is necessary for conduction when $U > t$.

Spin and charge excitations are thus decoupled by coulombic interactions in the one-dimensional electron gas. However, the one-dimensional Fermion system is *not* a Fermi liquid, as indicated by the behavior of the momentum distribution function, which does not exhibit a Fermi step at k_F and presents a single-particle density of states vanishing according to a power law singularity at E_F . This is a Luttinger liquid [29] with

$$n_k \approx n_{k_F} - \beta \operatorname{sign}(k - k_F)|k - k_F|^\alpha, \quad \beta > 0$$

$$N(\omega) \approx |\omega|^\alpha \quad \text{where} \quad \alpha = \frac{1}{4} \left(K_\rho + \frac{1}{K_\rho} - 2 \right)$$

K_ρ determines the long-distance decay of all correlation functions of the system. The temperature dependence of the response functions becomes

$$\chi_{\text{SDW,CDW}}(2k_F) \approx T^{K_\rho-1} \quad \text{and} \quad \chi_{\text{SS,TS}} \approx T^{1/K_\rho-1} \quad (13)$$

The noninteracting gas corresponds to $K_\rho \approx 1$ and density waves or pairing correlations are divergent at low temperature for $K_\rho < 1$ and > 1 , respectively. The observation of power law dependences for the response functions in an extended domain of temperatures should thus be taken as the signature of one-dimensionality. One-dimensionality is indeed limited at low temperature by the crossover regime toward a physics at higher dimensionality.

The response functions that diverge logarithmically at low temperature in the one-dimensional noninteracting electron gas level off at a value $\log(t_{\perp}/\pi E_F)$ corresponding to $T \approx t_{\perp}$ [30] when the interchain coupling t_{\perp} is taken into account. Band structure calculations would thus suggest a bare crossover temperature for the single-particle motion of $T_x^0 \sim 80$ K or so. However, it has been suggested [31] that the single-particle interchain tunneling can be impeded by one-dimensional correlations. The crossover regime is further reduced and reads

$$T_x \sim T_x^0 \left(\frac{t_{\perp}}{E_F} \right)^{(1-K\rho)/K\rho} \quad (14)$$

This effect can be quite significant even for relatively small coupling $K\rho \lesssim 1$ and may lead to a suppression of the dimensionality crossover down to, say, $T_x \approx 10$ K given $t_{\perp}/E_F \approx 10$.

Below the crossover, both channels are decoupled. A Fermi-liquid behavior is recovered using renormalized values of the interactions at the crossover temperature. We may expect mean-field treatments for dimensionality 2 or 3 to become valid at $T < T_x$ (see, e.g., the critical exponents for the SDW instability in $(\text{TMTSF})_2\text{PF}_6$ (see Section III.B).

The existence of a finite interchain interaction in a quasi-one-dimensional system is a prerequisite for a phase transition. However, there exists no necessary relation between the strengths of intra- and interchain couplings. It is thus conceivable to observe for SDW and SC instabilities the existence (if not the predominance) of magnetic fluctuations above the superconducting transition or the reverse as well. Such situations are encountered in the study of the $(\text{TMTSF})_2\text{X}$ series.

III. THE TM_2X FAMILY

A. Electronic Structure and Phase Diagram

As mentioned above, all members of the TM_2X series are isostructural compounds and no major difference could be expected at first glance between the four sulfur $(\text{TMTTF})_2\text{PF}_6$ and the four selenium $(\text{TMTSF})_2\text{ClO}_4$ compounds. They both exhibit the typical zigzag molecular packing (triclinic symmetry) with two molecular units per unit cell (i.e., a formally half-filled band).

A model band structure has been calculated for TM_2X materials by Grant [32] using a tight-binding scheme with a few simplifications. An important one is the use of the highest occupied molecular orbital (HOMO) of the isolated molecules as the only state that is relevant for the band structure close to the Fermi level. The band structure calculated with six

near-neighbor transfer integrals obtained from quantum chemistry, which are summarized in Table 1 [33,34], is displayed in Fig. 4.

The energy dispersion along XV and Γ Y in Fig. 4a is the signature of the nonzero interstack coupling, and the gap along XV reflects the existence of the structural dimerization. An overall decreasing tendency for the band dimerization going from (TMTTF)₂PF₆ to (TMTSF)₂PF₆ is indicated in Table 1. The conduction band can accommodate four electrons per TM₂ units. Therefore, removing one carrier per unit cell leads to a half-filled situation for the upper band in Fig. 4b.

(TMTSF)₂ClO₄ is a fairly good metal-like conductor at room temperature ($\sigma_{||} \approx 500 \, \Omega^{-1} \cdot \text{cm}^{-1}$) and undergoes a transition toward a superconducting ground state at 1.2 K [10]. On the other hand, (TMTTF)₂PF₆ is a poor conductor ($\sigma_{||}$ (300 K) $\approx 30 \, \Omega^{-1} \cdot \text{cm}^{-1}$) which shows a semi-conducting behavior on cooling [35]. The ground state of the latter system is somewhat reminiscent of a Peierls state, as it displays (below 20 K) a lattice modulation with periodicity 2a along the stacking axis ($2k_F$ wave vector) [36]. In addition, there is zero-spin susceptibility in this ground state since the isolated spins are dimerized in a spin Peierls state [37].

For both systems the temperature dependence of the spin susceptibility is about similar, with a 40% monotonous drop from 300 K to 50 K [37,38]. Clearly, there is no close relation between transport and magnetic properties in the high-*T* regime of these salts. This is an experimental illustration of the spin-charge separation concept of one-dimensional conductors.

The compounds mentioned above are only two members of the TM₂X series, whose generic phase diagram is shown in Fig. 5a. The names of compounds along the *x* axis indicate their location at atmospheric pressure in the generalized diagram. In addition, the pressure scale shows that it is also possible for a given compound to be shifted throughout the entire

Table 1 Transfer Integrals Intrastacks (*t_s*) and Interstacks (*t_I*) of Selected One-Dimensional Conductors. All Energies are in Units of 10⁻³ eV

	<i>t_s</i>	<i>t_I</i>	$\Delta t_s/t_s^a$
(TMTSF) ₂ PF ₆	365	26.2	0.16
(TMTSF) ₂ ClO ₄	366	21.6	0.14
(TMTTF) ₂ Br	240	10	0.13
(TMTTF) ₂ PF ₆	115	12.3	0.38

^aThe value of $\Delta t_s/t_s$ reflects the amplitude of the structural dimerization.

Source: Ref. 33.

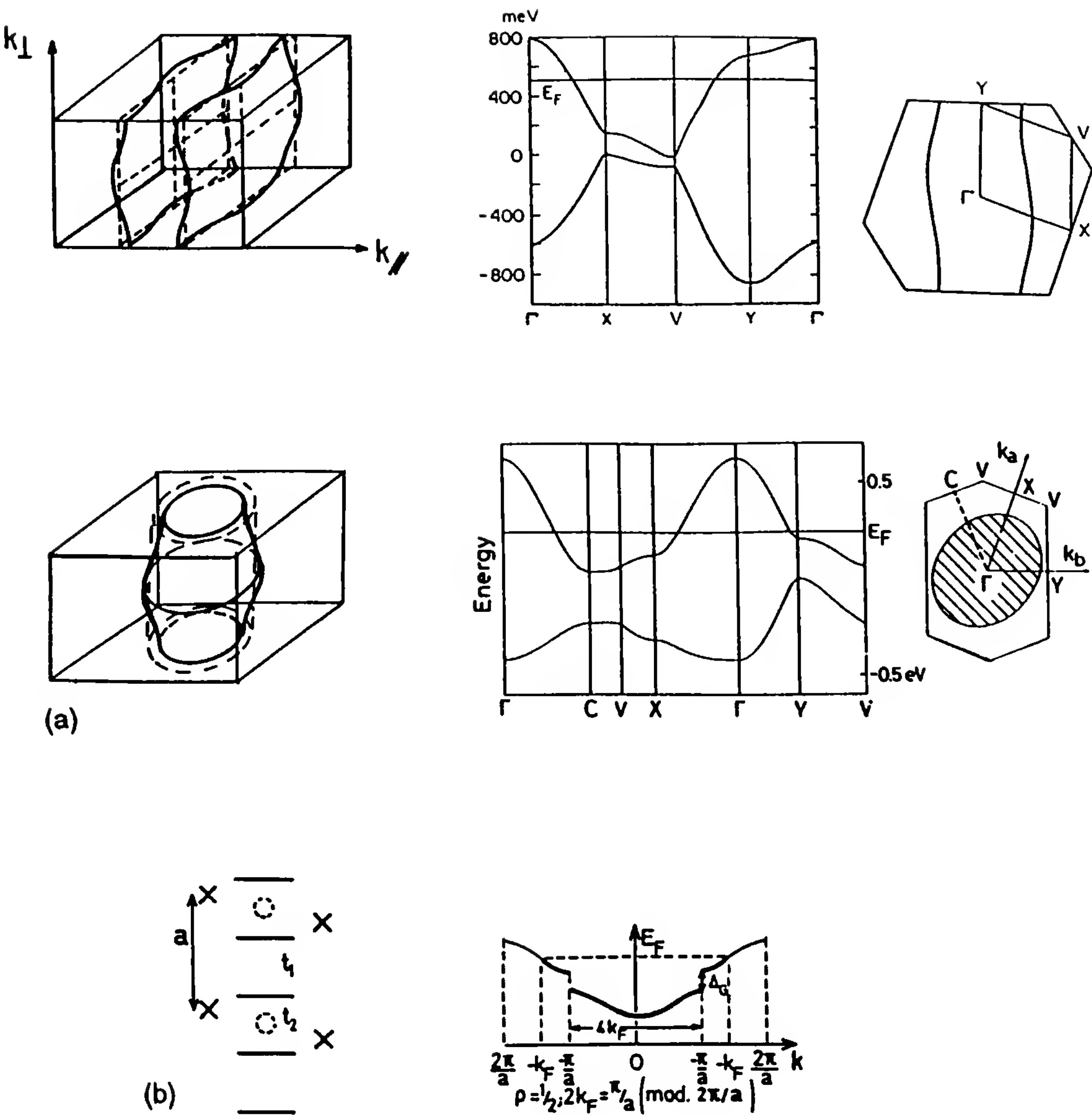


Figure 4 (a) Fermi surface (schematic) and band structure for $(TMTSF)_2X$ (after Ref. 32) and for $\beta(ET)_2X$ (after Ref. 32b); (b) schematic illustration of the structural dimerization giving rise to an half-filled upper band in $(TMTSF)_2X$ compounds.

diagram by applying hydrostatic pressure with a concomitant evolution of their physical properties. Materials shown in Fig. 5a all have centrosymmetric anions (with the noticeable exception of ClO_4), while noncentrosymmetric anions give rise to further problems (see Section III.E).

The long-range order which is stabilized at low temperature depends on the nature of the incipient instabilities that develop at high temperature along each stack on a short-range scale without any transverse correlation (i.e., one-dimensional fluctuations). It is therefore more illustrative to present the physical properties versus temperature for a few representative

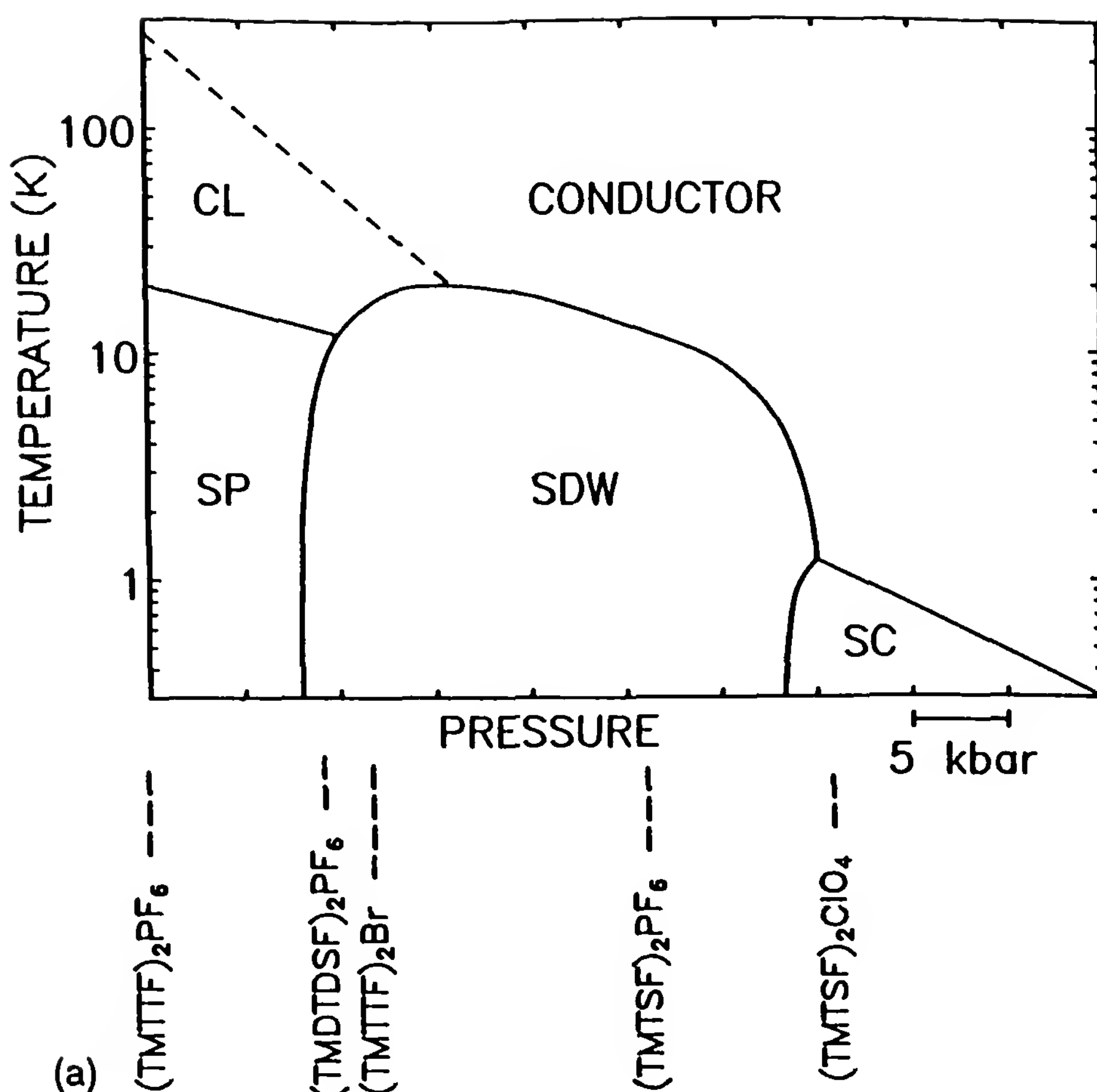
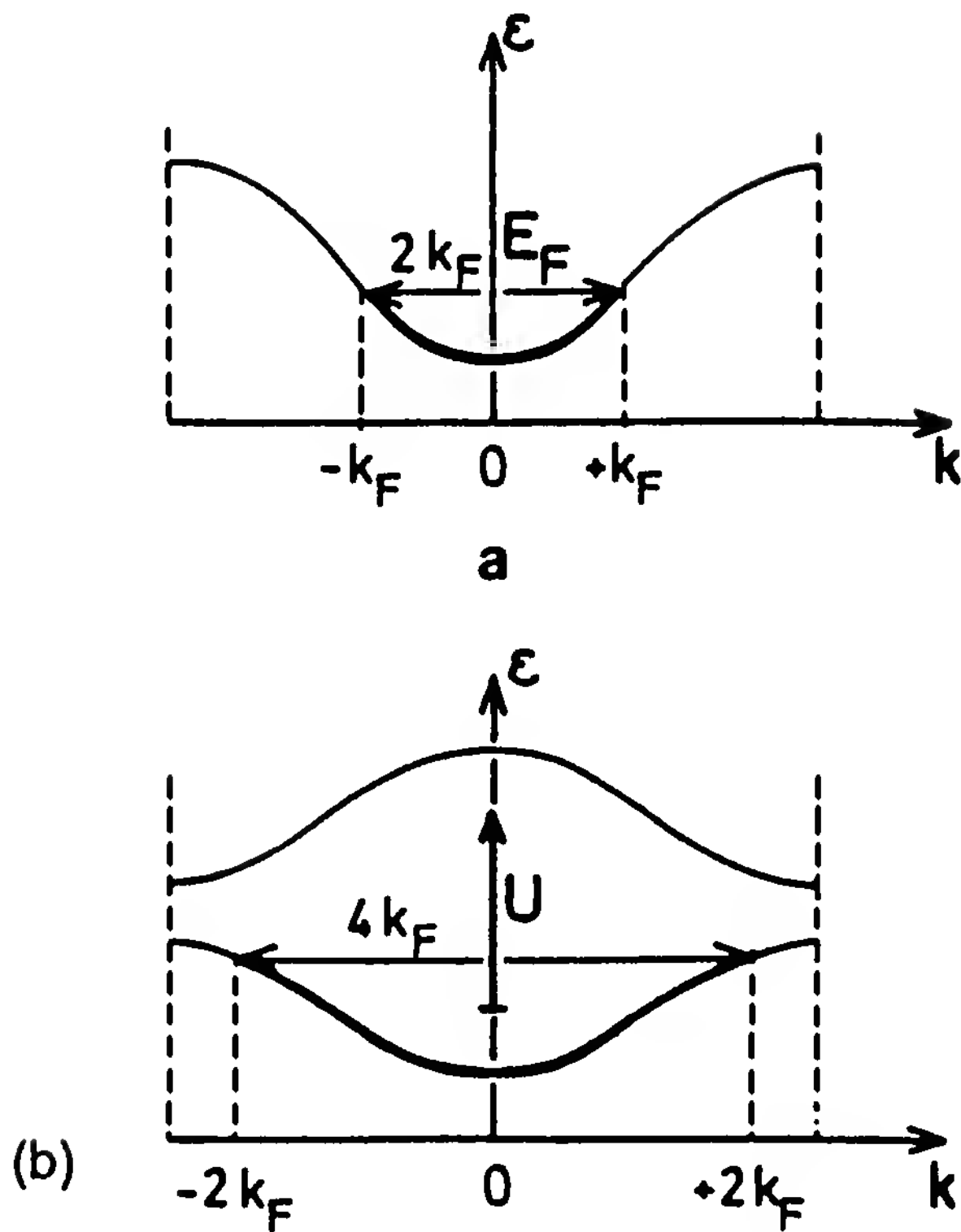


Figure 5 (a) Generalized phase diagram for the TM_2X series. Notations SP, SDW, and SC refer to spin-Peierls, spin density wave, and superconducting ground states, respectively. The dashed line marks the limit between metal-like and localized (CL) behavior. The zero-pressure locations of several prototype compounds are indicated [after Ref. 8]. (b) Electronic structure of the one-dimensional electron gas showing the $2k_F$ wave vector for noninteracting particles and the $4k_F$ wave vector in the lower Hubbard band of strongly interacting particles.

systems as shown in Fig. 5. We shall pay attention to spin and charge degrees of freedom making use of the experimental data obtained from transport, susceptibility, and NMR experiments.

B. Nuclear Magnetic Resonance and Transport Properties

NMR spin lattice relaxation measurements provide very direct information about the Fourier transform of the spin susceptibility $\chi(q, \omega)$ in a one-dimensional conductor [39]. The spin degrees of freedom constitute a relaxation channel for nuclear spin due to the modulation of the hyperfine interaction by the electron spin time dependence, which is given generally



in D dimensions by the Moriya relation [40],

$$(TT)^{-1} = 2\gamma_n^2 |A|^2 \int dq D \frac{\chi_{\perp}^{\parallel}(q, \omega_n)}{\omega_n} \quad (15)$$

where $\chi_{\perp}^{\parallel}(q, \omega_n)$ is the imaginary part of the transverse spin susceptibility taken at the nuclear Larmor frequency ω_n and integrated over all q vectors. The summation over q simplifies for a one-dimensional conductor, only $q = 0$ and $2k_F$ wave vectors giving rise to low-lying excited states. Hence T_1^{-1} for one-dimensional conductors contains only $q = 0$ and $q = 2k_F$ contributions probing uniform and antiferromagnetic correlations of the electron gas, respectively [41,42]. T_1^{-1} can be written formally as

$$[T_1 T]^{-1} = C_0 \chi_s^2(T) + C_1(T) \quad (16)$$

The first contribution in Eq. (16) probes the uniform ($q = 0$) spin correlations, $\chi_s(T)$ is the Faraday spin susceptibility, and C_0 is a constant depending on the hyperfine parameters. The second term probes the $q = 2k_F$ contribution. The $2k_F$ contribution can be temperature dependent or

independent, depending on the strength of the antiferromagnetic fluctuations since $C_1(T)$ is proportional to $\chi(2k_F, T)$, which follows a one-dimensional power law:

$$\chi(2k_F, T) \sim \left(\frac{T}{E_F^*} \right)^{-\gamma_{1D}} \quad (17)$$

where γ_{1D} is an exponent (> 0) describing the divergence of the antiferromagnetic fluctuations in the one-dimensional regime ($T > T_x$) and E_F^* is a renormalized cutoff ($E_F^* < E_F$) [43]. The relation between γ_{1D} and the correlation exponent K_ρ defined earlier reads

$$1 - \gamma_{1D} = K_\rho \quad (18)$$

The extreme situation of strongly repulsive interactions in a one-dimensional quantum antiferromagnet corresponds to γ_{1D} (or $K_\rho = 0$) and according to Eq. (16), $T_1^{-1}(2k_F)$ becomes temperature independent. The small \mathbf{q} spin excitations of the one-dimensional electron gas are not singular at low temperature, and as the temperature is increased, uniform fluctuations grow at the expense of diminishing antiferromagnetic correlations.

At the left side of the diagram, the compound $(\text{TMTTF})_2\text{PF}_6$ exhibits metal-like properties above room temperature but below a temperature T_ρ , where the resistivity passes through a shallow minimum [$T_\rho \approx 250$ K for $(\text{TMTTF})_2\text{PF}_6$], a loss of the charge degrees of freedom is observed, although the spin susceptibility remains unaffected (one-dimensional quantum antiferromagnet). The loss of the charge degrees of freedom has been explained in terms of coulombic repulsions in a one-dimensional conductor [44]. For the situation of one particle per site, there exists a correlation gap $\Delta\rho$ in the charge excitation spectrum (the Mott–Hubbard gap). Therefore, when T becomes smaller than $\Delta\rho/k_B$ charge excitations become frozen out. Hence the chain of localized spins with periodicity a ($4k_F$ wave vector); Fig. 5b is described by the Heisenberg linear model, where the antiferromagnetic interaction given by $2t_\parallel^2/U$ in the strong-coupling limit depends on the lattice spacing through the overlap integral t_\parallel . Thus the system of localized spins may gain energy by dimerizing, giving rise at low temperature to one-dimensional lattice fluctuations with a doubled periodicity ($2a$ or wave vector $2k_F$) which are detected by x-ray experiments [36]. Simultaneously, the spin susceptibility follows fairly well the temperature dependence of the Bonner–Fisher model [45] down to a temperature $T_{sp}^\circ \approx 60$ K for $(\text{TMTTF})_2\text{PF}_6$ [37], below which one-dimensional lattice fluctua-

tions are strongly developed and χ_s is decreased with respect to the one-dimensional quantum antiferromagnet by the opening of the spin-Peierls pseudogap at the Fermi level. Finally, below 20 K, these one-dimensional $2k_F$ fluctuations order three-dimensionally and the system undergoes a phase transition at $T_{sp} = 20$ K toward a nonmagnetic singlet ground state (total spin = 0) in which the lattice is tetramerized [36].

The NMR data of the ^{13}C relaxation rate of $(\text{TMTTF})_2\text{PF}_6$ are shown in a T_1^{-1} versus $T\chi_s^2(T)$ diagram [41b,46], where χ_s^2 is the spin susceptibility obtained from EPR or Faraday spin susceptibility experiments (Fig. 6). $T_1^{-1}(T)$ data follow very closely the law given by Eq. (17). The very good agreement with a law $C_1 \sim T^{-1}$, which is observed between 40 and 200 K, indicates that the $4k_F$ localized spins adopt the dynamics of a one-dimensional quantum antiferromagnet, with a weight of $2k_F$ spin correlations, which is dominant even up to room temperature ($K_p = 0$). The spin-Peierls ground state is accompanied by an activation of the relaxation, reflecting the freezing of the spin degrees of freedom in a spin-singlet ground state.

Moving to the right in the generic diagram, the metallic character becomes predominant as both the room-temperature conductivity increases and the positive temperature dependence of the resistivity extends to lower temperature [$T_p \approx 100$ K for $(\text{TMTTF})_2\text{Br}$] [47] and also for the mixed S–Se(TMDTDSF) $_2\text{PF}_6$ salt [48]. The role of one-dimensional coulombic repulsions is attenuated in the latter salts, as shown by the Mott localization taking place only below 100 K or so. Once more the temperature-dependent spin susceptibility above 100 K [47,48] does not depart significantly from that of $(\text{TMTTF})_2\text{PF}_6$ [37].

However, the nuclear relaxation rate behaves differently since the $T^{-1} \sim C_0\chi_s^2(T)$ law is followed accurately at all temperatures $T > T_p$, whereas the $2k_F$ contribution to T_1^{-1} grows only below T_p and gives rise to a temperature-independent term below $T \approx T_p/2$. The temperature dependence of the $2k_F$ contribution can be used to extract the exponent γ_{1D} (or K_p) for one-dimensional correlation functions. According to Fig. 7, γ_{1D} reaches the strong-coupling limit $\gamma_{1D} = 1$ below $T_p/2$, and the vanishing $2k_F$ part above T_p is also consistent with the power law dependence of Eq. (17) with $0 < \gamma_{1D} < 1$ in this high-temperature domain.

The data for $(\text{TMTTF})_2\text{Br}$ are somewhat less detailed, but they are qualitatively similar to those of the mixed S–Se compound. The observation of one-dimensional $2k_F$ lattice fluctuations is very marginal in these two compounds, with only a weak intensity arising below 60 K, which vanishes below 20 K in $(\text{TMDTDSF})_2\text{PF}_6$ [49]. However, the diffuse scattering does not condense into Bragg peaks as for the spin-Peierls transition

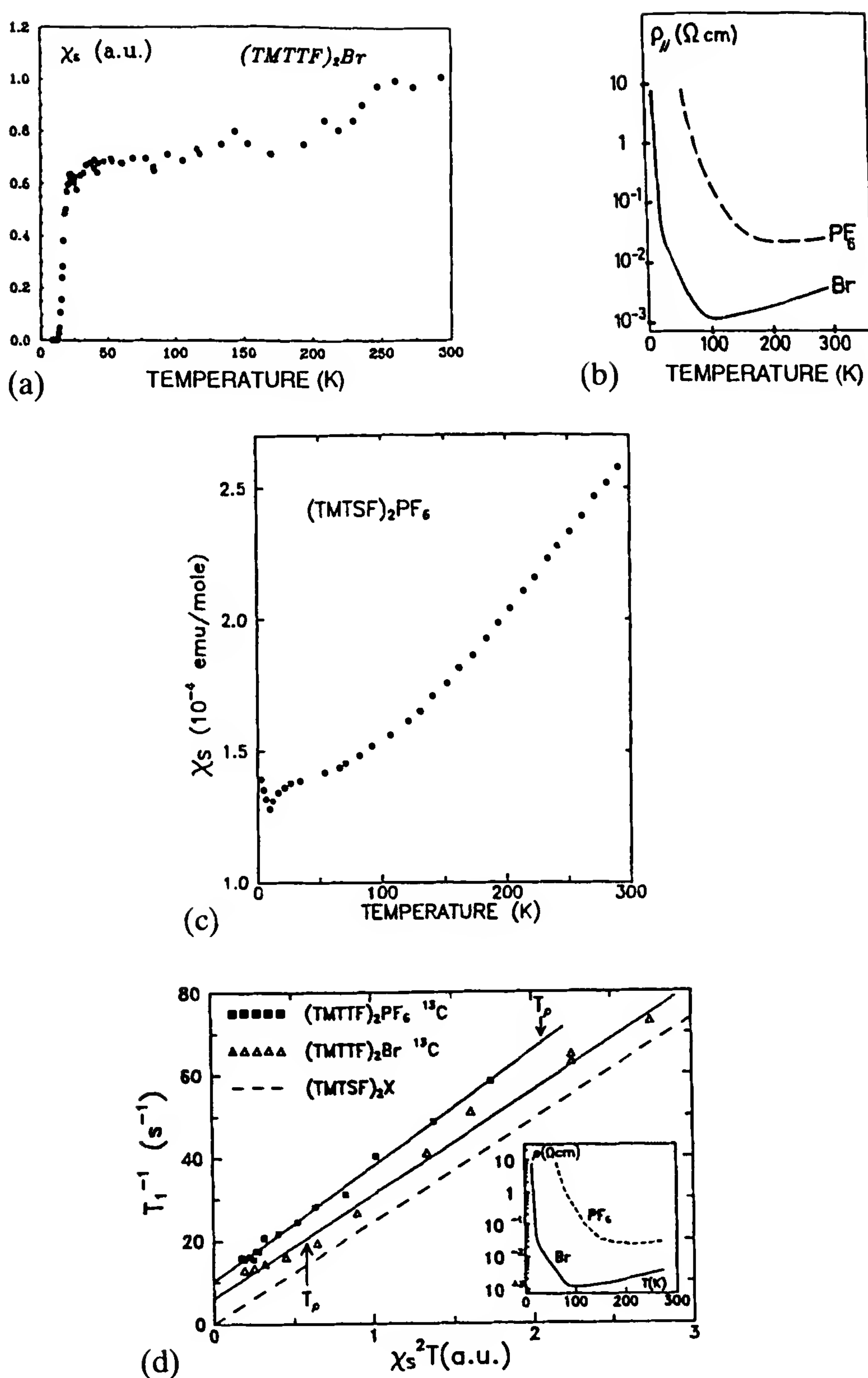


Figure 6 (a) Resistivity [after Ref. 47] and (b) EPR spin susceptibility of $(TMTTF)_2X$ compounds [after Ref. 46] undergoing a one-dimensional Mott–Hubbard localization below T_p ; (c) electron spin susceptibility of $(TMTSF)_2PF_6$ [after Ref. 38]; (d) plot of the ^{13}C spin lattice relaxation rate versus $T\chi_s^2(T)$ for three compounds in the TM_2X series. The temperature below which the charges are localized is indicated by T_p . No localization is observed for Se compounds (dashed line) above the SDW or SC ordering. (From Ref. 41b.)

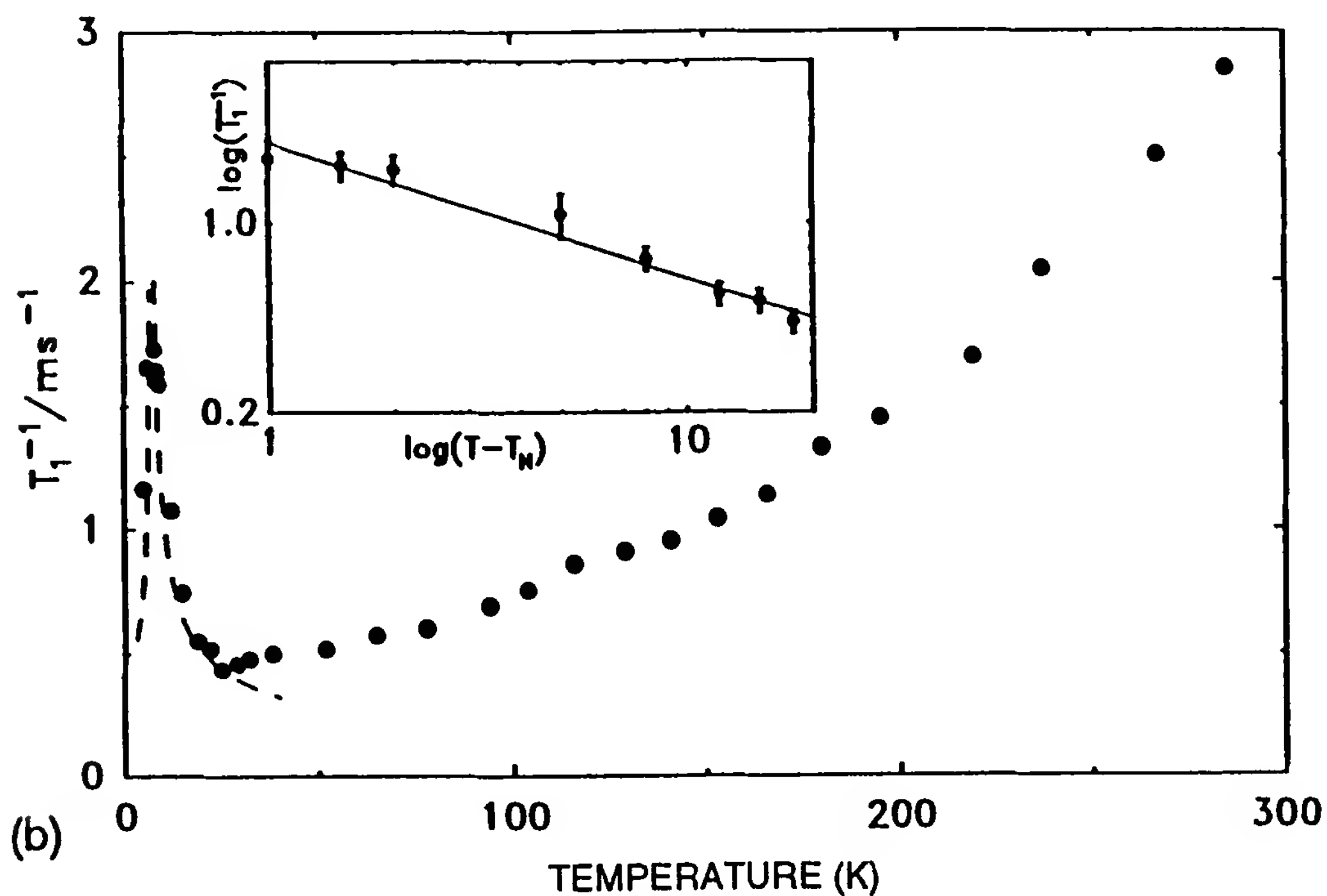
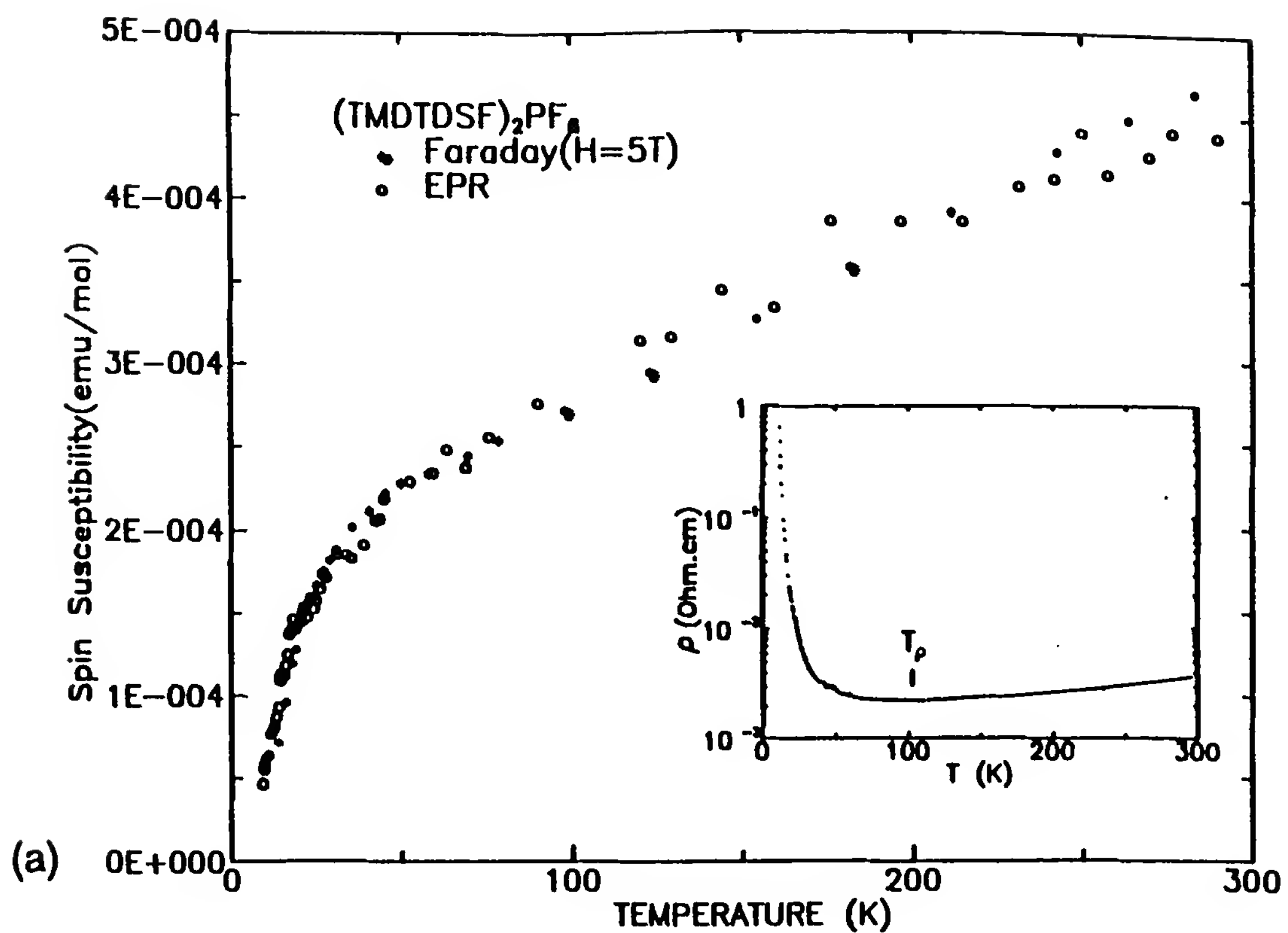


Figure 7 Properties of the mixed compounds $(\text{TMDTDSF})_2\text{PF}_6$: (a) Faraday susceptibility and resistivity (insert); (b) $^{77}\text{Se } T_1^{-1}$ versus temperature profile showing the onset of a SDW ground state at 7 K; (c) $^{77}\text{Se } T_1^{-1}$ versus $T\chi_s^2$, revealing the $2k_F$ SDW contribution below T_p which is plotted versus temperature in part (d). (e) $2k_F$ one-dimensional scattering amplitude and linewidth, which is the signature of spin-Peierls fluctuations vanishing below 2 K when SDW fluctuations are taking over (after Ref. 49). (From Refs. 48 and 51.)

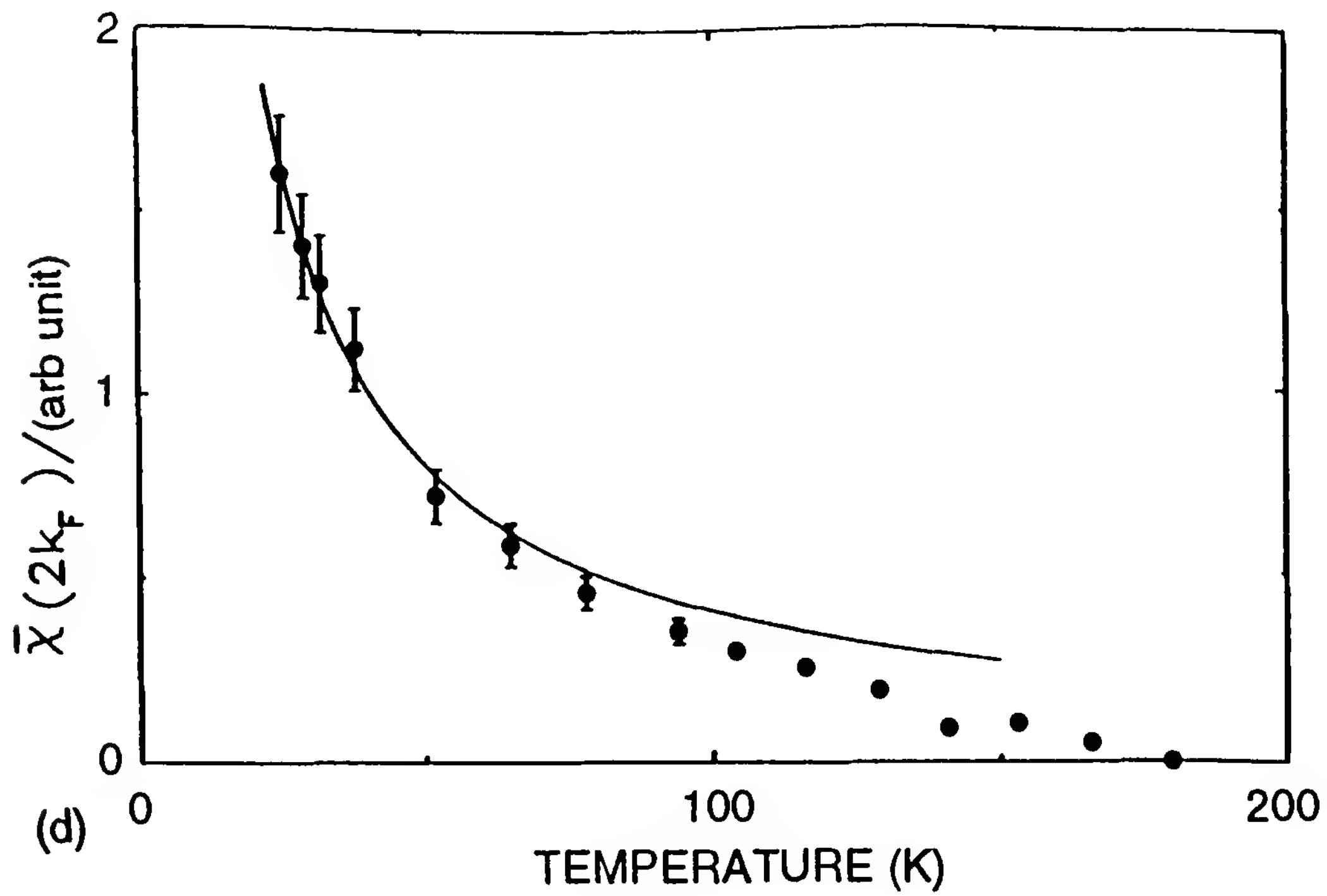
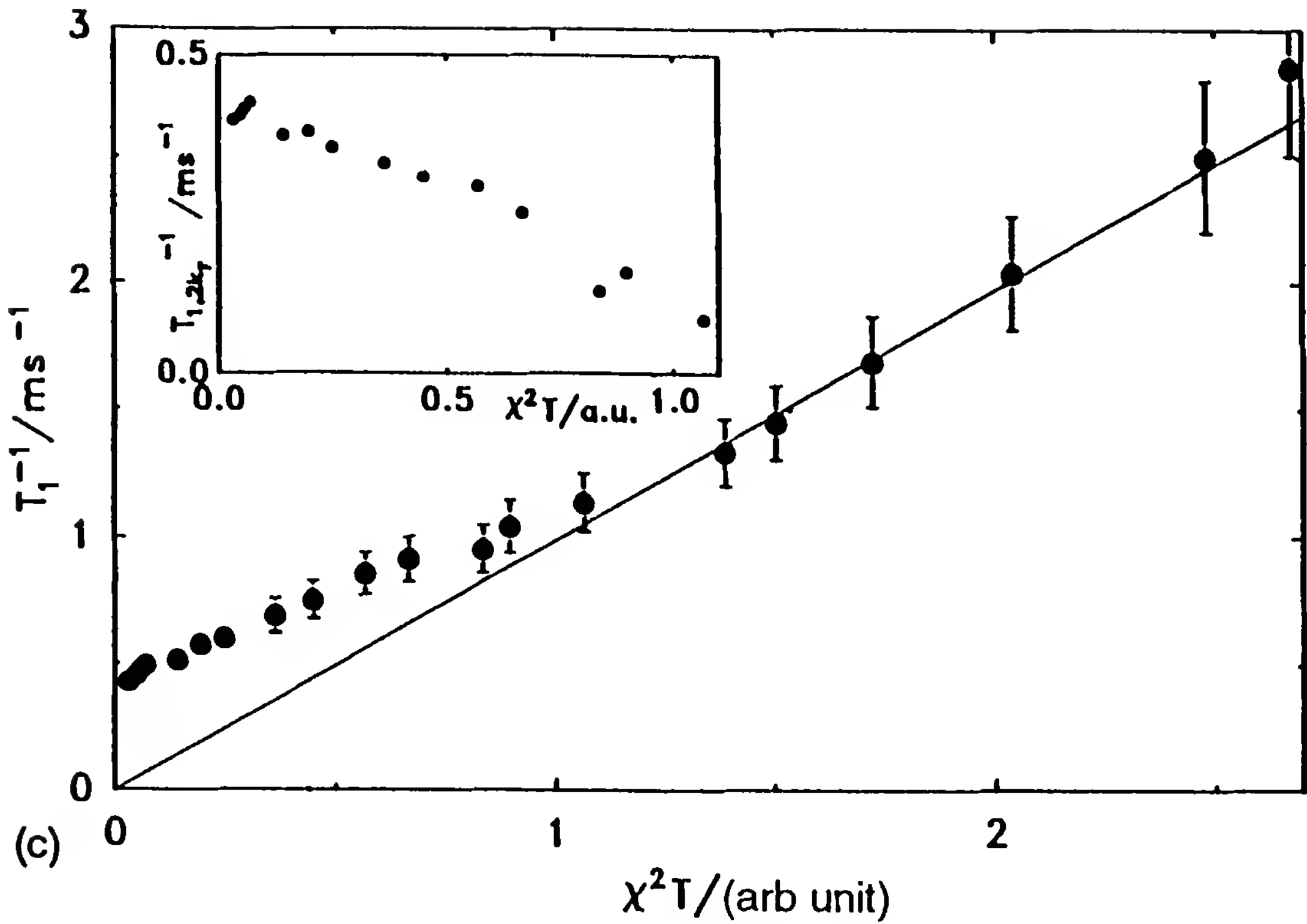
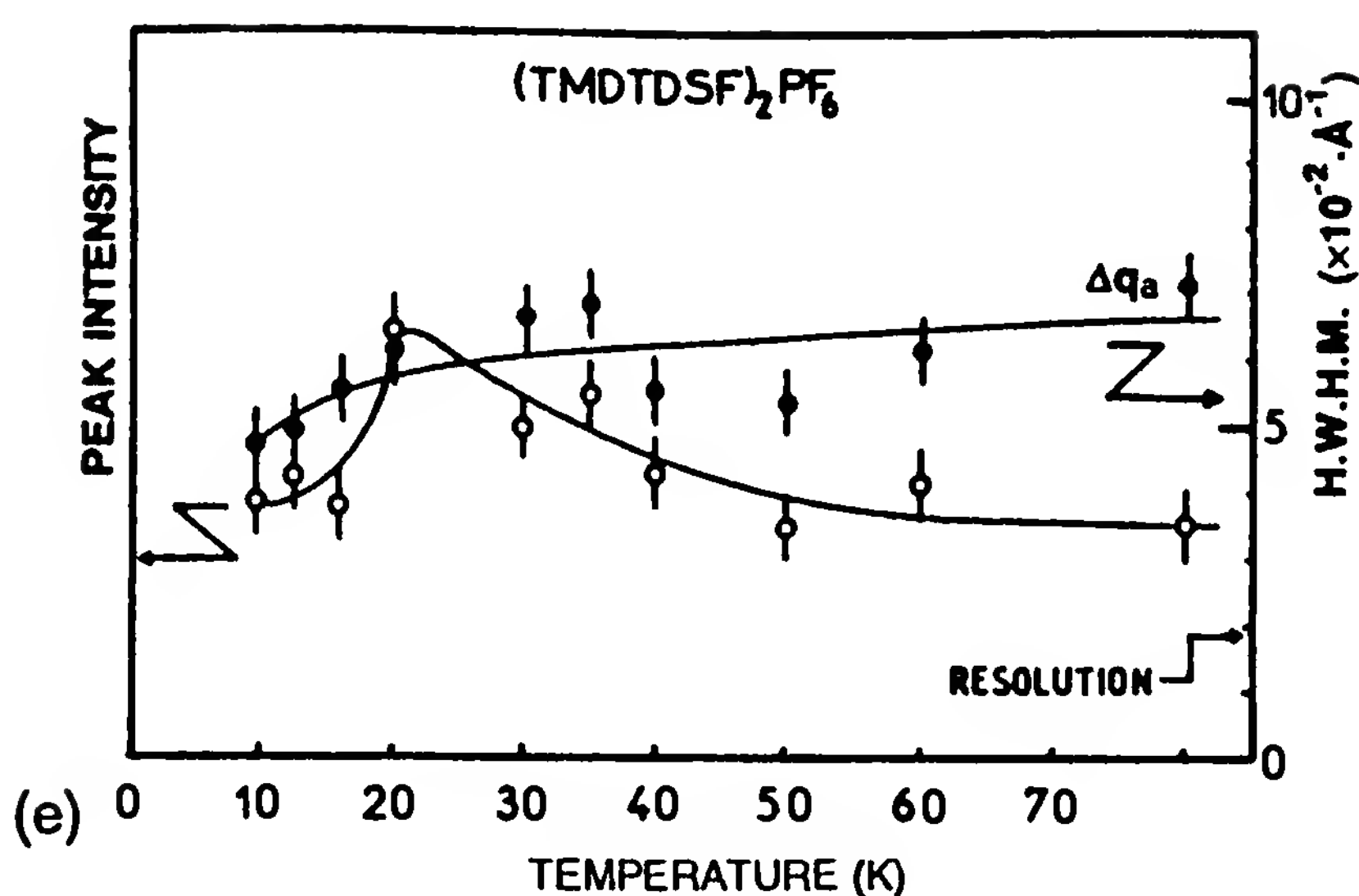


Figure 7 Continued



in (TMTTF)₂PF₆. Instead, the divergences of the relaxation rate which are observed at $T_N = 19$ and 7 K for (TMTTF)₂Br [50] and (TMDTDSF)₂PF₆ [51], respectively, show the signature of a ground state with low-lying magnetic excitation modes. This ground state is characterized by a finite modulation of the spin density with a wave vector \mathbf{Q} that is called a spin density wave phase.

The ¹³C-NMR line-shape analysis at $T < T_N$ in (TMTTF)₂Br has proved that the periodicity of the magnetic modulation is commensurate with the underlying lattice [52]. The spin lattice relaxation is activated in the SDW ground state since there exists a finite energy gap in the phason modes of this commensurate SDW phase (Fig. 8).

One may notice that the three-dimensional magnetic fluctuations are competing in (TMDTDSF)₂PF₆ against the $2k_F$ lattice fluctuations and finally, impose a magnetic long-range order at 7 K [51] instead of the spin-Peierls ground state, which could have been expected as a natural consequence of the one-dimensional $2k_F$ fluctuations visible at high temperature.

As far as all selenium molecular compounds are concerned, the shallow minimum of the resistivity is no longer observed, but different behaviors are observed for the representative compounds (TMTSF)₂PF₆ and (TMTSF)₂ClO₄. The conductivity of the former compound reaches $10^6 (\Omega \cdot \text{cm})^{-1}$ at 12 K and then vanishes abruptly as the system undergoes a metal-insulator transition [15] toward an antiferromagnetic (SDW) ground state, as indicated by NMR [53] and susceptibility measurements [54]. Furthermore, ¹³C NMR has proved the incommensurate nature of this SDW ground state [52]. It is the presence of this additional periodicity in

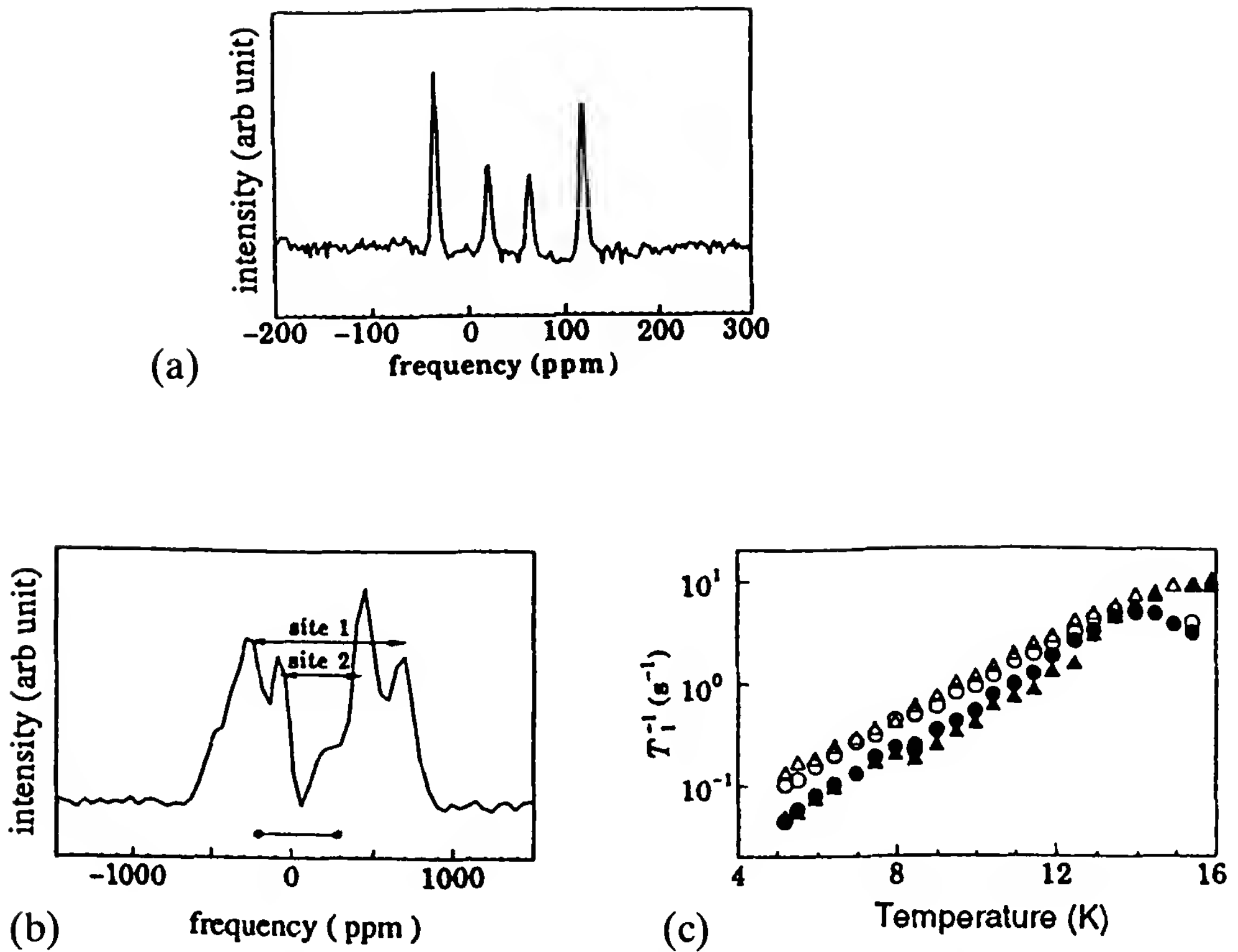


Figure 8 ^{13}C -NMR spectrum of the 100% ^{13}C -enriched central double bond of TMTTF in $(\text{TMTTF})_2\text{Br}$ at $T = 300\text{ K}$ (a) and of the NMR spectrum (b) showing the existence of a commensurate spin modulation with two distinct magnetic sites and an activated relaxation rate (c). (From Ref. 52.)

the exchange potential that is the cause of the gap opening at the Fermi surface (M–I transition). The various components of the wave vector \mathbf{Q} are determined as far as the PF_6 salt is concerned by the best nesting conditions of the Fermi surface of the quasi-one-dimensional conductor. These conditions do not necessarily coincide with commensurate values [55]. Finally, slowly cooled $(\text{TMTSF})_2\text{ClO}_4$ does not reveal any M–I and magnetic transition before the superconducting ground state is stabilized at 1.2 K [10].

Although the plot T_1^{-1} versus $T\chi_s^2$ in Fig. 6 does not reveal any finite intercept as $T\chi_s^2 \rightarrow 0$, the presentation of the NMR data as $\log T_1^{-1}$ versus $\log \chi_s^2$ in Fig. 9 [41b] shows a significant deviation to the law $T_1^{-1} \approx T\chi_s^2$ below 150 and 30 K in PF_6 and ClO_4 salts, respectively. A quantitative analysis of the T_1^{-1} temperature profile leads to the power law exponent $\gamma_{1D} \sim 0.90$ below 100 K in $(\text{TMTSF})_2\text{PF}_6$ and a similar value for ClO_4 below 30 K.

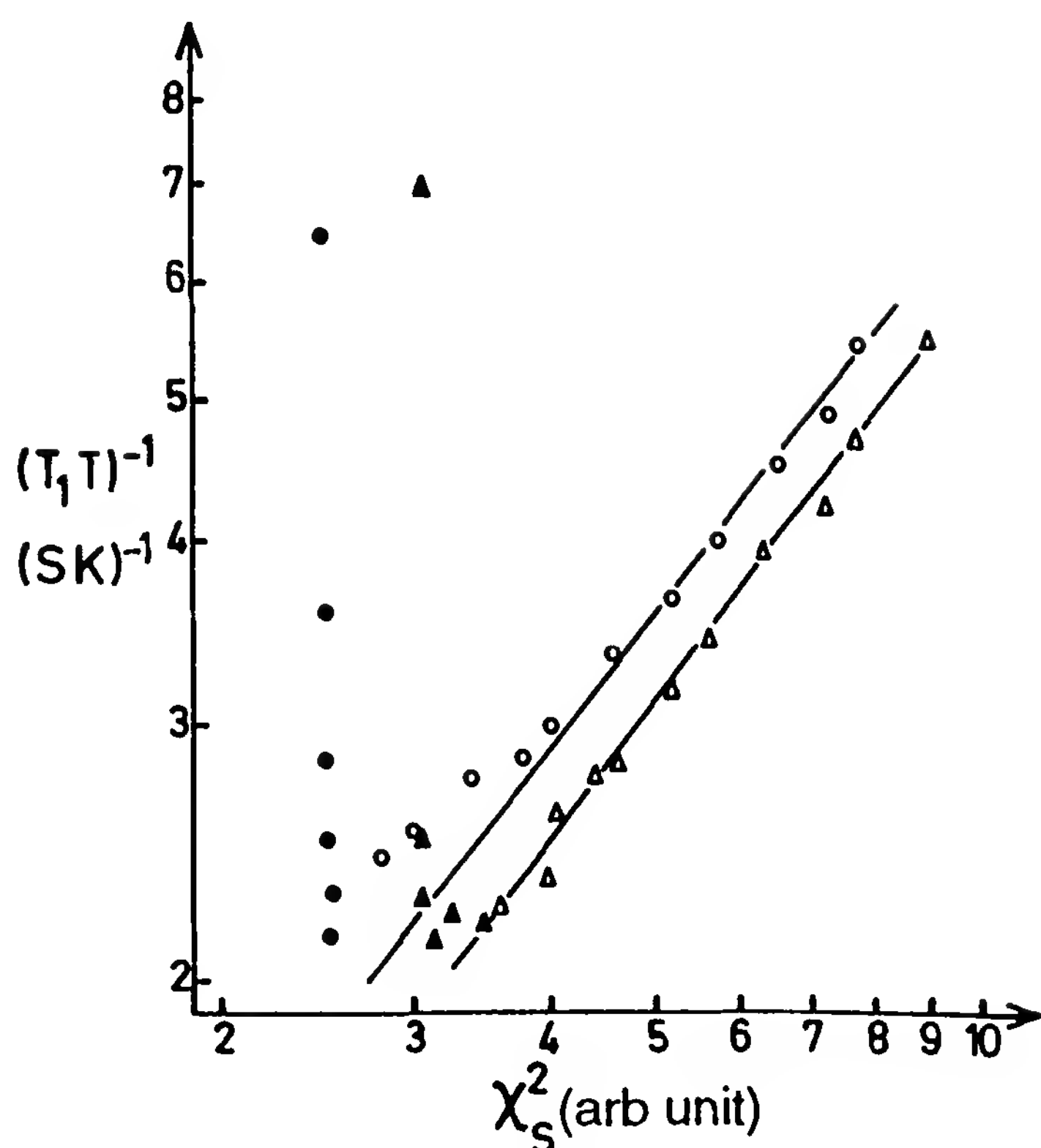


Figure 9 The plot of $(T_1T)^{-1}$ versus $\chi_S^2(T)$ shows a deviation to the $(T_1T)^{-1} \propto \chi_S^2$ law below 150 and 30 K for $(\text{TMTSF})_2\text{PF}_6$ (dots) and ClO_4 (triangles), respectively. (From Ref. 47b.)

The behavior of $(\text{TMTSF})_2\text{ClO}_4$ (Fig 10a) is indeed particularly illuminating as far as the non-Fermi liquid behavior is concerned. From the temperature independence of the Pauli susceptibility below 30 K [38], a linear temperature dependence of the spin-lattice relaxation rate could be expected following the theory of a regular Fermi liquid. The quasiplateau observed for T_1^{-1} between 30 and 8 K suggests that staggered correlations are involved in the relaxation enhancement and dominate the uniform contribution proportional to T_1^{-1} [41b]. However, the strong-coupling limit with $K_p = 0$ is never reached for a salt such as $(\text{TMTSF})_2\text{ClO}_4$ and even for $(\text{TMTSF})_2\text{PF}_6$, since there is no resistivity minimum at a T_p value higher than any phase-transition temperature toward either superconductivity or antiferromagnetism.

The quasiplateau for T_1^{-1} which is observed for ClO_4 and also for PF_6 salts under pressure (Fig. 10b) is therefore related to $2k_F$ correlations in a transient temperature regime when the nesting vector evolves from a purely one-dimensional situation $(2k_F, 0)$ to a vector that provides the best nesting of the two (three)-dimensional Fermi surface. Below the crossover temperature T_x a Fermi liquid behavior is recovered with an enhanced Korringa

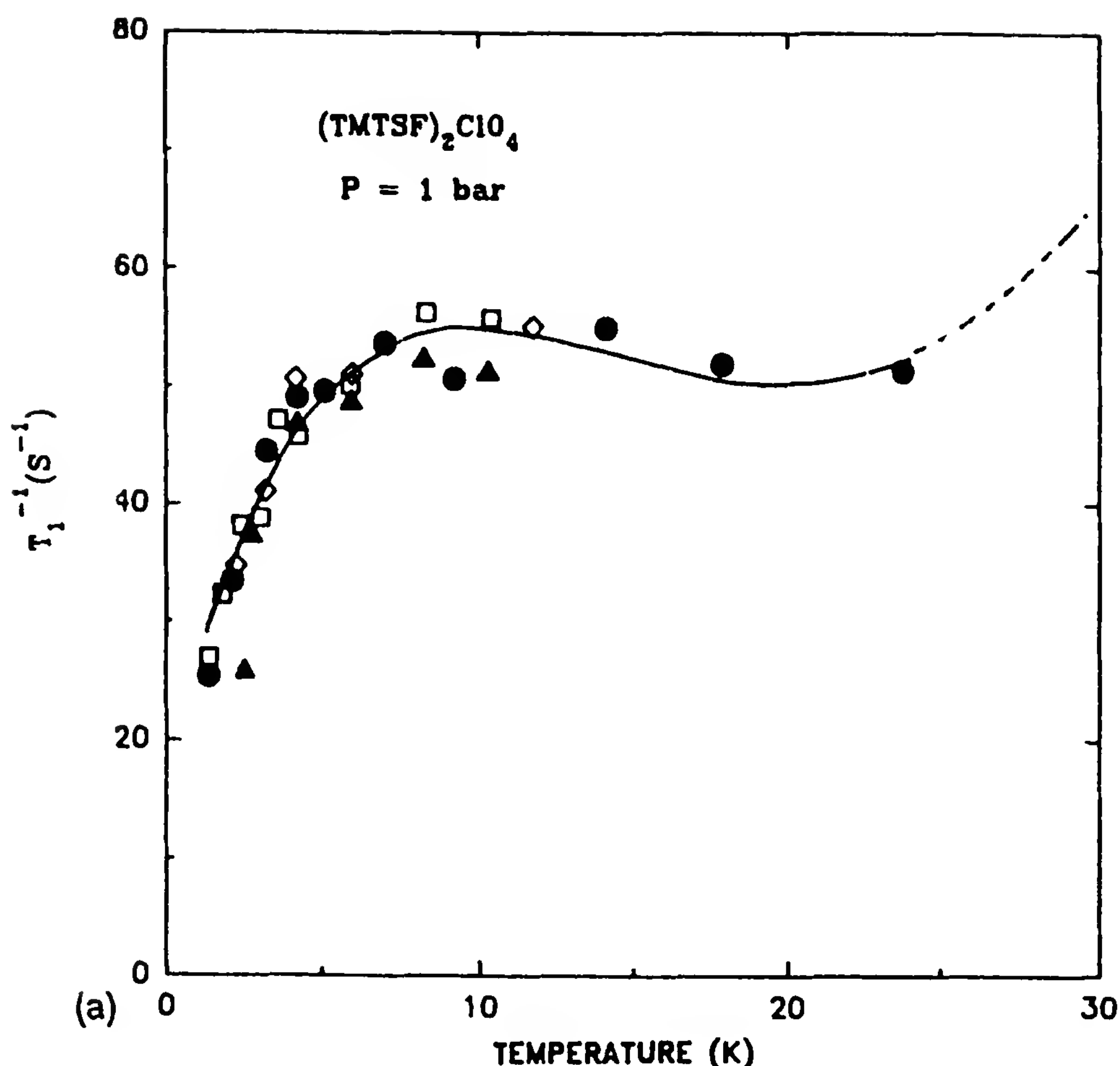


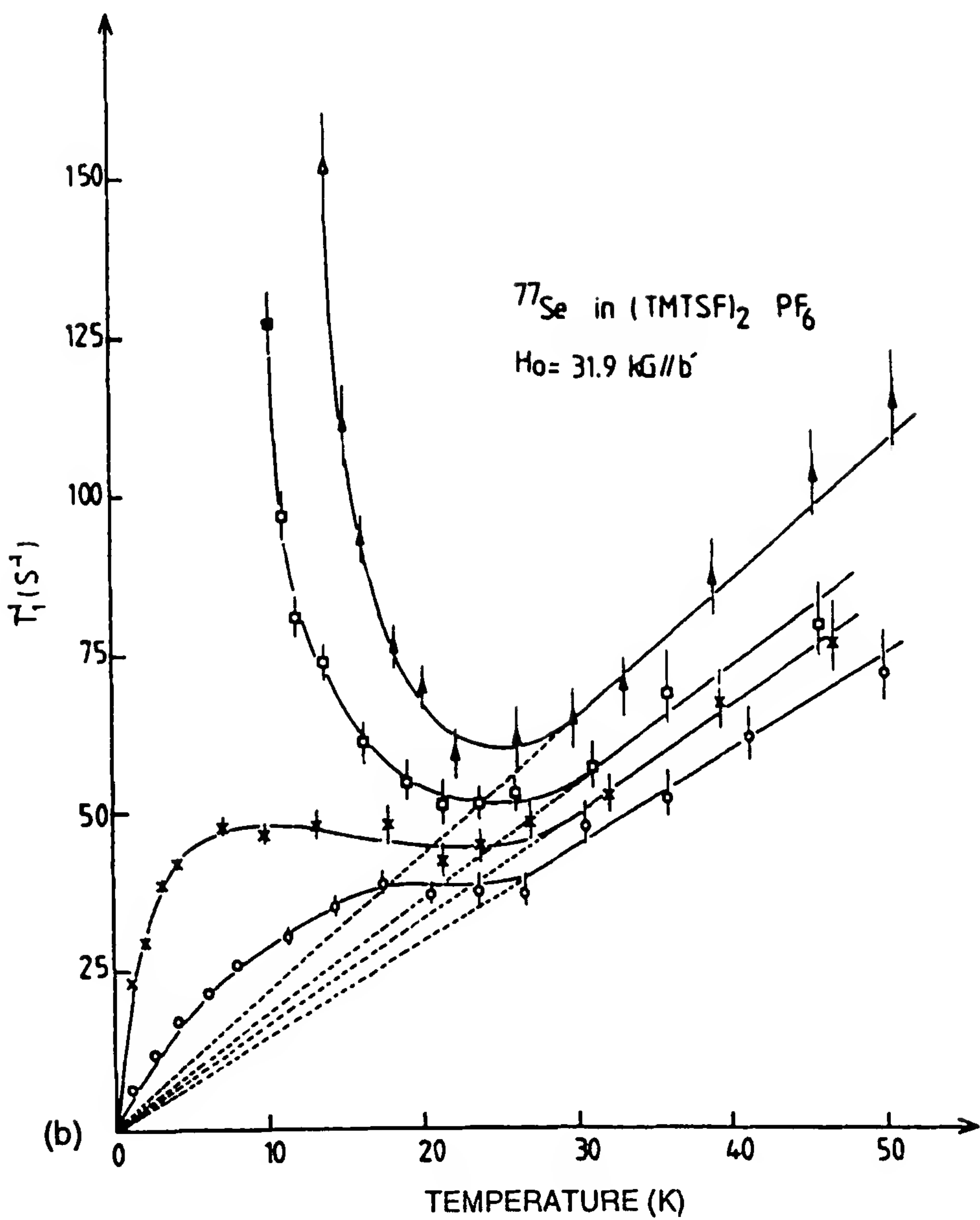
Figure 10 (a) Low-temperature ^{77}Se T_1^{-1} versus T data of $(\text{TMTSF})_2\text{ClO}_4$ in the relaxed state. (After Ref. 41b.) (b) Temperature dependence of ^{77}Se T_1^{-1} in $(\text{TMTSF})_2\text{PF}_6$ at $P = 1$ bar, 5.5 kbar, 9 kbar, and 11 kbar. (After Ref. 57.)

type of relaxation:

$$T_1^{-1} \sim T \left(\frac{T_x}{E_F^*} \right)^{-\gamma_{1D}} \quad (19)$$

where $0 \leq \gamma_{1D} \leq 1$.

The data of ClO_4 and PF_6 under pressure [41b] (Fig. 10) reveal that $T_x \approx 8$ K, which can be reconciled with the observed Korringa enhancement of 10 and a renormalized Fermi energy $E_F^* \approx 100$ K. Below T_x the two-dimensional electron gas undergoes a transition toward either a superconducting ground state (ClO_4 or PF_6 under pressure) or an antiferromagnetic ground state $(\text{TMTTF})_2\text{Br}$ or $(\text{TMTSF})_2\text{PF}_6$. Under such circumstances the nuclear relaxation is enhanced by three-dimensional critical fluctuations in



the vicinity of T_N with the critical exponent $\frac{1}{2}$ [56]:

$$T_1^{-1} \approx (T - T_N)^{-1/2} \tag{20}$$

The critical divergence of Eq. (20) is followed accurately for the onset of SDW ground states arising either from a quasi-one-dimensional metal as for $(\text{TMTSF})_2\text{PF}_6$ or from a one-dimensional Mott–Hubbard paramagnetic insulator [i.e., $(\text{TMTTF})_2\text{Br}$ at ambient pressure or $(\text{TMTTF})_2\text{PF}_6$ under 13 kbar] [57] (Fig. 11).

Relaxation and susceptibility data have been used to extract the values of the interactions governing the spin degrees of freedom, with $\chi_s(T)$ given

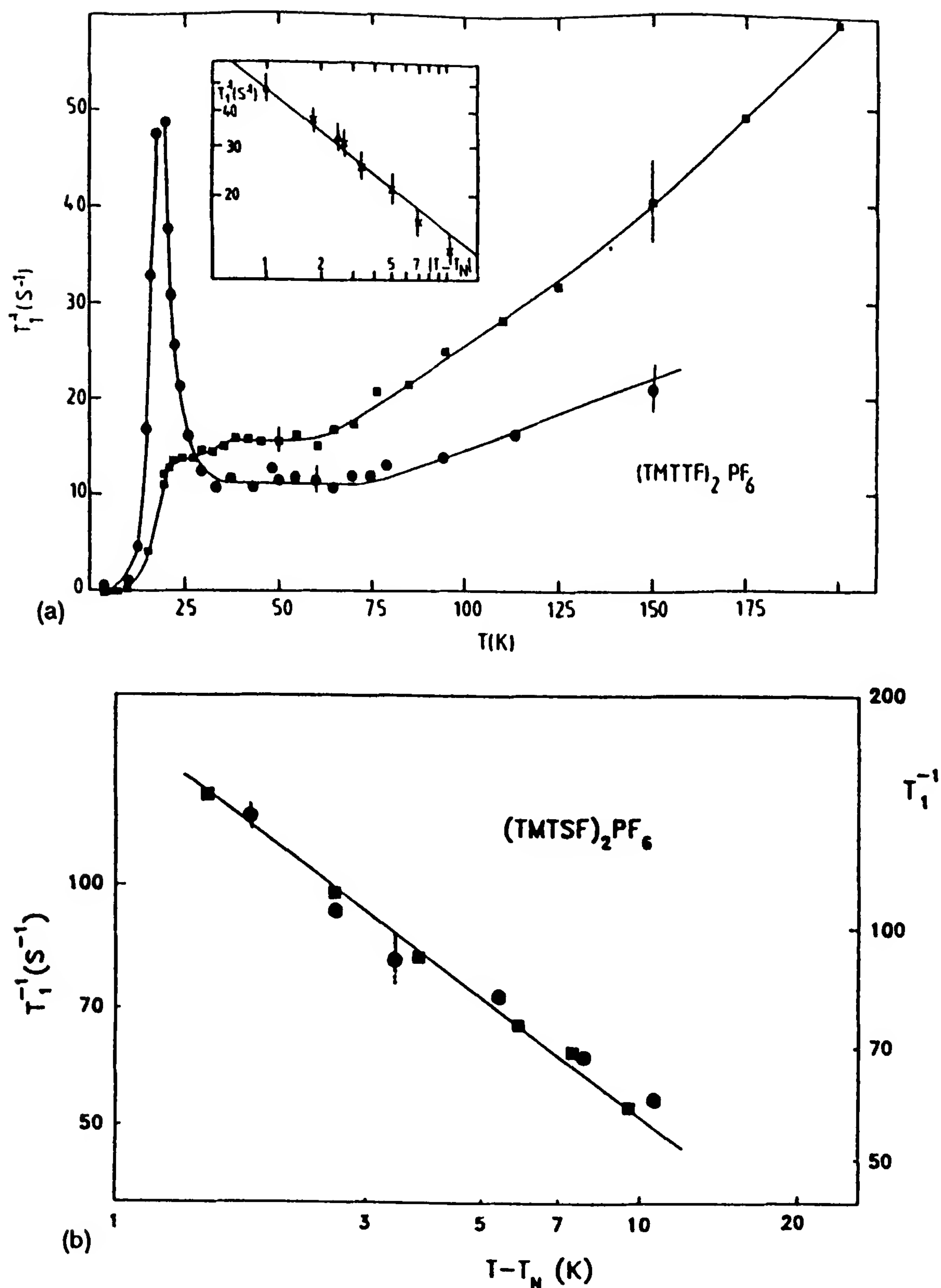


Figure 11 (a) $^{13}\text{C} - T_1^{-1}$ of $(\text{TMTTF})_2\text{PF}_6$ at ambient pressure showing a spin-Peierls transition below 20 K and under 13 kbar, where a SDW ground state is stabilized with a $(T - T_N)^{-1/2}$ divergence of T_1^{-1} as shown by the insert. (b) Log-log plot of T_1^{-1} versus $T - T_N$ in the critical domain of $(\text{TMTSF})_2\text{PF}_6$ at 1 bar (right scale, dots) and 5.5 kbar (left scale, squares). (After Ref. 41b.)

[26] by

$$\chi_s(T) = \chi_0 \left[1 - \frac{g_1(T)}{2} \chi_0 \right]^{-1}$$

(21)

where χ_0 is the bare susceptibility of the one-dimensional electron gas and $g_1(T)$ is the renormalized backward-scattering amplitude given by Eq. (11a). Values of $g_1/\pi\nu_F$ for several TM_2X salts and for TTF Ni[(dmit)₂]₂ are reported on Table 2 using E_F data derived from NMR experiments or band structure calculations.

We can see from Table 2 that the amplitude of $g_1/\pi\nu_F$ is nearly the same throughout the S and Se series, as expected from the similar amplitudes for the temperature variation of $\chi_s(T)$ up to 300 K in both cases. There is no scaling under pressure between the uniform susceptibility of S and Se compounds. However, such a scaling exists for $2k_F$ -spin correlations, which depend primarily on the amplitude of the Umklapp scattering g_3 . When g_3 is larger or smaller than $2g_2 - g_1$, the electron gas evolves toward a strong-coupling situation at low temperature with strongly developed AF correlations or toward the paramagnetic weak-coupling limit, respectively [58]. A crude approximation for g_3 is $g_3 = g_1(\Delta/E_F)$ [44], where Δ is given by the bandgap of the dimerized structure. Therefore, band parameters in Table 1 give $g_3/\pi\nu_F$ equal to 0.38 and 0.16 $g_1/\pi\nu_F$ for S and Se compounds,

Table 2 Parameters Describing the Behavior of Transport and Magnetic Properties of Some TM_2X Compounds in the Conducting (or Localized) Phase at High Temperature^a

Compound	T_p (K)	K_p	$g_1/\pi\nu_F$ (at 0 K, 1 bar)	E_F (K)
TMTTF ₂ PF ₆	250	0 $T < 250$ K	1.05	1600
TMDTDSF ₂ PF ₆	100	0 $T < 50$ K		
TMTTF ₂ Br	100	0 $T < 50$ K	0.94	1900
TMTSF ₂ PF ₆	No	0.1 $T < 100$ K	1.16	3100
TMTSF ₂ ClO ₄	No	0.2 $T < 30$ K		
TTF-Ni[(dmit)] ₂	No	0.4	1.1	1500

^a K_p , g_1 , and E_F have been derived from NMR experiments.
Source: Ref. 41b.

respectively. The dimerization gap of S compounds is expected to be suppressed under sufficiently high pressure [33,59]; then T_p goes to zero and the amplitude of AF fluctuations joins smoothly the one found in the selenide series at low pressure, which are less dimerized.

C. Transport Properties in the Metallic Regime

The room-temperature conductivity of different organic superconductors can vary in a large proportion, depending on the specific compound [6]. The conductivity is highest in the four Se-based systems, $(\text{TMTSF})_2\text{X}$ ($\sigma_{\parallel} \approx 600 (\Omega \cdot \text{cm})^{-1}$). The room-temperature conductivity decreases moving toward the left in the generic diagram of Fig. 5. The conductivity is governed by the character of longitudinal and transverse charge motions.

The transverse charge motion is incoherent for a quasi-one-dimensional conductor as long as the condition $t_{\perp} \ll \hbar/\tau_{\parallel}$ is fulfilled (where the intra-chain scattering time provides a broadening to the quasi-one-dimensional Fermi surface). This situation is encountered at high temperature. The interchain hopping rate is thus determined by the one-dimensional Fermi golden rule [60]:

$$\frac{1}{\tau_{\perp}} = \frac{|t_{\perp}|^2}{\hbar^2} \tau_{\parallel} \quad (22)$$

leading to a temperature-independent value for the conductivity anisotropy:

$$\frac{\sigma_{\parallel}}{\sigma_{\perp}} \sim \left(\frac{t_{\parallel}a}{t_{\perp}b} \right)^2 \quad (23)$$

The experimental data of $(\text{TMTSF})_2\text{PF}_6$ show that the prediction of a temperature-independent law is followed over an extended temperature domain down to ≈ 25 K (Fig. 12).

For $\hbar/\tau_{\parallel} < t_{\perp}$ the warping of the Fermi surface is pertinent and the transverse motion becomes coherent. Thus, assuming a Fermi surface broadening of $E_F/3 \approx 1000$ K at room temperature and decreasing down to 10 K at 25 K, according to the temperature dependence of the resistivity [5], a value of 10 K is obtained for the interchain coupling. This is a much smaller value than what can be derived from band structure calculations (i.e., 20 meV). The difference can be explained by the role of intrachain correlations improving the one-dimensional confinement, decreasing the effective interchain coupling and the crossover temperature [42].

The resistivity anisotropy of the TM_2X series is typically 1:200:30,000 along the a , b , and c axes, respectively, leading to the overlap anisotropy $t_a:t_b:t_c = 10:1:0.1$ with the assumption of incoherent transverse conduction

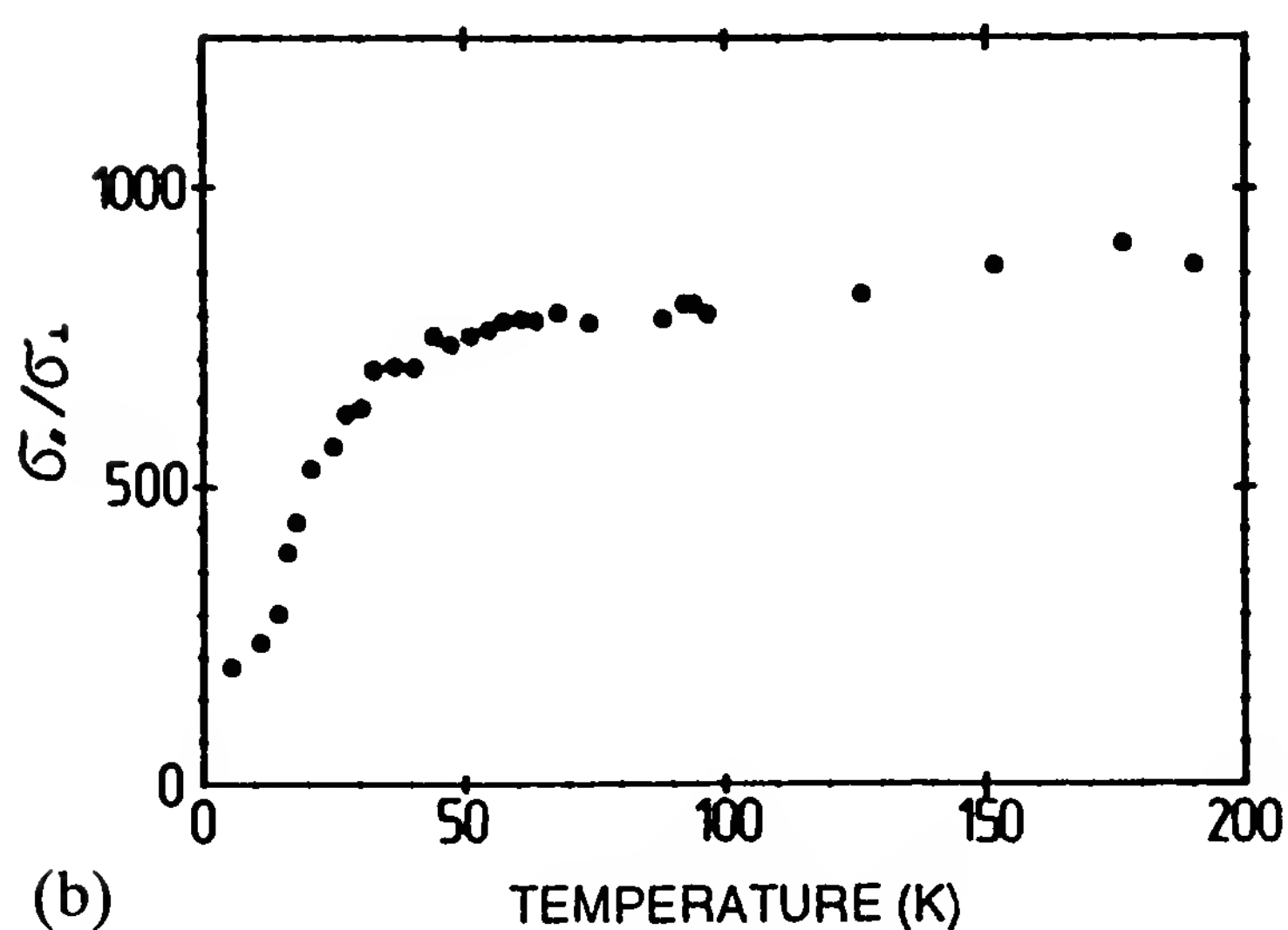
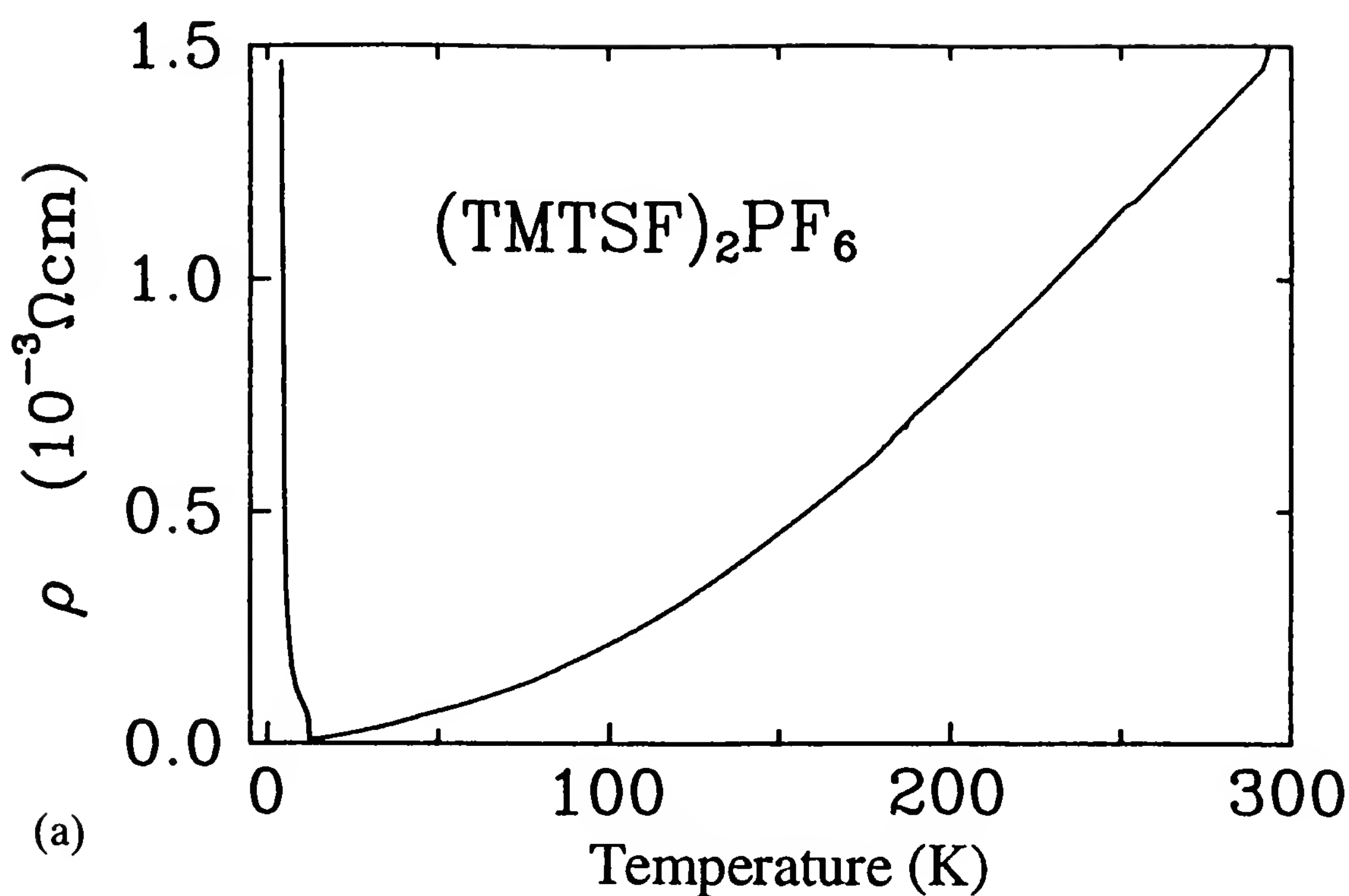


Figure 12 (a) Temperature dependence of the longitudinal resistivity of $(\text{TMTSF})_2\text{PF}_6$ obtained with the clamped contact technique. (From W. Kang, private communication, and O. Traetteberg, Thesis, Univ. Orsay, 1993.) (b) The conductivity anisotropy is temperature independent as long as the transverse motion remains incoherent. Data for $(\text{TMTSF})_2\text{PF}_6$ under 12 kbar. (After Ref. 6.)

at room temperature according to Eq. (23). Until very recently the temperature dependence of the longitudinal resistivity could not be measured with much accuracy because of voltage jumps occurring during the cooling procedure. However, a new contacting technique has significantly improved the quality of the data [61].

The temperature dependence of the longitudinal resistivity of $(\text{TMTSF})_2\text{PF}_6$ (or AsF_6) follows a power law $T^{1.4}$ from 300 K down to ≈ 100 K. Below 35 K, the resistivity follows the law $\rho_0 + AT^2$, which is valid down to the metal–insulator (SDW) transition [62] (Fig. 12). The term ρ_0 is close to zero for samples displaying large resistance ratios (RR) between room temperature and the temperature corresponding to the minimum of the resistance. Very different RR values can be found in a given batch of samples ranging from 800 to 30. For a sample with $\text{RR} = 260$, values of $\rho_0 = 0$ and $A = 0.04 \mu\Omega \cdot \text{cm} \cdot \text{K}^{-2}$ are found [62] (Fig. 13). This result suggests that the inelastic electron scattering is dominant in the conducting state at low temperature.

The very large pressure coefficient of the susceptibility (Fig. 14a) and conductivity in the metallic regime ($\partial \ln \sigma / \partial P \approx 25\% \text{ kbar}^{-1}$ for the $(\text{TMTSF})_2\text{X}$ series around room temperature [6]) raises a serious problem for the comparison with theory, which usually computes constant-volume temperature dependences. Hence the temperature dependence at constant pressure that is observed in actual experiments must be transformed into constant-volume data since the change of volume (due to the thermal expansion) cannot be ignored between 300 and 50 K. No detailed determinations of the constant-volume resistivity have been performed so far. However, a crude estimate of the intrinsic temperature dependence can be performed using the thermal expansion and the pressure dependence of the a axis at various temperatures [59] (Fig. 14b).

A dependence close to a linear law is observed down to 100 K. At low temperature, both the thermal expansion and the pressure coefficient are small. Therefore, the constant-volume temperature dependence of the resistivity does not deviate from the quadratic law observed under constant pressure. At this stage it is interesting to stress that the theory of the resistivity in a half-filled band conductor [63], including the strength of the coulombic repulsions as derived from NMR data (Section III.B), should lead to a more localized behavior than that observed experimentally in Fig. 14.

The Hall effect has been measured in some organic conductors. As far as $(\text{TMTSF})_2\text{ClO}_4$ is concerned, the low-field Hall constant measured at low temperature is small and positive (holes) in fair agreement with the value derived from the kinetic theory of the Hall constant for a one-

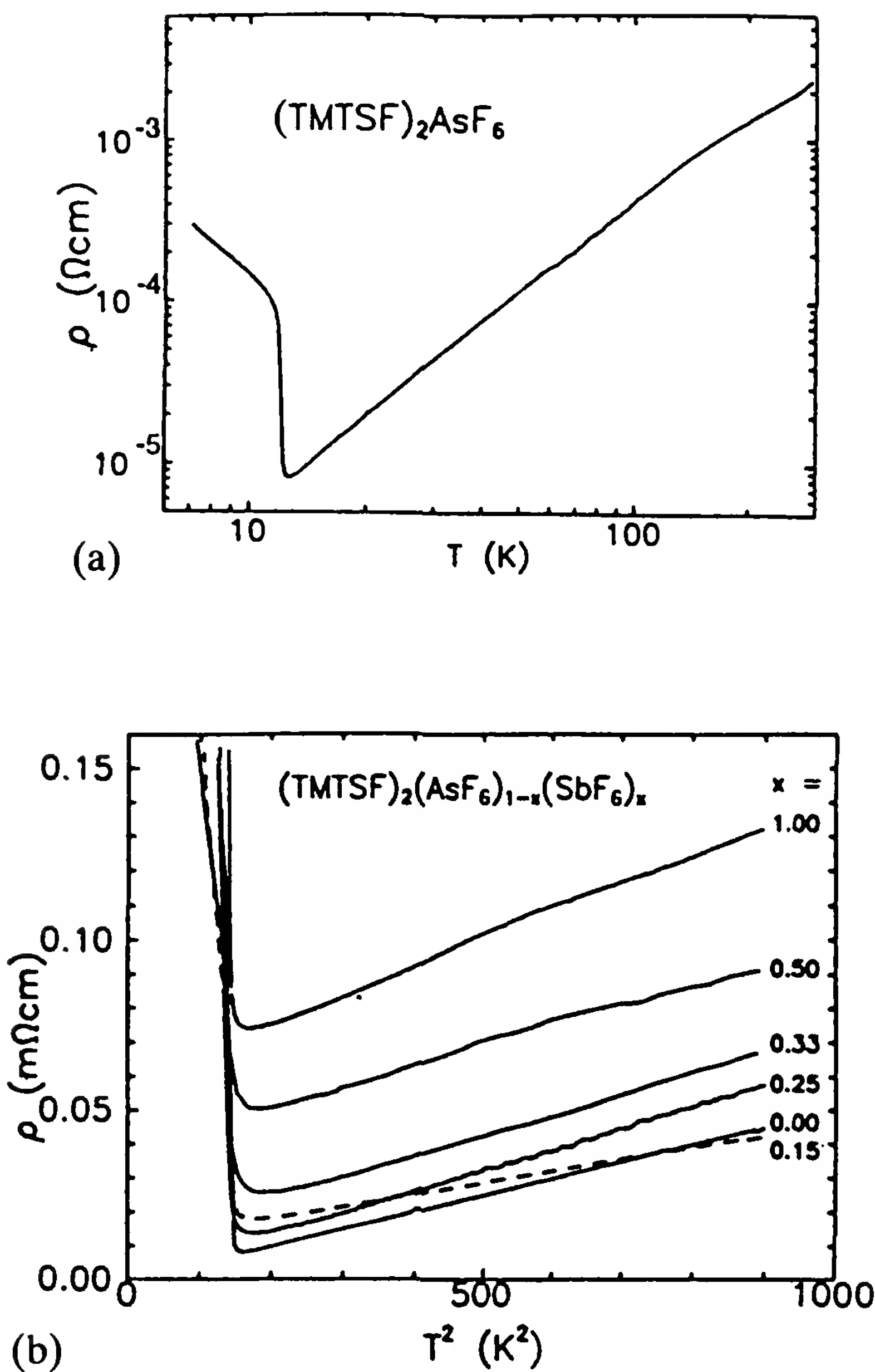


Figure 13 Temperature dependence of the resistivity of $(\text{TMTSF})_2\text{AsF}_6$, log-log plot (a) and versus T^2 (b) following the law $\rho = \rho_0 + AT_2$, where $\rho_0 = 0$ for the nonalloyed sample.

dimensional conductor [64]:

$$R_H = - \frac{\pi\rho}{2n|e|c \tan(\pi\rho/2)} \tag{24}$$

where n is the carrier density. Taking $n = 1.4 \times 10^{21} \text{ cm}^{-3}$, Eq. (24) leads to $R_{H+} = + 3.4 \times 10^{-9} \text{ m}^3/\text{A} \cdot \text{s}$ with $\rho = \frac{1}{2}$ in Eq. (24), as the weak

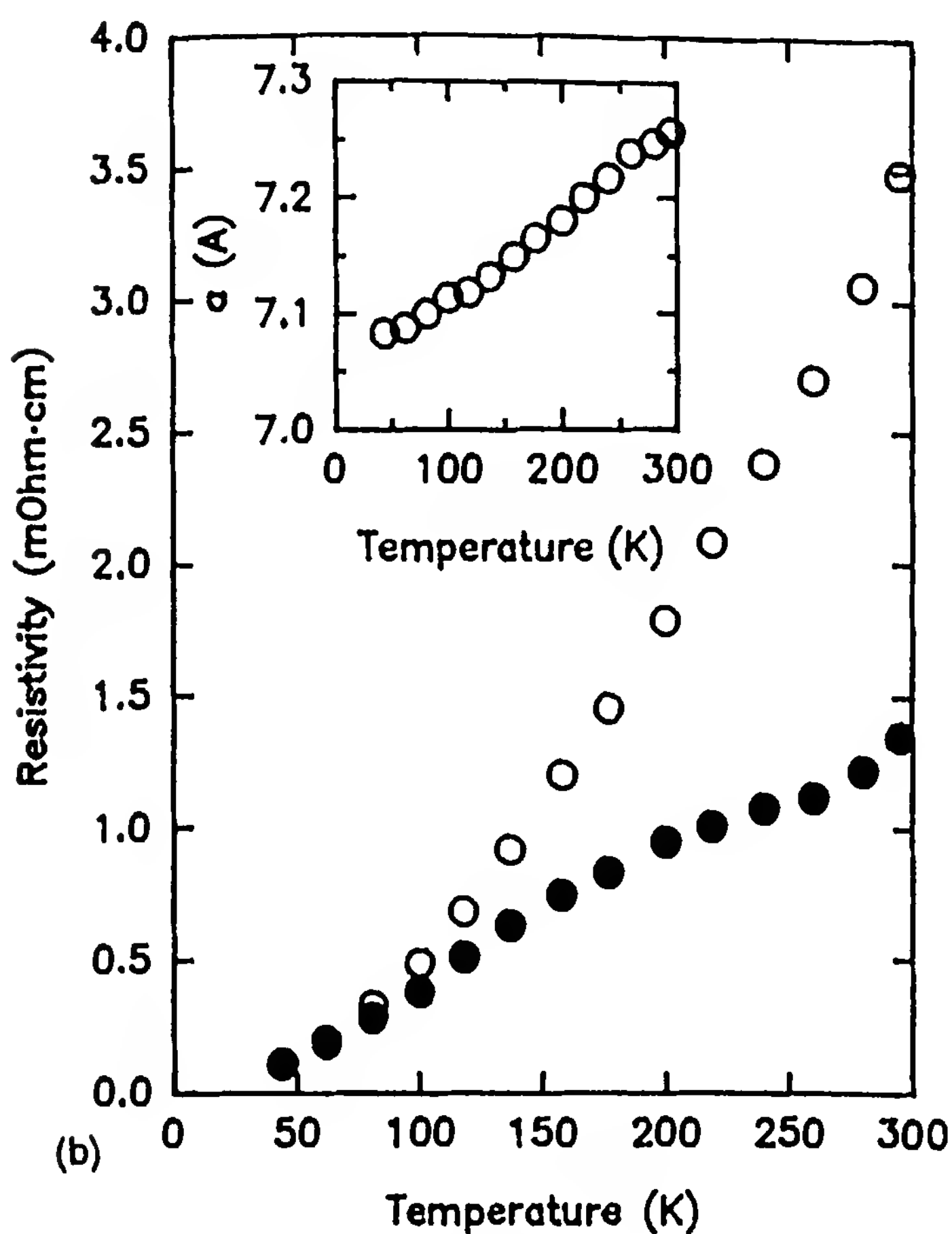
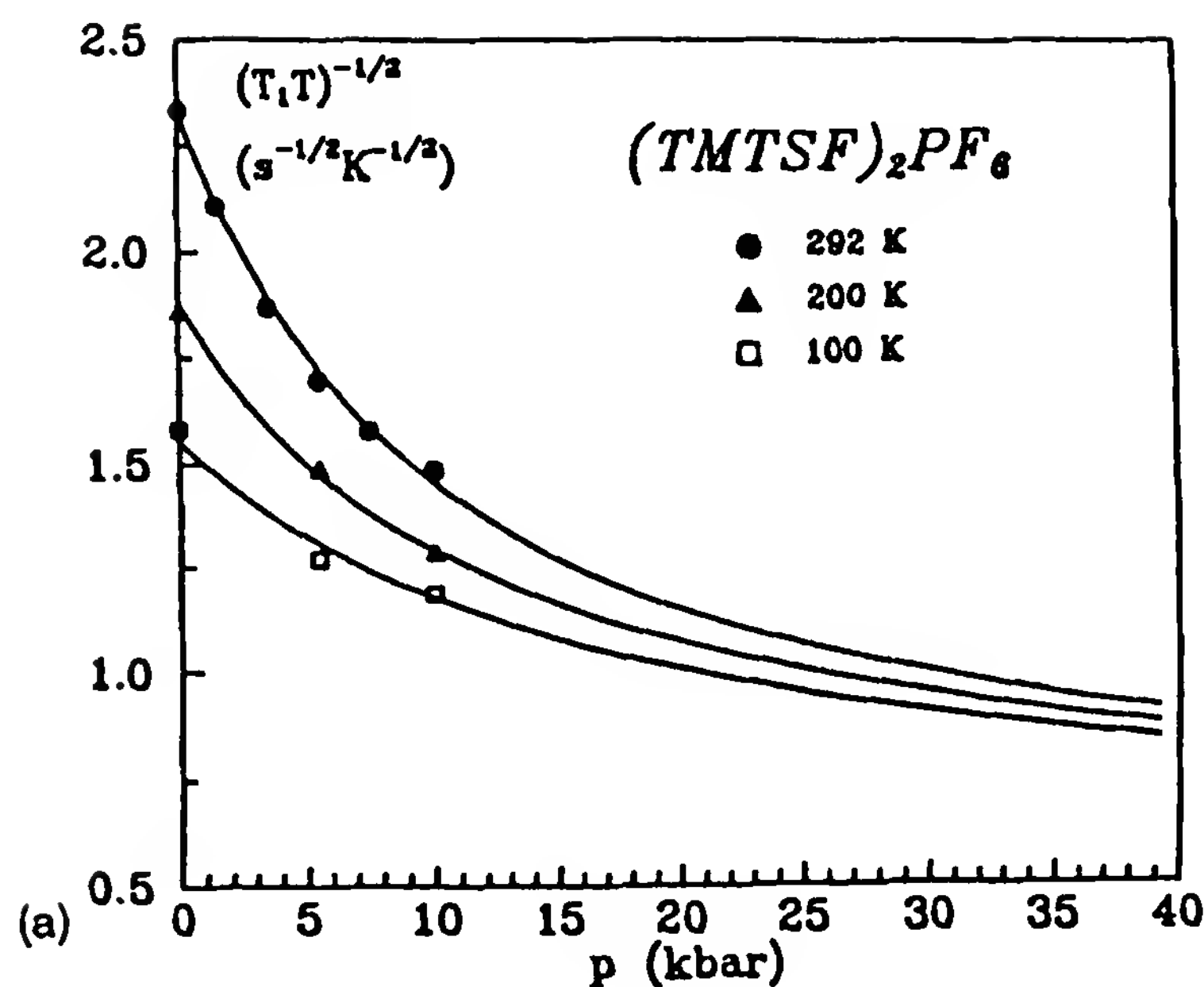


Figure 14 (a) Pressure dependence of the spin susceptibility $\chi \sim (T_1 T)^{-1/2}$ from NMR data. (From Ref. 41b.) (b) Constant-pressure and constant-volume temperature dependences of the resistivity of $(TMTSF)_2AsF_6$ derived point by point from the constant-pressure data of Fig. 12. The lattice parameters are from Ref. 33 and the pressure coefficient of the conductivity from Ref. 57.

dimerization of the TMTSF stacks does not modify significantly the band structure close to k_F . This value can be compared with the experimental determination at low-magnetic fields of $4 \times 10^{-9} \text{ m}^3/\text{A} \cdot \text{s}$ [65] (Fig. 15a).

The thermopower of single-chain conductors pertaining to the $(\text{TMTSF})_2\text{X}$ series ranges around $20 \mu\text{V/K}$ at room temperature [66]; it follows a quasi-linear temperature dependence and extrapolates to a value near zero at 0 K (Fig. 15b). The use of a one-dimensional tight-binding formulation [67a],

$$S = - \frac{\pi^2 k_B T}{3|e|} \frac{\cos(\pi\rho/2)}{2|t|\sin^2(\pi\rho/2)} \quad (25)$$

for a $\frac{3}{4}$ -filled band leads to a tight-binding band width of $\approx 1 \text{ eV}$. Both Hall effect and thermopower data suggest a rather simple picture for the electronic Fermi gas of $(\text{TMTSF})_2\text{X}$ superconductors very close to the straightforward one-dimensional model of two planar Fermi surfaces.

D. Suppression of the SDW Phase Under Pressure

Although the symmetry of TM_2X salts is triclinic, most physical features can be explained by taking an orthorhombic symmetry with the tight-binding energy dispersion written as

$$E(\mathbf{k}) = -2t_a \cos k_x a - 2t_b \cos k_y b - 2t_c \cos k_z c \quad (26)$$

with $t_a:t_b:t_c \approx 100:10:0.3$ and $t_a \approx 0.2 \text{ eV}$ for $(\text{TMTSF})_2\text{X}$ compounds [68].

The dispersion along the conducting axis can be linearized without significant modifications in the physical properties of the model provided that $kT < t_a$. Thus Eq. (26) becomes

$$E(\mathbf{k}) = E_0 + v_F(|k_x| - k_F) - 2t_\perp \cos k_y b - 2t'_\perp \cos 2k_y b \quad (27)$$

The linearized dispersion equation (27) leads to the same definition of the Fermi surface $E(\mathbf{k}) = E_F$ as that of Eq. (26) provided that $t'_\perp \approx t_\perp^2/t_a$, with $v_F \approx 2at_a$. We have neglected the dispersion along the c direction of very weak coupling.

Equation (27) leads to a Fermi surface that is only slightly distorted from the sinusoidal shape. If the last contribution in Eq. (27) is forgotten, both sheets of Fermi surface nest perfectly with the nesting vector $\mathbf{Q}_t = (2k_F, \pi/b)$. Then the spin susceptibility $\chi_0(\mathbf{q})$ becomes large near $\mathbf{q} = \mathbf{Q}_t$ and diverges logarithmically as $T \rightarrow 0$. A spin-modulated (SDW) ground state should thus be established below an ordering temperature $T_N \leq T_0$, where T_0 is the one-dimensional mean-field temperature for the SDW instability:

$$T_0 \sim E_F \exp \left[- \frac{1}{N(E_F)U} \right] \quad (28)$$

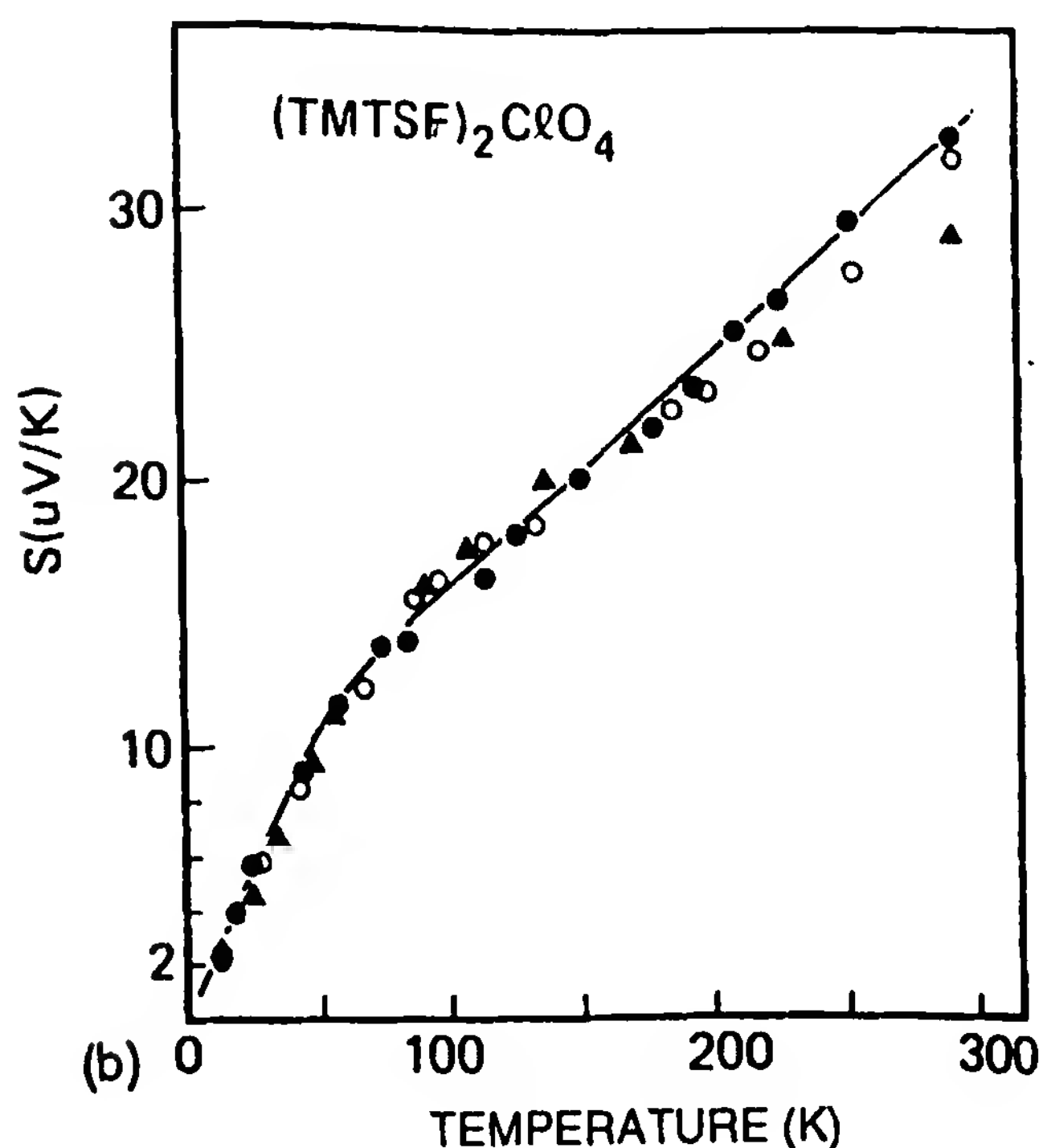
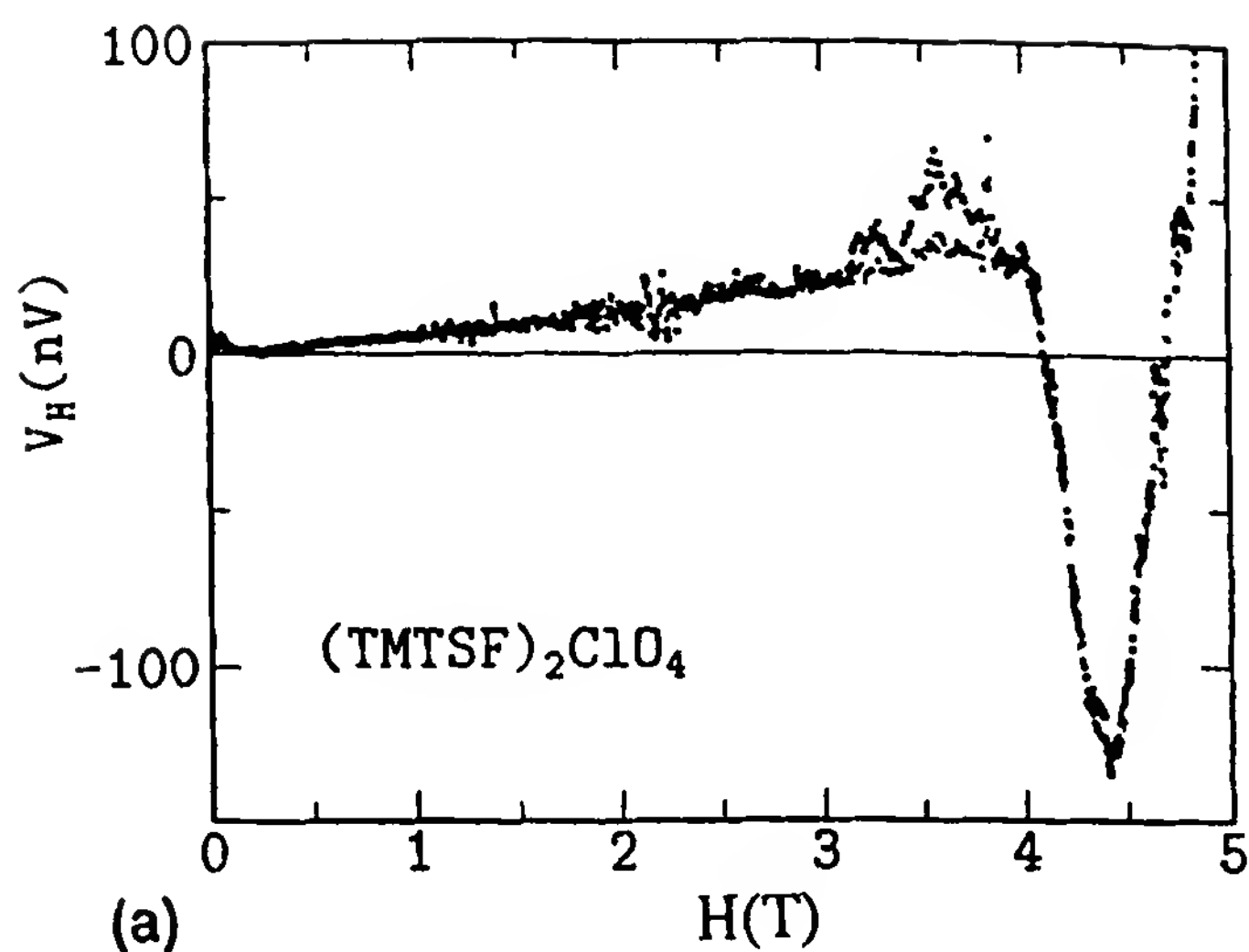


Figure 15 (a) Temperature dependence of the Hall voltage in the “relaxed” state of $(\text{TMTSF})_2\text{ClO}_4$ at $T = 0.35$ K. The outset of a FISHW phase is visible at 4 T. (From W. Kang, private communication.) (b) Thermopower data of $(\text{TMTSF})_2\text{ClO}_4$. (After Ref. 67b.)

The Fermi surface departs from perfect nesting when the second harmonic contribution in Eq. (27) becomes a relevant contribution, namely if $t'_\perp \approx T_0$. Thus the nesting of the Fermi surface is frustrated and the susceptibility $\chi_0(\mathbf{q})$ no longer presents any logarithmic divergence at $\mathbf{q} = \mathbf{Q}$, as $T \rightarrow 0$ but only a relative (nondivergent as $T \rightarrow 0$) maximum at a

vector \mathbf{Q}_0 (close to \mathbf{Q}_l), which optimizes the nesting of the nonsinusoidal Fermi surface (Fig. 16). This intermediate situation for t'_\perp can still lead to a SDW instability which is suppressed when t'_\perp is increased (by applying pressure or changing the anion $PF_6 \rightarrow ClO_4$). There thus exists a critical value for t'_\perp above which a nondistorted quasi-one-dimensional conductor is stabilized at low temperature (Fig. 16). This critical value amounts to about $t'_{\perp cr} \approx T_0 (\approx 1 - 2 \text{ meV})$. Given $t_\perp \approx 20 \text{ meV}$, the band structure anisotropy makes t'_\perp very close to the critical value already at ambient pressure. This situation explains why only a modest pressure of 9 kbar is enough to suppress the SDW ground state.

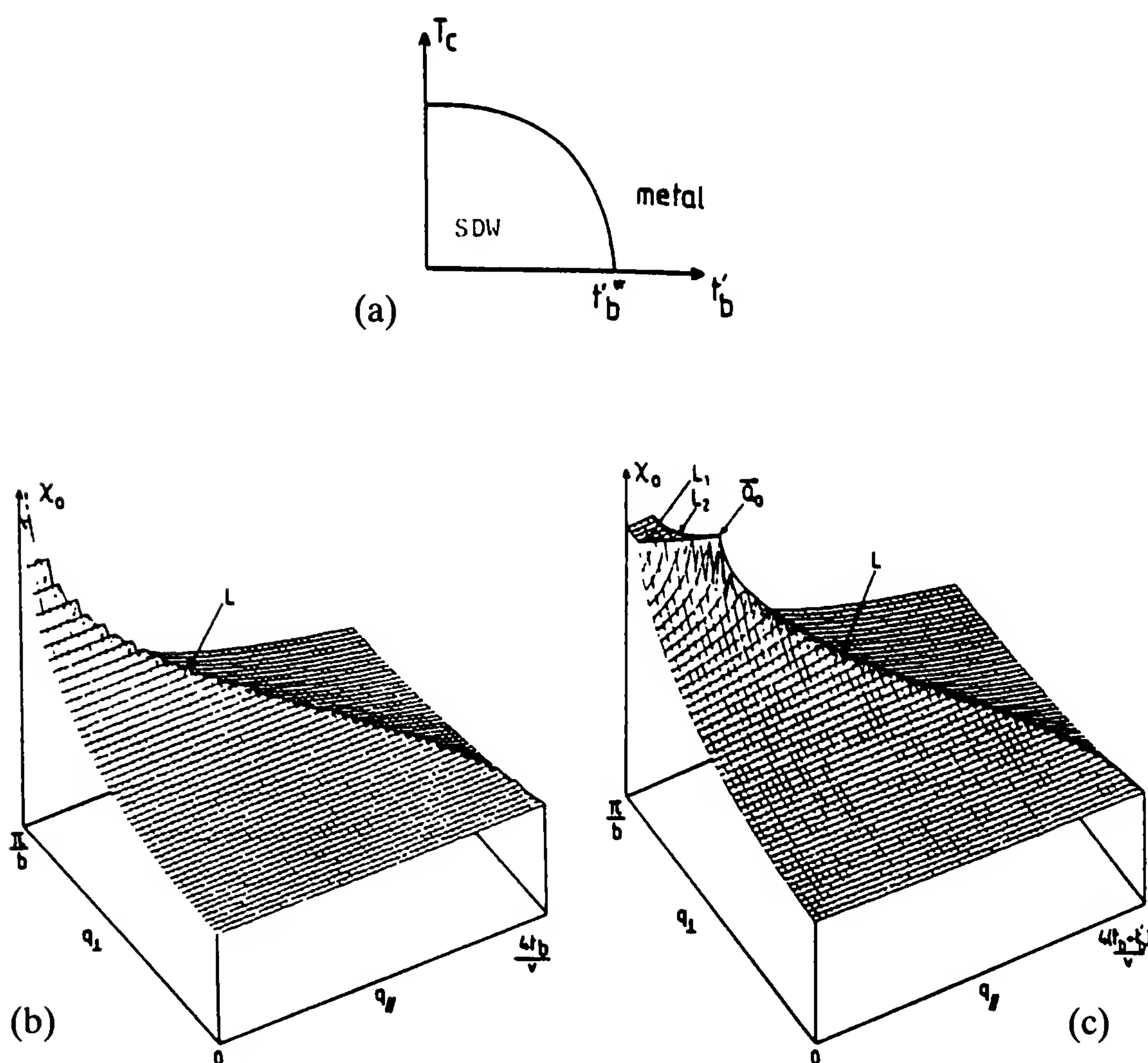


Figure 16 (a) The SDW ground state of $(TMTSF)_2X$ compounds is stable as long as $t'_b < t'_{cr}$. (b) At $t'_b = 0$, there is a logarithmic divergence of $\chi_0(\mathbf{q})$ at $\mathbf{Q} = (2k_F, \pi/b)$. (c) $\chi_0(\mathbf{q})$ is no longer divergent at $t'_b = 0$; the maximum of $\chi_0(\mathbf{q})$ occurs at $\mathbf{Q}_0 = (2k_F + \mathbf{Q}_\parallel, \mathbf{q}_\perp)$. (After Ref. 68a.)

E. Anion-Ordering Phase Transition

Another kind of semiconducting ground state is observed in the salts of the TM_2X series when the anion is noncentrosymmetric. That the sites occupied by anions are inversion centers of the structure thus implies two possible orientations for noncentrosymmetric anions. The anions are disordered at room temperature and both orientations have the same statistical occupancy. However, entropy is gained at low temperature if they order at a temperature T_{AO} . The new periodicity of the lattice is important for the one-dimensional electron gas, since a doubling of the anion periodicity along the stacking axis opens a gap at the Fermi level that stabilizes an anion-ordered semiconducting ground state [69].

Various ground states of salts with noncentrosymmetric anions can be classified according to their anion periodicity. In $(\text{TMTSF})_2\text{ClO}_4$, the anion order at $T_{\text{AO}} = 24$ K is characterized by the wave vector $(0, \frac{1}{2}, 0)$ [70]. The periodicity is doubled along the b direction but is left unchanged along the stacking axis (Fig. 17a,b). This kind of ordering should thus have a minor influence on the conducting properties, although it may significantly disturb the stability of the field-induced SDW phases (see Section VII.A).

The perfect long-range anion ordering of ClO_4 anions cannot be reached if the compound is quickly cooled through the anion-ordering temperature (<1 K/min). The compound is thus stabilized in a “quenched” state namely **Q** state at low temperature at variance with the “relaxed” state that is obtained after a slow cooling procedure (>1 K/min) [71]. The Fermi surface of the **Q** state does not present gaps at $k_y = \pm \pi/2b$. It thus resembles the quasi-one-dimensional Fermi surface of $(\text{TMTSF})_2\text{PF}_6$ [72], and a SDW ground state establishes below 6 K (Fig. 17c) [71]. The low value of the resistivity in the **Q**-SDW ground state of $(\text{TMTSF})_2\text{ClO}_4$ suggests that it may be more appropriately described by a semimetal.

The anion ordering in $(\text{TMTSF})_2\text{ReO}_4$ $(\frac{1}{2}, \frac{1}{2}, 0)$ [73] opens a large gap at 180 K which stabilizes an insulating ground state [6]. Moreover, the type of anion ordering can be changed by a pressure that modifies the balance between anion–anion electrostatic coupling and anion–organic stack coupling. For example, the anion order of $(\text{TMTSF})_2\text{ReO}_4$ becomes $(0, \frac{1}{2}, \frac{1}{2})$ at low temperature under a pressure of 12 kbar, and a superconducting state is stable below 1.3 K [74] (Fig. 17d).

The situation for $(\text{TMTSF})_2\text{NO}_3$ is somewhat different since the triangular NO_3 anion adopts a $(\frac{1}{2}, 0, 0)$ periodicity below $T_{\text{AO}} = 45$ K [74]. This new lattice symmetry implies a folding of the band structure about planes $k_x = \pm \pi/2a$. Consequently, the anion ordering triggers a transition between a quasi-one-dimensional conductor at high temperature and a two-

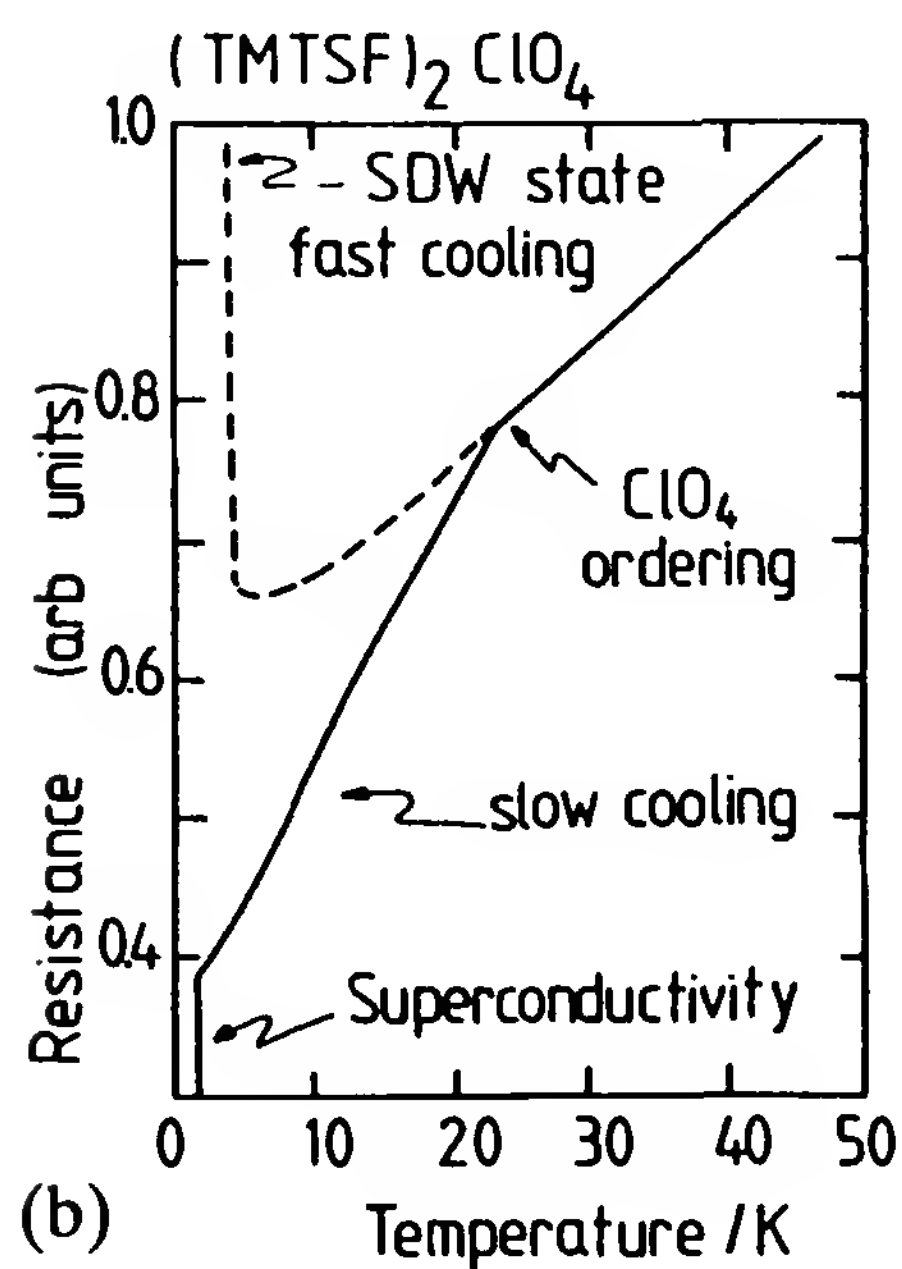
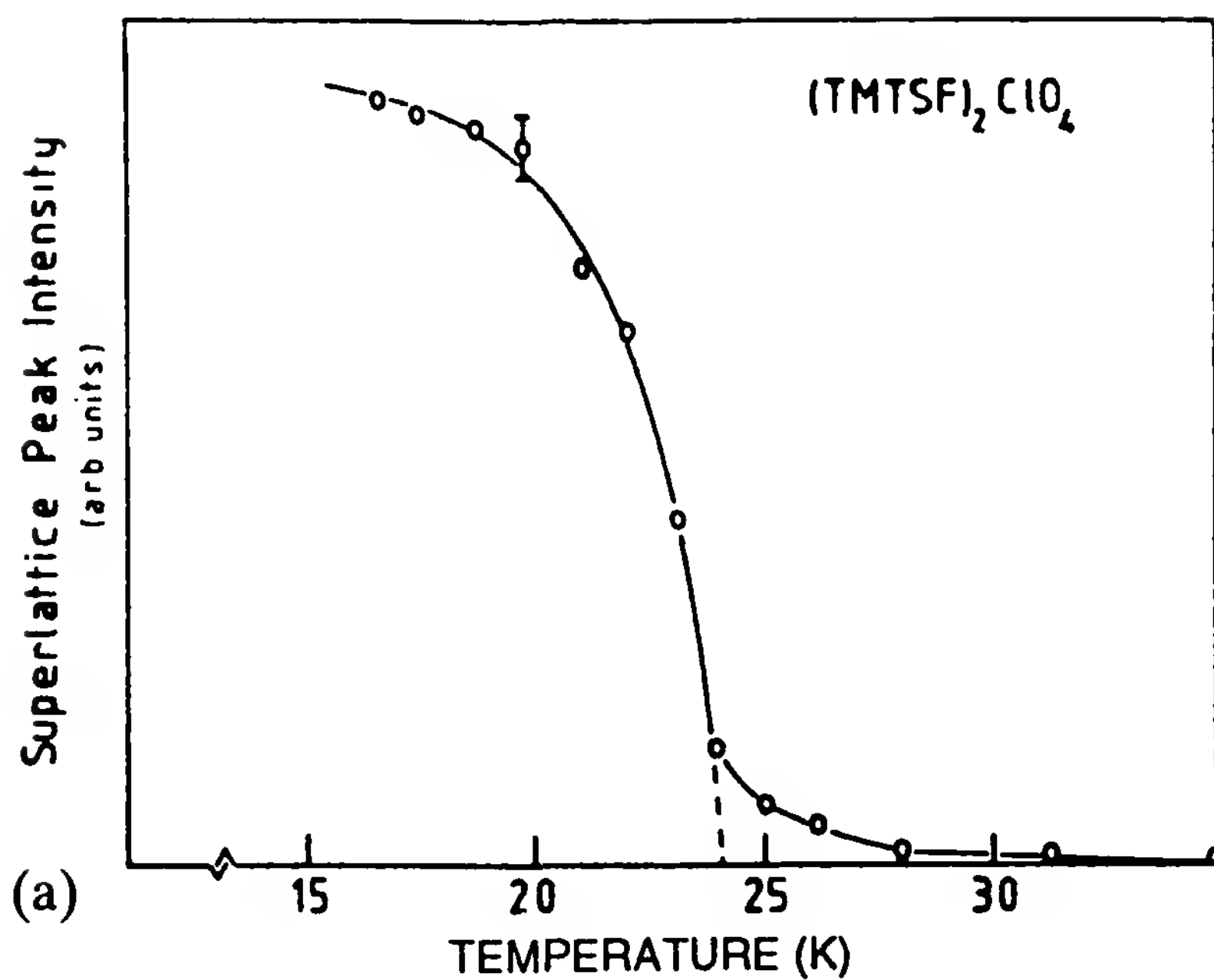


Figure 17 (a) Anion ordering $(0, \frac{1}{2}, 0)$ in $(\text{TMTSF})_2\text{ClO}_4$ at 24 K (from Ref. 75). (b) Different ground states are obtained in slow-cooled and quenched samples. (After S. Tomic, Thesis, Univ. Orsay, 1987, and Ref. 71.) (c, d) Phase diagram for the anion ordering [from Ref. 74] and transport properties of $(\text{TMTSF})_2\text{ReO}_4$. (From S. S. P. Parkin, D. Jérôme, and K. Bechgaard, *Mol. Cryst. Liq. Cryst.* 79:213 (1982).)

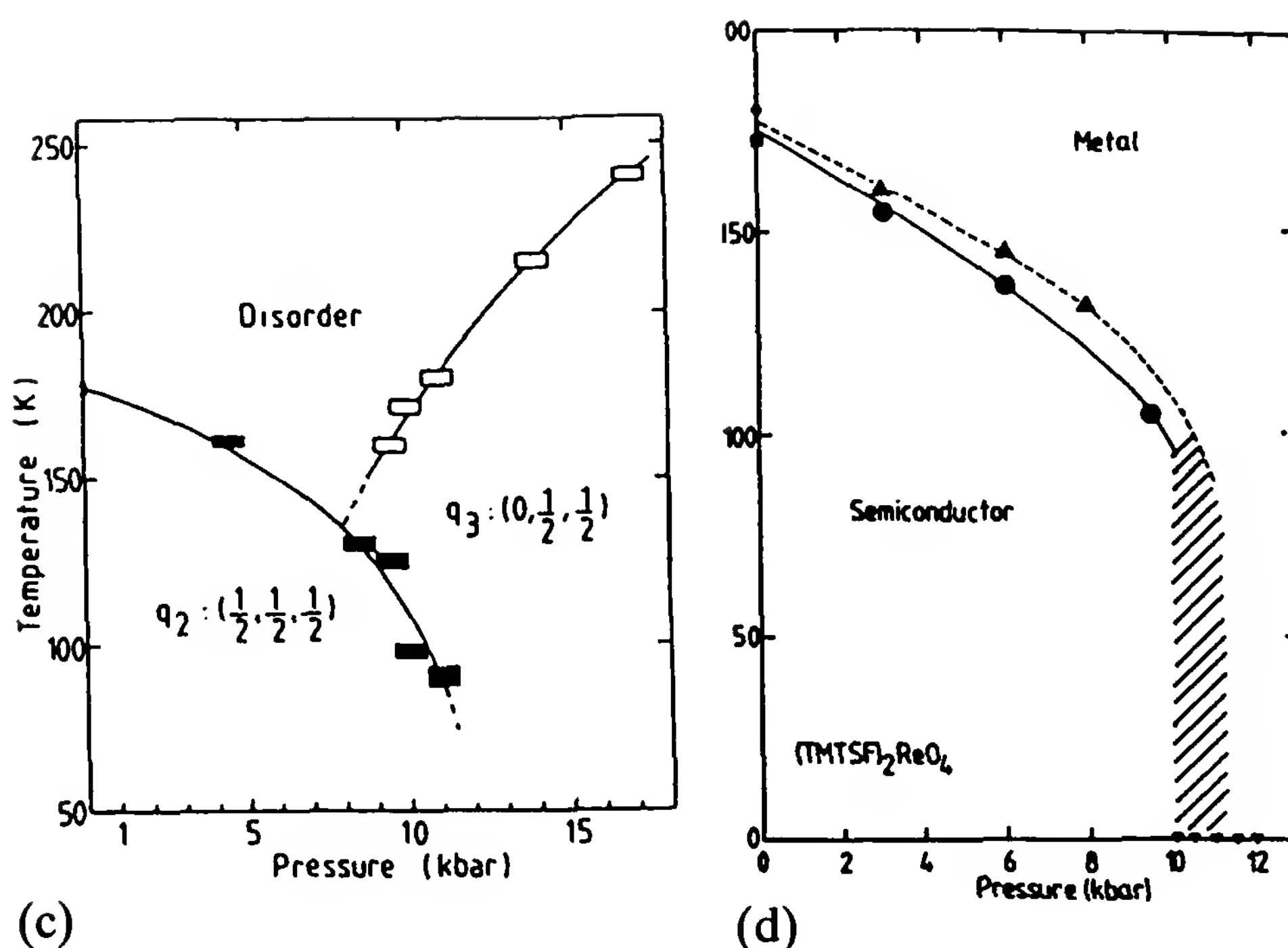


Figure 17 Continued

dimensional semimetal below 45 K. Hence the antiferromagnetic ground state that establishes below 9 K in this compound should be considered as the result of an excitonic instability of nested two-dimensional Fermi surfaces [76] instead of the quasi-one-dimensional instability observed in $(\text{TMTSF})_2\text{PF}_6$ (Fig. 18). The difference in anion-ordering structure may be responsible for the absence of field-induced SDW phases in $(\text{TMTSF})_2\text{NO}_3$ (see Section VII.A).

IV. SUPERCONDUCTING PROPERTIES OF MOLECULAR CONDUCTORS

A. Superconducting Parameters of Molecular Superconductors

Differences between the two major series of superconducting materials, TM_2X and ET_2X , are clear cut. A salient feature of superconductivity in the quasi-one-dimensional TM_2X series is the common border existing between superconducting and magnetic phases, which provides an upper limited value smaller than 2 K. This limitation is apparently independent of the anion symmetry since attempts to force the stabilization of superconductivity at lower pressures in the compound $(\text{TMTSF})_2\text{ReO}_4$, where a pressure of 12 kbar is necessary to prevent the ReO_4 anion ordering at low temperature from opening a gap at the Fermi level have failed to raise

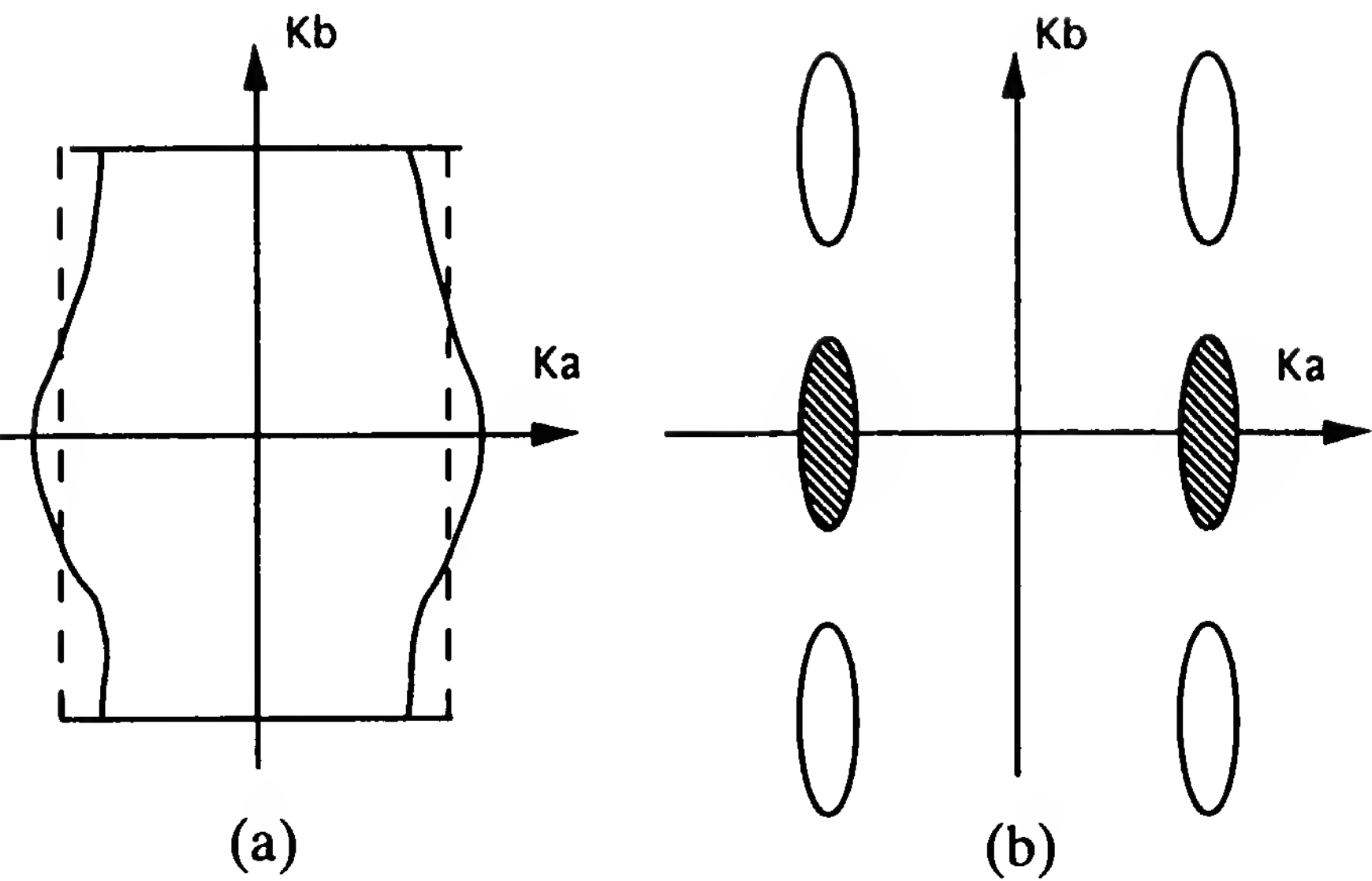


Figure 18 Fermi surface of $(\text{TMTSF})_2\text{NO}_3$ (schematic), in the quasi-one-dimensional regime (a) and below the anion ordering transition (b).

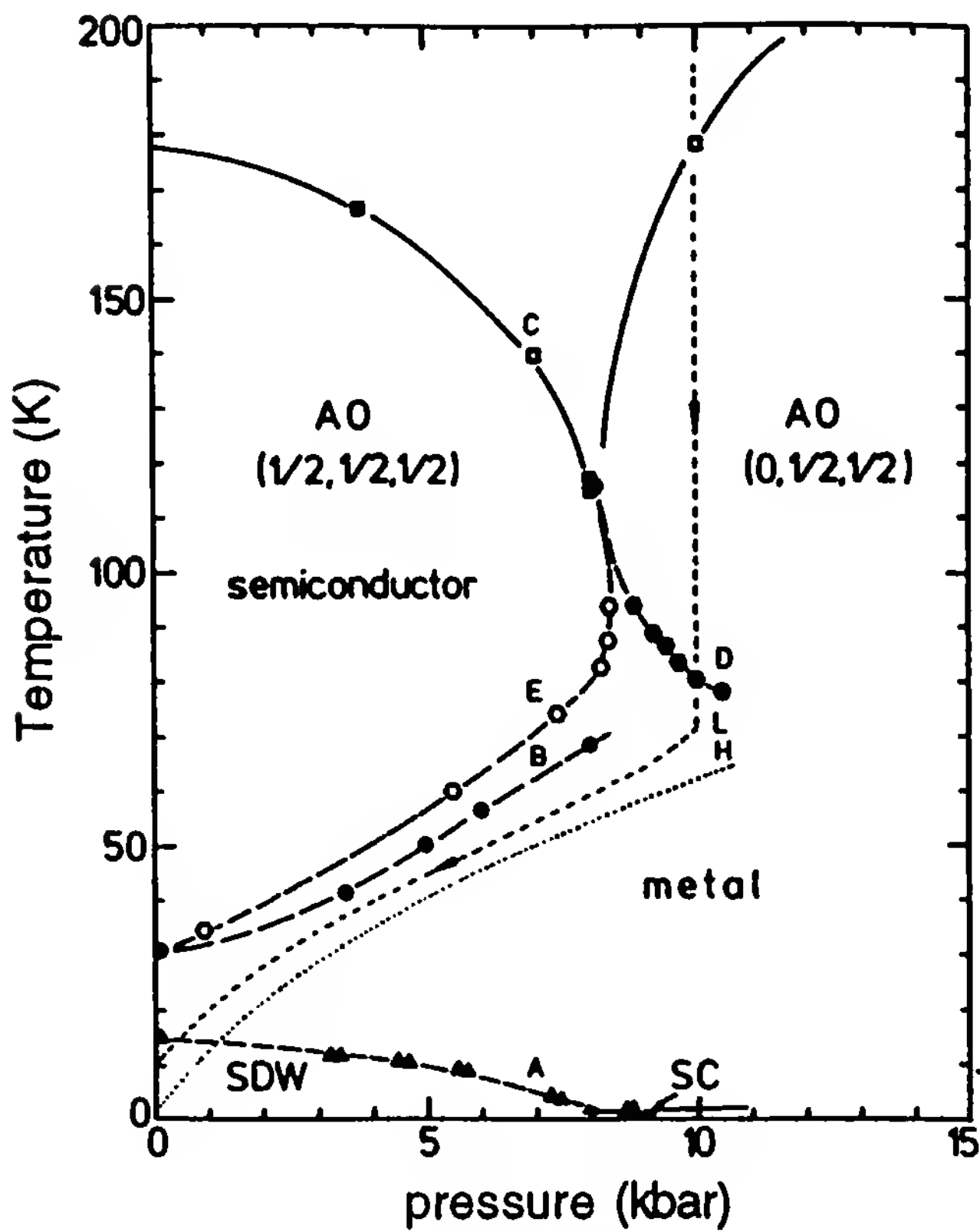


Figure 19 Hidden SDW ground state of $(\text{TMTSF})_2\text{ReO}_4$ obtained after depressurization of the sample at low temperature. (After Ref. 77.)

T_c above 1.2 K [77] (Fig. 19). The behavior of $(\text{TMTSF})_2\text{ReO}_4$ emphasizes the deeply rooted competition that exists between superconductivity and magnetism in the TM_2X series. It is clear that the low values of T_c are a direct consequence of the one-dimensional character of the Fermi surface. It is a situation where fluctuations can be very efficient in suppressing the superconducting long-range order down to low temperature. Consequently, T_c values higher than 1 to 2 K should be searched for in materials where the Fermi surface is less favorable for the stabilization of antiferromagnetism at low temperature.

Figure 20 displays the superconducting transition of $(\text{TMTSF})_2\text{PF}_6$ salts observed by resistivity data [6,9]. What is remarkable in Fig. 20 is the strong temperature dependence of $\rho(T)$ above T_c , unlike the behavior of regular metals, for which the resistivity is limited at low temperature by temperature-independent elastic scattering. The behavior of the temperature dependent resistivity at low temperature in TM_2X compounds has been ascribed to a precursor effect above T_c [6].

The observation of a Meissner flux expulsion [78] and of specific heat anomaly [79] supports the picture of bulk superconductivity (Fig. 21). On a C/T versus T^2 plot, the specific heat of $(\text{TMTSF})_2\text{ClO}_4$ displays a very large anomaly at 1.2 K and follows the law

$$\frac{C}{T} = \gamma + \beta T^2 \quad (29)$$

with $\gamma = 10.5 \text{ mJ} \cdot \text{mol}^{-1} \cdot \text{K}^{-2}$ corresponding to $N(E_F) = 2.1 \text{ states} \cdot \text{eV}^{-1} \cdot \text{mol}^{-1}$ [$N(E_F) = 3\gamma/2\pi^2k_B^2$] and $\beta = 11.4 \text{ mJ} \cdot \text{mol}^{-1} \cdot \text{K}^{-4}$. Superconductivity in the TM_2X series is not restricted to be containing molecules as shown by the stabilization of a superconducting state below 0.8 K in $(\text{TMTTF})_2\text{Br}$ under a pressure of 25 kbar, (see Note added in proof).

The $(\text{ET})_2\text{X}$ series with two-dimensional Fermi surfaces has indeed provided superconducting compounds with higher T_c : up to 8.1 K for $\text{X} = \text{I}_3^-$ [14,15] and even up to 10 to 12 K for $\text{X} = \text{Cu}(\text{SCN})_2^-$ [16], $\text{Cu}[\text{N}(\text{CN})_2]\text{Br}^-$ [18] (Fig. 22). Some parameters describing the superconducting state of molecular superconductors are summarized in Table 3.

It is not yet clear whether these layered superconductors should be considered as three-dimensional anisotropic superconductors or as two-dimensional superconductors with a three-dimensional ordering resulting from a Josephson coupling between the layers [80]. The nature of the pairing mechanism for one- and two-dimensional superconductors has obviously been the matter of several conjectures, but this question is still open.

The most salient feature of one-dimensional organic superconductivity is the strong sensitivity to the presence of impurities and even nonmagnetic lattice defects as observed in both families of superconductors [81] (the

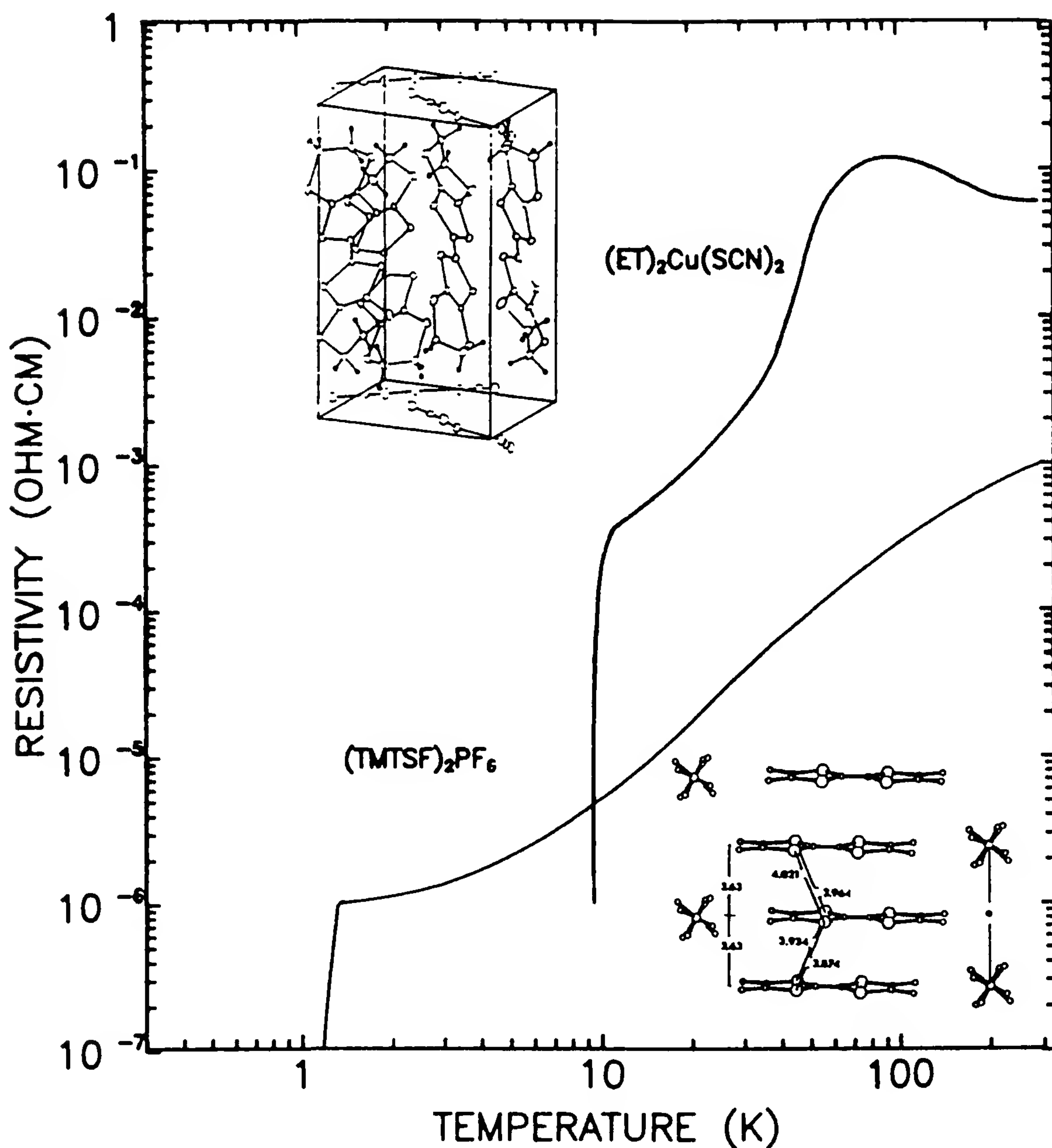


Figure 20 Superconducting transition of $(\text{TMTSF})_2\text{PF}_6$ under 8 kbar and $\kappa - (\text{ET})_2\text{Cu}(\text{SCN})_2$ at ambient pressure.

latter being unusual in conventional superconductors), which could point toward the existence of an anisotropic gap in the superconducting state. Pairing of carriers through the exchange between neighboring chains of an antiferromagnetic fluctuation is a possibility for gap anisotropy in the TM_2X series [82]. The absence of spin-lattice relaxation time anomaly at T_c in the TM_2X [83] series (Fig. 22) can also support the possibility of gap anisotropy [84].

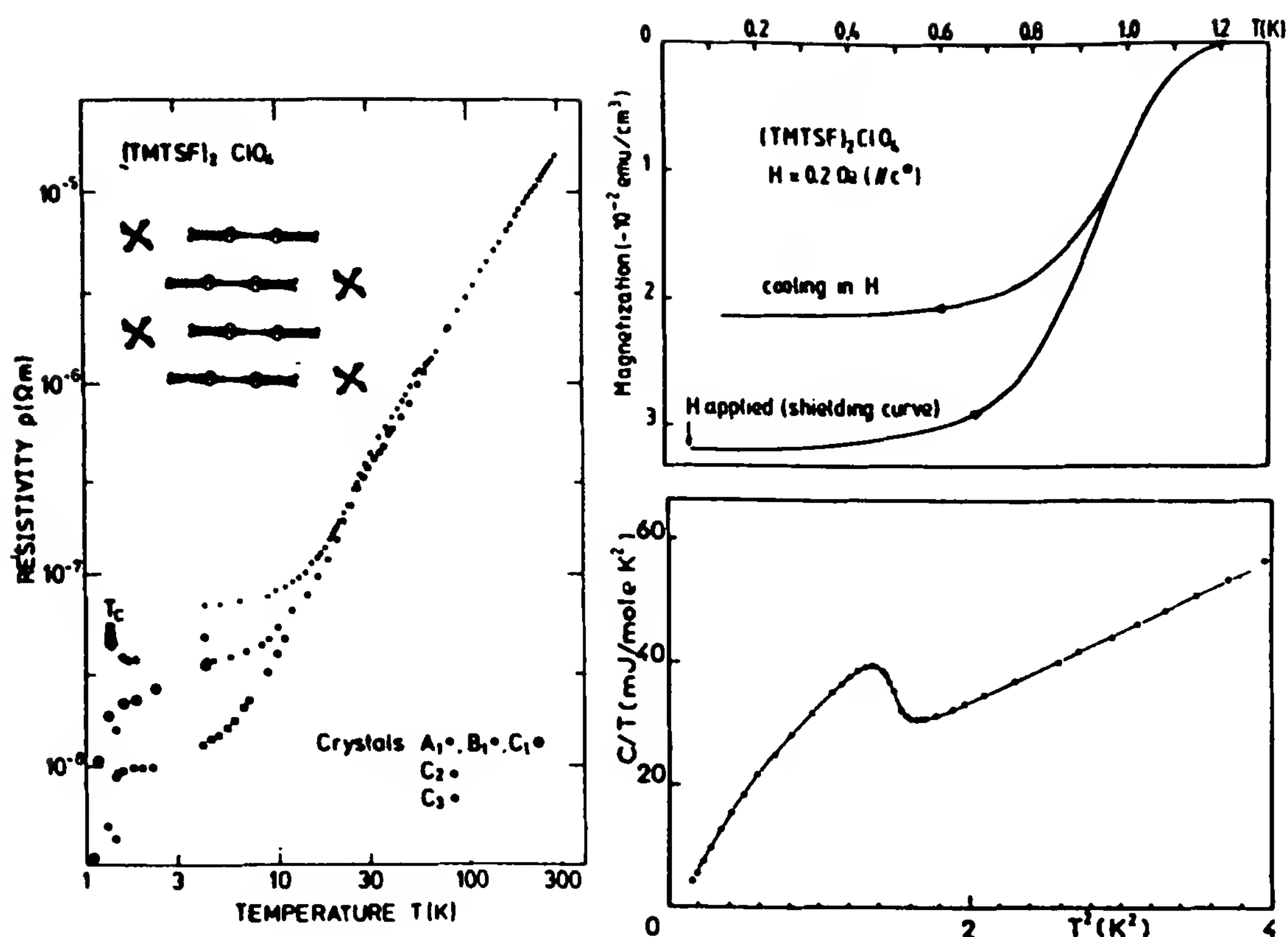


Figure 21 Superconductivity in $(\text{TMTSF})_2\text{ClO}_4$ by transport [10], magnetic [78], and specific heat data [79].

It is also remarkable to point out that superconductivity has also been discovered in a family of charge-transfer compounds based on the molecule $\text{M}(\text{dmit})_2$, with $\text{M} = \text{Ni}, \text{Pd}$ with $T_c = 1.6 \text{ K}$ under 7 kbar [12] (Fig. 23). In this interesting series, structural and NMR studies support the picture of a one-dimensional Fermi surface, and the ground state competing with superconductivity is a charge density wave modulation driven by the $\text{Ni}(\text{dmit})_2$ stacks [85].

B. Isotope Effect

Isotopic shift experiments are also important in organic superconductors, but their interpretation in all three classes must be treated with great caution, as many extrinsic effects may affect T_c in these materials. The isotopic deuterium labeling of methyl or ethylene groups located at the outskirts of the molecule may result in a significant T_c shift, which can be related to the known very large pressure coefficient of T_c in organic su-

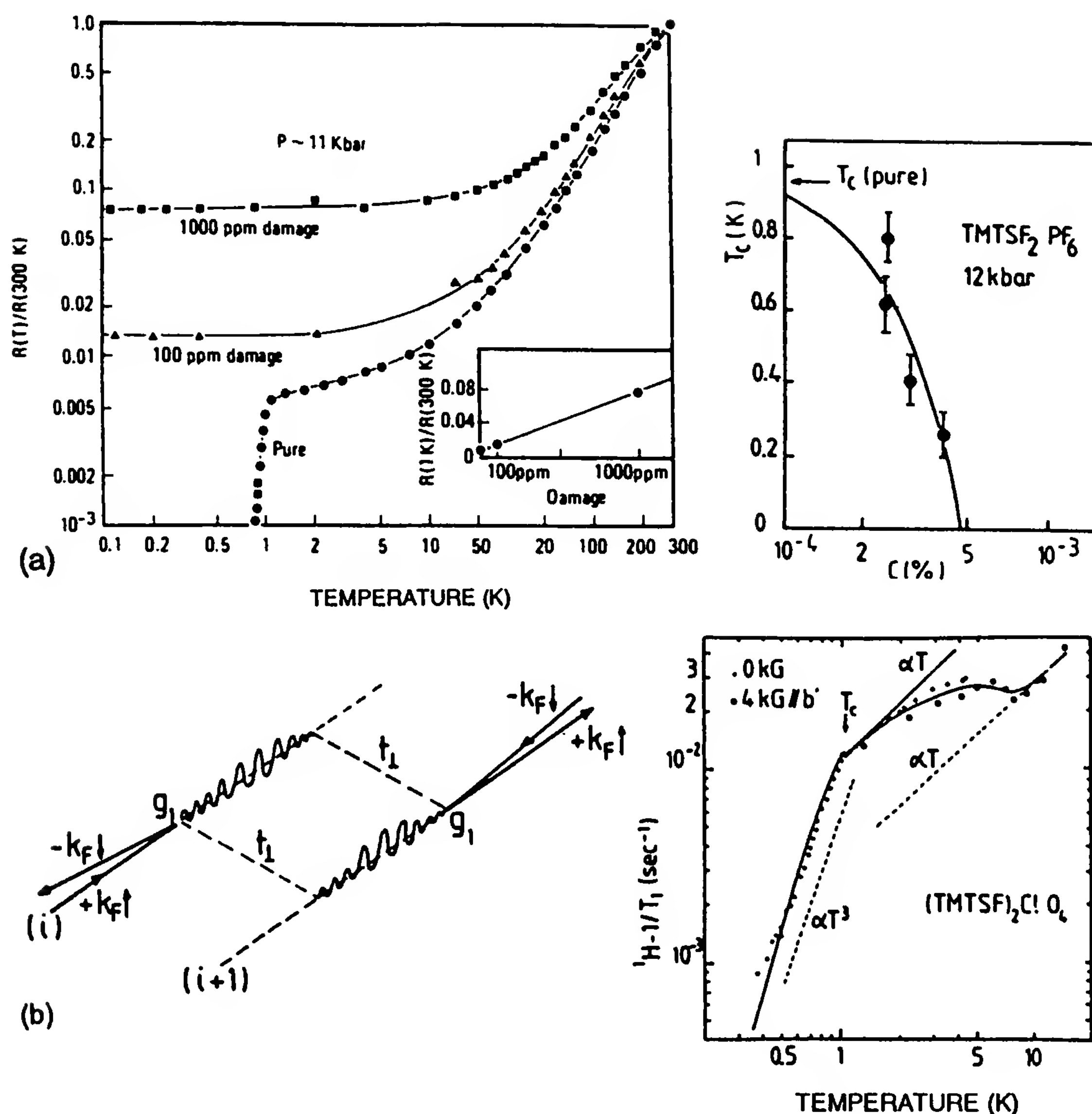


Figure 22 (a) The superconducting transition temperature is very sensitive to defects created by proton irradiation (left) (after Ref. 81a) and neutron irradiation (right) (after Ref. 81b). (b) Schematic representation of the interchain exchange of $2k_F$ spin fluctuations proposed by Bourbonnais and Caron [82] and temperature dependence of $1/T_1$ in $(\text{TMTSF})_2\text{ClO}_4$, showing the absence of any Hebel-Slichter anomaly at T_c and suggesting a power law temperature dependence in the superconducting state [83].

perconductors. A variety of data have been published in deuterated TM and ET salts [86,87].

T_c is also known to be extremely sensitive to disorder and sample purity [81,88]. Therefore, the most reliable experiments are those in which the isotopic substitution is performed on an active site of the molecule and

Table 3 Parameters Describing the Superconducting Phase of Molecular Superconductors

	One-dimensional	Two-dimensional	Three-dimensional
Compounds	TM ₂ X	�-ET ₂ X	A ₃ C ₆₀
T _c (K)	X = ClO ₄ 1.2	X = Cu(SCN) ₂ 9 X = Cu[N(CN) ₂]Br 12	A = K 19 A = Rb ₂ Cs 33
H _{c1} (0) (10 ⁻⁴ T)	a 0.2 b 1 c 10	(a, b) 1 c 45	1.3 (K ₃ C ₆₀)
H _{c2} (0) (T)	a 2.8 b 2.1 c 0.16	(a, b) 30 c 2	49 (K ₃ C ₆₀)
�(0) (�)	a 700 b 335 c 20	(a, b) 174 c 7	26 (K ₃ C ₆₀)
�(0) (�)		5000-10,000	2400-4800 (K ₃ C ₆₀)

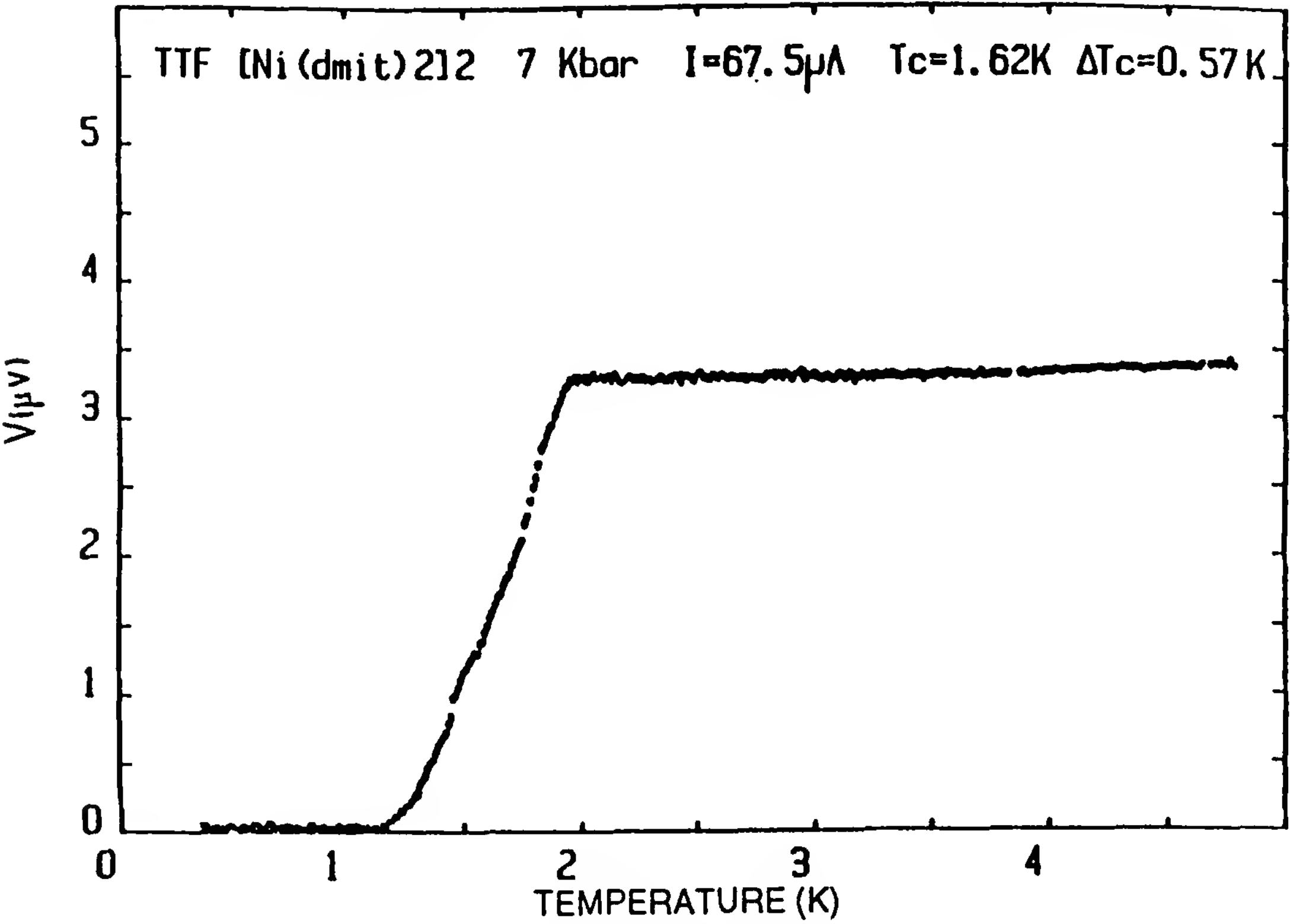


Figure 23 Superconductivity in TTF [Ni(dmit)₂]₂ under 7 kbar. (After Ref. 12.)

does not induce any lattice parameter modification. Two such studies have been reported, with ^{13}C substitution of the central double bond of the ET molecule in κ phases of $\text{Cu}[\text{N}(\text{CN})_2]\text{Br}$ and $\text{Cu}(\text{SCN})_2$ salts [89] and on the β_{H} phase of I_3 [90].

As far as κ phases are concerned, the isotope shift was found to be zero within a 0.1% accuracy [89] and confirmed in Ref. 90, whereas $\beta_{\text{H}}(\text{ET})_2\text{I}_3$ has revealed an isotopic downshift $\Delta T_c/T_c$ in between -1.25 and -3.75% [90]. In both cases the isotope shift of the Raman-active a_g $\text{C}=\text{C}$ stretching modes of the ET molecule were found to be in agreement with molecular dynamics predictions $\Delta\omega/\omega = -1.8\%$.

Within the canonical weak-coupling BCS theory assuming the $\text{C}=\text{C}$ modes to be the most strongly coupled to electrons should lead to a temperature shift of $\Delta T_c/T_c = \Delta\omega/\omega = -1.8\%$, which lies within the experimental window found for $\beta_{\text{H}}(\text{ET})_2\text{I}_3$ but is in clear disagreement with the κ phase reports. The present experimental status could support a pairing mechanism through intramolecular vibrations involving $\text{C}=\text{C}$ bonds in $\beta_{\text{H}}(\text{ET})_2\text{I}_3$ [91], but such a mechanism seems to be ruled out for the κ phases, which have a 30% higher T_c but do not show marked isotopic shifts for T_c .

A recent study of the isotope shift in ^{34}S -substituted κ phases [92] has ruled out either a dominant role for the $\text{C}-\text{S}$ stretching motions or a conventional BCS isotope effect involving the ET molecules as the relevant mass entity. There is still the possibility for the pairing in κ phases to be related to a non-phonon-mediated mechanism such as the interplane exchange of spin fluctuations as proposed by Bourbonnais and Caron [82] in the context of one-dimensional superconductors.

Understanding the pairing mechanism is apparently less of a problem for superconducting fullerenes. Although experiments on isotopic enrichment of C_{60} with ^{13}C atoms have led to a standard sign of the shift (T_c is smaller in ^{13}C -enriched samples), there remains much uncertainty about its amplitude, with α ranging from ~ 0.3 up to ~ 1.4 [93a] (where α is related to the C_{60} molecular mass by $T_c \sim M^{-\alpha}$ and amounts to 0.5 in a BCS formulation), high-pressure experiments have played an important role in clarifying the origin of the attractive pairing interaction.

C. Role of Pressure in Fullerenes

The critical temperatures of doped fullerenes pertaining to the series $(\text{M}_x\text{M}'_{1-x})_3\text{C}_{60}$ correlates very well with the lattice parameter of the face-centered cubic lattice [20]. As shown in Fig. 24, the transition temperature decreases as the C_{60} separation is decreased either by changing the composition or by the application of high pressure. This empirical law suggests

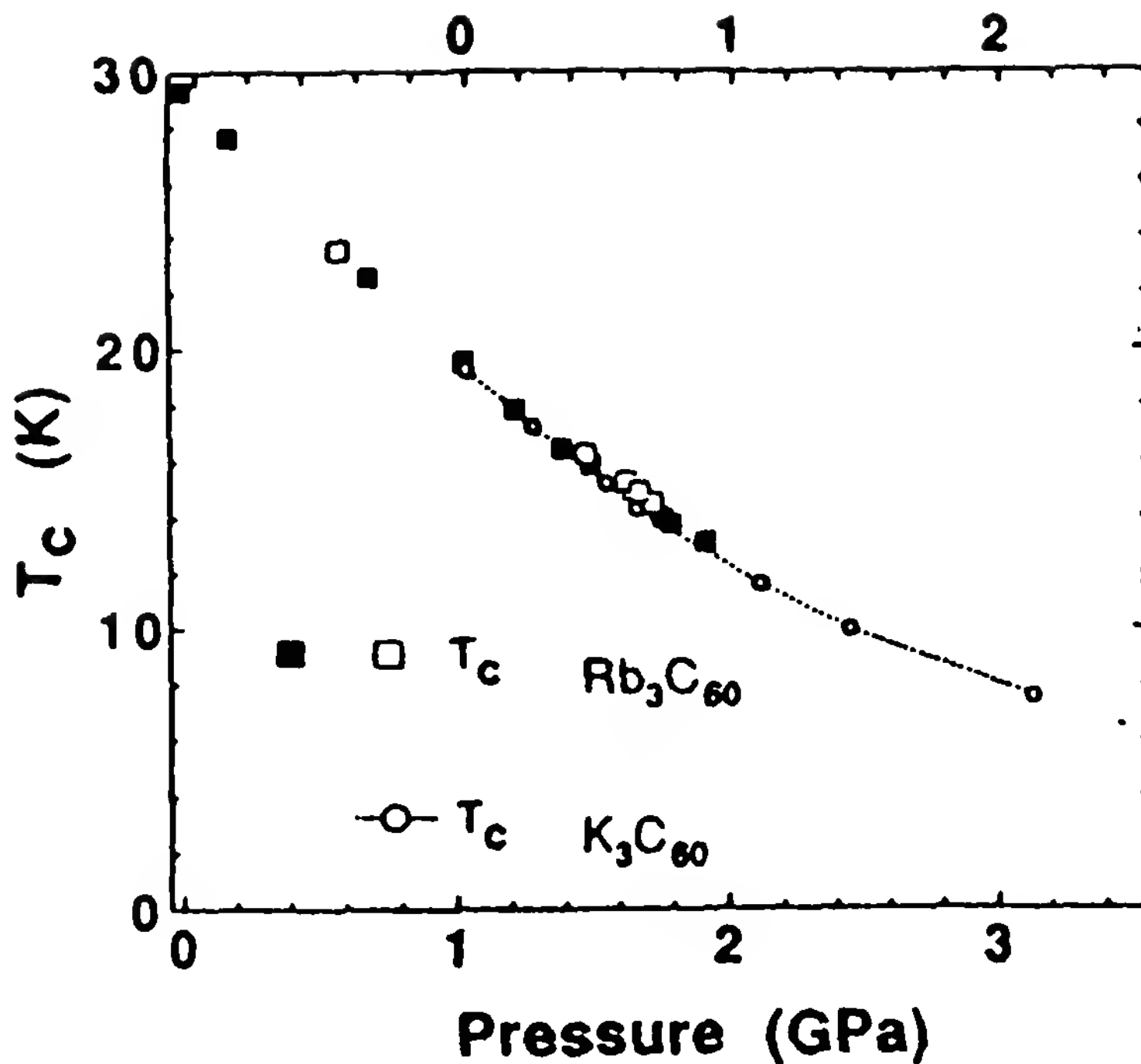


Figure 24 Pressure dependence of T_c in alkali-doped fullerenes. The K_3C_{60} data are shifted in the pressure leak to take into account the smaller lattice parameter. (After Ref. 93b.)

that T_c is essentially governed by the interball overlaps (or the density of states at Fermi level). In the weak-coupling BCS model for phonon-mediated electron pairing, T_c is given by

$$T_c = \Omega_{ph} e^{-1/VN(E_F)} \quad (30)$$

where Ω_{ph} is the energy of the phonons and V the electron–phonon coupling strength.

The pressure dependence of $N(E_F)$ has been measured recently through the pressure dependence of the ^{13}C -NMR Knight shift in K_3C_{60} [94]. In Fig. 25, a plot of $\ln T_c(P)$ versus $K(P)$ is presented. As shown by this plot, linear behavior is effectively observed, which intersects the y axis at $\Omega_{ph} = 600$ K and $\lambda = N(E_F)V = 0.3$ at ambient pressure [94]. Thus the value of T_c appears to be governed by $N(E_F)$ and the pressure data suggest that high-frequency intraball phonons are likely to be involved in the superconductivity of fullerenes [20,94].

V. OPTICAL PROPERTIES

A. Visible and Near-Infrared Properties

Optical studies of organic superconductors have provided a wealth of informations related to the bandwidth, the dimensionality of the electron

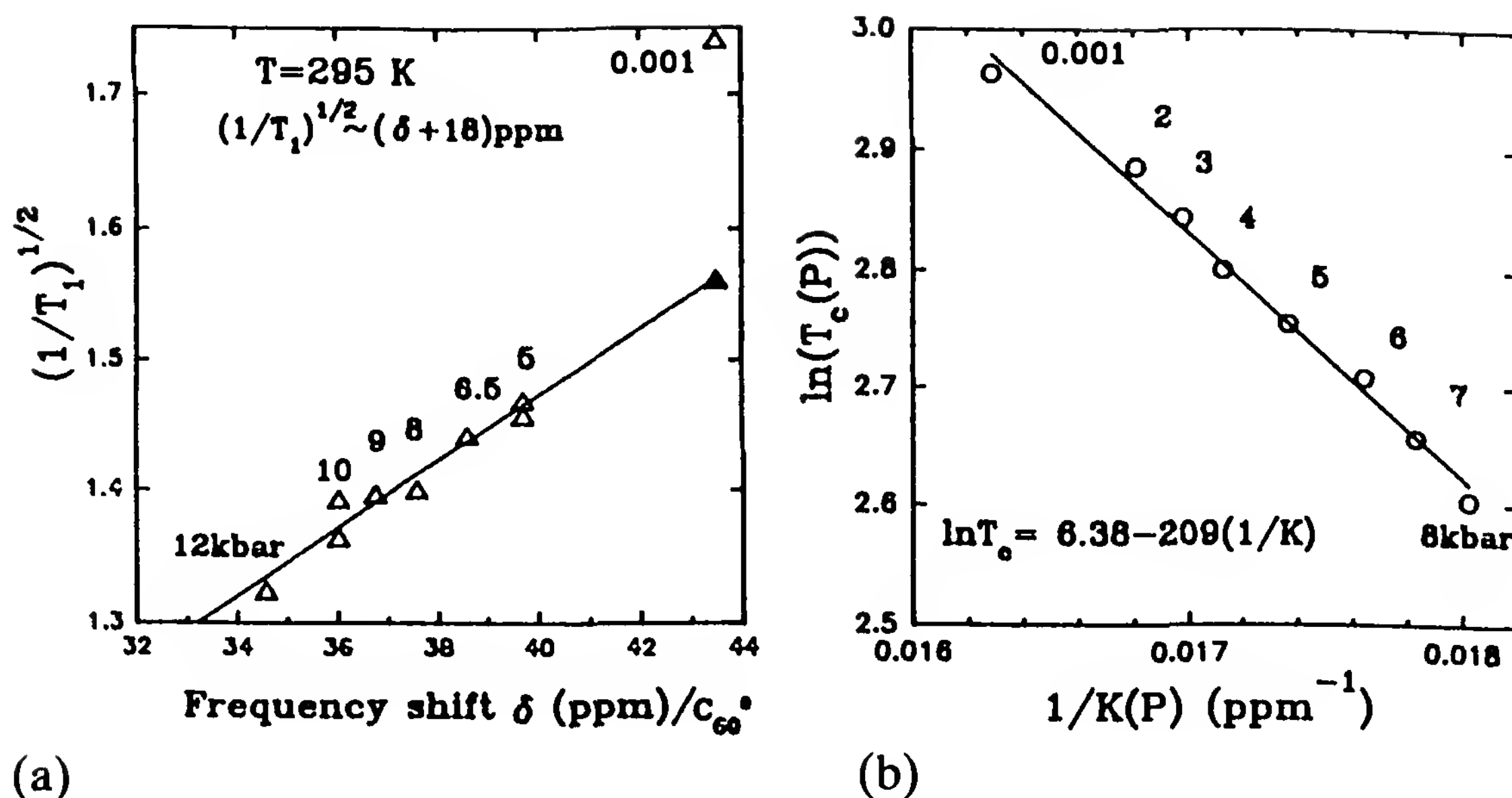


Figure 25 (a) Linear relation between $(1/T_1)^{1/2}$ and the ^{13}C -NMR frequency in K_3C_{60} under pressure leading to the determination of the C_{60}^{3-} chemical shift and (b) $\ln T_c$ versus the reciprocal Knight shift under pressure. The continuous line is the BCS prediction. (After Ref. 94.)

gas, and the role of electron correlations [95]. Most optical experiments measure the reflection coefficient, which is given in terms of the complex index $\tilde{N} = n + ik$ by the relation

$$R = \left| \frac{\tilde{N} - 1}{\tilde{N} + 1} \right|^2 = \left| \frac{\sqrt{\tilde{\epsilon}} - 1}{\sqrt{\tilde{\epsilon}} + 1} \right|^2 \quad (31)$$

where the complex dielectric constant reads

$$\tilde{\epsilon}(\omega) = \epsilon(\omega) + i \frac{\sigma(\omega)}{\epsilon_0 \omega} \quad (32)$$

Assuming that we have a metal in which the dominant contribution to the dielectric constant comes from intraband optical transitions $\epsilon(\omega)$ becomes

$$\tilde{\epsilon}(\omega) = \epsilon_\infty - \frac{\omega_{p0}^2}{\omega(\omega + i\gamma)} \quad (33)$$

In Eq. (33), ϵ_∞ is the core polarizability arising from high-frequency transitions and γ is the damping rate. The plasma frequency ω_{p0} is given by

$$\omega_{p0}^2 = \frac{Ne^2}{\epsilon_0} \frac{1}{m^*} \quad (34)$$

where N is the density of carriers in the band and m^* is the effective mass in the field direction.

A one-dimensional band with band filling defined by ρ (0.5 for the TM_2 salts forgetting about the structural dimerization) and a molecular volume V would lead to

$$\omega_{po}^2 = \frac{4t_{\parallel}a^2e^2}{\pi\epsilon_0\hbar^2V} \sin \frac{\pi\rho}{2} \quad (35)$$

The main goal of optical studies is to determine to what extent the law given by Eq. (33), namely the Drude behavior, is followed for one-dimensional conductors in the presence of strong correlations. Figure 26 gives a typical example of Drude behavior taken from the work of Jacobsen [95].

The conductivity sum rule is an important consequence of the Drude model, namely,

$$\int_0^{\infty} \sigma(\omega) d\omega = \omega_{po}^2 \quad (36)$$

for intraband transitions in a noninteracting electron gas. However, the observation of a well-defined plasma edge cannot be taken as proof of good metallic character. This is shown experimentally by the reflectance spectrum of a variety of $(\text{TM})_2\text{X}$ and $(\text{ET})_2\text{X}$ salts exhibiting quite different conductivity properties at room temperature (see Fig. 26 and Table 4).

The Drude parameters in Table 4 have been derived by fitting the reflectance spectra with the Drude-like dielectric constant, Eq. (33). It has been stressed by Jacobsen [98] and Yamaji [68b] that in the limit of highly anisotropic one-dimensional conductors the ratio of transfer integrals is not proportional to the ratio of plasma frequencies but to its square instead.

The near-infrared reflectance provides the response to plasmon oscillations of the electron gas (which are uniform excitations). This region of the spectrum is, however, not sensitive to the strength of the short-range coulombic interactions, which prevent conductivity in a Mott–Hubbard insulating state. This is illustrated by the frequency-dependent conductivity $\sigma(\omega)$ measured in various salts exhibiting very different values of the conductivity at room temperature (Fig. 27). The peak of the conductivity at the frequency ω_0 correlates with the metallic character: namely, a low frequency of the peak position corresponds to a high dc conductivity and vice versa. The structures below ω_0 are attributed to the coupling with intramolecular modes.

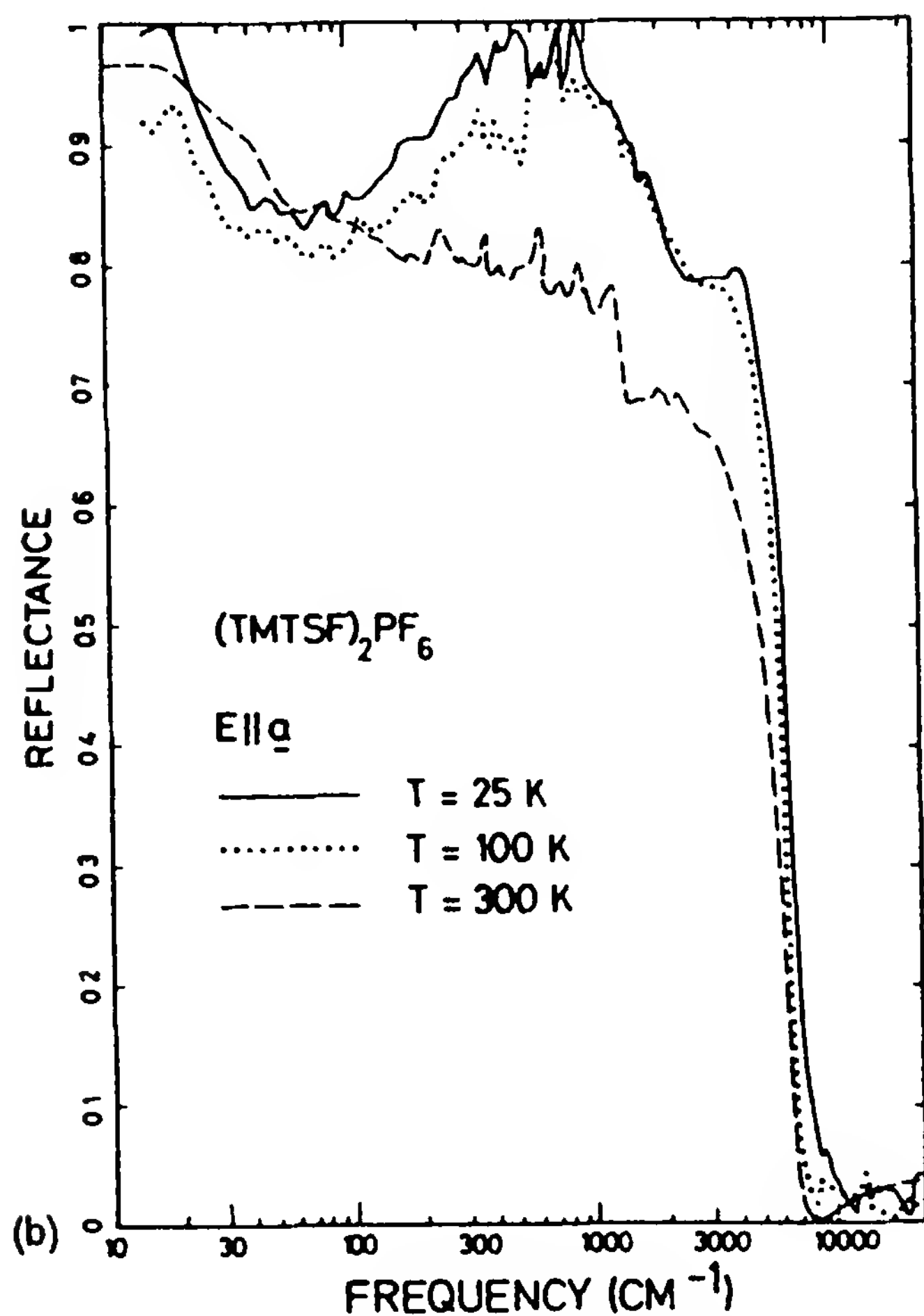
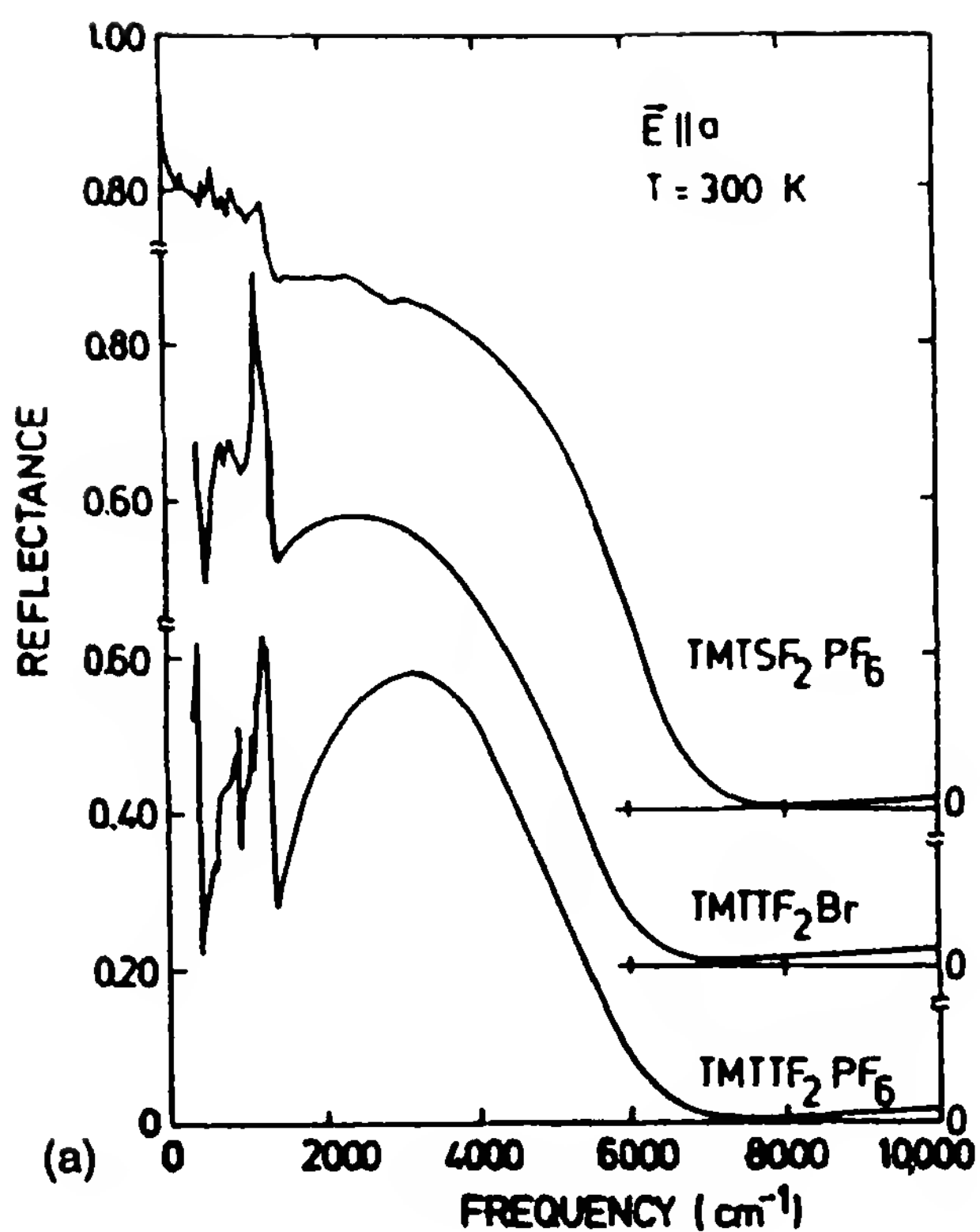


Figure 26 (a) Single-crystal optical reflectance data for organic conductors with decreasing conductivity from top to bottom (from Ref. 95); (b) optical reflectance of $(\text{TMTSF})_2\text{PF}_6$ at different temperatures in the conducting regime (from Refs. 95 and 98); (c) anisotropy of the optical reflectance (from Ref. 98); (d) optical reflectance of $\beta(\text{ET})_2\text{I}_3$ (from Ref. 97).

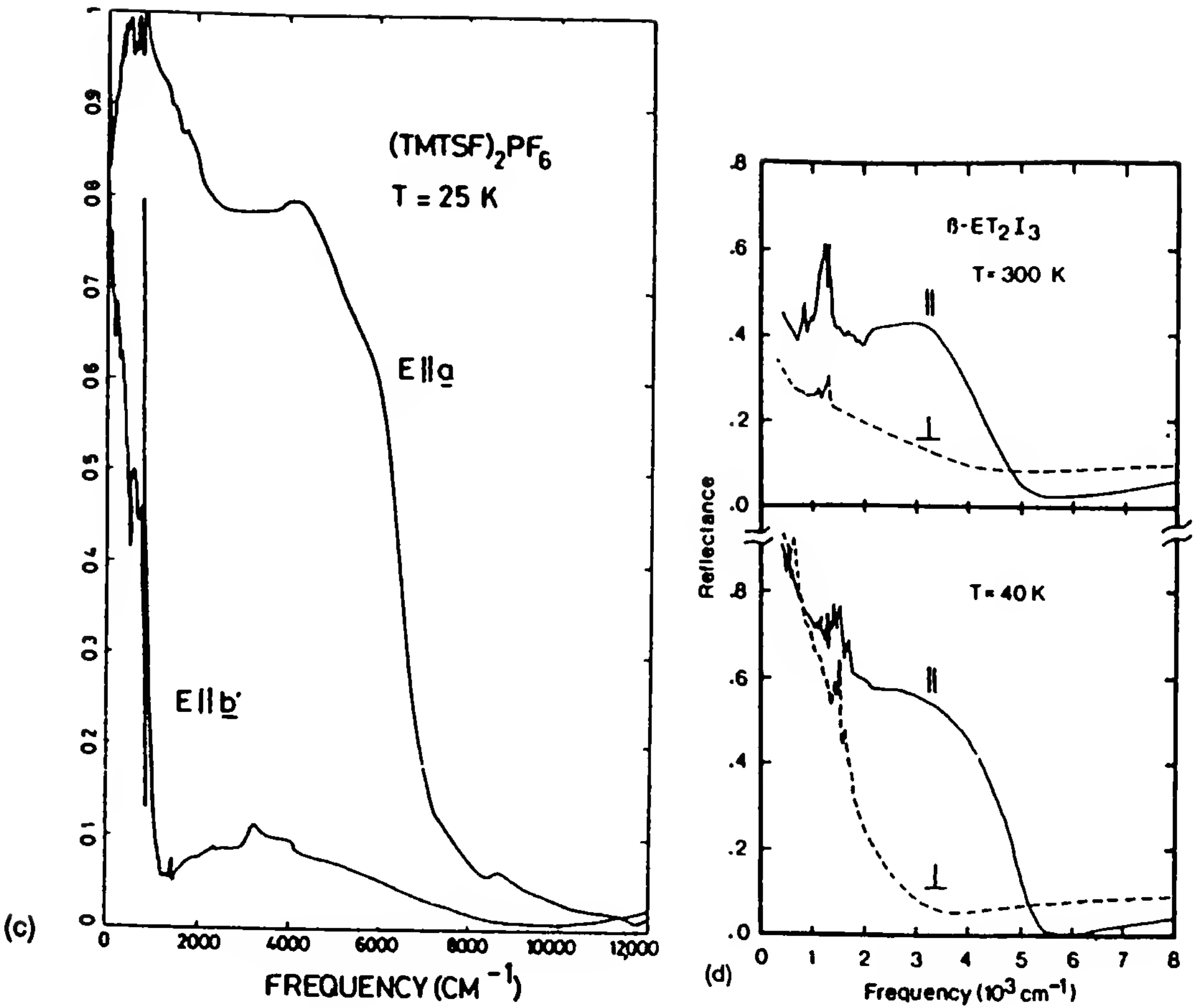


Figure 26 Continued

Table 4 Interpretation of the Reflectance Data of Organic Conductors in Terms of a Drude Model

Compound	σ (300 K) $(\Omega \cdot \text{cm})^{-1}$	ω_p (cm^{-1})	γ (cm^{-1})	t (eV)	ϵ_∞
$(\text{TMTTF})_2\text{PF}_6$	20	8860	1380	0.2	2.50
$(\text{TMTTF})_2\text{Br}$	250				
$(\text{TMTSF})_2\text{AsF}_6$	500	9900	1230	0.25	2.56
$(\text{TMTSF})_2\text{ClO}_4$	700	9900			
$\beta(\text{ET})_2\text{I}_3$	30	9100		0.17	

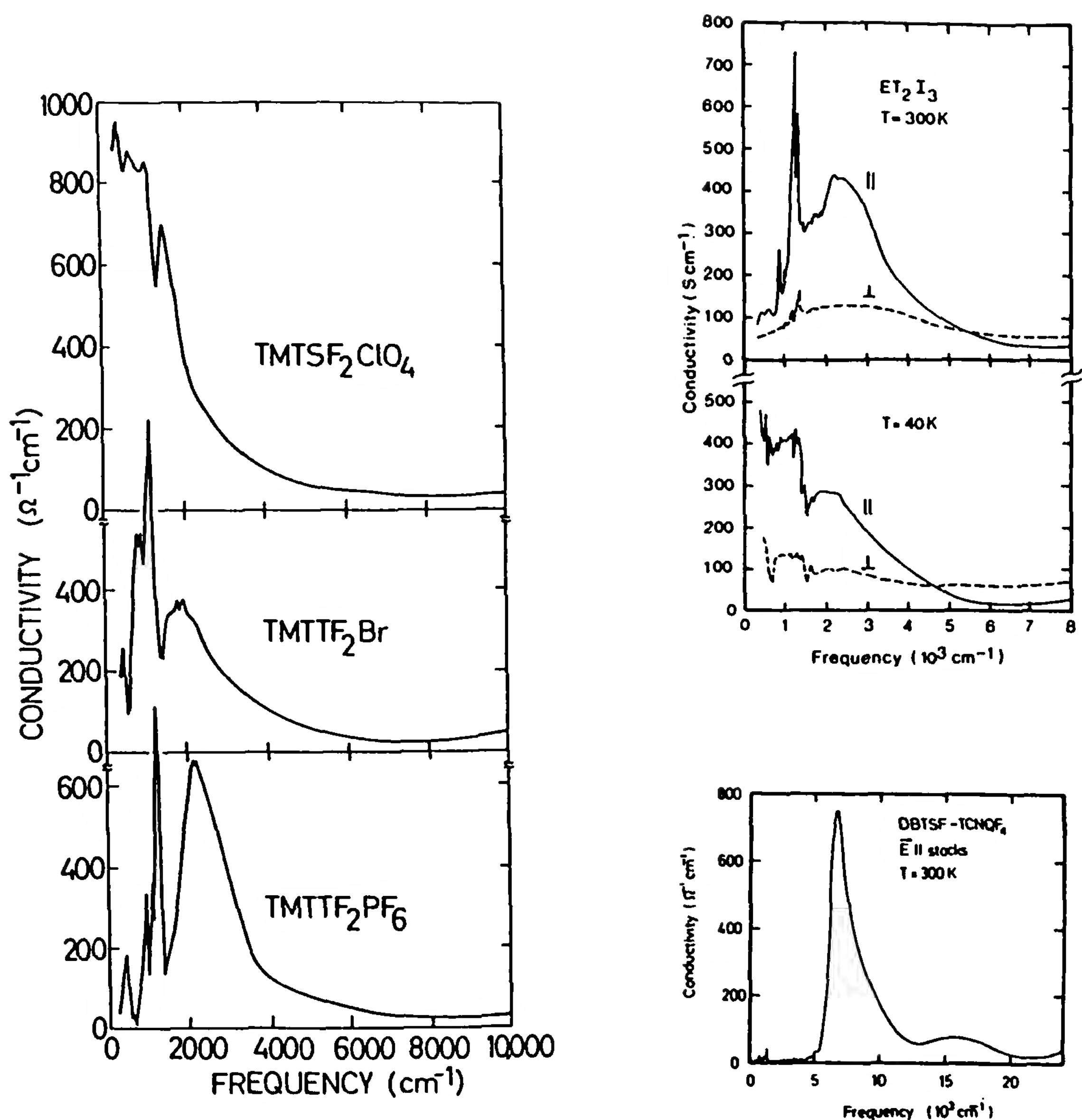


Figure 27 Frequency-dependent conductivity of various TM₂X compounds and β(ET)₂I₃. DBTSF-TCNQ F₄ is a Mott insulator at 300 K (after Ref. 96).

An estimate of the role of Coulomb correlations can be reached by computing the experimental intraband oscillator strength (see Ref. 96),

$$I_p = \int \sigma(\omega) d\omega \quad (37)$$

and comparing it either to the expected value for a noninteracting electron gas $I_o = \frac{2}{\rho_o}$ or to the sum rule for a gas of noninteracting spinless fermions in the limit of $U \rightarrow \infty$. For the latter situation, the plasma frequency is given by a formula such as Eq. (35), although the states are now occupied

up to $\pm 2k_F$ and the density of states is halved as compared to the $U = 0$ limit. Therefore, the oscillator strength of a one-dimensional Mott–Hubbard insulator should read

$$I_\infty = \omega_{po}^2 \cos \frac{\pi \rho}{2}$$

(38)

where $\rho = 0.5$ for the TM_2X series.

As shown in Table 5, a comparison between the Mott–Hubbard insulating compound $(TMTTF)_2PF_6$ and the metallic conductor $(TMTSF)_2ClO_4$ shows that the experimental oscillator strength I_p is close to the Mott–Hubbard insulator in $(TMTTF)_2PF_6$, but for the $(TMTSF)_2ClO_4$ conductor it is closer to the $U = 0$ limit. Table 5 shows that the suppression of oscillator strength correlates with the enhancement of the magnetic susceptibility over the Pauli value calculated with band parameters obtained from the plasma edge analysis.

Correlation effects are likely to be quite important in the compound $\beta(ET)_2I_3$ since they also are narrowband conductors. However, the reason why these strong interactions do not materialize in a Mott–Hubbard insulator could be attributed to the absence of one-dimensional character for this system, which precludes establishment of a Mott–Hubbard localized state.

The temperature dependence of reflectance and conductivity spectra of $\beta(ET)_2 I_3$ are very illuminating indeed (Fig. 27). At room temperature $\sigma(\omega)$ reveals a semiconducting behavior with a peak of conductivity at 2000 cm^{-1} while an approximate metallic behavior is obtained at low temperature; the plasma frequency remains almost temperature independent.

The shift of oscillator strength toward higher frequencies due to large on-site coulombic repulsion corresponds physically in the limit $U \gg 4t$ to charge-transfer transitions into states with doubly occupied sites. Using

Table 5 Comparison Between the Experimental Oscillator Strength I_p and the Sum Rule Computed in the Limit of Noninteracting Electrons I_0 and Spinless Fermions I_∞

Compound	I_0 (10^7 cm^{-2}) from reflectance		I_∞ (10^7 cm^{-2})	I_p (10^7 cm^{-2})	χ_s/χ_p
	edge				
$(TMTTF)_2PF_6$	7.9		5.6	5.8	3.3
$(TMTSF)_2ClO_4$	9.8		6.9	8.3	2.0
$\beta(ET)_2I_3(300\text{ K})$	8.3		5.9	6.2	~ 3
$\beta(ET)_2I_3(40\text{ K})$	9.2		6.5	6.2	~ 3

a Hubbard model Schulz [29] has computed the correlation exponent K_ρ and the weight of the dc conductivity in the total conductivity integrated from zero to infinity as a function of band filling for various U/t ratios. Figure 28 reveals a blue shift of the oscillator strength due to coulombic interactions. The role of interactions is dominant near $\rho = 1$ and at exact half filling all the oscillator strength is shifted above a frequency corresponding to the correlation gap Δ ($\sim kT\rho$). Close to quarter-band filling the sensitivity of the optical conductivity to correlations actually becomes much weaker.

B. Far-Infrared Properties

Using data obtained by far-infrared spectroscopy (FIR) we shall see that an interpretation of the conductivity of conducting TM_2X compounds at low temperature in the framework of a single-particle picture triggers some interesting problems. According to Drude's description of the conductivity, $\sigma(\omega)$ should be constant at low frequencies [$\approx \sigma(0)$] and should fall off as $1/\omega^2$ at a frequency of the order $\gamma = 1/\tau$, namely,

$$\sigma(\omega) = \frac{\omega_p^2 \tau}{1 + \omega^2 \tau^2} \quad (39)$$

The dc conductivity of all these systems becomes very large near 12 K [$\sigma(0) \geq 3 \times 10^5 (\Omega \cdot \text{cm})^{-1}$] while the experimental reflectance edge is

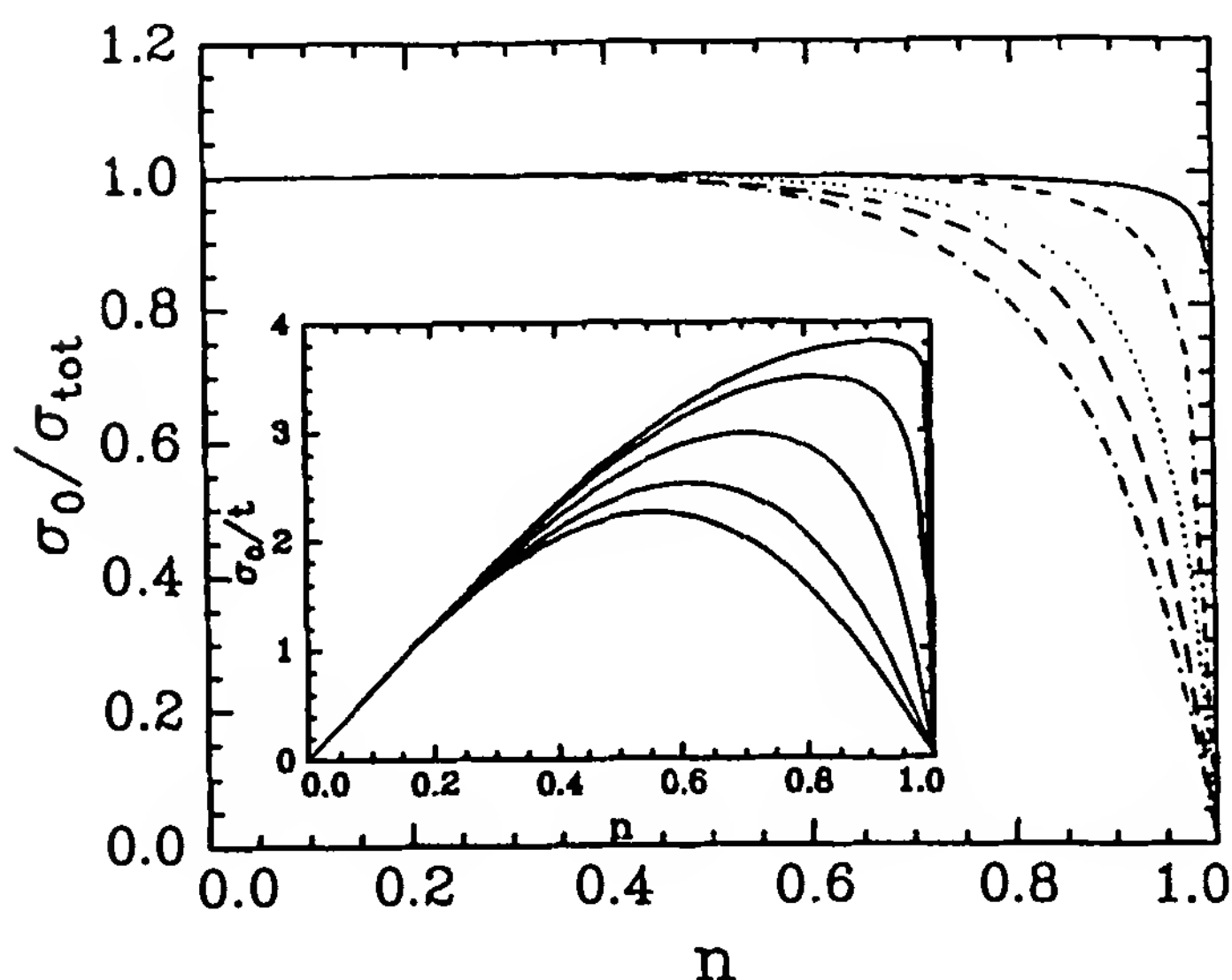


Figure 28 Relative weight of the dc peak in the total oscillator strength of the conductivity versus the band filling at different ratios of U/t , increasing from 1 to 256. The insert gives the weight of the dc peak versus bandfilling for different values of U/t , increasing from 1 to 16, top to bottom. (After Ref. 29.)

not affected by temperature [96]. Thus the use of Eq. (39) leads to a value $1/\tau(12\text{ K}) \sim 4\text{ cm}^{-1}$, which agrees reasonably well with the direct estimate of the electron lifetime at 12 K, based on the observed temperature dependence of σ_{dc} [10]. However, such a small value for $1/\tau$ predicts [Eq. (39)] the existence of a large conductivity in the FIR regime, say $\sigma \approx 4$ to $5 \cdot 10^3 (\Omega \cdot \text{cm})^{-1}$ at 40 cm^{-1} . This is about 10 times larger than the measured FIR conductivity (obtained via a Kramers–Kr  nig analysis of the FIR reflectance data) [99] (see Fig. 29). To reconcile the observed values of dc and FIR conductivities, the existence at low temperature of a collective mode centered around zero frequency has been proposed by several authors [6,100].

The oscillator strength of this mode can be derived using the frequency dependence of the dielectric constant of a damped oscillator at zero frequency, which reads

$$\epsilon_1(\omega) = \epsilon_H - \left(\frac{\Omega_p}{\omega} \right)^2 \quad (40)$$

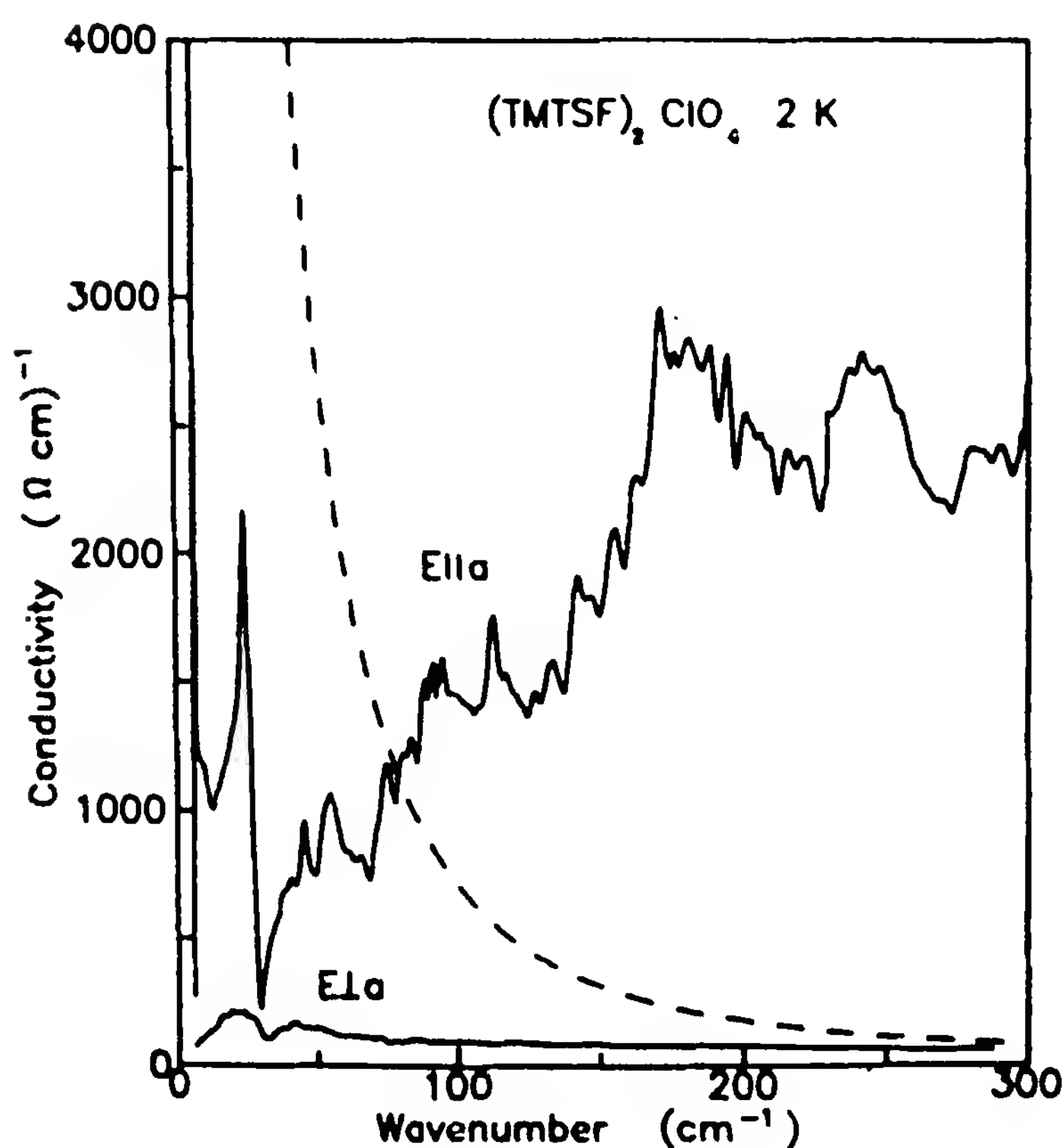


Figure 29 Far-infrared conductivity of $(\text{TMTSF})_2\text{ClO}_4$, relaxed phase. The dashed line is the Drude law with $1/\tau \sim 3.5\text{ cm}^{-1}$ and $\omega_p = 10^4\text{ cm}^{-1}$. (After Ref. 99.)

where $\epsilon_H \sim 500$ takes into account the high-frequency contribution to $\epsilon_1(\omega)$. The dielectric constant crosses zero at $\approx 10 \text{ cm}^{-1}$ (data for $(\text{TMTSF})_2\text{AsF}_6$ [101] (Fig. 30). Hence a value of 500 cm^{-1} is obtained for the plasma frequency of the collective mode. The Drude analysis of the conductivity of this mode gives rise to

$$\sigma(0) = \Omega_p^2 \tau_c \quad (41)$$

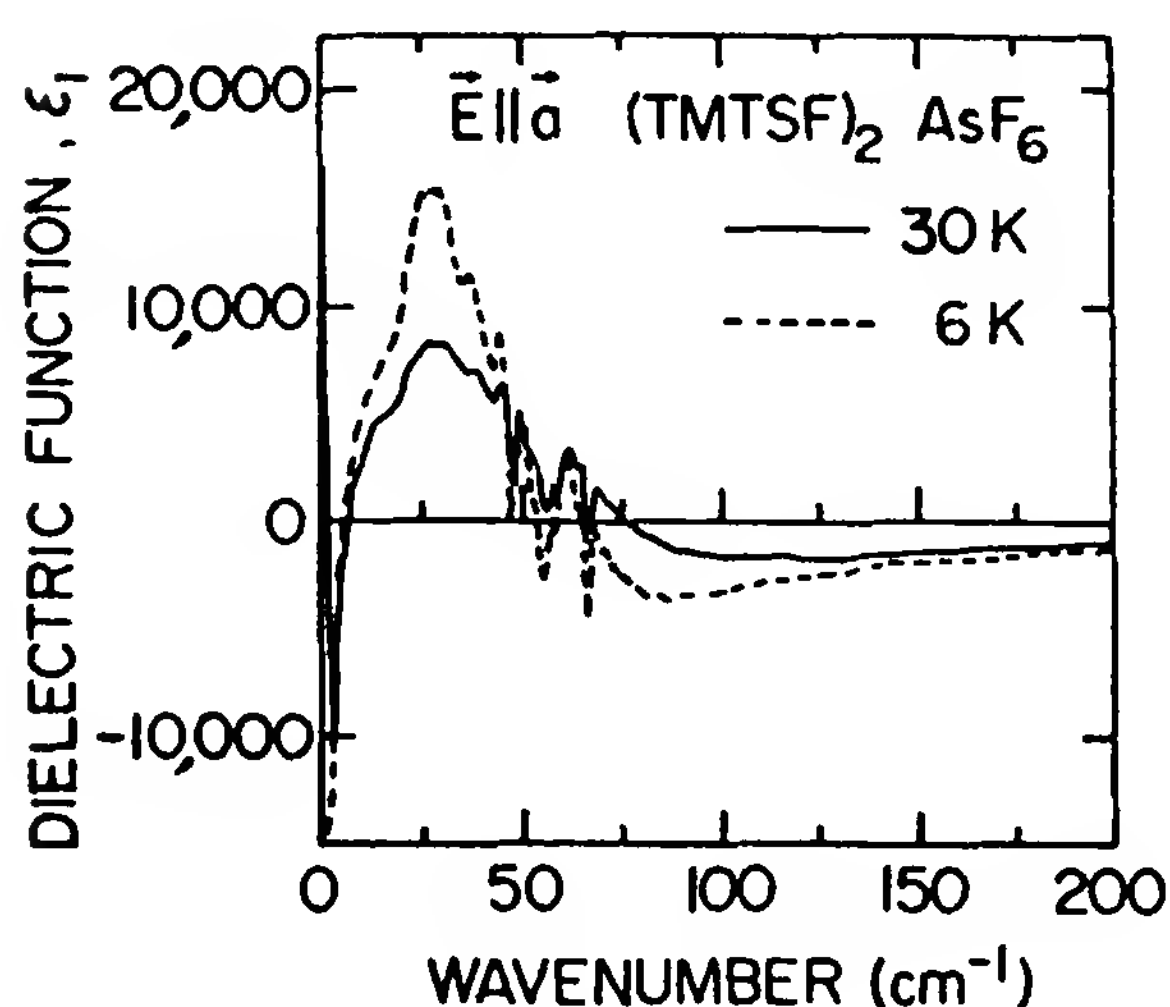
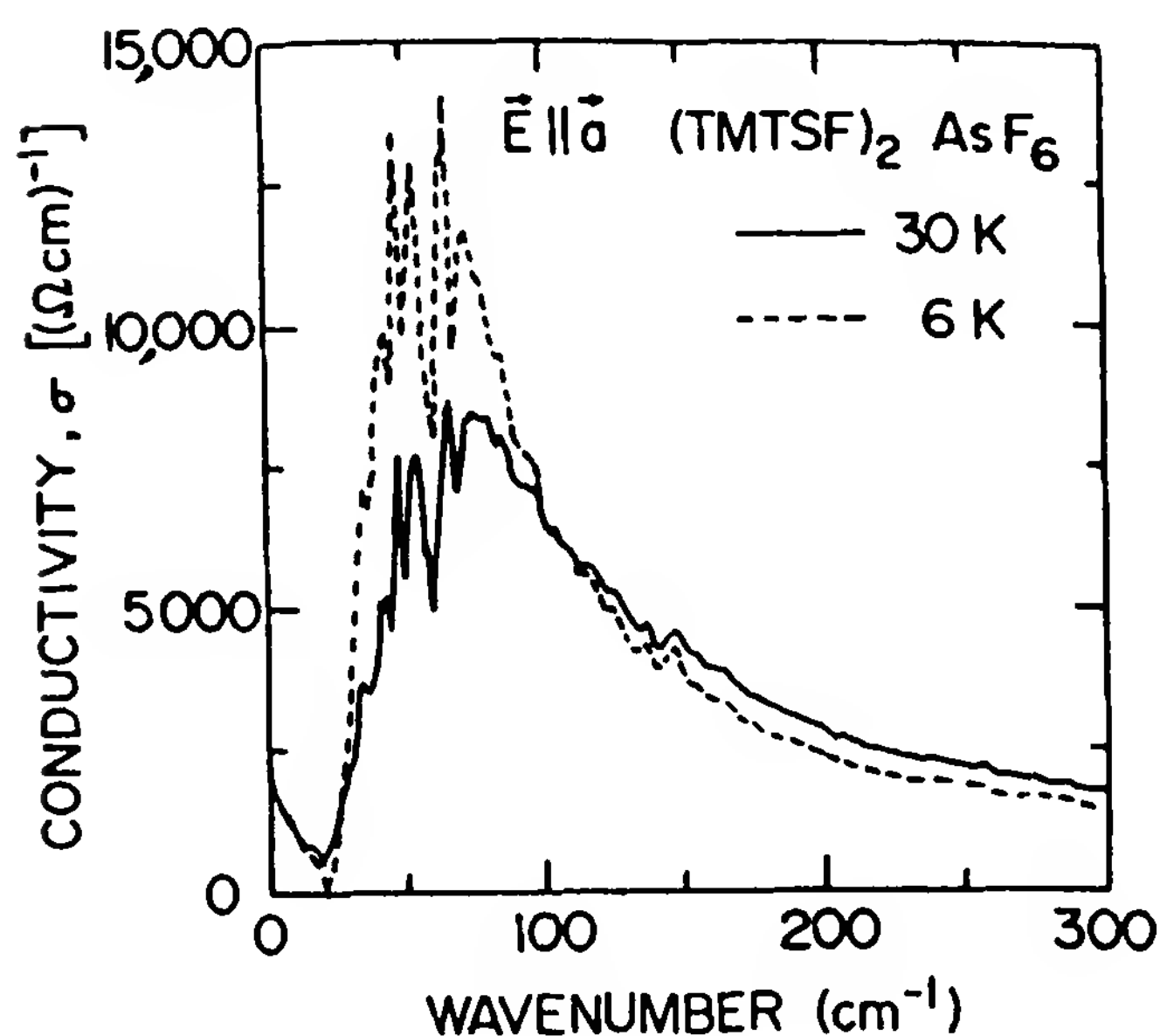


Figure 30 Far-infrared data of $(\text{TMTSF})_2\text{AsF}_6$, showing the FIR gap from conductivity and the zero crossing of the dielectric function at $\approx 6 \text{ cm}^{-1}$ which is relevant for the low-frequency collective mode. (After Ref. 100.)

where $1/\tau_c$ is the width of the collective mode. We thus obtain from the experimental values of Ω_p and $\sigma(0) \sim 3 \times 10^5 (\Omega \cdot \text{cm})^{-1}$ a collective mode width of $1/\tau_c \lesssim 0.5 \text{ cm}^{-1}$ at $T \approx 12 \text{ K}$.

Therefore, in the frequency range ($\omega \sim 30$ to 40 cm^{-1}) the collective mode contribution to the conductivity becomes negligible compared to the single-particle contribution (see Fig. 30) and the single-particle contribution in the oscillator strength is shifted down to the narrow zero-frequency mode.

The assumption of such a collective contribution to the low-temperature conductivity can be reconciled with direct measurement of the microwave conductivity at 20 K between 4.5 and 35 GHz [102]. As shown in Fig. 31, the development of the collective mode toward low temperatures can be predicted assuming a temperature-independent oscillator strength.

The physical origin of this zero-frequency collective mode is not yet clarified. Two possible mechanisms could be considered: (1) the onset of superconducting fluctuations below 30 K, and (2) the contribution of sliding

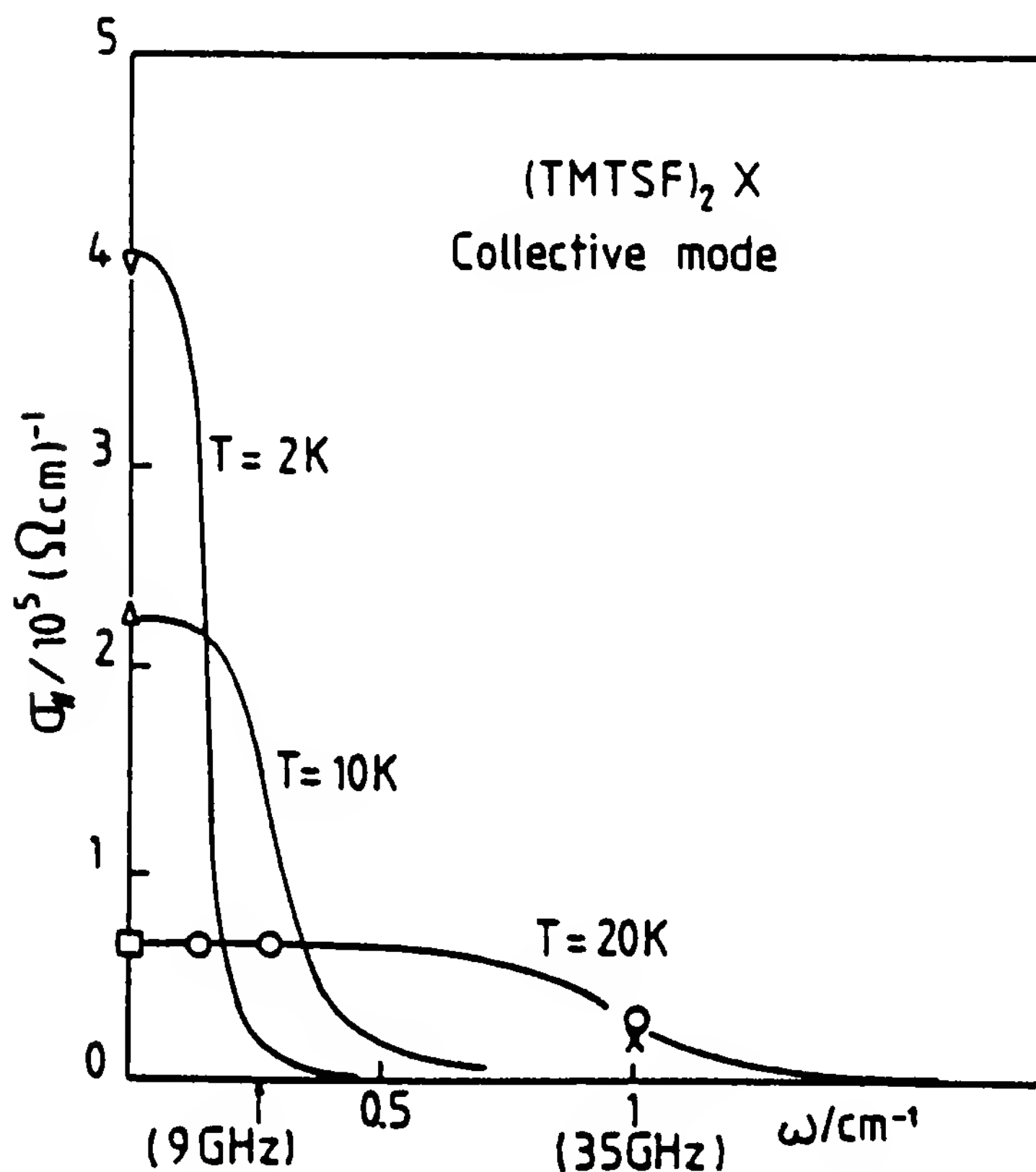


Figure 31 Schematic picture showing the development of the collective mode at low temperature. $T = 20 \text{ K}$ data are from Refs. 102 and 5. At $T = 10$ and 2 K only dc data are known and $\sigma(\omega)$ is drawn assuming a temperature-independent oscillator strength of the collective mode.

spin density wave fluctuations to the conductivity. The latter assumption is tempting since some examples of the contribution of fluctuating density waves to the conductivity of a conducting regime are already known (Fröhlich fluctuating conduction in TTF-TCNQ [6]) and also a three-dimensional ordered depinned SDW contribution to the conduction in the SDW state of $(\text{TMTSF})_2\text{PF}_6$, AsF_6 (see the following section). However, a magnetic density wave origin for the collective mode is hard to reconcile with a similar behavior of the FIR conductivity observed in $(\text{TMTSF})_2\text{ClO}_4$, where no SDW ground state is stable for the relaxed phase, which undergoes the superconducting transition below 1.2 K and also with the large and positive magnetoresistance coefficient which is measured between 12 and 30 K in $(\text{TMTSF})_2\text{PF}_6$ materials. It is thus tempting to attribute the large value of the conductivity to the development of superconducting correlations [6].

Using different microwave measurements of the conductivity from 3 up to 150 GHz (0.1 up to 5 cm^{-1}), Donovan et al. [103] reported nearly the same temperature dependence at all frequencies between 300 and 20 K. Consequently, they found no evidence for a narrow dc collective mode implied by the FIR studies. The question of the existence of a strongly conductive mode is still open, but an accurate determination of the temperature dependence of the resistivity which may not have been achieved in all cases is a prerequisite before comparing dc and high-frequency data.

VI. SPIN DENSITY WAVE COLLECTIVE CONDUCTION

A. Nonlinear Conduction and Narrowband Noise Generation

The antiferromagnetic state (Fig. 5) also reveals a lot of new physical properties. It is the nesting of the Fermi surface with the wave vector \mathbf{Q} that drives the transition from a metal at $T > 12\text{ K}$ for $(\text{TMTSF})_2\text{PF}_6$ into an insulator exhibiting a magnetic modulation or spin density wave at the same wave vector \mathbf{Q} [6]. The low-field susceptibility of the SDW phase behaves very much alike that of a regular antiferromagnet. For $(\text{TMTSF})_2\text{AsF}_6$ easy, intermediate, and hard axes are located approximately along the b , a , and c axes, respectively (Fig. 32) and a spin-flip transition arises around 5 kOe [104] (Fig. 32). Antiferromagnetic resonance studies have also been carried out in the SDW ground states of $(\text{TMTSF})_2\text{X}$ [105a] and of some S compounds [105b].

The broken symmetry of the SDW ground state characterized by a magnetic modulation at wave vector \mathbf{Q} in $(\text{TMTSF})_2\text{X}$, $\text{X} = \text{PF}_6$, NO_3 , and so on, is responsible for the activated behavior of the conductivity through the single-particle gap 2Δ . However, two kinds of collective excitations arise in the SDW condensate. They are, first, the magnon exci-

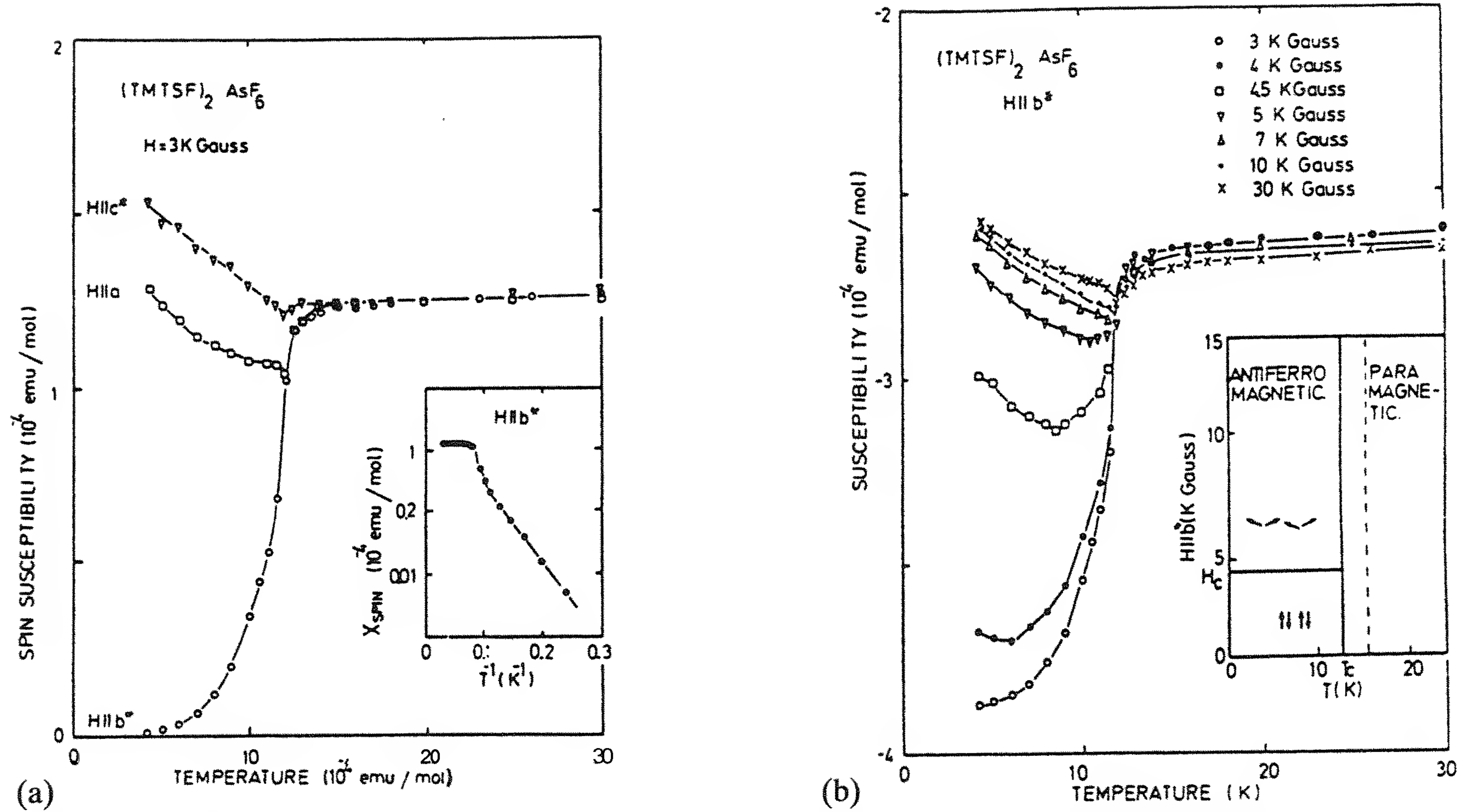


Figure 32 (a) Spin susceptibility of $(\text{TMTSF})_2\text{AsF}_6$ measured at a field lower than the spin-flop field and (b) measured versus field. The spin-flop field is around 4 kOe. After (Ref. 104.)

tations, which manifest themselves in the antiferromagnetic resonance [105], and second, the phase mode of the condensate, which is gapless provided that the spin modulation is noncommensurate, with the underlying lattice [106]. In $(\text{TMTSF})_2\text{PF}_6$, the wave vector corresponding to the optimum nesting of the Fermi surface is incommensurate, as shown by various measurements sensitive to local magnetic fields. Therefore, as long as \mathbf{Q} is incommensurate with the underlying lattice, a phason mode begins at $\omega = 0$ for $q = 0$; in other words, the electrons can slide freely without any cost in energy, almost as in a superconductor [106] (Fig. 33a). This translational invariance gives rise to a collective contribution to the conductivity:

$$\sigma(\omega) = \frac{ne^2}{m^*} \delta(\omega - \omega_0) \quad (42)$$

where n is the density of condensed carriers in the SDW state, m^* the effective mass of the condensate, and ω_0 is either zero, in an ideally pure material, or a finite frequency, when the collective mode is pinned by commensurability or impurities. (For a review, see Ref. 107.) This finite frequency is determined by the relation

$$\omega_0^2 \sim V^2 n_i N(E_F) \Delta \quad (43)$$

where n_i and V are the concentration of impurity centers and the SDW-impurity coupling potential, respectively.

However, in real materials the interaction between a SDW (or the associated CDW) and impurities or crystal defects provides a finite pinning energy, and a threshold electric field E_T must be reached before the condensate can contribute to the conduction at zero frequency. It is given by the balance between the energy provided by the electric field when the condensate is moved by the length $2\pi/k_F$ and the pinning energy:

$$eE_T \propto \omega_0^2 \quad (44a)$$

and

$$E_T = \frac{m^*}{m} \frac{\omega_0^2}{4ev_F} \quad (44b)$$

Describing the motion of the pinned SDW state by a harmonic oscillator and assuming that the displacement of the collective mode by ISDW leads to depinning, the following relation between the static dielectric constant and the threshold field is obtained:

$$\epsilon E_T = \text{const} \quad (44c)$$

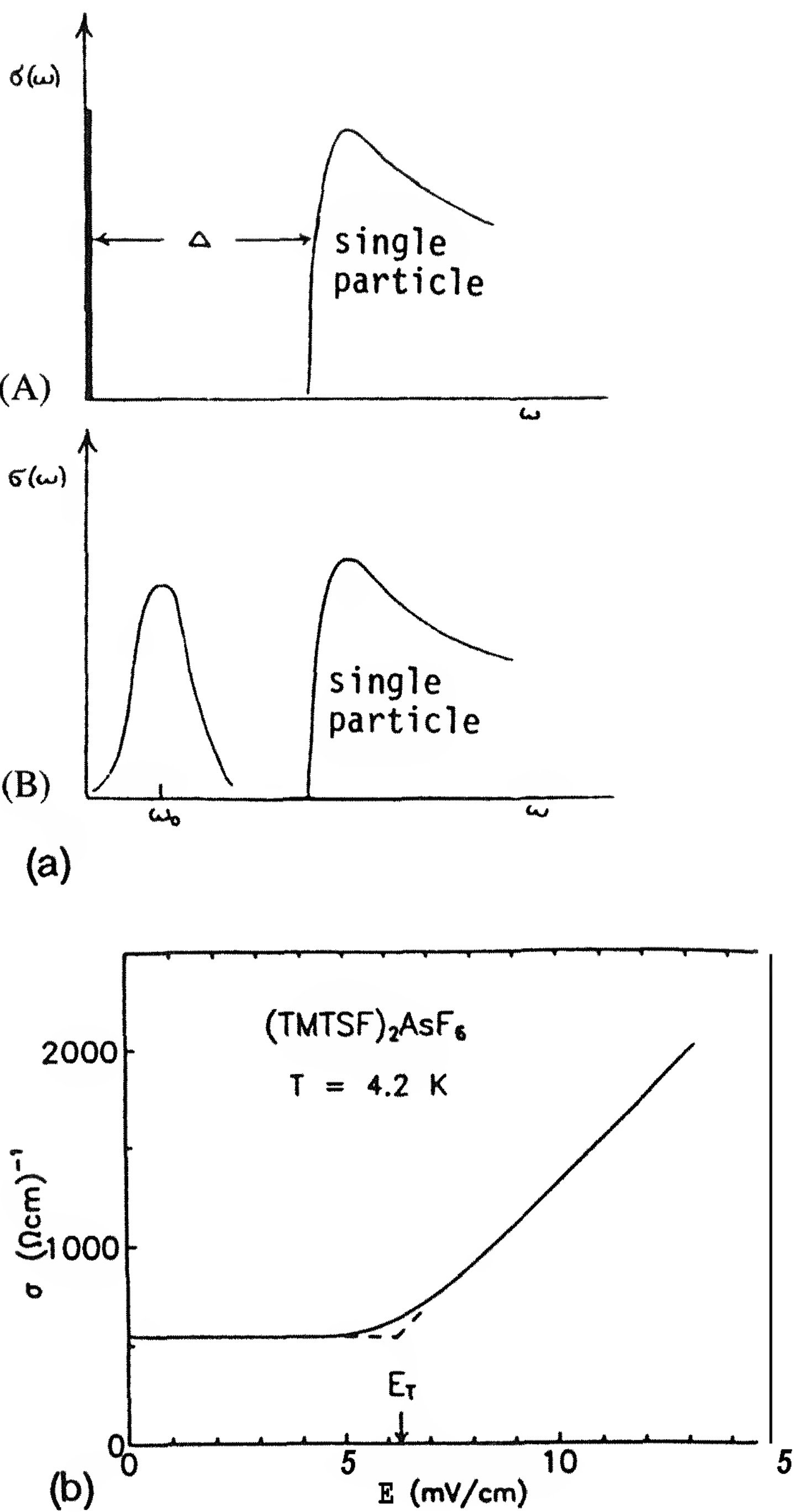
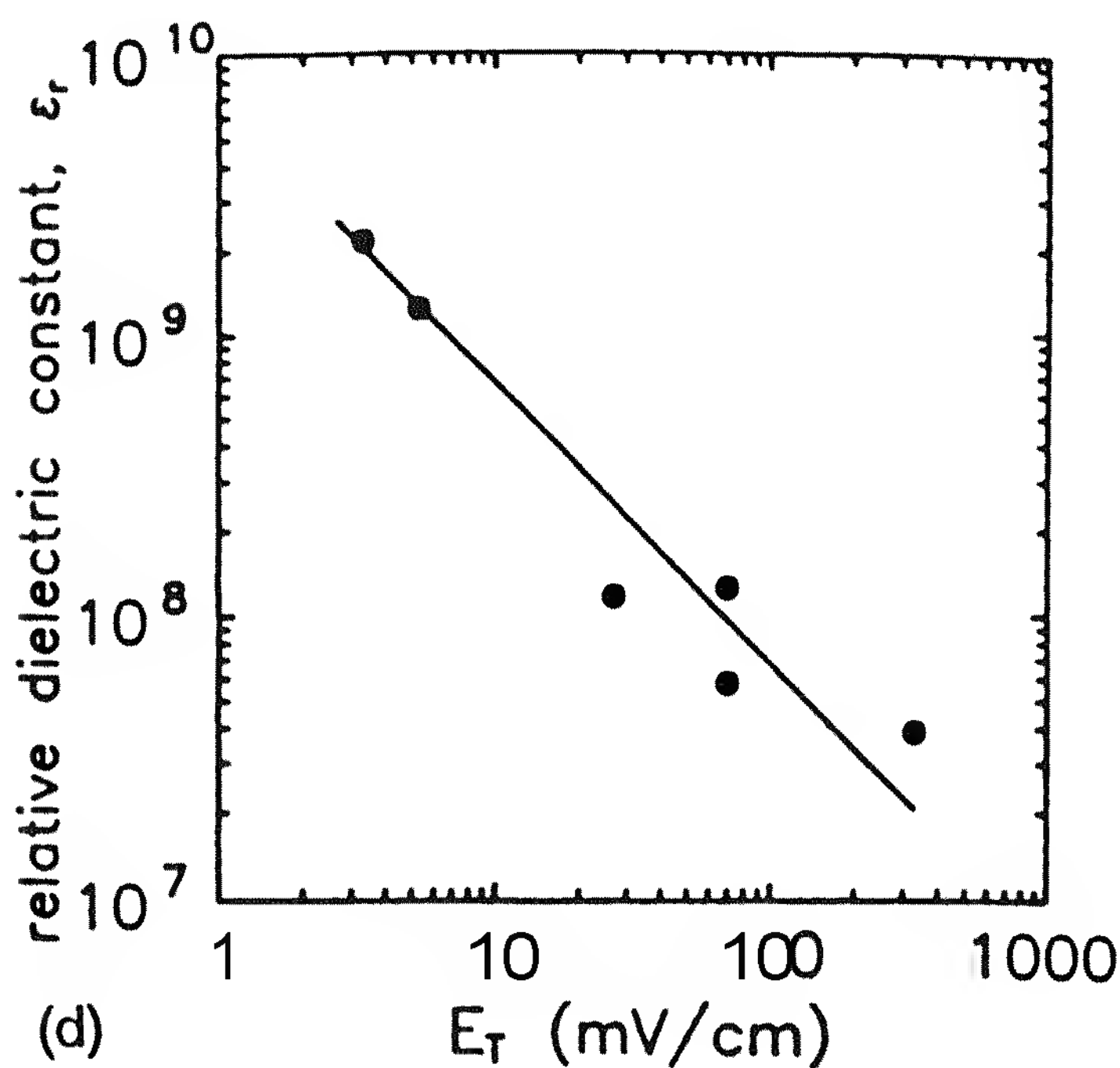
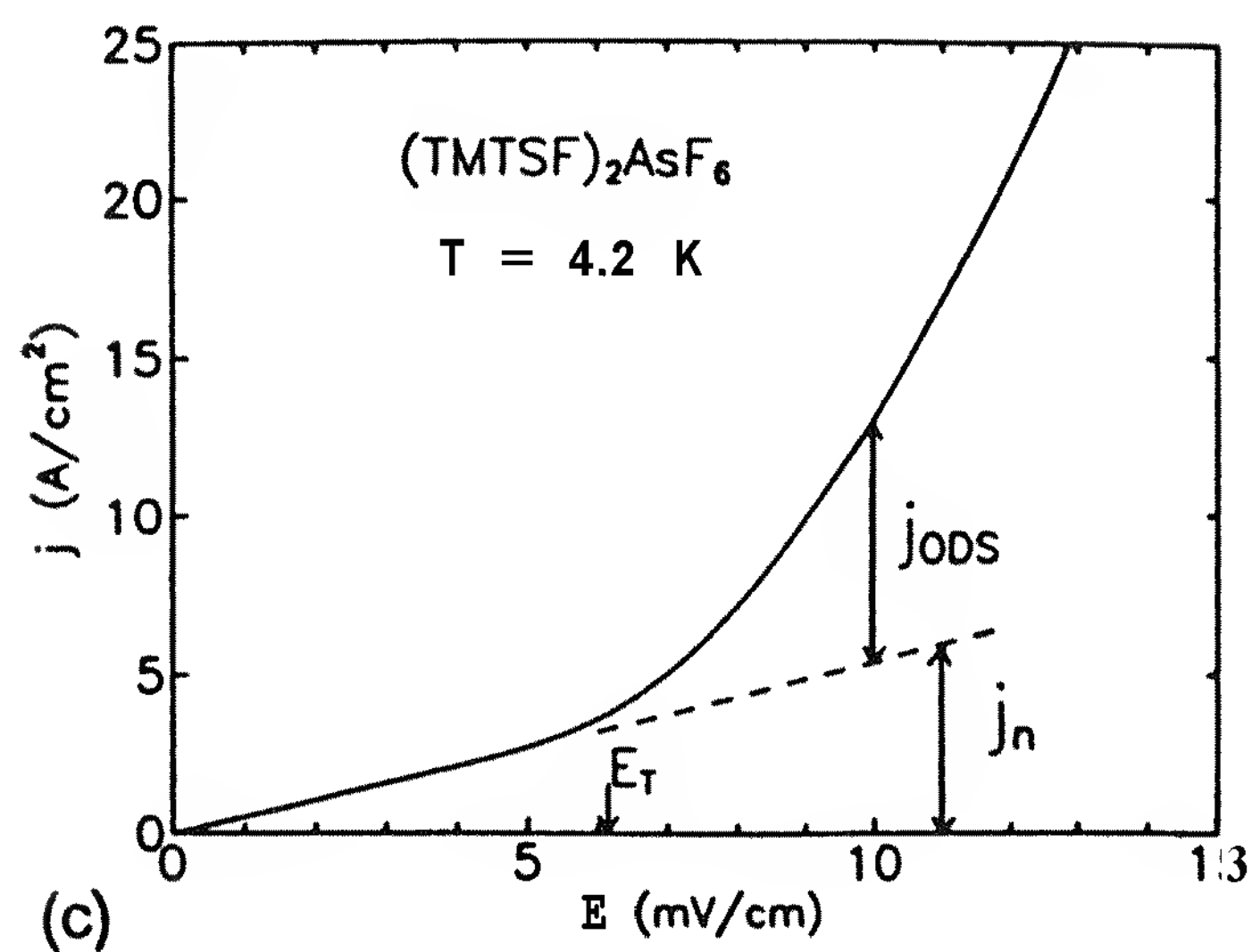


Figure 33 (a) Frequency-dependent conductivity in the absence of pinning (A) and with pinning and damping (B) (after Ref. 107); (b) nonlinear conductivity in the SDW phase of $(\text{TMTSF})_2\text{AsF}_6$; (c) current–voltage characteristics. (d) The $\epsilon E_{\perp} = \text{const.}$ relation is verified in the series of alloys $(\text{TMTSF})_2\text{AsF}_{6(1-x)}\text{SbF}_{6x}$ when the threshold field E_T is determined by the amount of lattice defects $x(1 - x)$, see also Fig. 34b. (After O. Traetteberg, thesis Univ Paris Sud (1993) unpublished.)



In all SDW phases of the $(\text{TMTSF})_2\text{X}$ series E_T is restricted to the range of a few mV/cm [108] (Fig. 33b), and for an electric field of twice the threshold field the collective current becomes a significant fraction of the total current (Fig. 33c). As shown in Fig. 33d, the relation $\epsilon E_T = \text{const}$ is followed very accurately over several decades in the series of alloys to be discussed below. Furthermore, the linear increase of E , versus the density of lattice defects suggests that the phase of the spin modulation is locally adjusted at each defect site to provide the largest pinning energy (strong pinning limit) [109a,b] (Fig. 34).

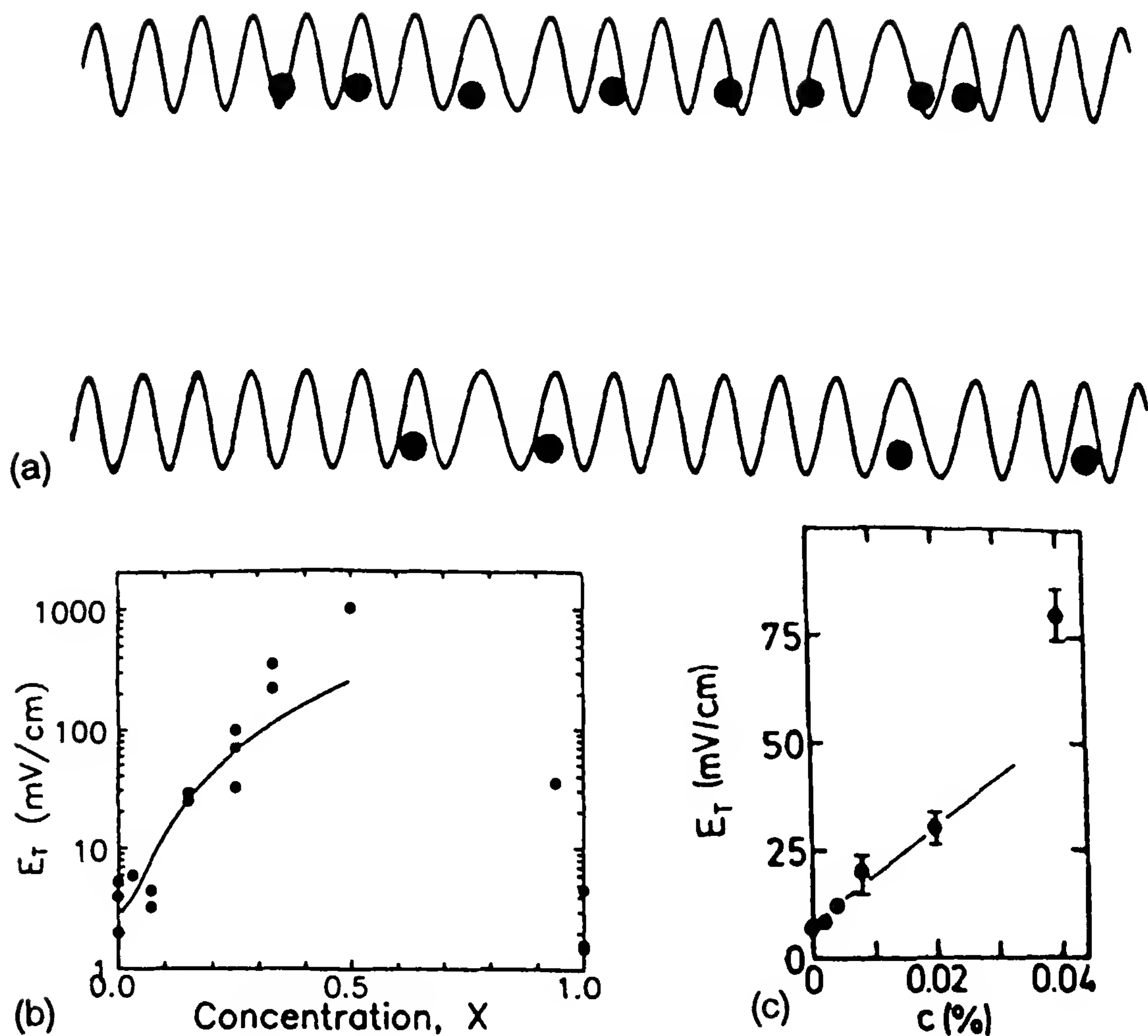


Figure 34 (a) Weak (top) and strong pinning (bottom) of a density wave. The phase of the modulation is locally adjusted at each defect site in the strong-pinning limit. (b) Threshold field in the $(\text{TMTSF})_2\text{AsF}_{6(1-x)}\text{SbF}_{6x}$ series (after Ref. 120); (c) threshold field of $(\text{TMTSF})_2\text{PF}_6$ versus the concentration of defects created by x-ray irradiation (after Ref. 109c).

Direct evidence for a spin density wave transport is the detection of a current oscillating at a frequency that is proportional to the dc current carried collectively. The recent observation of such oscillations; the harmonic and subharmonic locking of this oscillation to an external ac source and a motional narrowing of the NMR spectrum in the sliding SDW state have established firm evidence for the existence of a novel collective transport in a SDW condensate.

When a dc current flowing through the SDW state overcomes the threshold current, which is necessary for sliding the current density j_{SDW} carried by each chain is proportional to the phase winding rate $\nu_\phi = \frac{1}{2}\pi d\phi/dt$: that

is,

$$j_{\text{SDW}} = 2ef_c\nu_\phi \quad (45)$$

where f_c is the condensate density, reaching unity at 0 K. Furthermore, the sliding current generates a current oscillation at a frequency ν_n . Direct observation of the ac current is relatively easy in a sliding CDW. However, the amplitude of this coherent noise generation being much weaker in a SDW state has only been detected in $(\text{TMTSF})_2\text{PF}_6$ either by an interference between an external frequency ν_e whenever the ratio $\nu_n/\nu_e = p/q$ where p and q are two small integers (Fig. 35) or by a Fourier analysis [110,111a,b] (Fig. 36a). In addition, the proportionality law between the collective current and the noise frequency expected from Eq. (45) is very well followed (Fig. 36b). Similar results have been obtained in the quenched SDW state of $(\text{TMTSF})_2\text{ClO}_4$ via direct observation of the coherent noise oscillation [112]. However in both cases, the ratio j_{SDW}/ν_n has been found significantly smaller than expected (about 8 to 20 times) from Eq. (45) using dc current data. This discrepancy has been attributed to an underestimation of j_{SDW} due to a strongly inhomogeneous current distribution [110]. As far as CDWs are concerned [113], measured j_{CDW}/ν_n ratios give $2e$ at low temperature, which means that the winding rate frequency and the coherent noise frequency are equal. For such a situation direct measurement of ν_ϕ has been achieved by study of the motional narrowing of the NMR line in the DW state [114]. It has been recognized from motional narrowing experiments in $\text{Rb}_{0.3}\text{MoO}_3$ that $\nu_\phi = \nu_n$ [115]. However, the origin of these oscillations is still controversial, as it could be related to the pinning of the CDW state by local impurities (the washboard frequency) or to the conversion of normal into collective electrons at the sample's electrodes with the creation of a new SDW wavefront.

As far as a SDW state is concerned, the two interpretations of the noise generation lead to different values for $\nu_n/\nu_\phi = \alpha$: the washboard model [116] and the current contact conversion mechanism [117], leading to $\alpha = 2$ and 1, respectively (since the wave vector of the CDW associated with the SDW is now $4k_F$ instead of $2k_F$ [118]).

The period of the pinning SDW potential has been derived from two sets of NMR experiments which have been performed recently in a sliding SDW state. First, measurement of the SDW velocity from the proton spin echo amplitude of $(\text{TMTSF})_2\text{PF}_6$ [119] (Fig. 37) as a function of the dc current (above threshold field) and comparison with the SDW noise spectrum lead to a pinning potential period that is half the SDW wavelength (namely, $\alpha = 2$). Second, the result $\alpha = 1$ is inferred from a study of the amplitude of the motionally narrowed ^{13}C spectrum in $(\text{TMTSF})_2\text{PF}_6$ and of a SDW current and noise spectrum [111] (Fig. 38).

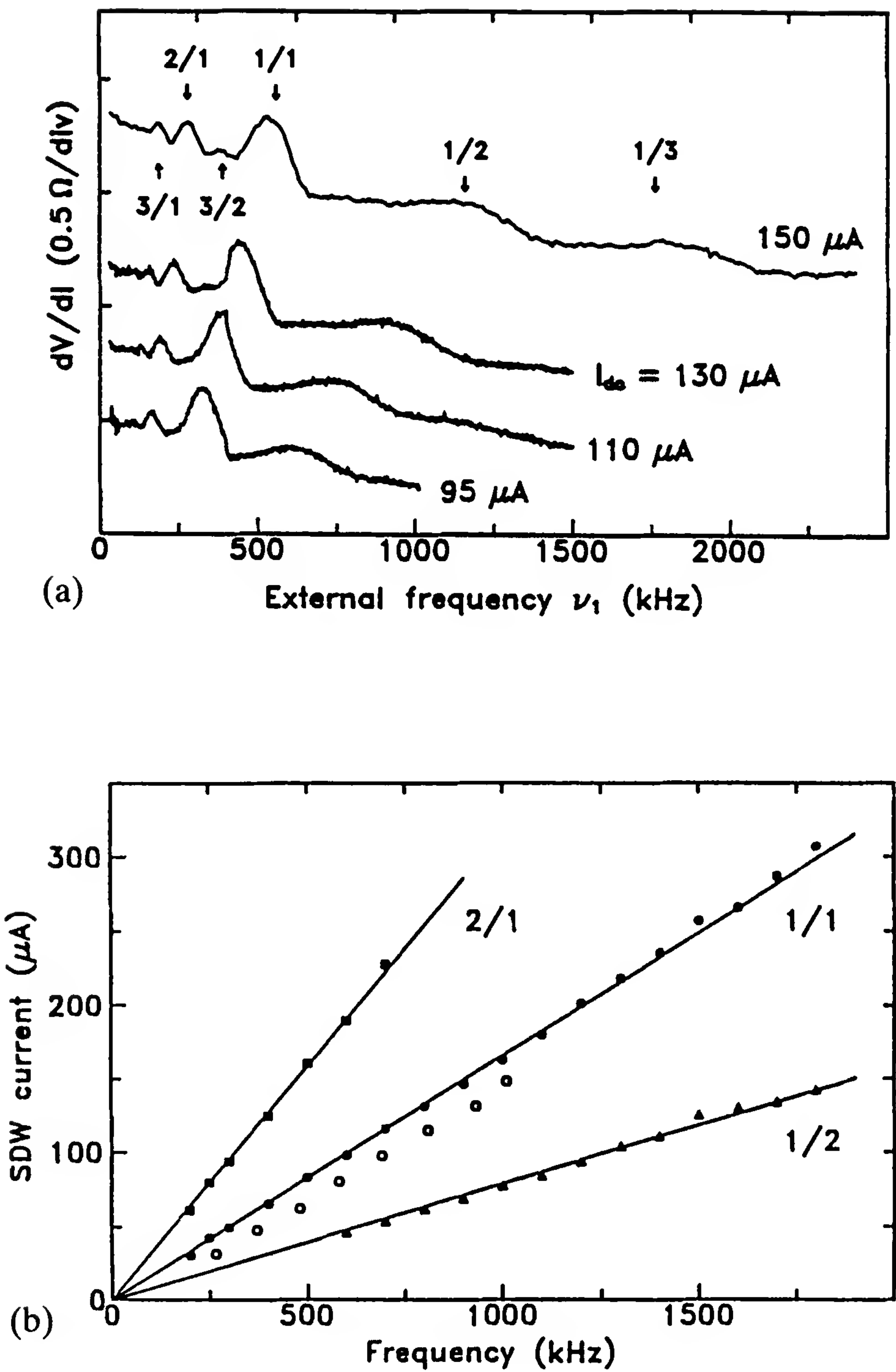


Figure 35 (a) Detection of a beating between the ac current provided by an external source and the internal current oscillation in the sliding SDW state; (b) linear dependence of the SDW current against the frequency of the internal current oscillation, harmonics, and subharmonics. (After Ref. 110.)

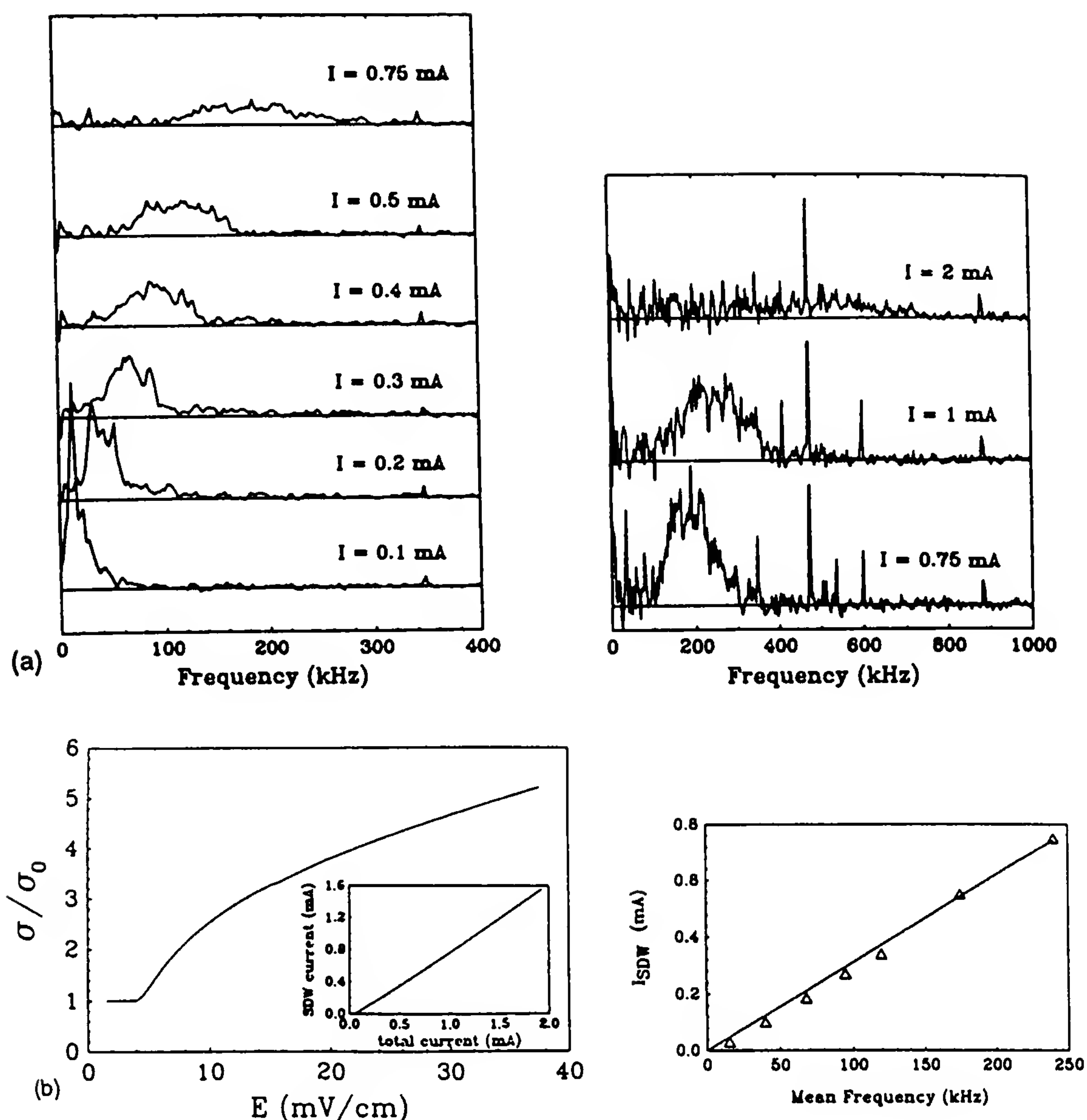


Figure 36 (a) Conduction noise amplitude versus frequency for various dc currents; (b) nonlinear conductivity and SDW current in the same $(\text{TMTSF})_2\text{PF}_6$ sample, $T = 4.2$ K as in (a). (After Ref. 111a.)

The weak pinning limit is encountered in the solid solution of two kinds of TM_2X salts with anions of similar shape (albeit different in their anionic volume): $(\text{TMTSF})_2\text{AsF}_{6(1-x)}\text{SbF}_{6x}$ [120]. The pinning induced by such defects is illustrated by the dependence of E_T on the defect concentration (Fig. 39). It is clear, considering the slope dE_T/dx for irradiation [109c] and solid solution-induced defects [120] that the latter kind of defect represents a weak pinning situation where the phase of the distortion is not fully adjusted to every defect at variance with the strong-coupling limit [109a,b].

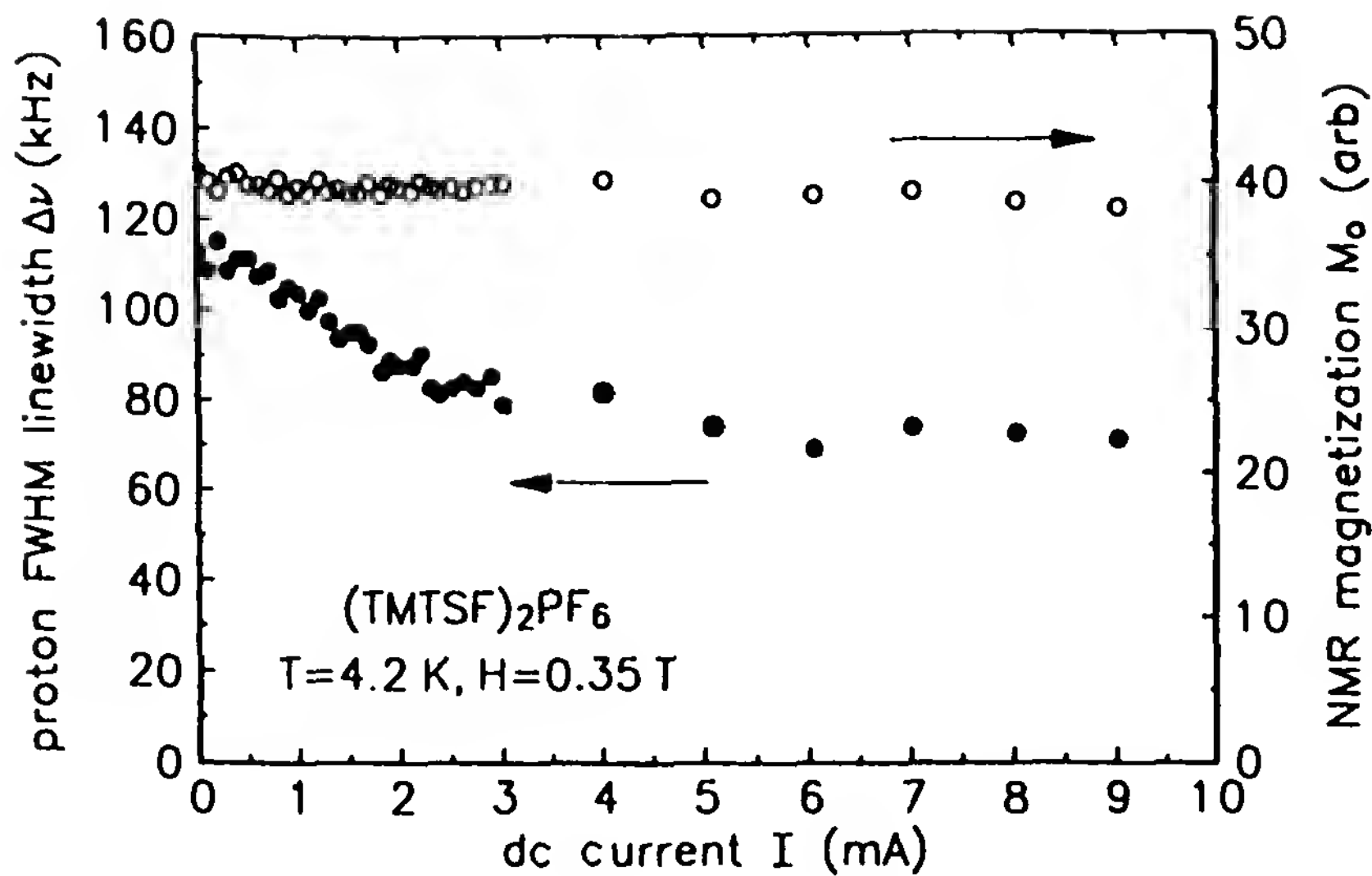


Figure 37 The proton line width in $(\text{TMTSF})_2\text{PF}_6$ at 4.2 K narrows as the current flowing through the sample increases while the constant magnetization shows that heating by the current is negligible. (After Ref. 119.)

The collective current in a sliding SDW state is not a superconducting current, as there exists a finite damping parameter γ which is usually defined by the nonlinear dc conductivity measured at $E = 2E_T$ by the relation

$$\gamma^{-1} = \sigma_{\text{SDW}}^{\text{dc}}(2E_T) - \sigma_n \quad (46)$$

where σ_n is the ohmic conductivity. The temperature dependences of $\sigma_{\text{SDW}}^{\text{dc}}$ and σ_n for the system $(\text{TMTSF})_2\text{AsF}_{6(1-x)}\text{SbF}_{6x}$ have revealed the existence of several damping mechanisms [120] (Fig. 39):

1. The good scaling between σ_{SDW} and σ_n that is observed between 2 and 4 K can be understood in terms of a collective-mode damping induced by thermally activated quasiparticles (as already known for CDW systems).
2. Above a crossover temperature (which is 4 K for the sample $x = 0.07$), σ_{SDW} becomes temperature independent and, furthermore, scales with E_T^{-1} when the concentration of pinning centers is varied. This behavior has suggested that the quasiparticle damping (small at high temperature) is overcome by a temperature-independent damping which is governed by the SDW–defect interaction.

B. Electrodynamic Response

The electrodynamic response of the SDW phase is dominated by a strong resonance of $\sigma(\omega)$ centered around 0.1 cm^{-1} (3 GHz) in $(\text{TMTSF})_2\text{PF}_6$

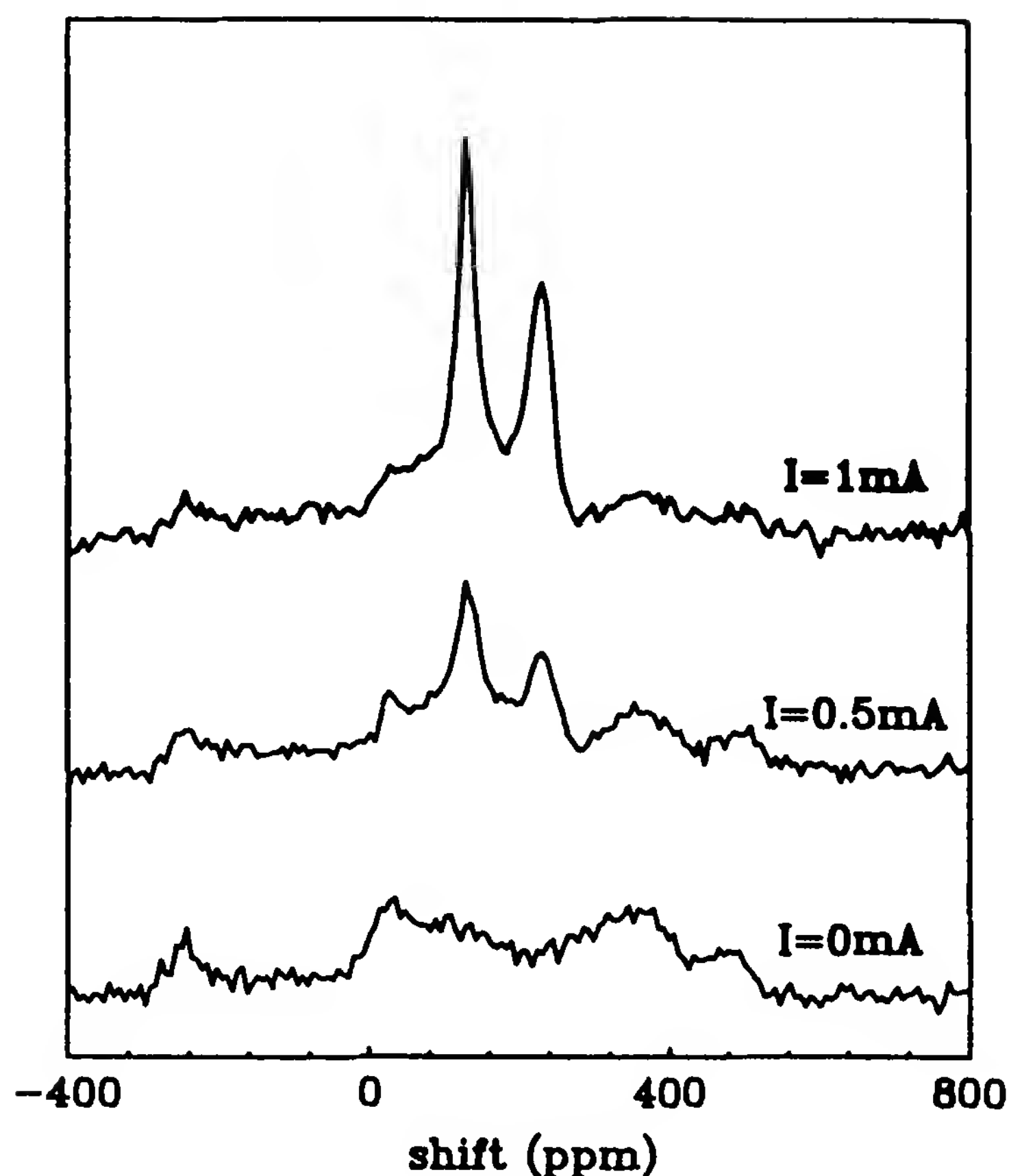


Figure 38 ^{13}C -NMR spectra in the SDW phase of $(\text{TMTSF})_2\text{PF}_6$ as a function of the total current at $T = 4.2$ K. (After Ref. 111b.)

[112] which has been attributed to the oscillation of the pinned phase mode. A weaker resonance at $\omega \approx 30 \text{ cm}^{-1}$ comes from the single-particle excitation across the gap Δ . In the clean limit situation ($1/\tau \ll \Delta$) which is fulfilled, nearly all the oscillator strength is associated with the collective mode resonance at ω_0 .

Two sum rules corresponding to the two resonances can be established theoretically: the collective contribution,

$$\int_0^\infty \sigma_{\text{SDW}} d\omega = \frac{n^2 e}{m^*} \quad (47)$$

and second, the total contribution,

$$\int_0^\infty (\sigma_{\text{SDW}} + \sigma_{\text{SP}}) d\omega = \frac{n^2 e}{m} \quad (48)$$

where m is the bare electron mass.

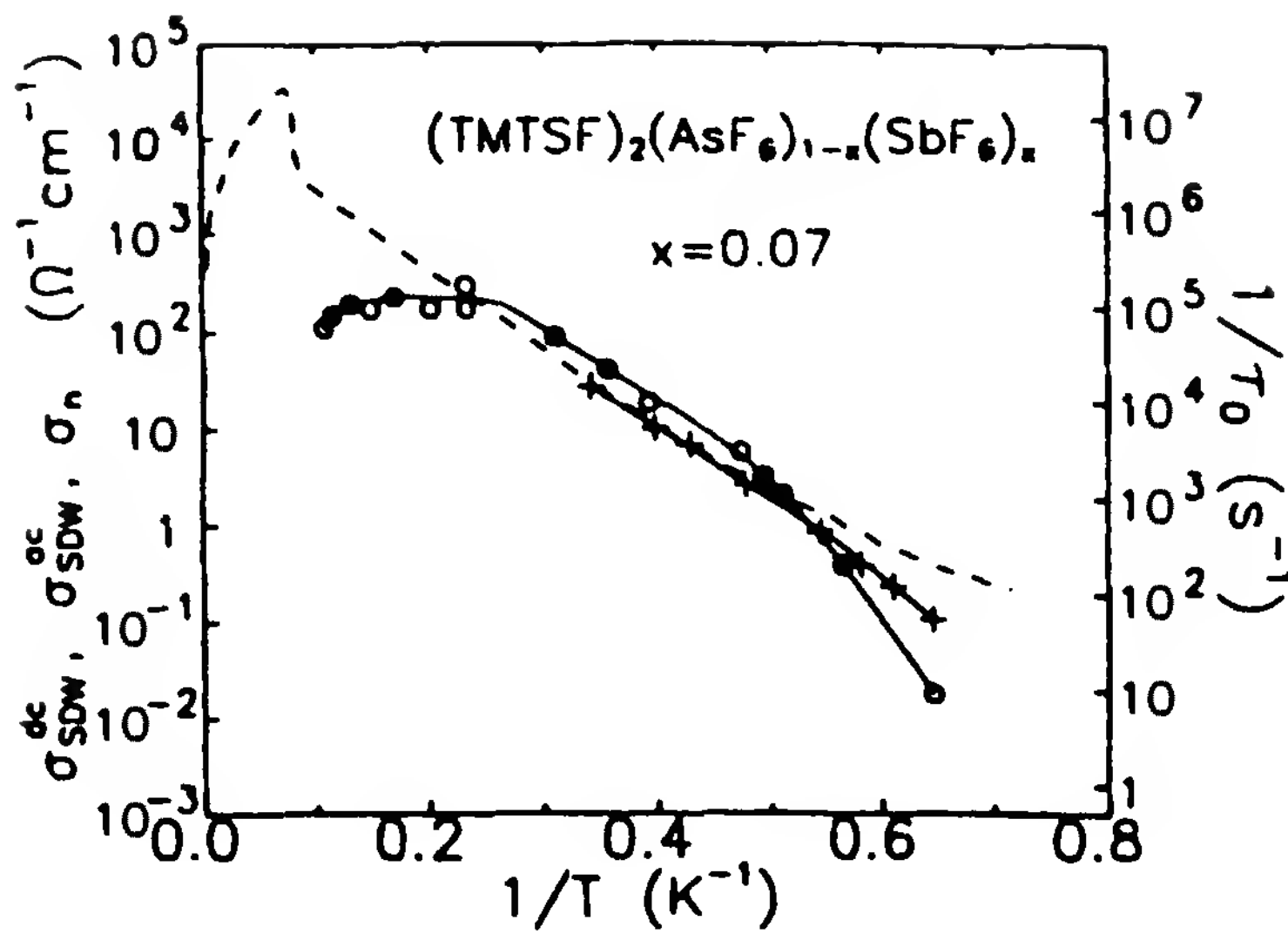


Figure 39 Temperature dependence of the normal conductivity (dashed line) and SDW conductivity (continuous line). [After O. Traetteberg et al., J. Phys. IV C-2:15 (1993).]

Experimentally (Fig. 40), the oscillator strength is about 10^{-2} the value expected from Eq. (48). It has been suggested that this reduction could be attributed to the strong effect of coulombic interactions on the electrodynamics of a SDW state rather than a large enhancement of the effective mass condensate with respect to the free-electron value, as it is the rule in a CDW ground state [122].

VII. LOW-DIMENSIONAL ELECTRONS IN HIGH MAGNETIC FIELDS

A. Field-Induced SDW Phases

The response of the quasi-one-dimensional electron gas to the application of a strong magnetic field has provided new and unexpected results: the transition from a quasi-one-dimensional conductor to a quasi-two-dimensional antiferromagnetic semimetal induced by a magnetic field at low temperature. The instability of the quasi-one-dimensional electron gas at high field can be inferred from observation of magnetoresistance oscillations above a certain threshold field in $(\text{TMTSF})_2\text{PF}_6$ under pressure [123] (Fig. 41). Moreover, NMR data have shown that the ground state which is stabilized by the magnetic field is characterized by the existence of a spin density wave [123] (Fig. 42). These phenomena are fairly well understood with a model in which, crudely speaking, the field restores enough

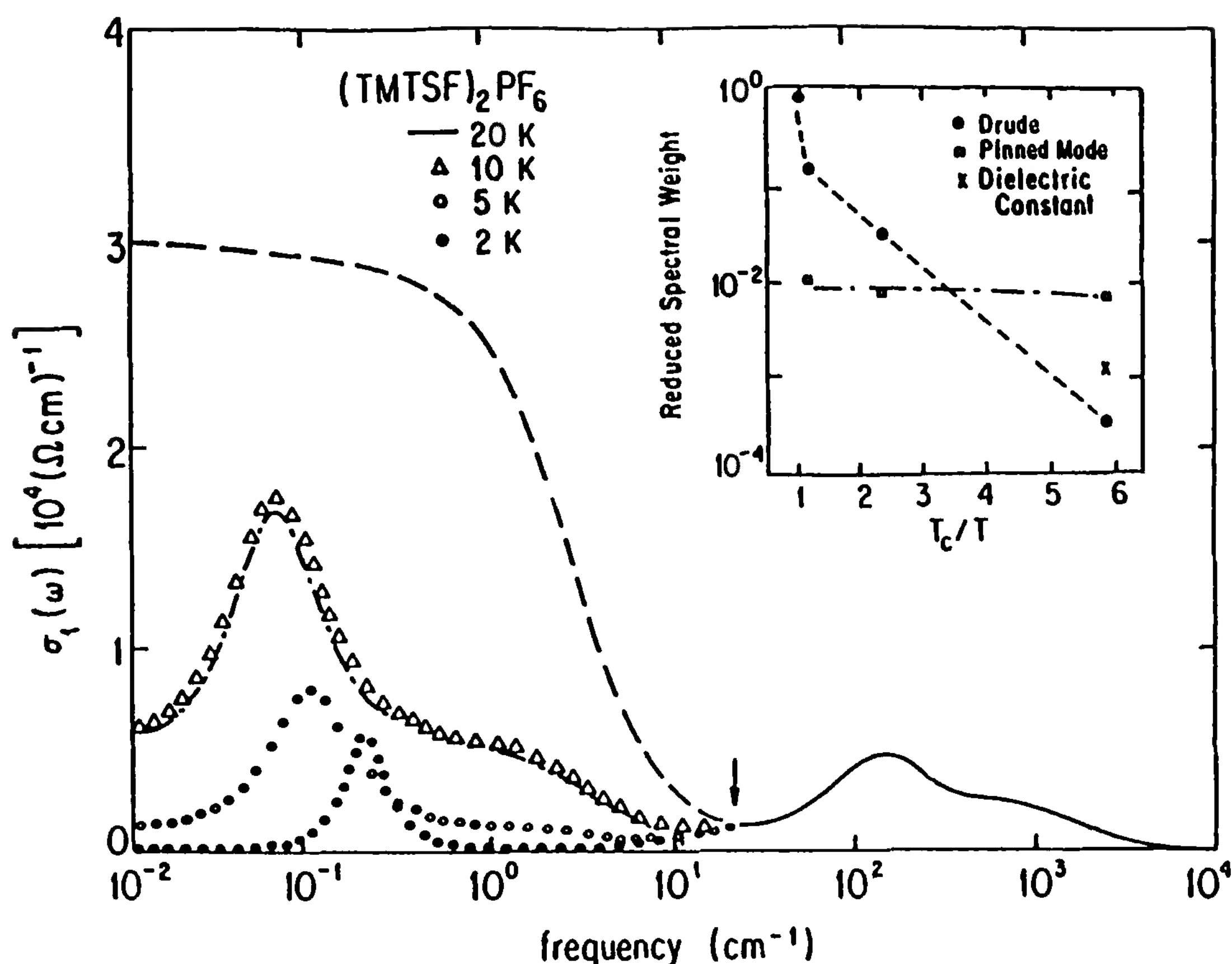


Figure 40 Pinned mode resonance of the SDW state in $(\text{TMTSF})_2\text{PF}_6$. (After Ref. 121.)

one-dimensional character in the energy dispersion for the SDW distortion to become stable at a finite temperature [125].

Again using the model sketched in Section III.D to explain the suppression of the SDW phase under pressure, the divergence of $\chi(\mathbf{q})$ at low temperature can, however, be reactivated as soon as a magnetic field is applied to this quasi-one-dimensional conducting electron gas along the direction c^* of lowest conductivity. $\chi(\mathbf{q}, H)$ thus displays logarithmically divergent peaks at $T \rightarrow 0$ for the set of different wave vectors defined by the relation

$$Q_x = 2k_F + \frac{NeHb}{h} \quad (49)$$

where N is an integer [126]. Crudely speaking, the field restores enough one-dimensional character in the energy dispersion for the SDW distortion to become stable at nonzero temperature (Fig. 43a).

However, the experimental data of $(\text{TMTSF})_2\text{PF}_6$ show that the problem is slightly more sophisticated [127,128]. A sequence of phases must be

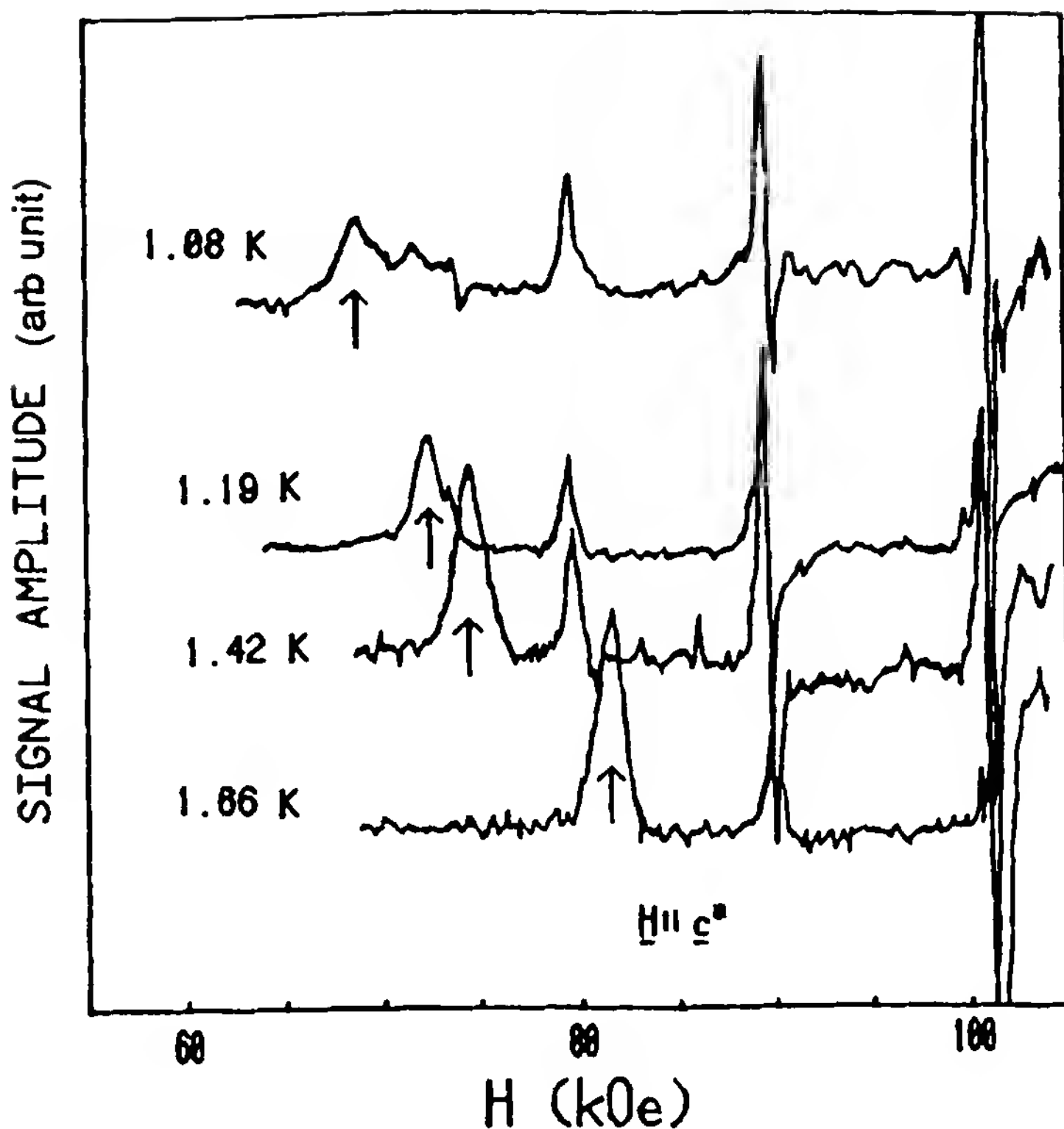


Figure 41 Detection of FISDW phases in $(\text{TMTSF})_2\text{ClO}_4$ via transport measurements. (After Ref. 123.)

crossed before the so-called “ $N = 0$ ” phase (which is believed to correspond to the insulating SDW ground state stable at ambient pressure) can be reached above 18 T (Fig. 44). The integer N , which is related to the deviation of Q_x from $2k_F$, labels the phase containing N fully occupied Landau levels. $N = 0$ means that there is no density of states at the Fermi level, namely, a gap opened over the whole Fermi surface. Phases with $N = 1, 2, 3, \dots$ which are observed below 18 T correspond to semimetallic phases with a very low density of carriers ($\approx 10^{-2}$ per unit cell) and a tubular Fermi surface along the c^* axis. In these subphases 1, 2, or 3, \dots Landau levels are completely filled, respectively.

The situation where the Fermi level falls between completely filled and completely empty levels minimizes the diamagnetic energy of the two-dimensional carriers. This situation prevails in a finite range of magnetic fields as long as the wave vector of the magnetic modulation within a given subphase can vary linearly with the field according to Eq. (49). First-order phase transitions are expected between various subphases, in agreement with the hysteresis shown in Fig. 44.

A direct consequence of the field-dependent \mathbf{Q} vector is the quantization of the Hall resistance at $\rho_{xy} = h/2Ne^2$ (where the factor 2 comes from spin

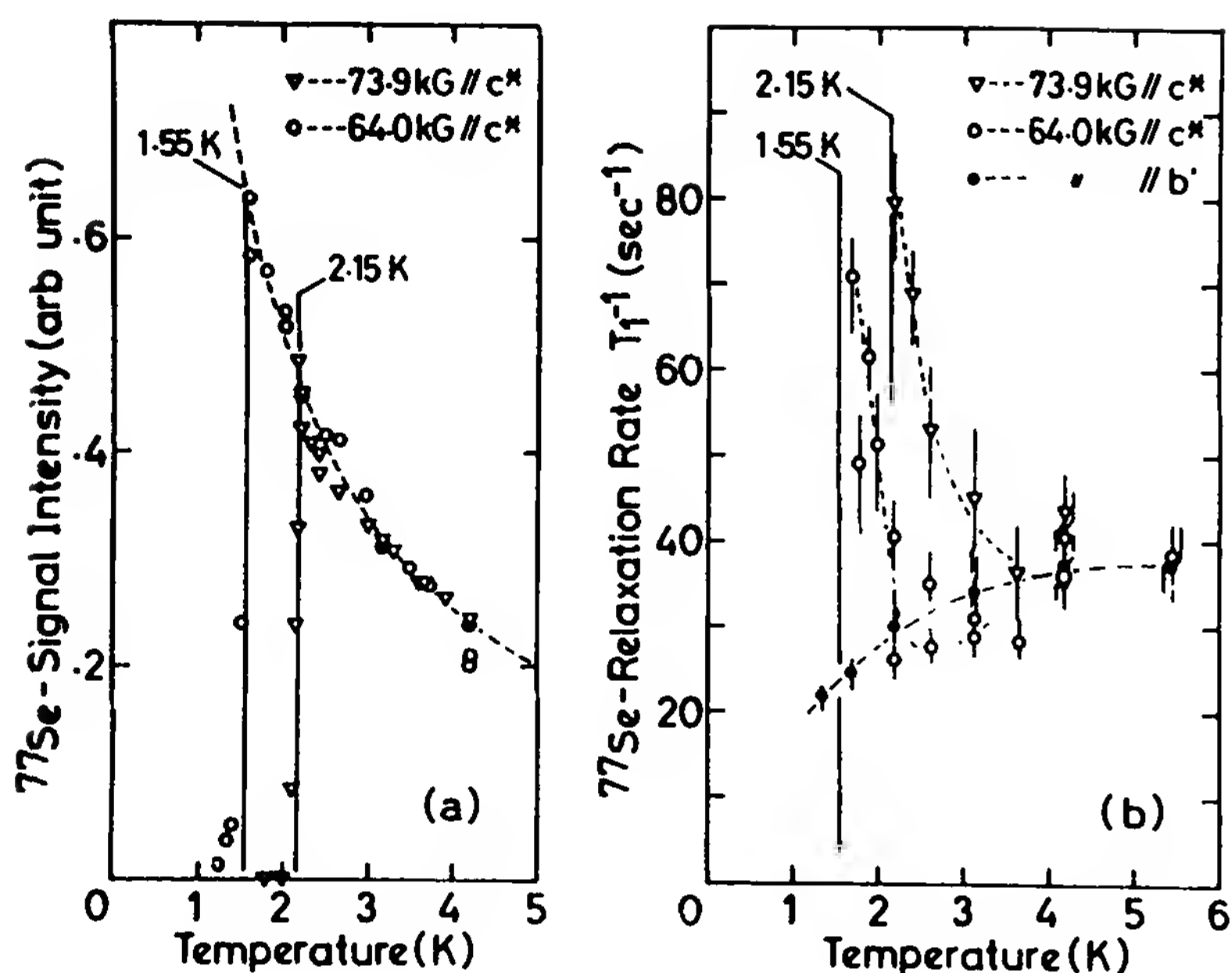


Figure 42 Proof for the magnetic nature of the new phases stabilized under magnetic field in (TMTSF)₂ClO₄. The ⁷⁷Se-NMR line broadens and vanishes (a), whereas the relaxation rate diverges (b). (After Ref. 124.)

degeneracy). The (TMTSF)₂PF₆ Hall data (Fig. 44) agree quantitatively with the quantized nesting theory (Fig. 43b). The almost perfect agreement between these data and the standard model is, however, not observed in other members of the (TMTSF)₂X series with noncentrosymmetric anions (X = ClO₄, ReO₄) [129,131].

The ClO₄ compound is particularly interesting for several reasons. First, the Hall resistance exhibits well-defined plateaus versus magnetic field and these plateaux can be indexed by the quantum numbers $N = 1, 3, 6, \dots$ [130]. The plateau $N = 2$ is apparently missing in the data of Fig. 45 and a sign reversal of the Hall resistance is observed between $N = 3$ and 6. Other authors have attributed a fractional number $N = \frac{1}{3}$ to the phase which is remarkably stable in magnetic field above 8 T [132]. Second, the standard quantized nesting model does not provide an interpretation for the destruction of the SDW observed at very high field with reentrance of the undistorted phase. A non-mean-field approach based on the enhancement of the fluctuations at high fields has been proposed to explain this reentrance [133]. However, a tentative interpretation for the reentrance of the FISDW phase of (TMTSF)₂ClO₄ which is based on the modification of the Fermi surface inferred by the ordering of the anion at 24 K has been suggested [134]. The wave vector that characterizes the ClO₄ ordering is known from x-ray studies to be $(0, \pi/b, 0)$ [69]. This means that the opening of gaps at the points $(2k_F, \pm \pi/b)$ in a two-dimensional picture of the Fermi

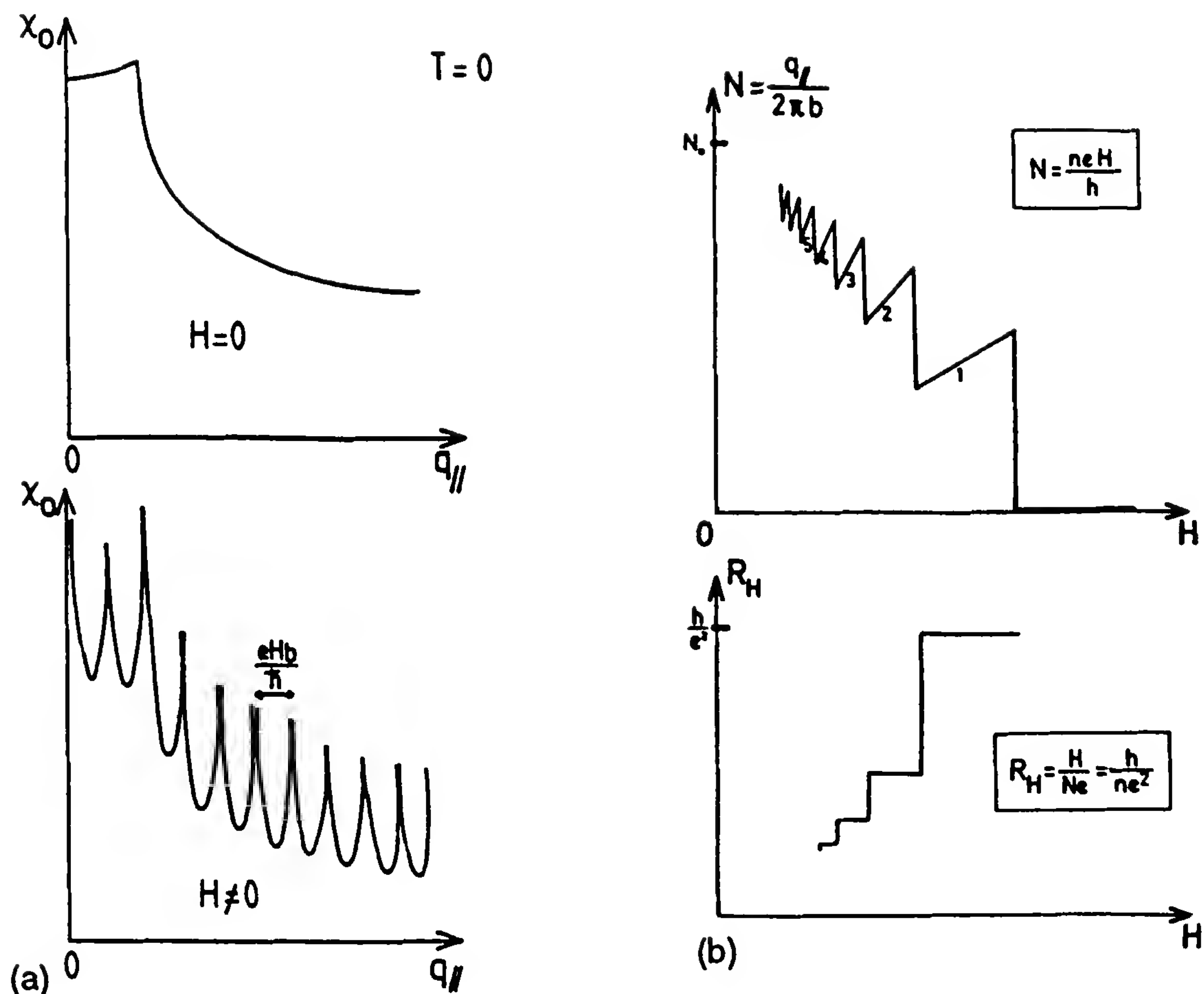


Figure 43 (a) The noninteracting spin susceptibility ($T = 0$ shows a nondivergent maximum at the optimum nesting vector $(2k_F + Q_{\parallel}, q_{\perp})$) (top). Logarithmic divergences are tested under a finite magnetic field (bottom). (b) In each FISDW subphase, the theory predicts a density of carriers, which varies linearly against magnetic field, and the Hall voltage, which is constant. (After Ref. 68a.)

surface is likely to perturb the possibilities of nesting close to the transverse vector $\mathbf{Q}_t = (2k_F, \pi/b)$.

In the standard model of FISDW states the quasi-one-dimensional electron gas is one-dimensionalized by the magnetic field. It is only when the quasi-one-dimensional Fermi surface is made sufficiently flat by a large magnetic field that the $N = 0$ state becomes stable. In the $N = 0$ insulating state a gap opens over the entire Fermi surface and the modulation wave vector of this phase should be closer to the transverse vector $(2k_F, \pi/b)$ than are the characteristic vectors of any semimetallic phases with $N = 1, 2, \dots$. We may reasonably assume that the nesting of the Fermi surface is rather poor in the vicinity of \mathbf{Q}_t (a consequence of the anion ordering). Therefore, the stabilization of the $N = 0$ state is *not* energetically favorable

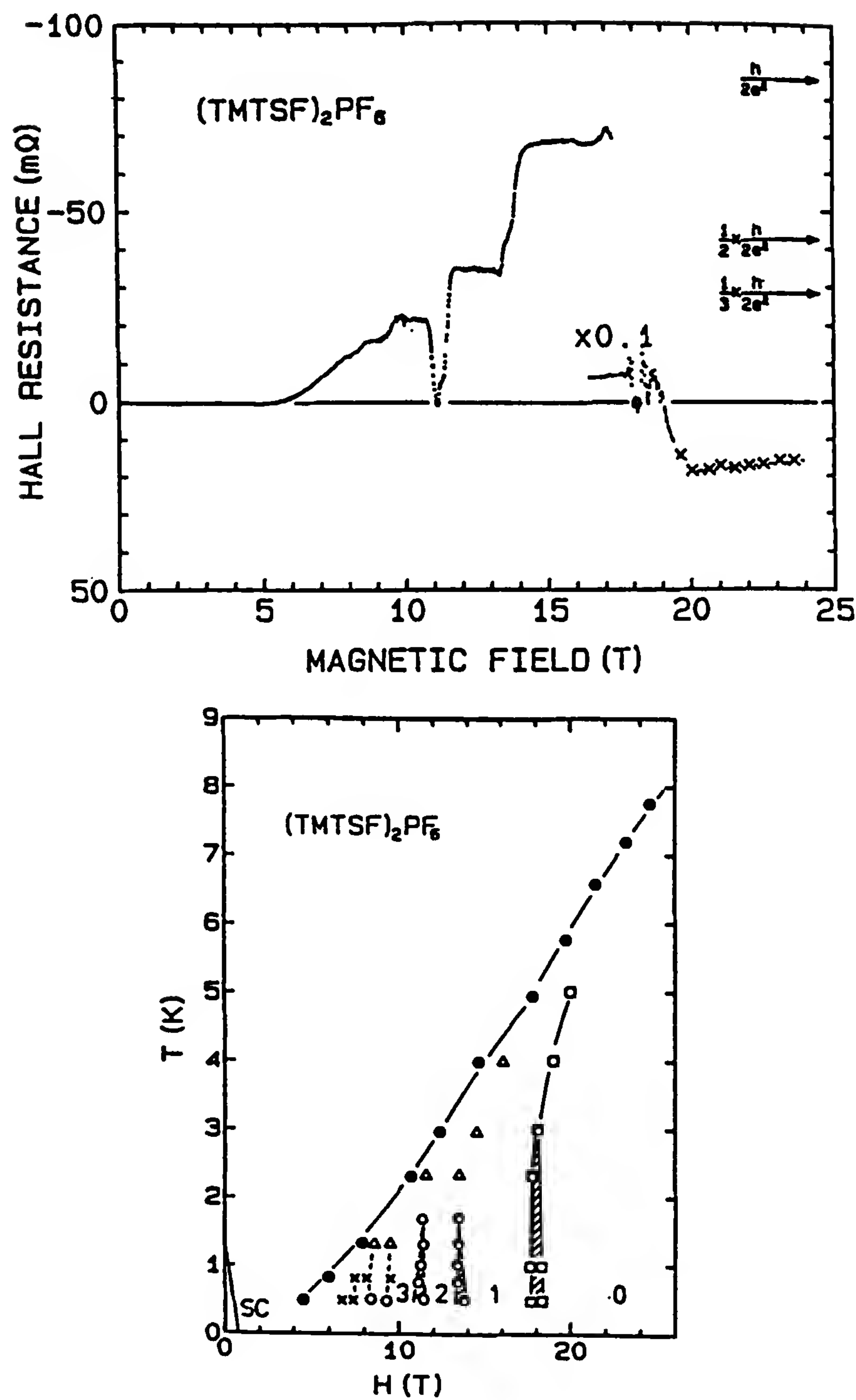


Figure 44 Quantized Hall voltage of $(\text{TMTSF})_2\text{PF}_6$ and phase diagram. The integers indicate the number of filled Landau levels in each subphase. (After Ref. 127.)

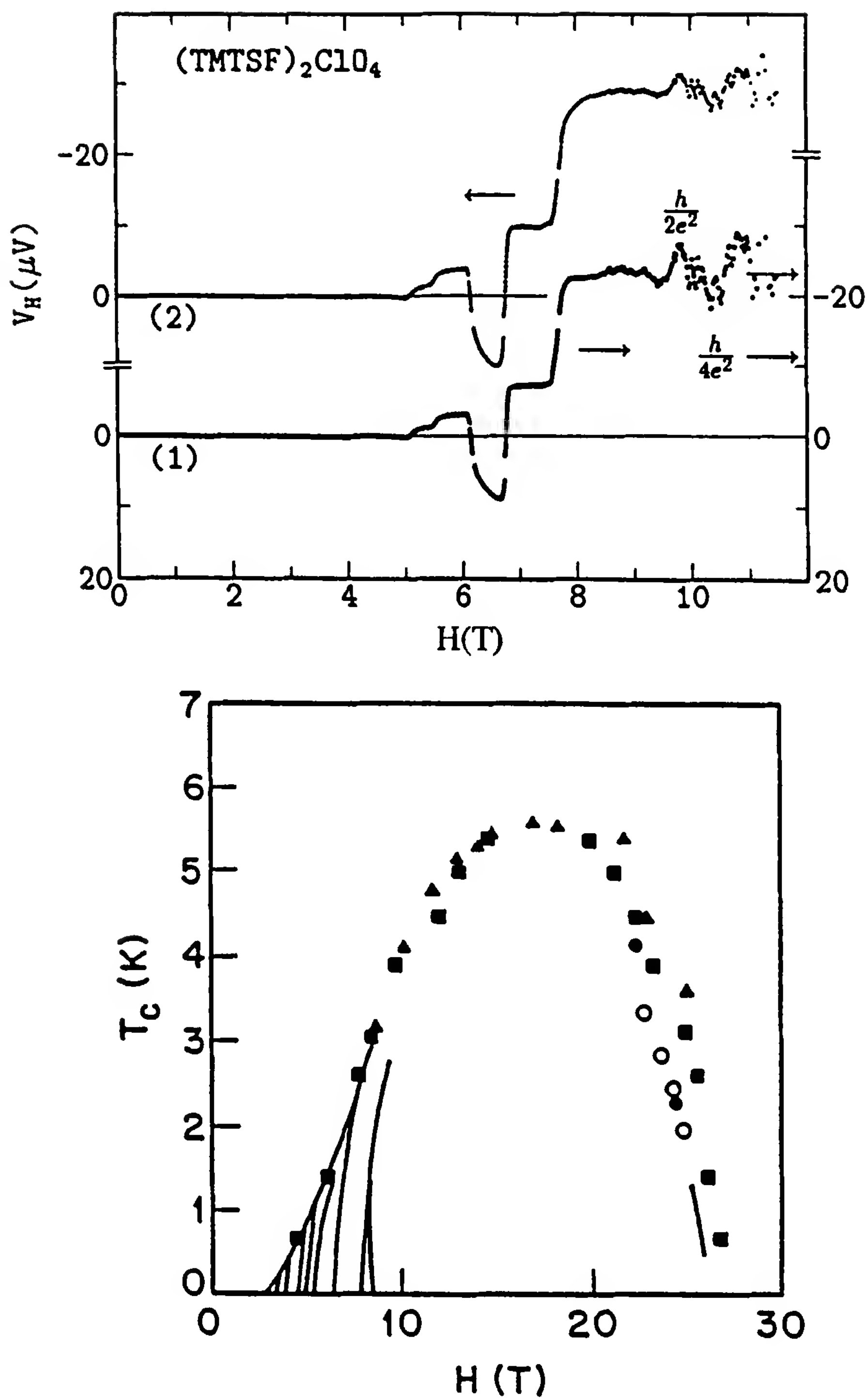


Figure 45 Quantized Hall voltage in $(TMTSF)_2ClO_4$ (two samples) (after Ref. 130) and phase diagram (from Ref. 132). A new phase line has been discovered around 1 K and 30 T (after R. C. Yu et al, *Phys. Rev. Lett*, 65:2458 (1990)). The phase that extends from 8 to 27 T is presumably $N = 1$ [130].

in $(\text{TMTSF})_2\text{ClO}_4$, unlike $(\text{TMTSF})_2\text{PF}_6$, where the Fermi surface is not affected by any anion-ordering potential. Consequently, the $N = 1$ phase of $(\text{TMTSF})_2\text{ClO}_4$ should remain stable in magnetic field since the semi-metallic electron gas ($N = 1$) cannot undergo any phase transition toward a state of lower energy. However, for the diamagnetic energy to be minimized, the only occupied Landau level has to be kept entirely full. As the degeneracy of the Landau level increases linearly with the magnetic field, the density of carriers must adapt to the change of the magnetic field. Such a situation can be achieved only if the magnetic distortion is weakened when the magnetic field is increased with a concomitant decrease in T_{SDW} .

The effect of anion ordering on the stability of FISDW phases has been confirmed quantitatively by calculation of the spin susceptibility following the standard approach and including an additional periodic potential with wave vector $\mathbf{Q} = (0, \frac{1}{2}, 0)$ [135]. After this numerical computation even phases ($N = 0, 2$) are suppressed, whereas odd phases $N = 1, 3$ are not. The same model also explains the normal-phase reentrance above 17 T. However, the predicted oscillation for T_c versus the magnetic field in the $N = 0$ phase is still lacking in the experimental data.

The quantization of the Hall resistance in the FISDW phases is indeed very reminiscent of the quantum Hall effect in the two-dimensional electron gas [136]. There is, however, an important difference between these two phenomena. In both cases the quantization requires a reservoir of non-conducting electronic states. This reservoir is provided either by localized states in the gap between conducting Landau levels or by the electron-hole (spin modulation) condensate for the two-dimensional electron gas and the FISDW of organics, respectively.

B. Angular-Dependent Magnetoresistance

Another new phenomenon has been discovered in the study of the angle dependence of magnetotransport properties of quasi-one-dimensional conductors such as $(\text{TMTSF})_2\text{ClO}_4$ and $(\text{TMTSF})_2\text{PF}_6$. The first report of this effect was made by Boebinger et al. [137] and Naughton et al. [138], who observed fine dips in the magnetoresistance of $(\text{TMTSF})_2\text{ClO}_4$ at characteristic angles when the magnetic field is rotated in the $b'c^*$ plane (which is perpendicular to the conducting a axis; Fig. 46). The presence of magnetoresistance dips in the metallic phase of $(\text{TMTSF})_2\text{ClO}_4$ [139] is clearly not ruled by the orientation dependence of the FISDW phase diagram since the threshold fields are governed only by the component of the external field along the c^* direction, as expected for two-dimensional systems. The unusual angular dependence of the magnetoresistance is related to “magic” angles [139] which satisfy the commensurability relation, given

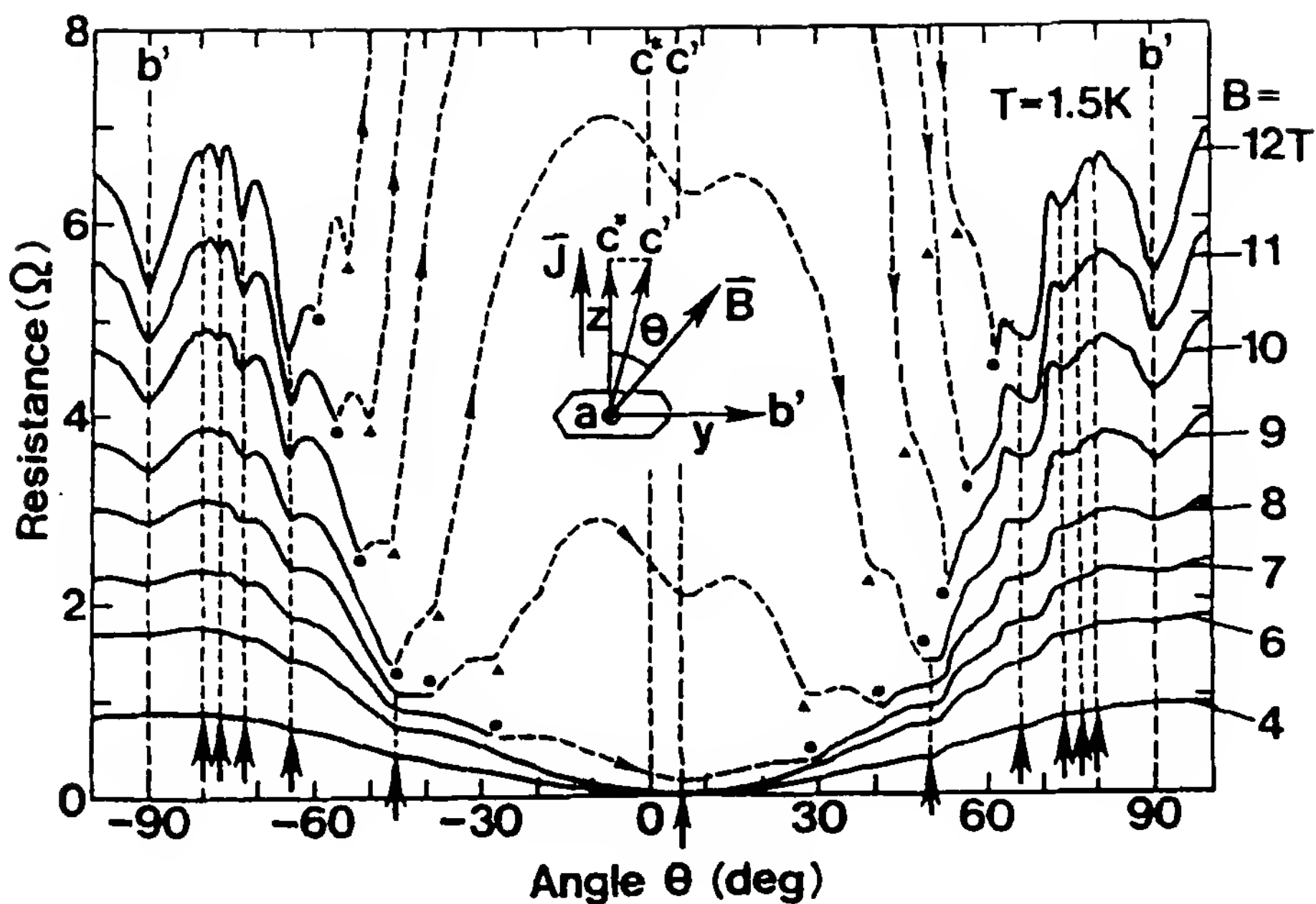


Figure 46 Angular oscillations of the magnetoresistance in $(\text{TMTSF})_2\text{ClO}_4$ [139] showing features at magic angles given by Eq. (50).

in an approximate form by

$$\tan \theta = \frac{m}{n} \frac{b}{c} \quad (50)$$

where b and c refer to the lattice periodicities and m, n are integers. The existence of fine-structure behavior in the magnetoresistance was first predicted theoretically by Lebed and Bak [140].

In a tilted magnetic field $H = (0, H \sin \theta, H \cos \theta)$ the electron can move along constant-energy trajectories. This motion is controlled by two periodic potentials with wave vectors $G_y = (e/\hbar) bH \cos \theta$ and $G_z = (e/\hbar) cH \sin \theta$. When the field angle satisfies the commensurability condition, $G_y/G_z = n/m$. The two periods become commensurate, and for “magic” angles given by Eq. (50), the periodic electron trajectories do not sweep out the entire Fermi surface as they do for arbitrary angles (Fig. 47).

This effect has been evidenced most clearly in $(\text{TMTSF})_2\text{PF}_6$, which is also a prototype system for the stabilization of FISDW [127,128] (Fig. 48). Very sharp dips of magnetoresistance are observed in the metallic phase at angles that satisfy the relation $m/n = 0, \pm 1, \pm 2$ [141,142]. A commensurability effect at the same angles is also seen in the FISDW state, although peaks instead of dips are observed there [141] and a drop in the FISDW threshold field is observed at magic angles, in agreement with a suggestion of Lebed [143] that at angles given by Eq. (50), the coupling

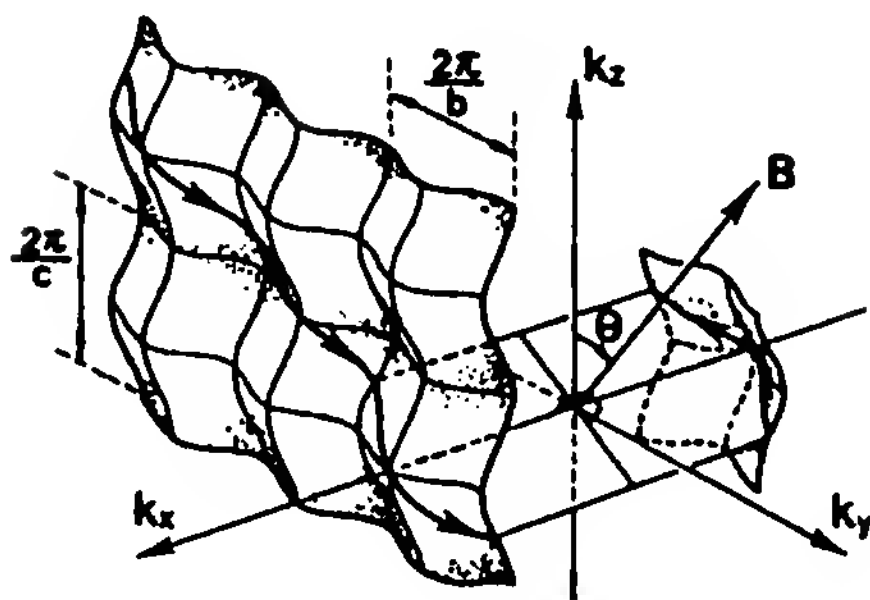


Figure 47 Electron trajectory on the Fermi surface of a quasi one-dimensional conductor under magnetic field satisfying the commensurability condition. (After Ref. 144.)

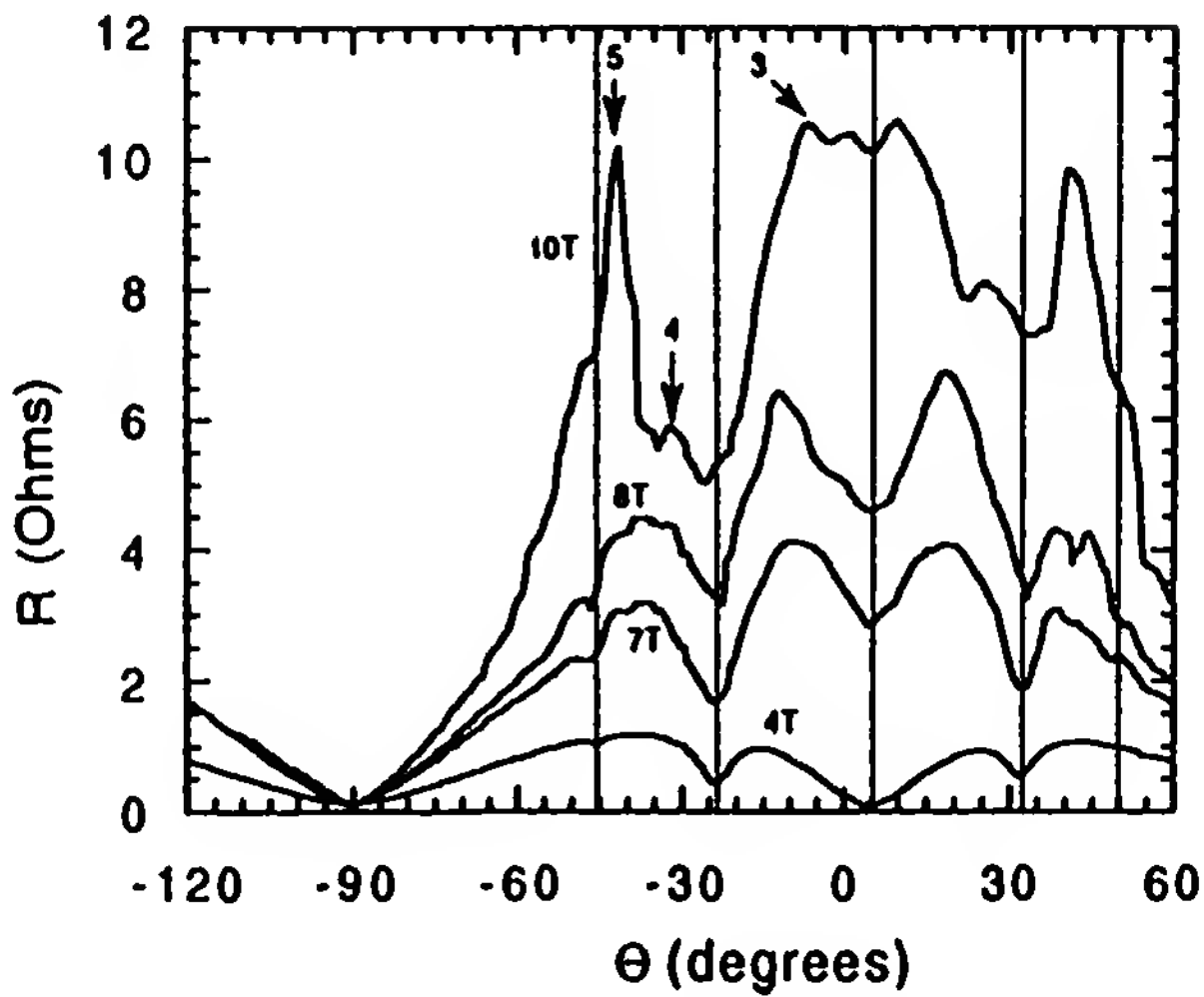
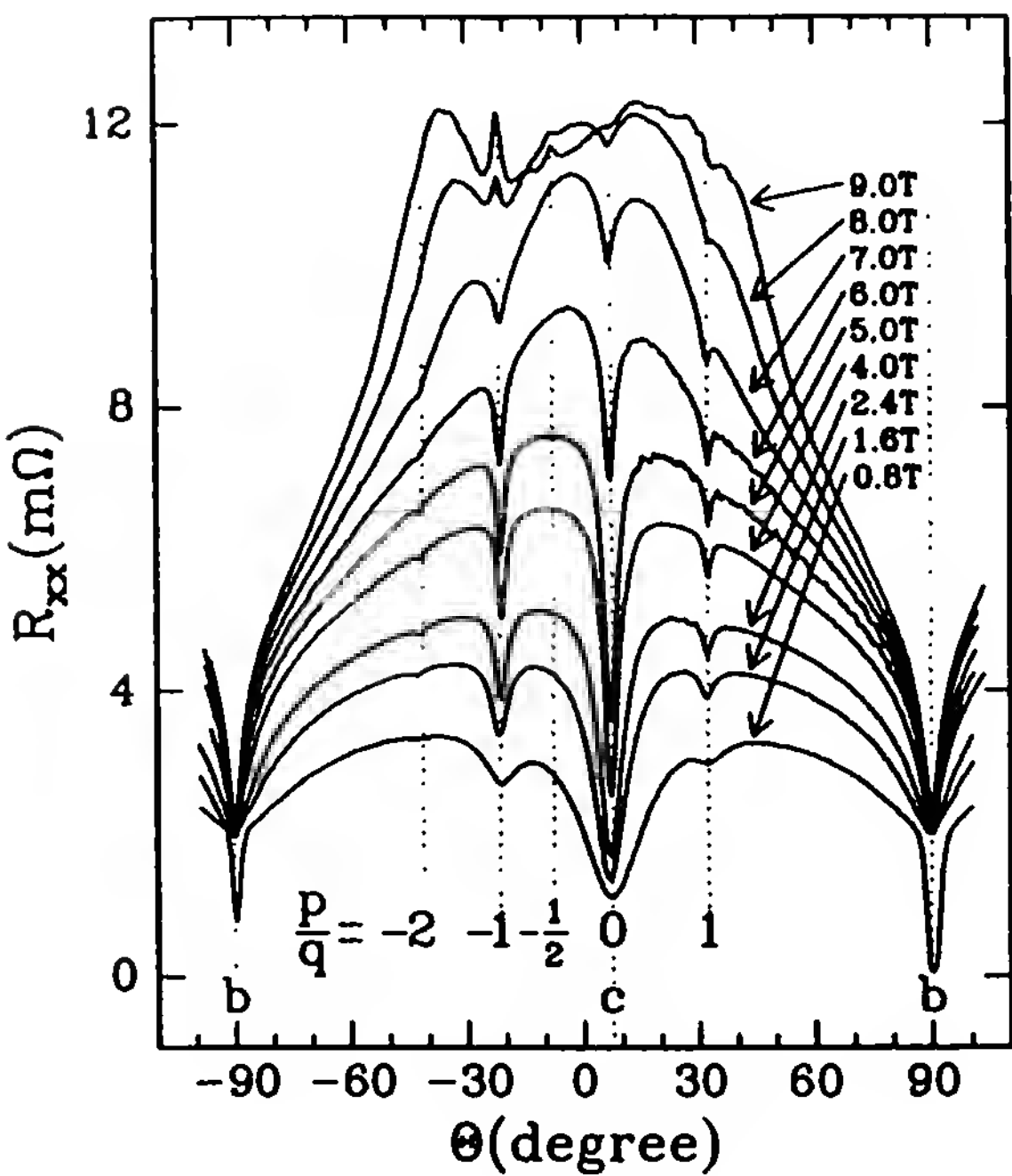


Figure 48 Lebed oscillations in $(\text{TMTSF})_2\text{PF}_6$. (Data from Refs. 141 (left) and 142 (right).)

along the third direction is eliminated and the electron gas becomes actually two-dimensional, making the FISDW state more stable at magic angles.

Several suggestions have been proposed to explain the fine structure of the angular dependence of the magnetoresistance. According to Lebed and Bak [140], a resonance of the electron scattering rate is expected at commensurate angles, but it should give rise to peaks in magnetoresistance instead of the minima that are observed. Kagoshima et al. [144] have shown the existence of a finite average velocity leading to a conductivity enhancement

along the magnetic field direction at magic angles. Other models predicting resistance dips have been proposed by Maki [145] and Chaikin [146].

C. Two-Dimensional Superconductors Under High Fields

Other spectacular effects of low dimensionality are observed in the series of $(\text{ET})_2\text{X}$ conductors with a two-dimensional tubelike Fermi surface. Figure 49 presents magnetoresistance data in the phase of $\beta_{\text{H}}(\text{ET})_2\text{I}_3$ which can be stabilized at low temperature following a special procedure [147]. Unlike the phase $\beta_{\text{L}}(T_c = 1.2 \text{ K})$ obtained after a regular cooling down, the β_{H} phase, which can be stabilized at atmospheric pressure after the special cooling procedure under pressure [148] (Fig. 49a), is free of any incommensurate lattice modulation and T_c rises up to 8.1 K (Fig. 49a) [15]. The oscillation of extremely large amplitude which is shown above 9 T (Fig. 49b) in the β_{H} phase is periodic in $1/H$ with a fundamental field $H_0 = 3730 \text{ T}$, which corresponds to the cross section of the tubular Fermi surface by a plane perpendicular to the field (H is thus perpendicular to the conducting sheets) agrees with a density of carriers of ≈ 1 per formula unit. In addition, the low-frequency beating is related to the deviation from perfect two-dimensionality. The low-frequency $H_1 = 36.8 \text{ T}$ provides an estimate for the interlayer coupling, namely $t_c \approx 0.5 \text{ meV}$ (if $t_{\parallel} = 70 \text{ meV}$). With the value of T_c derived from the experiment, the discrete Landau levels are actually broadened into minibands of width $4t_c = 2 \text{ meV}$ due to the energy dispersion along the k_z direction. It has been recognized [149] that the discretization can be restored when the magnetic field is no longer perpendicular to the conducting planes (i.e., $H \parallel c^*$) but tilted by an angle ϕ from the c^* axis, such as (Fig. 50a)

$$ck_F \tan \phi = \pi(n - \tfrac{1}{4}), \quad \text{with } n = 1, 2, 3, \dots \quad (51)$$

At magic angles given by the previous relation, the cross section of the Fermi surface normal to the magnetic field becomes independent of the k_z coordinate; the minibands are nearly discretized (the width of each miniband becomes smaller than the splitting between Landau levels). This model has explained the angle-dependent magnetoresistance oscillations which are observed in $\beta(\text{ET})_2\text{IBr}_2$ [150] (Fig. 50b) and in other two-dimensional $(\text{ET})_2\text{X}$ salts [144,151] (Fig. 51).

VIII. CONCLUSIONS

The study of the new class of synthetic conductors in which superconductivity has been discovered has contributed to a better experimental and theoretical understanding of the physics in low-dimensional electron gases

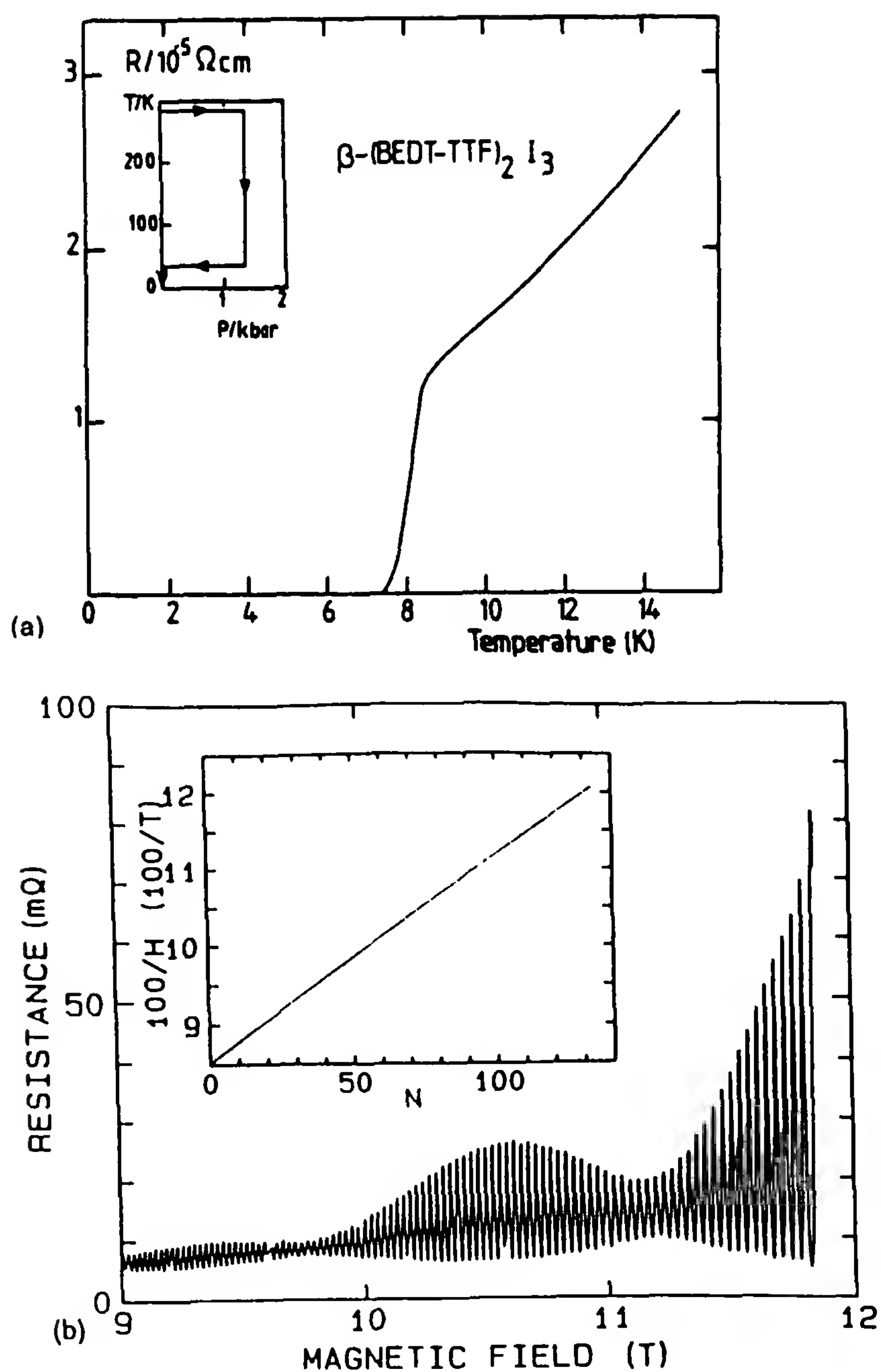


Figure 49 (a) Superconducting transition of $\beta_{\text{H}}(\text{ET})_2\text{I}_3$ at 8.1 K after a cooling procedure indicated in the inset. (From Ref. 15.) (b) Giant oscillations of the transverse magnetoresistance of $\beta_{\text{H}}(\text{ET})_2\text{I}_3$. (From Ref. 147.) The insert shows that fields corresponding to extrema are periodic versus $1/H$. The low-frequency beating is due to the finite but small interlayer coupling.

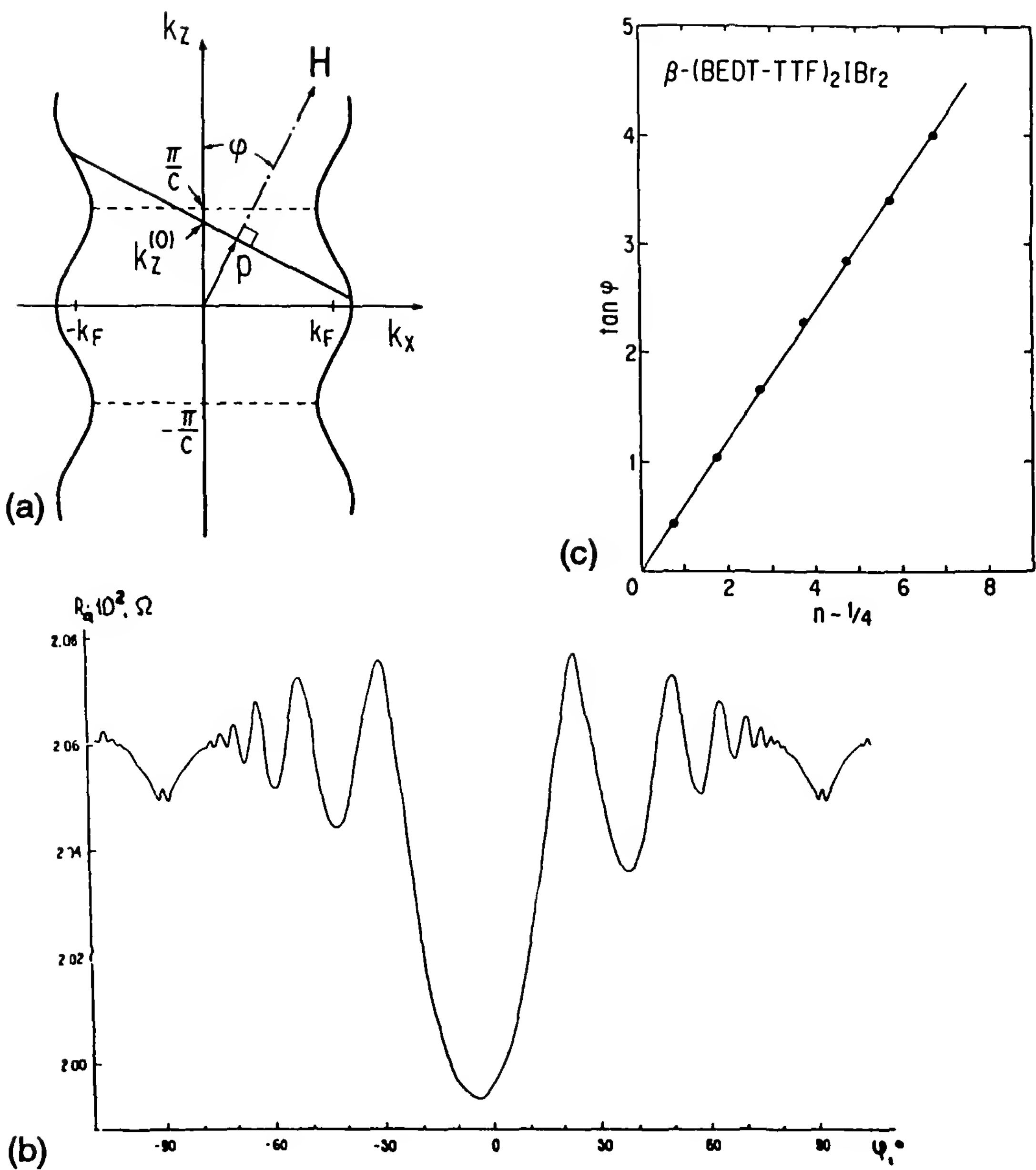


Figure 50 (a) The cross section of the Fermi surface normal to the magnetic field is independent of k_z at field orientations satisfying relation (51). (After Ref. 149.) (b) Angular oscillations of the magnetoresistance of the two-dimensional conductor $\beta\text{(ET)}_2\text{IBr}_2$. (After Ref. 150.) (c) Magic angles determined by the peaks of the magnetoresistance in (b) follow very accurately the relation (51).

(one- or two-dimensional), although there is still no firm explanation for the driving mechanism leading to the attractive pairing in organic superconductors. The interplay between antiferromagnetic and superconducting ground states in the TM_2X series, the role of coulombic interactions in the magnetic properties of the low-dimensional electron gas above T_c , and the

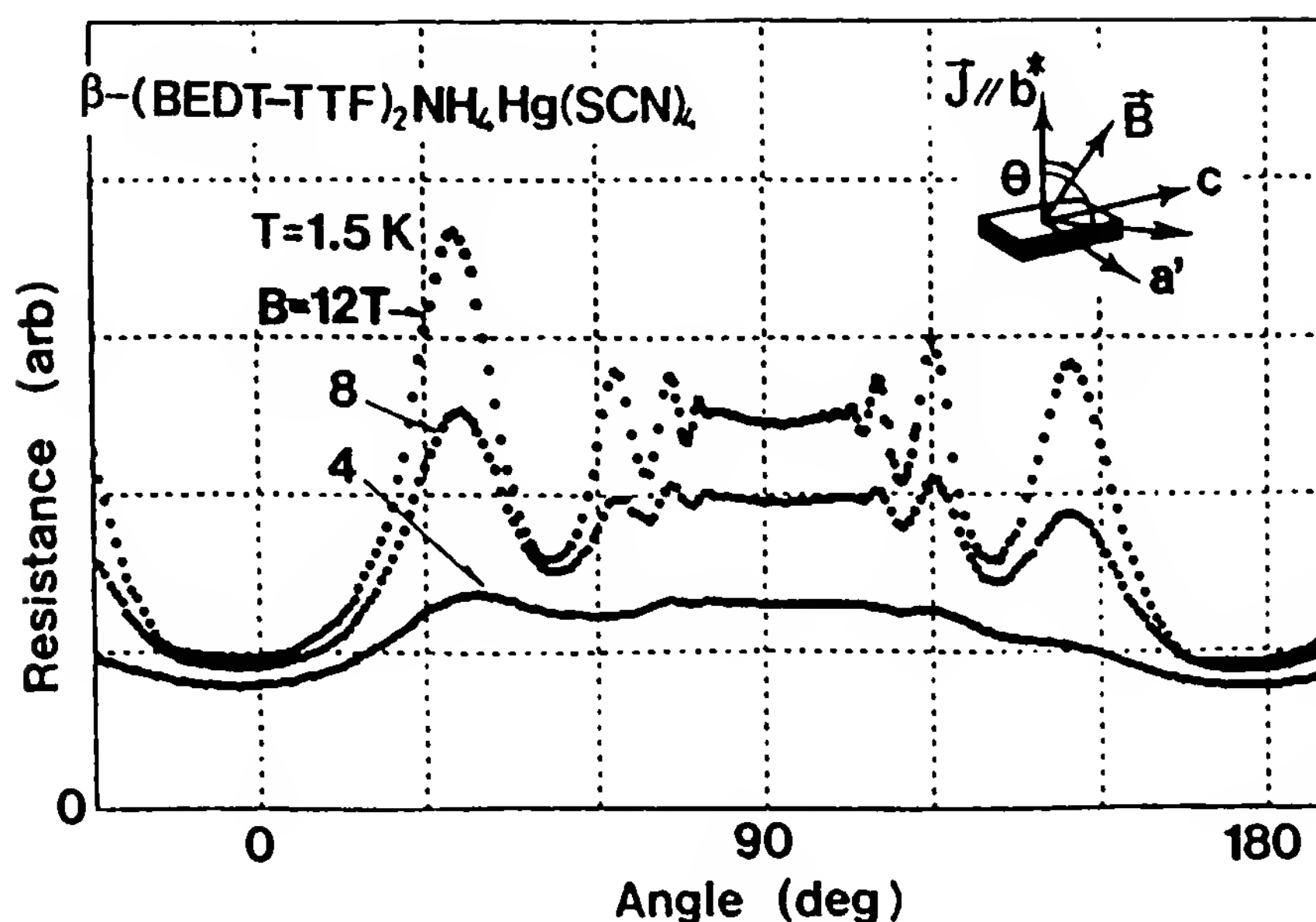


Figure 51 Angular oscillations of the κ -phase $(\text{ET})_2\text{NH}_4\text{Hg}(\text{SCN})_4$. (From Ref. 144.)

strong sensitivity of T_c to nonmagnetic impurities in both one- and two-dimensional organic superconductors are all factors playing in favor of a nonconventional superconducting mechanism. However, it is still premature to establish a close connection between the mechanism of superconductivity in existing organic superconductors and the model proposed 25 years ago by Little. Moreover, the stabilization of spin density wave phases at high magnetic field and the coherent motion of a SDW state under high electric field are remarkable products of the developments of these new compounds.

The recent discovery of superconductivity in compounds of fullerenes doped with alkali and alkaline-earth metals is very encouraging for the future of organic superconductors in which conductivity is governed by the formation of π orbitals. The fullerenes, in which the superconductivity is presumably mediated by high-energy intraball vibrations, represent a good compromise between a weak interball interaction and the on-site coulombic repulsion, which is sufficiently small to prevent the stabilization of an insulating Wigner crystal.

Several important and recent aspects of the physical properties of these molecular superconductors have been left by the roadside. It is the case, for example, for the physics of quasi-one-dimensional conductors at very high magnetic field when the undistorted phase exhibiting a metal-like behavior at zero field should become localized [152]. Reentrance of a superconducting instability is also expected at very low temperature under

high magnetic field [153]. The problem of the mixed superconducting phase of the two-dimensional organic compounds has not been discussed, although a magnetization irreversibility line, a vortex melting transition [154, 155], a slow dynamics of the vortex lines [156], and an intrinsic vortex pinning [157] have been observed experimentally in $(\text{ET})_2\text{X}$ superconductors.

The entire series of perylene salts comprising parallel segregated stacks of conducting chains and insulating spins are presented in Chapter 7. Transport and magnetic properties of organic superconductors as well as earlier compounds such as TTF-TCNQ and related systems are discussed in Chapter 9. A detailed presentation of the theory of one-dimensional conductors can be found in Chapter 2. The prospects for applications of organic superconductors are still in their infancy (see also Chapter 16). The future will depend very much on new openings for materials preparation.

However, when large areas of organic superconductors become available, it may be possible to take advantage of the Josephson effect and to use arrays of Josephson circuits prepared by lithographic techniques for the fabrication of low-current devices such as high-density memories and microwave detectors [158]. The very narrow electronic paramagnetic resonance of some organic conductors can be used in sensitive magnetic sensors [159].

ACKNOWLEDGMENTS

I gratefully acknowledge the constructive and fruitful cooperation which has been very active between Orsay and several laboratories in physics and chemistry all over Europe, Qu  bec, and South Korea. The list of colleagues and co-workers who have been involved in the research on molecular superconductors is so long that I would rather refer the reader to the reference list, where the names of colleagues who should be thanked for their cooperation can easily be found. This research has been supported partially by EEC Esprit Basic Research Action 3121, Stimulation Program CI-CT 90-0863 at DG XII, DRET contract 88/198, and CNRS-GDR C₆₀.

NOTE ADDED IN PROOF

The compound $(\text{TMTTF})_2\text{Br}$ occupies a key position in the generalized TM_2X phase diagram of Fig. 5. The small amplitude of the lattice dimerization, see Table 1, goes along with the observed weak one-dimensional $4k_F$ localization occurring below 80 K as displayed in Fig. 6a. Furthermore, the commensurate character of the spin modulation of the SDW ground state is very likely related to the localized character of the spins and to the concomitant absence of Fermi surface in the temperature regime 80–15

K. However, the one-dimensional localization at a temperature higher than the onset of the SDW state is known to be suppressed by a pressure exceeding 5 kbar or so [160]. ^1H -NMR data [161] have revealed a temperature independent spin-lattice relaxation rate in the SDW phase under 13 kbar (besides the strong temperature dependence related to the three-dimensional critical divergence) at variance with the activated behavior, Fig. 8, observed at 1 bar in the same temperature regime. As already reported in the study of $(\text{TMTSF})_2\text{PF}_6$ at 1 bar a temperature independent relaxation rate is a manifestation of the existence of low lying spin excitations such as phason modes, [52]. We may understand the behavior of NMR data under pressure as the signature of a pressure induced commensurate-incommensurate cross-over between 1 bar and 13 kbar. The commensurability cross over may be closely related to the suppression of the $4k_F$ localization as suggested by Fig. 5.

The investigation of transport properties under pressure has shown that the SDW ground state can be suppressed above a critical pressure of 25 kbar [160]. $(\text{TMTTF})_2\text{Br}$ was thus found to retain a strong metallic character down to 1.2 K. Furthermore, some samples showed a slight drop of the resistance down to a nonzero value near 3.5 K which was ascribed to a possible signature of superconductivity [160].

A recent reinvestigation of this compound down to 0.4 K has now proved unambiguously the existence of a transition toward a zero resistance state at $T_c = 0.8$ K under 25 kbar with a 10–90% width of 0.4 K [162]. It is possible that the 3.5 K anomaly observed previously was only related to precursor effects of a three-dimensional superconducting transition occurring below 1 K. This new finding of superconductivity in the $(\text{TMTTF})_2\text{X}$ family gives strong indications for TM_2X compounds to be considered as a whole as far as the theoretical interpretation is concerned.

However there remains an important problem with this material since FISDW phases are missing in $(\text{TMTTF})_2\text{Br}$ under 25 kbar at 0.4 K up to 20 Tesla. The absence is puzzling in comparison with other quasi one-dimensional superconductors in which the threshold fields for the stabilization of FISDW phases have always been located below 10T at $T = 0.5$ K, Figs. 44, 45 and reference 131 for $(\text{TMTSF})_2\text{ReO}_4$. Within the standard theory of FISDW phases the logarithmic divergence in temperature of the susceptibility under magnetic field at a wave vector governed by the magnetic field is preserved provided the amount of non-nesting along the weak coupling direction is smaller than the cyclotron energy, namely $t_c^2/t_a < \hbar\omega_c$. The latter condition is easily fulfilled for all compounds undergoing FISDW transitions below 10T since $t_c \sim 1$ meV according to a calculation [163].

As far as $(\text{TMTTF})_2\text{Br}$ is concerned the c-axis parameter is the smallest within the TM_2X series [164,165]. The dominant role of interchain coupling

in (TMTTF)₂Br is also supported by the broadest EPR line width among compounds of the (TMTTF)₂X series [47]. This situation could lead to an increased three-dimensional coupling with a possible suppression of FISDW phases below 20T.

REFERENCES

1. W. A. Little, Phys. Rev. A 134:1416 (1964).
2. J. Friedel and D. J  rome, Contemp. Phys. 23:583 (1982).
3. F. Wudl et al., J. Chem. Soc. Chem. Commun., 1453 (1970).
4. D. R. Salahub et al., Phys. Rev. 13:4052 (1976); A. J. Berlinski et al., Solid State Commun., 19:1165 (1976).
5. K. Bechgaard et al., Solid State Commun., 33:1119 (1980).
6. D. J  rome and H. J. Schulz, Adv. Phys. 31:299 (1982).
7. G. Brun et al., C. R. Acad. Sci. 284:211 (1977).
8. D. J  rome, Science 252:1509 (1991).
9. D. J  rome et al., J. Phys. Lett. 41:L95 (1980).
10. K. Bechgaard et al., Phys. Rev. Lett. 46:852 (1981).
11. L. Alc  cer et al., Solid State Commun. 35:945 (1980).
12. L. Brossard et al., C. R. Acad. Sci. 302:205 (1986).
13. J. M. Williams et al., Science 252:1501 (1991).
14. V. N. Laukhin et al., JETP Lett. 41:81 (1985); K. Murata et al., J. Phys. Soc. Jpn. 54:1236 (1985).
15. F. Creuzet et al., J. Phys. Lett. 46:L1079 (1985).
16. H. Urayama et al., Chem. Lett., 55 (1988).
17. J. M. Williams et al., Inorg. Chem. 29:3272 (1990).
18. A. M. Kini et al., 29:2555 (1990).
19. H. W. Kroto et al., Nature 318:162 (1985).
20. R. Haddon et al., Acc. Chem. Res. 25:127 (1992).
21. W. Kr  tschmer et al., Nature 347:354 (1990).
22. A. F. Hebbard et al., Nature 350:600 (1991).
23. K. Holczer et al., Science 252:1154 (1991); A. F. Hebard et al., Nature 350:320 (1991).
24. K. Tanigaki et al., Nature 352:222 (1991).
25. (a) L. D. Landau and E. M. Lifshitz, *Statistical Physics*, Pergamon Press, Elmsford, N.Y., 1959, p. 482; (b) Y. A. Byschkov et al., Sov. Phys. JETP 23:489 (1966).
26. J. Solyom, Adv. Phys. 28:201 (1979).
27. V. Emery, in *Highly Conducting One-Dimensional Solids* (J. T. Devreese, R. P. Evrard, and V. C. E. van Doren, eds.), Plenum Press, New York, 1979, p. 247.
28. J. P. Pouget et al., Phys. Rev. Lett. 37:437 (1976).
29. H. J. Schulz, Int. J. Mod. Phys. B 5:57 (1991).
30. V. J. Emery, J. Phys. C3 44:977 (1983).

31. C. Bourbonnais et al., J. Phys. Lett. 45:L755 (1984); V. N. Prigodin and Y. A. Firsov, Sov. Phys. JETP 49:369 (1979).
32. (a) P. M. Grant, J. Phys. C3 44:847 (1983). (b) T. Mori et al., Chem. Lett. 957 (1984).
33. B. Gallois, Thesis, Univ. Bordeaux I, 1987.
34. L. Ducasse et al., J. Phys. C 19:3805 (1986).
35. C. Coulon et al., Mol. Cryst. Liq. Cryst. 79:249 (1982).
36. J. P. Pouget et al., Mol. Cryst. Liq. Cryst. 79:129 (1982).
37. S. S. P. Parkin et al., J. Phys. C3 44:111 (1983); A. Maaroufi et al., J. Phys. C3 44:p. 1091.
38. M. Miljak et al., J. Phys. C3 44:893 (1983).
39. C. Bourbonnais et al., Phys. Rev. Lett. 62:1532 (1989).
40. T. Moriya, J. Phys. Soc. Jpn. 18:516 (1963).
41. (a) C. Bourbonnais, J. Phys. I 3:143 (1993); (b) P. Wzietek et al., J. Phys. I 3:171 (1993).
42. C. Bourbonnais, in *Low Dimensional Conductors and Superconductors*, NATO-ASI Series, (D. Jérôme and L. G. Caron, eds.), Plenum Press, New York, 1987, p. 155.
43. P. Wzietek et al., Europhys. Lett. 12:453 (1990).
44. V. Emery et al., Phys. Rev. Lett. 48:1039 (1982).
45. J. C. Bonner and M. E. Fisher, Phys. Rev. 135 A640 (1964).
46. F. Creuzet, Thesis, Univ. Orsay, 1987.
47. C. Coulon, Thesis, Univ. Bordeaux, 1981; J. Phys. C3, 44:885 (1982).
48. P. Auban et al., J. Phys. 50:2727 (1989).
49. Q. Liu et al., J. Phys. I 3:803 (1993); J. Phys. I 3:821 (1993).
50. F. Creuzet et al., J. Phys. Lett. 43:L755 (1982).
51. B. Gotschy et al., J. Phys. I, 2:677 (1992).
52. F. Barthel et al., Europhys. Lett. 21:87 (1993).
53. A. Andrieux et al., J. Phys. Lett. 42:L87 (1982).
54. K. Mortensen et al., Phys. Rev. B 25:3319 (1982).
55. K. Yamaji, J. Phys. Soc. Jpn. 51:2787 (1982).
56. C. Bourbonnais et al., Phys. Rev. B 33:7608 (1986).
57. F. Creuzet et al., Synth. Metals 19:289 (1987).
58. M. Kimura, Prog. Theor. Phys. 53:995 (1975).
59. B. Gallois et al., Synth. Metals 19:321 (1987).
60. (a) G. Soda et al., Solid State Commun. 18:1417 (1976); (b) G. Soda et al., J. Phys. 38:931 (1977).
61. W. Kang, Thèse, Univ. Paris-Sud, 1989.
62. S. Tomic et al., J. Phys. I 1:1603 (1991).
63. T. Giamarchi, Phys. Rev. B 44:2905 (1991).
64. J. Cooper et al., J. Phys. (Paris) 38:1097 (1977).
65. M. Ribault et al., J. Phys. Lett. 44:L953 (1983).
66. K. Bechgaard et al., Solid State Commun. 33:1119 (1980).
67. (a) P. Chaikin et al., Phys. Rev. B 12:1627 (1976); (b) R. L. Greene et al., Mol. Cryst. Liq. Cryst. 79:183 (1982).

68. (a) G. Montambaux, in *Low-Dimensional Conductors and Superconductors* (D. Jérôme and L. G. Caron, eds.) Plenum Press, New York, 1987, p. 233; (b) K. Yamaji, in *Organic Superconductors* (T. Ishiguro and K. Yamagi, eds.), Springer-Verlag, Berlin, 1990.
69. J. P. Pouget, in *Low-Dimensional Conductors and Superconductors* (D. Jérôme and L. G. Caron, eds.), Plenum Press, New York, 1987, p. 17.
70. J. P. Pouget et al., J. Phys. C3 44:969 (1983).
71. S. Tomic et al., J. Phys. C3 44:1083 (1983).
72. M. Héritier et al., J. Phys. Lett. 45:L433 (1984) and G. Montambaux, M. Héritier, and P. Lederer, Phys. Rev. Lett. 55:2078 (1985).
73. R. Moret et al., Phys. Rev. Lett. 49:1008 (1982).
74. R. Moret et al., Phys. Rev. Lett. 57:1915 (1986).
75. J. P. Pouget et al., J. Phys. Lett. 42:543 (1981).
76. D. Jérôme, C. R. Acad. Sci. 317:569 (1993).
77. S. Tomic and D. Jérôme, J. Phys. Condensed Matter, 1:4451 (1989).
78. K. Andres et al., Phys. Rev. Lett. 45:1449 (1980); D. Mailly et al., J. Phys. C3 44:1037 (1983).
79. P. Garoche et al., J. Phys. Lett. 43:L147 (1982).
80. N. Bulaevskii, Adv. Phys. 37:443 (1988).
81. (a) R. L. Green et al., Mol. Cryst. Liq. Cryst. 79:183 (1982), (b) S. Bouffard et al., J. Phys. C 15:2951 (1981).
82. C. Bourbonnais and L. G. Caron, Europhysics 5:209 (1988).
83. M. Takigawa et al., J. Phys. Soc. Jpn. 56:873 (1987).
84. Y. Hasegawa and H. Iukuyama, J. Phys. Soc. Jpn. 56:877 (1987).
85. S. Ravy et al., Europhys. Lett. 9:391 (1989); Synth. Metals 41:2191 (1991).
86. C. P. Heidmann et al., Physica 143:B357 (1986); K. Andres et al., Physica 143:B334 (1986).
87. K. Oshima et al., J. Phys. Soc. Jpn. 57:730 (1988); M. Tokumoto et al., J. Phys. Soc. Jpn. 60:1426 (1991); J. E. Schirber et al., Phys. Rev. B 44:4666 (1991).
88. D. Schweitzer et al., Synth. Metals 27:A465 (1988).
89. K. D. Carlson et al., Inorg. Chem. 32:3356 (1992).
90. P. Auban-Senzier et al., J. Phys. I 3:871 (1993).
91. K. Yamaji, Solid State Commun. 61:413 (1987).
92. K. D. Carlson et al., Physica, C 215:195 (1993).
93. (a) A. P. Ramirez et al., Phys. Rev. Lett. 68:1058 (1992); T. W. Ebbesen et al., Nature 355:620 (1992); C. C. Chen and C. M. Lieber, J. Am. Soc. Chem. 114:3141 (1992); P. Auban-Senzier et al., Synth. Metals 55:3027 (1993); A. A. Zakhidov et al., Phys. Lett. A 164:355 (1992). (b) G. Sparn et al., Phys. Rev. Lett. 68:1228 (1992).
94. R. Kerkoud et al., Europhys. Lett. (1994 not yet published); and G. Quirion et al., Europhys. Lett. 21:233 (1993).
95. C. S. Jacobsen, in *Low-Dimensional Conductors and Superconductors* (D. Jérôme and L. G. Caron, eds.), Plenum Press, New York, 1987, p. 253.
96. C. S. Jacobsen et al., Phys. Rev. Lett. 27:1142 (1981); Phys. Rev. B 28:7019 (1983).

97. C. S. Jacobsen et al., *Solid State Commun.* 54:937 (1985).
98. C. S. Jacobsen, Thesis, Technical Univ. Denmark, 1986; C. S. Jacobsen et al., *Phys. Rev. Lett.* 53:194 (1984).
99. H. K. Ng et al., *J. Phys. C3* 44:859 (1981).
100. K. Kornelsen et al., *Phys. Rev. B* 35:9162 (1987).
101. T. Timusk, in *Low-Dimensional Conductors and Superconductors* (D. Jérôme and L. G. Caron, eds.), Plenum Press, New York, 1987, p. 275; H. K. Ng et al., *Phys. Rev. B*, 32:8041 (1985).
102. H. H. S. Javadi et al., *Phys. Rev. Lett.* 55:1216 (1985).
103. S. Donovan et al., *Europhys. Lett.* 19:433 (1992).
104. K. Mortensen et al., *Phys. Rev. B* 25:3319 (1982).
105. (a) J. B. Torrance et al., *Phys. Rev. Lett.* 49:881 (1982); (b) C. Coulon et al., *Physica* 143 B425 (1986).
106. P. A. Lee et al., *Solid State Commun.* 14:703 (1974).
107. L. P. Gork'ov and G. Grüner, eds., *Charge Density Waves in Solids*, North-Holland, Amsterdam, 1989; G. Grüner, *Synth. Metals* 43:3767 (1991).
108. S. Tomic et al., *Phys. Rev. Lett.* 62:462 (1989).
109. (a) H. Fukuyama and P. A. Lee, *Phys. Rev. B* 17:513 (1987); (b) P. A. Lee and T. M. Rice, *Phys. Rev. B* 19:3970 (1979); (c) W. Kang, S. Tomic, and D. Jérôme, *Phys. Rev. B* 43:1264 (1991).
110. G. Kriza et al., *Phys. Rev. Lett.* 66:1922 (1991).
111. (a) E. Barthel et al., *Phys. Rev. Lett.* 71:2825 (1993); (b) E. Barthel et al., *J. Phys. I* 3:1501 (1993).
112. K. Nomura et al., *Solid State Commun.* 72:1123 (1989).
113. P. Monceau et al., *Phys. Rev. B* 25:931 (1966).
114. P. Segransan et al., *Phys. Rev. Lett.* 56:1854 (1986).
115. A. Janossy et al., *Phys. Rev. Lett.* 59:2348 (1987).
116. G. Grüner et al., *Phys. Rev. Lett.* 46:511 (1981); J. Richard et al., *Phys. Rev. B* 25:948 (1982).
117. N. P. Ong et al., *Phys. Rev. Lett.* 52:663 (1984).
118. I. Tutto and A. Zawadowski, *Phys. Rev. Lett.* 60:1442 (1988).
119. W. H. Wong et al., *Phys. Rev. Lett.* 70:1882 (1993).
120. G. Kriza and O. Traetteberg, *J. Phys. IV C2*:15 (1993).
121. D. Quinlivan et al., *Phys. Rev. Lett.* 65:1816 (1990).
122. K. Maki and G. Grüner, *Phys. Rev. Lett.* 66:782 (1990).
123. J. J. Kwak et al., *Phys. Rev. Lett.* 46:1296 (1981).
124. T. Takahashi et al., *J. Phys.* 45:945 (1984).
125. L. P. Gork'ov and A. G. Lebed, *J. Phys. Lett.* 45:L433 (1984).
126. M. Héritier et al., *J. Phys. Lett.* 45:L943 (1984).
127. J. R. Cooper et al., *Phys. Rev. Lett.* 63:1988 (1989).
128. S. T. Hannahs et al., *Phys. Rev. Lett.* 63:1988 (1989).
129. M. Ribault et al., *J. Phys. Lett.* 44:L953 (1983).
130. W. Kang and D. Jérôme, *J. Phys. I* 1:449 (1991).
131. W. Kang et al., *Phys. Rev. B* 43:11467 (1991).
132. M. J. Naughton et al., *Phys. Rev. Lett.* 61:2276 (1988).

133. Y. Yakovenko, Phys. Rev. Lett. 61:2276 (1988).
134. K. Bechgaard and D. J  rome, Phys. Scri. T 39:37 (1991).
135. T. Osada, S. Kagoshima, and N. Miura, Phys. Rev. Lett. 69:1117 (1992); K. Machida and Y. Hori, J. Phys. Soc. Jpn. 61:2216 (1992).
136. K. V. Klitzing, Rev. Mod. Phys. 58:519 (1986).
137. G. S. Boebinger et al., Phys. Rev. Lett. 64:591 (1990).
138. M. J. Naughton et al., MRS Symp. Proc. 173:257 (1990).
139. T. Osada et al., Phys. Rev. Lett. 66:1525 (1991).
140. A. G. Lebed and P. Bak, Phys. Rev. Lett. 63:1315 (1989).
141. W. Kang et al., Phys. Rev. Lett. 69:2827 (1992).
142. K. Behnia et al., Europhys. Lett. 25:285 (1994).
143. A. G. Lebed, JETP Lett. 43:174 (1986).
144. S. Kagoshima et al., Jpn. J. Appl. Phys. 7:381 (1992).
145. K. Maki, Phys. Rev. B 45:5111 (1992).
146. P. M. Chaikin, Phys. Rev. Lett. 69:2831 (1992).
147. W. Kang et al., Phys. Rev. Lett. 62:2559 (1989).
148. W. Kang et al., J. Phys. 48:1035 (1987).
149. K. Yamaji, J. Phys. Soc. Jpn. 58:1520 (1989).
150. M. V. Kartsovnik et al., JETP Lett. 48:541 (1988).
151. K. Kajita et al., Solid State Commun. 70:1189 (1989).
152. N. Dupuis and G. Montambaux, Phys. Rev. B 46:9603 (1992).
153. N. Dupuis et al., Phys. Rev. Lett. 70:2613 (1993); A. G. Lebed, JETP Lett. 44:114 (1986).
154. M. Lang et al., Synth. Metals. 55:2401 (1993).
155. T. Takahashi et al., Jpn. J. Appl. Phys. Ser. 7 414 (1992); S. M. De Sot  to, Phys. Rev. Lett. 70:2956 (1993); H. Mayaffre et al. (Orsay work to be published).
156. A. C. Mota et al., Physica C 153:1153 (1988); D. Prost et al., Phys. Rev. B to be published (1994).
157. D. E. Farrel et al., Phys. Rev. B 42:8694 (1990); P. A. Mansky et al., Phys. Rev. Lett. 70:1323 (1988).
158. U.S. Patent, 4,586,062.
159. French Patent, 88,007214; U.S. patent 5,149,946.
160. S. S. P. Parkin, J. Physique 44:975 (1983).
161. T. Takahashi et al., J. Physique C3, 44:1095 (1983) and F. Creuzet et al., J. Physique Lett. 43:L-755 (1982).
163. P. M. Grant, J. Physique C3 44:1121 (1983).
164. J. L. Galign   et al., Acta Cryst. B34:620 (1978).
165. P. Delhaes et al., Mol. Cryst. Liq. Cryst 50:43 (1979) and also Ref. 47.

Introduction to Conjugated and Conducting Polymers

Michel Schott

Université Paris VII (Denis Diderot), Paris, France

Maxime Nechtschein

Centre d'Etudes Nucléaires de Grenoble, Grenoble, France

I. INTRODUCTION

In a book such as this, it may be worth beginning a chapter by stressing several points where conducting (or, more generally, conjugated, polymers) differ from conducting organic crystals made of small molecules.

1. The polymers that we discuss are, in principle at least, linear and unbranched chains, so there is an infinitely extended, or at least very long, one-dimensional chain of covalent bonds. Therefore, one-dimensional electron energy bands in the chain are broad, their scale being that of overlap integrals, on the order of a few eV. In the three-dimensional solids built from such chains, the chains interact somewhat, but the corresponding integrals are now similar to those found in organic crystals, so the electron bandwidths in the corresponding directions are now one order of magnitude or more smaller. This is a very anisotropic, quasi-one-dimensional structure. Within the chains, the electron–phonon interaction is very strong, leading to strong relaxation effects: large Peierls gaps and large lattice relaxation around carriers.

2. All conjugated polymers (CPs) are semiconductors with wide forbidden gaps, generally on the order of 2 eV or more. Some have a low conductivity of extrinsic origin, others are insulators. They become conductors by injection of electrons or holes onto the chains, with simultaneous intercalation of compensating ions between the chains. This is the so-called

doping process. Doping is, in principle, reversible and its level can be adjusted continuously between zero and a maximum corresponding to one counterion for two to a few polymer repeat units, although there is evidence in some cases of the occurrence of stages, as in intercalated graphite. This produces a continuous variation of the conductivity between the very small value characteristic of an insulator and 1 to 10^3 S/cm, depending on the material. In the case of I_2 -doped polyacetylene, a value of 10^5 S/cm has been obtained. Usually, the counterions do not contribute to the (electronic) conduction.

3. Disorder is a central issue for CPs. Real materials are almost always highly disordered; the crystalline regions—in fact, better described as paracrystalline, for instance—are small (lateral dimensions ca. 10 nm). Accurate description of the structures at all scales and understanding of their influence on the electronic properties have not been achieved. Doping–undoping cycles, corresponding to large-scale motion of often bulky ions, usually increase the disorder irreversibly.

4. Many applications have been proposed in the past decade or so. Some have already reached the market. Few require high conductivity; rather, they use semiconducting or modestly doped materials.

II. CONJUGATION

A. Conjugated Molecules

It is well known that the $2s$ and three $2p$ atomic orbitals of carbon can hybridize in several ways: for instance, to yield either four equivalent sp^3 orbitals, or three equivalent sp^2 orbitals and one orbital antisymmetric with respect to the sp^2 plane, the $2p_z$ orbital. The sp^2 orbitals are directed along the line joining two atoms, generating a covalent bond, and in the language of chemistry, each electron can be assigned to a single pair of atoms: these are the σ electrons. On the other hand, if there are more than two sp^2 hybridized carbons in a row, each $2p_z$ orbital overlaps two similar ones belonging to two neighboring carbon atoms (possibly three in a polycyclic system), and consequently, the corresponding electron cannot be assigned to a particular bond: This is the phenomenon of *conjugation*, and the electrons involved are the π electrons.

Conjugated molecules have been studied actively by chemists for over a century. Since electronic excitation of a π -electron-containing molecule requires only a modest amount of energy, typically 1 to 3 eV, the corresponding optical absorptions occur in the visible; organic dyes are conjugated molecules. This small excitation energy is also at the origin of the interesting properties of conjugated and conducting polymers. These mol-

ecules have been the subject of intensive theoretical work for at least 60 years. A not too recent, but still not outdated review is that of Salem [1].

B. Conjugated Polymers

This chapter and the two following deal with conjugated and conducting polymers (CPs). Ideally, these should be infinite, perfectly ordered, linear systems regularly built from repeat units containing π electrons, in such a way that there is no interruption of the conjugation; the π -electron system is extended infinitely along the system. A number of such structures are shown on Table 1. In most of them, the repeat unit is a quite simple conjugated cycle or heterocycle, such as pyrrole. In several cases these units can be connected in different ways—hence the existence of isomers.

Real systems differ from that idealization in a number of ways, and the question of to what extent the real systems conform to the behavior predicted by theory for ideal ones has no general answer, not even in many cases a clear answer. These problems are discussed in more detail in Section II.B.

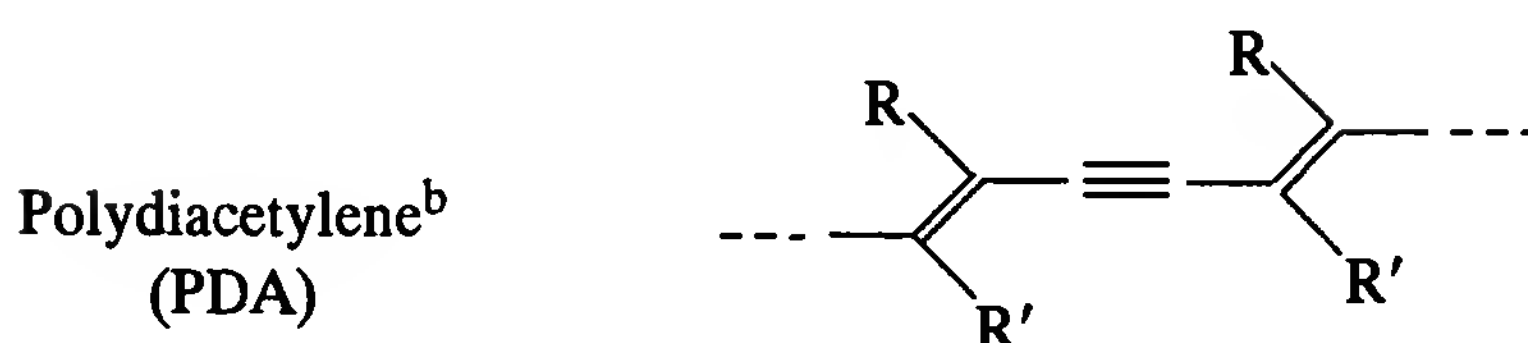
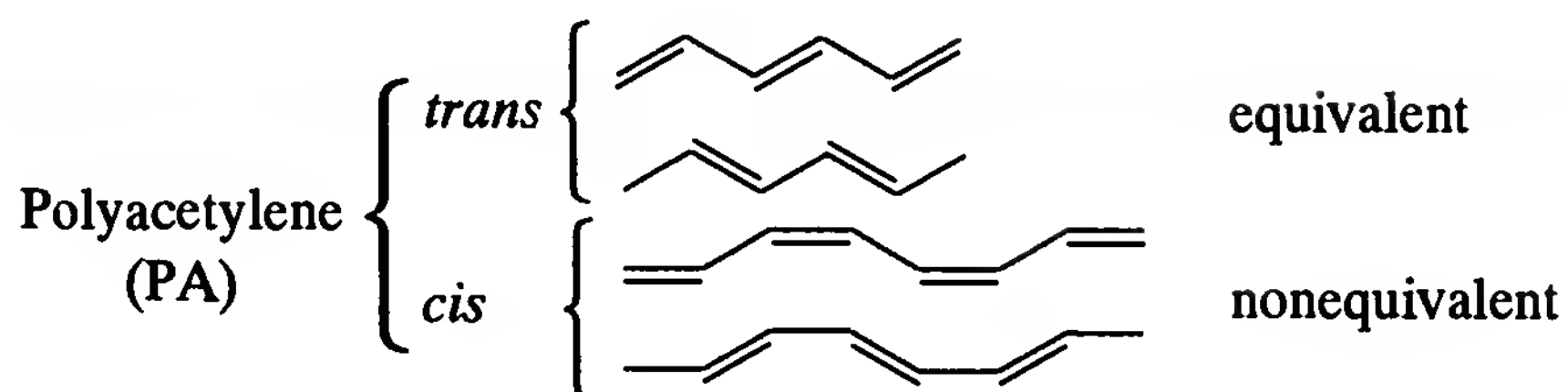
C. Conjugation Length: Interest in Studying Oligomers

The existence of π -electron conjugation in a molecule produces a kind of “propagation” of electronic influences along the corresponding carbon chain. As the π system (assumed here to be one-dimensional) is made longer, most of the electronic properties vary; for instance, the electronic transition energies decrease. The case of polyenes has been studied extensively [2,3]. So it is a quite natural idea that a conjugated polymer is the limit for $N \rightarrow \infty$ of shorter molecules made of a precise number N of the same repeat unit as the polymer (e.g., $-\text{CH}=\text{CH}-$) and terminated at both ends with an electronically inactive group such as CH_3 .

It is found that in a series of oligomeric molecules several molecular quantities increase with N faster than N : for instance, optical nonlinear susceptibilities [4]. So such a quantity referred to one repeat unit (i.e., the molecular value divided by N) increases with N . Still, in a macroscopic polymer sample, that same property is extensive: that is, proportional to the sample volume. Hence the idea that the supralinear variation ceases beyond some N : The effects of conjugation do not “propagate” beyond that characteristic distance—hence the notion of *conjugation length* [5]. Such behavior is not generally observed in nonconjugated polymers, which for such properties behave as mere addition of monomers, a rule used extensively in chemical physics. Other properties, such as electronic transition energy, often follow, in a series of oligomers empirical laws of the

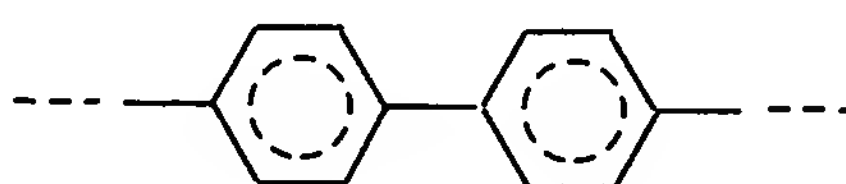
Table 1 Common Conjugated Polymers^a

1. Linear carbon chains

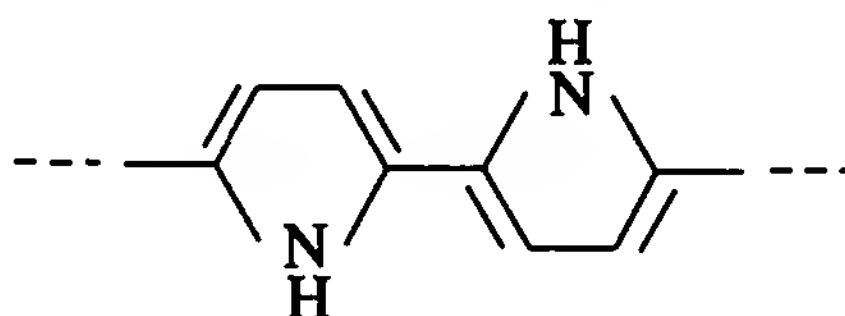


2. Linear chains of conjugated rings

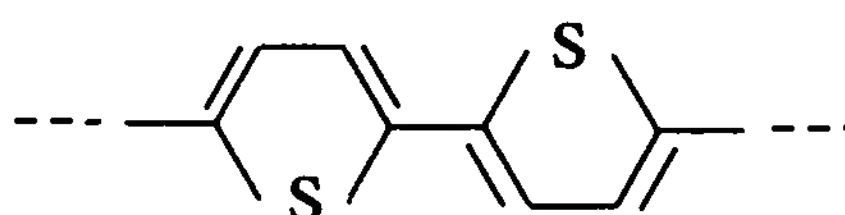
Polyparaphenylene
(PPP)



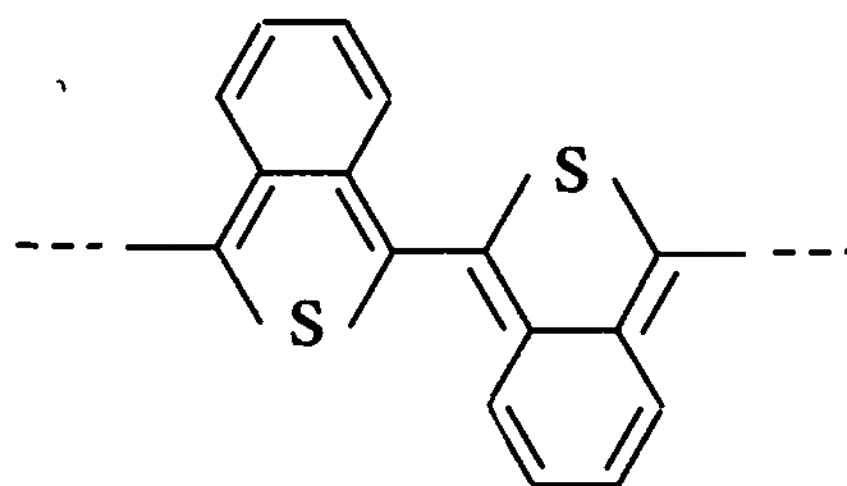
Polypyrrole
(PPy)



Polythiophene
(PT)

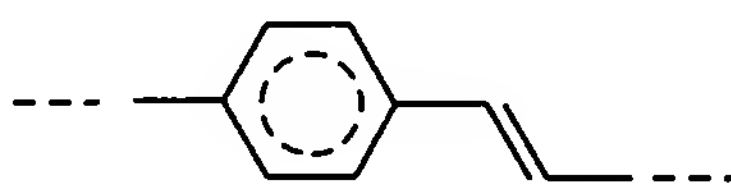


Polyisothianaphthene



3. Chains of alternating rings and C=C bonds

Polyphenylenevinylene
(PPV)



Polythienylenevinylene
(PTV)

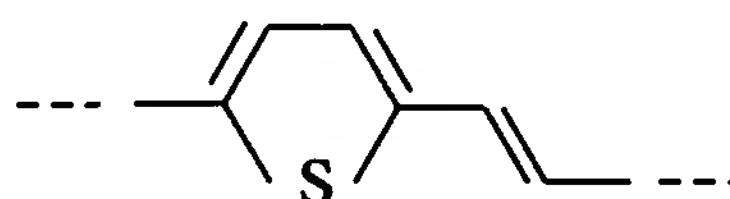
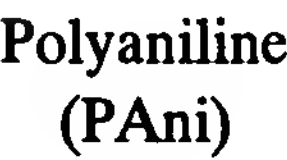
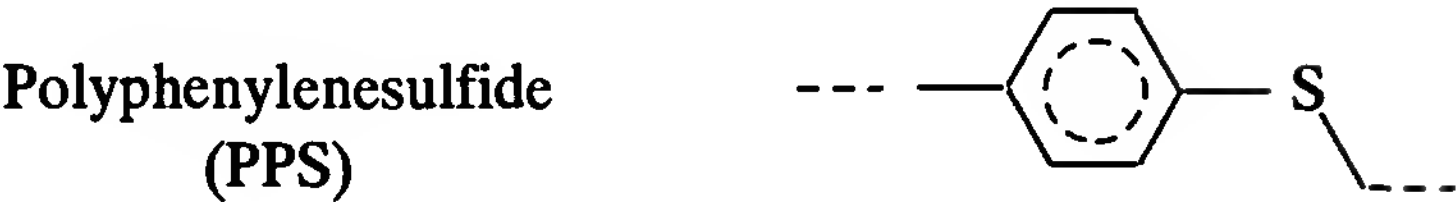
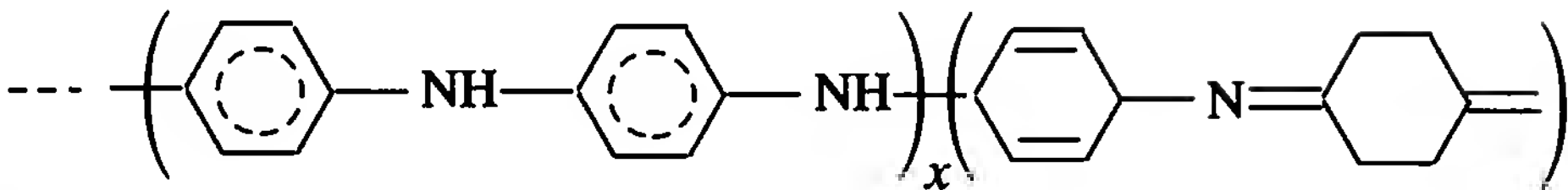


Table 1 (Continued)

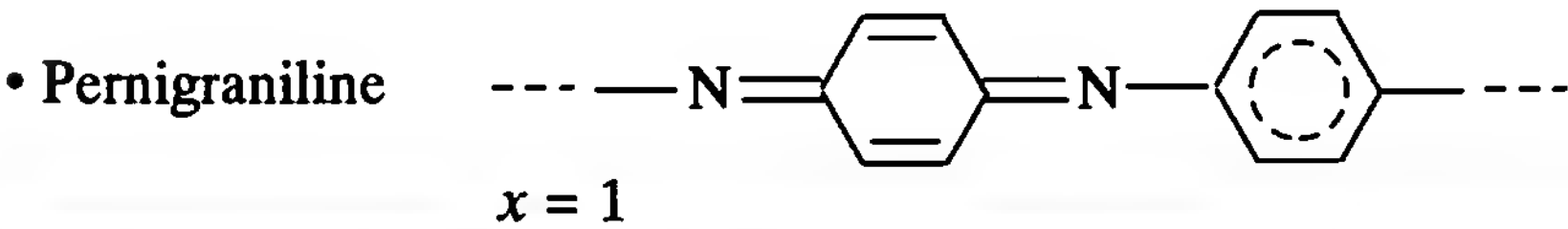
4. Chains of alternating rings and heteroatoms



• General formula



• Emeraldine $x = y = 0.5$



^a H atoms are not shown. They can be replaced by substitutes.
^b R and R' are side groups (which may be identical). PDAs are always substituted.

form

$$E(N) = A + BN^{-1}$$

where A represents the value corresponding to the infinite perfect conjugated polymer. Beyond a certain N , E changes negligibly.

Clearly, if one is interested in such a property, one need not attempt to prepare the longest possible polymer chain: It suffices that its length be comparable to or larger than the conjugation length. This is not true, however, of macroscopic *transport* properties, particularly of dc conductivity; intermolecular transport, not only intrachain properties, should be considered. As shown in Chapter 13, one should then optimize the intermolecular interactions and in general reduce the number of interchain hops, so the longest possible chain may be an advantage.

But a true conjugated polymer is anything but infinite and perfect (see Section III.C). Physical or chemical defects will hinder or interrupt the conjugation. A simple (in fact, oversimplified) model is to view a CP chain as a sequence of finite conjugated boxes uncoupled electronically from one another. In such a model the polymer is characterized by a distribution of box lengths (i.e., conjugation lengths). For instance, if a transition energy E is observed experimentally, it will be assigned to an effective conjugation

length N such that $E = A + BN^{-1}$. This approach has been used extensively for assessing the quality of CP samples, in particular polyacetylene samples, from their resonance Raman spectra (for a recent discussion of this, see Ref. 6).

Thus there are two notions of the conjugation length, corresponding to two different points of view. In the first, it is a characteristic quantity, intrinsic to the perfect polymer. It may be that different properties yield different lengths for the same polymer. Some CPs (notably polyacetylene) seem to have very large conjugation lengths, while they are much shorter in others. In the second definition the conjugation length is extrinsic, and to the extent that the “boxes” are effectively uncoupled, it should be the same for all properties. Of course, it is the extrinsic value that is commonly observed, except in the polydiacetylenes (PDAs). However, this box model is certainly oversimplified, and it is wrong for CPs in solution, in which the dynamic curvature fluctuations introduce random potentials along an otherwise perfect chain. The absorption spectrum of PDAs in solution is not a sum of the spectra of oligomers of various lengths [7].

In any case, the study of oligomers has proved to be very useful in understanding the electronic properties of conjugated polymers. They can also be used as a testing bench for quantum chemical calculations. Recently, some oligomers have emerged as interesting materials as such. This is particularly true of thiophene oligomers, which have been used in field-effect transistors (FETs) with performances now approaching those of amorphous silicon FETs [8,9].

D. Role of π -Electron Conjugation in Polymers

Insofar as obtaining a high electrical conductivity in a polymer generally requires conjugation and heavy doping, it is worth discussing briefly the reasons why π electrons are necessary. That is not to provide wide one-dimensional valence and conduction bands, and consequently, small effective masses for the carriers: σ overlap integrals being generally larger, bands built from σ electrons tend to be wider than π bands when σ - π coupling is neglected. A very pedagogical introduction by Hoffmann et al. [10] illustrates this point well and compares the simplest σ -bonded non-conjugated polymer, polyethylene (PE), or $(\text{CH}_2)_n$ to polyacetylene. But the bandgap of PE is about 9 eV and the bottom of its conduction band is above vacuum level; in chemical terms its electron affinity is negative [11,12]. Doping corresponds to transfer of an electron from a donor to the polymer, or from the polymer to an acceptor (see Chapter 13). Such transfers are clearly impossible with PE. The role of π electrons is then to

provide low-energy excitations and therefore small bandgaps and large electron affinities and small ionization potentials.

III. HISTORICAL BACKGROUND

A. New Materials

The search for “conducting plastics” has been going on for some time. There was a fair amount of work in the 1950s and 1960s on “semiconducting polymers,” and room-temperature conductivities up to 10^{-5} S/cm were reported. (For a review of that early work, see, e.g., Ref. 13.) Several materials investigated actively today were known and studied at that time: for instance, polyaniline (PAni) [14–16] (the chemical structure of the repeat units of all polymers mentioned in this and the following two chapters are given in Table 1) and polyacetylene (PA), which was to become around 1980 and for some time after the prototype conjugated polymer. However, the repeat units of these polymers were often quite complicated, the materials were usually poorly defined, and no general theoretical or phenomenological framework emerged.

On the other hand, interest in the theory of conjugated molecules, particularly the polyenes (linear molecules which, in chemical terms, are made of alternating single and double bonds, for instance hexatriene $\text{H}-\text{CH}=\text{CH}-\text{CH}=\text{CH}-\text{CH}=\text{CH}-\text{H}$) dates back to the early days of quantum chemistry and in the 1960s reached a high level of understanding [1], which was immediately available to formulate a theoretical framework for the study of the conjugated polymers, of relatively simple formula, which were to be studied in the 1980s.

But the more recent, enormous development of the study of conjugated and conducting polymers (tens of thousands of papers have been published), which started from a renewed interest in PA, is not a direct continuation of that early work. PA had been synthesized by Natta et al. in the late 1950s, using Ziegler–Natta catalysts, a method that is still a major method of synthesis of this and related materials. It had been observed that the room-temperature conductivity of PA—typically, a few 10^{-6} S/cm, a value still valid today—could be increased (respectively, decreased) by three to four orders of magnitude by exposure to electron acceptors (respectively, donors), so the conductivities thus obtained, albeit significant, remained modest [17]. But the “new start” was the consequence of two discoveries made in the 1970s. The first was a modification of Natta’s synthesis, yielding self-standing fibrillar films with metallic luster, a consequence of very strong absorption in the visible, not of a true metallic

state, as discussed below [18]. The second and decisive discovery was that such films can be made highly conducting ($\sigma \sim 50$ to 500 S/cm, an increase of about eight orders of magnitude) by exposing them to strong acceptors such as I_2 [19] or AsF_5 [20]. The exposure produces incorporation of large amounts of the acceptor, up to one molecule for four CH repeat units, certainly facilitated by the large effective surface of the material (up to 10^2 m²/g) due to its fibrillar morphology. So although this process is now universally referred to as doping, it is more akin to intercalation into graphite. But neat graphite is already a semimetal, whereas PA is a low- σ semiconductor. It was then shown that doping can be produced electrochemically, whereby, for instance, ClO_4^- ions are intercalated to compensate for the positive charges injected onto the PA chains, with resultant conductivities of about 10^3 S/cm [21]. It was also found that PA can be doped using strong donors, by intercalating alkali ions, and that conductivities larger than 100 S/cm were obtained [22].

The doping is reversible; the dopants can be removed from the film, which returns to its original semiconducting state (see Chapter 13). That property makes conducting polymers very different from the other organic conductors discussed in this book. It was soon found that acceptor and donor doping (known as *p*-type and *n*-type doping, after the nature of the charge carriers on the polymer chains) is a common property among CPs: for instance, polyparaphenylene (PPP; see Table 1), a wide-bandgap insulator, can be chemically *n*- or *p*-doped to conductivities $\sigma \gtrsim 100$ S/cm [23].

Even more important, because it opened the way to a general preparation method, was the electrochemical polymerization of pyrrole by anodic oxidation [24,25]: smooth, highly conducting doped films (σ ca. 100 S/cm) were obtained, which could be dedoped and redoped electrochemically, although the very high resistivity of the undoped states makes complete undoping difficult. The same method was then used to prepare polythiophene (PTh), with similar results [26]. The latter polymer is stable both as doped or undoped, and its study was to have a very large development. Finally, a renewed interest in PANi started around 1985 (for a review, see Ref. 27). PANi has the unique property that its electronic conductivity is modulated by orders of magnitude by pH changes. It is also cheap, and as such it has potential industrial interest. Electrochemical syntheses have been reviewed [28].

Many other CPs have been prepared during the past decade or so; some of them are shown on Table 1, but most properties discussed in Chapters 11 to 13 can be presented using PA, PTh, and PANi, and a few of their derivatives, with, in addition, polyphenylenevinylene (PPV) when electroluminescence is discussed.

B. Theory

As new materials were developed, it appeared clear that CPs are a new class of solids, with new and unexpected properties, the first being the enormous range that the conductivity of any of these CPs could span, which is now, in the case of PA, about 15 orders of magnitude.

The theoretical problems raised by the study of CPs will be discussed below as the need arises. Many special properties of CPs are related to their quasi-one-dimensional character: for instance, the large influence of disorder, the importance of residual three-dimensional coupling, and the importance of electron–phonon interactions, which, among other consequences, manifests itself in the case of a half-filled band by the occurrence of the Peierls instability. Much of the early theoretical work was concerned with PA, which, as we shall see, is peculiar among presently known CPs by having a degenerate ground state (see Section IV.B).

It had been realized very early in the study of polyenes that paramagnetic ($s = \frac{1}{2}$) defects similar to Bloch walls in a ferromagnet can exist [29,30] and be mobile. This idea was taken up in the context of the late 1970s [31,32]; this excitation is known in the CP literature as a soliton—although, unlike true solitons, two such excitations do not cross each other without interaction in their motion along the polymer chain. The soliton idea was at the basis of the first theoretical development on CPs, which is well reviewed in Ref. 33. In particular, it provided an elegant explanation of the surprising fact that as PA is doped to 10^2 S/cm, its Pauli susceptibility does not increase—in other words, that the corresponding charge carriers are spinless [34]: ionization of a soliton by addition or removal of an electron will indeed produce an excitation with spin zero and charge 1.

There are a few other degenerate ground-state CPs, such as poly(1,6-heptadiyne) [35], or pernigraniline, a fully oxidized state of polyaniline [36]. But in most CPs other than PA, no soliton exists, and the electron–phonon interaction will generate other types of charge-carrying excitations: polarons (spin $\frac{1}{2}$ and charge 1) and bi-polarons (spin 0 or 1 and charge 2). Only recently has the exciton (with charge zero and spin zero or 1) been seriously considered as a possible excitation in CPs (see Section IV.C5).

This theoretical approach is essentially an independent-electron theory. The importance and role of electron correlations in explaining the properties of CPs have been hotly debated. We return to this below. A balanced review focused on PA can be found in Ref. 37.

C. Processibility

All materials mentioned above are neither soluble nor fusible. They are obtained generally as poorly ordered and noncompact films, which mor-

phology is determined by the chemical or electrochemical growth conditions and cannot be modified after growth. An exception is the solubility in a few solvents, essentially concentrated strong acids, of relatively low-molecular-weight polyaniline (PAni) [38]. This is certainly a drawback, not only for fundamental studies but much more if it comes to potential applications: one of the motives for the search of plastic conductors was to combine interesting electrical properties with the processibility and mechanical properties usually associated with polymers, and it appeared that while gaining the former, the latter was lost.

Once the interest of CPs had become clear, several strategies were tried to recover processibility while keeping (most of) the conductivity. They are still under development but they all seem to be potentially successful. The earliest attempt was to generate a CP from a soluble precursor polymer by thermal elimination of part of each repeat unit. In fact, polyene sequences had been produced long before by such a method from vinyl polymers, for instance from PVC by HCl elimination. The idea is to process the precursor polymer and then to perform the transformation so as to preserve the shape and morphology throughout the elimination step. This was indeed achieved for PA in 1980, by the method now known as the "Durham route" to PA [39]. But this is hardly a general method: The chemical problem must be considered anew for each CP separately. Only one other case has at present some practical importance in relation to electroluminescence studies—the synthesis of polyphenylenevinylene (PPV) through a precursor [40].

In the second method, solubility and in some cases fusibility are achieved by replacing one or several hydrogen atoms of the repeat unit by suitable substituents, for instance alkyl chains. Since any substituent is bulkier than a hydrogen atom, this adds new geometrical constraints that may decrease the chain conjugation, as explained below; and indeed this occurs with substituted PAs [41,42]. (For a review on substituted polyacetylenes, see Ref. 42.) In 1986, the first soluble alkyl-substituted polythiophene was synthesized [43]; its electronic properties were similar to those of PTh, and high-quality films were easily formed from solution. Melt-processed films were generally of poorer quality, due to thiophene thermal degradation and cross-linking. (For a review, see Ref. 44.) This is, in principle, a fairly general method: Alkyl substitution does not drastically affect reactivity, so the existing polymerization methods remain practicable. The bulkiness of most substituents has structural consequences, which in turn affect the electronic properties; the conjugated chains are more distant than in the corresponding unsubstituted polymer, so the fraction of the total volume and the interchain coupling are decreased, and generally, although not always, the chains tend to be less ordered. On the other hand, judiciously

chosen substituents (such as OCH_3) allow tuning of the gap; others introduce desirable properties such as chirality, liquid crystallinity, or catalytic properties [45,46]. Others still allow “self-doping”: The substituent is terminated by an ionizable group such as SO_3^- , which can act in the doping process as a compensating counterion, covalently attached to the chain [47].

Another promising method for processibility of the doped polymers is to use large counterions, which can be surfactants, or polymers themselves, to induce solubility and generate structural order [48]. For many present and potential applications, the conductivities levels currently obtained are more than enough: hence the idea of obtaining a processible material by blending a CP with a nonconjugated processible polymer, or by making a copolymer.

A copolymer is a macromolecule containing two types of sequences, A and B (in the present case A would be a processible polymer and B a conjugated chain). In a graft copolymer, B sequences are grafted as side chains onto a single A sequence forming the main chain. In a block copolymer, the main chain itself is made of successive A and B sequences called “blocks.” A chain formed of a single A sequence followed by a single B sequence is a diblock copolymer. Both graft and block copolymers containing conjugated sequences have been prepared. However, since the two blocks have very different solubilities and are highly immiscible, microscopic segregation occurs and complicated mesoscopic structures may form. These questions are presently far from being understood, so while preparation of CP–non-CP copolymers may be a promising path toward processibility, much remains to be done; for a short discussion, see Ref. 49.

On the other hand, it may be useful for some applications to have short conjugated segments all of the same length. Obtaining blue electroluminescence may be an example: Large photon energies require short conjugation, but small molecules tend to crystallize, and the device lifetime is short. A copolymer may solve the problem; a first example has been reported recently [50].

D. Polydiacetylenes

The discussion above left aside an entire class of CPs, the polydiacetylenes (PDAs) (see Table 1). Their study has followed a path similar to that of other CPs, but with only occasional intersections. Indeed, they differ greatly from other CPs in many respects. PDAs have a feature that is almost unique in the entire polymer field, and not only among CPs; single crystals of macroscopic size can be obtained. They owe that to their peculiar polymerization mechanism, which is a topotactic reaction occurring in the mon-

omer single crystal, with, in several of these materials, preservation of the crystallinity [51,52]. In such polymer crystals, all chains are completely extended; they have precisely the same geometry and the same relative arrangement, so they are more like the theoreticians' chain than is any other CP. In addition, several PDAs are soluble; in fact, these were the earliest soluble CPs found [53,54], and homogeneous amorphous films can be prepared by spin casting, for instance. So the influence of various types of disorder can be studied by comparison with the properties of the highly regular chains in the crystal. However, the larger part of the theoretical work has been devoted to PA (or, rather, "idealized perfect PA") from which the PDAs differ in two important aspects: they have a nondegenerate ground state and the influence of electron correlations is large.

Another feature that sets the PDAs aside from other CPs is that most attempts at doping them have been unsuccessful. In the days where obtaining the highest (reversible) conductivity was a major goal, that was a severe drawback. On the other hand, PDAs have large third-order nonlinear optical susceptibilities, even compared to other CPs (in fact, this property of undoped CPs was discovered on a PDA in 1976 [55]), and this is presently an active field of study [56].

IV. SOME PHYSICS NOTIONS RELEVANT TO CPs

A. Bond-Length Alternation: Polyacetylene as a Semiconductor

Alternation of the CC bond lengths along the chain and the existence of a large energy gap are well-established facts in PA (see Chapter 12, Section II.C.2). However, since each carbon atom contributes one π electron, there is at first sight no obvious reason why CC bonds should not be equivalent. If they were, and taking into account the electron spin, the π electrons should generate a half-filled band; such a material is a metal. If there is bond alternation, the one-dimensional unit cell is doubled and a gap opens at the Brillouin zone boundary: the material is a semiconductor.

The origin of these effects has been debated. One possibility is the Peierls instability [57], which is discussed elsewhere in this book: In a one-dimensional system with a half-filled band and electron-photon coupling, the total energy is decreased by relaxing the atomic positions so that the unit cell is doubled and a gap opens in the conduction band at the Brillouin zone boundary. However, this is again within an independent electron approximation, and electron correlations should not be neglected. They certainly are important in polyenes, and the fact that the lowest-lying excited state in polyenes is a totally symmetric (A_g) state instead of an antisymmetric (B_u) state, as expected from independent electron models, is a consequence

of these correlations [2,3]. It was shown in the early 1970s that the existence and value of the energy gap observed could be accounted for in the frame of a one-dimensional Hubbard model [58], and the same authors claimed that the Peierls instability could not account for a gap of about 2 eV. In that model, correlations produce the gap and electron–phonon interactions the bond alternation.

On the other hand, the SSH Hamiltonian introduced in 1979 [59] assigns both facts to the Peierls instability. It is a one-electron tight-binding Hamiltonian in which the electron–phonon interaction is explicitly included, such that

$$\mathcal{H} = -t_0 \sum (c_{n+1,s}^+ c_{ns} + c_{ns}^+ c_{n+1,s}) + \alpha \sum (u_{n+1} - u_n)(c_{n+1,s}^+ c_{ns} + c_{ns}^+ c_{n+1,s}) + \mathcal{H}_{\text{ph}}$$

The index n labels successive CH groups along the chain, s is the spin, c^+ and c are creation annihilation operators, and u_n is the displacement of the CH group of index n from its equilibrium position in the undimerized chain (here supposed straight). The first term in \mathcal{H} is the π -electron Hamiltonian describing π -electron hopping along the chain, with transfer integral t_0 corresponding to the undimerized chain ($u_i = 0$); the second term expresses the electron–phonon interaction written as a variation of the transfer integral t with atomic displacement in the weak-coupling limit where only terms linear in the displacements are important. No electron–electron interaction is explicitly included. This is equivalent to what is known in quantum chemistry as the Hückel model with σ -bond compression [1]. \mathcal{H}_{ph} is the phonon Hamiltonian:

$$\mathcal{H}_{\text{ph}} = \sum \frac{p_n^2}{2M(\text{CH})} + \frac{K}{2} \sum (u_{n+1} - u_n)^2$$

For a discussion of this theory, its continuum equivalent (the TLM model) [60,61], and their consequences, we refer to detailed reviews [33,37]. This approach played a very important role in the development of a qualitative understanding of CP electronic properties.

In the ground state thus obtained, CC bonds are alternately lengthened and shortened by a quantity u (the bond alternation parameter) much smaller than the average bond length, with corresponding effective transfer integrals t_1 and t_2 . The total width of the π -electron bands (still neglecting σ – π interactions) is $4t_0$ (≈ 11 eV for PA), and there is now in their center a forbidden gap of width $\Delta = t_1 - t_2$ (≈ 1.8 eV for PA). In this approach, bond alternation and gap have a common origin and they are related by $\Delta = 4\alpha u$. The π -electron band structures corresponding to the undimerized and dimerized structures are shown on Fig. 1. The strength of the electron–

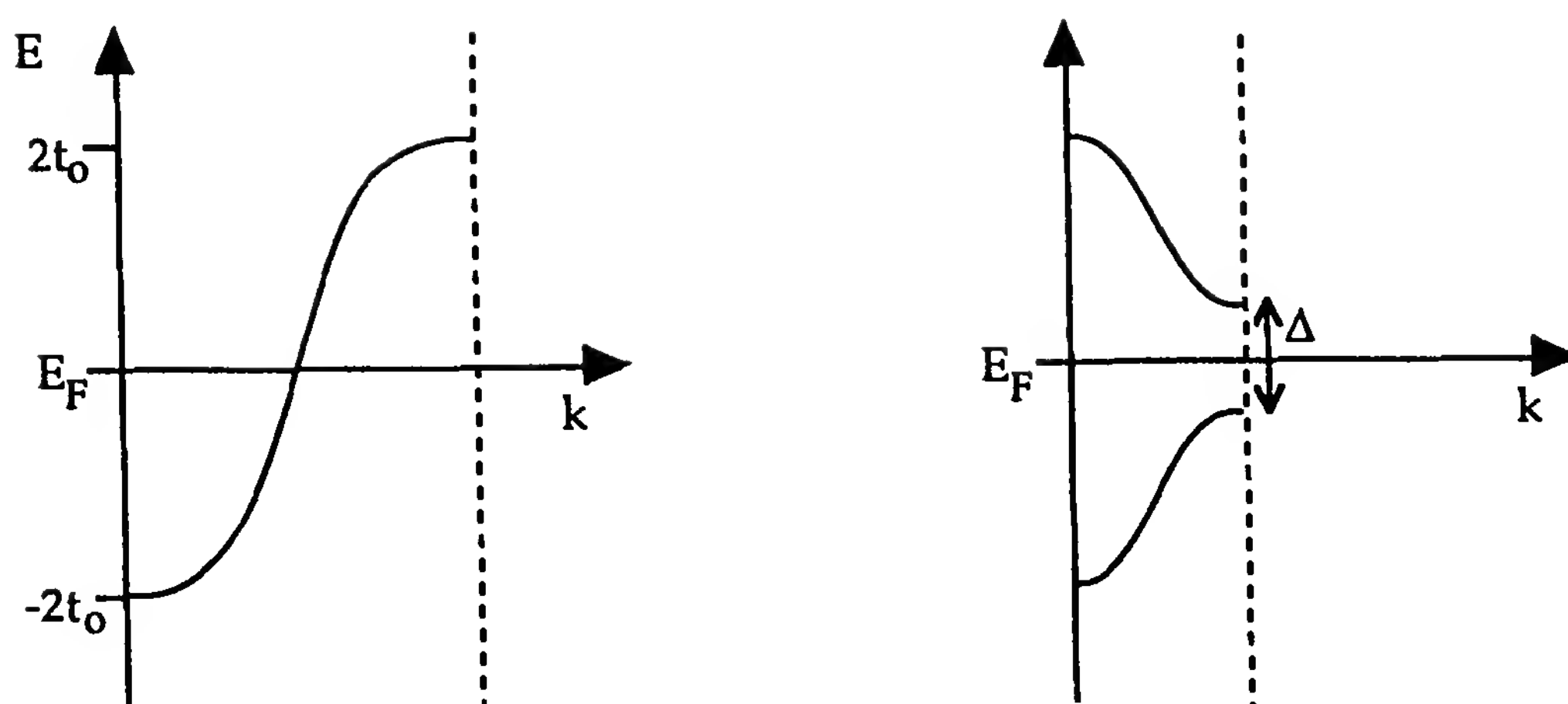


Figure 1 Dispersion relation of the half-filled valence band of a 1-D conductor. Upon dimerization, the Brillouin zone is halved, and a gap Δ opens at the new zone boundary: the material is now an insulator.

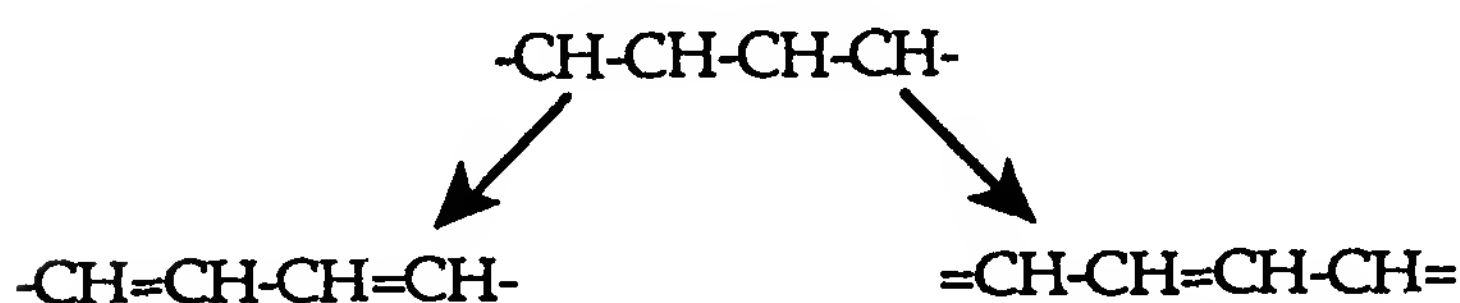


Figure 2 Two equivalent ways of introducing bond alternation in a *trans*-PA chain.

phonon coupling is expressed by the dimensionless parameter $\lambda = 2\alpha^2/\pi t_0 K$, K being the elastic force constant in the Hamiltonian.

When both electron–phonon and electron–electron interactions are included, in general one or the other dominates, with corrections due to the less important interaction becoming large near the transition region; and using the experimental gap and bond alternation values for PA (which are not very accurately known, for reasons discussed below), it seems that *trans*-PA is near the transition, so that the SSH approach, although incomplete, is still qualitatively very fruitful [37,62,63].

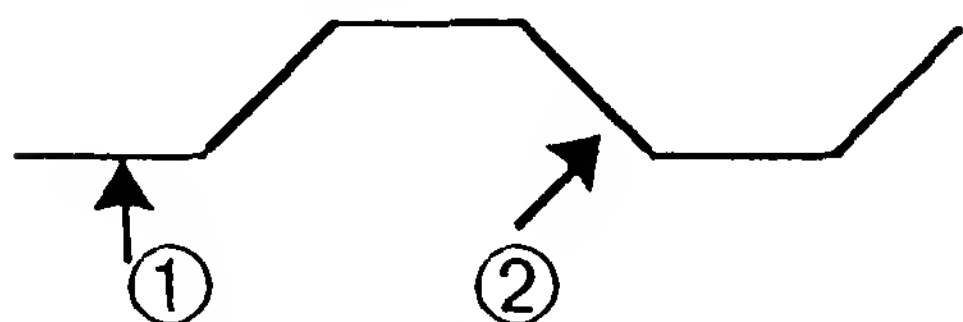
B. Degenerate Versus Nondegenerate Ground State

1. Bond Alternation

Starting from a straight nonalternating CH chain, there are two ways of introducing bond alternation (Fig. 2). Although a given CC bond is a single one in one scheme and a double one in the other, these two structures are equivalent; the alternating CH chain above has a degenerate ground state. This remains true of the actual *trans*-PA chain, which is not straight but a linear zigzag. Note that there are now two ways of defining the bond

alternation parameter u : the difference of bond lengths can be said to be $2u$; or the projection of each C atom onto the mean chain direction can be said to be $\pm u$ (with an obvious trigonometric relation between the two definitions). As a consequence of the degeneracy, such a chain can support a very interesting special kind of defect, known in the CP field as a soliton, to which we return shortly.

But not all CPs have degenerate ground states; except for *trans*-PA, pernigraniline, and polyheptadiyne (and the chain of C atoms, which can assume three configurations, $=C=C=C=C=$, $-C\equiv C-C\equiv C-$, and $\equiv C-C\equiv C-C\equiv$, the latter two being degenerate), all CPs known to date have nondegenerate ground states. The simplest example is *cis*-PA, in which there are only two kinds of CC bonds, as seen immediately if one draws the “ σ backbone” of the molecule without a priori introducing bond-length differences:



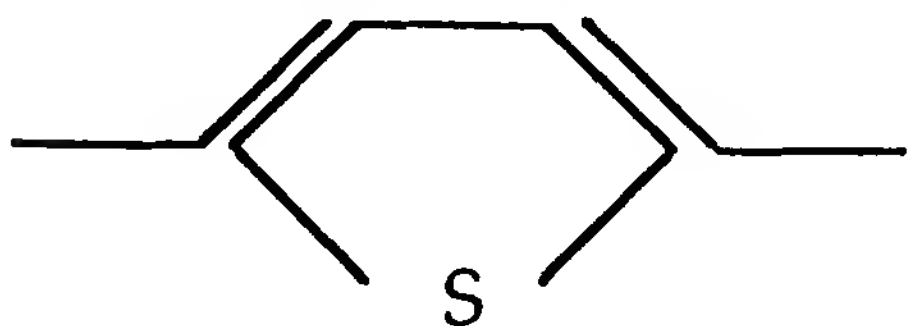
Bonds 1 and 2 are already nonequivalent at this level of approximation; their lengths have no reason to be equal, and the corresponding integrals t_1 and t_2 are different. This generates a forbidden gap between a full and an empty π band. Note that this does not tell us which one of bonds 1 and 2 is shorter in the true ground state; so there are two inequivalent isomers of this polymer:



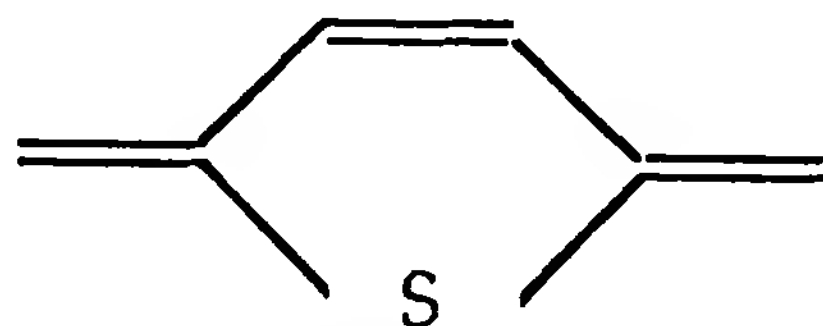
and



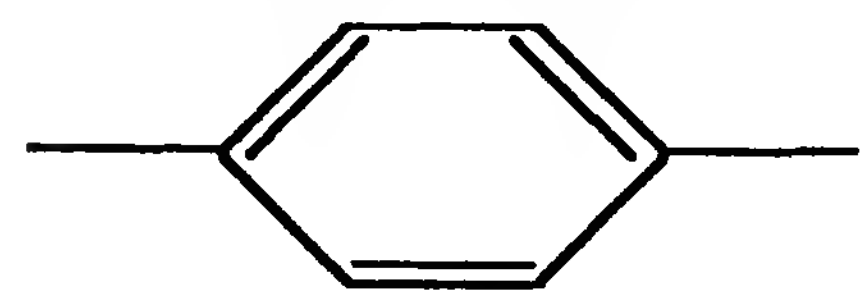
A similar diagram can be found in the literature for polythiophene (see Ref. 33); that is,



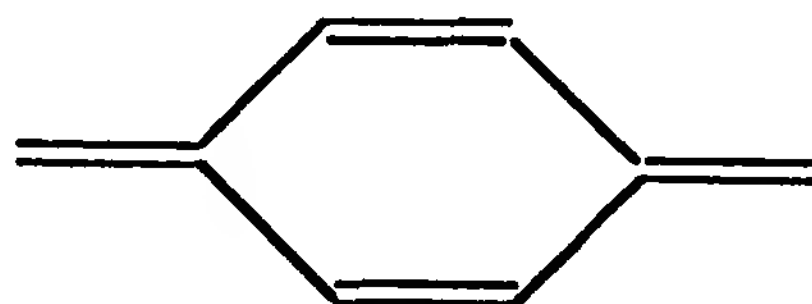
and



in which, in fact, coupling of the S atom to the C π electrons is neglected, or for polyparaphenylene,



and

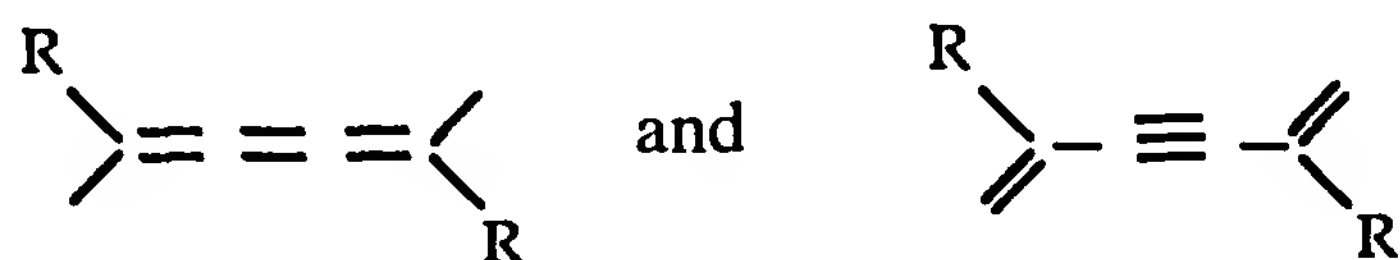


In general, there may be more than two types of bonds, and more complicated band structures result.

This gap may be further widened by electron–phonon interaction effects, as in the Peierls process. An accepted terminology [64] is to partition the gap Δ into the sum of an “extrinsic” one Δ_e coming from the nonequivalence of bonds (including the effect of the σ electrons), and an “intrinsic” one Δ_i due to π -electron effects alone. The relative importance of Δ_e and Δ_i , or the magnitude of the bond alternation, are more difficult to calculate.

2. Energy as a Function of Distortion

The total ground-state energy is plotted on Fig. 3a as a function of displacement for a degenerate ground-state system: The nondimerized case is seen to be an extremum, but a maximum; the two equivalent dimerized ground states correspond to $u = \pm u_0$. Figure 3b shows the corresponding plot for a nondegenerate ground-state chain with two possible structures, in the case where there is indeed a secondary minimum. There is a difference ΔE *per repeat unit* between the energies of the two minima. A secondary minimum does not always exist: in the case of PDAs; the two bond schemes can be written as



known, respectively, as the butatrienic and the acetylenic structures, and the former may not even correspond, for an infinite chain, to a local energy minimum [65].

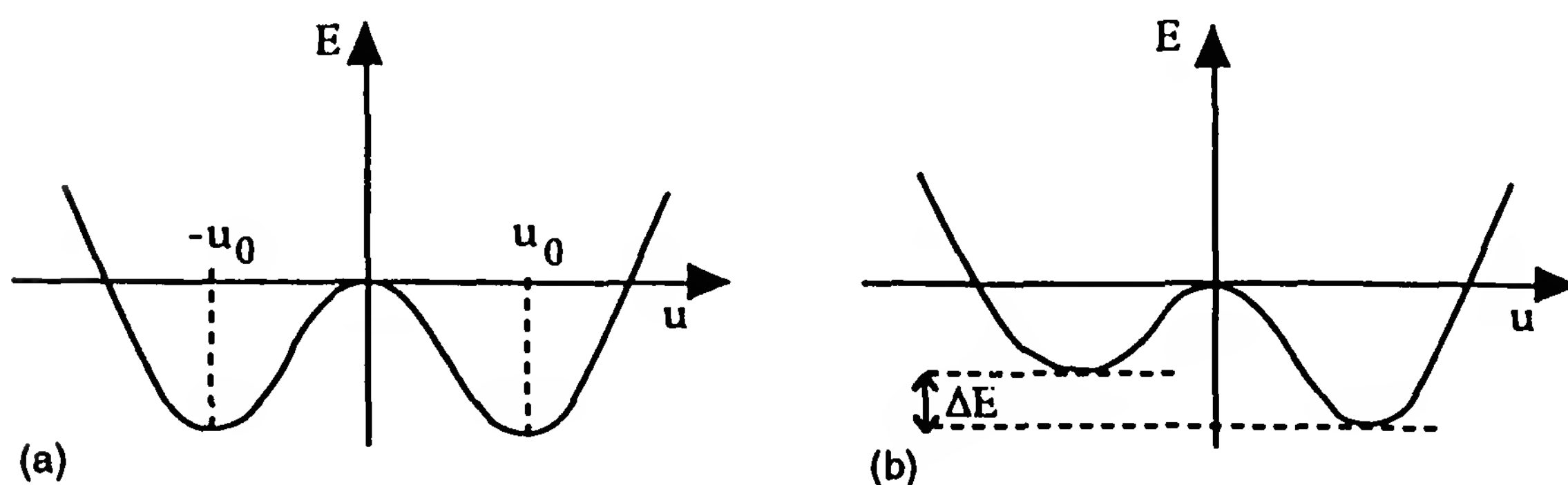


Figure 3 Ground state energy of a chain: (a) The dimerized, degenerate, ground state chain (equilibrium atomic displacement u_0); (b) The nondegenerate ground state case, with a secondary minimum at an energy ΔE above the ground state. Such a minimum may be absent.

C. Distortions of the Regular Chain Geometry: Solitons, Polarons, and Bipolarons

1. Solitons

In a degenerate ground chain as in Fig. 1, excitations corresponding to bond alternating defects can exist (Fig. 4). This is a domain wall separating two isoenergetic regions with an “opposite” sense of bond alternations. In chemical language, there is a nonbonding orbital which, in the neutral, uncharged (i.e., undoped) chain is occupied by a single electron that we can think as given by the $2p_z$ orbital of the C atom without a double bond on Fig. 4. This excitation of the chain is a $spin-\frac{1}{2}$ and $charge-0$ state: in other words, a free radical. But its position along the chain is arbitrary; it is a mobile “intrinsic” defect. Because it can move along the chain without distortion, it has become known in the CP literature as a soliton, although two such defects do not cross each other without distortion! The possible existence of such defects had been pointed out long ago [1,66], but the SSH theory allowed numerical calculation of the extension of the soliton [59]. It was found that the inversion of the bond length, shown in Fig. 4 as occurring on a single C atom, and the corresponding spin density are distributed over ≈ 14 atoms, as shown in Fig. 5a, which displays the variation of the bond alternation parameter within the soliton.

A free radical with a large extension of the spin density distribution has indeed been found experimentally in *trans*-PA by ESR and ENDOR, but differences with predictions of the SSH model are observed, corresponding to electron correlations; for a discussion of these studies, see Ref. 67. The nonbonding orbital corresponds to a soliton level at the middle of the forbidden gap. It may contain $n = 0, 1$, or 2 electrons; addition or removal of an electron to the neutral $n = 1$ state corresponds to a $\pm e$ charged soliton, which now has spin zero.

If electron correlations are neglected, all three levels are isoenergetic and the charged solitons are mobile. Doping is adding an electron or a hole on a CP chain (see Chapter 13), so if a neutral soliton is present, the added charge will naturally be accommodated on the corresponding midgap

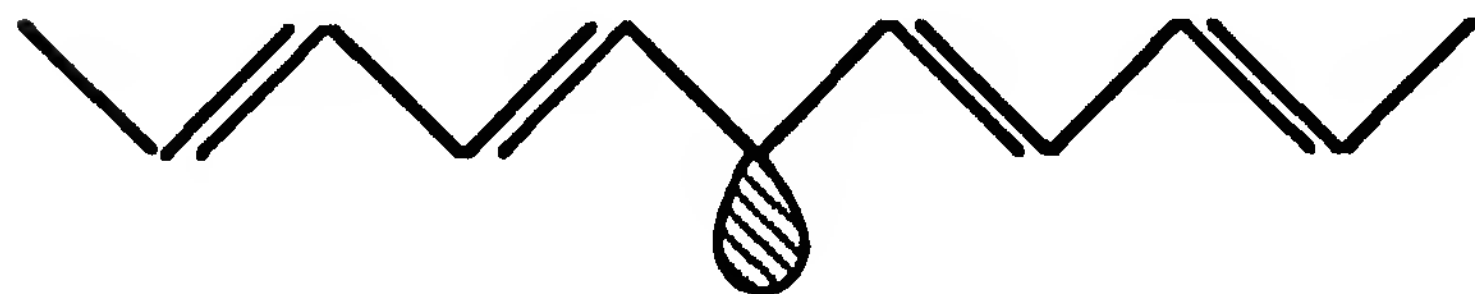


Figure 4 A bond alternation defect, shown here localized on a single site, bearing an unpaired electron.

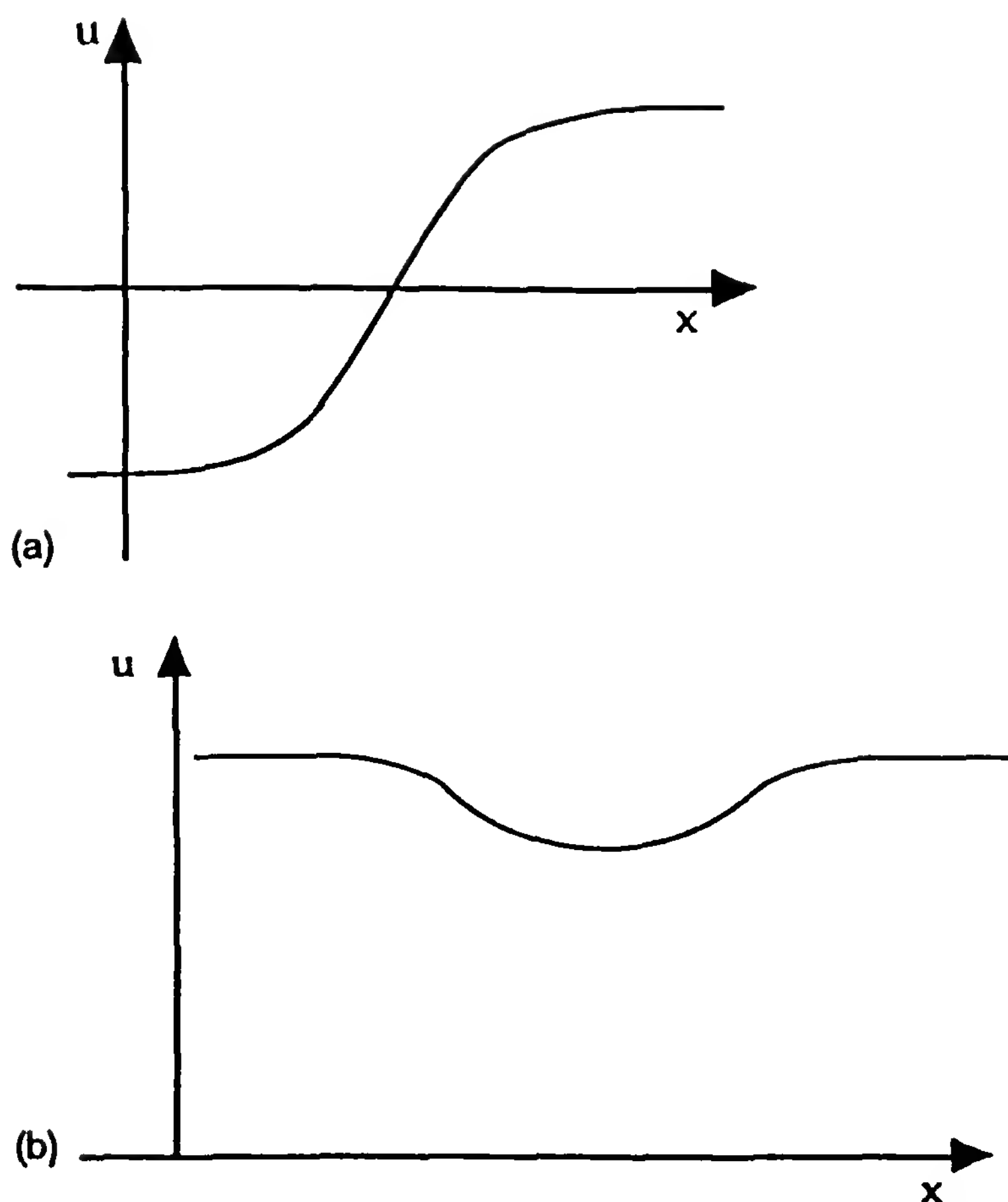


Figure 5 Variation of the distortion amplitude along a chain bearing (a) a soliton; (b) a polaron.

state. Pairs of oppositely charged solitons may also be created. In these cases *spinless charge carriers* are created. This is indeed what is observed in the early stages of doping of *trans*-PA, up to conductivities of about 10^2 S/cm, corresponding to an average of one dopant for 20 double bonds; this striking property did much to ensure the success of the SSH approach and of the notion of soliton.

2. Polarons

A single bond alternation defect in a nondegenerate ground-state CP would have very different consequences: the energies of the two semi-infinite chains on either side of the defect now differ by an amount ΔE per repeat unit (Fig. 3b), that is, an infinite amount. In a finite-length chain, the defect would move to the end corresponding to the vanishing of the high-energy structure: no soliton can exist, and the radicals that are observed in such CPs must have a different origin.

An electron or a hole injected on such a chain cannot then be present as a charged soliton. However, here again the electron–phonon interaction is important. If a charge is put on a true one-dimensional system, it always becomes dressed by a lattice distortion; that is, it will self-trap and form a polaron [68], an extension that depends on the ratio of the electron–phonon coupling to the electronic intersite coupling t . Presumably, the time needed to relax the one-dimensional lattice around the charge is very short, on the order of one vibrational period or 100 fs.

The polaron extension will often be large. The situation is quite different from that in a three-dimensional crystal, in which, in most cases, either the carrier will not become self-trapped, or it will form a “small polaron,” a strongly bound state of small extension. Quantum chemical calculations (Hückel type with σ -bond compression) yielded polaron binding energies compared to the bottom of the corresponding band on the order of 30 to 12 meV, a fairly small value, and effective masses of a few times the free electron mass [69,70], with extension of the geometrical deformation around the charge, within which the bond alternation parameter varies as shown on Fig. 5b; the geometry is the same on either side of the polaron (compare to the soliton case, Fig. 5a). The polaron, like an ordinary free carrier, has *charge* $\pm e$ and *spin* $\frac{1}{2}$.

Studies of oligomers can be of interest here. Radical ions of such molecules can be obtained in solution or in the solid state. In short oligomers the excess charge would be distributed homogeneously, in longer oligomers that is no longer true, which can be checked, for instance, by measuring the associated spin density. This has been done primarily on oligomers of thiophene, suggesting that in polythiophene the polaron extends over 6 to 10 cycles (i.e., 25 to 40 Å) [71] (for similar work on PPV oligomers, see Ref. 72). Note that degenerate ground-state chains can sustain a polaron as well, so that one should calculate which kind of excitation is more stable.

3. Bipolarons

Several cases of spinless conductivities have been observed in the doping of nondegenerate ground-state polymers, suggesting that polarons are not the appropriate excitations in these cases [73]. It has been proposed that the pairing of polarons would produce a new species of *charge* $\pm 2e$ and *spin zero*. Of course, the energy gained by forming a bipolaron must be large enough to overcome the coulombic repulsion between two nearby charges of the same sign and the entropic term. This may become quite natural if one thinks in terms of solitons, as was done when the idea was proposed. A nondegenerate ground-state chain cannot contain an isolated soliton, but if there are two nearby solitons sandwiching a short segment of the higher-energy geometry—a so-called soliton–antisoliton pair—as

shown in Fig. 6a for the case of *cis*-PA, the excess energy is finite. A bipolaron is then viewed as a doubly ionized soliton–antisoliton pair, such as on Fig. 6b [33]. Quantum chemical calculations similar to those performed for the polaron have yielded bipolaron energies lower than that of two polarons by about 0.4 eV [69,70].

The size of the soliton pair as on Fig. 6a is determined by the so-called confinement parameter $\gamma = \Delta_e/(2\lambda\Delta_0)$ [27,29]. Its meaning is qualitatively quite clear: If the energy difference ΔE between the two structures increases, the extension of the high-energy one decreases and the pair is “more confined.” For very small γ (i.e., $\Delta_e \sim 0$), the soliton pair or the bipolaron will tend to dissociate into independent solitons or polarons.

Contrary to polarons that form “instantaneously” upon injection or photogeneration of a charge, bipolarons are not created directly but must form by coupling of preexisting polarons, or possibly by addition of a charge to a preexisting polaron. Therefore, besides the question of their stability relative to two polarons, that of their kinetics of formation must be considered, to evaluate their relevance in a given experiment. The thermodynamics of polaron–bipolaron equilibrium is treated in Chapter 13. Again, bipolarons are possible excitations of degenerate ground-state chains, so the spinless conductivity of *trans*-PA could in principle be associated with bipolarons; we return to this question in Chapter 13.

4. Optical Signatures of Solitons, Polarons, and Bipolarons

The formation of these excitations generates energy levels corresponding to optical transitions below the fundamental absorption: that between the valence and the conduction band in one-electron models (but see Section

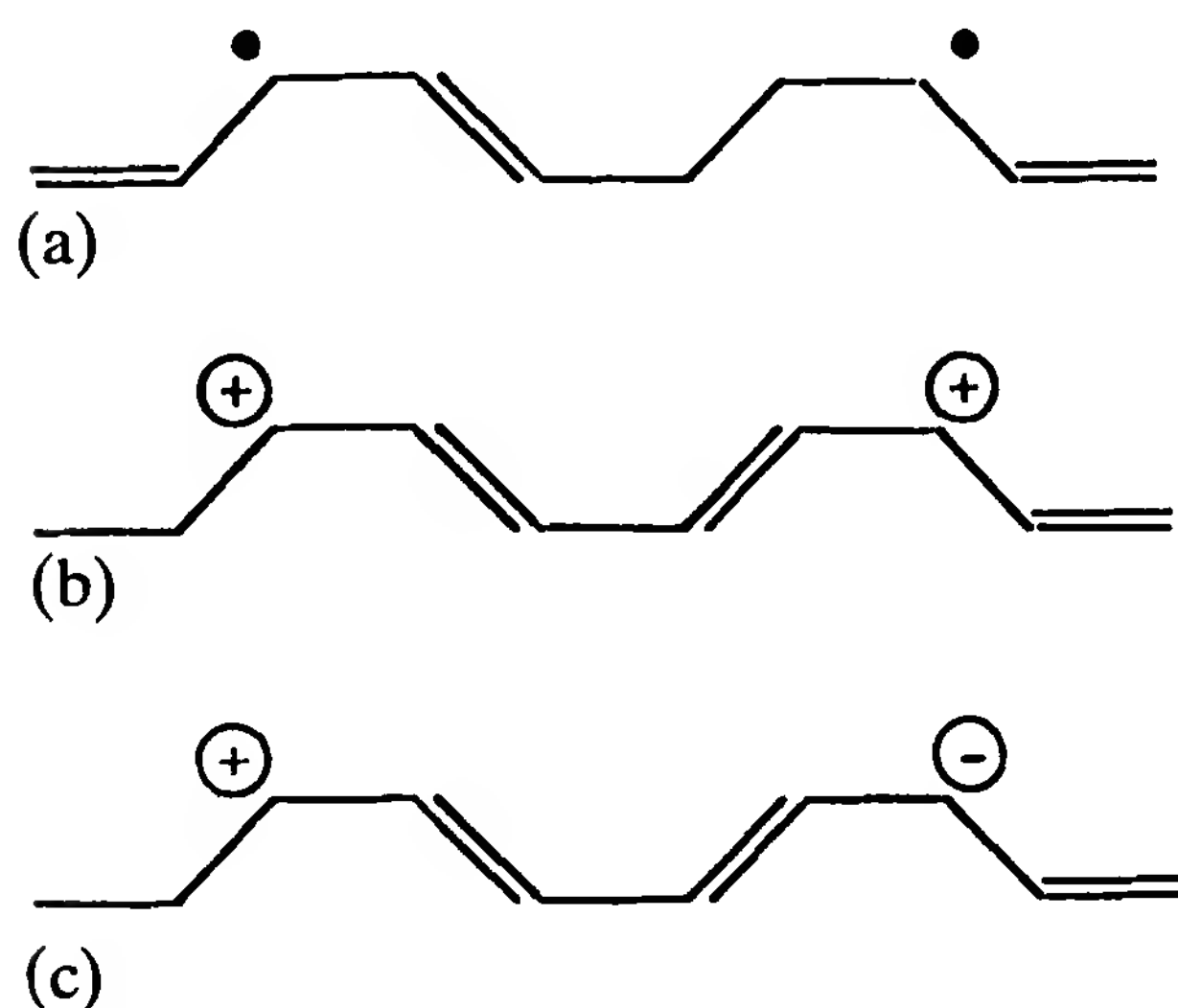


Figure 6 Comparison of: (a) a pair of solitons; (b) a positively charged bipolaron; and (c) an electron-hole pair bound by the lattice relaxation of the chain.

IV.C.5). The subject is not completely obvious and is discussed here within the independent electron approximation (no electron correlation is included), in which electron–hole symmetry is preserved. In fact, most numerical calculations have been performed using the valence effective Hamiltonian (VEH) method [74], which although it is supposed to deal with electronically occupied states only, is parametrized in such a way that it yields energy gaps (implying the lowest empty levels), in good agreement with optical absorption experiments [75], so, it seems that such calculations yield reasonably robust predictions for states derived mainly from band-edge levels, such as the soliton, polaron, and bipolaron. The corresponding energy states are usually drawn as shown on Fig. 7, on which for the conduction and valence bands only band edges are shown (renormalization of the bands due to the creation of the defect is neglected).

In this figure, small thick arrows indicate electron spins symbolizing the electron occupation of the levels, and dashed vertical arrows indicate the possible absorption transitions. Electron–hole symmetry is preserved, so the electron or hole levels are at the same distance from their corresponding band edge, and the various transition energies do not depend on the sign

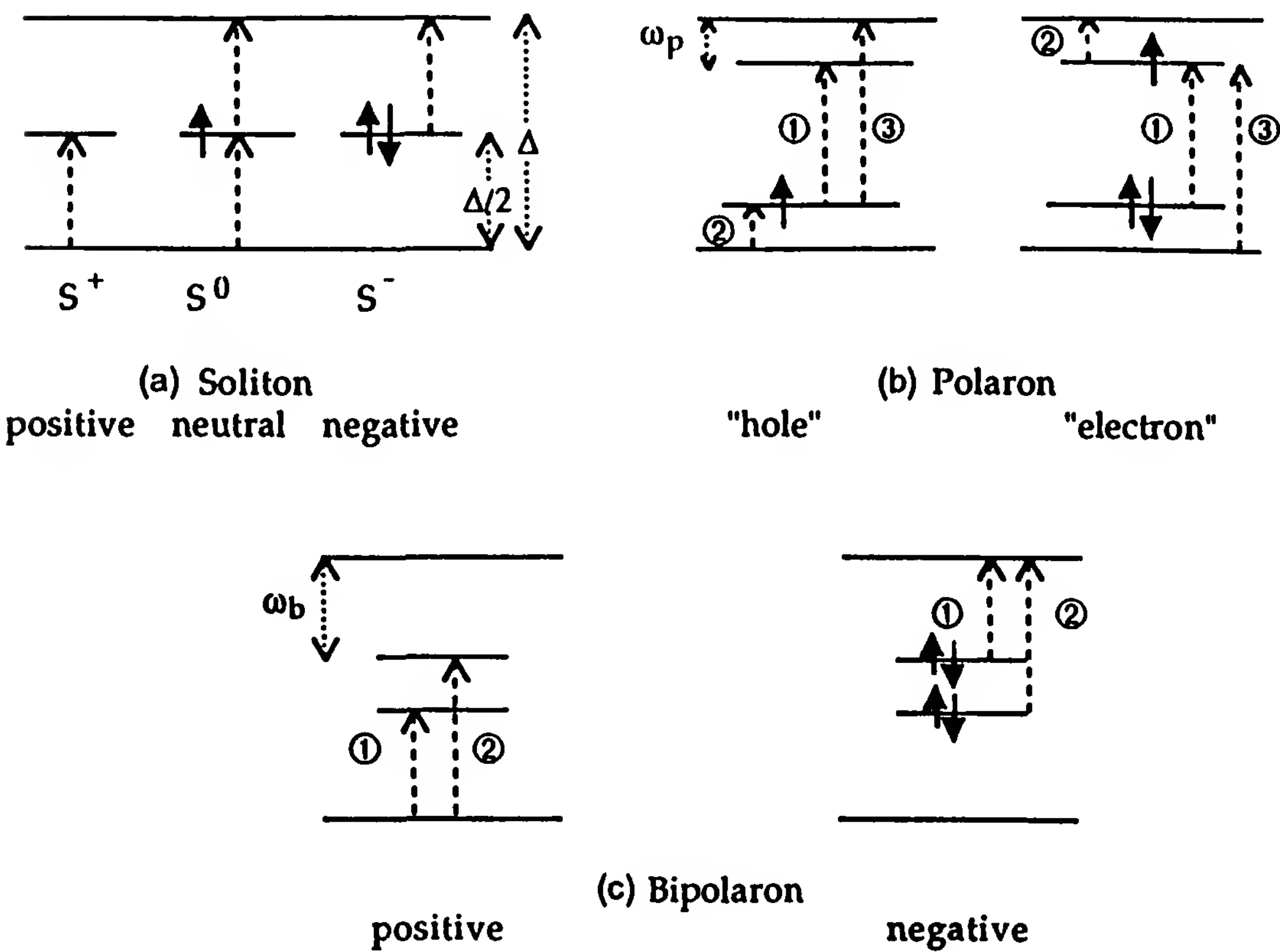


Figure 7 Electronic states, their charge, spin state, and the corresponding electronic transitions for: (a) solitons; (b) polarons; and (c) bipolarons.

of the carrier. New absorption bands are indeed predicted, and the model yields simple relations between the interband transition energy Δ and the new transitions; for instance, the soliton absorption (Fig. 7a) is at midgap $E_s = \Delta/2$, for the polaron $E(1) = \Delta - 2\omega_p$, and so on.

On the basis of this figure, it was claimed that absorption provides a test for discriminating among these excitations: solitons generate one new absorption, polarons generate three, and bipolarons generate two. In fact, things are much less clear cut. These transitions may have very different cross sections; a detailed study [76] has shown that the high-energy absorptions, number 3 in the polaron and number 2 in the bipolaron, have very small intensities unless the binding energies are large (i.e., the levels are near midgap), which is not what is found. So only two and one transitions, respectively, might be seen in most cases, one transition being expected to lie in the middle IR, where many vibrational absorption bands are already present.

Second, the simple energetic relations above are no more valid when electron correlations are included. For instance, the three soliton levels now occur at different energies, depending on their charge. This indeed seems to be shown by experiment: upon doping of *trans*-PA an intense and broad infrared absorption band appears, peaking near 0.7 eV (see, e.g., Ref. 77); this could be taken as evidence of the midgap state associated with S^- ; on the other hand, even very sensitive methods failed to give evidence for a band associated with the neutral soliton S^0 below 1.3 eV, and in particular near 0.7 eV [78]. For a theoretical discussion of these problems see Ref. 79. In fact, such differences might provide an experimental handle to estimate the importance of correlations.

Third, the reasoning above neglects any interaction of these species with other charges that may be present in the material and may generate static electric fields, which may modify the energy of the defects, especially the charged defects, and possibly immobilize ("pin") them. The counterions injected in the doping process will do just that, whereas charges injected from an electrode into the undoped material will not be compensated: that properties of these defects are independent of the way they are introduced in the material is not granted.

Finally, charged excitations on the chain also generate new and intense infrared absorptions (IRAS lines) which are other manifestations of the strength of the electron-phonon coupling.

5. Excitons

Another type of quasiparticle is the exciton, a *neutral* excitation well known in semiconductors, where it often dominates the onset of electronic optical absorption. Frenkel excitons, either singlet (spin 0) or triplet (spin 1), are

in fact the most important excitations for understanding the electronic properties, the visible and near-UV absorption to begin with, of crystals of small conjugated molecules such as naphthalene [80–82]. Again, their existence is a manifestation of electron interactions. Their status in CPs is not yet clear. For a long time they have been totally ignored, although it had been shown that the optical properties of PDAs are dominated by a strong excitonic transition to a fairly strongly bound singlet state, 0.5 eV below the gap energy (for a discussion, see Ref. 52).

In the spirit of Section IV.C.3, one could think of constructing an excitation by coupling two charges of opposite signs, confining a sequence of the high-energy structure, as on Fig. 6c. This would be a neutral excitation of spin 0 or 1. In the approximation of Section IV.C.4 and Fig. 7, its binding energy would be the same as that of the charged bipolaron and independent of its spin, but an independent electron framework does not seem to be a good starting point for studying strongly bound excitons! There is no adequate general exciton theory for CPs yet, and only general remarks are to the point here.

We mentioned above that in real materials, disorder of any kind localizes the excitations over a limited length on the chain, generating effective “conjugation lengths” so that, for instance, the optical properties are those of a finite, often quite small, molecule. It may well be that excitons are very important in such cases. This has been proposed, for instance, for substituted PPV and polythiophene [83]. This is not by itself a proof that were it possible to prepare the corresponding perfect chain, the excitons would still be important there, although this is precisely what is found in PDAs, because electron correlations have different intensities on different CPs.

If the exciton binding energy relative to the separate charge pair is larger than that of the polarons relative to their free particle bands, the polaronic optical transitions will be “hidden” under the excitonic ones, and a one-electron approximation of the polaron certainly fails. This is yet another reason why optical signatures of the polaron may give dubious results (see Section IV.C.4). Such a situation can have practical consequences, to which we return in the discussion of electroluminescence in Chapter 12, Section V.C.

In conjugated molecular crystals, the triplet exciton energy is always much lower than the singlet one, by up to 1.5 eV. Thus the triplet is the lowest-lying electronic excitation in these systems, but the optical transition between the (singlet) ground state and the triplet is spin forbidden [82]. The unique signature of the triplet is magnetic. Besides, higher-lying triplets exist and the transitions between these and the lowest triplet may be strongly allowed; intense triplet–triplet absorptions are known in conju-

gated molecules. In CPs, the energy of the lowest triplet has not been measured directly yet, but it is known to exist both by electron spin resonance (ESR) and triplet–triplet absorption. Particularly useful has been the optical detection of magnetic resonance (ODMR), which has been applied to date to PDAs [84] and polythiophene [85]. A strong absorption, induced in PDAs by pumping in the singlet-exciton absorption, has been shown to be triplet–triplet absorption [86,87]. Interestingly, a similar photoinduced absorption in *trans*-PA at 1.4 eV has been assigned completely different origins [88,89]. Thus although triplet excitons clearly exist and should be considered in CPs, their role is even less clear now than that of the singlet. That singlet and triplet excitons are important in at least several CPs is also shown by the occurrence of exciton interactions similar to those well studied in molecular crystals [80]; for instance, singlet-exciton fission has been found in PDAs [87] and triplet-exciton fusion in PPV [90].

To summarize this section, we can say that the picture of CP excitation in terms of solitons, polarons, and bipolarons is certainly incomplete, particularly when considering optical and, to a lesser extent, magnetic properties. However, there is presently no clear-cut and generally accepted picture of how and when excitons are important, although they certainly are.

D. Three-Dimensional Coupling

Up to now, we have considered CPs (almost) exclusively as being perfectly periodic, infinite, and isolated one-dimensional chains. This is not what real materials are made of. In this and the following sections, we move closer to real materials by considering the effects of three-dimensional coupling and of disorder (both intrachain and interchain). Not surprisingly, less theoretical work has been done on these issues. On the other hand, considerable experimental effort has been devoted to characterizing the disorder, which is discussed in Chapter 12, where the structure of CPs is considered.

Let us first discuss the effects of three-dimensional coupling of CP chains, still supposed to be perfect and in perfect three-dimensional order, a situation for which theoretical results are available. The coupling can affect the electronic structure and excitations of the chain; and a new problem appears, that of three-dimensional transfer of excitation. This is crucial to understanding the dc conductivity of CPs, both undoped and doped.

Three-dimensional coupling is characterized by the interchain transfer integrals t_{\perp} . Generally, only nearest-neighbor interactions are taken into account, so only one or two t_{\perp} are relevant. They may differ, even in sign, depending on the relative positions of the interacting chains. In this qual-

itative discussion we consider a single t_{\perp} ; the pertinent parameter can then be expressed as the ratio of t_{\perp} to the intrachain integral t_{\parallel} (called t above), which determines the order of magnitude of the band structure anisotropy, or the ratio of t_{\perp} to the polaron binding energy. Indeed, it was mentioned in Section IV.C.2 that the one-dimensional polaron is qualitatively different from the three-dimensional polaron [68].

The question then arises of the amount of three-dimensional coupling—that is, the value of t_{\perp}/t_{\parallel} —sufficient to establish three-dimensional behavior. It has been studied in different ways, showing that three-dimensional behavior wins at least if $t_{\perp}/t_{\parallel} \geq 10^{-2}$, that is, t_{\perp} on the order of 20 meV [91,92]. This is a stringent condition.

For quantitative calculation on a specific CP, a three-dimensional band structure calculation is needed, which requires knowledge of the crystal structure. Except for PDAs, only incomplete data are available, because ordered regions in a real sample are always imperfect and of limited size. Unit cells and space groups that have been determined in several cases correspond to monoclinic structures with two chains (actually two repeat units) per unit cell. But the geometry is not completely specified. First, the setting angle, which defines the orientation of the average plane of the chain relative to the cell axes, is known only approximately. Second, on a given chain there are different types of bonds or groups, such as long and short bonds in PA, rings and double bonds in PPV; the two chains within the unit cell are related by such operations as a glide plane or screw axis, so that identical bonds or groups on the two chains may or may not be staggered (Fig. 8), yielding different space groups, usually $P2_1/a$ or $P2_1/n$, and correspondingly large differences in the interchain interactions. Third, if the chains contain rings, the chains may be planar, or, more probably, rings are rotated in alternating directions, thus affecting both the one-dimensional electronic structure and the interchain interactions.

Two recent and detailed three-dimensional band calculations on *trans*-PA [93] and on PPV [94] yield similar results: t_{\perp}/t_{\parallel} is at least 3×10^{-2} , so three-dimensional behavior should be observed and no polaron state should

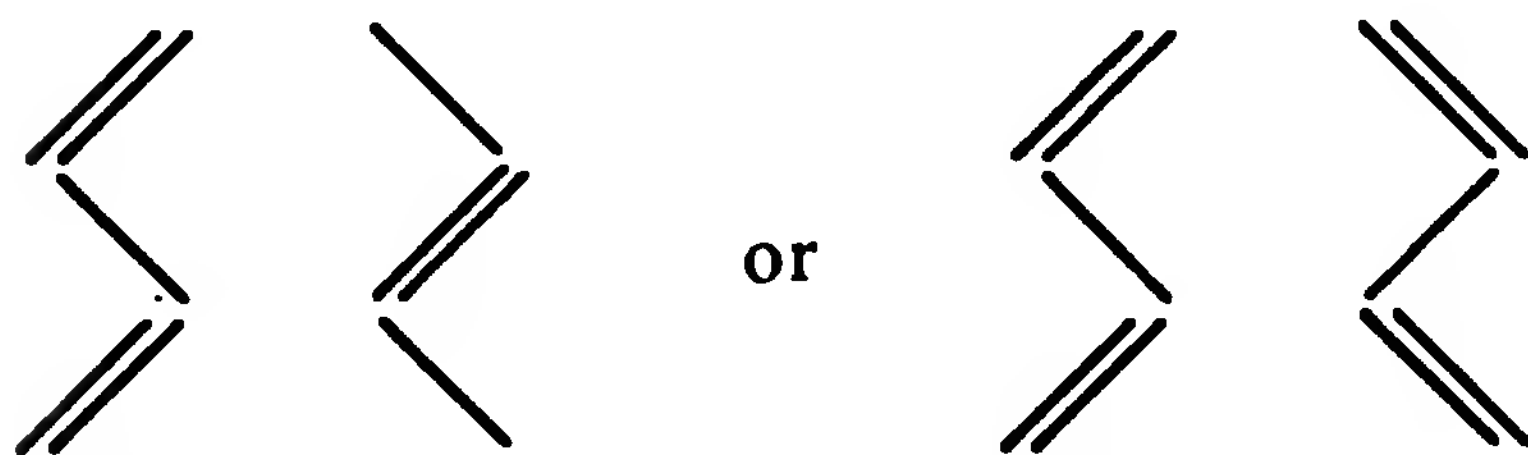


Figure 8 Relative disposition of two PA chains in the unit cell.

form; even the bipolaron may be unstable. Explicit numerical calculations of polaron and bipolaron localization as a function of interchain coupling have recently been carried out within the SSH approach, and they confirm this picture. Polarons are not formed for reasonable values of the coupling, and the bipolaron is dissociated in *trans*-PA, although not in *cis*-PA nor presumably in other nondegenerate ground-state CPs [95]. In addition, it is found that optical spectra are greatly affected by interchain coupling, even in the range of couplings where similar one-dimensional behavior is preserved.

However, in all these calculations, the conjugated chains bear H atoms only. As bulkier side groups are introduced, the overall interchain interaction decreases and it becomes more anisotropic. If chains form stacks, relatively strong two-dimensional coupling will persist and may still have consequences similar to those of three-dimensional coupling. The question remains open. But substituted CPs are generally even more disordered than the simple ones, and we shall see now that disorder will then have more important consequences than the details of interchain interaction.

E. Effect of Disorder

An important and general feature of CPs is that they are not well-ordered materials; an amorphous phase is always present, sometimes dominant; and the crystalline phase is always made of small, imperfectly ordered crystallites. These problems are seldom reviewed and are discussed at some length in Chapter 12, Section II.

Even neglecting gross inhomogeneities, disorder has an important electronic consequence: localization. It is a well-known property of one-dimensional and quasi-one-dimensional systems. It is all the more important in CPs, where the conformation of the chain in the paracrystalline solid (see Chapter 12, Section II.C.1) has static fluctuations along its length, and the interchain interactions fluctuate as well. The potential fluctuations due to these effects are spread over some distance and usually are not very deep ("weak disorder"). On the other hand, chemical defects, such as nonconjugated carbon atoms inserted in the chain, or impurities may result in very local and strong potential variations ("strong disorder"). Both types of disorder, not only the second one, are important in limiting the conjugation length [5].

The effect of disorder in CPs is a complicated problem and only a few model studies have been carried out. Geometrical fluctuations have been modeled by considering the effects of rotations of rings or bonds around another bond within the chain; such a distortion is known to decrease conjugation [96]. Experimentally, the best characterized situation to achieve

such a disorder is the isolated chain in solution [49], and calculations of the resulting overall conformation agree quite well with experiment [97]. Spectroscopically, the absorption of such chains is structureless and blue-shifted. Figure 13 of Chapter 12 shows a comparison of solution and crystal spectra of a PDA, the best characterized system in this regard, since the crystal spectrum shows that strong disorder is not significant. The solution spectrum in the figure suggests a distribution of conjugation lengths between about 20 and 50 Å, one order of magnitude smaller than the persistence length of the chain [54]; these values and the absence of structure in the absorption imply that there is a rather continuous distribution of conjugation lengths, so that they are not integral multiples of the repeat unit length.

Thus weak disorder may be the main source of localization and conjugation length limitation. The variations in electronic properties such as absorption will then not always follow laws such as those given in Section II.C: N^{-1} variations are well verified for polyenes, but then would not give the correct extrapolation for $N \rightarrow \infty$. Weak disorder also localizes excitations: for instance, photoexcited charge carriers. It will induce the presence of “polarons” even if they were not bound states of the perfect chain, or of bipolarons, modify the transport properties, and increase the lifetime of charge carriers against recombination [98].

Strong disorder has been studied both experimentally by purposely introducing chemical defects, and theoretically (see, e.g., Refs. 99 to 101). It is shown that a single atom “breaking the conjugation” is not enough to remove coupling completely between its two sides [99]. The actual energy of the defect level is greatly influenced by electron–phonon coupling [101]. Trapping of a charge by such a defect will generate a “localized” (i.e., trapped) polaron, which may be very long lived, seconds or more. Such levels are needed to explain some transient absorption experiments, for instance. Disorder is now put to use to adjust the emission wavelength of CP light-emitting diodes (see Chapter 12, Section VI.C.5).

The discussion above is concerned with undoped CPs. Doping almost always decreases the structural order (see Chapter 12, Section II.C.4) and may proceed inhomogeneously. As in graphite intercalates, stages may be present, and gross inhomogeneities, up to a situation in which doped, metallic regions coexist with undoped ones, have been reported [102]. If the free carriers on the chains are compensated by static counterions (thus excluding other processes by which free charges are injected onto the chains, for instance by carrier photogeneration or injection by the electrodes, processes that are sometimes termed “doping” [103]), these ions generate strong and random electrostatic potentials which strongly affect the free carriers, their transport, and their magnetic properties (see Section

IV.F). Even in the case of high doping levels leading to the highest dc conductivity to date in *trans*-PA [104,105], the temperature dependence of the conductivity can be accounted for by a model of tunneling through small barriers, corresponding to unspecified sample defects or inhomogeneities. The influence of disorder on conductivity is discussed in more detail in Chapter 13, Section III. A thorough description of disorder and its electronic effects in CPs has yet to be made.

F. Doping

A survey of the basic notions relevant to CP physics cannot be concluded without a brief review of doping. More details on this process are given in Chapter 13. Doping [i.e., addition (or withdrawal) of electrons to (or from) the conjugated chains] is a central process that governs the main properties of CPs, in particular the crossover from an insulating to a conducting state. It is also a process that makes a major difference between CPs and crystal organic conductors. While the latter exist only in the doped form, CPs can be doped and dedoped reversibly. The doping level then appears as an additional and crucial parameter.

As charges are injected in the chains, electrical neutrality is maintained by counterion insertion in the polymer matrix. In this way conducting polymers resemble intercalation compounds, with the difference that usually the counterions arrange randomly. In some cases, however (more especially in polyacetylene, but also in polyaniline), ordering of the counterions, or stages, has been observed. The ion insertion can thus be compatible with a crystalline structure. It has been observed, however, that the crystallinity is degraded on cycling (see Chapter 12, Section II.C).

Doping is a redox reaction that implies electron transfer between a given conjugated chain and surrounding donor or acceptor dopants, which become the counterions. It can be obtained either chemically or electrochemically. The electrochemical doping enables continuous and reversible variation of the doping level. The CP sample is then a film deposited on an electrode of an electrochemical cell. By controlling the electrical voltage of this electrode with respect to a reference electrode, the chemical potential of the film is controlled, and therefore the doping level. The maximum doping level corresponds to one charge per approximately 10 to 12 carbon atoms (or heavy atoms such as O, N, or S). This value seems practically independent on the polymer structure, which can be linear as in PA, or includes aromatic rings, as in PPP, PTh, and PANI. It is noteworthy that about the same value for the maximum doping level is also found for graphite or C₆₀ compounds.

Both p -type and n -type doping have been obtained in a few CPs, in particular PA and PPP. Generally, however, p -doping, which has been obtained in all CPs, leads to more stable compounds. In the case of n -doping the dopants are alkali metals which are unstable in air atmosphere. Furthermore, oxygen can act as an oxidant and neutralize n -doping. Even p -doping can be unstable in air if the oxidation potential of the polymer is higher.

Although the role of the counterions is often neglected when discussing CP properties, there is no doubt that their presence near the conjugated chains can play a major role in various processes. It has been observed in many cases that the transport and magnetic properties can depend on the nature of the dopant. The counterions create an electrical potential on the chains, which can shift and even modify the relative positions of the polaron and bipolaron levels. If randomly distributed, they can be a strong source of disorder. It has been shown that the positions of the self-trapped carriers on the chains are determined essentially by the position of the dopants [106]. Their influence on interchain coupling can also be considered. By placing the chains farther from each other, the counterions weaken the interchain couplings. Their role as interchain bridges that would favor conduction can be considered however. It can, for instance, be envisaged that the electrical charge coming from a counterion is distributed over two or even several chains, giving rise to a new kind of interchain polaron (or bipolaron) species.

V. APPLICATIONS

A. Overview

Approaching the field of the applications of conducting polymers (CPs) is a rather delicate task. It is a matter of fact that the hope for possible applications has always been one of the strong motivations in this domain. A basic idea was, of course, to combine “the important electronic and optical properties of semiconductors and metals with the attractive mechanical properties and the processing advantages of polymers” [48]. Another exciting feature is connected to the capability of CPs to have their properties changed with the doping level. Lists of numerous and promising applications have been available in different reports and review papers since the discovery of these materials in the late 1970s. Over 50 utilizations have been proposed (see Table 2), which is evidence of the richness and vitality of the domain. However, for a period in the 1980s, it was rather unclear how to distinguish between potential applications and those really

Table 2 Representative Proposed Applications of Conducting Polymers

Actuators	Electromechanical actuators for biomedical devices, micropositioners, microtweezers, microvalves, etc.
Antiradiation coating	Electron-beam resists
Antistatic carpets, coatings, fibers, films, paints, etc.	Fuses (reversible)-Gas separation membranes
Artificial muscles	Heating elements (e.g., clothing)
Batteries (lightweight, high energy density, rechargeable, flexible, odd-shaped)	Infrared reflectors
Capacitors and supercapacitors	Lithographic resists
Catalysts	Loudspeakers (electrostatic)
Coating for metal plating on plastics	Memory devices (electrical, optical)
Conductors (lightweight)	Molecular electronics
Controlled-release medicine delivery systems	Nonlinear optics
Corrosion-preventive paints	Packaging materials
Displays	pH modulator
Electrochromic displays, smart windows	Polymer/solid electrolytes
Electrodes (catalysts, fuel cells, etc.)	Semiconducting devices: <i>p-n</i> junctions, photovoltaics, Schottky diodes, light-emitting diodes, transistors, etc.
Electromagnetic shielding	Transparent conductors

Source: Ref. 108.

used. This rather fuzzy situation has begun to disappear, with the development of several applications now in use on an industrial scale. Discovered in the late 1970s, CPs have become industrial products in the 1990s. In 1992, there were about 100 companies at the stage of test production [107], a number that is increasing rapidly. A rough estimate is that the worldwide market for synthetic metals (mostly conducting polymers) will reach about \$1 billion in the year 2000 [48].

Applications of CPs can be classified in various ways. Besides the alphabetical order used in Table 2, one can, for instance, distinguish between (1) those that are commercialized, (2) those whose feasibility has been demonstrated, and (3) those that are only at the stage of laboratory investigation. Of course, these categories are separated by borders that are moving with time.

As explained before, a specificity of CPs is the capability of having their properties changed as a function of the doping level. Based on this feature, in Table 3 we give a presentation according to (1) the physical properties and (2) the various methods of doping. As a generalization, the word "doping" is often used to name any process changing the effective number

Table 3 Schematic Presentation of the Main Applications of Conducting Polymers and Fundamental Associated Problems Versus Properties and Charge Injection Modes

		Charge Injection Modes (Doping)				
		Chemical	Protonic	Electro-chemical	Optical	Electric
Type of Property	Conductivity Transport properties	<div>Nature of the conducting state</div> <div>Conduction mechanism</div> <div>Role of disorder</div> <div>Antistatics</div> <div>Electromagnetic Shielding</div> <div>Sensors</div>		<div>Electrochemical Transistors</div> <div>Sensors</div> <div>Doping process</div> <div>Insulating-to- Conducting Transition</div>	<div>Photoconductivity</div> <div>Solar cells</div>	<div>Schottky Diodes</div> <div>Electronic Components</div> <div>MISFET</div> <div>Carrier Mobility</div>
	Doping level Electrochemical properties			<div>Batteries</div>		
	Optical properties			<div>Smart Windows</div>	<div>Non Linear Optics</div>	<div>Electro-Optic Switch</div> <div>Light Emitting Diodes</div>
	MECHANICAL properties		<div>Loudspeaker</div>	<div>Actuators, Microtweezers... Artificial muscles</div>		
		Applications		Fundamental Problems		

of π electrons of the conjugated system. Such a classification is far from being complete but has the advantage of making clear the links between the specific properties of CPs and their possible applications, and consequently, to make apparent the relationship between fundamental problems and applied research.

According to the charge injection mode, three classes of materials can be defined.

1. *Permanently doped polymers*, concerned with chemical or protonic doping. The charges that appear on the polymer chains are compen-

sated by counterion insertion. Protonic doping concerns essentially polyaniline, a material that plays an important role for applications. Such materials are used for applications that require electronic conductivity (which need not be high).

2. *Redox cycled polymers*, which electrochemically doped and dedoped, are used for energy storage (batteries) and when one wants to have a property tuned by a potential. For instance, in the case of “smart windows” the color or absorbance of a glass window can be controlled electrically.
3. *Undoped polymers*, which remain in the semiconducting state. In this case charge injection is operated by photoexcitation (simultaneous creation of an electron in the conduction band and a hole in the valence band), or by action of an electric field at a junction.

The main characteristics of these different classes of materials can be sketched as follows. Class 1 materials can be obtained cheaply, in large quantities. They are suitable for big chemical companies interested in commercializing tons of industrial products. Class 3 materials require a high level of sophistication and advanced technology. Today, they are fabricated only on a laboratory scale. Interest in applications using class 3 materials is concentrated primarily in small high-tech companies, (such as UNIAX in Santa Barbara, California). Applications already on the market are concerned mainly with class 1 materials. Applications using class 3 are essentially at the stage of laboratory investigation. The situation of class 2 materials is somewhat intermediate. Batteries using CPs have been commercialized, but to our knowledge, this is not yet the case for other electrochemical devices.

B. Applications with Permanently Doped Polymers

Using chemical or protonic doping, the electric charges on the polymer chains are compensated by counterion injection. In the case of protonic doping (essentially in polyaniline), the addition of protons does not change the overall number of electrons in the chain skeleton. But one of the two electrons of the nitrogen doublet become caught in the N—H bond, and then the effective number of electrons available for the π system is modified.

High doping levels can be achieved (5 to 15% charge per carbon, or heavy atoms), giving rise to high conductivity. These types of doping are suitable for applications concerned with electronic conducting materials. Use in electricity transport has been envisaged, taking advantage of the light weight of the polymer materials; for instance, replacement of copper wires by conducting polymers in aircrafts would lead to appreciable weight gain. However, polyacetylene, the only conducting polymer approaching

copper conductivity, is still a very unstable material at ambient atmosphere. In fact, CPs are interesting in applications for which intermediate or low conductivities are required.

In this range we put applications in which CPs are used to make an electrical contact. In particular, with CPs contacts can be made on specific surfaces (e.g., on microporous electrodes). In the case of supercapacitors an electrical contact should be realized on a microporous surface covered by aluminum oxide. Liquids are capable of penetrating the micropores intimately and of covering all parts of the surface at a nanoscopic scale. Electrolytic capacitors use liquid conductors, but because the conductivity is ionic, such components suffer from polarization effects. Thus it is advantageous to replace the liquid ionic conductor by a solid electronic conductor. This has been achieved with polypyrrole obtained by polymerization of pyrrole in the presence of an oxidant (generally FeCl_3) in situ in the micropores, so that intimate contacts with the electrode are realized. Capacitors based on polypyrrole are available from Panasonic [107]. Based on the same principle, contacts can be made on porous silicon with the purpose of making porous silicon-conducting polymer LEDs.

Printed circuit boards for the electronics industry using a conducting polymer coating on a plastic substrate have been fabricated by various firms (e.g., BASF). The coating is obtained by direct polymerization of monomeric pyrrole (brought in the gaseous phase) on the substrate, which is impregnated by the oxidant. The polypyrrole layer is then used as an electrode for further electroplating of copper. Similarly, the polymerization of pyrrole has been used to obtain conducting textiles. Large quantities of such materials are produced. If heating clothes does not seem a real aim, numerous uses exist. For instance, Mulliken markets a camouflage net that thwarts visual, near-infrared, and radar detection [109].

A good illustrative example showing an elegant combination of conducting and plastic properties is a new type of electrostatic loudspeaker manufactured by Zipperling-Kessler under the trade name Final Elektrost. In principle it relies on the vibrations of a thin membrane suspended between two grid electrodes. It is essential that the membrane be both conducting and flexible. Natural metal would not fill these requirements. A sheet of metal would not be flexible enough; and a thin metal layer deposited on a plastic membrane would become brittle through vibrations. The solution is obtained with a 6- μm polyethylene film coated with 0.2 μm of conducting polyaniline [48].

Fabrication of conducting plastics, mostly blends in which the conducting polymer is associated with another polymer that has higher mechanical properties, is probably the most developed application to day. Such polymeric blends appear to be much better solutions than carbon black-loaded

polymers. There are several reasons in favor of CPs. First, their mechanical properties, although generally inferior to those of nonconjugated polymers, are much better than those of carbon black. Second, due to the one-dimensional characteristics of polymeric materials, the percolation threshold for conductivity is reached at much lower concentration (typically, $c < 1\%$) than with a loading material such as carbon black, which is essentially three-dimensional. This is also a reason for reinforced mechanical properties. Furthermore, the change of conductivity versus concentration around the threshold is not abrupt as in the usual cases, but is smooth. Hence intermediate values of conductivity can be obtained easily.

Antistatic protective films and bags constitute a very important domain of applications (probably the most important today). For instance, an antistatic layer made of polyaniline is used to protect computer disks recently introduced by Hitachi-Maxwell. Also, CPs would be valuable for the packaging of electronic items damageable by static discharges. The films should also be transparent, to enable direct vision of the items protected. Several chemical companies that manufacture plastic foils are in the process of commercializing films coated with CPs. Hoechst AG has developed polythiophene-coated films. Zipperling-Kessler, Americhem, and Allied Signal Corporation have formed a consortium to develop polyaniline-based products, including transparent films of PVC with polyaniline. Conductivities for antistatics applications need not to be high. Typical surface conductances in the range 10^{-9} to 10^{-5} S are sufficient.

For electromagnetic shielding, somewhat higher conductivities are required. While low-frequency shielding would require a metal-like level of conductivity not easily attainable with conducting polymers, absorption in the microwave domain corresponds to a range of conductivities quite suitable for CPs, typically 10^{-3} to 10^{-1} S/cm. Thus CPs appear to be interesting materials for antiradar protection; they present a good compromise between absorption bandwidth and surface mass [110]. The dielectric absorption parameters, ϵ' and ϵ'' , can be adjusted by dilution in a polymeric host matrix, which will also ensure reinforced mechanical properties. The conductivity-absorption range can also be adjusted by the doping level. Very conveniently, in the case of polyaniline the transport properties are tuned by the protonation level, which is controlled by the equilibrating pH, and any intermediate value for the parameters can be obtained.

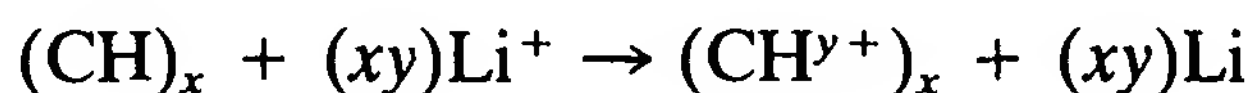
Finally, still in the area of permanently doped polymers, we mention gas separation, which has a very large potential market in the domain of chemical separation. Preliminary work has shown that membranes very promising for gas separation can be made with CPs [111], typically polyaniline or polypyrrole [112]. The basic points are as follows: (1) thin CP

membranes demonstrate gas permeability, (2) the gas transport properties are highly selective (i.e., the permeability depends on the nature of the gas), and (3) both permeability and selectivity can be changed reversibly by the doping level. Very high selectivity has been reported. For instance, the permeability of oxygen has been reported to be 30 [110] (or 8 [111]) times larger than that of nitrogen. Thus membranes for separation of oxygen from air can be conceived. Whether the electronic properties of CPs are involved in the process is unclear. Rather intuitively, permeability is depicted as being due to holes, or to fissures of a few angstroms left in the polymer matrix by ions when they are inserted and removed in doping–dedoping cycles. The permeability, which depends critically on the gas molecule size, would be adjusted by the amount of ions in the polymer matrix as the doping level is changed.

C. Applications with Electrochemical Doping

1. Energy Storage

The capability of CPs to be reversibly doped and dedoped electrochemically was pointed out and their use as electroactive material for rechargeable batteries was proposed from the beginning. The attractive basic idea relied on the light weight of organic polymers compared to the usual active materials, such as lead. A number of battery designs using CPs have been described. The active CP electrode can be either the anode or the cathode of the cell. Battery cells with CP as the anode are most common. That case corresponds to *p*-type doping for the polymer. When the battery is charged, positive charges are present on the polymer chains. These charges are compensated by anions entering the polymeric matrix. The cathode is made of a low-work-function metal. Lithium has been used intensively. It has the advantage of light weight and a high open-circuit voltage, typically 3 to 4 V. The battery has two redox couples: CP/CP⁺ at the anode and Li⁺/Li at the cathode. For instance, with (CH)_x as CP, the overall charging reaction is



Between the two electrodes, the electrolyte is a solution of a dissociated salt (e.g., Li⁺ClO₄[−] in propylene carbonate). It has the use of a reservoir of ions available for charge compensation at the electrodes. A schematic of a typical battery is shown in Fig. 9.

A number of prototype batteries have been fabricated, using different CPs: PA [113–115], PPy [116,117], PTh [118], PPP [119], and PAni [120,121].

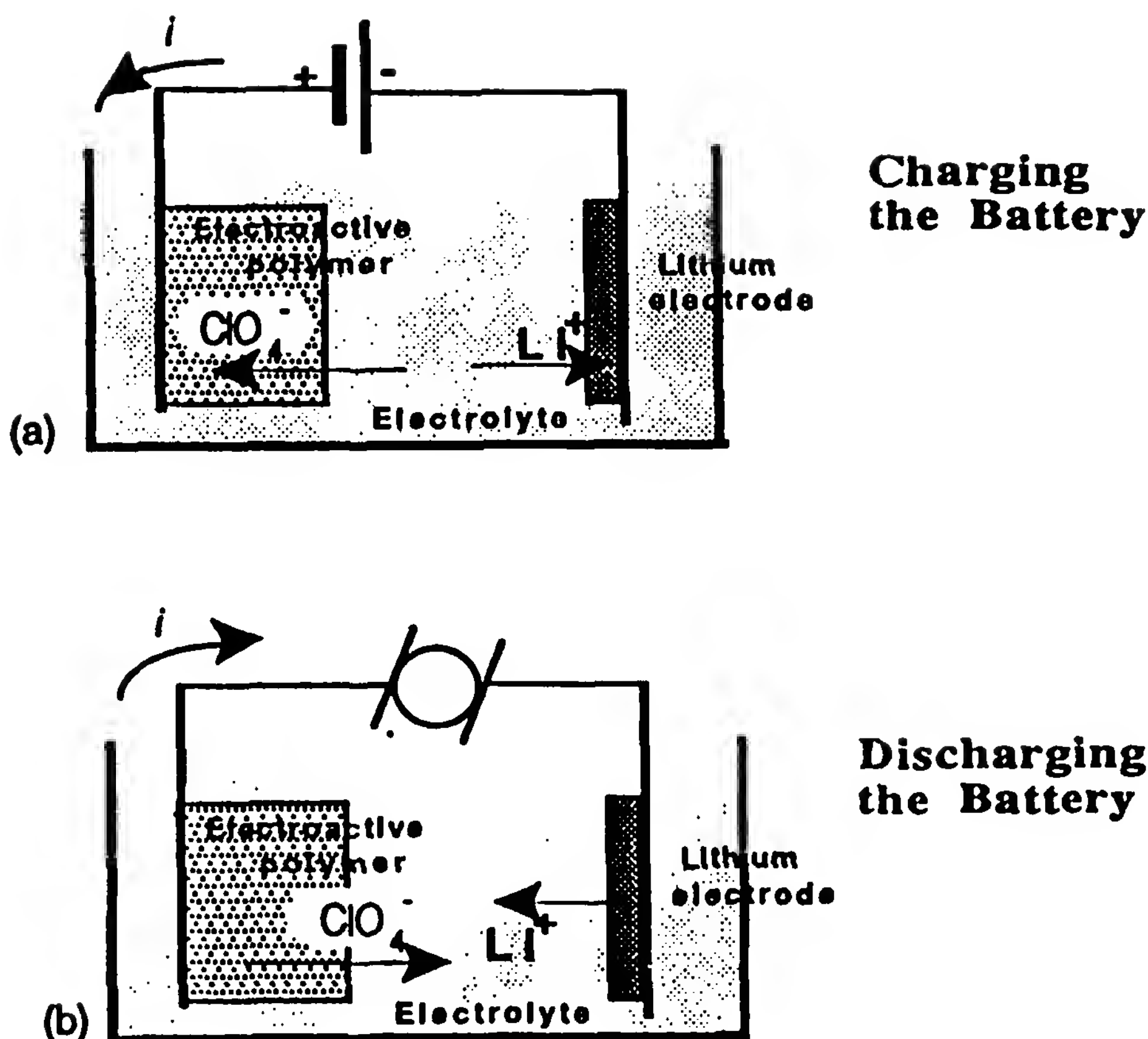


Figure 9 Electroactive Polymer/Lithium battery. (a) During charging of the battery, ClO_4^- anions enter into the polymer matrix, while Li^+ cations move to the lithium cathode where they are reduced to the metallic state: $\text{Li}^+ + e^- \rightarrow \text{Li}$. (b) During the discharge, both ClO_4^- and Li^+ ions move back into the electrolyte.

Work with PPy and PANi has reached the industrial stage. Bridgestone-Seiko has been selling coin-shaped 3-V polyaniline-based batteries for 5 years (1987–1992), and polypyrrole-based batteries were developed by Varta/BASF in the same period. Such batteries have lower energy densities than those of conventional batteries, but they are superior in terms of self-discharge. The main characteristics of a typical PANi battery are compared to those of lead and Cd-Ni batteries in Table 4. The values mentioned for energy density and electric capacity density refer to the active material alone.

2. Electrochromic Devices

The considerable changes in the optical absorption of CPs during the doping–undoping process are at the basis of many proposals for electrochromical devices, such as “smart windows,” whose light transmission can be electrically controlled, and various display devices. Due to the drastic change that appears in their visible spectrum, PTh [122–124] and PANi [125] are

Table 4 Characteristics of Conventional Lead and Ni-Cd Batteries and a Typical Polyaniline Battery

	Ni in Ni-Cd	Lead	Polyaniline
Electric capacity density (Ah/kg)	290	90	100–140
Energy density (Wh/kg)	348	180	300–420
Open-circuit voltage (V)	1.2	2	3
Power density (mW/cm ²)	540	400	10
Current density (mA/cm ²)	400–500	200	3
Usable energy for a time discharge of 1 h (Wh/kg)	310	60	225–315
Self-discharge (%/day)	1	0.3	0.15

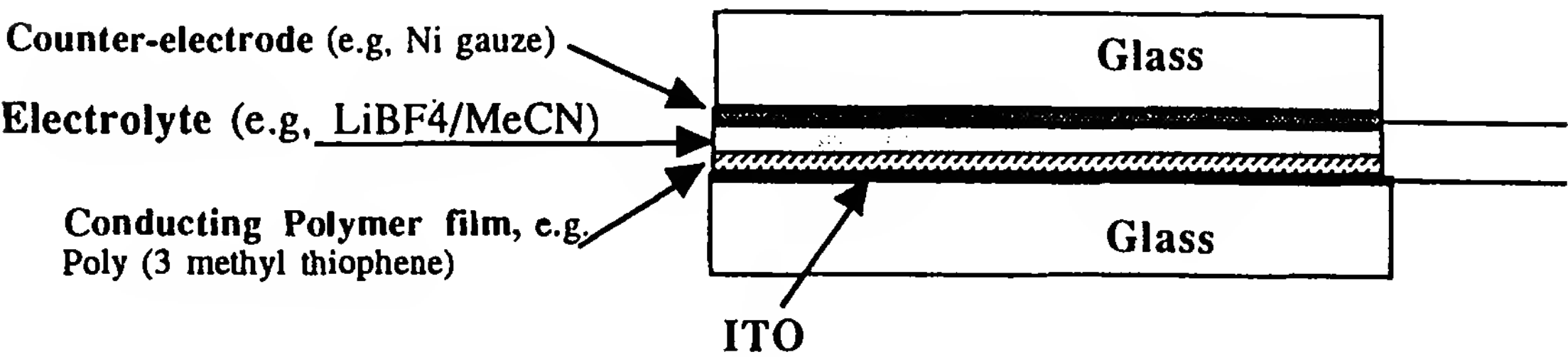


Figure 10 Electrochromic device, or “smart window” using a conducting polymer as the active material.

excellent candidates for optical switch applications. A thin film of polymer (0.1 to 0.5 μm) is deposited (usually by electropolymerization) on a transparent conducting electrode (typically, ITO on glass). It constitutes the anode of a flat electrochemical cell, as sketched in Fig. 10. The time response of such displays is in the range 10 to 300 ms, which is sufficient for some practical applications. In the case of PANi, switching times in the microsecond range are possible. More stringent is the limitation due to cyclability and polymer lifetime. Up to about 10^5 cycles has been achieved in various laboratories, which is one or two orders of magnitude below the necessary lifetime of commercial devices. Let us note, however, that cycle numbers exceeding 10^7 have been obtained on alkyl- and polyether-substituted PThs [126]. To our knowledge, electrochromical devices based on CPs have not yet been commercialized (in 1993).

3. Miscellaneous

Numerous other possible applications based on the change of a given property upon electrochemical doping have been proposed. Control of

conductivity of a CP film by an applied voltage, via doping level, can be used to fabricate electrochemical transistors. Microcircuit technology with PPy and PANi has been developed from 1983 at MIT, with the purpose of manufacturing microelectronic devices, diodes, and transistors [127]. The principle of an electrochemical transistor is shown in Fig. 11.

A CP film is deposited on a split electrode, making a bridge between the two parts. By tuning the potential of the film with respect to a reference electrode, the doping level, and thus the conductivity of the film, is controlled. Hence, the "drain" current can be controlled by the "gate" voltage. The feasibility of such transistors has been demonstrated, but they are still far from competitive with silicon technology, in particular due to the slowness of electrochemical (ionic) processes compared to solid-state electronics.

Dimensional changes in CP during the doping–dedoping process can be used to design microelectromechanical devices, as first proposed by R. Baughman at Allied Signal. As a result of ion insertion, the size change can be as high as $\Delta L/L \sim 10\%$ (compared to $\Delta L/L \sim 0.1\%$ obtained with piezoelectric polymers). Various electrochemically controlled devices have been described, such as microtweezers, microvalves, actuators, and artificial muscles [128,129].

Finally, we mention the use of CPs for controlled drug release, with the purpose of optimizing medicine action. An ionic function must be attached to the drug molecules. In the doped state the medicine molecules are then

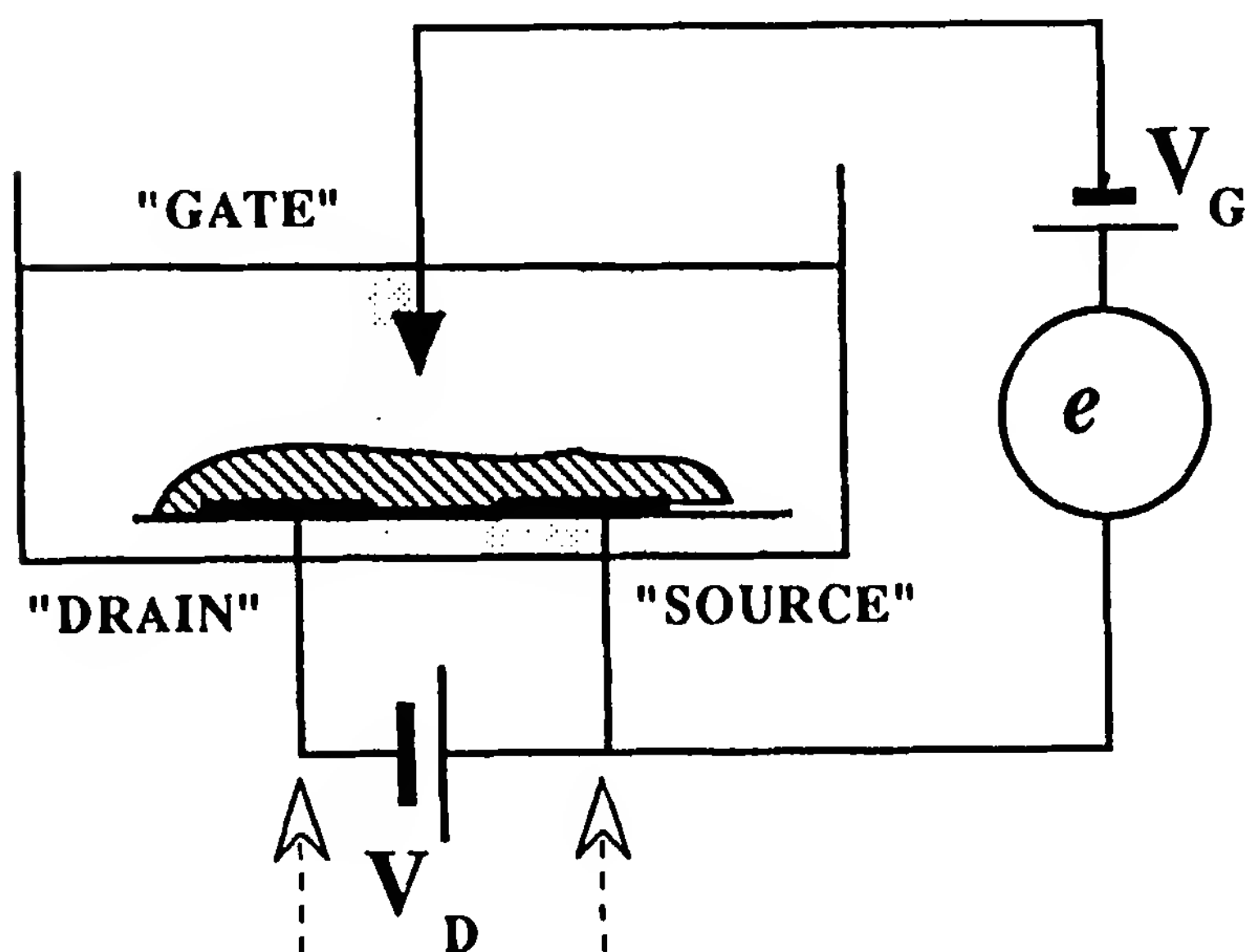


Figure 11 Electrochemical transistor using a conducting polymer.

trapped in the CP matrix. During electrochemically controlled dedoping, they can be slowly released in vivo.

D. Applications in the Semiconducting State

Applications of undoped (semiconducting) CPs fill only one line in Table 2. None has reached the market yet, and as for other classes of CPs, several applications that were advocated in the past have failed to meet the necessary requirements. In the early 1980s, for instance, a significant amount of work was invested in the study of CP photovoltaic cells [130], but the subject is no longer active.

In the next chapter, two more recent potential applications in electronics are discussed at some length: field-effect transistors (FETs) and light-emitting diodes (LEDs). The CP FETs have now reached specifications not far from those of amorphous Si FETs, but industrial development will require more—a decisive advantage of some sort over existing technologies (Chapter 12, Section V.B). Discovery of electroluminescence in CPs, the basic process in LEDs, is only 3 years old, but intense activity has produced impressive progress (Chapter 12, Section V.C). There, performances are still evolving, but novel potential applications are considered, from simple ones such as flat LCD-panel rear illumination sheets, to active matrix flexible flat display panels. Further work is required for serious evaluation of these possibilities.

Applications in electronics are not the only ones that have been considered. CPs have very large third-order nonlinear susceptibilities. This was found first for PDAs [55] and is a general property of these materials. Their nonresonant response is very fast, in the 100-fs range [131,132], due to π electrons. Reviews of this quite active research can be found in [133,134]. In relation to current research on optical signal processing, a few simple devices using a CP as an active material have been investigated: waveguiding in a PDA crystal [135] or spin-cast film [136], a directional coupler, and an all-optical phase modulator [137]. But these are still very far from practical applications.

REFERENCES

1. L. Salem, *The Molecular Orbital Theory of Conjugated Systems*, W. A. Benjamin, New York, 1966.
2. B. S. Hudson, B. E. Kohler, and K. Schulten, in *Excited States*, Vol. 6 (E. C. Lim, ed.), Academic Press, Orlando, Fla., 1982, p. 2.
3. B. E. Kohler, in *Conjugated Polymers* (J. L. Brédas and R. Silbey, eds.), Kluwer, Dordrecht, The Netherlands, 1991, p. 405.

4. C. P. De Melo and R. Silbey, *J. Chem. Phys.* 88:2558 (1988); *Chem. Phys. Lett.* 140:537 (1987).
5. J. L. Fave and M. Schott, *J. Chim. Phys. (Paris)* 89:931 (1992).
6. J. Kürti and H. Kuzmany, *Phys. Rev. B* 44:597 (1991).
7. M. L. Shand, R. R. Chance, M. Le Postollec, and M. Schott, *Phys. Rev. B* 25:4431 (1982).
8. G. Horowitz, X. Peng, D. Fichou, and F. Garnier, *J. Appl. Phys.* 67:528 (1990).
9. K. Waragai, H. Akimichi, T. Inoshita, S. Hotta, and H. Sakaki, *Proceedings of the 51st Annual Technical Conference of Plastics Engineers*, Society of Plastics Engineers, Brookfield, Conn., 1993, p. 2331.
10. R. Hoffmann, C. Janiak, and C. Kollmar, *Macromolecules* 24:3725 (1991).
11. D. Bloor, *Chem. Phys. Lett.* 40:323 (1976).
12. M. Rei Vilar, G. Blatter, P. Pfluger, M. Heyman, and M. Schott, *Europhys. Lett.* 5:375 (1988).
13. A. Rembaum, J. Moacanin and H. A. Pohl, in *Progress in Dielectrics*, Vol. 5 (J. B. Birks and J. Hart, eds.), Heywood, London, 1965, p. 41.
14. M. F. Combarel, G. Belorgey, M. Jozefowicz, L. T. Yu, and R. Buvet, *C. R. Acad. Sci. Ser. C* 262:459 (1966), and references therein.
15. L. T. Yu, M. S. Borredon, M. Jozefowicz, and R. Buvet, *J. Polym. Sci. Symp. C* 16:2931 (1967).
16. M. Doriomedoff, F. Hautière-Cristofini, R. de Surville, M. Jozefowicz, L. T. Yu, and R. Buvet, *J. Chim. Phys. (Paris)* 68:39 (1971).
17. D. J. Berets and D. S. Smith, *Trans. Faraday Soc.* 64:823 (1968).
18. T. Ito, H. Shirakawa, and S. Ikeda, *J. Polym. Sci. Polym. Chem. Ed.* 12:11 (1974).
19. H. Shirakawa, E. J. Louis, A. G. MacDiarmid, C. K. Chiang, and A. J. Heeger, *Chem. Commun.*, 578 (1977).
20. C. K. Chiang, C. R. Fincher, Y. W. Park, A. J. Heeger, H. Shirakawa, E. J. Louis, S. C. Gan, and A. G. MacDiarmid, *Phys. Rev. Lett.* 39:1098 (1977).
21. P. J. Nigrey, A. G. MacDiarmid, and A. J. Heeger, *Chem. Commun.*, 594 (1979).
22. A. G. MacDiarmid and A. J. Heeger, *Synth. Metals* 1:101 (1980).
23. D. M. Ivory, G. G. Miller, J. M. Sowa, L. W. Shacklette, R. R. Chance, and R. H. Baughman, *J. Chem. Phys.* 71:1506 (1979).
24. A. F. Diaz, K. K. Kanazawa, and G. P. Gardini, *Chem. Commun.*, 635 (1979).
25. K. K. Kanazawa, A. F. Diaz, R. H. Geiss, W. D. Gill, J. F. Kwak, J. A. Logan, J. F. Rabolt, and G. B. Street, *Chem. Commun.*, 854 (1979).
26. G. Tourillon and F. Garnier, *J. Electroanal. Chem.* 135:173 (1982).
27. E. M. Geniès, A. Boyle, M. Lapkowski, and C. Tsintavis, *Synth. Metals* 36:139 (1990).
28. J. Heinze, *Topics Current Chem.* 152:1 (1993).
29. H. C. Longuet-Higgins and L. Salem, *Proc. R. Soc. A* 251:172 (1959).
30. J. A. Pople and S. H. Walmsley, *Mol. Phys.* 5:15 (1962).

31. M. J. Rice, *Phys. Lett.* 71:152 (1979).
32. W. P. Su, J. R. Schrieffer, and A. J. Heeger, *Phys. Rev. Lett.* 42:1698 (1979).
33. A. J. Heeger, S. Kivelson, J. R. Schrieffer, and W. P. Su, *Rev. Mod. Phys.* 60:781 (1988).
34. S. Ikehata, J. Kaufer, T. Woerner, A. Pron, M. A. Druy, A. Sivak, A. J. Heeger, and A. G. MacDiarmid, *Phys. Rev. Lett.* 45:1123 (1980).
35. H. W. Gibson, F. C. Bailey, A. J. Epstein, H. Rommelmann, S. Kaplan, J. Harbor, X. Yang, D. B. Tanner, and J. M. Pochan, *J. Am. Chem. Soc.* 105:4417 (1983).
36. M. C. Dos Santos and J. L. Brédas, *Phys. Rev. Lett.* 62:2499 (1989); *Synth. Metals* 29:E321 (1989).
37. H. Kiess, ed., *Conjugated Conducting Polymers*, Springer Series in Solid State Sciences, Vol. 102, Springer-Verlag, Berlin, 1992.
38. A. Andreatta, Y. Cao, J. C. Chiang, A. J. Heeger, and P. Smith, *Synth. Metals* 26:383 (1988).
39. J. H. Edwards and W. J. Feast, *Polymer* 21:595 (1980).
40. R. A. Wessling, *J. Polym. Sci. Polym. Symp.* 72:55 (1985), and references therein.
41. P. Garrin, J. P. Aimé, J. L. Fave, S. Ramakrishnan, and G. L. Baker, *J. Phys. II (France)* 2:529 (1992).
42. T. Masuda and T. Higashimura, *Adv. Polym. Sci.* 81:121 (1986).
43. R. L. Elsenbaumer, K. Y. Jen, and R. Oboodi, *Synth. Metals* 15:164 (1986).
44. G. Gustafsson, O. Inganäs, W. R. Salaneck, J. Laakso, M. Lojonen, T. Taka, J.-E. Österholm, H. Stubb, and T. Hjertberg, in *Conjugated Polymers* (J. L. Brédas and R. Silbey, eds.), Kluwer, Dordrecht, The Netherlands, 1991, p. 315.
45. D. Delabouglise and F. Garnier, *Synth. Metals* 39:117 (1990).
46. S.-H. Jin, S.-J. Choi, W. Ahn, H.-N. Cho, and S.-K. Choi, *Macromolecules* 26:1487 (1993).
47. Y. Ikenoue, J. Chiang, A. D. Patil, F. Wudl, and A. J. Heeger, *J. Am. Chem. Soc.* 110:2983 (1985), and references therein.
48. A. J. Heeger, *Synth. Metals* 55–57:3471 (1993).
49. J. P. Aimé, in *Conjugated Polymers* (J. L. Brédas and R. Silbey, eds.), Kluwer, Dordrecht, The Netherlands, 1991, p. 229.
50. Z. Yang, I. Sokolik, and F. E. Karasz, *Macromolecules* 26:1188 (1993).
51. V. Enkelmann, *Adv. Polym. Sci.* 63:91 (1984).
52. M. Schott and G. Wegner, in *Nonlinear Optical Properties of Organic Molecules and Crystals*, Vol. 2 (D. S. Chemla and J. Zyss, eds.), Academic Press, Orlando, Fla., 1987, p. 1.
53. G. N. Patel, *Polym. Prepr. Am. Chem. Soc. Div. Polym. Chem.* 19:154 (1978).
54. M. Rawiso, J. P. Aimé, J. L. Fave, M. Schott, M. A. Müller, M. Schmidt, H. Baumgartl, and G. Wegner, *J. Phys. (France)* 49:861 (1988), and references therein.

55. C. Sauteret, J. P. Herrmann, R. Frey, F. Pradère, J. Ducuing, R. H. Baughman, and R. R. Chance, *Phys. Rev. Lett.* 36:956 (1976).
56. G. L. Baker and Z. Vardeny, eds., *Proceedings of the Conference on Optical Probes of Conjugated Polymers*, Synth. Metals 49–50 (1992).
57. R. E. Peierls, *Quantum Theory of Solids*, Oxford Univ. Press, Oxford, 1955, p. 108.
58. A. A. Ovchinnikov, I. I. Ukrainskii, and G. V. Kventsel, *Sov. Phys. Usp.* 15:575 (1973).
59. W. P. Su, J. R. Schrieffer, and A. J. Heeger, *Phys. Rev. Lett.* 42:1698 (1979); *Phys. Rev. B* 22:2099 (1980); 28:1138 (1983).
60. M. Takayama, Y. R. Lin-Liu, and K. Maki, *Phys. Rev. B* 21:2388 (1980).
61. D. K. Campbell, A. R. Bishop, and M. J. Rice, in *Handbook of Conducting Polymers*, Vol. 2 (T. A. Skotheim, ed.), Marcel Dekker, New York, 1986, p. 937.
62. S. Kivelson and D. E. Heim, *Phys. Rev. B* 26:4278 (1982).
63. C. Aslangul and D. Saint-James, *J. Phys. (France)* 44:953 (1983).
64. S. A. Brazovskii and N. N. Kirova, *JETP Lett.* 33:4 (1981).
65. C. Kollmar and H. Sixl, *J. Chem. Phys.* 88:1343 (1988).
66. J. A. Pople and S. H. Walmsley, *Mol. Phys.* 5:12 (1962).
67. P. K. Kahol, G. C. Clark, and M. Mehring, in Ref. 29, Chap. 5.
68. D. Emin and T. Holstein, *Phys. Rev. Lett.* 36:323 (1976).
69. J. L. Brédas, R. R. Chance, and R. Silbey, *Phys. Rev. B* 26:5843 (1982).
70. J. L. Brédas, J. C. Scott, K. Yakushi, and G. B. Street, *Phys. Rev. B* 30:1023 (1984).
71. D. Fichou, G. Horowitz, B. Xu, and F. Garnier, *Synth. Metals* 39:243 (1990).
72. P. Brendel, A. Grupp, M. Mehring, R. Schenk, K. Müllen, and W. Huber, *Synth. Metals* 45:49 (1991).
73. J. Chen and A. J. Heeger, *Solid State Commun.*, 58:251 (1986).
74. G. Nicolas and P. Durand, *J. Chem. Phys.* 72:453 (1980).
75. J. L. Brédas, in *Handbook of Conducting Polymers*, Vol. 2 (T. A. Skotheim, ed.), Marcel Dekker, New York, 1986, p. 860.
76. K. Fesser, A. R. Bishop, and D. K. Campbell, *Phys. Rev. B* 27:4804 (1983).
77. A. Feldblum, J. H. Kaufman, S. Etemad, A. J. Heeger, T.-C. Chung, and A. G. MacDiarmid, *Phys. Rev. B* 26:815 (1982).
78. B. R. Weinberger, C. B. Roxlo, S. Etemad, G. L. Baker, and J. Orenstein, *Phys. Rev. Lett.* 53:86 (1984).
79. D. Baeriswyl, D. K. Campbell, and S. Mazumdar, in Ref. 29, p. 7.
80. M. Pope and C. E. Swenberg, *Electronic Processes in Organic Crystals*, Oxford Univ. Press, London, 1982.
81. D. P. Craig and S. H. Walmsley, *Excitons in Molecular Crystals*, W. A. Benjamin, New York, 1968.
82. M. R. Philpott, in *Advances in Chemical Physics*, Vol. 31 (I. Prigogine and S. A. Rice, eds.), Academic Press, Orlando, Fla., 1973, p. 97.
83. H. Bässler, M. Gailberger, R. F. Mahrt, J. M. Oberski, and G. Weiser, *Synth. Metals* 49–50:341 (1992).

84. M. Winter, A. Grupp, M. Mehring, and H. Sixl, *Chem. Phys. Lett.* **133**:482 (1987).
85. L. S. Swanson, J. Shinar, and K. Yoshino, *Phys. Rev. Lett.* **65**:1140 (1990).
86. L. Robbins, J. Orenstein, and R. Superfine, *Phys. Rev. Lett.* **56**:1850 (1986).
87. R. H. Austin, G. L. Baker, S. Etemad, and R. Thompson, *J. Chem. Phys.* **90**:6642 (1989).
88. J. D. Flood and A. J. Heeger, *Phys. Rev. B* **28**:2356 (1983).
89. S. R. Phillpot, B. Horowitz, and A. R. Bishop, *Synth. Metals* **28**:D419 (1989).
90. L. S. Swanson, J. Shinar, A. R. Brown, D. D. C. Bradley, R. H. Friend, P. L. Burn, A. Kraft, and A. B. Holmes, *Phys. Rev. B* **46**:15072 (1992).
91. D. Emin, *Phys. Rev. B* **33**:3973 (1986).
92. Yu. N. Gartstein and A. A. Zakhidov, *Solid State Commun.*, **60**:105 (1986).
93. P. Vogl and D. K. Campbell, *Phys. Rev. B* **41**:12797 (1990).
94. P. Gomes da Costa, R. G. Dandrea, and E. M. Conwell, *Phys. Rev. B* **47**:1800 (1993).
95. J. A. Blackman and M. K. Sabra, *Phys. Rev. B* **47**:15437 (1993).
96. J. L. Brédas, G. B. Street, B. Thémans, and J. M. André, *J. Chem. Phys.* **83**:1323 (1985).
97. G. Rossi, R. R. Chance, and R. Silbey, *J. Chem. Phys.* **90**:7594 (1989).
98. H. Bässler, *Phys. Status Solidi (b)* **107**:9 (1981), **175**:15 (1993).
99. P. R. Surjan and H. Kuzmany, *Phys. Rev. B* **33**:2615 (1986).
100. K. S. Schweitzer, *J. Chem. Phys.* **85**:4181 (1986).
101. S. R. Phillips, D. Baeriswyl, A. R. Bishop, and P. S. Lomdahl, *Phys. Rev. B* **35**:7533 (1987).
102. H. H. S. Javadi, K. R. Cromack, A. G. MacDiarmid, and A. J. Epstein, *Phys. Rev. B* **39**:3579 (1989).
103. A. J. Heeger, in *Conjugated Polymers and Related Materials* (W. R. Salaneck, I. Lundström, and B. Rånby, eds.), Oxford Univ. Press, Oxford, 1993, p. 27.
104. J. Tsukamoto, *Adv. Phys.* **41**:509 (1992).
105. T. Schimmel, D. Gläser, M. Schwoerer, and H. Naarman, in *Conjugated Polymers* (J. L. Brédas and R. Silbey, eds.), Kluwer, Dordrecht, The Netherlands, 1991, p. 49.
106. M. N. Bussac and L. Zuppiroli, *Phys. Rev. B* **47**:5493 (1993).
107. S. Roth, *Synth. Metals* **55**:3623 (1993).
108. J. S. Miller, *Adv. Mater.* **5**:587, 671 (1993).
109. H. H. Kuhn, W. C. Kimbrell, J. E. Fowler, and C. N. Barry, *Synth. Metals* **55**:3707 (1993).
110. L. Olmédó, P. Hourquebie, and F. Jousse, *Adv. Mater.* **5**:373 (1993).
111. M. R. Anderson, B. R. Mattes, B. R. Reiss, and R. B. Kaner, *Science* **252**:1424 (1991).
112. C. R. Martin, W. Liang, V. Menon, R. Parthasarathy, and A. Parthasarathy, *Synth. Metals* **55**:3766 (1993).

113. M. Maxfield, S. L. Mu, and A. G. MacDiarmid, *J. Electrochem. Soc.* **132**:838 (1985).
114. G. C. Farrington, B. Scrosati, D. Fridrych, and J. De Nazzio, *J. Electrochem. Soc.* **7**:1312 (1984).
115. T. Nagatomo, C. Ichikawa, and O. Omoto, *Synth. Metals* **18**:649 (1987).
116. R. Bittihn, G. Ely, F. Woeffler, H. Münstedt, H. Naarmann, and D. Naegele, *Makromol. Chem. Macromol. Symp.* **8**:51 (1987).
117. M. Mermillod, J. Tanguy, and F. Petiot, *J. Electrochem. Soc.* **133**:1073 (1986).
118. K. Kaneto, K. Yoshino, and Y. Inuishi, *Jpn. J. Appl. Phys.* **22**:L467 (1983).
119. L. W. Shacklette, R. L. Elsenbaumer, and R. H. Baughman, *J. Phys. (Paris)* **C3 44**:559 (1983).
120. A. G. MacDiarmid, L. S. Yang, W. Huang, and B. D. Humphrey, *Synth. Metals* **18**:393 (1987).
121. E. M. Genies, M. Lapkowski, C. Santier, and E. Vieil, *Synth. Metals* **18**:631 (1987).
122. K. Yoshino, K. Kaneto, and S. Takeda, *Synth. Metals* **18**:741 (1987).
123. K. Yoshino, K. Kaneto, and Y. Inuishi, *Jpn. J. Appl. Phys.* **22**:L157 (1983).
124. F. Garnier, G. Tourillon, M. Gazard, and J. C. Dubois, *J. Electroanal. Chem.* **148**:299 (1983).
125. T. Kobayachi, H. Yoneyama, and H. Tamura, *J. Electroanal. Chem.* **161**:419 (1984).
126. J. Roncali et al., European Patent 88,202,679.2 Dec. 16, 1988.
127. J. Ricco, and M. S. Wrighton, *J. Phys. Chem.* **89**:1441 (1985).
128. T. F. Otero, J. Rodriguez, E. Angulo, and C. Santamaria, *Synth. Metals* **55**:3713 (1993).
129. Q. Pei and O. Inganäs, *Synth. Metals* **55**:3718 (1993).
130. J. Kanicki, in *Handbook of Conducting Polymers*, Vol. 1 (T. A. Skotheim, ed.), Marcel Dekker, New York, 1986, p. 543.
131. G. M. Carter, *J. Opt. Soc. Am. B* **4**:1018 (1987).
132. T. Hattori and T. Kobayashi, *Chem. Phys. Lett.* **133**:230 (1987).
133. D. S. Chemla and J. Zyss, eds., *Nonlinear Optical Properties of Molecules and Crystals*, Vol. 2, Academic Press, Orlando, Fla., 1987.
134. F. Kajzar and J. Messier, in *Conjugated Polymers* (J. L. Brédas and R. Silbey, eds.), Kluwer, Dordrecht, The Netherlands, 1991, p. 509.
135. M. Thakur, R. Frye, and B. Greene, *Appl. Phys. Lett.* **56**:1187 (1990).
136. W. J. Blau, in *Electronic Properties of Polymers*, Springer Series in Solid-State Science, Vol. 107 (H. Kuzmany, M. Mehring, and S. Roth, eds.), Springer-Verlag, Berlin, 1992, p. 183.
137. M. Thakur and D. M. Krol, *Appl. Phys. Lett.* **56**:1213 (1990).

Undoped (Semiconducting) Conjugated Polymers

Michel Schott

Université Paris VII (Denis Diderot), Paris, France

This chapter is not meant to be a comprehensive review of undoped conjugated polymers. Rather, we consider the structural and electronic (mostly spectroscopic) properties of CPs from the perspective of their potential applications in electronics, which are discussed in the final section.

I. MATERIALS

Physical properties of conjugated and conducting polymers (CPs) could be studied as they have been, only because chemists and electrochemists have developed many new monomer molecules and new polymerization processes. The former resulted in a wide gamut of physical properties, the latter in better controlled materials. Examples are the synthesis of substituted monomers modifying the electronic transition energies of the conjugated part (see Section V.C) and yielding soluble and processible polymers (see Section II); the use of new conditions of catalyst preparation yielding self-standing fibrillar films of polyacetylene (PA); or the development of CP preparation routes by transformation of a nonconjugated “precursor” polymer, which is a new way of processing and of obtaining well-oriented samples.

The molecular structures of the best studied CPs are given in Table 1 of Chapter 11, and there are many others. But the chemistry of CPs is rich, not only in the large number of molecules produced but also for the

many and clever synthetic methods that have been developed. This is outside the scope of this review of CP physical properties. There are several good reviews, both of the chemical synthesis work (see, e.g., Refs. 1 to 3) and of the electrochemistry [4]. Information can be found in several chapters of a handbook published in 1986 [5]. There are, in addition, topical reviews concerned with one material, such as PA [6], polyparaphenylene (PPP) [7], or polyaniline (PAni) [8], in which some chemical or electrochemical information is given.

Almost all the chemical and physical studies have been concerned with homopolymers, in which all monomers (repeat units) are identical. In polymer science in general, the synthesis and study of copolymers, where there are two or more different types of repeat units arranged in various types of order, have been developed enormously. Copolymers may, for instance, be a way of giving to a material simultaneously two properties that would be incompatible, or would not even exist, in a homopolymer, and they also exhibit a rich variety of structures and morphologies at the scale of 100 Å or more. The synthesis and study of copolymers involving CPs are only beginning and will be mentioned briefly (see Section II.E).

A characteristic feature of CPs is the interplay between the structure and the physical properties. The structure is not defined for all samples of a given polymer as it may be for a crystalline material. The macromolecular chains of a given polymer are not all alike; not even considering cross-linking of chains or many possible types of local defects (which are studied by spectroscopic methods), the chains can have different lengths, local conformations, overall geometries, interactions with their neighbors, and so on. Polymer physicists have developed experimental methods for characterization of single chains in solution or in the melt. There are several outstanding books on polymer physics (e.g., Refs. 9 and 10, and a thorough theoretical treatment of polymers in solution in Ref. 11); and polymer solids, particularly their crystallization, are discussed thoroughly, for example, in Ref. 12.

All these methods and concepts apply in principle to CPs. But several CPs, particularly the early ones, are insoluble and infusible, among them the most studied of all, which has been the prototype CP for about 10 years, polyacetylene. This has limited the knowledge we have of CPs, so some generally accepted notions, such as that they are “intrinsically rigid,” could not be proved.

The length of a polymer chain is an important characteristic of a CP. As discussed in Chapter 11, electron conjugation couples several (often many) repeat units along the chain, and there is a “conjugation length” whose intrinsic value may be large. For the properties of the infinite chain (the system generally discussed in theory) to be experimentally accessible,

an obvious necessary (but not sufficient) condition is that the chain length is much larger than the conjugation length. This is not a trivial condition since several methods used in CP polymerization do produce samples with a wide distribution of chain lengths, including small ones [1–4].

The synthesis of soluble CPs [13,14], and the discovery for some CPs of somewhat unusual solvents such as H_2SO_4 or NMP for PANi [8,15], allowed direct measurement of molecular weights, hence of chain lengths, confirming that these materials are true polymers, sometimes very long ($>1\ \mu\text{m}$) and in a few cases a detailed study of the conformation in solution [16]. It was also observed that in some cases the material indeed contains large amounts of oligomers (i.e., short chains).

In fact, in most cases the conjugation is not limited by the chain length, but by disorder along it, and the physical properties are also governed by interchain interactions (see Chapter 11). Determination of the structure of the actual samples studied, and possibly its modification to change (improve) the physical properties, are therefore important and are discussed in Section II. Electronic properties are then considered in Sections III (optical properties) and IV (conductivity in the undoped state). All that information is then used to present a few selected potential applications in Section V.

II. STRUCTURES

A. Introduction

So it is worth beginning a study of the physical properties of conjugated polymers with a discussion of structural problems. Although there are several excellent review discussions of electronic properties (in a broad sense) of CPs, data on structures are more scattered. In conjugated polymers, unsubstituted materials, such as polyacetylene, and substituted ones, such as the polyalkylthiophenes, pose different structural problems, so the two classes will be discussed separately, with more emphasis on the first class of polymers.

The structure of an usual crystal, or of the perfectly regular chain of a “theoretical CP,” is specified completely by a small number of parameters, whatever the size of the system. Defects in these perfect structures, such as a dislocation or a soliton, are well defined in the same way. Except for PDAs, which are not considered in this section, this is not true of a real CP sample. It is usually disordered at all scales in a variable way, up to macroscopic dimensions; for instance, the morphologies of the two surfaces of a fibrillar PA film are different (see, e.g., Fig. 5 in Ref. 17), or that of an electrochemically synthesized CP film varies continuously along its thick-

ness [18]. Depending on the physical or technical property of interest, disorder at some particular scale, or at all scales (as for dc conductivity), may be important.

This makes CPs quite different from organic conducting crystals, so we devote some space to a discussion of structural problems in CPs; moreover, evaluation of the relevance to real CPs of theoretical results requires consideration of the structure of the material, a question that is often not given the interest it deserves. We discuss general properties or problems, using particular materials as examples, but not entering into detail in complicated cases even if the material may become technically important, such as PANi. We consider microscopic order and disorder. Polyacetylene and several electrochemically prepared CPs have inhomogeneous large-scale morphologies, often fibrillar. Scanning electron microscopic (SEM) and scanning transmission microscopic (STM) images abound but are not discussed here, since we would soon be presenting mainly a description.

Like many semicrystalline polymers, a CP material is almost always “partly crystalline”; that is, it contains regions that can be classified as crystalline or at least well ordered on the basis of their diffraction pattern, and others that are amorphous (for a thorough treatment of polymer crystallization in general, see Ref. 12; CPs are too recent to be discussed to any extent in that book). All cases are found, from an almost completely ordered material such as well-ordered stretched PA [19] to an essentially amorphous material such as polypyrrole [20]. The same material, depending on the synthesis method, can be either crystalline or amorphous; for instance, electrochemical polythiophene is amorphous [21], whereas the chemically prepared polymer is partly crystalline [22,23]. Similar differences are found in polyaniline [24], and PA prepared via the Durham precursor route can show very variable crystallinity, depending on the stretching of the precursor during processing [25].

The term *crystalline* itself may be somewhat misleading when applied to CPs. Well-defined Bragg peaks can be obtained under less stringent conditions of order: for instance, in the paracrystalline state [26] (see also Ref. 12, Vol. 1, p. 438), and this applied to all CPs, with the exception of PDAs, which form crystals in the usual sense of the word.

B. Experimental Methods

Diffraction methods and work in the reciprocal space are prominent in atomic position determinations, but in poorly ordered materials such as CPs the amount of information that can be obtained from a typical x-ray or neutron or electron diffraction pattern (some typical examples of “good” x-ray diffraction patterns are shown on Fig. 1) is not enough for all pertinent

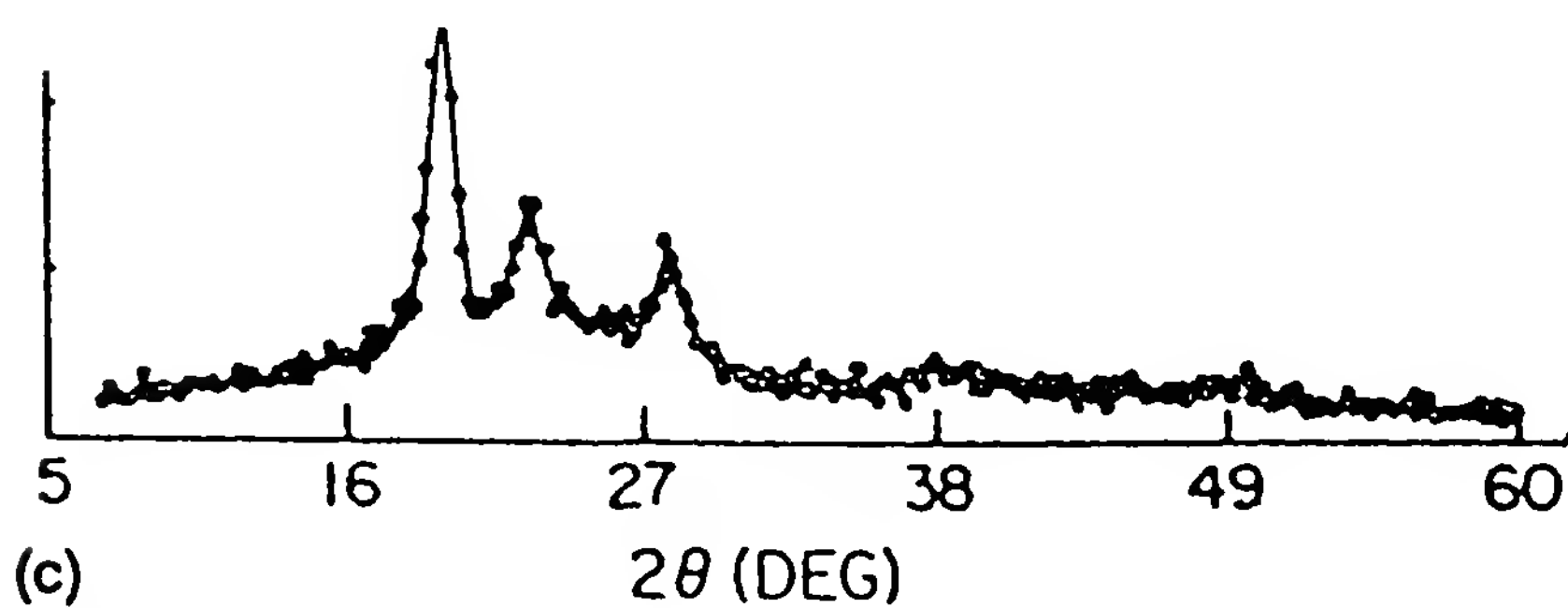
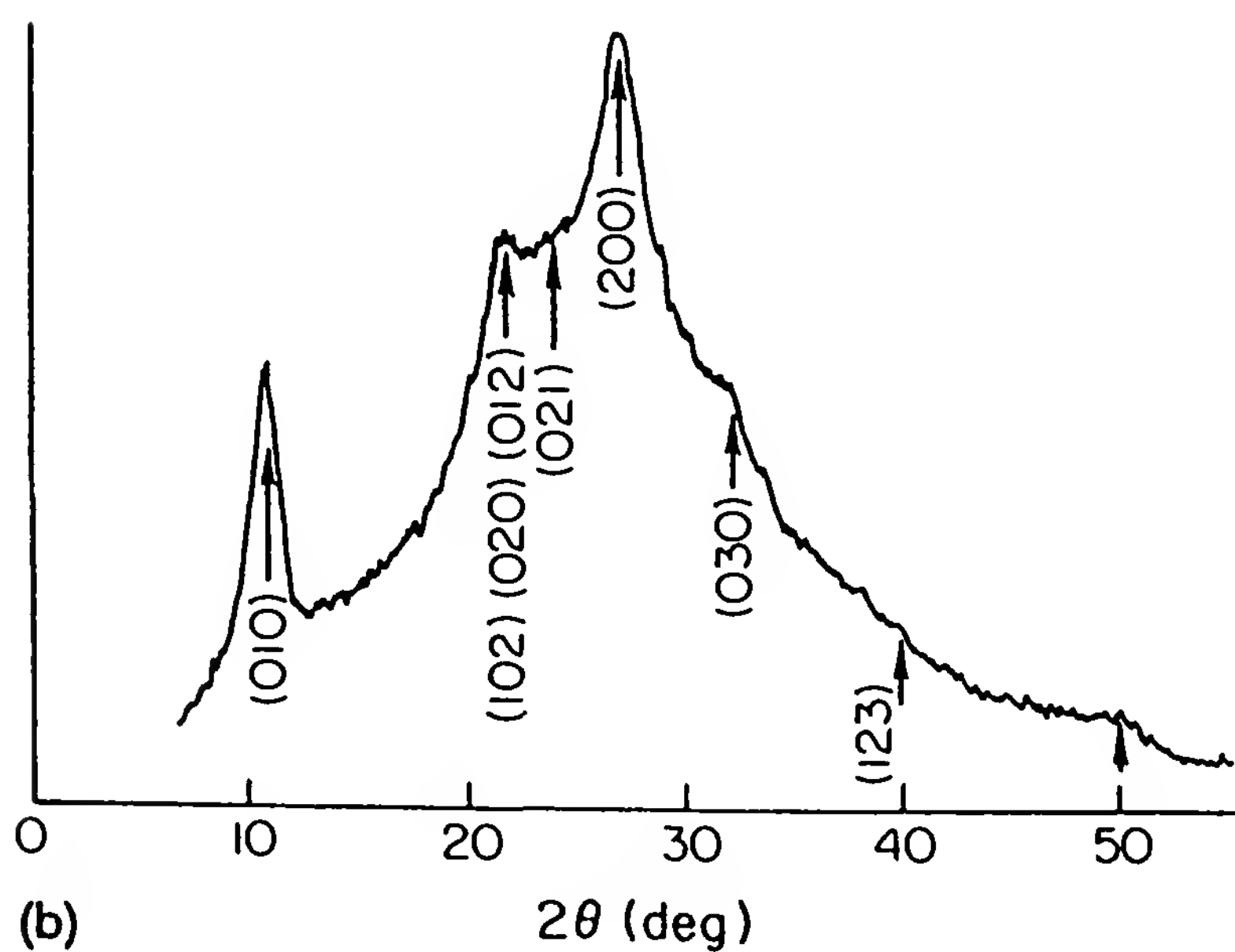
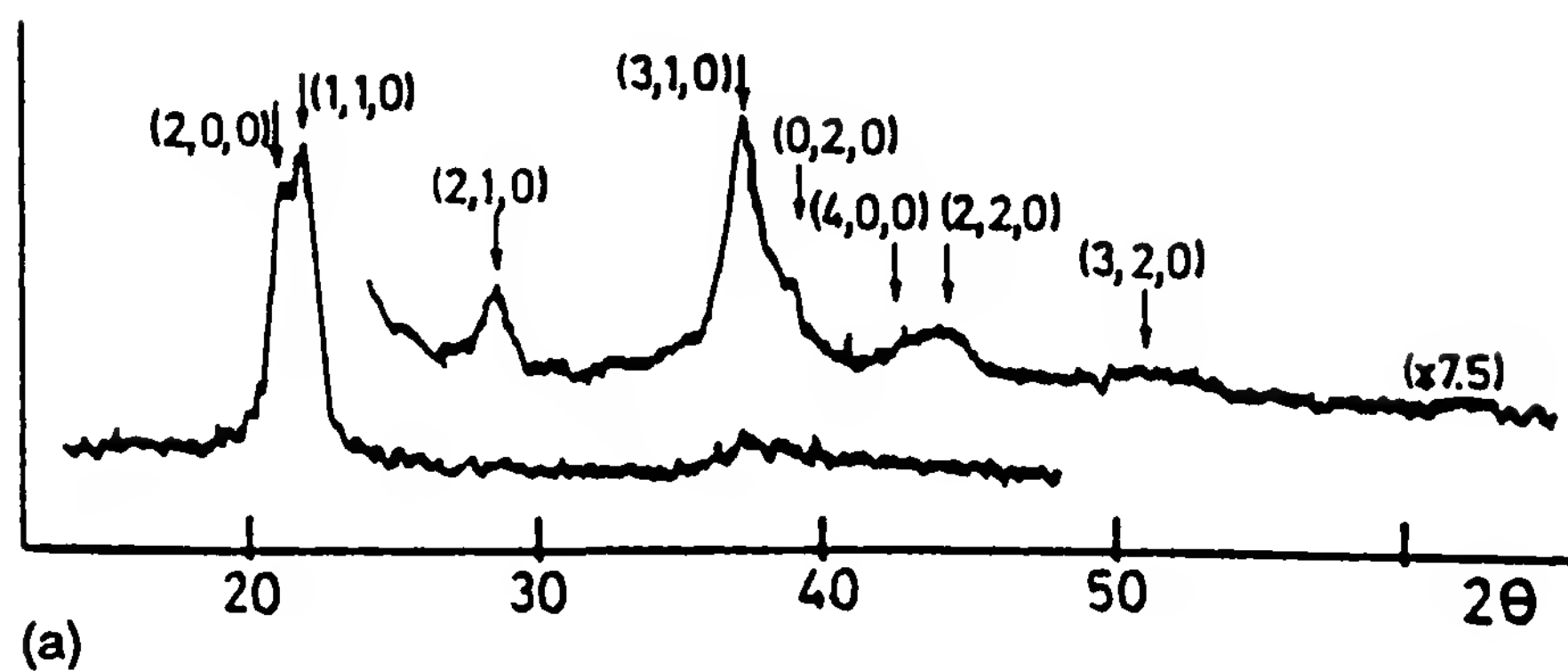


Figure 1 Typical diffraction patterns from undoped CPs: (a) *trans*-polyacetylene, Shirakawa-type, from Ref. 34; (b) polyaniline, emeraldine salt form II, from Ref. 24; (c) polythiophene, from Ref. 22.

parameters to be determined. This is discussed in more detail in Section II.C. Therefore, information provided by other methods is sometimes used in conjunction with diffraction data. CPs are often partly or completely amorphous. Usual diffraction methods do not yield much information on the local order in these regions, which one would like to know and to compare to the structure of the crystalline parts of the same material. A technique that yields such information has been introduced in the field of CPs and applied to PANi (see Section II.C.4.c) [27,28].

X-ray scattering can also yield information about structural features on a larger than atomic scale: the size of ordered regions, the mass ratio of ordered versus amorphous regions, or the overall texture of a sample in cases where it is macroscopically anisotropic, as for fibers or stretched films. Real space methods, such as scanning electron microscopy or “local microscopies” (i.e., STM and AFM), are major sources of information about morphology at mesoscopic scales, mainly of surface regions. Other techniques, either quite new (real space methods) or quite specific to CPs (spectroscopic methods), are currently used. On the angstrom scale, NMR has been used to measure a CC bond length accurately without a complete structure determination [29]; this was important with regard to determination of the dimerization amplitude in *trans*-PA. On the scale 10 to 100 Å, resonance Raman spectroscopy (RRS) is very generally used to infer conjugation lengths (see Chapter 11, Section II.C), taken as a measure of the spatial extent of order along the conjugated chain in many CPs [30]. Images in real space have been obtained by AFM, usually at scales of 100 Å to 100 μm [18], or to a lesser extent by STM [31], in some cases at the 10-Å scale. Information from some of these methods is used in the following discussion.

C. Local Organization of Crystalline Regions

This problem is relevant to most of the theoretical work, which assumes perfectly regular and ordered chains. For instance, the observed value of the dimerization parameter (see Chapter 11, Section IV.A) yields information on the relative importance of electron–electron versus electron–phonon interactions. More generally, experimental bond lengths and angles can be used to validate geometry calculations using MNDO, for instance. This structural information is, of course, essential to the calculation of three-dimensional band structures, yielding the interchain couplings, with their consequences on the stability of polarons, and so on, noted in Chapter 11, Section IV.D, and necessary for realistic inclusion of the effects of disorder (Chapter 11, section IV.E).

A significant difference between CPs and organic CT crystals should be pointed out. Whereas in the latter, order within a molecular stack depends on intermolecular interactions, in CPs there is a one-dimensional covalent bonding throughout a macromolecule. The corresponding structural constraints are therefore stronger—such as a smaller thermal expansion coefficient. On the other hand, bending of a polymer chain may be easier than bending a stack of planar molecules. In fact, although it is often said that conjugated polymers are “intrinsically rigid,” actual measurements show that isolated CP chains in solution that have been studied are rather flexible [16].

1. Pertinent Information

Several types of information are sought here.

a. Bragg peak positions and their presence or absence yield *lattice parameters* and the *space group*, from which, for instance, the geometrical relations between the chains in a unit cell (e.g., their relative orientation) can be obtained.

b. Determination of *atomic positions* requires knowledge of x-ray diffraction intensities for a large enough number of reflections. A well-known criterion, due to Hamilton [32], is that the number of independent data (i.e., intensities) should be about 10 times the number of independent parameters in the structure; there are typically seven such parameters per atom, three defining the position, and four the anisotropic and isotropic thermal factors. The diffraction spectra of Fig. 1 illustrate that this condition is never met with CPs. Therefore, the determination of chain geometry by diffraction methods uses simplifying assumptions and informed guessing. So some conclusions should be taken with a grain of salt, but on the whole the amount of information thus obtained is quite remarkable. One should not assume bond lengths taken from chemically similar smaller molecules, since precisely these lengths carry information about the effect of conjugation and the properties of the electronic ground state. However, for lack of better information, this assumption is often made (see Section II.C.3). Implicitly, the intermonomer coupling within a chain is therefore taken to be only a perturbation of the monomer electronic structure.

c. Not only are the Bragg peaks few in number, but they are also broad and their height quickly decreases at a large scattering angle. These features are associated with *disorder*. For simplicity, we discuss the case of a one-dimensional system of parameter d . Equations for the three-dimensional case are more complicated, but no new physics is introduced. One source of peak width is the finite size of a diffracting crystalline region, within which perfect periodicity is assumed (except for small thermal fluctuations around the lattice points). In that case, if the diffracting intensity is plotted

as a function of scattering angle θ , the width Δ_c of a peak is related to the size L of the crystallite by the Scherrer formula, written here for the one-dimensional case [33]:

$$\Delta_c(2\theta) \approx \frac{\lambda}{L \cos \theta} \quad (1)$$

In the θ range in which Bragg peaks typically appear for CPs, experimental values of $\Delta_c(2\theta)$ increase with θ much more rapidly than predicted by Eq. (1). The observed broadening must have, at least in part, another origin. It is found in the cumulative effect of small static disorder—in the fact that chain distances and orientations (i.e., setting angles φ) are not strictly constant and that chains can be displaced statically along their axis by random amounts (translational disorder). This state of matter, named paracrystalline, and diffraction by it, have been studied in depth by Hosemann [26]. In the case of CPs, and although even in one dimension d and φ both fluctuate, this disorder has always been characterized up to now by a single parameter δ (or σ) in which mean-square variations of both d and φ are lumped together, and the corresponding broadening is then written as

$$\Delta_p(2\theta) \approx \frac{\pi^2 \delta^2}{d} \left(\frac{2 \sin \theta}{\lambda} \right)^2 = \frac{\pi^2 \delta^2 s^2}{d} \quad (2)$$

where s is the scattering vector. Therefore, values of δ deduced from experiment are only indicative; no detailed description of paracrystalline disorder in CPs is available. In fact, crystalline regions are certainly both of limited size and imperfect order. Assuming further that the two contributions to disorder are additive, plots of the $[\Delta(2\theta)]^2$ experimental values corrected for the instrument linewidth as a function of the fourth power of the scattering vector s^4 yields both L and δ , as shown on Fig. 2 for three types of *trans*-PA.

2. *Trans*-Polyacetylene

Trans-PA will now be used to illustrate the kind of data that are actually obtained for a real CP, using the approaches described above. It is chosen as an example for several reasons. A large amount of work has been performed on this material, both experimental and theoretical, and in both the undoped state (considered in this chapter) and the conducting state. It has by far the largest conductivity in the doped state, up to $\sigma \sim 10^5$ S/cm at room temperature [36]. So it has been used as a prototype CP. It is the most “crystalline” CP (except, of course, the PDAs); as much as 90% of the total mass may be in the crystalline regions [4], so interference by the amorphous CPs may be minimal. Its repeat unit is the simplest of all CPs. Figures 1 and 2 show data for *trans*-PA. Although it has been helpful in

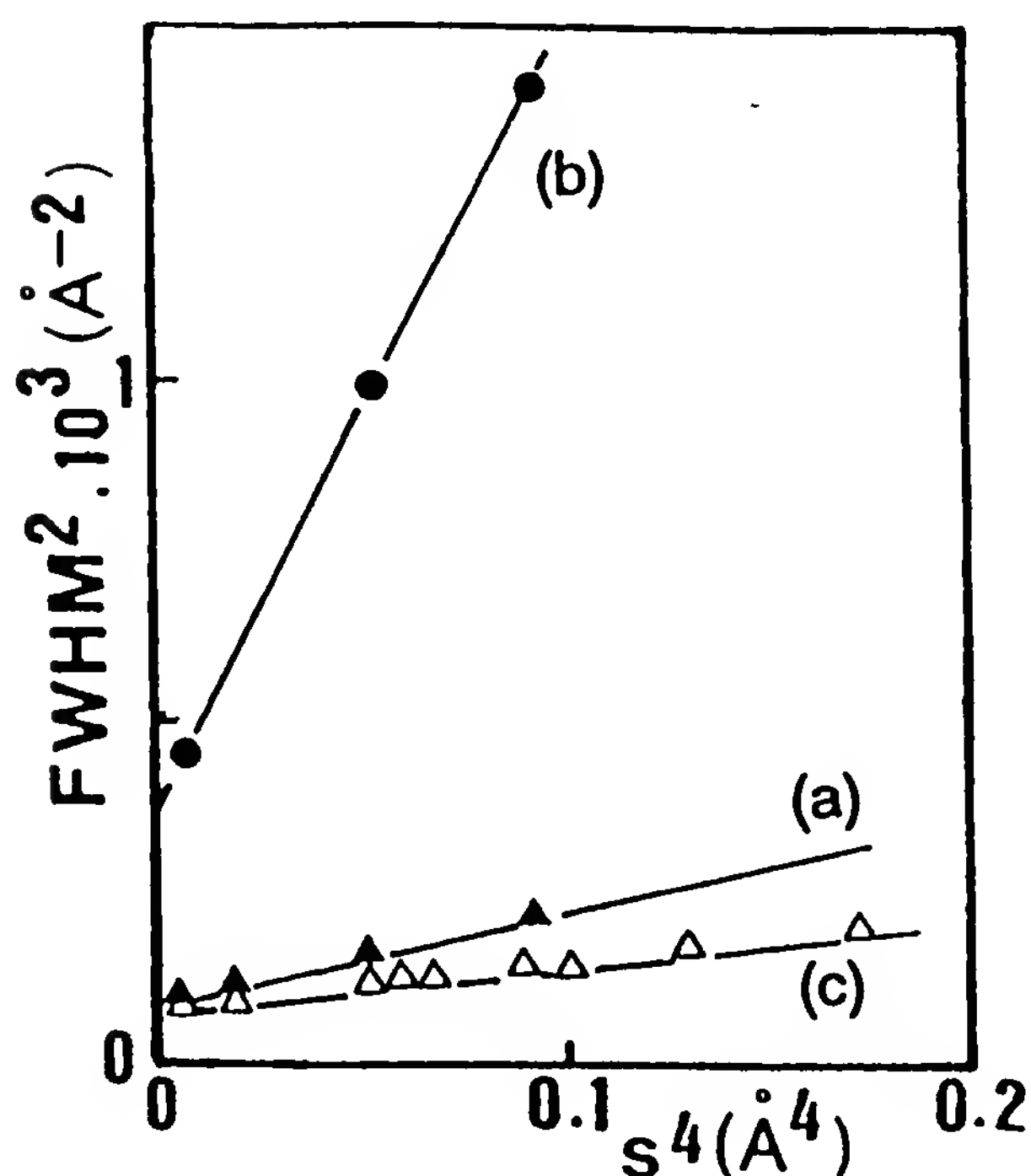


Figure 2 Linewidth variations with scattering angle in several forms of *trans*-PA. The square of the fwhm of the observed (*hk*0) lines is plotted versus the fourth power of the scattering vector [see Eq. (2) in the text]: (a) Shirakawa type, from Ref. 34; (b) Durham type, from Ref. 35; (c) Akagi type, from Ref. 19. (From Ref. 19.)

unraveling the structure of *trans*-PA, the structure of *cis*-PA and its isomerization into the trans isomer will not be discussed here; for these problems, see [25,37].

Trans-PA has been prepared by several methods: Ziegler–Natta catalytic polymerization of acetylene, ring-opening metathesis, or modification of a soluble precursor polymer, the so-called Durham route [1–3]. Various morphologies are thus obtained, fibrils or dense films, and preferential orientation can be induced by stretching. This orientation is useful in structural studies since it makes it possible to assign separately reflections related to order along the average chain direction or perpendicular to it.

As already shown in Fig. 1, the amount of information contained in a diffraction pattern of *trans*-PA is limited. In this discussion, the three points a to c in Section II.C.1 will be taken up in the same order.

a. Fiber diffraction patterns of stretch-oriented samples have been used to determine the unit cell parameters of *trans*-PA. Based on many x-ray and electron diffraction studies, it is now generally agreed that the structure is monoclinic with approximately $a \approx 4.24 \text{ \AA}$, $b \approx 7.3 \text{ \AA}$, $c \approx 2.46 \text{ \AA}$, and $\beta \approx 92 \pm 1$ degrees, with c the chain axis direction. This is close to

orthorhombic; in addition, $b^2/a^2 \sim 3$, so the structure is also close to a hexagonal packing of disks in the (a,b) plane, each having six nearest neighbors. Upon cooling, b/a increases, so the structure distorts further away from hexagonal [38]. Generally, different studies yield slightly different parameters. It is not known whether this dispersion is due to experimental difficulties or reflects real differences from sample to sample, depending on details of preparation or processing. This is possible, since *trans*-PA is never really obtained in its equilibrium state.

Most diffraction spectra are compatible with either a $P2_{1/b}$ or a $P2_{1/n}$ space group. These groups correspond to the same two-dimensional group pgg (full name p2gg) upon projection along the chain direction (see Fig. 3). The difference is not trivial, since the two three-dimensional groups correspond to the two chain periodicity relations sketched in Fig. 8 of Chapter 11 (Fig. 4), hence to different interchain interactions, so this point has been actively debated. Systematic extinctions differ in the two groups, odd (00l) reflections being allowed in $P2_{1/b}$ but not in $P2_{1/n}$, so observation of the (001) line would in principle settle the matter. This line has indeed been observed [39], but in some spectra only [40], so at least in some cases bond alternations are “in phase,” contrary to several calculations (see, e.g., Refs. 41 and 42). It could also be that there is no order in the relative positions of alternation in neighboring chains, either because of static disorder or because of soliton motion (see Chapter 11, Section IV.C.1), which would flip the bond alternation, hence average it out on the time scale of a diffraction experiment. This would then yield a higher symmetry group, such as Pnam, as was assumed, for instance, in Ref. 43. However, this assumption does not seem to have been borne out by further experiments.

b. Since the exact atomic positions cannot be determined using standard crystallographic methods, the organization of the atoms in the unit cell is conventionally described using the dimerization amplitude: for instance, the difference in length δl of the two C—C bonds (see Chapter 11, Section IV.B) and the setting angle φ , that is, the angle between the (010) plane and the plane containing a chain. This assumes planar chains. In such a case the setting angle φ is important, since it determines the number of interchain interactions between two nonparallel π -electron systems; if $\varphi = 45^\circ$, these systems are nearly perpendicular.

For instance, from a thorough analysis of their diffraction data, Fincher et al. [44] deduce that $\varphi \approx 55^\circ$ and $\delta l \sim 0.07 \text{ \AA}$, with limited precision. The NMR determination of $\delta l \approx 0.08 \text{ \AA}$ [29], which can be considered more accurate, is not in disagreement with their value. Early crystal packing calculations [45] also led to $\varphi \approx 50$ to 60° . These values of φ and δl are generally accepted today. The value of δl is of some theoretical importance (see Chapter 11, Sections IV.A and IV.B). Numerical predictions from

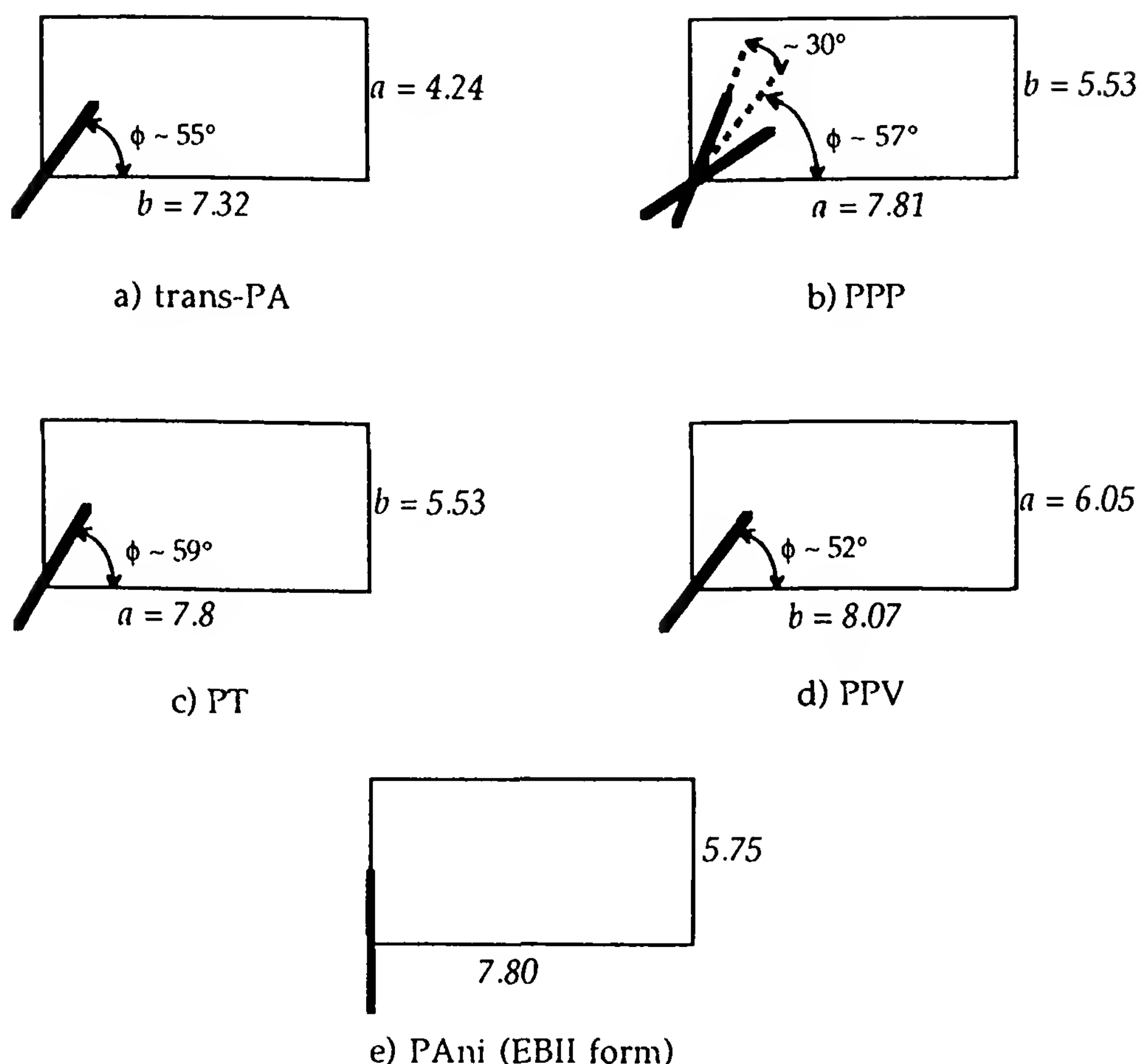


Figure 3 Two-dimensional projected unit cells of several unsubstituted CPs. Units cells are drawn so as to emphasize the similarities. Axes are labeled according to the rules for three-dimensional space group $P2_{1/c}$ where appropriate. Cell parameters in angstroms. (a) *Trans*-PA, average of several results (see the text); (b) PPP from Ref. 49, assuming similarity with oligophenylene unit cells; (c) PT from Refs. 22 and 23, no determination of c -axis orientation; (d) PPV from Ref. 47 but with a and b directions interchanged; (e) PANi from Ref. 24, orthorhombic structure. Thick bars indicate the average chain orientations, or for PPP the two orientations of the phenyl rings (for PPP the dashed line is drawn midway to the thick bars). ϕ is the setting angle. In all cases there is another chain at the cell center, its orientation deduced from the one shown by the appropriate symmetry operation.

the SSH theory require $\delta l \approx 0.08 \text{ \AA}$ to agree with experiment, but a theoretical calculation including electron correlations leads to a similar value, $\delta l \approx 0.084 \text{ \AA}$ [46].

c. Although, for instance, the maximum conductivities achieved upon complete p -doping may differ by two orders of magnitude [36], all variants of Shirakawa-type (fibrillar) *trans*-PA give similar values of the parameters

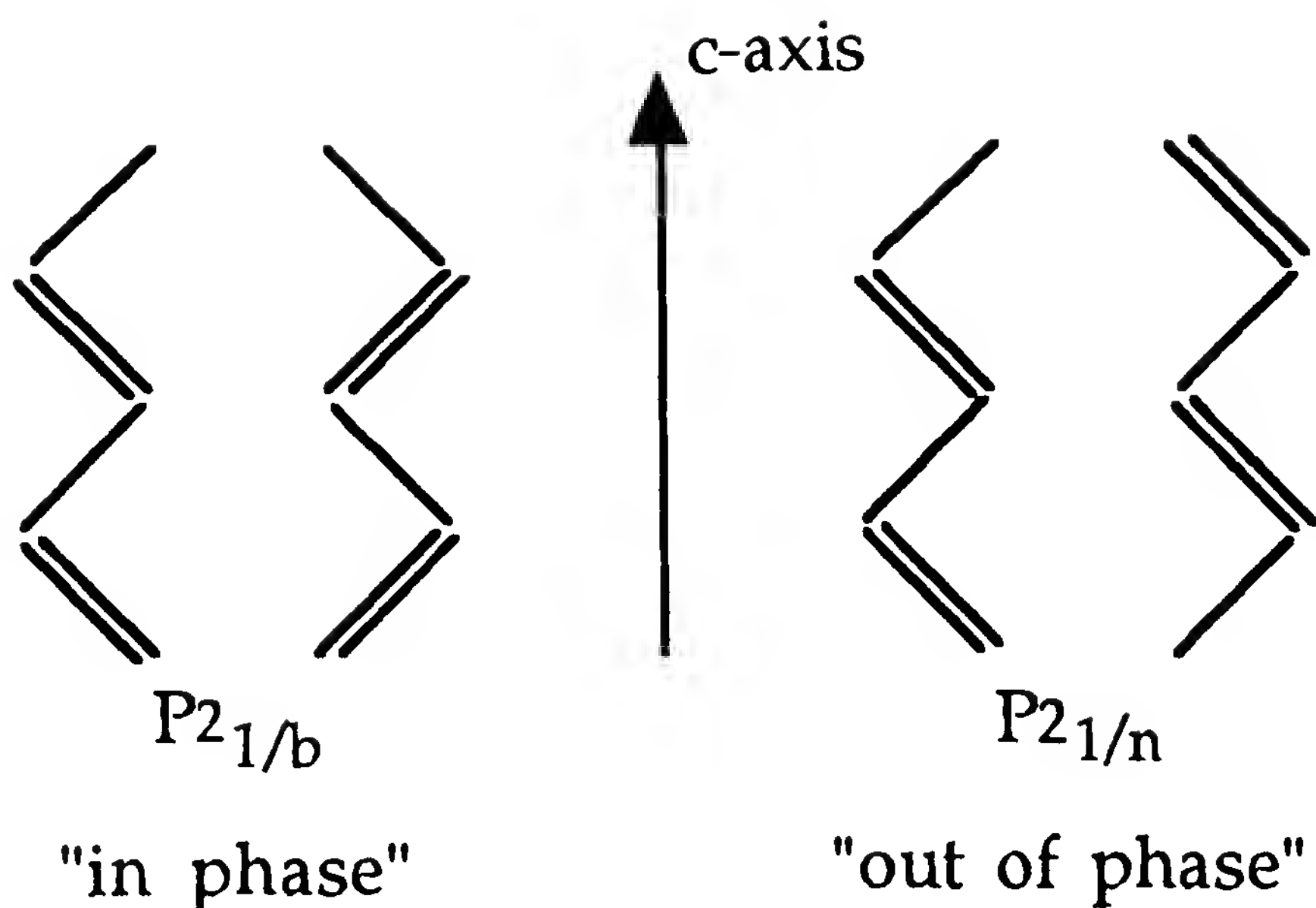


Figure 4 Relative positions along c axis of the alternating double and single bonds of the two chains in the cell, for the two possible three-dimensional space groups.

describing the degree of local order. The average crystallite size along the chain direction is $L_p \approx 100$ to 150 \AA , and in the perpendicular plane $L_{\perp} \approx 50$ to 80 \AA . The former value corresponds to 40 to 50 double bonds, many fewer than the average number of repeat units in the chains as far as is known, so that a given chain is part of several crystallites. And the latter value corresponds to a little more than 10 unit cells; in other words, a crystallite contains 100 to 150 chains. Correlatively, δ is 3 to 4% of the unit cell parameter. It is then likely that the "crystallite" has no sharp boundary. Nonfibrillar, dense *trans*-PA prepared from a stretched "Durham" precursor polymer is slightly less ordered, with $L_p \leq 70 \text{ \AA}$, $L_{\perp} \approx 50 \text{ \AA}$, and $\delta \approx 5\%$ [35]; the unstretched material is highly disordered. By comparison, in polyethylene $L_p \approx 300 \text{ \AA}$.

Paracrystalline disorder will cause electron localization, but there is no reason for the corresponding characteristic length to be equal to L . It will therefore be interesting to compare L_p in particular to the average conjugation lengths inferred from resonance Raman scattering studies (see Section III).

3. Other Nonsubstituted CPs

The structure described above for PA is in fact typical of most nonsubstituted undoped CPs studied to date. Among the more extensively studied CPs, polyparaphenylene (PPP), polythiophene (PTh), and polyphenyl-

enevinylene (PPV) structures resemble that of *trans*-PA and are discussed first. Polyaniline (PAni), which has several potential applications, is quite different and is considered briefly next. All these materials are nondegenerate ground-state materials, contrary to *trans*-PA.

In these polymers, data are often of poorer quality than is PA, so, for instance, analysis in terms of paracrystallinity has rarely been performed. Disorder in the translational position of the chains along their axis may exist, especially in PPV [47]. The unit cell invariably contains more independent atoms than in PA, so that a larger number of simplifying assumptions are required; it is difficult, for instance, to determine experimentally from diffraction data the geometry of the conjugated cycle that these chains contain.

The amorphous fraction in these polymers is often larger than in PA. However, the ordered regions appear quite similar. The unit cell itself is usually not completely determined: in PTh [23] or PPP [48,49]; for instance, only the two-dimensional projection along the chain direction has actually been measured. Figure 3 shows the two-dimensional unit cells, all of space group pgg, containing two chains with very similar relative orientations in all materials. Except for PAni, these are, or are likely to be, two-dimensional projections of monoclinic structures $P2_{1/a}$ or similar. Conventionally, the binary axis in these structures is the *b* axis, so the axis labeling has been adapted to conform to that rule whenever necessary [47]. Note that the *b/a* ratio may be larger or smaller than 1, so the chain axis (the *c* axis) is not tilted off the perpendicular to the (*a,b*) plane in the same way in all materials. Except for PPV, in which the monoclinic angle $\beta \approx 123^\circ$, it is likely to be near 90° in the other cases. Note also that all structures except *trans*-PA are far from hexagonal: $b^2/a^2 \leq 2$ instead of ≈ 3 . It is much less obvious than in PA that each of these chains lies in a plane; in the case of PPP it is almost certainly not so. The angle between successive cycles in phenylene oligomers is known to be about 30° , not zero [50], due to steric hindrance between the H atoms belonging to neighboring cycles, a phenomenon present in PPP as well. Indeed, the experimental second moment in H-NMR spectra is only about half the value calculated for a planar chain, and agrees reasonably well with that calculated assuming that successive benzene rings are tilted by 30° [51]. Steric hindrances are less in PTh and PPV, so that all-*trans* planar chains have been assumed, based on unit cell dimensions. If this is indeed so, these structures can be seen as packings of thick ribbons, not cylinders; since φ clearly deviates from 45° , there is some π - π interchain interaction (i.e., a sizable interchain overlap and perpendicular electron bandwidth).

It is also noteworthy that coherence lengths in these materials are comparable to those in *trans*-PA (see Table 1). It is difficult to compare these

Table 1 Coherence Lengths and Crystalline Fractions Inferred from Diffraction Results^a

	L_{\parallel}	L_{\perp}	Crystal fraction
<i>trans</i> -PA	100–150	50–80	70–90
PPP		60–150	70–80
PTh		100–150	30–55
PPV	50–90 ^b	40–60 ^c	0 to large
PAni (EBII form)	150	50–100	~50

^aCoherence lengths in angstroms. Crystalline fractions in percents of total mass.

^bLarge translational disorder.

^cValue of 250 Å quoted in D. D. C. Bradley, J. Phys. D 20:1387 (1987).

lengths to the conjugation lengths obtained from resonance Raman spectra as done in *trans*-PA, since the variation of Raman frequencies with conjugation is usually much smaller in the other CPs.

Polyaniline differs from other CPs in that the doping process may be associated with protonation of the N atoms in the chain (i.e., to a base ↔ salt equilibrium in the presence of acid, in addition to the usual redox reactions). This is discussed further in Chapter 13. The related processes are therefore more complex. On the other hand, the low cost and processibility of PAni makes it a prime candidate for several applications.

In the undoped state, PAni is a base. Three molecular structures are possible, one of them being the so-called emeraldine base (EB) shown in Fig. 1 of Chapter 11 [52]. There are several differences between it and the other CP chains discussed above: Due to the presence of the N atoms, the chain has a zigzag shape and the benzene rings have either a benzene-like or a quinone-like bond pattern (see Chapter 11, Section IV.B.1) and may be twisted. In principle, the number of independent structural parameters is even larger than for the other CPs. However, quite a good (albeit partial) understanding of the structure has been achieved, as shown in Ref. 24, for instance.

EB is obtained as a totally amorphous solid (EB I) or a partially crystalline one (EB II), depending on the preparation or processing conditions [24]; the crystallinity of EB II is about 50%. But stretching a film containing a plasticizer can increase its crystallinity (see Section II.D.2) [59]. The coherence lengths and dimensions of the two-dimensional projection of the structure are very similar to those of the other CPs (see Table 1), but

the packing of the chains within the unit cell is quite different (see Fig. 3). The average chain planes, defined by the N atoms and their C neighbors, are parallel to the (a,c) plane, with the rings alternately twisted by $\approx \pm 30^\circ$ from that plane, and the three-dimensional structure is orthorhombic [24]. Thus it is similar to that of other polymers of the type $-\text{Z}-\text{X}-_n$, with X being O or S and Z a conjugated cycle.

4. Structural Consequences of Doping

Doping of CPs to increase their conductivity is in fact an intercalation of anions or cations together with injection of an equal number of positive or negative mobile charges onto the polymer chains. These ions are too big to accommodate into the undoped polymer structure, which is quite closely packed, as shown in Figs. 5a and 6d. Structural changes are therefore produced.

While in lamellar structures such as graphite, intercalation always occurs as insertion of planes of ions or molecules sandwiched between host material planes which are left structurally largely unchanged, in CPs where the covalent bonds form a one-dimensional structure, there are three possible cases: intercalants can form chains parallel to the polymer chain direction, or planes separating planes of parallel polymer chains, a third possibility being that a plane is of mixed composition, consisting of alternating polymer chains and dopant linear stacks. In all cases, structural changes can include rotations or translations of the CP chains, motions that do not occur in two-dimensional systems. The two cases are indeed observed, an important factor being the size of the intercalated ion.

An important aspect of the intercalation in lamellar systems is the existence of stages: periodic arrangements in which neighboring intercalated planes are separated by a given constant number of host planes, from 1 up to about 10 in some cases. Stages can exist in CP doping as well. During doping, the average amount of dopant in a sample increases progressively from zero to a maximum of one dopant for about two to three polymer repeat units, depending on the polymer and the dopant. Whereas the fully doped materials may well contain a single crystalline phase, at least for highly crystalline CPs, this is not obvious at intermediate doping levels. This continuous variation of relative intercalant-polymer concentration during doping is an important difference with crystalline organic CT crystals, which usually have a precise, often $\frac{1}{2}$, stoichiometry. Since this is not so in CPs, intercalants and polymer structures, if both exist, are usually incommensurate, or only the polymer has periodic order, the dopant being disordered, amorphous, or even liquid-like.

Another difference with graphite, for example, is the imperfect order in CPs discussed above and the existence of amorphous regions. In such

materials, intercalation may be highly inhomogeneous for thermodynamic or kinetic reasons. Indeed, a model has been proposed in which doping in PANi proceeds by formation, growth, and percolation of fully doped ("metallic") regions in an undoped (insulating) medium [54,55].

The structure of doped CPs will not be studied in further detail here; a few representative examples will be given.

(a) *Polyacetylene n-Doped by Alkali Ions*

The fully K^+ -doped material (approximate composition $CHK_{0.17}$) is a good example of a system in which dopants form one-dimensional chains, filling channels parallel to the polymer chain direction. The diffraction patterns obtained are as good as those of highly ordered undoped *trans*-PA. The projections along that direction of the undoped and fully doped *trans*-PA structures are compared in Fig. 5 [56] (see also Ref. 57). The area of the two-dimensional projected cell is increased by only 13%. The chains are rotated to open channels just filled by the K^+ ions (radius 1.33 Å), the distance between chains being almost unchanged. The doped structure is now tetragonal. The lateral coherence length is practically unchanged, and after dedoping, the material regains its initial crystallinity. This is an optimum case: Cs^+ , for instance, is too big to fit into these channels, the corresponding doped structure is less well ordered, and order is not fully recovered on dedoping. Na^+ is too small to fill these channels, so another structure, in which an ion chain is surrounded by three polymer chains, is found at least at some doping level [58].

The doping level can be controlled electrochemically or by doping from the metal vapor phase. This has been studied extensively for alkali insertion, and the existence of stages has been clearly demonstrated and studied thoroughly [56], as well as the corresponding conductivity changes [59].

(b) *p-Doped Trans-PA*

Anions involved in *p*-doping, such as AsF_6^- or ClO_4^- , are bulkier than alkali cations. They would not fit into a channel structure such as the above one; different structures implying larger chain motions are expected. We consider in some detail iodine-doped PA, since it shows by far the highest conductivity to date of all conducting polymers [36]. Most structural studies have not been performed on the actual material showing this large σ , but to the level of information that can be obtained from presently available diffraction patterns there do not seem to be significant differences between differently prepared I_2 -doped PAs. The system is further complicated by the fact that the actual counterions present in the structure are I_3^- and I_5^- in variable proportions.

Early diffraction patterns showed a small number of reflections only [60]. The degree of order that remains in a sample after doping depends

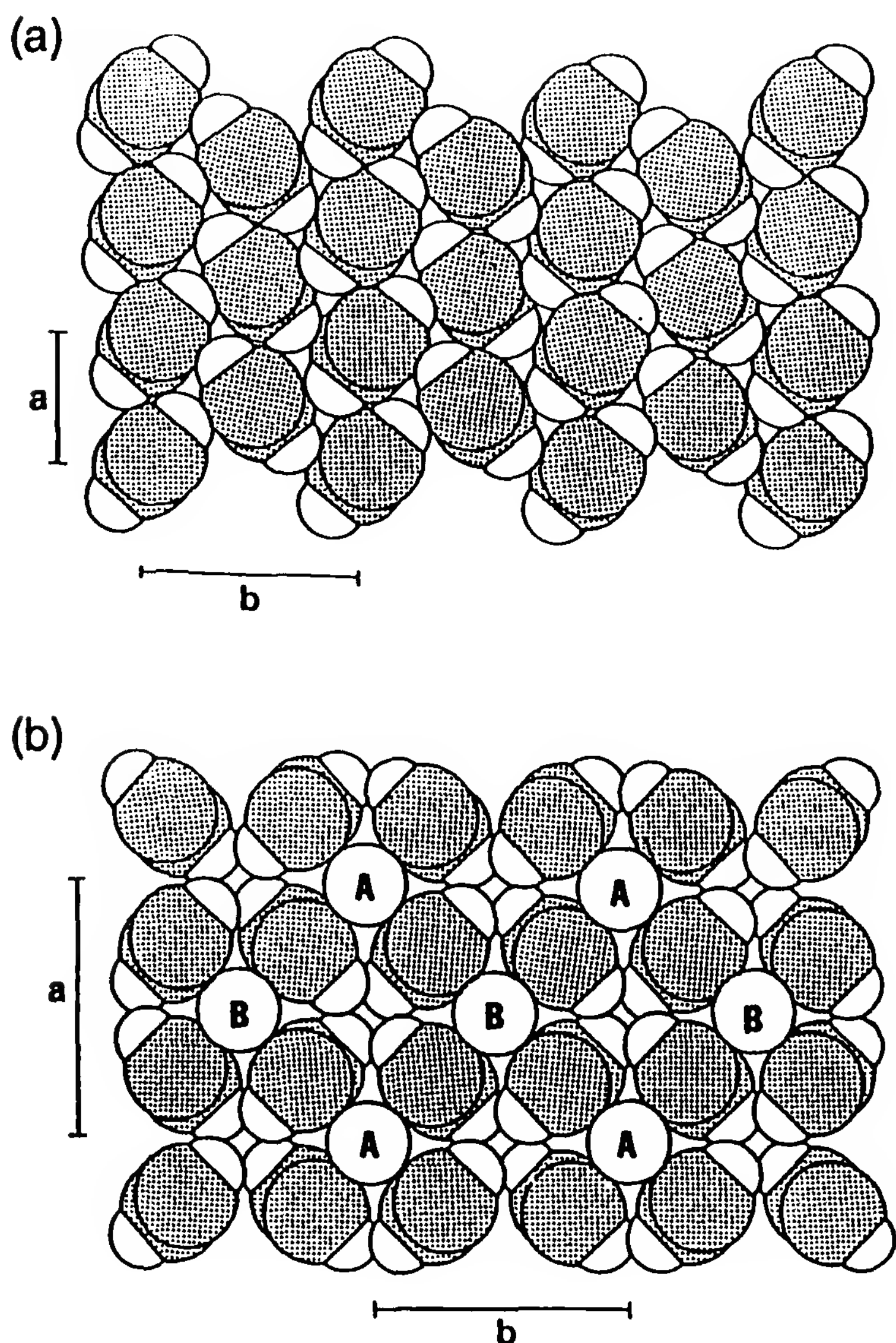


Figure 5 Comparison of undoped (a), and alkali-metal doped (b), *trans*-PA crystal packings. Alkali ions occupy channels labeled A and B in (b). In stage 1, both are filled equally; in stage 2, only set A is occupied. (From Ref. 56.)

on the kinetics of doping and is often very low. Use of oriented PA and careful control of doping kinetics made it possible more recently to obtain better resolved patterns (see Fig. 1) [61]. Correlatively, different models have been proposed, all assuming intercalation of planes made either of dopants only, or of alternating chains of dopants and polymer, between planes of pure polymer [62]. X-ray scattering is produced primarily by the heavy I ions, whereas neutron scattering tends to be dominated by the polymer [63]. A recently proposed model is shown on Fig. 6; differently intercalated structures (i.e., stages) occur [61]. There is also some evidence of stages in conductivity or spectroscopic data at intermediate doping levels.

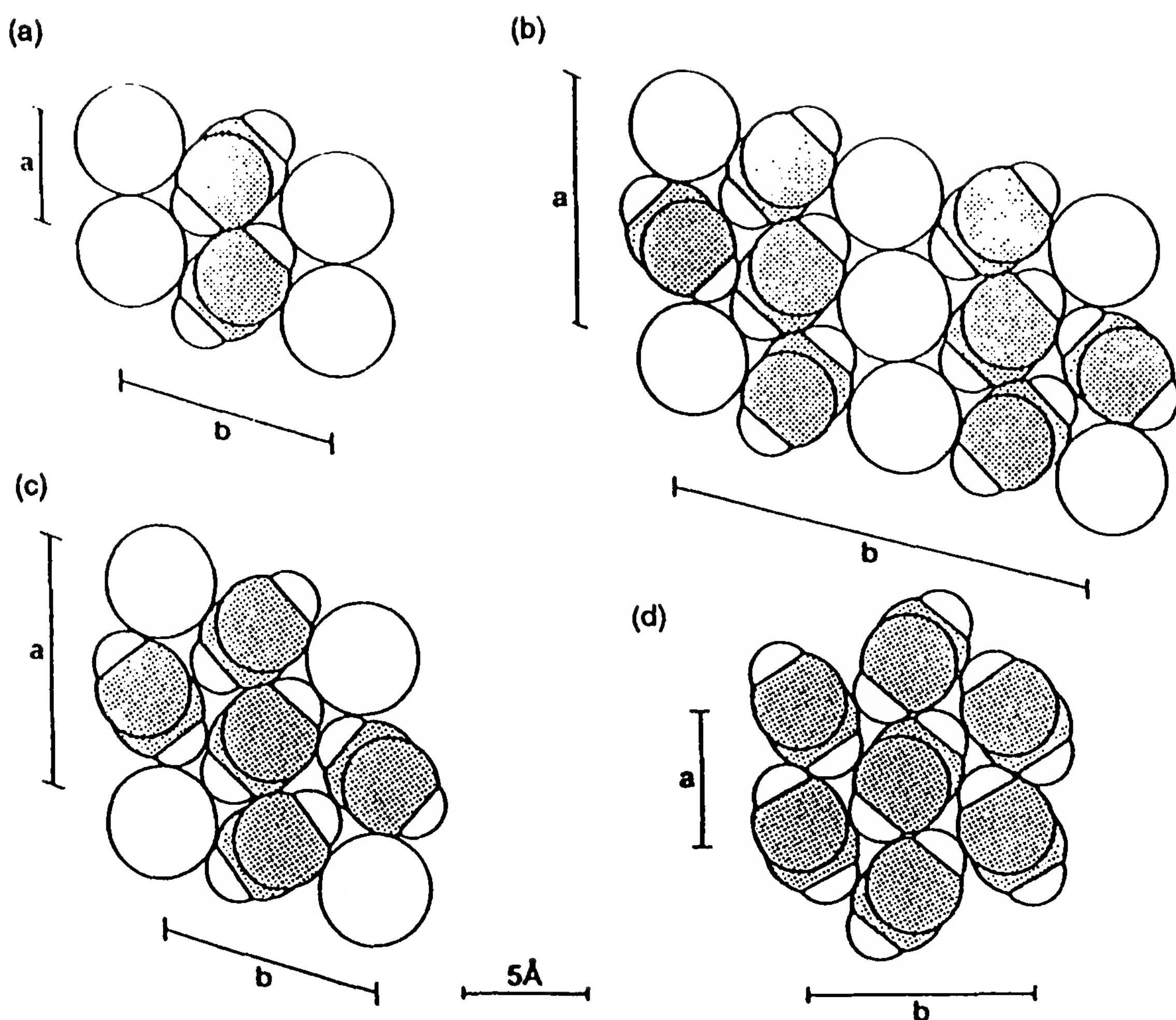


Figure 6 Proposed structures for iodine-doped *trans*-PA arranged in decreasing I contents from (a) to (d): average I/C₂H₂ ratio is 0.78 for (a), 0.48 for (b), 0.26 for (c); structure (d) is for undoped *trans*-PA. (From Ref. 61.)

However, the model implies that a sample almost always contains a mixture of stages. Unfortunately, there is also evidence in some cases of inhomogeneous doping not obviously related to staging [64]. In addition, the short coherence lengths found imply that the order does not extend beyond a few unit cells. There is clearly not enough data to obtain information on other properties, such as chain setting angles.

This model has been carried over to other *p*-doped systems. But the dimensions of ions such as AsF₆[−] or ClO₄[−] are larger than the I[−] ion diameter, so planes where columns of such ions and polymer alternate can hardly occur. What is known is not inconsistent with the planar intercalation model. Finally, let us note that this model is also supported by the structure of doped oligomers, that is, of stoichiometric radical cation salts in which the cation is, for instance, that of quaterphenyle [65].

(c) *Doped Polyaniline*

Polyaniline is structurally much more complicated than PA, even if we restrict our attention to the emeraldine base (EB) and salt (ES) forms. There are two classes of base forms, to which correspond two classes of salt forms ESI and II [28], and the $EB \leftrightarrow ES$ interconversion does not mix the classes. This interconversion corresponds to addition or removal of a proton onto the N atom in the chain without changing the total number of electrons; this causes a conductivity change by more than 10 orders of magnitude, from $\sim 10^{-10}$ S/cm to > 1 S/cm [52].

Crystallinity is an important factor in the control of doping kinetics. Doping may proceed inhomogeneously in partially crystalline material. It is also important in the final conductivity obtained at high doping; it has been proposed that carriers are highly mobile and delocalized in the crystalline regions, transport through the amorphous ones limiting the macroscopic dc conductivity observed (see Chapter 13) [52].

Recent structural investigations give evidence of a situation too complicated to be described in detail here. It now appears that both EBI and EBII may be amorphous, but that their local orders differ. EBI is always amorphous, and ESI partly crystalline, whereas EBII may be amorphous or partly crystalline. In all cases the amorphous region's local order is very reminiscent of the organization of the crystalline regions of the same material. Since coherence lengths in the crystallites are $L_p \approx 40$ to 50 \AA , or about five repeat units, these similarities are quite understandable. These relations in local order explain why $I \leftrightarrow II$ class interconversion does not occur until the material is dissolved and reprecipitated, thus destroying the local order.

It is also observed that several structural features, such as cell volume, depend on sample history. The situation is made more difficult by the existence of slow relaxation effects (see Chapter 13). Information on chain conformation or bond length, which would be useful in theoretical modeling, is therefore hard to get. These problems are still under study, and the interested reader is referred to the original articles (e.g., Refs. 24, 27, and 28).

5. Substituted Conjugated Polymers

Substituents replacing H atoms are almost always relatively large. Unit cells similar to those shown on Fig. 3 are impossible. Chains and side groups have very different mechanical properties, electronic structures, and packing requirements, so the resulting structures may bear no relation to those of the "parent" unsubstituted polymer. In particular, one may expect chains and side groups to show a tendency to segregate (as occurs for other types of polymers), since substituents are usually attached to

induce the solubility of the very insoluble CP chain, implying that the chain and side group have very different thermodynamic properties (see Section II.E).

These segregated side groups will either shield conjugated chains from one another, or induce a partial two-dimensional ordering of CP chains (i.e., an incipient lamellar structure). In all cases, interchain interactions will be affected. Substitutions have therefore also been attempted to modulate and control interchain interactions and therefore electrical conductivity [66].

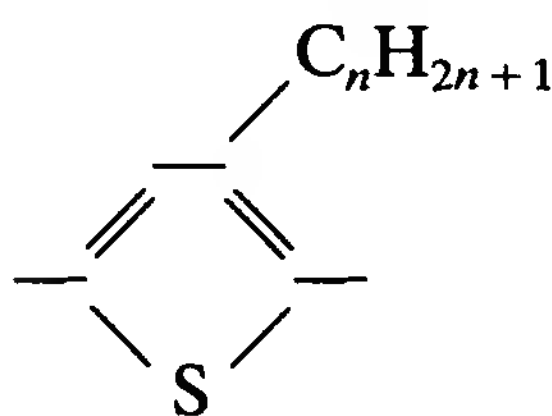
Large side groups will also directly affect the conjugated chain geometry in at least two ways: bulky substituents such as the cycloalkanes used in Ref. 66, or almost any substituent on the PA chain whose repeat unit length is very short, will impose steric constraints and may force the CP chain out of planarity, thus decreasing the conjugation, or possibly induce helicity [12]. On the other hand, long substituents, having large moments of inertia, will stiffen the chain [16]. Specific chemical interactions, both intra- and interchain, will occur as well. So substituents can decrease as well as increase electronic transition energies, and both have indeed been observed.

The solubility acquired by the polymer upon substitution makes it possible in principle to measure molecular weights and to study the geometry of the isolated chain in solution. However, this has been done in a few cases only, but it seems that conjugated chains are in fact not intrinsically rigid as often claimed [67], and that the large statistical lengths sometimes observed [68] are imposed by the presence of long side groups [16]. Energy barriers to rotation in conjugated systems are indeed calculated to be low [69].

Many types of substituents have been attached to several kinds of CPs. We shall restrict the discussion to substituted polythiophenes (P3ATs) and PPVs, on which most of the work has been performed and which are the materials used most often in the study of physical properties and potential applications (see Section VI).

(a) *Poly(3-alkylthiophenes)*

The most studied substituted conjugated polymers are presently the poly(3-alkylthiophene)s or P3ATs [70], for which the repeat unit is



P3AT

A number of materials have been prepared from the methyl to the docosyl ($n = 22$) derivatives. For $n \geq 4$, the P3ATs are soluble in many solvents. In addition, reported melting points T_m also decrease with increasing n , down to $\leq 120^\circ\text{C}$ for $n \geq 10$ [71], so the corresponding polymers are also melt processible. However, it seems that for all processible P3ATs the glass transition temperature T_g is below room temperature [72]; indeed, better resolved diffraction patterns are obtained at low temperature [73]. So there would be limitations to the long-term mechanical stability of structures using P3ATs, such as field-effect transistors (FETs) (see Section VI.B); this point does not seem to have been studied much up to now.

The structure of these CPs have been studied in some detail since it was observed that the absorption spectrum of cast films changes quite rapidly and reversibly upon heating ("thermochromism") [74], and the transition temperature decreases with alkyl chain length. The structural origins of these changes have been sought.

Room-temperature diffraction patterns (Fig. 7) of unstretched P3AT films (for the effect of stretching, see Section II.D.3) indicate that they

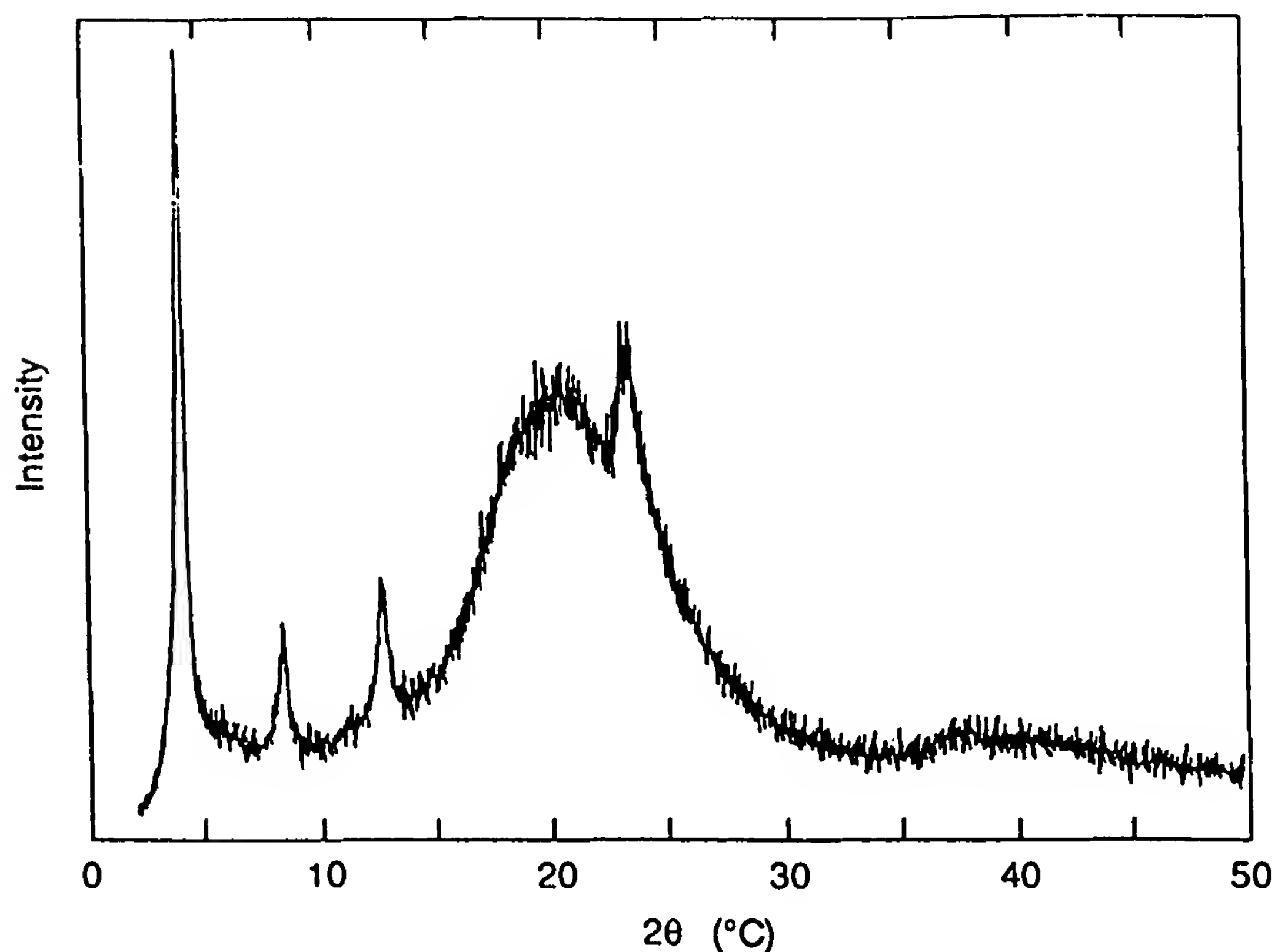


Figure 7 X-ray diffraction pattern from a melt-processed polyoctylthiophene film. (From Ref. 70.)

are only partly "crystalline": $\leq 30\%$ and often less than 10% , for reasons (thermodynamic or other) yet unknown. This crystallinity is less than that found in chemically synthesized PT [22,23], but with completely different diffraction patterns (compare Fig. 1c). What is analyzed in a diffraction experiment is therefore a minor fraction of the material, so not too much concerning the electronic properties can be inferred. The absorption spectra recorded in the study of thermochromism are dominated by the amorphous fraction and also by the kinetics of spontaneous thermal dedoping of these materials (which is not discussed here) [75].

Why is the crystalline fraction so small? This is not yet well understood, and we can only speculate. It may be for kinetic reasons, the nucleation and growth of crystalline nuclei being too slow, or cooling much too rapid, so that most of the chains will remain entangled; the molecular weights are usually large enough for entanglement to occur. There may also be structural reasons. For instance, one obvious cause of disorder-impeding crystallization is that side groups may not always be attached to the same C atom in successive monomers, so that steric constraints on the chain and therefore its conformation vary along its length [76]. That this will impede crystallization is well known [12]. A specific example is given in Fig. 8, on which the geometries of dimers with head-to-head and head-to-tail conformations are compared [77]. Polymerization, not of substituted thiophene but of the corresponding dimer, almost eliminates that problem [78]. More crystalline PATs may be forthcoming.

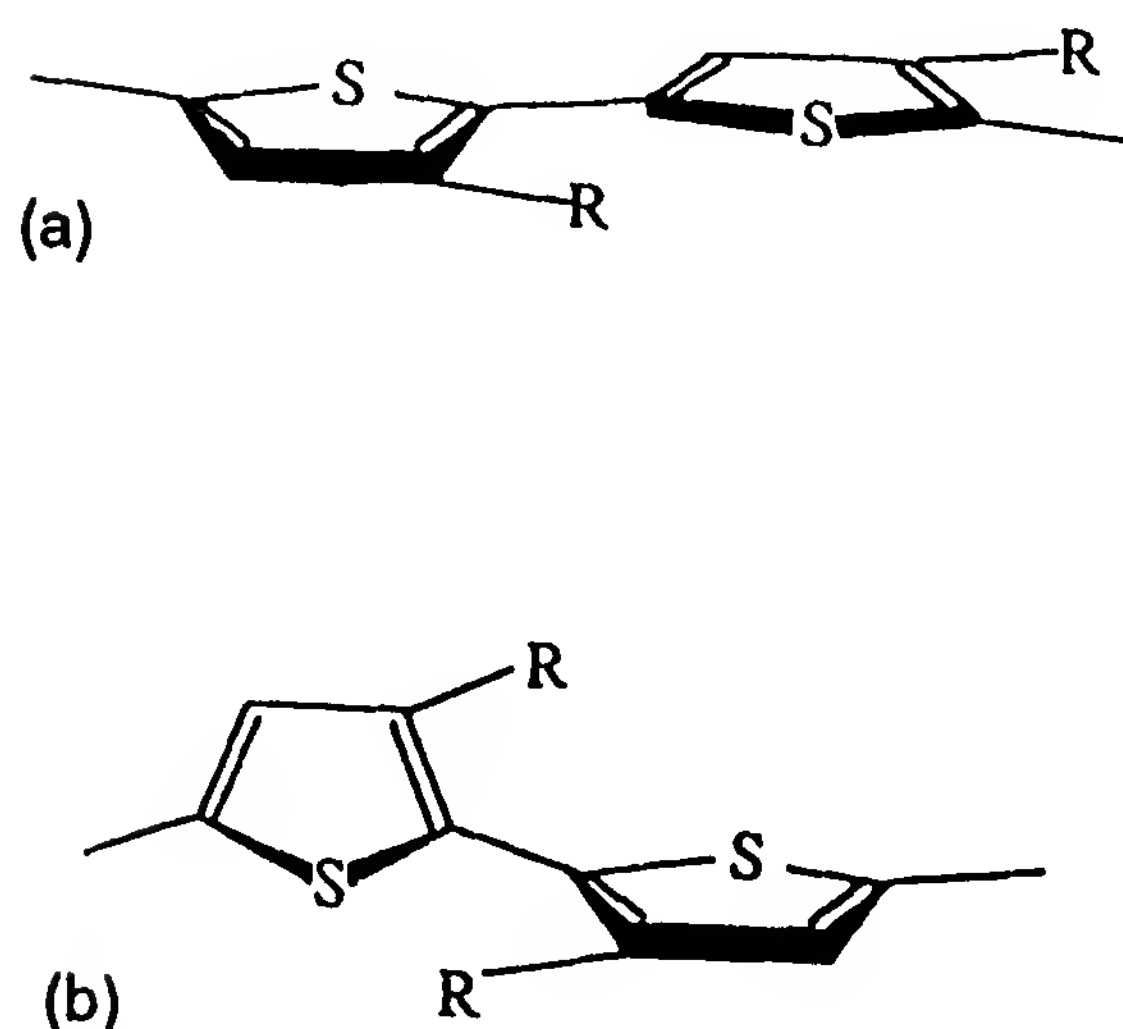


Figure 8 Sketch of (a) head-to-tail and (b) head-to-head conformations of thiophene dimers. (From Ref. 82.)

Whatever the cause of this small amount of crystalline phase, the dimensions of a crystallite (ca. 100 Å) are much smaller than a chain length, and it is likely that a given chain will “go through” two or more crystallites, which will then be connected by one or more covalent links. This situation is similar to the one known in polymer physics as the fringed micelle model (see Ref. 12, p. 187), and is sketched on Fig. 9. This has consequences on the behavior of films upon stretching (see Section II.D.3).

Well-defined peaks are observed at small angle, corresponding to a “long” spacing, increasing nearly linearly with alkyl chain length. Weak second- and third-order related peaks are present, together with a weak peak at a greater angle, which corresponds to a distance of 3.8 to 4 Å, independent of alkyl chain length [72,73,79].

The long spacing has been assigned to a distance between conjugated PT chains, extended and straight and in the all-trans conformation and separated by an interpenetrating network of extended alkyl side chains. This is likely, since that distance increases by about 2.6 Å upon addition of two carbons to the side chains, and this is the repeat distance along an alkane molecule. The long spacing is more than one side-chain length but less than twice this length, so side chains are partly interdigitated or more probably tilted [80].

It has also been argued that the polymer chains are stacked with a distance between thiophene rings of 3.8 Å, based on the weak large-angle peak [79]. A kind of two-dimensional lamellar ordering of the PT chains would then occur [80]. The distance between successive rings along the PT chain, and also the distance between close-packed alkane chains measured

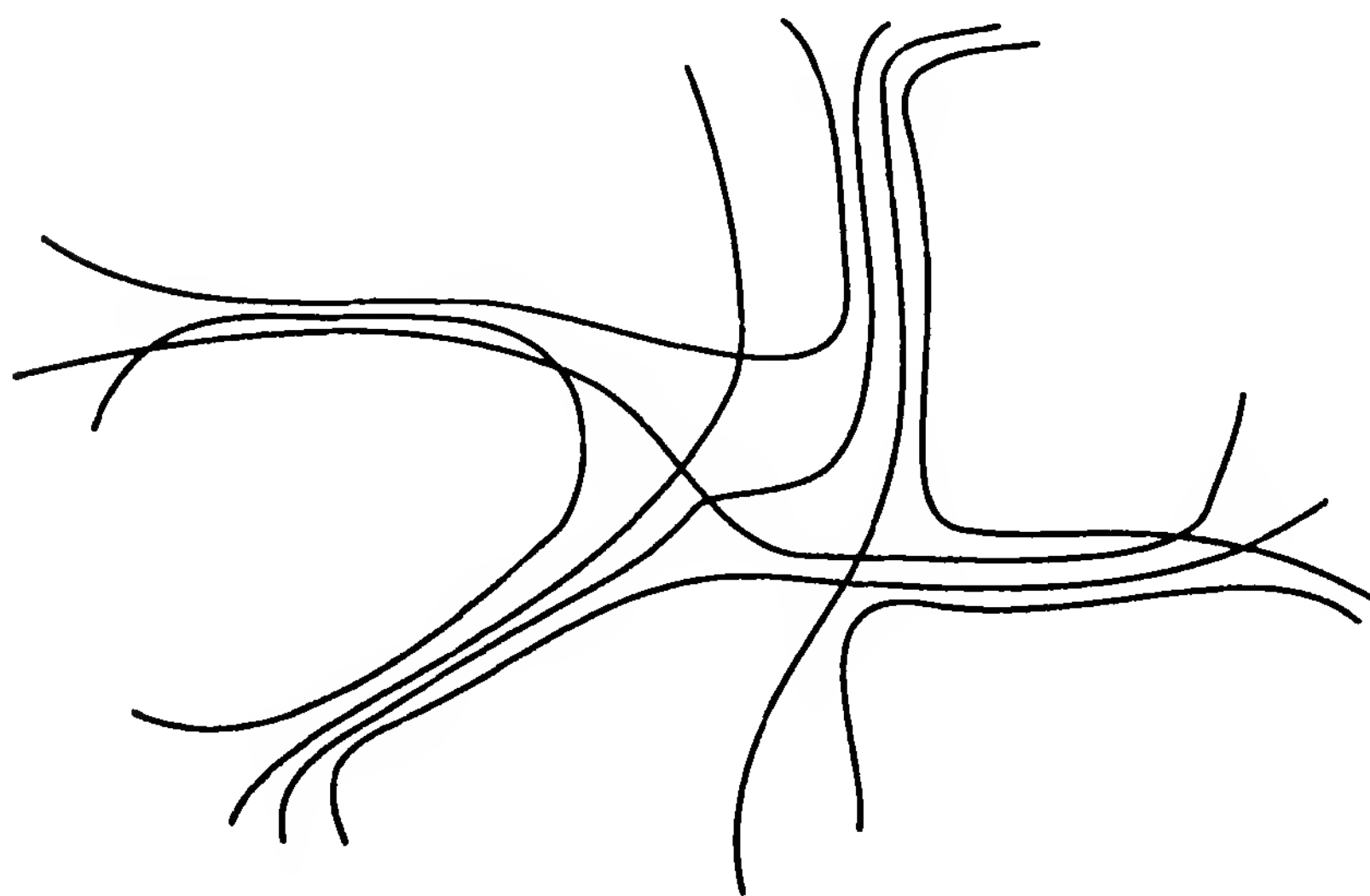


Figure 9 Sketch of a few chains forming fringed micelles.

perpendicularly to their axes, is approximately 3.85 Å (see Ref. 12, p. 89). That these two distances are equal certainly helps the material to order. Diffraction patterns of oriented samples contain more information since diffraction by planes parallel or perpendicular to the stretching direction are now distinct. Recent studies [80,81] conclude that in the crystallites the chains are arranged in planes separated by extended alkane chains, the PT chains in successive planes being mostly uncorrelated. For instance, the structure shown in Fig. 10 for the octyl polymer has been proposed [81]. The smallest distance between translationally equivalent thiophene rings is 4.8 Å, and for rings related by a 180° rotation it is 3.9 Å. This order extends over ≤ 70 Å. These distances do not correspond to very large interchain couplings, but they are smaller than most corresponding interchain distances in crystals of unsubstituted CPs (see Fig. 3). Considering the present impossibility of quantifying the disorder in these struc-

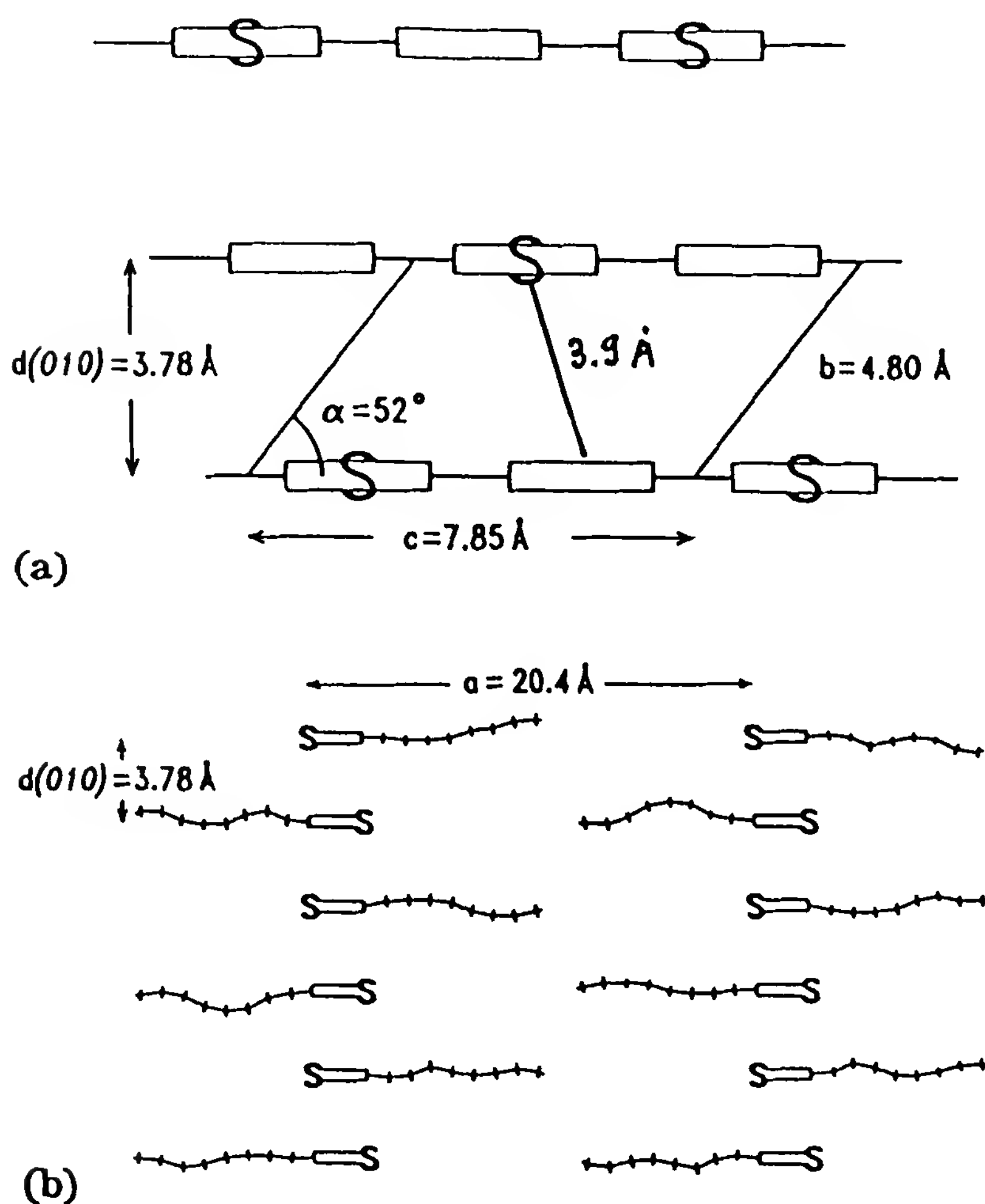


Figure 10 Proposed structure for polyoctylthiophene. (From Ref. 81.)

tures, the crystal packings sometimes drawn in the literature may be a bit misleading.

All diffraction peaks disappear upon heating above T_m . It is known, however, that “comblike” polymers (i.e., those with long side groups) may show two melting transitions, the lower one corresponding to side-group melting only [82,83]. This may be occurring for $n \geq 12$ [72]. And indeed, in the dodecyl ($n = 12$) compound, changes in diffraction pattern with temperature occur in two steps [84]. The relation between thermochromism and side-group melting merits further study.

When thermochromism is completed, conjugation lengths have decreased greatly. The wavelength of maximum absorption is shorter in the “melt” than in good solvents near room temperature, in which the chains have statistical lengths on the order of 50 Å [16], corresponding to an average angle between successive monomers on the order of 30°. Thus P3AT melts seem to be well-behaved flexible polymer melts, another indication that PT chains are not “intrinsically rigid.”

(b) *Substituted PPVs*

Substituted PPVs are of particular interest in relation to electronic applications (Section V) both because processibility can be improved and because electronic structure can be “fine tuned” by suitable substitution. However, no homogeneous series such as the P3ATs exists for PPV. Up to now most substitution of PPV has been by alkoxy groups (i.e., $\text{OC}_n\text{H}_{2n+1}$), and in many cases only low-molecular-weight materials are obtained, so less is known than for the P3ATs. There are few long side groups, with the notable exception of MEH-PPV.

The properties that probably help to ensure order in at least part of the P3ATs films—side groups long enough to crystallize and a match between the CP repeat unit distance and the alkane close-packing distance—are missing in the substituted PPVs prepared to date. Indeed, the corresponding oriented films are less well ordered than those of PPV [85]. The volume fraction of crystallinity is not known.

Even though the study is not complete, it shows an interesting effect of the side groups, quite different from the P3AT case. In PPV itself, although the chains are parallel, there is a large translational disorder along their direction (see Section II.C.3). When two methyl or two methoxy substituents are attached to the phenyl ring, opposite effects result: With $-\text{OCH}_3$, a more three-dimensional structure is formed, although the order is very local; $-\text{CH}_3$ substitution results in loss of the regular chain geometry [85]. This can be rationalized by using the results of theoretical calculations on the corresponding substituted stilbenes: $-\text{OCH}_3$ interacts with the double bonds of a neighboring molecule, thus contributing to their three-dimensional

ordering [86], whereas $-\text{CH}_3$ substitution merely results in chain distortion.

Thus, although substitution generally increases the proportion of amorphous phase and leads to more disordered crystalline phases, the reverse effect can be obtained using specific molecular interactions between side groups and conjugated chains. This suggests that interaction of a CP chain with another, nonconjugated polymer could be used to orient the former. In a sense, this is what is achieved in “blends” (see Section II.E).

D. Effects of Stretching

Stretching of CP films was mentioned above on several occasions: post-synthesis stretching of Ziegler–Natta-type PA; preparation of aligned PA films via the precursor route through stretching of the polymer during transformation; high-temperature stretching of spin-cast, initially un-oriented P3AT films; and so on. Thus stretching seems to be a promising processing route and is considered here in more detail.

Stretching should produce an anisotropic, oriented material. In some cases, one aims at increasing the crystallinity: either the volume fraction of crystal, or its order, or both. In all cases, the induced anisotropy produces optical dichroism and anisotropic conductivity, usually studied in the doped state, and the hope is to reach true intrachain properties, either electronic or mechanical (Young’s modulus or tensile strength of an infinite conjugated chain should be very high [87]). As discussed in Section II.C.5, it is also useful in diffraction experiments if it can be assumed or shown that the crystal structure is not modified by stretching. The stretching, or draw, ratio λ (i.e., the length of the sample divided by its length before drawing) is an immediately available parameter, but it may not be the most pertinent one, since stretching may result in many structural or morphological effects, and structural relaxation may occur at constant λ .

1. Stretching of a Highly Crystalline CP: Polyacetylene

PA is a highly crystalline polymer in which the crystalline fraction can be $\geq 80\%$ of the total volume [19]; when prepared by one of the variants of the Ziegler–Natta method [19,36], it is a fleece of fibrils of diameter 1 to a few hundred angstrom, so these films are never completely compact. Despite this overall similarity, the reported maximum draw ratios λ_{max} of such PA films before rupture vary widely, from about 1 to 15, at least.

It seems that the major effect at small λ is to orient entire crystalline fibers along the stretching direction; the void volume is then decreased and the film is more dense. Something else must occur for $\lambda > 2$. Apparently, fibers begin to slide past one another without much internal change; beyond $\lambda \sim 6$, cracks appear [88]. Orientation would then be limited by

entanglement of fibrils in the starting material rather than by cross-linking of individual chains, which would operate at a more microscopic scale. Indeed, films produced directly in highly oriented and anisotropic morphology by synthesis in an oriented liquid-crystalline solvent [89] are difficult to stretch. So a better measure of alignment than λ would be variance of the chain orientation function α , which can be deduced from diffraction patterns. Typical values of α are about 5 to 15°.

However, larger values of λ , up to 15, have been reported for films that had been swelled in a liquid supposedly acting as a plasticizer, then stretched [90], and in that case an increase of the coherence length L_p from ≤ 100 to ≈ 200 Å was reported, but no detailed analysis in terms of paracrystallinity was done. This seems to be the only report of a truly microscopic intrafibril change in stretched PA.

Variations with λ or α of the conductivity σ or its anisotropy in the undoped state do not seem to have been studied, only that of the doped state. Orientation is preserved upon doping, the conductivity along the stretching direction increases, and anisotropies of σ on the order of 25 are currently reported (although larger anisotropies have been reported, for instance ≤ 120 for $\lambda = 5$ [91]); these changes seem to “saturate” at a small value of $\lambda \leq 4$. Quite surprisingly, they do not seem, for a given sample, to depend on the magnitude of σ nor on temperature [92], suggesting that this may be a geometric effect and that “true” anisotropies could be larger. The highly oriented “plasticized” samples mentioned above behave quite differently: the conductivity does not saturate nor does its anisotropy (an anisotropy of at least 250 has been claimed [87,90]). The Young’s modulus and tensile strength increase in parallel with σ up to quite large values: about 50 and 0.7 GPa, respectively.

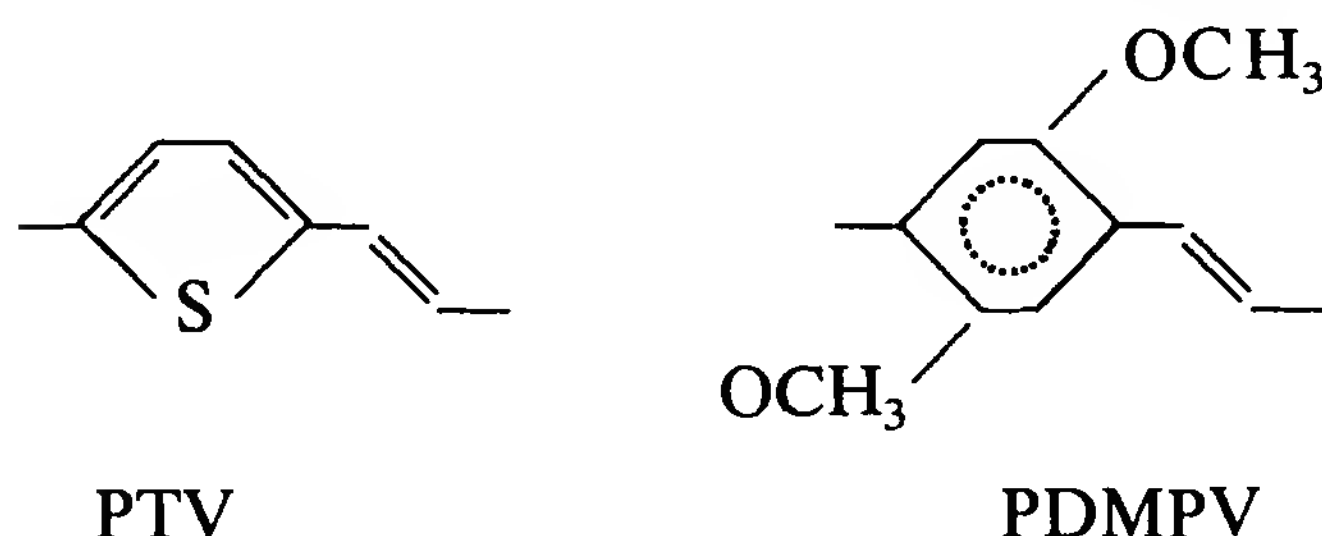
2. Crystallization by Stretching

a. CP films prepared from precursor films, such as the Durham PA, are amorphous. But transformation into the CP is generally performed at temperatures well above the T_g of the precursor. For instance, this $T_g \approx 100^\circ\text{C}$ for PA; so if the transformation into PA is carried out on a statically stretched, and therefore aligned, precursor film, the resulting CP film is oriented and highly crystalline [93,94], allowing more structural information to be obtained (see Section II.C.2 [35,38,39]) and many other structural studies to be carried out (see, e.g., Fig. 1 of Section III). Similarly, the T_g of the precursor to PPV is $\approx 110^\circ\text{C}$, well below the transformation temperature as well [95,96], and stretching up to $\lambda \approx 16$ has been achieved [97]. Several other cases have been studied [87].

In this process, precursor chains are first brought into parallel orientation well above T_g , which is favorable to subsequent crystallization of the re-

sulting CP chains. Since the melting point of the CP is far higher, the resulting structure is stable. The films are very anisotropic and dense, but microscopically less well ordered than Shirakawa-type PA, as evidenced by Fig. 2.

b. If the conversion of the precursor into the CP can be made fast enough, a continuous process is possible. This has been achieved, for instance, for PTV and PDMPV, whose repeat units are



Fibers from the corresponding precursors were drawn through an oven in which they were simultaneously elongated up to $\lambda \approx 16$ and $\lambda \approx 8$ for PTV and PDMPV, respectively, and transformed into the CP [87,98]. Highly oriented crystalline fibers are obtained; Young's modulus and tensile strength increase approximately linearly with λ up to 30 GPa and 0.6 GPa, respectively, for PDMPV, for instance, and the conductivity of the fibers (parallel to their axis) after doping increases more than linearly with λ , up to values above 1000 S/cm.

c. Clearly, the fact that a "soft" material (above T_g) is stretched is important. A possible method for softening high- T_g materials is to swell them with a molecule acting as a plasticizer. The application of this method to PA has already been mentioned in Section II.D.1, but in that case orientation of an already crystalline polymer was sought for, and the molecules used were not real solvents of the polymer.

The method has also been applied to PAni [53]. The plasticizer is a solvent of the polymer *N*-methylpyrrolidone (NMP), and the film to be stretched is not, or is very poorly, crystalline and may contain up to 20 wt% NMP. T_g decreases as the NMP content increases, down to $\approx 110^\circ\text{C}$; heating and stretching swollen EB films above that T_g value produces $\lambda > 6$, increased crystallinity (Fig. 11), and sizable orientation and anisotropic properties [27,99,100]. Such films, doped with HCl, show a conductivity anisotropy ≈ 25 [99–101]. Contrary to what is observed with PPV, the mechanical properties of stretched PAni remain modest; the Young's modulus is below 0.5 GPa [53].

3. Stretching of Predominantly Amorphous CPs

It was mentioned in Section II.C.5.a that PAT films contain a relatively small crystalline fraction, usually $\leq 15\%$, and have T_g values around or

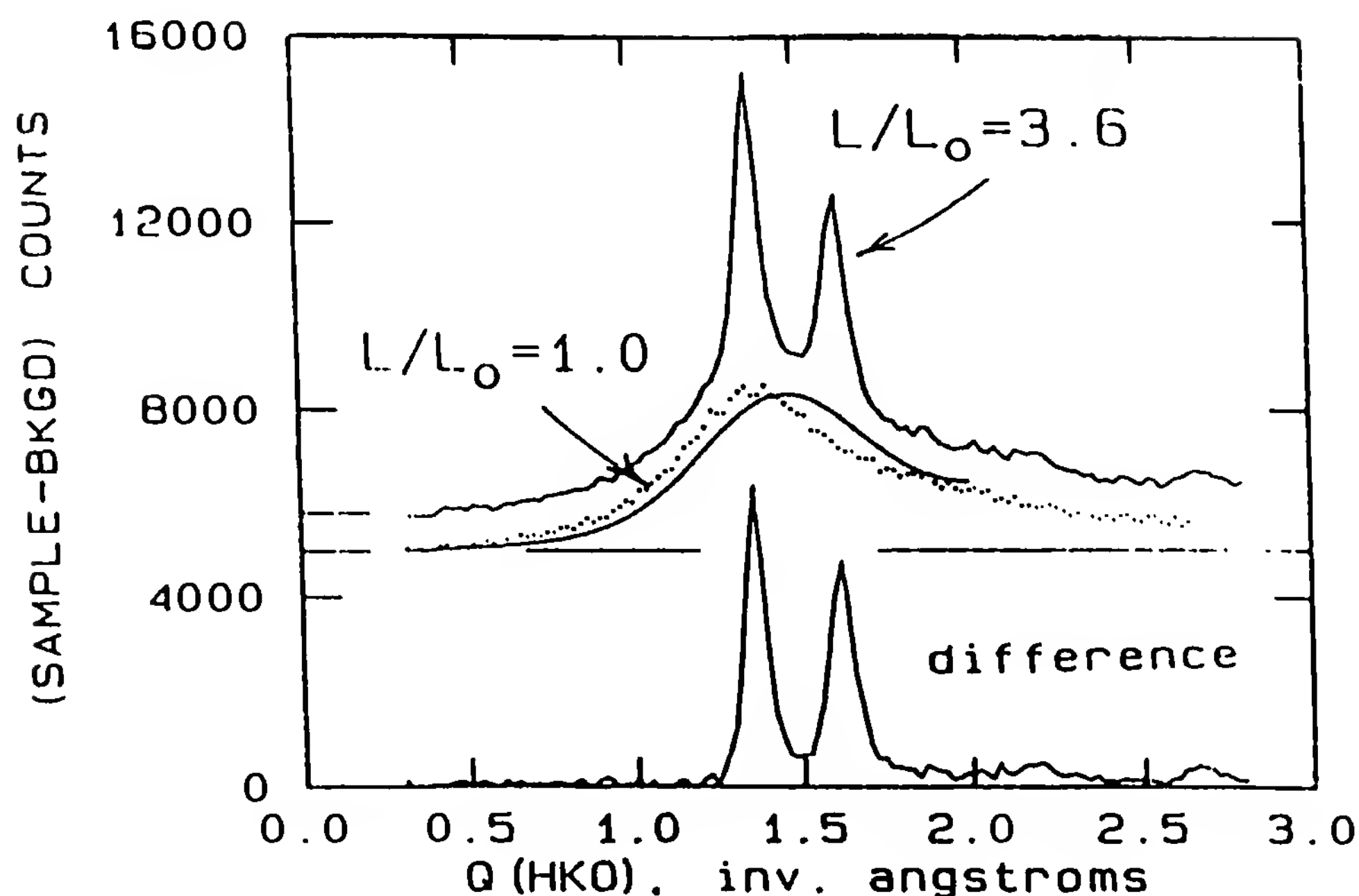


Figure 11 Part of the diffraction pattern of a stretched PANi film. L/L_0 indicates the value of λ , the stretching ratio. (From Ref. 99.)

below room temperature and melting points not far above 100°C. As above, one would then expect that such films can be stretched and are modified by stretching.

This is indeed the case [102]. $\lambda_{\max} \approx 3$ to 4 for stretching at room temperature [103], and $\lambda_{\max} \approx 5$ at the optimum temperature of 100°C [87,104]. Fibers have been spun in similar conditions [87,105]. A significant orientation is obtained, sufficient for allowing real progress in the understanding of crystal structure [81]. However, the results are quite different from those reported in Sections II.D.1 and II.D.2. Crystallites are oriented, but less than expected, even for samples rapidly quenched after drawing [104], and their volume fraction in the sample does not increase significantly. So the amorphous phase only is stretched and thereby reorients the crystals. The amorphous phase is still dominant and much less well oriented than the crystalline phase. Mechanical properties remain modest and degrade as longer alkyl chains are studied [105]: Young's modulus for fibers with $\lambda \approx 5$ is ≈ 2 GPa for the hexyl derivative and less than 0.5 GPa for octyl and longer alkyl chains [87,106].

The origin of this behavior can be understood only qualitatively at present. At the drawing temperature, well above T_g , the chain mobility is quite large, and is larger for longer alkyl chains, for which melting temperatures are lower. Therefore, relaxation will occur even at constant λ during cooling and even possibly at room temperature. Rapid quenching, which could

minimize that relaxation, seems to have been done only once [104]. Dynamical mechanical studies are only beginning [72].

If the fringed micelle model (see Section II.C.5.a) is applicable, large values of λ , which would correspond to distances between crystallites greater than the length of the chain connecting them, imply breaking of covalent bonds; this may place the limit for fracture of the sample.

E. Blends and Copolymers

1. Introduction: The Compatibility Problem

Another way for processing and orienting a CP might be to use a “mixture” of it and a nonconjugated, processible polymer in such a way that the mixture keeps the desirable properties of each of its components. This has been tried in two ways.

1. One can simply blend the two polymers either in the molten state or in a common solvent. The solid thus obtained contains two types of chains, say A and B, with no covalent link between them.
2. It is also possible to incorporate one or several sequences of a conjugated polymer A and of a nonconjugated polymer B in a single chain. This is a block copolymer: all chains in the resulting solid are in principle identical, but composite. The simplest such structure is a diblock AB copolymer; each chain contains one sequence of each type, A and B.

However, a fundamental question arises immediately. As a rule, different polymers are not miscible [9,10], and certainly the two components of a CP/non-CP blend or copolymer are microscopically quite different! They will therefore try to *segregate* into two phases, one pure or almost pure CP, the other containing no or a very small amount of CP.

The morphology generated by segregation will be very different in the cases of blends and copolymers, since in the latter case a covalent bond between A and B constrains at least one dimension of each phase to be on the order of the length of one A or B sequence; copolymer demixtion must occur at microscopic scale. This generates a rich family of structures reminiscent of those found, for instance, with surfactants, in particular lamellar structures. The crystal structure of alkyl-substituted polythiophenes (Section II.C.5) is related to this effect. No such constrain exists for a blend. This must be taken into account when one considers properties requiring a continuous path through one of the phases, such as dc conductivity; the percolation threshold will be dependent of the geometry of the phases. One important consequence is apparent if one considers the conductivity of the mixed solid; dc conductivity requires a continuous path

through the conducting phase between the electrodes. A few representative examples of both kinds of studies are given below.

2. Blends

For these experiments we refer to the review article by Heeger and Smith [87]. Two quite interesting results will be discussed briefly. The first takes advantage of the possibility of “tailoring” the morphology of a blend to avoid the usual percolation threshold conditions. In several cases, the thresholds as measured by dc conductivity of blends are around 16% of doped CP in volume [87], corresponding to percolation of globular conducting particles. It is known, however, that if the conducting phase is in the form of long rods, the percolation threshold is much lower, and this has indeed been demonstrated for dispersions of organic conductor crystals in an insulating matrix.

Ultrahigh-molecular-weight polyethylene (PE) can be processed into a gel. Blends of such a PE with polyoctylthiophene were prepared, and conductivities above 10^{-4} S/cm were measured for POT volume fractions $\leq 1\%$. Data at even lower POT content suggest a percolation threshold below a volume fraction of 3×10^{-4} . Presumably, POT is rejected by PE and adsorbs on the threads forming the gel.

The second study shows that such gels, once dried, can be drawn to a remarkable extent, $\lambda_{\text{max}} \approx 200$, and that very highly oriented CP chains are obtained [107]. The CP used was MEH-PPV, a soluble polymer of current interest in the development of light-emitting diodes (see Section II.C.5); well-resolved and strongly dichroic absorption spectra (dichroic ratio ≈ 10) were obtained. More surprisingly, the low-temperature luminescence is also very dichroic (ratio > 50) [108]. It was suggested that this results from spontaneous orientation of the CP on the PE internal surfaces, lamellae or fibers depending on the draw ratio λ .

3. Copolymers

There is an enormous literature on copolymers in general, but only a very tiny part involves CPs. Polystyrene–polyacetylene diblock copolymers (PS-PA) are the most studied systems to date. The earliest CP/non-CP copolymer reported was a PS-PA copolymer [109]. PA is very insoluble, so it already seems difficult to obtain true solutions of such copolymers; the (usually short) PA sequences aggregate, with the PS sequences swollen around the aggregate. Moreover, demixing of these aggregate solutions occurs (see, e.g., Ref. 110). So although there may be very interesting physics to do with those systems, their structure, behavior, and practical potential are far from being understood.

F. Summary

The discussion above shows that structural problems in CPs are very different from those in organic conductor crystals. They also differ somewhat from those in other polymers; the dominant polymer crystal morphologies, lamellae and spherulites [12] are not found. Rather, fibrils are often observed.

CPs are rarely “crystalline” polymers in that they always contain an amorphous fraction $\geq 50\%$ the total volume. The crystalline fraction may be $\leq 10\%$ the volume. It is the latter that is selected in “structural studies,” but the amorphous phase may often dominate the physical properties.

Unsubstituted CP crystals all have quite similar chain packings. The crystal sizes are always small (ca. 100 Å in all directions) and imperfectly ordered; usually, chains are longer than the crystal dimensions. Therefore, the “ideal CP” is not found in practice; chain geometries fluctuate along their length, as well the interchain interactions. This disorder is to be taken seriously in physical study, not as a small perturbation.

Substituted CPs were initially prepared to achieve processibility; they are even less well organized. Many such CPs can be cast into homogeneous films, extrusion molded, drawn into fibers, and therefore oriented. In all these shapes they are generally dopable to sufficiently high conductivity for applications. Attempts to prepare various types of composites have begun.

III. OPTICAL PROPERTIES AND ELECTRONIC STRUCTURE

A. Introduction: Typical Experimental Spectroscopic Results

In this section the electronic structure of conjugated polymers is discussed. They form a special class of materials with particular types of excitations (such as the solitons) and properties, introduced briefly in Chapter 11. These problems are discussed here essentially in relation to the spectroscopic properties. The related but distinct subject of electrical conductivity is treated in Section IV. To set the scene, we first present some typical results: visible absorption and emission spectra and resonance Raman spectra. We consider the theoretical issues in Section III.B, then return to the meaning of the experimental results in Section III.C. The interesting non-linear optical properties of CPs will be considered in Section III.D. These sections are concerned with electronic states within the gap or near the band edges; the structure (i.e., the dispersion relations) of valence and conduction bands is also of theoretical interest and is considered in Section III.E.

1. Typical Visible Absorption and Luminescence Spectra: The Optical Gap

The visible absorption of all CPs shows a broad and intense band; its threshold is anywhere between 12,500 Å (or 1 eV) for isothianaphthene [111] to 4000 Å (or 3 eV) for PPP [112], and at 8000 to 9000 Å (or 1.35 to 1.5 eV) in *trans*-PA, depending on the preparation conditions [113]. Precise definition of the threshold would require a theoretically sound extrapolation law. This absorption band is usually well separated from further absorption at higher energy. The corresponding transition is naturally assigned to the π electrons. The threshold of this intense absorption, or the energy of maximum absorption, is often referred to in the literature as the “optical gap.” The initial implication was that it corresponds to the threshold of band-to-band transitions as in semiconductors, but as we shall see, this is debatable.

The absorption is very intense, so direct measurement of absorption spectra requires very thin films. When the sample surface is smooth enough, the absorption can be calculated by Kramers–Kronig inversion of the reflectance, which can be done rather accurately for a well-isolated transition [113]. A strongly scattering sample must be studied by attenuated total internal reflectance.

Next we show a number of representative absorption and photoluminescence spectra of CPs and the corresponding oligomers (hexamers). Figure 12a shows the absorption spectra of a *trans*-PA produced via the precursor route [113] and of the corresponding hexamer, dodecahexaene [114]. Two differences are immediately apparent in the absorption spectra:

1. There is a large difference in the maximum absorption energies, ≈ 1.5 eV. In the language of conjugation lengths (see Chapter 11, Section II.C) this means that conjugation extends in PA over much more than six repeat units.
2. The oligomer spectrum is well structured, typical of a molecular spectrum; the data shown are for molecules in solution. Although no pure solid spectrum is available, it is claimed that solid polyene spectra are not grossly different from the solution ones and are red-shifted (due to the larger dielectric constant of the solid) by not more than ~ 0.4 eV [115]. Solid-state spectra of conjugated molecules of similar size are relatively well structured exciton ones, not much red-shifted compared to solution spectra either [115]. On the contrary, the polymer spectrum appears structureless. In fact, there is a hint of a structure on the rising edge of the reflection spectrum [113]. In some cases this structure is slightly more pronounced, as shown for a Shirakawa-type

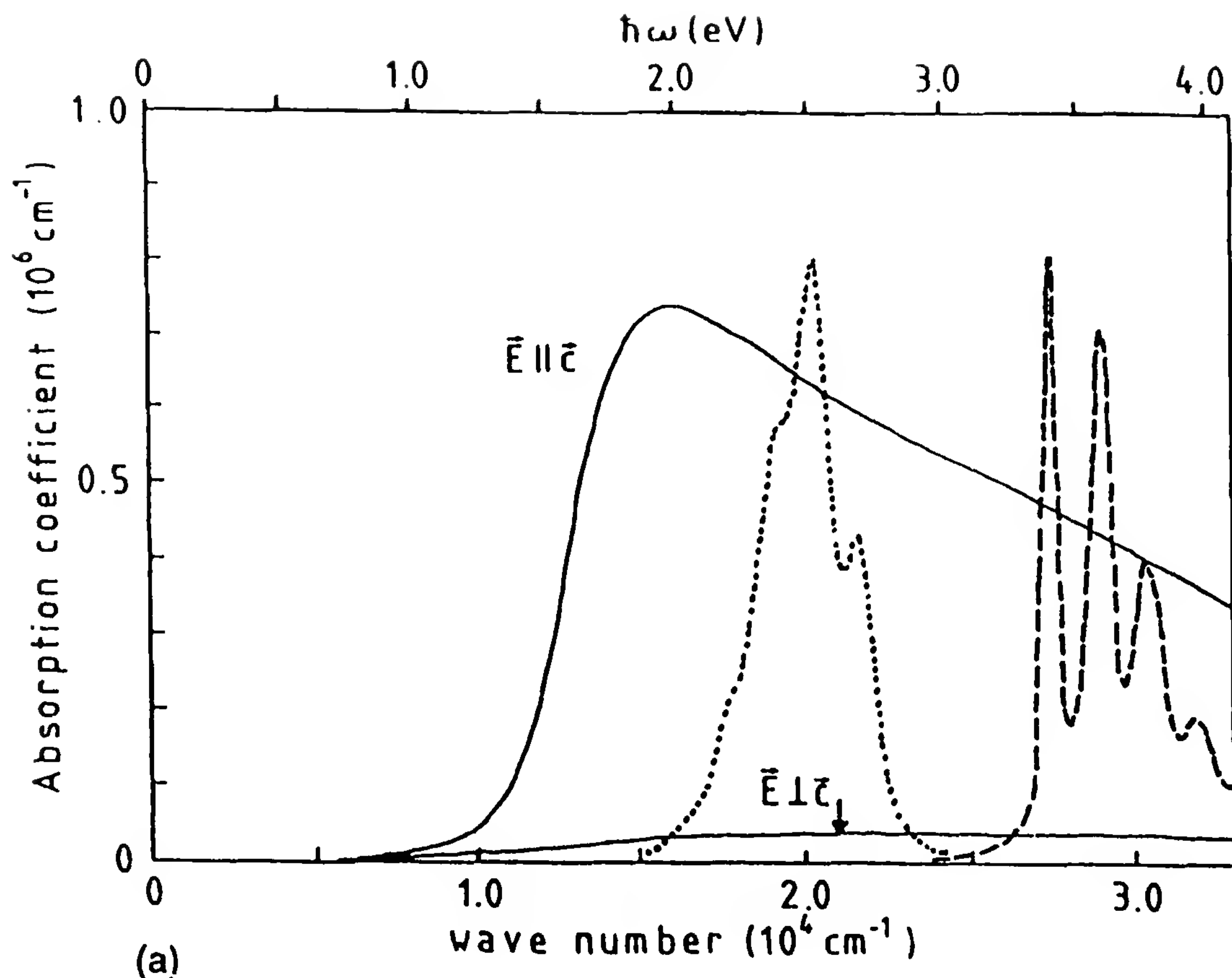


Figure 12 (a) Optical absorption of *trans*-PA and a related oligomer. Solid lines: polarized absorptions of an oriented PA film (precursor route), calculated from the reflection spectrum (from Ref. 113). The polymer chains are parallel to *c*. Dashed line: absorption of the hexamer all-*trans* dodecahexaene, in solution in hexane (from Ref. 114). Dotted line: hexamer emission in hexane. (b) Optical absorption and reflectivity of unoriented *cis*- and *trans*-PA films (Shirakawa type) (from Ref. 116).

unoriented PA on Fig. 12b [116]. The question is then: Is the absorption of a perfect PA actually structureless, or is this lack of structure due to sample inhomogeneity? Indeed, samples with more defects than those used for the data shown have blue-shifted, still structureless absorption bands. This important problem is discussed below.

The polymer absorption is intense: $\alpha_p \approx 7.5 \times 10^5 \text{ cm}^{-1}$ for light polarized parallel to the PA chains and the dichroic ratio is ≈ 25 . The polymer is not fluorescent.

Figure 13 shows spectra corresponding to a PDA which can be studied as a macroscopic single crystal [117,118], a disordered solid (see, e.g.,

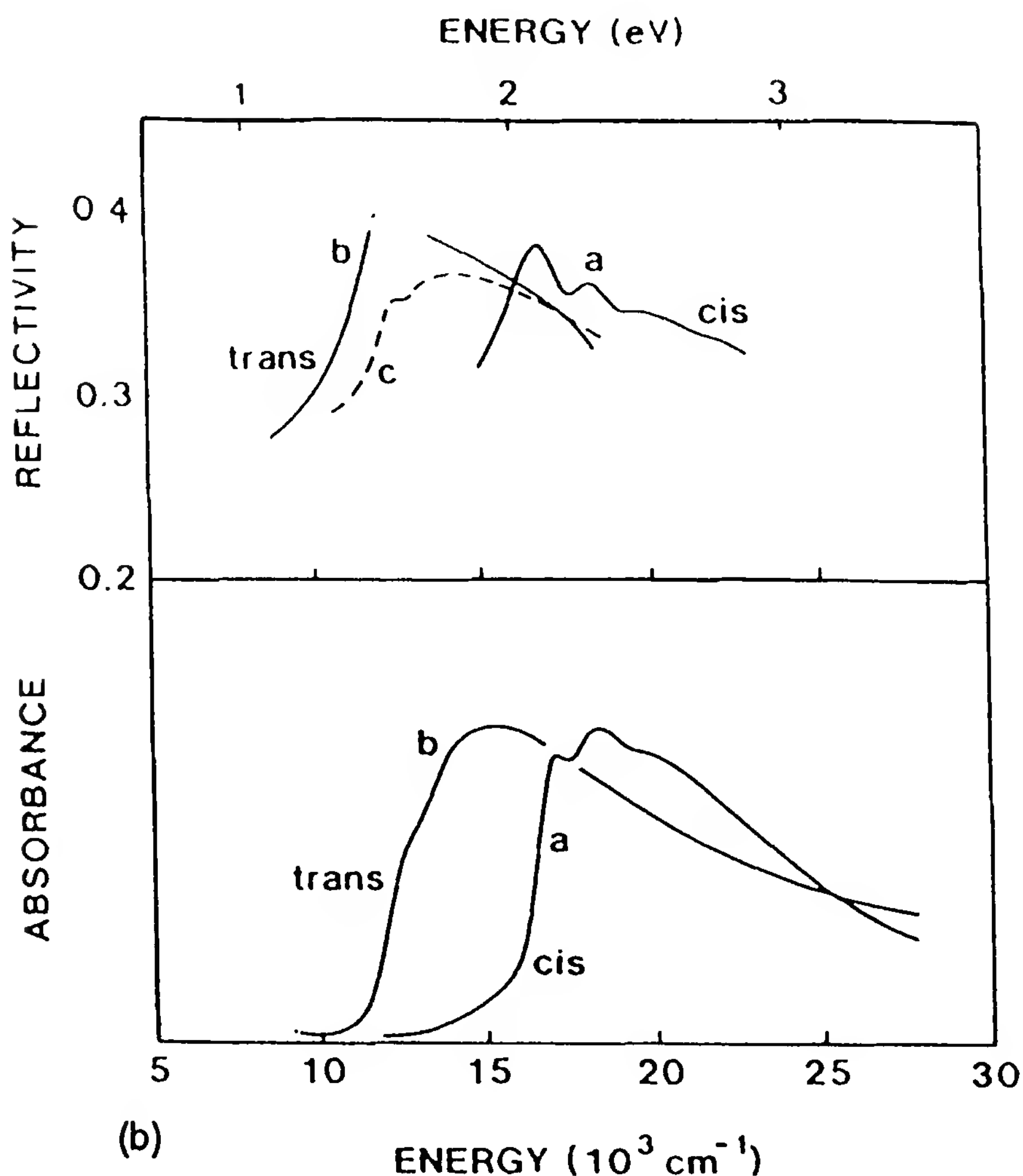


Figure 12 Continued

spectra in [119,120]), or a gel [68], and in solution [68,121], poly-4BCMU. The crystal spectrum is typical of most PDA crystals. In some cases (e.g., poly-3BCMU [121,122]), the disordered solid spectrum is very similar to the single-crystal spectrum, not blue-shifted as for poly-4BCMU shown in Fig. 13. The differences between spectra in Fig. 13 correspond purely to conformational differences of the PDA chains. Spectrum (c) is that of a real single crystal; all PDA chains in it have identical geometries, constant along their entire length, and they are long [16,68]. It should not be broadened inhomogeneously as the structureless PA spectra shown in Fig. 12 may be.

An obvious difference with Fig. 12 is the presence of structure on spectra (b) and (c). In fact, structure is even more resolved on low-temperature

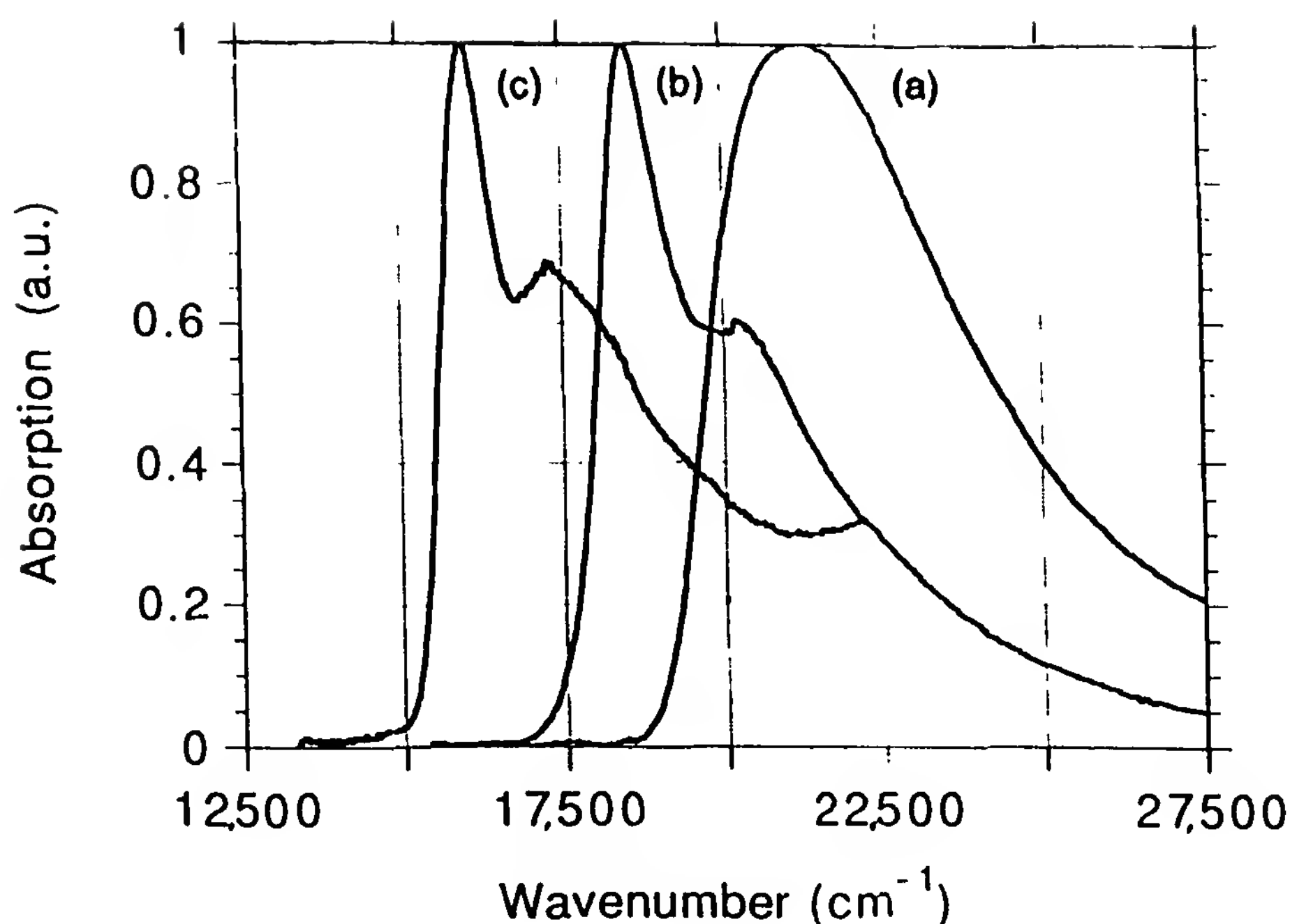


Figure 13 Optical absorption of the PDA poly-4BCMU in three differently ordered states: (a) solution in chloroform; (b) gel from toluene (dense homogeneous films cast from solution have similar, though slightly less structured, spectra); (c) single crystal.

spectra of the crystal, and all of it can be accounted for by vibronic progressions built on an electronic origin at the position of the most intense peak. These spectra therefore resemble that of the oligomer in Fig. 12a.

The maximum absorption per chain for light polarized parallel to the PDA chains is at least as intense as for PA. The measured dichroic ratio is about 120 [117,118]. It may be smaller in other PDAs: for instance, about 25 in pTS [123]. As for *trans*-PA, solid PDAs are not fluorescent (there is a small solution fluorescence).

Figure 14 shows the unpolarized absorption spectra of films of polythiophene [124] and its hexamer α -sexithienyl [125]. The hexamer solution spectrum is at almost the same energy. As in Fig. 12a, the oligomer shows structure on its rising edge, and the polymer spectrum is structureless. But in Fig. 14 the absorption thresholds differ by ≈ 0.2 eV only; one would then say that conjugation extends in PT over only about six monomers. One could show similar data for many other CPs.

The unstructured polymer spectrum on Fig. 14 corresponds to an un-oriented film. It has now been shown, for instance on MEH-PPV [108], that orientation and stretching can result in much more structured absorption spectra. Moreover, the corresponding emission is highly structured, even more than the hexamer emission on Fig. 12a; and the wavelength of

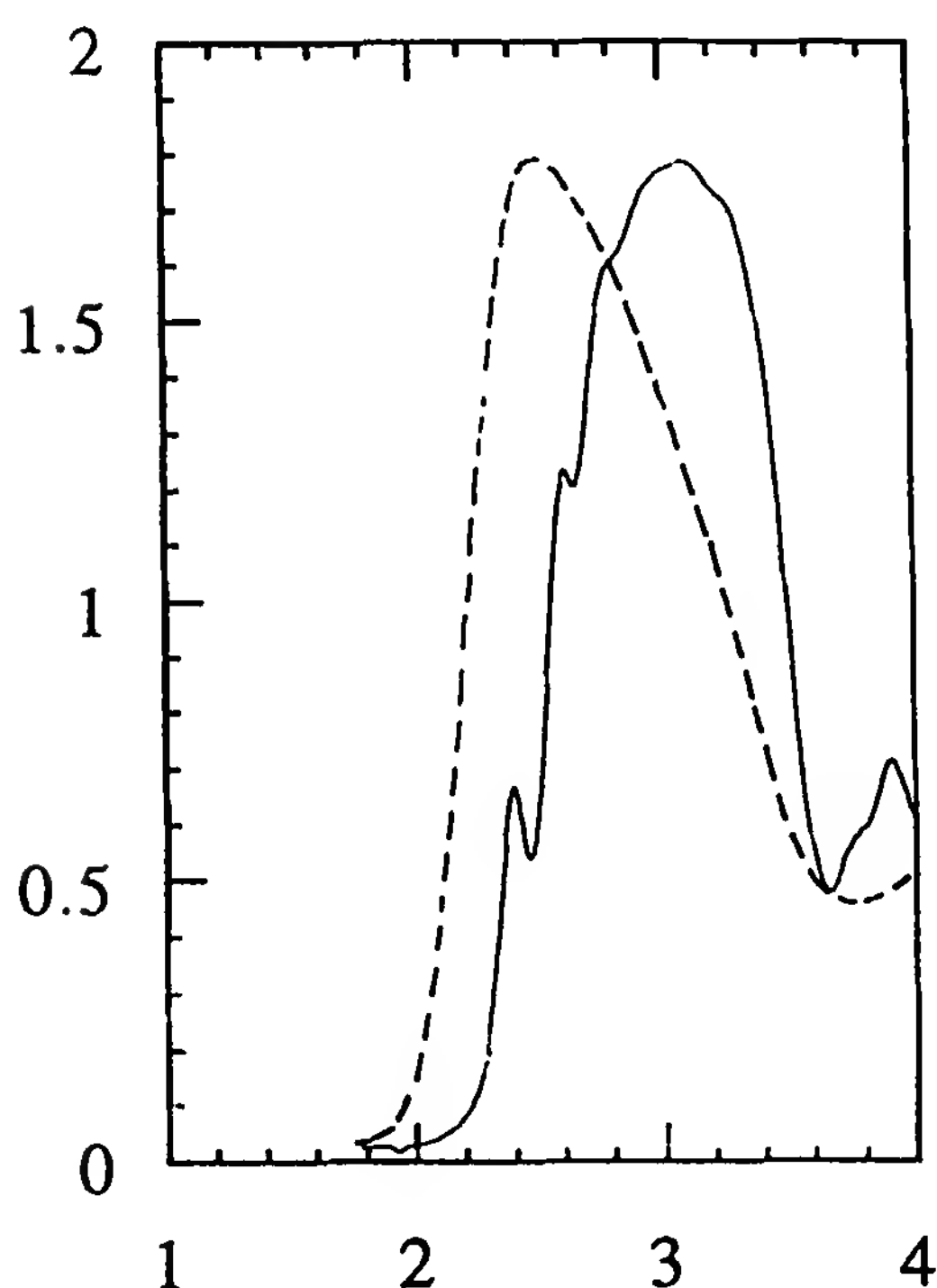


Figure 14 Optical absorption of polythiophene (dashed line) and of the corresponding hexamer α -sexithienyl (solid line).

maximum emission is red-shifted by 0.05 eV only from that of the absorption. Similarly, it has been shown that better control of the transformation into PPV of its precursor greatly changes the absorption spectrum, which is red-shifted and much more structured than the spectra obtained previously. The new spectra shown in Fig. 15 resemble those of PDAs (Fig. 13) rather than those of PA (Fig. 12). Moreover, the emission is highly structured, too, and its maximum is shifted by 0.07 eV only from the absorption maximum [126].

2. Electronic Absorptions Below the Optical Gap: Gap States

In the energy window between the relatively intense infrared vibrational absorptions and the optical gap, only weak vibrational combinations and overtones are present, so low-lying electronic transitions might be observable. Several types of such transitions may be present at these energies. As discussed in Chapter 11, Section IV.C, a degenerate ground-state polymer may contain solitons, which in the SSH model are midgap levels; slight doping may create charged solitons, polarons, or bipolarons, with specific optical absorption patterns. On the other hand, from the exciton point of view, low-lying exciton states may exist: A_g singlets known to be present in polyenes [127] and which cause the large Stokes shift between absorption and emission of the hexamer in Fig. 12a; or triplet (spin 1) excitons, which

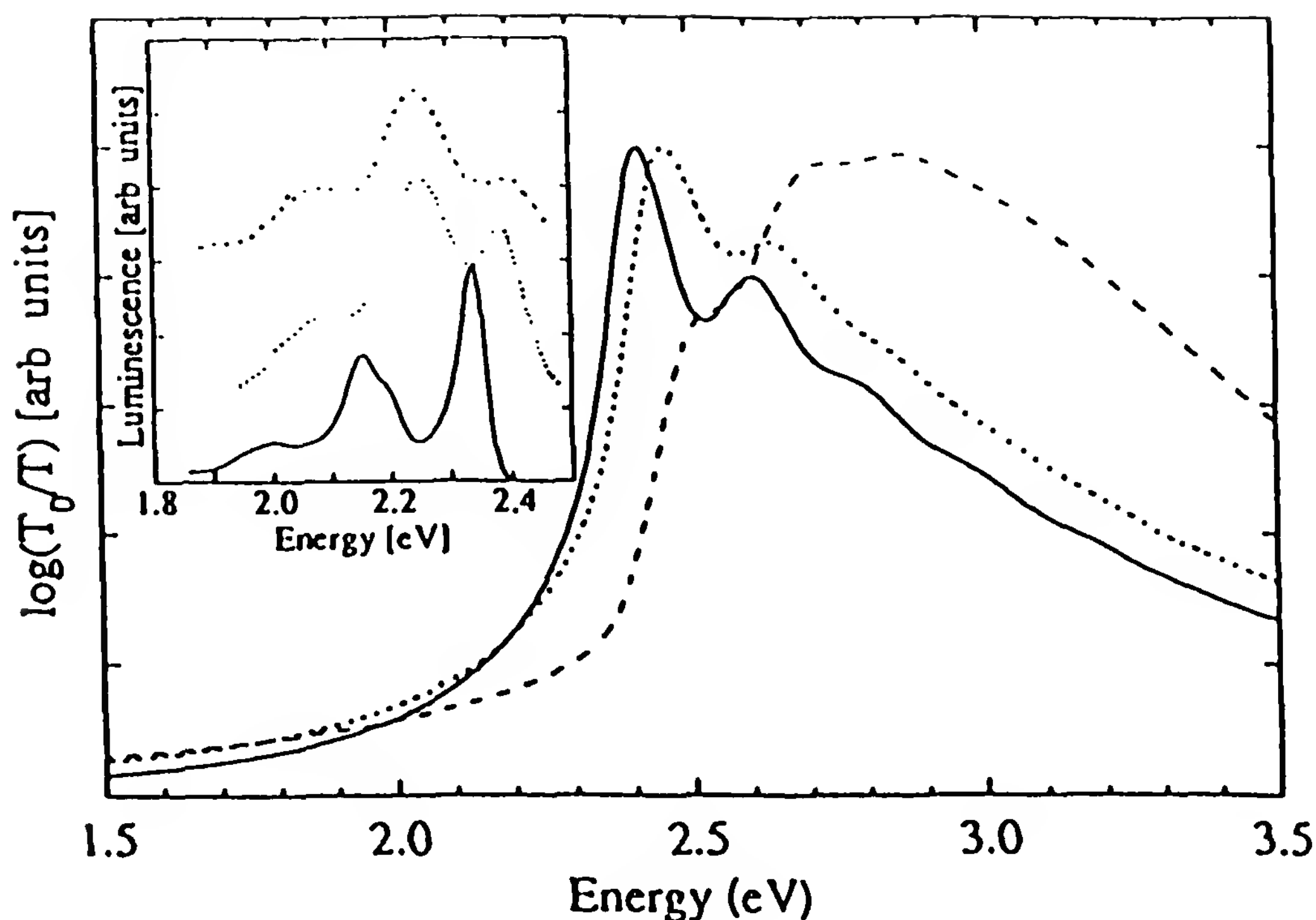


Figure 15 Comparison of emission (insert) and absorption spectra of PPV. Dashed lines: ordinary PPV at 300 K. Dotted lines: PPV prepared as in Ref. 126, at 300 K. Solid lines: same at 80 K. (From Ref. 126.)

are the lowest-lying electronic excited state in almost any molecular crystal [128] or molecule [129]. These are intrinsic excitations present in a perfect pure CP. In addition, impurities may have low-lying excitations of their own, and disorder may generate tails of density of states, extending well below the band edge in amorphous materials.

All CP films are more or less microscopically heterogeneous, so they scatter light. This effect is very large in fibrillar films such as those of *trans*-PA (except when prepared by the precursor route): several percent of the incident light may be scattered, so any “measured” absorption coefficient $\leq 10^3 \text{ cm}^{-1}$ in such films is uncertain [130]. Scattering is almost eliminated in PDA single crystals (but not completely in cast films) [120,131]. To obtain absorption spectra of weak transitions in the presence of scattering requires using methods such as photothermal deflection spectroscopy (PDS) [132]. For these reasons there are not many studies of CP absorption in this energy range. Two examples are given here: PDAs and Shirakawa-type PA.

In PDA crystals, PDS shows that an absorption tail extends on the low-energy side of the intense 2-eV absorption [133]. In poly-pTS, for instance,

the absorption coefficient is down from its maximum value of $>5 \times 10^5 \text{ cm}^{-1}$ [123] by four orders of magnitude at 700 nm, about 0.25 eV to the red of the absorption peak, and is below 1 cm^{-1} beyond 900 nm. Conventional absorption measurements failed to give evidence of any absorption other than vibrational overtones up to $3 \mu\text{m}$ [131,134]. Similarly, in poly-4BCMUs crystals [135] and films [131], the absorption coefficient is everywhere smaller than a few cm^{-1} in that region.

Because of their special polymerization process [136], PDA crystals should not contain any dopant or associated residual polaron or bipolaron concentration. These negative results give some constraints on other low-lying states, especially exciton states. Triplet-state absorption from the ground state would probably be too strongly spin-forbidden to have absorption coefficients as high as 1 cm^{-1} [129]. As for *g* states, the absorption coefficient depends sensitively on how far from the intense absorption they are (for the polyene case, see Ref. 127). That they are not found in these experiments means that they are either above the main transition at 2 eV or not far below it and buried in its tail. Indeed, evidence of a weak absorption $\approx 0.1 \text{ eV}$ below the main transition has recently been found at low temperature [118]; it would be buried in the absorption tail at higher temperatures.

PDS experiments have also been performed on PA [130]; results are shown in Fig. 16. As-grown films show a relatively intense absorption at energies below the absorption edge, which can be eliminated completely by treatment with ammonia. A brief exposure to air restores the absorption, and again NH_3 removes it. As-grown *trans*-PA films have conductivities $\sigma \sim 10^{-5} \text{ S/cm}$ [137,138], much more than the expected σ value of an intrinsic semiconductor with a gap of about 1.8 eV; they are therefore slightly doped, presumably by residual oxygen. NH_3 compensates this doping, and indeed σ decreases by several orders of magnitude. Thus, compensated PA shows no measurable absorption beyond the optical gap except for a relatively broad exponential tail, extending from 1.5 to 0.8 eV at least, which is probably a consequence of disorder. Any absorption observed is related to states involved in the conductivity, either charge carriers (e.g., charged solitons in the SSH model) or electrically active impurities. The experiment does not find neutral soliton absorption where the SSH theory places it (sketched by the solid line on Fig. 16). Any such absorption, if it exists, must be buried in the exponential absorption tail, since it is not found farther in the IR either.

In summary, beyond an exponential (Urbach) tail, which can be due either to phonons or to disorder, there is no low-energy absorption that can be assigned to a neutral state. This conclusion is probably valid for all

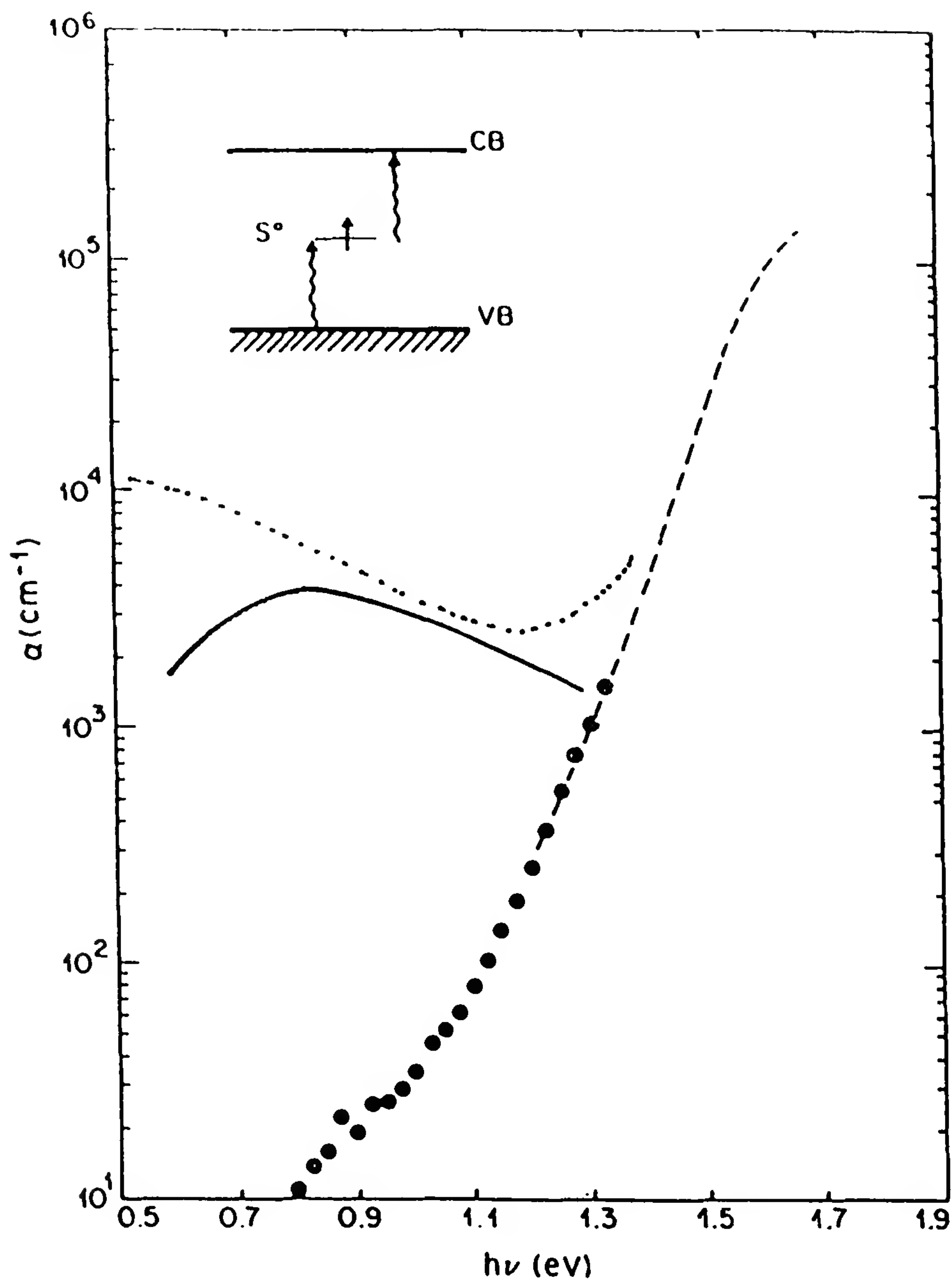


Figure 16 Photothermal deflection spectrum of a NH_3^- -compensated *trans*-PA. Dots and dashed line show the absorption edge recorded on two films, 4 μm and 0.1 μm , respectively. Dotted line shows the residual absorption of an uncompensated sample. Solid line sketches the expected neutral soliton absorption in the absence of electron correlation. (From Ref. 130.)

CPs. This does not mean that there are no such states. Other spectroscopic methods have therefore been applied to this problem: photoinduced absorption and nonlinear optical methods, which we consider next.

3. Photoinduced Absorption Spectroscopy

(a) *Definition and Properties of Photoinduced Absorption*

In most optical transitions, such as those shown on Figs. 12 to 16, the initial state of the system is the ground state, possibly including thermal excitation of phonons, molecular vibrations (called “hot bands” in molecular spectroscopy), or even free carriers in a semiconductor (leading to free carrier absorption in the IR).

A nonequilibrium, nonnegligible concentration of excited states, whatever they are, prepared in a material can serve as an initial state in an optical absorption process. The most common and easiest way to prepare such a nonequilibrium state is by light (although, as mentioned below, other ways can be used), so the corresponding absorption spectra are usually called *photoinduced absorption*. Strongly allowed transitions, different from those from the ground state, can originate from an excited state. If its lifetime is long enough, it may be possible to accumulate, using, for instance, an excitation of sufficient duration or a very intense pulse, a significant concentration of excited states, and the corresponding photoinduced absorption may be quite intense. Whatever the nature of these states, their accumulation in the material implies a corresponding depletion of the ground state, therefore a bleaching of its absorption. Simultaneous study of photobleaching and photoinduced absorption may make it possible to understand the excited-state generation process and to determine its concentration and therefore the absorption cross sections.

In most cases of interest to us, the excited states to be studied are not directly accessible from the ground state, either by light absorption (see Section III.A.3) or thermally. They must therefore be prepared indirectly. Two examples will be given, which correspond to excited states that are thought to be important in CPs: triplet excitons and charged species.

Preparation of *triplet excitons* from states generated by the intense optical absorption is possible in several ways: from the singlet exciton, by intersystem crossing [129], or by a process known as exciton fission, whereby a pair of triplets (of total spin 0) is generated from a singlet (of spin 0) by a spin-allowed process. This is very efficient provided that energy conservation allows it [128,139]; triplets can also result from electron–hole recombination [128]. The triplet lifetime is limited by spontaneous, and generally nonradiative, decay to the ground state [129], or by bimolecular interactions, mainly between triplets [128,139]. It is usually in the microseconds to milliseconds range.

Charge carriers. Free electrons and holes, and the resulting polarons, bipolarons, or charged solitons (see Chapter 11, Section IV.C), can be prepared either by light absorption (as in semiconductors), possibly followed by conformational relaxation, or in the case of bipolarons, by binding, or through ionization of singlet excitons if they exist as in molecular crystals [128]. Note that charge carriers can also be injected in the dark from the electrodes. Their lifetime is limited by recombination. But an important process, almost always neglected in CPs, is trapping of a charge carrier: immobilization onto a chemical or physical defect. Depending on the binding energy of the carrier in the trap, the lifetime can reach milliseconds to hours.

Triplets, and most kinds of charge carriers (see Chapter 11, Section IV.C), have spin, so they can be monitored magnetically, and changes in their concentrations under various conditions can be investigated by methods such as optically detected magnetic resonance (ODMR). An example of such a method applied to CPs is presented in Ref. 140.

After photoexcitation (i.e., preparation of excited states) has stopped, photoinduced absorption will decay with a kinetics characteristic of the excited state concerned. When several photoinduced absorption spectra are present simultaneously, this makes it possible to determine the various spectra separately and therefore to identify the corresponding excited states. Conversely, if the nature of the excited state is known, this is a means of measuring its lifetime.

(b) *Photoinduced Absorption in CPs*

Rather than surveying the entire literature, we shall give three illustrative examples.

PDA seems to be the simplest case among CPs. Leaving aside very rapid (picosecond) processes, only one long-lived excited state has been observed conclusively up to now. It is characterized by a relatively intense absorption near 1.40 eV (the exact energy depends slightly on the PDA chosen and on temperature) [141,120]. Based on ODMR measurements, it has been shown that the corresponding initial state is a triplet [141], and by magnetic field modulation experiments [139] that the triplet is produced primarily by fission of a singlet exciton [142]. Recently, this has been used to determine the energy of the lowest triplet, approximately 1.1 eV above the ground state [143]; this is the first measurement of the absolute position of a triplet exciton in a CP.

The situation in other CPs seems to be more confused. PIA spectra often depend on temperature and time delay after pulse excitation. In *trans*-PA, at low enough temperature and a sufficiently long time, the PIA spectrum consists of three features: a low-energy (LE) asymmetric ab-

sorption band peaking at 0.45 eV, a high-energy (HE) relatively narrow and symmetric absorption peaking at 1.35 eV, and bleaching of the strong absorption above 1.6 eV [144]. These are discussed in several reviews, sometimes with different conclusions [145–147]. LE should be associated with a charged excited state, since it occurs concurrently with IR absorption bands which have been shown to be due to the presence of charges on the chains [146,147]. Recent ODMR studies (see, e.g., Ref. 148) confirm the identification of LE [146] as absorption by a charged soliton; how such states have the long lifetime implied by some experiments [145] is, however, not well understood. On the other hand, HE seems to be associated to a neutral excited state having spin $\frac{1}{2}$ [148], in which case it could not be a triplet as had been proposed [149]; it must be a free radical, and it has been concluded that HE corresponds to absorption by neutral solitons [145,148].

In PPV a PIA peak at ≈ 1.4 eV has been assigned to a triplet–triplet transition from the triplet exciton [148,150], as in PDA (it is not known if the near equality in the energies is accidental). But, in addition, two other induced absorptions are observed near 0.6 and 1.6 eV, and since they are associated with the characteristic IR bands (such as the 0.45-eV band in PA), they should be due to a charged state. The absence of ODMR signal suggests that they have no spin and would then be bipolarons. In “improved PPV” (see Fig. 15), the PIA spectrum contains only the triplet peak [151], suggesting that the presence of the other features is a consequence of strong localization in a defective polymer. Similar results are found in other CPs, but up to now evidence for PIA due to polarons is elusive.

4. Light Emission

Only photoluminescence (i.e., emission following optical excitation) is discussed here. The increasingly important electroluminescence is presented in Section V.C, where its potential application to light-emitting diodes is discussed.

Absolute emission quantum yields η_f are not easily measured in the solid state. However, to a good approximation CPs can be placed in two distinct classes. Some CPs are practically nonfluorescent (yields $\leq 10^{-4}$): for instance, *trans*-PA or PDAs in the solid state. Others have η_f yields greater than 1% and sometimes much more: for instance, about 35% for MEH-PPV [152]. The yields may be limited in the solid state by quenchers for excitons or dark recombination centers for carriers, so they might be improved in better quality materials.

Emission spectra are always structured even if the corresponding absorption is not, and in cases where the absorption is somewhat structured, such as in Fig. 15 or Fig. 17, the two structures are similar. Two examples

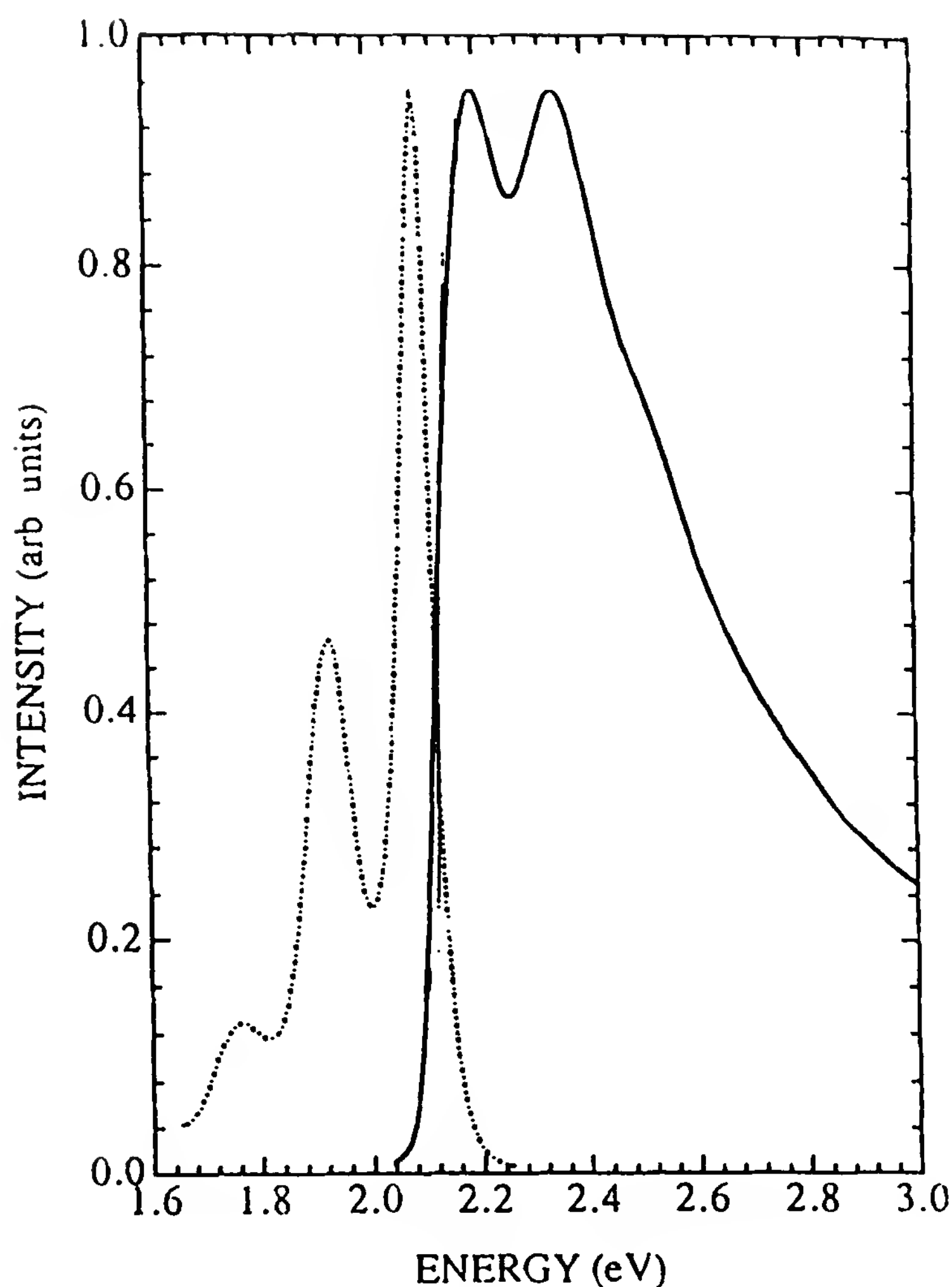


Figure 17 80-K spectra of MEH-PPV/PE blend. Unoriented film. Solid line: absorption. Dash-dotted line: emission. (From Ref. 107.)

are given, in Fig. 17 for an unoriented film of the MEH-PPV/PE blend mentioned above [107] and in Fig. 18 for PPP [153]. The wavelength of maximum emission is often red-shifted (Stokes shifted) from the absorption maximum (Fig. 18), but this is not true at least of PPV (Fig. 16) and of MEH-PPV (Fig. 17). These structured spectra are reminiscent of molecular crystal emissions [128]; indeed, the PPP spectrum is almost identical to that of the hexamer α -sexiphenyl [154]. They are very different from typical radiative recombination spectra in semiconductors, which usually consist of quite narrow lines near the band edge, having no relation in shape with the absorption.

5. Resonance Raman Scattering

Resonance occurs in Raman scattering when the incident energy is equal (or nearly equal) to an allowed electronic transition of the material under

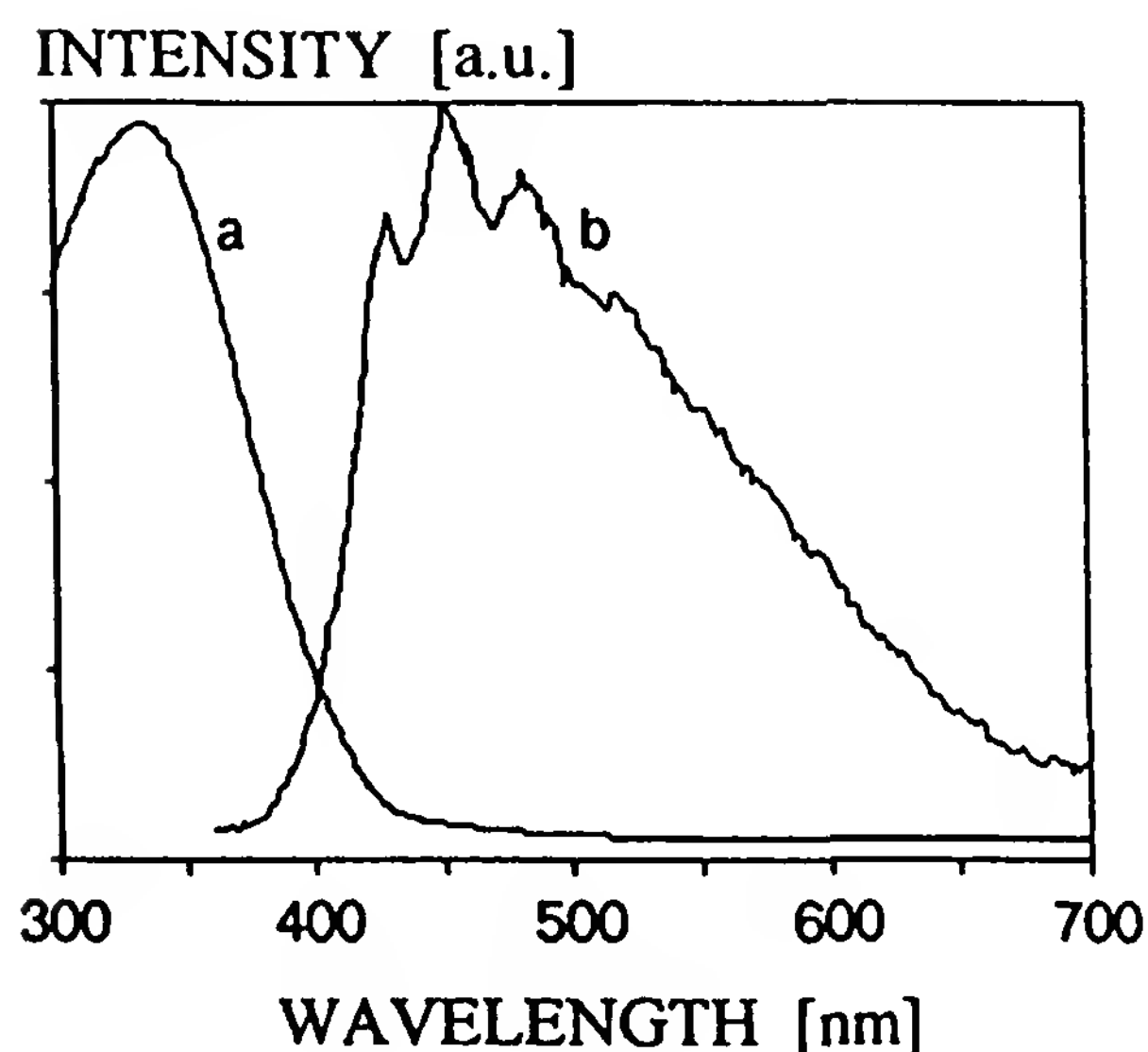


Figure 18 Emission (b) and absorption (a) of PPP at 300 K. (From Ref. 157.)

study. The scattering cross sections for Raman-active vibrations which are strongly coupled to the electronic state may be increased by up to six orders of magnitude. The enhancement decreases as the incident photon energy becomes more different from that of the electronic transition but is still perceptible at a distance of several tenths of an electron volt. Clearly, such a technique has many attractive features for the study of CPs:

1. Conjugated chain vibrations are selectively enhanced. If side groups are attached to the chain, their vibrational Raman lines will not be enhanced. Thus simple resonance Raman scattering (RRS) spectra are often obtained, free of interference from the medium.
2. Resonance depends sensitively on the electron–phonon coupling, which is an important property of CPs. In fact, in the SSH model of PA, it is important in the mere occurrence of the Peierls dimerization.
3. Information on the excited state can be obtained by studying the variation of RRS cross sections with incident photon energy.
4. RRS requires only small amounts of matter: an RRS spectrum of a single PDA chain has even been obtained [155].

RRS, in particular its application to polyenes and PDAs, and the information that can be extracted have been reviewed thoroughly in Ref. 156. Here, only one point will be stressed, which has been the essential issue in RRS studies of CPs: namely, the fact that the position and shape of CP Raman lines may depend on the incident photon energy within the absorption band. A thorough discussion of the theoretical issues may be found in Ref. 14.

This effect is particularly conspicuous in *trans*-PA. Figure 19 shows RRS spectra of *trans*-PA excited at four wavelengths within the absorption band [157]. The spectra contain two main bands, in agreement with theory [158]. For 676-nm excitation, each band has a single maximum and is asymmetric, with a trailing edge toward larger Raman shifts. Essentially similar results are obtained for all longer excitation wavelengths; the lines become narrower and more symmetrical, the minimum fwhm at 2 K being $\approx 10 \text{ cm}^{-1}$ [159]. As the excitation increases, that is, as one goes up into the absorption band, a shoulder develops and turns into another maximum at larger Raman shifts. This second feature becomes dominant and is almost the only one left for excitation in the near ultraviolet.

Similarly, the RRS spectra of polyenes contain two main bands, which shift toward lower frequencies as the number N of double bonds is in-

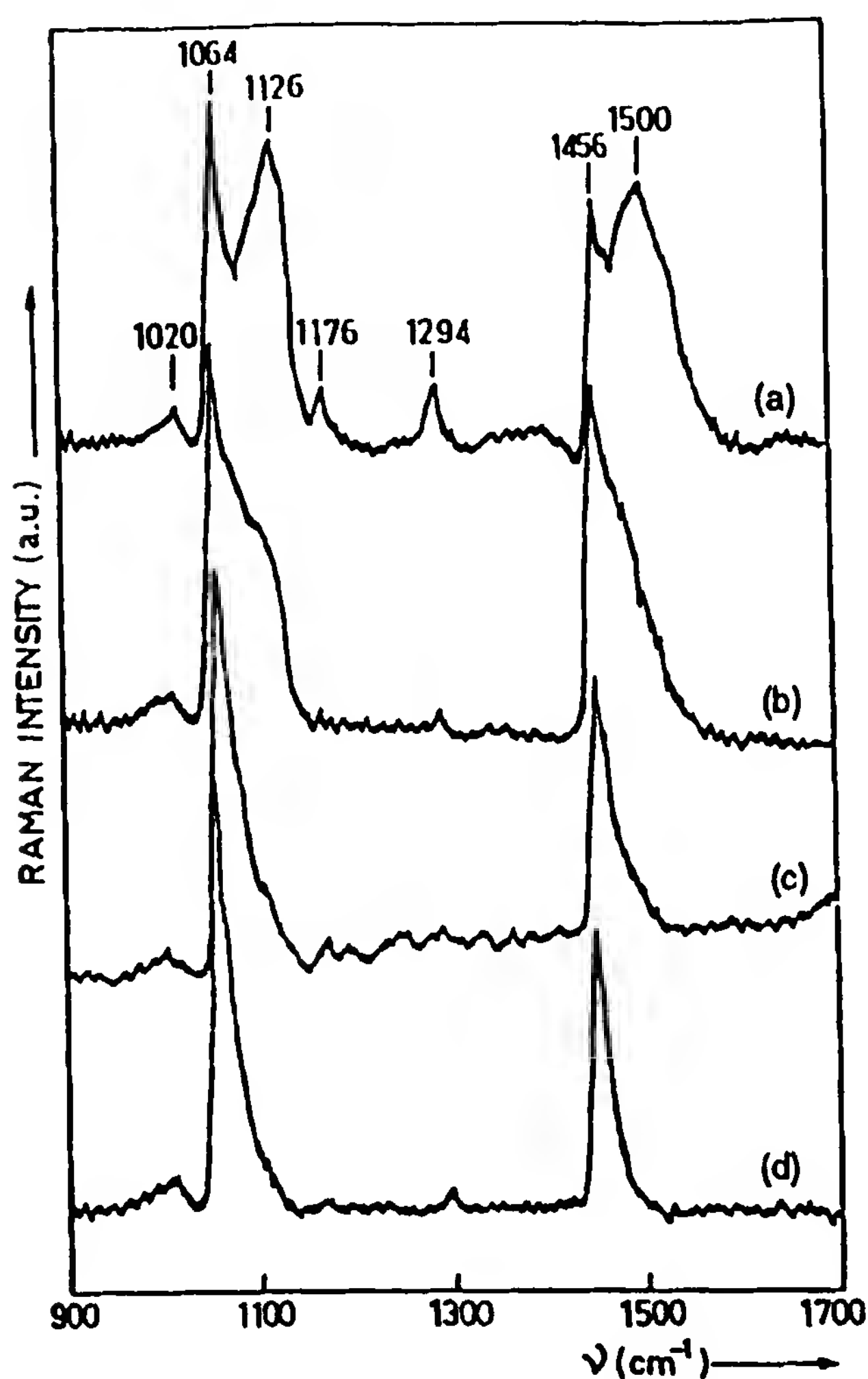


Figure 19 Resonance Raman spectra of *trans*-PA at four excitation wavelengths: (a) 4579 Å; (b) 5145 Å; (c) 6000 Å; (d) 6764 Å. (From Ref. 157.)

creased, following laws of the form

$$\omega_R = A + BN^{-1}$$

with somewhat different values of A and B from different authors [160]. So it was assumed that the changes in *trans*-PA RRS spectra were due to the presence in actual samples of distributions of conjugation lengths bi-univocally related to polyene lengths. This is a good example of the usefulness of oligomer studies. The presence of two features in a single Raman band was then associated with a bimodal distribution of such lengths, with the “short” chains having spectra of the corresponding polyenes, and the long chains having spectra similar to the “infinite” chain but with selection rules relaxed due to the actual finite length [161]. In fact, the subject has been debated hotly, and two other theoretical approaches were proposed; in one, the amplitude-mode formalism, it is a distribution of electron–phonon couplings, related to a distribution of energy gap values, which determines the changes in the RRS spectra [162,163]. This will not be discussed here, and the reader is referred to [14,159,163,164] for discussion; these approaches may not be as contradictory as had been claimed.

Some variations in RRS spectra with excitation energy for polymers or with N for the corresponding oligomers have been observed in several CPs. But these effects are much smaller than in the *trans*-PA case, and less information has been obtained [162,163]. The variations in RRS cross sections with excitation energies have been less well studied than those of the line shapes. It has been found that cross sections have maxima near 1.4 eV, within the absorption edge, approximately where the weak shoulder is shown in Fig. 12 [159].

B. Discussion

1. Nature of the Visible Optical Absorption: Band-to-Band Transitions Versus Excitons

(a) “Pure” Cases. Semiconductors Versus Molecular Crystals

The reason for the existence of an energy gap in *trans*-PA has been much debated and is discussed critically, for example, in [147]: Is it due essentially to electron–phonon interactions (a Peierls gap) [146] or to electron correlations [165]? Both processes are thought to be important, but there is still no agreement on the details of the appropriate description. As for other CPs whose ground state is nondegenerate, a gap is a natural consequence of this fact, but again the role of the Peierls process in increasing its value has been debated. These problems were noted in Chapter 11.

There is, however, a related but distinct question that can be asked for any CP: What is the nature of the states involved in the intense visible

optical absorption; that is, do we observe band-to-band transitions with electron–hole pair generation as was taken for granted for some time? Electron correlations can generate, or contribute to, an energy gap; they can also generate bound electron–hole states below the electron–hole pair creation energy threshold (i.e., excitons).

Two well-known limiting cases are the semiconductors, on the one hand, and the aromatic molecular crystals on the other. In semiconductors, the absorption corresponds to transitions at constant momentum, which can be at any point of the Brillouin zone, so it is proportional to the corresponding joint density of states [166]. In the independent electron approximation and in the textbook case of an isotropic semiconductor with spherical energy surfaces, the absorption coefficient near threshold is proportional to $(E - E_g)^{1/2}$, where E is the photon energy. The overall absorption will then be weakly structured, and the structure will reflect that of the joint density of states. For instance, the absorptions of Si or Ge increase steadily above the gap energy over several eV without any structure. In a one-dimensional system such as an “ideal” CP, the densities of states of each band have a singularity at each edge, as does the absorption coefficient: It is infinite at threshold. In practice, this singularity is suppressed for several reasons, and the absorption will have a maximum near threshold which is sharper the closer the material is to the one-dimensional case and the more perfectly periodic it is. In that limit there are no excitons; they come in when electron interactions are introduced. Their effect on the optical absorption spectrum is not only to add narrow absorption lines near the band edge, but the absorption coefficients within the band near the edge are modified in a way that is sketched in Fig. 20 [167]. The interactions greatly enhance the probability of transition near the band edge, so that the $\Delta E^{1/2}$ dependence is replaced essentially by a step function.

On the other hand, molecular crystals are characterized by the existence of strongly bound (Frenkel type) excitons, and it has been shown that the lower-energy part of the absorption spectrum (say, the first 2 eV) is completely dominated by these excitons [168], even to the extent that the absorption corresponding to electron–hole pair generation is completely hidden in the exciton spectrum [128] and is revealed only by such methods as modulated electroreflectance [169]. The only states in the exciton bands that are accessible by photon absorption are those at the center of the Brillouin zone, so the absorption is not a continuous band as for semiconductors, but a sharp line. The existence of this sharp line therefore does not mean that the exciton band is narrow (i.e., that its dispersion relation in the Brillouin zone is flat). On the contrary, since that dispersion is caused by dipolar interactions, exciton bandwidths can be several eV [168,170]; the total bandwidth is four times the coupling term. This will be particularly

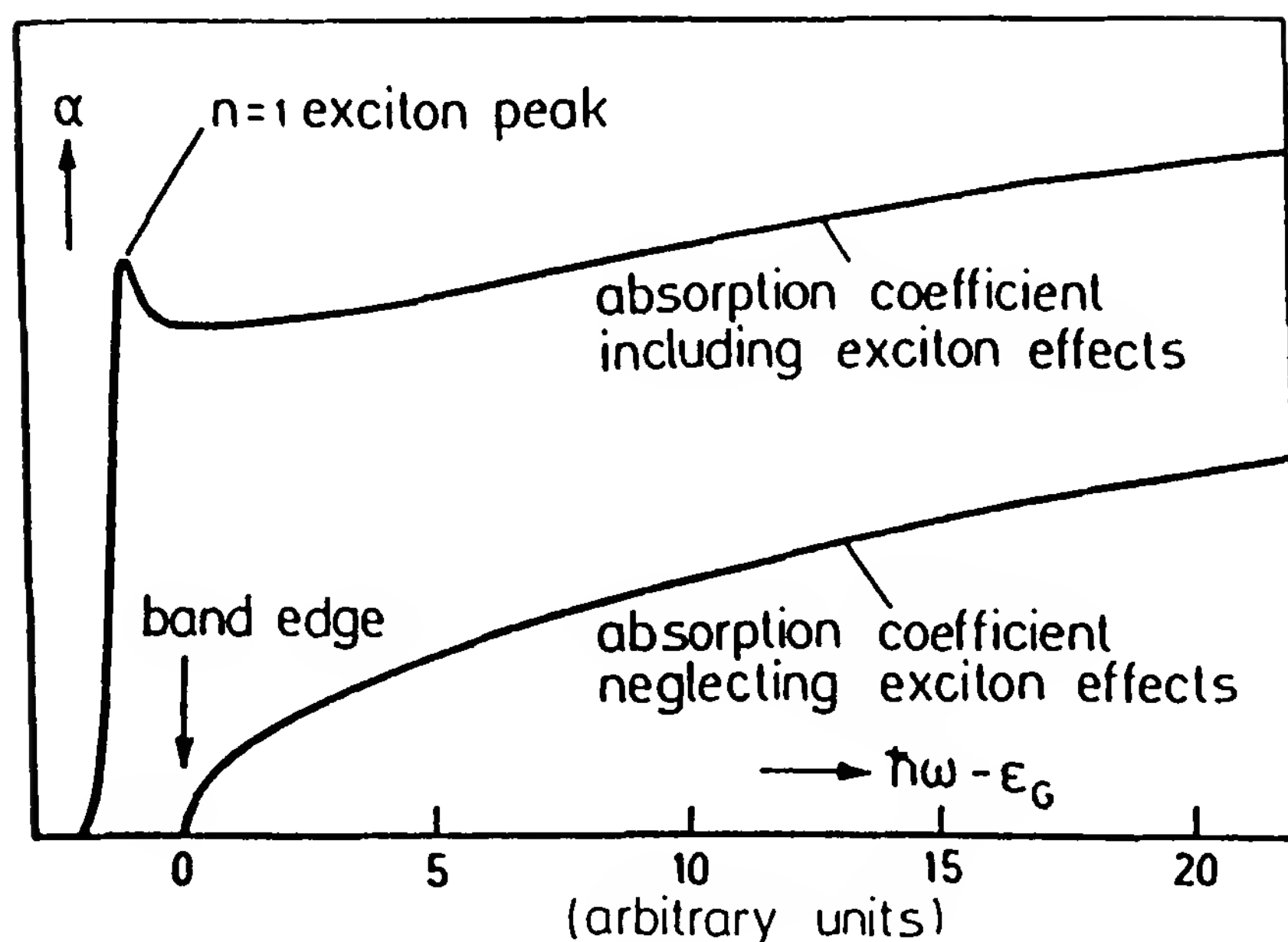


Figure 20 Effect of the exciton on the band-edge absorption in a direct gap semiconductor such as GaAs. (From Ref. 167.)

true in CPs. In addition to the pure electronic transition considered above, joint electron–phonon excitations generate vibronic absorption lines corresponding to simultaneous generation of an exciton and a molecular vibration; the differences in energy between these lines and the pure exciton line are the vibrational quanta in the excited state. Coupling with lattice phonons generates phonon side bands to all these lines. In practice, of course, these features are broadened, particularly by disorder, but amorphous molecular solids still have absorption spectra reminiscent of their crystalline counterparts; some vibrational structure is often still perceptible (see, e.g., Ref. 171).

Exciton luminescence spectra obey the same momentum selection rule, the initial state being almost exclusively, whatever the photon energy, the pure exciton level, since relaxation from the vibronic levels is extremely rapid (in the subpicosecond range), and the final state can be any vibrationally excited sublevel of the electronic ground state, so the emission spectrum should look very similar to the absorption one, and generally it does in crystals. In highly disordered or amorphous molecular solids, however, emission spectra are in general red-shifted from the absorption and much more highly structured. This corresponds to migration of the excitation to a subset of localized lower energy levels with relatively well defined energy. So one should be able to tell the relevance of excitons by analyzing the absorption and emission spectra. This criterion is not too

easy to apply, as the current discussion about CPs amply demonstrates. So, another criterion, based on photoconductivity, has been proposed.

Excitons are neutral quasiparticles, so their creation by light absorption does not generate a current directly. Hence a test for the presence of excitons: If photoconductivity is absent, absorption is excitonic; the onset of band-to-band transitions would then be signaled by the photoconductivity threshold. It is, in fact, not so clear cut, since there are many ways by which exciton decay can generate charge carriers; this is well documented in molecular crystals [128].

(b) A Case of Excitonic Absorption in a CP: PDAs

As PDAs (several of them at least) form true single crystals, all chains are identical and well ordered, thus minimizing the effects of disorder, which is there due primarily to thermal vibrations. No dispersion of Raman frequencies is observed in PDA crystals [156]. Very well resolved absorption spectra are obtained at low temperature (Fig. 21) [118]. All absorption bands shown in Fig. 21, except the small, lowest-energy band, can be accounted for by vibronic transitions associated to a purely electronic transition at 1.8 eV. At the same temperature there is a weak fluorescence whose spectrum is nearly a mirror image of the absorption. The RRS excitation spectrum shows strong, narrow lines similar to the absorption [156]. These are clear spectroscopic signatures of an exciton absorption. This has been generally accepted for some time, and the fact that the

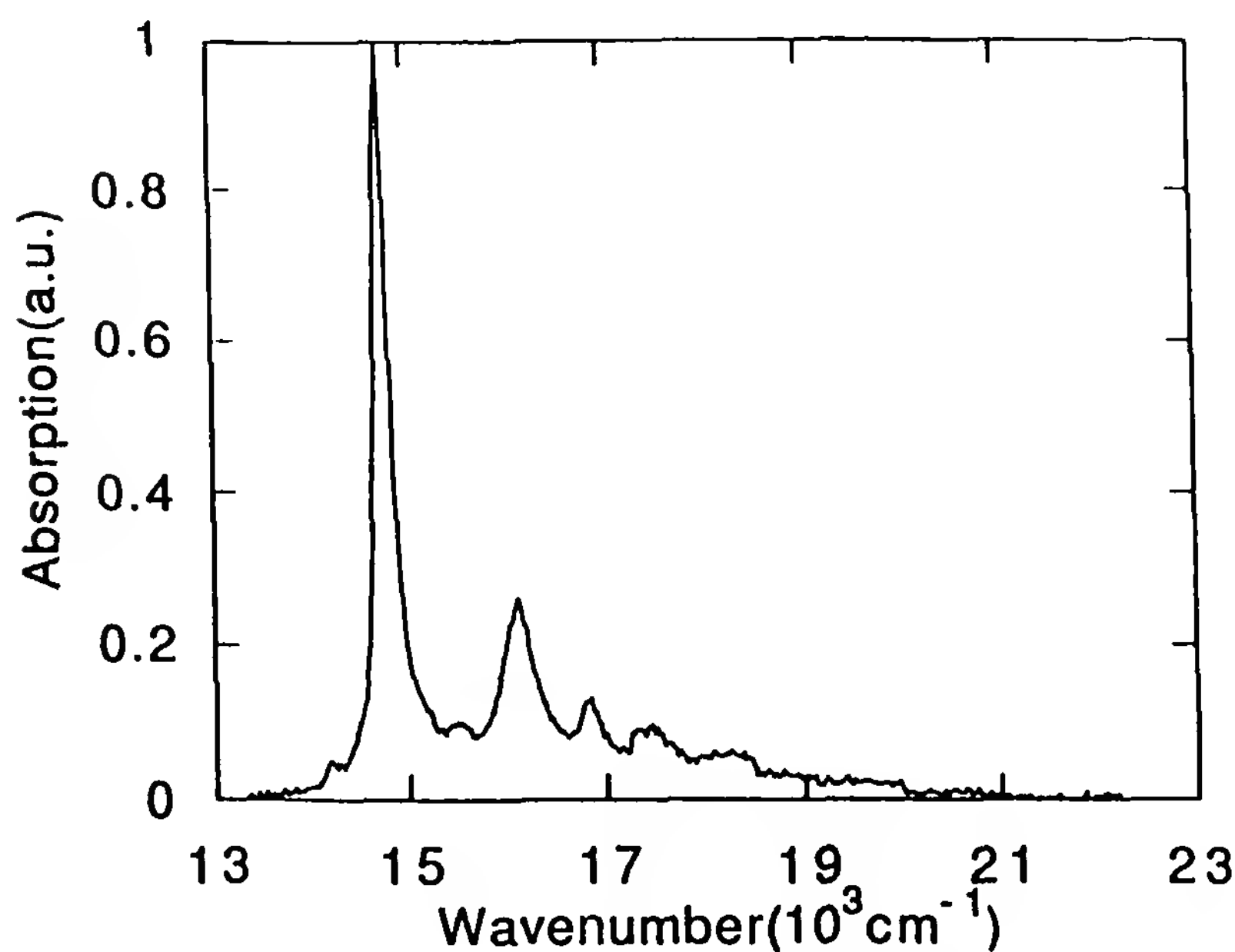


Figure 21 Absorption spectrum of poly-4BCMU chains at 20 K. (From Ref. 118.)

photoconductivity threshold is in some cases well above the optical gap was an important argument for that (this is discussed at length in Ref. 136). There is no reason to believe that the same absorption at room temperature would be no more excitonic. Sill, the PDA spectrum of Fig. 13c is much less resolved than in Fig. 21 and not much more than the PPV spectrum on Fig. 15.

Electroreflectance experiments have been used to locate the bandgap energy [172]. There is no conspicuous feature in the ordinary absorption spectrum at that energy; again, this is typical of a molecular crystal [128]. Recent calculation of the optical absorption of a conjugated polymer, starting from a tight-binding SSH Hamiltonian to which on-site (Hubbard) and long-range intersite electron–electron interactions have been added, yields predictions very similar to the experimental results of Fig. 21: an intense absorption line at the (strongly bound) exciton energy, and an asymmetric band two orders of magnitude weaker, corresponding to band-to-band transitions [173].

These experiments yield an exciton binding energy of 0.5 eV relative to separate electron and hole. This is a large value. An important consequence, although one that is never mentioned, is that in such a case, the polaron binding energy ω_p (see Fig. 7 of Chapter 11) must be larger than 0.25 eV for the absorption between polaron levels in the gap to occur below that of the exciton: in practice, the polaron absorption, if it exists, will remain hidden under the excitonic absorption.

This exciton is just one of the several possible excited states. The lowest electronic excitation is certainly a triplet exciton, noted in Section III.A.3, whose energy is about 1.1 eV [143]. In molecules or crystals with a center of symmetry, states are either symmetrical (*g* states) or antisymmetrical (*u* states) relative to inversion, and optical transitions are allowed to *u* states only [174]; in PDAs, the two excitons discussed above are *u* states. But the lowest singlet state in polyenes is not the *u* state giving the intense absorption shown, for instance, in Fig. 12, but a *g* state 0.4 to 0.6 eV below [127]—hence the red-shifted oligomer emission in Fig. 12. This is a fairly uncommon situation, and in most molecules and molecular crystals, the lowest excited singlet and triplet states are *u* states. The situation in PDAs is not settled: the lowest energy absorption band in Fig. 21 might be a *g* state (perhaps a false origin), and there is some independent evidence of such a state just below the *u* exciton [175]. This could provide a nice explanation for the lack of fluorescence in PDAs, but more work is required.

The final picture of PDAs excitations is distinctly “molecular.” How much of it is applicable to other CPs?

(c) *Trans-PA*

The present situation for PA is opposite that in PDAs. There is no unambiguous evidence for excitons, either in absorption or in the PIA spectra. Variations in Raman frequencies as the excitation energy is increased through the absorption band indicate that this band is broadened inhomogeneously, primarily on its high-energy side, to which the contribution of “short chains” is dominant. This does not seem to be enough to wash out a structure near the band edge, if there was one. The absorption really seems to be a highly asymmetric structureless band, with an exponential low-energy tail, and a decrease on the high-energy side of its maximum very much like what the dielectric function calculated in the SSH model predicts [176]. Electron energy loss spectroscopy (EELS) failed to reveal any other transition below 10 eV [177], in agreement with band structure [178] and dielectric constants [176] calculations. So the case for a band-to-band transition seems strong.

One might then expect a situation similar to the one sketched in Fig. 20, and perhaps assign the weak shoulder on the rising edge of the absorption (Fig. 12) to the exciton. This might explain the large increase in the RRS cross section near that energy, an effect that is known in semiconductors [179,180].

The cause or causes of the opening of a gap in the band structure of *trans*-PA has been the subject of many theoretical papers and of much debate (see Chapter 11, Section IV.A and reviews and discussions in [17,146,147,181]). It would seem that electron–phonon and electron–electron interactions are of comparable importance. If electron correlations are treated by adding a Hubbard on-site interaction term to the SSH Hamiltonian, the available experimental results for *trans*-PA are best accounted for by taking about equal values for the electron–phonon coupling λ and for the Hubbard U . It might be that in other CPs the importance of electron correlations is greater. Note, however, that a U term (on-site interactions) is not enough to treat the correlations correctly, especially if excitons are to be studied (see the discussion of the PDA case above).

This picture of *trans*-PA raises another question. There are extensive studies of polyenes up to at least 12 conjugated double bonds [115,127,160]. The energies of the neutral and ionic excited states decrease smoothly as the molecules become longer, with an ordering similar to the one discussed for PDA. The lowest excited state is a u triplet, then a g singlet, then a u singlet to which corresponds the optical gap, all well below the ionic states [160,182]. How, and for which oligomer length, does this situation evolve to the situation for the polymer? For instance, where is the state that would correspond to the lowest triplet state, which has not been found in the PIA

in *trans*-PA? This is related to the question of the intrinsic conjugation length discussed in Chapter 11, Section II.C.

(d) *Other Conjugated Polymers*

Because of the role played by *trans*-PA as a “prototype CP,” other CPs have been discussed in the same terms as band-to-band transitions without excitons. The spectroscopic data reported above cast doubt on that approach, although recent results are still being so discussed [107]; no consensus has yet been reached.

The PPV spectra of Fig. 16 show all the signatures of exciton absorption and emission, such as in typical molecular crystals. The existence of well-defined structure in the absorption spectrum is not so easily accounted for in a band-to-band absorption model. In semiconductor theory, the main source of structure is in the joint density of states, and none is predicted in one-dimensional band structure calculations (see below). However, CPs have high-energy phonons (molecular vibrations) which are known (see, e.g., RRS spectra) to be coupled to the electron states. The influence of these vibrations has not been included in previous theories of band-to-band transition spectra in the case of such wide bands [176,183]. For excitons, the vibronic structure is washed out in the case of very intense transitions, corresponding to very wide exciton bands, the strong-coupling case [168,170]. Does a similar effect occur for one-electron bands? Further theoretical work would be useful.

The absence of energy shift between absorption and emission thresholds indicates minimal conformational relaxation in the excited state. There is an overall similarity to the PDAs, including the presence of a very strongly bound triplet exciton. The absence of polaron-related transitions in the PIA could be explained if the singlet were as strongly bound as in PDAs. All these properties are important in the electroluminescence processes discussed in Section V.C.

The case of other CPs, such as PT or PPP, is at first sight less clear, since their absorption spectra are almost structureless. The situation here is complicated by the large amount of disorder. However, one may note that the spectra are very similar to those of the corresponding hexamers; for PPP, for instance, the sexiphenyl spectrum is also structureless, and this is related to large conformational changes in the excited state, which is much more quinoid than the ground state (see below). Hexamers still clearly form molecular crystals, so it seems safe to assume that the actual CPs fit into the excitonic picture as well; but that does not disclose what a theoretical infinitely perfect PPP or PT would be (one again encounters the problem of the intrinsic conjugation length). Again, it is the actual polymer that counts in the study of electroluminescence.

2. Band Structure Calculations and Experimental Results

The spectroscopic properties discussed above are related primarily to intrachain electronic structure. One exception is the stability of gap states (e.g., polarons) versus the three-dimensional interaction effects mentioned in Chapter 11, Section IV.D. Energy and charge transport are, of course, dependent on interchain transfers. So while there are only a few three-dimensional band structure calculations (e.g., for PA [184] and PPV [185]), there are many theoretical calculations concerning infinite perfectly periodic one-dimensional chains, the effects of local perturbations, and the elementary excitations of these chains: solitons, polarons, and bipolarons. Only a few hints of that work will be given here. It has been discussed and reviewed several times (see, e.g., Refs. 186 to 188).

There have been two main types of calculations. Elaborate (*ab initio*) methods have been applied to small molecules, essentially oligomers, and mainly to PA oligomers, that is, polyenes (see, e.g., [182]). These methods are accurate and powerful but computer time consuming and therefore limited to relatively small molecules. They yield a precise description of the evolution of the various excited states with the number of repeat units, and they provide a benchmark for other types of calculations. They have been particularly useful in understanding the importance of electron correlations in polyenes, of which the most conspicuous effect is that the lowest singlet excited state is an A_g state [127]. Nonlinear optical susceptibilities have been calculated as a function of length: third-order susceptibilities of conjugated molecules are quite large, and they are predicted to increase as N^4 to N^5 [188]. This cannot go on indefinitely, and understanding how this behavior leads to the finite (and very large) value for the polymer is an interesting problem, connected to the very notion of conjugation length.

(a) *VEH Method*

Most calculations on CPs have used semiempirical methods. The Hückel method yields useful results and many properties can be qualitatively understood [188,190], but numbers are not quite reliable. The valence effective Hamiltonian (VEH) method [191] has been applied successfully to CPs [187,192]. It uses atomic potentials parametrized on the results of *ab initio* HF-SCF calculations on small molecules, and not on experimental data; in that sense, it is a purely theoretical method.

Thus the VEH method can yield reliable results about the occupied states: Valence-band structures and ionization potentials (the absolute value of the energy of the topmost occupied electronic level), and as we shall see, agreement is indeed good. The lowest empty states can be calculated as well, and surprisingly, that yields energy gaps in quite good agreement

with observed optical gaps, although no excited state has been included in the parametrization. Why this is so is not well understood, but that observation prompted use of the VEH method to the study of the effects of doping on the band structure and of the energies of gap states.

The molecular geometries used in these calculations have generally been calculated using MNDO [193,194], a semiempirical method that is known to yield reliable geometries; for polymers, the repeat-unit geometry used is taken from the central part of a long enough oligomer, at least a tetramer. Different VEH calculations on the same polymer do not always give the same results: Compare, for instance, Refs. 124 and 187, and see Table 3. This may be related to slightly different choices of geometry.

(b) Comparison to Experiments

Experimental information on the valence levels comes essentially from photoemission: XPS and UPS measure densities of states (DOSs) convoluted with absorption cross sections, and these DOS values can be compared with those computed from VEH valence-band structures [195]. This has now been done for several CPs and the agreement is good. It would be more instructive to compare the actual band structure to angle-resolved (ARUPS) measurements, but this has never been done. What comes nearest is an ARUPS study of a series of long alkanes taken as models for polyethylene, a nonconjugated polymer [196].

An important parameter is the ionization potential I_p . It is needed to model the energetics of p -doping, in which an electron is removed from the topmost valence levels (see Chapter 13), and also electrical contacts on CPs, in order to understand charge injection, and therefore Schottky barriers, field-effect transistors, and light-emitting diodes, which are studied in Section V.

Two examples of experimental UPS data and their comparison to VEH band calculations are given in Fig. 22a and b for *trans*-PA and PPV [197]. The DOS values calculated have been broadened by an arbitrary Gaussian line shape (the energy resolution of UPS is no more than a fraction of 1 eV) but not corrected for the energy dependence of the cross sections. They have been shifted in energy as discussed below. There is good overall agreement in the top 5 eV of the valence band, and the main features of the experimental spectrum correspond to calculated maxima of the DOS.

The VEH energies correspond to isolated chains in vacuo. It is therefore no surprise that the ionization potentials turn out to be too large, since in the solid state a chain is surrounded by a polarizable medium of dielectric constant 2 to 4. Analysis of a very large amount of data on molecular solids has shown that the difference between the ionization potentials of a conjugated molecule and the corresponding solid, that is, the polarization

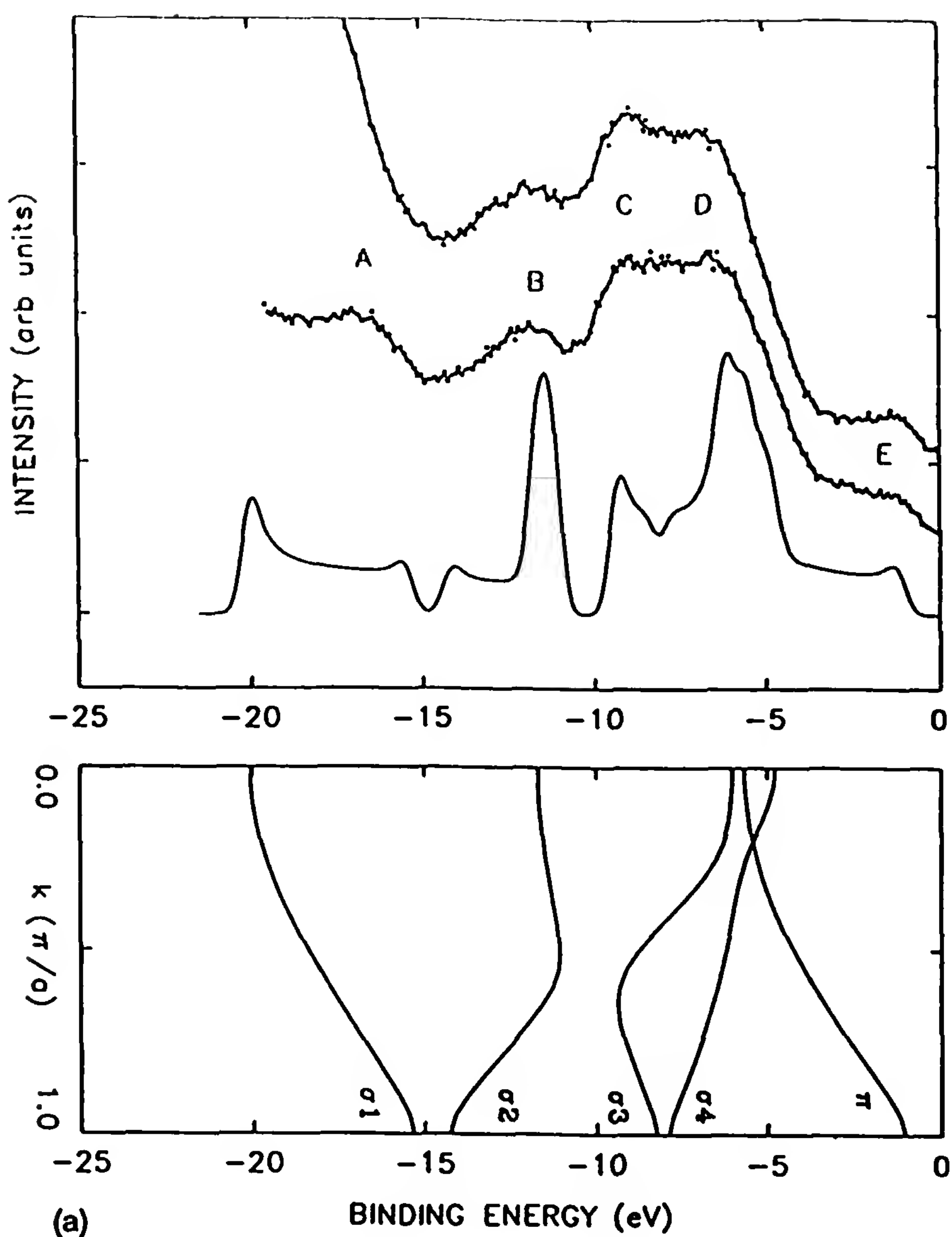


Figure 22 (a) Valence-band spectra of PA, recorded using synchrotron radiation at 27 eV photon energy, and the corresponding VEH DOS curves. The VEH band structure, at the same energy scale, is shown in the lower part of the figure. (b) HeI and HeII valence-band spectra of PPV and the corresponding VEH DOS curves. The VEH band structure, at the same energy scale, is shown in the lower part of the figure. (From Ref. 197.)

energy of the solid by the remaining hole, is about 1.5 eV [128,198]. The value for unsubstituted CPs is likely to be slightly larger, due to the larger polarizability of the chains. In PA, the theoretical estimate differs from the experimental UPS energy by about 1.9 eV [199], and consequently, VEH values of I_p are usually scaled down by subtracting 1.9 eV. The resulting agreement with experiment is quite good, as shown in Table 2.

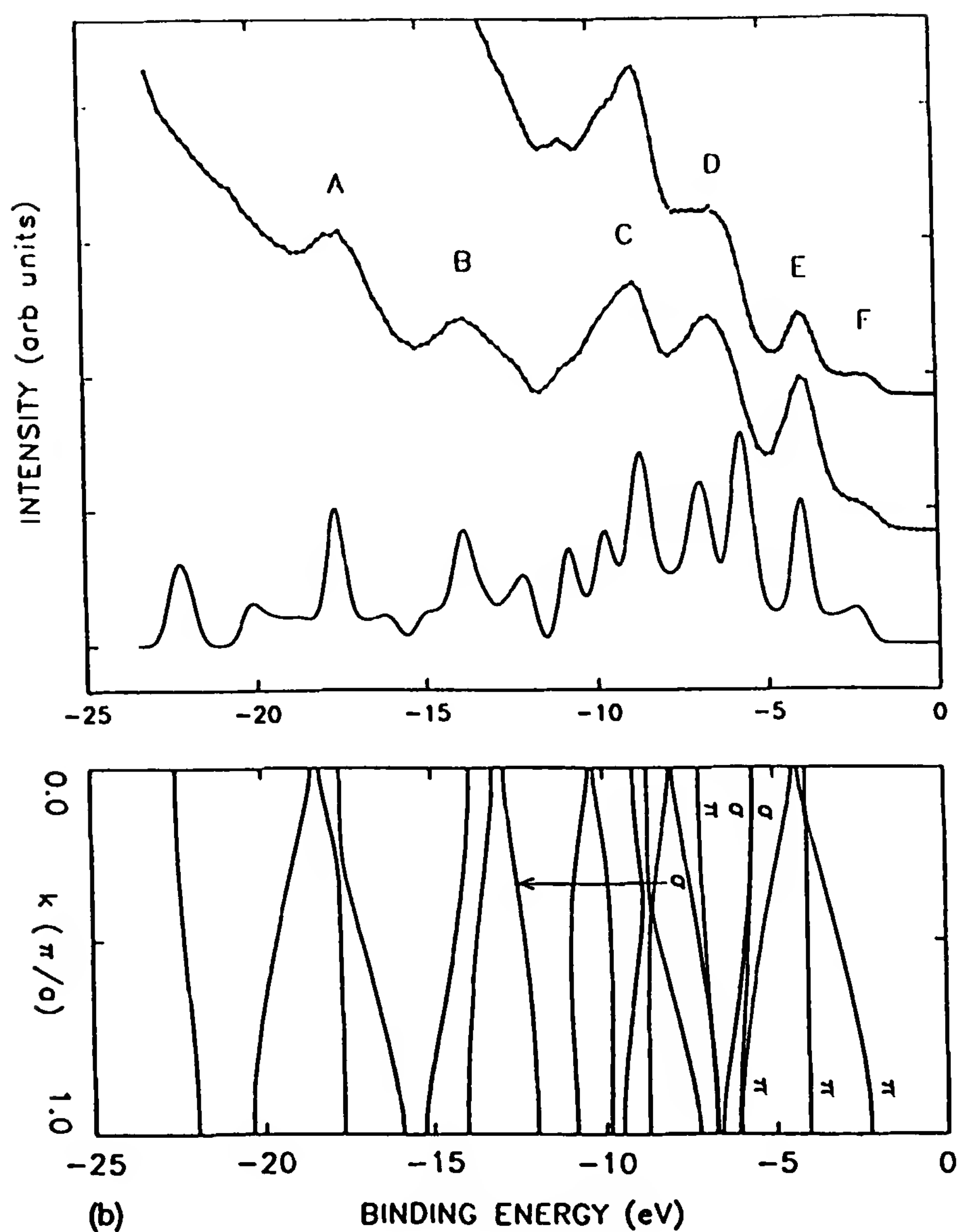


Figure 22 Continued

Another important property is the position of the lowest unoccupied levels, the electron affinity A . Symmetrically to I_p , it determines the efficiency of potential n -dopants and the energy-band positions at an electron injecting contact, which is very important in LEDs (Section V.C). Moreover, the quantity $(A - I_p)$ is the bandgap E_g , which should be accessible to experiment. The two VEH calculations that have been mentioned [186,194] yield more different values for E_g than for I_p , as shown in Table 3.

In the literature, calculated E_g values have been compared to the optical gap (Section III.A.2), assuming implicitly that one-electron band-to-band transitions dominate the optical spectrum. The discussion above has shown

Table 2 Ionization Potentials

	VEH calculations ^a	Experiment	
		Value	Ref.
<i>trans</i> -PA	4.7	4.7	199
PDA ^b	5.1	5.3	201
PPP	5.4–5.6	5.65	202
PPV	5.1–5.2	5.2	200
PT	5.0–5.1		

^aFrom Refs. 187 and 124; after subtraction of 1.9 eV.

^bSince the large side groups are less polarizable than the chains, the polarization correction is probably less in PDAs.

Table 3 Energy Gaps

	Calculated VEH values		Experimental optical gap: absorption		Electro- chemistr [124]
	[187]	[124]	Threshold	Maximum	
<i>trans</i> -P	1.4		1.4	1.8	
PDA	2.1		1.9	2	
PPP	3.5	2.9	2.9	3.2	2.85
PPV	2.5	2.2	2.4	2.55	2.4
PT	1.6	1.7	2.0	2.55	2.25

that this is not obvious; if exciton effects are important, E_g should be larger than the optical gap by a fraction of a volt. E_g has also been compared (e.g., in Ref. 124) to the difference between the electrochemical reduction and oxidation threshold potentials. The latter values tend to be smaller than the optical gap, suggesting a systematic bias of unknown origin and importance. Results are given in Table 3, which shows that calculated values of E_g tend to be too small. In the only case where it is experimentally known (for PDA), the difference is ≈ 0.5 eV.

Several recent calculations have considered the effect of substituents on the band structure, I_p and E_g , as, for example, in Ref. 124. The effect of a substituent can be chemical, by direct electronic interaction with the chain (a methoxy group $-\text{OCH}_3$ may be an example). In other cases, it would, rather, change the chain conformation by, for example, forcing a torsion, either regular (hence a helicoidal conformation) or not; long alkanes may be examples. So VEH calculations at varying geometries for a

given polymer have been performed, for instance, on PT as a function of intermonomer torsion [203].

Finally, let us just recall that the VEH method, and others as well, have been used to study the evolution of gap states into polaron or soliton bands, for example, upon doping [146] (see, e.g., Ref. 204 for *trans*-PA and PT).

(c) Exciton Band Calculations

Excitons have energy–momentum dispersion relations as well, and exciton band structures have been studied in molecular crystals in the past [168,205], but to date, theoretical work on excitons in CPs has been concerned primarily with calculating the binding energies and electronic structure (i.e., charge-transfer character and extension of wave packets) of the various types of excitons and the position of their absorption lines (see, e.g., Ref. 173). Most theoretical studies to date have for obvious reasons been concerned with PDAs [206–208]. Calculations on PDA predict excitons bandwidths of ≈ 3 eV [207].

In fact, an exciton approach was applied to carotenoids many years ago [209]. This approach was revived recently and applied to polythiophene solutions and oligomers [210]. The experimental spectroscopic results are easily accounted for, so this type of work should be continued, especially if excitons turn out to be quite strongly bound in other polymers of practical interest, such as PPV. It will also be needed to understand the vibronic interactions apparent in some spectra.

IV. SOME REMARKS ON ELECTRICAL CONDUCTIVITY

A. Electronic Energy Levels and Experimental Techniques

1. Introduction

Almost all the work on conductivity of CPs has been on doped materials. These problems are discussed in Chapter 13 and have been critically reviewed several times (e.g., in Refs. 5, 17, 36, 52, 92, 146, 147, and 211). Here we are concerned with undoped, meaning, in fact, nonintentionally doped, CPs, such as those used in the potential electronic applications considered in Section V. Their electrical properties are still poorly understood.

The transport properties of such disordered materials (see Section II) are difficult to study, for several reasons. One is that the microscopic theory of transport is not clear even for perfectly ordered CPs, as discussed in the reviews mentioned above. Another is that a dc or low-frequency conductivity measurement on an inhomogeneous material can be viewed as measuring several resistances in series, the larger playing the major role. For instance, in a fibrillar material interfibril transport is important, in a mixed crystalline–amorphous medium the amorphous regions may limit

the current, and so on. Even for highly conducting *trans*-PA [36,92], the measured values of σ seem to be limited by tunneling through barriers and not by the transport properties of the chains. Recent progress toward more homogeneous or better oriented materials may open new possibilities.

So the discussion in Section IV.B will be limited to a few problems: the conduction in PDAs, taken as CPs with minimal disorder; and some recent work on oligomers and polymers, mainly in the PT family, that has used mainly the field effect. Early work had concentrated on *trans*-PA, with interest in the possible role of charged solitons; for this we refer to the reviews cited above.

2. Electronic Levels Involved

The optical properties presented in Section III show clearly that CPs are all wide-bandgap semiconductors, E_g being 2 to 3 eV. In their undoped state, the room-temperature dark conductivities vary widely for the different materials, the most conducting being Shirakawa-type *trans*-PA with $\sigma \approx 10^{-5}$ S/cm [137,138,212], but some CPs, such as the PDAs, have very small σ and the current flowing in such crystals is mostly injection current [213]. The latter situation is more in line with a wide-bandgap semiconductor with no shallow levels. Whatever the conductivity observed, it must be of extrinsic origin, corresponding to shallow enough acceptors, since the conductivity is always *p*-type. It has been proposed, for instance, that the active levels in *trans*-PA may be associated with catalyst residues [216], and since compensation by NH_3 decreases σ by orders of magnitude [130], that oxygen plays the role of a dopant. Thus acceptors are present in the forbidden gap, and they influence the position of the Fermi level and the free carrier concentration.

This is not the entire story, however, for two reasons:

1. All real CP samples except PDAs are disordered, as shown in Section II. Disorder is usually associated with band tails, that is, energy levels extending from the band edge into the gap and corresponding to states localized in space. That this is so in CPs as well is shown by the absorption tails extending below the optical gap [130]. These states will influence the motion of carriers.
2. Molecular solids always contain traps, localized levels deep into the gap in which carriers can be immobilized. These levels are important in transport and recombination [128] and in injection currents [215]. In particular, they can greatly decrease the apparent mobilities (this is discussed further in Section V).

3. Experimental Techniques

Most measurements have been concerned with σ and the thermoelectric power S as a function of T . S is always positive and on the order of 1 mV/K.

σ decreases rapidly with temperature and the variations have been fitted by various theoretical expressions, such as $\sigma \propto T^n$ with $n \approx 14$, or $\ln \sigma \propto T^{-1/3}$ or $T^{-1/4}$, with comparable degrees of agreement [17]. All attempts at galvanomagnetic studies are on doped samples. All this is not enough to establish a microscopic theory of transport.

In molecular crystals, a great deal of information has been obtained by measuring the drift mobility of carriers [128]. At least three methods are available: time-of-flight measurements [216], variation of injected space-charge-limited current with applied voltage [215], and field-effect measurements (see Section V.B). What is obtained in general is a quantity averaged over a distance large compared to a chain length, so it at least includes many interchain hops; the result is not unambiguously related to intrachain transport, which is the problem of interest in most theories, but it may yield an empirical parameter of great interest for electronic applications.

B. A Few Experimental Results

1. PDAs: A Model of CPs Without Disorder

In PDAs one would expect to have only two processes to consider: transport along a really periodic chain, and all similar interchain hopping events. The case of PDAs illustrates the ambiguities of transport studies on CPs. Early time-of-flight experiments yielded mobilities $\approx 5 \text{ cm}^2/\text{V} \cdot \text{s}$ along the chains, and $\sim 10^{-3}$ along the perpendicular directions [217]. A mobility of a few $\text{cm}^2/\text{V} \cdot \text{s}$ is typical of a molecular crystal, and the polymer character was not apparent.

Soon after, photoconductivity experiments were interpreted totally differently. It was proposed that electrons have in fact very high low-field mobilities, on the order of $10^4 \text{ cm}^2/\text{V} \cdot \text{s}$ or more, their velocity saturating at the sound velocity as field is increased above a value of a few V/cm. The moving carriers were supposed to be polarons dressed with acoustic phonons [218,219]. This has not generally been accepted nor conclusively disproved. However, space-charge injection current experiments yielded electron mobilities on the order of $6 \times 10^3 \text{ cm}^2/\text{V} \cdot \text{s}$ [220].

More recent work [221–225] has not yet resolved the puzzle. It seems, however, that the small mobilities obtained initially were influenced by trapping, and the intrinsic value should be larger. Evidence for a sublinear increase in drift velocity with electric field and a tendency toward saturation has been found [224], but at a much higher field than proposed earlier. The lower limit of the low-field mobility would be about $10^3 \text{ cm}^2/\text{V} \cdot \text{s}$. But since the chain length in the PDAs investigated to date is not known, the relative influence of intrachain transport and interchain hopping in this value is uncertain. It will be some time before values to be compared to a theory of transport in a CP are available. The high electron mobilities

(the behavior of holes is not known) are limited in practice by trapping by a factor on the order of 10^{-3} . Trapping can be expected to be even more severe in disordered CPs—that is, almost all of them.

2. Use of Field Effect to Evaluate Mobilities

As discussed in Section V.B, the drain current I_d of a field-effect transistor is proportional to a carrier mobility, and since all other parameters can be determined, this provides a way of measuring the so-called field-effect mobility μ_{FE} .

This is useful, but the value obtained may not be, and generally is not, easily interpreted. First, the carriers are confined to a very thin channel near the CP–insulator interface of the transistor, and such a region may be structurally different from the bulk and contain different impurities. Second, this is an effective value, influenced by any trap present and by the surface states. These difficulties are shown clearly by the fact that the value of μ_{FE} in a given material depends on the nature of the insulating material used, by up to an order of magnitude [226].

There are a few such measurements on polythiophene, where a μ_{FE} value of 10^{-5} to 10^{-4} $\text{cm}^2/\text{V} \cdot \text{s}$ has been found [227]. Even accounting for trapping, this is a very small value. The most systematic measurements have been performed on several unsubstituted or substituted thiophene oligomers [226,228]. Values of μ_{FE} are between 10^{-7} and 10^{-1} $\text{cm}^2/\text{V} \cdot \text{s}$, the largest values for the hexamers. For instance, α -sexithienyl has a μ_{FE} value of 2×10^{-3} to a few 10^{-2} , depending on the insulator. The carriers are holes.

It is interesting to compare these values with the result of another method, the analysis of current–voltage relation for space-charge-limited currents. Such a study on α -sexithienyl [229] has given an effective mobility $\mu \approx 2 \times 10^{-2}$ $\text{cm}^2/\text{V} \cdot \text{s}$, limited by traps 0.28 eV above the top of the valence band. Thus the trap-free “microscopic” mobility is likely to be at least two orders of magnitude larger, a typical value for a molecular crystal.

V. SELECTED POTENTIAL APPLICATIONS

A. Metal–CP Contacts

1. Introduction

It was seen above that as obtained from synthesis and isomerization, *trans*-PA has an optical absorption threshold near 1.5 eV, and a room-temperature conductivity $\sigma \approx 10^{-5}$ S/cm due to slight unintentional *p*-doping, possibly by oxygen or catalyst residues [137,138,212]. It can be increased by slight deliberate doping. Other undoped CPs usually have higher absorption energy thresholds and higher resistivities; generally, $\sigma \leq 10^{-8}$ S/cm for those used in electronic device studies (see, e.g., Ref. 226). They can be

considered as high-resistivity semiconductors, which could possibly find applications in electronics or optoelectronics. Electronic applications would require controlled doping and/or a good knowledge of metal–CP interfaces (i.e., electrodes). Two research fields related to two such potential applications will be briefly reviewed: thin-film transistors and light-emitting diodes. These studies are now in the state where practical applications appear possible.

Optical applications that have been considered do not require the presence of free electrons, only that of extended conjugation; doping is unnecessary. Several CPs, particularly the PDAs, have very large third-order susceptibilities $\chi^{(3)}$; their nonlinear optical properties are currently under active study, and operation of simple devices has been demonstrated, but we are far from being able to consider actual technical developments.

The standard method of adjusting the conductivity of a semiconductor and choosing the nature (electrons or holes) of the dominant, majority, carriers is by controlled doping. Dopants are incorporated into the solid's covalent bond network. This allows the construction of *p-n* junctions in which the concentration profiles of the dopants, and therefore the spatial dependence of the energy-level positions, remain stable despite the existence of high internal electric fields. *p-n* junctions have been the basic element of many electronic components [230].

Doping in CPs is, as already mentioned, an intercalation of ions. Dopants move relatively easily at room temperature (cf. the fast kinetics of electrochemical doping or undoping), and attempts at preparing *p-n* junctions by selective diffusion of two dopants eventually lead to compensation of the donor by the acceptor and to an homogeneous insulating material. Consequently, stable *p-n* junctions could not be developed in CPs. To control and adjust the positions and spatial variations of energy levels, interfaces between a metal and a CP were therefore used; one could use a heterojunction between a semiconductor and a CP, but most studies use fairly highly doped (or even metallic) CPs, such as in Ref. 231. A brief survey of some basic properties of metal–semiconductor contacts, with application to CPs, is given in Section V.A.2, where ohmic contacts and Schottky barrier contacts are discussed.

Early studies of metal–CP interfaces, particularly Schottky barrier metal–CP diodes, were motivated primarily by possible applications in photovoltaic energy conversion. Work on *trans*-PA as of 1985 was reviewed by Kanicki [232]. Unfortunately, the photovoltaic yield of CPs never exceeded about 1%, so interest in that field subsided, and it will not be considered further here. A more recent review is given in Ref. 233.

The study of metal–CP junctions also led to that of thin-film field-effect transistors (TFT-FET). The fibrillar or at least inhomogeneous morphology of early CPs certainly was a drawback, so the new processing methods (see

Chapter 11, Section III.C) that allow preparation of homogeneous films of controlled thickness, gave a boost to such studies. FETs using conjugated polymers or oligomers are discussed in Section V.B. Although CP FETs still have relatively poor performances, devices using oligomers now approach the characteristics of amorphous-Si devices used, for instance, in liquid-crystal flat-screen panel multiplexing [234], so there is some hope that organic FETs may find a market (although the emergence of a new technology requires more, i.e., that it is not equivalent to existing ones but better, simpler, and/or cheaper).

More recently, emission of light by a metal–CP–metal sandwich has been observed [235]. This is again a thin-film device, analogous to conventional MIM devices [230]. To some extent, such a light-emitting diode (LED) can be considered as the reciprocal of a photovoltaic cell. In the latter, absorption of a photon creates an electron–hole pair that is collected in the external circuit, whereas in the former, recombination of an electron and a hole that have been injected from the electrodes generates an emitted photon. LEDs using CPs are discussed in Section V.C.

2. Metal–Semiconductor or Metal–CP Contacts

Up to now, metal–CP interfaces have in most cases been discussed within a very simplified model: an abrupt separation, with no localized electronic states (interface states), between two media which are homogeneous right to the interface. The vast amount of work on semiconductors [236,237] has shown that this is not usually true. Nevertheless, some basic properties are already evidenced in that model, which we shall use to begin with, but with the caveat that one should not expect from it a detailed understanding; this is considered further in Section V.C.

Almost by definition, an electronic device has at least two contacts. Here we consider a single one; therefore, it is assumed that the bulk conductivity of the material and the distance between contacts are large enough, so that over most of that distance the material's energy levels are not influenced by the contacts. This is not true in the case of space-charge-limited currents [215], especially in double injection, a situation that may occur in CP LEDs (see Section V.C).

At equilibrium, the Fermi energy is the same on both sides of the interface. But since this energy is not, in general, the same in the bulk of the materials before contact, relative to vacuum level, the positions of the valence- and conduction-band levels in the semiconductor must adjust: band bending occurs. The two most probable cases are sketched in Fig. 23, for a *p*-type semiconductor, since CPs are generally so.

The position ϕ_m of the metal Fermi level versus vacuum level (its “work function”) is known experimentally and varies from ≈ 2.15 eV for cesium

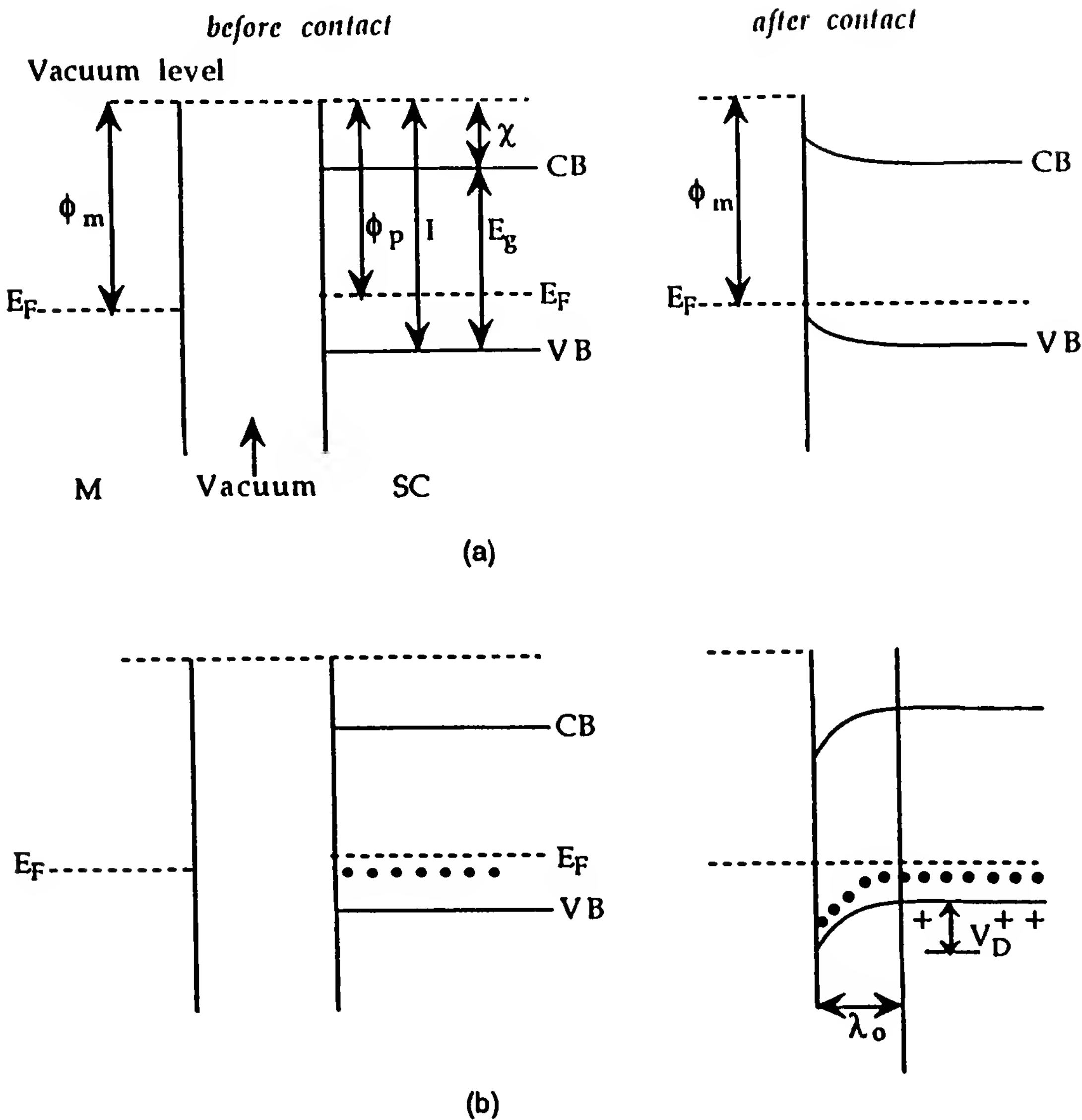


Figure 23 Ohmic contact (a) and Schottky barrier contact (b) between a metal M and a *p*-type semiconductor SC. Energies ϕ , I , χ , and E_g are defined in text. E_F , Fermi level; VB valence band, or hole conducting levels; CB, conduction band, or electron conducting levels. Dots indicate the acceptors; crosses indicate the holes in the SC outside the depletion layer.

to ≈ 5.7 eV for platinum or rhenium [238]. However, it is also known that these values can be greatly affected by surface contamination, so there may be a doubt about the value relevant to a real metal–CP contact.

On the CP side, the situation at the interface and the spatial variation of the energy-level positions away from the contact depend on two parameters: the Fermi level position ϕ_p and the energy of either the top of the valence band I (the ionization potential) for the holes, or the bottom of

the conduction band χ (the electron affinity) for the electrons, with the relation $I = \chi + E_g$, where E_g is the forbidden gap width. In CPs as in semiconductors, ϕ is not an intrinsic property of the material. It depends on the nature and concentration of the gap states; consequently, it is rarely known, and almost never accurately, in undoped polymers. In cases where the doping has been adjusted electrochemically, the potential that has been applied to the CP layer defines ϕ_p (see Chapter 13 or any textbook on electrochemistry), assuming that ϕ_p does not change subsequently. The ionization potential I can, in principle, be measured as the photoemission threshold, but this has been done for a few CPs only. In most cases the values quoted and used are calculated, often using the VEH method [239], or inferred from electrochemical redox potential measurements [124], and systematic errors are possible in both cases. Generally accepted values are between about 4.8 eV (for *trans*-PA) and 5.4 eV (for PPP), most being between 5 and 5.2 eV.

The electron affinities of the CPs are even less well known. They are difficult to measure directly, so χ is generally inferred from $\chi = I - E_g$, or from electrochemical measurements [124]. Unfortunately, both methods are unreliable (see Section V.C.3.b). The generally quoted values for E_g , hence for χ , vary in a larger range among CPs than do values of I , from $E_g \approx 1.8$ eV, hence $\chi \approx 3$ eV for *trans*-PA (and even $E_g \approx 1$ eV for the less studied polymer isothianaphthene [240]), to $E_g \geq 3.5$ eV, hence $\chi < 2$ eV, for PPP, most values clustering around $\chi \sim 2.5$ eV.

Figure 23 shows the two main situations; both are important in electronics. An ohmic contact on a semiconductor is usually defined [230,237] as a contact whose impedance is negligible compared to the total impedance of the device, and which does not affect the bulk carrier concentrations far into the semiconductor. In some cases this is equivalent to saying that it can furnish any required current of the carriers for which it is ohmic, and does not prevent carriers from leaving the material. The words *ohmic contact* are usually used in that sense, meaning, in the case of insulators, injecting contacts (i.e., contacts capable of providing space-charge-limited currents under any circumstance) [215].

Ohmic contacts such as shown in Fig. 23a for holes (the majority carriers in CPs) require $I - \phi_m$ to be as small as possible, or even negative. For $I \approx 5.1 \pm 0.3$ eV, this can be achieved with several metals, such as gold. The corresponding condition for electrons is $\phi_m - \chi$ as small as possible, or even negative, and this condition is met by highly reactive metals only. Obtaining electron injecting contacts on CPs will therefore be difficult. This is not a problem for FETs, which with CPs work exclusively with the majority carriers, holes; but it is a problem for LEDs, whose operation requires injection of both types of carriers.

If $I - \phi_m$ or $\phi_m - \chi$ is large, bands on the semiconductor side are strongly bent so as to form a barrier, as shown in Fig. 23b. This is known as a Schottky barrier. In the region adjacent to the interface within the semiconductor, the valence-band edge is moved farther from the Fermi level, so the free carrier density is very much decreased: this is called the depletion region.* The theory is treated in detail in many textbooks [236,237] and will not be repeated here. Two important parameters in describing a Schottky barrier are the thickness λ of the depletion region and the barrier height, which is (for holes) $\phi_{ps} = I - \phi_m$ on the metal side and $V_D = \phi_m - \phi_p$ on the CP side when no external potential V_B is applied to the barrier. V_D is known as the diffusion potential. Both depend on the density of acceptors N_a or trap states in the material. Some fundamental relations are

$$V_D = \frac{N_a e \lambda_0^2}{2 \epsilon \epsilon_0} \quad (3)$$

which at $V_B = 0$ relates the barrier thickness λ_0 to the barrier height; but the coulombic screening length in the CP (Debye length) is

$$\lambda_D^2 = \frac{kT}{e} \frac{\epsilon \epsilon_0}{e N_a} \quad (4)$$

so

$$2 \frac{V_D}{kT/e} = \left(\frac{\lambda_0}{\lambda_D} \right)^2 \quad (5)$$

Upon application of a voltage V_B to the barrier, its thickness and shape change and a current flows. For instance, the barrier width is now λ_B , given approximately by a relation similar to Eq. (3),

$$\lambda_B^2 = \frac{2 \epsilon \epsilon_0 (V_D + V_B)}{N_a} = \frac{2 \epsilon \epsilon_0 V_B}{N_a} + \lambda_0^2 \quad (6)$$

The measurement of the impedance $Z(\omega)$, especially that of the barrier capacitance C_B , given by

$$(C_B)^{-2} = \left(\frac{\lambda_B}{\epsilon \epsilon_0} \right)^2 = \frac{2}{\epsilon \epsilon_0 e N_a} (V_D + V_B) \quad (7)$$

*There is another model of interface barriers, due to Mott, which is rarely used in semiconductors but might be relevant to CPs in some cases since it assumes that the depletion of free carriers in the semiconductor surface region is due to the absence of acceptors (or donors) in that region [236]. In a CP this would correspond to chemical compensation or destruction of the dopants unintentionally present, which give the CP its conductivity.

provides a way of proving that a Schottky barrier is present and of determining N_a and V_D . The current may flow over or through the barrier by a variety of processes (i.e., by thermionic emission or, if it is narrow enough, by tunneling), yielding $J(V)$ relations of the general form

$$J = J_{\text{sat}} \exp\left(-\frac{eV_B}{kT}\right) \quad (8)$$

where J_{sat} is the saturation current (i.e., the current value reached at large enough reverse voltage). If the current over the barrier is by thermionic emission, J_{sat} is proportional to

$$A^* T^2 \exp\left(-\frac{e\phi_{ns}}{kT}\right) \quad (9)$$

where A^* is an “effective” Richardson constant. In fact, current often flows by tunneling and Eq. (8) is still obeyed, but not Eq. (9). In practice, the exponent of the exponential in Eq. (8) is often empirically written $eV_B/\eta kT$, η being the nonideality factor, which may differ from 1 for a number of reasons, among others the existence of interface layers (see below). But if η is very different from 1, which is the case in several CP barrier studies [231], it is most likely that the entire theoretical approach is inapplicable. For further discussion, see Refs. 236 and 237. The current is a function of the voltage applied to the barrier, that is, to the total film if the bulk conductance is large enough and the other contact is ohmic, a property that will be useful in the study of electroluminescence in Section V.C.

In this simplified model, two important factors have been neglected: interface states and interface layers. These may greatly modify the properties of the contact. For instance, let us return to the problem of forming an ohmic contact for electrons onto a CP. In fact, the majority of actual ohmic contacts on semiconductors do not work, as shown in Fig. 23a. They depend on the presence of a thin highly doped semiconductor layer adjacent to the metal. The width of the depletion region in the Schottky barrier thus formed is then so small [Eq. (3)] that injection occurs by field emission [237]. Such a process could in principle be used in CPs, for electron injecting metals such as K are also n -dopants of all CPs. But this would require that we get rid of most, if not all of the oxide at the interface. An example of the difficulty of forming such an injecting Ca contact on PPV is given in [241].

The presence of a thin insulating layer made of a wide-bandgap material such as an oxide between the metal and the semiconductor is actually the most common situation. For instance, an Al_2O_3 layer will grow very rapidly on Al to a thickness of ≈ 25 Å except in UHV. This is likely to be very common with CPs. This layer will influence the situation in several ways.

First, there is a potential drop in the insulator, which will be large since its conductivity is negligible compared to that of the semiconductor. Consequently, the zero-bias barrier height (the difference between the top of the valence band at the CP–insulator interface and the metal Fermi level) will be lowered. Second, the insulator bandgap is large, so the layer is a high barrier for both carriers. Current can flow through the insulator by tunneling only, but if the barrier is thin enough, say $\approx 20 \text{ \AA}$, the metal and the semiconductor levels will be well coupled, and the current can be high. Under bias, the barrier height is a function of voltage, changing the slope of the $J(V)$ dependence, hence introducing nonideality. The situation is illustrated in Fig. 24.

Finally, interface states, that is, electronic states localized at the interface, are always present in the case of semiconductors and may be very important in fixing the Fermi level at the interface (Fermi level pinning) and modify the barrier height. In the case of organic solids in general, and of CPs, the existence of a surface does not imply that of dangling (i.e.,

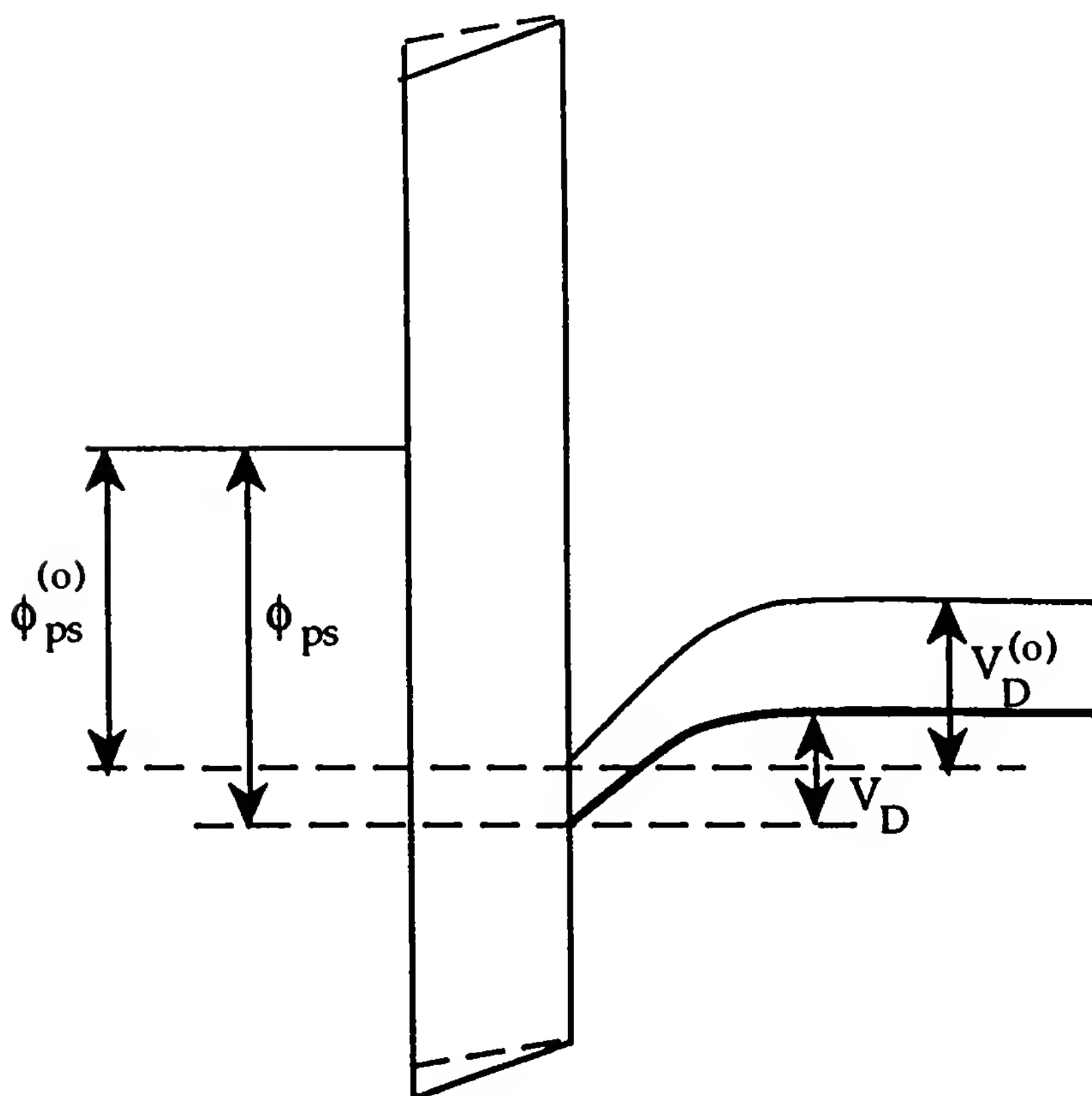


Figure 24 Schottky barrier contact with an insulating interfacial layer. In the semiconductor and the insulator, the valence and conduction levels are shown as solid lines at zero bias (barrier heights $V_D^{(0)}$ and $\phi_{ps}^{(0)}$) and as dashed lines at forward bias (barrier heights V_D and ϕ_{ps}).

free) covalent bonds, and the possible origin of interface states is not clear. Not much is known about them, and this topic is not discussed further.

Early CP Schottky barriers were made and studied as photovoltaic devices, but heterogeneous, noncompact CP films were used, and they were not electrically well characterized as barriers. Examples are Al/fibrillar *trans*-PA [242] or Al/PT [243] barriers (see Ref. 232 for a review).

More recently, the use of homogeneous films deposited from solution or obtained from a soluble precursor allowed preparation of geometrically well defined diodes; this, and a more thorough exclusion of oxygen, led to improved characteristics. For instance, Fig. 25 shows the $J(V)$ relation of an Al/*trans*-PA/Au diode in which the Au contact is ohmic and the Schottky barrier is at the Al electrode [244]. The polymer film thickness is 1 μm . The current does not saturate at large negative (reverse) voltages, perhaps because of the presence of the interfacial layer; in fact, such an increase is expected in the case of a Mott barrier (see Ref. 236, p. 83). The slow increase at large forward V is due to the series resistance of the CP film. Apart from that, the device follows the Schottky barrier behavior given by the equations above, with a nonideality factor $\eta \approx 1.3$ (i.e., close to 1) ("ideality"). However, if In is used instead of Al, the η value rose to about 2.

From these measurements, and assuming all impurities to be ionized in the bulk (which is far from certain), acceptor concentrations $N_a \approx 10^{16}$ to

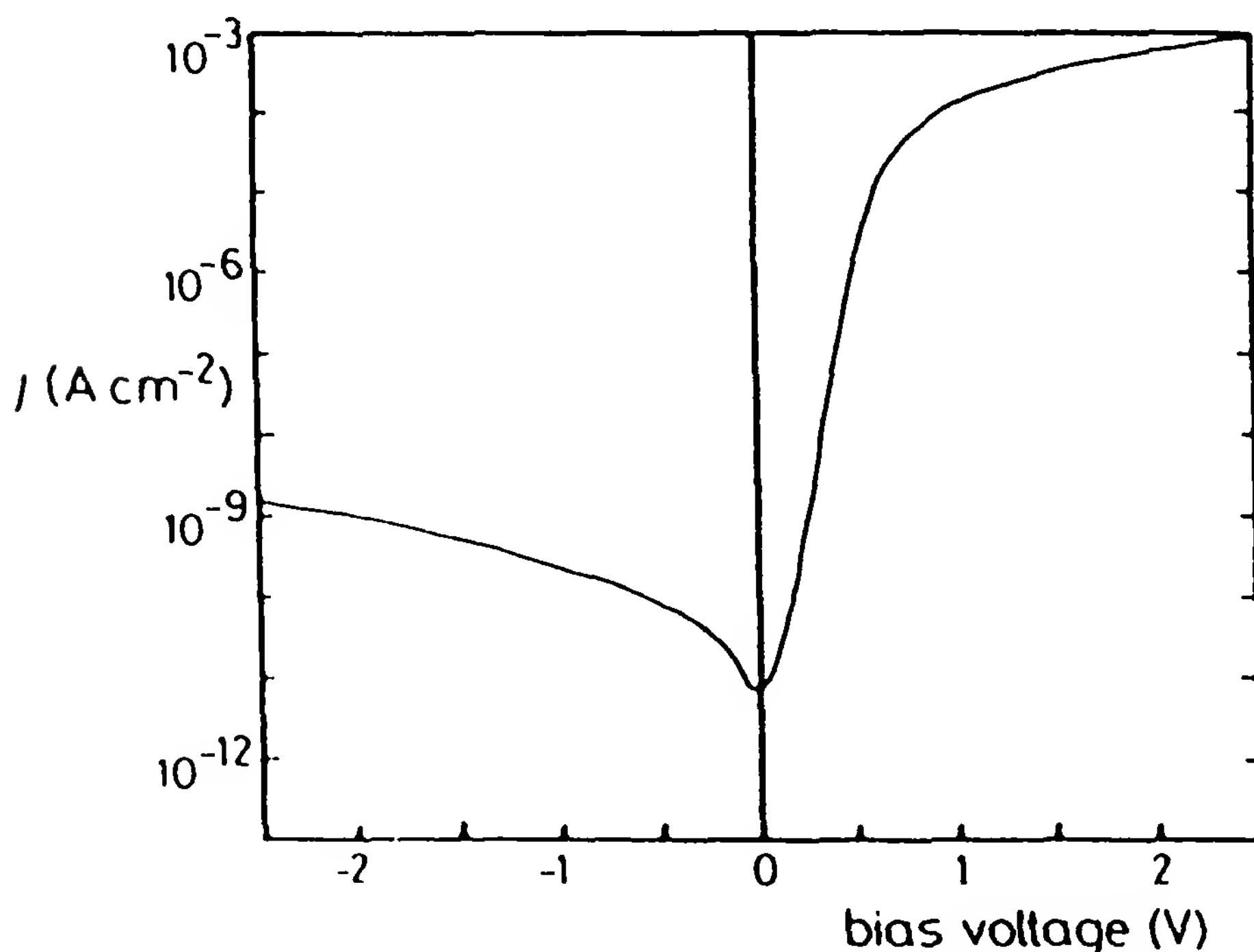


Figure 25 Current–voltage relation [$\log|J|$ versus V] of an Al/*trans*-PA/Au Schottky diode. (From Ref. 245.)

a few 10^{17} cm^{-3} are inferred, leading to barrier thicknesses of $\lambda_0 \leq 2000 \text{ \AA}$, small enough compared to the actual film thickness. But these values should be borne in mind when LEDs are discussed below, since smaller thicknesses are used there.

Note that ordinary Schottky behavior is observed, although it has been assumed that charged solitons play a role in transport (see Section V) [244,245]; one would have expected that direct hole injection into soliton midgap states modifies the $J(V)$ behavior. Similar well-behaved Schottky barriers have also been obtained on other systems, including oligomers: for instance, In/polyalkylthiophenes [246] with a relatively high value of $\eta \approx 2$, Ag/ α -sexithienyl [247], or Al/PPV [248], the latter being part of a light-emitting diode. In all cases, barriers heights are comparable to the difference in work functions (as far as they are known), and acceptor densities range from a few 10^{16} to a few 10^{17} cm^{-3} . As will be seen below, ohmic contacts are used in field-effect transistors and light-emitting diodes, in which evidence of the role played by Schottky barriers in at least some devices has been obtained [248].

B. Thin-Film Transistors

1. Field Effect

Consider a plane-parallel condenser of capacitance C_i , whose plates are a p -type semiconductor (e.g., a CP) and a metal, and polarize the latter negatively. Excess positive charges (i.e., holes) appear at the surface of the semiconductor, and since its conductivity is low, they are in fact distributed over a certain thickness within the material. These excess holes, or at least part of them, should take part in the conduction. Applying a voltage to an external electrode not in contact with the semiconductor modulates its conductivity. This is the principle of the field effect, and clearly this control of the current through a “gate” electrode opens the possibility of transistor action without requiring the existence of p - n junctions.

If the semiconductor surface bears localized bound states (surface states), part of the induced charge will reside in these states, thus decreasing the conductivity modulation induced by the transverse field. For a long time, field effect was therefore not used in devices but was a very useful tool for studying semiconductor surfaces and surface states [249] (see also Ref. 236, p. 285).

2. Thin-Film Transistor

If the insulating medium between the plates of a condenser is not air or vacuum but a solid insulator, decreasing its thickness can increase its capacitance C_i by orders of magnitude, so it becomes possible to fill (saturate) completely the surface states that may be present. Based on this idea, the

insulated-gate thin-film transistor was proposed by Weimer in 1961 [250]. In this device, current is transported by carriers of one sign only, in CP FETs, the holes: this is a unipolar device. Several geometries are possible, as shown on Fig. 26 [250], the one used commonly with CPs at present being a slight modification of geometry (b).

The theory of insulated-gate transistors is given in Ref. 230. It is usually carried over from crystalline semiconductors to amorphous semiconductors or conjugated polymers without change, which is not quite correct (see below). The pertinent parameters are defined in Fig. 27. Using this notation, the fundamental equation relating the current into the drain electrode I_D to the gate and drain voltages V_G and V_D is

$$I_D = \frac{W\mu C_i}{L} \left[(V_G - V_T)^2 - \frac{1}{2} V_D^2 \right] \quad (10)$$

where μ is the carrier mobility, $C_i = \epsilon\epsilon_i/d$ is the capacitance of the gate insulator of thickness d , and the threshold voltage $V_T = -(ehp_0)/C_i$, where p_0 is the hole density at zero voltage and h is the film thickness. Equation

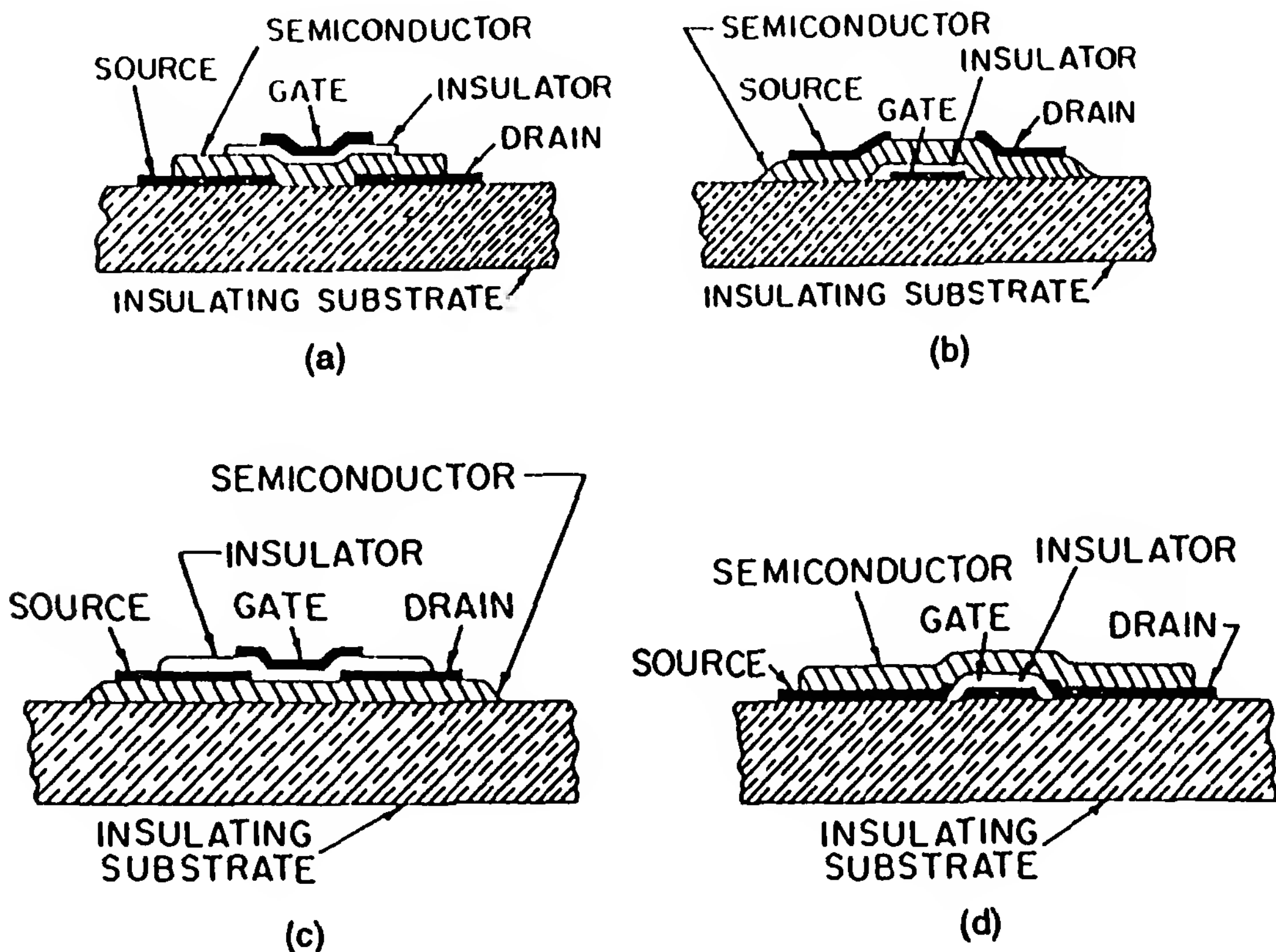


Figure 26 Four TFT geometries. In (a) and (b) the three electrodes are staggered, in (c) and (d) they are coplanar. Most CP TFTs use a geometry similar to (b) but in which the gate and insulator almost completely cover the substrate. (From Ref. 250.)

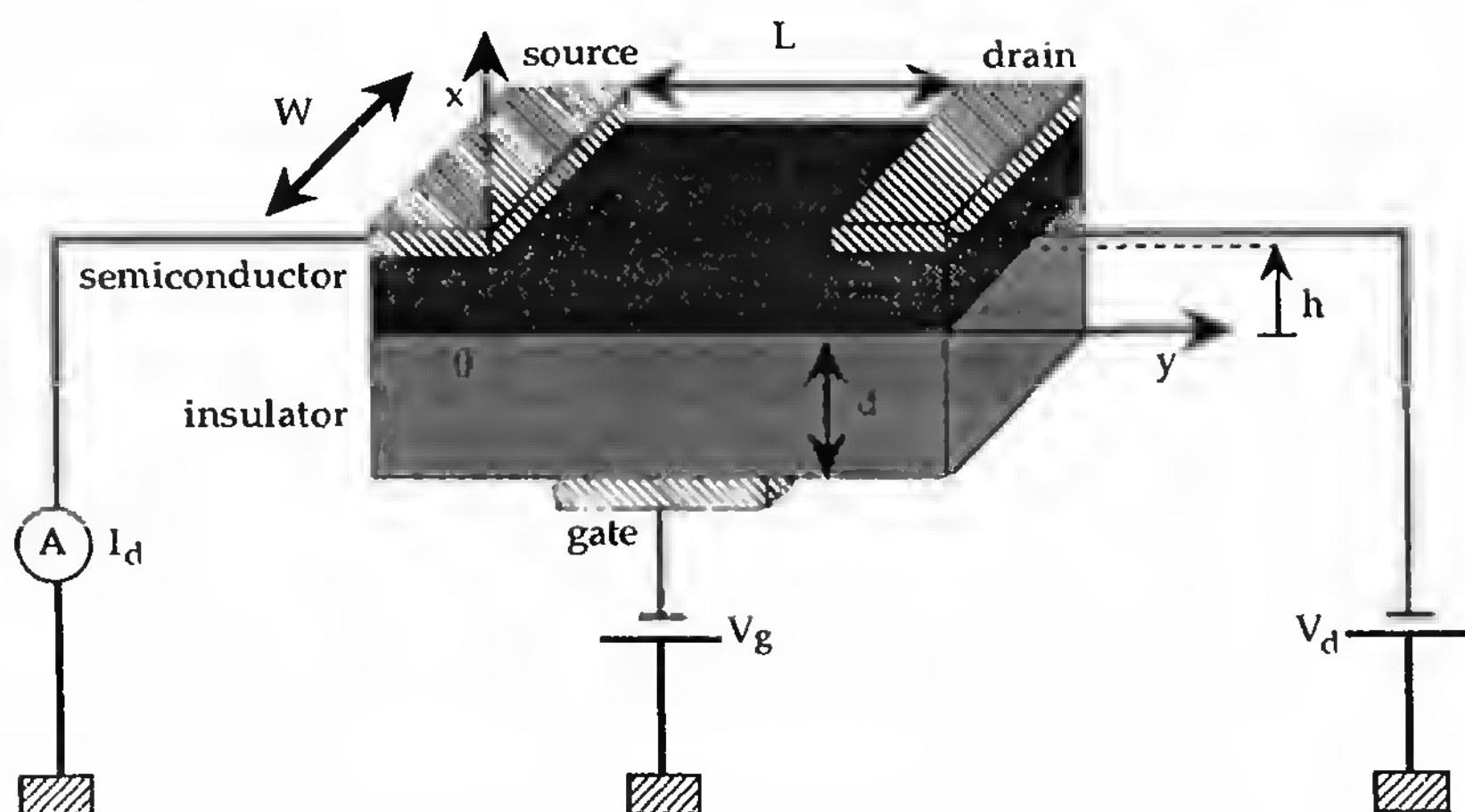


Figure 27 Schematic view of the organic thin-film transistor. W and L are the channel width and length, respectively. (Adapted from Ref. 251.)

(10) holds for drain voltages between 0 and $V_G - V_T$. At $V_D = V_G - V_T$ the drain saturation current I_D^{sat} is attained:

$$I_D^{\text{sat}} = \frac{W\mu C_i}{2L} (V_G - V_T)^2 = \frac{1}{2} g_m (V_G - V_T) \quad (11)$$

where g_m is the transconductance of the device. For $V_D > V_G - V_T$ the current is assumed constant. Thus the current–voltage relations of a thin-film field-effect transistor are as shown on Fig. 28.

In Eq. (10), all quantities are set or measured independently except μ and p_0 , which can therefore in principle be deduced from the experimental $I(V_D, V_G)$ curves. In fact, the field-effect mobility thus obtained may differ from the microscopic bulk mobility for a variety of reasons, such as confinement effects in the conducting channel or change in the transport properties near the surface. More important, a complete analysis must allow for the presence of surface states and of traps in the bulk and the distribution of total field-induced charge among them. The elements of this analysis are given in Ref. 230.

In organic solids, traps due to chemical impurities tend to have fairly well defined energies [218]. This certainly applies to oligomers. Such solids are therefore very different from amorphous Si, for instance, in which localized state energies form continuous distributions (“band tails”) extending deep into the gap. In CPs, the situation is not yet clear. The thin-film transistor (TFT) equations incorporating a single trapping level at a

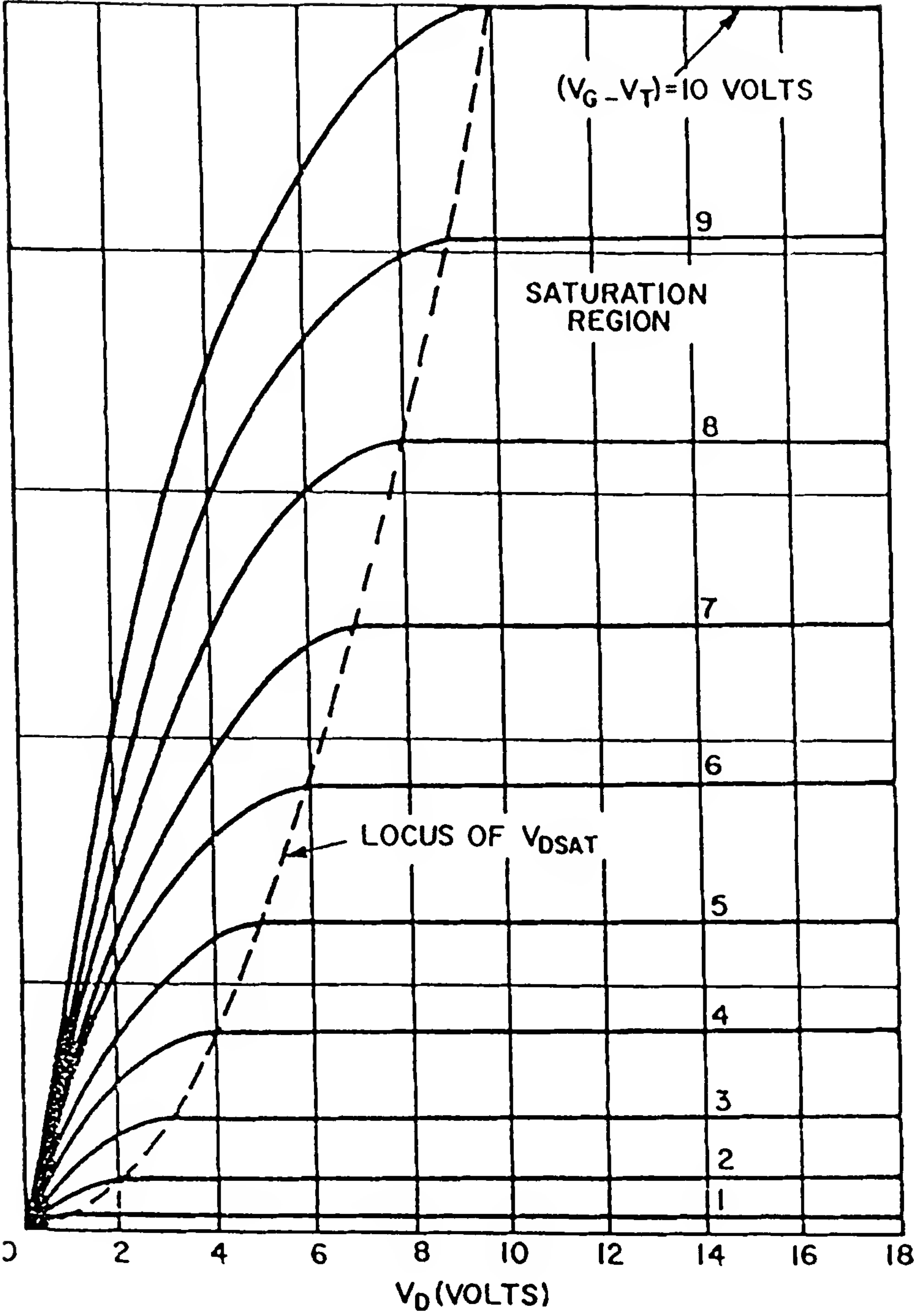


Figure 28 Idealized output $I_D = f(V_D)$ of a FET. The dashed line shows the saturation drain voltage V_{Dsat} . (From Ref. 230.)

well-defined energy have been analyzed in the case of a TFT working in an accumulation mode, which is the usual case with such materials [251]. Although a unique case, it is nevertheless quite illuminating. If the trap depth is ΔE_t and its concentration N_t , the thermal equilibrium ratio of free to trapped charges is

$$\theta_0 \approx \frac{N_v}{N_t} \exp\left(-\frac{\Delta E_t}{kT}\right) \quad (12)$$

where N_v is the density of states near the top of the valence band (or the density of molecules or repeat units in the case of a narrow band). Due to that distribution of charges, the saturation current [Eq. (11)] at low V_G is modified, μ is now $\theta_0\mu_0$, μ_0 being the microscopic hole mobility. But as V_G increases, the field-induced charge density reaches and exceeds N_t . All traps are then filled and the value of μ entering Eq. (11) is now μ_0 . This transition is similar to the trap-filled limit in space-charge-limited currents [215]. Experimental data on α -sexithienyl TFTs are in good agreement with these predictions using trap parameters agreeing with those inferred from other experiments such as SCL currents [251].

Generally, traps are expected to yield field-effect mobilities which are both much lower than microscopic ones and varying with physical or electrical parameters. It would be worth taking this into account in CP TFT data. Apparently, low threshold voltages will require trap densities in the range 10^{17} cm^{-3} , or less than 100 ppm, for trap depths of a few tenths of 1 eV. This does not seem impossible; but the very low localized level densities sometimes quoted seem unrealistic, considering the poor structural order and limited chemical purity of most CPs to date.

3. CP- and Oligomer-Based TFTs

Up to now, TFTs have mainly been prepared using either *trans*-PA [244,245], polythiophene [252] or derivatives (i.e., soluble polyalkylthiophenes) [226,253], or oligomers [227,254,255]. The original insulated-gate field-effect transistor (IGFET) has two back-to-back barriers, one at the source, the other at the drain. These are either n^+ - p junctions (on a p -type semiconductor) or Schottky barriers. The current flowing at $V_G = 0$ is therefore only the corresponding saturation current J_{sat} . As V_G is increased, a surface inversion layer (channel) is formed, connecting the two electrodes, and a large current flows [230]. Organic TFTs prepared up to now do not work in that way. Source and drain are ohmic contacts (generally of Au) and application of a large enough negative V_G (for p -type) creates a surface accumulation layer through which a large current flows.

In that case the equations above are in fact exact, but the current in the bulk of the film, parallel to the surface but outside the channel is not

blocked and runs in parallel to the controlled, channel, current: this leakage current is a useless loss, and it prevents current saturation at large negative V_D . So the material conductivity should be kept low, and the TFT geometrical and electrical parameters may be difficult to optimize.

The bulk conductivity of presently used materials is in the range 10^{-8} to 10^{-7} S/cm. The field-effect mobilities are around 10^{-5} cm²/V · s, generally depending on applied voltages or the nature of the gate insulator; this suggests that it is not the microscopic mobility and that different results would be obtained with better controlled materials. The mobilities also depend on time, suggesting that ionic motions in the insulator and corresponding changes of the interface may in some cases transiently affect the device characteristics. Most devices operate at V_D and V_G around 10 V and at currents I_D around 100 nA, with transconductances around 10^{-8} S. These are modest performances.

Work with α -sexithienyl TFTs yielded more promising values: The field-effect mobility reaches $\approx 3 \times 10^{-2}$ cm²/V · s, with currents and voltages similar to those with CPs [227,254]. For comparison, amorphous silicon FETs [256] usually have $\mu \approx 0.1$ to 0.3 cm²/V · s, sometimes nearly reaching 1 cm²/V · s [257], with $I_D \approx 1$ to 100 μ A at voltages of about 10 V, and such devices are used in liquid-crystal display panels [234].

It is difficult to predict the future of CP FETs based on the limited amount of data available. It is encouraging that α -sexithienyl FETs are approaching the performances that are required to control a pixel in a LCD panel, but structural and/or chemical problems remain, as indicated by the large range of quoted mobilities [227,254,255]. The lifetime of such a device is unknown. CPs should show a clear superiority over a-Si, possibly a very inexpensive process, before they can compete. It is clearly easier to prepare a flexible panel with organic materials, but the market for such a device is unknown. Moreover, it is not known whether the difference between conjugated polymers and oligomers is only a question of chemical purity and structural control, or has a deeper cause (e.g., oligomers have narrow bands in three dimensions, whereas CPs, at least in principle, have wide bands in one dimension). In fact, in the last two years, interest in CP FETs has somewhat decreased, due in part to the rapid development of research on light-emitting diodes, to which we now turn.

C. Light-Emitting, Electroluminescent Diodes

1. Introduction and Historical Background

When a suitable CP is sandwiched between two suitable electrodes and a high enough voltage is applied, visible light is emitted. Such an emission produced by the passage of an electric current, but not by the heat gen-

erated by it, is named electroluminescence (EL). The first published report of EL in a CP is only 3 years old [235]. It was immediately considered as an important potential application, and activity in this field has grown very rapidly. In this section, the present understanding of the phenomenon and the state of the art of presently reported devices are reviewed.

One may, in fact, wonder why this occurred so late. Electroluminescence has been known for about 70 years, has been actively studied for about 40, and has been developed into feasible and important devices at least 30 years ago (useful, if not very recent, reviews, are found in Ref. 258). EL in organic materials was known at least 30 years ago [259,260], and EL organic diodes with high brightness and high quantum yield were demonstrated more than 20 years ago [261,262]. CPs have been studied actively for more than 15 years (see Chapter 11) and indeed, as early as Kanicki's review [232] the potential interest of EL in CPs was pointed out. One reason for this delay may be that CPs studied in the early 1980s for their semiconducting properties (e.g., *trans*-PA or polypyrrole) were not, or barely, luminescent.

Several more recently studied CPs are, on the other hand, much more luminescent. For instance, the luminescence quantum yield of MEH-PPV in solution is 35%, and laser emission at ≈ 600 nm from a solution pumped at 530 nm by frequency-doubled Nd pulses has been reported, with outputs comparable to those of typical laser dyes [152].

It may be interesting to place the present discussion of EL in CPs in the perspective of organic EL as a whole since there are lessons to be learned from the study of smaller molecules. Organic crystal properties will therefore be used to infer CP behavior in Section V.C.3 and new diode geometries using organic layers will be recalled in Section V.C.4.

Before embarking in the discussion of EL processes (Section V.C.2), the elementary steps of CP EL (Section V.C.3), the possible diode geometries (Section V.C.4), and present performances (Section V.C.5), it is worth giving typical experimental data. So Fig. 29 shows an example of the dependence of current and light-emission intensity on applied voltage, and Fig. 30 the corresponding emission spectrum. In all cases this spectrum is identical to or only slightly different from the photoexcited luminescence spectrum.

2. EL Processes: General Model for Polymer LEDs

By electroluminescence we mean nonthermal emission of light by a solid through which an electrical current is passing under an applied voltage. The emitted photons correspond to electronic transitions within the material, so EL and photoluminescence (light emission following light absorption) are closely related processes. Several EL mechanisms are known.

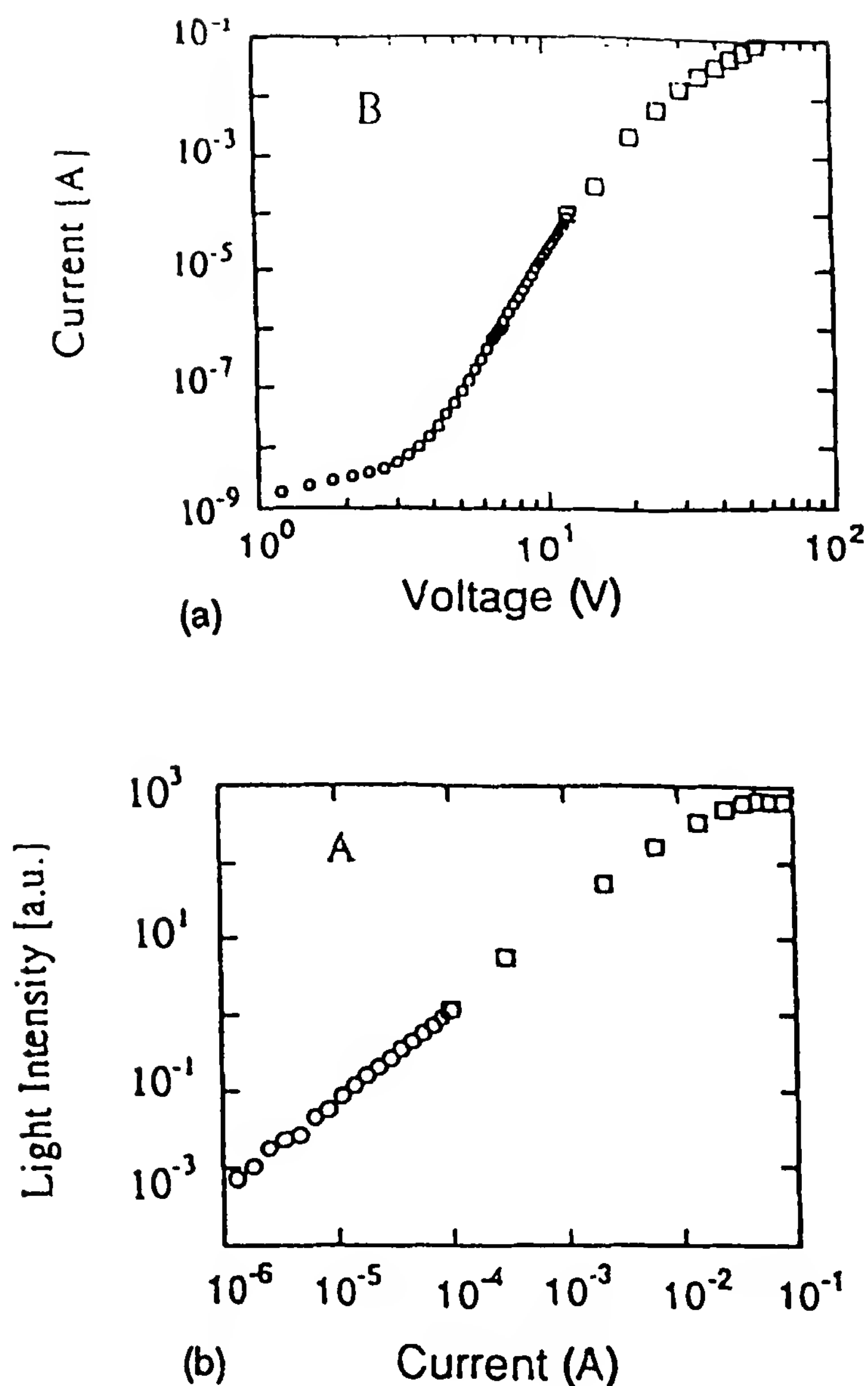


Figure 29 (a) Current–voltage relation; (b) light intensity-injected current relation for a MEH–PPV diode. (From Ref. 298.)

In many classes of materials, free carriers can gain sufficient kinetic energy from an applied field (i.e., become “hot”) to be able to excite electronic transitions, for instance to bring a localized level of an impurity ion or atom to an excited state, which then decays radiatively. This is impact excitation. ZnS:Mn phosphors work in that way. Charge carrier multiplication by impact ionization may occur as well. These mechanisms are not likely to be of importance in polymers, and generally in organic EL: no evidence of carrier heating by an applied field has ever been observed in these materials at room temperature, and studies of the energy

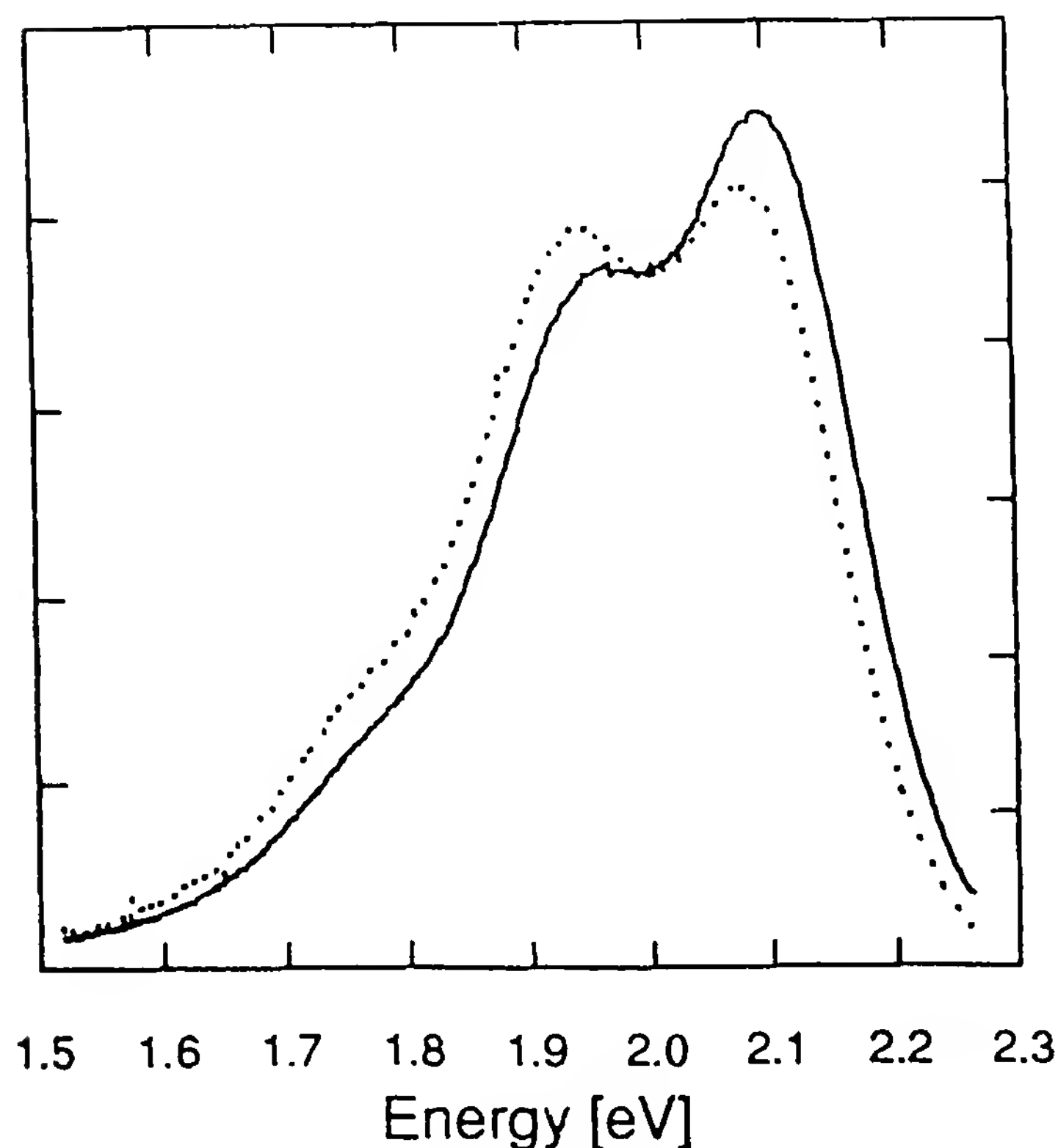


Figure 30 Emission spectrum for the same diode as on Fig. 29 at high (solid line) and low (dotted line) currents. Emission intensities in arbitrary unit.

relaxation of electrons initially injected high in the conduction band of a polymer indicate that the mean free path for excitation of molecular vibrations (of energy 100 to 400 meV) is very short, on the order of 20 Å [263]. This inelastic process is likely to prevent excitation of electronic transitions in CPs. However, since the applied fields are large, the possibility should not be forgotten: the energy gained over a distance of 20 Å in a field of 10^6 V/cm is 200 meV!

A very important EL mechanism—in fact, the most important today in practice—is radiative recombination (by any of several possible processes) of thermal carriers in a forward-biased p - n junction. This process is not important in CPs today because attempts at making stable p - n junctions have essentially failed, probably because, as mentioned above, the dopants are only intercalated between the chains and are therefore mobile in an electric field.

In fact, almost all polymer EL experiments to date have been interpreted in terms of the recombination of electrons injected from the cathode with holes injected from the anode, that is, a situation of *double injection in an insulator*, implicitly assuming that the carriers are not heated by the applied

field. Some of the conjugated polymers or oligomers studied in EL have significant conductivities, up to 10^{-7} S/cm at least, and in these cases the thermal carriers should not be neglected. Considering the large bandgaps, these conductivities must be extrinsic, and some of the corresponding localized centers are likely to be quite deep (i.e., incompletely ionized). In that case, the injection of minority carriers, not present at equilibrium, will be an important factor.

Nevertheless, most experiments are discussed in the literature in terms of rigid-band diagrams of the type shown on Fig. 31, in which the only effect of the applied field is to tilt the band edges. What these band edges really mean will be discussed later. We shall use the same model below, but the possible existence of Schottky barriers in materials of sufficient

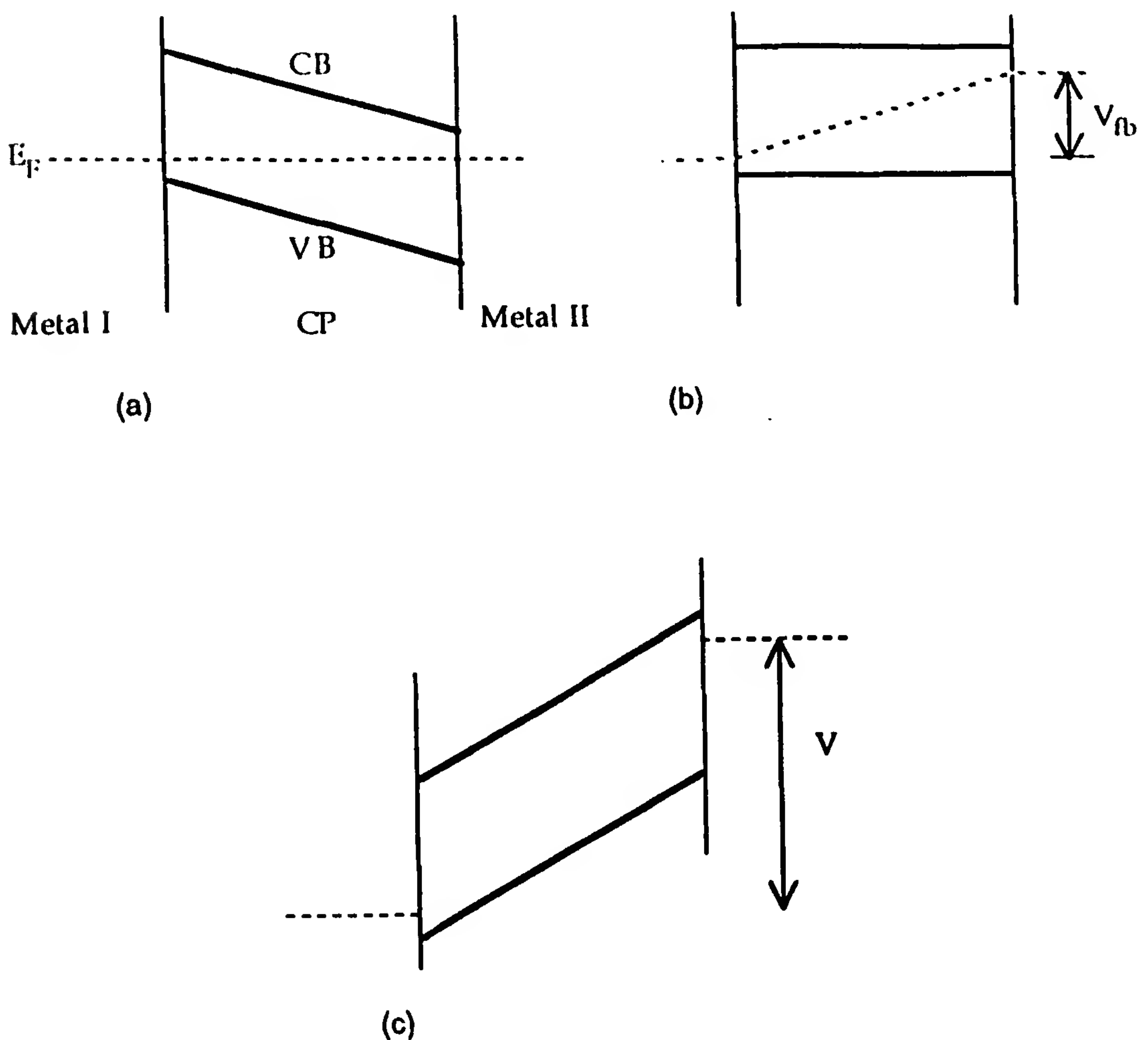


Figure 31 Rigid-band model of the energy levels in a diode: (a) zero voltage; (b) flat band (voltage V_{fb} applied); (c) large forward voltage V .

conductivity must be considered first. If such a barrier is formed at one electrode, the band edges there now look as on Fig. 23.

There is a depletion region of width $\lambda \sim N_a^{-1/2}$ [Eq. (6)], where N_a is the density of acceptors responsible for the conductivity, beyond which extends a low-field region. This is, of course, a very simplified view. If N_a is small enough, λ will be comparable to or larger than the total sample thickness L , and the rigid-band approximation will apply. This is quite possible since films used in practice are thin, $L \approx 500$ to 5000 \AA , whereas in a medium of static dielectric constant $\epsilon \approx 2$ to 3 , $\lambda \approx 1000 \text{ \AA}$ for $N_a \approx 10^{16} \text{ cm}^{-3}$. In a Schottky barrier, formed in a material of significant conductivity, the first effect of application of a voltage V is to vary λ roughly proportionally to $V^{1/2}$, whatever L if it is large enough [Eq. (6)]. This provides a way of saying whether a Schottky barrier or a rigid-band picture is an appropriate start for modeling an experiment, since in the latter case it is the slope of the band edge that matters (i.e., the applied electric field), not the voltage. Study of several diodes having different L but being otherwise (hopefully) identical will tell, for instance, if the current depends on V or E . In most experimental cases it has been found that the rigid-band picture is appropriate, but clear Schottky behaviors have also been found [248]. When observed at room temperature, Schottky barrier behavior tends to disappear at low temperature [248]. Measured forward currents in rigid-band diodes are usually only weakly temperature dependent around room temperature. This tells us that if there is a barrier (as on Fig. 29), carriers are injected by tunneling through it and not by thermal emission above it.

To summarize, the model within which polymer EL is at present mostly discussed is therefore the following. EL is the (final) result of recombination of thermal negative and positive carriers, which drift in the field corresponding to rigid-band conditions after they have been injected either by an ohmic contact or by tunneling through a barrier at the corresponding electrode. Internal space charge within the diode material, resulting from this double-injection process, is neglected; otherwise, due to the Poisson equation, the field would not be constant. The physical problems associated with all these processes is considered further next.

3. Elementary Steps in Polymer EL Operation: Physical Principles

There are five steps to consider: electron or hole injection and transport, and recombination, shown schematically in Fig. 32.

(a) Hole Injection

Hole injection into the hole-conducting states of the CP occurs from states above the anode Fermi level. One should then compare the positions,

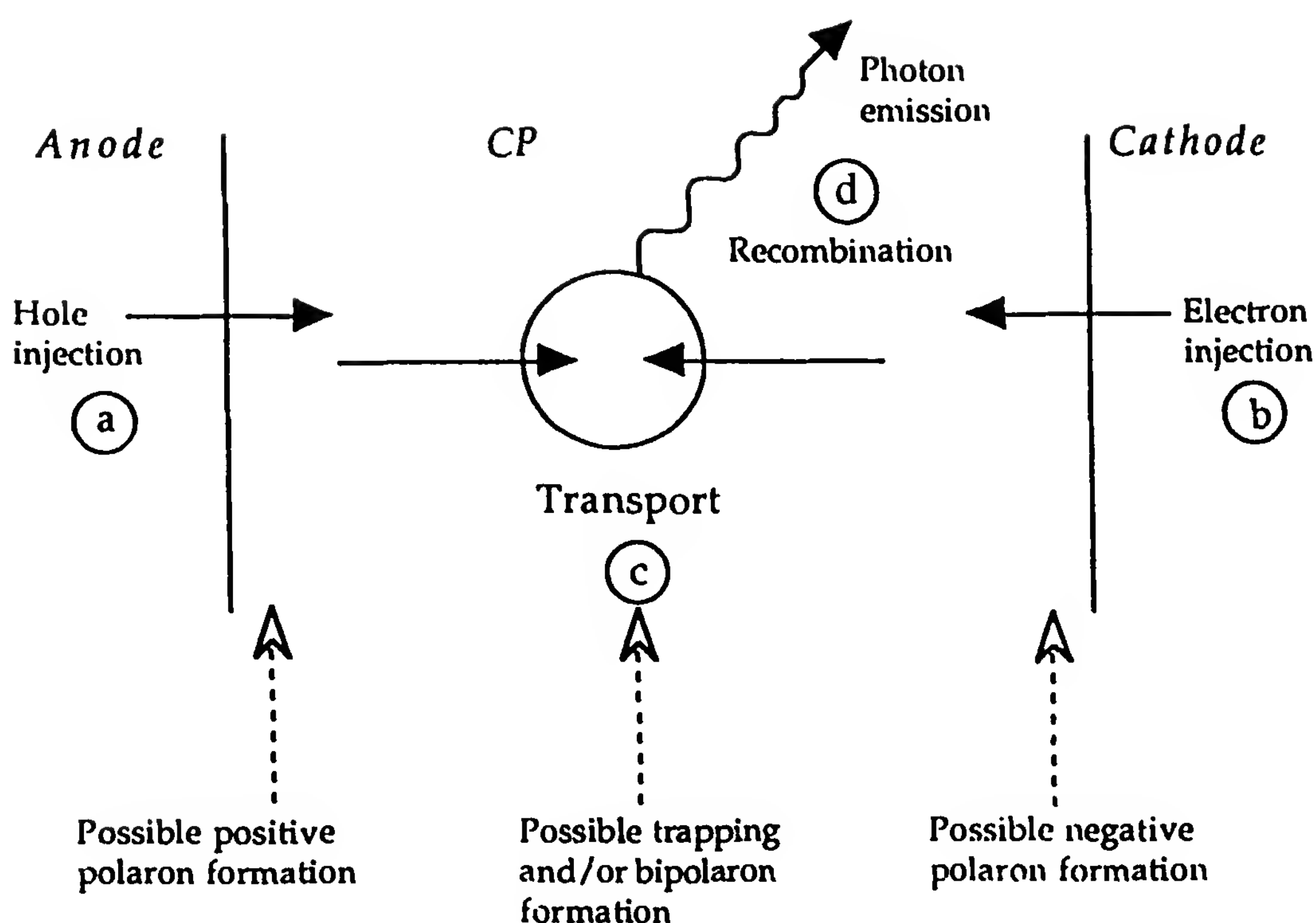


Figure 32 Various steps leading to electroluminescence. The letters a to d refer to corresponding paragraphs in the text.

relative to the vacuum level, of the highest occupied state in the CP and the anode Fermi level. In the usual way in semiconductor physics, this level is drawn as the top of the valence band in all energy diagrams, although depending on the nature of charge carriers, the actual situation in CPs may be more complicated.

Typically, the highest filled electronic level, corresponding to the photoemission threshold, is $I_c \approx 5.1 \pm 0.3$ eV for the CPs of interest here (see Section V.A.2). The highest I_c is for PPP ≈ 5.4 eV, which has been measured directly. This is not too high for double-injection EL, since early organic diodes [261,262] used crystalline materials with even higher I_c . Several potential electrode materials (e.g., gold) have work functions comparable to the values above, so they should form an ohmic contact to any CP. But interface states may greatly modify interface barrier shapes, so the choice of the value applicable to a real interface may be a problem. A particularly promising anode material is ITO conducting glass since, being transparent throughout the visible, it transmits the emitted light out from the diode. It has been almost universally chosen in all CP EL studies to date. ITO (indium–tin oxide) is a degenerate *n*-type semiconductor; the position of its Fermi level within the conduction band depends on the

composition: the indium/tin ratio and oxygen stoichiometry. Various values are quoted in the literature between 4.2 and 4.9 eV [264]. Values of 4.6 eV [265] to 4.9 eV [266] are often assumed, implying a relatively low barrier-to-hole injection into most CPs.

A highly *p*-doped CP (or a degenerate *p*-doped semiconductor) should also be able to serve as anode. This has been achieved with polyaniline, in what is an almost all-organic, flexible LED [267]. The work function of PAni is at least as uncertain as that of ITO, but it should be comparable, since the diodes using either material as anode have very similar properties.

More surprisingly, materials with much lower work functions, such as Al, have been found to inject holes in PPV, for instance [235]. Al is known to bind covalently to molecules such CPs in ultrahigh vacuum [268], but in conventional vacuum an oxide layer forms immediately. As discussed above, such a layer may act as a tunnel injecting barrier under a high enough applied field. This mechanism has long been used in inorganic EL, but it is not yet understood in organic EL and has not been exploited systematically, in the sense that no such layer has been made and used in a controlled way.

(b) *Electron Injection*

Again, one should compare the position of the Fermi level of the cathode with that of the lowest empty electronic level of the CP, corresponding to the electron affinity χ (see Section V.A.2). But the latter cannot easily be measured directly and is usually inferred either from electrochemical measurements [124], or by subtracting from the photoemission threshold the optical absorption threshold energy (or that corresponding to the maximum absorption), assumed to be identical to the forbidden energy gap (see Section III). But this neglects exciton effects (and the influence of disorder), and the true energy gap is likely to be at least a few tenths of 1 eV, and possibly up to 1 eV, larger.

Finally, the most likely value of χ in the CPs of interest here is about 2.5 eV or less. Therefore, an ohmic contact for electrons should have a work function of at most 3 eV. This is the case for the alkali metals from Li (2.9 eV) to Cs (2.15 eV); these elements are also, for the same reason, good *n*-dopants of the CPs; slight diffusion into the polymer may then generate an n^+ contact favorable for electron injection. The most widely used low-work-function cathode in CP EL is, however, Ca (2.9 eV) [269]. One could try to increase χ by a proper choice of the monomer chemical structure, but unless one succeeds in avoiding having E_g reduced simultaneously, the emission will be shifted to the red part of the spectrum.

However, all these metals are highly reactive toward oxygen and will first form an oxide layer with any oxygen available at the polymer surface,

even in ultrahigh vacuum [241]. The neglect of the corresponding thin, wide-bandgap barrier layer, although customary up to now, is certainly not granted. Thus tunnel injection is likely to be important for electrons, too. This is clearly shown by the fact that metals with work functions much larger than 3 eV, such as Mg or Mg/Ag alloy (3.7 eV) or Al (4.3 eV), are able to inject enough electrons to generate relatively intense EL. The Fermi level of Al would be slightly below midgap of PPV. Certainly, in such a case, field-assisted tunnel injection through the Al_2O_3 layer will be important. A sizable fraction of the total voltage drop probably occurs through the oxide layer.

It is therefore expected that, in general, hole injection into CP films will be easier than electron injection. This imbalance may imply that most majority carriers (the holes) will leave the film by passing into the cathode. Preventing this from occurring may therefore increase the EL yield. An insulating interface layer may inhibit, or at least slow down, this hole extraction, depending on the relative positions of the bands. This indeed has been realized long ago, during the early studies on CdS EL, as shown on Fig. 33, taken from a 30-year-old paper [270]. It might be even more interesting to use degenerate wide-bandgap semiconductors as injecting electrodes.

(c) *Transport*

The effect of electric charge imbalance within the material (injected space charge) has not been taken into account up to now in CP EL studies. Space-charge-limited currents have been discussed thoroughly, for instance, in Ref. 215. With the advent of geometries in which one carrier is confined within the film and large local charge densities and electric field variations occur (see Section V.C.4), space-charge effects might become important. It is too early to consider them here.

Nature of charge carriers. Once injected, an electron and a hole must be brought at small enough distance to allow their recombination. This will depend on the nature and transport properties of the charge carriers. All CPs used in EL are nondegenerate ground-state polymers. The relevant notions of polaron and bipolaron and their relative stability were introduced in Chapter 11, Section IV.C. Some characteristic times pertinent to polaron or bipolaron formation will be discussed first, then the influence of traps.

If a carrier mobility μ can be defined in the field E , the time needed for one carrier to cross a homogeneous film of thickness L (the so-called transit time) is $\approx L/\mu E = L^2/\mu V$. If $L = 10^{-5}$ cm and $V = 10$ V, this time is 1 μs for $\mu = 10^{-5}$ $\text{cm}^2/\text{V} \cdot \text{s}$ (see Section V.B.3), and 1 ns for $\mu = 10^{-2}$ $\text{cm}^2/\text{V} \cdot \text{s}$, as in thiophene oligomers [227,254]. On the other hand, the

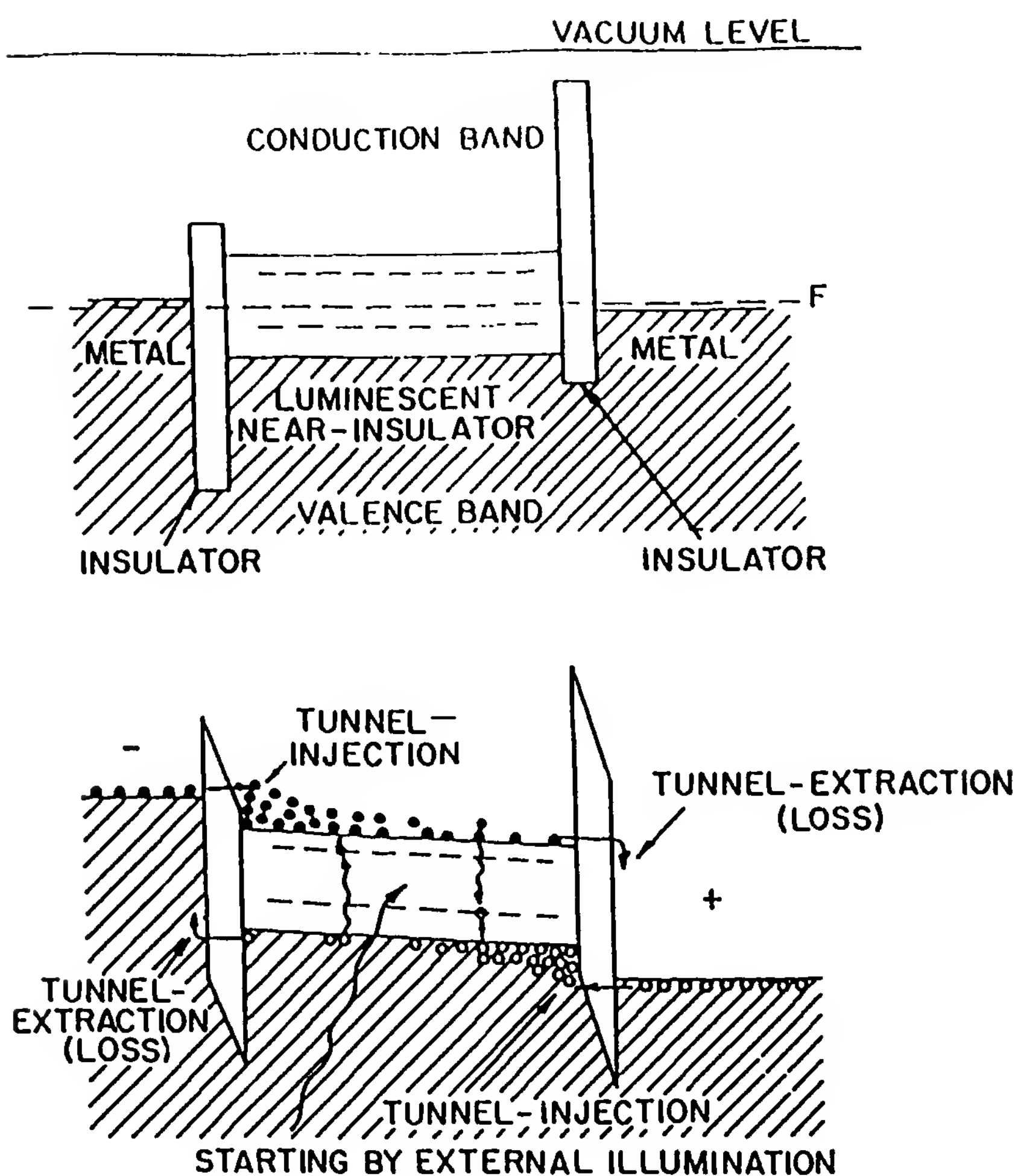


Figure 33 Double-tunnel-injection electroluminescence (metal contacts). (From Ref. 270.)

dielectric relaxation time $\tau_\sigma = \epsilon\epsilon_0\sigma^{-1}$ measures the decay time of a charge fluctuation in a material of conductivity σ . It will be $\geq 1 \mu\text{s}$ for $\sigma \leq 10^{-7} \Omega^{-1} \text{cm}^{-1}$, which is the case in all EL CP diodes. The transit time is then an intrinsic lower limit of the device response time, and a reference duration for other processes that can occur during transit, such as polaron or bipolaron formation. In a disordered medium there is no well-defined mobility, but a quantity related to a transit time still exists [271]; for our purposes, this does not significantly alter the discussion.

The time needed to dress an injected free carrier with phonons (i.e., to form a polaron) is on the order of a phonon period $< 1 \text{ ps}$. Therefore, if polaron formation occurs at all, it will be instantaneous compared to a transit time: the moving charges begin their transit as polarons. In fact, if the polaron binding energy relative to the free carrier state is small [272], there is a sizable probability that the corresponding nuclear geometric

configuration occurs spontaneously and the carrier can tunnel directly from the electrode Fermi level into a polaron state. If this energy is very small or negative, polarons will not be present; there will be no lattice relaxation around the moving charge. Apart from its large effective mass and small mobility, there is nothing special with the polaron, which is a charge $\pm e$ and spin- $\frac{1}{2}$ excitation; this will be important in Section V.C.d when we discuss recombination.

The case of the bipolaron is quite different. It must be formed by binding of two preexisting polarons of the same kind, and this may take time since the polarons must move to contact. So even if bipolarons are stable, their formation may not be important in actual LED operation conditions. Optical evidence for bipolaron formation in a PPV LED has recently been reported [273], as it had previously in P3AT MIS diodes [273]. This is again important for recombination, since the bipolaron binding energy relative to the free carriers is calculated to be large [272]. It seems that indeed they do not take part in EL [273]. Bipolaron–bipolaron or even bipolaron–polaron recombination are new processes about which nothing is known (see Section V.C.d). The nature of charge carriers is thus important in the recombination.

Role of traps. An important feature of organic solids is the existence of trapping centers, which will affect both transport and recombination. A trap is a localized center (chemical or physical defect) which is normally neutral (empty) but which can bind and therefore immobilize an electron or a hole, or the corresponding polarons (there is no information about bipolaron trapping, but it should occur as well). In three dimensions, trapping is independent of the electric field E up to very large fields, but diffusion and therefore the kinetics of trapping in quasi-one-dimensional solids are peculiar [274,275]. The influence of anisotropy on trapping has not been considered up to now in CPs.

Traps play a very important role in the electrical properties of organic, nonmetallic solids [128,218]. At equilibrium, the charges are partitioned between mobile and trapped carriers; the fraction of carriers that are free is given by Eq. (12). Therefore, unless $E_t \leq 0.2$ eV, most of the carriers will be immobilized in traps; and a given carrier will spend most of its time in traps, its effective transit time being lengthened accordingly. Moreover, a trapped charge does not contribute to the current, but it does to the recombination, through interaction with a free charge of the opposite sign, generally yielding an emission spectrum and yield characteristic of the trap [128,218]. So it may be a nuisance, but on the other hand, it may provide a way of adjusting the emission color, or even of obtaining multicolor emission by balancing the emissions of several traps.

In molecular crystals with small μ , trap capture cross sections σ_t are usually close to the geometric dimensions of the impurity, typically 10 to 100 Å², or 10^{-15} to 10^{-14} cm² [128,218]. The trapping time associated with trap density N_t is

$$\tau_t = (N_t \sigma_t \nu_{th})^{-1} \quad (13)$$

where ν_{th} is the carrier thermal velocity, assumed large compared to the drift velocity $\mu_0 E$. With $N_t \approx 10^{16}$ cm⁻³, $\tau_t \sim 1$ μs. On the other hand, the detrapping time τ_{dt} (i.e., the carrier dwell time in a trap) is

$$\tau_{dt} = \nu \exp\left(-\frac{E_t}{kT}\right) \quad (14)$$

where ν is a frequency factor (often $10^{11 \pm 2}$ s⁻¹) and E_t an effective depth, which is the trap depth at zero field decreased in high field by the Poole–Frenkel effect [276]. If $E_t \geq 0.7$ eV, τ_{dt} can exceed 1 s at 300 K, and $\tau_{dt} \approx 10$ μs would correspond to $E_t \approx 0.4$ eV. Thus the time needed to equilibrate the charge populations according to Eq. (12) will often be long compared to the transit times and govern the response time of the system.

Summarizing, whatever the nature of charge carriers, mobilities indicate hopping transport. At low-enough injection levels, most of the charges may reside in traps, but these can be filled completely at high current (as discussed in Section V.B.3 for FETs); their role in recombination and photon emission will depend on voltage.

Significant time scales. In several applications, for instance in multiplexing, LEDs would operate in a pulse mode. The question of rise and decay times is therefore important. Many characteristic times arose in the previous discussion, and some of them, associated with the equilibration of charges with traps, may be quite long.

The trapping and detrapping times are not important only because they influence the type of charges present in the device and therefore influence the time of equilibration of a Schottky barrier, for instance; in all cases where one of the injection processes implies tunneling through a barrier, the field there must first increase; as seen in Section V.C.4, this may be achieved by accumulation of the other carrier at the barrier, creating a space charge, therefore a field, a process whose time constant may also be governed by traps.

(d) Recombination and Photon Emission

The small or very small carrier mobilities imply hopping transport, or a mean free path (if it can be defined) comparable to monomer dimensions, so recombination occurs by diffusive motion of the carriers toward each other within the potential well generated by their mutual attraction. This

is called in the organic crystal literature [128] coulombic or Langevin recombination, the latter name by reference to Langevin's theory of recombination in dense gases. Since the dielectric constants are small, the capture distances are large ($>100 \text{ \AA}$), corresponding to a very large capture cross section of 10^{-12} to 10^{-11} cm^2 . The process is almost as efficient if only one carrier is mobile, the other being trapped. Anisotropy of μ will modify these values, as it does for trapping, but the coulombic recombination will still be orders of magnitude more efficient than the recombination processes usual in semiconductors.

The efficiency of coulombic recombination is a potential advantage of organic materials over conventional semiconductors. Double-injection theory [215] shows that it is possible to reach a state in which almost all injected charges recombine within the organic film. EL will follow only if recombination is radiative. Here the nature of the charge carriers, and the relative energies of the various excitations in the organic medium, are important. This will be discussed by considering first the two limiting cases of molecular aromatic crystals and conventional semiconductors.

In the case of molecular aromatic crystals, which were used in the first generation of organic LEDs (see Section V.C.1), the situation is well understood [128]. The energy of an electron-hole pair at infinite separation (i.e., the bandgap E_g) is much larger than either the singlet exciton or the triplet exciton energies E_s and E_t , respectively. In anthracene, for instance, $E_g - E_s \approx .1 \text{ eV}$ and $E_g - E_t \approx 2.5 \text{ eV}$. The energy of an electron-hole pair at minimum distance which is bound by its mutual coulombic attraction is difficult to measure but is also calculated to be well above E_s [128]. The electron-hole recombination then always produces an exciton. Because the spins of the electron and the hole are uncorrelated, $\frac{1}{4}$ of the events produce a singlet and $\frac{3}{4}$ a triplet. The singlet binding energy $E_g - E_s$ is so large that the singlet cannot thermally ionize again into an electron-hole pair during its lifetime of a few nanoseconds, even in a large electric field in which the Poole-Frenkel effect is operative [276], and the same is true of the triplet: Formation of the exciton is irreversible. The exciton will then decay to the ground state, either radiatively or by emission of phonons. In molecules containing only light atoms and at room temperature, triplet decay is essentially nonradiative [129]. On the other hand, the radiative quantum yield of the singlet can approach 1. The maximum EL quantum yield to be expected in that scheme would then be 0.25; however, it is possible to generate singlet excitons by triplet fusion [128,139], in such a way that the maximum attainable yield is about 0.35.

In conventional semiconductors, the situation differs in many ways: In such materials, transport in extended states is the rule, and the mean free paths are much larger than atomic dimensions; Langevin theory does not

apply. Briefly (see any textbook on semiconductor physics), an electron–hole pair can recombine in the volume either by formation of an exciton, or by direct emission of a photon, or by successive trappings of both carriers on the same center (recombination center). The latter process is extrinsic. Direct recombination essentially produces emission near the band edge, not a spectrum that would be the mirror image of the absorption. Its yield is not limited by spin considerations as above. The calculated recombination cross sections are much smaller than above, 10^{-22} to 10^{-18} cm² (see, e.g., Ref. 277). So, the corresponding radiative lifetimes are long, typically more than 200 ns at a carrier concentration of 10^{17} cm⁻³ [278], which is a larger density than can be expected in a CP EL device.

CPs. Which of these two schemes applies in CPs? The question is still under discussion, since many observations can be, at least approximately, understood in both ways. For instance, the EL and the photoluminescence spectra are often very similar and occur near the absorption band edge; it may be claimed that photoexcitation generates the singlet either directly (as in molecular crystals [128,168]) or through electron–hole recombination; or that both processes are due to direct radiative recombination. In the opinion of this author, which seems to be the general one, evidence is decidedly in favor of the molecular picture. In most cases, transport is clearly diffusive and through localized states. The occurrence of very high order and high absorption dichroism in stretch-aligned MEHPPV [108] is not in itself a proof of the importance of extended states and of the dominance of direct radiative recombination. Photoluminescence lifetimes and the fastest rise and decay times observed in EL are, for CPs with quantum yields of 10% or more, in the nanosecond range, typical of exciton lifetimes. This combination of yield and lifetime is not easily accounted for by the direct process.

Clearly, an important question is whether the singlet exciton is bound, not only relative to a pair of infinitely distant polarons, but also to a pair of polarons at minimum distance, after subtraction of their mutual coulombic attraction energy. If it is not so, polarons can radiatively recombine only by direct emission of a photon, or through some deeper, localized, presumably extrinsic level. What is required, then, is a direct determination of the bandgap (i.e., the electron–hole pair creation threshold energy). In only one class of CPs, the PDAs, is this information available: $E_g - E_s \approx 0.5$ eV. This binding seems large enough to ensure that two polarons can indeed recombine into an exciton; but probably bipolarons cannot: The calculated energy difference between a bipolaron and two isolated carriers seems too large [273]. One can only speculate about bipolaron recombination; it might, for instance, occur in two steps, the first (probably non-

radiative) one generating a pair of opposite charged polarons, which could in a second step recombine as discussed above, hence a decrease in total radiative yield.

Conjugated polymers may, however, differ from organic molecular crystals in a very important way, and some indeed do. In these crystals, the lowest singlet exciton is always of ungerade (*u*) symmetry; hence the radiative decay to the ground state, which is always of gerade (*g*) symmetry, is always allowed. But it is well documented that in polyenes (the oligomers of PA) the lowest singlet state is of *g* symmetry, and consequently, the radiative lifetimes are long and the fluorescence quantum yields are very small [127]. This is also true in at least one diacetylene oligomer [279], and indeed PDAs are not fluorescent.

Therefore, at least in some CPs, the lowest singlet exciton is a *g* state. If recombination in such a CP is by the exciton process, no EL, or only a very weak one, is expected. The case of direct (nonexciton) recombination has not been considered yet, but one may expect that if a low-lying *g* state exists, it will be formed by recombination just as well, and no EL will be emitted.

Spectroscopy of CP *g* states is a subject of current interest, up to now mainly because these states are important in the optical nonlinear properties of these molecules [280,281]. It has recently been shown that in PPV, a CP frequently used in EL, the lowest *g* excited state is 0.5 eV above the *u* exciton [282], and indeed the fluorescence quantum yield of PPV is high. Calculations relating the extent of bond-length alternation (see Chapter 11, Sections IV.A and IV.B) to the energy ordering of excited states indeed predict the situation observed in PPV [283]. Similar experimental and theoretical studies are certainly forthcoming.

To summarize, the microscopic recombination processes in CPs are still debated. If recombination proceeds via the formation of a singlet exciton, a good CP for LED applications should have at least three properties: It should not form bipolarons, or only slowly; the *u* exciton should be the lowest singlet state; and that state should, of course, have minimal non-radiative decay processes, in particular to the triplet state [129]. But, in addition, the diode geometry and the electrodes should be chosen so as to maximize carrier recombination and minimize carrier extraction through the electrodes.

4. Diode Geometries: Multilayer or Single Layer

All early work on polymer LEDs was performed using a single polymer layer between two electrodes, as in the early organic crystal LEDs [259–262]. However, new progress in LED using vapor-deposited small molecules as active materials had been made possible by using multilayer struc-

tures in order to spatially control carrier transport and recombination [284–286]. The material of the hole transporting layer deposited near the anode was chosen so as to block the transport of electrons injected at the cathode into the electron transporting layer. It was claimed that holes accumulated near the interface between the two organic layers and that recombination occurred there. Quite interesting performances were reported: for instance, a brightness of 100 cd/m² under 5.5 V bias, corresponding to a power conversion efficiency of about 0.5%. More complicated multilayer structures were subsequently prepared in an effort to increase quantum and power efficiencies and to adjust color [287], and indeed, performances improved (brightness up to 1000 cd/m²).

The two-layer geometry has now been used with CPs [288] (Fig. 34). In principle, several improvements results:

1. The holes injected by ITO into PPV are blocked by the PMMA layer before reaching the Ca electrode. PMMA is a wide-bandgap insulator, so electron transport requires dispersion of electron-accepting molecules into it, between which electron hopping occurs.
2. The electric fields at the electrodes are different and can adjust toward equalization of the electron and hole currents (although electron extraction by ITO is not prevented), thus increasing the recombination yield.
3. The excitons are created away from the electrodes, so they are protected against nonradiative quenching at the metal–polymer interfaces.

Such diodes have quantum efficiencies (photon/electron) of up to 0.8% and a brightness of 500 cd/m². Further progress is forthcoming.

5. Materials and Performances

In a rapidly moving field it is difficult to describe a “state of the art.” What is given here is merely what was known by the author as of September 1993; it may not even be a balanced account of what had been done by then.

(a) Materials

The number of polymeric materials in which EL has been demonstrated is increasing rapidly. Very different molecular formulas have been reported. The main aims are to obtain all colors and to improve the yields, the quantum yield expressed in photons per electron as well as the power yield, and to improve device lifetime. We shall not describe the chemistry involved, merely hint at some underlying principles.

All *colors* have now been obtained. Table 4 shows six examples of polymers for which the wavelength of monomer emission spans most of the visible spectrum. In fact, three basic unit structures are used: the phenyl

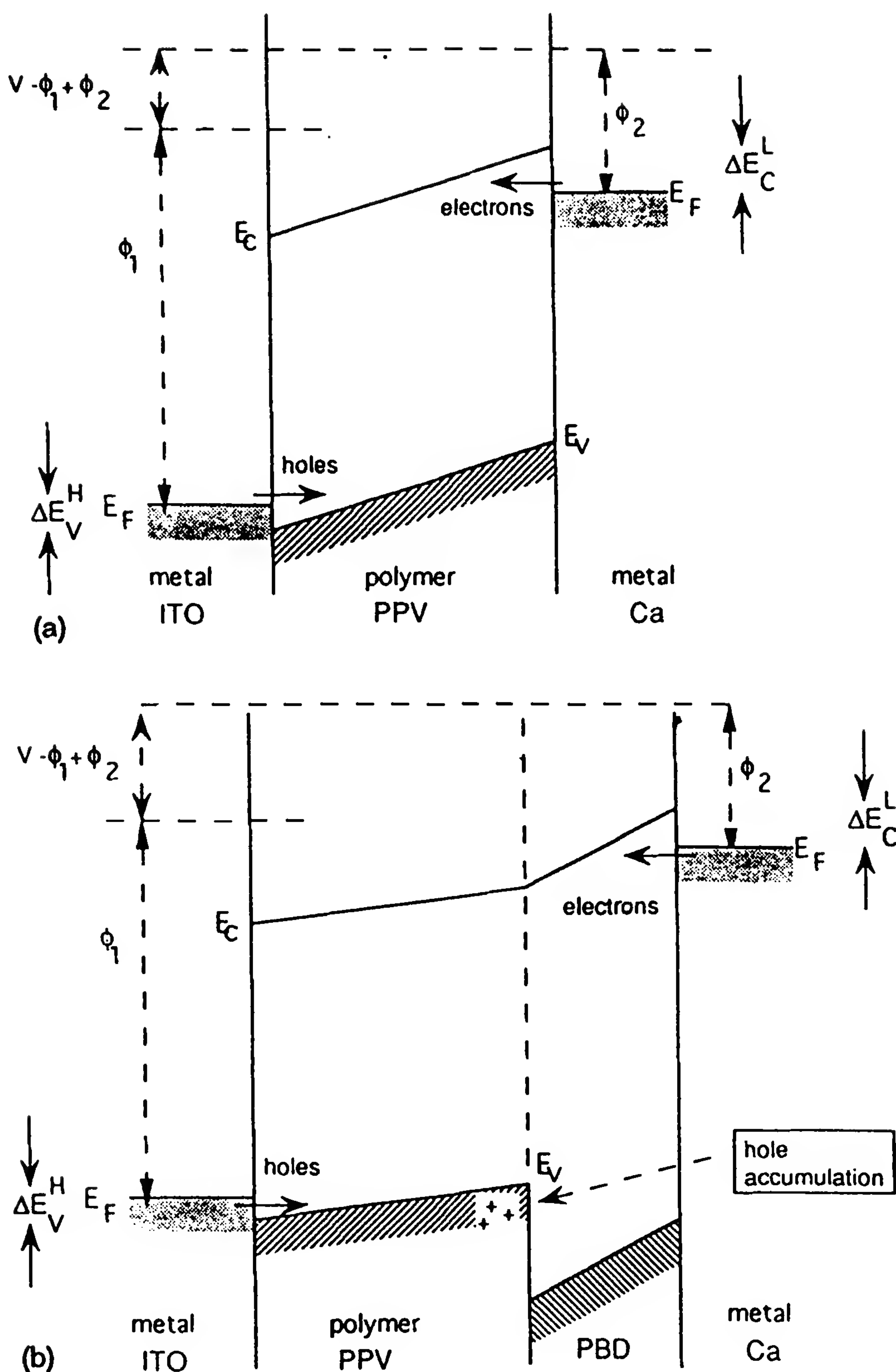

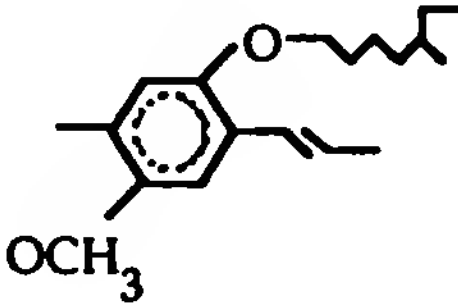
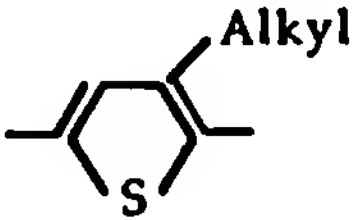
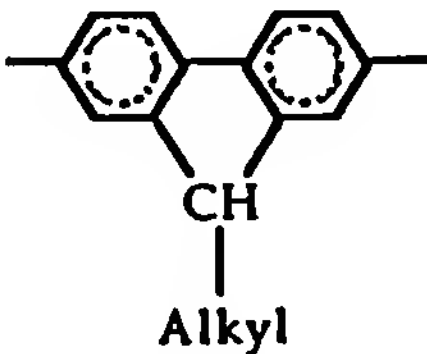

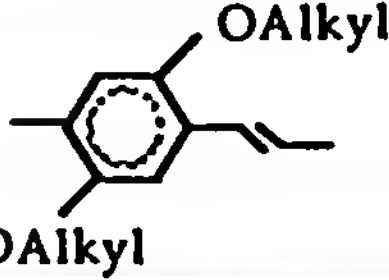


Figure 34 Comparison of the single organic layer geometry (a), with the double layer obtained by insertion of an electron transporting, hole blocking layer (b). The energy-level positions are highly simplified. Recombination should occur preferentially within the hole accumulation layer. (From Ref. 288.)

Table 4 Six Processible Polymers, Covering the Entire Visible Spectrum, in Order of Publication Dates^a

S, or SP	Repeat unit	Polymer	λ_{max} (Å)	Ref.	Date
SP		PPV	5600	235	1990
S		MEH-PPV	6000	269	1991
S		P3AlkylT	6500	289	1991
S		PAlkyl Fluorene	4700	290	1991
SP		PPP	4800	291	1992
S		RO-PPV*	6000		1993

^aS, soluble polymer; SP, soluble precursor.
*Maximum brightness obtained, 7000 cd/m².

ring for blue emission, and thiophene or phenylenevinylene for yellow to red. Examples of absorption spectra are shown on Fig. 35; emission spectra are roughly mirror images of these. New basic units are due to appear. Color can be adjusted in at least two ways:

1. By suitable substituents, used at the same time to increase the yield and facilitate processibility. Substitution usually shifts emission toward the red (see Table 4). However, the absorption and emission spectra of phenylPPV (PPPV), in which the phenyl is substituted to one of the H atoms on the phenyl ring in the conjugated chain, is blue-shifted by several hundred angstroms [292].
2. By adjusting the extent of electron conjugation. This has been done by purposely introducing disorder to shorten the conjugation length (see Chapter 11, Section II). For instance, imperfect conversion of a

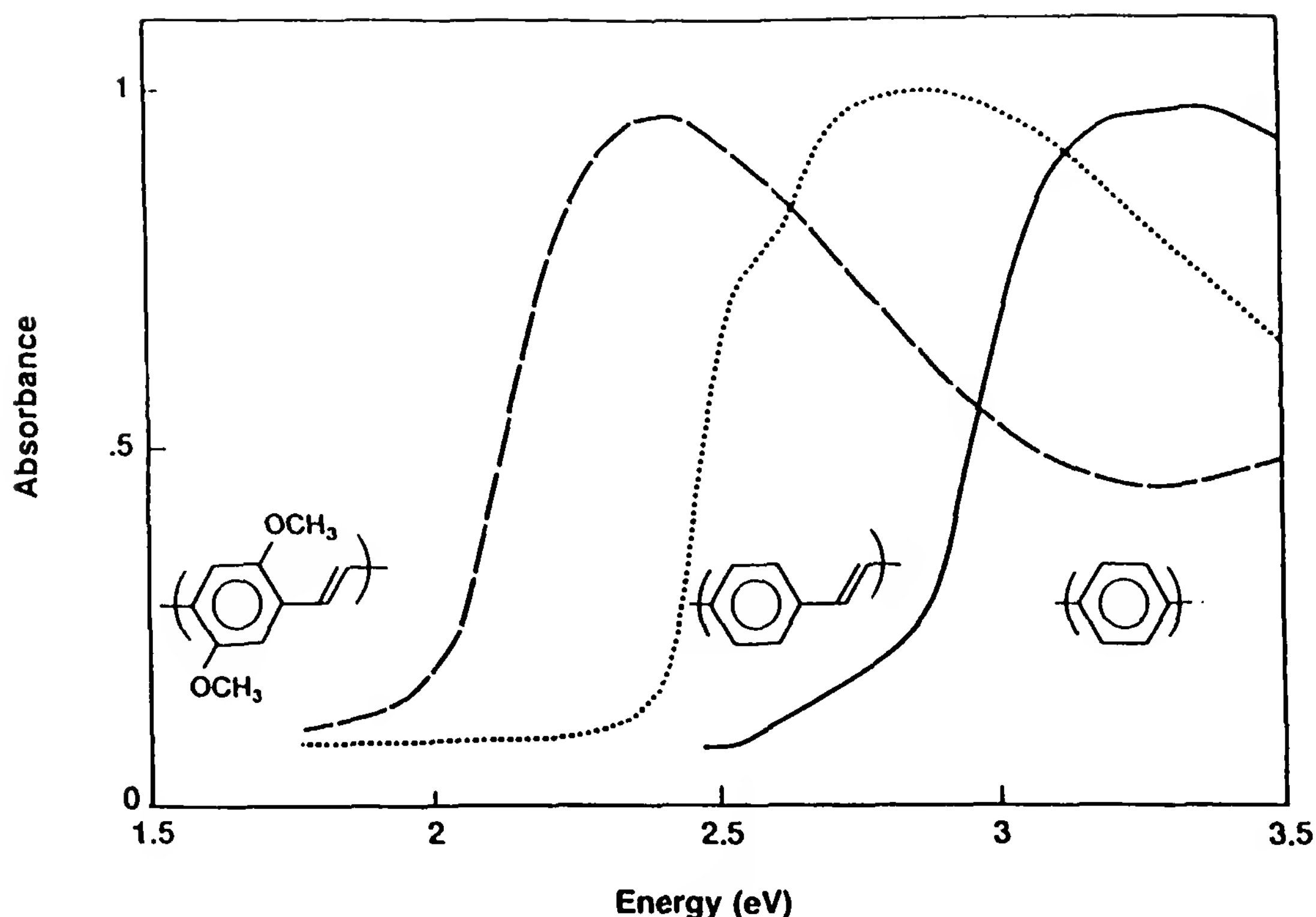


Figure 35 Absorption spectra of three CPs commonly used in LED studies, showing how the entire visible spectrum can be spanned. (From Ref. 124.)

precursor will leave unconjugated spacers in the resulting CP [265]; it has also been shown that the regularity of relative orientations of successive monomers (in polyhexylthiophene) can be controlled, thus adjusting the electron localization [77]. These are ways of shifting the emission toward the blue.

These two strategies are illustrated on Fig. 36. More generally, it is possible to conceive regular block copolymers in which both components would be CPs, so as to adjust the bandgap and/or the electron localization [293].

Another possibility is to use oligomers [266], as in FETs. Oligomer diodes are, in fact, similar to “small molecule” LEDs. Block copolymers with short conjugated blocks all of equal lengths provide a means for having the oligomer electronic properties together with the polymer processibility [294].

Increased yields imply reduction of radiationless loss processes. These may be intrinsic to the polymer itself; for instance, the singlet exciton may have a small fluorescence yield η_f . Rigid molecules tend to have larger η_f ,

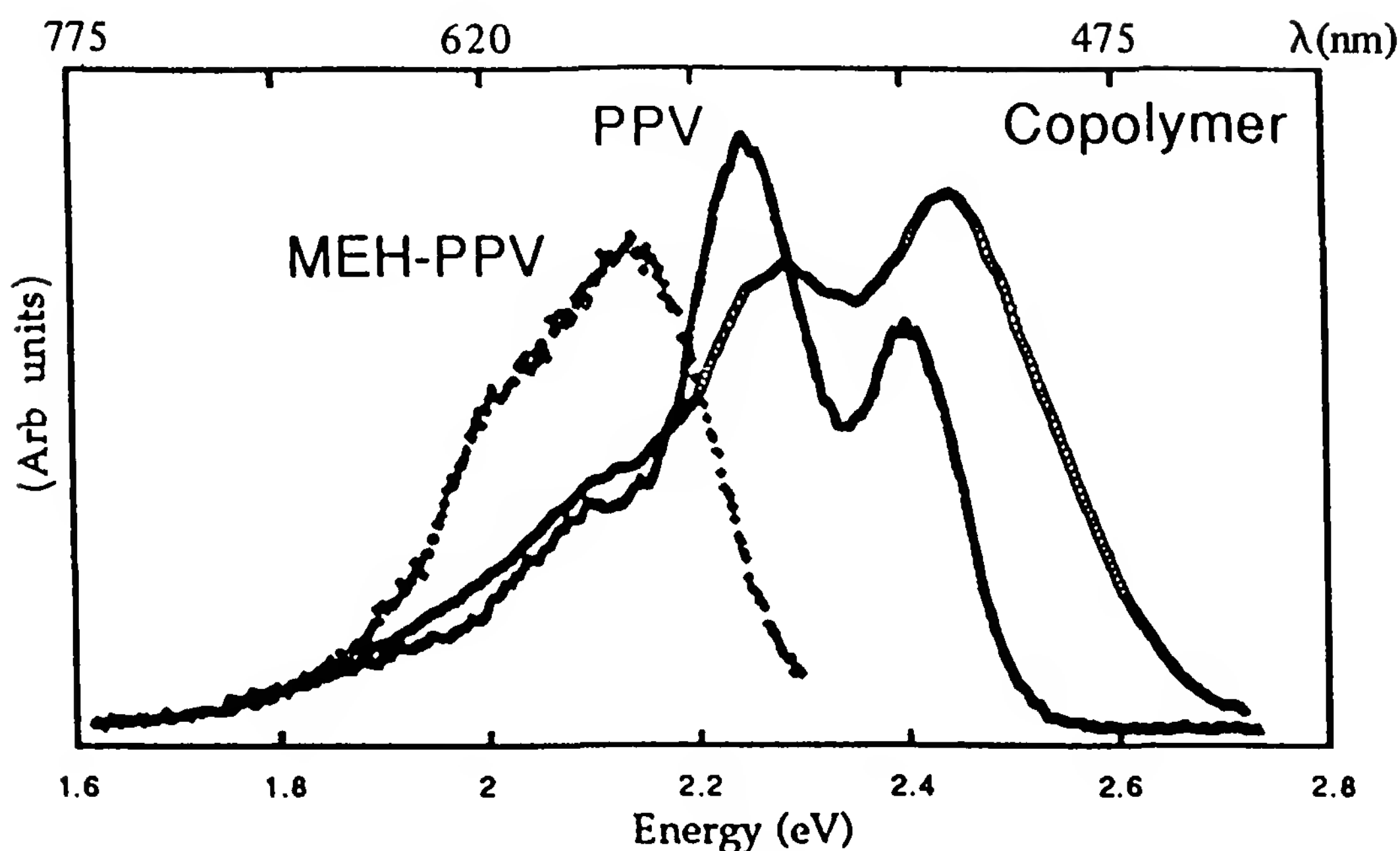


Figure 36 Emission of PPV and derivatives. It is red-shifted by substitution in MEH-PPV, and blue-shifted by insertion of nonconjugated “spacers” in the copolymer. (From Ref. 265.)

so a large effort is invested in producing more rigid chains; note that large side groups can also sufficiently hinder rotation and play a similar role.

Radiationless losses can also occur by migration of the excitation to nonemitting “killer” quenching centers [295]. Surfaces and interfaces are also well-known quenchers. To obviate this migration, two (mutually compatible) strategies are pursued. One is to remove the killer centers (i.e., to improve purity). The other one is to hinder exciton motion by increasing disorder or favoring localization. To achieve that, regular or random copolymers are being synthesized, the units having different energy levels (this also shifts the emission spectrum; see above). Confining the recombination zone away from the interfaces in a multilayer geometry (see Section V.C.4) is also useful.

It is also possible to adjust both the color and the quantum yield by doping the material with highly fluorescent recombination centers, as often done in inorganic LEDs. This has not yet been much explored in CPs. However, a new type of polymer LED has been demonstrated in which the active element is a dye in the form of small clusters or isolated molecules dispersed in a nonconjugated polymer such as poly(methylmethacrylate) [296] or polystyrene. Performances are comparable to those of present CP LEDs: this may yield a new generation of polymer LEDs.

(b) Performances

This is a survey of typical results obtained to date (some not yet published). Not all performances are present simultaneously in a given device, but there is no fundamental reason precluding that.

1. *Color.* All colors are now available (Figs. 35 and 36). Fine adjustments are possible (see above). However, the emission spectra are broader than those defining the primary colors [258]. Narrower and more structured emission bands have now been obtained by fine tuning of the polymerization conditions [296] or processing conditions [108] (see Fig. 15), so there is hope that this problem can be solved.
2. *Electrical operation conditions.* Almost all high-brightness CP LEDs have a threshold voltage for light emission (perhaps related to the flat-band conditions shown in Fig. 31) of 1.8 to 2 eV. Beyond that voltage, current and brightness increase rapidly with V (Fig. 29). Good brightness without too much heating or device lifetime shortening is usually achieved at 10 to 20 V. Therefore, operating voltages compatible with today's electronics are within reach. Operating currents are still high, 10 to 100 mA/cm². Progress is needed, perhaps from multilayer structures.
3. *Yields* are still low (and often not even measured). They improved very quickly to about 4×10^{-2} (quantum yield). More progress seems harder to come by, but the physical limits are almost one order of magnitude larger (see above).
4. *Brightness* values above 100 cd/m² are currently obtained; this is on the order of that of a computer screen. Maximum brightness reported is 7000 cd/m², larger than that of a fluorescent bulb. The problem is with the yields, not with intrinsic brightness limits; operation well above 1000 cd/m² means voltages above 20 V and high operating temperatures over 100°C.
5. *Switching times* are very dependent on electrical operation conditions. They can reach several tens of microseconds at low voltage, but are much shorter at high voltages: 50 ns [298] or even less. Therefore, multiplexing appears possible. There has not been much discussion of this point yet (however, see Ref. 299).
6. *Light-emitting areas* are in most cases small, a few square millimeters, but diodes having areas as large as 100 cm² have been prepared. As long as processible polymers are used, it seems possible to prepare very large area emitting panels. This may well be the first practical application of CP LEDs. Flexible LEDs have been fabricated [267].
7. *Lifetimes* larger than 700 h, or a month, of continuous operation have already been reported. This is still one to two orders of magnitude too short. There is a dearth of research on this point, but failure processes

are beginning to be understood and controlled: for instance, peeling of the CP film off the ITO electrode.

In conclusion, prospects for practical uses of CP LEDs seems better than for FETs. Progress in 3 years has been significant, and physical or technological limits seem to be far away. Although simple devices might appear in the near future, use of CPs in high-definition screens such as those used in TV sets is many years ahead, if it ever occurs.

REFERENCES

1. W. J. Feast, in *Handbook of Conducting Polymers*, Vol. 1 (T. A. Skotheim, ed.), Marcel Dekker, New York, 1986, p. 1.
2. N. C. Billingham and P. D. Calvert, *Adv. Polym. Sci.* **90**:1 (1989).
3. C. B. Gorman and R. H. Grubbs, in *Conjugated Polymers* (J. L. Brédas and R. Silbey, eds.), Kluwer, Dordrecht, The Netherlands, 1991, p. 1.
4. J. Heinze, *Topics Current Chem.* **152**:1 (1993).
5. T. A. Skotheim, ed., *Handbook of Conducting Polymers*, Marcel Dekker, New York, 1986.
6. J. C. W. Chien, *Polyacetylene*, Academic Press, Orlando, Fla., 1984.
7. L. M. Goldenberg and P. C. Lacaze, *Synth. Metals* **58**:271 (1993).
8. E. M. Geniès, A. Boyle, M. Lapkowski, and C. Tsintavis, *Synth. Metals* **36**:139 (1990).
9. P. J. Flory, *Principles of Polymer Chemistry*, Cornell Univ. Press, Ithaca, N.Y., 1953.
10. P. G. de Gennes, *Scaling Concepts in Polymer Physics*, Cornell Univ. Press, Ithaca, N.Y., 1979.
11. J. des Cloizeaux and G. Jannink, *Les Polymères en Solution: leur Modélisation et leur structure*, Ed. de Physique, Les Ulis, France, 1987.
12. B. Wunderlich, *Macromolecular Physics*, 2 volumes, Academic Press, New York, 1973.
13. G. N. Patel, *Polym. Prepr. Am. Chem. Soc. Div. Polym. Chem.* **19**(2):154 (1978).
14. R. L. Elsenbaumer, K. Y. Jen, and R. Oboodi, *Synth. Metals* **15**:164 (1986).
15. (a) A. Andreatta, Y. Cao, J. C. Chiang, A. J. Heeger, and P. Smith, *Synth. Metals* **26**:383 (1988); (b) M. Angelopoulos, G. E. Asturias, S. P. Erner, A. Ray, E. M. Scherr, A. G. MacDiarmid, M. Akhtar, Z. Kiss, and A. J. Epstein, *Mol. Cryst. Liq. Cryst.* **160**:151 (1988).
16. J. P. Aimé, in *Conjugated Polymers* (J. L. Brédas and R. Silbey, eds.), Kluwer, Dordrecht, The Netherlands, 1991, p. 229.
17. S. Roth and H. Bleier, *Adv. Phys.* **36**:385 (1987).
18. F. Chao, M. Costa, and C. Tian, *Synth. Metals* **53**:127 (1993).
19. F. Saldi, M. Lelaurain, and D. Billaud, *J. Chim. Phys. (Paris)* **89**:997 (1992).
20. G. B. Street, in Ref. 5, Vol. 1, p. 265.
21. G. Tourillon, in Ref. 5, Vol. 1, p. 293.

22. Z. Mo, K.-B. Lee, Y. B. Moon, M. Kobayashi, A. J. Heeger, and F. Wudl, *Macromolecules* 18:1972 (1985).
23. S. Brückner and W. Porzio, *Makromol. Chem.* 189:961 (1988).
24. J. P. Pouget, M. E. Jozefowicz, A. J. Epstein, X. Tang, and A. G. MacDiarmid, *Macromolecules* 24:779 (1991).
25. C. S. Brown, M. E. Vickers, P. J. S. Foot, N. C. Billingham, and P. D. Calvert, *Polymer* 27:1719 (1986).
26. R. Hosemann and S. N. Baghchi, *Direct Analysis of Diffraction by Matter*, North-Holland, Amsterdam, 1962.
27. M. Laridjani, J. P. Pouget, E. M. Scherr, A. G. MacDiarmid, M. E. Jozefowicz, and A. J. Epstein, *Macromolecules* 25:4113 (1992).
28. M. Laridjani, J. P. Pouget, A. G. MacDiarmid, and A. J. Epstein, *J. Phys. (France) I* 2:1003 (1992).
29. C. S. Yannoni and T. C. Clarke, *Phys. Rev. Lett.* 51:1191 (1983).
30. J. Kürti and H. Kuzmany, *Phys. Rev. B* 44:597 (1991).
31. M. Schott, in *Conjugated Polymers and Related Materials; The Interconnexion of Chemical and Electronic Structure* (W. R. Salaneck, I. Lundström, and B. Rånby, eds.), Oxford Univ. Press, Oxford, 1993, p. 377.
32. W. C. Hamilton, *Acta Cryst.* 18:502 (1965).
33. A. Guinier, *Théorie et technique de la radiocristallographie*, Dunod, Paris, 1950; *X-ray Diffraction in Crystals*, W. H. Freeman, San Francisco, 1963.
34. J. P. Pouget, in *Electronic Properties of Polymers and Related Compounds*, Springer Series in Solid-State Science, Vol. 63 (H. Kuzmany, H. Mehring, and S. Roth, eds.), Springer-Verlag, Berlin, 1985, p. 26; J. Pouget, P. Robin, R. Comes, H. W. Gibson, A. J. Epstein, and D. Billaud, *Physica* 127 B:158 (1984).
35. M. M. Sokolowski, E. A. Marseglia, and R. H. Friend, *Polymer* 27:1714 (1986).
36. J. Tsukamoto, *Adv. Phys.* 41:509 (1992).
37. P. Robin, J. P. Pouget, R. Comès, H. W. Gibson, and A. J. Epstein, *Phys. Rev. B* 27:3938 (1983).
38. J. Ma, J. E. Fischer, E. M. Scherr, A. G. MacDiarmid, M. E. Jozefowicz, A. J. Epstein, C. Mathis, B. François, N. Coustel, and P. Bernier, *Phys. Rev. B* 44:11609 (1991).
39. H. Kahlert, O. Leitner, and G. Leising, *Synth. Metals* 17:467 (1987).
40. Y. B. Moon, M. Winokur, A. J. Heeger, J. Barker, and D. C. Bott, *Macromolecules* 20:2457 (1987).
41. R. H. Baughman and G. Moss, *J. Chem. Phys.* 77:6321 (1982).
42. D. Baeriswyl and K. Maki, *Phys. Rev. B* 28:2068 (1983).
43. K. Shimamura, F. E. Karasz, J. A. Hirsch, and J. C. W. Chien, *Makromol. Chem. Rapid Commun.* 2:473 (1981).
44. C. P. Fincher, Jr., C.-E. Chen, A. J. Heeger, A. G. MacDiarmid, and J. B. Hastings, *Phys. Rev. Lett.* 48:100 (1982).

45. R. H. Baughman, S. L. Hsu, L. R. Anderson, G. P. Pez, and A. J. Signorelli, in *Molecular Metals*, NATO Conference Series (W. E. Hatfield, ed.), Plenum Press, New York, 1979, p. 187.
46. S. Suhai, Phys. Rev. B 27:3506 (1983).
47. D. Chen, M. J. Winokur, M. A. Masse, and F. E. Karasz, Phys. Rev. B 41:6759 (1990).
48. H. W. Hässlin and C. Riekkel, Synth. Metals 5:37 (1982).
49. M. Stamm and J. Hocker, J. Phys. (France) C3 44:667 (1983).
50. K. N. Baker, H. C. Knachel, A. V. Fratini, and W. W. Adams, Mater. Res. Soc. Symp. Proc. 134:497 (1989).
51. P. K. Kahol, W. G. Clark, and M. Mehring, in *Conducting Polymers*, Springer Series in Solid-State Science, Vol. 102 (H. Kiess, ed.), Springer-Verlag, Berlin, 1992, p. 217.
52. A. J. Epstein, in *Conjugated Polymers* (J. L. Brédas and R. Silbey, eds.), Kluwer, Dordrecht, The Netherlands, 1991, p. 211.
53. E. M. Scherr, A. G. MacDiarmid, S. K. Manohar, J. G. Masters, Y. Sun, X. Tang, V. B. Cajipe, J. E. Fischer, K. R. Cormack, M. E. Jozefowicz, J. M. Ginder, R. P. McCall, and A. J. Epstein, Synth. Metals 41–43:735 (1991).
54. F. Zuo, M. Angelopoulos, A. G. MacDiarmid, and A. J. Epstein, Phys. Rev. B 36:3475 (1987).
55. Q. Li, L. Cruz, and P. Phillips, Phys. Rev. B 47:1840 (1993).
56. N. S. Murthy, L. W. Shacklette, and R. H. Baughman, Phys. Rev. B 41:3708 (1990).
57. F. Saldi, M. Lelaurain, and D. Billaud, Solid State Commun. 76:595 (1990).
58. M. J. Winokur, Y. B. Moon, A. J. Heeger, J. Barker, D. C. Bott, and H. Shirakawa, Phys. Rev. Lett. 58:2329 (1987).
59. N. Coustel, P. Bernier, and J. E. Fischer, Phys. Rev. B 43:3147 (1991).
60. R. H. Baughman, N. S. Murthy, G. G. Miller, and L. W. Shacklette, J. Chem. Phys. 79:1065 (1983).
61. N. S. Murthy, G. G. Miller, and R. H. Baughman, J. Chem. Phys. 89:2523 (1988).
62. S. L. Hsu, A. J. Signorelli, G. P. Pez, and R. H. Baughman, J. Chem. Phys. 69:106 (1978).
63. C. Riekkel, H. W. Hässlin, K. Menke, and S. Roth, Synth. Metals 10:31 (1984).
64. G. Perego, G. Lugli, U. Pedretti, and G. Allegra, Makromol. Chem. 189:2687 (1988).
65. V. Enkelmann, K. Göckelmann, G. Wieners, and M. Monkenbusch, Mol. Cryst. Liq. Cryst. 120:195 (1985).
66. G. Wegner and J. Rühle, Disc. Faraday Soc. 88:333 (1989).
67. D. S. Spiegel, P. Pincus, and A. J. Heeger, Synth. Metals 28:C385 (1989).
68. M. Rawiso, J. P. Aimé, J. L. Fave, M. Schott, M. A. Müller, M. Schmidt, H. Baumgartl, and G. Wegner, J. Phys. (France) 49:861 (1988).
69. G. Rossi, R. R. Chance, and R. Silbey, J. Chem. Phys. 90:7594 (1989).

70. G. Gustafsson, O. Inganäs, W. R. Salaneck, J. Laakso, M. Lojonen, T. Taka, J.-E. Österholm, H. Stubb, and T. Hjertberg, in *Conjugated Polymers* (J. L. Brédas and R. Silbey, eds.), Kluwer, Dordrecht, The Netherlands, 1991, p. 315.
71. K. Yoshino, S. Nakajima, M. Fujii, and R. I. Sugimoto, *Polym. Commun.* 28:309 (1987).
72. S.-A. Chen and J.-M. Ni, *Macromolecules* 25:6081 (1992).
73. A. Bolognesi, M. Catellani, S. Destri, and W. Porzio, *Makromol. Chem. Rapid Commun.* 12:9 (1991).
74. O. Inganäs, W. R. Salaneck, and J. E. Österholm, *Synth. Metals* 22:395 (1988).
75. M. Granström and O. Inganäs, *Synth. Metals* 48:21 (1992).
76. M. Leclerc, F. M. Diaz, and G. Wegner, *Makromol. Chem.* 190:3105 (1989).
77. B. Xu and S. Holdcroft, *Macromolecules* 26:4457 (1993).
78. R. M. Souto Maior, K. Hinkelmann, H. Eckert, and F. Wudl, *Macromolecules* 23:1268 (1990).
79. M. Winokur, D. Spiegel, Y. Kim, S. Hotta, and A. J. Heeger, *Synth. Metals* 28:C419 (1989).
80. T. J. Prosa, M. J. Winokur, J. Moulton, P. Smith, and A. J. Heeger, *Macromolecules* 25:4364 (1992).
81. J. Mårdalen, E. J. Samuelsen, O. R. Gautun, and P. H. Carlsen, *Synth. Metals* 48:363 (1992).
82. N. A. Platé and V. P. Shibaev, in *Comb-Shaped Polymers and Liquid Crystals* (J. M. G. Cowie, ed.), Plenum Press, New York, 1987, p. 40.
83. D. Aubrey and A. Barnatt, *J. Polym. Sci. Polym. Phys. Ed.* 6:241 (1968).
84. K. Tashiro, K. Ono, K. Kobayashi, T. Kawai, and K. Yoshino, *Synth. Metals* 41–43:571 (1991).
85. J. H. F. Martens, E. A. Marseglia, D. D. C. Bradley, R. H. Friend, P. L. Burns, and A. B. Holmes, *Synth. Metals* 55–57:449 (1993).
86. O. Lhost and J. L. Brédas, *J. Chem. Phys.* 96:5279 (1992).
87. A. J. Heeger and P. Smith, in *Conjugated Polymers* (J. L. Brédas and R. Silbey, eds.), Kluwer, Dordrecht, The Netherlands, 1991, p. 141.
88. D. Gläser, T. Schimmel, M. Schwoerer, and H. Naarman, *Makromol. Chem.* 190:3217 (1989).
89. J. L. Ribet, M. Rolland, A. Montaner, M. Galtier, Z. Lakhiai, J. L. Sauvajol, M. Brunet, R. Almairac, and P. Bernier, *Synth. Metals* 24:1 (1988).
90. Y. Cao, P. Smith, and A. J. Heeger, *Polymer* 32:1210 (1991).
91. Y. W. Park, C. Park, Y. S. Lee, C. O. Yoon, H. Shirakawa, Y. Suezaki, and K. Akagi, *Solid State Commun.* 65:147 (1988).
92. T. Schimmel, D. Gläser, M. Schwoerer, and H. Naarman, in *Conjugated Polymers* (J. L. Brédas and R. Silbey, eds.), Kluwer, Dordrecht, The Netherlands, 1991, p. 49.
93. G. Leising, *Polym. Bull.* 11:401 (1984).
94. D. E. White and D. C. Bott, *Polym. Commun.* 25:98 (1984).

95. D. R. Gagnon, J. D. Capistran, and F. E. Karasz, *Polym. Bull.* 12:293 (1984).
96. I. Murase, T. Ohnishi, T. Noguchi, and M. Hirooka, *Polym. Commun.* 25:327 (1984).
97. J. H. F. Martens, D. D. C. Bradley, P. L. Burns, R. H. Friend, A. B. Holmes, and E. A. Marseglia, *Synth. Metals* 41–43:301 (1991).
98. S. Tokito, P. Smith, and A. J. Heeger, *Synth. Metals* 36:183 (1990).
99. J. E. Fischer, X. Tang, E. M. Scherr, V. B. Cajipe, and A. G. MacDiarmid, *Synth. Metals* 41–43:661 (1991).
100. K. R. Cromack, M. E. Jozefowicz, J. M. Ginder, A. J. Epstein, R. P. McCall, G. Du, J. M. Leng, K. Kim, C. Li, Z. H. Wang, M. A. Druy, P. J. Glatkowski, E. M. Scherr, and A. G. MacDiarmid, *Macromolecules* 24:4157 (1991).
101. A. P. Monkman and P. Adams, *Synth. Metals* 40:87 (1991).
102. S. Hotta, M. Soga, and N. Sonoda, *Synth. Metals* 26:267 (1988).
103. J. Mårdalen, E. J. Samuelson, O. R. Gautun, and P. H. Carlsen, *Solid State Commun.* 77:337 (1991).
104. G. Gustafsson, O. Inganäs, H. Österholm, and J. Laakso, *Polymer* 32:1574 (1991).
105. J. Moulton and P. Smith, *Polymer* 33:2340 (1992).
106. J. Moulton and P. Smith, *Synth. Metals* 40:13 (1991).
107. T. W. Hagler, K. Pakbaz, J. Moulton, F. Wudl, P. Smith, and A. J. Heeger, *Polym. Commun.* 32:339 (1991).
108. T. W. Hagler, K. Pakbaz, K. F. Voss, and A. J. Heeger, *Phys. Rev. B* 44:8652 (1991).
109. F. S. Bates and G. L. Baker, *Macromolecules* 19:704 (1983).
110. P. Garrin, J. P. Aimé, D. Reibel, and C. Mathis, *Synth. Metals* 51:37 (1992).
111. M. Kobayashi, N. Colaneri, M. Boysel, F. Wuld, and A. J. Heeger, *J. Chem. Phys.* 82:5717 (1985).
112. M. Satoh, M. Tabata, F. Uesugi, K. Kaneto, and K. Yoshino, *Synth. Metals* 17:595 (1987).
113. G. Leising, *Phys. Rev. B* 38:10313 (1988).
114. K. L. D'Amico, C. Manos, and R. L. Christensen, *J. Am. Chem. Soc.* 102:1777 (1980).
115. R. E. Schaffer, R. R. Chance, K. Knoll, R. R. Schrock, and R. Silbey, in *Conjugated Polymeric Materials: Opportunities in Electronics, Optoelectronics and Molecular Electronics* (J. L. Brédas and R. R. Chance, eds.), Kluwer, Dordrecht, The Netherlands, 1990, p. 365.
116. H. Eckhardt, *J. Chem. Phys.* 79:2085 (1983).
117. R. R. Chance, G. N. Patel, and J. D. Witt, *J. Chem. Phys.* 71:206 (1979).
118. S. Spagnoli, J. Berréhar, C. Lapersonne-Meyer, and M. Schott, *J. Chem. Phys.* (May 1994).
119. W. E. Torruellas, K. B. Rochford, R. Zanoni, S. Aramaki, and G. I. Stegeman, *Opt. Commun.* 82:94 (1991).
120. P. Gass, I. Abram, R. Raj, and M. Schott, *J. Chem. Phys.* 100:88 (1994).

121. R. R. Chance, J. M. Sowa, H. Eckhardt, and M. Schott, *J. Phys. Chem.* **90**:3031 (1986).
122. M. L. Shand, R. R. Chance, M. Le Postollec, and M. Schott, *Phys. Rev. B* **25**:4431 (1982).
123. D. Bloor and F. H. Preston, *Phys. Status Solidi (a)* **37**:427 (1976).
124. H. Eckhardt, L. W. Shacklette, K. Y. Jen, and R. L. Elsenbaumer, *J. Chem. Phys.* **91**:1303 (1989).
125. D. Fichou, G. Horowitz, B. Xu, and F. Garnier, *Synth. Metals* **48**:167 (1992).
126. D. A. Halliday, P. L. Burns, D. D. C. Bradley, R. H. Friend, O. M. Gelsen, A. B. Holmes, A. Kraft, J. H. F. Martens, and K. Pichler, *Adv. Mater.* **5**:40 (1993).
127. (a) B. S. Hudson, B. E. Kohler, and K. Schulten, in *Excited States*, Vol. 6 (E. C. Lim, ed.), Academic Press, New York, 1982, p. 1; (b) B. E. Kohler, in *Conjugated Polymers* (J. L. Brédas and R. Silbey, eds.), Kluwer, Dordrecht, The Netherlands, 1991, p. 405.
128. M. Pope and C. L. Swenberg, *Electronic Processes in Organic Crystals*, Oxford Univ. Press, Oxford, 1982; and in *Quantum Chemistry of Polymers: Solid State Aspects* (J. Ladik and J. M. André, eds.), D. Reidel, Dordrecht, The Netherlands, 1984, p. 137.
129. S. P. McGlynn, T. Azumi, and M. Kinoshita, *Molecular Spectroscopy of the Triplet State*, Prentice Hall, Englewood Cliffs, N.J., 1969.
130. B. R. Weinberger, C. B. Roxlo, S. Etemad, G. L. Baker, and J. Orenstein, *Phys. Rev. Lett.* **53**:86 (1984).
131. W. Krug, E. Miao, M. Derstine, and J. Valera, *J. Opt. Soc. Am. B* **6**:726 (1989).
132. A. C. Boccara, D. Fournier, W. Jackson, and N. M. Amer, *Opt. Lett.* **5**:377 (1980).
133. M. Thakur, R. C. Frye, and B. I. Greene, *Appl. Phys. Lett.* **56**:1187 (1990).
134. H. Eichele, E. Herath, and Ch. Kröhnke, *Chem. Phys. Lett.* **71**:211 (1980).
135. J. Berréhar, C. Lapersonne, M. Schott, and S. Spagnoli (in preparation).
136. M. Schott and G. Wegner, in *Nonlinear Optical Properties of Organic Molecules and Crystals*, Vol. 2 (D. S. Chemla and J. Zyss, eds.), Academic Press, Orlando, Fla., 1987, p. 1.
137. C. K. Chiang, C. R. Fincher, Jr., Y. W. Park, A. J. Heeger, H. Shirakawa, E. J. Louis, S. C. Gau, and A. G. MacDiarmid, *Phys. Rev. Lett.* **39**:1098 (1977).
138. H. Shirakawa, T. Ito, and S. Ikeda, *Makromol. Chem.* **179**:1565 (1978).
139. C. E. Swenberg and N. E. Geacintov, in *Organic Molecular Photophysics*, Vol. 1 (J. B. Birks, ed.), Wiley, London, 1973, p. 489.
140. Z. V. Vardeny and X. Wei, *Synth. Metals* **54**:99 (1993).
141. H. Sixl and W. Rühle, in *Conjugated Polymeric Materials: Opportunities in Electronics, Optoelectronics and Molecular Electronics* (J. L. Brédas and R. R. Chance, eds.), Kluwer, Dordrecht, The Netherlands, 1990, p. 457.
142. R. H. Austin, G. L. Baker, S. Etemad, and R. Superfine, *J. Chem. Phys.* **90**:6642 (1989).

143. C. Jundt, G. Klein, and J. LeMoigne, *Chem. Phys. Lett.* 203:37 (1993).
144. J. Orenstein and G. L. Baker, *Phys. Rev. Lett.* 49:1043 (1982).
145. R. H. Friend, D. D. C. Bradley, and P. D. Townsend, *J. Phys. D Appl. Phys.* 20:1367 (1987).
146. A. J. Heeger, S. Kivelson, J. R. Schrieffer, and W. P. Su, *Rev. Mod. Phys.* 60:781 (1988).
147. D. Baeriswyl, D. K. Campbell, and S. Mazumdar, in *Conjugated Conducting Polymers*, Springer Series in Solid-State Science, Vol. 102 (H. Kiess, ed.), Springer-Verlag, Berlin, 1992, p. 7.
148. X. Wei, B. C. Hess, Z. V. Vardeny, and F. Wudl, *Phys. Rev. Lett.* 68:666 (1992).
149. W.-P. Su, *Phys. Rev. B* 36:2988 (1986); 36:6040 (1987).
150. N. F. Colaneri, D. D. C. Bradley, R. H. Friend, P. L. Burns, A. B. Holmes, and C. W. Spangler, *Phys. Rev. B* 42:11670 (1990).
151. K. Pichler, D. A. Halliday, D. D. C. Bradley, R. H. Friend, P. L. Burns, and A. B. Holmes, *Synth. Metals* 55:234 (1993).
152. D. Moses, *Synth. Metals* 55–57:22 (1993).
153. G. Grem and G. Leising, *Synth. Metals* 55–57:4105 (1993).
154. L. Athouël, Thesis, Univ. Limoges (France), 1992, unpublished.
155. M. A. Taylor, J. A. Odell, D. N. Batchelder, and A. J. Campbell, *Polymer* 31:1116 (1990).
156. D. N. Batchelder and D. Bloor, in *Advances in Infrared and Raman Spectroscopy*, Vol. 11 (R. J. H. Clark and R. E. Hester, eds.), Wiley-Heyden, 1984, New York, p. 133.
157. E. Mulazzi, G. P. Brivio, E. Faulques, and S. Lefrant, *Solid State Commun.* 46:851 (1983).
158. E. J. Mele, *Solid State Commun.* 34:339 (1980).
159. J. Berréhar, J. L. Fave, C. Lapersonne, M. Schott, and H. Eckhardt, *Mol. Cryst. Liq. Cryst.* 117:393 (1985).
160. H. E. Schaffer, R. R. Chance, R. J. Silbey, K. Knoll, and R. R. Schrock, *J. Chem. Phys.* 94:4161 (1991).
161. G. P. Brivio and E. Mulazzi, *Phys. Rev. B* 30:876 (1984).
162. B. Horowitz, *Mol. Cryst. Liq. Cryst.* 77:286 (1981).
163. Y. Yacobi and E. Ehrenfreund, in *Light Scattering in Solids VI*, Topics in Applied Physics, Vol. 68 (M. Cardona and G. Güntherodt, eds.), Springer-Verlag, Berlin, 1991, p. 73.
164. G. Zerbi, M. Gussoni, and C. Castiglioni, in *Conjugated Polymers* (J. L. Brédas and R. Silbey, eds.), Kluwer, Dordrecht, The Netherlands, 1991, p. 435.
165. A. A. Ovchinnikov, I. I. Ukrainskii, and G. V. Kventsel, *Sov. Phys. Usp.* 15:575 (1973).
166. K. Seeger, *Semiconductor Physics*, Springer-Verlag, Berlin, 1973 (5th ed., 1991).
167. M. D. Sturge, *Phys. Rev.* 127:768 (1962).
168. M. R. Philpott, in *Advances in Chemical Physics*, Vol. 23 (I. Prigogine and S. A. Rice, eds.), Academic Press, Orlando, Fla., 1973, p. 207.

169. L. Sebastian, G. Weiser, G. Peter, and H. Bässler, *Chem. Phys.* 75:103 (1983).
170. D. P. Craig and S. H. Walmsley, *Excitons in Molecular Crystals*, W. A. Benjamin, New York, 1968.
171. K. O. Lee and T. T. Gan, *Chem. Phys. Lett.* 51:120 (1977).
172. L. Sebastian and G. Weiser, *Phys. Rev. Lett.* 46:1156 (1981); *Chem. Phys.* 62:447 (1981).
173. S. Abe, W. P. Su, and J. Yu, *Phys. Rev. B* 45:8264 (1992).
174. R. M. Hochstrasser, *Molecular Aspects of Symmetry*, W. A. Benjamin, New York, 1966.
175. F. Kajzar and J. Messier, *Thin Solid Films* 132:11 (1985).
176. D. Baeriswyl, G. Harbeke, H. Kiess, E. Meier, and W. Meyer, *Physica* 117–118:B617 (1983).
177. J. Fink and G. Leising, *Phys. Rev. B* 34:5320 (1986).
178. J. Ashkenazi, E. Ehrenfreund, Z. Vardeny, and O. Brafman, *Mol. Cryst. Liq. Cryst.* 117:193 (1985).
179. R. M. Martin and L. M. Falicov, in *Light Scattering in Solids*, Topics in Applied Physics, Vol. 8 (M. Cardona, ed.), Springer-Verlag, Berlin, 1975, p. 80.
180. C. Weisbuch and R. G. Ulbrich, in *Light Scattering in Solids III*, Topics in Applied Physics, Vol. 51 (M. Cardona and G. Güntherodt, eds.), Springer-Verlag, Berlin, 1982, p. 207.
181. S. Kivelson and D. E. Heim, *Phys. Rev. B* 26:4278 (1982).
182. P. Tavan and K. Schulten, *Phys. Rev. B* 36:4337 (1988).
183. W. P. Su, J. R. Schrieffer, and A. J. Heeger, *Phys. Rev. B* 22:2099 (1980).
184. P. Vogl and D. K. Campbell, *Phys. Rev. B* 41:12797 (1990).
185. P. Gomes da Costa, R. G. Dandrea, and E. M. Conwell, *Phys. Rev. B* 47:1800 (1993).
186. J. M. André, V. P. Bodard, J. L. Brédas, J. Delhalle, and J. G. Fripiat, in *Quantum Chemistry of Polymers: Solid State Aspects* (J. Ladik, J. M. André, and M. Seel, eds.), D. Reidel, Dordrecht, The Netherlands, 1984, p. 1.
187. J. L. Brédas, in *Handbook of Conducting Polymers*, Vol. 2 (T. A. Skotheim, ed.), Marcel Dekker, New York, 1986, p. 860.
188. R. Hoffmann, C. Janiak, and C. Kollmar, *Macromolecules* 24:3725 (1991).
189. C. P. De Melo and R. Silbey, *J. Chem. Phys.* 88:2558, 2567 (1988).
190. M. H. Whangbo, R. Hoffmann, and R. B. Woodward, *Proc. R. Soc. London A* 366:23 (1979).
191. G. Nicolas and P. Durand, *J. Chem. Phys.* 70:2020 (1979); 72:453 (1980).
192. J. L. Brédas, R. R. Chance, R. Silbey, G. Nicolas, and P. Durand, *J. Chem. Phys.* 75:255 (1981).
193. M. J. S. Dewar and W. Thiel, *J. Am. Chem. Soc.* 99:4899 (1977).
194. M. J. S. Dewar and M. L. McKee, *J. Comput. Chem.* 4:84 (1983).
195. W. R. Salaneck, in *Handbook of Conducting Polymers*, Vol. 2 (T. A. Skotheim, ed.), Marcel Dekker, New York, 1986, p. 1337.

196. K. Seki, N. Ueno, U. O. Karlsson, and R. Engelhardt, *Chem. Phys.* **105**:247 (1986).
197. M. Lögdlund, W. R. Salaneck, F. Meyers, J. L. Brédas, G. A. Arbuckle, R. H. Friend, A. B. Holmes, and G. Froyer, *Macromolecules* **26**:3815 (1993).
198. K. Seki, *Mol. Cryst. Liq. Cryst.* **171**:255 (1989).
199. W. R. Salaneck, H. R. Thomas, C. B. Duke, A. Paton, E. W. Plummer, A. J. Heeger, and A. G. MacDiarmid, *J. Chem. Phys.* **71**:2044 (1979).
200. K. Seki, S. Asada, T. Mori, H. Inokuchi, I. Murase, T. Ohnishi, and T. Noguchi, *Solid State Commun.* **74**:677 (1990).
201. S. Arnold, *J. Chem. Phys.* **76**:3842 (1982).
202. K. Seki, U. O. Karlsson, R. Engelhardt, E. E. Koch, and W. Schmidt, *Chem. Phys.* **91**:459 (1984).
203. B. Thémans, W. R. Salaneck, and J. L. Brédas, *Synth. Metals* **28**:C359 (1989).
204. S. Stafström and J. L. Brédas, *Phys. Rev. B* **38**:4180 (1988).
205. S. A. Rice and J. Jortner, in *Physics and Chemistry of the Organic Solid State*, Vol. III (D. Fox, M. M. Labes, and A. Weissberger, eds.), Interscience, New York, 1967, p. 199.
206. M. R. Philpott, *Chem. Phys. Lett.* **50**:18 (1977).
207. S. Suhai, *Phys. Rev. B* **29**:4570 (1984).
208. H. Tanaka, M. Inoue, and E. Hanamura, *Solid State Commun.* **63**:103 (1987).
209. W. T. Simpson, *J. Am. Chem. Soc.* **77**:6164 (1955).
210. J. L. Fave, in *Electronic Properties of Polymers*, Springer Series in Solid-State Science, Vol. 107 (H. Kuzmany, M. Mehring, and S. Roth, eds.), Springer-Verlag, Berlin, 1992, p. 60.
211. W. Rehwald and H. G. Kiess, in *Conjugated Conducting Polymers*, Springer Series in Solid-State Sciences, Vol. 102 (H. Kiess, ed.), Springer-Verlag, Berlin, 1992, p. 135.
212. D. Berets and D. S. Smith, *Trans. Faraday Soc.* **64**:823 (1968).
213. A. S. Siddiqui and E. G. Wilson, *J. Phys. C Solid State Phys.* **12**:4237 (1979).
214. J. C. W. Chien and G. N. Babu, *J. Chem. Phys.* **82**:441 (1985).
215. M. A. Lampert and P. Mark, *Current Injection in Solids*, Academic Press, New York, 1970.
216. N. Karl, *Festkörperprobleme* **14**:261 (1974).
217. B. Reimer and H. Bässler, *Phys. Status Solidi (b)* **85**:145 (1978).
218. K. J. Donovan and E. G. Wilson, *Phil. Mag. B* **44**:9 (1981).
219. E. G. Wilson, *J. Phys. C, Solid State Phys.* **16**:6736 (1983).
220. W. Spannring and H. Bässler, *Chem. Phys. Lett.* **84**:54 (1981).
221. T. Blum and H. Bässler, *Chem. Phys.* **123**:431 (1988).
222. D. Moses and A. J. Heeger, *J. Phys. Condensed Matter* **1**:7395 (1989).
223. Y. Yang, J. Y. Lee, P. Miller, L. Li, J. Kumar, and S. K. Tripathy, *Solid State Commun.* **77**:763 (1991).
224. Y. Yang, J. Y. Lee, J. Kumar, A. K. Jain, S. K. Tripathy, H. Matsuda, S. Okada, and H. Nakanishi, *Synth. Metals* **49–50**:439 (1992).

- 225. N. E. Fisher and D. J. Willock, *J. Phys. Condensed Matter* 4:2517, 6613 (1992).
- 226. A. Assadi, C. Svensson, M. Willander, and O. Inganäs, *Appl. Phys. Lett.* 53:195 (1988).
- 227. G. Horowitz, F. Deloffre, F. Garnier, R. Hajlaoui, M. Hmyene, and A. Yassar, *Synth. Metals* 54:435 (1993).
- 228. H. Akimichi, K. Waragai, S. Hotta, H. Kano, and H. Sakati, *Appl. Phys. Lett.* 58:1500 (1991).
- 229. G. Horowitz, D. Fichou, X. Peng, and P. Delannoy, *J. Phys. (France)* 51:1489 (1990).
- 230. S. M. Sze, *Physics of Semiconductor Devices*, Wiley-Interscience, New York, 1969 (2nd ed., 1981).
- 231. A. Watanabe, S. Murakami, K. Mori, and Y. Kashiwaba, *Macromolecules* 22:4231 (1989).
- 232. J. Kanicki, in *Handbook of Conducting Polymers*, Vol. 1 (T. A. Skotheim, ed.), Marcel Dekker, New York, 1986, p. 543.
- 233. G. Horowitz, *Adv. Mater* 2:287 (1990).
- 234. D. G. Ast, in *Semiconductors and Semimetals*, Vol. 21D (R. K. Willardson and A. C. Beer, eds.), Academic Press, Orlando, Fla., 1984, p. 115.
- 235. J. H. Burroughes, D. D. C. Bradley, A. R. Brown, R. N. Marks, K. Mackay, R. H. Friend, P. L. Burns, and A. B. Holmes, *Nature* 347:539 (1990).
- 236. H. K. Henisch, *Semiconductor Contacts*, Oxford Univ. Press, Oxford, 1984.
- 237. E. H. Rhoderick and R. H. Williams, *Metal-Semiconductor Contacts*, Oxford Univ. Press, Oxford, 1988.
- 238. H. B. Michaelson, *J. Appl. Phys.* 48:4729 (1977).
- 239. J. L. Brédas, R. R. Chance, R. H. Baughman, and R. Silbey, *J. Chem. Phys.* 76:3673 (1982).
- 240. M. Kobayashi, N. Colaneri, M. Boysel, F. Wuld, and A. J. Heeger, *J. Chem. Phys.* 82:5717 (1985).
- 241. Y. Gao, K. T. Park, and B. R. Hsieh, *J. Appl. Phys.* 73:7894 (1993).
- 242. B. R. Weinberger, S. C. Gau, and Z. Kiss, *Appl. Phys. Lett.* 38:555 (1981).
- 243. S. Glenis, G. Horowitz, G. Tourillon, and F. Garnier, *Thin Solid Films* 111:93 (1984).
- 244. J. H. Burroughes, C. A. Jones, and R. H. Friend, *Nature* 335:137 (1988).
- 245. J. H. Burroughes and R. H. Friend, in *Conjugated Polymers* (J. L. Brédas and R. Silbey, eds.), Kluwer, Dordrecht, The Netherlands, 1991, p. 555.
- 246. H. Tomozawa, D. Braun, S. Phillips, and A. J. Heeger, *Synth. Metals* 22:63 (1987).
- 247. G. Horowitz, D. Fichou, and F. Garnier, *Solid State Commun.* 70:385 (1989).
- 248. S. Karg, W. Riess, V. Dyakonov, and M. Schwoerer, *Synth. Metals* 54:427 (1993).
- 249. A. Many, Y. Goldstein, and N. B. Grover, *Semiconductor Surfaces*, North-Holland, Amsterdam, 1964.

- 250. P. K. Weimer, *Proc. IRE* 50:1462 (1962); and in *Physics of Thin Films*, Vol. 2 (G. Hass and R. E. Thun, eds.), Academic Press, New York, 1964, p. 147.
- 251. G. Horowitz and P. Delannoy, *J. Appl. Phys.* 70:469 (1991).
- 252. A. Tsumura, H. Koezuka, and T. Ando, *Appl. Phys. Lett.* 49:1210 (1986); *Synth. Metals* 25:11 (1988).
- 253. A. Tsumura, H. Fuchigami, and H. Koezuka, *Synth. Metals* 41–43:1181 (1991).
- 254. X. Peng, G. Horowitz, D. Fichou, and F. Garnier, *Appl. Phys. Lett.* 57:2013 (1990).
- 255. P. Ostoja, S. Guerri, S. Rossini, M. Servidori, C. Taliani, and R. Zamboni, *Synth. Metals* 54:447 (1993).
- 256. P. G. LeComber and W. E. Spear, in *Semiconductors and Semi-metals*, Vol. 21D (R. K. Willardson and A. C. Beer, eds.), Academic Press, Orlando, Fla., 1984, p. 89.
- 257. N. Lustig and J. Kanicki, *J. Appl. Phys.* 65:3951 (1989).
- 258. J. I. Pankove, ed., *Electroluminescence*, Topics in Applied Physics, Vol. 17, Springer-Verlag, Berlin, 1977.
- 259. M. Pope, H. P. Kallmann, and A. Magnante, *J. Chem. Phys.* 38:2042 (1963).
- 260. W. Helfrich and W. G. Schneider, *Phys. Rev. Lett.* 14:229 (1965).
- 261. J. Dresner, *RCA Rev.* 30:322 (1969).
- 262. D. F. Williams and M. Schadt, *Proc. IEEE*, 476 (1970).
- 263. E. Cartier, P. Pfluger, J. J. Pireaux, and M. Rei Vilar, *Appl. Phys. A* 44:43 (1987).
- 264. D. L. Feucht, *J. Vac. Sci. Technol.* 14:57 (1977).
- 265. A. B. Holmes, D. D. C. Bradley, A. R. Brown, P. L. Burns, J. H. Burroughes, R. H. Friend, N. C. Greenham, R. W. Gymer, D. A. Halliday, R. W. Jackson, A. Kraft, J. H. F. Martens, K. Pichler, and I. D. W. Samuel, *Synth. Metals* 55–57:4031 (1993).
- 266. C. Hosokawa, H. Higashi, and T. Kusumoto, *Appl. Phys. Lett.* 62:3238 (1993).
- 267. G. Gustafsson, Y. Cao, G. M. Treacy, F. Klavetter, N. Colaneri, and A. J. Heeger, *Nature* 357:477 (1992).
- 268. P. Dannetun, M. Boman, S. Stafström, W. R. Salaneck, R. Lazzaroni, C. Fredriksson, J. L. Brédas, R. Zamboni, and C. Taliani, *J. Chem. Phys.* 99:664 (1993).
- 269. D. Braun and A. J. Heeger, *Appl. Phys. Lett.* 58:1982 (1991).
- 270. A. G. Fischer and H. L. Moss, *J. Appl. Phys.* 34:2112 (1963).
- 271. H. Scher and E. W. Montroll, *Phys. Rev. B* 12:2455 (1975).
- 272. J. L. Brédas and G. B. Street, *Acc. Chem. Res.* 18:309 (1985).
- 273. A. R. Brown, K. Pichler, N. C. Greenham, D. D. C. Bradley, and R. H. Friend, *Chem. Phys. Lett.* 210:61 (1993).
- 274. D. Haarer and H. Möhwald, *Phys. Rev. Lett.* 34:1447 (1975).
- 275. H. Scher, S. Alexander, and E. W. Montroll, *Proc. Natl. Acad. Sci. USA* 77:3758 (1980).

- 276. R. M. Hill, *Phil. Mag.* 23:59 (1971).
- 277. J. S. Blakemore, *Phys. Rev.* 163:809 (1967).
- 278. R. N. Hall, *Proc. IRE* 106B(Suppl. 17):923 (1959).
- 279. B. E. Kohler and D. E. Schilke, *J. Chem. Phys.* 86:5214 (1987).
- 280. D. S. Chemla and J. Zyss, eds., *Nonlinear Optical Properties of Organic Molecules and Crystals*, Vols. 1 and 2, Academic Press, Orlando, Fla., 1987.
- 281. F. Kajzar and J. Messier, in *Conjugated Polymers* (J. L. Brédas and R. Silbey, eds.), Kluwer, Dordrecht, The Netherlands, 1991, p. 509.
- 282. C. J. Baker, O. M. Gelsen, and D. D. C. Bradley, *Chem. Phys. Lett.* 201:127 (1993).
- 283. Z. G. Soos, S. Ramasesha, D. S. Galvao, R. G. Kepler, and S. Etemad, *Synth. Metals* 54:35 (1993).
- 284. C. W. Tang and S. A. VanSlyke, *Appl. Phys. Lett.* 51:913 (1987).
- 285. C. Adachi, S. Tokito, T. Tsutsui, and S. Saito, *Jpn. J. Appl. Phys.* 27:L269 (1988).
- 286. C. Adachi, T. Tsutsui, and S. Saito, *Appl. Phys. Lett.* 55:1489 (1989).
- 287. C. W. Tang, S. A. VanSlyke, and C. H. Chen, *J. Appl. Phys.* 65:3610 (1989).
- 288. A. R. Brown, D. D. C. Bradley, J. H. Burroughes, R. H. Friend, N. C. Greenham, P. L. Burns, A. B. Holmes, and A. Kraft, *Appl. Phys. Lett.* 61:2793 (1992).
- 289. Y. Ohmori, M. Uchida, K. Muro, and K. Yoshino, *Jpn. J. Appl. Phys.* 30:L1938 (1991).
- 290. Y. Ohmori, M. Uchida, K. Muro, and K. Yoshino, *Jpn. J. Appl. Phys.* 30:L1941 (1991).
- 291. G. Grem, G. Leditzky, B. Ullrich, and G. Leising, *Adv. Mater.* 4:36 (1992).
- 292. S. Heun, R. F. Mahrt, A. Greiner, U. Lemmer, H. Bässler, D. A. Halliday, D. D. C. Bradley, P. L. Burns, and A. B. Holmes, *J. Phys. Condensed Matter* 5:247 (1993).
- 293. F. Meyers, A. J. Heeger, and J. L. Brédas, *J. Chem. Phys.* 97:2750 (1992).
- 294. Z. Yang, I. Sokolik, and F. E. Karasz, *Macromolecules* 26:1188 (1993).
- 295. U. Lemmer, R. F. Mahrt, Y. Wada, A. Greiner, H. Bässler, and E. O. Göbel, *Appl. Phys. Lett.* 62:2827 (1993).
- 296. J. Kido, M. Kohda, K. Okuyama, and K. Nagai, *Appl. Phys. Lett.* 61:761 (1992).
- 297. D. A. Halliday, P. L. Burns, D. D. C. Bradley, R. H. Friend, O. M. Gelsen, A. B. Holmes, A. Kraft, J. H. F. Martens, and K. Pichler, *Adv. Mater.* 5:40 (1993).
- 298. D. Braun, D. Moses, C. Zhang, and A. J. Heeger, *Appl. Phys. Lett.* 61:3092 (1992).
- 299. C. Hosokawa, H. Tokailin, H. Higashi, and T. Kusumoto, *Appl. Phys. Lett.* 60:1220 (1992).

13

Doped Conjugated Polymers: Conducting Polymers

Maxime Nechtschein

Centre d'Etudes Nucléaires de Grenoble, Grenoble, France

I. INTRODUCTION

It is widely recognized that the “doping” of polyacetylene in 1977 by Shirakawa et al. [1] at the University of Pennsylvania opened the door to research on conducting polymers (CPs). By doping conjugated polymers, previously called semiconducting polymers, their conductivity increased by more than 10 orders of magnitude. These compounds then took their full place in the family of organic conductors. It is fully recognized that doping is the central process that governs the main properties of conjugated polymers, in particular the crossover to the conducting state.

In a very general sense, any manner of changing the number of π electrons (addition or withdrawal), whose essential role is described in Chapter 11, can be called *doping* and gives rise to an increase in conductivity. Many different ways of transferring charge to the π -electron system can be listed and are currently used, including chemical, electrochemical, and protonic; by photoexcitation; and by electric field injection. But for the present purpose, only those processes that lead to a sufficient and permanent doping level will be discussed here: namely, the chemical, electrochemical, and protonic doping processes. Charge injection in the π -electron system is accompanied by counterion admission for maintaining electroneutrality. In this respect CPs resemble other organic conductors based on charge-transfer complexes. The electrically charged polymer chains

are surrounded by the counterions and form a salt, or a “macrosalt.” However, the polymer chains and the counterions do not play equivalent roles in the molecular architecture. The polymer chains form a host matrix, which can be filled up with counterions or can be emptied. In this way CPs are very similar to intercalation compounds.

In contrast to organic conducting crystals, in which the conduction is essentially an intermolecular process, for CPs, conduction along the polymeric chains should be considered first. This feature is a priori favorable for high conductivity since intrachain bandwidths are about one order of magnitude larger than intermolecular transfer integrals (several eV instead of a few tenths). However, interchain transfers are also necessary and can be the limiting factor for macroscopic dc conductivity.

Another major difference between CPs and organic conducting crystals concerns the structure, which is generally amorphous. “Generally” means for most of the material and unless special attention had been paid in the sample preparation. However, the crystallinity of CPs should not be ignored. In most cases crystalline regions are present, so that the material can be seen as a two-phase (amorphous and crystalline) system. Crystallinity is very dependent on the polymer and on synthesis, processing, and doping procedure. Polypyrrole, which is essentially amorphous, and polyacetylene, whose crystallinity is commonly around 80%, can be considered as the two extreme cases. In most cases crystallinity lies between 10 and 50%. Quite different properties—in particular for transport—should be expected for the amorphous and crystalline regions. However, in most experiments, an overall behavior is observed, and one cannot easily distinguish between the two types of contributions. This fact may be a major source of ambiguity in the interpretation of the data.

Disorder plays a leading role in governing the properties of CPs. Several types of disorder can be distinguished. First, the intrachain defects—chemical and conformational—account for the lack of perfection of the chain. At least, the finiteness of the chain length—commonly, a polymeric chain contains between 10 and 10^3 unit cells—puts real materials outside the pure infinite chains of theorists. Chemical defects originate in random polymerization events (e.g., in a polypyrrole chain, polymerization in the β position, instead of the α), chemical impurities, accidental sp_3 cross-linkings, partial degradation (in particular due to oxygen contamination), and so on. Conformational defects correspond to anything that breaks the translation symmetry. In particular, in the amorphous regions, the random character of the chain arrangement is a major source of disorder. Special attention should be paid to the counterion distribution. Random distribution of counterions in amorphous regions results in a random potential on the chain sites. Because interchain transfer is an essential step for conduction, disorder should also be considered at the interchain level. In

the crystalline parts the chain parallelism is compatible with coherent transport. In the amorphous regions the average interchain coupling is weakened by the randomness of the chain orientation, and only hopping is possible. Then the mesoscopic scale has to be taken into account. This is the scale of the interdomain connection, which accounts for the crystallite shape and size (50 to 200 Å), the form (powder versus film), and the morphology of the material.

If a single crystal of CP cannot be envisaged, we can approach such an ideal case with oriented films. Aligning the chains is an efficient way of reducing disorder. Straight chains result in reduced intrachain conformational disorder. Furthermore, in aligned chains the randomness of both the potential created on a given chain by the neighborhood, and the interchain coupling, tends to vanish. It is observed that the gain in conductivity achieved in stretched aligned films is much higher than one could expect just from geometrical considerations. Indeed, film orientation can induce a qualitative change from hopping to coherent transport.

Also in contrast to organic crystals, it should be noted that the properties of CPs are highly sensitive to numerous factors, some of which are not fully controlled at the present time. This explains the apparent “sample dependency” of different properties, the difficulty in obtaining reproducible data, and the frequent controversies among authors. One reason for the spread of the data probably lies in the difficulty in controlling the morphology, in particular the amorphous versus crystalline distribution. However, considerable progress in the processing and quality control of the materials has been accomplished in recent years. Oriented films can now be obtained which provide highly improved transport and mechanical properties.

About a decade after the first doping of polyacetylene, the improvement made in chemical synthesis and processing has enabled the passage from disorder-governed transport properties to metal-like behavior. Conductivity approaching the value of copper has been reported in highly conducting polyacetylene obtained by the Naarman–Theophilou synthesis, also called $n\text{-(CH)}_x$: $\sigma \sim 10^5$ S/cm. Furthermore, the temperature dependence of conductivity is beginning to behave as in a “true metal”: namely, an increase in σ for decreasing T has been observed.

II. ON THE DOPING PROCESS

A. Preliminary Remarks

A major difference between charge-transfer complex salts and CPs is that the latter can exist in either the doped or the undoped state. Thus passing from one state to the other is a specific and essential process that deserves

a special place in a review on CPs. In the present section we consider only processes leading to permanent doping: charge injection into the polymer chains, accompanied by counterion adjunction for charge compensation.

Basically, doping is a redox reaction (i.e., an electron transfer reaction) between the polymer chain and the counterions. For example, in the case of negative doping one can write



where P represents a polymer chain, D a donor molecule, and n the number of electrons transferred. Doping will proceed (reaction to the right) if the energy balance of the reaction is favorable: $\Delta E < 0$. This is given by

$$\Delta E = I_D - A_p - E_{coul} \quad (2)$$

where I_D is the ionization potential of D , A_p the polymer electron affinity [an “effective” affinity including the relaxation energy of the chain lattice as the transferred charge is accommodated (see Chapter 11)], and the term E_{coul} includes all electrostatic interactions between charges in the doped state. However, (1) and (2), which could account for the appearance of a charge-transfer compound when the two initial species are in contact (gas or liquid phase), are not very useful for the solid phase, the usual case for conjugated polymers. The case of soluble conjugated polymers is not purely academic, however, and is becoming an increasing part of the domain. When the polymer matrix remains in the solid state, Eqs. (1) and (2) should be considered as necessary but not sufficient conditions for the redox reaction to occur. The preliminary condition to be fulfilled is that species D should come into contact with P . This implies complicated migration or diffusion processes, which are highly dependent on the morphology and microscopic structure of the polymer matrix. It is clear that whether the counterions migrates in the liquid or in the gaseous phase is of crucial importance.

Furthermore, the kinetics of ion diffusion, and hence the kinetics of doping, are quite different in the amorphous and crystalline regions. Whereas in amorphous regions fast processes are expected, in the crystalline parts the ion-diffusion coefficients can be very small (values in the range 10^{-9} to 10^{-13} cm²/s are currently reported), which can give rise to nonequilibrium situations and nonhomogeneous doping.

When the counterion is in solution, the solvent, whose action cannot be ignored, is a third partner. In polar solvents the ion dopants are generally solvated. In other words, the ions are surrounded by solvent molecules attached by electrostatic forces. Thus the effective active species is a multimolecular cluster, which can be quite big. This causes a slowing down of the ion diffusion. Also, due to electrostatic screening and the increased

distance to the chain, the Coulomb chain–ion interaction is reduced significantly. This results in a depinning of the charge carriers and hence in increased mobility. Furthermore, when operating in solution, swelling phenomena can occur; the polymer matrix cannot be treated as a rigid skeleton, but rather, as a soft lattice.

In case of chemical doping, the redox reaction should be spontaneous, which implies that $\Delta E < 0$. In other words, in case of *p* doping, for instance, the redox potential of the dopant should be higher than the oxidation potential of the polymer. If this condition is not fulfilled, doping can be achieved by electrochemical means. In that case, the charge transfer is assisted electrochemically. The polymer forms an electroactive film deposited on the working electrode of an electrochemical cell. The great interest of this method is that it enables one to reversibly monitor the doping level simply by adjusting a voltage. This opportunity of tuning the doping level, and hence the related properties, is a unique feature of CPs. Therefore, a special section will be devoted to electrochemical doping. We should mention that electrochemistry has also been used extensively by some of the CP community because it is an easy method of polymerization. Using electropolymerization, polymer films are deposited in the doped state on an electrode plate and can be used directly for in situ studies.

Finally, another method of doping, specific to CPs, should also be mentioned: namely, “protonic” (or “acidic”) doping. In that case the doping consists of a proton addition to the polymer chain, with no change in the total number of electrons. This type of doping is concerned essentially with polyaniline. It is not a new effect—it was reported and carefully studied in the 1960s [2]. It was shown at that time that protonation of polyaniline in the emeraldine base form resulted in a tremendous increase in conductivity. It was also proved that electrons (and not protons) were involved in the conduction process. Then, in the 1980s, polyaniline was rediscovered [3–5] and has been the subject of hundreds of papers. (For references on polyaniline, see Ref. 6.) Indeed, the increase in conductivity after protonation can reach 10 orders of magnitude. Furthermore, polyaniline is one of the most stable organic conductors and can be made processible. The mechanism of the occurrence of a conducting state through protonation could appear somewhat puzzling. We can illustrate this in the following way. If it is true that the total number of electrons does not change when a proton is added to the chain skeleton, the bonding of the added proton (with an imine nitrogen) acts as a trap for one of the two electrons of the nitrogen-free doublet. Thus the number of electrons effectively available for the delocalized π -molecular orbitals diminishes. The Fermi level is shifted, and a transition to a conducting state can be conceived.

B. Electrochemical Doping

We should first briefly introduce a few notions of electrochemistry for the reader who is not familiar with this field [7]. To demonstrate the mechanism of electrochemical doping, we present a simplified picture—in reality, an oversimplified picture and consequently, not strictly correct. However, in our defense it should be noted that no comprehensive theory of the process of electrochemical doping at the microscopic scale exists at the present time.

In an electrochemical experiment the polymer is a film sandwiched between a metal electrode, the *working electrode*, and a liquid electrolyte (Fig. 1). Electrons can be exchanged between the polymer (\mathcal{P}) and the metal (\mathcal{M}). The exchange proceeds across the polymer–metal interface (\mathcal{P}/\mathcal{M}). In addition, to maintain electroneutrality in the polymer bulk, ions are exchanged between \mathcal{P} and the electrolyte (\mathcal{E}), across the polymer–electrolyte interface (\mathcal{P}/\mathcal{E}). In the case of *p* doping, which corresponds to oxidation of the polymer, electrons are transferred from \mathcal{P} to \mathcal{M} (and the reverse for *n* doping, which corresponds to a reduction). The cell includes a *reference electrode*, which is immersed in the electrolyte and connected to a high-impedance voltmeter. It measures the potential of the electrolyte with respect to that of a reference redox couple. Note that no current

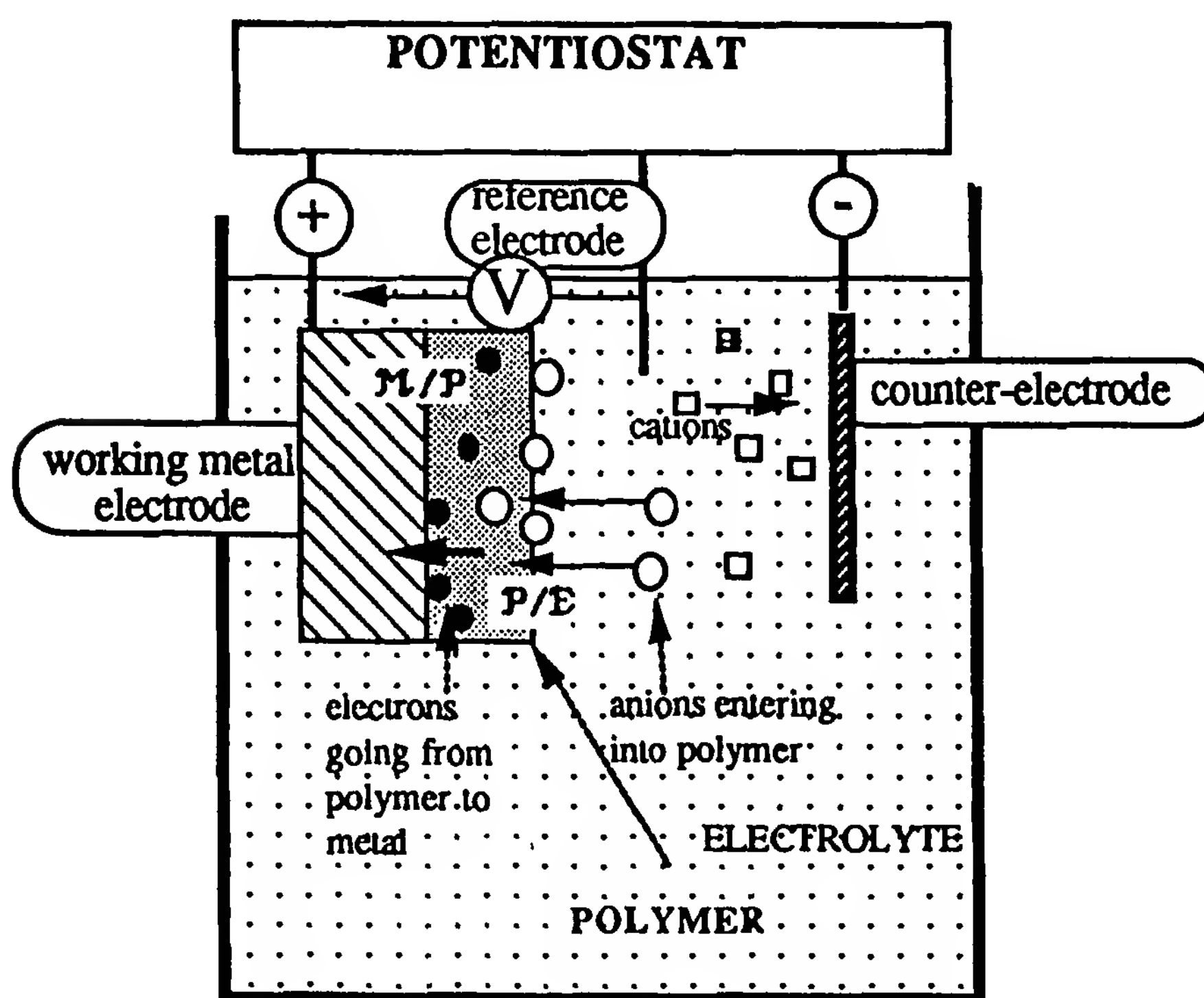


Figure 1 Schema of an electrochemical cell. The polymer is a film deposited on the metal working electrode.

passes through the reference electrode. Some current can be collected via a third electrode, the counterelectrode, which closes the electric circuitry.

The three electrodes are connected to a potentiostat, whose function (in the potentiostatic mode) consists of supplying a current, which is regulated in such a way that the voltage between the working and the reference electrodes remains at a chosen value $V_{\text{WR}} = V$. In fact, if an overall current crosses the cell, it proceeds in two steps: (1) electronic current in the polymer, and (2) ionic current in the electrolyte (which is not conducting for electrons). Since for electrons the electrical loop is interrupted at the electrolyte crossing, an electron transfer between \mathcal{M} and \mathcal{P} means that a redox reaction is taking place in the polymer. Electron transfer proceeds if the Fermi level of the metal, E_{FM} , is situated below the level of the polymer valence band E_{VP} (oxidation) or above the conduction band E_{CP} (reduction) (Fig. 2). The potentiostat enables us to shift the electronic levels of the polymer with respect to E_{MF} , just by varying V . The current $I(V)$ recorded during a linear scan of V ($V = \pm ut$, with u the scan rate) is the cyclic voltammogram (Fig. 3), well known in the electrochemistry community. It gives information on the redox processes in the polymer.

In particular, a peak current appears at V_{ox} , the potential characteristic of the redox reaction. The integral of the current gives the charge transferred with the polymer for a given applied voltage V . This integral is also the doping level: $(1/u) \int_V I(V') dV' = q(V)$.

Assuming that thermal equilibrium has been obtained, a simple two-level diagram enables us to calculate $q(V)$. Let us assume that the undoped and doped states can be represented by two levels, with energy 0 and E_{ox} , and populations n_0 and n_{ox} , respectively. If the doped state has a charge of m electrons (m electrons per site are transferred for the doping process), when the potential V is applied, its level will be shifted by $-meV$, as represented in Fig. 4. The Boltzmann distribution for the populations can be written as

$$n_{\text{ox}} = n_0 e^{-(E_{\text{ox}} - meV)/kT} \quad (3)$$

With the condition that $n_0 + n_{\text{ox}} = 1$ and since $q = mn_{\text{ox}}$, Eq. (3) can be rewritten as

$$V = V_{\text{ox}} + \frac{kT}{me} \ln \frac{q}{1 - q} \quad (4)$$

which is simply the Nernst law, where $V_{\text{ox}} = E_{\text{ox}}/e$ is the *normal* or *standard potential* (the potential at which 50% of the sites are oxidized). Expression (4) gives a symmetrical current peak, with a half-maximum width of $(90/m)$ mV at 25°C. This gives an estimate for the variation of the voltage that should be applied to go to the doped state. In fact, in most cases, the

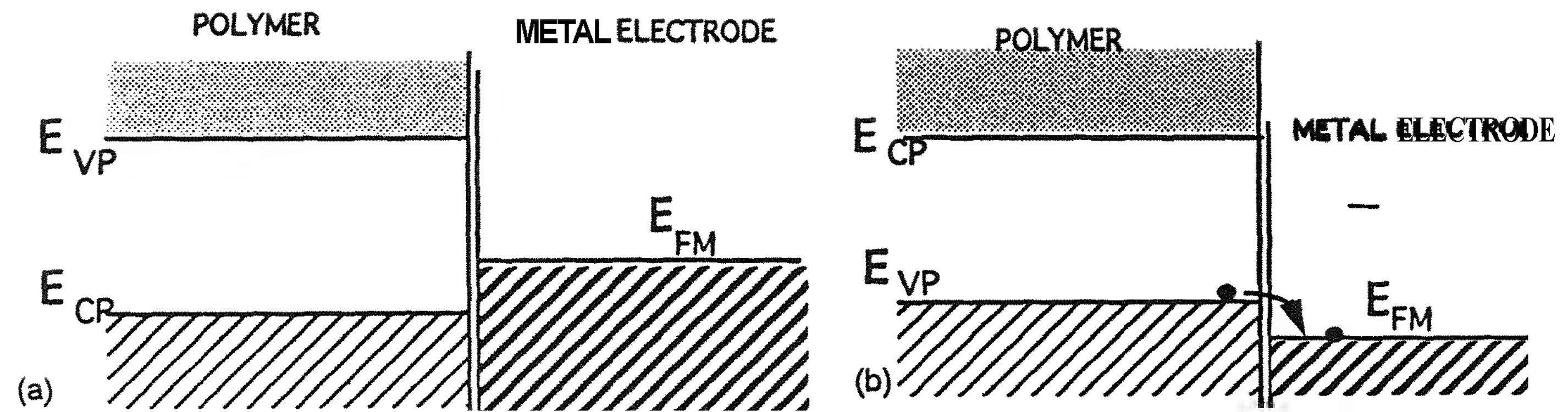


Figure 2 Energy-level diagram of the polymer in contact with the metal electrode: (a) Fermi level of the metal electrode is within the gap of the polymer: no transfer possible; (b) Fermi level of the metal electrode is below E_{VP} : electrons can transfer to the metal.

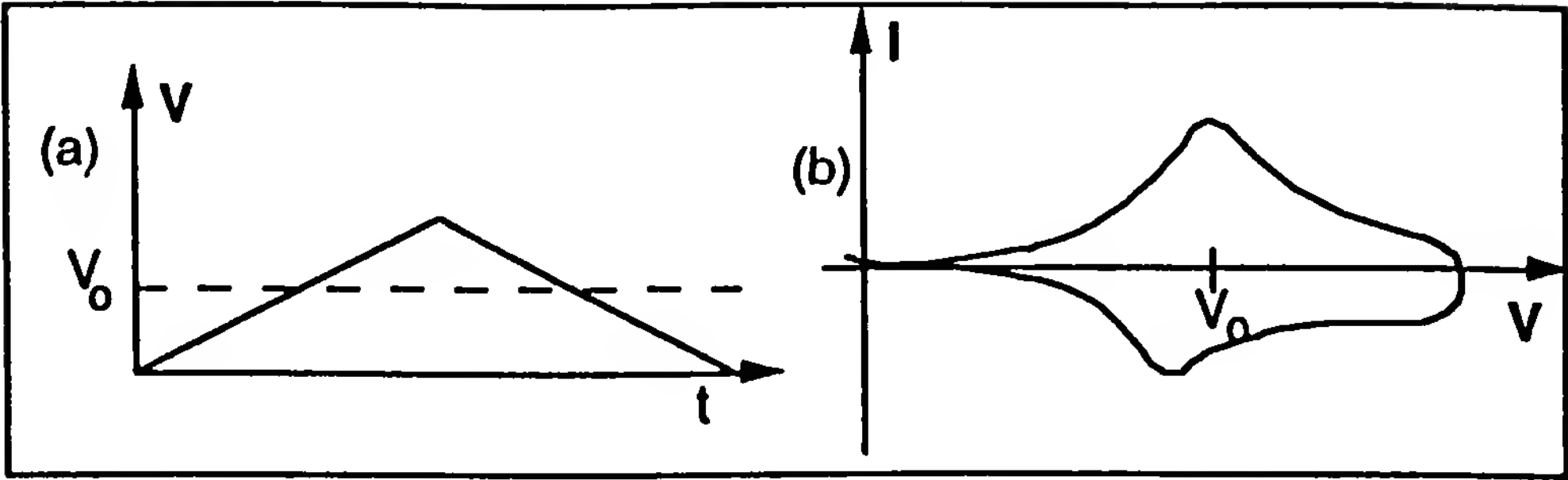


Figure 3 Cyclic voltammogram experiment: (a) applied voltage versus time; (b) current response versus applied voltage.

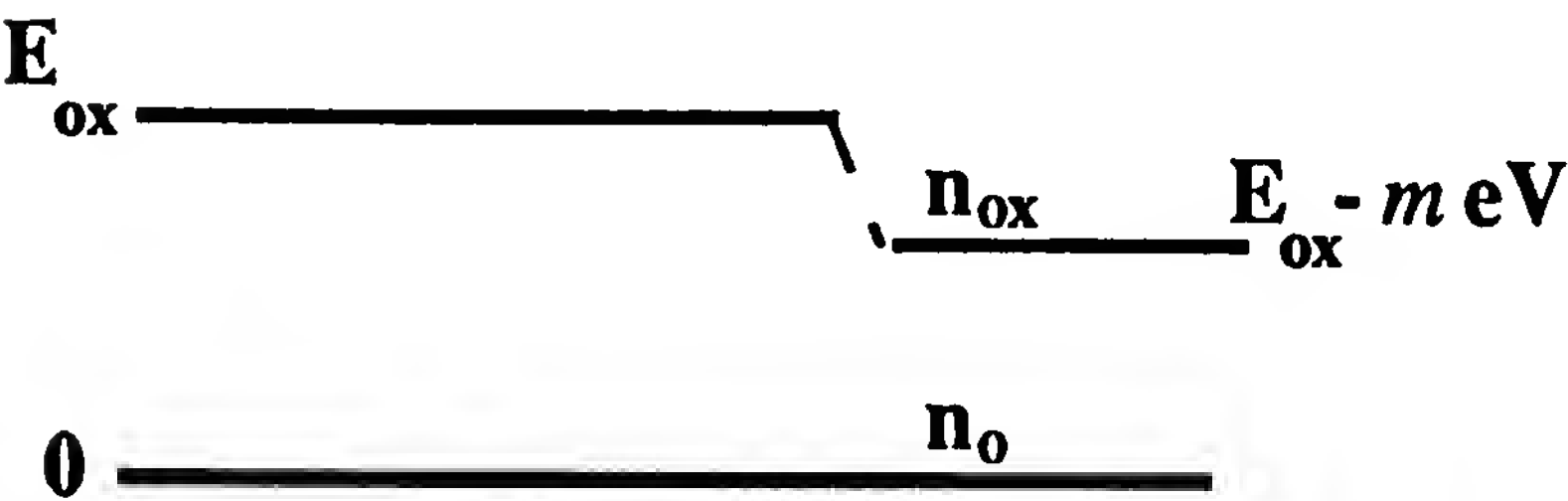


Figure 4 Energy levels of the undoped (0), and doped (E_{ox}) state. On the right a potential V has been applied.

voltage variation for the undoped-to-doped crossover extends over a quite broad range. Indeed, the Nernst law describes an “ideal” equilibrium situation. There are many factors that lead to deviations from Eq. (4), several of which we discuss next.

1. Counterion Transfer

In fact, at equilibrium, not only are electrons transferred across the \mathcal{P}/\mathcal{M} interface, but ions also cross the \mathcal{P}/\mathcal{E} interface. Taking into account this additional transfer yields non-Nernstian behavior. In the simple case of polarons being the predominant species, one obtains [8].

$$V = V_0 + \frac{kT}{e} \ln \frac{C_T}{A_e} + \frac{kT}{e} \ln \frac{q^2}{1 - q} \tag{5}$$

with (A_e) the anion concentration in the electrolyte and C_T the total site concentration in the film. This modified expression gives rise to a current peak that is broader and no longer symmetrical. The effect of ion pairs and of solvent molecules can also be taken into account: It results in broadening of the current peak.

2. Ion-Insertion Work

During ion insertion the polymeric matrix is rearranged, which implies that mechanical energy is involved in the doping process. Mechanical–electrochemical coupling results in adding a term to the right part of the Nernst law [Eq. (3)] [9]. The additional term is proportional to the charge q and induces a broadening of the current peak. This means that during the charging process, the more charge is injected, the more difficult it becomes to inject additional charge.

3. Interaction Between Charged Sites

Taking into account the interactions between the charged sites leads to an additional, q -dependent term. In the case of repulsive interactions, the most realistic case in reality (e.g., coulombic interactions), the current peak is broadened once again. In fact, the charges created on the polymer chains are (1) compensated by counterions at the nanoscopic scale and (2) partially screened when the compound becomes conducting. Thus the electrostatic interaction to be considered is a much reduced effective interaction. Such interactions have been accounted for in the “box model” [10], which is explained in Section IV. This model is a simple way to describe the charging of a polymer chain. The latter is divided into fixed sites, which can be neutral, singly charged (polaron with two spin states: up and down), or doubly charged (bipolaron state). The coulombic interactions between charges can be accounted for, in a phenomenological way, by introducing an additional term proportional to the charge of the state: Cq and $2Cq$, for polarons and bipolarons, respectively. It always results in a broadening of the current peak.

4. Kinetic Effects

Additional deviations from the Nernst law [Eq. (4)] can come from kinetic effects: in other words, if the potential scan is too fast to allow the system to reach thermal equilibrium. Two cases should be mentioned: (1) ion transport limitation, and (2) electron transfer limitation. In case 1 the redox reaction is limited because the ions do not diffuse across the film fast enough to compensate for the charge at the rate of the electron transfers. This case is characterized by a square-root dependence of the current peak intensity versus scan rate: $I_k \propto u^{1/2}$ instead of $I_k \propto u$. Since the time needed to cross the film, t_{cr} , decreases as the square of the film thickness: $t_{cr} \propto d^2$, the transport limitation is avoided in thin films (typically, $d < 1 \mu\text{m}$ for $u < 100 \text{ mV/s}$). The limitation by the electron transfer kinetics (case 2) is more intrinsic to the polymer properties. It originates from the fact that the redox reaction is not instantaneous: in particular, due to the fact that the electron transfer implies a jump over a potential barrier. If the scan

rate is not slow compared to the redox constant reaction, the current peak in the CV experiment is shifted and broadened.

An interesting question is concerned with the maximum speed at which a CP film can be switched from the undoped (insulating) state to the doped (conducting) state. This point is, of course, important for the purpose of devices based on electrochemical doping. To our knowledge, the polymer with the fastest response is polyaniline. Operating on thin polyaniline films deposited on a microelectrode (10 μm diameter), a switch time of about 10 μs has been reported for discharge (conducting-to-insulating crossover) [11]. More recently, times as short as 0.5 μs have been obtained for the conducting-to-insulating transition [12]. For such a high-speed estimate of the ion diffusion constant gives $D \propto 10^{-6} \text{ cm}^2/\text{s}$, a value comparable to that in the liquid phase. This result is evidence that the polymer is intimately impregnated by the electrolyte at the microscopic scale.

5. Nonthermal Equilibrium Effects

In addition to the above-mentioned kinetic effects (which in principle can be controlled) the response of a CP film is not a simple function of the applied potential. In particular, it depends on whether the voltage has been applied from increasing or decreasing values. In other words, for the same applied voltage, the doping level has different values on doping or undoping. Hysteresis effects are clearly present. They are evidence that thermal equilibrium situations have not been reached. Although different interpretations have been proposed for the hysteresis effects [13,14], no general understanding of such effects is yet available.

More evidence that thermal equilibrium is not attained is the existence of a “memory effect.” It has been observed that the kinetics of doping depends on the wait time spent in the insulating state [15]. After 10^5 s in the undoped state, steady-state behavior is still not obtained. This means that a slow relaxation process is taking place in the film maintained in the insulating state. This effect has been quite well characterized, but no microscopic explanation has yet been given [16].

C. In Situ Experiments

Due to the possibility of electrochemically monitoring the doping level by an applied voltage, a number of in situ experiments have been developed. In such experiments a given property is followed as a function of the doping level. The advantages of such experiments are threefold:

1. Measurements are made directly with no handling of the samples and thus no risk of contamination.

2. The doping level can be varied continuously and any intermediate value can be obtained.
3. Kinetic studies are feasible by recording the time response following a change in the doping level.

The appropriate form for the sample is a thin film deposited on the working electrode of an electrochemical cell. Of course, the cell should be made compatible with the experiment, which can be the major difficulty.

Among the large variety of in situ experiments that have been described one can distinguish (1) those whose purpose is investigation of the electrochemical doping process itself: cyclic voltammetry, quartz balance [17], mirage effect [18], and ellipsometry [19], and (2) those developed for studies of the properties of the CP: UV–near-IR spectroscopy [20], IR [21], ESR [22], conductivity [23], impedance [24], and so on.

III. TRANSPORT PROPERTIES

A. Overview

In Section II, charge carriers were introduced in CPs. Remember that we may deal with three different species of charge carriers: charged solitons (in the case of *trans*-polyacetylene), polarons, and bipolarons. The common feature of these charged species is that the charge is accompanied by a lattice distortion. In other words, the charge carrier is “dressed” by phonons. However, the mass of the particle is not necessarily large. For instance, the soliton mass is only $5m_e$ (m_e being the free electron mass).

We now consider the transport of these charge carriers across the material. Transport along a macroscopic distance involves different processes, which reflect the structure of the material at different scales. Let us look at the various levels in the conduction process. We will follow the theorist’s approach, which considers a pure and ideal one-dimensional system isolated from the rest of the world, going on to the point of view of the experimentalist, who has to deal with real matter: assemblies of macromolecular compounds with all kinds of imperfections, packed together in very complicated ways.

At first the charge has to migrate inside a given chain, that is, at the intrachain level. When interchain couplings are ignored, conduction in such a “molecular wire” is a one-dimensional process. Hence in one dimension, special aspects of physics will be involved. In particular, it is now well known (the “Anderson localization”) that in a pure one-dimensional system, any disorder, whatever its magnitude, will induce localization at $T = 0$ K [25]. In other words, instead of being delocalized over the entire chain, the charge-carrier wave functions are limited to a given localization length

λ . Thus as soon as the chain length is larger than the localization length ($L \gg \lambda$), charge carriers are not able to cross along the chain; the chain is an insulator at $T = 0$. For $T > 0$, phonons are created that will have two opposing effects: (1) being assisted by phonons, charge carriers can now move along by hopping, but (2) scattering against the same phonons also restrains the motion of the charge carriers.

In a second step interchain coupling is taken into account. Interchain transport can now take place. Two limiting cases have to be considered. In the case of weak disorder (the chains are reasonably parallel to each other), interchain coupling, by reintroducing some three-dimensional features, can prevent “one-dimensional effects,” such as one-dimensional localization, which reduce conductivity. If $\Delta\epsilon$ (the mean-square deviation of the on-site energy) is a measure of the disorder, the condition for the one-dimensional localization to be removed is

$$\Delta\epsilon < (t_{\parallel}t_{\perp})^{1/2}$$

t_{\parallel} and t_{\perp} being the on-chain and interchain transfer integrals, respectively. Furthermore, taking advantage of the possibility of interchain transfers, coherent transport will take place if the anisotropy is not too high, that is, when

$$\frac{t_{\parallel}}{t_{\perp}} < \frac{\lambda}{a}$$

where a is the unit cell distance. This condition expresses a high probability of interchain transfer during the time a carrier is traveling through a coherence length (or a mean free path) [26]. In other words, before the coherent motion of a carrier on a given chain has been interrupted, the carrier has time to go to another chain. Such a process can be envisaged only if the chains are parallel to each other. In the case of strong disorder, the charge carriers have to jump from one chain to the next by hopping. This is the most usual case in CPs. However, the study of coherent transport in CPs is not purely academic, since chemists are now able to obtain samples (e.g., the best samples of “highly conducting polyacetylene”) that “behave coherently” or display tendencies for such behavior. At the level of the interchain transfer, the resulting transport properties are highly dependent on the way the chains are organized and arranged with respect to each other. In particular, the crystalline or amorphous molecular organization is of crucial importance.

The third level for macroscopic conduction will be that of intergrain (fibril, microcrystallite, etc.) transfer. At this level the charge carriers must travel over large distances (e.g., 1 μm), and heterogeneities of the sample have to be taken into account. The material can be depicted as a random

network of more conducting regions separated by fewer conducting borders or barriers. Essentially, the charges are supposed to follow the percolation path corresponding to the highest conductance.

The connection between the measured conductivity (which is a macroscopic measure) and the structural parameters of the compound at the various levels is a major problem. One can say that the conduction in CPs, at least concerning its temperature dependence, is intermediate between semiconductors and metals. As in semiconductors, σ decreases with decreasing T . In the overwhelming majority of cases, a steep decrease is observed:

$$\log \sigma \propto -T^{-\gamma}$$

This behavior resembles the law in semiconductors where $\gamma = 1$, but the decay is slower, $\gamma < 1$; commonly, $\gamma \approx 0.25$. As in metals, the number of charge carriers is constant. In the factors that determine conductivity, $\sigma = ne\mu$: the temperature dependence comes from the mobility μ . Accounting for the temperature behavior $\sigma(T)$ is a very delicate task since many different processes can give rise to the observed law. The difficult problem is to obtain the appropriate model for the case in question. The various possible processes have one common feature: disorder plays a leading role.

Nevertheless, there are cases in which conductivity is not governed by disorder, or at least in a less drastic way. This is the case of highly conducting polyacetylene [27]. Conductivity approaching the value of copper at room temperature has been reported, and a high value is still observed at low temperature. Recently, polyaniline with camphor sulfonic acid (CSA) as the counterion has been reported to present an almost flat temperature dependence of conductivity [28]. Such examples are quite rare, but they are of major importance for an understanding of the intrinsic conduction process.

B. Conduction in the "Molecular Wire"

We will start from a single, ideal, regular, and infinite chain, the perfect one-dimensionality system of the theorists. For several reasons one-dimensionality is unfavorable to conduction. (As a textbook for basic principles of transport properties in one dimension, see Ref. 29.) First, we know from Chapter 11 that the electronic structure of such a chain cannot be like that of a metal. Even the best chemist will not be able to prevent the Peierls transition. He will end up with a compound with a gap in the band structure: that is, an insulating, or at best a semiconducting material. Second, since we are dealing with a pure one-dimensionality system, any defect in the

chain, however small, will have a localizing effect (the Anderson localization). Thus the chain is an insulator at $T = 0$. More quantitatively, according to a calculation by Landauer [30], for a chain of length L , the conductivity at $T = 0$ is given by

$$\sigma = 4 \frac{e^2}{h} \frac{L}{e^{2L/\lambda} - 1}$$

So, for $L \gg \lambda$, one has $\sigma \sim e^{-2L/\lambda}$, which shows that the conductivity decreases exponentially to zero for increasing chain length.*

Another effect, connected to one-dimensionality, also reduces conduction. As we inject charges in the chain, they distort the lattice around themselves and become *self-trapped* in the distortions. The resulting species—charged soliton, polaron, or bipolaron—are then on localized states, and their energy levels are situated in the gap. This effect, which originates in the electron–phonon coupling, is typical of CPs. Continuing the charge injection up to high doping levels, we could expect that due to the overlap of the charged species wave functions, a band structure would finally emerge. Indeed, such a result has been obtained from quantum chemistry calculations [32,33], but the resulting bandwidth is strongly reduced compared to the initial π bandwidth.

Thus, in our attempt to obtain a polymeric organic conductor, many obstacles, due to the one-dimensional features of the material, have to be overcome. Return to the charge carrier, which tries laboriously to propagate in the polymeric chain. The one-dimensional system is so sensitive to imperfections that the motion of our charge carrier is interrupted after a mean free path λ , which even in the best cases is barely longer than a few unit distances (monomer length). Hopping then enables the carrier propagation to continue, a process that is favored by increasing the temperature. Thus, in contrast to the case of “true metallic behavior,” conductivity in CPs generally increases with temperature. However, before reviewing hopping conductivity processes, we can take a look at possible mechanisms for coherent transport. Since the problems related to obtaining high conductivity appear to be connected inherently to the one-dimensionality, one way of overcoming the difficulties is to introduce some three-dimensional characteristics.

*Let us note, however, that it has been proposed recently that the disorder-induced one-dimensional localization could not be effective in particular cases: namely, if the sites with random potential can be associated by pairs, or “dimers.” In that case the random dimer model shows that there should exist an energy spectrum of electrons that can propagate freely [31].

C. From the Single Chain to the Assembly of Chains

So far we have been dealing with a single chain. We now introduce other chains. Since our approach is to go progressively from perfect systems to real materials, we consider an assembly of chains parallel to each other, with the interchain transfer integral t_{\perp} . Due to the three-dimensional interactions, the Anderson localization can now be avoided if t_{\perp} is large enough: namely, if $(t_{\parallel}t_{\perp})^{1/2} > \Delta\epsilon$. Interchain transfers will also enable the charge carriers to pass around the chain defects (such as conjugation interruptions). Coherence will be kept during the interchain transfer if there is a high probability for such transfers over the mean free path (i.e., if $t_{\perp}/t_{\parallel} \gg 2a/\lambda$).

In such conditions, according to Kivelson and Heeger [26], the mainly *one-dimensional* feature of the system will now be favorable to conduction. The reason for this is that in a quasi-one-dimensional system only the phonons at $\pm 2k_F$ give efficient scattering to limit the mean free path. Thus, due to the small number of these phonons, a theoretical value of $\sigma \approx 2 \times 10^6$ S/cm has been derived for the conductivity at room temperature in polyacetylene. Note also the value $\sigma \approx 10^7$ S/cm obtained by Pietronero [34]. Such values for the room-temperature conductivity of polyacetylene would put this compound in a much better position than copper. Of course, these are theoretical estimates, and they could only be an upper limit for “perfect” materials. However, since the “new” synthesis of polyacetylene by Naarman and Theodorou [35], values as high as $\sigma \approx 1.5 \times 10^5$ S/cm have been reported a couple of times and σ in the range 2 to 5×10^4 S/cm has been measured in various laboratories. The main features of conduction in such highly conducting polyacetylene are reviewed in Section III.E. As we shall see, in this high-quality material, conduction could possibly be governed by a coherent process only within given segments of chains. At a larger scale, barriers between highly conducting regions are implied, in a way that resembles behavior in heterogeneous systems. For that reason we first give an insight into the conducting processes governed by disorder, which correspond to the overwhelming majority of real cases.

D. Conduction in a Disordered Medium

We now consider the situation in real materials. In addition to the localization effects inherent to in one-dimensional systems, all kinds of defects and disorders are present, so that the charge carriers are located on localized states, or possibly on limited conducting areas, which can be chain segments or more extended conducting regions. Conduction must then proceed by hopping from one place to another. Conduction in CPs is thus a particular example of the general problem of conduction in disordered

solids [36]. Since barriers have to be overcome, we are dealing with an activated process, resulting in very rapid temperature dependence. As the temperature is lowered, conductivity decreases exponentially as

$$\sigma \propto \exp\left[\left(\frac{T_0}{T}\right)^\gamma\right]$$

where the exponent γ has typical values between 0.25 and 0.5. This law is commonly observed in disordered materials, and good fits have been reported with the data of different CPs in the temperature range 300 to 10 K [5]. Although there are several models leading to such a temperature dependence, with values for the exponent from $\frac{1}{2}$ to $\frac{1}{4}$, a general and satisfactory theory accounting for the transport mechanism in disordered CPs is still lacking.

Start from the usual expression for conductivity,

$$\sigma = ne\mu$$

where n is the number of charges and μ their mobility. The number of charges is given by $n = kTN(E_F)$, where $N(E_F)$ is the density of states at the Fermi level; and for the mobility, we take the Einstein formula, $\mu = eD/kT$, where D is the charge diffusion coefficient. The diffusion coefficient is related to the hopping distance between sites R and to the hopping probability $p(T)$, which is temperature dependent: $D(T) = R^2p(T)$. Different methods have been proposed to estimate $p(T)$. The variable-range hopping (VRH) model, developed by Mott [37] for noncrystalline semiconductors, gives a qualitative agreement with experiment. It is assumed that the Fermi energy lies within the localized state energy levels. First, the hopping probability is proportional to the overlap between the site wave functions, which decreases exponentially with the intersite distance R_{ij} : $p_{ij} \propto \exp(-2\alpha R_{ij})$, where α is the wavefunction decay. Second, since an energy difference Δ_{ij} may exist between sites i and j , it is an activated process, $p_{ij} \propto \exp(-\Delta_{ij}/kT)$. The hopping probability is then written as $p_{ij} = \nu_{ph} \exp(-2\alpha R_{ij} - \Delta_{ij}/kT)$, where ν_{ph} is the frequency of phonons involved in the hopping process. The conductivity in the random medium can be reduced to the problem of calculating the current in a random resistor network governed by Kirchhoff's laws [38]. In the VRH model, the hopping distance is replaced by its optimum value R^* , which is a function of temperature (so it is a variable-range hopping: $R^* = [\frac{2}{3}\pi\alpha N(E_F)kT]^{-1/4}$ and one obtains

$$\sigma = \sigma_0 T^{-1/2} \exp\left(-\frac{T_0}{T}\right)^{1/4}$$

with $T_0 \approx 7.64 \alpha^3/kN(E_F)$ and $\sigma_0 = A\nu_{ph}[N(E_F)/\alpha]^{1/2}$. Optimization of R depends on the dimensionality of the system and yields values for the exponent γ which are dependent on dimensionality: $\gamma = 1/(d + 1)$. One obtains $\gamma = \frac{1}{2}, \frac{1}{3}, \frac{1}{4}$, for $d = 1, 2$, and 3 , respectively.

In most CPs the temperature dependence of conductivity has behavior resembling Mott's VRH law, that is,

$$\log \sigma \propto -T^{-\gamma}$$

where σ decreases exponentially as T decreases, but the decay is slower than for a simple activated process ($\gamma < 1$). Deviations of the exponent from $\gamma = \frac{1}{4}$ could possibly be explained in terms of dimensionality different from $d = 3$. However, the parameters $N(E_F)$ and α , which can be extracted from the data, are often unphysical. This suggests that if conduction can basically be described in terms of a hopping process in a random material, the VRH model is not fully correct for a precise description. Improvements in the model have been attempted in different ways. For instance, instead of taking Mott's assumption of a constant density of states over kT : $N(E_F) = cst$, the first terms of an expansion can be taken [39]: $N(E_F) = \rho_0 + \frac{1}{2}\rho_2(E - E_F)^2 + \dots$. Such treatment leads to $\sigma \sim \sigma_0 \exp[-(T_0/T)^{1/2}]$, with $T_0 \approx [6500 \alpha/(k^3\rho_2)]^{1/3}$, for a $3d$ system.

Another refinement of the VRH model consists in assuming that the charges are delocalized over segments of length L , instead of being strictly localized on point sites [40]. This is indeed a more realistic picture, leading to better fits with the data, but it has the drawback that an extra parameter has been added. Note that the temperature dependence, $\log \sigma \propto -T^{-\gamma}$, can be found by other approaches, such as the percolation model, the effective medium approximation (EMA), the extended pair approximation (EPA) [41], the random walk theory, and so on.

If the material can be depicted in terms of highly conducting regions separated by much less conducting areas, the concept of a granular metal can be applied. This model was proposed by Sheng et al. and applied to the case of granular Ni-SiO [42]. The charges are supposed to move freely within a metallic grain, but since the intergrain transfer requires overcoming coulombic attraction, the charge carriers have to be thermally activated. With tunneling occurring between nearest neighbors, and after optimization of the product mobility and number density of charge carriers, an expression of the form $\sigma \propto \exp(-b/T^\gamma)$ is derived with $\gamma = \frac{1}{2}$. However, a possible crossover to $\gamma = \frac{1}{4}$ can be expected at low temperature [43]. At high field the conductivity is expected to become nonohmic, with the field dependence $\sigma \propto \sigma_0 \exp(-E_0/E)$, where E is the applied electric field. The concept of a granular metal has been used to account for transport properties in polyaniline [44]. It is true that in polyaniline there is evidence for

nonhomogeneous doping upon protonation, giving rise to a material depicted in terms on conducting islands embedded in an insulating matrix [45,46].

The frequency dependence of the conductivity is also a signature of disorder. Here again, the behavior commonly observed in CPs is similar to that in other disordered solids. Namely, after a plateau where $\sigma(\omega) = \sigma_{dc}$, $\sigma(\omega)$ increases as a power law of frequency:

$$\sigma(\omega) \propto \omega^\beta$$

Basically, as frequency increases, during half a period of the external electric field, charge carriers can move through regions of decreasing size, so that with increasing frequency areas of decreasing size and increasing effective conductivity are probed. Some authors have applied theories developed for the general class of disordered solids to CPs (for a general review, see Ref. 47). For the exponent β , values somewhat lower than 1 are usually found: $\beta \sim 0.6$ to 0.9 . If the motion of the charge carriers can be described in terms of a random walk over a lattice of effective dimensionality \mathfrak{D} , β is simply given by [48] $\beta = 1 - \mathfrak{D}/d$ where $d = 3$ is the real dimensionality of the space.

E. The Case of Polyacetylene

Fifteen years after the doping of polyacetylene started the entire era of CPs, polyacetylene remains a model compound for various aspects. (For an extended report on the stage of the research on “transport properties in polyacetylene” in 1987, see Ref. 49.) In addition to the chemical and structural simplicity of the material (samples with more than 80% crystallinity are currently obtained), considerable progress has been made in the synthesis (the Naarman–Theodorou synthesis), giving rise to a material with ultralow concentration of defects. Conductivity as high as 10^5 S/cm has been obtained, with a temperature dependence approaching metallic behavior. The question of the ultimate value that can be expected in CPs is then raised. But prior to this question the problem of the real nature of the conducting state in doped polyacetylene has been addressed since the very beginning of CPs.

The problem of the nature of the conducting state in polyacetylene cannot be considered without a close investigation of the real nature of the samples, including characteristics such as morphology, crystallinity, defect concentration, chain length, and so on. In the early 1980s the studies were concerned with $(CH)_x$ obtained by the Shirakawa method. The doping level y appeared to be a crucial parameter. As a function of y , basically

three ranges can be distinguished, which differ from each other by their spin susceptibility χ_s behavior.

1. At first, starting from undoped polyacetylene ($y = 0$), χ_s decreases with y and goes to almost zero for $y \sim 0.1\%$. It is assumed that the neutral solitons present in the undoped material, whose spin $\frac{1}{2}$ is responsible for the initial χ_s , are progressively converted to charged spinless solitons. In pristine $(\text{CH})_x$ the charge carriers originate in impurities, which essentially give p -type doping. Direct charge hopping between impurities is hard to admit because the levels are essentially all empty. A possible mechanism has been proposed by Kivelson. In the Kivelson's model the charge transport is assisted by the mobile neutral solitons [50]. Hopping from a charged to a neutral soliton becomes feasible when the neutral soliton passes close to an impurity ion. Kivelson's model predicts a steep power law dependence for σ versus T : $\sigma \propto T^9$, which is close to that observed experimentally. In the very low doping range, as χ_s goes to zero with increasing y , conductivity increases drastically: more than five orders of magnitude increase as y is varied in the range 0 to 0.5%.

2. At the intermediate doping level, $0.5\% < y < 5\%$, conductivity increases more slowly and $\chi_s \approx 0$. In this range of *spinless conductivity* the charge carriers are very likely charged solitons, which carry charge but no spin. Impurity concentration is large enough so that the energies of soliton levels occupy a wide range and direct jumps should be enabled by thermal energy. The σ versus temperature data can be explained reasonably well in terms of the VRH model, especially in the case of iodine-doped $(\text{CH})_x$ [51]. The conduction process seems to depend on the nature of the counterion. In the case of Na-doped samples, doping is probably nonhomogeneous, giving rise to highly conducting Na-rich regions surrounded by less conducting Na-poor regions [52].

3. In highly doped samples a large Pauli susceptibility (temperature independent) suddenly appears for $y \geq 5$ to 6%. The spins must be due either to polarons or to free electrons. The nature of the conducting state has been a matter of discussion since the beginning of the 1980s. It is beyond the scope of this brief presentation to review the numerous models that have been developed. So far, the nature of the conducting state of highly doped polyacetylene is still an open question. A large part of the difficulty originates with the fact that the data appear ambiguous. On the one hand, the Pauli susceptibility and thermopower data (thermopower is small and decreases with T) are consistent with a "metallic" state. But on the other hand, there is strong evidence that dimerization persists at any doping level. The doping-induced infrared modes, which would not occur for a uniform chain, are seen even at high dopant concentration. This means that there is still a gap in heavily doped material, although it is no

longer at $2\Delta_0 \sim 1.4$ eV, as in the undoped $(\text{CH})_x$, but at lower values (e.g., ~ 0.3 eV in I_3 -doped material). Furthermore, in almost all cases, conductivity decreases with decreasing T , which is evidence that defects and disorder should play a major role in limiting the conductivity. However, this last statement has been shown to be incompatible with recent improvements in polyacetylene chemistry. In particular, with the Naarman–Theodorou synthesis developed since 1986, high-quality material has been obtained, giving rise to so-called “highly conducting” polyacetylene, whose conductivity approaches that of copper.

Basically, the Naarman-Theodorou synthesis of polyacetylene [36], like the Shirakawa synthesis, is a direct polymerization of acetylene on a substrate covered by a catalyst layer, but the catalyst [a mixture of $\text{Ti}(\text{OC}_4\text{H}_9)_4$ and $\text{Al}(\text{C}_2\text{H}_5)_3$] has been softened by aging at 120°C in silicon oil. Long $(\text{CH})_x$ chains with very few sp^3 defects are obtained. Quite long conjugation lengths are obtained. Furthermore, samples with stretched aligned chains have been prepared. The resulting material, commonly called “n- $(\text{CH})_x$ ” (“n” for “new” or “N” for “Naarman”), can be considered as an example of an “assembly of chains” and a good candidate to approach the ultimate conductivity of CPs. But do we observe a metallic conductivity in n- $(\text{CH})_x$ —basically an increase of σ as T decreases—consistent with the Kivelson–Heeger model [2]? In fact, n- $(\text{CH})_x$ samples are on the borderline between metallic behavior (σ increases with decreasing T) and defect-controlled conduction behavior (σ decreases as T decreases). In a few cases, samples have been obtained which exhibit a maximum in the temperature dependence of the conductivity [53]. But in most cases, σ decreases with decreasing T . However, the decrease is slow, much slower than in hopping conduction. Typically, on freshly prepared stretched aligned films one has $\sigma_{\parallel}(300) \approx 5 \times 10^4$ S/cm, and the decay between 300 and 0.4 K is less than one order of magnitude. Aging of the sample both decreases the high-temperature conductivity and increases the decay at low temperature. At low temperature, in the range 0.4 to 3 K, an almost linear dependence is observed: $\sigma(T) = \sigma_0 + \sigma T$. It is remarkable that the zero-temperature extrapolated value is not zero (typical value $\sigma_0 \sim 10^4$ S/cm). This result invalidates any conduction model based on thermal activation of the carriers.

At lower temperature, namely for T lower than a given “localization temperature” $T < T_{\text{loc}}$, there is a crossover to a power law decay $\sigma(T) \propto T^{\beta}$, which leads to zero conductivity at $T = 0$. For freshly prepared samples one has $T_{\text{loc}} \sim 0.3$ K. The value increases with aging, which indicates a stronger localization effect with larger defect concentration [54]. A reasonable explanation is that the localization effect is related to the nonzero-level spacing as long as the chain length N is not infinite. As kT becomes smaller than the energy difference ΔE between two neighboring levels near

the Fermi energy, the charge carriers are no longer mobile. This yields $T_{\text{loc}} = \Delta E/k_B$. The spacing goes like $\Delta E \propto 1/N$, with N the number of carbon atoms in the conducting region. The experimental value, $T_{\text{loc}} \sim 0.3$ K, gives a value for the length of the conjugated segments which is too high ($N \sim 500,000$) if one considers a purely one-dimensional system. On the other hand, considering a three-dimensional system leads to too-short chains. The reality probably lies between these two limiting cases. The experimental data support the picture of localization in a finite highly anisotropic system with three-dimensional interactions.

In the temperature range $T > T_{\text{loc}}$, the data give a remarkable fit to an expression derived by Sheng [55]: over almost three orders of magnitude in temperature

$$\sigma(T) = \sigma_{\infty} \exp\left(\frac{T_1}{T + T_0}\right)$$

This formula accounts for nonzero conductivity at $T = 0$. Tunneling through potential barriers between highly conducting regions is supposed to be the basic process for charge transfer at low temperature. In Sheng's model the effects of thermal fluctuations on the potential barriers are also considered. Such fluctuations result in an enhancement of the tunneling current. As discussed by Schimmel et al., Sheng's formula gives an excellent fit with the data, although the applicability of the Sheng's model is somewhat questionable. A phenomenological approach can, however, be proposed [29]. Basically, conductivity would reflect the crossing of potential barriers by two processes: (1) a thermally activated jump at temperatures higher than or approximating the barrier, and (2) crossing through the barrier by quantum tunneling at low temperature. The effective height V_0 and the effective width w , together with the high-temperature limit of conductivity σ_{∞} , are the three parameters of the model. Barrier heights of about 10 meV and barrier widths of 1 to 2 nm are obtained from the data. Concerning the high-temperature limit conductivity σ_{∞} , which is the conductivity one would obtain if it were not limited by barriers—or in other words, the conductivity between barriers in high-conducting regions—it turns out that it is only 30 to 50% more than the room-temperature conductivity. Thus at room temperature the conductivity of $n\text{-(CH)}_x$ is essentially the intrinsic conductivity of “perfect” chains. From the typical value $\sigma_{\infty} \sim (20 \text{ to } 100) \times 10^3 \text{ S/cm}$, with the assumption that the carrier concentration is 6% per C—H unit, one obtains a value for the mobility of $\mu \sim 50 \text{ to } 250 \text{ cm}^2 \text{ V}^{-1} \text{ s}^{-1}$. These are remarkably high values for organic conductors, about two orders of magnitude larger than usual at room temperature.

IV. MAGNETIC PROPERTIES

A. Introduction

The electronic spins responsible for the magnetic properties of CPs can be located on the conjugated chains themselves or on the counterions inserted in the polymer matrix during doping. We are concerned essentially with the spins on the chains, since they are more specifically related to the intrinsic properties of CPs. Different kinds of unpaired spins can be encountered. First, it has been known since the 1960s that unpaired spins are present in conjugated polymers, even in the absence of doping. The spin concentration, as measured by ESR, lies in the range 10^{17} to 10^{20} spins/g. Although the nature of these unpaired spins is difficult to establish accurately, it is clear that their appearance is associated with the existence of large π -electron systems. Very likely, structures with an odd number of π electrons are stabilized on conjugated macromolecules of sufficient size. Of particular interest are the spins observed in undoped *trans*-polyacetylene. The origin of these spins is probably similar to that of other conjugated polymers (such as interruption defects leaving conjugated segments with odd numbers of π electrons), but they present quite peculiar and original properties. In particular, they are highly mobile. Indeed, they behave quite similarly to that expected for neutral solitons. Upon doping conjugated polymers, another kind of spin carrier appears: polarons. Polarons appear in conjugated polymers with a nondegenerate ground state (i.e., in practically all CPs except *trans*-polyacetylene).

The unpaired spins in undoped *trans*-polyacetylene, whose origin is likely to be accidental, supply a good model for observing the properties of neutral solitons. Furthermore, these objects play a special role in various properties of polyacetylene. For instance, they enable a lower-energy doping process. They can also play a special role in the conduction mechanism of lightly doped polyacetylene, as proposed by Kivelson [50]. However, polarons, being more universal, play a more central role in the physics of CPs. They present a threefold interest since they are intimately related to (1) the doping process, (2) conduction, and (3) magnetic properties.

During doping, electrons are introduced into, or removed from, the chains. The following question arises: Since each electron (or hole) possesses a spin, how will all the spins arrange together in the chains? This is a basic question, which involves a large part of the physics of these systems. If at low doping levels, two well-defined and separate charged species are formed—polarons (with one charge and one spin $\frac{1}{2}$ and bipolarons (with two charges and no spin)—the situation is less clear when, with increasing doping level, the interspecies interactions become significative. In a general

way, the spin susceptibility, χ_s , versus doping is less than (or equal to) that expected if every injected charge would give rise to an additional spin. This means that there is currently no sign of χ_s enhancement, which would give evidence for ferromagnetic-like spin–spin interactions. Cases of ferromagnetic polymers have, however, been reported [56]. If the reproducibility of most data has been questionable in the past, a very recent work claiming that ferromagnetism has been observed at room temperature in a purely organic conjugated polymer could open the way to a new and fascinating area [57]. However, in the following, we will be concerned only with the paramagnetism of CPs.

B. Neutral Solitons in Undoped Polyacetylene

As explained in Chapter 11, the ground state of *trans*-(CH)_x is a twofold degenerate state, which allows for the possibility of excitations in the form of soliton-like bond alternation domain walls [58–60]. (For a review on solitons in conducting polymers, see Ref. 60.) The energy level of the soliton state is located at the midgap. The idea of bond alternation defects appearing in long polyene chains was proposed by Pople and Walmsley in the 1960s [61].

Such a “kink” is represented in Fig. 5, where the bond alternation has been supposed to take place on a single carbon atom. By counting the valence electrons on this carbon atom one can see that there is an odd electron left. Thus one unpaired spin is present. Indeed, the presence of spins was early detected by ESR in undoped *trans*-(CH)_x [62], with a spin concentration of about 1 spin per ca. 3000 CH units. However, with a theoretical soliton formation energy of ~ 0.45 eV, one would expect a much smaller concentration of thermal solitons at room temperature. Very likely the spins in *trans*-polyacetylene, which essentially appear during the *cis* \rightarrow *trans* isomerization [63], are related to an odd number of π electrons in conjugated segments accidentally formed during isomerization.

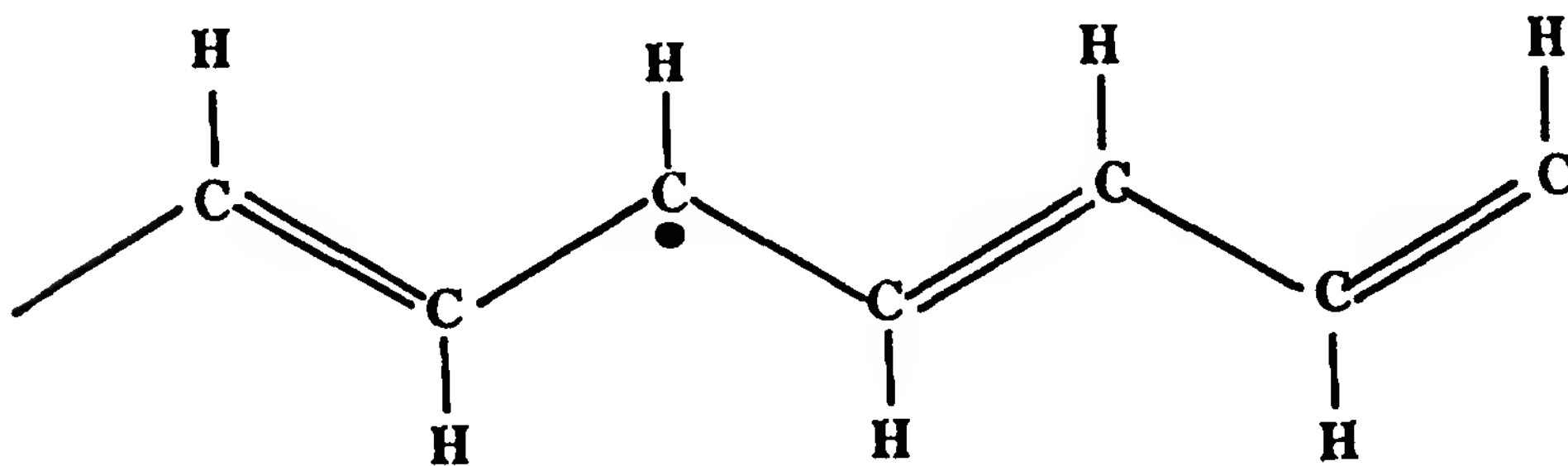


Figure 5 Bond alternation defect, or “neutral soliton” in *trans*-polyacetylene.

The remarkable point is that even if their very nature is something like macromolecular free radicals, they behave as topological solitons, which are nonlinear excitations of the dimerized chain. In particular, they are very mobile. The change in the bond alternation phase, instead of being located on a single carbon atom, extends over several C—H units. Over the soliton extension, denoted as ξ , the bond alternation and the Peierls gap $2\Delta_0$ vanish, which means that the Peierls dimerization is not operating. In other words, solitons are excitations that tend to violate the Peierls transition. So it is intuitive that their energy should be an increasing function of the Peierls gap (since larger Δ_0 increases the difficulty to suppress it). Within the continuous model [64,65] the formation energy of a soliton is simply given by $E_s = (2/\pi)\Delta_0$. Based on the same intuitive argument it can be understood that the soliton extension is inversely related to Δ_0 : $\xi/a \sim W/\Delta_0$ (from the SSH model), where a is the unit cell distance and W the π -electron bandwidth. This yields $\xi/a \sim 15$. The solitons should extend over ~ 15 carbon atoms. In fact, the soliton structure has been determined by ENDOR experiments [66,67] and a width about twice the theoretical value has been found [68] (Fig. 6).

Moreover, the spin density over the soliton, instead of being uniform, is alternatively positive and negative. This result provides strong evidence for the role of the correlation energy. The high mobility of solitons was proved by dynamic nuclear polarization experiments [69].

Dynamic nuclear polarization experiments consist of observing the proton NMR signal (at the nuclear Larmor frequency $\omega_N/2\pi \sim 10^7 \text{ s}^{-1}$), while pumping with microwave power near the ESR Larmor frequency $\omega_e/2\pi \sim 10^{10} \text{ s}^{-1}$ (Fig. 7). Two limiting results may occur according to whether the electron nuclear coupling is static or dynamic. In the static case, the elec-

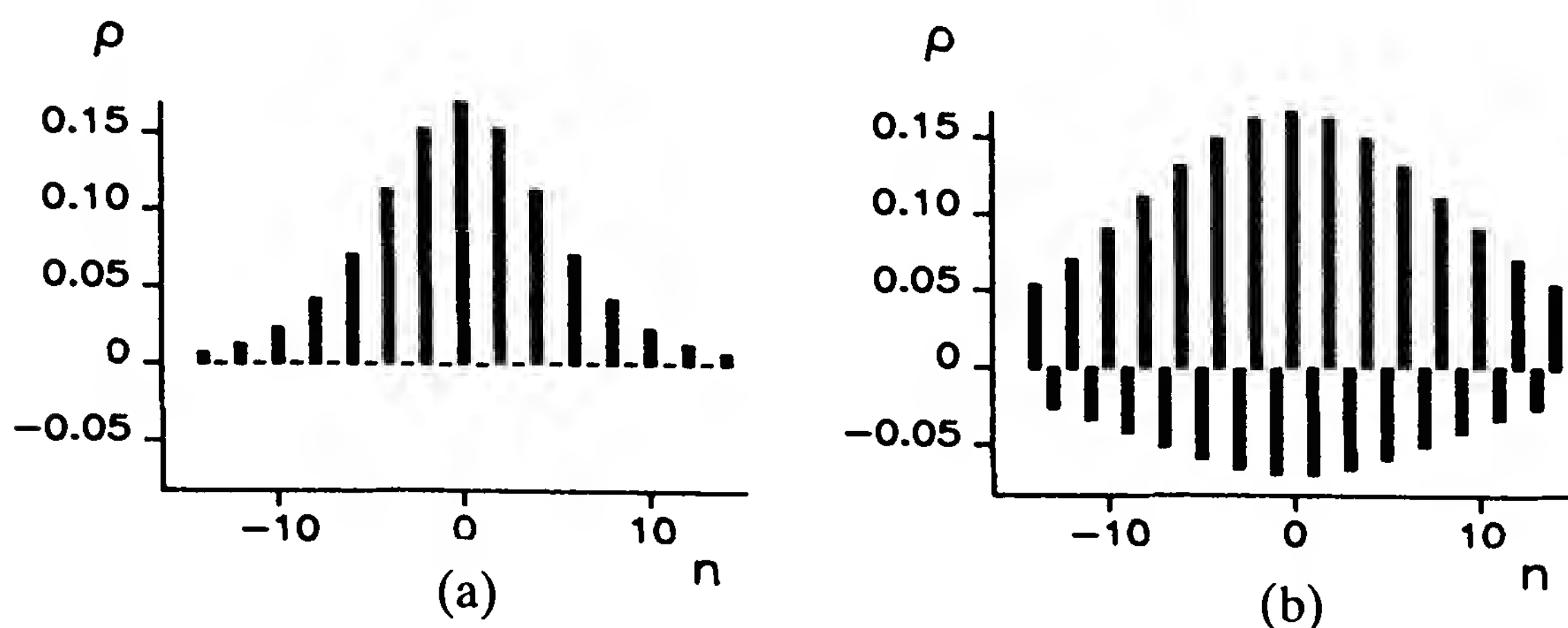


Figure 6 Spin density distribution in a soliton: (a) according to the SSH model; (b) as determined from pulsed ENDOR.

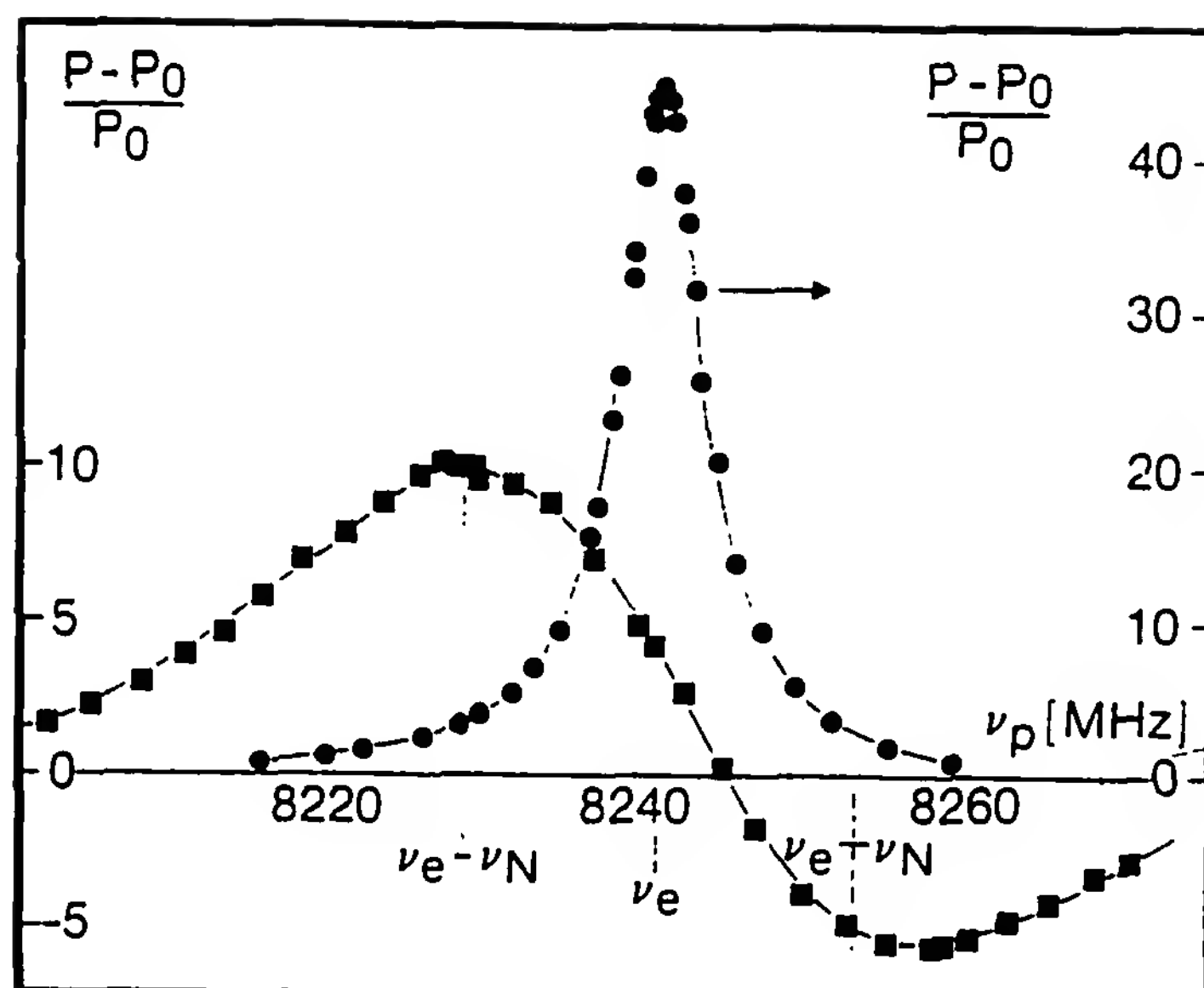


Figure 7 Proton NMR signal enhancement as a function of the electronic pumping frequency for *trans*-rich (solid circle), and *cis*-rich (solid square) polyacetylene samples.

tronic spin is fixed, and forbidden transitions at $\omega_e \pm \omega_N$ can be induced. This is the so-called *solid-state effect* (SSE). On the other hand, if the electronic spin is moving, at least at the rate ω_e , it is possible to enhance the NMR signal by pumping at the ESR frequency ω_e . This is the Overhauser effect (OE).

The experiments showed clear differences of behavior between polyacetylene in the *cis* and *trans* forms. Namely, SSE and OE are obtained in the *cis* and *trans* forms, respectively. In other words, the electronic spins are fixed in *cis*-polyacetylene, and they become mobile in the *trans* form. This result is quite consistent with the soliton picture. In *cis*-polyacetylene, a bond alternation defect divides the chain into two parts: *cis*-transoid and *trans*-cisoid, whose energies are different (Fig. 8a). Thus, to minimize energy, the spin defect will be trapped at one end of the chain (Fig. 8b). On the other hand, in *trans*-polyacetylene the chain is divided into two degenerate parts. The defect should therefore be free to move (Fig. 9).

Furthermore, quantitative characterizations of the spin motion in *trans*-(CH)_x have been performed by measurements of the proton NMR relaxation time T_1 and analysis of the ESR line width [70,71]. The spin motion can be described in terms of highly one-dimensional diffusion. The diffusion rate along the chains is very fast: $D_{\parallel} \sim 10^{13}$ rad/s (i.e., a diffusion coefficient of ca. 5×10^{-3} cm²/s), and the anisotropy is extremely high $D_{\parallel}/D_{\perp} > 10^5$. The very high anisotropy is also an argument for the soliton picture: neutral

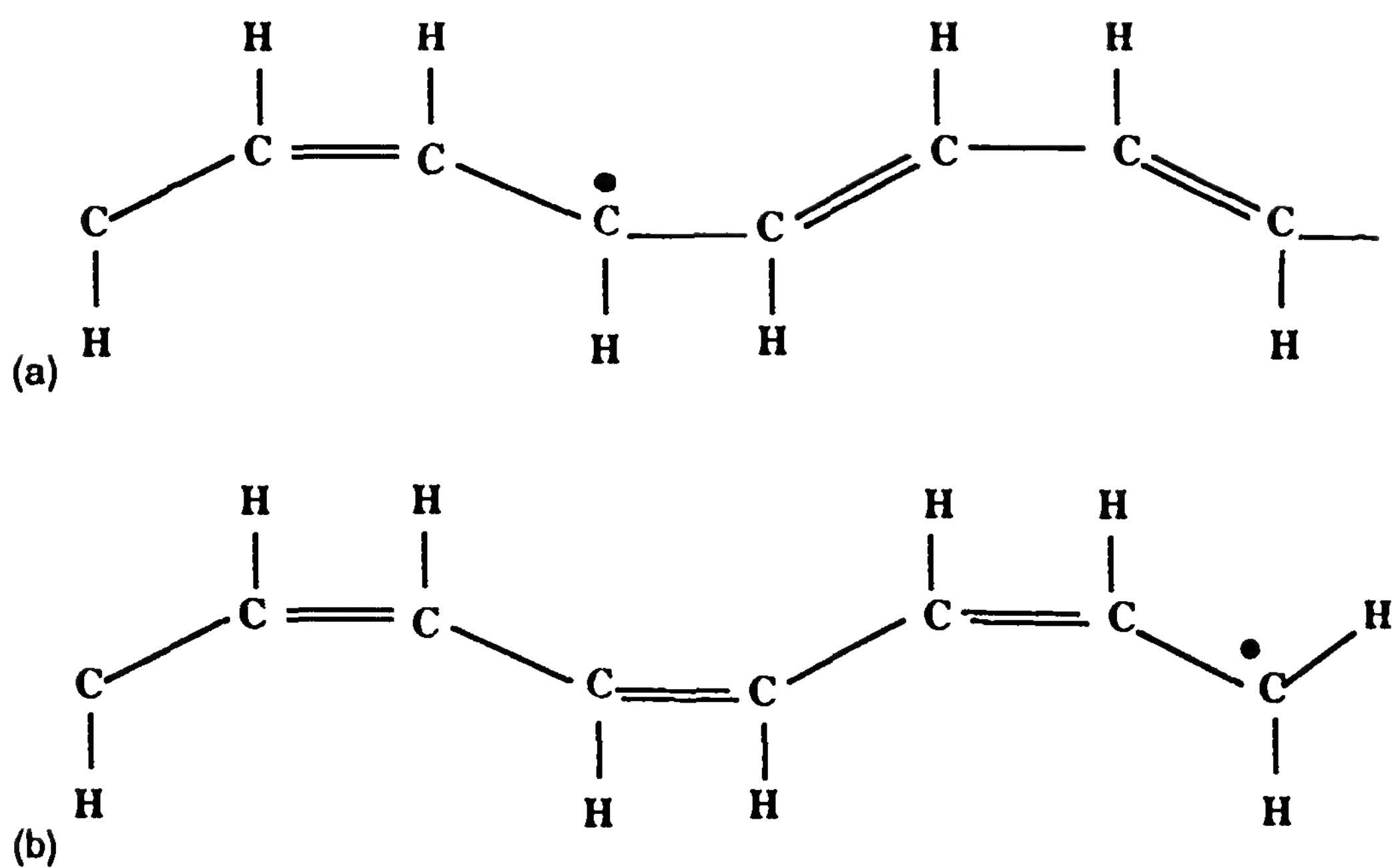


Figure 8 (a) The *cis-transoid* form (left of the defect) is more stable than the *trans-cisoid* form (right). (b) Spin defect trapped at one end of the chain.

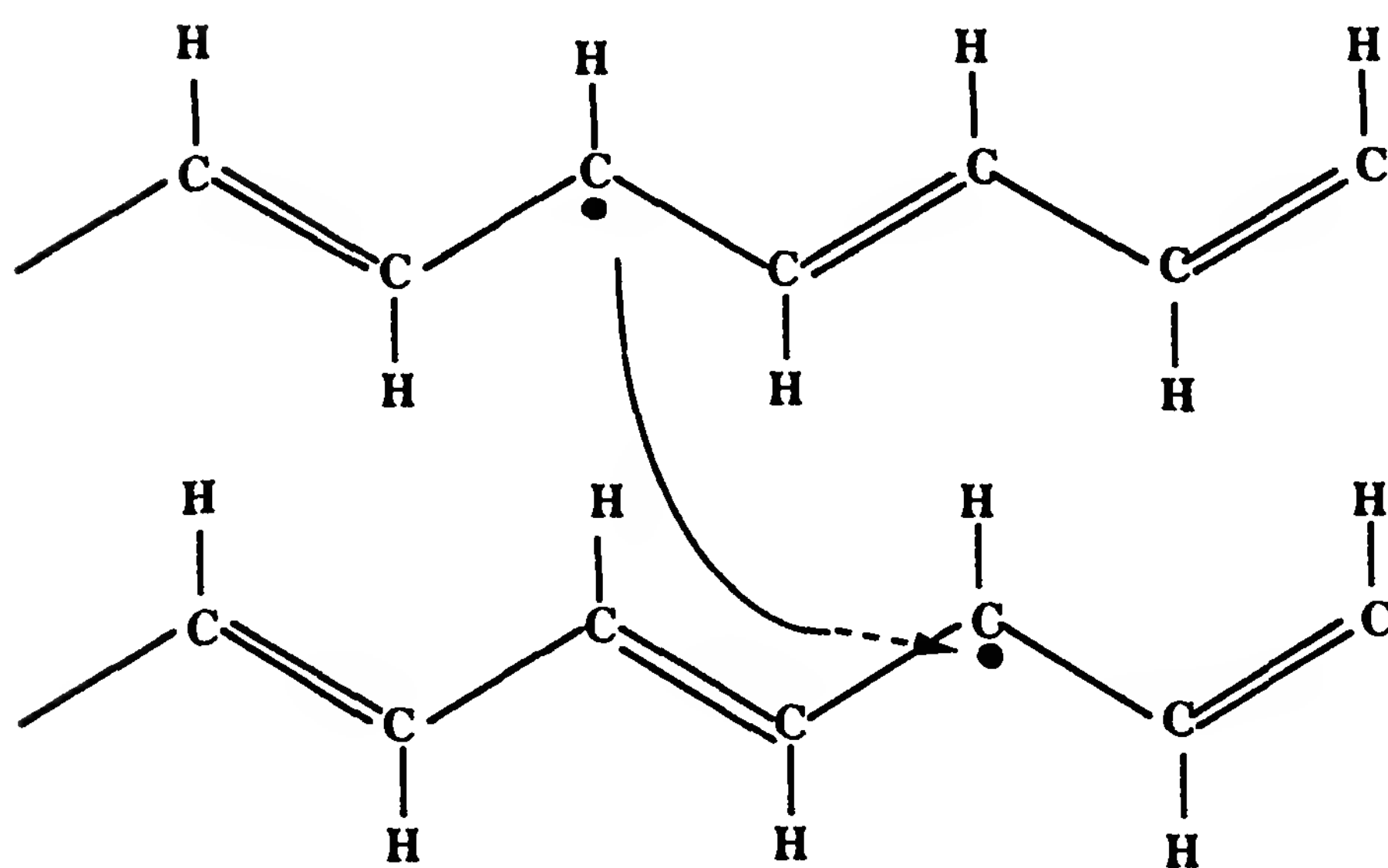


Figure 9 In *trans*-(CH)_x, both sides of the spin defect being degenerate, the latter is free to move.

solitons are objects whose interchain transfer is not allowed. At low temperature the solitons are less and less mobile, and become progressively trapped [68,72].

C. Spin Appearance Upon Doping

1. Different Charged Species

As noted in Section II, doping consists of injecting charge carriers into the polymer chains. These injected charges may or may not result in spin carriers, depending on the type of charged species involved. The spin-charge relationship for the different species in CPs is represented in the following table:

Species	Number of charges/electron	Spin
Neutral soliton	0	$\frac{1}{2}$
Charged soliton	1	0
Polaron	1	$\frac{1}{2}$
Bipolaron	2	0

The soliton species is concerned with systems with a degenerate ground state (in fact, *trans*-polyacetylene), and the polaron-bipolaron species is encountered in systems with a nondegenerate ground state (all conjugated polymers except *trans*-polyacetylene). The soliton species presents an “inverse” spin-charge relationship. It is “inverse” since when a charge is present there is no spin, and vice versa. It is also “inverse” as compared to the effects of doping in semiconductors. The polaron behavior is more regular in the sense that charge injection is accompanied by the appearance of spins. However, the bipolaron behavior is similar to that of charged solitons. A bipolaron can be depicted as a charged soliton-antisoliton pair.

2. Charged Solitons in Doped Polyacetylene

Numerous studies have been devoted to the magnetism of polyacetylene as a function of doping. After pioneering work with controversial results [73], the use of in situ techniques for doping, either chemical or electrochemical, enabled a rather consensual description of the evolution of the spin susceptibility upon doping to be reached. Both *n*-type doping (e.g., $[\text{Na}_y^+(\text{CH})^{-y}]_x$ [74] and *p*-type doping (e.g., $[(\text{CH})^{+y}(\text{ClO}_4^-)_y]_x$ [75]) have been investigated. It is now established that up to a doping level of $y \sim 5$ to 6% (dopant per carbon atom), the injected charges result in spinless charge carriers. As a function of the doping level, there is first a slight decrease of the initial spin susceptibility, which is attributed to a conversion of the neutral solitons with spin $\frac{1}{2}$ present in undoped *trans*-polyacetylene

to spinless charged solitons. The residual χ_s follows the Curie law and corresponds to a spin concentration of $\sim 2 \times 10^{-2}\%$ (spin per carbon). This small Curie spin susceptibility is maintained while the doping level increases up to $y \sim$ of 5 to 6%. This result demonstrates that the overwhelming majority of the charge carriers are spinless. Note, however, that at this range of doping, the conductivity has become quite high ($\sigma \sim 10^2 \text{ S cm}^{-1}$). The charged soliton model is thus strongly supported. At $y \sim 5$ to 6%, a sudden increase in χ_s is observed, which presents characteristics of a first-order phase transition. In the high-doping-level region, χ_s is temperature independent. It is thus a Pauli-type spin susceptibility, which is usually considered as a signature of the metallic state. Its value is in the normal range for organic conductors ($\chi_s \sim 10^{-6} \text{ emu/mol}$). χ_s , as well as the critical dopant concentration, is rather independent of the nature of the dopant. Spin susceptibility data, together with conductivity data, collected for different dopants [39] are shown in Fig. 10.

The susceptibility data are normalized to the Pauli susceptibility of undimerized $(\text{CH})_x$. This correspond to a one-dimensional metal with a 10-eV-wide half-filled conduction band. Tight-binding calculations with no coulombic interactions give $\chi_p = 3.9 \times 10^{-6} \text{ emu/mol}$. The nature of the conducting state in highly doped $(\text{CH})_x$ (i.e., for $y > 5$ to 6%), as noted

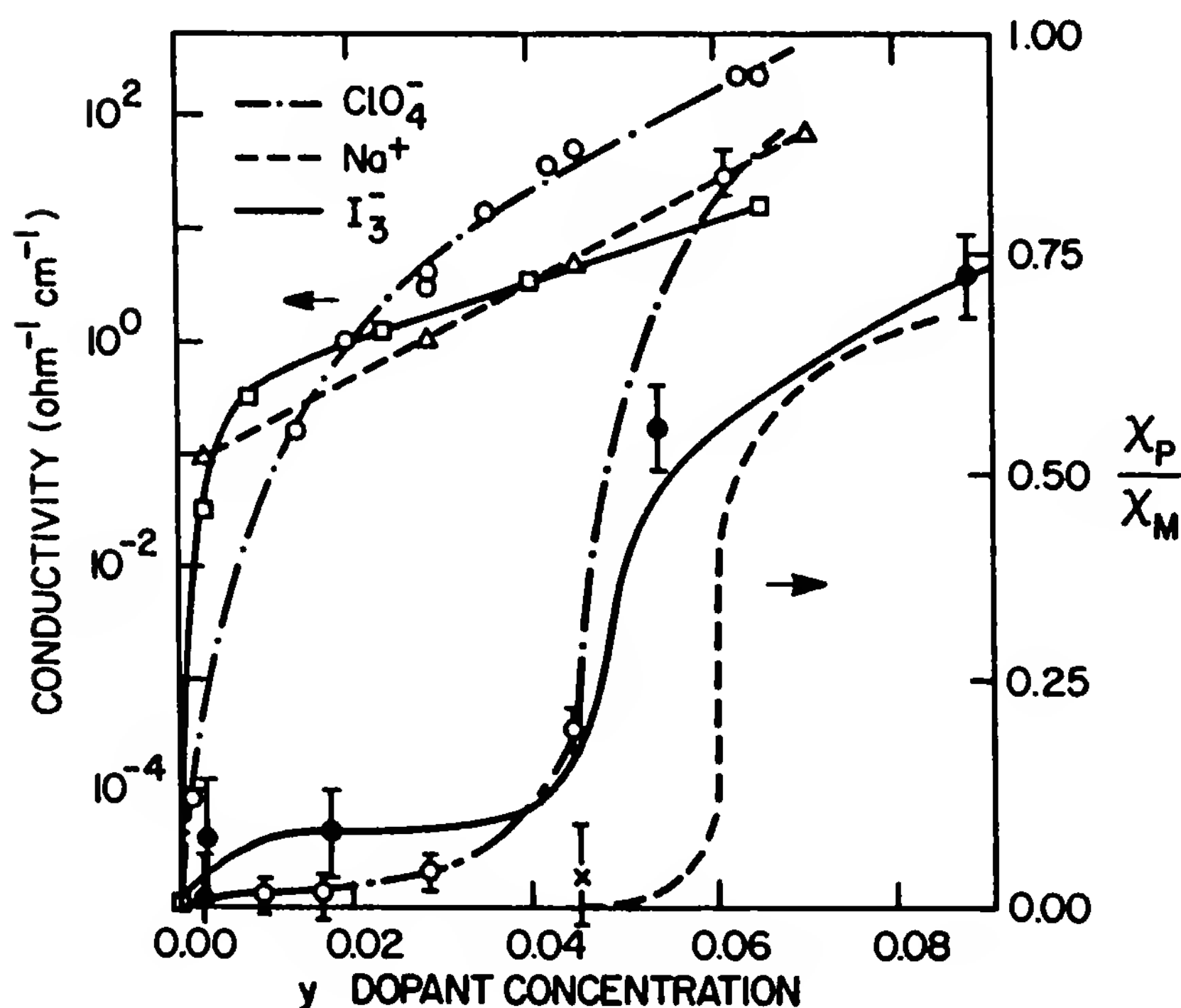


Figure 10 σ_{dc} (left-hand scale) and χ_p (right-hand scale) as function of y for various dopants. (From Ref. 39.)

in Section III, has been the subject of considerable work but is still an open question.

3. Polarons/Bipolarons

We turn now to conjugated systems with nondegenerate ground states. The charged states are thus expected to be polarons or bipolarons. Numerous studies have been devoted to the problem of determining which of these two objects corresponds to the basic species. Let us call E_p and E_b the energy for polarons and bipolarons, respectively. A simple argument shows that creating a bipolaron would be more favorable than two polarons. The energy difference

$$U = E_b - 2E_p$$

is expected to be negative. As a polaron is created, lattice relaxation takes place, giving rise to a lattice distortion. The lattice distortion costs energy E_d . When a bipolaron is created, about the same lattice distortion is used to accommodate the two electrical charges. Consequently, by creating a bipolaron instead of two polarons, energy E_d is saved. However, this argument ignores the coulombic repulsion between the two charges in the same lattice distortion. The importance of coulombic interactions in the physics of CPs has been pointed out by various authors [76]. Basically, the energy U we have introduced is the difference between the energy gain as the chain relaxes to accommodate a charge and the coulombic repulsion between two charges in the same chain distortion: $U \approx E_d - E_{\text{Coul}}$. Each of these two terms being on the order of a few tenths of eV, U is a quantity hardly predictable by theory. Although some idea has been drawn from quantum chemistry calculations [77], U is a complicated and subtle balance depending on the compounds, the local environment of charge carriers, and the microscopic arrangement of the chains. Contradictory data have been published on this question, probably corresponding to different experimental conditions. The case of polypyrrole is a good example. First, Scott et al. [78] found that the charges were essentially in the form of bipolarons. This result was contradicted by Genoud et al. [79], who concluded from in situ ESR measurements that polarons and bipolarons were almost degenerate: $U \approx 0$. It should be noted that Scott's samples were oxidized by oxygen exposure, while Genoud's samples were oxidized electrochemically. More recently, in chemically prepared samples by a layer-by-layer deposition method, conductive thin films with no detectable spins have been obtained [80].

With the development of in situ ESR experiments [23], which enable one to follow the spin concentration during electrochemical doping, quantitative studies of the polaron creation versus injected charges have become

feasible. In different CPs—polypyrrole, polyaniline, polythiophene—similar behavior has been observed [10,81] (Fig. 11). As a function of the doping level, χ_s , at first, increases at a rate of one spin per charge injected. Then the number of spins goes to a maximum, and finally it decreases to a small value at high doping levels.

This behavior is described simply in terms of a “box model” [10]. The polymer chain is divided into fixed sites, which can be neutral, singly charged (polaron with two spin states: up and down), or doubly charged (bipolaron state). Increasing the doping level corresponds to filling up the boxes with charges. For a given doping level, the polarons and bipolarons are supposed to be in thermal equilibrium, with their relative populations governed by the parameter U/kT , according to the Boltzmann law.

The problem can be expressed as follows. Assume there are N_c charges, or “balls,” to be distributed over N boxes. The rule is that a maximum of two balls can be put in each box. How many boxes will you obtain containing zero, one, and two balls? N_0 is the number of neutral sites, N_1 the number of polarons, and N_2 the number of bipolarons. Of course, N_1 is also the spin number $N_1 \equiv N_s$. It is clear that one has

$$N = N_0 + N_1 + N_2$$

and

$$N_c = N_1 + 2N_2$$

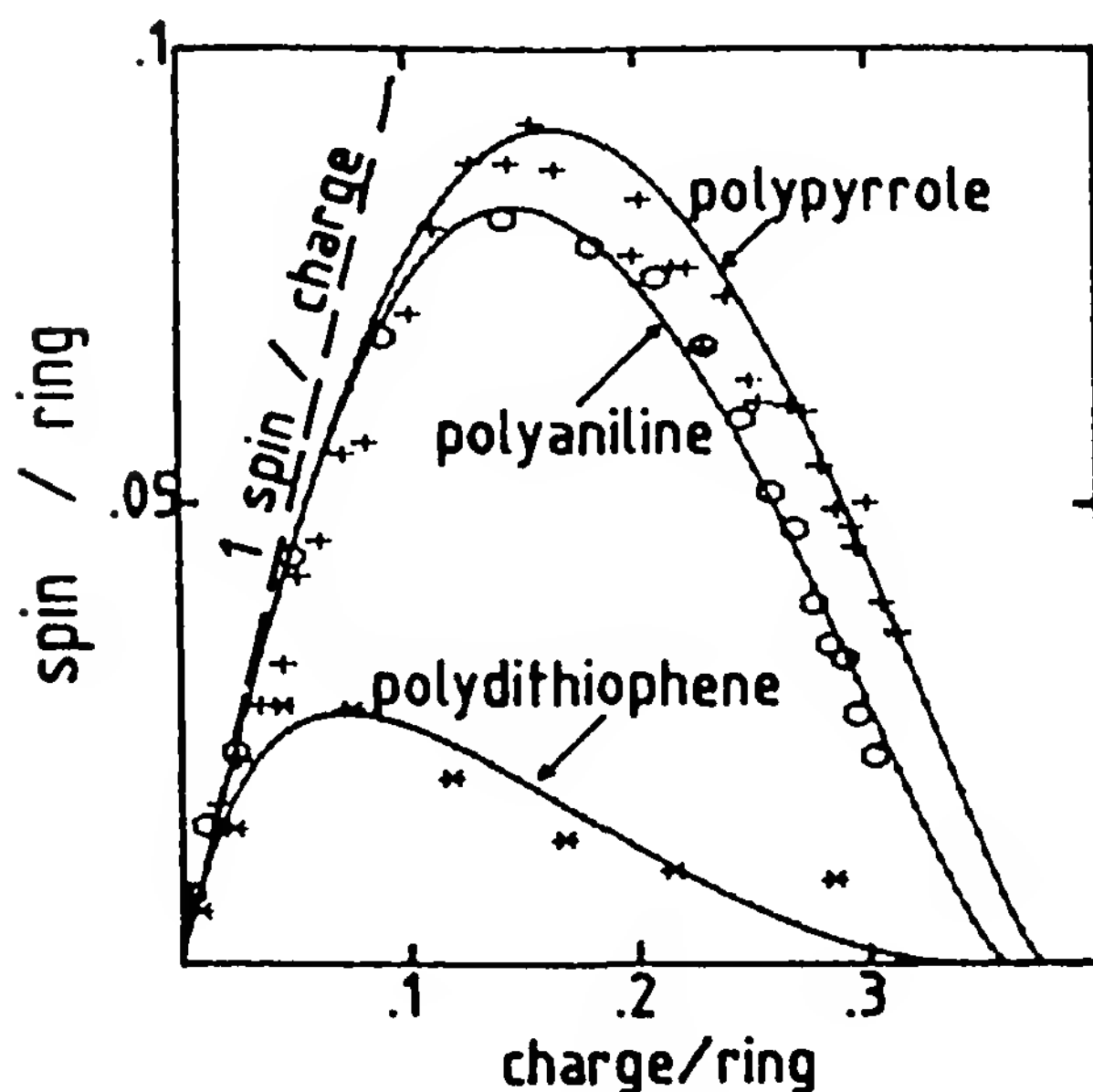


Figure 11 Spin concentration as a function of the injected charge concentration, for three different CP values. (From Ref. 81.)

In the following the reduced quantities $n_i = N_i/N$ ($i = 0, 1, 2, s$) and $q = N_c/N$ are considered. Add some physics to the problem with the additional rules as follows. Placing one ball in a box requires energy E_1 , and placing two balls requires E_2 . Furthermore, our balls are particles with spin $s = \frac{1}{2}$, so in the case of single occupancy (polaron), there is a twofold degeneracy. One obtains

$$n_1 = 2n_0 \exp\left(-\frac{E_1}{kT}\right)$$

$$n_2 = n_0 \exp\left(-\frac{E_2}{kT}\right)$$

Taking into account that $n_0 + n_1 + n_2 = 1$, and with $U = E_2 - 2E_1$, one obtains the spin concentration as a function of charge level q and temperature:

$$n_s = \frac{1 - \{1 - q(2 - q)[1 - \exp(-U/kT)]\}^{1/2}}{1 - \exp(-U/kT)}$$

The charge level varies between 0 (undoped material) and 2 (fully doped). Spin concentration is zero in these two limiting cases. It is maximum at half charge ($q = 1$) and the maximum value is

$$n_s^{(\max)} = \frac{1}{1 - \exp(-U/2kT)}$$

The case $U = 0$ is of special interest. In such a case, making one bipolaron from two polarons does not cost energy. The maximum spin concentration is $\frac{1}{2}$, which means that 50% of the boxes possess unpaired spins. This result can be explained as follows. Since (1) at the maximum spin concentration one has $q = 1$, and (2) placing one or two balls in the box is equivalent, there are four equiprobable cases: (1) neutral site (no ball), (2) polaron up, (3) polaron down, and (4) bipolaron (two balls). Two among four of these states are magnetic, which gives $\frac{1}{2}$ for the spin concentration. The room-temperature data for polypyrrole and polyaniline can almost be fitted with $U \approx 0$, which means that in these compounds polarons and bipolarons would be degenerate.

The box model is a very crude picture. It accounts correctly for the room-temperature behavior of spin susceptibility versus doping level in different conducting polymers, but its validity can be disputed. First, interactions between charged species can be added, in a phenomenological way, as in Ref. 10, but this does not change the essential basis of the model. In the statistical model [82] the charges are allowed to migrate along the chain and adjust to each other to minimize the free energy. Neutral sites,

polarens, and bipolarons may also have different lengths: l_n , l_p , and l_b , respectively. The statistic model gives qualitatively the same results as the box model, unless $l_b > 2l_p$. Indeed, if the length of a bipolaron is more than twice that of a polaron, it would be more favorable to create two polarons rather than a bipolaron at high doping levels. A magnetic state would then be obtained at full charge. However, such a case seems unlikely to be really physical.

D. Spin Susceptibility Versus Temperature: Curie Versus Pauli, Role of Disorder

Although the models presented above account qualitatively for the room-temperature spin–charge relationship, they generally fail to account for the temperature dependence of χ_s . In various cases, χ_s data deviate from the Curie law and cannot be explained simply in terms of temperature-dependent polaron population. There is certainly not a unique and general magnetic behavior for all CPs. The magnetic behaviors depend on the compound, and also, for a given compound, they may depend on the way it has been prepared and doped. Note, however, that there is a behavior that has *not* been observed (to our knowledge): a spin susceptibility decreasing toward zero for decreasing temperature, as expected if bipolarons were the basic species ($U < 0$). There is no reliable indication of a maximum in the χ_s data as a function of temperature. If one admits that a state of thermodynamic equilibrium exists (which might not be the case), one is lead to the conclusion that $U \geq 0$, in all cases. In other words, polarons would be the basic species. According to the box model, this conclusion sets a minimum value for the unpaired spin concentration. At 50% doping level ($q = 1$), one should have $n_s \geq \frac{1}{2}$ ($n_s = \frac{1}{2}$ for $q = 1$). Such a high value for the spin concentration is not consistent with data for compounds that present a significantly lower χ_s (e.g., polythiophene). This apparent contradiction can be overcome if one takes into account the role of disorder. However, before introducing the effect of disorder on the spin susceptibility, its temperature dependence should be reviewed.

The data of $\chi_s(T)$ are often interpreted as a sum of two terms:

$$\chi_s = \chi_c + \chi_p$$

in which we have introduced two contributions to the spin susceptibility:

1. *Curie-like*: $\chi_c = C/T$ with $C = N\mu_B^2/k$ is the spin concentration, μ_B the Bohr magneton, and k the Boltzmann constant.
2. *Pauli-like (temperature independent)*: $\chi_p = \mu_B^2 N(E_F)$, where $N(E_F)$ is the density of states at the Fermi level E_F .

The presence of a Pauli-like term is associated with a nonzero density of states at the Fermi level: it has been presented by different authors as evidence for metallic behavior. Before mentioning other possible interpretations, we would point out that the decomposition $\chi_s = \chi_c + \chi_p$ is not unambiguous. Indeed, in the case of polyacetylene in the heavily doped regime ($y > 6\%$), the existence of Pauli susceptibility is well established [83], since in all the temperature range χ_s is almost constant ($\chi_p \gg \chi_c$). But this is generally not the case in other compounds in which a significant “Curie term” remains present.

The case of polyaniline is of particular interest. Polyaniline undergoes an insulator-to-metal transition not only as a function of oxidation, as in other CPs, but also as a function of protonation level. Only the polyaniline form, which is both oxidized (emeraldine) and protonated (emeraldine salt) is conducting. Spin susceptibility, as well as conductivity, increases with protonation level [84]. The temperature dependence of χ_s has been interpreted as the sum of Curie-like and Pauli-like contributions. Furthermore, the Pauli-like term seems to vary approximately proportionally to the protonation level [85,86]. In particular, even at low protonation levels when the conductivity is still very low, some Pauli-like contribution is already present. Since Pauli susceptibility is usually associated with metallic material, it has been proposed that protonation, instead of being a homogeneous process, is concentrated in isolated regions, depicted as “metallic islands” embedded in an unprotonated insulating sea. By increasing the protonation level, the number and/or the size of the metallic islands increases, giving rise to an increase in the Pauli susceptibility. Conductivity starts to increase significantly at the percolation threshold. Such a picture is in agreement with spin dynamic measurements on emeraldine samples of different protonation levels [87]. Taking advantage of their spin, spin dynamics studies can follow the motion of the charge carriers (polarons) at a nanoscopic scale. The spin–charge diffusion coefficient can be determined both along the chains (D_{\parallel}) and perpendicular to the chains (D_{\perp}). It appears that the carrier motion along the chains (D_{\parallel}) remains about the same whatever the protonation level, and thus the overall conductivity. This is further evidence for metallic islands. Furthermore, from the spin dynamics data, these islands would be essentially one-dimensional. They can be described as consisting of a single chain. The macroscopic conductivity is then determined essentially by the interchain hopping (D_{\perp}). This statement is consistent with the parallel variations of D_{\perp} and σ as a function of protonation rate and of temperature [88].

The origin of paramagnetism in the conducting state of polyaniline has been attributed to a polaron lattice [89] which forms at 50% protonation,

as sketched in Fig. 12. In such a case, the magnetic state would be favored by a regular periodic lattice. Consistent with this picture, it has also been proposed that the magnetic state would be located in crystalline regions, while the amorphous part would be spinless [90]. However, the problem of the appearance of unpaired spins is very complicated, and the data are contradictory. For instance, according to other experimental evidence, the appearance of unpaired spins is more likely to be related to disorder [20]. In thin films obtained by in situ electropolymerization, the highly doped state contains very few spins. Moreover, data have been reported showing that for the few spins that are present, the Pauli-like term is practically zero [91].

The Pauli-like contribution to spin susceptibility (temperature independent) is associated with nonzero density of states at the Fermi level, but these states are not necessarily extended states. The Pauli-like term is therefore not necessarily related to a metallic state. In spin glasses, for instance, a nonzero density of states appears at the Fermi level. In particular, disorder can give rise to localized states with energy in the gap in the vicinity of E_F [92]. It can be shown explicitly that disorder introduces a contribution to the spin susceptibility that is independent of temperature.

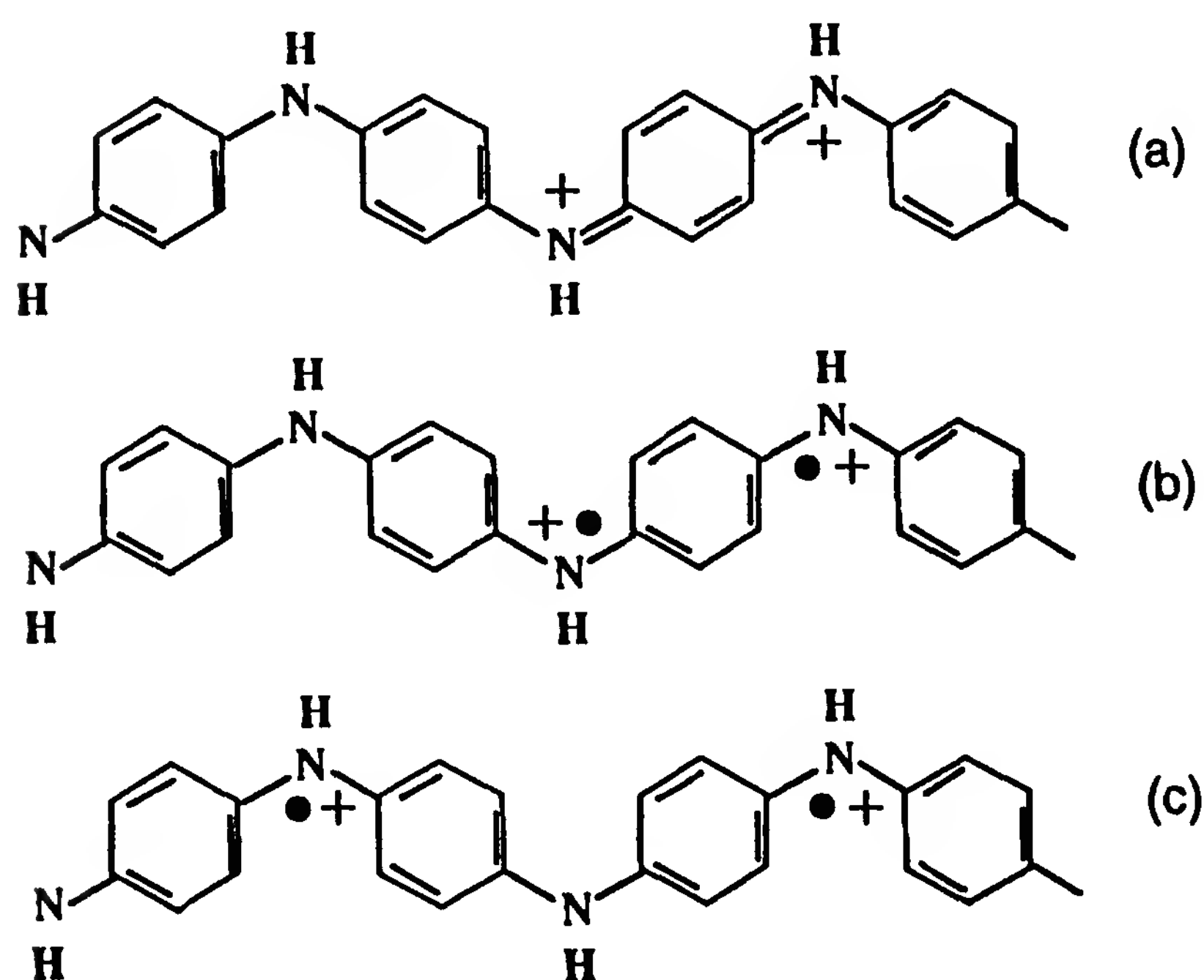


Figure 12 Formation of a polaron lattice according to Ref. 89: (a) emeraldine salt in bipolaron form; (b) dissociation of the bipolaron into two polarons; (c) rearrangement of the charges into a "polaron lattice."

If one assumes that disorder can be described by a distribution $g(\epsilon)$ of the site energy, one obtains [27,93]

$$\chi_p = \kappa N_c \mu_B^2 [g(\mu) + g(\mu - U)]$$

where κ is a numerical factor close to 1.

Furthermore, in addition to the temperature-independent term, disorder has the effect of favoring bipolaron formation rather than polarons. Consider, for instance, $U > 0$ and $q = 1$ ($N_c = N$, i.e., one charge per unit cell in average). In the absence of disorder, essentially the polaron states will be populated (for $kT \ll U$). With enough disorder ($\Delta\epsilon \sim U$), some doubly occupied sites (bipolarons) will be located below the singly occupied states (polarons), giving rise to an increase in the bipolaron number, and thus to a decrease in the spin susceptibility.

We should mention that another possible explanation of the Pauli-like behavior has recently been proposed in terms of contributions of the triplet-excited bipolaronic states to the spin susceptibility [94]. As shown by Bussac and Zuppiroli, the polaron–bipolaron energy difference U is essentially determined by the interdopant distance L_d . The authors also consider the bipolaron triplet state, which reduces to two separate polarons for large L_d . Due to disorder, the L_d are distributed, giving rise to a distribution for the energy of the magnetic states. Summing over the distribution yields a Curie-like contribution, plus a smoothy temperature-dependent term, which resembles a Pauli contribution.

V. CONCLUSIONS

We can now make some comparisons between CPs and organic crystals, their cousins in the organic conductor family. First, it is clear that an understanding of the fundamental processes is less advanced in CPs. Works in this domain started about a decade later. The main reason, however, is related to the large difference in the material definition. While conducting molecular crystals are well-defined objects at any scale of investigation, in the case of CPs one has to deal with materials with (1) high structural complexity, (2) the absence of long-range order, and (3) difficulty in reproducibility. These features, which are inherent to polymeric compounds, are reinforced in the doped materials, since doping introduces an additional source of heterogeneity and disorder. It is remarkable, however, that despite this difficult scenario, after about 15 years of active work, interest in the CP area has not begun to decline. One reason for this is probably that the dream of combining the mechanical properties of plastics with the conducting and optical properties of metals and semiconductors is still alive. The dream has become reality in various fields, as mentioned in Chapter

11, and is still more promising for the future. Another reason lies in the richness of the properties and phenomena encountered in these systems, of which we have presented an overview in Chapter 12 and in this chapter. Extremely wide ranges of characteristics are covered. For instance, in the case of conductivity, the measured values extend over more than 15 orders of magnitude (from 10^5 to less than 10^{-10} S/cm). All intermediate values can be obtained. We should also point out the interdisciplinary nature of the field. Cooperative work associating the effort of scientific communities from different origins—solid-state physics, synthesis and macromolecule chemistry, theory, electrochemistry, polymer science, and processing—is a stimulating aspect of the domain.

Also, an exciting aspect is related to the claim that in CPs we would be dealing with a “new physics.” This statement is based on the proposal that the electronic properties would be governed by nonclassical charge carriers: namely, the nonlinear excitations that are solitons, polarons, and bipolarons. After various controversies [95], as is usual in a living and growing science, a rather consensual agreement has been achieved on the concept of the soliton. The problem of deciding whether soliton-like particles are present or not in CPs is not trivial at all.

Solitons in polyacetylene, and polarons in conjugated polymers with nondegenerate ground states, are expected to occur as a direct consequence of electron–phonon coupling. If it is clear that electron–phonon coupling is of fundamental importance in one-dimensional organic solids, whether this interaction plays a leading role, surpassing all others, can be questioned. In particular, electron–electron interaction has also been shown to play a very important role. In the occurrence of the Peierls transition, for instance, Coulomb interaction makes a greater contribution than electron–phonon coupling [96]. It has also been proposed that polarons in three-dimensional lattices should be unstable with respect to delocalized free electrons [97]. However, rather than asking the question “Do soliton-like particles exist?” (a rather metaphysical question in reality), one should ask whether such objects are, or are not, necessary to account for experimental results. One can admit that after about 15 years of intensive research, the real *proofs* for solitons are quite rare. But nevertheless, some strong arguments in favor of the soliton picture do exist. Having already discussed arguments from optics (Chapter 12), we can now envisage the contributions related to properties reported in this chapter.

In electrochemical doping the presence of hysteresis has been noted. It is evidence that, for instance, after *n*-type doping in $(\text{CH})_x$, removal of an electron (dedoping) requires less energy than introducing it (doping). The energy difference is ~ 0.7 eV, which is about half the gap of $(\text{CH})_x$. This result can be interpreted as follows [98]. During doping, electrons are

placed in the conduction band (just above the gap). Lattice relaxation then takes place, and soliton levels appear at midgap (i.e., ~ 0.7 eV below the conduction band). Thus, upon dedoping, charges will be removed from energy levels located 0.7 eV below that at which they were introduced. Hysteresis in electrochemical doping could therefore be interpreted as evidence for lattice relaxation, which accompanies the creation of soliton-like particles. The same results and arguments are also valid for polarons in polymers with nondegenerate ground states. However, hysteresis in electrochemistry is a very common phenomenon, which can be due to numerous causes.

From transport properties, it does not seem possible to discriminate between charge carriers being solitonlike or having a more classical nature. Conductivity is concerned with the overall motion of charges, whether or not these charges are accompanied by lattice distortions. The most convincing argument for solitons relies on a combination of the three aspects that have been discussed in this chapter: doping, conductivity, and magnetic properties. Namely, the inverse spin–charge relationship encountered in polyacetylene and the spinless conductivity reported in different CPs are strong evidence that we are dealing with charge carriers with special properties. In the case of *trans*-polyacetylene, injection of charges—that is, electrons or holes which are particles with spin—does not result in the occurrence of spin susceptibility in the doped polymer. Spins have therefore disappeared. The only way to account for spin disappearance is in terms of spin pairing. In other words, as charges are injected they form pairs with opposite spins. Such a mechanism is well illustrated in terms of soliton–antisoliton pairs. Indeed, the inverse spin–charge relationship demonstrates the pairing of charge carriers, even if the charge carriers are not exactly solitons. The soliton–antisoliton pairing does not imply a confinement of the pseudoparticles. In conjugated polymers with nondegenerate ground states, the pairing is not as strong as in *trans*-(CH)_x, since spin susceptibility at first increases on doping. In terms of the polaron picture, the pairing can be broken by the entropy that is gained by having two free, independent polarons instead of one bipolaron. Nevertheless, at high doping levels, spin pairing does occur in all polymers. Moreover, in some cases, spinless conductivity has been reported. This result demonstrates that charge carriers have a tendency to form pairs, even in conjugated polymers with nondegenerate ground states. When the degeneracy of the ground state is lifted, the two charged partners become confined in the same lattice distortion: namely, they form a bipolaron.

The pairing of charge carriers induced by lattice distortion can be considered as the most specific feature in the physics of CPs, an aspect which, in the context of organic conductors, is reminiscent of superconductivity.

Even if superconductivity is not obtained in CPs, it should be noted that the charge pairing is efficient even at room temperature.

Finally, we can stress that the very nature of the conducting state, particularly for highly conducting compounds, such as $n\text{-(CH)}_x$, is still an open question. The achievement of conductivity close to that of copper at room temperature shows that charge mobility about two orders of magnitude larger than in organic crystals can be obtained, together with a high charge carrier concentration. Clearly, in such cases it is not inappropriate to speak of CPs in terms of synthetic "metals," although the temperature dependence of conductivity is not really metallic in almost all materials synthesized so far. Preparing materials in which disorder would play a negligible role is a considerable task, but considering the remarkable progress in synthesis achieved over the last 15 years, it does not seem out of the reach of chemists.

REFERENCES

1. H. Shirakawa, E. J. Louis, A. G. MacDiarmid, C. K. Chiang, and A. J. Heeger, *Chem. Commun.*, 578 (1977); C. K. Chiang, C. R. Fincher, Y. W. Park, A. J. Heeger, H. Shirakawa, E. J. Louis, S. C. Gau, and A. G. MacDiarmid, *Phys. Rev. Lett.* 39:1098 (1977).
2. L. T. Yu, J. Petit, M. Josefowicz, G. Belorgey, and R. Buvet, *C. R. Acad. Sci.* 262:459 (1966); M. Doriomedoff, F. H. Cristofini, R. De Surville, M. Josefowicz, L. T. Yu, and R. Buvet, *J. Chim. Phys.* 68:1055 (1971).
3. A. G. MacDiarmid, J. C. Chiang, M. Halpern, W. S. Huang, S. L. Mu, N. L. D. Somasiri, W. Wu, and S. I. Yaniger, *Mol. Cryst. Liq. Cryst.* 121:173 (1985).
4. E. M. Genies and C. Tsintavis, *J. Electroanal. Chem.* 195:109 (1985).
5. J. P. Travers, J. Chroboczek, F. Devreux, F. Genoud, M. Nechtschein, A. A. Syed, E. M. Genies, and C. Tsintavis, *Mol. Cryst. Liq. Cryst.* 121:195 (1985).
6. E. M. Genies, A. Boyle, M. Lapkowski, and C. Tsintavis, *Synth. Metals* 36:139 (1990).
7. A. J. Bard and L. R. Faulfner, *Electrochemical Methods: Fundamentals and Applications*, Wiley, New York, 1980.
8. M. Levy (to be published).
9. E. F. Bowden, M. F. Dautratas, and J. F. Evans, *J. Electroanal. Chem.* 219:91 (1987).
10. M. Nechtschein, F. Devreux, F. Genoud, E. Vieil, J. M. Pernault, and E. Genies, *Synth. Metals* 15:59 (1986).
11. M. Kalaji, L. M. Peter, L. M. Abrantes, and J. C. Mesquita, *J. Electroanal. Chem.* 274:289 (1989).
12. J. C. Lacroix, K. K. Kanazawa, and A. Diaz, *J. Electrochem. Soc.* 136:1308 (1989); C. Odin, M. Nechtschein, and P. Hapiot, *Synth. Metals* 47:329 (1992).

13. J. Heinze, M. Storzbach, and J. Mortensen, *Ber. Bunsenges. Phys. Chem.* 91:960 (1987); J. Heinze, R. Bilger, and K. Meerholz, *Ber. Bunsenges. Phys. Chem.* 92:1266 (1988).
14. S. W. Feldberg and I. Rubinstein, *J. Electroanal. Chem.* 240:1 (1988); T. C. Chung, A. J. Heeger, and F. Wudl, *Phys. Rev. B* 30:702 (1984).
15. B. Villeret and M. Nechtschein, *Phys. Rev. Lett.* 63:1285 (1989); C. Barbero, R. Kotz, M. Kalaji, L. Nyholm, and L. M. Peter, *Synth. Metals* 55:1545 (1993).
16. C. Odin and M. Nechtschein, *Phys. Rev. Lett.* 67:1114 (1991).
17. J. H. Kaufman, K. K. Kanazawa, and G. B. Street, *Phys. Rev. Lett.* 53:2461 (1984); C. K. Baker, and J. R. Reynolds, *J. Electroanal. Chem.* 251:307 (1988); C. Frubose and K. Doblhofer, *Synth. Metals* 55:1329 (1993); R. Bilger and J. Heinze, *Synth. Metals* 55:1424 (1993).
18. F. Decker, R. T. Neuenschwander, C. L. Cesar, and A. F. S. Penna, *J. Electroanal. Chem.* 228:481 (1987); A. Merle, E. Maurin, and J. P. Maurand, *J. Chem. Phys.* 86:173 (1989); T. Matencio and E. Vieil, *Synth. Metals* 44:349 (1991); T. F. Otero and Angulo, *Synth. Metals* 55:1430 (1993).
19. P. Lang, F. Chao, M. Costa, E. Lhéritier, and F. Garnier, *Ber. Bunsenges. Phys. Chem.* 92:1528 (1988); F. Chao, M. Costa, E. Museix, E. Levart, and L. M. Abrantes, *J. Chim. Phys.* 89:1009 (1992).
20. T. C. Chung, J. H. Kaufman, A. J. Heeger, and F. Wudl, *Phys. Rev. B* 30:702 (1983); E. M. Genies, G. Bidan, and A. Diaz, *J. Electroanal. Chem.* 149:101 (1983); G. Harbeke, E. Meyer, W. Kobel, M. Egli, H. Kiess, and E. Tassatti, *Solid State Commun.* 55:419 (1985); S. M. Yang and T. S. Lin, *Synth. Metals* 29:E227 (1989); E. M. Genies and Lapkowski, *Synth. Metals*, 21:117 (1987).
21. I. R. H. Kuzmany, N. S. Sariciftci, H. Neugebauer, and A. Neckel, *Phys. Rev. Lett.*
22. F. Moraes, J. Chen, T.-C. Chung, and A. Heeger, *Synth. Metals* 11:271 (1985); F. Genoud, M. Guglielmi, M. Nechtschein, E. Genies, and M. Salmon, *Phys. Rev. Lett.* 55:118 (1985); S. H. Glarum and J. H. Marshall, *J. Phys. Chem.* 90:6076 (1986); A. El-Khodary and P. Bernier, *J. Chem. Phys.* 85:2243 (1986).
23. E. W. Paul, A. J. Ricco, and M. S. Wrighton, *J. Phys. Chem.* 89:1441 (1985); B. J. Feldman, P. Burgmayer, and R. W. Murray, *J. Am. Chem. Soc.* 107:872 (1985); G. Schiavon, S. Sitran, and G. Zotti, *Synth. Metals* 32:209 (1989); L. Olmédo, I. Chanteloube, A. Germain, M. Petit, and E. M. Genies, *Synth. Metals* 28:C165 (1989); J. Kruszka, M. Nechtschein, and C. Santier, *Rev. Sci. Instrum.*, 695 (1991).
24. J. Tanguy, M. Slama, M. Hoclet, and J. L. Baudouin, *Synth. Metals* 28:C145 (1989).
25. P. W. Anderson, *Phys. Rev.* 109:1492 (1958).
26. S. Kivelson and A. J. Heeger, *Synth. Metals* 22:371 (1988).
27. N. Basescu, K.-X. Liu, D. Moses, A. J. Heeger, H. Naarmann, and N. Theophilou, *Nature* 327:403 (1987).

28. R. Reghu, Y. Cao, D. Moses, and A. J. Heeger, *Phys. Rev. B* 47:1758 (1993).
29. L. Zuppiroli, *Le Fil Moléculaire*, Rapport CEA-R-5543, Saclay, France, 1990.
30. R. Landauer, *Phil. Mag.* 21:863 (1970).
31. P. Phillips and H. Wu, *Science* 252:1805 (1991).
32. J. L. Brédas, B. Thémans, J. G. Fripiat, and J. M. André, *Phys. Rev. B* 29:6761 (1984).
33. J. L. Brédas and R. Silbey, eds., *Conjugated Polymers*, Kluwer, Dordrecht, The Netherlands, 1991, p. 49.
34. L. Pietronero, *Synth. Metals* 8:285 (1983).
35. H. Naarmann and N. Theodorou, *Synth. Metals* 22:1 (1987).
36. H. Botteger and V. V. Bryksin, *Hopping Conduction in Solids*, Akademie-Verlag, Berlin, 1985.
37. N. F. Mott and E. A. Davis, *Electronic Processes in Noncrystalline Solids*, Clarendon Press, Oxford, 1979.
38. A. Miller and S. Abrahams, *Phys. Rev.* 120:745 (1960).
39. A. J. Epstein, R. W. Bigelow, H. Rommelmann, H. W. Gibson, R. J. Weagley, and A. Feldum, *Mol. Cryst. Liq. Cryst.* 117:147 (1985).
40. S. Yueqiang, K. Carneiro, C. Jacobsen, Q. Renyuan, and Q. Jinjin, *Synth. Metals* 18:77 (1987).
41. S. Summerfield and P. N. Butner, *J. Phys. C Solid State Phys.* 15:7003 (1982); J. A. Chroboczek and S. Summerfield, *J. Phys. (Paris) C3* 44:517 (1983).
42. P. Sheng, B. Abeles, and Y. Arie, *Phys. Rev. Lett.* 31:44 (1973).
43. P. Sheng and J. Klafter, *Phys. Rev. B* 27:2583 (1983).
44. F. Zuo, M. Angelopoulos, A. G. MacDiarmid, and A. J. Epstein, *Phys. Rev. B* 36:3475 (1987).
45. A. J. Epstein, J. M. Ginder, R. W. Bigelow, F. Zuo, H. S. Woo, D. B. Tanner, A. F. Richter, W. S. Huang, and A. G. MacDiarmid, *Synth. Metals* 18:303 (1987).
46. Q. Li, L. Cruz, and P. Phillips, *Phys. Rev. B* 47:1840 (1993).
47. J. C. Dyre, *J. Appl. Phys.* 64:2456 (1988).
48. F. Devreux and H. Lecavellier, *Phys. Rev. Lett.* 56:2585 (1987).
49. E. M. Conwell, *IEEE Trans. Electr. Insul.* EI-22:591 (1987).
50. S. Kivelson, *Phys. Rev. B* 25:3797 (1982).
51. A. J. Epstein, H. Rommelmann, R. Bigelow, H. W. Gibson, D. M. Hoffman, and D. B. Tanner, *Phys. Rev. Lett.* 50:1866 (1983).
52. L. W. Shacklette and J. E. Toth, *Phys. Rev. B* 32:5892 (1985).
53. W. Pukacki, R. Zuzok, S. Roth, and W. Göpel, in *Electronic Properties of Polymers*, Springer Series in Solid-State Science, Vol. 107 (H. Kuzmany, M. Mehring, and S. Roth, eds.), Springer-Verlag, Berlin, 1991, p. 106.
54. Th. Schimmel, D. Glasser, M. Schwoerer, and H. Naarmann, in *Conjugated Polymers* (J. L. Brédas and R. Silbey, eds.), Kluwer, Dordrecht, The Netherlands, 1991, p. 49.
55. P. Sheng, *Phys. Rev. B* 21:2180 (1980).
56. J. B. Torrance, S. Oostra, and A. Nazzal, *Synth. Metals* 19:709 (1987); A. A. Ovchinnikov and V. N. Specktor, *Synth. Metals* 27:B615 (1988); Y.

- Cao, P. Wang, Z. Hu, S. Li, and L. Zhang, *Synth. Metals* 27:B625 (1988); D. A. Kaisaki, W. Chang, and D. A. Dougherty, *J. Am. Chem. Soc.* 113:2764 (1991).
57. S. Galaj, A. Le Méhauté, et al. *Nature* (1993) (submitted).
 58. W. P. Su, J. R. Schrieffer, and A. J. Heeger, *Phys. Rev. Lett.* 42:1698 (1979); *Phys. Rev. B* 22:2099 (1980).
 59. M. J. Rice, *Phys. Lett.* 71A:152 (1979).
 60. A. J. Heeger, S. Kivelson, J. R. Schrieffer, and W. P. Su, *Rev. Mod. Phys.* 60:781 (1988).
 61. J. A. Pople and S. H. Walmsley, *Mol. Phys.* 5:15 (1962).
 62. B. R. Weinberger, E. Ehrenfreund, A. J. Heeger, and A. G. MacDiarmid, *J. Chem. Phys.* 72:4749 (1980).
 63. A. El-Khodari and P. Bernier, *J. Chem. Phys.* 85:2243 (1986).
 64. S. A. Brazovskii and N. Kirova, *JETP Lett.* 33:4 (1981).
 65. H. Takayama, Y. R. Lin-Liu, and K. Maki, *Phys. Rev. B.* 21:2388 (1980).
 66. S. Kuroda, H. Bando, and H. Shirakawa, *Solid State Commun.* 52:893 (1984); S. Kuroda and H. Shirakawa, *Synth. Metals* 17:423 (1987).
 67. H. Thomann and L. R. Dalton, in *Handbook of Conducting Polymers*, Vol. 2 (T. J. Skotheim, ed.), Marcel Dekker, New York, 1986, p. 1157, and references therein.
 68. M. Mehring, A. Grupp, P. Höfer, and H. Käss, *Synth. Metals* 28:D399 (1989).
 69. M. Nechtschein, F. Devreux, R. L. Greene, T. C. Clark, and G. B. Street, *Phys. Rev. Lett.* 44:356 (1980).
 70. K. Holczer, J. P. Boucher, F. Devreux, and M. Nechtschein, *Phys. Rev. B* 23:1051 (1981); M. Nechtschein, F. Devreux, F. Genoud, M. Guglielmi, and K. Holczer, *Phys. Rev. B* 27:61 (1983).
 71. K. Mizoguchi, K. Kume, and H. Shirakawa, *Solid State Commun.* 50:213 (1984).
 72. W. G. Clark, K. Glover, G. Mozurkewich, S. Etemad, and M. Maxfield, *Mol. Cryst. Liq. Cryst.* 117A:447 (1985).
 73. Y. T. Tomkiewicz, T. D. Schultz, H. B. Brown, A. R. Taranko, T. C. Clarke, and G. B. Street, *Phys. Rev. B* 24:4348 (1981).
 74. F. Moraes, J. Chen, T.-C. Chung, and A. Heeger, *Synth. Metals* 11:271 (1985); J. Chen, T. C. Chung, F. Moraes, and A. J. Heeger, *Solid State Commun.* 53:757 (1985).
 75. J. Chen and A. J. Heeger, *Phys. Rev. B* 33:1990 (1986).
 76. D. K. Campbell, T. A. Degrand, and S. Mazundar, *Phys. Rev. Lett.* 52:1717 (1984); D. Baeriswyl and K. Maki, *Phys. Rev. B* 31:6633 (1985); D. Baeriswyl, *Synth. Metals* 55:4213 (1993).
 77. J. L. Brédas, B. Thomans, J. G. Fripiat, J. M. André, and R. R. Chance, *Phys. Rev. B* 29:6761 (1984).
 78. J. C. Scott, P. Pfluger, M. T. Krounbi, and G. B. Street, *Phys. Rev. B* 28:2140 (1983).
 79. F. Genoud, M. Guglielmi, M. Nechtschein, E. Genies, and M. Salmon, *Phys. Rev. Lett.* 55:118 (1985).

80. Y. F. Nicolau, S. Davied, F. Genoud, M. Nechtschein, and J. P. Travers, *Synth. Metals* 41:1491 (1991).
81. F. Devreux, F. Genoud, M. Nechtschein, and B. Villeret, in *Electronic Properties of Conducting Polymers*, Springer Series in Solid-State Science, Vol. 76 (H. Kuzmany, ed.), Springer-Verlag, Berlin, 1987, p. 270.
82. F. Devreux, *Europhys. Lett.* 1:233 (1986).
83. S. Ikehata et al., *Phys. Rev. Lett.* 45:1123 (1980).
84. J. P. Travers, J. Chroboczek, F. Devreux, F. Genoud, M. Nechtschein, A. A. Syed, and C. Tsintavis, *Mol. Cryst. Liq. Cryst.* 121:195 (1985); F. Zuo, M. Angelopoulos, A. G. MacDiarmid, and A. Epstein, *Phys. Rev. B* 36:3475 (1987).
85. A. J. Epstein et al., *Synth. Metals* 21:63 (1987).
86. M. Nechtschein, F. Genoud, C. Ménardo, K. Mizoguchi, J. P. Travers, and B. Villeret, *Synth. Metals* 29E:211 (1989).
87. K. Mizoguchi, M. Nechtschein, J. P. Travers, and C. Menardo, *Phys. Rev. Lett.* 63:66 (1989).
88. K. Mizoguchi, M. Nechtschein, and J. P. Travers, *Synth. Metals* 41:113 (1991).
89. S. Stafstrom, J. L. Brédas, A. J. Epstein, H. S. Woo, D. B. Tanner, W. S. Huang, and A. G. MacDiarmid, *Phys. Rev. Lett.* 59:1464 (1987).
90. M. E. Jozefowicz, R. Laversanne, H. H. S. Javadi, A. Epstein, J. P. Pouget, X. Tang, and A. G. MacDiarmid, *Phys. Rev. B* 39:12958 (1989).
91. F. Genoud, M. Nechtschein, and C. Santier, *Synth. Metals* 55:642 (1993).
92. D. Baeriswyl, in *Electronic Properties of Conducting Polymers*, Springer Series in Solid-State Physics, Vol. 91 (H. Kuzmany, ed.), Springer-Verlag, Berlin, 1989, p. 54.
93. P. Le Guennec, M. Nechtschein, and J.-P. Travers, *Synth. Metals* 55:630 (1993).
94. M. N. Bussac and L. Zuppiroli, *Phys. Rev. B* 47:5493 (1993).
95. Y. Tomkiewicz, T. D. Schulz, H. B. Brown, A. R. Taranko, T. C. Clarke, and G. B. Street, *Phys. Rev. Lett.* 43:1532 (1979); S. Roth, K. Ehinger, K. Menke, M. Peo, and R. J. Schweitzer, *J. Phys. Colloq. Paris C3*, 44:69 (1983).
96. G. König and G. Stollhoff, *Phys. Rev. Lett.* 65:1239 (1990).
97. D. Baeriswyl and K. Maki, *Synth. Metals* 28:D509 (1989).
98. C. K. Chung, J. H. Kaufman, A. J. Heeger, and F. Wudl, *Phys. Rev. B* 30:702 (1984).

This Page Intentionally Left Blank

Related Topics I: Charge-Transfer Complexes in Biological Systems

Vivian C. Flores, Hendrik Keyzer, Cissy Varkey-Johnson, and Karen Leslie Young

California State University, Los Angeles, Los Angeles, California

I. INTRODUCTION

A. Scope

Regular and periodic organization of molecules is essential for the living state, and fundamental to its processes are structured instabilities, which are reflected in the solid state by, for example, charge-transfer complexes. Many *in vivo* phenomena are difficult to explain by classical chemical processes but appear to fit solid-state physical processes in cells. Solid-state events involving charge-transfer complexation are evident in inanimate aggregations and may well be an essential characteristic of life embedded in electromagnetic phenomena. Charge and electron transfer processes are replete in biological systems such as membranes, mitochondria, vesicles, and a host of biological molecules.

Our apologia will embrace as much as possible charge-transfer interaction of biological molecules with other biological molecules *in vitro*. The exposition necessitates largely a physical-chemical approach imposed by the very nature of charge transfer. For an early review of charge transfer in biological systems, the reader is referred to the lucid and seminal work by Michael A. Slifkin [1] to whom the writers are much indebted, and to some general texts on charge transfer [2]. This chapter is intended to introduce to the reader some concepts of charge transfer in complexes,

and some of the principal forms of methodology in the field, followed by a brief survey of examples.

B. Definition of Charge-Transfer Complexes

Mulliken [3] introduced the term *charge-transfer complex* (CTC) for a new type of complex with distinctive features to explain the behavior of certain molecules or classes of molecules that did not conform to classical patterns of ionic, covalent, coordination, or hydrogen bonding. These mixtures, as solids or in solution, formed colors or exhibited other spectral absorptions or emissions absent from the individual components. While such mixtures largely retained the properties of the components, some changes were apparent (e.g., in solubility, diamagnetic, and paramagnetic susceptibility). Other differences have also been found with electrochemical techniques. More strikingly, some complexes were isolated as crystals of regular stoichiometry and structure [2]. One important feature of most charge-transfer complexes is that the original components can readily be recovered in unreacted form. Another aspect is the temperature dependence of charge transfer in a complex; the association constant of the complex decreases with increasing temperature. The effect is due to the thermal motion disorienting the partners of the complex. The most commonly measured interplanar distance between components of a complex is about 3.25 Å [4].

C. Electron and Proton Complexes

Charge transfer may not be confined to electron donation; transfer can also involve protons in certain cases to yield proton transfer complexes [5]. This often occurs in surface reactions, say, at electrodes, and a fortiori in nonaqueous media, because the proton affinity of water is extremely high (i.e., about 8.9 eV) [6]. Hydroxydinitropyridines, for instance, may be electron acceptors and/or proton donors with respect, say, to naphthalene derivatives [7].

Dumas and Gomel [8], urged by theoretical and experimental considerations, claim that little energetic difference exists between bonds conventionally classed as purely electrostatic, Debye, Keesom, London dispersion, electron and proton transfer, and hydrogen bonds. They claim [8] the hydrogen bond to be merely a special case of charge transfer, a view to which Slifkin [1] subscribes, but we will avoid this to limit our topic.

1. Electron Donor–Acceptor (EDA) Complexes

Undoubtedly, the most successful theoretical explanation of charge-transfer phenomena was due to Mulliken [3,9]. He showed that charge-transfer

interactions within a molecular complex consisting of an electron donor D and an electron acceptor A involved a resonance with a transfer of charge from D to A:



In the limit, complete charge transfer leads to an ionic bond in a simple ion–radical pair interaction. In the solid state, the simple pair interaction may not be limited to two molecules but may extend further in a crystal. The ground state is thus partly ionic and may be described by a wavefunction Ψ_{DA} :

$$\Psi_{DA}(D,A) = a\Psi_0(D,A) + b\Psi_1(D^+A^-) \quad (2)$$

where Ψ_0 represents a nonbonding, and Ψ_1 a charge-transfer wavefunction, involving the transfer of an electron from D to A. If the interaction is weak, $a \gg b$, a tends to 1 and b tends to 0. The ground state is then essentially nonbonding. On the other hand, if $b \gg a$, the ground state will be essentially ionic. For the excited state we can write a wavefunction Ψ_E given by

$$\Psi_E(D,A) = a^*\Psi_1(D^+A^-) - b^*\Psi_0(D,A) \quad (3)$$

This is responsible for the characteristic color of the complex. It is seen that for weakly interacting complexes, that is, for $a^* \gg b^*$, the excited state will be essentially ionic. The ionic character in either case arises from at least a partial transfer of electrons from the donor D to acceptor A; partial in this context means that on the average, the electron will spend more time in the vicinity of A than in the proximity of D. For high stability of the complex, charge transfer must be incomplete [10].

Thus we have to distinguish between strongly interacting systems in which the ground state already has at least partially ionic character, and weakly interacting complexes in which only the excited state is ionized. It appears that those charge-transfer complexes which are strongly interacting, that is, those in which the ground state is already ionic, have very high conductivities [11], while the weaker interactions lead to room-temperature conductivities which are much lower, but higher than those encountered in ordinary molecular crystals.

All charge-transfer complexes show a markedly increased conductivity compared with that of either component. The resistivity minimum is most pronounced in the strongly interacting complexes, as exemplified by the *p*-chloranil/*p*-phenylenediamine complex: complexing lowers the resistivity by about 10^8 relative to that of either component [12].

The increase in conductivity is usually understood [12] to be caused by changes in both quantities appearing on the right side of Eq. (4), since a

charge carrier encounters ion–dipole forces as well as the ion-induced dipole forces that it would experience in an ordinary molecular crystal. It is assumed that for conduction to take place, it is first necessary to ionize a molecule and then to remove the electron until its coulombic energy has become negligibly small compared to kT , the thermal energy:

$$\sigma = \sigma_0(T) \exp\left(\frac{-E_a}{kT}\right) \quad (4)$$

where σ is the electrical conductivity and $\sigma_0(T)$ represents any function of temperature, T , subject to certain conditions, such as uniform convergence; E_a is the activation energy, and k has the usual meaning. The experimental value of E may really be the first term in a series and may be temperature independent only to a first approximation. In a molecular solid, this energy E_0 is given by

$$E_0 = I_P - E_A - \frac{e^2}{\epsilon r - I_X - P} \quad (5)$$

where I_P is the ionization potential, E_A the electron affinity, and the next term represents the coulombic interaction: e is the electronic charge, ϵ the permittivity, and r the intercomponent distance. I_X represents the resonance energy and P the polarization energy. For a charge-transfer complex, this expression must be modified to include the charge-transfer interaction, which will affect primarily I_X and P . Thus an increased polarizability will increase P and therefore reduce E_0 . The reasoning is supported by the experiments of Uchida and Akamatu [11] on violanthrene–iodine complexes.

Basically, electron donors and acceptors may be classed into three groups: (1) π donors and π acceptors, so that charge transfer is delocalized over the π system of the molecule; (2) σ donors and σ acceptors, in which the electron originates from or enters a σ orbital; and (3) n donors, in which the charge comes from an electron more or less localized on the donor (e.g., an N atom). Thus six donor–acceptor combinations, not necessarily mutually exclusive, are possible as follows (donor is identified first): π – π , π – σ , σ – π , σ – σ , n – π , and n – σ .

Although this classification of electron donors and acceptors often proves useful, these terms are only relative [14], under appropriate conditions, such as when the highest occupied molecular orbital is located between the orbitals of the potential donor and acceptor. Any molecule can exhibit both electron-donor and electron-acceptor properties [15]. Thus dimethylalloxazine, for example, acts as a donor to the strong acceptor TCNE (tetracyanoethylene) and as an acceptor to the strong donor pyrene [16]. This dual character applies particularly to π -bonded molecules and is es-

pecially true for large biological molecules [17] such as the purines [18] or cyclophanes [19]. Even the classic electron acceptor, oxygen, has been shown [20] capable of donating an electron to the magnesium phthalocyanine molecule, which has a high electron affinity of 14 eV, thus matching the ionization potential of O₂ (i.e., 13 eV). The resulting CTC is of biological interest. The donor, then having donated an electron, may act as an acceptor, and vice versa; reverse charge-transfer complexes are known [17] in which, for example, the π -electron system of an aromatic compound acts as an electron acceptor rather than as a donor, such as the ferrocenes [21] or benzoporphyrazines [22].

Complexes may also sometimes be classified into the following groups: autocomplexes (self- or intramolecular), in which different regions of one molecule interact; ternary complexes, which involve guest molecules in a host matrix, where the host forms the EDA complex: α -cyclodextrin forms such complexes with mononuclear aromatic hosts in solution [23]; surface complexes, such as those between cytochrome *b* and cytochrome *c*, as well as substrate⁺ porphyrin⁻ complexes [24]; and micellar and colloidal complexes. The latter are involved in many biological systems, such as with acetylcholine [25], melanin [26], and phenothiazine tranquilizers [27]. A micellar structure contributes considerably to the free energy of the system, the gain of which can be as high as 0.8 eV [14]. The energy required for the photoionization of micellar phenothiazines is much lower than that for the gas-phase reaction [28]. Similar effects have been noted in exciplexes of micellar adducts [29]. Another class of complexes involves charge transfer between localized regions of positive and negative charges in adjacent molecules but is not attributed to classical electrostatic attraction; some movement of charge occurs from one region to another, while motion in the molecular entities is restricted. Slifkin [1] points out that such an event is usually termed charge complementarity.

2. Proton Complexes

The field of protonic charge-transfer complexes was introduced by Matsunaga and co-workers [5]. Morokuma [30] cites the close exchange in such adducts between proton and electron transfer; one occurs concurrently with the other, as with proton complexes of some amines. In some cases electron transfer is catalyzed by the presence of a proton and thus enhanced above its thermally controlled rate [31].

Proton transfer could sometimes be nothing more than a case of conventional hydrogen bonding, but in many cases the concurrent transfer of an electron and a proton produces a new type of adduct, and complex formation may indeed be dramatic [32]. Arnett and Mitchell [32] point out that no correlation existed between the heats of protonation and of hy-

drogen bonding. The average residence time of the proton at a temporary equilibrium site is about one vibrational period of the —OH group and of the average lifetime of H_3O^+ (i.e., about 2.5×10^{-13} s); since the dielectric relaxation time of water is about 10^{-11} s, dielectric relaxation and frictional processes are not involved in proton transfer [33]. However, for aliphatic amines, a considerable increase in viscosity is reported [34].

In organic solvents, proton transfer involves [35] an AH—B complex formation. The important solvent dimethylsulfoxide (DMSO) is an efficient proton donor [36]. Ultrasonic experiments indicate [37] that proton transfer plays a major role in nucleotides in aqueous solution, even at pH 5.

The 1:1 and 1:2 complex formation of oxalic acid and α -amino acids proceeds via a proton transfer from the carboxyl group of the oxalic acid to the carboxyl ion of the amino acid. A similar interaction in the 1:1 complex between malonic acid and glycine has been noted [38].

3. Activated Charge-Transfer Complexes

Activated charge-transfer complexes involve an excited state termed an excimer when two like molecules interact and an exciplex when two unlike molecules interact. The activation energy usually arises from irradiation, or sometimes by nonradiative stimuli (i.e., electrochemical means).

If an electron in a substance is raised not from the Fermi level but from a higher excited state, the effective ionization energy is correspondingly lowered; similarly, if the electron is shifted not to the bottom of the conduction band but to an excitation level within the band gap, the effective electron affinity is raised. Both effects may occur simultaneously and increase the probability of complexation in an aggregate.

In solution, exciplex formation may be written as

$$\Psi_E = a\Psi_{(D,A^*)} - b\Psi_{(D^+A^-)} \quad (6)$$

where Ψ is a wavefunction, the coefficient $b \gg a$, and A^* refers to an excited acceptor. These energies follow a volume integral relationship of the form

$$W_0 = \int_{V(AD)} H(\Psi_{(AD)}) dV \quad (7)$$

where H is a Hamiltonian operator. The wavefunctions are all real, hence require no multiplication with the complex conjugate.

Tavares [39] includes a polarization term P in the binding energy E_B of an exciplex consisting of D with an ionization potential I_P and an acceptor A with an electron affinity E_A :

$$E_B = I_P - E_A - P \quad (8)$$

An energy profile is given by Christov [40] for the formation of an exciplex similar to that shown in Fig. 1. The exciplex is confined within

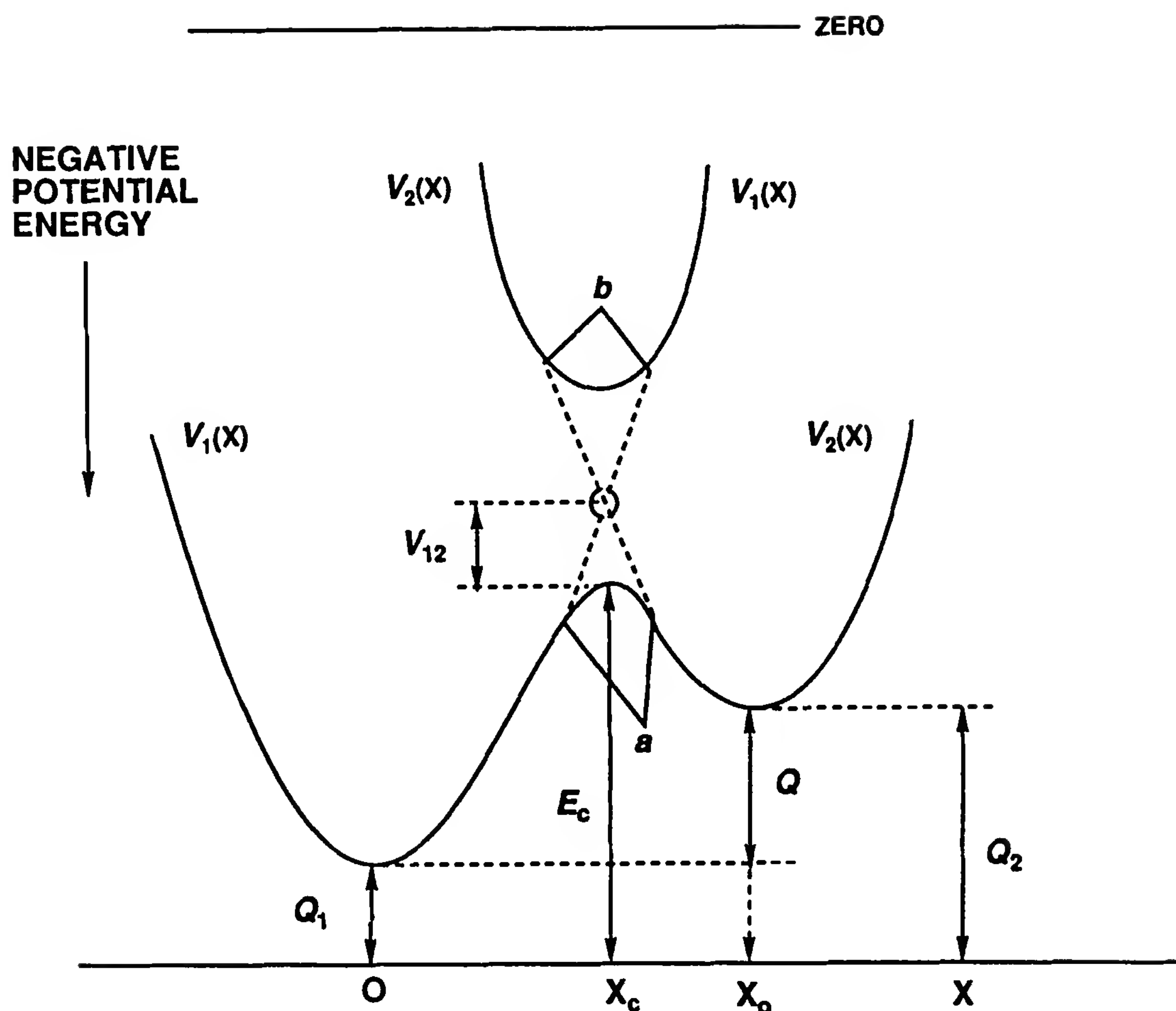


Figure 1 Energy profile for exciplex formation. (Adapted from Ref. 240.)

the potential energy well at b , which represents the adiabatic curve for the excited electronic state formed by the overlap of the energetic interaction of the donor and acceptor molecules, respectively, indicated by the parabolic adiabatic curves $V_1(x)$ and $V_2(x)$. The potential well is stabilized by the resonance energy V_{12} gained by the overlap of $V_1(x)$ and $V_2(x)$. A quantum-mechanical no-crossing rule stipulates that an energy barrier exists at the electronic ground state represented by the parabolic, and necessarily asymmetric, curve a , the top of which represents the classical activation energy E_c at the crossover point $x = x_c$. It is seen that E_c is usually larger than the heat of reaction Q at 0 K, which equals $Q_2 - Q_1$; the process of an electron being transferred over the top of the barrier equivalent to a classical chemical reaction is strongly temperature dependent, obeying an *Arrhenius*-like relationship. For a more detailed treatment of exciplex energy profiles the reader should consult other sources [14,39,40].

Many photochemical reactions, especially those involving dyes, occur via an exciplex, in which the solvent provides a ligand between the two

components of an excimer. Exciplexes, including excimers, may migrate, either by thermally activated hopping or via a dipole–dipole interaction leading to contraction, by means of the shift or the rotation of a neighboring unexcited molecule; this then may result in local spacing equal to the exciplex–exciplex equilibrium distance. The system may then be considered as a type of soliton because it involves a localized elastic deformation coupled to a transfer of electrical energy.

The biological significance of exciplexes involves their ability to transfer energy from one location to another (i.e., from an energy donor to an energy acceptor). Because of its large dipole moment the exciplex may move vectorially in an external, inhomogeneous electric field as provided by biomembranes. Many biomolecules exhibit low-lying states of very small energy [1,41]. Melanin forms exciplexes with antibiotics such as tetracycline, which may lead to the side effect of iatrogenically mediated sunburn [41,42].

The exciplex may decay, after the supply of excitation energy has ceased, by a variety of radiative and/or nonradiative processes. An electron may be transferred from the donor to the acceptor within an external energy supplied by a process called tunneling (i.e., through the barrier a in Fig. 1). However, for this the barrier must be narrow. If additional energy is supplied externally (e.g., by illumination) an electron is raised to a higher energy level within its potential well, $V_1(x)$ (Fig. 1), but below E_C , where the barrier is narrower and tunneling may become possible. Tunneling is virtually independent of temperature. At very low temperatures, any transfer can occur only by tunneling. As the temperature is raised, activated (over the top) transfer becomes more and more probable until a temperature is reached where the tunneling and the activated transfer probabilities are equal: namely, the *Christov characteristic temperature*, T_k [40]. For a typical parabolic, asymmetric barrier 1 eV high and 20 Å wide, T_k is about 1400 K. Thus, in vitro, all transfer must take place by tunneling. However, in vivo, say, on a biological membrane, there are other sources of energy readily available; 1400 K represents about 0.12 eV. The membrane potentials are of the order of 60 mV, so that on a membrane the formation of exciplexes is quite a probable event.

An exciplex may degrade in the continued presence of the exciting radiation. There are two routes to exciplex formation: excitation of either donor or acceptor followed by complexation, or excitation of the preformed complex. The excitation energies are often quite low, even only a few kT , but must be supplied in a one-quantum process involving a virtual photon. Thus excitation may be produced by nonradiative means, especially electrochemically. Exciplexes are rather weak adducts. The electronic transi-

tion involved requires the shift of an electron into a more delocalized orbital, usually an $n-\pi^*$ transition; this has a low probability—hence the adducts are weak—but relatively long lifetimes as would be required for biological reactions. The $n-\pi^*$ state is very reactive, the lifetime depends on the deactivation reaction most probable in a given case; thus it may range from 10 ns to, frequently, microseconds and longer. Its dynamics are greatly affected by the environment (e.g., solvation effects). It may dissociate, giving rise to free carriers, the additional (dissociation) energy being derived, for example, from a local field. This is likely to be of biological significance in view of the strong local electric fields that exist on and in membranes.

Intramolecular proton transfer in electronically excited transfer in, say, salicylic acid ester and other aromatic compounds leads to deexcitation of the energized electron [43–45]. In photoreduction processes, electron transfer often precedes proton transfer [46]; the stability of the protonic bond is at least partially due to an $n-\sigma^*$ interaction [47]. The strength of the protonic interaction appears to be proportional to the ionization potential of the donor and is sensitive to solvent polarity [48]. These effects have hardly been touched on in biologically important transitions and represent an important new field of research.

4. Dipole Moments of Charge-Transfer Complexes

The formation of a CTC is generally accomplished by an increase in the dipole moment [49,50], although complexes between a polar and a non-polar component result in a reduction of the molecular polarization. Thus measurement of changes in the molecular polarization following complexation provides an indication, although by no means an infallible proof, of the formation of CTC. The changes are small differences between comparable quantities if both donor and acceptor are polar and are also small if both are apolar [51]. It is important that the changes in the molecular dipole moment be shown to be temperature reversible in order to establish a charge-transfer interaction. However, being nonadditive, the polarization indicates, although it falls short of proving, a charge-transfer interaction: for example, *m*-cresol/pyridine and *m*-cresol/quinoline complexes were initially studied in this way, the interaction then being confirmed by means of conductimetric titrations [52]. For strong complexes the measured permittivity is linearly related to the weight fraction of the dissolved complex using the same solvent [53].

For a discussion of dipole moment changes influenced by irradiation, the reader is referred to work by Gutmann et al. [14]. Suffice it to say that excitation to higher singlet and triplet states is accompanied by intra-

molecular charge transfer and changes in dipole moments, although there is no relationship between the extent of this transfer and the energy of the transitions [54].

5. Thermodynamic Parameters

The dipole moment of the adduct has been related to the enthalpy of formation [55], which is usually of the order of a few kilocalories per mole [56], in contradistinction to the tens of kilocalories per mole involved in conventional chemical reactions. Complex formation usually involves a lowering of the entropy of the system, because of the increased order, although in solution this may be masked by clustering, association, and solvation effects [14].

Thermodynamic parameters have greater utility than equilibrium constants (K_C). The majority of workers use ΔH_d , the enthalpy of dissociation, as the index for complex stability, which can be derived from the variation of K_C with temperature T :

$$\frac{d}{dT}(\ln K_C) = \frac{-\Delta H_d}{RT^2} \quad (9)$$

The standard free energy ΔF_d is also used:

$$\Delta F_d = \Delta H_d - T \Delta S_d \quad (10)$$

where ΔS_d is the entropy change. The entropy change is a particularly useful parameter for determining conformational and solvent interaction changes in large molecules such as proteins [1,14,57–59]. The enthalpy of dissociation is an index of the energy required to break the bond between components of the complex. ΔF_d measures the difference in energy of the free and associated states and includes changes due to conformational and solvation changes also. However, for organic adducts, ΔS_d is usually proportional to ΔH_d , whereas ΔF_d is not.

Iwatsuki et al. [57–59] have related the modification of the free energy for complexes of macromolecular donors with small acceptors with solvation and with intra- and/or intermolecular interactions of donor functional groups which alter such aspects as dipole moment and *Brownian* motion of the donor polymer chain. The free-energy change involved in intramolecular proton transfer of electronically excited molecules changes from 0.13 eV to 0.22 eV [45]. The enthalpy change of hydrogen bonding due to electronic excitation is about 0.0044 eV [60].

6. Summary of Charge-Transfer Complex Main Features

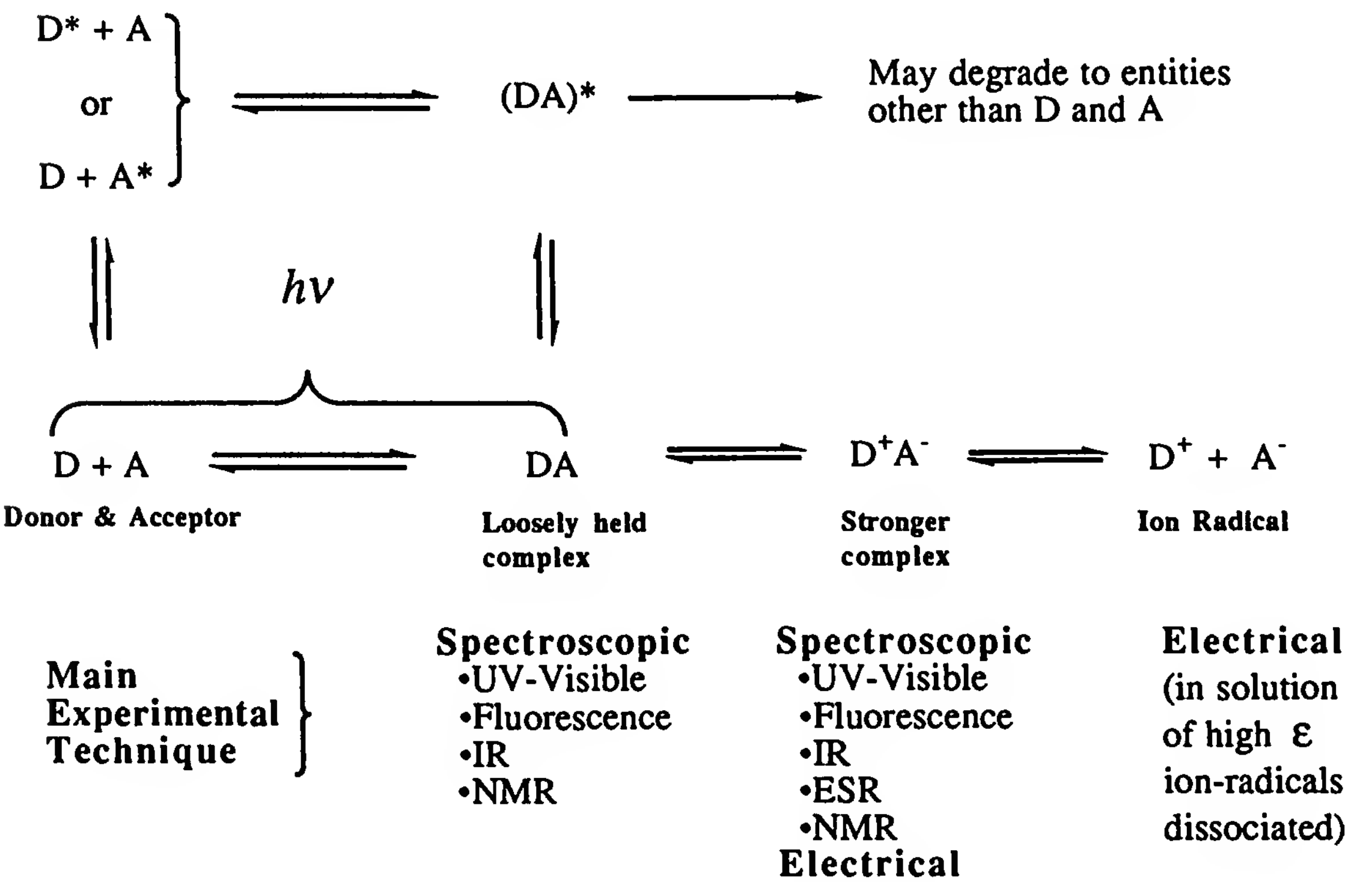
The general features of a stable electron charge-transfer complex follow:

1. **Reversibility:** the components of the complex are usually recoverable.

- 2. The association constant of the complex decreases with increasing temperature.
- 3. The electrical (dark) conductivity of the complex increases compared to those of the individual components.
- 4. The activation energy of the complex is less than that of the individual components.
- 5. Complex formation often leads to increased dipole moments.
- 6. Complex formation lowers the entropy of the system.
- 7. The spectrogram of the complex should differ from the sum of those of the individual components. (Color changes often occur.)
- 8. Complexation usually quenches fluorescence.
- 9. The most common interplanar distance between the individual components in the complex is about 3.25 Å.

II. METHODOLOGY

A considerable variety of methods now exist for following charge-transfer complex formation. These generally rely on comparing properties of the complex with those of the individual components. A brief schematic guide to methodology may be gathered from Fig. 2.



A. Absorption and Emission Spectroscopy

1. Ultraviolet and Visible Measurements

Relatively inexpensive ultraviolet (UV)-visible spectroscopy is one of the most widely used methods for the investigation of charge-transfer complexes, and a description can be found in any number of excellent texts [2]. All EDA complexes produce a specific absorption band, usually broad because the electron transfer is a statistical phenomenon influenced profoundly by the orientation of the donor and acceptor molecules. The new charge-transfer absorption band should diminish in intensity upon heating, and revert again upon cooling. Multiple charge-transfer bands [61] sometimes complicate evaluation of the spectra, as will spectral shifts due to solvatochromism [62] and thermochromism [63]. Triplet emission processes may also produce extra bands [14]. Electronic absorption spectra of EDA complexes may be repeated for different stoichiometric ratios. A plot of absorbance against wavelength will intersect at one or more isosbestic points [64]. This method also applies to ternary and autocomplexes.

The position of the absorption maximum $h\nu_{DA}$ is dependent on the ionization potential I_P of the donor, the electron affinity E_A of the acceptor, and the dissociation energy W of the complex, which depends on the coulombic attraction and the environment [65,66].

$$h\nu_{DA} = I_P + E_A + W \quad (11)$$

For the energetics of complexes of different donors with a common acceptor, the reader is referred to the work by Briegleb and Czekalla [67], and that of Kuroda et al. [68]. Batley and Lyons [69] have established the following relationship for complexes with analogous configurations for a series of acceptors interacting with a common donor:

$$h(\nu_{CT1} - \nu_{CT2}) = E_{A2} - E_{A1} \quad (12)$$

This equation allows approximate determination of the electron affinity of small individual acceptor molecules as well as acceptor groups in macromolecules.

When charge-transfer bonds are obscured by those of the original donors and acceptors, one may find of value a difference method [1] (e.g., *Forster's tandem* method [70]). Four cuvetts of equal path length are used, two containing the charge-transfer complex solutions in series in the indicator beam of a double-beam spectrophotometer, and two cuvetts, one with the unreacted donor and the other with unreacted acceptor solution, also in series in the reference beam. A difference spectrum is thus obtained which, however, needs special care in its interpretation.

Benesi and Hildebrand [71] derived a relationship for EDA complexes in solution as follows:

$$\epsilon_{CT} = \frac{\log(I_0/I)}{d[DA]} \quad (13)$$

where ϵ_{CT} is the extinction coefficient, d the path length, $\log(I_0/I)$ the optical density of the complex, and $[DA]$ the concentration of the complex. Equation (13), for $[D] \gg [A]$, may be modified to include the association constant, K_C :

$$[A] \frac{d}{\log(I_0/I)} = \frac{1}{K_C} \frac{1}{[D]} + \frac{1}{\epsilon_{CT}} \quad (14)$$

A plot for this equation at constant $[A]$ and varying $[D]$ allows $1/K_C$ and $1/\epsilon_{CT}$ to be determined.

Scott [72] utilized a variant of Eq. (13). Carter et al. [73] have derived equations for the association constants of solvated complexes. Caution must be applied to cases where a large amount of donor may affect the behavior of the solvent, which can seriously affect the application of Eq. (13) [74,75].

2. Infrared (IR) Measurements

The (IR) spectra of EDA complexes are often different from those of the superposed individual components. The electronic interaction of an EDA complex changes bond lengths and angles in the molecules affected. However, these changes may be minute because many of the complexes determined by this method are relatively weak. Strongly dative complexes (ionic in the ground state) simply sum the spectra of the components. The advantage of infrared spectroscopy arises from the possibility of identification of structural changes, the charge-transfer site, and possibly new absorption bands involved with particular chemical bonds. For instance, this technique has shown that amino acid zwitterions in the free state are nonionized when complexed [76]. Kagiya et al. [77] have correlated ionization potentials of organic donors complexed with a common acceptor by infrared band shifts. This has definite application to biological systems.

3. Fluorescence Spectroscopy

Many charge-transfer complexes do not fluoresce. Thus, fluorescent probes, either as donor or acceptor, cause fluorescence quenching proportional to the association constant K_C of the complex. Fluorescence quenching may be utilized in the study of small molecules, as well as, particularly, macromolecules, to determine energy migration and transfer [78,79]. The fluorescence yield of the acceptor alone (F_0), and that in the presence of

the donor (F) are related by the *Stern–Volmer* equation [80]:

$$\frac{F_0}{F} = 1 + K_C[D] \quad (15)$$

where $[D]$ is the donor concentration. K_C , the association constant, obtained in this manner is often in good agreement with that of the *Benesi–Hildebrand* equation.

4. Excited Complexes

A new broad, red-shifted emission band is often observed in the fluorescence spectra of organic molecules with increasing concentration [81]. The new band is due to short-lived dimers between an excited molecule and a like unexcited molecule (i.e., excimers). A case can be made for excimer formation which may involve charge transfer, and a good correlation exists for the wavelength of excimer emission bands and the difference between the I_P and E_A values of the molecule [82]. However, it may well be that the binding in excimers involve interaction forces differing from charge transfer. It is more likely that exciplex fluorescence emission is based on charge transfer [39].

B. Magnetic Resonance Spectroscopy

1. Electron Spin Resonance Measurements

There was a time when some workers in the field of electron donor–acceptor (EDA) complexes would accept evidence of charge transfer only when one could observe a spin signal originating from a free radical. Indeed, electron spin resonance (ESR) is the most direct method for determining the degree of uncoupling of an electron in a molecule. The energy of the electron in the $+\frac{1}{2}$ - and $-\frac{1}{2}$ -spin states in a magnetic field H equals $(+/-)\frac{1}{2}(g\beta_0 H)$, where $g\beta_0$ is the inverse gyromagnetic ratio: g is 2.0023 for free spin, and β_0 is the Bohr magneton ($eh/4mc$), in which the symbols have the usual meaning. When the electron spin is coupled to its angular orbital momentum a slightly different g factor is obtained. This feature should be expected in the case of EDA complexes. While the g shift gives one item of information, the area under the absorption peak yields the number of free electrons in the sample, and the half-width of the signal is inversely proportional to the half-life of the uncoupled electron. This technique is fraught with difficulties because in a solution of high-permittivity, microwave radiation is strongly absorbed. Weak complexes yield such poor signals that they are virtually undetectable. Several good texts on this topic are available [83]. Several representative examples in biological systems

are studies involving complexes of amino acids [84], melanin [85], and phenothiazines [86,87].

2. Nuclear Magnetic Resonance Measurements

The continued improvement of high-resolution nuclear magnetic resonance (NMR) instrumentation makes this tool more and more desirable for the study of EDA complexes. To identify a CTC one observes chemical shifts associated with a disturbance of the local chemical environment of a proton, or appropriate NMR-sensitive probe, in the EDA complex compared to the individual components. NMR data so acquired may be utilized to provide K_C from Benesi–Hildebrand plots. One may now also obtain information on transfer sites and molecular conformation, as well as thermodynamic properties of components of EDA complexes in a variety of solvents. V. Gutmann [88] relates so-called donicities (donor strengths) of molecules in EDA complexes to chemical shifts in different solvents. Donicity of a molecule is defined as the negative value of the total enthalpy change measured in a complex with antimony pentachloride. Unfortunately, donicity cannot be equated with ionization potential. Tables of values of donicities for a considerable number of molecules are available [14,88]. Acceptance numbers are determined analogously; these are also not related directly to electron affinities.

The strength of the NMR method is made evident, for example, in the study of the behavior of phenothiazine derivatives and their EDA complexes in solution [89]. First, the solution properties of, for example, the tranquilizer chlorpromazine hydrochloride and base in a variety of solvents were established leading to the unambiguous notion of self-association and micellization, with the HCl form being the more stable. Second, the conformation of these compounds in self-adducts were discovered to be virtually unchanged as a function of temperature in the range 20 to 60°C. Iodine stabilized both molecular forms. Third, the complexation sites in these molecules were clearly established, as well as the stoichiometry of the complexes. The stability of these CTC can be followed with time.

In low-molecular-weight aromatic charge-transfer complexes the chemical shifts of aromatic protons decrease linearly with the degree of complexation. A small effect suggests that such chemical shifts are determined on the whole by ring currents, due to the layering of complexing groups and not by charge transfer [90]. In this case the proton chemical shifts for both donor and acceptor are not only numerically alike but also have the same sign: namely, an upfield shift compared to those of the unreacted components. One would expect that significant charge transfer would cause a downfield shift of the proton absorptions of the donor in the complex.

However, excimerization and exciplexation, in these cases, cannot be excluded.

C. Electrical Methods

1. Conductivity

The electrical properties of organic EDA complexes are determined by the orbitals involved in the electron transfer. Accordingly, Matsunaga [91] and Seanor [92] have classed them as weak or strong complexes. In the solid state the conductivity of strong complexes, compared to those of the individual components, is relatively high, generally decreasing with increasing temperature typical of organic semiconductors [14,93]. Their activation energies, E_a , can be estimated from conductivity measurements as a function of temperature, T , as follows:

$$\sigma_T = \sigma_0 \exp\left(\frac{-E_a}{kT}\right) \quad (16)$$

where σ_0 is the conductivity at absolute zero and k is Boltzmann's constant [cf. Eq. (4)]. Over relatively large ranges of temperature more than one activation energy region may surface, similar to doped semiconductors [14]. The reader should appreciate that the activation energy depends on the presence of n -type carriers (usually electrons), and at the same time p -type carriers (positive holes), and Eq. (16) should be modified to read $-E_a/2kT$ [14].

The number of charge carriers (n) and their mobilities (μ) are related to conductivity by the relationship

$$\sigma = e \sum_i n_i \mu_i \quad (17)$$

The increase of electrical conductivity attendant upon complexation is thought to be due to the increase of carrier mobility as electroactive groups rearrange [14,93–95]. Generation of charge carriers in EDA complexes arises from dissociation of the complex into ion radicals [Eq. (1)]. Low donor ionization potentials and high acceptor electron affinities lead to strong complexes (i.e., dative in the ground state).

2. Alternating-Current Measurements

In organic solvents the probability of charge transfer increases with increasing permittivity of the environment. High permittivity promotes ion formation, and it is this feature that allows simple alternating-current (ac) titrations to determine the stoichiometry and relative charge-transfer strength of an EDA complex [14]. Alternating-current methods prevent the EDA components from plating out at the electrodes and have thus been used

for the study of a wide variety of complexes of pharmacologically active agents, neurohumoral transmitters, and protein and protonic complexes [1,53,96–99]. Increasing the temperature increases the conductivity of EDA complexes in solution, due to increased concentrations of ions [14]. Conductivity titrations are usually complementary to spectroscopic methods of investigation.

3. Permittivity Measurements

Surface-active agents have relatively high capacitances, which often track conductivities closely, exhibiting the same stoichiometries as those obtained from conductivity measurements [14,100]. The capacitance peaks observed in the course of conductivity titrations of charge-transfer complexes cannot possibly be caused by any reasonable increase in the bulk permittivity of the solutions, which were only of the order $10^{-3} M$, and which is determined by that of the solvent. These changes must then be due to processes occurring within an “active space” or reaction zone associated with the double layer [101]. During the titration, the electrochemical concentrations differ greatly from the bulk concentrations. Thus, for example, acetylcholine [92] adsorbs on the electrode to a lesser degree than the more surface-active chlorpromazine (CPZ) and fails to displace the CPZ from the double layer in proportion to its bulk concentration. The measured electron-transfer rate is markedly affected by the material of which the supposedly inert electrode is made. This is due to the extent of orbital overlap between the electroactive species and the electrode. Capacitance measurements as a function of frequency may also be used to investigate the aggregate nature of amphiphiles in solution [102]

4. Polarography

Polarography of an acceptor A will yield a half-wave potential for the reduction of A to A^- at the dropping mercury electrode. If a donor D is added, several complexes of different stoichiometries generally form, having the composition D_iA , where the integer i varies from 1 upward. The half-wave potential is not identical to the electron affinity, or analogously, to the ionization potential. A number of workers [103] have derived equations that allow equilibrium constants of the EDA complexes to be determined, for example, for tetramethyl porphyrin complexes [104]. The polarography of CTC in nonaqueous solvents, such as acetonitrile, has been discussed in a number of publications [105,106]. Polarography need not be confined to direct-current methods. Alternating-current polarography has enjoyed success in the study of EDA complexes [107,108]. Activation energies of complexes may readily be obtained by means of such polarographic waves [14].

5. Voltammetry and Potentiometry

Cyclic voltammetry and potentiometry have also been used for the study of complexes of biologically important compounds such as tranquilizers and dilantin [109], and surface CTC on membranes [110].

6. Photoconduction

All photoeffects involve the absorption of photons to produce an excited state in the absorber or liberate electrons directly. With the direct release of electrons, photoemission may occur from the surface of solids. While the excited state may revert to the ground state, it may proceed further to a photochemical reaction to provide an electron–hole pair (exciton) as the primary photoproduct. The exciton may dissociate into at least one free carrier, the other generally remaining localized. In an externally applied electric field, photoconduction occurs. Photomagnetic effects arise in a magnetic field. Absorption of photons yield photoelectric action spectra which resemble optical absorption spectra. Photoeffects are involved in many biological systems in which charge transfer takes place (e.g., as observed in the chlorophylls and carotenoids) [14].

D. Other Methods

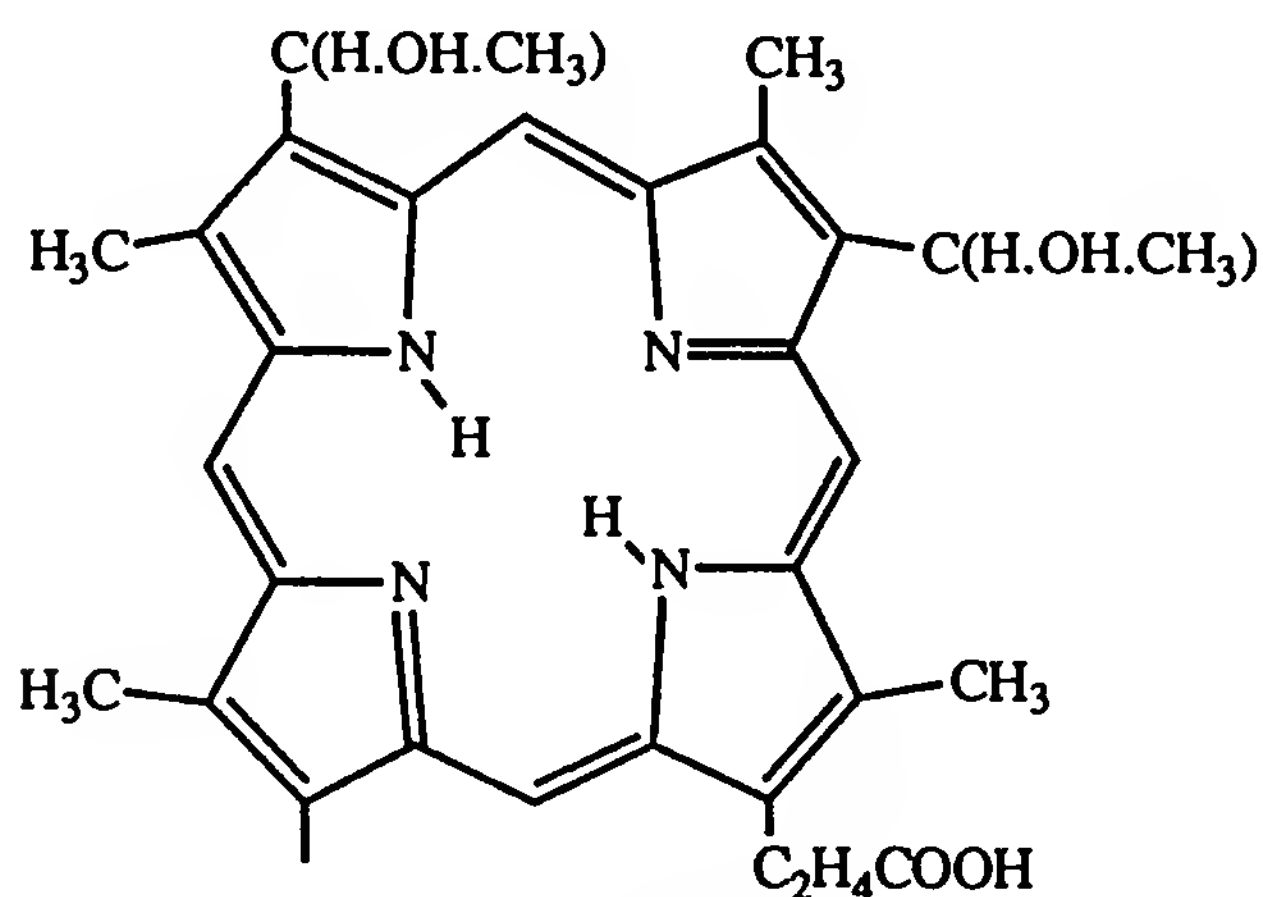
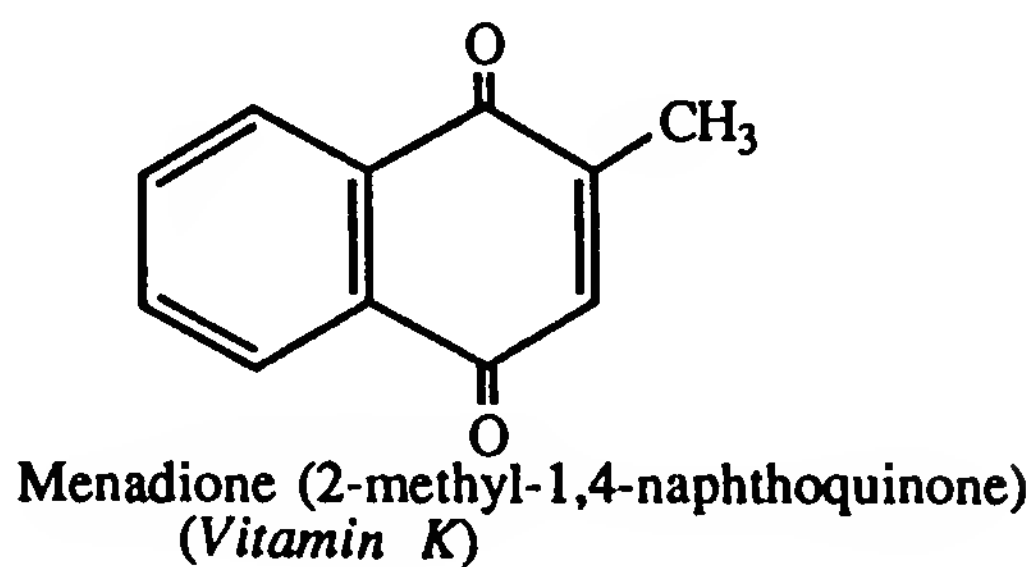
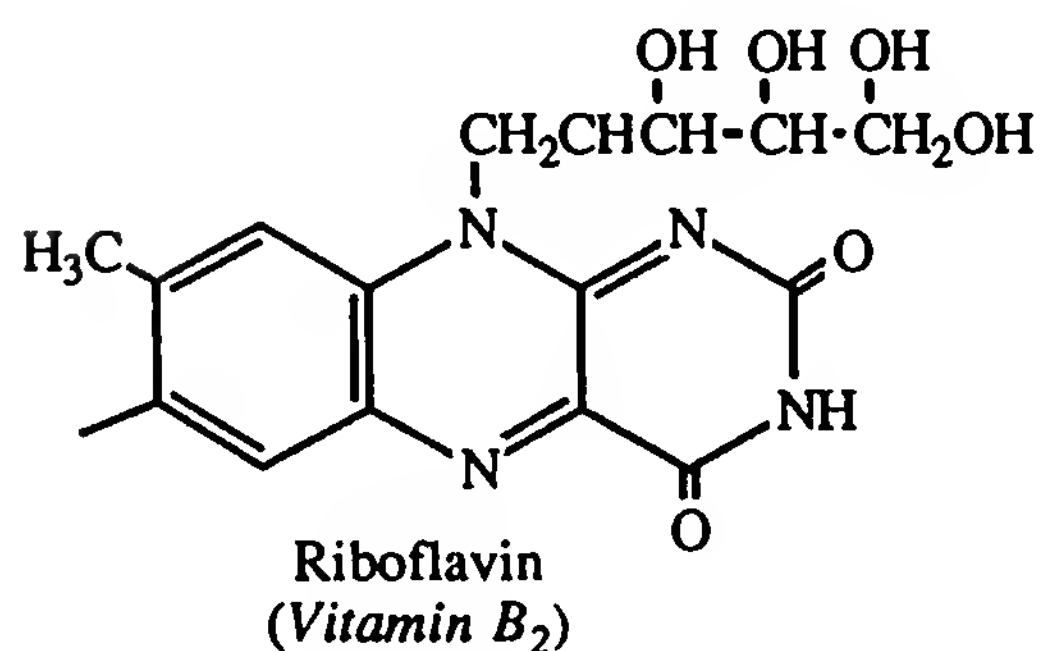
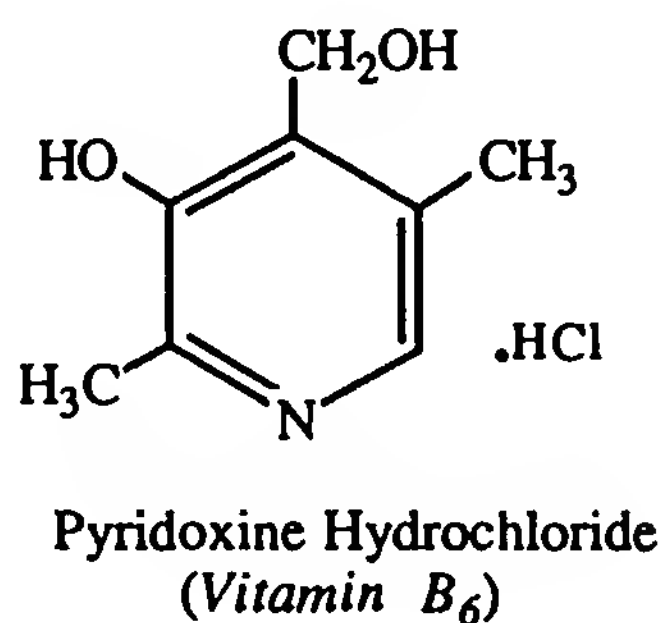
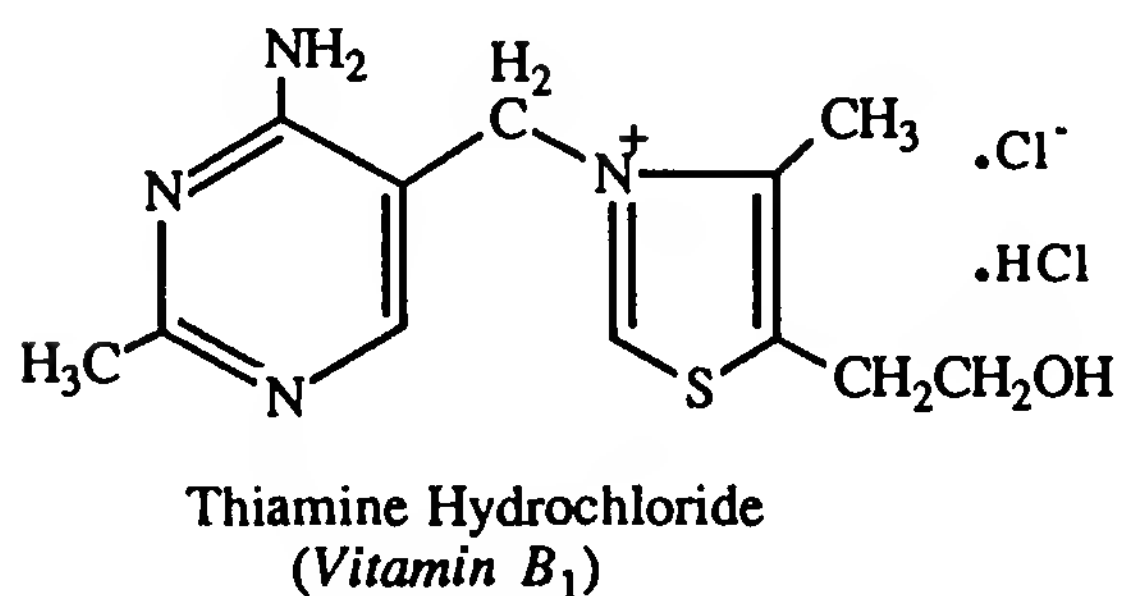
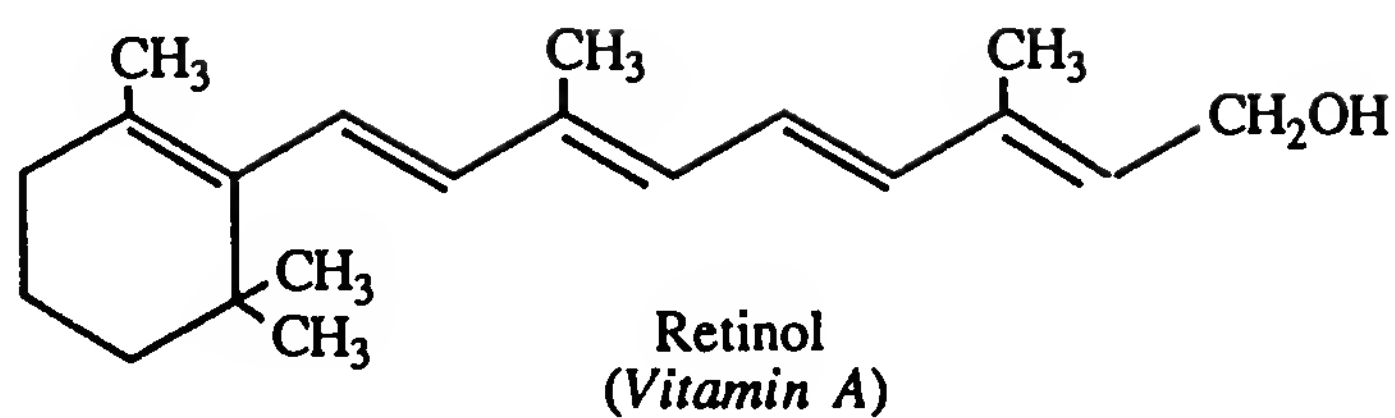
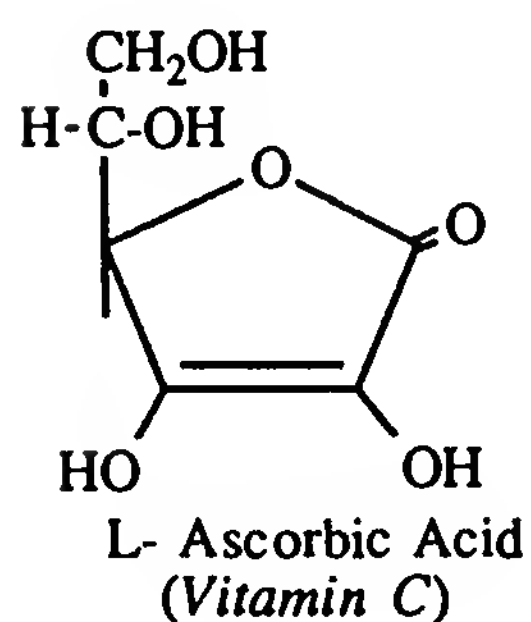
Many other methods have been employed to study CTC in biological systems, such as calorimetry, mixed fusion analysis, solubility and partition methods, ultrasonic methods, spectropolarimetry, reflective infrared spectroscopy, Raman spectroscopy, flash photolysis spectroscopy, nuclear quadrupole resonance spectroscopy, and magnetic susceptibility methods, to name several of a very long list. X-ray photoelectron spectroscopy (XPS) has also been used to elucidate some EDA interactions in electrically active macromolecules. XPS is useful for detecting the redistribution of charges in complexes of such compounds, (e.g., in the presence of phosphate acceptors, the nature of the semiconductive environment of S, O, and N bridges in macromolecules is affected profoundly [111].

III. EXAMPLES OF CHARGE-TRANSFER COMPLEXES IN BIOLOGICAL SYSTEMS

Some representative molecular structures are given in Figs. 3 to 5.

A. Vitamins

Vitamins occupy a central position in the successful operation of living processes, and many are capable of forming charge-transfer complexes.



Hematoporphyrin
(Vitamin B₁₂ is based on a porphyrin)

Figure 3 Structures of selected vitamins.

1. Vitamin A

β -Carotene has been mixed with iodine to yield products of low activation energy and high conductivity typical of charge-transfer complexes; I_3^- was found to be present. Strong ESR signals were obtained [112]. However, these signals do not correlate with increased conductivity. This may reflect the mobility of the carriers rather than the conductivity. Slifkin [1] suggests that the carotene forms a complex with I^+ ions after dissociation of $2I_2$ to I^+ and I_3^- , and that the spectral data obtained are due to a charge-transfer transition between the complex in the ground state, carotene/ I^+ , and the excited complex carotene $^+/I$ [112]. With bovine serum albumin Eley and Snart [113] found that the carotene interaction product exhibited increased conductivity and reduced activation energy. Gaseous electron donors produced a similar effect [114], leading to the notion that carotene is an electron acceptor.

One might have expected similar results for retinol (vitamin A), (Fig. 3); however, the retinol needs to be in the colloidal state to give a blue-green product [115,116]. Tetracyanoquinodimethane (TCNQ) cations are produced by both β -carotene and retinol, with the former showing a stronger interaction [117]. In ethanol the retinol- I_2 complex is not as stable as in water, which, according to Slifkin [1], suggests the possibility of two separate processes for electron transfer to iodine to produce I^- . Self-complexes of retinol in saline solution, probably as cation-anion forms, oxidize rapidly in air [118,119], presumably because the retinol cation is more reactive than the neutral molecule, similar to the autooxidation of catecholamine [120].

2. Vitamin B

Vitamin B_1 (thiamine) and the thiamine pyrophosphate undergo typical complex formation with tryptophan and other indoles [121–123]. Association constants of such complexes increase as electron-donating groups are substituted, while they decrease with increasing ionic strength, which indicates little dative character in the ground state [38,121–123].

Vitamin B_{12} (cyanocobalamin), related to porphyrins (see e.g., Fig. 3) was suggested by Pullman [124] to be a good electron acceptor, but it was shown experimentally to be an electron donor in the presence of, say, glutaric acid [125]. Amino acids form 1:1 complexes with vitamin B_{12b} [1]. However, in this case n -electron donation is said to occur from the amino acid amine to the vitamin, the complexes weakening with the addition of sterically hindering groups on the amino acids (17). Increasing the chain length of the peptides showed that the terminal free nitrogen was involved, although the C-terminal group had a slight effect on complexing, in the same order as those of the amino acids. Vitamin B_{12} also forms complexes

with purines and pyrimidines [1,126]. Vitamin B₁ forms 2:1 adducts with acetylcholine, noradrenaline, and serotonin [127]. If it is present, charge transfer is very small, confined mostly to a slight blue shift of the vitamin's absorption band and the nonadditivity of the electrical conductivity of the individual components.

3. Vitamin C

Ascorbic acid interacts as a donor with nicotinamide to produce a temperature-dependent 1:1 yellow complex [128], the color increasing with decreasing temperature. The absorbance of this complex is pH-dependent peaking at pH 4, in contrast to the pH-independent *N'*-methyl nicotinamide, suggesting an interaction between the protonated nicotinamide base and the ascorbic cation.

4. Vitamin K

Vitamin K₃ (menadione) complexed with polycyclic hydrocarbons (e.g., pyrenes) was investigated by Laskowski using a mixed fusion method [129]. Similar 1:1 complexes exhibited intensification of color upon cooling. These complexes have small association constants [130], and their small, sometimes even positive enthalpies of dissociation are probably due to contact charge transfer in the melt because the colors disappear on solidification of the products, probably due to loss of favorable orientation of the interacting components [1,131].

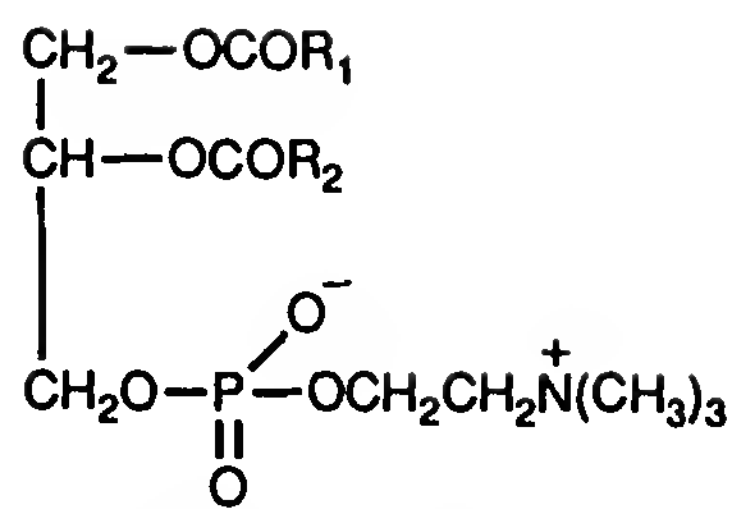
B. Lipids

Like the lecithins (see Fig. 4), lipids appear to behave as electron donors [1]. With I₂, Rosenberg et al. [132,133] observed that lecithin yielded 2:1 iodine complexes with the appearance of the triiodide spectrum, and a decrease of the iodine spectrum, similar to the changes caused by amino acids [134].

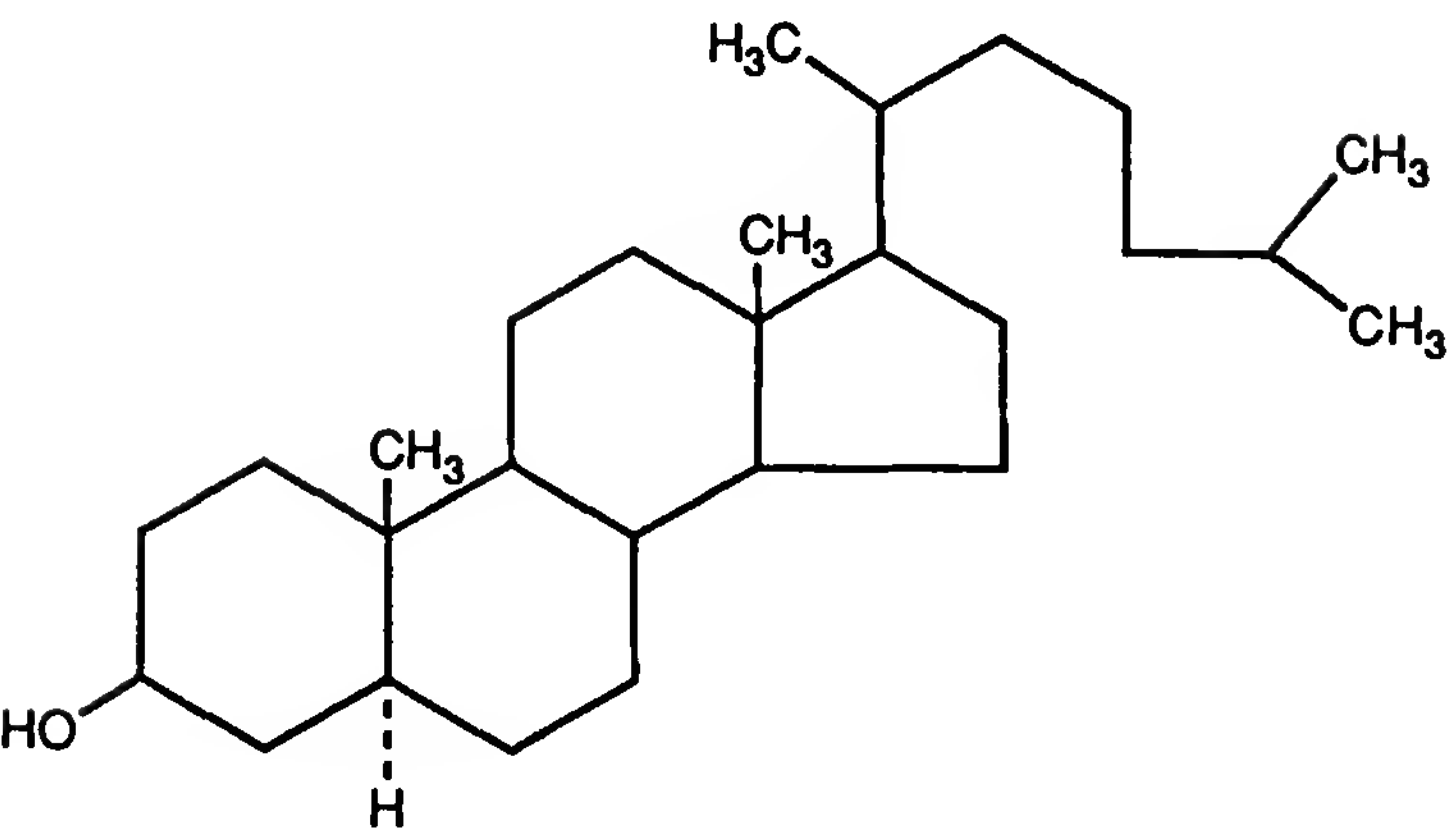
Cholesterol (see Fig. 4) also acts as an electron donor with I₂ and various organic electron acceptors which lower the activation energy and resistivity [1,133]. The cholesterol was studied in various states: dry and fully and partially hydrated. The fully hydrated cholesterol complexes had the lowest activation energies and resistivities [1,133].

C. Carbohydrates

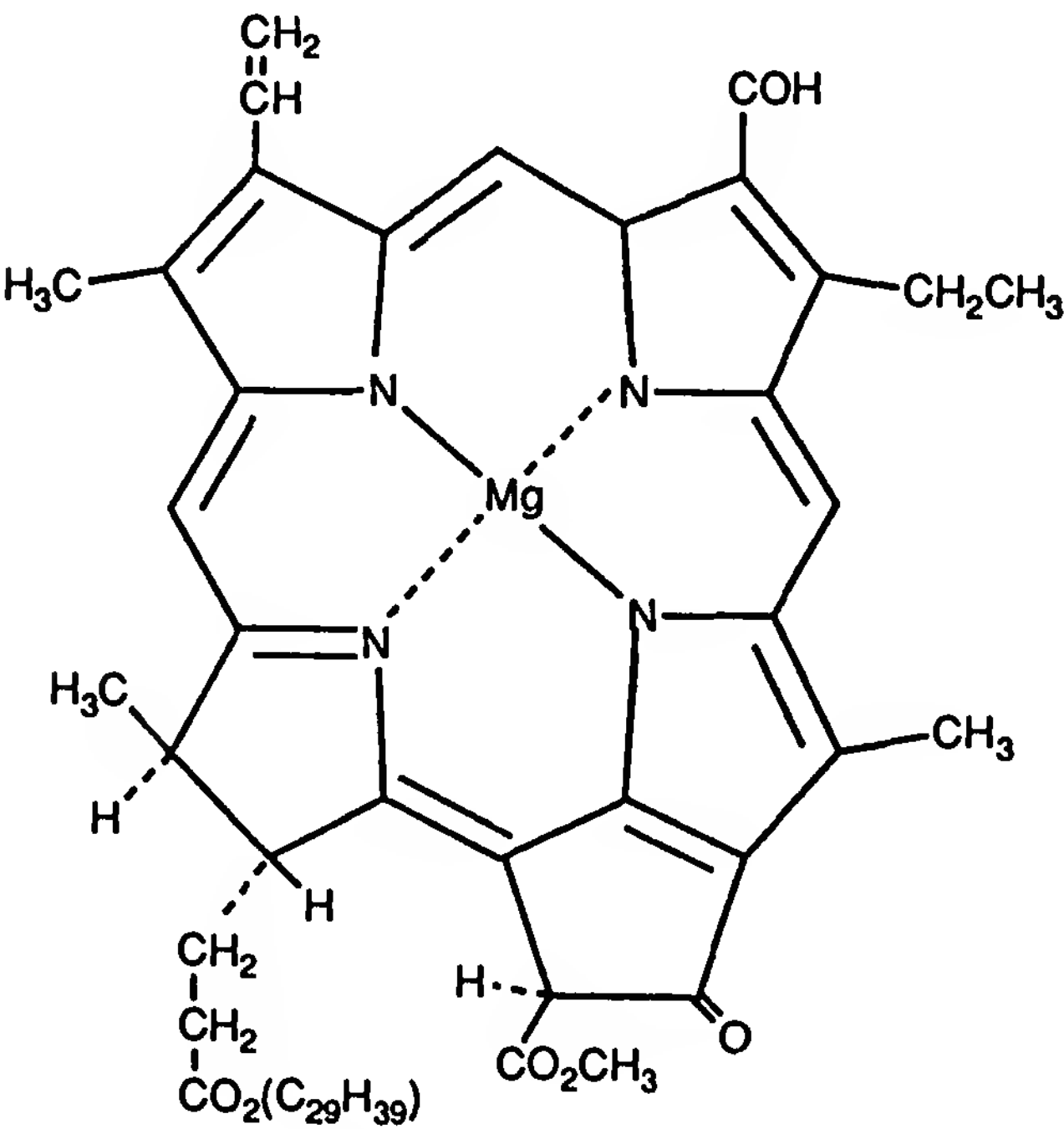
The blue starch iodine complex has been used from time immemorial as an indicator in aqueous iodometric titrations; water is required for development of the blue color. The color sensitivity is decreased with increasing temperature and also with increasing concentration of ethanol [134]. Although one might imagine this to be evidence for a charge-transfer complex,



Lecithin. R₁ and R₂ are fatty acid residues.



5-α-Cholestan-3, β-ol (cholestanol)



Chlorophyll-*b*

Figure 4 Structures of lecithin, cholestanol (cholesterol derivative), and chlorophyll *b*.

Bersohn and Isenberg [135] suggest that these adducts involve covalent bonding of a metallic kind. This complex is formed by inclusion of I_3^- in the spiral starch molecule with a stoichiometry of six glucose units per I_3^- . With amylose a green-to-blue I_2 complex is formed in which one glucose unit traps an I_3^- . Amylopectin, a branched-chain molecule, reacts with one I_3^- molecule per spiral to form a reddish-purple adduct [136]. While steroids are not carbohydrates, oxygen-bearing steroid dimer triiodide ion complexes are known, for example, in which the I_3^- bridges the two steroids via keto-oxygens [137]. A similar mechanism may operate in the starch complexes.

Very few studies are extant on the electron charge-transfer interactions of carbohydrates with electron donors or electron acceptors. This may be because carbonyl groups are generally poor electron acceptors. However, see the discussion of methyl glyoxal in Section III.I. Those that do exist involve mainly DNA, RNA, and nucleosides, adenosine, and related derivatives of the purines and pyrimidines. Basu and Greist [138] have suggested that some purine and pyrimidine nucleosides form autocomplexes. The UV spectra of very concentrated solutions produced new UV- and blue-shifted absorption bands. However, Slifkin [1] observed similar bands for the same purine and pyrimidine bases, which were independent of temperature. Mono- and dinucleotides, on the other hand, exhibit red-shifted fluorescence spectra suggestive of self-association [139]. Such spectral changes were observed during exciplex and excimer formation, consistent with the behavior of purines and pyrimidines [140].

1:1 Complexes of adenosine, guanosine, and deoxyguanosine with various caffeines are well established [1]. Adenosine also forms a complex with riboflavin in aqueous solution at pH 7 [141]. Whether the ribose or deoxyribose form direct charge-transfer complexes is moot. Although the introduction of electron-accepting phosphate linkage groups to form the backbone of DNA and RNA may contribute to charge-transfer phenomena, it is more likely that these provide the scaffolding on which the purines and pyrimidines form the stacking unit alignment favorable to electron charge transfer.

Flavin mononucleotide (FMN)–adenosine and flavin adenine dinucleotide (FAD)–adenosine complexes show quenched triplet lifetimes compared to FMN alone, which is cited as evidence of intramolecular complexation between the flavins and adenosine by Shiga and Piette [142]. Adenosine phosphates also form complexes with FAD [143]. The complexation between a flavin and adenosine is identical to the intermolecular complexing of adenosine and flavin moieties, in the latter case enforced by hydrophobic bonding [144–146]. Rath and McCormick [147] have examined the riboflavin complexes of a series of purine ribose derivatives

and confirm the correlation of their stability with the energy of the highest filled molecular orbitals (Fig. 5).

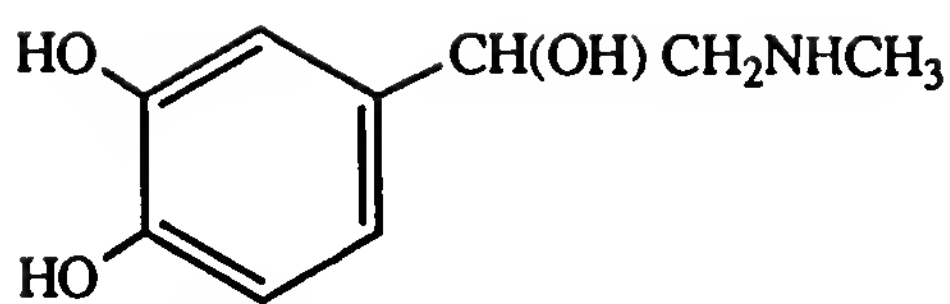
D. Purines and Pyrimidines

Much of the work on charge-transfer complexes in biological systems has been done on the purines and pyrimidines, not only because these form an important fundamental group of biological compounds but because they contain readily distinguishable electron donor and acceptor groups (Fig. 5). Actinomycin forms adducts with purine derivatives, complexation decreasing in the order of guanosine, adenosine, and the adenosine phosphates AMP, ADP, and ATP [148–150] corresponding roughly to the energy of the highest filled molecular orbital computed by Pullman [151].

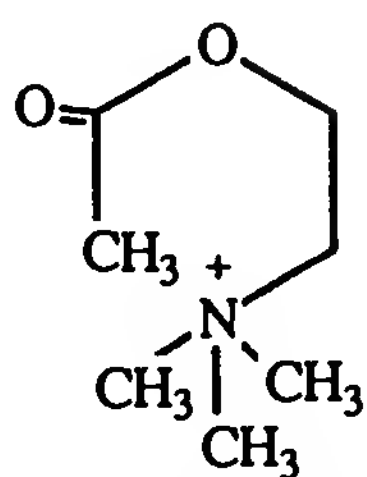
Fluorescence quenching has been one of the major techniques for the study of purines and pyrimidines, the probe molecules being flavins. Weber [141] studied the temperature-reversible 1:1 complexes of adenosine and caffeine with riboflavin. While several workers [1,139] have demonstrated purine-FAD, purine-3-methyl RFN, FMN, and RFN complexes, Slifkin [152], from absorption spectroscopy studies, excluded the reactive uric acid and 8-azaverdenine from these groups. Adenine was found to complex more strongly with RFN than with adenosine [153]. Similar behavior generally was determined for the free bases compared to the nucleosides. N₆ substitution of purines or pyrimidines increases the complexing ability with RFN, as does alkylation of an amino group at this position [147,153,154]. Surprisingly, the order of alkylation of this amine group in purines is not homologous, (i.e., ethyl > methyl > propyl) [147]. MacIntyre [155] claims that 8-azaguanine forms a dimeric self-complex with an intermolecular separation of 3.25 Å. These molecules are not superposed perfectly but displaced slightly to allow π -orbital overlap for complexation. The low electron affinity of this compound would require observation of the charge-transfer band in the far ultraviolet [156].

Wenzl et al. [157] claim to observe charge-transfer interaction between Cu²⁺ and uracil derivatives in DMSO mediated by hydrogen bonding. Pullman [158,159] predicted that purines were good donors and pyrimidines good electron acceptors. Purine–pyrimidine α -nucleotide complexes upon irradiation invariably localize damage on the pyrimidine nucleotide consistent with electron transfer to the latter. Olast and co-workers [160] also showed spin transfer from amino acids to pyrimidine nucleotides. The relative degree of stacking between the amino acids and pyrimidine bases as well as the relative electron affinities affect transfer intensity in the molecular aggregates. To tease out each of these two factors, Mathur-De Vré and Bertinchamp [161] studied pyrimidine nucleosides and 5-halo-

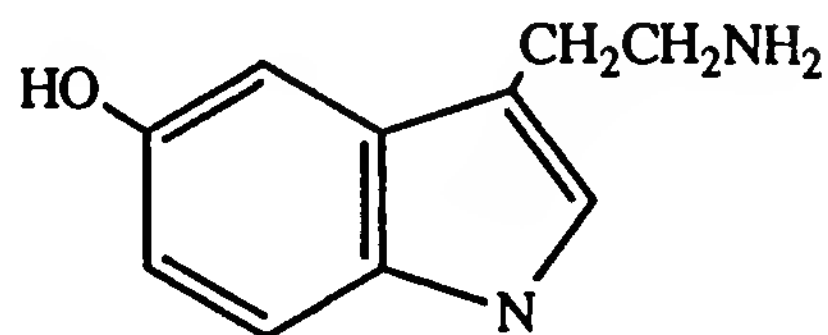
Neurohumoral Transmitters:



Adrenaline

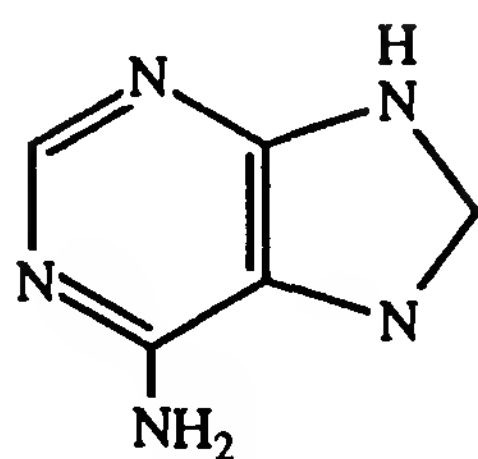


Acetylcholine

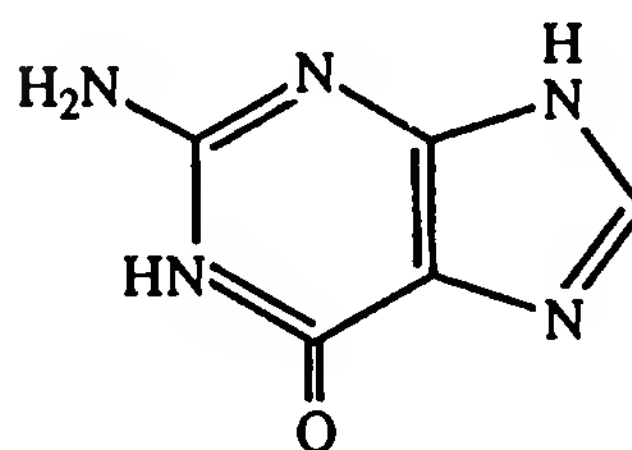


Serotonin (5-hydroxytryptamine)

Purine:

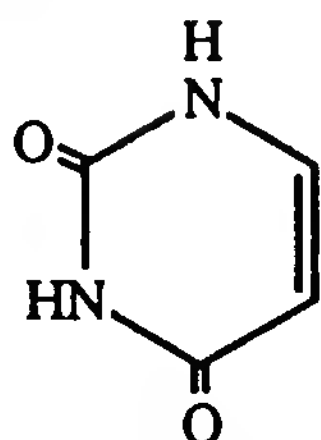


Adenine

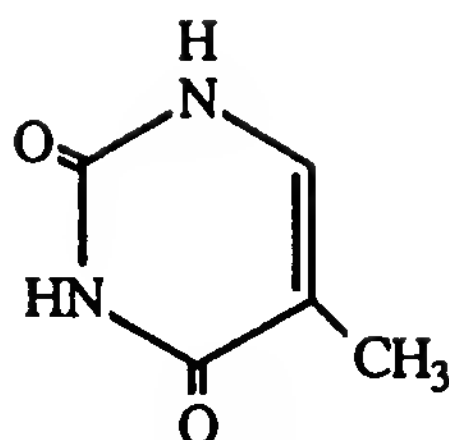


Guanine

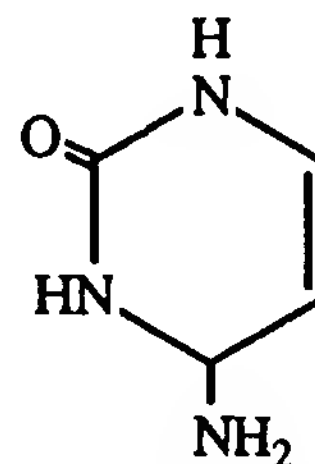
Pyrimidine:



Uracil

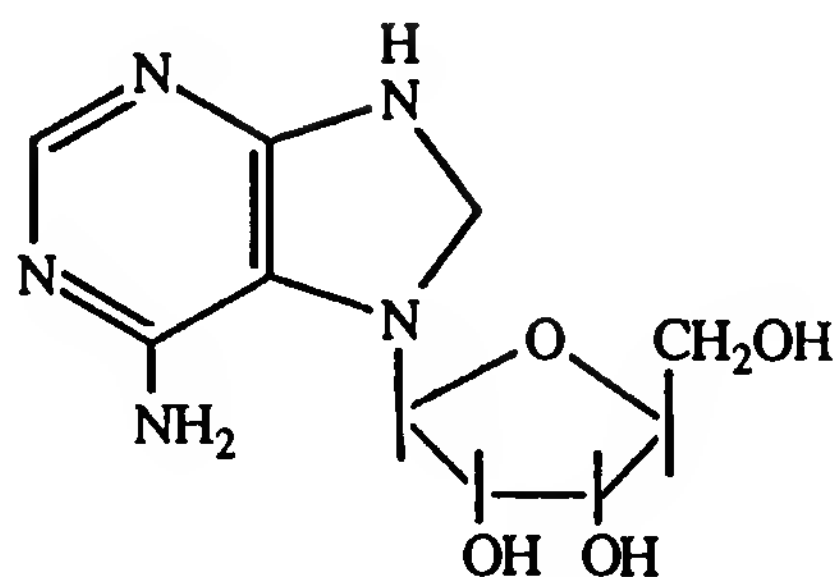


Thymine



Cytosine

Nucleoside:



Adenosine

Figure 5 Structures of selected molecules.

nucleosides with electron donors, such as 5-hydroxytryptamine (serotonin) and 5-methoxytryptamine (5-MTA) by means of NMR spectroscopy. They show that charge transfer from serotonin and 5-MTA to nonhalopyrimidines base rings is not significant but that with stacking charge transfer may be promoted, as it certainly is with the halogenated pyrimidine derivatives. The relative electron affinities in a series of pyrimidine nucleosides are said to play an important role in these events. Ts'o et al. [162] showed that in water, purine nucleosides and nucleotides self-associate extensively, while pyrimidines show such behavior to a much lesser extent, probably due to the small density of their delocalized π -electron clouds.

DNA and RNA, containing purines and pyrimidines, have been studied in terms of charge-transfer complexes, no doubt because of their importance in genetics and biological phenomena, such as cancer. Some of the earlier studies were sketchy in this regard. For instance, DNA mixed with acridines are yellow in DMSO [163]. However, the color change mentioned above cannot constitute a priori evidence of electron charge transfer, especially in an active solvent such as DMSO, which can affect the steric properties of DNA normally found in aqueous environments.

Controversy exists as to whether DNA forms complexes with polycyclic aromatic hydrocarbons [164–170]. The evidence suggests that while intercalation of the hydrocarbons into the DNA strands occurs, the presence of electron charge transfer is not entirely established. Nevertheless, the weight of evidence tilts toward electron charge-transfer complexation rather than a colloidal trapping phenomenon. However, it is not unlikely that the formation of aqueous colloids may assist the process of charge transfer as discussed previously. For these mixtures, DNA behaves as a donor [170–173]. Certainly, ESR signals have been obtained for DNA and RNA mixed with cationic dyes [174]. These signals were undiminished by denaturation of the nucleic acid.

Mutagens such as acridine and proflavine are known to form adducts with DNA [1,175,176]. The mutagens are believed to intercalate between base pairs of the nucleic acid, and the mechanism of action was believed to be charge transfer. However, another study suggests that the mutagens act electrostatically at external sites of the nucleic acids [176]. Intercalative binding is also excluded for the interaction with DNA of antitumor antibiotics isolated from *Streptomyces zelenais*, and some derivatives [177]. The binding is largely hydrophobic and is established by van der Waals contact. Such binding spans about one-half of the helical turn of double-stranded DNA, or about five base pairs, with a substantial preference for adenosine–thymine- rather than guanine–cytosine-rich areas.

DNA forms an intercalation product with the trypanoacids and ethidium [178,179]. Olinsted and Kearns [180] studied the fluorescence quench-

ing by aqueous dilution studies of the ethidium–DNA adduct, and concluded that quenching involved a proton transfer mechanism. The addition of amsacrine, an antitumor derivative of acridine, to the DNA–ethidium adduct quenches the fluorescence of the DNA-bound ethidium [181]. The authors of this work [181] strongly implicate the electron donor properties of amsacrine and exclude the possibility of a resonance energy transfer mechanism as proposed [182] to explain the DNA–ethidium–H₂O observations. Amsacrine's electron donor interaction with DNA is also implicated as electron transfer complexation with cupric ion, leading to DNA cleavage [183].

E. Porphyrins

Minkov [184] maintains that the reaction of metal phthalocyanines (MPc) with organic hydroperoxides which are of the type MPc—HOOR involves proton complexation with a peripheral nitrogen atom. Electron charge transfer is implicated in intermediate complexes during oxidative decomposition of phthalocyanines of so-called active metals, such as Co²⁺, Ni²⁺, and the Pt metals [185]. Chlorophyll and heme (Figs. 3 and 4) are representatives of some of the more important class of biological systems. In 1960, Calvin's group [186] showed that chloranil mixed with metal-free phthalocyanine yielded a charge-transfer complex exhibiting an ESR signal and increased dark conductivity. Upon illumination the ESR signal decreased but the conductivity increased. This was ascribed to a one-electron transfer from the donor phthalocyanine in the dark and a two-electron transfer in the photonic event. Kearns and Calvin [171] also produced solid iodine phthalocyanine complexes. As early as 1943, Keilin [187] prepared complexes of caffeine and porphyrins. Related studies in which the porphyrins behave as electron acceptors were done by Mauzerall [188]. He produced porphyrin adducts of purines, adenine, and caffeine.

Other studies have brought out the ambivalent characteristics of many porphyrins in charge-transfer adducts [189–192]. Porphyrin fluorescence quenching, a characteristic of complexation, occurs for a variety of aromatic donors and acceptors. The porphyrins are known [189–192] to form charge-transfer complexes with some amino acids and the indole tryptophan [193], some steroids [194], and some vitamins [194].

Chlorophyll studies of adducts with various biological molecules are also known (bovine plasma albumin and β -carotene [195], quinone riboflavin [196], and NADH [173]. Mitsui et al. [196] have shown that in porphyrin complexes of viologen the counterion (I⁻, Cl⁻, Br⁻) affects the electron transfer process by reduction of the electron-accepting properties of viol-

ogen units by means of charge-transfer interaction and enhancement of intersystem crossing of the photogenerated radical pair.

Phthalocyanine (PHTH), mesophenyltetrabenzoporphyrin (MTBP), and metallo-MTBP EDA complexes have been studied in solution and the solid state [197]. The stoichiometry of the TCNQ complexes of Mg-MTBP and Zn-MTBP, 1:4, indicates that the porphyrins are oriented with the metal core toward the N of the electron acceptor. However, the interaction is weak. In the case of iodine complexes ESR data demonstrated [198] that preferential oxidation of the ligand takes place. This infers that the coordinated complexed metals do not play an important role in the conduction process of iodinated metallo-MTBP and metallo-PHTH. An exception is Ni-tetrabenzoporphyrin in which charge transfer occurs both via ligands and the metal [199]. Freeman [200] confirmed that metalloorganics can accept or donate electrons without affecting the coordination number of the metal in poplar plastocyanin, which has a free Cu center. This center is embedded deep in the protein, thus avoiding contact with the external environment.

Dihematoporphyrin derivatives (DHPD) have been introduced in tumor therapy [201]. These derivatives develop high cytotoxicity in light-sensitized cells. Although structurally, the active component appears to be a dimer [202], some suggest it to be the ester [203], and others the ether and the ester [204], it is clear that the cytotoxic complexation occurs via exciplexation [42]. Several other esters (mesochlorine and bonellin) of DHPD ether are claimed [205] to be five times more lethal than DHPD.

F. Neurohumoral Transmitters

Gutmann et al. [206] have prepared solution complexes of acetylcholine, serotonin creatine sulfate, and 6-hydroxydopamine (Fig. 5) with chlorpromazine hydrochloride, identified by conductivity measurements. Noradrenaline was found to form a charge-transfer complex with 6-hydroxydopamine yielding a typical charge-transfer band at 20.4 kK.

Our conductrimetric work [207] with three hydrochloride psychotropes—chlorpromazine, trifluoperazine, and methotrimeprazine—also showed that these formed charge-transfer complexes with acetylcholine, 6-hydroxydopamine, and noradrenaline which were not highly associated. Two different types of interaction occurred, one in which a single product was formed, and a second which involved two almost simultaneous reactions. In the former case the product was stable to ultraviolet light, while in the latter case the more slowly formed product was strongly UV sensitive. The reactions in solution were first order.

Galzigna [208] investigated the complex formed between acetylcholine and catecholamines and discovered that the product led to oxidation of

the catecholamines. For example, noradrenaline oxidized to noradrenochrome. The autooxidation rate of noradrenaline was enhanced by complexation. Nicotinamide, as the donor, increased this effect. Slifkin [1], and Cilento and Zimmer [209], give alternative schemes to explain the same results.

Riboflavin was discovered by Isenberg and Szent-Györgyi [210] to form a complex with serotonin, colored at low temperature in solution and the solid state. Unprotonated nicotinamide adenine dinucleotide (NAD^+) forms a charge-transfer complex with serotonin creatinine sulfate [211]. Douzou [212] noted that decreasing temperature caused a partially reversible increase in optical density of the NAD –serotonin complex. He claims that aggregation of the complex constituents is followed by oxidation. Serotonin complexes of pteridines are also known [1].

G. Macromolecules

Macromolecular complexes are those in which at least one component belongs to a chain. Simionescu and Stigoras [213] distinguish between complexes of donor polymers, or acceptors with small molecules (intermolecular), complexes between a donor polymer and acceptor polymer (interpolymer), and complexes of a donor–acceptor copolymer (intramolecular). Intermolecular polymer complexes are common among polypeptides involving both donors and acceptors. Biological interpolymer complexes are also known [214]. Copolymerization in a heterogeneous medium generates stronger complexes than those obtained in a homogeneous phase [215]. The quantum efficiency of photoactive donor–acceptor copolymers is higher than that of doped systems [216].

Although charge transfer in macromolecules is of fundamental interest and has been studied piecemeal, often with model systems, this field is in its infancy. DNA and RNA complexes have been discussed in Section III. D. The oxidized and reduced forms of flavin mononucleotide produce charge-transfer complexes as precursors of the semiquinone free radical [217]. A similar charge-transfer interaction was expected to exist in the NAD coenzyme and was observed in the complex of NAD with NADH [218]. Shinkai and co-workers [219] discovered that association constants for complexes of indole derivatives with 1-lauryl-3-carbamoylpyridinium bromide (LCP) were considerably higher than those for the monomer and those in the micellar system. They also observed enhanced charge-transfer interaction with increased nicotinamide group concentration between LCP and LCPH in the micellar form. Enhanced charge-transfer interactions with LCP were also noted for adenosine and indole derivatives. The absorption spectra from which these authors deduced their conclusions are

of interest because they are similar to those of the interaction between NAD and glyceraldehyde-3-phosphate dehydrogenase [220]. Velick [221] assumed that the NAD coenzyme is bound at the top or bottom of the tryptophan stack in the enzyme. Similar behavior was observed for the intramolecular-associated model compound 1-(β -indolyethyl)-3-carbamoylpyridinium chloride [222,223].

Cope [224] linked the enzymic charge-transfer behavior of cytochrome oxidase conclusively to its solid-state semiconductivity based on the fact that this molecule is embedded in a fragment of the mitochondrial wall. Pelletier and Kraut [225] demonstrated the existence of cytochrome *c*/cytochrome *c* peroxidase complexes. Electron transfer tunneling is said [225] to proceed along the cytochrome *c* peroxidase backbone.

Mieloszyk and colleagues [226] determined that flavins which form charge-transfer complexes with proteins exist in both the ground and excited electronic states. In the flavin–riboflavin-binding protein the tryptophan is considered to be the donor. Other such complexes of flavin coenzymes and apoenzymes are known [227–229].

H. Aggregates (Micelles)

Aggregation of amphiphiles in solution is the rule rather than the exception [230]. Aggregation is one of the commonest phenomena in biology—to wit, the existence of membranes and vesicles, to draw attention to a few. Aggregation, may, as in the case of micelles, affect dramatically rates of a multitude of organic and inorganic reactions by many orders of magnitude, for example, as in the case of protonation of indicator dyes [231–236], and the reaction of mercuric ions with cobalt complexes in the presence of sodium hexadecyl sulfates. For nonpolar media, micellar catalysis has also been observed [231]. In such media, polar reactants in the hydrophilic micellar cavity, in, for example, globular proteins, may be affected strongly by small amounts of water which would behave very differently from bulk water because of extensive binding and organization. Thus aquation of the tris(oxalato)chromium III anion is almost seven orders of magnitude faster in a nonpolar medium containing octadecyltrimethyl ammonium tetradecanoate than in water [237]. At least two kinds of cases can be distinguished: one in which the aggregate acts only as a reaction medium, and another in which the amphiphile is directly involved as the catalyst or substrate [232]. Self-association and mutual association are of great importance for many physiological molecules and aggregates. Kuroda [238] showed that columnar structures existed in Langmuir–Blodgett films composed of amphiphilic CTC. Budyka [239] showed that unlimited coaggregation or polycomplexes can occur via charge-transfer complexation.

It is conceivable that if organization at the molecular level can promote chemical reaction, charge-transfer interactions may also be enhanced (or decreased) or come into play in such environments. Florence [240] gives examples of the implication of biological aggregates: for example, the interaction of ATP with serotonin and with noradrenaline, the aggregation of glycoproteins, self-association of alamethacin, a compound obtained from microorganisms [241], and the interactions of chlorophyll and protoporphyrin [14].

Aggregation is a reversible form of molecular aggregation and is probably one of the many control mechanisms in living systems. While macromolecules are often involved with reception or act as barriers, aggregates (i.e., micelles), because of their amphiphilic nature, behave like macromolecules. Cell membranes with nonpolar interiors and hydrophilic surfaces are prime examples, and many drug molecules, local anesthetics, and tranquilizers, the majority being amphiphiles, exert their activity by interaction with these membranes [242]. The charge-transfer interaction between ATP and biogenic amines leads to concentrations of about 20% in storage vesicles [243]. Self-charge transfer in the case of biogenic amines, leading to micelle formation, effectively reduces the pH of cationic drugs, such as promethazine, chlorpromazine, and thioridazine [240]. Such a reduction increases the rate of transport of the drug through the biological membrane [244]. The interaction of bilirubin with chlorpromazine is stabilized by micellar exciplex charge transfer, which may explain the condition known as *xanthomata* in chronically dosed patients [245]. Melanosis as a late side effect of long-term chlorpromazine therapy is manifested as skin pigmentation or ocular opacities [245]. This effect is also attributed to exciplexation [245].

I. Integrated Biological Systems

The oxygen molecule is preeminent in living systems because it is a universal electron acceptor. Oxygen, however, tends to accept electrons in pairs, which renders it unsuitable as a direct electron acceptor for proteins, because these would then be degraded too rapidly. Charge-transfer interaction usually involves single electron transfer, which may lead to a bi-radical complex with an unpaired electron on both the donor and the acceptor molecule. The majority of charge-transfer interactions are weaker, generally transferring electronic charge only fractionally. A charge-transfer complex is formed in which no new chemical bonds arise but in which the electron shuttles between the donor and the acceptor, preferring the neighborhood of the donor parent. This behavior may convert a “dead” molecule to a “living” molecule.

The carbonyl molecule is an alternative to the oxygen molecule as an electron acceptor even though it has poor acceptance characteristics. However, in methylglyoxal this problem is overcome by joining two $\text{C}=\text{O}$ groups to form glyoxal and adding a methyl group to form methylglyoxal (CH_3CHOCHO). This molecule has an aldehyde group quite reactive to proteins, and a ketonic group with a low-lying energy level ideal for accepting single electronic charge [246].

Methylglyoxal has been found [246] to bind to structural proteins of beef liver. A very active and widespread enzyme, glyoxalase [247], transforms methylglyoxal efficiently to *D*-lactic acid. If this were the sole purpose of glyoxalase, a puzzle would exist because methylglyoxal and *D*-lactic acid together lie on no presently known metabolic pathway. However, the problem acquires a solution when solid-state concepts of charge transfer and electronic desaturation are applied to proteins interacting with methylglyoxal. Proteins suspended in water in the dark with methylglyoxal assume a stable brown color, and the dc conductivity increases by two orders of magnitude [248]. Large ESR signals are observed [248]. Methylglyoxal binds to form colored complexes with bovine serum albumin (BSA), casein, lysozyme, chymotrypsin, chymotrypsinogen, cytochrome *c*, and fibrinogen [248–250]. Lorand showed [251] that all the arginine and 85% of the lysine groups in these proteins are involved in the interaction with methylglyoxal. It has further been shown by Pethig and colleagues [248] that the color and electron spin resonance signal intensities are directly related to the number of unblocked lysine groups.

A lysine residue is also found in rhodopsin and bacteriorhodopsin isolated from *Halobacterium halobium* [248]. Sulfhydryl groups [248] may be involved in producing the color of the protein–methylglyoxal complexes, but this is not the case in complexes with bacteriorhodopsin which contain no sulfhydryl groups [252]. The electron spin resonance signals observed in the methylglyoxal–protein complexes, three orders of magnitude higher than for proteins alone [253], probably arise directly from the polypeptide backbone.

From the energies for linear polyacenes, determined accurately by Silinsh [254], it appears that as the number of rings increased, charge separation in the charge-transfer state was facilitated. This could be significant [255] for biological systems containing highly conjugated molecules such as chlorophyll.

Solutions of chlorophyll have been shown to be photoconductive even in the absence of extrinsic acceptors [256]. In acetonitrile as solvent, ions were formed from two molecules in the triplet state. In petroleum ether, red light yielded ions from dimers if the concentration exceeded $10^{-4} M$, the dimerization point [257]. In chlorophyll solutions containing ascorbic

acid (here a donor) or acceptors such as quinones, triplets were involved to produce positive or negative ions [258–262]. Bromberg et al [263] concluded that in films of chlorophyll-*a* carrier generation occurred via a one-photon process involving a singlet state. They excluded triplet states because the rise time of photoconduction was less than 1 s. The subject of photosynthesis [264] has now become so large, involving an enormous wealth of published work, that it is impossible to do it justice within the necessarily limited confines of this chapter.

Watanabe et al. [265] report quantum efficiencies of about 15% in chlorophyll *a* films monolayered with 50% stearic acid and immersed in an electrolyte, similar to efficiencies found by Meilanov et al. [266] Photoconduction similar for both polarities was found [267] in chlorophyll *a*/H₂O adducts at 820 nm (i.e., at 1.5 eV). Lyons [255] suggests that this may be the energy needed to form a CT state. Chlorophylls in condensed states can produce separated charges, sometimes with high efficiencies. In chloroplasts energy transfer and charge generation at reaction centers involving more than one electron acceptor are likely to be the key processes. Lyons [255] has deduced from his experiments with model compounds (phthalocyanines) that the primary process in photosynthesis involves a carrier generation rate which is associated with acceptors and exceeds the generation of carriers without the acceptors.

Bacteriorhodopsin is a pigment found as a single protein component of the purple membrane of *H. halobium* [268–270] and similar extreme halophiles. The purple membrane converts light energy by translocating protons across the membrane to generate an electrochemical potential. A review [271] of this subject is available. The naturally recurring crystalline structure has been determined by electron microscopy at 7-Å resolutions. The protein is folded into seven α -helical chains, all of which span the hydrophobic core of the membrane [271]. The chromophore has been located in a lysine residue in the sequence of the second helical chain from the terminal group [272] (cf. previous discussion of methyl glyoxal–protein complexes).

A unique feature of the structure of higher plant chloroplasts is the differentiation of the internal membranes of the chloroplasts (thylakoids) into stacked and unstacked regions. Boardman et al. [264] show that the degree of thylakoid stacking depends on electrostatic screening rather than ion binding. The light-absorbing pigments, chlorophyll and carotenoids, are associated with proteins and organized into energy-transferring units within the thylakoid membrane. Quanta absorbed by approximately 200 light-harvesting molecules are transferred to one special molecule of chlorophyll *a*, where primary conversion of light into chemical free energy takes place. This reaction center of chlorophyll *a* is in close association

with an electron donor and an electron acceptor in the thylakoid membrane. Electron transfer takes place in the membrane of chloroplasts in a predominantly nonaqueous phase; it begins vectorially at each chlorophyll, so that one component of transfer is perpendicular to the membrane. This is achieved by anisotropically arranged molecules with the electron donor at the inner surface and the electron acceptor at the outer surface [273].

Chance and Nishimura [274] demonstrated electron transfer between cytochrome *c* and light-activated bacterial chlorophyll in *Chromatium vinosum* which was ascribed to long-range tunneling. This phenomenon was suggested to be common and necessary for long-range electron transfer in chloroplasts and mitochondria. Gochev and Christov [275] have given a quantum-mechanical treatment of the primary event in photochemical cycles and of the primary reaction in the photochemical cycle of *H. halobium*, the electron transfer between primary and secondary acceptors in bacterial photosynthesis and the photoinduced oxidation of cytochrome *c* by bacterial chlorophyll. The transfer is said [276,277] to be extremely fast, thus avoiding a back reaction; an electron transfers from the photoexcited state of a chlorophyll dimer to a pheophytin in about 10^{-11} s. The resulting hole is filled by electron transfer from cytochrome *c*, taking 20 μ s. The transfer to the chlorophyll dimer is reported [276,277] to occur by adiabatic tunneling.

IV. CONCLUSIONS

The processes of living cells appear manifold and complex beyond anything that are encountered in the physics or chemistry of inanimate matter. Long gone are the days when cells, for example, were viewed as mere lipid bags filled with watery fluids. Even water, tenuously structured in the bulk, acquires structure near and in systems, all also structured. They provide the matrix in and on which small and large biologically active substances interact by a variety of bonds of which the more subtle involve partial electron and proton transfer, as in charge-transfer complexes.

Experts in the field of biology, chemistry, and physics know very well that boundaries must be crossed, which can only be done effectively with the present and emerging concepts of dynamical systems, quantum theory, electrostatics, and the solid state, among others. Submolecular biology is becoming more accessible by means of sophisticated research methods based on microtechniques, microcircuitry, and computers. The steps from in vitro to in vivo experimentation, although still tentative, have already taken place and will accelerate rapidly.

The field of in vitro charge transfer and charge-transfer interactions has become exceedingly large, and one should expect a burgeoning of its subdivision involving the interaction of biological materials, as this brief work

has begun to indicate. The process of charge transfer has been shown to have a profound influence on biological systems and explains many phenomena not accessible by conventional classical bonding. A charge-transfer bond, an indisputable feature of integrated biological systems, has the magnitude and capacity to direct microscopic molecular architecture similar to that of the conventional hydrogen bond. While weak, the charge-transfer bond has another dimension less apparent in the hydrogen bond: namely, it mediates and modulates energy transfer. As such, it represents a major frontier in research of the integrated living state.

ACKNOWLEDGMENT

K. L. Young is grateful for support from the National Institutes of Health grant 5T34GM08228.

REFERENCES

1. M. A. Slifkin, *Charge Transfer Interactions of Biomolecules*, Academic Press, New York, 1971.
2. G. Briegleb, *Elektronen Donator-Acceptor Complexes*, Springer-Verlag, Berlin, 1961; L. J. Andrews and R. M. Keefer, *Molecular Complexes in Organic Chemistry*, Holden-Day, San Francisco, 1964; J. Rose, *Molecular Complexes*, Pergamon Press, Oxford, 1967; R. S. Mulliken, and W. B. Person, *Molecular Complexes*, Wiley-Interscience, New York, 1969; R. Foster, *Organic Charge-Transfer Complexes*, Academic Press, New York, 1969.
3. R. S. Mulliken, J. Am. Chem. Soc. 74:811 (1952); J. Phys. Chem. 56:801 (1952); J. Phys. Chem. 56:801 (1952).
4. J. C. A. Boeyens and I. H. Herbstein, J. Phys. Chem. 69:2160 (1965).
5. S. G. Christov, J. Res. Inst. Catal. Hokkaido Univ. 24:27 (1970); G. Saito and Y. Matsunaga, Bull. Chem. Soc. Jpn. 46:1609 (1973); 45:963 (1972); 47:2873 (1974); 47:1020 (1974); 46:714 (1973); Y. Matsunaga, Bull. Chem. Soc. Jpn. 48:37 (1975); Y. Matsunaga and R. Osawa, Bull. Chem. Soc. Jpn. 47:1589 (1974); J. M. Dumai et al., J. Chem. Phys. Chem. Biol. 72:1185 (1975); H. Ratajczak et al., Chem. Phys. 17:197 (1976); A. Kofler, Elektrochemistry, 50:200 (1974); G. I. Krishtalik et al., J. Res. Inst. Catal. Hokkaido Univ. 22:101 (1974); R. R. Dogonadze and A. M. Kuznetsov, J. Res. Inst. Catal. Hokkaido Univ. 26:15 (1978); I. Yu Martynov et al., Russ. Chem. Rev. 46:1 (1977); W. Klopffer, Adv. Photochem. 10:311 (1977).
6. M. J. Rice and W. L. Roth, J. Solid State Chem. 4:294 (1972); L. J. Gagliardi, J. Chem. Phys. 57:2193 (1973).
7. J. Koziol and P. Tomasik, Bull. Acad. Pol. Sci. Ser. Sci. Chim. 25:689 (1977).
8. J. M. Dumas and M. Gomel, J. Chim. Phys. 22(10):1185 (1975).
9. R. S. Mulliken, Recl. Trav. Chim. 75:845 (1956); J. Am. Chem. Soc. 72:600 (1950); S. P. McGlynn, Chem. Rev. 58:113 (1958).

10. B. D. Silverman, *Phys. Rev. B* 16:5153 (1977).
11. T. Uchida and H. Akamatu, *Bull. Chem. Soc. Jpn.* 35:981 (1952).
12. A. Ottenberg, C. J. Hoffmann, and J. Osiecki, *J. Chem. Phys.* 38:1898 (1962).
13. L. E. Lyons, *J. Chem. Soc.*, 5001 (1957); J. Fox, *Phys. Chem. Solids* 8:439 (1959); W. P. Person, *J. Chem. Phys.* 38:109 (1963).
14. F. Gutmann, H. Keyzer, and L. E. Lyons, *Organic Semiconductors*, Part B, R. E. Krieger, Malabar, Fl., 1983.
15. O. Kh. Poleshuk and Yu. K. Maksyutin, *Russ. Chem. Rev.* 45:1077 (1976).
16. Y. Matsunaga, *Nature (London)* 211:182 (1966).
17. R. S. Mulliken and W. B. Person, *Molecular Complexes*, Wiley, New York, 1969.
18. T. Montenay-Garestier and C. Helene, *Nature (London)* 217:844 (1968).
19. I. Schroff et al., *Tetrahedron Lett.*, 1649 (1973).
20. V. F. Gachkovskii, *Russ. J. Phys. Chem.* 47:208 (1973).
21. D. W. Slocum et al., *Tetrahedron Lett.* 46:4429 (1971).
22. Z. Witkiewicz, *Viul-Wojsk. Akad. Technol.* 20:69 (1971).
23. F. Cramer, *Einschluss-Verbindungen*, Springer-Verlag, Heidelberg, 1974; J. P. Behr and J. M. Lehn, *J. Am. Chem. Soc.* 98:1743 (1976).
24. J. P. Williams, 5th Keilin Memorial Lecture, *Biochem. Soc. Trans.* 1:1 (1973); G. M. Schwab, *Fortschr. Chem. Forsch.* 25:105 (1972); O. Johnson, *Fortschr. Chem. Forsch.* 22:157 (1974).
25. F. Gutmann et al., *Adv. Biochem. Psychopharmacol.* 9:15 (1974).
26. N. G. Gaylord, *Polym. Prepr. Am. Chem. Soc. Div. Polym. Chem.* 13:505 (1972).
27. J. F. J. Kibblewhite and A. J. Tench, *J. Chem. Soc. Faraday Trans. I* 70:72 (1974).
28. Y. M. Thomas and P. Piciulo, *J. Am. Chem. Soc.* 100:3239 (1978).
29. E. A. G. Aniansson, *Ber. Bunsenges. Phys. Chem.* 82:981 (1978); H. Hoffmann, *Ber. Bunsenges. Phys. Chem.* 82:988 (1978); B. Katusin-Razem et al., *J. Am. Chem. Soc.* 100:1679 (1978); J. H. Fendler and L.-J. Liv, *J. Am. Chem. Soc.* 97:999 (1975).
30. K. Morokuma, *Acc. Chem. Res.* 10:294 (1977).
31. K. Kalnins et al., *Dokl. Akad. Nauk. USSR* 244:400 (1979).
32. E. M. Arnett and E. J. Mitchell, *J. Am. Chem. Soc.* 93:4052 (1971).
33. M. J. Rice and W. L. Roth, *J. Solid State Chem.* 4:294 (1972); L. F. Gagliardi, *J. Chem. Phys.* 58:2193 (1973).
34. G. N. Felix and P. C. Huyskens, *J. Phys. Chem.* 79:316 (1975).
35. F. Strohmusch et al., *J. Phys. Chem.* 82:2447 (1978).
36. W. B. Nixon et al., *Int. J. Mass Spectrom. Ion. Phys.* 26:115 (1978).
37. L. M. Rhodes and P. R. Schimmel, *J. Am. Chem. Soc.* 96:2609 (1974).
38. J. Nishijo, *Bull. Chem. Soc. Jpn.* 47:1539 (1974).
39. M. A. F. Tavares, *Trans. Faraday Soc.* 66:2431 (1970).
40. S. G. Christov, *Collision Theory and Statistical Theory of Chemical Reactions*, Springer-Verlag, Berlin, 1980.

41. B. W. Carey, J. Am. Med. Assoc. 172:1196 (1960).
42. G. M. Eckert, F. Gutmann, and H. Keyzer, Appl. Phys. Commun. 12(3&4):351 (1993) (in press).
43. I. Deperasinska and J. Prochorov, Adv. Mol. Relaxation Interact. Processes 11:51 (1977).
44. W. Klöpffer, Adv. Photochem. 10:311 (1977); I. Yu. Martynov et al., Russ. Chem. Rev. 46:1 (1977).
45. Yu. I. Martinov et al., Khim. Vys. Energ. 11:443 (1977).
46. G. G. Wubles et al., J. Am. Chem. Soc. 95:1281 (1973); A. Cu and A. C. Testa, J. Am. Chem. Soc. 96:1963 (1974).
47. P. Kollman, J. Am. Chem. Soc. 99:4875 (1977).
48. T. Yahabe, J. Chem. Soc. Faraday Trans I 73:1860 (1977).
49. P. Durand and R. Fournie, *Dielectric Materials, Measurement, and Applications Conference*, IEE Conf. Publ. 67, IEE, London, 1970.
50. K. Ishii et al., in *Energy and Charge Transfer* (K. Masuda and M. Silver, eds.), Plenum Press, New York, 1974, p. 183; J. Prakash, J. Chim. Phys. 73:696 (1976); H. Takagi et al., Bull. Chem. Soc. Jpn. 50:1807 (1977).
51. J. M. Bonnier and R. Arnard, J. Chim. Phys. 68:423 (1971); W. Wacklawek, Bull. Acad. Sci. Ser. Sci. Math. Astron. Phys. 21:189 (1973); M. A. Slifkin, in Ref. 1.
52. Y. Y. Borovikov, Izv. Vyssh. Uchebn. Zaved. Khim. Technol. 11:20 (1968).
53. F. Gutmann and H. Keyzer, J. Chem. Phys. 50:550 (1969); Electrochim. Acta 13:693 (1968); A. Brau et al., Electrochim. Acta 17:1803 (1972); J. Caldoford, *Complex Permittivity*, English Univ. Press, London, 1971; D. Bauer et al., J. Phys. Chem. 74:4504 (1970); W. E. Vaughan, Dig. Lit. Dielect. 35:1973 (1971).
54. N. Tyutyulkov et al., Theoret. Chim. Acta (Berlin) 20:385 (1971); H. Beens et al., J. Chem. Phys. 47:1183 (1967).
55. J. Giera et al., *3rd International Symposium on the Specific Interactions of Molecular Ions Proceedings*, Vol. 1, Institute of Chemistry, Univ. Wroclaw, Poland, p. 154.
56. L. Abate and G. Siracusa, Thermochim. Acta 29:157 (1979); I. G. Orlov et al., in *Proceedings of the 3rd All-Union Conference*, 1968 (A. A. Petrov, ed.), Nauk Publishing House, Moscow, 1972.
57. S. Iwrauki and K. Inukai, Makromol. Chem. 179:189 (1978).
58. S. Iwatsuki and K. Inukai, J. Polym. Sci. Polym. Chem. Ed. 12:1437 (1984).
59. S. Iwatsuki and K. Arai, Makromol. Chem. 178:2307 (1977).
60. T. G. Meister and V. P. Klindukhov, Adv. Mol. Relaxation Interact. Processes 13:107 (1978).
61. S. Bagchi and M. Chowdhury, J. Phys. Chem. 83:629 (1979); E. M. Kosower, *An Introduction to Physical Chemistry*, Wiley, New York, 1968.
62. A. Hantzsch, Ber. Deut. Chem. Ges. 52:1535, 1544 (1979); E. M. Kosower, J. Am. Chem. Soc., 3253, 3261, 3267 (1958); J. S. Brinen et al., J. Phys. Chem. 69:3761 (1965).
63. S. Bagchi and M. Chowdhury, J. Phys. Chem. 80:2111 (1976).

64. L. Skulski et al., *Bull. Acad. Pol. Sci. Ser. Sci. Chem.* 21:369 (1973); R. P. Lang, *J. Phys. Chem.* 78:1657 (1967).
65. G. Briegleb, *Angew. Chem.* 76:326 (1964).
66. H. McConnell, J. S. Ham, and J. R. Platt, *J. Chem. Phys.* 21:66 (1953).
67. G. Briegleb and J. Czekalla, *J. Elektrochem.* 63:6 (1959).
68. H. Kuroda, M. Kobayashi, M. Kinoshita, and S. Takimoto, *J. Chem. Phys.* 36:457 (1962).
69. M. Batley and L. E. Lyons, *Nature (London)* 196:573 (1962).
70. E. O. Forster, *J. Chem. Phys.* 37:1021 (1962); 40:869 (1964).
71. H. A. Benesi and J. H. Hildebrand, *J. Am. Chem. Soc.* 71:2703 (1949).
72. R. L. Scott, *Recl. Trav. Chim.* 75:787 (1956).
73. S. Carter, J. N. Murrell, and E. J. Rosch, *J. Chem. Soc.*, 2048 (1965).
74. R. Foster, *Organic Charge-Transfer Complexes*, Academic Press, New York, 1969.
75. R. S. Mulliken and W. B. Person, *Molecular Complexes*, Wiley-Interscience, New York, 1969.
76. M. A. Slifkin and R. H. Walmsley, *Experientia* 25:930 (1969).
77. T. Kagiya, Y. Sumida, and T. Inoue, *Bull. Chem. Soc. Jpn.* 41:767 (1968).
78. S. Beck, A. Hallan, and A. M. North, *Polymer* 20:1177 (1979).
79. S. Arora and C. G. Overberger, *J. Polym. Sci. Polym. Phys. Ed.* 24:2275 (1986).
80. O. Stern and M. Volmer, *Physik Z.* 20:183 (1919).
81. J. B. Birks, *Photophysics*, Wiley-Interscience, London, 1970.
82. M. A. Slifkin, *Nature (London)* 200:766 (1963).
83. F. Gerson, *High Resolution ESR Spectroscopy*, Wiley, New York, 1970; E. E. Budzinski et al., *J. Chem. Phys.* 59:2899 (1973); D. J. Ingram, *Free Radicals As Studied by ESR*, Butterworth, London, 1958; Varian Associates, *NMR and EPR Spectroscopy*, Pergamon Press, Oxford, 1960; P. G. Lykos, in *Advances in Quantum Chemistry* (P. O. Lowdin, ed.), *Electron Spin Relaxation in Liquids* (L. Muus and P. W. Atkins, eds.), Plenum Press, New York, 1972; G. I. Subbotin and R. V. Grechishkins, in *Magnetic Resonance Phenomena: Proceedings of the 16th Ampere Congress, 1970* (I. Ursu, ed.), North-Holland, Amsterdam, 1971; Y. Tomkiewicz et al., *Phys. Rev. Lett.* 32:1363 (1974).
84. J. B. Jones et al., *Nature (London)* 211:309 (1966); K. Tsuji et al., *J. Chem. Phys.* 46:2808 (1967).
85. I. S. Forrest, F. Gutmann, and H. Keyzer, *Rev. Aggressol. (Paris)* 7:147 (1966).
86. F. Gutmann and H. Keyzer, *Electrochim. Acta* 13:693 (1968); H. Keyzer, Ph.D. thesis, Univ. New South Wales, Australia, 1966; *Edit. Note Z. Phys. Chem. (Leipzig)* 259:177 (1978).
87. D. N. Gillbanks, M.Sc. thesis, Victoria Univ. Wellington, New Zealand, 1973.
88. V. Gutmann, *Electrochim. Acta* 21:661 (1976); *Chimia* 31:1 (1977).

89. P. K. Dea and H. Keyzer, *7th International Phenothiazine Conference*, Marseille (J. Barbe et al., eds.), Enlight Associates, San Gabriel, California, 1994.
90. R. Foster, *Organic Charge-Transfer Complexes*, Academic Press, New York, 1969.
91. Y. Matsunaga, *J. Chem. Phys.* 41:1609 (1964).
92. D. A. Seanor, in *Textbook of Polymer Science* (A. D. Jenkins, ed.), North-Holland, Amsterdam, 1972.
- 93.
94. D. K. Davies, *J. Phys. D* 5:162 (1972).
95. W. D. Gill, *J. Appl. Phys.* 43:5033 (1972).
96. F. Gutmann et al., *Adv. Biochem. Psychopharmacol.* 9:15 (1974).
97. G. Eckert et al., *J. Biol. Phys.* 6:161 (1978); *J. Electroanal. Chem. Interfacial Electrochem.* 62:267 (1975); see also Ref. 87.
98. W. B. Nixon et al., *Int. J. Mass Spectrom. Ion. Phys.* 26:115 (1978).
99. M. V. Ramamurthy and A. Quayum, *J. Electrochem. Soc. India* 27:33 (1978).
100. F. Gutmann and H. Keyzer, in *Thiazines and Structurally Related Compounds* (H. Keyzer, ed.), R. E. Krieger, Malabar, Fl., 1992.
101. B. Breyer and H. H. Bauer, *AC Polarography and Tensammetry*, Interscience, New York, 1963; B. Breyer and F. Gutmann, *Austral. J. Sci.* 8:163 (1946); B. Breyer and S. Hacobian, *Austral. J. Chem.* 7:225 (1954); D. Smith, *Crit. Rev. Anal. Chem.* 2:247 (1971).
102. H. Keyzer et al., *7th International Phenothiazine Conference*, Marseille, 1993 (in preparation).
103. Yu. A. Karbainon et al., *Nov. Polyarogr. Tezisydokl. Vses Soveshla Polyarogr., 6th* (J. Stradins, ed.), 1975; B. Kastening, *Prog. Polarogr.* 3:195 (1973); M. E. Peover, *Trans. Faraday Soc.* 60:417, 479 (1964).
104. J. P. Williams, *Diss. Abstr. Int.* 36(8):3950 (B-1976).
105. L. R. Ramaley and S. Gual, *Can. J. Chem.* 56:2381 (1978).
106. J. Wolfe et al., *Melliand Textilber. Int. Ed.* 54:61 (1973); N. Nagy et al., *J. Chem. Soc. Perkins Trans.* 2:1048 (1972); E. J. Rudd and B. E. Conway, *Trans. Faraday Soc.* 67:440 (1971); E. G. Chikayzova, *Usp. Perspekt. Razv. Polyarogr. Metoda*, 164 (1972); R. N. Adams, *Acc. Chem. Res.* 2:175 (1969); G. Dayhurst and P. J. Elving, *Talanta* 16:885 (1969).
107. L. V. Mirovich, *Ostsiologr. Peremenotok Polyarogor.* 126 (1971); K. G. Boto and F. G. Thomas, *Austral. J. Chem.* 26:1669 (1973); V. F. Toropova et al, *Zh. Obsch. Khim.* 43:711 (1973).
108. M. Barigandi et al., *Bull. Soc. Chim. Belges* 79:625 (1970); A. Deslout, *Memoire de License en Sci. Centre Univ., Mons., Belgium*, 1969.
109. G. Eckert and F. Gutmann, *J. Electroanal. Interfacial Electrochem.* 62:267 (1975); G. Eckert et al., *J. Biol. Phys.* 6:161 (1978).
110. M. E. Starzak, *J. Biol. Phys.* 2:57 (1974); D. V. Lamsweerde-Gallez and A. Meessen, *J. Biol. Phys.* 2:75 (1974); R. A. Llenado, *Anal. Chem.* 47:2243 (1975); P. Groll and F. Grass, *Electrochim. Acta* 16:31 (1971).

111. H. S. Nalwa, *J. Mater. Sci. Lett.* 9:1296 (1990).
112. C. M. Huggins and O. H. LeBlanc, *Nature (London)* 186:552 (1960).
113. D. D. Eley and R. S. Snart, *Biochim. Biophys. Acta* 102:379 (1965).
114. B. Rosenberg, T. N. Misra, and R. Switzer, *Nature (London)* 217:423 (1968).
115. J. A. Lucy and F. U. Lichti, *Biochem. J.* 103:34 (1967).
116. J. A. Lucy and F. U. Lichti, *Biochem. J.* 112:231 (1969).
117. R. Foster and T. J. Thomson, *Trans. Faraday Soc.* 58:860 (1962).
118. J. A. Lucy, *Am. J. Clin. Nutr.* 22:1033 (1969).
119. J. A. Lucy, *Proc. Biochem. Soc.* 96:12 (1965).
120. G. Cilento and K. Zinner, *Biochim. Biophys. Acta* 120:84 (1966).
121. H. Z. Sable and J. E. Biaglow, *Proc. Natl. Acad. Sci. USA* 54:808 (1965).
122. J. E. Biaglow, J. J. Mieyal, J. Suchy, and H. Z. Sable, *J. Biol. Chem.* 244:4052 (1968).
123. J. J. Mieyal, J. Suchy, J. E. Biaglow, and H. Z. Sable, *J. Biol. Chem.* 244:4063 (1968).
124. A. Veillard and B. Pullman, *J. Theoret. Biol.* 8:307 (1965).
125. J. G. Heathcote and M. A. Slifkin, *Biochim. Biophys. Acta* 158:167 (1968).
126. J. G. Heathcote and M. A. Slifkin, *Biochim. Biophys. Acta* 158:167 (1968); M. A. Slifkin and J. G. Heathcote, in *Molecular Associations in Biology* (B. Pullman, ed.), Academic Press, New York, 1968.
127. L. Galzigna, *Biochem. Pharmacol.* 18:2485 (1969).
128. D. E. Guttman and D. Brooke, *J. Pharm. Sci.* 52:941 (1963).
129. D. E. Laskowski, *Anal. Chem.* 32:1171 (1960).
130. L. Shutsung and H. C. Williams-Ashman, *Biochem. Pharm.* 6:53 (1961).
131. G. Cilento and M. Berenholc, *Biochem. Biophys. Acta* 120:84 (1966).
132. B. Rosenberg and G. L. Jendrsiak, *Chem. Phys. Lipids* 2:47 (1968).
133. B. Rosenberg and B. B. Bhowmik, *Chem. Phys. Lipids* 3:109 (1968).
134. M. A. Slifkin, *Spectrochim. Acta* 20:1391 (1964).
135. R. Bershon and I. Isenberg, *J. Chem. Phys.* 35:1640 (1961).
136. A. I. Vogel, *Quantitative Inorganic Chemistry*, Longman, London, 1961.
137. J. B. Jones, M. Bershon, and G. C. Neice, *Nature (London)* 211:309 (1969).
138. S. Basu and J. H. Greist, *J. Chim. Phys.*, 407 (1963).
139. C. Helene and A. M. Michelson, *Biochem. Biophys. Acta* 142:12 (1967).
140. M. A. Slifkin, *Nature (London)* 200:766 (1963); see also Ref. 81.
141. G. Weber, *Biochem. J.* 47:114 (1950).
142. T. Shiga and L. H. Petit, *Photochem. Photobiol.* 3:213 (1964); 4:769 (1965).
143. K. Burton, *Biochem. J.* 48:458 (1951).
144. D. W. Miles and D. W. Urry, *Biochemistry* 7:2791 (1968).
145. P. S. Song, *J. Am. Chem. Soc.* 91:1850 (1969).
146. R. H. Sarma, P. Dannies, and N. O. Kaplan, *Biochemistry* 7:4359 (1968).
147. J. A. Roth and D. B. McCormick, *Photochem. Photobiol.* 6:657 (1967).
148. W. Kersten, *Biochim. Biophys. Acta* 47:610 (1961).
149. E. Reich, *Science* 143:684 (1964).
150. L. D. Hamilton, W. Fuller, and E. Reich, *Nature* 196:538 (1963).
151. B. Pullman, *Biochim. Biophys. Acta* 88:440 (1964).

152. M. A. Slifkin, *Biochim. Biophys. Acta* 103:365 (1965).
153. J. C. M. Tsibris, D. B. McCormick, and L. D. Wright, *Biochemistry* 4:504 (1965).
154. B. M. Chassy and D. B. McCormick, *Biochemistry* 4:2612 (1965).
155. W. M. MacIntyre, *Science* 147:507 (1965).
156. B. Pullman and A. Pullman, *Quantum Biochemistry*, Wiley-Interscience, New York, 1963.
157. H. Wenzl, W. Lohmann, and M. Hillerbrand, *Biophys. Struct. Mech.* 1:147 (1975).
158. H. Berthod, C. Greissner-Prettre, and A. Pullman, *Theor. Chim. Acta* 5:53 (1966).
159. B. Pullman and A. Pullman, *Quantum Chemistry*, Interscience, New York, 1963.
160. M. Olin and A. Bertinchamps, in Ref. 157.
161. E. Mathur-De Vré and A. J. Bertinchamps, *Radiat. Environ. Biophys.* 11:135 (1974).
162. P. O. P. T'so, M. P. Schweizger, and D. P. Hollis, *Ann. N.Y. Acad. Sci.* 158:256 (1969).
163. J. Duchesne and P. Machmer, *C.R. Acad. Sci. (Paris)* 260:4279 (1965).
164. J. Booth and E. Boyland, *Biochim. Biophys. Acta* 12:75 (1953).
165. A. M. Licori, B. DeLerma, B. Ascoli, C. Botre, and M. Trasciatti, *J. Mol. Biol.* 8:20 (1964); P. O. P. T'so and P. Lu, *Proc. Natl. Acad. Sci. USA* 51:17 (1964); E. Boyland and B. Green, *Br. J. Cancer* 16:507 (1962).
166. B. S. Giovanella, L. E. McKinney, and C. Heidelberger, *J. Mol. Biol.* 8:20 (1964).
167. E. Boyland and B. Green, *Biochem. J.* 92:4c (1964); E. Boyland, B. Green, and S. L. Liu, *Biochim. Biophys. Acta* 87:653 (1964).
168. B. Green and J. A. McCarter, *J. Mol. Biol.* 29:447 (1967).
169. J. K. Ball, J. A. McCarter, and M. F. Smith, *Biochim. Biophys. Acta* 103:275 (1965).
170. R. S. Snart, *Trans. Faraday Soc.* 63:2384 (1967).
171. D. R. Kearns and M. Calvin, *J. Am. Chem. Soc.* 83:2110 (1961).
172. G. Tollin and G. Green, *Biochim. Biophys. Acta* 60:524 (1962).
173. G. Tollin and G. Green, *Biochim. Biophys. Acta* 66:308 (1962).
174. D. E. Lakowski, *Anal. Chem.* 32:1171 (1960).
175. L. S. Lerman, *Proc. Natl. Acad. Sci. USA* 49:94 (1963).
176. B. L. Van Duuren, B. M. Goldschmidt, and H. H. Seltzman, *Ann. N.Y. Acad. Sci.* 153:744 (1969), and references therein.
177. D. L. Boger et al., *Chem.-Biol. Interact.* 73:29 (1990).
178. M. J. Waring, *J. Mol. Biol.* 13:269 (1965).
179. J. B. Le Pecq and A. Paoletti, *J. Mol. Biol.* 27:87 (1967).
180. J. O. Olmsted III and D. R. Kearns, *Biochemistry* 16:3647 (1977).
181. L. M. Davis, J. D. Harvey, and B. C. Baqule, *Chem.-Biol. Interact.* 62:45 (1985).
182. T. Forster, *Disc. Faraday Soc.* 27:7 (1959).

183. J. L. Julina, A. Lindsay, B. C. Baguley, and W. A. Denny, *J. Med. Chem.* 30:473 (1987).
184. A. I. Minkov, Dissertation, Institute of Catalysis, Siberian Branch of the USSR Academy of Sciences, Novosibirsk, 1967.
185. B. D. Beregin and G. V. Sennikova, *Kinet. Katal.* 9:528 (1968); *Zh. Fiz. Khim.* 43:2499 (1969).
186. D. R. Kearns, G. Tollin, and M. Calvin, *J. Chem. Phys.* 32:1020 (1960).
187. J. Keilin, *Biochem. J.* 37:281 (1943).
188. D. Mauzerall, *Biochemistry* 4:1801 (1965).
189. J. R. Cann, *Biochemistry* 6:3427 (1967).
190. J. R. Cann, *Biochemistry* 6:3435 (1967).
191. J. G. Heathcote, G. J. Hill, P. Rothwell, and M. A. Slifkin, *Biochim. Biophys. Acta* 153:13 (1968).
192. J. R. Cann, *Biochemistry* 8:4036 (1969).
193. M. Gouterman and P. E. Stevenson, *J. Chem. Phys.* 37:2266 (1962).
194. H. A. O. Hill, A. J. MacFarlane, and R. J. P. Williams, *J. Chem. Soc. (A)*, 1704 (1969).
195. D. D. Eley and R. S. Snart, *Biochim. Biophys. Acta* 102:379 (1965).
196. A. Mitsui, A. Ueharata, H. Nakamura, and T. Matsuo, *Chem. Lett. Chem. Soc. Jpn.* 1445 (1989).
197. G. Geib, H. Keyzer, and K. G. Reimer, in *Conducting Polymers*, (L. Alcácer, ed.), D. Reidel, New York, 1987.
198. F. Gutmann and H. Keyzer, *J. Chem. Phys.* 46:1969 (1967).
199. W. B. Euler, J. Martinsen, L. J. Pace, B. M. Hoffman, and J. A. Ibers, *Mol. Cryst. Liq. Cryst.* 81:949, 231 (1982).
200. H. C. Freeman, *J. Proc. R. Soc. N. S. W.* 112:60 (1979).
201. T. J. Dougherty, in *Advances in Experimental Medicine and Biology*, Vol. 160 (A. Cubbedu, ed.), Plenum Press, New York, 1983.
202. D. Kessel, *Photochem. Photobiol.* 44(2):193 (1986).
203. G. Gadonas et al., *Chem. Phys. Lett.* 129:603 (1986).
204. E. J. Land, *J. Radioanal. Nucl. Chem.* 101(2):189 (1986).
205. D. Kessel, *Cancer Res.* 46(5):2248 (1986).
206. F. Gutmann, L. C. Smith, and M. A. Slifkin, in *Phenothiazines and Structurally Related Drugs* (E. S. Forrest, C. J. Carr, and E. Usdin, eds.), Raven Press, New York, 1974.
207. D. N. Gillbanks, in Ref. 87.
208. L. Galzigna, *Nature (London)* 225:1058 (1970).
209. G. Cilento and K. Zinner, *Biochim. Biophys. Acta* 143:93 (1967).
210. I. Isenberg and A. Szent-Györgyi, *Proc. Natl. Acad. Sci. USA* 44:857 (1958).
211. A. Fulton and L. E. Lyons, *Aust. J. Chem.* 20:2267 (1967).
212. P. Douzou, in *Molecular Associations in Biology* (B. Pullman, ed.), Academic Press, New York, 1968.
213. C. I. Simonescu and M. Grigoras, *Prog. Polym. Sci.* 16:907 (1991).
214. S. Tazuke and H. Nagahara, *Makromol. Chem.* 181:2217 (1980).
215. V. Percec, A. Natansohn, and C. I. Simionescu, *Polym. Bull.* 5:217 (1981).

- 216. S. Tazuke and H. Nagahara, *J. Polym. Sci. Polym. Lett. Ed.* 16:525 (1978).
- 217. Q. H. Gibson, V. Massey, and N. M. Atherton, *Biochem. J.* 85:369 (1962).
- 218. J. Ludowieg and A. Levy, *Biochemistry* 3:373 (1964).
- 219. S. Shinkai, K. Tamaki, and T. Kunitake, *Bull. Chem. Soc. Jpn.* 48(6):1918 (1975).
- 220. E. M. Kosower, *J. Am. Chem. Soc.* 78:3497 (1956).
- 221. S. F. Velick, *J. Biol. Chem.* 233:1455 (1958).
- 222. S. Shifrin, *Biochim. Biophys. Acta* 81:205 (1964).
- 223. S. Shifrin, *Biochemistry* 3:829 (1964).
- 224. F. W. Cope, in *Bioelectrochemistry* (H. Keyzer and F. Gutmann, eds.), Plenum Press, New York, 1980.
- 225. H. Pelletier and J. Krout, *Science* 258:1748 (1992).
- 226. S. Mieloszyk, K. Ulbrich, and R. Drabent, *Stud. Biophys.* 115(3):181 (1986).
- 227. E. Dale, D. Edmonson, B. A. C. Ackrell, and E. B. Kearney, *Arch. Biochem. Biophys.* 228:69 (1981).
- 228. M. R. Eftink and G. A. Ghiron, *Arch. Biochem. Biophys.* 209:706 (1981).
- 229. T. E. Mifflin and N. Langerman, *Arch. Biochem. Biophys.* 224:319 (1983).
- 230. K. L. Mittal, ed., *Micellization, Solubilization, and Microemulsions*, Vol. I, Plenum Press, New York, 1977.
- 231. J. H. Fendler, *Acc. Chem. Res.* 9:153 (1976).
- 232. E. H. Cordes and R. B. Dunlap, *Acc. Chem. Res.* 2:329 (1969).
- 233. E. J. Fendler and J. H. Fendler, *Adv. Phys. Org. Chem.* 8:271 (1970).
- 234. E. H. Cordes and C. Gitler, *Prog. Bioorg. Chem.* 2:1 (1973).
- 235. C. A. Bunton, *Prog. Solid State Chem.* 8:239 (1973).
- 236. I. V. Berezin, K. Martinek, and A. K. Yatsimirski, *Russ. Chem. Rev.* 42:787 (1973).
- 237. C. J. O'Connor, E. J. Fendler, and J. H. Fendler, *J. Am. Chem. Soc.* 95:600 (1973); *J. Chem. Soc. Dalton Trans.*, 625 (1974).
- 238. S. Kuroda, K. Ikegami, and M. Sugi, *Mol. Cryst. Liq. Cryst.* 190:111 (1990).
- 239. M. F. Budyka, A. G. Rachinsky, and M. V. Alfimov, *Chem. Phys. Lett.* 181(1):59 (1991).
- 240. A. T. Florence, in Ref. 230.
- 241. S. S. Brody, *J. Theor. Biol.* 7:352 (1964).
- 242. A. T. Florence, *Adv. Colloid Interface Sci.* 2:115 (1968).
- 243. R. J. Baldessarini, in *Handbook of Psychopharmacology*, Vol. 3 (S. D. Iverson and S. H. Snyder, eds.), Plenum Press, New York, 1975; H. G. Weder and U. W. Wiegand, *FEBS Lett.* 38:64 (1973).
- 244. H. Keyzer, C. Lowe, W. Plumtree, and F. Gutmann, in *4th International Conference on Phenothiazines and Related Drugs* (H. Eckert, I. S. Forrest, and E. Usdin, eds.), Elsevier, Amsterdam, 1980.
- 245. G. M. Eckert, F. Gutmann, and H. Keyzer, *Xenobiotica* 19(5):567 (1989).
- 246. G. Foder, R. Mujunder, and A. Szent-Györgyi, *Proc. Natl. Acad. Sci. USA* 75:4317 (1978).
- 247. H. D. Dakin and H. W. Dudley, *J. Biol. Chem.* 14:155 (1913); C. Neuberg, *Biochem. Z.* 49:202 (1913).

- 248. R. Pething and A. Szent-Györgyi, in *Bioelectrochemistry* (H. Keyzer and F. Gutmann, eds.), Plenum Press, New York, 1980.
- 249. S. Bone et al., *Proc. Natl. Acad. Sci. USA* 75(1):315 (1978).
- 250. A. Bonsignore et al., *Ital. J. Biochem.* 26:162 (1977).
- 251. L. Lorand, in R. Pething, *Int. J. Quantum Chem. Quantum Biol. Symp.* 5:159 (1978).
- 252. R. A. Bogomolni, in Ref. 224.
- 253. R. Pethig and A. Szent-Györgyi, *Proc. Natl. Acad. Sci. USA* 74:226 (1977).
- 254. E. Silinsh, *Phys. Status Solidi (a)* 25:339 (1974).
- 255. L. E. Lyons, in Ref. 224.
- 256. T. Imura, T. Furutsuka, and K. Kawabe, *Photochem. Photobiol.* 22:129 (1975).
- 257. V. B. Estigneev et al., *Dokl. Akad. Nauk SSSR* 230:726 (1976).
- 258. A. Chibisov, *Dok. Akad. Nauk SSSR* 175:230 (1967); *Photochem. Photobiol.* 10:331 (1969).
- 259. K. Seifert and H. T. Witt, *Naturwissenschaften* 55:222 (1968).
- 260. A. R. Kelly and G. Porter, *Proc. R. Soc. London A* 319:319 (1970).
- 261. R. Livingston and P. J. McCartin, *J. Am. Chem. Soc.* 80:4826 (1963).
- 262. V. B. Estigneev et al., *Dokl. Akad. Nauk SSSR* 203:1346 (1972).
- 263. A. Bromberg, C. W. Tang, and A. C. Albrecht, *J. Chem. Phys.* 60:4058 (1974).
- 264. N. K. Boardman, W. S. Chow, J. T. Duniec, and S. W. Thorne, in Ref. 224; G. A. Seely, *Photochem. Photobiol.* 27:639 (1978).
- 265. T. Watanabe, T. Muiasaka, A. Fujishima, and K. Honda, *Chem. Lett.* 4:443 (1978).
- 266. Y. S. Meilanov, V. A. Benderskii, and L. A. Blyumenfeld, *Biophysics* 15:851 (1970).
- 267. J. Nakata, T. Imura, and K. Kawabe, *J. Phys. Soc. Jpn.* 42:146 (1971).
- 268. P. Oesterhelt and W. Stoeckenius, *Nature (New Biol.)* 233:149 (1971).
- 269. A. E. Blaurock and W. Stoeckenius, *Nature (New Biol.)* 233:152 (1971).
- 270. S. C. Kushawa, M. Kates, and W. Stoeckenius, *Biochem. Biophys. Acta* 426:703 (1976).
- 271. W. Stoeckenius, R. H. Lozier, and R. A. Bogomolni, *Biochem. Biophys. Acta* 505:215 (1979); P. N. T. Unwin and R. Henderson, *J. Mol. Biol.* 94:425 (1975); R. Henderson and P. N. T. Unwin, *Nature (London)* 94:957 (1975).
- 272. Yu. Orchinnokov, N. G. Abdulaev, M. Yu. Feigina, A. V. Kiselev, N. A. Lobanov, and I. V. Nasimov, *Bioorg. Chim.* 4:1593 (1978).
- 273. H. T. Witt, *Quart. Rev. Biophys.* 4(4):365 (1971).
- 274. B. Chance and M. Nishimura, *Proc. Natl. Acad. Sci. USA* 46:19 (1960).
- 275. A. D. Gochev and S. G. Christov, *Dokl. Bulg. Akad. Nauk.* 32(3):321 (1979).
- 276. M. Redi and J. J. Hopfield, *Bull. Am. Phys. Soc.* 24:346 (1979).
- 277. M. J. Potasek and K. W. Beeson, *Bull. Am. Phys. Soc.* 24:344 (1979).

Related Topics II: Thallium-Based High- T_c Superconducting Oxides

M. Paranthaman

Oak Ridge National Laboratory, Oak Ridge, Tennessee

Allen M. Hermann

University of Colorado at Boulder, Boulder, Colorado

I. INTRODUCTION

Since the discovery of high-temperature superconducting oxides in the La–Ba–Cu–O system with a superconducting transition temperature (T_c) up to 40 K by Bednorz and Muller [1], many researchers all over the world have been striving for an understanding of the mechanism of high-temperature superconductivity and searching for new materials with even higher T_c values. Accordingly, Wu et al. [2] have discovered a superconductor with a T_c value up to 91 K (above liquid nitrogen temperature) in the Y–Ba–Cu–O system. Michel et al. [3] found a superconductor near 20 K in the Bi–Sr–Cu–O system. The addition of Ca to this system by Maeda et al. [4] has led to the discovery of 80 K and 110 K superconducting phases in the Bi–Sr–Ca–Cu–O system. Following this work, Sheng and Hermann's [5] discovery of superconductivity in the Tl–Ba–Ca–Cu–O system led to the discovery of 125 K superconductors. Cava et al. [6] subsequently have discovered a superconductor near 70 K in the Pb–Sr–Ca–Y–Cu–O system. Recently, Putlin et al. [7] have discovered a superconductor in the Hg–Ba–Cu–O system with a T_c value of 94 K. The superconducting properties of this material are found to be encouraging [8–10]. Very recently, Schilling et al. [11] have discovered a superconductor with a T_c value of 133 K (the highest T_c value of a known oxide superconductor to date) in the Hg–Ba–Ca–Cu–O system. During the last seven years, several high-

temperature superconductors were discovered. A summary of all the known copper oxide superconductors is shown in Table 1. These high-temperature superconductors have the properties of low-dimensional (highly anisotropic) materials similar to those of organic superconductors. Both classes of materials have relatively small and quite similar carrier concentrations [12]. The first organic superconductors were the Bechgaard salts, (TMTSF)₂X (X = PF₆, ClO₄, etc.) discovered in 1980 by Jerome et al. [13] with a *T_c* value ~ 1 K. Following this work, several organic superconductors were discovered. These organic superconductors are mostly electron charge-transfer salts [14]. In 1991, Hebard et al. [15] discovered K₃C₆₀, a potassium salt of buckminsterfullerene, C₆₀, with a *T_c* value of 19 K. Immediately, a compound of rubidium, cesium, and buckminsterfullerene, Rb₂CsC₆₀, with

Table 1 Summary of the Known Copper-Oxide Superconductors

Composition ^a	<i>T_c</i> (K)
(La _{2-x} Sr _x)CuO ₄ (T-structure) (Ca,Ba)	20–40
(Nd _{2-x} Ce _x)Cu(O _{4-y} F _y) (T-structure) (Th)	10–27
(La _{1.8-x} Dy _x Sr _{0.2})CuO ₄ (T*-structure)	20
YBa ₂ Cu ₃ O ₇	70–91
(Cu ₄ O ₈ or Cu ₇ O ₁₅) (Sr ₂ Cu ₂ GaO ₇)	
Bi ₂ Sr ₂ Ca _{n-1} Cu _n O _{2n+4+x} (<i>n</i> = 1–3) (Pb)	10–110
Tl ₂ Ba ₂ Ca _{n-1} Cu _n O _{2n+4-x} (<i>n</i> = 1–3)	90–128
Tl ₁ Ba ₂ Ca _{n-1} Cu _n O _{2n+3-x} (<i>n</i> = 1–4)	10–122
(Tl,Pb)Sr ₂ Ca _{n-1} Cu _n O _{2n+3-x} (Hg)	0–122
Pb ₂ (Sr _{2+x} Pr _{1-x})Cu ₃ O ₈	70–85
(Pb,Cu)Sr ₂ (Ca,Y)Cu ₂ O ₇ (Cd,Hg,Mg)	60–92
Bi ₂ Sr ₂ (Sm _{2-2x} Ce _{2x})Cu ₂ O ₁₀	20–25
Ba _{1.33} Nd _{0.67} Sm _{1.33} Ce _{0.67} Cu ₃ O ₉	40
(La _{2-x} Sr _x)CaCu ₂ O ₆ (two-layer)	60
NbSr ₂ (Nd,Ce) ₂ Cu ₂ O _x (Ta)	28
(Sr _{0.84} Nd _{0.16})CuO ₂ (infinite-layer) (La,Eu)	40
Hg ₁ Ba ₂ Ca _{n-1} Cu _n O _{2n+2+x} (<i>n</i> = 1–4)	95–133

^aPossible partial substitutions are given in parentheses.

a T_c value of 33 K (the highest T_c value of a known organic superconductor until today) [16] was discovered. For more details regarding organic superconductors, refer to Chapter 10 in this book. Since one of us (Allen M. Hermann) is the co-discoverer of the thallium-based high-temperature superconductors, and since these superconductors represent a prototypical and important class nearing commercialization, it is appropriate for us to provide a summary of the thallium-based high-temperature superconductors in this chapter. For more details on the other high-temperature superconductors, the reader is referred to the literature [17–24].

Soon after the discovery of high-temperature superconductivity in the Tl–Ba–Ca–Cu–O system by Sheng and Hermann [5], two families of Tl compounds were identified [25–36]. They are (1) single-Tl-O layered compounds with the general formula $\text{TlBa}_2\text{Ca}_{n-1}\text{Cu}_n\text{O}_{2n+3}$ ($n = 1$ to 4), and (2) double Tl-O-layered compounds with the general formula $\text{Tl}_2\text{Ba}_2\text{Ca}_{n-1}\text{Cu}_n\text{O}_{2n+4}$ ($n = 1$ to 3). The single-Tl-O-layered compounds, $\text{TlBa}_2\text{CuO}_5$ (hereafter denoted as Tl-1201), $\text{TlBa}_2\text{CaCu}_2\text{O}_7$ (Tl-1212), $\text{TlBa}_2\text{Ca}_2\text{Cu}_3\text{O}_9$ (Tl-1223), and double-Tl-O layered compounds, $\text{Tl}_2\text{Ba}_2\text{CuO}_6$ (Tl-2201), $\text{Tl}_2\text{Ba}_2\text{CaCu}_2\text{O}_8$ (Tl-2212), $\text{Tl}_2\text{Ba}_2\text{Ca}_2\text{Cu}_3\text{O}_{10}$ (Tl-2223) are basically intergrowth structures with the conducting $\text{Ca}_{n-1}(\text{CuO}_2)_n$ layers and blocking BaO-TlO-TlO-BaO (for double-Tl-O layers) layers. The ideal crystal structures of these phases are shown in Fig. 1.

II. VARIOUS SITE SUBSTITUTIONS IN $\text{Tl}_2\text{Ba}_2\text{CuO}_6$ SYSTEMS

$\text{Tl}_2\text{Ba}_2\text{CuO}_6$ is the $n = 1$ member of the $\text{Tl}_2\text{Ba}_2\text{Ca}_{n-1}\text{Cu}_n\text{O}_{2n+4}$ family. A very interesting feature of this material is that by annealing the superconductor in oxygen at around 350°C, one can achieve a normal metallic state. On reannealing the normal metallic sample in N_2 or Ar, one can regain the superconducting state even with a loss of oxygen of only about 0.04. Hence, by varying the oxygen content in Tl-2201 by differing annealing conditions, one can vary the electronic properties from those of a normal metal to those of a high-temperature superconductor with varying T_c values [30,34,36–40]. Due to Tl toxicity and volatilization during synthesis, safety procedures must be followed carefully.

Tl-2201 exists in two crystal symmetries, tetragonal and orthorhombic. Even though Hewat et al. [36] claimed that the tetragonal symmetry is responsible for the superconducting behavior, Shimakawa et al. [37] showed that the superconducting properties do not depend on the symmetry of the structure (tetragonal versus orthorhombic) but on the total oxidation state of the sample. Hence by using different synthetic conditions, one can prepare either tetragonal or orthorhombic superconducting samples [37,41]. Several sources of oxidation have been suggested in the literature: the

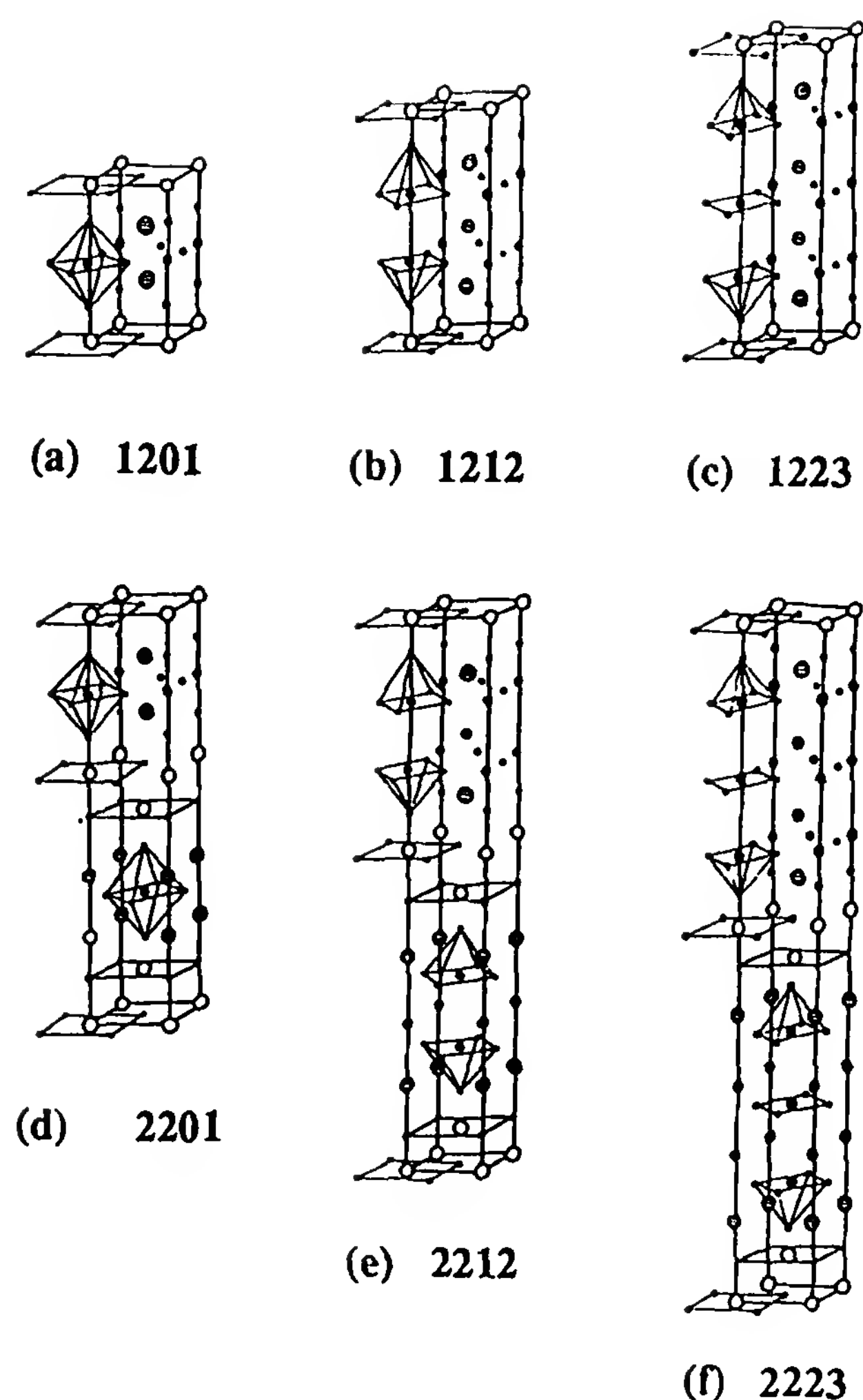


Figure 1 Ideal crystal structures of (a) $\text{TlBa}_2\text{CuO}_5$; (b) $\text{TlBa}_2\text{CaCu}_2\text{O}_7$; (c) $\text{TlBa}_2\text{Ca}_2\text{Cu}_3\text{O}_9$; (d) $\text{Tl}_2\text{Ba}_2\text{CuO}_6$; (e) $\text{Tl}_2\text{Ba}_2\text{CaCu}_2\text{O}_8$; (f) $\text{Tl}_2\text{Ba}_2\text{Ca}_2\text{Cu}_3\text{O}_{10}$. \bigcirc , Tl; \ominus , Ca; \oplus , Ba; \bullet , Cu; \cdot , O.

presence of Tl vacancies [30,36,37], mixed-valent Tl in the Tl_2O_2 layer [40,42–45], and/or excess oxygen in the Tl_2O_2 layer [41,46]. Band-structure calculations [45], XPS measurements [42], and wet-chemical analysis [40] have proved the existence of mixed valency ($3+$ and $1+$) for Tl, and hence the origin of hole concentration in Tl-2201 is the overlap of the Tl-6s band with the conduction band of the CuO_2 sheets. This can be represented by a simple equation:



Tl-2201 has high anisotropy [47–52] with two-dimensional behavior as well [50–52]. The details of the crystal structure, bulk synthesis, crystal growth, calculated band structure, electronic transport properties, and pressure

dependence of T_c on Tl-2201 have been reported elsewhere [51,52]. A summary of the various site substitutions in the Tl-2201 system is shown in Table 2.

A. Substitution of La at Ba Sites

In the $\text{Tl}_{2-y}\text{Ba}_{2-z}\text{La}_z\text{CuO}_{6-x}$ system, single-phase material can be prepared only in the range $0 \leq z \leq 0.2$ [42,53,54]. Attempts to make a single phase of semiconducting $\text{Tl}_2\text{Ba}_2\text{CuO}_6$ by using higher La concentrations ($z > 0.2$) [54] have failed. Nakajima et al. [42] have demonstrated an overdoped state of Tl-2201 by annealing $z = 0.2$ (La-doped) sample in oxygen; they obtained an 80 K superconductor. In contrast, pure Tl-2201 sample on annealing in oxygen becomes a normal metal down to 4.2 K. In the $\text{Tl}_{2-y}\text{Ba}_{2-z}\text{La}_z\text{CuO}_{6-x}$ system, samples with a starting $y = 0.00$ and 0.35 for $0 \leq z \leq 0.2$ are synthesized at 860 to 880°C in sealed gold tubes and quenched in liquid N_2 by Paranthaman et al. [54]. All the samples are tetragonal. During the O_2 anneal, samples with starting $y = 0.00$ extruded thallium to form Tl_2O_3 and were transformed from a tetragonal to an orthorhombic structure; samples with starting $y = 0.35$ were not transformed. Recently, Shimakawa et al. [55] have obtained results similar to Paranthaman et al. [56,57] on pure Tl-2201 samples (i.e., they observe a transformation of tetragonal to orthorhombic with extrusion of Tl_2O_3).

B. Substitution of Sr at Ba Sites

In the $\text{Tl}_2\text{Ba}_{2-z}\text{Sr}_z\text{CuO}_6$ system, Ganguli and Subramanian [58] have obtained single-phase materials in the range $0 \leq z \leq 1.2$. All the samples

Table 2 Summary of the Various Site Substitutions in $\text{Tl}_2\text{Ba}_2\text{CuO}_6$ Systems

Composition	Structural and physical properties	Refs.
1. $\text{Tl}_2\text{Ba}_2\text{CuO}_6$	$T_c = 0\text{--}90$ K, tetragonal I4/mmm, $a = 3.866$, $c = 23.239$ Å	26
2. $\text{Tl}_2(\text{Ba}_{2-z}\text{Sr}_z)\text{CuO}_6$	$z = 0.0$, $T_c = 90$ K; $z = 1.0$, $T_c \sim 20$ K; $z = 1.2$, metal down to 4.2 K	58
3. $\text{Tl}_2(\text{Ba}_{2-z}\text{La}_z)\text{CuO}_6$	$z = 0\text{--}0.2$, single phase	42,54
4. $(\text{Tl}_{2-z}\text{Cd}_z)\text{Ba}_2\text{CuO}_6$	$z = 0\text{--}0.7$, single phase; $z = 0.0$, $T_c = 92$ K; $z = 0.5$, metal	46
5. $\text{Tl}_{2.2}\text{Ba}_2\text{CeCu}_3\text{O}_{9.3}$	$T_c = 90$ K, multiphase	59
6. $\text{Tl}_{2.2}\text{Ba}_2\text{ThCu}_3\text{O}_{9.3}$	$T_c = 75$ K, multiphase	60

were tetragonal and similar to the parent $\text{Tl}_2\text{Ba}_2\text{CuO}_6$ phase. Both the lattice parameters a and c decrease with increasing Sr content. T_c also decreases very slowly as a function of z . Above $z = 0.8$, T_c drops sharply, and at $z = 1.2$, the material becomes normal down to 4.2 K. Substitution of the less electropositive Sr for the more electropositive Ba in $\text{Tl}_2\text{Ba}_2\text{CuO}_6$ should bring down the Tl-6s band and should increase the overlap of Tl-6s band with Cu $3d_{x^2-y^2}$ and hence increase the hole concentration. Hence the decrease of T_c value with increase of z is probably associated with the overdoping of the CuO_2 sheets.

C. Substitution of Cd at Tl Sites

In the $\text{Tl}_{2-z}\text{Cd}_z\text{Ba}_2\text{CuO}_6$ system, Parise et al. [46] obtained the single-phase material in the range $0 \leq z \leq 0.7$ using BaO or BaO_2 as sources of barium. The T_c varied smoothly (downward) from 92 K at $z = 0.0$ to normal metallic behavior at $z = 0.5$ when BaO_2 was used. When BaO was used as the Ba source, however, T_c increased from 65 K at $z = 0.0$ to 90 K at $z = 0.2$ and decreased as z increased further, and finally, the material became a normal metal at $z = 0.7$. These observations suggest that (1) the T_c depends on the average Cu oxidation state, and (2) the hole concentration can be adjusted by varying oxygen or by cation doping. Also, a decrease in the Cu—O bond length (usually half of lattice parameter a in Tl compounds) is correlated with the oxidation of the CuO_2 sheets. An increase in the c -axis parameter results from substitution of the larger Cd^{2+} for Tl^{3+} .

D. Substitution of Ce and Th in Tl-2201 Phase

Wang et al. [59] obtained a T_c value of 90 K with a nominal starting composition of $\text{Tl}_{2.2}\text{Ba}_2\text{CeCu}_3\text{O}_{9.3}$. Since the product is a multiphase with mainly Tl-2201 phase, the research is still open to find whether or not Ce is really going inside the Tl-2201 lattice. Following this work, Thomas et al. [60] have attempted to incorporate Th, Pr, Tb, Pb, and Te. However, they also obtained multiphase samples with mainly Tl-2201 phase. Also, the T_c value obtained was 75 K for Th, and other dopants showed still lower T_c . Since all these samples are multiphase; we cannot comment about the variation of hole concentration with T_c .

III. VARIOUS SITE SUBSTITUTIONS IN $\text{Tl}_2\text{Ba}_2\text{CaCu}_2\text{O}_8$ SYSTEMS

$\text{Tl}_2\text{Ba}_2\text{CaCu}_2\text{O}_8$ is the $n = 2$ member of the $\text{Tl}_2\text{Ba}_2\text{Ca}_{n-1}\text{Cu}_n\text{O}_{2n+4}$ family. The $\text{Tl}_{2-y}\text{Ba}_2\text{CaCu}_2\text{O}_{8-x}$ samples can be obtained as a single phase with

y in the range $0 < y < 0.5$ by both the gold-foil and the sealed-gold-tube methods [56,57]. The crystal symmetry is tetragonal. Unlike Tl-2201, on annealing in oxygen, the T_c value does not vary much [57]. Also, this system does not exhibit any macroscopic transformation from tetragonal to orthorhombic symmetry with the extrusion of Tl to form Tl_2O_3 [57]. The lack of any orthorhombic distortion where the Cu has only one apical c -axis oxygen near neighbor rather than two as in the Tl-2201 case would seem to suggest that a cooperative tilting of the CuO_6 octahedra in the Tl-2201 system may accompany an ordered removal of Tl to induce a long-range ordering. But this speculation needs to be verified by neutron diffraction. The insensitivity of T_c to both Tl and O content would seem to suggest that the charge transfer between CuO_2 planes and Tl-6s states tends to be self-adjusted so as to maximize T_c .

$\text{Tl}_2\text{Ba}_2\text{CaCu}_2\text{O}_8$ single crystals have been grown by the self-flux technique [51]. The out-of-plane resistivity ρ_c is greater than in-plane resistivity ρ_{ab} by about two orders of magnitude [51,61]. Morosin et al. [62] have suggested that strain, Tl content, and Tl/Ca site disorder might also be important as the oxygen content in determining T_c . A summary of various site substitutions in polycrystalline Tl-2212 systems is shown in Table 3.

A. Substitution of Sr or Mg at Ba Sites

In the $\text{Tl}_2\text{Ba}_{2-x}\text{Sr}_x\text{Cu}_2\text{O}_8$, Hayri and Greenblatt [64] have made the solid solutions in the range $0 \leq x \leq 2$. Some line broadening of x-ray peaks and impurity peaks are observed for $x = 1.0$. As x approaches 2.0, more impurity peaks are observed along with the major Tl-2212 phase. The lattice

Table 3 Summary of the Various Site Substitutions in $\text{Tl}_2\text{Ba}_2\text{CaCu}_2\text{O}_8$ Systems

Composition	Structural and physical properties	Refs.
1. $\text{Tl}_2\text{Ba}_2\text{CaCu}_2\text{O}_8$	$T_c = 110$ K, tetragonal I4/mmm, $a = 3.855$, $c = 29.318$ Å	63
2. $\text{Tl}_2(\text{Ba}_{2-x}\text{Sr}_x)\text{CaCu}_2\text{O}_8$	$x = 0.0$, $T_c = 105$ K; $x = 2.0$, $T_c = 44$ K	64
3. $\text{Tl}_2(\text{Ba}_{2-x}\text{Mg}_x)\text{CaCu}_2\text{O}_8$	$x = 0\text{--}0.2$, single phase; $x = 0.0$, $T_c = 110$ K; $x = 0.1$, high J_c	65,66
4. $\text{Tl}_2\text{Ba}_2(\text{Ca}_{1-x}\text{Y}_x)\text{Cu}_2\text{O}_8$	$x = 0\text{--}0.6$; $x = 0.48$, AF semiconductor $x = 0\text{--}0.3$; single phase; $x = 0.3$, AF semiconductor	67 68

parameters a and c and also T_c decrease very slowly as a function of x . At $x = 2.0$, the T_c obtained is 44 K.

In the $\text{Tl}_2\text{Ba}_{2-x}\text{Mg}_x\text{CaCu}_2\text{O}_8$ system, Paranthaman et al. [65,66] obtained the single phase in the range $0 \leq x \leq 0.2$. The sample with $x = 0.3$ was multiphase with a majority of Tl-2212 phase. Magnetization measurements on these samples at 5 K between 0 and 4.5 T have shown that the 5 at % Mg-doped Tl-2212 ($x = 0.1$) samples have enhanced pinning, as demonstrated by a field-dependent increase in the magnetic critical-current density J_c by 18 to 25% over that of pristine Tl-2212 [65,66]. Excess Mg (10 to 15 at %; $x = 0.2$ to 0.3), however, is deleterious. Rietveld refinement of the x-ray diffraction pattern showed Mg on the Tl sites. Auger electron spectroscopy (AES) analysis showed part of the Mg on grain boundaries. The flux-creep activation energies are higher for flux expulsion than for flux penetration in both Tl-2212 [69] and 5 at % Mg-doped Tl-2212 [65,66] samples.

B. Substitution of Y at Ca Sites

In the $\text{Tl}_2\text{Ba}_2\text{Ca}_{1-x}\text{Y}_x\text{Cu}_2\text{O}_8$ system, Poddar et al. [67] produced single-phase superconductors in the range $0 \leq x \leq 0.6$. The T_c decreases with x . At $x = 0.48$, a metal–insulator transition is observed. In contrast, Paranthaman et al. [56,68] obtained single-phase material only in the range $0 \leq x \leq 0.3$. Also, at $x = 0.3$, the samples become antiferromagnetic semiconductors. The variation of hole concentration and T_c in this system has been reported elsewhere [68]. The hole concentration and T_c decreases with x . The discrepancies between two groups could be due to chemical inhomogeneity and to the partial substitution of Ca at the Tl sites.

IV. VARIOUS SITE SUBSTITUTIONS IN $\text{Tl}_2\text{Ba}_2\text{Ca}_2\text{Cu}_3\text{O}_{10}$ SYSTEMS

$\text{Tl}_2\text{Ba}_2\text{Ca}_2\text{Cu}_3\text{O}_{10}$ is the $n = 3$ member of the $\text{Tl}_2\text{Ba}_2\text{Ca}_{n-1}\text{Cu}_n\text{O}_{2n+4}$ family. The T_c value obtained for this phase was 125 K [28]. $\text{Tl}_2\text{Ba}_2\text{Ca}_2\text{Cu}_3\text{O}_{10}$ single crystals can be grown using a self-flux technique with different starting compositions [27,70–73]. The resistivity anisotropy (ρ_c/ρ_{ab}) is quite high and is on the order of 50 to 60 at 300 K [72]. The presence of mixed valency (Tl^{3+} and Tl^+) in Tl-2223 phase has been established from band-structure calculations [45], XPS analysis [43], and from wet-chemical analysis data [74–76]. Meyer et al. [77] have measured the density of states (DOS) by photoemission and inverse photoemission experiments on polycrystalline Tl-2223 samples and have found good correlation between their results and the DOS calculated by Marksteiner et al. [78] using full-potential

linearized augmented-plane-wave (FLAPW) calculations of the band structures. A summary of various site substitutions in polycrystalline Tl-2223 system is shown in Table 4.

A. Substitution of Ca at Tl sites

Single-phase Tl-2223 samples are prepared in the $Tl_{2-x-z}Ba_2Ca_{2+x}Cu_3O_{10-y}$ system (z represents Tl vacancies in the range 0.22 to 0.27 and y represent oxygen vacancies in the range 0.17 to 0.33) with x between 0 and 0.4 [75,76]. All samples were found to be tetragonal. The T_c value varied between 112 and 118 K for the “as-synthesized” samples. The T_c value increased with increasing hole concentration. The origin of holes for all these samples is due to Ca^{2+} substitution on the Tl^{3+} sites and overlap of Tl-6s band with the conduction band of the CuO_2 layers. This behavior was confirmed by XPS core-level studies [82] and ultraviolet photoemission spectroscopic (UPS) studies [83].

In the $Tl_{2-x}Ba_2Ca_{2+x}Cu_3O_{10}$ system, Kaneko et al. [79] have postannealed the as-synthesized $x = 0.3$ sample in an evacuated quartz tube at 750°C for 250 h and obtained a T_c of 127 K. Similarly, Liu et al. [80] have done similar postannealing treatments on $x = 0.4$ samples and obtained a T_c value of 128 K. This is the highest T_c value known for thallium cuprate superconductors. Usually, starting with little excess calcium helps in the phase formation of Tl-2223.

B. Substitution of Sn at Tl Sites

Ren et al. [81] showed that the critical-current density J_c can be enhanced from 7.6×10^3 A/cm² at 77 K and zero magnetic field to 1.2×10^4 A/cm² under the same conditions by the addition of 0.1 formula weight of SnO_2 to Tl-2223 superconductor. Also, they have suggested that the role of SnO_2

Table 4 Summary of the Various Site Substitutions in $Tl_2Ba_2Ca_2Cu_3O_{10}$ Systems

Composition	Structural and physical properties	Refs.
1. $Tl_2Ba_2Ca_2Cu_3O_{10}$	$T_c = 125$ K, tetragonal I4/mmm, $a = 3.85$, $c = 35.88$ Å	28
2. $Tl_{2-x}Ba_2Ca_{2+x}Cu_3O_{10}$	$x = 0-0.4$, single phase, $T_c = 112-118$ K (as synthesized) $x = 0.3$, $T_c = 127$ K (vacuum anneal) $x = 0.4$, $T_c = 128$ K (after postanneal)	75,76 79 80
3. $(Tl_{2-x}Sn_x)Ba_2Ca_2Cu_3O_{10}$	$x = 0.2$, high J_c	81

is to stabilize the Tl-2223 phase and to improve intergranular or interfacial contact.

V. VARIOUS SITE SUBSTITUTIONS IN $\text{TlBa}_2\text{CuO}_5$ SYSTEMS

$\text{TlBa}_2\text{CuO}_5$ is the $n = 1$ member of the $\text{TlBa}_2\text{Ca}_{n-1}\text{Cu}_n\text{O}_{2n+3}$ family. It is very difficult to synthesize the stoichiometric Tl-1201 phase by the usual solid-state reaction. This difficulty is associated with the necessity of copper being $3+$. Hence one can make a single phase and a superconductor out of $\text{TlBa}_2\text{CuO}_5$ phase by substituting part Ba^{2+} by La^{3+} and thereby reducing the hole concentration to the optimum level [56,57,84–87]. Halder et al. [88] and Parkin et al. [89], however, reported a nonsuperconducting $\text{TlBa}_2\text{CuO}_5$ phase. Later, Ku et al. [84] and Gopalakrishnan et al. [90] have reported a T_c value of 10 K for pure $\text{TlBa}_2\text{CuO}_5$ phase. A summary of various site substitutions in polycrystalline Tl-1201 system is shown in Table 5.

A. Substitution of Sr or La at Ba Sites

Gopalakrishnan et al. [90] have synthesized a single-phase TlBaSrCuO_5 with a T_c value of 33 K for the air-quenched samples. They have also enhanced the T_c up to 43 K by slow cooling the air-quenched sample in a nitrogen atmosphere. Annealing in an inert atmosphere probably decreases the oxygen content and thereby reduces the hole concentration to the optimum level and increases the T_c value in $\text{TlBaSrCuO}_{5-\delta}$. The end member, $\text{TlSr}_2\text{CuO}_5$, has been obtained as a metal [97,98].

In the $\text{TlBa}_{2-x}\text{La}_x\text{CuO}_5$ system, single phase has been obtained in the region $0.5 \leq x \leq 1.0$ [57,85]. Many groups have reported superconductivity in different ranges of x : Manako et al. [85] give $0.64 \leq x \leq 0.99$, Paranthaman et al. [57] $0.5 \leq x \leq 0.8$, Sundaresan et al. [87] $0.3 \leq x \leq 0.6$, and Ku et al. [84] $0 \leq x \leq 0.4$. Subramanian et al. [86,91] have reported a T_c of 52 K at $x = 0.8$ and 57 K at $x = 0.75$. The $x = 1.0$ sample (TlBaLaCuO_5) has been reported as an antiferromagnetic semiconductor [56,57,85]. The discrepancies in the reporting of different x ranges for superconductivity among various groups could be due to chemical inhomogeneity, different Tl content, and varying oxygen contents.

In the $\text{TlSr}_{2-x}\text{RE}_x\text{CuO}_5$ ($\text{RE} = \text{La}, \text{Nd}$), Subramanian et al. [92,96] obtained single phase for the range $0.5 \leq x \leq 1.0$ for La and $0.6 \leq x \leq 1.0$ for Nd with entire region superconducting ($T_c = 35$ to 48 K). X-ray diffraction suggests that the rare earth substitution occurs mainly at the Sr site rather than at the Tl site [92]. However, Bourgault et al. [109] have stabilized the $\text{TlSr}_2\text{CuO}_5$ phase by Pr and concluded that the substitution

Table 5 Summary of the Various Site Substitutions in $\text{TlBa}_2\text{CuO}_5$ Systems

Composition	Structural and physical properties	Refs.
1. $\text{TlBa}_2\text{CuO}_5$	Nonsuperconductor, tetragonal P4/mmm, $a = 3.896$, $c = 9.694 \text{ \AA}$ $T_c = 10 \text{ K}$	88,89 84,90
2. $\text{Tl}(\text{Ba},\text{Sr})\text{CuO}_5$	$T_c = 43 \text{ K}$	90
3. $\text{Tl}(\text{Ba}_{2-x}\text{La}_x)\text{CuO}_5$	$x = 0.5\text{--}1.0$, single phase; $x = 0.5\text{--}0.85$, superconductor $x = 1.0$, AF semiconductor $x = 0.75$, $T_c \sim 57 \text{ K}$	57,85 56,57,85 91
4. $\text{Tl}(\text{Sr}_{1-x}\text{Ba}_x,\text{La})\text{CuO}_5$	$x = 0.0$, $T_c \sim 42 \text{ K}$; $x = 0.3$, $T_c \sim 37 \text{ K}$; $x = 0.4\text{--}0.5$, semimetal $x = 0.6\text{--}1.0$, AF semiconductor	92–94 95
5. $\text{Tl}(\text{Sr}_{2-x}\text{La}_x)\text{CuO}_5$	$x = 0.5\text{--}1.0$, single phase, whole range superconducting	92,96
6. $\text{TlSr}_2\text{CuO}_5$	Metal	97,98
7. $(\text{Tl}_{1-x}\text{Cd}_x)(\text{Ba},\text{La})\text{CuO}_5$	$x = 0\text{--}0.4$; single phase; $x = 0.2\text{--}0.4$; $T_c = 38\text{--}50 \text{ K}$	96
8. $\text{TlSr}_2(\text{Cu}_{1-x}\text{M}_x)\text{O}_5$	$\text{M} = \text{Co}$; $x = 0.3\text{--}0.5$; AF semiconductor; $\text{M} = \text{Fe}$; $x = 0.5\text{--}0.75$; AF semiconductor	99
9. $(\text{Tl}_{0.75}\text{Bi}_{0.25})\text{Sr}_2\text{CuO}_5$	Metal	88,100
10. $(\text{Tl}_{1-x}\text{Bi}_x)\text{Sr}_2\text{CuO}_5$	$x = 0.2\text{--}0.3$; $T_c \sim 45 \text{ K}$ $x = 0.2\text{--}0.5$; metal $x = 0.2\text{--}0.5$; AF semiconductor	101 102 103
11. $(\text{Tl},\text{Pb})\text{Sr}_2\text{CuO}_5$	Metal AF semiconductor; $T_c = 60 \text{ K}$	104 105
12. $(\text{Tl},\text{Pb})(\text{Sr}_{2-x}\text{La}_x)\text{CuO}_5$	$x = 0.0$; metal; $x = 0.5$; $T_c \sim 43 \text{ K}$	106
13. $(\text{Tl},\text{Pb})(\text{Sr},\text{Nd})_2\text{CuO}_5$	$T_c = 45 \text{ K}$	107
14. $(\text{Tl},\text{Pb})(\text{Sr},\text{Pr})_2\text{CuO}_5$	$T_c = 40 \text{ K}$	108
15. $(\text{Tl},\text{Pb})\text{Sr}_2(\text{Cu}_{1-x}\text{Fe}_x)\text{O}_5$	$x = 0.1\text{--}0.5$; AF semiconductor	99

occurs either at Tl or Tl and Sr sites. The two compositions reported are $\text{Tl}_{0.8}\text{Sr}_{1.6}\text{Pr}_{0.6}\text{CuO}_5$ (weak superconductivity) and $\text{Tl}_{0.7}\text{Pr}_{0.3}\text{Sr}_2\text{CuO}_5$ (traces of diamagnetism). This could be possibly due to the existence of Pr in both 3+ and 4+.

In the $\text{TlSr}_{1-x}\text{Ba}_x\text{LaCuO}_5$ system, single phase is obtained in the range $0 \leq x \leq 1.0$ [92,93]. The superconductivity occurs in the range $0 \leq x \leq 0.3$. The $x = 0.6$ to 1.0 samples have been reported to be antiferromagnetic

semiconductors [95]. The observation of superconductivity in TlSrLaCuO_5 could be due to very short in-plane Cu—O distance, this might raise the conduction band ($d_{x^2-y^2}$) high enough in energy for the Tl—O layer to create holes in the Cu—O sheets [91].

B. Substitution of Co or Fe at Cu Sites

Ganguli et al. [99] have reported the existence of single phase of the $\text{TlSr}_2\text{Cu}_{1-x}\text{M}_x\text{O}_5$ ($\text{M} = \text{Co}, \text{Fe}$) system over the range $0.3 \leq x \leq 0.5$ for Co and $0.5 \leq x \leq 0.75$ for Fe. They have also co-doped Pb at Tl sites and Fe at Cu sites [i.e., $(\text{Tl,Pb})\text{Sr}_2\text{Cu}_{1-x}\text{Fe}_x\text{O}_5$ with the single-phase region $0.1 \leq x \leq 0.5$]. All of these phases are reported to be antiferromagnetic semiconductors [99].

C. Substitution of Pb, Bi, or Cd at Tl Sites

It is easy to stabilize $\text{TlSr}_2\text{CuO}_5$ phase by substituting either Bi or Pb at Tl sites [88,100–105]. In the $\text{Tl}_{1-x}\text{Bi}_x\text{Sr}_2\text{CuO}_5$ system, a T_c of ~ 45 K has been obtained in the region $x = 0.2$ to 0.3 [101]. It is also possible to form a metal [88,102] or a semiconductor [103] in the foregoing region. Similarly, in $\text{Tl}_{0.5}\text{Pb}_{0.5}\text{Sr}_2\text{CuO}_5$ samples, one can produce a metal [104], semiconductor [105], or a superconductor with a T_c value as high as 60 K [105], depending on the annealing procedures. Thus a strong correlation between T_c and oxygen content is observed in all these systems.

It is also possible to achieve superconductivity by co-doping (i.e., Pb at Tl sites and La, Nd, or Pr at Sr sites) [106–108]. A T_c value of 45 K is observed for $(\text{Tl,Pb})(\text{Sr,Nd})_2\text{CuO}_5$ [107]. Similarly, in the $(\text{Tl}_{1-x}\text{Cd}_x)(\text{Ba,Lu})\text{CuO}_5$ system, Ganguli and Subramanian [96] have obtained a single phase in the region $0 \leq x \leq 0.4$. The $x = 0.2$ to 0.4 samples are reported to be superconductors with T_c values of 38 to 50 K.

VI. VARIOUS SITE SUBSTITUTIONS IN THE $\text{TlBa}_2\text{CaCu}_2\text{O}_7$ SYSTEMS

$\text{TlBa}_2\text{CaCu}_2\text{O}_7$ is the $n = 2$ member of the $\text{TlBa}_2\text{Ca}_{n-1}\text{Cu}_n\text{O}_{2n+3}$ family. It is possible to obtain a single phase of Tl-1212 with a T_c of 90 K [63]. The crystal symmetry is reported to be tetragonal. The T_c value can be increased up to 100 K [110] in this system by substituting part Ca^{2+} by Y^{3+} , thereby reducing the hole concentration (oxygen content) to the optimum level. A summary of various site substitutions in polycrystalline Tl-1212 system is shown in Table 6.

Table 6 Summary of the Various Site Substitutions in $\text{TlBa}_2\text{CaCu}_2\text{O}_7$ Systems

Composition	Structural and physical properties	Refs.
1. $\text{TlBa}_2\text{CaCu}_2\text{O}_7$	$T_c = 90$ K, tetragonal $P4/mmm$, $a = 3.856$, $c = 12.75$ Å	63
2. $\text{Tl}(\text{Ba},\text{Sr})\text{CaCu}_2\text{O}_7$	$T_c = 94$ K	111
3. $\text{TlBa}_2(\text{Ca}_{1-x}\text{RE}_x)\text{Cu}_2\text{O}_7$	(RE = Nd, Gd, or Y); $x = 0.0$ – 1.0 , single phase; $x = 0.0$, $T_c = 80$ K; $x = 0.2$ – 0.35 , $T_c = 100$ K; $x = 0.4$ – 0.5 , AF semiconductor	110
	RE = Pr, $x = 1.0$, $T_N = 8$ K	112
	RE = Nd	113
4. $\text{TlSr}_2(\text{Ca},\text{RE})\text{Cu}_2\text{O}_7$	$T_c = 60$ – 90 K	114
5. $(\text{Tl},\text{Bi})\text{Sr}_2\text{CaCu}_2\text{O}_7$	$T_c \sim 95$ K	115
	$T_c \sim 106$ K	116
6. $(\text{Tl},\text{Pb})\text{Sr}_2\text{CaCu}_2\text{O}_7$	$T_c = 85$ K	33
7. $(\text{Tl}_{1-y}\text{Pb}_y)\text{Sr}_2(\text{Ca}_{1-x}\text{Y}_x)\text{Cu}_2\text{O}_7$	$y = 0.5$, $x \sim 0.7$, $T_c \sim 100$ K	117

A. Substitution of Sr at Ba Sites

Gopalakrishnan et al. [111] have obtained a single phase of $\text{TlBaSrCaCu}_2\text{O}_{7-\delta}$ with a T_c of 90 K for air-quenched samples. They have also obtained a T_c value of 94 K for slow-cooled air-quenched samples in a nitrogen environment. The occupancy of Sr at Ba sites has been confirmed by x-ray diffraction analysis. Doi et al. [118] obtained a single phase of $\text{TlSr}_2\text{CaCu}_2\text{O}_7$ with a nonsuperconducting behavior. However, one can achieve superconductivity and metallic behavior in the $\text{TlSr}_2\text{CaCu}_2\text{O}_7$ phase by annealing in oxygen.

B. Substitution of Y at Ca Sites

In the $\text{TlBa}_2\text{Ca}_{1-x}\text{RE}_x\text{Cu}_2\text{O}_7$ (RE = Y, Nd, or Gd) system, single phase is obtained in the range $0 \leq x \leq 1.0$ [110,113]. The T_c value of 80 K (for $x = 0.0$ sample) increases to 100 K (for $x = 0.2$ to 0.35 samples). The samples with $x \geq 0.4$ are reported to be antiferromagnetic semiconductors. $\text{TlBa}_2\text{PrCu}_2\text{O}_7$ has also been reported to be an antiferromagnetic semiconductor with T_N of 8 K [112]. In the $\text{TlBa}_{2-x}\text{Sr}_x\text{YCu}_2\text{O}_7$ system, samples with $x = 0$ to 1.0 are found to be antiferromagnetic semiconductors [94].

C. Substitution of Pb or Bi at Tl Sites

Li and Greenblatt [115] have reported a T_c value of 95 K for a $(\text{Tl}_{0.5}\text{Bi}_{0.5})\text{Sr}_2\text{CaCu}_2\text{O}_7$ phase. The T_c of 95 K for a $(\text{Tl},\text{Bi})\text{Sr}_2\text{CaCu}_2\text{O}_7$ is believed to be higher than those of $\text{TlBa}_2\text{CaCu}_2\text{O}_7$ and $(\text{Tl},\text{Pb})\text{Sr}_2\text{CaCu}_2\text{O}_7$ [115]. Dong et al. [116] have obtained a T_c value as high as 106 K for the multiphase $\text{Tl}-\text{Bi}-\text{Sr}-\text{Ca}-\text{Cu}-\text{O}$ samples. Similar to Bi, one can also substitute Pb^{4+} at the Tl^{3+} sites in Tl-1212 phase and achieve superconductivity by optimizing the hole concentration [33,119–121]. Subramanian et al. [33] have obtained a T_c value of 85 K for $(\text{Tl},\text{Pb})\text{Sr}_2\text{CaCu}_2\text{O}_7$.

In the $(\text{Tl}_{1-y}\text{Pb}_y)\text{Sr}_2(\text{Ca}_{1-x}\text{Y}_x)$ system, Vijayaraghavan et al. [117] studied the dependence of T_c on hole concentration. The T_c reaches a maximum at an optimal Cu–O distance. Also, the maximum is found at slightly larger Cu–O distances as the Pb content (y value) increases. Recently, Subramanian et al. [122] measured the thermoelectric power in the foregoing system. Liu and Edwards [123] have obtained a multiphase superconductor $(\text{Tl}_{0.5}\text{V}_{0.5})\text{Sr}_2(\text{Ca}_{0.8}\text{Y}_{0.2})\text{Cu}_2\text{O}_{7-\delta}$.

VII. VARIOUS SITE SUBSTITUTIONS IN $\text{TlBa}_2\text{Ca}_2\text{Cu}_3\text{O}_9$ SYSTEMS

$\text{TlBa}_2\text{Ca}_2\text{Cu}_3\text{O}_9$ is the $n = 3$ member of the $\text{TlBa}_2\text{Ca}_{n-1}\text{Cu}_n\text{O}_{2n+3}$ family. The highest T_c value of 115 K is obtained for the tetragonal $\text{TlBa}_2\text{Ca}_2\text{Cu}_3\text{O}_9$ samples [29]. Kim et al. [124] have shown recently that the magnetic field-induced broadening of the resistive transitions of high- T_c superconductors depends strongly on the Cu–O layer spacings. Accordingly, they have suggested that the Tl-1223 materials will be the suitable candidates for the practical applications since Tl-1223 phase has a shorter distance of 9.59 Å between the Cu–O layers. Deluca et al. [125] have, in fact, reported transport critical-current densities as high as of $1.05 \times 10^5 \text{ A/cm}^2$ at 77 K and zero magnetic field on Tl-1223 thick films. A summary of various site substitutions in polycrystalline Tl-1223 system is shown in Table 7.

A. Substitution of Sr at Ba Site

Martin et al. [126] have made single-phase $\text{TlBaSrCa}_2\text{Cu}_3\text{O}_{9-\delta}$ with a T_c value of 103 K. On annealing in a reducing atmosphere, the T_c value has been shown to increase up to 116 K. It has also been proven that the irreversibility line does not depend on T_c (i.e., oxygen nonstoichiometry does not influence the nature of the irreversibility line in this phase). The $\text{TlSrCa}_2\text{Cu}_3\text{O}_9$ phase has not been made in a pure phase yet since the Tl-1223 structure needs all Cu to be $2.33+$. But it is possible to stabilize this

Table 7 Summary of the Various Site Substitutions in $\text{TlBa}_2\text{Ca}_2\text{Cu}_3\text{O}_9$ Systems

Composition	Structural and physical properties	Refs.
1. $\text{TlBa}_2\text{Ca}_2\text{Cu}_3\text{O}_9$	$T_c = 115 \text{ K}$, tetragonal P4/mmm, $a = 3.853$, $c = 15.913 \text{ \AA}$	29
2. $\text{Tl}(\text{Ba},\text{Sr})\text{Ca}_2\text{Cu}_3\text{O}_9$	$T_c = 116 \text{ K}$	126
3. $(\text{Tl}_{1-x}\text{Bi}_x)\text{Sr}_2\text{Ca}_2\text{Cu}_3\text{O}_9$	$x = 0.1\text{--}0.5$, $T_c = 115\text{--}120 \text{ K}$	127
4. $(\text{Tl},\text{Pb})\text{Sr}_2\text{Ca}_2\text{Cu}_3\text{O}_9$	$T_c = 122 \text{ K}$	33
	$T_c = 124 \text{ K}$	128
5. $(\text{Tl},\text{Pb})(\text{Sr}_{1.6}\text{Ba}_{0.4})\text{Ca}_2\text{Cu}_3\text{O}_9$	High J_c	129–132

phase by doping part Bi or Pb at Tl sites and thereby reducing the Cu valency to the optimum level [33,127].

B. Substitution of Pb or Bi at Tl Sites

Subramanian et al. [127] have produced $(\text{Tl}_{1-x}\text{Bi}_x)\text{Sr}_2\text{Ca}_2\text{Cu}_3\text{O}_9$ ($x = 0.1$ to 0.5) samples with T_c values in the range 115 to 120 K . All samples were reported to have tetragonal symmetry. The absence of any superstructure has been confirmed by electron diffraction studies. Similarly, Subramanian et al. [33] produced $(\text{Tl}_{0.5}\text{Pb}_{0.5})\text{Sr}_2\text{Ca}_2\text{Cu}_3\text{O}_9$ samples with a T_c value of 122 K . Later, Liu et al. [128] increased the T_c value up to 124 K (diamagnetic onset) by postannealing the “as-synthesized” samples in an evacuated quartz tube at about 700 to 750°C for 5 to 10 days. The magnetization properties of $(\text{Tl}_{0.5}\text{Pb}_{0.5})\text{Sr}_2\text{Ca}_2\text{Cu}_3\text{O}_9$ samples were superior to those of the Tl-2223, Tl-2212, Bi-2212, and Bi-2223 phases [133]. Matsuda et al. [129–131] obtained a high (magnetically measured) J_c (critical-current density) of $2 \times 10^4 \text{ A/cm}^2$ at 77 K and 1 T magnetic field for both films and bulk samples of $(\text{Tl}_{0.5}\text{Pb}_{0.5})(\text{Sr}_{1.6}\text{Ba}_{0.4})\text{Ca}_2\text{Cu}_3\text{O}_9$. Ren and Wang [132] have produced uniform and flexible 24-m superconducting tape of silver-sheathed $(\text{Tl}_{0.5}\text{Pb}_{0.5})(\text{Sr}_{1.6}\text{Ba}_{0.4})\text{Ca}_2\text{Cu}_3\text{O}_{8.2}$ exhibiting a transport J_c value of 10^4 A/cm^2 at 77 K and zero magnetic field. From the band-structure calculations, Kang et al. [134] have shown that the Bi atoms of $(\text{Tl}_{0.5}\text{Bi}_{0.5})\text{Sr}_2\text{Ca}_2\text{Cu}_3\text{O}_9$ phase are half in the $+3$ and half in the $+5$ oxidation states. Also, the most likely oxidation state of Pb in $(\text{Tl}_{0.5}\text{Pb}_{0.5})\text{Sr}_2\text{Ca}_2\text{Cu}_3\text{O}_9$ phase is $+4$. The role of partial barium substitution at the strontium site in $(\text{Tl}_{0.5}\text{Bi}_{0.5})(\text{Sr}_{1.6}\text{Ba}_{0.4})\text{Ca}_2\text{Cu}_3\text{O}_9$ is not yet clear and needs to be addressed.

Recently, Bhattacharya et al. [135] have a high J_c value of $3.2 \times 10^4 \text{ A/cm}^2$ at 76 K and zero magnetic field for the electrodeposited Tl-2223

films. Tatarskii et al. [136] have recently presented the complete results of tight-binding calculations of the band structures and Fermi surfaces for the $\text{TlBa}_2\text{Ca}_{n-1}\text{Cu}_n\text{O}_{2n+3}$ and $\text{Tl}_2\text{Ba}_2\text{Ca}_{n-1}\text{Cu}_n\text{O}_{2n+4}$ ($n = 1, 2$, and 3) superconducting phases. Wet-chemical methods are now available to determine Tl and oxygen contents in thallium cuprate superconductors [40,56,57,74,137–140].

VIII. CONCLUSIONS

Our detailed review on the summary of various site substitutions in thallium-based high- T_c superconducting oxides has led us to the following conclusions.

1. Due to Tl toxicity and volatilization during synthesis, safety procedures must be followed carefully.
2. Single crystals of thallium cuprate superconductors can be grown by the self-flux technique.
3. $\text{Tl}_2\text{Ba}_2\text{CuO}_6$ phase exists in two crystal symmetries, tetragonal and orthorhombic. All the other phases are found to exist mostly in tetragonal symmetries.
4. Wet-chemical procedures are now available to define the Tl and oxygen contents.
5. The highest T_c value of 128 K is known for the Tl-2223 phase.
6. The valency of thallium in double-Tl-O layered compounds is between +3 and +1, whereas in mono-Tl-O layered compounds it is mostly +3.
7. Thallium-based superconductors are found primarily to be both Tl and oxygen deficient.
8. These superconductors typically exhibit weak-link behavior and are highly anisotropic.
9. Tl-2212 and Tl-1223 phases are suitable candidates for practical applications.
10. High transport J_c values (critical-current densities) have been obtained for Tl-1223 phases. This could be due to the shorter distance of 9.59 Å between the Cu–O layers.
11. It is possible to introduce defects in the crystal structure by site-selective substitutions in thallium phases.
12. The T_c value can be varied by changing the oxygen content. By annealing in oxygen, one can achieve metallic behavior in the $\text{Tl}_2\text{Ba}_2\text{CuO}_6$ and $\text{TlSr}_2\text{CaCu}_2\text{O}_7$ phases. This is due to the presence of an overdoped state.

ACKNOWLEDGMENTS

AMH gratefully acknowledges the support of the Office of Naval Research under ONR grant N00014-90-J-1571. A portion of the work of MP was supported by the Oak Ridge National Laboratory, Postdoctoral Research Program, administered jointly by the Oak Ridge Institute for Science and Education and ORNL. Also, part of the work of MP was sponsored by the Division of Materials Sciences, Office of Basic Energy Sciences, U.S. Department of Energy, and technology development was funded by the U.S. Department of Energy Office of Advanced Utility Concept-Superconductor Technology Program, both under contract DE-AC05-84OR21400 with Martin Marietta Energy Systems, Inc.

REFERENCES

1. J. G. Bednorz and K. A. Muller, *Z. Phys. B* 64:189 (1986).
2. M. K. Wu, J. R. Ashburn, C. J. Torng, P. H. Hor, R. L. Meng, L. Gao, Z. J. Huang, Y. Q. Wang, and C. W. Chu, *Phys. Rev. Lett.* 58:908 (1987).
3. C. Michel, M. Hervieu, M. M. Borel, A. Grandin, F. Deslandes, J. Provost, and B. Raveau, *Z. Phys. B* 68:421 (1987).
4. H. Maeda, Y. Tanaka, M. Fuksutumi, and T. Asano, *Jpn. J. Appl. Phys.* 27:L209 (1988).
5. Z. Z. Sheng and A. M. Hermann, *Nature* 332:55 (1988); 332:138 (1988).
6. R. J. Cava, B. Batlogg, J. J. Krajewski, L. W. Rupp, L. F. Schneemeyer, T. Siegrist, R. B. van Dover, P. Marsh, W. F. Peck, Jr., P. K. Gallagher, S. H. Glarum, J. H. Marshall, R. C. Farrow, J. V. Waszczak, R. Hull, and P. Trevor, *Nature* 336:211 (1988).
7. S. N. Putilin, E. V. Antipov, O. Chmaissem, and M. Marezio, *Nature* 362:226 (1993).
8. U. Welp, G. W. Crabtree, J. L. Wagner, D. G. Hinks, P. G. Radaelli, J. D. Jorgensen, and J. F. Mitchell, *Appl. Phys. Lett.* 63:693 (1993).
9. M. Paranthaman, J. R. Thompson, Y. R. Sun, and J. Brynestad, *Physica C* 213:271 (1993).
10. M. Paranthaman, J. R. Thompson, Y. R. Sun, J. Brynestad, and D. M. Kroeger, *Appl. Supercond.* (1994) (in press).
11. A. Schilling, M. Cantoni, J. D. Gud, and H. R. Ott, *Nature* 363:56 (1993).
12. R. L. Greene, in *Proceedings of the International Conference on Organic Superconductors*, Lake Tahoe, Calif. (W. A. Little and V. Kresin, eds.), Plenum Press, New York, 1990.
13. D. Jerome, A. Mazaud, M. Ribault, and K. Bechgaard, *J. Phys. Lett. (Paris)* 41:L95 (1980).
14. D. Carlson and J. Williams, *New Sci.* 14:26 (Nov. 1992).
15. A. F. Hebard, M. J. Rosseinsky, R. C. Haddon, D. W. Murphy, S. H. Glarum, T. T. M. Palstra, A. P. Ramirez, and A. R. Kortan, *Nature* 350:600 (1991).

16. K. Tanigaki, T. W. Ebbesen, S. Saito, J. Mizuki, J. S. Tsai, Y. Kubo, and S. Kuroshima, *Nature* 352:222 (1991).
17. *High-Temperature Superconductivity*, reprints from *Phys. Rev. Lett.* and *Phys. Rev. B*, The American Physical Society, New York, 1987–1994.
18. A. V. Narlikar, ed., *Studies of High Temperature Superconductors*, Vols. I–XI, Nova Science Publishers, New York, 1989–1994.
19. A. M. Hermann and J. V. Yakhmi, eds., *Thallium-Based High-Temperature Superconductors*, Marcel Dekker, New York, 1994.
20. D. M. Ginsberg, ed., *Physical Properties of High Temperature Superconductors*, Vols. I–III, World Scientific, Singapore, 1990–1992.
21. A. Manthiram and J. B. Goodenough, in *Advances in the Synthesis and Reactivity of Solids*, Vol. I, JAI Press, Greenwich, Conn., 1991, pp. 1–80.
22. A. W. Sleight, *Science* 242:1519 (1988); *Phys. Today*, June 1991, p. 24.
23. R. J. Cava, *Science* 247:656 (1990); *Sci. Am.*, Aug. 1990, p. 42.
24. T. Vanderah, ed., *Chemistry of Superconductor Materials*, Noyes Publications, Park Ridge, N.J., 1992.
25. R. M. Hazen, L. W. Finger, R. J. Angel, C. T. Prewitt, N. I. Ross, C. G. Hadidiacos, P. J. Heaney, D. R. Veblen, Z. Sheng, A. El Ali, and A. M. Hermann, *Phys. Rev. Lett.* 60:1657 (1988).
26. C. C. Torardi, M. A. Subramanian, J. C. Calabrese, J. Gopalakrishnan, E. M. McCarron, K. J. Morrissey, T. R. Askey, R. B. Flippen, U. Chowdhry, and A. W. Sleight, *Phys. Rev. B* 38:225 (1988).
27. C. C. Torardi, M. A. Subramanian, J. C. Calabrese, J. Gopalakrishnan, K. J. Morrissey, T. R. Askew, R. B. Flippen, U. Chowdhry, and A. W. Sleight, *Science* 240:631 (1988).
28. S. S. P. Parkin, V. Y. Lee, E. M. Engler, A. I. Nazzal, T. C. Huang, G. Gorman, R. Savoy, and R. Beyers, *Phys. Rev. Lett.* 60:2539 (1988).
29. S. S. P. Parkin, V. Y. Lee, A. I. Nazzal, R. Savoy, R. Beyers, and S. J. La Placa, *Phys. Rev. Lett.* 61:750 (1988).
30. T. C. Huang, V. Y. Lee, R. Karini, R. Beyers, and S. S. P. Parkin, *Mater. Res. Bull.* 23:1307 (1988).
31. D. E. Cox, C. C. Torardi, M. A. Subramanian, J. Gopalakrishnan, and A. W. Sleight, *Phys. Rev. B* 38:6624 (1988).
32. H. Ihara, R. Sugise, M. Hirabayashi, N. Terada, M. Jo, K. Hayashi, A. Negishi, M. Tokumoto, Y. Kimura, and T. Shimomura, *Nature* 334:510 (1988).
33. M. A. Subramanian, C. C. Torardi, J. Gopalakrishnan, P. L. Gai, J. C. Calabrese, T. R. Askew, R. B. Flippen, and A. W. Sleight, *Science* 242:249 (1988).
34. M. Kikuchi, T. Kajitani, T. Suzuki, S. Nakajima, K. Hiraga, N. Kobayashi, H. Iwasaki, Y. Syono, and Y. Muto, *Jpn J. Appl. Phys.* 28:L382 (1989).
35. M. Hervieu, A. Maignan, C. Martin, C. Michel, J. Provost, and B. Raveau, *J. Solid State Chem.* 75:212 (1988).

36. A. W. Hewat, P. Bordet, J. J. Capponi, C. Chaillout, J. Chenavas, M. Godinho, E. A. Hewat, J. L. Hodeau, and M. Marezio, *Physica C* 156:369 (1988); 156:375 (1988).
37. Y. Shimakawa, Y. Kubo, T. Satoh, S. Iijima, T. Ichihashi, and H. Igarashi, *Physica C* 157:279 (1989).
38. K. V. Ramanujachary, S. Li, and M. Greenblatt, *Physica C* 165:377 (1990).
39. M. Kikuchi, S. Nakajima, Y. Syono, K. Nagase, R. Suzuki, T. Kajitani, N. Kobayashi, and Y. Muto, *Physica C* 166:497 (1990).
40. M. Paranthaman, A. Manthiram, and J. B. Goodenough, *J. Solid State Chem.* 87:479 (1990).
41. J. B. Parise, C. C. Torardi, M. A. Subramanian, J. Gopalakrishnan, and A. W. Sleight, *Physica C* 159:239 (1989).
42. S. Nakajima, M. Kikuchi, T. Oku, N. Kobayashi, T. Suzuki, K. Nagase, K. Hiraga, Y. Muto, and Y. Syono, *Physica C* 160:458 (1989).
43. T. Suzuki, M. Nagoshi, Y. Fukuda, Y. Syono, M. Kikuchi, N. Kobayashi, and M. Tachiki, *Phys. Rev. B* 40:5184 (1989).
44. D. R. Hamann and L. F. Mattheiss, *Phys. Rev. B* 38:5138 (1988).
45. D. Jung, M.-H. Whangbo, N. Herron, and C. C. Torardi, *Physica C* 160:381 (1989).
46. J. B. Parise, N. Herron, M. K. Crawford, and P. L. Gai, *Physica C* 159:255 (1989).
47. H. M. Duan, R. M. Yandrofski, T. S. Kaplan, B. Dlugosch, J. H. Wang, and A. M. Hermann, *Physica C* 185–189:1283 (1991).
48. T. Manako, Y. Shimakawa, Y. Kubo, and H. Igarashi, *Physica C* 185–189:1327 (1991).
49. T. Manako, Y. Shimakawa, Y. Kubo, and H. Igarashi, *Physica C* 190:62 (1991).
50. A. M. Hermann, H. M. Duan, W. Kiehl, and M. Paranthaman, *Physica C* 209:199 (1993).
51. M. Paranthaman, H. M. Duan, and A. M. Hermann, in *Thallium-Based High-Temperature Superconductors* (A. M. Hermann and J. V. Yakhmi, eds.), Marcel Dekker, New York, 1994, pp. 177–194.
52. M. Paranthaman, W. Kiehl, and A. M. Hermann, in *Studies of High Temperature Superconductors*, Vol. XI (A. V. Narlikar, ed.), Nova Science Publishers, New York, 1994, and references therein.
53. M. Paranthaman, A. Manthiram, and J. B. Goodenough, *Proceedings of the ICMC '90 Topical Conference on High-Temperature Superconductors: Materials Aspects*, Garmisch, Partenkirchen, Germany, 1990.
54. M. Paranthaman, A. Manthiram, and J. B. Goodenough, *J. Mater. Chem.* 2:317 (1992).
55. Y. Shimakawa, Y. Kubo, T. Manako, and H. Igarashi, *Physica C* 185–189:639 (1991).
56. A. Manthiram, M. Paranthaman, and J. B. Goodenough, *Physica C* 171:135 (1990).

57. M. Paranthaman, A. Manthiram, and J. B. Goodenough, in *Thallium-Based High-Temperature Superconductors* (A. M. Hermann and J. V. Yakhmi, eds.), Marcel Dekker, New York, 1994, pp. 147–175.
58. A. K. Ganguli and M. A. Subramanian, *J. Solid State Chem.* **90**:382 (1991).
59. J. H. Wang, Z. Z. Sheng, C. Dong, X. Fei, L. Sheng, A. M. Hermann, and Z. X. Zhao, *Physica C* **158**:507 (1989).
60. K. A. Thomas, U. V. Varadaraju, G. V. Subba Rao, C. V. Tomy, and S. K. Malik, *J. Solid State Chem.* **88**:177 (1990).
61. H. M. Duan, W. Kiehl, C. Dong, A. W. Cordes, M. J. Saeed, D. L. Vlar, and A. M. Hermann, *Phys. Rev. B* **43**:12925 (1991).
62. B. Morosin, R. J. Baughman, D. S. Ginley, J. E. Schirber, and E. L. Venturini, *Physica C* **161**:115 (1990).
63. K. Yvon and M. Francois, *Z. Phys B* **76**:413 (1989).
64. E. A. Hayri and M. Greenblatt, *Physica C* **156**:775 (1988).
65. M. Paranthaman, M. Foldeaki, and A. M. Hermann, *J. Electron. Mater.* **22**:1205 (1993).
66. M. Paranthaman, M. Foldeaki, D. Balzar, H. Ledbetter, A. J. Nelson, and A. M. Hermann, *Supercond. Sci. Technol.* (1994) (in press).
67. A. Poddar, P. Mandal, A. N. Das, B. Ghosh, and P. Choudhury, *Phys. Rev. B* **44**:2757 (1991).
68. M. Paranthaman, A. Manthiram, and J. B. Goodenough, *J. Solid State Chem.* **98**:343 (1992).
69. M. Foldeaki, H. Ledbetter, M. Paranthaman, H. M. Duan, and A. M. Hermann, *J. Supercond.* **6**:185 (1993).
70. T. Kotani, T. Kaneko, H. Takei, and K. Tada, *Jpn. J. Appl. Phys.* **28**:L1378 (1989).
71. T. Kajitani, K. Hiraga, S. Nakajima, M. Kikuchi, Y. Syono, and C. Kabuto, *Physica C* **161**:483 (1989).
72. C. P. Tigges, E. L. Venturini, J. F. Kwak, B. Morosin, R. J. Baughman, and D. S. Ginley, *Appl. Phys. Lett.* **57**:517 (1990).
73. B. Morosin, E. L. Venturini, and D. S. Ginley, *Physica C* **175**:241 (1991).
74. A. Manthiram, M. Paranthaman, and J. B. Goodenough, *J. Solid State Chem.* **96**:464 (1992).
75. M. Paranthaman, M. Foldeaki, and A. M. Hermann, *Physica C* **192**:161 (1992).
76. M. Paranthaman, M. Foldeaki, A. Naziripour, and A. M. Hermann, *Mater. Res. Soc. Proc.* **275**:41 (1992).
77. H. M. Meyer III, T. J. Wagener, and J. H. Weaver, *Phys. Rev. B* **39**:7343 (1989).
78. P. Marksteiner, J. Yu, S. Massidda, A. J. Freeman, J. Redinger, and P. Weinberger, *Phys. Rev. B* **39**:2894 (1989).
79. T. Kaneko, H. Yamauchi, and S. Tanaka, *Physica C* **178**:377 (1991).
80. R. S. Liu, J. L. Tallon, and P. P. Edwards, *Physica C* **182**:119 (1991), and references therein.
81. Z. Ren, M. Qi, and J. H. Wang, *Physica C* **184**:24 (1991).

82. C. S. Gopinath, S. Subramanian, M. Paranthaman, and A. M. Hermann, *J. Solid State Chem.* (1994) (in press).
83. C. S. Gopinath, S. Subramanian, M. Paranthaman, and A. M. Hermann, *Physica C* 214:153 (1993).
84. H. C. Ku, M. F. Tai, J. B. Shi, M. J. Shieh, S. W. Hsu, G. H. Hwang, D. C. Ling, T. J. Watson-Yang, and T. Y. Lin, *Jpn. J. Appl. Phys.* 28:L923 (1989).
85. T. Manako, Y. Shimakawa, Y. Kubo, T. Satoh, and H. Igarashi, *Physica C* 158:143 (1989).
86. M. A. Subramanian, G. H. Kwei, J. B. Parise, J. A. Goldstone, and R. B. Von Dreele, *Physica C* 166:19 (1990).
87. A. Sundaresan, A. K. Rajarajan, L. C. Gupta, M. Sharon, and R. Vijayaraghavan, *Physica C* 178:193 (1991).
88. P. Haldar, A. Roig-Janicki, S. Sridhar, and B. C. Giessen, *Mater. Lett.* 7:1 (1988).
89. S. S. P. Parkin, V. Y. Lee, A. I. Nazzari, R. Savoy, T. C. Huang, G. Gorman, and R. Beyers, *Phys. Rev. B* 38:6531 (1988).
90. I. K. Gopalakrishnan, J. V. Yakhmi, and R. M. Iyer, *Physica C* 175:183 (1991).
91. M. A. Subramanian and A. K. Ganguli, in *Thallium-Based High-Temperature Superconductors*, (A. M. Hermann and J. V. Yakhmi, eds.), Marcel Dekker, New York, 1994, pp. 347–356.
92. M. A. Subramanian, *Mater. Res. Bull.* 25:191 (1990).
93. A. Sundaresan, C. S. Gopinath, A. S. Tamhane, A. K. Rajarajan, M. Sharon, S. Subramanian, R. Pinto, L. C. Gupta, and R. Vijayaraghavan, *Phys. Rev. B* 46:6622 (1992).
94. M. Paranthaman, M. Foldeaki, D. Balzar, H. Ledbetter, and A. M. Hermann, reprint.
95. M. Huve, C. Michel, C. Martin, M. Hervieu, A. Maignan, J. Provost, and B. Raveau, *Physica C* 179:214 (1991).
96. A. K. Ganguli and M. A. Subramanian, *Mater. Res. Bull.* 26:91 (1991).
97. A. K. Ganguli and M. A. Subramanian, *J. Solid State Chem.* 93:250 (1991).
98. J. S. Kim, J. S. Swinnea, and H. Steinfink, *J. Less-Common Metals* 156:347 (1989).
99. A. K. Ganguli, M. A. Subramanian, and G. H. Kwei, *J. Solid State Chem.* 91:397 (1991).
100. P. Haldar, K. Chen, B. Maheswaran, A. Roig-Janicki, N. K. Jaggi, R. S. Markiewicz, and B. C. Giessen, *Science* 241:1198 (1988), and references therein.
101. S. Li, M. Greenblatt, and A. J. Jacobson, *Mater. Res. Bull.* 26:229 (1991).
102. M. H. Pan and M. Greenblatt, *Physica C* 184:235 (1991).
103. M. Greenblatt and M. H. Pan, in *Thallium-Based High-Temperature Superconductors* (A. M. Hermann and J. V. Yakhmi, eds.), Marcel Dekker, New York, 1994, and references therein.
104. G. H. Kwei, J. B. Shi, and H. C. Ku, *Physica C* 174:180 (1991).
105. M. H. Pan and M. Greenblatt, *Physica C* 176:80 (1991).

106. J. B. Shi, M. J. Shieh, T. Y. Lin, and H. C. Ku, *Physica C* 162–164:721 (1989).
107. T. Itoh and H. Uchikawa, *Jpn. J. Appl. Phys.* 28:1790 (1989).
108. S. Adachi, O. Inoue, H. Hirano, Y. Takahachi, and S. Kawashima, *Jpn. J. Appl. Phys.* 28:L775 (1989).
109. D. Bourgault, C. Martin, C. Michel, M. Hervieu, J. Provost, and B. Raveau, *J. Solid State Chem.* 78:326 (1989).
110. S. Nakajima, M. Kikuchi, Y. Syono, N. Kobayashi, and Y. Muto, *Physica C* 168:57 (1990).
111. I. K. Gopalakrishnan, J. V. Yakhmi, and R. M. Iyer, *Physica C* 172:450 (1991).
112. C. C. Lai, B. S. Chiou, Y. Y. Chen, J. C. Ho, and H. C. Ku, *Physica C* 202:104 (1992).
113. C. Michel, E. Surad, V. Caignaert, C. Martin, A. Maignan, M. Hervieu, and B. Raveau, *Physica C* 178:29 (1991).
114. C. N. R. Rao, A. K. Ganguli, and R. Vijayaraghavan, *Phys. Rev. B* 40:2565 (1989).
115. S. Li and M. Greenblatt, *Physica C* 157:365 (1989).
116. C. Dong, Z. Z. Sheng, X. Fei, L. Sheng, J. H. Wang, and A. M. Hermann, *Physica C* 161:257 (1989).
117. R. Vijayaraghavan, J. Gopalakrishnan, and C. N. R. Rao, *J. Mater. Chem.* 2:327 (1992).
118. T. Doi, K. Usami, and T. Kamo, *Jpn. J. Appl. Phys.* 29:L57 (1990).
119. A. K. Ganguli, K. S. Nanjundaswamy, and C. N. R. Rao, *Physica C* 156:788 (1988).
120. C. Martin, J. Provost, D. Bourgault, B. Domenges, C. Michel, M. Hervieu, and B. Raveau, *Physica C* 157:460 (1989).
121. J. B. Parise, P. L. Gai, M. A. Subramanian, J. Gopalakrishnan, and A. W. Sleight, *Physica C* 159:245 (1989).
122. C. K. Subramanian, A. B. Kaiser, H. J. Trodahl, A. Mawdsley, and R. G. Buckley, *Physica C* 203:98 (1992).
123. R. S. Liu and P. P. Edwards, *J. Solid State Chem.* 91:407 (1991).
124. D. H. Kim, K. E. Gray, R. T. Kampwirth, J. C. Smith, D. S. Richeson, T. J. Marks, J. H. Kang, J. Talvacchio, and M. Eddy, *Physica C* 177:431 (1991).
125. J. A. Deluca, P. L. Karas, J. E. Tkaczyk, C. L. Briant, M. F. Garbauskas, and P. J. Bednarczyk, *Mater. Res. Soc. Symp. Proc.* 275:669 (1992).
126. C. Martin, M. Huve, M. Hervieu, A. Maignan, C. Michel, and B. Raveau, *Physica C* 201:362 (1992).
127. M. A. Subramanian, P. L. Gai, and A. W. Sleight, *Mater. Res. Bull.* 25:101 (1990).
128. R. S. Liu, S. F. Hu, D. A. Jefferson, and P. P. Edwards, *Physica C* 198:318 (1992).
129. S. Matsuda, T. Doi, A. Soeta, T. Yuasa, N. Inoue, K. Aihara, and T. Kamo, *Physica C* 185–189:2281 (1991).

130. T. Doi, T. Nabatame, T. Kamo, and S. Matsuda, *Supercond. Sci. Technol.* **4**:488 (1991).
131. T. Kamo, T. Doi, A. Soeta, T. Yuasa, N. Inoue, K. Aihara, and S. P. Matsuda, *Appl. Phys. Lett.* **59**:3186 (1991).
132. Z. Ren and J. H. Wang, *Appl. Phys. Lett.* **61**:1715 (1992).
133. R. S. Liu, D. N. Zheng, J. W. Loram, K. A. Mirza, A. M. Campbell, and P. P. Edwards, *Appl. Phys. Lett.* **60**:1019 (1992).
134. D. B. Kang, D. Jung, and M.-H. Whangbo, *Inorg. Chem.* **29**:257 (1990).
135. R. N. Bhattacharya, P. A. Parilla, and R. D. Blaugher, *Physica C* **211**:475 (1993).
136. V. V. Tatarskii, M. Paranthaman, and A. M. Hermann, *Phys. Rev. B* **47**:14489 (1993), and references therein.
137. J. Gopalakrishnan, R. Vijayaraghavan, R. Nagarajan, and C. Shivakumara, *J. Solid State Chem.* **93**:272 (1991).
138. S. Nakajima, M. Kikuchi, Y. Syono, T. Oku, K. Nagase, N. Kobayashi, D. Shindo, and K. Hiraga, *Physica C* **182**:89 (1991).
139. T. S. Krishnamoorthy, N. Mahadevan, and S. S. Desai, *J. Solid State Chem.* **100**:182 (1992).
140. M. Karppinen, A. Fukuoka, T. Kaneko, and H. Yamauchi, *Supercond. Sci. Technol.* **6**:265 (1993).

This Page Intentionally Left Blank

Applications of Organic Conductors: Molecular Electronics

Mutsuyoshi Matsumoto, Hiroaki Tachibana, and Takayoshi Nakamura

*National Institute of Materials and Chemical Research, Tsukuba,
Ibaraki, Japan*

I. INTRODUCTION

Organic materials are used in the existing electronics industries mainly for passive purposes: insulating and structural support materials. There are, however, exceptions, such as photoresists, liquid crystal displays, and electrocopying. More challenging to many researchers in a diversity of fields is the application of organic conductors from the viewpoint of the fabrication of molecular electronics, to which this chapter is devoted.

The importance of the idea of molecular electronics was reemphasized by Carter in the famous workshop on molecular electronics devices in 1981 [1]. By this term he meant that a single molecule or a cluster of molecules can act as a device. This concept was presented since it is foreseen that the silicon semiconductor technology might suffer, in the near future, from limits on the size and properties of ICs arising from processing considerations, materials properties, and operational constraints.

One of the most famous molecular devices is the Aviram–Ratner molecular rectifier using a molecule of the type D- σ -A, shown in Fig. 1 [2,3]. If a molecule (supermolecule) of this type is assembled and sandwiched between two metal electrodes, it is expected to work as a rectifier since the energy necessary to allow the electron transfer reaction shown in Eq. (1) to proceed is considered to be several eV lower than the one shown

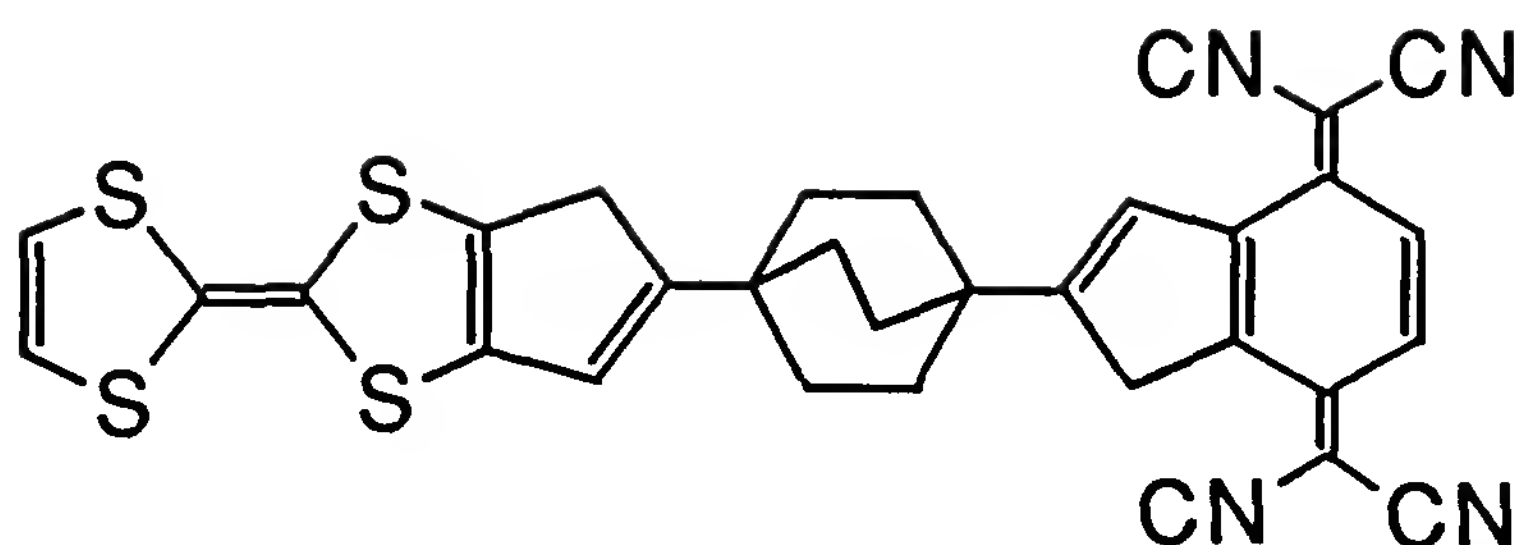


Figure 1 Structure of D-σ-A type of molecule. (From Ref. 2.)

in Eq. (2).



A rectifier of this type has not been realized despite considerable effort [4].

The demonstration of molecular electronics has been really difficult, as can be seen for the Aviram–Ratner rectifier. The only molecular device that has been demonstrated experimentally is the molecular photodiode, by Fujihira et al. [5–7]. In the course of time, the term *molecular electronics* has acquired a broader definition, such as that of being the field in which organic molecular materials perform an active function in the processing and its transmission and storage [8].

To realize molecular electronics, one of the key issues is how to fabricate the ordered structures in a planned manner since organic molecules, especially when they are to be used in active forms, are anisotropic in terms of various properties, and consequently, the functions of the molecular assemblies depend strongly on the way molecules are arranged in them, as is the case for single crystals. The assembling process is called *molecular engineering* or *supramolecular engineering*, depending on the species that attracts attention [9–11]. There are several ways to assemble molecules, among which the Langmuir–Blodgett (LB) technique has been considered to be most promising. To use single-crystalline materials is usually difficult since the processing technique for single crystals has not been exploited sufficiently.

Typical LB films are constructed through transferring monolayers of amphiphilic molecules at the air–water interface onto solid substrates [8,12,13]. The amphiphilic molecules are first dissolved in an organic solvent that is immiscible with water, spread on a water surface, and compressed by decreasing the area in which the molecules are confined, to form a monolayer at the air–water interface. Then the monolayer is transferred onto a solid substrate by moving the substrate vertically or horizontally. This procedure allows us to obtain ultrathin films with the struc-

tures and thicknesses controlled at the molecular level [14,15]. Figure 2 illustrates the structures of X,Y,Z-type LB films. All three structures make possible dense packing and segregation of the hydrophilic and hydrophobic moieties of the amphiphilic molecule, which makes the LB technique suitable for the fabrication of functional materials.

Generally speaking, there are two ways by which molecular electronics is to be realized. The first employs a molecular component system consisting of different molecules with different functions. These molecules are expected to act cooperatively and form a device. In this system, the point is how to assemble different molecules in a desired manner and how to endow the molecular assemblies with the specific functions that are aimed at. The alternative method relies on a "supramolecular system" that takes advantage of the multiple functions of the supermolecules. The functions of this system depend not only on the relative arrangement of the supermolecule in the material but also on the position of each functional unit in the supermolecule, which stresses the importance of the molecular design and its synthesis. The more sophisticated way would be to fabricate the materials consisting of different supermolecules, which is yet to be realized.

II. CONDUCTIVE LANGMUIR-BLODGETT FILMS

Conductive LB films have attracted considerable attention not only as active elements of molecular electronics but also in terms of the low-dimensional nature of the LB film structure, which may give rise to new

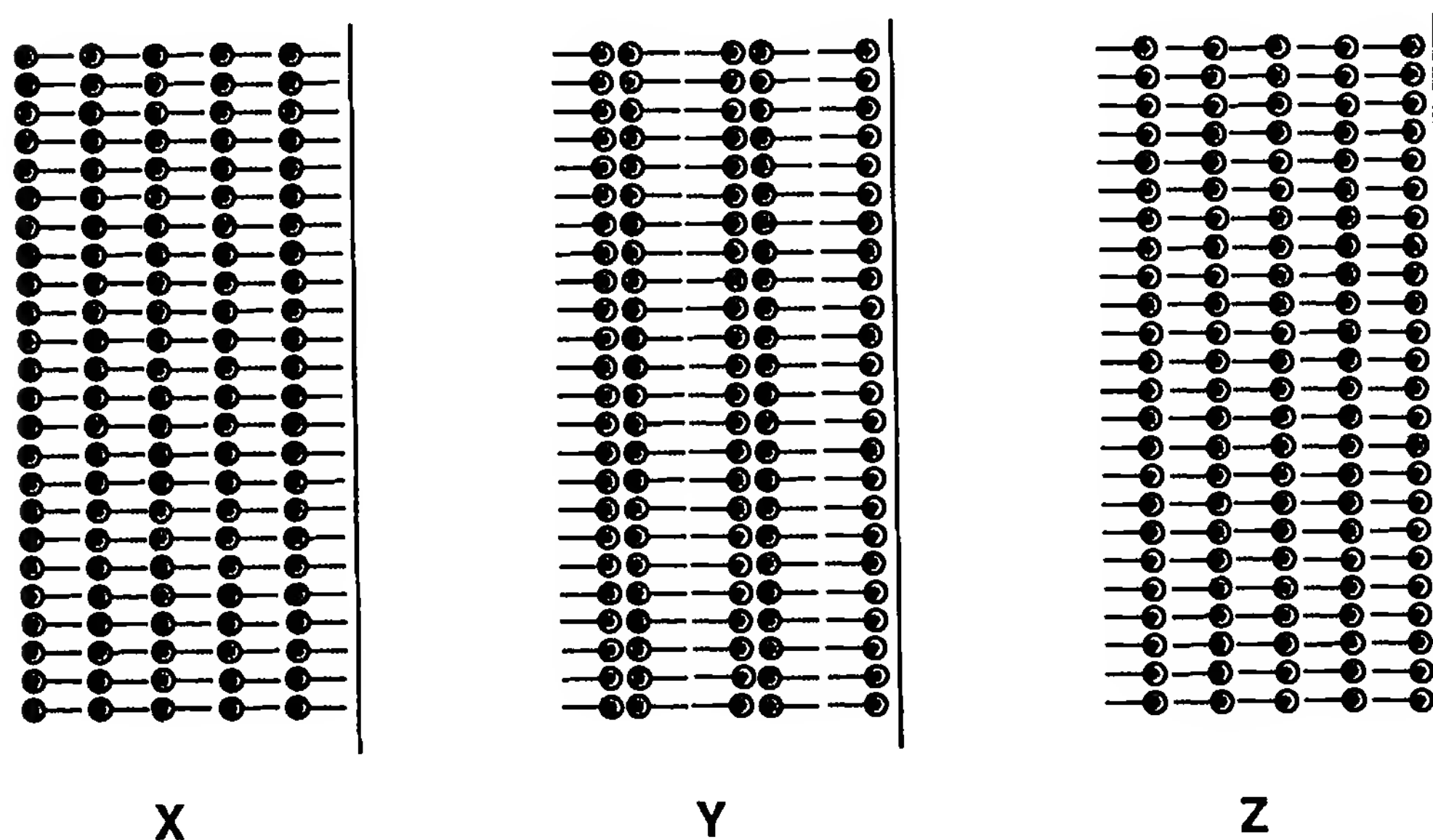


Figure 2 Structures of X-, Y-, Z-type LB films.

mechanisms of conduction such as those proposed by Little and Ginzburg [16–19]. The molecular design of the film-forming molecule is rather straightforward. In most cases, long alkyl chains or those having hydrophilic groups at the ends are attached to the electrically active moieties, which are known to give high conductivities or superconducting transitions in bulk forms. When the conductive compounds are immiscible with the usual solvent or unstable in the solvent or at the air–water interface, the precursor LB films, which are usually insulating, are first transferred onto solid substrates and then subject to secondary treatments such as gas doping and electrochemical oxidation to obtain high conductivities. Until now, no conductive LB films have shown higher conductivities or higher superconducting transition temperatures than those of the corresponding bulk materials having the same active elements under appropriate conditions. In this chapter the term *conductivity* is used as the lateral conductivity measured in the direction parallel to the film surface, unless stated otherwise.

A. History of Conductive LB Films

Until the fabrication of the first conductive LB film by Ruaudel-Teixier et al. [20], LB films had been considered as insulators or at most as semiconductors with very low conductivities. This is understandable since the typical film-forming molecules are long-chain fatty acids, which can act only as insulators. It is no wonder that the first systematic investigations of the electrical properties of LB films were carried out for insulating LB films [21–30]. Mott's variable-range-hopping model [31] is employed to explain the results [21,24].

Tens of conductive LB films have been developed so far, including metallic and superconductive LB films. These LB films are classified into the categories anion radical salt, charge-transfer complex, cation radical salt, conducting polymer, and transition metal complex in this section. The LB films, with metallic temperature dependences of conductivity, and the fullerene LB films, which exhibit a superconducting transition, are discussed separately.

1. Anion-Radical Salt

The first conductive LB film, consisting of $C_{22}Py(TCNQ)$ doped with iodine (Fig. 3) belongs to the class of anion-radical salts [20]. The insulating $C_{22}Py(TCNQ)$ LB film was rendered conductive by iodine doping, and the bulk conductivity was about 0.01 S/cm.* The nominal charge of TCNQ of

*The reported value was divided by ca. 10 or 5 to reduce it into the value of the bulk conductivity, since the volume of the insulating part such as alkyl chains has been excluded from the estimation of the conductivity in the literature.

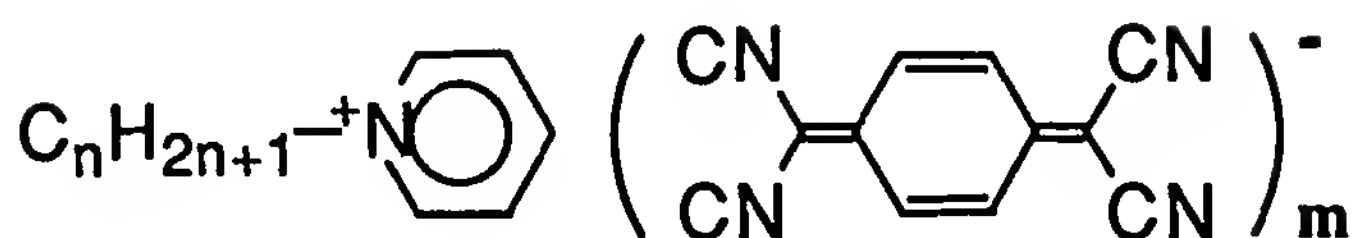


Figure 3 Structure of $\text{C}_n\text{Py}(\text{TCNQ})_m$.

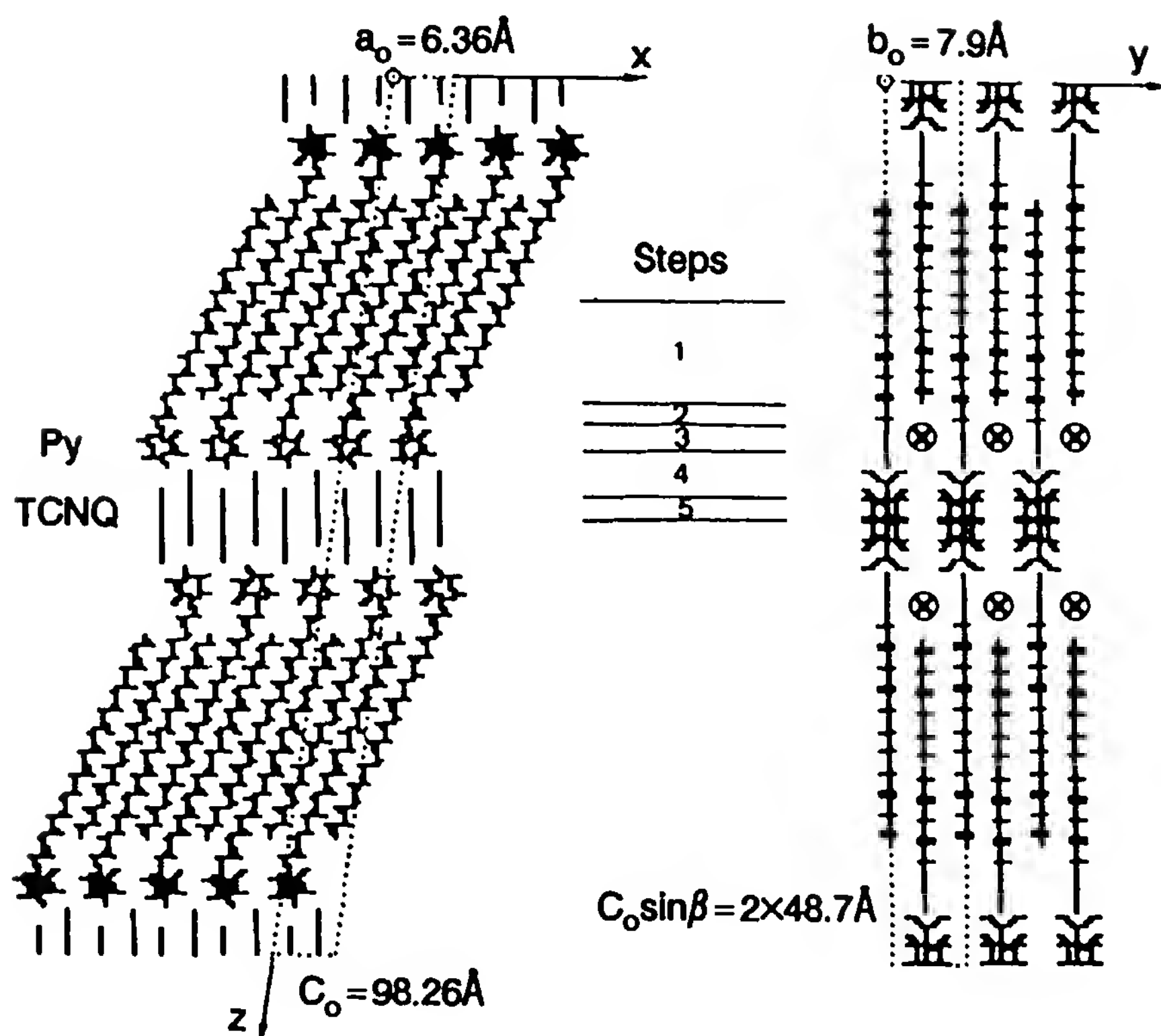


Figure 4 Structure of $\text{C}_{22}\text{Py}(\text{TCNQ})$ LB film doped with iodine. (From Ref. 33.)

the as-deposited LB film (insulator) is -1 and the high conductivity obtained shows the partial oxidation of TCNQ anion radical caused by the presence of iodine.

In the precursor film, the spectroscopic analyses showed that TCNQ molecules form slipped dimers with their molecular planes almost parallel to the film surface [32]. On the other hand, the structure of the conductive film is very different from this, due to iodine doping. The presence of iodine ions enables calculation of the linear electron density function along the normal of the film by x-ray diffraction analyses [33]. The results are explained by a model that involves the interdigitation of adjacent molecules shown in Fig. 4, which is consistent with the spectroscopic results [32].

Temperature-dependent dc and microwave conductivities are of activation type, with the activation energies 0.15 and 0.08 eV, respectively.

Thermoelectric power measurements show that by its nature, this film is a semiconductor [34]. It is to be noted that the conductivity of the precursor film is controlled by the subphase temperature at which the LB film is fabricated [35]. By changing the amphiphilic octadecylpyridinium cation to octadecyldimethylsulfonium, octadecylmethylethylsulfonium, or octadecyltrimethylphosphonium cation, another three conductive LB films were formed by iodine doping of the precursor films [36,37]. These conductive LB films need iodine doping as the secondary treatment to achieve high conductivities, which is unnecessary for materials in which partial charge-transfer states are achieved without doping.

The conductive LB film in an as-deposited form was obtained using $C_{22}Py(TCNQ)_2$, in which TCNQ anion radical is in a partially oxidized state without doping [38,39]. The bulk conductivity of this film is 0.01 S/cm, which is similar to the value of the doped $C_{22}Py(TCNQ)$ film. This value is four orders of magnitude higher than the value of the compaction sample of the 1:2 salt, due probably to the ordered arrangement of the molecules realized in the LB film. The activation energy of the temperature dependence of dc conductivity is 0.3 eV. This $C_{22}Py(TCNQ)_2$ LB film is stable for at least 2 months in air, due to the absence of a volatile component in the film. UV–visible and infrared (IR) spectra show that the TCNQ moiety is oriented with its long axis almost perpendicular to the film surface and that the TCNQ stacking axis is parallel to the film surface. No in-plane anisotropy is observed, which is consistent with the direct observation of the film by polarizing microscopy and scanning electron microscopy [40]. The distinct blue shift of the absorption bands due to the TCNQ moiety in the UV–visible region compared with the powder sample is explained by the difference in energy between the three-dimensional solid and the quasi-two-dimensional LB system using a Hubbard-like model [41].

This LB film does not require secondary treatment to obtain a high conductivity, which enables measurement of the conductivity–area isotherm at the air–liquid interface [38,39] using the instrument shown in Fig. 5. The conductivity of the monolayer on a glycerin subphase increases with compression of the monolayer and is about 0.02 S/cm at 25 mN/m, which is on the same order as the value of the LB film.

The magnetic properties of the $C_{22}Py(TCNQ)_2$ LB film was studied intensively by ESR spectroscopy to obtain microscopic information on the structure and conduction mechanism of the film [43,44]. The characteristic temperature dependences of the spin susceptibility and linewidth are well explained by the random-exchange Heisenberg antiferromagnetic chain (REHAC) model of Soos and Bondeson [45–47]. The REHAC system is characterized by the development of one-dimensional spin chains with regular exchange J and weak exchange ϵJ . This model predicts that the

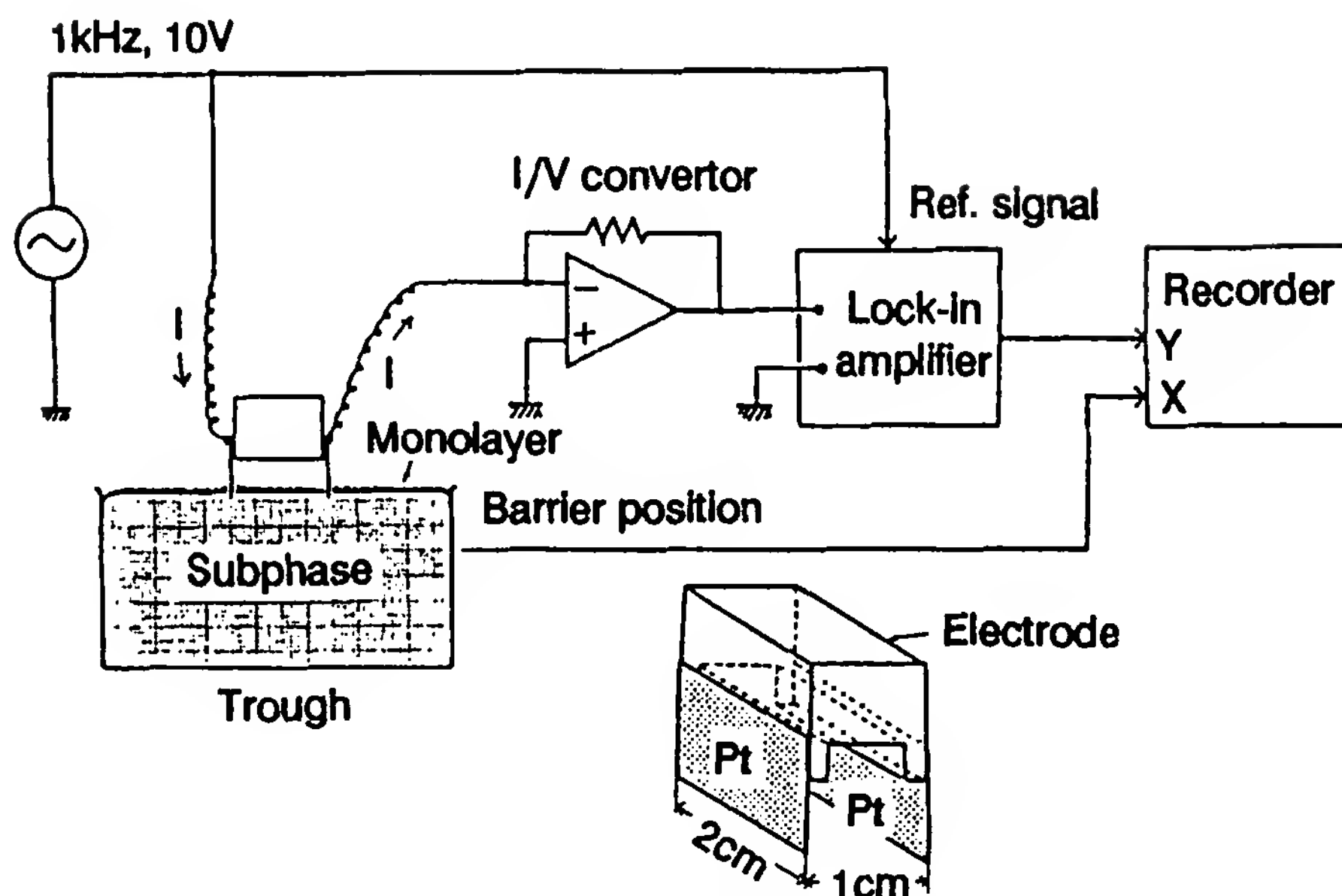


Figure 5 Apparatus for measuring the monolayer conductivity at the air-liquid interface. (From Ref. 42.)

spin susceptibility behaves as a regular antiferromagnetic chain at higher temperatures, whereas it obeys a power law at low temperatures, which is really observed for this LB film with $J/k_B \approx 700$ K. Precise analysis of electron spin resonance (ESR) line shapes using the spectrum simulation method [48–50] reveals that the linewidth anisotropy is dominated by the exchange-narrowed secular dipolar width peculiar to quasi-one-dimensional spin systems [51,52]. The interchain exchange integral within the two-dimensional crystallites in the film is estimated to be $J'/k_B \approx 0.65$ K, which is three orders of magnitude smaller than the intrachain exchange integral J/k_B , showing that this system is considered to be quasi-one-dimensional. The orientation of TCNQ in the film obtained by ESR spectroscopy is consistent with the results of UV-visible and IR spectroscopies. Completely different results were reported by Vandevyver et al. using the LB film of the same 1:2 salt, in which the ESR spectra are essentially the same as those of the 1:1 salt, with the TCNQ molecular plane parallel to the film surface [53].

Another conductive LB film was reported using $C_{18}Py(TCNQ)$ without a doping process [54]. The conductivity is 0.02 S/cm, with an activation energy of 0.13 eV. This compound should be a Mott insulator, and oxidation of the film should have occurred during or after film preparation.

The recently proposed *homodoping method*, by which an amphiphilic TCNQ having a long alkyl chain is mixed with $C_{22}Py(TCNQ)$ to achieve partial oxidation of TCNQ moiety in the form of LB film, gives conductivities on the order of 10^{-3} S/cm [55].

2. Charge-Transfer Complex

The monolayer assemblies of charge-transfer complexes have been fabricated since they do not require any secondary treatments to obtain high conductivities [42,56–58]. The molecules used are the charge-transfer complexes of TMTTF and long-chain derivatives of TCNQ (Fig. 6). The conductivities of the LB films of TMTTF- C_{14} TCNQ and TMTTF- C_{18} TCNQ are 0.4 and 0.1 S/cm, respectively, which are an order of magnitude higher than the values of the compaction samples. These films are stable for at least 3 months in air at room temperature. The temperature dependence of the conductivity of the LB film shows a semiconductor-like behavior with the activation energy 0.08 eV, which probably originates from the defects and disorders present in the film. The monolayer conductivity of TMTTF- C_{18} TCNQ on a glycerin subphase is shown in Fig. 7. The conductivity increases with increasing surface pressure and reaches a maximum of about 1 S/cm. Polarized UV–visible absorption spectra indicate that the long axis of TCNQ is parallel to the film surface, which is very different

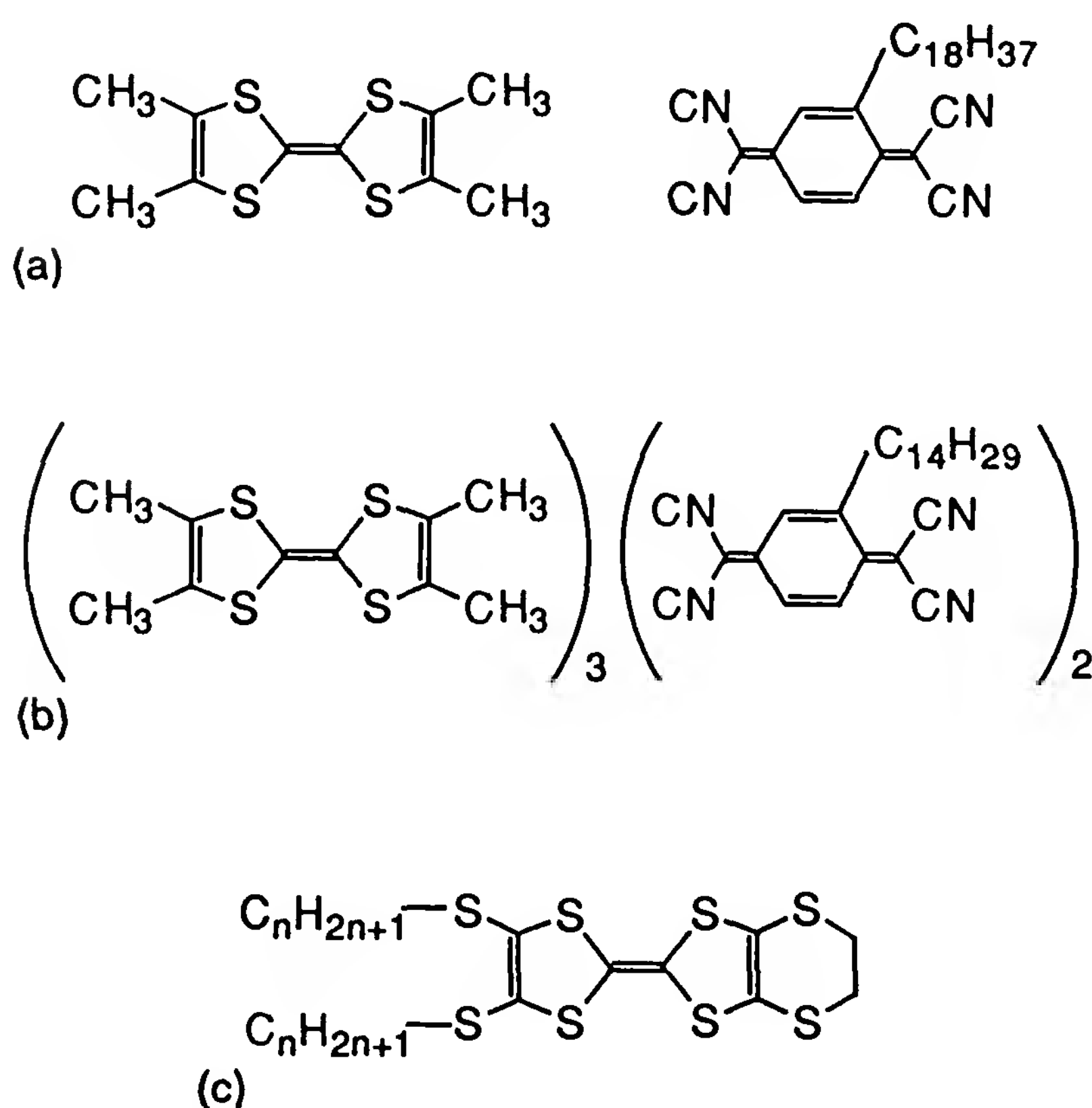


Figure 6 Structures of (a) TMTTF- C_{18} TCNQ, (b) TMTTF- C_{14} TCNQ, and (c) C_n TET-TTF.

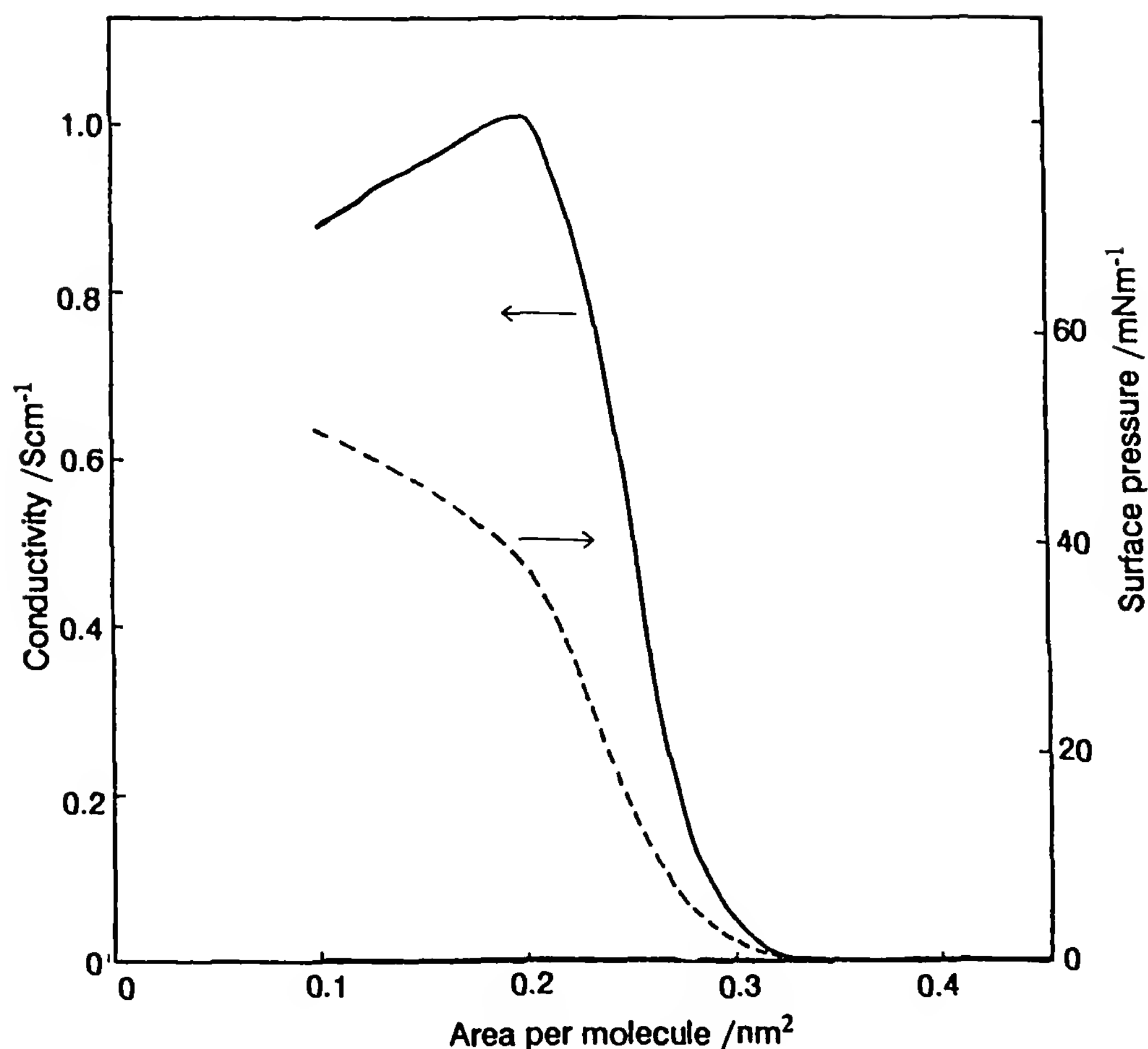


Figure 7 Conductivity–area and surface pressure–area isotherms of TMTTF- C_{18} TCNQ. (From Ref. 56.)

from the $C_{22}Py(TCNQ)_2$ LB film case, in which the long axis of TCNQ is almost perpendicular to the film surface.

ESR spectra of the LB film of TMTTF- C_{18} TCNQ show a single line without structures, which together with the observed g value indicates that there is strong coupling between TMTTF radical spins and TCNQ radical spins [59] as in the TTF-TCNQ crystal [60]. The temperature dependence of the spin susceptibility of the film suggests the presence of spin species due to conduction electrons.

Anomalous behavior was observed in the ESR spectra of the TMTTF- C_{14} TCNQ LB film shown in Fig. 8 [61,62]: a decrease in spin susceptibility with decreasing temperature, a prominent maximum linewidth, and a maximum g value. These features are similar to those observed in TTF-TCNQ crystals around the Peierls transition temperature [60,63,64]. The results can be reconciled if the system is an organic metal: the observed anomalies

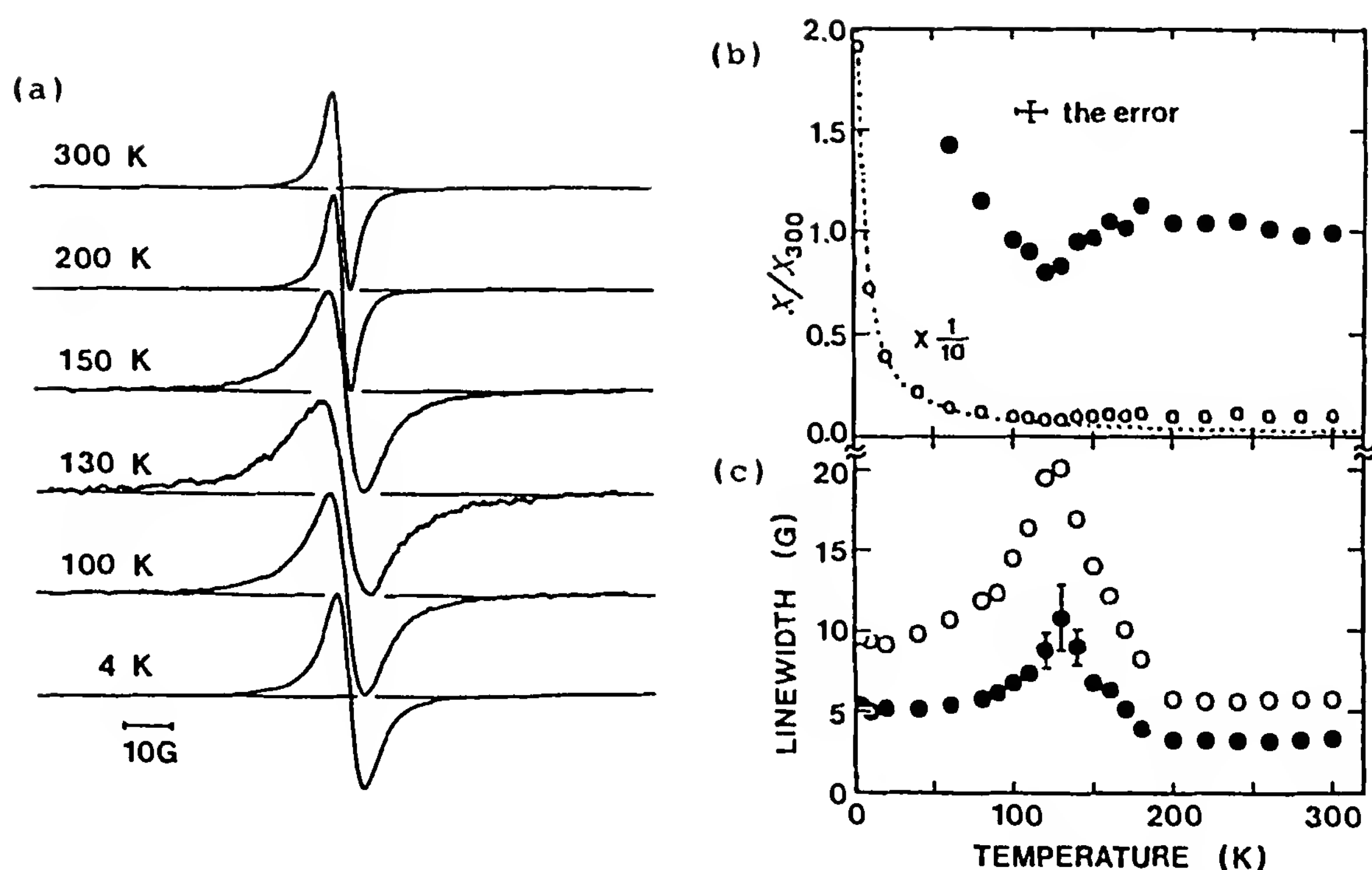


Figure 8 (a) ESR signals observed for an LB film of TMTTF- C_{14} TCNQ at various temperatures with the external magnetic field parallel to the plane normal of the sample. (b) Temperature-dependent spin susceptibility corresponding to lines (a); the dashed line refers to a Curie-like ($1/T$) law. (c) Temperature-dependent peak to peak linewidth ΔH_{PP} (\bullet), and full width at half maximum of the integrated signal, ΔH_{HM} (\circ), corresponding to the lines in part (a). (From Ref. 61.)

should be due to Peierls fluctuations, which are prominent in typical one-dimensional systems.

The orientation of the donor and acceptor moieties is elucidated by ESR and optical measurements [65,66]. The long axes of TMTTF and TCNQ lies in the film plane, while the short axes of the two components are almost perpendicular to the film surface.

The LB films of charge-transfer complexes of C_n TET-TTF, long-chain derivatives of BEDT-TTF, with F_4 TCNQ were fabricated to try to obtain high conductivities [67–69]. The iodine doping of the LB film yields a conductivity on the order of 10^{-2} S/cm, which is considered to be due to reduction of the donor. The LB films of a series of 3,4,5-(alkylthio)-1,2-dithiolium and TCNQ were also fabricated [70,71]. The binary mixed LB films were investigated for amphiphilic donors, TTF and BEDT-TTF derivatives, amphiphilic acceptors, TCNQ, and anthraquinodimethane derivatives [72]. There is an LB film based on a charge-transfer complex with

a metallic temperature dependence of conductivity, which will be discussed later.

3. Cation-Radical Salt

The LB films of TTF [73,74] and BEDT-TTF [75–81] derivatives were investigated and secondary treatments, such as iodine or ICI doping, rendered the films conductive. The structure of the LB film of C_{18} TET-TTF doped with iodine is investigated by UV/visible and IR spectroscopies [76–79]. The initial stage of the chemical reaction involves formation of the cation radical of the donor, which is converted spontaneously into a dimeric form. At this step the film is insulating. Gradual evaporation of I_2 from the film takes place afterward and the conductivity of the film reaches a maximum of about 0.1 S/cm. (See the footnote in Section II.A.1.)

4. Conducting Polymer

The LB film of a conducting polymer was first prepared by Iyoda et al. [82–85] using an amphiphilic pyrrole derivative mixed with octadecane. This precursor LB film is electropolymerized to give a lateral conductivity of 0.1 S/cm, with the conductivity in the perpendicular direction being 10^{-11} S/cm. The procedure of the electropolymerization is shown in Fig. 9: The precursor film is immersed in an acetonitrile solution of $LiClO_4$ by a few millimeters, and the electropolymerization starts near the liquid surface and proceeds upward.

Propagation of the polymerization is seen by a change in color of the LB film: from the semitransparent white of the precursor LB film to the blackish green or reddish brown of the conductive film. Several other methods were demonstrated to obtain conductive polypyrrole LB films [86,87]. The conductive LB films of polyaniline [85,87] and polythiophene [85,88–93] were also reported. For the latter LB films, a maximum conductivity of 5 S/cm was obtained by $NOPF_6$ doping [91].

5. Transition Metal Complex

The molecules used in this class are metal–dithiolate complexes with amphiphilic cations such as long-chain ammonium or long-chain pyridinium cations [94–107]. Among others, metal–(dmit) $_2$ systems have been investigated extensively [95–107] since superconductors are found in the metal–(dmit) $_2$ complexes in single-crystalline forms [108–110]. The conductivities of the LB films of mC_n -M (Fig. 10) after Br or electrochemical oxidation were investigated systematically and are summarized in Table 1. Roughly, the shorter the length of the substituted alkyl chains, the higher the conductivity of the resultant LB film. The LB film of $3C_{10}$ -Au gives the best

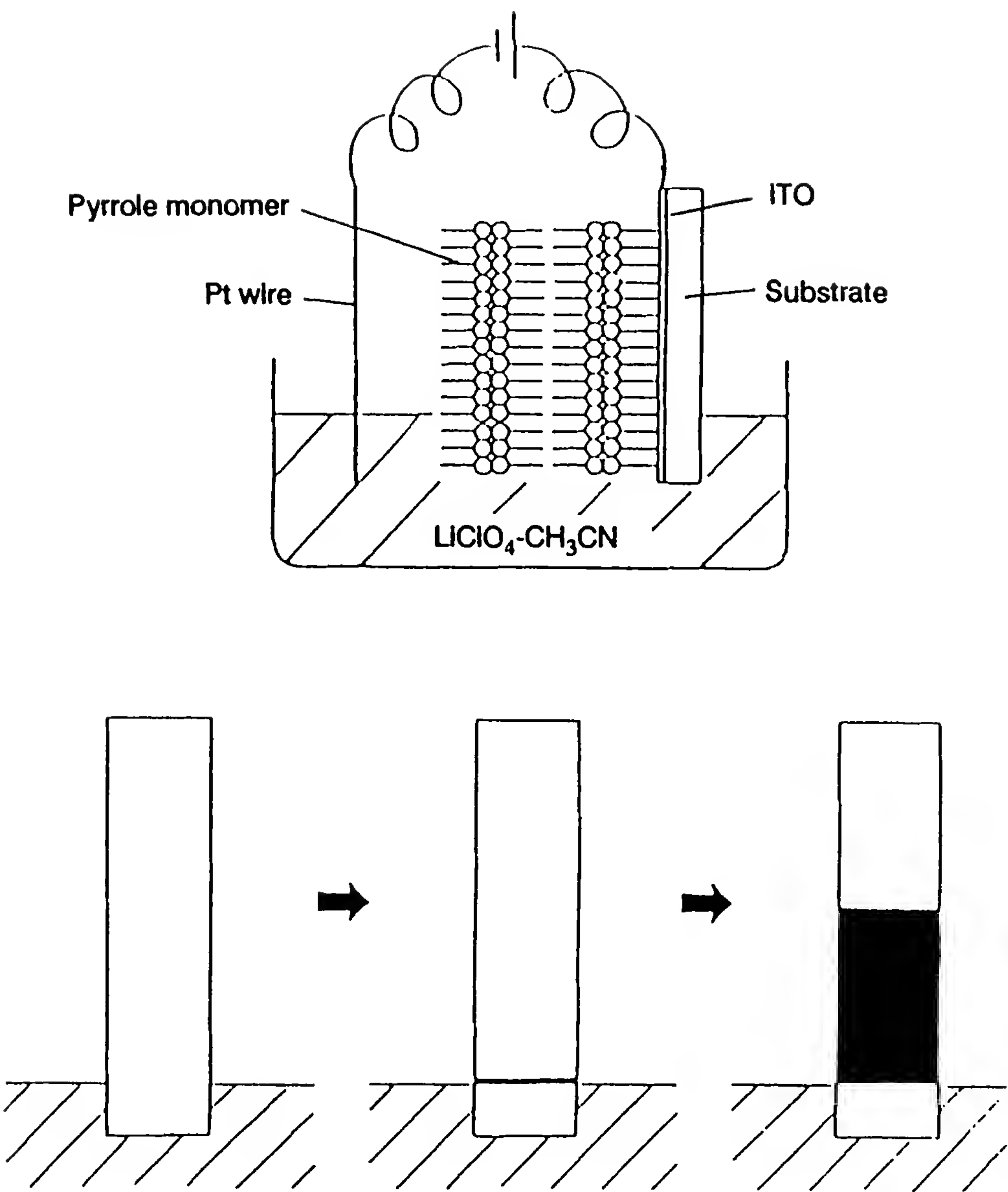


Figure 9 Electrochemical polymerization of polypyrrole LB film. (From Ref. 84.)

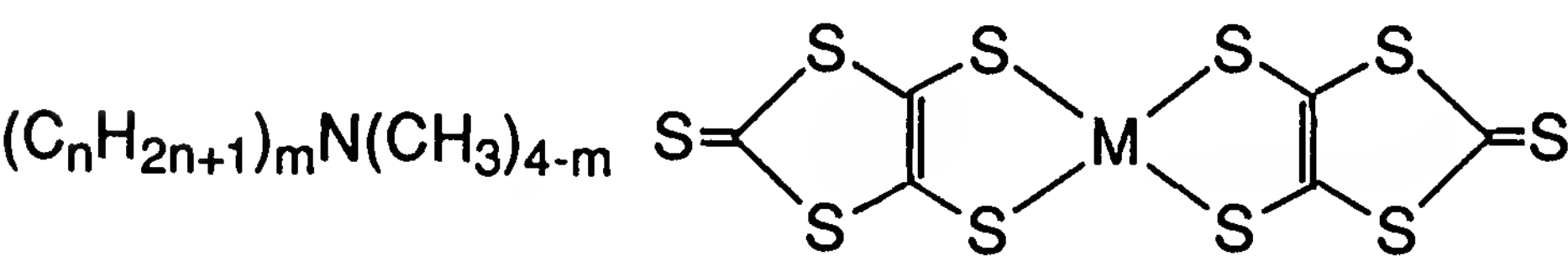


Figure 10 Structure of $m\text{C}_n\text{-M}$.

Table 1 Conductivity of the LB Film of Metal–(dmit)₂

Material ^a	Ratio ^b	Dipping method ^c	Bulk conductivity (S cm)	
			Bromine oxidation	Electrochemical oxidation
1C ₁₈ -Ni	1:1	H	0.11	0.9
2C ₁₀ -Ni	1:1	H	1.0	1.4
2C ₁₂ -Ni	1:1	H	0.03 ^d	
2C ₁₄ -Ni	1:1	H	0.09 ^d	
2C ₁₆ -Ni	1:1	V	0.05 ^d	
2C ₁₈ -Ni	1:1	V	0.009 ^d	
2C ₂₂ -Ni	Pure	V	0.002 ^d	
2C ₁₀ -Au	1:1	H	0.12 ^d	1.4
2C ₁₄ -Au	1:1	H	0.15 ^d	
2C ₁₈ -Au	1:1	H	0.005 ^d	
2C ₂₂ -Au	1:1	H	— ^e	
3C ₁₀ -Ni	1:1	H	1.5	1.4
3C ₁₄ -Ni	1:1	H	1.3	0.87
3C ₁₀ -Au	1:1	H	15	33
3C ₁₄ -Au	1:1	H	5.4	19
3C ₁₆ -Au	1:1	H	2.6	0.46
3C ₁₈ -Au	1:1	H	1.4	0.12
4C ₁₀ -Ni	1:1	H	1.6	0.012
C ₁₄ Py-Ni	1:1	H	1.5	1.2
C ₂₂ Py-Ni	1:1	H	0.23	0.32
2C ₁₀ -Pd ^f	Pure	H	0.3 ^g	1.0
2C ₁₀ -Pt ^f	Pure	H	0.001 ^g	

^aPy, pyridinium.
^bMolar mixing ratio with icosanoic acid.
^cH, horizontal lifting method; V, vertical dipping method.
^dSilver paste was used as electrodes.
^eBelow the limit of detection.
^f2:1 salt.
^gOxidized by iodine vapor.
Source: Ref. 98.

result, and the conductivity of LB film after the electrochemical oxidation is about 30 to 40 S/cm, which is the highest value in the LB field. Moreover, the temperature dependence of conductivity of this LB film is metallic from room temperature down to around 200 K (i.e., the conductivity increases with decreasing temperature, which is discussed in the next section).

B. Metallic LB Film

Most of the conductive LB films are semiconductors in a macroscopic scale, which means that the macroscopic conductivity decreases with a decrease in temperature. At present there are only two LB films, the conductivities of which increase with decreasing temperature. It is to be noted that the ESR analyses of the LB films of TMTTF-C₁₄TCNQ and TMTTF-C₁₈TCNQ show that these LB films include metallic parts, although the macroscopic conductivities are semiconductor-like [59,61,62]. This suggests that the defects and disorders present in the LB films are sometimes the reason why the LB films behave like semiconductors when metallic domains exist in the films. Due to the strong intermolecular interaction between the molecules used for conductive LB films, domain structures are generally observed using a polarizing microscope, a scanning electron microscope, or an atomic force microscope [40,53,106].

Organic conductors could be categorized in terms of the conduction mechanism. One-dimensional conductors seem to be sensitive to defects and disorders and become insulators at low temperatures due to the metal–insulator transitions even when the materials are metals at room temperature. On the other hand, more-than-one-dimensional conductors seem to be relatively insensitive to defects and disorders. Superconductors are found in this class of compounds. Taking the foregoing features into account, more-than-one-dimensional conductors have an advantage over one-dimensional conductors when they are to be used as the active elements of the conductive LB films. Actually, the active parts of the two metallic LB films belong to the more-than-one-dimensional conductors.

1. 3C₁₀-Au LB Film

As mentioned earlier, the LB film of 3C₁₀-Au shows a metallic temperature dependence of dc conductivity [97,98,100,101,107]. Figure 11 shows the temperature-dependent conductivity of the film in the temperature range 300 to 4 K. The conductivity increases with decreasing temperature from room temperature down to around 200 K and decreases below that temperature down to 4 K. This curve is reproducible both for cooling and heating cycles, although T_{max} , the temperature at which the conductivity takes a maximum, is scattered in the temperature range 100 to 240 K, depending on the sample [101].

The temperature dependence of the thermoelectric power in the range 300 to 4 K is shown in Fig. 12. The thermoelectric power decreases gradually with decreasing temperature, and no anomaly corresponding to the maximum in conductivity is seen, which suggests that the maximum in conductivity is not of the Peierls type but is attributable to the strong carrier

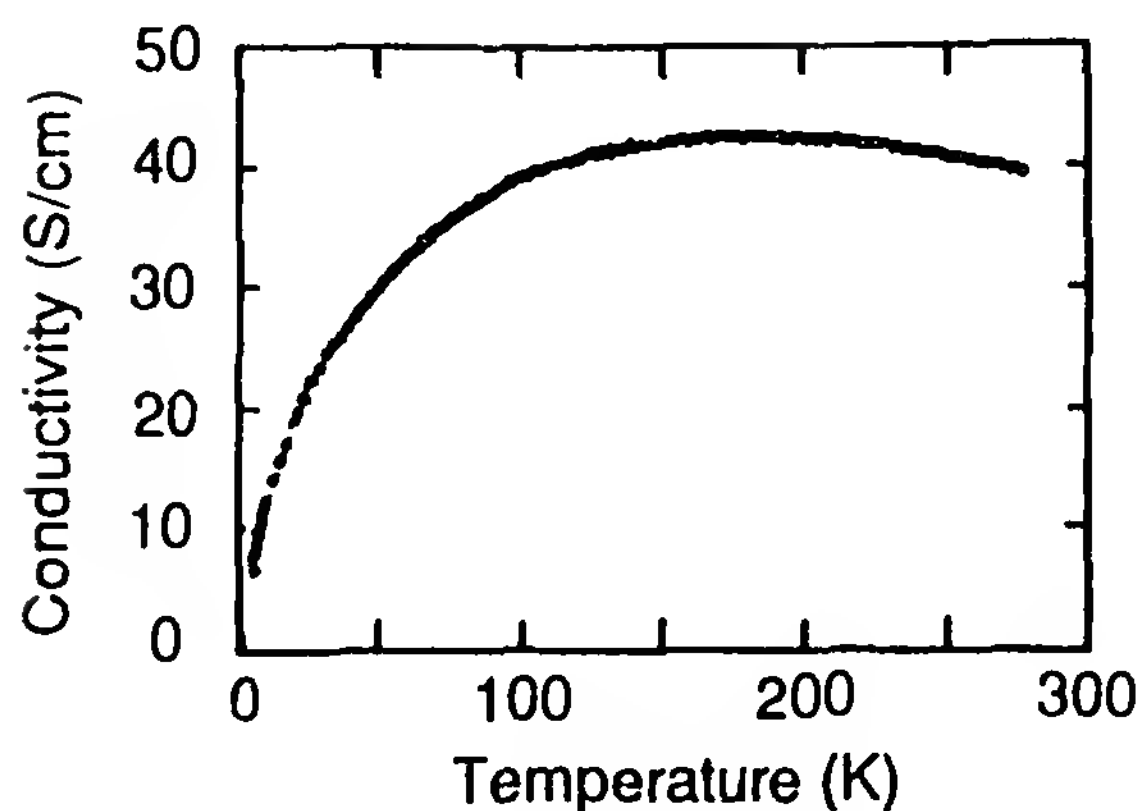


Figure 11 Electrical conductivity of the $3C_{10}$ -Au LB film in the temperature range 300 to 4 K. (From Ref. 101.)

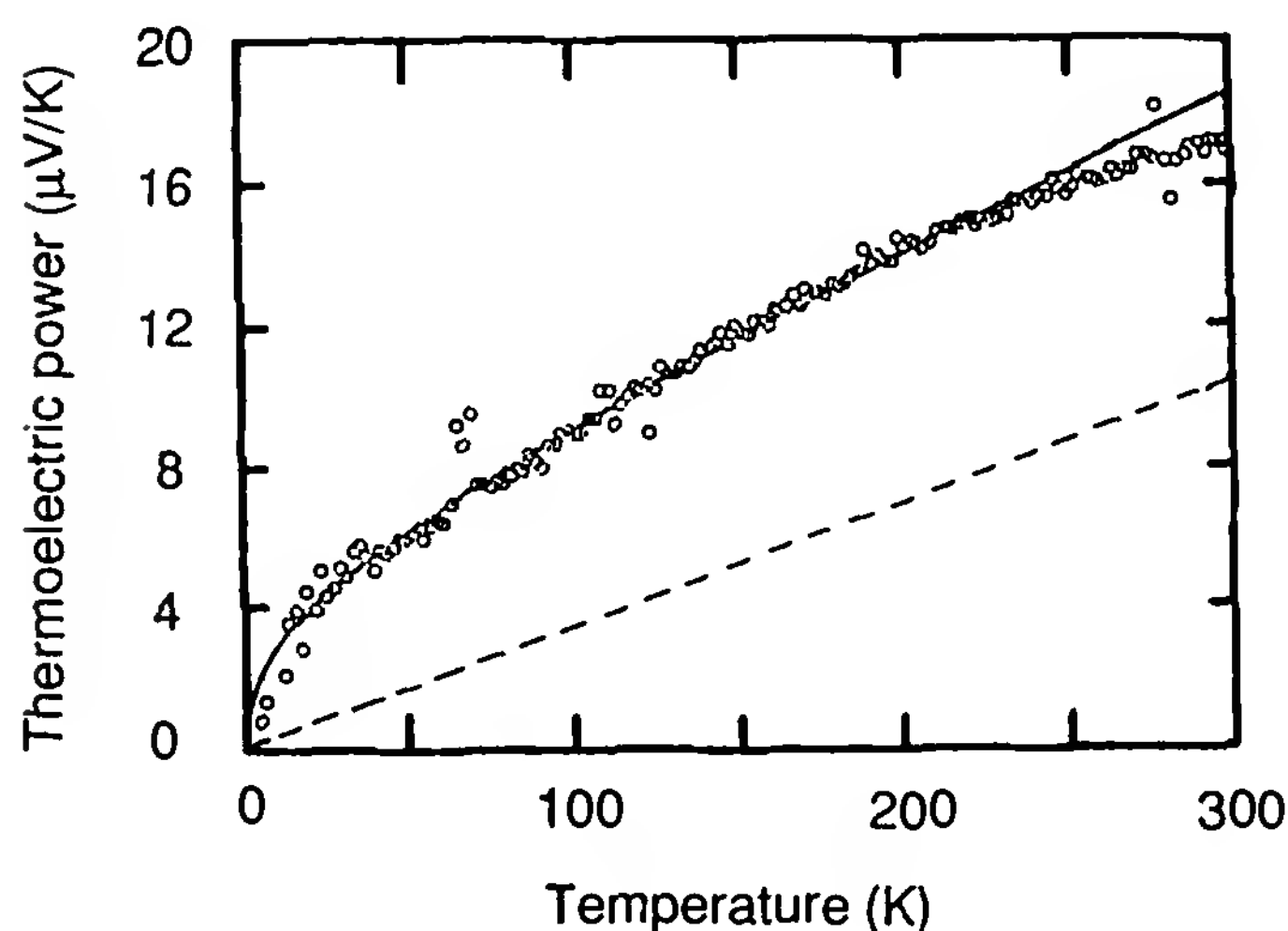


Figure 12 Thermoelectric power of the $3C_{10}$ -Au LB film in the temperature range 300 to 4 K. (From Ref. 101.)

localization, which is characterized by the variable range hopping (VRH) regime. The thermoelectric power is characterized by the linear combination of a metallic and a VRH behavior. This picture indicates that the metallic and VRH regions coexist in the film.

As the compressibilities of the organic compounds are larger than those of inorganic compounds in most cases, the electrical properties of the organic metals are strongly affected by the application of pressure, and in some cases, even the superconducting transitions at low temperatures are induced [111]. Hence the conductivity measurements of this LB film has been made under hydrostatic pressure [107]. The conductivity increased with applied pressure, reaching about a threefold larger value at 14 kbar

than the conductivity under ambient pressure, which is comparable to the values of the single crystals of $\text{TTF}[\text{Pd}(\text{dmit})_2]_2$ and $\text{TTF}[\text{Ni}(\text{dmit})_2]_2$ [109] or doped bulk polymers of poly(3-alkylthiophene) [112]. The temperature dependence of conductivity did not show any evidence of superconducting transition. Phenomenologically, the metallic nature of the conductivity becomes more enhanced under higher pressure since T_{max} decreases with increasing pressure.

2. $\text{BO-C}_n\text{TCNQ}$ LB Film

The LB films of charge-transfer complexes of BO (bisethylenedioxytetra-thiafulvalene)- C_nTCNQ (Fig. 13) are investigated and one of them shows a metallic temperature dependence of conductivity [113]. This donor had provided a number of metallic complexes not only with inorganic anions [114–117] but also with a large variety of organic acceptors [118,119]. The point is that they exhibit metallic temperature-dependent conductivities even in the form of a compressed pellet, which suggests the strong self-assembling ability of BO to form a two-dimensional network and presents an advantage for this donor to be used for conductive LB films since the presence of the defects and disorders is in a sense inherent in conductive LB films.

The elemental analyses show the stoichiometry of the complexes, $\text{BO}:\text{C}_{10}\text{TCNQ}:\text{H}_2\text{O} = 10:4:1$ and $\text{BO}:\text{C}_{14}\text{TCNQ}:\text{H}_2\text{O} = 9:4:2$. The exact composition is not obtained for the complex with C_{18}TCNQ . Figure 14 shows the temperature dependence of conductivity of the LB films of the foregoing complexes with icosanoic acid as a matrix. The room-temperature conductivities are ca. 10 and 3 S/cm for the C_{10}TCNQ and C_{14}TCNQ complexes, respectively. The value of 10 S/cm is the highest value for an LB film without secondary treatment. Moreover, the conductivity of the C_{10}TCNQ complex is metallic from room temperature down to about 250 K. It is to be noted that this high conductivity has enabled measurement

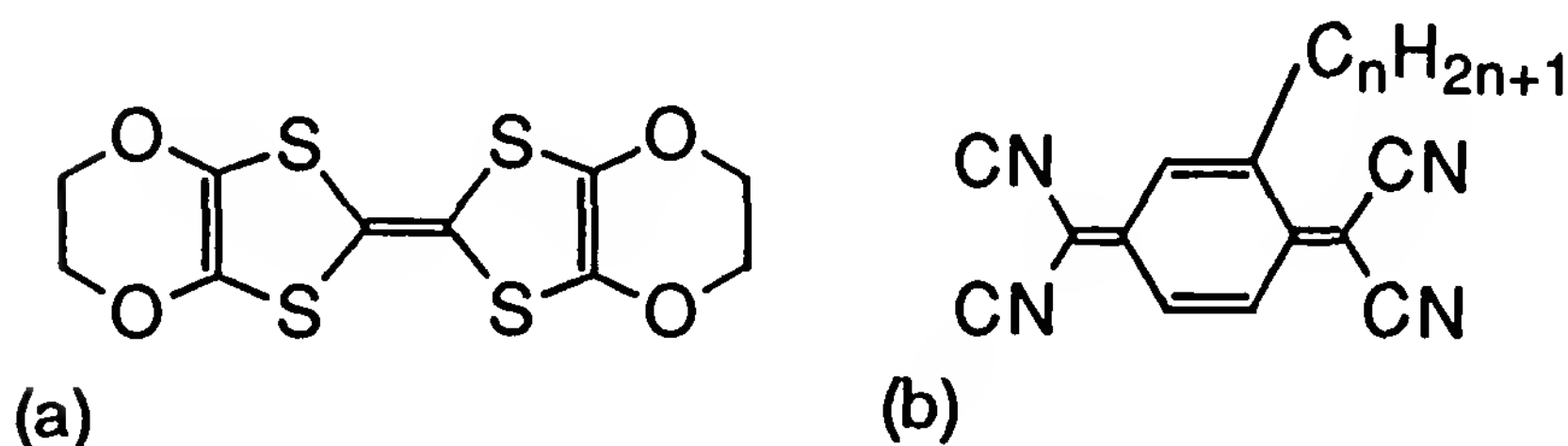


Figure 13 Structure of (a) BO and (b) C_nTCNQ .

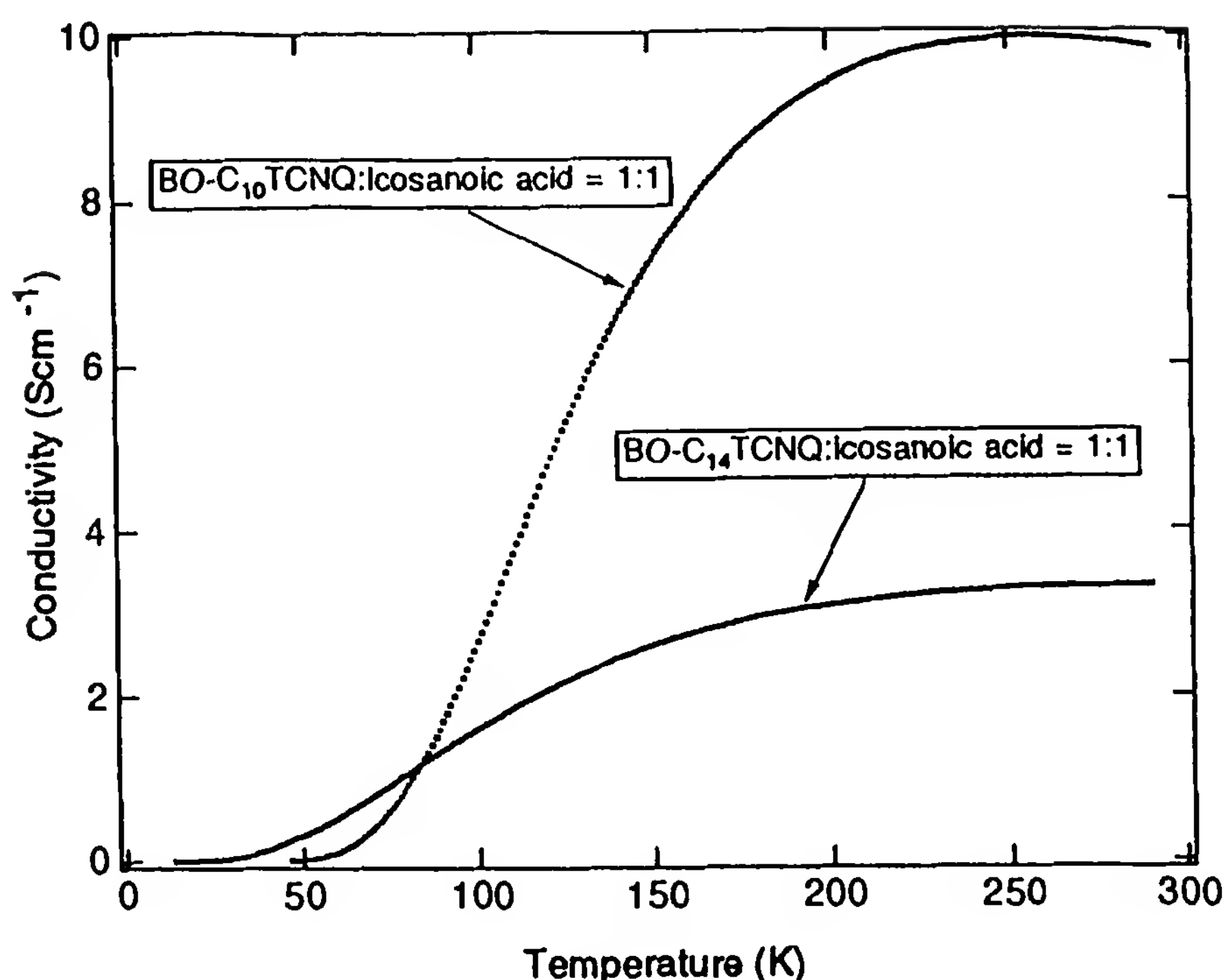


Figure 14 Electrical conductivity of the LB film of BO- C_n TCNQ mixed with icosanoic acid in the temperature range 300 to 4 K. (From Ref. 113.)

of the conductivity–area isotherm on a water surface for the first time [120].

C. Fullerene LB Film

Details of the characteristics of the fullerenes have been given in Chapter 10. The discovery [121] of an efficient synthesis for C_{60} has led to intense research on the properties of fullerene and its derivatives [122]. The first monolayer experiment on C_{60} was done by Obeng and Bard [123,124]. They reported the monolayer formation of C_{60} at the air–water interface, which has been a controversial subject [125–133]: most groups found the multilayer formation on a water surface [125–132]. The interesting point is that a superconducting transition was observed around 8 K in a 50-layer LB film of C_{60} doped with potassium [134], which is significantly lower than the critical temperature $T_c = 18.6$ K observed in bulk K_3C_{60} [135,136]. Because of the small amount of material in the LB film, probably a few micrograms per layer, the doping level was adjusted by controlling the doping time. The superconducting phase was evidenced by a low-magnetic-field microwave absorption signal, or low-field signal, and not by a con-

ductivity measurement. In any case, this is the first time that a superconductivity has been observed in an LB film.

III. FIELD-EFFECT TRANSISTOR

Direct applications of LB films to electronic devices can be made by substituting the LB films for a part or parts of the existing devices based on inorganic materials. Naturally, this has been done for insulators of Josephson junctions [137–139] MIS (metal–insulator–semiconductor) structures, and so on [140–143]. It would be more interesting to fabricate electronic devices composed solely of LB films. Photoelectric cells based on LB films were fabricated using dye monolayers as photoconductors and $C_{22}Py(TCNQ)_2$ monolayers as one of the electrode materials [144]. The results show that the $C_{22}Py(TCNQ)_2$ films can be used as a wiring material instead of high-work-function metals such as silver or Ni–Cr. In comparison with photoelectric cells using conventional metals, use of the organic electrode is reflected in the changes in spectral shape and transient response of I_{sc} , which are assignable to the difference between the LB film–metal and the LB film–LB contacts.

The first LB field-effect transistors (FETs) utilizing organic semiconductors as the active material have been prepared by Paloheimo et al. using poly(3-hexylthiophene)/icosanoic acid and quinquethiophene/icosanoic acid LB films with thicknesses ranging from a monolayer to some 10 monolayers [145,146]. Transistor action was actually recognized for the devices even in structures containing one monolayer. The transport properties of the LB films were characterized by fabricating these molecular transistors. Since the holes in these materials are stored into self-localized polaronic states, the field-effect (hole) mobilities were low, especially in thin films. In this context, a method has been devised for fabricating metal electrodes for thin-film FETs having a source-to-drain distance in the sub-100-nm range, based on a lift-off process with sidewall spacers [147].

IV. PHOTOCHEMICAL SWITCHING DEVICE

The LB technique enables us to obtain ultrathin films with the structures and thicknesses controlled at the molecular level, which promises applications to various fields. One of the challenges is to construct a new type of switching device based on conductive LB films. For this purpose, a supramolecular system is used since the geometrical alignment of the functional units are defined by the molecular design of the supermolecules to be used.

A. Switching Phenomenon Based on the Multifunctional Molecule

The scheme of the switching device using the conductive LB film is shown in Fig. 15. A multifunctional supermolecule having switching, transmission, and working units assembled in a proper manner can form a new type of switching device. The basic idea of the switch is that the external stimulus received by the switching unit is conveyed through the transmission unit to the working unit, causing a change in the structure and hence the function of the working unit. Photons are chosen as the external stimulus out of a variety of candidates, such as electric and magnetic fields and heat and chemical substances. The conductivity of the LB film serves as an output signal. These choices are made on the foresight that electricity and light will still play a major role in information processing in the near future. The actual supermolecule consists of photochromic azobenzene as the switching unit, conductive pyridinium(TCNQ)₂ as the working unit, and an alkyl chain as the transmission unit that connects the switching and working units [148–151].

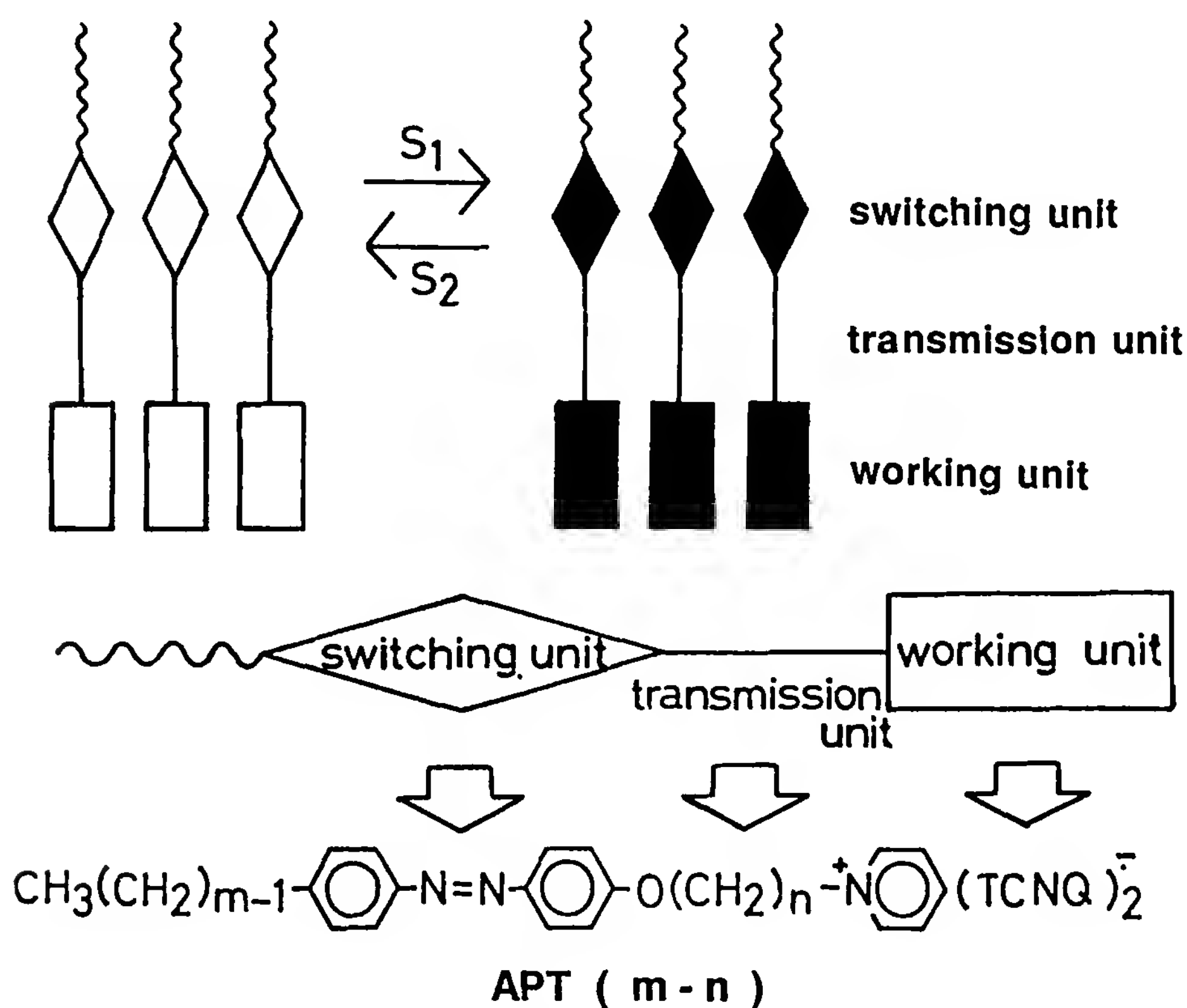


Figure 15 Schematic representation of switching device using conductive LB film. (From Ref. 150.)

Figure 16 shows a change in the absorption spectrum of the LB film of APT(8-12) with UV (365 nm) and visible (436 nm) photoirradiation. The strong band around 360 nm is due to the trans isomer of azobenzene. The absorption due to the local excitation of TCNQ polarized along the long axis is located at about 315 nm but is indiscernible in this spectrum since the transition moment of this band is oriented almost perpendicular to the film surface and the electric field of the light is parallel to the film surface [149].

With the irradiation of UV, the trans-to-cis photoisomerization of the azobenzene proceeds, which is seen by a decrease in the absorption assigned to the trans isomer and a simultaneous increase in the absorption assigned to the cis isomer in the region 400 to 500 nm. The conversion to the cis isomer in the photostationary state is estimated to be about 25% from the change in the absorbance of the trans isomer, which serves as a measure of the cis content. The formed cis isomer isomerizes back to the trans isomer with the irradiation of visible light.

The switching behavior of this LB film with photoirradiation is shown in Fig. 17 together with the results of the LB films with transmission units of different lengths. Figure 17a shows the change in absorbance of the LB

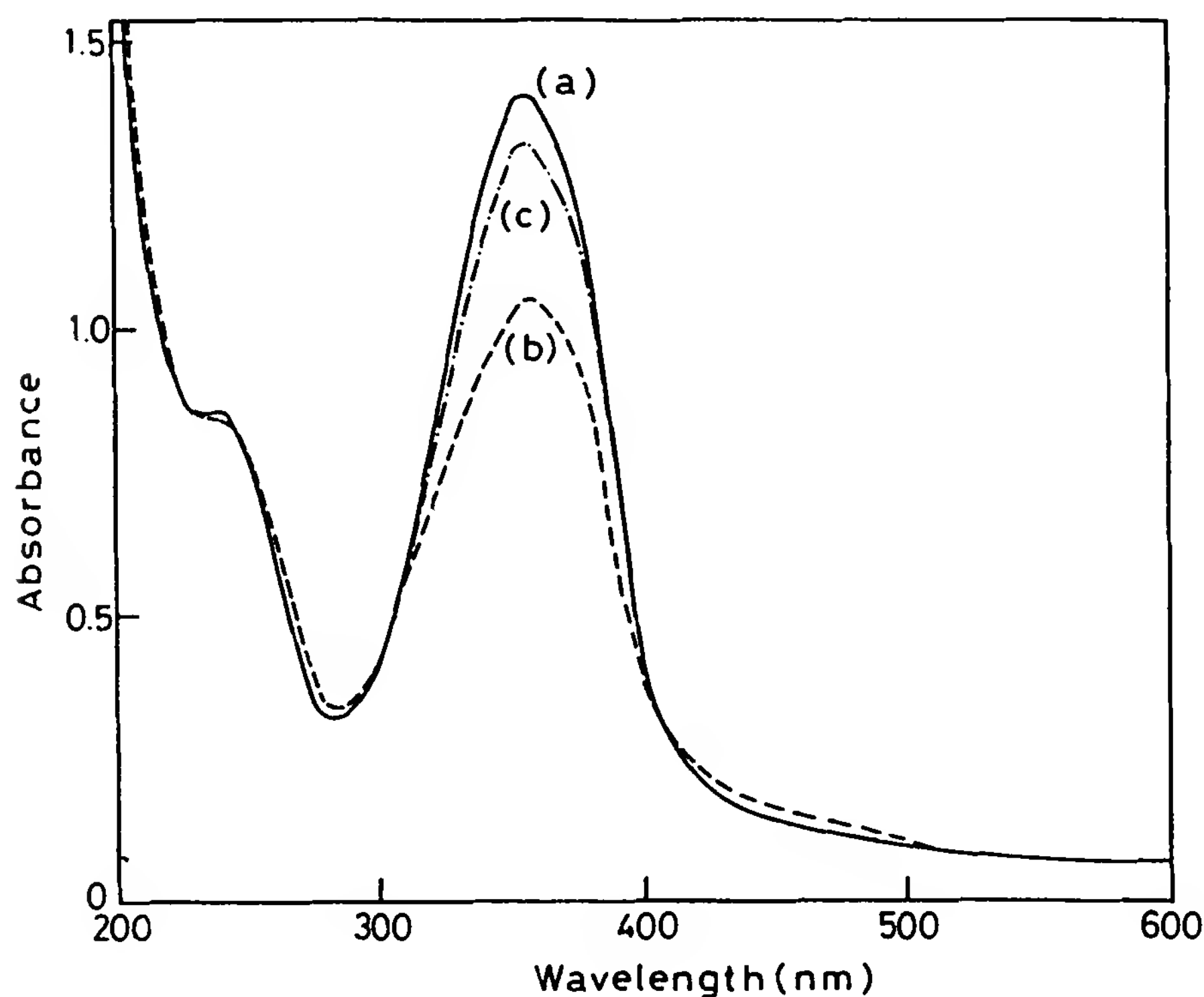


Figure 16 Change in absorption spectrum of LB film of APT(8-12): (a) as-deposited; (b) after irradiation with UV; (c) after irradiation with visible light. (From Ref. 150.)

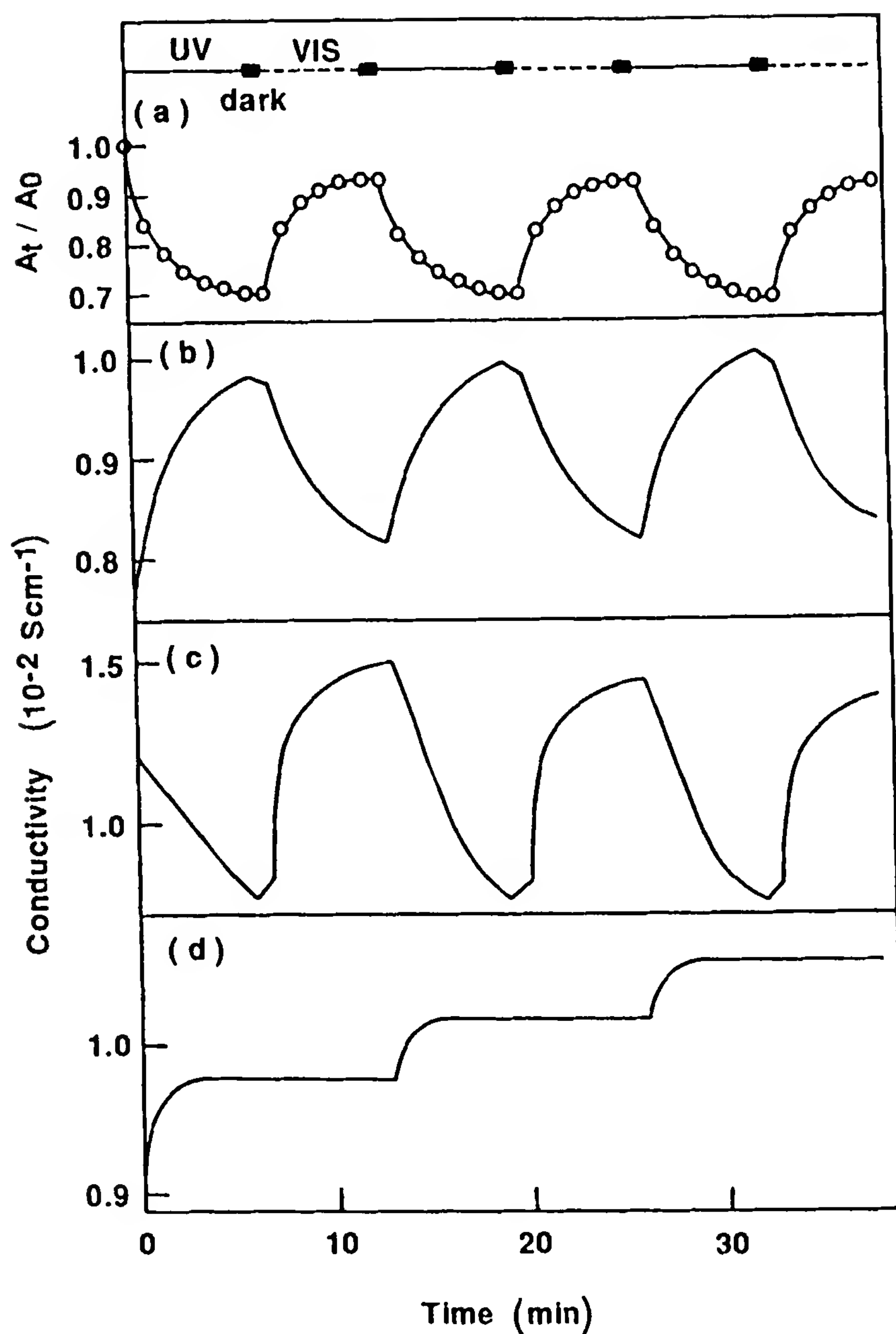


Figure 17 Change in fraction of *trans*-azobenzene for (a) APT(8-12) and change in conductivity of the LB films of (b) APT(8-12), (c) APT(8-14), and (d) APT(8-6) on alternate irradiation with UV and visible light. (From Ref. 152.)

film of APT(8-12) at 356 nm corresponding to the maximum value of the absorption of *trans*-azobenzene on alternate irradiation with UV and visible light [148,150,152,153]. The value of A_t/A_0 represents the fraction of *trans*-azobenzene of APT(8-12) on photoirradiation, where A_t is absorbance at time t and A_0 is absorbance at $t = 0$. When the *trans*-to-*cis* isomerization occurs, this absorbance decreases, and vice versa. Similarly, reversible

photoisomerization was observed for the other two LB films except for the magnitude.

Figure 17b shows the switching behavior of the LB film of APT(8-12). It is apparent that the conductivity of the film associated with the TCNQ moiety is controlled through the photoisomerization of the azobenzene. In other words, the conformational change in the switching unit changes the function of the working unit as designed. The apparent slow switching speed seems to be due to the low intensity of the used light, and the actual switching speed is less than 100 μ s when a laser pulse is employed [148,150].

B. Different Switching Behavior

The role of the transmission unit was investigated by changing the length of the alkyl chain [152,153]. Figure 17c shows the conductivity switching of the LB film of APT(8-14), the transmission of which is longer than the previous transmission by only two carbons. Like the previous switching, this switching is reversible but is different in that the direction of the switching is the opposite in this case. The change in conductivity of the foregoing two LB films is reversible more than several tens of times on alternate irradiation with UV and visible light.

Figure 17d shows the switching behavior of the LB film of APT(8-6), which is very different from the two cases above. The conductivity increases with the trans-to-cis isomerization of azobenzene as in the case of APT(8-12), and the increase in conductivity is about 6% in the photostationary state. The conductivity stays, however, unchanged with the cis-to-trans isomerization. Further irradiation with UV light causes the conductivity to show another increase. This stepwise behavior is observed about 30 times. The increment per cycle decreases with an increasing number of cycles and the conductivity tends to become constant in a cycle repeated more than 30 times.

The behavior of APT(8-6)LB film is compared with the learning process based on the plasticity of synaptic transmission [154,155], since the LB film gains in “skill” (the conductivity of the film increases) due to repeated practice (alternate photoirradiation). In other words, electrons can pass through the LB film more easily as the stimulation (photoirradiation) is repeated. The mechanisms involved in the plasticity in this case are unknown. A tentative explanation is as follows: As deposited, the LB film is in a quasi-stable state, but the activation energy to be overcome is not small. In this case the film will be relaxed to a more stable form when a stimulus with sufficient energy is imposed. In the present case, the switching phenomena having plasticity would be understood if we assume that stimulation by trans-to-cis isomerization of azobenzene has sufficient energy

but stimulation by cis-to-trans isomerization does not. This is supported by the fact that trans-to-cis isomerization is generally more difficult than cis-to-trans isomerization in monolayers or LB films since the former includes the process in which the area per molecule increases [156].

C. Multiple Switching Device

The absorption band associated with the switching unit of the molecule is determined by its molecular structure, which means that the wavelength of the control light is changed by chemical modification of the switching unit. This is easily realized by substituting a naphthalene ring for one of the benzene rings in the azobenzene shown in Fig. 18 [157], which causes the LB film of the chemically modified species to absorb in the longer-wavelength region since the NAPT(8-14) molecule has a more extended π -conjugated skeleton [158].

The absorption band of *trans*-NAPT(8-14), which is located around 410 nm and which represents the absorption of the switching unit, is really shifted toward a longer-wavelength region compared with the LB film of *trans*-APT(12-12). Similarly, the absorption band of the cis isomer is shifted toward a longer-wavelength region.

The photochemical switching device can be fabricated by using either of the two LB films as observed in the APT(8-12) LB film case [148,150]. The wavelengths of control light for the two LB films are summarized in Table 2. Photoirradiation at 365 nm (UV) and at 436 nm (VIS) causes trans-to-cis and cis-to-trans isomerization of the switching unit of APT(12-12), respectively, and irradiation with 405 nm (VIS I) and 546 nm (VIS II) works similarly for NAPT(8-14). The fraction of cis isomer in the photostationary state is about 25% and 17% for APT(12-12) and NAPT(8-14), respectively. The change in conductivity accompanied by the photo-

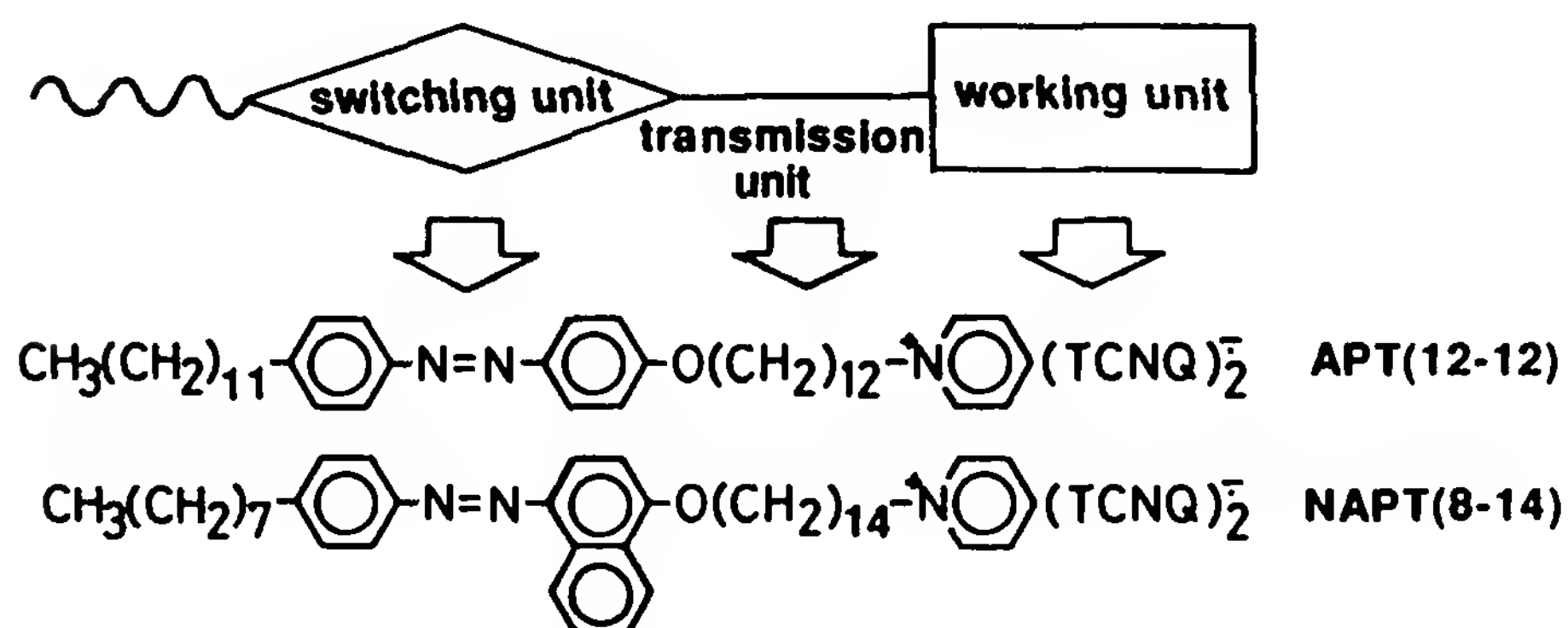


Figure 18 Structure of APT(12-12) and NAPT(8-14). (From Ref. 157.)

Table 2 Wavelength of Control Light Corresponding to Photoisomerization of Switching Unit

Photoisomerization	trans to cis	cis to trans
APT(12-12)	365 nm (UV)	436 nm (VIS)
NAPT(8-14)	405 nm (VIS I)	546 nm (VIS II)

Source: Ref. 157.

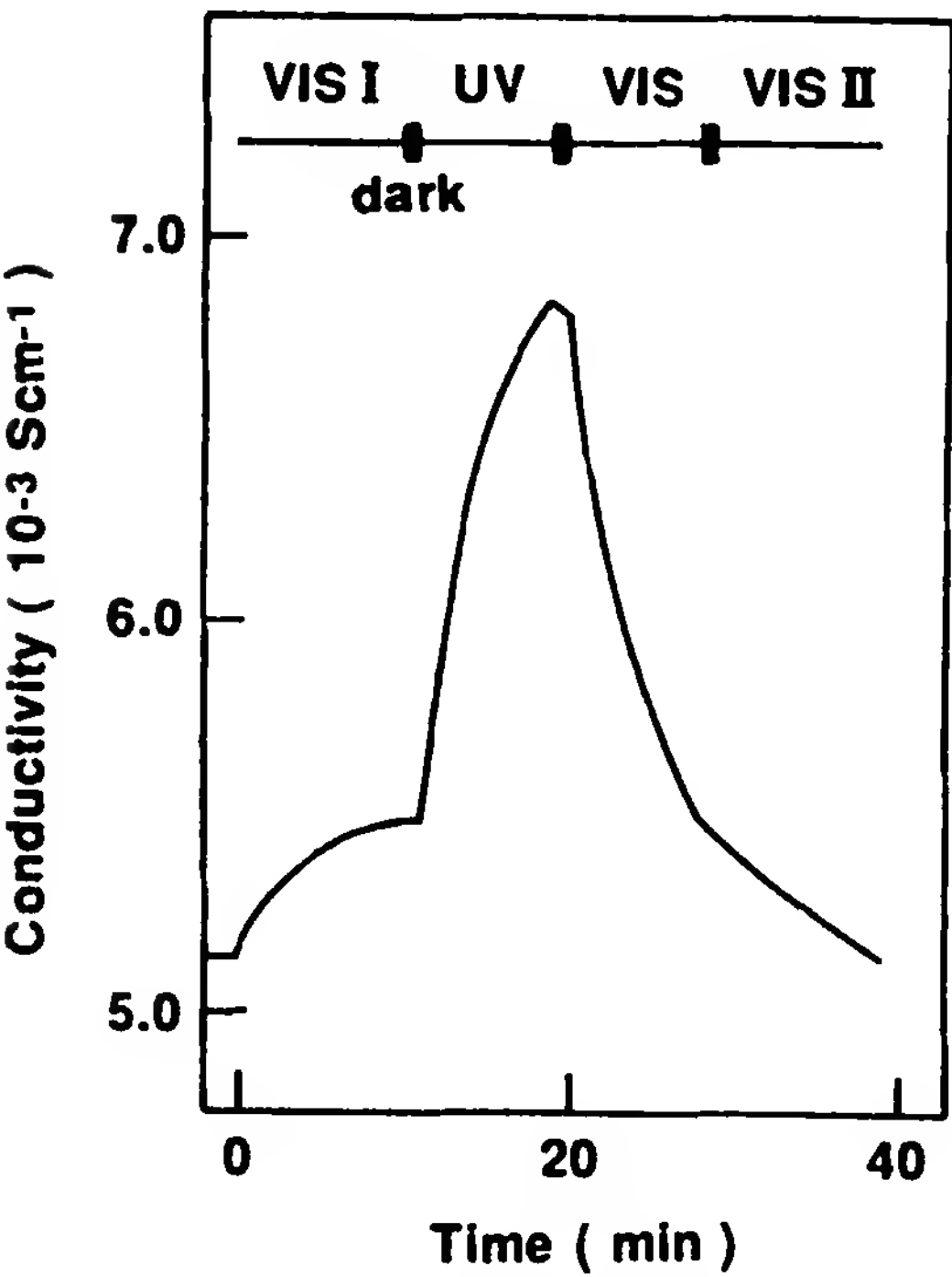


Figure 19 Switching behavior of a multiple switching device by sequential photoirradiation. (From Ref. 157.)

isomerization is about 35% and 13% for APT(12-12) and NAPT(8-14), respectively [157].

A multiple switching device can be fabricated by combining the two photochemical switching LB films noted above, consisting of molecules with different switching units, NAPT(8-14) and APT(12-12): 20 monolayers of APT(12-12) are first transferred onto a hydrophobized quartz plate on which 20 monolayers of NAPT(8-14) are deposited.

A multiple switching device of this type can utilize all four types of control light as external stimuli. Actually, the conductivity of the multiple photochemical switching device is controlled by sequential photoirradiation, as shown in Fig. 19. Irradiation with VIS I causes trans-to-cis isomerization of the naphthylbenzyl azo dye of NAPT(8-14), the conductivity

increasing by about 5%. The irradiation with UV increases the conductivity by 20%, due to trans-to-cis isomerization of azobenzene of APT(12-12). The conductivity of the LB film is changed in a stepwise fashion back to the initial value by sequential irradiation with VIS I and VIS II, each causing cis-to-trans isomerization of the switching unit of APT(12-12) and NAPT(8-14), respectively.

The change in conductivity obeys the additive rule. When the multiple switching device is irradiated with the UV–VIS cycle or the VIS I–VIS II cycle, the conductivity changes reversibly by about 20% or 5%, respectively. These values are the same as the values when a sequence of four types of control light is used, as shown in Fig. 19.

V. CONCLUDING REMARKS

As shown in Section II, this field has expanded enormously in less than 10 years since the first conductive LB film was reported in 1985 [20]. During this time, the research has shifted from one-dimensional conductors to two- and three-dimensional conductors. The reason is clear: Due to the small amount of material involved in an LB film, it is crucial to deal with a highly conductive material if precise conductivity measurements are to be made to elucidate the electrical properties of the material. In this regard, two- and three-dimensional conductors have an advantage over one-dimensional conductors when considered for use as the active parts of the conductive LB films since two- and three-dimensional conductors seem to be relatively insensitive to the defects and disorders present in conductive LB films compared with one-dimensional conductors.

The fabrication of LB FETs and photochemical switching devices is encouraging to researchers working in the field of molecular electronics. The active parts of devices really consist of LB films. The latter could be considered a molecular device.

Another type of electrical switching based on a molecular system has been demonstrated by Potember et al. using polycrystalline organic semiconductor films of metal–TCNQ [159–162]. Switching and memory effects were also observed using an STM tip as a trigger [163,164]. At present these devices do not seem to compete with existing inorganic systems based on single crystals or superlattices. However, improvement in terms of reliability and stability may lead to actual applications of these devices based on molecular systems.

REFERENCES

1. F. L. Carter, ed., *Molecular Electronic Devices*, Marcel Dekker, New York, 1982.

2. A. Aviram and M. A. Ratner, *Chem. Phys. Lett.* 29:277 (1974).
3. A. Aviram, M. J. Freiser, P. E. Seiden, and W. R. Young, U.S. Patent 3,953,874 (Apr. 27, 1976).
4. R. M. Metzger and C. A. Panetta, *New J. Chem.* 15:209 (1991).
5. M. Fujihira, K. Nishiyama, and H. Yamada, *Thin Solid Films* 132:77 (1985).
6. M. Fujihira and H. Yamada, *Thin Solid Films* 160:125 (1988).
7. M. Sakomura and M. Fujihira, *6th International Conference on Organized Molecular Films*, Trois-Rivières, Quebec, Canada, 1993, Abstr. P-8.28.
8. G. G. Roberts, ed., *Langmuir-Blodgett Films*, Plenum Press, New York, 1990.
9. H. Kuhn, *Naturwissenschaften* 54:429 (1967).
10. H. Kuhn, *Thin Solid Films* 99:1 (1983).
11. H. Kuhn, *Thin Solid Films* 178:1 (1989).
12. G. L. Gaines, Jr., *Insoluble Monolayers at Liquid-Gas Interfaces*, Wiley-Interscience, New York, 1966.
13. H. Kuhn, D. Möbius, and H. Bücher, in *Physical Methods of Chemistry*, Vol. 1, Pt. IIIB (A. Weissberger and B. W. Rossiter, eds.), Wiley, New York, 1972, p. 577.
14. For example, *Thin Solid Films* 210-211 (1992).
15. R. M. Leblanc, ed., *Abstracts of the Sixth International Conference on Organized Molecular Films*, Trois-Rivières, Quebec, Canada, 1993.
16. W. A. Little, *Phys. Rev. A* 134:1416 (1964).
17. W. A. Little, in *Low Dimensional Cooperative Phenomena* (H. J. Keller, ed.), Plenum Press, New York, 1975, p. 35.
18. V. L. Ginzburg, *J. Polym. Sci. C* 29:3 (1970).
19. V. L. Ginzburg, *Contemp. Phys.* 9:355 (1968).
20. A. Ruaudel-Teixier, M. Vandevyver, and A. Barraud, *Mol. Cryst. Liq. Cryst.* 120:319 (1985).
21. B. Mann and H. Kuhn, *J. Appl. Phys.* 42:4398 (1971).
22. M. Sugi, K. Nembach, D. Möbius, and H. Kuhn, *Solid State Commun.* 15:1867 (1974).
23. E. E. Polymeropoulos, *J. Appl. Phys.* 48:2404 (1977).
24. M. Sugi, T. Fukui, and S. Iizima, *Chem. Phys. Lett.* 45:163 (1977).
25. M. Sugi and S. Iizima, *Phys. Rev. B* 15:574 (1977).
26. M. Sugi, T. Fukui,[†] and S. Iizima, *Phys. Rev. B* 18:725 (1978).
27. G. G. Roberts, P. S. Vincett, and W. A. Barlow, *J. Phys. C* 11:2077 (1978).
28. M. Sugi, T. Fukui, and S. Iizima, *Mol. Cryst. Liq. Cryst.* 50:183 (1979).
29. M. Sugi and S. Iizima, *Appl. Phys. Lett.* 34:290 (1979).
30. M. Sugi, T. Fukui, S. Iizima, and K. Iriyama, *Bull. Electrotech. Lab.* 43:625 (1979).
31. N. F. Mott, *Phil. Mag.* 19:835 (1969).
32. J. Richard, M. Vandevyver, P. Lessieur, A. Ruaudel-Teixier, and A. Barraud, *J. Chem. Phys.* 86:2428 (1987).
33. B. Belbeoch, M. Roulliay, and M. Tournaire, *Thin Solid Films*, 134:89 (1985).

34. J. Richard, M. Vandevyver, P. Lesieur, A. Barraud, and K. Holczer, *J. Phys. D. Appl. Phys.* **19**:2421 (1986).
35. T. Nakamura, M. Tanaka, T. Sekiguchi, and Y. Kawabata, *J. Am. Chem. Soc.* **108**:1302 (1986).
36. A. Barraud, M. Lequan, R. M. Lequan, P. Lessieur, J. Richard, A. Ruaudel-Teixier, and M. Vandevyver, *J. Chem. Soc. Chem. Commun.*, 797 (1987).
37. M. Vandevyver, J. Richard, A. Barraud, A. Ruaudel-Teixier, M. Lequan, and R. M. Lequan, *J. Chem. Phys.* **87**:6754 (1987).
38. T. Nakamura, M. Matsumoto, F. Takei, M. Tanaka, T. Sekiguchi, E. Manda, and Y. Kawabata, *Chem. Lett.* 709 (1986).
39. M. Matsumoto, T. Nakamura, F. Takei, M. Tanaka, T. Sekiguchi, M. Mizuno, E. Manda, and Y. Kawabata, *Synth. Metals* **19**:675 (1987).
40. H. Komizu, M. Matsumoto, T. Nakamura, M. Tanaka, E. Manda, Y. Kawabata, and K. Honda, *Nippon Kagaku Kaishi*, 2180 (1987).
41. T. Nakamura, M. Matsumoto, H. Tachibana, M. Tanaka, E. Manda, and Y. Kawabata, *Thin Solid Films* **178**:413 (1989).
42. T. Nakamura, F. Takei, M. Matsumoto, M. Tanaka, T. Sekiguchi, E. Manda, Y. Kawabata, and G. Saito, *Synth. Metals* **19**:681 (1987).
43. K. Ikegami, S. Kuroda, M. Saito, K. Saito, M. Sugi, T. Nakamura, M. Matsumoto, and Y. Kawabata, *Phys. Rev. B* **35**:3667 (1987).
44. K. Ikegami, S. Kuroda, M. Saito, K. Saito, M. Sugi, T. Nakamura, M. Matsumoto, and Y. Kawabata, *Thin Solid Films* **160**:139 (1988).
45. Z. G. Soos and S. R. Bondeson, *Solid State Commun.* **35**:11 (1980).
46. Z. G. Soos and S. R. Bondeson, *Solid State Commun.* **39**:289 (1981).
47. S. R. Bondeson and Z. G. Soos, *Phys. Rev. B* **22**:1793 (1980).
48. J. Messier and G. Marc, *J. Chim. Phys.* **32**:799 (1971).
49. S. Kuroda, K. Ikegami, M. Sugi, and S. Iizima, *Solid State Commun.* **58**:493 (1986).
50. S. Kuroda, K. Ikegami, Y. Tabe, K. Saito, and M. Sugi, *Phys. Rev. B* **43**:2531 (1991).
51. K. Ikegami, S. Kuroda, M. Sugi, T. Nakamura, H. Tachibana, M. Matsumoto, and Y. Kawabata, *J. Phys. Soc. Jpn.* **61**:3752 (1992).
52. K. Ikegami, S. Kuroda, M. Sugi, T. Nakamura, M. Matsumoto, H. Tachibana, and Y. Kawabata, *Synth. Metals* **55–57**:1899 (1993).
53. M. Vandevyver, A. Barraud, P. Lesieur, J. Richard, and A. Ruaudel-Teixier, *J. Chim. Phys.* **83**:599 (1986).
54. A. S. Dhindsa, M. R. Bryce, J. P. Lloyd, and M. C. Petty, *Synth. Metals* **22**:185 (1987).
55. J.-P. Bourgoin, A. Ruaudel-Teixier, M. Vandevyver, M. Roulliay, and A. Barraud, *Thin Solid Films* **210–211**:250 (1992).
56. T. Nakamura, F. Takei, M. Tanaka, M. Matsumoto, T. Sekiguchi, E. Manda, Y. Kawabata, and G. Saito, *Chem. Lett.* 323 (1986).
57. Y. Kawabata, T. Nakamura, M. Matsumoto, M. Tanaka, T. Sekiguchi, H. Komizu, E. Manda, and G. Saito, *Synth. Metals* **19**:663 (1987); see also *Synth. Metals* **22**:92 (1987).

58. M. Matsumoto, T. Nakamura, E. Manda, Y. Kawabata, K. Ikegami, S. Kuroda, M. Sugi, and G. Saito, *Thin Solid Films* 160:61 (1988).
59. K. Ikegami, S. Kuroda, K. Saito, M. Saito, M. Sugi, T. Nakamura, M. Matsumoto, Y. Kawabata, and G. Saito, *Synth. Metals* 19:669 (1987).
60. Y. Tomkiewicz, B. A. Scott, L. J. Tao, and R. S. Title, *Phys. Rev. Lett.* 32:1363 (1974).
61. K. Ikegami, S. Kuroda, K. Saito, M. Saito, M. Sugi, T. Nakamura, M. Matsumoto, Y. Kawabata, and G. Saito, *Synth. Metals* 27:B587 (1988).
62. K. Ikegami, S. Kuroda, K. Saito, M. Saito, M. Sugi, T. Nakamura, M. Matsumoto, Y. Kawabata, and G. Saito, *Thin Solid Films* 179:177 (1989).
63. Y. Tomkiewicz, A. Z. Taranko, and J. B. Torrance, *Phys. Rev. B* 15:1017 (1977).
64. Y. Tomkiewicz, *Phys. Rev. B* 19:4038 (1979).
65. K. Ikegami, S. Kuroda, Y. Tabe, K. Saito, M. Saito, M. Sugi, T. Nakamura, H. Tachibana, M. Matsumoto, and Y. Kawabata, *Thin Solid Films* 210–211:303 (1992).
66. K. Ikegami, S. Kuroda, Y. Tabe, K. Saito, M. Saito, M. Sugi, T. Nakamura, M. Matsumoto, and Y. Kawabata, *Jpn. J. Appl. Phys.* 31:1206 (1992).
67. G. Saito, *Pure Appl. Chem.* 59:999 (1987).
68. A. Otsuka, G. Saito, T. Nakamura, M. Matsumoto, Y. Kawabata, K. Honda, M. Goto, and M. Kurahashi, *Synth. Metals* 27:B575 (1989).
69. J. Richard, M. Vandevyver, A. Barraud, J. P. Morand, R. Lapouyade, P. Delhaes, J. F. Jacquinet, and M. Roullay, *J. Chem. Soc. Chem. Commun.* 754 (1988).
70. V. Gionis, O. Fichet, M. Izumi, J. Amiell, C. Garrigou-Lagrange, G. C. Papavassiliou, and P. Delhaes, *Chem. Lett.* 871 (1991).
71. O. Fichet, V. Gionis, J. Amiell, B. Agricole, P. Delhaes, D. Ducharme, A. Perrier, and R. M. Leblanc, *Thin Solid Films* 210–211:330 (1992).
72. S. V. Ayrapietants, T. S. Berzina, S. A. Shinkin, and V. I. Troitsky, *Thin Solid Films* 210–211:261 (1992).
73. A. S. Dhindsa, M. R. Bryce, J. P. Lloyd, and M. C. Petty, *Thin Solid Films* 165:L97 (1988).
74. F. Bertho, D. Talham, A. Robert, P. Batail, S. Megtert, and P. Robin, *Mol. Cryst. Liq. Cryst.* 156:339 (1988).
75. C. Lalanne, P. Delhaes, E. Dupart, Ch. Garrigou-Lagrange, J. Amiell, J. P. Morand, and B. Desbat, *Thin Solid Films* 179:171 (1989).
76. J. Richard, M. Vandevyver, A. Barraud, J. P. Morand, and P. Delhaes, *J. Colloid Interface Sci.* 129:254 (1989).
77. M. Vandevyver, M. Roullay, J. P. Bourgoïn, A. Barraud, J. P. Morand, and O. Noel, *J. Colloid Interface Sci.* 141:459 (1991).
78. M. Vandevyver, M. Roullay, J. P. Bourgoïn, A. Barraud, V. Gionis, V. C. Kakoussis, G. A. Mousdis, J. P. Morand, and O. Noel, *J. Phys. Chem.* 95:2095 (1991).
79. M. Vandevyver, *Thin Solid Films* 210–211:240 (1992).

80. J. P. Morand, L. Brzezinski, and M. C. Lopez, *Thin Solid Films* 210–211:280 (1992).
81. T. S. Berzina, S. L. Vorobyova, V. I. Troitsky, V. Yu. Khodorkovsky, and O. Ya. Neiland, *Thin Solid Films* 210–211:317 (1992).
82. T. Iyoda, M. Ando, T. Kaneko, A. Ohtani, T. Shimidzu, and K. Honda, *Tetrahedron Lett.* 27:5633 (1986).
83. T. Iyoda, M. Ando, T. Kaneko, A. Ohtani, T. Shimidzu, and K. Honda, *Langmuir* 3:1169 (1987).
84. T. Shimidzu, T. Iyoda, M. Ando, A. Ohtani, T. Kaneko, and K. Honda, *Thin Solid Films* 160:67 (1988).
85. M. Ando, Y. Watanabe, T. Iyoda, K. Honda, and T. Shimidzu, *Thin Solid Films* 179:225 (1989).
86. K. Hong and M. F. Rubner, *Thin Solid Films* 160:187 (1988).
87. J. H. Cheung, E. Punkka, M. Rikukawa, R. B. Rosner, A. T. Royappa, and M. F. Rubner, *Thin Solid Films* 210–211:246 (1992).
88. I. Watanabe, K. Hong, M. F. Rubner, and I. H. Loh, *Synth. Metals* 28:C473 (1989).
89. I. Watanabe, K. Hong, and M. F. Rubner, *Thin Solid Films* 179:199 (1989).
90. P. Y.-Lahti, E. Punkka, H. Stubb, and P. Kuivalainen, *Thin Solid Films* 179:221 (1989).
91. I. Watanabe, K. Hong, and M. F. Rubner, *Langmuir* 6:1164 (1990).
92. I. Watanabe, J. H. Cheung, and M. F. Rubner, *J. Phys. Chem.* 94:8715 (1990).
93. I. Watanabe and M. F. Rubner, *Brit. Polym. J.* 23:165 (1990).
94. M. Watanabe, H. Kamiyama, K. Sanui, and N. Ogata, *Polym. Prepr. Jpn.* 36:3242 (1987).
95. T. Nakamura, H. Tanaka, M. Matsumoto, H. Tachibana, E. Manda, and Y. Kawabata, *Chem. Lett.* 1667 (1988).
96. T. Nakamura, H. Tanaka, M. Matsumoto, H. Tachibana, E. Manda, and Y. Kawabata, *Synth. Metals* 27:B601 (1988).
97. T. Nakamura, K. Kojima, M. Matsumoto, H. Tachibana, M. Tanaka, E. Manda, and Y. Kawabata, *Chem. Lett.* 367 (1989).
98. T. Nakamura, H. Tanaka, K. Kojima, M. Matsumoto, H. Tachibana, M. Tanaka, and Y. Kawabata, *Thin Solid Films* 179:183 (1989).
99. K. Ikegami, S. Kuroda, K. Saito, M. Saito, M. Sugi, T. Nakamura, H. Tachibana, M. Matsumoto, and Y. Kawabata, *Thin Solid Films* 179:245 (1989).
100. Y. F. Miura, M. Takenaga, A. Kasai, T. Nakamura, M. Matsumoto, and Y. Kawabata, *Jpn. J. Appl. Phys.* 30:L647 (1991).
101. Y. F. Miura, M. Takenaga, A. Kasai, T. Nakamura, M. Matsumoto, and Y. Kawabata, *Jpn. J. Appl. Phys.* 30:3503 (1991).
102. C. Pearson, A. S. Dhindsa, M. C. Petty, and M. R. Bryce, *Thin Solid Films* 210–211:257 (1992).
103. D. M. Taylor, S. K. Gupta, A. E. Underhill, and C. E. Wainwright, *Thin Solid Films* 210–211:287 (1992).

104. Y. F. Miura, M. Takenaga, A. Kasai, T. Nakamura, Y. Nishio, M. Matsumoto, and Y. Kawabata, *Thin Solid Films* 210–211:306 (1992).
105. D. M. Taylor, S. K. Gupta, P. Dynarowicz, E. Barlow, C. E. A. Wainwright, and A. E. Underhill, *Langmuir* 8:3057 (1992).
106. M. Yumura, T. Nakamura, M. Matsumoto, S. Ohshima, Y. Kuriki, K. Honda, M. Kurahashi, and Y. F. Miura, *Synth. Metals* 57:3865 (1993).
107. Y. F. Miura, H. Isotalo, K. Kawaguchi, T. Nakamura, and M. Matsumoto, *Appl. Phys. Lett.* 63:1705 (1993).
108. M. Bousseau, L. Valade, J. P. Legros, P. Cassoux, M. Garbauskas, and L. V. Interrante, *J. Am. Chem. Soc.* 108:1908 (1986).
109. L. Brassard, H. Hurdequint, M. Ribault, L. Valade, J. P. Legros, and P. Cassoux, *Synth. Metals* 27:B157 (1988).
110. A. Kobayashi, H. Kim, Y. Sasaki, R. Kato, H. Kobayashi, S. Moriyama, Y. Nishio, K. Kajita, and W. Sasaki, *Chem. Lett.* 1819 (1987).
111. J. M. Williams, J. F. Ferraro, R. J. Thorn, K. D. Carlson, U. Geiser, H. H. Wang, A. M. Kim, and M. H. Whangbo, *Organic Superconductors*, Prentice Hall, Englewood Cliffs, N.J., 1992, and references therein.
112. H. Isotalo, M. Ahlskog, and H. Stubb, *Synth. Metals* 48:313 (1992).
113. T. Nakamura, G. Yunome, R. Azumi, M. Tanaka, M. Yumura, M. Matsumoto, S. Horiuchi, H. Yamochi, and G. Saito, *Synth. Metals* 57:3853 (1993).
114. M. A. Beno, H. H. Wang, A. M. Kini, K. D. Carlson, U. Geiser, W. K. Kwok, J. E. Thompson, J. M. Williams, and M.-H. Whangbo, *Inorg. Chem.* 29:1599 (1990).
115. H. Yamochi, T. Nakamura, G. Saito, T. Kikuchi, S. Saito, K. Nozawa, M. Kinoshita, T. Sugano, and F. Wudl, *Synth. Metals* 42:1741 (1991).
116. T. Suzuki, H. Yamochi, H. Isotalo, C. Fite, H. Kasmai, K. Liou, G. Srdanov, F. Wudl, P. Coppens, K. Maly, and A. Frost-Jensen, *Synth. Metals* 42:2225 (1991).
117. S. Kahlich, D. Schweitzer, I. Heinen, S. E. Lan, B. Nuber, H. J. Keller, K. Winzer, and H. W. Helberg, *Solid State Commun.* 80:191 (1991).
118. H. Yamochi, S. Horiuchi, and G. Saito, *Phosphorus Sulphur Silicon Relat. Elem.* 67:305 (1992).
119. H. Yamochi, S. Horiuchi, G. Saito, M. Kusunoki, K. Sakaguchi, T. Kikuchi, and S. Sato, *Synth. Metals* 56:2096 (1993).
120. H. Isotalo, G. Yunome, M. Abe, S. Horiuchi, H. Yamochi, G. Saito, H. Tachibana, T. Nakamura, and M. Matsumoto, *J. Chem. Soc. Chem. Commun.* 573 (1994).
121. W. Krätschmer, L. D. Lamb, K. Fostiropoulos, and D. R. Huffman, *Nature* 347:354 (1990).
122. F. Wudl, *Acc. Chem. Res.* 25:157 (1992).
123. Y. S. Obeng and A. J. Bard, *J. Am. Chem. Soc.* 113:6279 (1991).
124. C. Jehoulet, Y. S. Obeng, Y.-T. Kim, F. Zhou, and A. J. Bard, *J. Am. Chem. Soc.* 114:4237 (1992).

125. T. Nakamura, H. Tachibana, M. Yumura, M. Matsumoto, R. Azumi, M. Tanaka, and Y. Kawabata, *Langmuir* 8:4 (1992).
126. G. Williams, C. Pearson, M. R. Bryce, and M. C. Petty, *Thin Solid Films* 209:150 (1992).
127. C.-F. Long, Y. Xu, F.-X. Guo, Y.-L. Li, and D.-F. Xu, Y.-X. Yao, and D.-B. Zhu, *Solid State Commun.* 82:381 (1992).
128. R. Back and R. B. Lennox, *J. Phys. Chem.* 96:8149 (1992).
129. M. Iwahashi, K. Kikuchi, Y. Achiba, I. Ikemoto, T. Araki, T. Mochida, S. Yokoi, A. Tanaka, and K. Iriyama, *Langmuir* 8:2980 (1992).
130. Y. Tomioka, M. Ishibashi, H. Kajiyama, and Y. Taniguchi, *Langmuir* 9:32 (1993).
131. P. Wang, M. Shamsuzzoha, X.-L. Wu, W.-J. Lee, and R. M. Metzger, *J. Phys. Chem.* 96:9025 (1992).
132. T. Nakamura, H. Tachibana, M. Yumura, M. Matsumoto, and W. Tagaki, *Synth. Metals* 55–57:3131 (1993).
133. N. C. Maliszewskyj, P. A. Heiney, D. R. Jones, R. M. Strongin, M. A. Cichy, and A. B. Smith III, *Langmuir* 9:1439 (1993).
134. R. Wang, R. M. Metzger, S. Bandow, and Y. Maruyama, *J. Phys. Chem.* 97:2926 (1993).
135. A. F. Hebard, M. J. Rosseinsky, R. C. Haddon, D. W. Murphy, S. H. Glarum, T. T. M. Palstra, A. P. Ramirez, and A. R. Kortan, *Nature* 350:600 (1991).
136. A. A. Zakhidov, A. Ugawa, K. Imaeda, K. Yakushi, H. Inokuchi, K. Kikuchi, I. Ikemoto, S. Suzuki, and Y. Achiba, *Solid State Commun.* 79:939 (1991).
137. J. L. Miles and H. O. McMahon, *J. Appl. Phys.* 32:1176 (1961).
138. G. L. Larkins, E. D. Thompson, E. Oritz, C. W. Burkhart, and J. B. Lando, *Thin Solid Films* 99:277 (1983).
139. T. Kubota, M. Wada, M. Iwamoto, H. Noshiro, and M. Sekine, *Thin Solid Films* 210–211:277 (1992).
140. J. Tanguy, *Thin Solid Films* 13:33 (1972).
141. G. G. Roberts, K. P. Pande, and W. A. Barlow, *Electron. Lett.* 13:581 (1977).
142. I. M. Dharmadasa, G. G. Roberts, and M. C. Petty, *Electron. Lett.* 16:201 (1980).
143. M. Tabib-Azar, A. S. Dewa, and W. H. Ko, *Appl. Phys. Lett.* 52:206 (1988).
144. K. Saito, M. Yoneyama, M. Saito, K. Ikegami, M. Sugi, T. Nakamura, M. Matsumoto, and Y. Kawabata, *Thin Solid Films* 160:133 (1988).
145. J. Paloheimo, P. Kuivalainen, H. Stubb, E. Vuorimaa, and P. Yli-Lahti, *Appl. Phys. Lett.* 56:1157 (1990).
146. J. Paloheimo, H. Stubb, P. Yli-Lahti, P. Dyreklev, and O. Inganäs, *Thin Solid Films* 210–211:283 (1992).
147. S. Franssila, J. Paloheimo, and P. Kuivalainen, *Electron. Lett.* 29:713 (1993).
148. H. Tachibana, T. Nakamura, M. Matsumoto, H. Komizu, E. Manda, H. Niino, A. Yabe, and Y. Kawabata, *J. Am. Chem. Soc.* 111:3080 (1989).

149. H. Tachibana, H. Komizu, T. Nakamura, M. Matsumoto, M. Tanaka, E. Manda, Y. Kawabata, and T. Kato, *Chem. Lett.* 841 (1989).
150. H. Tachibana, A. Goto, T. Nakamura, M. Matsumoto, E. Manda, H. Niino, A. Yabe, and Y. Kawabata, *Thin Solid Films* 179:207 (1989).
151. H. Tachibana, H. Komizu, T. Nakamura, M. Matsumoto, E. Manda, and Y. Kawabata, *Thin Solid Films* 179:239 (1989).
152. H. Tachibana, R. Azumi, T. Nakamura, M. Matsumoto, and Y. Kawabata, *Chem. Lett.* 173 (1992).
153. H. Tachibana, Y. Nishio, T. Nakamura, M. Matsumoto, E. Manda, H. Niino, A. Yabe, and Y. Kawabata, *Thin Solid Films* 210–211:293 (1992).
154. T. V. P. Bliss and T. Lomo, *J. Physiol. (London)* 232:331 (1973).
155. J. C. Eccles, *Neuroscience* 10:1071 (1983).
156. D. G. Whitten, *J. Am. Chem. Soc.* 96:594 (1974).
157. H. Tachibana, E. Manda, R. Azumi, T. Nakamura, M. Matsumoto, and Y. Kawabata, *Appl. Phys. Lett.* 61:2420 (1992).
158. K. Yoshida, T. Koujiri, T. Horii, and Y. Kubo, *Bull. Chem. Soc. Jpn.* 63:1658 (1990).
159. R. S. Potember, T. O. Poehler, and D. O. Cowan, *Appl. Phys. Lett.* 34:405 (1979).
160. R. S. Potember, T. O. Poehler, A. Rappa, D. O. Cowan, and A. N. Bloch, *J. Am. Chem. Soc.* 102:3660 (1980).
161. R. S. Potember, T. O. Poehler, and R. C. Benson, *Appl. Phys. Lett.* 41:548 (1982).
162. R. S. Potember, T. O. Poehler, R. C. Hoffman, K. R. Speck, and R. C. Benson, in *Molecular Electronic Devices II* (F. L. Carter, ed.), Marcel Dekker, New York, 1987, p. 91.
163. S. Yamaguchi, C. A. Viands, and R. S. Potember, *J. Vac. Sci. Technol. B* 9:1129 (1991).
164. M. Matsumoto, Y. Nishio, H. Tachibana, T. Nakamura, Y. Kawabata, H. Samura, and T. Nagamura, *Chem. Lett.* 1021 (1991).

Organic Photoconductors and Photovoltaics

Piergiulio Di Marco and Gabriele Giro

*Istituto di Fotochimica e Radiazioni d'Alta Energia del CNR,
Bologna, Italy*

I. PHOTOCONDUCTIVITY OF ORGANIC SOLIDS

A. Introduction

In general, *photoconductivity* may be defined as the enhancement of electrical conductivity following the absorption of a photon of electromagnetic radiation. The phenomenon is due to a sum of several processes, such as absorption of radiation, photogeneration of charge carriers, their separation and transport under applied electric field, and charge collection at electrodes to yield current. The initial interest of researchers was focused on covalent solids, such as germanium and silicon. However, some pioneering studies on organic solids were carried out, starting in 1906 by Pochettino [1], who described for the first time photoconduction in anthracene. In the recent past the electrical and photoelectronic properties of organic solids have received a considerable amount of attention. Many review and books have been published on this subject [2–6].

B. Generality

In the dark, the conductivity of an organic solid is

$$\sigma = \frac{J}{E} = ne\mu_n + pe\mu_p \quad (1)$$

where J is the current density, E the applied electric field, n and p the density of negative and positive charges, e the electron charge, and μ_n and μ_p the mobilities of the negative and positive charges, respectively. The light produces additional charges Δn and Δp . The photocurrent σ_{ph} is then

$$\sigma_{\text{ph}} = \Delta n e \mu_n + \Delta p e \mu_p \quad (2)$$

In inorganic covalently bonded materials such as Ge, Si, and CdS, photoconductivity is described using the band model. The bands (valence and conduction bands) refer to states of allowed electron energies in a finite and quasi-continuous array, separated by a forbidden gap (E_g). In this model, the photogeneration is due to the excitation, by means of light, of electrons from the valence band to the conduction band.

In organic materials the direct process is not usual. The main reason comes from energetic considerations. The forbidden gap of organic solids, in fact, is considerably greater than the optical absorption edge of the highly allowed singlet–singlet transition. However, since the light absorption in this spectral region produces photocurrent, other photogeneration processes should be operative. The characterizing peculiarity of organic solids (i.e., their molecular nature) arises from the strength of the intermolecular interactions governed by weak van der Waals or electrostatic forces.

Photon absorption obeys the well-known Lambert–Beer law:

$$I_t = I_i e^{-\alpha d} \quad (3)$$

where I_t is the transmitted light intensity, I_i the incident light intensity, α the absorption coefficient, and d the sample thickness.

Light absorption does not produce free carrier through a direct mechanism but leads to the formation of excited states (excitons) that are subjected to many different photophysical processes, both radiative (fluorescence, phosphorescence) and nonradiative (internal conversion, intersystem crossing) (Fig. 1). The excitons may also migrate nonradiatively, from one molecule to another, many times before being trapped on some molecule. One of these processes may consist of an electron transfer to a neighboring molecule, giving rise to an excited charge-transfer state. The final step under an applied electric field could be the formation of mobile charge carriers if the coulombic attraction between the electron and hole becomes lower than the thermal energy kT .

In conclusion, photogeneration is one of the several photophysical processes in competition with one another in which the excited state may be involved. In this view, the primary photogeneration quantum yield (ϕ), defined as the number of charge pairs that are formed per absorbed light

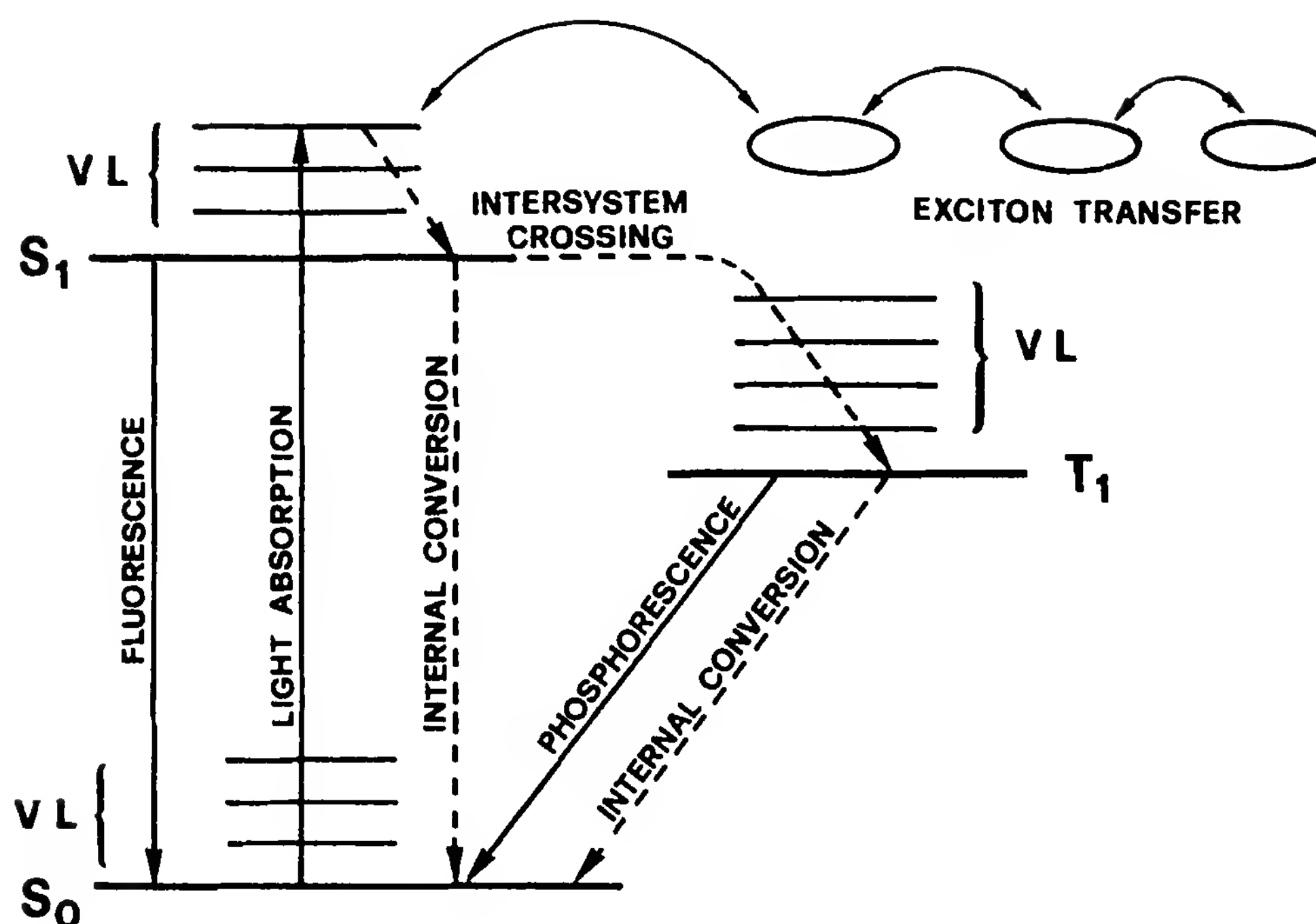


Figure 1 Energy-level diagram showing transitions by light absorption and deactivation pathways for an organic molecule. S_0 , ground state; S_1 , first singlet excited state; T_1 , first triplet excited state; VL, vibrational levels.

quantum, is related to the other processes through the following relation:

$$\phi = \frac{k_{ph}}{k_{ph} + k_n + k_{isc} + k_q [Q]} \quad (4)$$

where k_{ph} represents the rate of carrier production, k_n the rate constant of the nonradiative deactivation processes, k_{isc} the rate of transition to the triplet state, k_q the rate of quenching processes, and $[Q]$ the concentration of the quenchers. The quantum yield of carrier generation depends on the absorption coefficient [7], the temperature, and the electric field strength (E).

A theory that explains the field dependence of the yield was originally proposed by Onsager [8]. In his theory an electron that possesses energy in excess becomes thermalized at a certain distance r from a hole in a Coulomb electric field. The probability of an e^-/h^+ pair dissociation is expressed by

$$\phi = \exp \left(-\frac{r_c}{r} \right) \quad (5)$$

where $r_c = e^2/\epsilon\epsilon_0 kT$ is the Onsager radius, e the electron charge, ϵ the dielectric constant, and ϵ_0 the vacuum permittivity.

The photosensitivity of a photoconductor is defined as the number of carriers passing through the outer circuit divided by the number of photons absorbed by the photoconductor during the same period of time. This ratio is called gain (G). The gain may be expressed as the ratio between the charge carrier lifetime (τ) and the charge transit time ($T_t = d^2/\mu V$, where d is the sample thickness, μ the drift mobility, and V the applied voltage):

$$G = \frac{\tau}{T_t} = \frac{\tau\mu V}{d^2} \quad (6)$$

This expression correlates the gain with the carrier mobility μ and the sample thickness d .

C. Photogeneration Processes

There are numerous mechanisms of charge photogeneration. The most common are the direct production of electron–hole pairs, exciton dissociation, and photoinjection from electrodes.

1. Direct Production of e^-/h^+ Pairs

Intrinsic e^-/h^+ pair generation depends on the width of the forbidden energy gap and therefore takes place at high photon energies. The gain is in general very low ($10^{-6} < G < 10^{-4}$) and with similar values for electrons and holes. Moreover, the photoconductivity action spectrum does not generally resemble the absorption spectrum.

2. Exciton Dissociation

The excitons can react with the surface and, owing to the presence of absorbed oxygen, impurities and structural defects or due to electrode interactions may dissociate to produce separated electrons and holes. The probability of the generation of charge carriers will be higher for excitons created near the surface. The extrinsic exciton-surface mechanism may be distinguished from the direct process as follows:

1. The photoconductivity action spectrum generally resembles the solid absorption spectrum.
2. The quantum efficiencies for holes and electrons are not the same and depend on the electrode.
3. The G values range between 10^{-2} and 10^{-3} .
4. At low light intensity and high electric field, the photocurrent varies linearly with the light intensity. For high I_i values, the I_{ph} versus I_i characteristics may follow a sublinear dependence.

Several other charge carrier generation mechanisms involve excitons: (1) field or thermal ionization of excitons, (2) exciton interaction with trapped carriers, (3) exciton–exciton interaction, and (4) exciton–photon interaction.

3. Photoinjection from Electrodes

Internal photoemission of charge carriers from metal electrodes takes place when a metal, placed in contact with an insulator, absorbs light so that it promotes electrons from its Fermi level to the conduction band of the insulator. This happens only if the incident photon energy is equal to or greater than the barrier height between the insulator and the metal electrode. On the basis of Fowler's theory [9], the measured photocurrent is given by the expression

$$I_{\text{ph}}^{1/2} = h\nu - \Phi_{\text{e/h}} \quad (7)$$

where $\Phi_{\text{e/h}}$ is the barrier height for electrons or holes. Plotting the square root of the photocurrent against the photon energy, a straight line is obtained that allows determination of the internal photoemission threshold by intersection with the photon energy axis. Photoinjection processes may be distinguished from others on the basis of:

1. The dependence of the photocurrent action spectrum by the nature of the metal electrode
2. The square-root dependence of the photocurrent from the photon energy
3. A G value below 10^{-4}

D. Experimental Methods

The relationship between steady-state photoconductivity [performed on surface or sandwich cells (Fig. 2a)] and several parameters, such as photon energy, illumination intensity, applied electric field, temperature, electrode materials, sample thickness, sensitizer materials, and relative concentration, provides information on spectral sensitivity, photoconductivity threshold, and photocarrier generation mechanisms. From these measurements, however, no direct information regarding basic parameters such as μ , ϕ , and τ is obtained. For this purpose the transient techniques are more appropriate. For high-resistivity materials, the time-of-flight (TOF) technique is particularly suitable [10,11]. In fact, this technique allows determination of the charge carrier mobility μ and the quantum efficiency ϕ separately, the sign of the carriers drifting across the sample and the free carrier lifetime τ .

In TOF experiments (Fig. 2b), a small number of carriers are generated by short pulses of strongly absorbed light. Under the effect of a constant

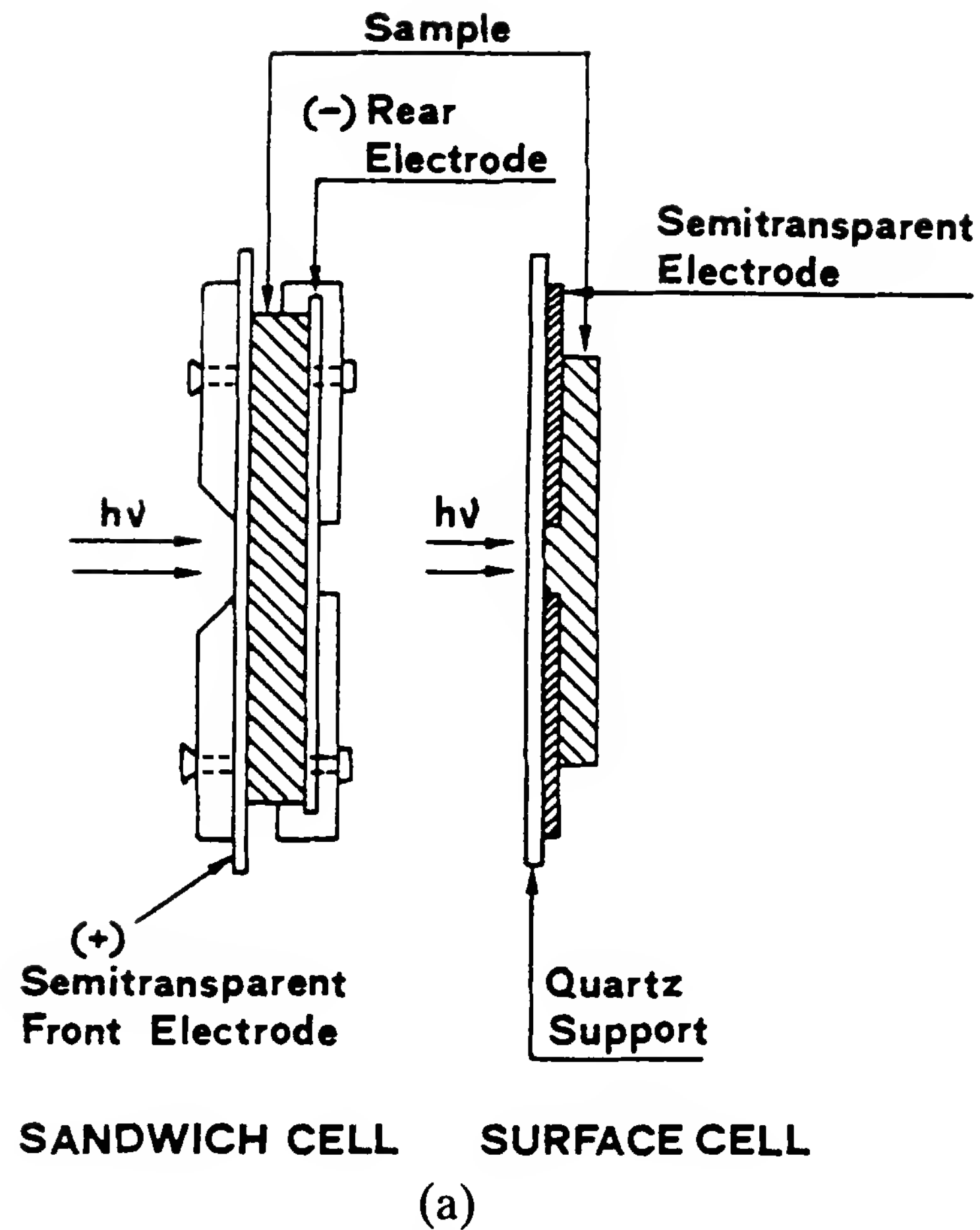


Figure 2 (a) Schematic representation of measuring cells in photoconductivity experiments; (b) typical experimental arrangement for transient photoconductivity studies (TOF) (R is the load resistance); (c) I_{ph} versus time transient as a result of the drifting charge in the external circuit and registered by the scope.

electric field the carriers will move through the solid, generating a current in the external circuit. The current will stop moving when the carrier packet reaches the opposite electrode. The drift mobility μ can be determined from the transit time T_t since $\mu = d^2/T_t V$. If the sample contains trapping centers, the transient current is characterized by a trap-free lifetime t_f (the average time spent by a carrier before being captured) and by a release time t_r (the average time spent by a carrier in a trap) other than the transit time T_t . If the traps are “shallow” and $\tau_f \ll \tau_t \ll T_t$, the carriers may undergo many trapping events during the transit, the number of which depends on the concentration of the traps. If n_f and n_t are the number of free and trapped carriers, respectively, the result is that a fraction $n_t/(n_f + n_t)$ of carriers will reside in shallow traps and the remaining fraction $n_f/(n_f + n_t)$ will be “free.” The carriers still drift as a well-defined coherent packet, but the transit time will increase. The trap-controlled drift mobility μ_{tc} (independent of the transport mechanism) is given as

$$\mu_{tc} = \mu_o \left(\frac{n_f}{n_f + n_t} \right) = \mu_o \left(\frac{\tau_f}{\tau_f + \tau_t} \right) \quad (8)$$

where μ_o is the trap-free mobility.

E. Carrier Transport Mechanism

In organic materials, the weak intermolecular interactions lead to the formation of narrow conduction or valence bands and to low charge carrier mobilities. In some cases the validity of the band theory can be questioned. For the band theory to be valid, in fact, the bandwidth W must be greater than the uncertainty in the energy of the charge carrier,

$$W \geq \frac{h}{\tau_r} \quad (9)$$

where τ_r is the relaxation time of the carrier. But bandwidth and mobility are strictly correlated, and Eq. (9) poses a limit of 0.4 cm²/Vs for the validity of a transport mechanism within the framework of band theory. In wideband materials, as in inorganic semiconductors, the drift mobility is generally higher than 1 cm²/Vs and the transport properties are well explained by the band theory approach.

In crystalline organic solids such as anthracene, in which the mobility is on the order of 1 cm²/Vs, the transport mechanism may still be explained by a band theory formalism. But for most organic solids (especially if disordered), the mobility values are far below the lower limit value and a hopping transport mechanism seems to be more appropriate. Organic polymers are classic examples of hopping transport materials. In poly-*N*-

vinylcarbazole [12], for instance, the charges are transported by hopping through chromophores that are linked to the main vinyl chain. In these materials, the transport is thermally activated, the charge carrier mobilities are very low (10^{-8} to 10^{-5} cm²/Vs) and depend strongly on the electric field. Moreover, the transit from TOF profile curves can be very dispersive. A variety of theories for hopping transport have been developed. Among them, nonadiabatic small polaron hopping [13] and phonon-assisted hopping [14] are worth mentioning.

II. XEROGRAPHY

A. Introduction

The biggest opportunity for organic photoconductors to enter the business of application was given by the discovery of electrophotography by Carlson [15] in 1938. Carlson suggested a method for utilizing the photoconductive properties of insulating surfaces to produce electrostatic latent images, and his invention became the basis for the first practical electrophotographic system, together with the beginning of the electrophotography history. The electrophotographic process can be divided into four categories, depending on the type of image formed. At present, xerography, which utilizes electrostatic image formation, as stated above, is the most highly developed form of electrophotography.

B. Xerographic Processes

The basic steps of the xerographic processes may be schematized as follows:

1. **Charge.** The surface of a photoconductive layer deposited onto a conductive support is charged by corona discharge at a potential of several hundred volts. The acceptance of a high charge level must be rapid; moreover, the amount of charge the photoconductor can accept and hold in the dark is a function of the film resistance. The acceptance potential corresponds to the equilibrium point beyond which the charges leak away as fast as they are supplied. The dark decay of the surface potential must be very low, and its rate gives a measure of the time that the electrostatic latent image is retained on a xerographic plate.

2. **Exposure.** The charged surface is exposed successively to reflected light from the document. When the light falls on the photoconductive layer, the electrical charge is removed from the layer surface. In the dark regions, on the contrary, the electrical charges create a latent electrostatic image that reproduces the document information. The spectral sensitivity of a xerographic plate is determined by the rate of decay of the electrical potential when illuminated and is measured by determining the exposure

necessary to reduce to one-half the value of the initial surface potential at different wavelengths.

3. Development. This is obtained through the electrical attraction of a toner (thermoplastic pigment mixed with carbon black), whose fine particles carry electrical charges that are opposite in polarity to the latent electrostatic image charges.

4. Transfer. The developed image is transferred from the photoconductor to the paper by intimate contact between the layer and the paper, charged with the same polarity of the image.

5. Fixing. The transferred image is made permanent and fixed to the paper by heating or by fixing with a fixative coating.

The toner particles are removed from the photoconducting layer surface by a successive uniform light exposure that removes any traces of surface charges in order to be able to repeat the cycle. Many reviews and books deal with this subject; among them the readers are directed to Refs. 16 to 20. The samples for xerography are cycled several times. A decrease in charge acceptance, an increase in the dark discharge, or an increase in the residual potential constitute a test to measure the fatigue effects. Light, heat, electric field, and chemical exposure may also cause fatigue effects on photoreceptor samples.

C. Materials for Application in Xerography (Photoreceptors)

Photoreceptors must satisfy the following requisites: (1) good insulating properties in the dark, (2) low dark decay of the surface potential, (3) high rate of photodischarge, (4) cycle stability, (5) low cost, and (6) environmental aspects. In the past, inorganic material such as selenium, selenium–arsenic or selenium–tellurium alloys, cadmium sulfide, and zinc oxide were widely used as photoreceptors. Since from 1980 the inorganic materials have been replaced progressively with organic photoreceptors. In fact, the chemical constituents of the photoreceptor, unlike inorganic materials, can be varied at will in order to answer the specific requirements of the various operating characteristics of xerographic systems. Moreover, the major advantages of organic photoreceptors are a lower cost than inorganics, ease of manufacturing, flexibility, panchromatic response, and high light sensitivity.

The poly-*N*-vinylcarbazole:trinitrofluorenone (PVK:TNF) charge-transfer complex [21–23] was the first commercial organic photoreceptor used in electrophotography by IBM. The photoconductivity of this material is comparable to that of amorphous selenium, but its utilization in practical devices was limited, owing to its toxicity and long transit-time value, comparable, as for most single-layer photoreceptors, to the development process time.

The number of organic materials showing both good photogeneration and good transport properties is limited. To improve the characteristics of organic photoreceptors, a multilayer structure was developed in which a thin charge generation layer (CGL) is put into intimate contact with a thicker charge transport layer (CTL) (Fig. 3). The photogeneration of charge carriers occurs in the thin (about 0.1 to 3 μm) CGL layer, made of photoconductive materials such as dyes or pigments. The charges are then injected into the thicker CTL layer (about 10 to 30 μm), which provides the transport of the carriers across the bulk to the surface. This configuration allows independent optimization of both CGL and CTL layers. In this way the organic photoreceptors considerably improved their sensitivity, panchromatic response, speed, and durability, satisfying the strong demand for xerographic technology.

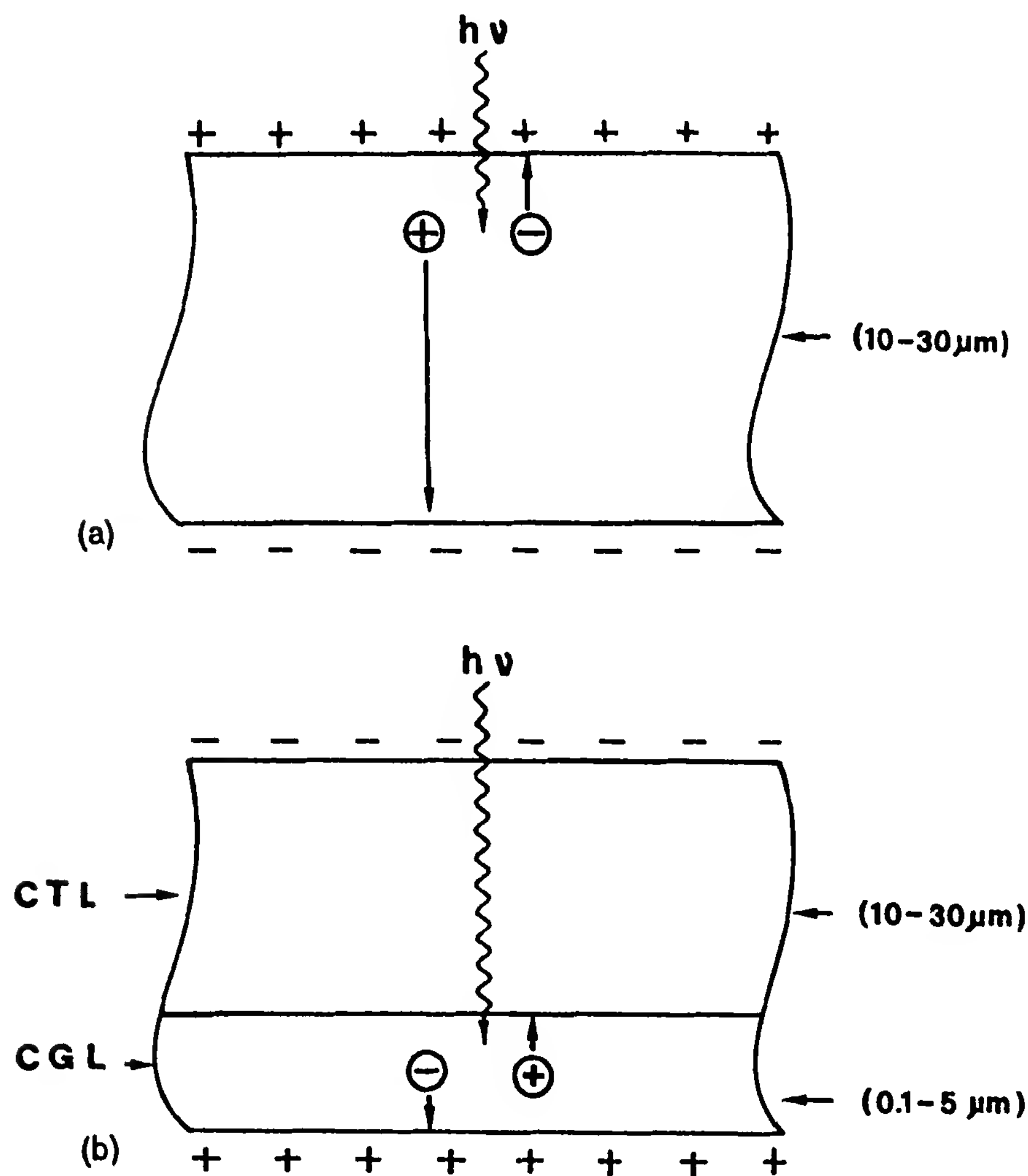


Figure 3 Cross section of (a) mono- and (b) dual-layer photoreceptors.

D. Charge Generation Materials

Several classes of organic compounds have been developed as carrier generation materials. The most important characteristics of a charge generation material are the spectral response, which is determined by the absorption spectrum, and the sensitivity, which depends on the charge generation efficiency.

1. Charge Generation Materials for Visible Region

In the following, some examples of organic photoconductors developed for office copiers are shown. They are designed to absorb light in the visible region of the spectrum and with a high photosensitivity in the same region (Fig. 4a).

(a) *Polyaromatics*

Perylene pigments are commercial products used, for example, in automotive paints and are readily available. Perylenes show many different polymorphic structures, which depend on the substituents [24–27]. Enhancement of the absorption spectrum has been achieved by morphology changes [28]. By vacuum deposition, the α form is produced, which may be converted into β by solvent treatment or solvent-based overcoating [28,29]. 2,7-Dibromoanthanthrone as the charge generation layer active component has been studied in a dual-layer arrangement [30]. Substituting Br^- with various halogen atoms, the photodischarge shape became slower and the best result was obtained with the unsubstituted parent compound. The decrease in sensitivity in the anthanthrone dye has been ascribed to the heavy-atom effect, which increases the rate of intersystem crossing from the singlet state to the triplet state [31].

(b) *Azo Compounds*

Among the polyazo compounds, the bis-azo pigments dominate the field of charge-generation-layer components in the visible region (400 to 700 nm). These materials are generally composed of bridging substituents and azo-coupling substituents; the coupling group seems to affect the photosensitivity [32–34]. The increase in the number of azo groups leads to long-wavelength-absorption materials [35]. The first azo pigment used in a practical device was chlorodiane blu (IBM copiers: 1977). It was used in both single- and dual-layer arrangements, the latter being more sensitive [36,37].

(c) *Aggregate Materials*

Polyaromatics such as perylene and bis-azo pigments have been employed in low-volume copiers that normally utilize low intensity and relatively long exposures. For high-volume copiers, instead, it is necessary to employ photoreceptors with high speed and high charge photogeneration quantum

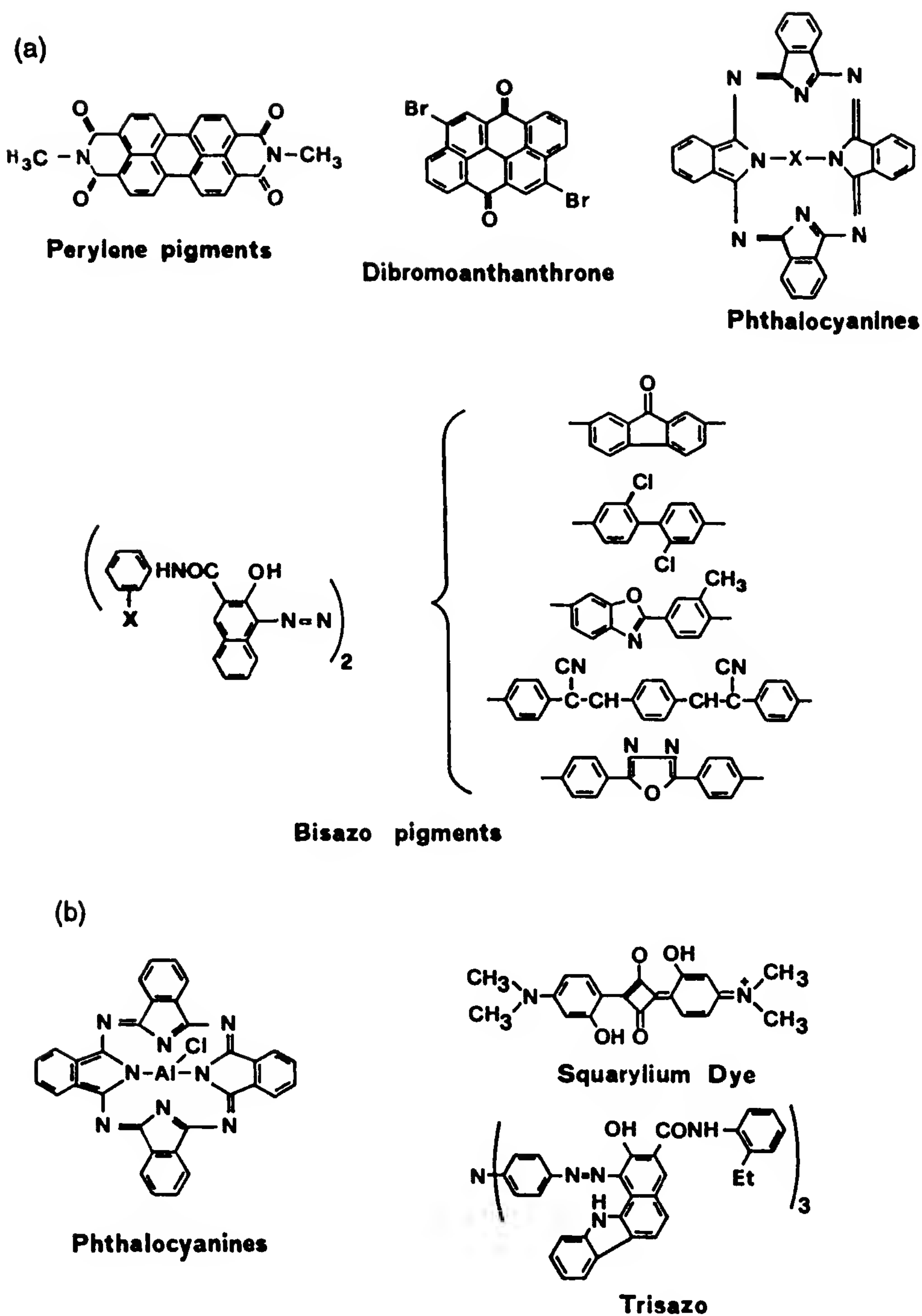


Figure 4 Examples of organic compounds used as charge-generation materials for practical image reproduction systems in the (a) visible and (b) near-IR ranges.

efficiency. For this kind of application the utilization of aggregate photoconductors [38] was suggested.

The aggregate consists of a two-phase material of photoconducting crystalline dye molecules dispersed in an amorphous inert matrix. The aggregation takes place from an interaction between the organic dye and the polymer matrix. The dye used is one of the numerous aryl-substituted thiapyrilium salts, while the inert polymer matrix is bisphenol-A-polycarbonate. Aggregation, which occurs spontaneously in the presence of suitable solvents such as dichloromethane [39] or by solvent fuming [38] of homogeneous coating of dye and polymer solutions gives rise to a shift in the absorption spectrum from 580 to 700 nm and a 100-fold speed increase in xerographic sensitivity compared with the homogeneous film.

(d) *Phthalocyanines*

The phthalocyanines have recently received great attention as charge-generating materials in xerographic photoreceptors. Copper phthalocyanine was one of the first dyes to be employed as a photoreceptor and its performance varied as a function of the crystallinity, morphology, and dispersion preparation [40].

2. Charge-Generation Materials for the Near-Infrared Region

The utilization of laser diodes and LED as light sources for nonimpact printing devices (laser printers), which are operative in the near-infrared region of the spectrum, induced the development of new photoreceptor materials with long-wavelength sensitivity. For this purpose, materials such as phthalocyanines, squarylium dyes, and triazo pigments are employed (Fig. 4b).

(a) *Phthalocyanines*

Besides phthalocyanine pigments developed for office copiers, new polymorph materials for laser printer utilization have been prepared. These materials, whose absorption characteristics were extended to the near-infrared region, were prepared by vacuum sublimation techniques. Recently, for safety reasons and to reduce the cost of production, solvent-pigment interactions have received great attention [41].

(b) *Squaraines and Trisazo Compounds*

Among the materials for laser printer utilization, we may consider squarylium dyes and trisazo compounds (Fig. 5). Squaraines, for instance, give rise to photoreceptors with superior electrical characteristics, as they can form different crystalline modifications throughout the introduction of suitable impurities at low concentration [42]. This characteristic is due to the ability of squaraines to form aggregates having very broad absorption spectra (400 to 1000 nm).

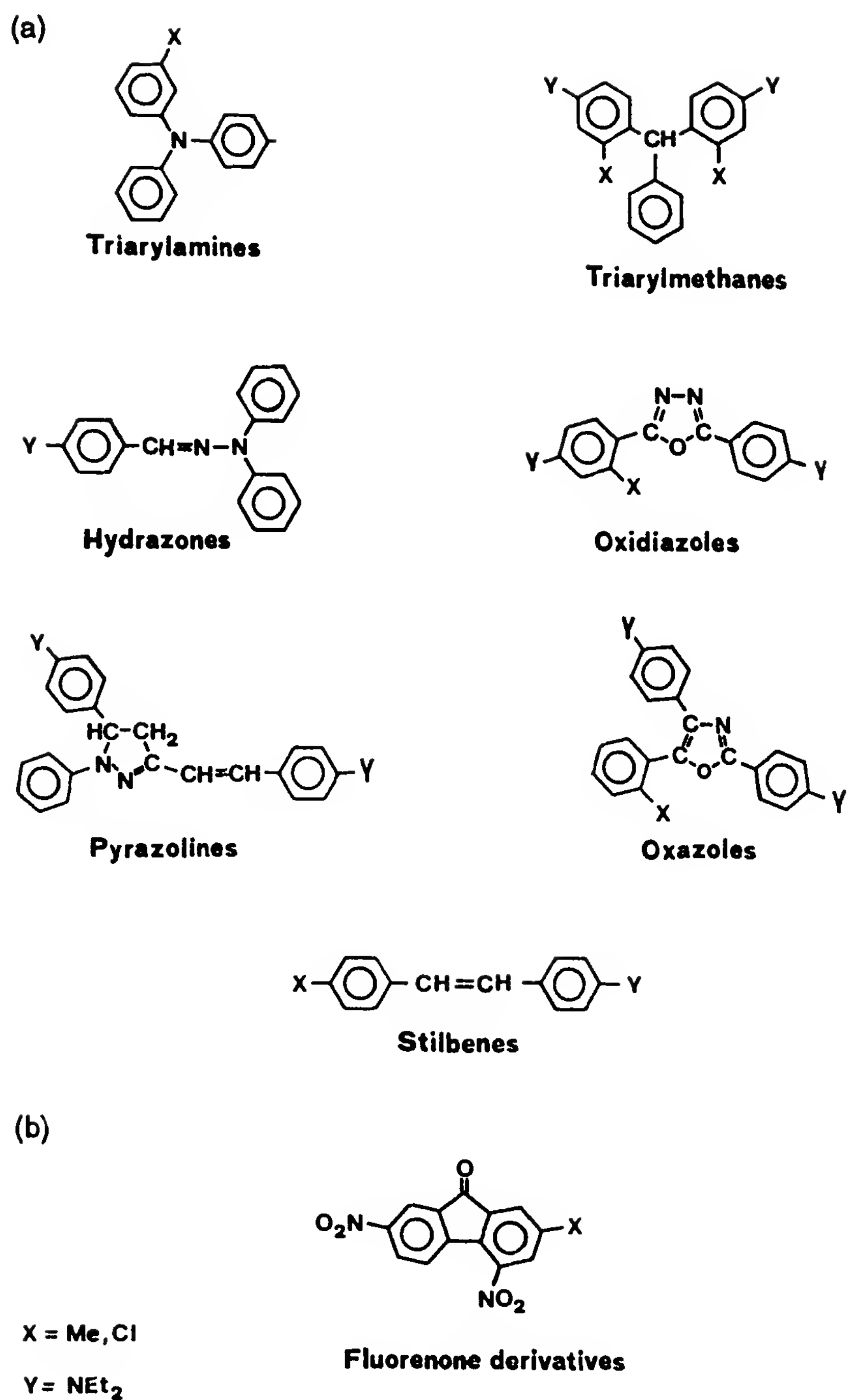


Figure 5 Examples of (a) hole- and (b) electron-transporting materials for mono- and dual-layer photoconductive systems.

E. Transport Materials

In xerography, both hole and electron transport materials are employed; the synthesis of efficient electron transport materials was slow mainly due to the difficulty in obtaining materials having a reduction potential lower than that of oxygen, and second, for the recognized toxicity of these compounds [2,4,7-trinitro-9-fluorenone (TNF) is an example]. Hole-transporting materials must have an ionization potential below 6.6 eV, and both molecularly doped polymers and/or transport active polymers may be utilized. Molecularly doped polymers, however, offer greater flexibility, owing to the possibility of overcoming the mobility limitation (e.g., by varying the concentration of dopant molecules) and for other characteristics, such as good adhesion, low curl, and improved wear [40,43].

1. Hole Transport Materials

The current organic photoreceptors are triarylaminines, triarylmethanes, hydrazones, oxadiazoles, pyrazolines, oxazoles, and more recently, stilbene derivatives. The polymer matrix, on the other hand, is constituted by polyesters and polycarbonates (Fig. 5). The common presence of aromatic amines as substituents in all these materials contributes to efficient hole transport [44]. The nonbonding electron pair on the nitrogen atom, in fact, confers on these molecules a low oxidation potential, and consequently, the production of a chemically stable radical cation with the possibility of an effective overlap of nonbonding molecular orbitals between neighboring molecules.

For efficient hole transport the materials should be constructed such as to prevent dimer formation in both the ground and excited states. Excimer forming sites, in fact, may constitute traps for charge transport materials [45–47]. More recently, it has been shown that the host polymer can also affect the transport properties of the film [48].

2. Electron Transport Materials

As reported above, the utilization of these materials was limited, owing to their toxicity and low miscibility. Recently, a new class of substituted fluorenone compounds has been suggested [49,50]. These compounds show improved solubility and polymer compatibility combined with an electron drift mobility higher than that of TNF molecules. However, the presence of electron-withdrawing substituents in TNF, such as nitro and dicyanomethylene molecules, designed for achieving the desired reduction potential, were found to reduce their solubility and compatibility with the host polymer, thereby preventing the formation of good amorphous films at high dopant concentration [51].

III. ORGANIC SOLAR CELLS

A. Introduction

The photovoltaic cell is a solid-state device able to convert light into electricity. The greatest success in this field has been obtained with solar cells based on inorganic materials. During recent years, however, increasing interest has been shown in the application of organic materials in various photovoltaic devices, due primarily to their low cost and easy processibility. Moreover, the organic compounds are so numerous that among them many should meet the proper requisites for a practical application in this field.

The organic photocells are described as being mainly of two types [3,52–55]:

1. *Schottky-type cell*. A thin organic film is sandwiched between two different metals, which form a blocking and an ohmic contact.
2. *p-n cell*. In this case the organic film is composed of two layers, constituted of a *p*- and an *n*-type conductor.

Before taking into consideration the photovoltaic effects in organics, let us briefly review the general concepts of this argument as developed for inorganic semiconductors [56,57].

B. Theoretical Aspects

In inorganic cells, the conversion of light into electrical energy follows these main steps: (1) absorption of light, (2) photogeneration of hole–electron pairs, (3) charge separation and transport assisted by an existing internal field, and (4) charge collection to yield current. In a *Schottky cell*, the internal field, essential for producing current, is due to the formation of a potential barrier between the metal and the semiconductor. This occurs when $\Phi_m > \Phi_s$ for an *n*-type semiconductor or $\Phi_m < \Phi_s$ for a *p*-type semiconductor, where Φ_m and Φ_s are the work functions of the metal and the semiconductor, respectively. The energy band diagram for the contact between a metal and an *n*-type semiconductor with $\Phi_m > \Phi_s$ is shown in Fig. 6. The conduction band of the metal and the semiconductor conduction and valence bands are depicted when they are completely separate from each other (Fig. 6a). If they are brought in contact in order to attain thermal equilibrium, the energy levels of the semiconductor must be lowered with respect to those of the metal so that their Fermi levels are aligned to the same height. This occurs via a transfer of electrons from the semiconductor conduction band to the metal (Fig. 6b), leaving behind a positive charge due to immobile donor atoms, distributed over a distance W_d from the junction (depletion region). This sets up an electric field that tends to

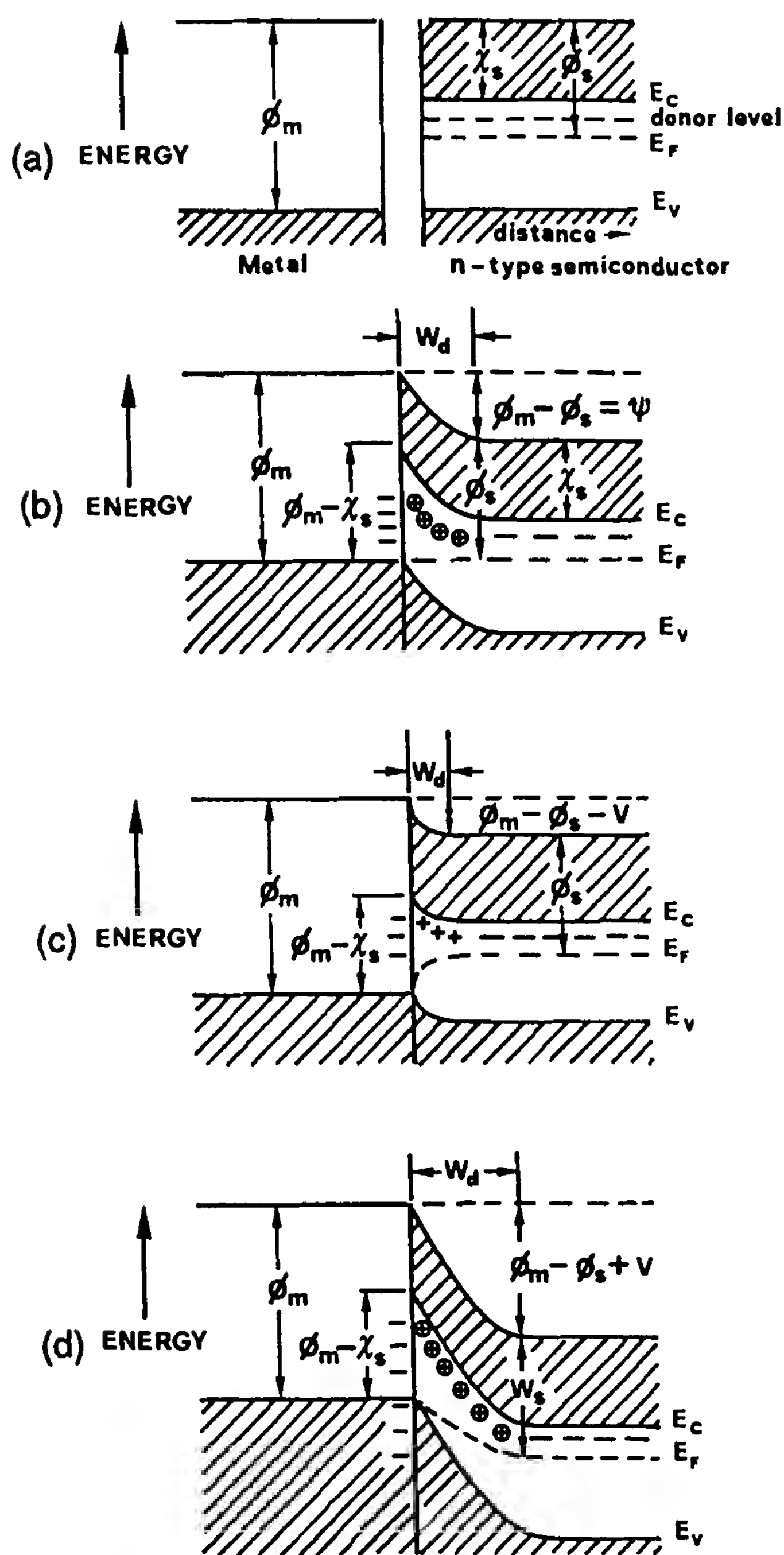


Figure 6 Schottky junction between a metal and an *n*-type semiconductor: (a) before contact; (b) after contact, without bias; (c) forward bias; (d) reverse bias.

discourage the flow of additional electrons from the semiconductor, and an equilibrium potential barrier $\Phi_m - \Phi_s$ results, as shown in the same figure. There is also diffusion of electrons from the metal over the larger barrier $\Phi_m - \chi_s$, where χ_s is the electron affinity of the semiconductor. At equilibrium the current I_F from the semiconductor to the metal is equal

and opposite to the current I_0 from the metal to the semiconductor. $\Phi_m - \Phi_s$ is called the diffusion potential Ψ .

The Schottky junction is characterized by asymmetry of the current flow following the application of a forward or reverse potential bias (Fig. 6c, d). The bias will appear almost entirely across the depletion layer, whose resistance, being void of mobile charges, is much greater than that of the bulk of the semiconductor. At reverse bias (n -type semiconductor positive with respect to the metal) the energy of the electrons in the semiconductor is lowered and the potential barrier is raised to $\Psi + V = \Phi_m - \Phi_s + V$ (Fig. 6d). This reduces I_F to zero and increases W_d . On the other hand, the bias pushes the electrons in the metal toward the barrier, but since the barrier $\Phi_m - \chi_s$ is unaffected by the voltage, I_0 remains unchanged. Therefore, with reverse bias the net current I is constant and equal to I_0 . With a forward bias the potential barrier is reduced to $\Phi_m - \Phi_s - V$ (Fig. 6c); now the electrons from the conduction band of the semiconductor can flow more easily into the metal. I_0 remains constant, since the height of the barrier $\Phi_m - \chi_s$ is unchanged. For $I_F \gg I_0$, $I = I_F$. The relationship between current I and voltage V can be approximated by the expression

$$I = I_F - I_0 = I_0 \left[\exp\left(\frac{eV}{kT}\right) - 1 \right] \quad (10)$$

where e is the electronic charge and k is the Boltzmann constant (Fig. 7). The same arguments can be applied to the case of a metal and a p -type semiconductor with $\Phi_m < \Phi_s$.

When a Schottky junction between a metal and an n -type semiconductor is illuminated and photons having enough energy for the creation of an electron-hole pair are absorbed in the depletion region, the electric field at the junction is able to separate the photogenerated charges, preventing recombination. Electron movement toward the semiconductor and hole

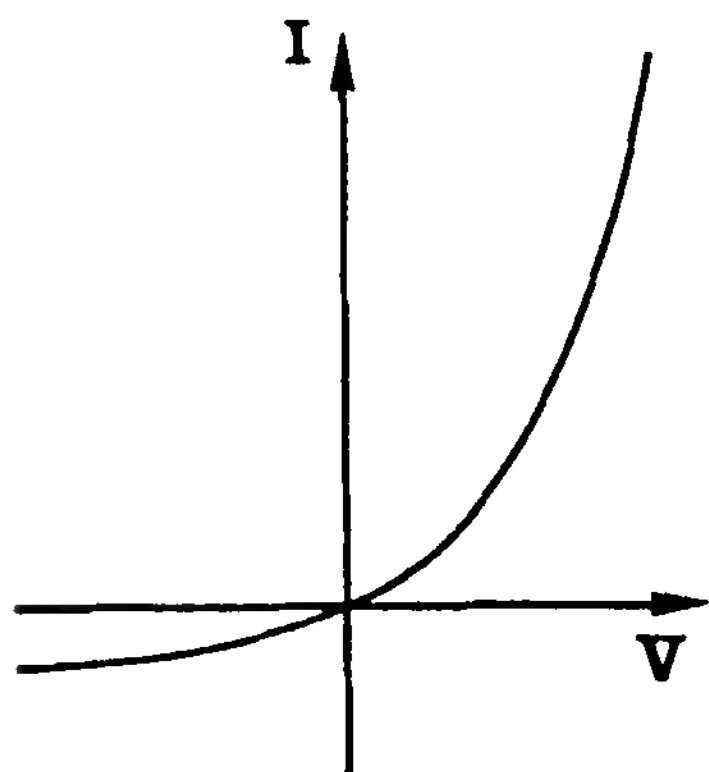


Figure 7 Current-voltage characteristic of a rectifying contact.

movement toward the metal are equivalent to an increase in I_0 . But since the net current I must be zero, I_F must increase by the same amount. This is possible only if there is a reduction of the field at the junction. The light therefore induces a lowering of the barrier equivalent to the application of a forward bias. The photovoltage is equal to the amount by which the barrier potential is decreased, and its maximum value should correspond to $\Phi_m - \Phi_s$. The photocurrent (I_{Ph})–voltage relationship is

$$I_{Ph} = I_0 \left[\exp\left(\frac{eV}{kT}\right) - 1 \right] - I_L \quad (11)$$

where I_L is the photocurrent at zero bias and zero load resistance.

A potential barrier is also obtained at the contact between an n -doped and a p -doped semiconductor. The n -doped part is characterized by fixed positive donor ions and by mobile electrons, the p -doped part by fixed negative acceptor ions and by mobile holes, the two parts being electrically neutral. When they are joined together, due to the density gradient across the junction, there will be diffusion of holes from the p -region to the n -region and of electrons from the n -region to the p -region. Near the junction the p -side will acquire a net negative charge and the n -side a net positive charge. As a result, an electric field will appear across the junction in a direction in which drift currents will tend to flow in the opposite direction to counterbalance the diffusion currents. Equilibrium will be established again when the field is large enough that the drift currents are equal to the diffusion currents. In the unbiased p - n junction the net current I across the junction must be zero, and therefore the drift and diffusion currents must be equal and opposite.

Let us now consider applying a negative potential to the p -region and a positive potential to the n -region of a p - n junction (reverse bias). The electrons of the n -region are attracted to the positive terminal, and the holes of the p -region to the negative one. Thus the depletion region is widened and the height of the junction barrier increases, preventing majority carrier flow across the junction. Reverse bias has the opposite effect on the minority carriers since their motion is favored by the potential barrier. The minority-carrier currents will increase with the applied voltage, but when the voltage is enough to allow all thermally generated carriers to cross the junction, the minority-carrier currents cannot increase further, even though the reverse bias is increased. In conclusion, the only current that flows is the current due to the minority carriers (reverse saturation current), and this current remains almost constant as the reverse bias is increased.

If the p -region is now made positive with respect to the n -region (forward bias), the majority carriers are pulled toward the junction, thus neutralizing some of the donor and acceptor ions and reducing the junction potential.

At low voltage the diffusion currents due to the majority carriers will increase while the drift currents will remain unchanged. Further increase in voltage will eventually reduce the potential barrier to zero, and the electrons and holes will move across the junction and recombine with the majority carriers of the other side of the junction. Thus a forward current consisting of majority carriers now flows across the junction and increases rapidly with only a small increase in voltage.

In a forward-biased p - n junction, the I - V characteristics are similar to those valid for a Schottky cell:

$$I = I_0 \left[\exp\left(\frac{eV}{kT}\right) - 1 \right] \quad (12)$$

When a p - n junction is illuminated, photogeneration of free electrons and holes near the junction take place, leading to an increase in the minority currents. The majority currents must increase the same amount to maintain the total current equal to zero. This increase is possible only if the barrier at the junction is lowered. The lowering of the barrier appears as a photovoltaic emf at the terminals of the junction. The photocurrent-voltage relationship is again

$$I_{\text{Ph}} = I_0 \left[\exp\left(\frac{eV}{kT}\right) - 1 \right] - I_L \quad (13)$$

C. Characterization of Organic Photovoltaic Devices

For the characterization of an organic photovoltaic cell, the following parameters are often used:

1. Short-circuit current (I_{SC}). This is the current output when the load impedance is much smaller than the device impedance.
2. Open-circuit voltage (V_{OC}). This is the voltage output when the load impedance is much greater than the device impedance.
3. Maximum output power (P_m) and fill factor (FF). P_m is the product of the current I_m and voltage V_m at maximum output power:

$$P_m = I_m V_m = \text{FF} \cdot I_{\text{SC}} V_{\text{OC}} \quad (14)$$

$$\text{FF} = \frac{P_m}{I_{\text{SC}} V_{\text{OC}}} \quad (15)$$

4. Power conversion efficiency (η). Photovoltaic devices should be used for the direct conversion of sunlight to electricity. The intensity of solar radiation on the earth's surface when the sun's rays form an angle of 60° is about 691 W/m^2 (AM2). The power conversion efficiency (η) is

the ratio of the maximum power output P_m to the incident power P_{in} :

$$\eta = \frac{P_m}{P_{in}} = \frac{I_{sc}V_{oc}FF}{P_{in}} \quad (16)$$

Sometimes the use of the power conversion efficiency of the barrier region is preferable, defined as

$$\eta' = \frac{I_{sc}V_{oc}FF}{P_T} \quad (17)$$

where P_T is the transmitted light power through the metal electrode.

5. Quantum efficiency (ϕ). It is worth mentioning that in organics ϕ increases with the field and that high fields can be obtained using very thin films.

D. Models

In general, the organic materials are characterized by wide energy gaps and low electrical conductivities, and as a consequence, charge injection from the electrodes is a common phenomenon. Furthermore, as a rule, light absorption does not produce mobile charge pairs, but excitons. Finally, the generation of mobile charges is strongly field dependent. Despite these differences, the photovoltaic effects in organic materials are generally explained using the models developed for the case of a junction between a metal and a p - or n -doped semiconductor. This approach has been questioned by some authors [58–60], since the concepts of semiconductor physics suggest high carrier concentration and the presence of a depletion layer at the contact.

The width of the depletion layer in inorganics is [56]

$$W_d = \left[\frac{2\epsilon\epsilon_0}{eN} (\Phi_s - \Phi_m + V) \right]^{1/2} \quad (18)$$

where V is the applied voltage and N is the donor or acceptor density. Under bias, if W_d increases, the capacitance of the layer decreases in agreement with

$$C = \frac{\epsilon\epsilon_0}{W_d} \quad (19)$$

From Eqs. (18) and (19),

$$\frac{1}{C^2} = \frac{2(\Phi_s - \Phi_m + V)}{e\epsilon_0 kN} \quad (20)$$

A plot of $1/C^2$ versus V should result in a straight line if the capacitance is attributable to a Schottky depletion region. Capacitance measurements versus V on organics should therefore be able to prove the existence of a depletion layer, thus confirming the applicability to organic materials of the concepts developed for inorganics [61].

If, on the other hand, the organic photoconductor is considered an insulator, the bulk carriers can no longer play a significant role and charge redistribution between the two metals, when the circuit is closed, takes place through the external circuit. The electric field E will be

$$E = \frac{\Phi_{m1} - \Phi_{m2}}{d} \quad (21)$$

where d is the thickness of the organic layer [62]. This model gives a capacitance independent from the voltage and corresponding to the geometric capacitance of the system. The key for a correct interpretation of C - V experiments is the frequency of the applied voltage. Some experiments [61,63] indicate that the capacitance remains constant with the applied voltage; however, when the frequency of the applied voltage is at 10^{-2} Hz, the capacitance begins to show a voltage dependence [61]. This behavior was taken as proof of the existence of a depletion layer formed by trapped, quasi-immobile charges [61]. Only very slow voltage changes can enlarge or reduce the thickness of the trapped charge cloud.

Within the framework of the Schottky junction theory, many models have been developed to explain the photovoltaic spectral response of organic materials. Assuming a direct formation of carriers, without diffusion of exciton to the surface but taking into account the charge diffusion length $L_{n,p}$, the photocurrent density J_{SC} for light incident on the junction side is [64]

$$J_{SC} = e\phi N_{\text{phi}} \left[\alpha W_d + \frac{\alpha}{\alpha + \beta} \exp(-\alpha W_d) \right] \quad (22)$$

for $\alpha W_d < 1$, where ϕ is the quantum efficiency, N_{phi} the number of incident photons/cm²s, α the absorption coefficient, and $\beta = 1/L_{n,p}$. The first term on the right gives the contribution of the carriers generated within the barrier of width W_d , and the second term gives the contribution of the carriers generated in the bulk. If $\beta \gg \alpha$, the expression (22) becomes

$$J_{SC} = e\phi N_{\text{phi}} \alpha W_d \quad (23)$$

When the light is incident on the opposite side,

$$J_{SC} = e\phi N_{\text{phi}} \left\{ \frac{\alpha}{\alpha - \beta} \{ \exp[-\beta(d - W_d)] - \exp[-\alpha(d - W_d)] \} + \exp(-\alpha d) [\exp(-\alpha W_d) - 1] \right\} \quad (24)$$

where d is the cell thickness. If $\beta \gg \alpha$,

$$J_{SC} = e\phi N_{\text{phi}} \exp(-\alpha d) [\exp(-\alpha W_d) - 1] \quad (25)$$

In organic cells, however, the steps involved in the generation of photocurrent are (1) light absorption, (2) exciton creation, (3) exciton diffusion, (4) exciton dissociation in the bulk or at the surface, (5) field-assisted carrier separation, (6) carrier transport, and (7) carrier delivery to external circuit. Assuming that only the excitons which reach the junction interface produce free carriers, if the blocking contact is illuminated [65],

$$J_{SC} = e\phi N_{\text{phi}} \frac{\alpha}{\alpha + \beta'} \quad (26)$$

where $\beta' = 1/l_d$ and l_d is the diffusion length of the exciton. For light incident on the opposite electrode, if $\exp(-\beta' d) \ll 1$,

$$J_{SC} = e\phi N_{\text{phi}} \frac{\alpha}{\beta' - \alpha} \exp(-\alpha d) \quad (27)$$

An alternative model [58] considers the photovoltage, at least in the first singlet absorption region, where direct generation of electron-hole pair can be neglected as due to photoinjection of charges at the electrode interfaces. The band model of conduction is assumed and the organic is considered a pure insulator (no donors or acceptors) with a narrow conduction band. Only the open circuit was considered. Both electrodes inject the same carrier into the insulator by two processes: a dark process occurring at a constant rate, and a photo process occurring at a rate proportional to the light intensity. In the trap-free single-carrier case, the additional injection of charges due to the light absorbed near the front electrode induces a shift in the Fermi level with respect to the Fermi level of the back electrode. The difference in Fermi level between the two electrodes is the observed photovoltage. If the cell is thin enough that some light reaches the back electrode, photoinjection occurs there also, thus

generating a photovoltage component opposed to that at the front. The net photovoltage is then

$$V = V_1 - V_2 = \frac{kT}{e} \ln \frac{1 + X_f/D_f}{1 + X_b/D_b} \quad (28)$$

where D_f and D_b are the rate of injection in the dark at the front and back electrode, while X_f and X_b are the rate of photoinjection. If X_f and X_b are proportional to N_{phi} and a and b are the ratios of the photoinjection efficiency to the dark injection rate at the front and back electrode, respectively, Eq. (28) becomes

$$V = \frac{kT}{e} \ln \frac{1 + aN_{\text{phi}}}{1 + bN_{\text{phi}}} \quad (29)$$

where $aN_{\text{phi}} = X_f/D_f$ and $bN_{\text{phi}} = X_b/D_b$. There are four cases to be considered:

$$\text{Case I: } V = \frac{kT}{e} (a - b)N_{\text{phi}} \quad aN_{\text{phi}} \ll 1, \quad bN_{\text{phi}} \ll 1 \quad (30)$$

$$\text{Case II: } V = \frac{kT}{e} \ln (aN_{\text{phi}}) \quad aN_{\text{phi}} \gg 1, \quad bN_{\text{phi}} \ll 1 \quad (31)$$

$$\text{Case III: } V = -\frac{kT}{e} \ln (bN_{\text{phi}}) \quad aN_{\text{phi}} \ll 1, \quad bN_{\text{phi}} \gg 1 \quad (32)$$

$$\text{Case IV: } V = \frac{kT}{e} \ln \frac{a}{b} \quad aN_{\text{phi}} \gg 1, \quad bN_{\text{phi}} \gg 1 \quad (33)$$

At very low light intensity, case I holds and the photovoltage varies linearly with light intensity with a sign that depends on the relative magnitude of a and b . When both electrodes are identical and the light is strongly absorbed, $a \gg b$. If the back electrode has a much higher work function than the front electrode, it is possible that $b > a$, in which case the sign of V is reversed. As the light increases, the case II becomes relevant and the photovoltage become logarithmically dependent on the light intensity at the front surface. If the front electrode has a much lower work function than the rear electrode, the case III may be obtained. At very high light intensity or with very thin crystals, saturation is approached and V becomes independent of light intensity (case IV). To get some idea of the type of spectral response, supposing that X_f and X_b are proportional to the absorption coefficient α and N_{phi} , through the approximations (30–33), the following four cases are obtained (where ϕ_f and ϕ_b are the quantum ef-

iciencies of charge generation in the front and rear electrodes, respectively):

$$\text{Case I: } V = (kT)(\alpha N_{\text{phi}}) \left[\frac{\phi_f l_d}{D_f} - \frac{\exp(-\alpha d) \phi_b l_d}{D_b} \right] \quad (34)$$

$$\text{Case II: } V = \frac{kT}{e} \ln \frac{e\alpha\phi_f l_d N_{\text{phi}}}{D_f} \quad (35)$$

$$\text{Case III: } V = \frac{kT}{e} \left(\alpha d - \ln \frac{e\alpha\phi_b l_d N_{\text{phi}}}{D_b} \right) \quad (36)$$

$$\text{Case IV: } V = \frac{kT}{e} \left(\alpha d + \ln \frac{D_b \phi_f}{D_f \phi_b} \right) \quad (37)$$

In case I, V is almost linear on α and N_{phi} ; in case II V is a weak function of N_{phi} and α ; in case III the action spectrum is antibatic with the absorption spectrum; and in case IV the photoresponse is again symbatic and independent of light intensity. The presence of surface traps modifies the earlier equation:

$$V = \frac{kT}{e} \ln \frac{1 + a'N_{\text{phi}} + a''N_{\text{phi}}^2}{1 + b'N_{\text{phi}} + b''N_{\text{phi}}^2} \quad (38)$$

where a' , b' , a'' , and b'' are constants that are functions of the injection, ejection, detrapping, and trapping processes operative at the surface.

E. Experimental Results

The choice of the organic material to be used in a Schottky or p - n device should take into account some necessary requirements: broad light absorption in the visible and near-IR region to create charge carriers; high absorption coefficient to reduce the thickness of the organic layer, thus increasing the electric field; chemical and photochemical stability; electrodes stability; inexpensive materials; and simple methods for the production of devices. The ambient conditions during the film preparation and during the electrical measurements require careful control. It is well known, in fact, that the presence of oxygen greatly influences the behavior of organic photovoltaic cells [59].

1. Schottky Cells

The Schottky cell is constituted of an organic compound sandwiched between two metals. Several organic materials have been tested (Fig. 8): aromatic hydrocarbons [60,61,63,66–68], chlorophyll [69–74], porphyrins [75–77], phthalocyanines [78–84], merocyanines [65,85–90], squarylium

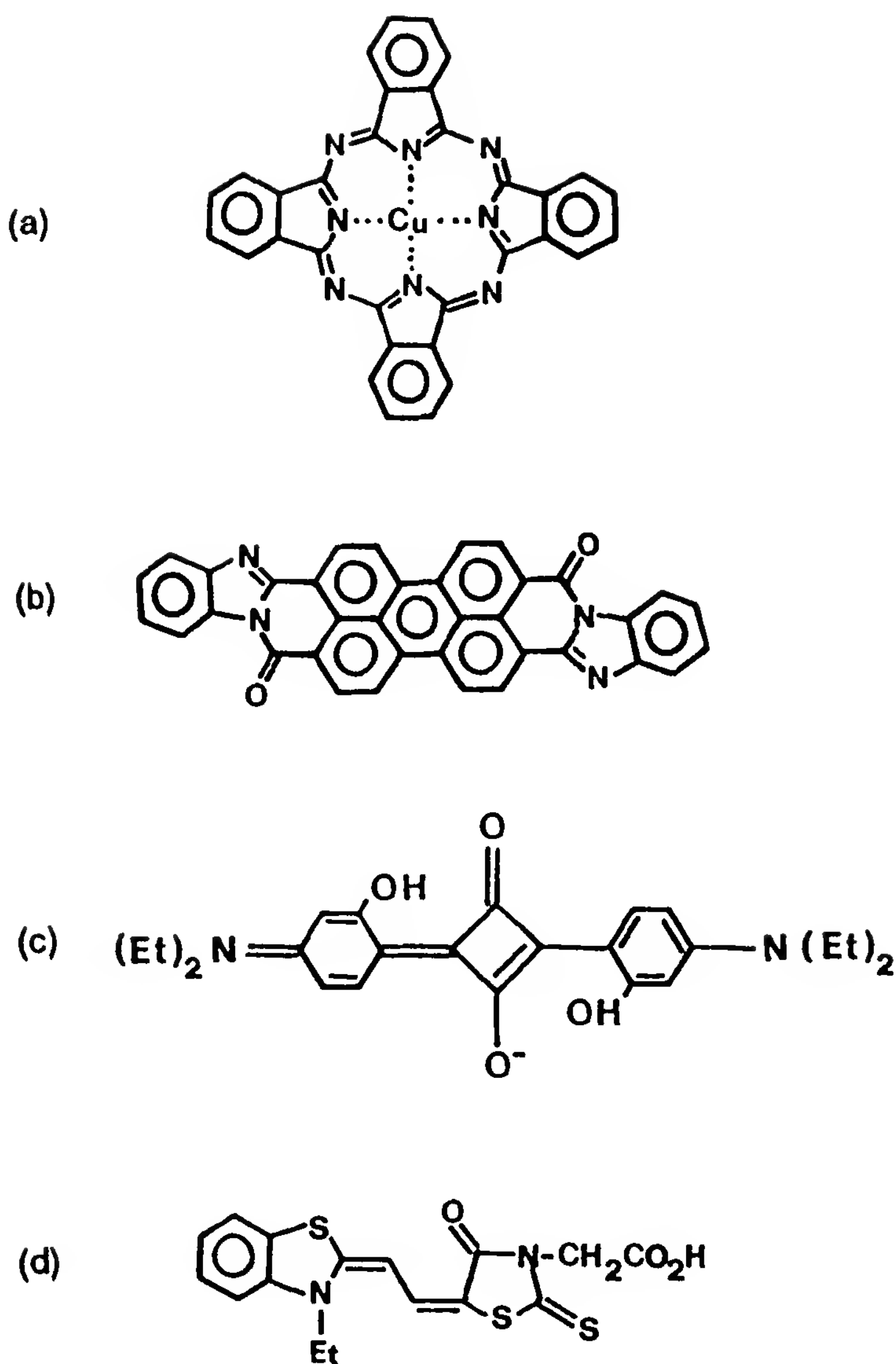


Figure 8 Molecular structures of some interesting materials: (a) copper phthalocyanine (CuPc); (b) perylene tetracarboxylic derivative (PV); (c) hydroxysquarylium; (d) merocyanine dye.

dyes [91], rhodamines [92], quinacridones [93], polyvinylcarbazole (PVK) [94,95], and doped polymers [96–98]. Various methods have been utilized for the production of thin films: vacuum sublimation, spin coating, and electrochemical deposition. The optimum film thickness depends on the absorption coefficient of the material, but if the thickness is below a certain critical value, the risk of short circuits greatly increases. In general, the thickness ranges between 100 and 10,000 Å. Since the organic materials almost invariably show a *p*-type conductivity, the ohmic contact is realized using a high-work-function metal (Au, Ag) or ITO conducting glass, while the rectifying contact requires a low-work-function metal (Al, In). The

illumination of the active region occurs through the low-work-function metal, whose thickness should meet the opposing requirements concerning the electrical resistance and optical transmission of the layer. The cell efficiencies are in general very low; interesting results were obtained with hydroxysquarilium (0.23%) [91] and merocyanines (0.7%) [65,85].

Schottky cells produce satisfactory open-circuit voltages but poor short-circuit currents. These depend strongly on the thickness of the organic layer because of its low conductivity. The thinner the layer, the lower the series resistance R_s . This, however, will increase the probability of pinhole formation. Other causes could explain the low efficiencies observed, especially at high light intensities. Among these are (1) the poor chemical stability of the aluminum electrode; (2) the presence of a high density of traps; (3) low carrier generation efficiency; (4) the electrical and optical characteristics of the electrodes (indium, for instance, has a high sheet resistance which can be reduced only by increasing the film thickness, to the detriment of its transmittance); and (5) low overall sunlight absorption.

2. *p-n* Junction Cells

If the Schottky barrier cells are by far the most extensively studied, the limited absorption spectra of single-layer films, combined with the narrow widths of their depletion layer, restrict the ultimate sunlight conversion to about 4% [55]. An organic *p-n* junction, in contrast, should have a higher efficiency because of improved matching of absorption and solar spectra by the use of more than one absorber in the depletion layer. The *p-n* junction, in fact, is composed of two layers, constituted of a *p*-type and an *n*-type organic conductor.

Another advantage is that the cell can be illuminated through a transparent (indium tin oxide, for instance) electrode that forms an ohmic contact with *n*-type materials. In a Schottky barrier, instead, cells illumination has to be transmitted through one of the two semitransparent metal electrodes (preferably the rectifying one if the radiation is strongly absorbed), and thus part of the available sunlight is lost at the outset [99]. The *p-n* cells should be fabricated taking into account the existence of a proper hierarchy among the materials that dictate that the *n*-type one, in contact with the transparent electrode, should be the shorter-wavelength absorber and its fluorescence band should overlap the absorption band of the *p*-type material [100]. These requirements are particularly striking with materials having exciton diffusion lengths shorter than the distance between the *p-n* junction and the transparent illuminated electrode. In merocyanines, for instance, the diffusion lengths range between 50 and 80 Å, while the thickness of the layer ranges between 200 and 400 Å. If the dye hierarchy noted above is violated, excitons generated from photons absorbed

preferentially near the illuminated electrode, and thus lying more than an exciton diffusion length away from the dye–dye junction, cannot then find their way to that interface by either diffusion or radiationless transfer [100].

Rectification and photovoltaic effects in organic *p-n* junctions were first reported by Kearns and Calvin [101] and by Meier [3]. The combination of rhodamines or triphenylmethane dyes (both *n*-type) with merocyanines or phthalocyanines (both *p*-type) generated photovoltages up to 200 mV and photocurrents of about 10^{-8} A at low light intensity, with power conversion efficiency much less than 1%. More recent studies have been performed on merocyanine and malachite green [89,90] and on phthalocyanines and TPyP (a porphyrin derivative) [102,103]. These devices showed stronger spectral sensitization and better spectral match to a solar spectrum than those of Schottky barrier cells using only one component.

A notable improvement was obtained by Tang [105]. The cell, composed of ITO/copper-phthalocyanine (CuPc, *p*-type)/perylene tetracarboxylic derivative (PV, *n*-type)/Ag, (Fig. 9), showed the following characteristics under AM2 illumination: $V_{oc} = 450$ mV, $I_{sc} = 2.3$ mA, $FF = 0.65$, $\eta = 1\%$, without correction for reflection or absorption losses (Fig. 10). Tang assumes that the absorption of light by both CuPc and PV layers creates excitons, which can diffuse in the bulk of the film. The interface, or junction, between CuPc and PV was taken as the location of active sites for the dissociation of excitons, which leads to holes transported through the CuPc layer and collected by the ITO electrode, while the electrons are transported through the PV layer toward the Ag electrode. The exciton dissociation may be associated with a high built-in field of unknown origin, perhaps a dipole field or a field due to trapped charges at the interface.

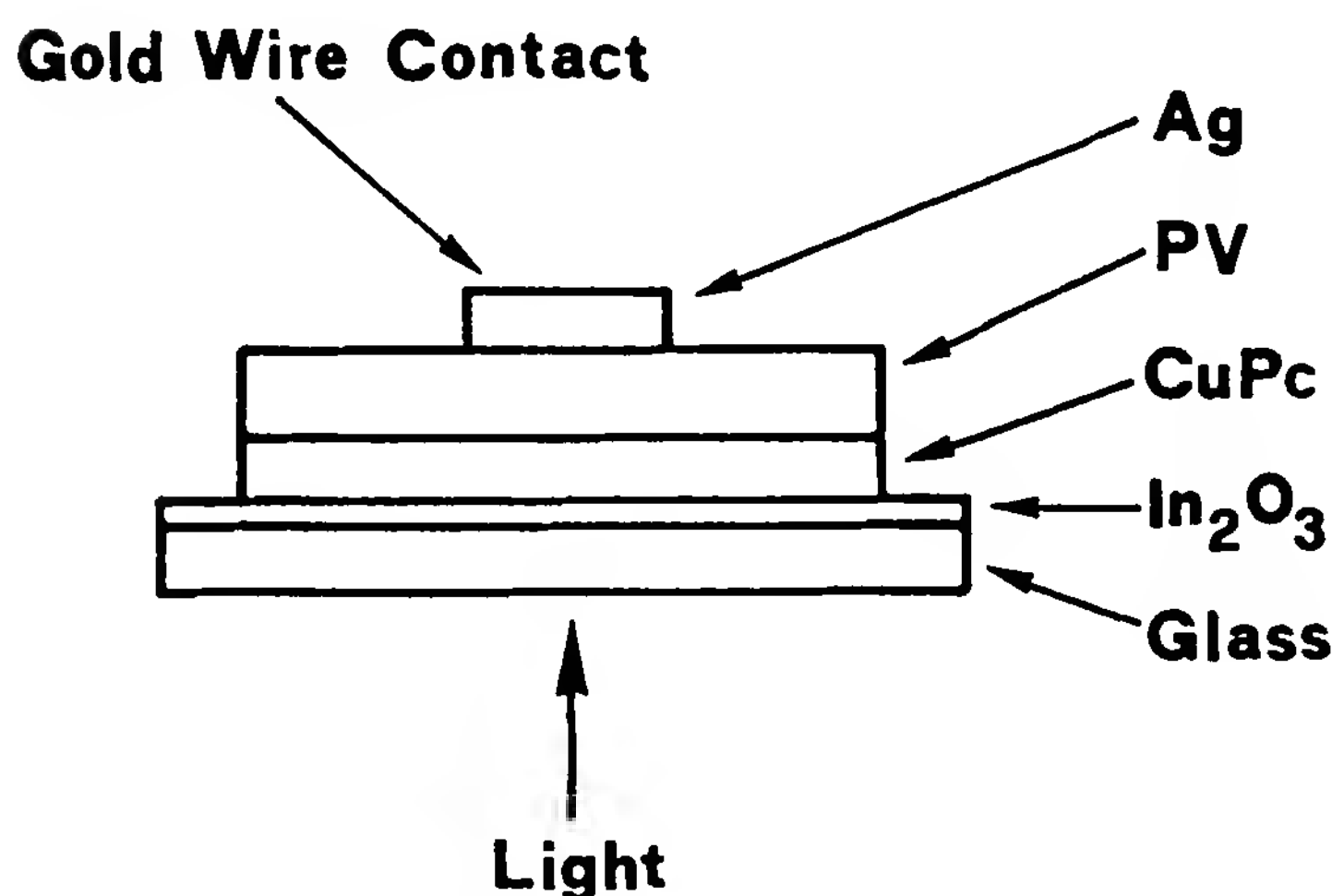


Figure 9 Configuration of a *p-n* organic cell. (After Ref. 105.)

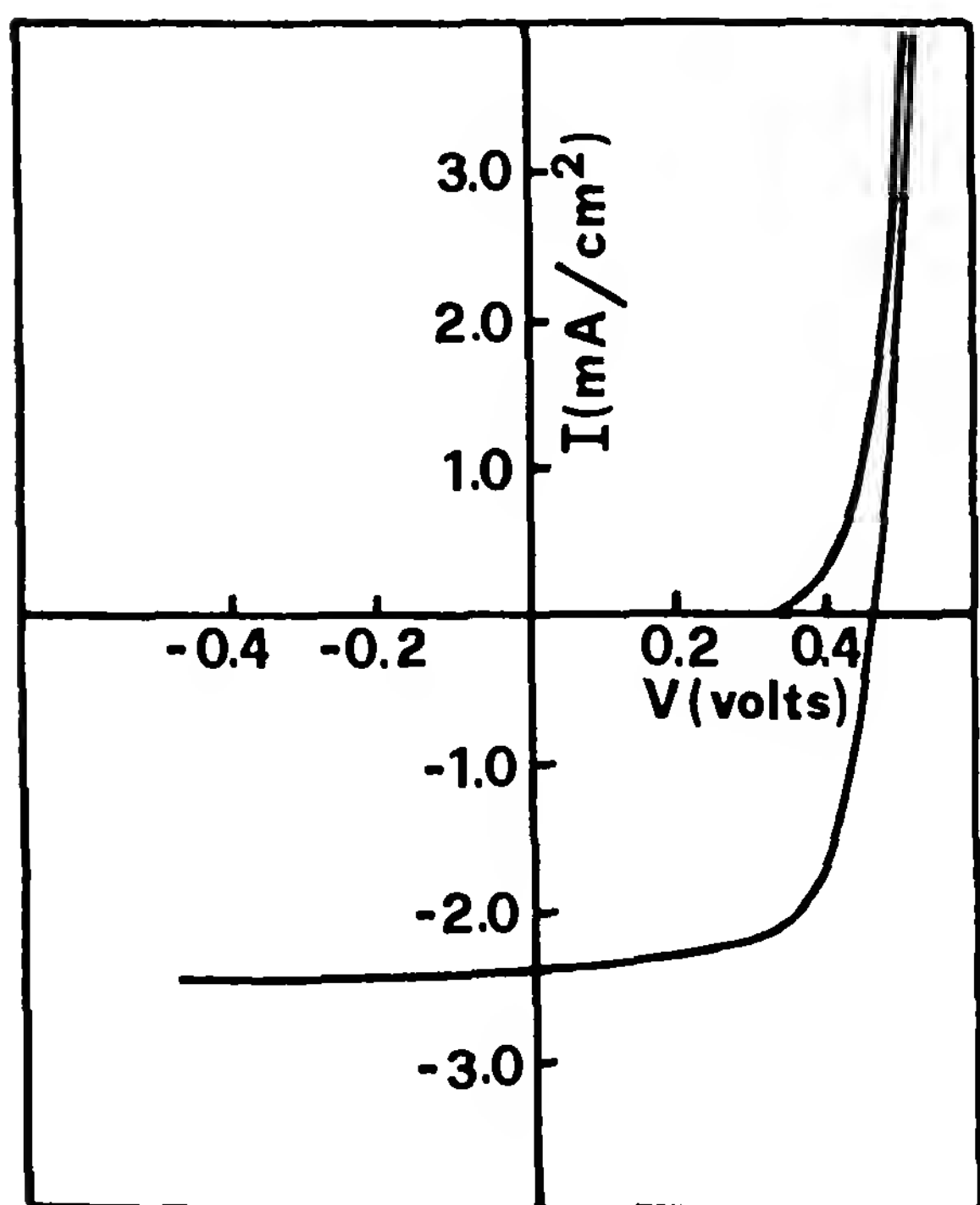


Figure 10 Dark and photocurrent–voltage characteristics of a *p-n* organic cell. (After Ref. 105.)

If the field is sufficiently high, the carrier generation efficiency would be virtually saturated and is limited primarily by the diffusion of excitons into this interface region.

On the basis of the *p-n* junction theory, to have an appreciable interface barrier, the organic materials should be carefully chosen by taking into account their electrochemical potentials [99]: the best materials should have widely separated Fermi levels [100]. The potential difference can be increased further with the insertion in donor dye molecules of an electron-donating group (methyl, methoxy) and in acceptor dyes of an electron-withdrawing group (fluoro, trifluoromethyl, cyano, chloro). Good results were obtained with the system SnO_2 /dimethylimide of perylene-3,4,9,10-tetracarboxylic acid/Al–Cl-substituted phthalocyanine/Ag. Doping could also be used to produce a shift of the Fermi levels, giving rise to an increase in the junction potential and carrier generation efficiency [105].

A factor limiting the conversion efficiency of these devices is the thickness of the active layer. Some studies were devoted to the realization of a more extended junction layer by doping [106]. Concentration of dopant in the range 10^{-6} to 10^{-3} extends the active layer to 5000 to 20,000 Å. The main limitation of many organic *p-n* devices is a poor short-circuit current. As in Schottky cells, the short-circuit current depends strongly on

layer thickness. Its optimization should greatly improve device performance [83].

REFERENCES

1. A. Pochettino, *Atti Accad. Naz. Lincei Sci. Fis. Mat. Nat. Rend.* **15**:355 (1906).
2. F. Gutmann and L. Lyons, *Organic Semiconductors*, Wiley, New York, 1967.
3. H. Meier, *Organic Semiconductors: Dark and Photoconductivity of Organic Solids*, Verlag Chemie, Weinheim, Germany, 1974.
4. J. Mort and D. M. Pai, *Photoconductivity and Related Phenomena*, Elsevier, New York, 1976.
5. K. C. Kao and W. Hwang, *Electrical Transport in Solids*, Pergamon Press, Elmsford, N.Y., 1981.
6. M. Pope and C. E. Swenberg, *Electronic Processes in Organic Crystals*, Clarendon Press, Oxford, 1982.
7. J. W. Steketee and J. Jonge, *Philips Rev. Rep.* **17**:363 (1962).
8. L. Onsager, *Phys. Rev.* **54**:554 (1938).
9. R. H. Fowler, *Phys. Rev.* **38**:45 (1931).
10. W. E. Spear, *Proc. Phys. Soc. B* **70**:669 (1957).
11. R. G. Kepler, *Phys. Rev.* **119**:1226 (1960).
12. J. Mort and G. Pfister, *Electronic Properties of Polymers*, Wiley, New York, 1982.
13. T. Holstein, *Ann. Phys.* **8**:343 (1959).
14. N. Mott, *Electronic and Structural Properties of Amorphous Semiconductors*, Academic Press, New York, 1972.
15. C. F. Carlson, U.S. Patent 2,221,776 (1938).
16. J. H. Dessauer and H. E. Clark, *Xerography and Related Processes*, Focal Press, New York, 1965.
17. R. M. Schaffert, *Xerography*, Focal Press, New York, 1975.
18. R. O. Loutfy, A.-M. Hor, C.-H. Hsiao, G. Baranyi, and P. Kazmaier, *Pure Appl. Chem.* **60**:1047 (1988).
19. H. Baumann, W. Helmstreit, and R. Ackermann, *J. Inf. Rec. Mater.* **19**:29 (1991).
20. M. G. Carter, in *Xerographic Materials from Silicon to Organics* (L. S. Miller and J. B. Mullin, eds.), Plenum Press, New York, 1991, Chap. 18, p. 267.
21. H. Hoegl, German Patent 1,068,115 (Sept. 7, 1957).
22. M. D. Shattuck and U. Vatra, U.S. Patent 3,484,237 (1969).
23. R. M. Schaffert, *IBM J. Res. Dev.* **15**:75 (1971).
24. E. G. Schlosser, *J. Appl. Photogr. Eng.* **4**:118 (1978).
25. D. Winkelman and K. Reuter, in *Advances in Non-impact Printing Technologies for Computer and Office Applications* (J. Gaynor, ed.), Van Nostrand Reinhold, New York, 1982, p. 446.
26. S. T. Takano, T. Enokida, A. Kakuta, and Y. Mori, *Chem. Lett.*, 2037 (1984).

27. K. Ohaku, H. Nakano, T. Kawara, S. Yokota, O. Takenouchi, and M. Aizawa, *Electrophotography* 25:258 (1986).
28. P. M. Borsenberger, M. T. Regan, and W. J. Staudenmayer, U.S. Patents 4,578,334 and 4,618,556 (1985).
29. W. J. Staudenmayer and M. T. Regan, U.S. Patent 4,719,163 (1988).
30. S. Takenouchi, A. Hirano, H. Yoshioka, Y. Fujimaki, and H. Moriguchi, in *SPSE 4th International Congress on Advances in Non-impact Printing Technologies*, New Orleans, La., Mar. 20–25, 1988, p. 22.
31. N. S. Allen, E. T. Robinson, C. M. Scott, and F. Thompson, *Dyes Pigments* 10:183 (1989).
32. Q. Takehouchi, N. C. Khe, T. Kawara, and H. Tanaka, U.S. Patent 4,504,560 (1985).
33. M. Hashimoto, *Electrophotography* 25:230 (1986).
34. S. Ofsuke, T. Murayama, and H. Nagasaka, *3rd International Congress on Advances in Non-impact Printing Technologies*, San Francisco, Aug. 24–28, 1986, p. 111.
35. M. Ohta, Ricoh Tech. Rep. 8:4 (1982).
36. D. McMurty, M. Tinghitella, and R. Svendsen, *IBM J. Res. Dev.* 28:257 (1984).
37. N. C. Khe, O. Takenouchi, T. Kawara, H. Tanaka, and S. Yokota, *Photogr. Sci. Eng.* 28:195 (1984).
38. W. J. Dulmage, W. A. Light, S. I. Marino, C. D. Salzberg, and W. J. Staudenmayer, *J. Appl. Phys.* 49:5543 (1978).
39. M. Sasaki, U.S. Patent 4,777,296 (1988).
40. P. M. Borsenberger and D. S. Weiss, in *Handbook of Imaging Materials* (A. S. Diamond, ed.), Marcel Dekker, New York, 1991, Chap. 9, p. 379.
41. N. C. Khe and M. Aizawa, *J. Chem. Soc. Jpn. Chem. Ind. Chem.* 3:393 (1986).
42. K. Y. Law and F. C. Bailey, *J. Imag. Sci.* 31:172 (1987).
43. D. M. Pai, *Proceedings of the First International Conference on Frontiers of Polymer Research*, New Dehli, India, Jan. 1991.
44. J. Stevens and K. A. Zaklika, *Photogr. Sci. Eng.* 26:75 (1982).
45. M. Yokoyama, K. Akiyama, N. Yamamori, H. Mikawa, and S. Kusabayashi, *Polym. J.* 17:545 (1985).
46. G. Giro and P. G. Di Marco, *Chem. Phys. Lett.* 162:221 (1989).
47. G. Giro, P. G. Di Marco, V. Fattori, and R. Degli Esposti, *Mol. Cryst. Liq. Cryst.* 186:107 (1990).
48. T. Sasakawa, T. Ikeda, and S. Tazuke, *J. Appl. Phys.* 65:2750 (1989).
49. B. S. Ong, B. Keoshkerian, T. I. Martin, and G. K. Hamer, *Can. J. Chem.* 63:147 (1985).
50. R. O. Loufty, C. K. Hsiao, B. S. Ong, and B. Keoshkerian, *Can. J. Chem.* 62:1877 (1984).
51. J. E. Kuder, J. M. Pochan, S. R. Turner, and D. F. Hinman, *J. Electrochem. Soc.* 125:1750 (1978).

52. V. Y. Merritt, in *Electrical Properties of Polymers*, Vol. 4 (D. A. Seanor, ed.), Academic Press, New York, 1982.
53. J. Simon and J. J. André, in *Molecular Semiconductors*, Springer-Verlag, Berlin, 1985.
54. J. Kanicki, in *Handbook of Conducting Polymers* (T. A. Skotheim, ed.), Marcel Dekker, New York, 1985.
55. G. A. Chamberlain, *Solar Cells* 8:47 (1983).
56. S. M. Sze, *Physics of Semiconductor Devices*, Wiley, New York, 1981.
57. H. G. Hovel, *Semiconductors and Semimetals*, Vol. 11, *Solar Cells*, Academic Press, New York, 1975.
58. J. S. Bonham, *Aust. J. Chem.* 29:2123 (1976).
59. K. J. Hall, J. S. Bonham, and L. E. Lyons, *Aust. J. Chem.* 31:1661 (1978).
60. R. Signerski, J. Kalinowski, I. Koropeczky, and S. Nespurek, *Thin Solid Films* 121:175 (1984).
61. A. J. Twarowski and A. C. Albrecht, *J. Chem. Phys.* 70:2295 (1979).
62. J. S. Bonham and D. H. Jarvis, *Aust. J. Chem.* 30:705 (1977).
63. A. K. Gosh and T. Feng, *J. Appl. Phys.* 44:2781 (1973).
64. A. K. Gosh, D. L. Morel, T. Feng, R. F. Shaw, and C. A. Rowe, Jr., *J. Appl. Phys.* 45:230 (1974).
65. A. K. Gosh and T. Feng, *J. Appl. Phys.* 49:5982 (1978).
66. P. H. Fang, A. Golubovic, and N. A. Dimond, *Jpn. J. Appl. Phys.* 11:1298 (1972).
67. P. H. Fang, *Jpn. J. Appl. Phys.* 13:1232 (1974).
68. J. Twarowski and A. C. Albrecht, *J. Chem. Phys.* 72:1797 (1980).
69. C. W. Tang and A. C. Albrecht, *J. Chem. Phys.* 62:2139 (1975).
70. C. W. Tang and A. C. Albrecht, *Nature* 254:507 (1975).
71. G. A. Corker and I. Lundstrom, *J. Appl. Phys.* 49:686 (1978).
72. I. Lundstrom, G. A. Corker, and M. Stenberg, *J. Appl. Phys.* 49:701 (1978).
73. A. F. Janzen and J. R. Bolton, *J. Am. Chem. Soc.* 101:6342 (1979).
74. J. P. Dodelet, J. Le Brech, C. Chapados, and R. M. Le Blanc, *Photochem. Photobiol.* 31:143 (1980).
75. T. Kawai, K. Tanimura, and T. Sakata, *Chem. Phys. Lett.* 56:541 (1978).
76. F. J. Kampas, K. Yamashita, and J. Fajer, *Nature* 284:40 (1980).
77. K. Tanimura, T. Kawai, and T. Sakata, *J. Phys. Chem.* 84:751 (1980).
78. Fu-Ren Fan and L. Faulkner, *J. Chem. Phys.* 69:3341 (1978).
79. R. O. Loutfy and J. Sharp, *J. Chem. Phys.* 71:1211 (1979).
80. R. O. Loutfy, J. H. Sharp, C. K. Hsiao, and R. Do, *J. Appl. Phys.* 52:5218 (1981).
81. M. Martin, J. J. André, and J. Simon, *Nouv. J. Chim.* 5:485 (1981).
82. B. Sh. Barkhalov and Y. A. Vidadi, *Thin Solid Films* 40:L5 (1977).
83. S. Siebentritt, S. Gunster, and D. Meissner, *Synth. Metals* 41-43:1173 (1991).
84. G. A. Chamberlain and P. J. Cooney, *Chem. Phys. Lett.* 66:88 (1979).
85. D. L. Morel, A. K. Gosh, T. Feng, E. L. Stogryn, P. E. Pumwin, R. F. Shaw, and C. Fishman, *Appl. Phys. Lett.* 32:495 (1978).
86. K. Kudo and T. Morizumi, *Jpn. J. Appl. Phys.* 19:L63, (1980).

87. G. A. Chamberlain, P. J. Cooney, and S. Dennison, *Nature* 289:45 (1981).
88. T. Morizumi and K. Kudo, *Appl. Phys. Lett.* 38:85 (1981).
89. K. Kudo and T. Moriizumi, *Jpn. J. Appl. Phys.* 20:L553, (1981).
90. G. A. Chamberlain, *Proceedings of the 6th International Conference on the Chemistry of the Organic Solid State*, Freiburg, Germany, Oct. 4–8, 1982.
91. V. Y. Merrit, *IBM Res. Dev.* 32:353 (1978).
92. J. Muto and Y. Tsunekawa, *Phys. Status Solidi (a)* 79:K109 (1983).
93. M. Tomida, S. Kusabayashi, and M. Yokoyama, *Chem. Lett.*, 1305 (1984).
94. P. J. Reucroft, K. Takahashi, and H. Ullal, *Appl. Phys. Lett.* 25:664 (1974).
95. P. J. Reucroft, K. Takahashi, and H. Ullal, *J. Appl. Phys.* 46:1975 (5218).
96. S. Glenis, G. Horowitz, G. Tourillon, and F. Garnier, *Thin Solid Films* 111:93 (1984).
97. *Thin Solid Films* 139:221 (1986).
98. S. Glenis and A. J. Frank, *Synth. Metals* 28:C681 (1989).
99. P. Panayotatos, D. Parikh, R. Sauers, G. Bird, A. Piechowski, and S. Husain, *Solar Cells* 18:71 (1986).
100. P. Panayotatos, G. Bird, R. Sauers, A. Piechowsky, and S. Husain, *Solar Cells* 21:301 (1987).
101. R. Kearns and M. Calvin, *J. Chem. Phys.* 29:950 (1958).
102. Harima et al., *Appl. Phys. Lett.* 45:1144 (1984).
103. S. Antohe and L. Tugulea, *Phys. Status Solidi (a)* 128:253 (1991).
104. M. Hiramoto, Y. Kishigami, and M. Yokoyama, *Chem. Lett.*, 119 (1990).
105. C. W. Tang, *Appl. Phys. Lett.* 48:183 (1986).
106. J. J. André, J. Simon, R. Even, B. Boudjema, G. Guillaud, and M. Maitrot, *Synth. Metals* 18:683 (1987).

This Page Intentionally Left Blank

Index

- Acceptors molecules, 6, 15–19,
75–108, 116, 692–708, 819
electron affinity, 2, 80, 92, 93, 102,
341, 405, 500, 594, 604, 621,
650, 694–707
- Acetylcholine, 695, 707, 718
- Acetylene, 547
- Ag(TCNQ), 257
- Aggregate materials, 569, 720–721,
801–803
- Alkali metal TCNQ salts, 332,
338–342
Cs₂(TCNQ)₃, 348
K(TCNQ), 239, 240, 248, 257, 339,
391
Rb(TCNQ), 338–341
- 3,4,5-(alkylthio)-1,2-dithiolium, 768
- Amines, 696, 805
- Amino acids, 696, 703, 705, 710
- Amino-substituted derivatives, 84
- Ammonium ions, substituted, 3
- Amphiphiles, 707, 720, 721, 768, 769
- Anion (or counterion) ordering (*see*
Phase transitions)
- Anion (or counterion) symmetry, 63,
161, 261, 288, 419, 477
- Anthanthrone, dye, 801
- Anthracene, 4, 626, 791, 797
- Anthraquinodimethane, 768
- Antibiotics, 698
- Antiferromagnetic resonance
(AFMR), 278–279, 284, 289,
463, 465
- Antiferromagnetism (AFM), 13, 17,
32–35, 54, 61–67, 203,
272–299, 365, 366, 415–465
- Applications, magnetic properties,
270, 303–306
biocompatibility, 306
insulating magnets, 306
integrated optical devices, 306
magnetic and magnetooptic storage,
305
magnetic field detectors, 303
magnetic imaging, 305, 306
magnetic ink, 306
magnetic sensors, 303, 488
magnetic tapes and disks, 305

- [Applications, magnetic properties]
 - narrow ESR signals, 303–305, 488
 - object identification, 303
 - patent, fast adiabatic pass method, 305
 - photomagnetic switches, 306
 - processibility, 305
 - soluble materials, 305
 - submarine mine detectors, 303
 - ultrahigh-density optical storage, 305
- Applications, molecular electronics,
 - Langmuir-Blodgett films, 108–109, 759–790
 - contacts (or electrodes), 759, 776
 - dye monolayers, 776
 - electrocopying, 759
 - engineering
 - molecular, 20, 311, 760
 - supramolecular, 760, 761
 - functional materials, 761
 - active elements, 761, 772, 776, 783
 - hydrophobized quartz plate, 782
 - information processing, 777
 - liquid crystal displays (LCD), 759
 - multifunctional supramolecule, 776
 - switching unit, 777–783
 - transmission unit, 777–780
 - working unit, 777, 780
 - operational constraints, 759
 - ordered structures, 760, 764
 - photodiodes, 760
 - photoelectric cells, 776
 - photoresists, 759
 - processing, 759, 760
 - realization, 760, 761
 - rectifiers, 759, 760
 - Aviram-Ratner molecular rectifier, 759, 760
 - switching devices, 776–783
 - based on multifunctional molecule, 777–780
 - chemical modifications, 781
 - control light, 781–783
 - learning process and plasticity of
- [Applications, molecular electronics
 - Langmuir-Blodgett films]
 - synaptic transmission, 780–781
 - multiple switching device, 781–783
 - photochemical switching device, 781, 783
 - photoirradiation, alternate UV/visible, 778–783
 - photoisomerization, *cis-to-trans/trans-to-cis*, 778–783
 - realization, 782–783
 - reversibility, 779, 780
 - switching speed, 780
 - transistors, field-effect (FET)s, 776, 783
 - fabrication, 776
 - field-effect mobilities, 776
 - lift-off process, 776
 - source-to-drain distance, 776
- Applications, photoconductors,
 - photovoltaics, 798–806
 - acceptance potential, 798
 - contacts (electrodes), 794, 795, 809–817
 - blocking, rectifying, 806, 808, 813, 816–818
 - charge collecting, 791, 806
 - charge injection, photoinjection, 794, 795, 811–814
 - conducting glass, ITO, 816, 818
 - ohmic, 806, 816, 817
 - semitransparent, metallic, 817, 818
 - stability, 815, 817
 - work function, 806, 814–817
 - corona discharge, 798
 - dyes, 800–803, 815–819
 - electrochemical deposition, 816
 - electrophotography, 798
 - electrostatic latent images, 798, 799
 - materials for application in
 - xerography, 799–800
 - materials for charge generation, 801–805
 - coating, 801, 803

- [Applications, photoconductors, coating, 801, 803
- dispersion preparation, 803
- dual-layer arrangement, 801
- efficiency, 801
- near-infrared region, 803–805
- new polymorph materials, 803
- substituents, 801–805
- visible region, 801–803
- materials for charge transport, 805–806
- pigments, 800–803
 - pigment-solvent interaction, 803
- p-n* junction cells, 806–810, 815–820
 - advantages over Schottky cells, 817
 - capacitance-voltage (C-V) measurements, 812
 - current-voltage (I-V) characteristics, 810
 - depletion layer, 811, 812, 817, 819
 - diffusion currents, 809
 - drift currents, 809, 810
 - forward bias, 810
 - junction potential, 810
 - majority/minority carriers, 809, 810
 - photovoltaic emf, 810
 - potential barrier, 809, 810, 819
 - recombination, 810
 - reverse bias, 809, 810
- printing devices, 803
- sandwich cells, 795, 796, 806, 815
- Schottky cells, 806–810, 815–817
 - current asymmetry, 808
 - current-voltage (I-V) characteristics, 808
 - depletion layer, 807–812
 - diffusion potential, 808
 - forward bias, 808, 809
 - illuminated, 808
 - photocurrent-voltage characteristic, 809
 - potential barrier, 806–809
 - recombination, 809
 - reverse bias, 808
- [Applications, photoconductors, photovoltaics]
- solar cells (photovoltaic cells), 806–820
 - charge diffusion length, 812
 - controls, 815
 - cost, 806, 815
 - devices, characterization, 810–811, 815–820
 - efficiencies, 811–819
 - excitons, 813, 817–819
 - field-assisted carrier separation, 813
 - fill factor, 810
 - limiting factor, 819
 - losses, 818
 - maximum output power, 810
 - models, 811–815
 - open-circuit voltage, 810, 817
 - oxygen effect, 815
 - photocurrent/photovoltage, 812–814, 818
 - processibility, 806
 - short-circuit current, 810, 817, 819
 - solar spectrum, absorption/conversion, 811, 817, 818
 - spectral response, 801, 812, 814, 818
 - stability, 815, 817
- surface cells, 795, 796
- thin film production, 815, 816
 - electrochemical deposition, 816
 - short circuits, risk for, 816
 - single-/two-layer, 817
 - spin coating, 816
 - thickness, 816, 817
 - vacuum deposition/sublimation technique, 801, 803, 816
- xerography, 798–806
 - amorphous films, 806
 - automotive paints, 801
 - charge generation/transport layers (CGL/CTL), 800, 801
 - copiers, high/low-volume, 801
 - cost, 799, 803
 - cycle stability, 799

- [Applications, photoconductors, photovoltaics]
 - development, process time, 799
 - durability, 800
 - exposure, 798
 - fatigue effects, 799
 - fixing, fixative coating, 799
 - flexibility, 799
 - manufacturing, ease of, 799
 - miscibility, 805
 - multilayer structures, 800
 - panchromatic response, 799, 800
 - photoconductive layer, 798
 - photodischarge, 799, 801
 - photoreceptors, 799–805
 - polymer matrix compatibility, 803–806
 - processes, 798–799
 - requisites, for applications, 799
 - sensitivity to light, 799–803
 - solubility, 805, 806
 - speed, 800, 803
 - technology, 800
 - toner particles, 799
 - toxicity, 799, 805
 - transfer, 799
 - xerographic plate, 798
- Applications, polymers, 496, 504, 505, 523–533, 539, 541, 563, 597, 599, 601
 - industrial scale, world market, 524
 - overview, 523–526
- Applications, polymers permanently doped, 525–529
 - antiradar protection, 528
 - antistatic protective (transparent) films, 528
 - conducting and plastic properties, 526, 527
 - electrolytic capacitors, 527
 - electromagnetic shielding, 528
 - electroplating of copper, 527
 - electrostatic loudspeaker, 527
 - gas separation, 528, 529
 - porous Si-conducting polymer LEDs, 527
- [Applications, polymers permanently doped]
 - printed circuit boards, 527
 - selectively permeable membranes, 529
 - supercapacitors, 527
- Applications, polymers redox cycled (electrochemical doping), 526, 529–532
 - actuators, 532
 - artificial muscles, 532
 - batteries, light, rechargeable, 529
 - controlled drug release, 532
 - cyclability, 531
 - diodes, 532
 - drain current, 532
 - electroactive materials, 529
 - electrochromic devices, 530–531
 - energy storage, 526, 529
 - gate voltage, 532
 - microcircuit technology, 532
 - microelectromechanical devices, 532
 - microtweezers, 532
 - microvalves, 532
 - open-circuit voltage, 529
 - optical switch, 530
 - smart windows, 526, 530
 - time response, 531
 - transistors, 532
- Applications, polymers undoped, 526, 533, 600–635
 - active matrix flexible flat display panel, 533
 - all-optical phase modulator, 533
 - contacts (or interfaces or electrodes)
 - electric field action at a junction, 526
 - electrode materials, 620–622, 628
 - injection, 594–629
 - interface layers, 606–608, 614, 620–622, 633
 - metal-conjugated polymer, 600–609, 629
 - ohmic, 601–621
 - work function, 620–622
- diode geometries, 608, 628–635

[Applications, polymers undoped]

diodes, Al/trans polyacetylene/Au, 608

diodes, light-emitting

(electroluminescent) (LED)s,
533, 569, 594, 601–604, 609,
614–635

applied voltage, 615

brightness, 634

color adjustment, 629–631, 633,
634

device lifetime, 634

dye, 633

electrical operation conditions,
634

flexible LEDs, 621, 634

high-definition screens, 635

laser emission, 615

light-emitting areas, 634

materials, 629–633

multicolor emission, 624, 629

multiplexing, 625

performances, 629, 633

pulse mode, 625

quantum yields, 615, 626, 629,
633, 634

quenching centers, 633

radiationless losses, 632, 633

response time, 623, 625

switching times, 634

threshold voltage, 634

transit time, 623, 625

vapor deposited molecules, 628

diodes, Schottky, 601

directional coupler, 533

field emission, 606

heterojunctions, 601

liquid crystal display (LCD) panels,
533, 614

Mott barrier, 608

optical signal processing, 533

optoelectronic devices, 601

photovoltaic

cell, 533, 602

devices, 608

energy conversion, 601

yield, 601

[Applications, polymers undoped]

p-n junctions, 601 609, 613, 617

Schottky barriers, 601–625

Ag/ α -sexithienyl, 609Al/fibrillar *trans*-polyacetylene,
608

Al/polyphenylenevinylene, 609

Al/polythiophene, 608

barrier height, 605–609

depletion region, thickness, 605–
609, 619

diffusion potential, 605

In/polyalkylthiophenes, 609

saturation current, 606

thin film devices (TF)s, 602

spin-cast film, 533

thickness, 602, 619

transistors, field effect, (FET)s, 500,
533, 559, 600–604, 609–614,
632transistors, thin-films field-effect,
(TFT-FET)s, 602, 609–614
comparison with amorphous-Si
FETs, 614

current-voltage characteristics, 611

device lifetime, 614

drain electrode, 610–613

field effect, 609–614

gate electrode, 609, 610, 614

geometries, 610

insulated-gate field-effect
transistor (IGFET), 613insulated-gate thin films
transistors, 610

parameters, optimization of, 614

saturation current, 613

surface accumulation layer, 613

theory, 610–613

threshold voltage, 610, 613

unipolar device, 610

Applications, semiconductors,
343–353

conducting composites, 349–351

ionizing radiation dosimetry,
351–353

negative-resistance devices, 339–344

[Applications, semiconductors]

- switching, 343–344, 783
 - memory effect, 783
 - reproducibility, 343–344
- thermistor effect, 344–349
 - current-voltage characteristics, 346–349
 - theory, 344–347

Applications, superconductors, 488, 750

- Josephson circuits
 - high-density memories, 488
 - lithographic techniques, 488
 - microwave detectors, 488

Arenes, 80–84, 408

Aromatic molecules, crystals, 586, 626, 705, 815

Arrhenius plot, 697

Azobenzene,

- naphtalene substituted, 781
- NATP LB films, 781–783
- photochromic, *cis*, *trans*, 777–783
- ATP LB films, 778–783

Azo compounds, 801, 803

Band

- bending, at interfaces, 602, 806
- edges, 515, 618, 619, 627
- filling, 34, 36, 44, 61, 65, 292, 319, 373, 418, 454, 459, 503, 506
 - half-, 30, 34, 49–52, 54, 60, 61
- model, 4, 5, 28, 32, 76, 191, 197–199, 213, 230, 244, 245, 269–293, 313, 319, 360, 365–396, 406–459, 495–519, 544, 551, 570–620, 648–684, 696, 792–813

BCPTTF, 332, 337

(BCPTTF)₂AsF₆, 290, 295(BCPTTF)₂PF₆, 290(BCPTTF)₂X salts, 332, 337Bechgaard salts (*see* (TMTSF)₂X salts)(BEDO-TTF)₂X salts, 17, 237 α' -(BEDT-TTF)₂Ag(CN)₂, 180(BEDT-TTF)₂(ClO₄)₃, 373(BEDT-TTF)₂Cu[N(CN)₂]Br, 446 κ -(BEDT-TTF)₂Cu[N(CN)₂]Cl, 161 κ -(BEDT-TTF)₂Cu(NCS)₂, 201

BEDT-TTF (ET), 75, 87, 91, 96, 99, 100, 119, 120, 136, 162, 184

derivatives, 99, 768, 769

(BEDT-TTF)₂GaCl₄, 289, 338(BEDT-TTF)₂I₃, 99

polymorphs, 99, 138

 α -(BEDT-TTF)₂I₃, 238, 239, 257 β -(BEDT-TTF)₂I₃, 156, 161–162, 175, 180, 184–186, 197, 201, 213, 217, 238, 239, 257, 361, 362, 371, 375, 379, 380, 387, 388, 484 θ -(BEDT-TTF)₂I₃, 156, 161 κ -(BEDT-TTF)₂I₃, 156, 161 β -(BEDT-TTF)₂IBr₂, 484(BEDT-TTF)₂ICl₂, 289 α -(BEDT-TTF)₃(NO₃)₂, 238(BEDT-TTF)₂TlHg(SCN)₄, 60, 65 α' -(BEDT-TTF)₂X salts, 198, 338(BEDT-TTF)_{*n*}X salts, 191

polymorphs, 161

(BEDT-TTF)₂X salts ((ET)₂X salts), 17, 32, 59, 65, 67, 99, 139, 140, 164, 174, 179, 180, 191, 196, 198–203, 217, 237–245, 257, 359, 387, 444–458, 484, 487–488Benzocyclopentyltetrathiafulvalene (*see* BCPTTF)

Benzodimethyltetrathiafulvalene, 126

Benzoporphyrazines, 695

Benzoquinones, 93

Biethylenedioxytetrathiafulvalene (BO), 774

Biological systems, 2, 3, 7, 8, 312, 691–734

biological cells, 691

biosynthesis, 20

experimentation, *in vitro*, *in vivo*, 691, 698, 724

integrated, 721–724

living state, 2, 6, 7, 20, 691, 708, 721–725

membranes, 691, 698, 699, 708, 721, 723, 724

- [Biological systems]
 - mitochondria, 691, 724
 - submolecular biology, 724
 - vesicles, 691
- Bisbidentated ligands, 298
- Bis-dithiolene-transition metal
 - conductors, 134
- Bis(ethylenedioxy)tetrathiafulvalene (BEDO-TTF or BO), 120
- Bis(ethylenediseleno)tetraselenafulvalene (BEDS-TSF), 129
- Bis(ethylenediseleno)tetrathiafulvalene (BEDS-TTF or BEST), 125, 131
- Bis(ethylenedithio)tetraselenafulvalene (BEDT-TSF or BETS), 131
- Bis(ethylenedithio)tetrathiafulvalene (BEDT-TTF or ET) (*see* BEDT-TTF)
- Bismaleonitriledithiolate ($M(mnt)_2$), 291
- Bisphenol-A/polycarbonate, 803
- Bis(propylenedithio)tetrathiafulvalene (BPDT-TTF), 242
- Bis(tetramethylenetetraselenafulvalene- (4,5-dimercapto-1,3-dithiole-2-thione)Ni [OMTSF-Ni(dmit)₂], 242
- Bloch walls, 503
- BO-C₁₀TCNQ LB films, 774
- BO-C₁₄TCNQ LB films, 774
- BO-C_nTCNQ LB films, 774
 - stoichiometries, 774
- Bogoliubov transformation, 412
- Boltzmann transport theory, 377, 394, 396
- Bond-ordering-wave (BOW), 26, 42–63, 339
- Bonner-Fisher law, 275–296, 328–338, 422
- Bose-Einstein condensation, 6
- Bosonization, 35–36, 40, 53
 - (BPDT-TTF) salts, 242
- Brillouin zone, 12, 61, 506, 586, 587
- Buckminsterfullerene (C₆₀) (*see* Fullerenes)
- Cancer, role of CTC, 716, 718
- Carbohydrates, 711–714
- Carbon, 1, 2
 - atomic orbitals, 496, 511
 - black, 527, 528
- Carotenoids, 597, 708, 723
 - β -carotene/I₂ complex, 710
- Charge
 - distribution (density), 12, 14, 17, 164, 190–196, 214, 242, 261, 279, 326, 454, 605, 611, 613, 664, 685, 706
 - free carriers, 33–34, 579–625, 651, 658–674
 - hot, 616
 - majority, minority, 601, 604, 622, 809
 - mean free path, 368–395, 625, 659, 661, 662
 - relaxation time, 794–797
 - spinless, 503, 512–514, 674, 675
- itinerant electrons, 293, 294
- localization/delocalization, 15, 53–55, 87, 98, 99, 159, 191, 198, 209, 243, 254, 261, 262, 273–303, 312, 337, 394–397, 405, 406, 458, 550, 557, 581, 591, 598, 624, 632, 633, 659–668, 772
 - scaling theory of localization, 378
- mobilities, 4, 312, 324, 336, 349, 383, 434, 598–625, 651, 660–668, 685, 706, 792–798, 805
 - mobility edge, 373
- mobility measurements
 - field effect, 598–600
 - photoconductivity measurements, 599
 - space-charge-limited (SCL)
 - current, 599, 600
 - time-of-flight, 599
- motion, 598, 599, 648, 684
 - coherent, 56, 649, 659, 661, 662
 - diffusive, 55, 625, 627, 663
- response, 35–36, 43–44

[Charge]

- self trapped (*see* Polarons)
- single and double site occupancy, 235, 415, 458

Charge density waves ($2k_F, 4k_F$)

- (CDW) (*see also* Peierls transition), 13, 15, 26, 33–63, 149, 164, 180, 181, 192, 204, 205, 208, 217, 233, 244, 255, 256, 260, 283–285, 365, 380–383, 392, 411–414, 448, 465–474, 767

- coherent noise generation, 469
- conduction, 383
- current oscillations, 469
- depinning, 256
- interaction between CDWs, 380, 383
- pinning, 244, 255, 256, 469
 - washboard model, 469
- sliding, 383, 465, 469
- winding rate, 469

Charge transfer, 4, 8, 30, 48, 692, 693, 764, 792

- back transfer, 191
- charge oscillator model, 242, 245, 391
- degree of, 96–103, 159, 164, 192–196, 240, 242, 251, 252, 274, 275, 317–343, 367, 380, 408
- measurement of, 190–196, 200, 209, 239–243
 - bond length method, 192, 195–196, 200
 - Raman spectroscopy, 257
 - x-ray or neutron, 192–195
- photo and thermal excitation, 102
- transition, 458

Charge-transfer complexes (CTC), 4, 8, 96–98, 190, 230, 232, 298, 761, 799**Charge transfer complexes, biological systems, 691–734**

- activated CTC, 696–699
- association constant, 692, 701–705
- autocomplexes, 695, 702, 705, 710

[Charge transfer complexes, biological systems]

- charge complementarity, 695
- charge transfer interaction, 692–694, 699
- colloidal complexes, 695
- conductimetric titrations, 699, 707, 718
- dipole moments, 699–701
- dissociation energy, 700, 702, 706
- dual donor/acceptor character, 694, 695
- electron donor-acceptor (EDA) complexes, 692–695, 701–708
- examples, 708–724
- excimers, 696, 698, 704, 706
- exciplexes, 695–699, 704, 706
- gas-phase reaction, 695
- irradiation, 696, 699
- methodology, 701–708
- micellar complexes, 695, 705
- photochemical reactions, 697
- photoionization, 695
- polarization energy, 694, 699
- polarography, 707
 - half-wave potential, 707
- potentiometry, 708
- protonic CTC, 692, 695–696, 699, 707
- resonance, 693, 694, 697
- reversibility, 700
- in solution, 692, 696, 702–707
- solvation effects, 699–703
- stability, 699, 700, 705
- stoichiometric ratios, 702–707
- strong, weak CTC, 693–706
- structural changes, 703
- summary of main features, 700–701
- surface processes, 692, 695, 707, 708
- ternary complexes, 695, 702
- thermodynamic properties, 700, 701, 705
- ultrasonic experiments, 696
- viscosity, 696
- voltammetry, 708

Charge-transfer complexes, Langmuir-Blodgett films, 766–769

- Charge-transfer salts (*see* Ion-radical salts)
- Chemical synthesis, 6, 15, 17–19, 80–109, 115–146, 162, 202, 735–737
- S-alkylation, 125
- H-shaped glass reaction, 135, 138
- molecular fastener effect, 100
- new conductors, 115
- organometallic chemistry, 115
- phase-transfer catalyst, 121
- photochemical coupling, 123
- precursor, synthesis, 118–135
- acceptors, 132–135
 - donors, 118–132
 - yield and cost, 118
- selenone precursor, 129
- solubility problem, 100
- solution reaction procedures, 135
- solvation, energy, 82, 97
- substituent groups, 116, 133
- supramolecular chemistry, 19, 108–109
- transition metal-promoted coupling, 122
- trivalent phosphorus route, 119
- vapor phase diffusion, 136
- voltammetry, cyclic, 80–84, 90, 91, 138
- Chemical synthesis, polymers, 501, 539–542, 560, 648
- catalyst preparation, 539, 667
 - crystallization by stretching, 565–566
 - electrochemical, 502, 541, 542
 - fusibility, 504
 - growth conditions, 504
 - layer-by-layer deposition method, 676
 - miscibility, 568
 - Naarman-Theodorou synthesis, 649, 662, 665, 667
 - Natta's synthesis, 501
 - new monomers, 539
 - in oriented liquid-crystalline solvent, 565
- [Chemical synthesis, polymers]
- polymerization mechanisms, 504, 539, 541, 547, 577, 634, 648, 651, 667
 - electropolymerization, 531, 651, 681
 - topotactic reaction, 505
- precursor polymers, 539, 565, 566
- Durham route, 504, 542, 547, 550, 564, 565
 - soluble, 504, 513, 547, 571, 576, 608
- preparation routes, 539
- processibility, 503–505, 559, 563, 568, 570, 602, 631–634, 648–651
- reactivity, 504
- redox reactions, 552, 650–657
- ring-opening metathesis, 547
- Shirakawa synthesis, 566, 598, 647, 665, 667
- solubility, 503–506, 558
- spin-casting, 505, 564
- substitution, 504, 539, 557
- use of large counterions, 505, 568
- Ziegler-Natta catalyst, 501, 547, 564
- Chloranil, 93
- p*-Chloranil/*p*-phenylenediamine complex, 693
- Chlorodiane blue, 801
- Chlorophyll, 708, 717, 721–724, 815
- Chloroplasts, 723, 724
- Chlorpromazine, 705, 707, 718, 721
- Cholesterol, 711
- mC_n*-M LB films, 769, 772–774
- Coherence, 17, 26, 27, 36–39, 48, 53–65, 149, 204, 205, 208, 286
- Color changes, 103, 341, 692, 693, 701, 769
- Commensurability effects (*see also* Periodic lattice distortions), 44–49, 62–65, 149, 193, 202, 257
- commensurability condition, 481–482
 - discommensurations, 49, 55
 - incommensurate systems, 44–46

- [Commensurability effects]
 - under pressure, 380–383
 - weakly commensurate systems, 47–49
- Compressibility, 148, 149, 176–177, 180, 198, 395
- Conjugated polymers (*see* Polymers)
- Cooling effects, 442, 484
- Correlations, 26–68, 413–463
- Coulomb interactions (*see* Interactions, electron-electron)
- C_nPy (TCNQ) LB films, 762–767, 776
- m*-Cresol/pyridine (quinoline) complexes, 699
- Critical exponents, 417, 422, 431
- Crossover, 472, 647, 657, 667, 697
 - adiabatic-nonadiabatic, 46, 52
 - classical, 57–58
 - dimensionality, 27, 55–64, 283, 288, 366, 416, 417, 429, 434
 - localization, 54
 - quantum-classical, 46, 57, 59
 - undoped-doped polymer, 655
- {Cr[(ox)Ni(Me₆-[14]ane-N₄)₃](ClO₄)₃}, 300
- Crystal growth, 20, 115, 116, 135–140
 - chemical redox methods, 135–138
 - electrochemical synthesis, 212
 - electrocrystallization, 18, 135, 138–140
 - growth from viscous medium, 137
 - recrystallization, 135–138, 212
- Crystal imperfections (*see also* Disorder)
 - crystal order, 3, 505, 506, 519, 520, 542, 588, 597
 - dislocations, 15, 214, 541
 - grain boundaries, 15
 - imperfect order, 553, 554, 597, 613
 - microchannels/microcracks, 214, 370, 385, 396
 - mosaic, 213–214
 - reconstructed surfaces, 217
 - solvent inclusions, 214
 - structural control, 614
 - topography, 213–214
- [Crystal imperfections]
 - twinning, 152, 158, 199–201, 207, 208
- Crystallographic techniques, 147–228, 542–544
 - angle-dispersive method, 153, 155, 165
 - automated diffractometers, 153
 - Bragg reflection, 150–155, 171–188, 214, 215, 423, 542, 545, 546
 - diffraction pattern, 152, 165, 542–565
 - diffuse scattering, 149, 150, 157, 179–218, 284–296, 372, 373, 380, 386, 416, 423
 - electron density maps, 193, 209–212, 763
 - electron microdiffraction, 181, 193, 205–209
 - electrons, technique, 148, 216, 542, 547
- Guinier-Lenne camera, 176
- Hamilton criterion, 545
- at high pressure, 168–176, 218
 - clamp-pressure cells, 171
 - clamps, 175
 - diamond anvil cells, 175
 - gasketed anvil cells, 172
 - gas-pressurized cells, 171
 - helium-pressurized cells, 175
- instrument geometries, 154–155
 - four-circle with Euler geometry, 154–174
 - four-circle with κ -geometry, 154–174
 - three-circle with normal-beam geometry, 154–183
- 2k_F, 4k_F scattering, 149, 182–192
- Laue technique, 153, 201
 - fixed-crystal-fixed film technique, 181, 186, 193
- at low temperature, 164–176, 183, 218
 - cryocoolers, 166–186
 - gas-flow cryostats, 166, 175
 - gas-stream cryostats, 165

[Crystallographic techniques]

- microdensitometer, 188
 - neutrons, technique, 18, 147–219, 380, 542, 555
 - inelastic scattering, 212, 213
 - polarized neutron diffraction, 212–216
 - pulsed sources, 153
 - oriented (polymer) samples, 562
 - on powders, 149–152, 168, 176
 - quantum detectors, 153
 - real space methods, 544
 - on single crystals, 149–153, 165, 168, 176
 - structure factors, 151, 193, 214
 - atomic scattering factor, 151, 155, 188, 210
 - Debye-Waller factor, 151, 155, 181, 203, 210
 - elastic scattering length, 151
 - magnetic structure factor, 214
 - superspace, 181, 183
 - superstructure reflections, 161, 183, 204, 205
 - synchrotron radiation, 153, 168, 173, 183, 188, 208, 212
 - techniques requiring large samples, 212–213
 - Weissenberg cameras, 188
 - white beams, 153, 201
 - x-rays, technique, 18, 147–219, 422, 477, 542–547, 555, 763
 - topography, x-ray transmission, 213–214
- Crystal packing, 20, 149, 155, 180, 406, 548, 551, 553, 557, 563, 761
- Crystal size, 212–213, 497, 505, 506, 519, 570, 572
- Crystal structures, 147–228, 316–327, 333–335, 447, 482, 735–757, 765, 772, 773, 801–803
- control, 19
 - at high pressure, 147–154, 164–176
 - at low temperature, 147–154, 164–176

[Crystal structures]

- at room-temperature, 147, 149, 160–164
 - structure-conductivity correlations, 100
- Crystal structures, polymers, 519, 540–570
- amorphous phase, 520, 542–610, 648–650
 - crystalline phase, 496, 520, 542–610, 648, 650
 - crystallinity, 519, 540–570, 648, 649, 659, 662, 665, 681
 - crystallization, disorder impeded, 560
 - effect of doping, 553–557
 - entanglement, 560
 - fringed micelle model, 561, 568
 - geometry calculations, 544
 - glide plane, 519
 - granularity concept, 664
 - incommensurability with
 - intercalants, 553
 - lamellar structures, 553, 561, 568
 - lattice parameters, 290, 506, 541, 545, 552, 660
 - local organization, 544–564
 - mesoscopic structures, 505, 544, 649
 - molecular structures, 539
 - morphologies, 540, 542, 547, 564, 569, 570, 602, 649, 650, 665
 - fibers, 544, 547, 566, 570
 - fibrillar, nonfibrillar, 539–542, 547, 564, 565, 570, 597, 659
 - oriented samples, 539
 - and physical properties, 540
 - sample history dependence, 557
 - screw axis, 519
 - setting angle, 519, 546, 548, 556
 - space group, 519, 545
 - surface regions, 544
 - symmetry group, 548
 - thermal degradation, 504
 - thermal factors, 545, 548
 - three dimensional, 553, 563
 - unit cells, 519, 545, 551, 556, 659

- $\text{Cs}_2(\text{TCNQ})_3$, 252
 $\text{C}_n\text{TET-TTF}$ LB films, 768, 769
 $\text{Cu}(2,5\text{-DMDCNQI})_2$, 133
 $\text{Cu}[\text{N}(\text{CN})_2]\text{Br}^- (\text{Cl}^-)$, 408
 $\text{Cu}(\text{SCN})_2$, 408
 $\text{Cu}(\text{TCNQ})$, 257, 344
 Cycloalkanes, 558
 α -Cyclodextrin, 695
 Cyclophanes, 695
 Cytochrome, 8, 695
- DCNQI, 93, 94, 133
 Dddt ligand, 96, 134
 $\text{M}(\text{dddt})_2$, 134, 408
 $[\text{M}(\text{dddt})_2]_m\text{X}_n$, 96
 metal derivatives, 96
 Debye length, 605
 Decamethylferrocenium(TCNQ), 248
 Defects (*see* Disorder)
 Deformation tensor, 177
 Deuterated molecules (*see* Isotopically substituted molecules)
 Diacetylene, 628
 Diaminodiacetylenes, 19
 Dibenzotetrathiafulvalene (DBTTF), 117, 123
 2,7-Dibromoanthanthrone, 801
 Dichlorodicyano-*p*-benzoquinone (DDQ), 93
N,N'-Dicyanoquinonediimine (*see* DCNQI)
 Dielectric properties, 6, 14, 230–236, 244, 303, 453, 454, 460–461, 465, 590, 619, 626, 696, 707, 793
 4,5-Dihydro-1,4-dithiin-2,3-dithiolate (*see* dddt)
 Dilantin, 708
 Dimensionality effects, 7–10, 15, 25–73, 229, 312, 362–370, 376, 396, 406, 408, 416, 417, 446, 452, 458, 474, 484, 495, 513, 519, 528, 624, 659–668, 736, 764
 on magnetic systems, 279, 288, 290, 304
- cis*-(2,3-Dimercapto-2-butene-dinitrile) (or mnt) ligand, 291
 4,5-Dimercapto-1,3-dithia-2-thione (*see* dmit)
 Dimers 805 (*see also* Molecular chains)
 biradical dimers, 239, 240, 254, 258
 Dimethylalloxazine, 694
S,S-Dimethyl-
 bis(ethylenedithio)tetrathiafulvane *S,S*-DMBEDT-TTF), 125
 (Dimethylcicyanoquinodiimine) $_2\text{Ag}$ ((DMDCNQI) $_2\text{Ag}$), 336
 Dimethyldibenzophosphonium(TCNQ) $_2$, 249
 Dimethyl(ethylenedithio)diselenadithiafulvane (DMET), 125, 131
 Dimethyl(ethylenedithio)tetraselenafulvane (DMEDT-TSF), 125
 Dimethylimide, 819
 Dimethyltetracyanoquinodimethane (*see* DMTCNQ)
 Dimethyltetrathiafulvalene, 126
N-dimethylthiomorpholinium ((TCNQ) $_2$ (*see* DMTM (TCNQ) $_2$), 249, 260–261
 Diphenylpicrylhydrazil (DPPH), ESR standard, 304
 Diquinone derivatives, 103
 Disorder/defects/impurities, 8, 15–16, 53–55, 66, 149, 153–162, 177, 193–209, 261–262, 288, 327, 334–336, 370, 387–398, 442, 446, 449, 465, 469, 496–523, 540–633, 648–685, 766, 772, 774, 783, 794, 797
 chemical substitution (solid solutions, alloys), 370, 389, 393, 396, 471
 and conductivity, 53–55, 662–667
 conformational, 648
 controlled, 199, 393
 dynamic, 149, 179, 203
 irradiation induced defects, 149, 199, 204, 205, 261, 288, 381–396, 471

[Disorder/defects/impurities]

- isotopic defects, 392
- magnetic impurities, 55, 341, 503
- and optical properties, 261–262
- positional disorder, 202–204
- static, 149, 203, 396, 546, 548
- Dispersion theory, classical, 232
- Disproportionation, 77
- Di(tetrathiafulvalenyl) ditelluride, 108
- Dithiolate salt, 119, 120, 123
- 1,3-Dithiole-2-iminium salts, 126
- 1,3-Dithiole-2-phosphonates, 126
- 1,3-Dithiole-2-phosphoranes, 126
- 1,3-Dithiole-2-thione-4,5-thiolate dianion, 121
- 1,3-Dithiole-2-thiones, 122, 123, 125
- 1,3-Dithiole, in TTF, 87
- 1,3-Dithiolium salts, 118–126
- Divergencies, 366, 414–417, 427, 431, 475
- Dmit ligand, 95, 99, 121, 134, 769
 - metal (superconductor) derivatives, 95, 96, 406, 448
 - $M(\text{dmit})_2$, 134, 408, 769
- DMTCNQ, 352
- DMTM(TCNQ)₂, 335–336
- (DMTTSF)₂X salts, 397
- DNA (desoxyribonucleic acid), 7, 20, 713–719
- Donor molecules, 6, 15, 18, 19, 75–108, 116, 131, 692–708, 769, 819
 - ionization potential, 2, 80–82, 102, 341, 405, 500, 592, 593, 604, 650, 694–707
- Doping, 15, 258, 312, 495–528, 546–633, 647–689
 - chemical or protonic, 525, 528, 647, 651, 665, 674, 680
 - clusters, 650
 - compensating counterions, 495, 521–529, 553–556, 601, 647–669
 - controlled, 601
 - donor-acceptor compensation, 601

[Doping]

- doping-undoping cycles, 496, 526–532, 560, 684
- effect on structures, 553–557
- heavy doping, 500, 526, 601, 606, 661, 666–668, 675, 677, 680, 681, 806
- inhomogeneous, 650, 665, 666, 680
- injection, 495, 513–516, 553, 580, 602–609, 617–625, 647, 650, 661, 674, 676, 684
- intercalation, stages of, 553–557
- ion diffusion, 657
- ion diffusion, insertion, 656–657
- ion solvation, in solution, 650
- kinetics, 554–560, 601, 650
- lifetime of carriers, 521, 580
- magnetic monitoring, 580
- from metal vapor phase, 554
- n*-type, 502, 523, 554, 594, 620, 621, 650, 652, 674, 683, 706, 806–820
- permanent, 650
- photoexcitation, 258, 514, 521, 526, 627, 647
- p*-type, 502, 523, 529, 549, 554–556, 598–602, 609, 621, 651, 652, 666, 674, 706, 806–820
- self-doping, 505
- stability, 523
- swelling phenomena, in solution, 651
- doping, electrochemical, 522, 526, 529, 531, 554, 601, 604, 647–657, 674–684
- cyclic voltammetry, 653, 658
- electroactive films, 651
- electrochemical cell (three electrodes), 651–658
- ellipsometry, 658
- hysteresis effect, 657, 683, 684
- in situ experiments, 657–658
- kinetic effects, 656, 658
- memory effect, 657
- mirage effect, 658

[Doping]

- Nernst law, 653–656
- quartz balance, 658
- reference electrode, 652
- reversible doping, 496, 502, 651
- undoped-doped switching time, 657
- working electrode, 652
- doping, extrinsic, 598, 627
 - due to catalyst residues, 598, 600
 - due to oxygen, 598, 600, 621
 - surface contamination, 603, 621
- Doping, LB films, 762–765, 769, 775
 - electrochemical oxidation, 762
 - gas doping, 762
 - homodoping method, 765
 - iodine-, 762–764, 768
- Drude model, 230, 244, 245, 454, 459
- Drugs, 217, 721
- Dyes, 496, 697, 716, 720, 776, 800–803, 815–819

Effective medium approximation (EMA), 664

Electrical properties, conductivity (see also Hall effect, Magnetoresistance, Thermopower), 1–16, 30, 53, 54, 156, 158, 159, 177, 193, 196, 197, 235, 244, 245, 270, 289, 302, 303, 313–351, 359–396, 408–474, 495–531, 541–623, 647–685, 693, 694, 701, 706, 761–776

conductivity

- anomalies, 380
- charge density wave, 383
- collective, nonlinear, 46, 339–340, 381, 463–474
- after exposure to electron acceptor/donor, 501, 502
- extrinsic, 495, 496
- granularity concept, 664
- maximum, 63, 64, 198, 391, 422, 427, 429, 436, 772, 774

[Electrical properties, conductivity]

- metal-like behavior, in polymers, 649, 660, 662, 666, 667
- tensor, 361, 367, 368
- frequency dependence, 665, 763
- measurements
 - alternating-current, 706–707
 - contacting technique, 383, 385, 436
 - equivalent isotropic sample, 361
 - Montgomery method, 361
 - van der Pauw method, 361
 - voltage jumps, 436
- recombination, radiative,
 - nonradiative, 521, 580, 582, 598, 602, 617–633
- resistivity, T^2 power law, 361, 363, 369, 370, 375
- space-charge injection, 599–604, 613, 622, 625
- Electrochemical redox reactions (*see also* Donors and Acceptors), 77–98, 135, 138, 595, 604, 819
- oxidation, 76, 82–92, 116, 405, 763–765, 769, 771, 805
- reduction, 76, 93–96, 116, 405, 768, 805
- Electrochemistry, 312, 540, 604, 621, 651, 652, 684, 692, 698
- Electron gas, system, 62, 197, 409–422, 442, 454, 457, 486, 506, 586
 - electron-hole pair formation, 14, 409, 579, 585, 587, 602, 626, 627
 - electron-hole symmetry, 515
 - electronic states, 597–599, 607–613
 - in high magnetic field, 475–484
 - interacting, 44, 409, 412, 416, 421, 422, 454
 - of spinless fermions, 416, 457
 - two dimensional, 430, 476–484
- Electron spin resonance (ESR), 215, 276–280, 288–289, 305, 370, 379, 423, 511, 518, 658, 669–676, 704–705, 764–772

[Electron spin resonance (ESR)]

- g-tensor, 276–278, 286, 287, 294, 373, 704, 767
- g shift, 277, 704
- linewidth, 276–278, 289, 293, 303–305, 370, 380, 704
- narrowness in organic conductors, 288
- measurement, 279, 371
- relaxation times, 276, 277, 284
- spin-orbit coupling, 289, 304, 305
- Elliot relation, 278
- Emeraldine, 552, 557, 651
- ENDOR experiments, 511, 671
- Energy gap/activation energy (*see also*: Optical properties, Organic superconductors), 4, 5, 11, 13, 34–67, 197, 247, 320–345, 348, 406–481, 495–517, 570–632, 660, 666, 681, 683, 694–707, 763–765, 780, 792, 794, 811
- charge/spin excitation, 34–36, 40, 41, 52–55, 63, 64, 263, 373
- correlation gap, 422, 459
- dimerization (or bond-order) gap, 13, 48–52, 63, 65, 434
- gap function, 314, 315
- gap states, 575–578, 591, 592, 604
- midgap states, 49, 51, 511, 575, 609, 622, 670
- pseudogap, 45, 46, 57, 256, 286, 289, 297, 423
- Enzymes, 2, 719, 720
- ESR (*see* Electron spin resonance)
- (ET)₂X salts (*see* (BEDT-TTF)₂X salts)
- Exchange, 67, 271–296, 299, 301, 327–332, 416, 447, 451, 764, 765
- superexchange, 273
- Excimers, 805
- Excitations, 238–242, 255, 501, 506, 517, 518, 570, 579, 589, 592, 617, 628, 670
- charge/spin, 34–36, 40–42, 46, 54, 55, 63, 64, 373, 415, 422, 503, 516

[Excitations]

- collective, 34, 272, 278, 369, 463
- gapless, 26, 27, 33–35, 49
- localized, 517, 520, 521, 587
- magnons, 463
- nonlinear, 671, 683
- spectrum, 45
- spin-charge decoupling, 8, 34, 415–418
- spin-wave, 373
- Excitons, 516–518, 579, 585–597, 621–633, 708, 792–795, 811, 813, 817
- singlet, 516, 517, 575–592, 626, 628, 632
- exciton fission, 518, 579, 580
- triplet, 575–591, 626
- exciton fusion, 518, 626
- triplet-triplet transition, 581
- Extended pair approximation (EPA), 664
- Extensive property, 497
- External potential, 333
- Fe(C₅Me₅)₂(TCNE), 301
- (FeCp₂)(TCNE), 299
- Fe(Me₅Cp)₂(TCNE), 298
- Fermi
- density of states, 34, 35, 46, 60, 452, 586, 591, 593, 613, 663, 664, 679, 681
- singularity (van Hove), 60, 61, 586
- tails, 576, 598, 611
- golden rule, 434
- liquid, 61, 416, 417, 429
- non-Fermi liquid behavior, 429
- surface, 6, 11, 17, 28–67, 148–149, 164, 181, 193, 197–199, 245, 270–284, 319, 336, 365–367, 380, 406–484, 598–624, 651, 653, 663, 679–681, 696, 795, 806, 813, 819
- closed, 59–61, 65, 197, 198
- nesting, 12, 17, 34, 58–66, 197, 198, 366, 380, 428–481

- [Fermi]
 - open, 30, 65, 197, 366
 - pinning, 607
 - quantized nesting theory, 477
 - two-dimensional, 17, 32, 58, 429–430, 439–446
- Ferrimagnetic state, 272, 273
- Ferrocenes, 695
- Ferromagnetic state, 26, 61, 67, 68, 272, 297, 299, 412, 413, 690
- Flavins, 719, 720
- Fluctuations (*see also* Excitations), 10, 17, 18, 26–62, 177–190, 218, 281, 369, 411–427, 446, 451, 462–463, 500, 520, 545, 623, 668, 768
 - antiferromagnetic, 421, 422, 434, 447
 - enhancement, 477
 - pretransitional, 148, 179–192, 284–296, 331, 332, 462–463
 - quantum, 27–68
 - superconducting, 43, 52–53
 - thermal, 26, 27, 45–48, 55, 57, 62, 68, 413
 - three dimensional, 427, 430
- Fluoranthene, 304
- (Fluoranthene)₂PF₆, 286
- Fluorenones, 805
- Free radicals (*see also* Solitons), 511, 512, 581, 671, 704, 719
- Frölich mode, 46, 55, 62, 65, 463
- Fullerenes, 19, 32–33, 67–68, 76, 96, 116, 134, 405–409, 522, 736
 - A₃C₆₀ compounds, 9, 68, 134, 136, 409, 451, 452, 487, 736, 775
 - role of pressure, 451–452
 - superconducting films of, 136
- LB films, 762, 775–776
- microtubes, 33
- preparation route, 409
- Glass, metallic, 396
- Glycine, 696
- G-ology model, 30, 37, 410
 - diagrammatic representation, 410, 414
- Graphite, 304, 405 (*see also* Intercalation compounds)
- Ground state, degenerate versus nondegenerate, 508–513, 520, 551, 575, 585, 622, 669–684
- Hall effect, 64, 366–368, 383–387, 436–440
 - measurements, 383–386
 - quantized, 64, 387, 476–481
 - difference with ordinary quantum effect, 481
 - sign change, 387, 477
- Hartree-Fock approximation, 13, 272, 275
- Heisenberg chain, 272, 275, 288, 301, 327–328, 331, 422
 - random-exchange, antiferromagnetic (REHAC), 764, 765
- Heterocycles, 82
- Hexamer α -sexiphenyl, 582
- Hexathioorthoxates, 122, 125
- High temperature superconductors (HTSC), 9, 32, 35, 59–68, 312, 397, 735–757
 - comparison with organics, 17–18, 67, 68, 736–737
 - a summary, 736
- Tl-Ba-Ca-Cu-O system (thallium salts), 735–757
 - substitutions in Tl₂Ba₂CaCu₂O₈, 740–742
 - substitutions in Tl₂Ba₂Ca₂Cu₃O₁₀, 742–744
 - substitutions in Tl₂Ba₂CuO₆, 737–740
 - substitutions in TlBa₂CaCu₂O₇, 746–748
 - substitutions in TlBa₂Ca₂Cu₃O₉, 748–750
 - substitutions in TlBa₂CuO₅, 744–746

[High temperature superconductors (HTSC)]

- toxicity aspects, 737, 750
- Y-Ba-Cu-O system, 17, 200, 735
- HMTSF, 365
- HMTSF-TCNQ, 287–289, 365, 371, 380, 383, 387, 388
- HMTSF-TNAP, 288, 373
- HMTTF-TCNQ, 373, 380
- Holons, 35
- Hopping, 28–30, 55–66, 283, 288, 377, 390, 395, 434, 499, 599, 625–667, 680, 698, 797
 - models, 394, 396, 798
 - variable range hopping (VRH), 15, 303, 663–666, 762, 773
- Hubbard model (*see also* Interactions), 5, 29–64, 230, 239, 274–288, 312, 319, 330, 373, 406, 415, 416, 422, 454–459, 487, 507, 589, 590, 764
 - extended, 29, 30, 274, 275, 285, 330
 - two-dimensional, 32, 60, 61, 64, 67
- Hume-Rothery rules, 12
- Hund rule, 68
- Hydrazones, 805
- Hydroxydinitropyridines, 692
- 6-Hydroxydopamine, 718
- Hysteresis (*see* Phase transitions)

Impurities (*see* Disorder)

- Instabilities, 10–18, 63, 65, 150, 179, 230, 255–256, 270, 283–285, 292, 296, 313, 380, 408, 412–418, 479
 - one-dimensional, summary, 284–285
- Interactions, 27–33, 198, 230
 - electron-electron/spin-spin (*see also* Hubbard model), 4–6, 10–17, 27–68, 90, 179, 198, 229, 245, 262, 269–304, 312–339, 365–390, 406–486, 503–517, 544–627, 656–683, 767
 - electron-molecular vibration (e-mv, vibronic coupling), 230–260,

[Interactions]

- 369, 391–393, 454, 573, 587, 591, 597
- electron-phonon/electron-ion/spin-phonon, 29–66, 179, 192, 218, 229, 230, 245–255, 257, 262, 269–287, 312–333, 366, 369, 370, 381, 414, 451–452, 495–521, 544–590, 683
- phonon softening, 12, 44–52, 259, 365
- screened, 14–17, 29, 230, 406, 605, 650, 656
- Intercalation compounds, 496, 502, 553, 648
- Ion-radical salts (*see also* specific salts), 29–32, 43, 65, 76, 98, 190, 191, 230, 232, 305, 360, 762–769
 - anion-radical salts, 80, 116, 327, 330, 334–336
 - cation radical salts, 77–84, 90, 101, 116, 556
- Ising chain, 26, 27, 55, 412
- Isomerization, *cis-to-trans*, *trans-to-cis*, 778–783
- Isostructural materials, 164
- Isothianaphtalene, 571, 604
- Isotopically substituted molecules, 117, 279, 287, 391–393, 423, 427, 448–451
 - deuterated molecules, 193, 215, 216, 258, 289, 325, 380, 449
- Josephson junctions, 446, 488, 776
- $2k_F$, $4k_F$ (*see* Phase transitions)
- K-chloranil, 240
- Kinks, 26, 48, 200, 670
- Kohler's rule, 366, 368, 387–389, 396
 - deviations from, 388
- Kramers-Kronig analysis, 231, 236, 277, 460, 571

- Landau-Ginzburg theory, 27, 45–49, 53
- Landau levels, 476, 481, 484
- Langmuir-Blodgett (LB) films, 109, 124, 263, 720, 760–776
- air-liquid interface, 760–764, 775
- amphiphilic molecules, 760–762
- binary mixed, 768
- charge-transfer complexes, 766–769
- conductive films, 761–776
- fullerene, 762, 775–776
- glycerine subphase, 764, 766
- ion-radical salts, 762–766, 769
- interdigitation, 763
- long-chain fatty acid, 762
- magnetic, 306
- miscibility, 760, 762
- molecular design, 760–762, 776
- molecular orientation, 764–767, 768
- monolayers, 760–766, 775
- precursors, 762, 764, 769
- stability, 764, 766, 783
- substrate, 760
- surface pressure, 766
- ultrathin films, 760, 776
- Lecithin/iodine complex, 711
- Libron model, 369
- Lindhard function, 281
- Lipids, 711
- Little's model, 7, 75, 218, 405, 487, 762
- Living organisms, 1, 2, 6
- Luttinger liquid, 35, 42, 411, 416
- Macrometal, 19
- Madelung energy, 97
- Magnetic properties (*see also* Electron spin resonance, Nuclear magnetic resonance, Spin susceptibility), 182, 198, 214–215, 269–306, 327–332, 365, 370–372, 379, 380, 486, 704–706, 764
- magnetization, 270–273, 297
- Magnetic techniques, 270
- Faraday balance, 271, 370, 379, 421, 423
- SQUID magnetometer, 271, 370
- Magnetoresistance, 17, 360–397, 463, 474, 481–484
- magic angles, 368, 389–390, 397, 481–484
- Malachite green, 818
- Malonic acid, 696
- Matthiessen's rule, 370
- deviations from, 396
- Mean field approximation (MFA), 43–67, 319, 333, 366, 409–412, 417
- beyond MFA, 412–415, 477
- Mechanical properties, polymers, 527, 528, 557, 567, 568, 649, 682
- flexibility, 545, 563
- intrinsic rigidity, 540, 545, 558, 563
- tensile strength, 564–566
- Young's modulus, 564–567
- Melanin, 695, 705
- MEM(TCNQ)₂, 216, 248, 259, 290, 315–339
- Mermin-Wagner theorem, 26, 27, 45
- Merocyanines, 815–818
- Metallic ions, 3
- Metallic regime, 270
- 1-Methyl-1,4-dithianium(TCNQ)₂ (MDT(TCNQ)₂), 337
- Methylenedithiotetrathiafulvane (MDT-TTF), 125
- Methyl-*N*-ethyl-benzimidazolium(TCNQ)₂ (MNEB(TCNQ)₂), 213, 214, 249
- N*-Methyl-*N*-ethylmorpholinium(TCNQ)₂ (*see* MEM(TCNQ)₂)
- Methylglyoxal/protein complexes, 722
- N*-methyl-2,6-methylpyridinium(TCNQ)₂, 248
- N*-Methylpyrrolidone (NMP), 566
- S*-methylthiuronium salt ((MT)₂(TCNQ)₃·2H₂O), 252

- Methyltriphenylarsonium (TCNQ)₂
(MTPA(TCNQ)₂), 237
- Methyltriphenylphosphonium(TCNQ)₂
(MTPP(TCNQ)₂), 205, 213,
214, 252, 261
- Micelles, 720–721
- Microscopy, 150
- atomic force microscopy (AFM),
216–217, 544, 772
 - polarizing microscope, 235–238,
764, 772
 - scanning electron microscopy
(SEM), 542, 544, 764, 772
 - scanning tunneling microscopy
(STM), 216–217, 542, 544
 - topography, 216
- Microtubes, 33
- Mixed valance salts, 75, 133
- Mn(Cp₂)(TCNQ), 299
- MnO, 273
- Molecular bonds/orbitals, 405, 408,
496, 692
- bonding/antibonding/nonbonding
character, 48–52, 148, 197, 209,
511, 693, 805
 - bond lengths, 26, 31, 164, 192–196,
200, 209, 519, 544, 545, 557
 - alternation, 13, 506–513, 544,
548, 628, 670–672
 - charge-transfer bonds, 693, 702,
703, 725
 - σ - π coupling, 500, 507
 - covalent bonds, 5, 31, 495, 496, 507,
513, 553, 561, 568, 601, 608,
621, 692
 - double bonds, 87, 584
 - σ -electron system, 496, 500, 502,
694
 - π -electron system, 3, 28–32, 405,
487, 496–510, 524, 533, 548,
571, 647, 651, 669, 670, 694,
695, 781
 - highest occupied (HOMO), 417, 694
 - hydrogen bonds, 20, 692–696, 700,
725
 - ionic, 692, 693
- [Molecular bonds/orbitals]
- lowest unoccupied (LUMO), 594
 - overlap, 405, 406, 409, 495, 496, 551
- Molecular chains (*see also* Specific
compounds), 76, 98–102, 149,
155, 162, 312, 319, 338, 360,
406, 417, 495, 497, 507–518,
564, 764
- alkyl chains, 504, 561, 596, 762, 765,
769, 777, 780
 - cross-linking, 504, 540, 565, 648
 - dimerization, 11, 15, 49–51, 63, 76,
77, 99, 161, 164, 184, 200,
234–260, 276, 292, 317–342,
370–376, 408, 418, 422, 433,
439, 454, 507, 510, 544, 548,
552, 583, 593, 633, 666, 671,
763, 769
 - geometry, 545–596
 - helicity, 558, 596, 723
 - interrupted, 659–662, 669
 - lengths, 540, 541, 561, 563, 599,
659, 665
 - macromolecules (*see also* Polymers),
7, 540, 700–703, 708, 719–720
 - n*-merization, 234, 235
 - rigid-body approximation, 164, 183–
186
 - segregated, 29, 76, 102–108, 159,
244, 259, 260, 274
 - tetramerization, 156, 203, 248, 252,
261, 292, 317–339, 360, 423
 - trimerization, 48, 49, 235, 252, 360
 - two-chain systems, 360, 361, 370,
373, 380, 386
 - two-dimensional, 105, 161, 162, 184,
186, 203, 774
- Molecular crystal (MC) Hamiltonian,
31, 43–53
- Molecular design, 75–114
- prototype molecules, 101–105
 - recent advances, 105–108
- Molecular ferromagnets, 270, 297–303
- coercive field, 298, 302, 305
 - demagnetization field, 305
 - design strategy, 298

- [Molecular ferromagnets]
 - domains, 297
 - examples, 300–303
 - ferrimagnetic approach, 299
 - hard, soft, 298
 - hysteresis, 298, 302
 - magnetization, 298–301
 - organometallic derivatives, 298, 300
 - topological degeneracy, 299
 - transparent films, 298
- Molecular field approximation, 272
- Molecular interactions, 148, 417, 418, 442, 499, 540, 545, 558, 564, 579, 651, 792, 797
 - interchain, 27, 32, 33, 63, 64, 149, 179, 204, 244, 361, 408, 417, 418, 484, 519, 520, 523, 541, 544, 547, 551, 558, 562, 570, 649, 658, 659
 - steric site inequivalence, 249, 252
 - three-dimensional, 503, 518–520, 591
 - van der Waals, 5, 20, 163, 194, 197, 237, 405, 792
- Molecular vibrations, 232, 234, 240, 242, 255, 257, 369, 391–393, 451–452, 587, 591, 617
 - totally symmetric (a_g) modes, 47, 232, 255, 257, 261, 391
- Mulliken theory, 235, 252, 692
- Mutagens, 716
- Naphtacene, 4
- Naphtalene, 390, 517, 692
- Naphtho-1,4-dioxin derivatives, 108
- Naphthoquinone, 93
- NBu₄[CuCr(ox)₃], 301
- Neurohumoral transmitters, 707, 718–719
- Nicotinamide, 711, 719
- N-Methylphenazinium-TCNQ (*see* NMP-TCNQ)
- NMP-TCNQ, 16, 192, 203, 288
- NMP_x(phenazine)_{1-x}-TCNQ, 192
- NMR (*see* Nuclear magnetic resonance)
- Noise generation, narrowband, 463, 469–472
- Noradrenaline, 719, 721
- Nuclear magnetic resonance (NMR) (*see also* Magnetic properties), 63, 66, 68, 177, 279–297, 420–434, 447–474, 544, 548, 705–706
 - ¹³C, 336, 423, 427, 452
 - chemical shift, 280, 404, 705
 - crossover from one to three dimensional regime, 283, 288
 - dynamic nuclear polarization experiments, 671
 - ¹H, 279, 336, 551, 671, 672, 705
 - high-resolution NMR techniques, 280, 705
 - hyperfine interaction, 280–283, 293, 420, 421
 - Knight shift, 280, 281, 286, 452
 - Korringa relaxation, 66, 281, 282, 289, 293, 297
 - enhanced, 429, 430
 - Larmor frequency, 280, 282, 421, 671
 - motional narrowing, 468–469
 - Overhauser effect, 672
 - relaxation rate, 280–282, 335, 420, 423, 427, 429, 447
 - divergency, 427
 - in SDW state, 468–469
 - second moment, 334, 551
 - solid-state effect, 672
 - strong/weak coupling, 423, 429, 433
- Nucleotides, 696
- Octadecane, 769
- Octadecyldimethylsulfonium, 764
- Octadecylmethylethylsulfonium, 764
- Octadecylpyrimidium, 764
- Octadecyltrimethylphosphonium, 764
- Olefins, 20
- Oligomers, 497, 500, 513, 541–632
- Optical properties, spectroscopy, 229–267, 452–463, 539–544, 555, 559, 570–597, 658, 763, 768

[Optical properties, spectroscopy]

absorption, 231–258, 496–530, 559–563, 576, 577, 589, 631, 692, 702–704, 708, 764, 778–781, 792–817
 Benesi-Hildebrand equation, 703–705
 edge, 585, 590, 627, 792
 Stokes shift, 575, 581
 tail, 576, 577, 590, 598
 threshold, 571, 574, 586, 600, 621
 anisotropy, 229–245
 basics, 230–235
 birefringence, 236–238
 conductivity, 232, 233, 244, 249, 255, 454, 459–463
 collective mode, 460–463
 optical gap, 244–258, 571–575, 588–598
 damping rate, 453
 dichroism, 564, 569, 572, 574, 627
 electroluminescence (EL), 502–505, 517, 533, 591, 606, 614–635
 emission, 570–634, 692, 702–704
 fluorescence, 572, 574, 589, 628, 632, 633, 701–704, 792, 817
 quenching, 703, 714, 717
 index of refraction, 231, 452
 infrared, 229, 230, 232, 243, 258, 405, 575, 581, 666, 703
 activation of infrared nonactive modes, 232–235, 252, 259–262, 391
 far-infrared (FIR), 459–463
 indentations, 258
 intramolecular or vibrational, 229–242, 255, 261, 575, 587
 irradiated samples, 261–262
 luminescence, 569, 571–575, 587
 non-linear susceptibility, 497, 506, 533, 570, 592, 601, 628
 and phase transitions, 258–261
 phosphorescence, 792

[Optical properties, spectroscopy]

photoluminescence, 518, 571, 581, 615, 627
 polarizability tensor, 229, 235, 236–239
 Raman light scattering, 229, 236, 242, 256–258, 323, 405, 544, 552, 582–590
 resonant Raman, 236, 257, 500, 550, 570, 582–585, 588, 591
 reflectivity, 47, 229–236, 244, 245, 249, 252, 255, 259, 323, 333, 453, 459, 571
 electroreflectance, 587, 589
 metallic, 240, 243
 plasma reflectance, 243–245
 signatures of solitons, polarons, bipolarons, 514–516
 solid-state spectra, 571–573
 solution spectra, 571, 574
 solvatochromism, 702
 spectral shift, 702, 703
 blue-shift, 631, 632, 764
 red-shift, 571, 574, 575, 581, 587, 589, 621, 631, 781
 thermochromism, 559, 560, 563, 702
 transitions, electronic, 229, 238, 239, 243, 339, 453, 454, 460, 497, 517, 518, 539, 570–597, 615
 oscillator strength, 239, 256, 457–460
 visible, 570–575, 585–591
 visible-near infrared, 452–459
 UV-visible, 236–243, 702–703
 UV-visible-IR, 764–766, 769
 Optical techniques, 235–236, 238
 bolometric technique, 255
 electron energy loss spectroscopy (EELS), 590
 indicatrix, 229–239
 infrared absorption spectra, 242, 326
 light scattering, 257
 microspectroscopy, 238
 non linear optical methods, 577

[Optical techniques]

optical detection of magnetic resonance (ODMR), 518, 580, 581

photobleaching, 579

photoemission, 593, 604, 620, 621

photoinduced absorption (PIA)

spectroscopy, 577–581, 589–591

photothermal deflection

spectroscopy (PDS), 576, 577

spectrophotometers, double beam, 702

Order, 48, 64, 365, 415, 518, 544, 545, 550, 551, 557–564

long range, 8, 12, 26, 27, 45, 60–65, 244, 278, 406, 413, 414, 419, 423, 442, 446, 463

parameter, 6, 26, 27, 45, 46, 49, 55, 61, 62, 411, 413

Ordinary metals, 1–17, 230, 244, 271, 277, 281, 286, 365, 371, 396, 405, 447, 660, 776

Ordinary semiconductors (insulators), 8, 233, 586–626, 660

Organic alloys, 393, 467 (*see also* Disorder)

Organic conductors, 1–823

biosynthesis, 20

classification, 311–313

early history, 3

more-than-one-dimensional, 772

overview, 1–24

future prospects, 18–20

key issues, 9–11

physical concepts, 25–73

ternary, 157, 244

three dimensional, 363, 396, 409

two dimensional, 184, 186, 242, 245, 359, 361, 396, 406, 481

Organic metal components, 76

Organic metals, 5–6, 155, 197, 278, 311, 338, 359–494, 767

Organic molecules

closed/open shell, 116, 135, 291, 292, 405

[Organic molecules]

planarity/symmetry, 75, 76, 102, 105, 133, 134

Organic photoconductors/

photovoltaics, 587, 588, 599, 708, 722, 723, 776, 791–823

action spectrum, 794

carrier generation, 708, 792–795, 800, 806–817

quantum yield, 792–795, 803

carrier transport mechanisms, 797–798

deactivation processes, 792, 793, 801

experimental methods, 795–797

time-of-flight (TOF) techniques, 795, 798

transient techniques, 795

gain, 794, 795

photocurrent, 792–795

photovoltaic effect, 806–820

sensitivity, 794, 795, 801

threshold, 588, 795

transit time, 794–799

Organic semiconductors/insulators,

3–5, 8, 155, 197, 198, 311–360, 383, 390, 409, 458, 495–516, 706, 776

metal-like behavior, 315, 336–337

mixed chains materials, 341–343

non-metallic state, 313

segregated chains materials, 315–341

Organic superconductors, 2, 6–9,

63–68, 76, 96, 99, 100, 108, 109, 115–138, 155–161, 179, 183, 204, 245, 255, 257, 263, 270, 289, 298, 312, 359, 392, 396, 405–494, 684–685, 762, 772–776

BCS theory, 6–7, 44, 451

BCS gap, 60, 66–67, 257, 263, 333, 446–447

pairing mechanism, 6, 41, 53, 60, 66–68, 446, 451, 486

[Organic superconductors]

- comparison with high T_c
 - superconducting oxides, 17–18, 67, 68, 736–737
- isotope effect, 448–451
- Kosterlitz-Thouless transition, 27, 60, 62
- low magnetic field detection
 - method, 775
- Meissner flux expulsion, 446
- penetration depth, 67
- precursor effect, 446
- sensitivity to impurities, 446, 487
- singlet (SS), triplet (TS), 33–68, 283, 411–414
- specific heat anomaly, 446
- stabilization by repulsive interactions, 412
- superconducting gap, BCS
 - gap equation, 66, 67
- two-dimensional, 156, 161, 179, 203, 359, 361, 369, 446, 484, 487, 488
- unconventional superconductivity, 67, 396, 487
- vortices, 62, 488
 - s*-, *p*-, *d*-waves, 60, 61, 66–68
- Oxadiazoles, 805
- Oxalic acid, 696
- Oxazoles, 805

Pariser-Parr-Pople Hamiltonian, 29

Pentachloride, antimony, 705

Pentamethylcyclopentadienyl (or Me_5Cp), 298

Percolation mechanism, 351, 528, 554, 568, 569, 660, 680

Periodic lattice distortions (PLD) (*see also* Commensurability effects, Phase transitions), 11, 44–58, 148, 150, 177–190, 203, 208, 218, 283, 284, 406, 413, 414, 418, 427, 428, 465

displacive modulations, 181, 218

[Periodic lattice distortions (PLD)]

- incommensurate, 44–46, 162, 177–190, 218, 256, 373, 380, 413, 427, 465
- intramolecular, 183, 247
- magnetic modulation, 427, 463, 476, 481
- quenched, 46
- superstructures, 63, 161, 181–191, 203, 205, 256, 257, 291, 335

Pernigraniline, 503, 509

Perylene, 801, 818, 819

Perylene-bromide complex, 4

(Perylene) $_2$ [M(mnt) $_2$] salts, 291–297

Perylene salts, 304, 408, 488

Pharmacologically active agents, 707

Phase transitions (*see also*

Superconductivity), 7, 71, 179–191, 208, 259, 283–285, 311, 315, 320–324, 330–331, 335, 363–365, 373, 380, 392, 417, 423

anion (or counterion) ordering, 63, 179–203, 389, 442–444, 477–481

and broken symmetry, 25–27, 319

commensurate-incommensurate, 62, 149, 158

competition between superconducting and magnetic (dielectric) phase, 362, 387, 409, 429, 446, 486

crystallographic study, 147–164, 177–190

first-order, 205, 259, 476, 675

generic phase diagram, 417–420

hysteresis, 380, 476

metal-to-semiconductor/insulator, 13–15, 63, 98, 99, 208, 260, 269–297, 313, 336, 337, 387, 418–476, 657, 680, 772

Anderson localization, 378, 658, 661, 662

localization under very high magnetic field, 487

[Phase transitions]

- Mott-Hubbard localization, 15, 284, 291, 313, 328, 336, 339, 416, 422, 431, 454, 458, 765
- Wigner crystal, 487
- metal-to-superconductor, 61–67, 235, 269, 274, 313, 387, 408–463
- neutral-to-ionic transition, 341–343
 - color change, 341
- order-disorder, 149, 161, 179, 180, 204, 261, 335
- Peierls ($2k_F$, $4k_F$), 11–13, 16, 44, 61–66, 98, 148, 158, 180–208, 233–260, 283–296, 313–333, 339, 363–392, 413–418, 495, 503–510, 583, 585, 660, 671, 683, 767, 772
 - inverted Peierls transition, 260, 336
 - sensitivity to defects, 204
- reentrance, 477, 481, 487
- semiconductor-to-semiconductor, 313, 314, 333
- spin-Peierls ($2k_F$), 63–64, 148, 180, 188, 204, 205, 216, 259, 283–296, 327–342, 418–427
- Phasons, 47–49, 427, 465, 473
- Phenothiazines, 695, 705
- m*-Phenylenecarbenes, 299
- Phenyl ring, 631
- Phonon
 - anomalies, 258, 260, 325
 - softening (*see* Interactions)
- Photosynthesis, 723, 724
- Phtalocyanine dyes, 803, 815–819
- Phtalocyanines (PHTH)s, 304, 695, 717, 718, 723
- Physical concepts of organic conductors, 25–73
 - low-dimensional physics, 26–55
 - physics in one dimension, 33–55, 270, 366, 488, 503, 658, 660
 - physics in three dimensions, 62–68
 - physics in two dimensions, 55–62

[Physical concepts of organic conductors]

- quasi one-dimensional conductors, 29–32, 55–59, 66
 - classical crossover, 57–58
 - dimensionality crossover, 55–58
 - single particle crossover, 55–56
 - two-dimensional regime, 58–59
 - two particle crossover, 56–57
- Pinning, 47, 55, 65, 461, 465–473
- Plasma edge/frequency, 230, 235, 244, 245, 368, 374, 453, 454, 457, 458, 461
- Plasmon, 244, 454
- Plastics, conducting, 501, 504
- Polarizable molecules, 7, 15, 405, 715
- Polarization energy, 6, 369, 593
- Polaron, 51, 65, 254, 503–523, 544, 577–627, 656–684
 - binding energy, 513, 516, 519, 589, 623, 624
 - bipolaron, 51, 52, 65, 503–521, 579–628, 656–684
- Polyacetylene (prototype polymer), 2, 10, 26, 258, 500–526, 529–628, 648–685
 - iodine-doped, 8, 258, 496, 554, 666, 667
 - isomerization cis-trans, 670
 - n*-doped by alkali ions, 554, 666
 - new synthesis, 649, 662
 - cis-PA, 502–520, 547, 672
 - p*-doped trans PA, 554–556
 - stretching of, 564–565
 - trans*-PA, 508–520, 544–615, 658–684
- Polyalkylthiophene, 541, 609, 613, 774
- Polyaniline (PAni), 501–504, 522, 526–532, 540–621, 651–680, 769
- Polyaromatics, 801
- Polycarbenes, 300
- Polycarbonates, 805
- Polycyano compounds, 95
- Polydiacetylenes (PDA)s, 500–521, 546, 572–628

Polyenes, 7, 497–521, 583–628, 670
Polyesters, 805
Polyethylene (PE), 500, 527, 569, 581, 593
Polyheptadiyne, 503, 509
Poly(3-hexylthiophene)/isocaicacid LB films, 776
Polymeric films, 502–504, 528–532, 539–613, 651, 652, 658, 676, 681
 electropolymerization, 769
 extrusion molded, 570
 fibrillar, 501, 502, 576, 602
 heterogeneous, 576, 608
 homogeneous, 506, 570, 608, 622
 in situ studies, 651
 LB films, 769
 melt processed, 504
 membranes, 529
 self-standing, 539
 stretched, 544, 564–566, 649, 667
 thickness, 609, 610, 622
 transparent, 528
Polymers, 7, 8, 13–19, 26, 31, 32, 42, 49, 61, 65, 236, 256–263, 339, 344, 352, 405, 495–689
 blends, 505, 564, 568–570, 581, 774, 797, 805, 816
 catalytic properties, 505
 chirality, 501, 505
 coherence lengths, 551–565
 conjugated, doped (conducting), 647–689
 conjugated, undoped (semiconducting), 539–646
 conjugation, 496–501, 520, 524, 540–631, 662, 669, 670
 box model, 499, 500
 breaking, 499, 521
 lengths, 497–500, 517, 520, 521, 540–631, 667
 copolymers, 505, 540, 568–570, 632, 633
 block, diblock, 505, 568
 CP-non-CP, 505, 569
 donor-acceptor, 719

[Polymers]
 electropolymerization, 769
 ferromagnetic polymers, 298, 300, 306
 gel formation, 569, 572
 glass transition temperature, 559, 565, 566
 homopolymers, 540
 isomers, 497
 liquid crystallinity, 505
 macromolecules, 545, 658, 669
 macrosalt, 648
 in the melt, 540, 559, 563–568
 molecular weights, 540, 558, 560, 569
 molecular wire, 658, 660–661
 new materials, 501–503
 nonconjugated, 497, 500, 528
 perfect, 497, 499, 541, 545, 668
 persistence length, 521
 piezoelectric, 532
 repeat unit, 496–521, 540–613
 solubility, 503–505, 541, 569, 613
 acquired on substitution, 557
 in solution, 521, 540, 541, 558, 569–572, 597, 615, 650, 651, 803
 stability, 526, 559
 stretching, 542–569
 oriented samples, 547, 564–570, 598, 627, 649
 with a plasticizer, 552, 565, 566
 substituents, 520, 531, 557–564, 570, 596, 631
 side chains, side groups, 520, 557–564, 633
Polymethylmethacrylate, 633
Polyoctylthiophene (POT), 562, 569
Polyparaphenylene (PPP), 502, 522, 529, 540, 551, 571, 581, 582, 591, 604
Polyphenylenevinylene (PPV), 502, 513, 517–519, 551–631
 substituted, 563–564, 615, 627
Polypyrrole (PPy), 527–542, 615, 648, 676–678

- Polystyrene, 633
 Polystyrene-polyacetylene (PS-PA), 569
 Polythiophenes (PT), 502, 513–529, 542, 551, 574, 591–613, 677, 679, 769
 substituted, 504, 560, 568, 600
 poly(3-alkylthiophene) (P3AT), 558–566, 624
 Polyvinylcarbazole (PVK), 504, 528, 798, 816
 Porphyrins, 695, 717–718, 815
 Power law dependences, 35–66, 361–370, 375, 415–436, 666, 765
 Pressure effects, 16–17, 63, 64, 341–343, 365–387, 418–475, 773–774
 N-Propylquinolinium(TCNQ)₂ (NPrQn(TCNQ)₂), 337
 Proteins, 153, 707, 720–723
 Purines, 695, 711, 714–717
 PVK:TNF, 799
 Pyranthrone, 4
 Pyranylidenes, 82
 Pyrazolines, 805
 Pyrene, 304, 694
 Pyrimidines, 711, 714–717
 Pyrimidium(TCNQ)₂, 777
 Pyrrole, 497, 502, 527, 769

 Qn(TCNQ)₂, 5, 203, 288, 289, 336–337, 352
 Quantum chemistry, 418, 500, 501, 513, 514, 661, 676
 ab initio methods, 197, 592
 HF-SCF, 592
 semiempirical methods
 Hückel, 197, 507, 513, 592
 MNDO, 592
 Valence effective Hamiltonian (VEH), 515, 592–597, 604
 Quasi-particles, 33–40, 230, 472, 511–518, 587
 Quaterphenyle, 556
 Quinacridones, 816
 Quinolinium(TCNQ)₂ (*see* Qn(TCNQ)₂)
 Quiquethiophene/isocatic acid LB films, 776

 Random phase approximation (RPA), 39–62
 Random walk theory, 664
 Reciprocal space, 151, 154, 187, 188, 207, 542
 Relaxation rate/time, 230, 244, 365–367, 377, 388, 623
 Renormalization group (RG) method, 36–64, 414, 415
 Resonance valence bond (RVB), 61
 Response function, 33–64, 373, 410–416
 Retinol/iodine complex, 710
 Rhodamines, 816, 818
 RNA (ribonucleic acid), 713, 716, 719
 Ruderman-Kittel interaction, 273

 Salicylic acid, 699
 Scaling, 36–41
 Scattering (*see also* Interactions), 30, 53–54, 288, 365, 372, 394, 659, 662
 backward/forward, 30, 44, 53–54, 256, 281, 282, 289, 304, 379, 409, 411, 433
 diffusive/nondiffusive, 282, 304, 390
 elastic/inelastic, 378, 379, 396, 446, 617
 interchain/intrachain, 30, 278, 434
 mechanisms, 368, 369, 375
 rate, time, 368–370, 377, 396, 483
 Umklapp, 30–63, 331, 336, 369, 411, 433
 Semimetallic state, 365, 380, 387, 442, 502
 two dimensional, 444, 474–478
 Serotonin, 718–721
 α-sexithienyl, 600, 609, 613, 614
 Shubnikov-de Hass method, 17, 197
 (SN)_x, 8, 10

- Solid-solid charge-transfer reactions, 349–351
- Solitons, 8, 26, 47–55, 65, 373, 503–516, 541, 570, 592, 671, 674, 683, 698
 charged/neutral, 51, 55, 511, 575–609, 658–676
 defect-like, 340, 342
 domain wall, 511, 670
 motion, 340, 511, 548, 669, 671
 soliton-antisoliton pair, 65, 513, 514, 674, 684
- Solvation, 6
- Solvents, 6, 19, 84, 135, 139, 302, 305, 504, 541, 559–568, 650, 655, 696–707, 760, 762, 769, 801, 803
- Specific heat, 182, 387, 446
- Spin, 214, 215, 272, 278, 669–684
 concentration, 511, 513, 669–679
 doping produced, 674–684
 glass, 54, 681
 motion, 282, 669, 672, 680
 wave, 13, 272
- Spin density wave ($2k_F$) (SDW), 13–17, 33–66, 204, 263, 283–286, 365–396, 411–465, 469, 474
 coherent noise generation, 463, 469–472
 current oscillations, 468
 damping, 472
 electrodynamic response, 472–474
 field induced (FISDW), 17, 64–65, 366, 387, 390, 444, 474–487
 magnetoresistance, 481–484
 novel collective nonlinear
 conduction, 64, 365, 463–475, 487
 threshold electric current/field, 465–468
 phason modes, 427, 465, 473
 pinning, 461, 465–473
 quenched state, 469
 sliding, 393, 462, 468
- [Spin density wave ($2k_F$) (SDW)]
 suppression of, under pressure, 475
 velocity, 469
 winding rate, 468
- Spin flop transition, 365, 463
- Spinons, 34, 35
- Spin susceptibility (*see also* Magnetic properties), 34, 35, 42–43, 54, 63, 269–309, 369–380, 387, 420–423, 431–433, 458, 463, 481, 517, 518, 523, 666–684, 692, 764, 767
 box model, 677–679
 Curie law, 273, 297, 302, 305, 675
 versus Pauli law, 679–682
 Curie-Weiss law, 273, 275, 295–297, 301, 328
 diamagnetic susceptibility (Landau-Peierls), 270, 271, 288, 371, 387
 enhanced susceptibility, 274, 286, 293–296, 330, 373, 458, 670
 Stoner-type enhancement factor, 43, 60, 274
 Landé factor, 272, 273
 Pauli law, 34, 60, 271, 274, 281, 286, 293, 429, 459, 503, 666, 675
 singlet-triplet, 64, 215, 276, 297, 299, 327
 two-chain systems, 281, 283, 286–289
- Squaraines, 803, 805
- Squarylium dyes, 803, 815
- Starch/iodine complex, 711
- Steric effects, 94, 103, 331–336, 551, 558
- Stilbene derivatives, 805
- Structural transitions (*see* Phase transitions)
- Su-Schrieffer-Heeger (SSH)
 Hamiltonian, 31, 43, 44, 48, 49, 53, 507–512, 520, 549, 575, 577, 589, 590, 671
- Symmetry
 broken symmetry, 26, 27, 463

[Symmetry]

crystal symmetry, 177, 368
 and Neumann's principle, 177
 Synthetic metals, 685

TCNE, 694
 TCNQ, 5, 18, 84, 132, 232, 242,
 350–351, 710, 762–768, 778
 derivatives, 93, 94, 103, 108, 766,
 768
 TCNQ salts, 132, 162, 191, 195, 200,
 212, 237–242, 252–261, 360,
 365, 392, 762–769, 783
 TEA(TCNQ)₂, 47–48, 155–157, 177,
 183, 195–196, 203, 204, 214,
 215, 232, 242, 247–252,
 315–337, 348–352, 383, 391
 Tetraalkylammonium salts, 134
 Tetrachalcogenafulvalenes, 82, 118,
 125
 Tetrachalcogenapolyacenes, 132
 Tetrachalcogenotetracenes, 85
 Tetracyanodiphenoquinodimethane, 94
 Tetracyanoethylene (TCNE), 93, 298
 11,11,12,12-Tetracyanonaphthoquinodi-
 methane (TNAP), 133
 Tetracyano-*p*-benzoquinone, 93
 7,7,8,8-Tetracyano-*p*-quinodimethane
 (*see* TCNQ)
 Tetracyanotetrahydropyrenoquino-
 dimethane, 94
 Tetracycline, 698
 Tetraethylammonium(TCNQ)₂
 (TeEA(TCNQ)₂), 248
 Tetrafluorotetracyanoquinodi-
 methane, 133
 Tetrahalotetrathiafulvalene, 124
 Tetrahydrol,2,7,8-
 dicyclopentaperylene, 305
 Tetrakis(alkylthio)tetrathiafulvalenes,
 100
 Tetrakis(methyltelluro)tetrathiaful-
 valenes, 100, 343
 Tetramethylammonium cation, 99
 3,3',5,5'-Tetramethylbenzidine-TCNQ
 (TMB-TCNQ), 343

(Tetramethyl-*p*-phenylene
 diamine)ClO₄ ((TMPD)-ClO₄),
 240, 248
 Tetramethyl-porphyrin complexes, 707
 Tetramethyltetraselenafulvalene (*see*
 TMTSF)
 Tetramethyltetrathiafulvalene (*see*
 TMTTF)
 Tetraselenafulvalene (TSF), 118, 126,
 129
 Tetraselenatetracene, 132
 Tetrasubstituted ethylenes, 86
 Tetratellurafulvalene (TTeF), 100,
 118, 131, 132
 Tetrathiafulvalene (*see* TTF)
 Tetrathianaphthalene (TTN), 85
 Tetrathiatetracene (TTT), 132, 352
 (Tetrathiatetracene)₂I₃ (TTT₂I₃), 352
 Thermal expansion, 148, 149,
 175–177, 286, 375, 545
 Thermal hysteresis, 259
 Thermal losses, 345
 Thermal motion, 150, 203, 588, 692
 Thermionic emission 606
 Thermopower, 330, 337, 350–351,
 439, 598, 666, 764, 772, 773
 Thiapendione, 121
 Thiapyrilium salt, 803
 Thin-films (*see also* LB and polymeric
 films), 230, 396, 397
 Thiophene, 500, 513, 561, 562, 622,
 631
t-*J* model, 32, 43, 61, 64, 67
 TMA-TCNQ-I, 244
 (TMDTDSF)₂PF₆, 64, 423, 427
 TMTSF, 129, 140, 161, 210, 370, 396,
 406
 (TMTSF)₂AsF₆, 210, 365
 (TMTSF)₂(AsF₆)_{1-x}(SbF₆)_x, 393, 471–
 472
 (TMTSF)₂BF₄, 184
 (TMTSF)₂ClO₄, 63–65, 156, 159, 160,
 183–184, 200, 203–205, 352,
 371, 375, 389–396, 408, 469,
 477–481
 (TMTSF)₂(ClO₄)_{1-x}(ReO₄)_x, 394, 396

- TMTSF-DMTCNQ, 289, 352–353, 380, 394
 (TMTSF)₂PF₆, 9, 16, 17, 63–64, 160, 175, 245, 249, 287, 289, 365, 373, 379, 381, 389, 390, 405, 408, 417, 465, 469–483
 (TMTSF)₂ReO₄, 175, 184, 370
 {(TMTSF)_x(TMTTF)_{1-x}}₂ClO₄, 394
 {(TMTSF)_x(TMTTF)_{1-x}}₂PF₆, 393
 (TMTSF)₂X salts (Bechgaard salts), 17, 48, 63–65, 99, 100, 164, 168, 173, 184, 191, 213, 244–250, 257, 270, 288–293, 337, 360–396, 408–467, 477, 736
 generic phase diagram, 417–420
 TMTTF, 396, 766–768
 TMTTF-C₁₄TCNQ LB films, 766, 767, 772
 TMTTF-C₁₈TCNQ LB films, 766, 767, 772
 (TMTTF)₂PF₆, 63, 289, 293, 336
 (TMTTF)₂(SbF₆)_{1-x}(AsF₆)_x, 177
 TMTTF-TCNQ, 373
 (TMTTF)₂X salts, 48, 63, 64, 100, 161, 179, 180, 184, 191, 198, 205, 217, 244, 249, 250, 257, 261, 270, 288, 331, 332, 337, 408–459
 generic phase diagram, 417–420
 TM₂X salts (*see* (TMTSF)₂X salts and (TMTTF)₂X salts)
 Tranquilizers, 705, 708, 721
 Transfer (overlap) integrals, 28, 29, 149, 163, 164, 197, 198, 209, 211, 244, 245, 261, 274, 299, 366, 418, 422, 454, 495, 507, 509, 513, 519, 659
 interchain/intersheet, 209, 278, 366, 388, 406, 418, 484, 518, 591, 648, 662
 Transition metal complexes
 LB films, 769–771
 metal-dithiolate complexes, 769
 Transport properties (*see* Electrical properties)
- Traps, 580, 598–625, 651, 674, 797–818
 Triarylamines, 805
 Triarylmethanes, 805
 Triethylammonium(TCNQ)₂ (*see* TEA(TCNQ)₂)
 Trimethylammonium-TCNQ-I (TMA-TCNQ-I), 155–158, 181, 182, 188, 200–202, 208
 2,4,7-Trinitro-9-fluorenone (TNF), 799, 805
 Triphenylmethane dyes, 818
 Tri(tetrathiafulvalenyl)phosphine ((TTF)₃P), 91
 TSeF-TCNQ, 373, 380
 (TSeF)_x(TTF)_{1-x}TCNQ, 393
 (TSeT)₂Cl, 361, 362, 365, 370, 371, 375, 376, 380
 TSF, 90
 TTeF, 90
 TTF, 5, 18, 84–100, 118, 123, 124, 134, 251, 337, 350–351, 359, 360, 392, 768
 derivatives, 86–100, 118–125
 giant analogs, 250–251
 TTF-*p*-chloranil, 341, 342
 TTF-Cl, 240
 TTF-Ni[(dmit)₂]₂, 289, 293, 433
 TTF[Ni(dmit)₂]₂, 774
 TTF[Pd(dmit)₂]₂, 774
 TTF salts, 240, 242, 250, 257
 TTF-TCNQ, 5, 10, 29, 46, 65, 97, 98, 132, 136, 155–217, 237–259, 287, 289, 338–339, 350, 359–393, 463, 488, 767
 TTF-TCNQ composites, 350–351
 (TTT)₂I₃, 167, 202, 288
 Tunneling (*see also* Hopping), 10, 28, 47–49, 55–57, 66, 394, 598, 606, 607, 619–625, 664, 668, 698
 two-particle, 56, 57, 66
- V(C₆H₆), 298
 Vibronic or e-mv coupling (*see also* Interactions), 230–260, 369,

- [Vibronic or e-mc coupling]
 - 391–393, 454, 573, 587, 591, 597
 - microscopic theory, 230–235, 247–252, 260
- Violanthrene-iodine complex, 694
- Violanthrone, 4
- Vitamins, 708–711
 - vitamin A (retinol), 710
 - vitamin C (ascorbic acid), 711, 722
- [Vitamins]
 - vitamin K, 711
 - vitamins B, 710–711
- V(TCNE)_x.y(solvent), 302
- Weiss field, 272
- XY model, 413
- Yukawa potential, 14